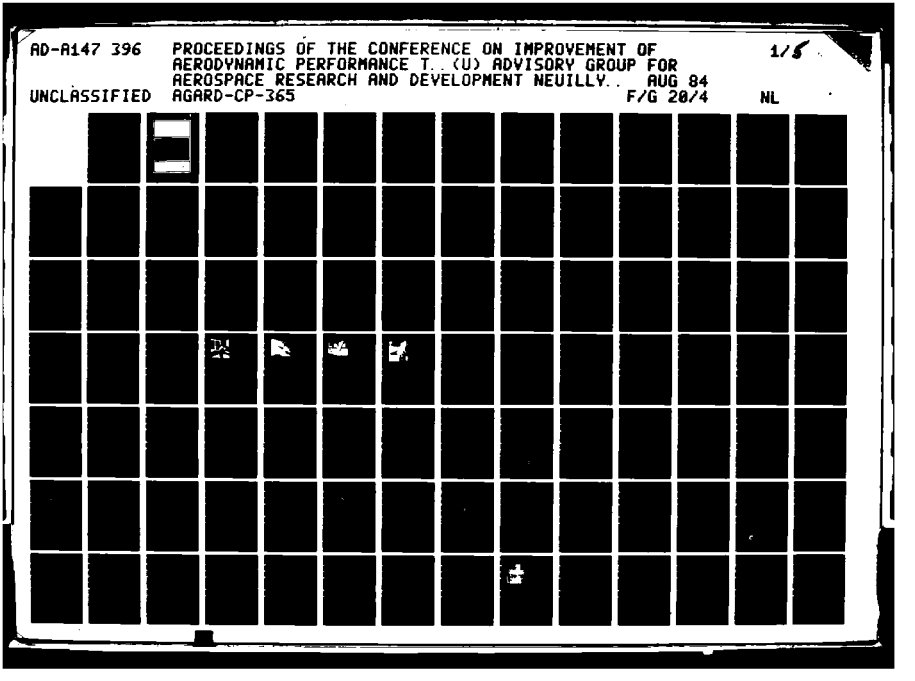
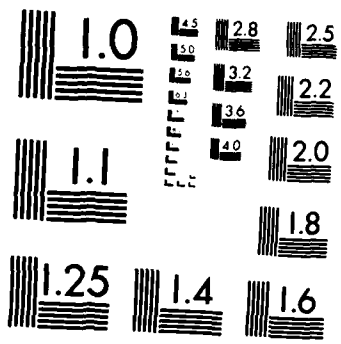
AD-A147 396 PROCEEDINGS OF THE CONFERENCE ON IMPROVEMENT OF AERODYNAMIC PERFORMANCE T..(U) ADVISORY GROUP FOR AEROSPACE RESEARCH AND DEVELOPMENT NEUILLY.. AUG 84 1/5

UNCLASSIFIED AGARD-CP-365 F/G 20/4 NL





MICROCOPY RESOLUTION TEST CHART
NATIONAL BUREAU OF STANDARDS-1963-A

REPRODUCED AT GOVERNMENT EXPENSE

AGARD-CP-365

AGARD-CP-365

AGARD

ADVISORY GROUP FOR AEROSPACE RESEARCH & DEVELOPMENT

7 RUE ANCELLE 92200 NEUILLY SUR SEINE FRANCE

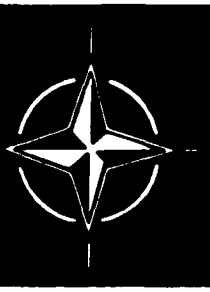
AD-A147 396

AGARD CONFERENCE PROCEEDINGS No.365

Improvement of Aerodynamic Performance Through Boundary Layer Control and High Lift Systems

DTIC
ELECTE
NOV 6 1984
S D
D

NORTH ATLANTIC TREATY ORGANIZATION



DISTRIBUTION AND AVAILABILITY
ON BACK COVER

DISTRIBUTION STATEMENT A
Approved for public release;
Distribution Unlimited

84 10 24 007

COMPONENT PART NOTICE

THIS PAPER IS A COMPONENT PART OF THE FOLLOWING COMPILATION REPORT:

(TITLE): Proceedings of the Conference on Improvement of Aerodynamic Performance through Boundary Layer Control and High Lift Systems Held at the Fluid Dynamics Panel Symposium in Brussels, Belgium on 21 23 May 1984.

(SOURCE): Advisory Group for Aerospace Research and Development, Neuilly-sur-Seine (France).

REPRODUCED AT GOVERNMENT EXPENSE

TO ORDER THE COMPLETE COMPILATION REPORT USE AD A147 396.

THE COMPONENT PART IS PROVIDED HERE TO ALLOW USERS ACCESS TO INDIVIDUALLY AUTHORED SECTIONS OF PROCEEDINGS, ANNALS, SYMPOSIA, ETC. HOWEVER, THE COMPONENT SHOULD BE CONSIDERED WITHIN THE CONTEXT OF THE OVERALL COMPILATION REPORT AND NOT AS A STAND-ALONE TECHNICAL REPORT.

THE FOLLOWING COMPONENT PART NUMBERS COMPRISE THE COMPILATION REPORT:

AD#:	TITLE:
P004 052	Recent Progress on Development and Understanding of High Lift Systems.
P004 053	Investigations into the Effects of Scale and Compressibility on Lift and Drag in the RAE 5m Pressurised Low-Speed Wind Tunnel.
P004 054	Recent Advances in Computational Methods to Solve the High-Lift Multi-Component Airfoil Problem.
P004 055	Inviscid Compressible Flow Past a Multi-Element Aerofoil.
P004 056	Design of an Airfoil Leading Edge Slat Using an Inverse Aerodynamic Calculation Method.
P004 057	Modelling Circulation Control by Blowing.
P004 058	Turbulent Bubbles behind Airfoils and Wings at High Angle of Attack.
P004 059	Aerodynamic Issues in the Design of High-Lift Systems for Transport Aircraft.
P004 060	An Update of the Canada/U.S.A. Augmentor-Wing Project.
P004 061	Aircraft Drag Reduction Technology.
P004 062	Theoretical Study of Boundary-Layer Control.
P004 063	Drag Reduction due to Boundary-Layer Control by Combined Blowing and Suction.
P004 064	Design Studies of Thick Laminar-Flow Airfoils for Low Speed Flight Employing Turbulent Boundary Layer Suction over the Rear Part.
P004 065	Technology Developments for Laminar Boundary Layer Control on Subsonic Transport Aircraft.
P004 066	Turbulent Drag Reduction Research.
P004 067	On the Relaxation of a Turbulent Boundary Layer after an Encounter with a Forward Facing Step.
P004 068	Full Scale Experiments into the Use of Large-Eddy-Breakup Devices for Drag Reduction on Aircraft.

COMPONENT PART NOTICE (CON'T)

AD#: P004 069 TITLE: Pneumatic Turbulators - A Device for Drag Reduction at Reynolds Numbers below 5, 000, 000.

P004 070 Active and Passive Shock/Boundary Layer Interaction Control on Supercritical Airfoils.

P004 071 Transonic Shock Interaction with a Tangentially-Injected Turbulent Boundary Layer.

REPRODUCED AT GOVERNMENT EXPENSE

AGARD-CP-365

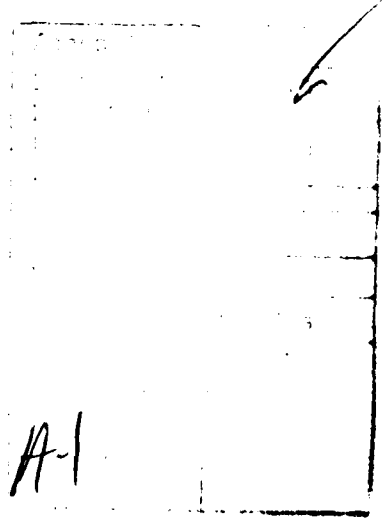
NORTH ATLANTIC TREATY ORGANIZATION

ADVISORY GROUP FOR AEROSPACE RESEARCH AND DEVELOPMENT

(ORGANISATION DU TRAITE DE L'ATLANTIQUE NORD)

AGARD Conference Proceedings No.365

IMPROVEMENT OF AERODYNAMIC PERFORMANCE THROUGH BOUNDARY LAYER CONTROL AND HIGH LIFT SYSTEMS



Papers presented and Discussions held at the Fluid Dynamics Panel Symposium in Brussels, Belgium, 21—23 May 1984.

THE MISSION OF AGARD

The mission of AGARD is to bring together the leading personalities of the NATO nations in the fields of science and technology relating to aerospace for the following purposes:

- Exchanging of scientific and technical information;
- Continuously stimulating advances in the aerospace sciences relevant to strengthening the common defence posture;
- Improving the co-operation among member nations in aerospace research and development;
- Providing scientific and technical advice and assistance to the North Atlantic Military Committee in the field of aerospace research and development;
- Rendering scientific and technical assistance, as requested, to other NATO bodies and to member nations in connection with research and development problems in the aerospace field;
- Providing assistance to member nations for the purpose of increasing their scientific and technical potential;
- Recommending effective ways for the member nations to use their research and development capabilities for the common benefit of the NATO community.

The highest authority within AGARD is the National Delegates Board consisting of officially appointed senior representatives from each member nation. The mission of AGARD is carried out through the Panels which are composed of experts appointed by the National Delegates, the Consultant and Exchange Programme and the Aerospace Applications Studies Programme. The results of AGARD work are reported to the member nations and the NATO Authorities through the AGARD series of publications of which this is one.

Participation in AGARD activities is by invitation only and is normally limited to citizens of the NATO nations.

The content of this publication has been reproduced
directly from material supplied by AGARD or the authors.

Published August 1984

Copyright © AGARD 1984
All Rights Reserved

ISBN 92-835-0358-9



Printed by Specialised Printing Services Limited
40 Chigwell Lane, Loughton, Essex IG10 3TZ.

THEME

There has been an increased experimental understanding of boundary layer structure and behaviour particularly in the turbulent regime as well as significant improvements in our knowledge of the factors affecting the boundary-layer transition in arbitrary flow fields.

It was intended that this Symposium bring together the practitioners of the various applications of boundary layer control with those interested in the underlying fluid mechanics for the purpose of mutual learning and understanding.

Contributions covered theoretical and experimental developments in the use of both traditional and non-traditional means of boundary layer control for external flow applications such as lift-augmentation, drag reduction and improved effectiveness of controls, and for internal flow applications such as air intakes and exit configurations. Techniques included: shaping (geometry) suction and blowing; transverse blowing; vortex generators; heating and cooling; and turbulent boundary layer manipulators.

The special emphasis on high-lift systems included consideration of the techniques of boundary layer control on characteristics of wings and wing-body arrangements that involve flaps, slats and jets (blown flaps), and vortex flaps.

***

L'expérience nous a permis de mieux comprendre la structure et le comportement de la couche limite, en particulier en régime turbulent, et notre connaissance des facteurs affectant la transition de la couche limite dans les champs d'écoulement arbitraires s'est considérablement améliorée.

L'objectif du symposium était de réunir les praticiens travaillant sur les applications diverses du contrôle de la couche limite avec ceux qu'intéressent la mécanique des fluides, en tant que base de ces applications pour procéder à un échange de connaissance mutuelles.

Les communications présentées traitaient des développements théoriques et expérimentaux intervenus dans l'utilisation des moyens, traditionnels ou non, de contrôle de la couche limite, en ce qui concerne (1) les applications intéressant l'écoulement externe: augmentation de la portance, réduction de la résistance aérodynamique, meilleure efficacité des commandes; et (2) les applications intéressant l'écoulement interne: configuration des prises et sorties d'air. Les techniques étudiées comprennent: la géométrie, l'aspiration et le soufflage, le soufflage transversal, les générateurs de tourbillons, l'échauffement et le refroidissement, et les manipulateurs de couches limites turbulentes.

Une attention particulière était consacrée aux systèmes hypersustentateurs et, dans ce domaine, à l'influence des techniques de contrôle de la couche limite sur les caractéristiques des ailes et sur les configurations aile-fuselage comportant des volets de courbure, des becs de bord d'attaque, des jets (volets soufflés) et des volets générateurs de tourbillons.

AGARD FLUID DYNAMICS PANEL

Chairman: Dr L.Roberts
Joint Institute for Aeronautics
& Acoustics
Department of Aeronautics
and Astronautics
Stanford University
Stanford
California 94305, USA

Deputy Chairman: Dipl. Ing. P.W.Sacher
Messerschmitt-Bölkow-Blohm GmbH
UFFE 12
Postfach 80 11 60
D-800 München 80
Federal Republic of Germany

PROGRAM COMMITTEE MEMBERS

Professor E.Reshotko (Chairman)
Dept. of Mechanical & Aerospace Eng.
Case Western Reserve University
Cleveland
Ohio 44106, USA

Professor J.J.Ginoux
Director
Von Kármán Institute for Fluid Dynamics
Chaussée de Waterloo 72
B-1640 Rhode-Saint-Genèse, Belgium

Dr K.J.Orlik-Ruckemann
National Aeronautical Establishment
National Research Council
Montreal Road, Ottawa, Ontario
K1A OR6

M. l'Ing. Général C.Capelier
Directeur de l'Aérodynamique
ONERA
B.P. 72
92322 Châtillon, France

Professor M.Onorato
Politecnico di Torino
Insituto di Meccanica Applicata alle
Macchine Aerodinamica e
Gasdinamica
Corso Duca Degli Abruzzi 24
10129 Torino, Italy

Professor Dr Ir. J.L.van Ingen
Department of Aerospace Engineering
Delft University of Technology
Kluyverweg 1
2629 HS Delft, Netherlands

Professor A.D.Young
Queen Mary College, Aeronautics Dept
Mile End Road
London E1 4NG, UK

Professor Dr Ing. K.Gersten
Institut für Thermo und Fluiddynamik
Ruhr-Universität Bochum
Postfach 10 21 48
D-4630 Bochum 1, Germany

PANEL EXECUTIVE

Robert H.Rollins II

Mail from US and Canada
AGARD/NATO
APO New York 09777

Mail from Europe
AGARD/NATO
7 rue Ancelle
92200 Neuilly-sur-Seine
France

CONTENTS

	Page
THEME	iii
MEETING AND PANEL OFFICIALS	iv
	Reference
SESSION 1 – HIGH LIFT SYSTEMS I	
RECENT PROGRESS ON DEVELOPMENT AND UNDERSTANDING OF HIGH LIFT SYSTEMS by D.J.Butter	1
INVESTIGATIONS INTO THE EFFECTS OF SCALE AND COMPRESSIBILITY ON LIFT AND DRAG IN THE RAE 5m PRESSURISED LOW-SPEED WIND TUNNEL by S.P.Fiddes, D.A.Kirby, D.S.Woodward and D.H.Peckham	2
RECENT ADVANCES IN COMPUTATIONAL METHODS TO SOLVE THE HIGH LIFT MULTI-COMPONENT AIRFOIL PROBLEM by B.Oskam, D.J.Laan and D.F.Volkers	3
ETUDE DETAILLEE DE L'ECOULEMENT AUTOUR D'UN PROFIL HYPERSUSTENTE. COMPARAISONS AVEC LES CALCULS par B.Porcheron et J.J.Thibert	4
SESSION 2 – HIGH LIFT SYSTEMS II	
INVISCID COMPRESSIBLE FLOW PAST A MULTI-ELEMENT AEROFOIL by I.M.Hall and A.Suddhoo	5
DESIGN OF AN AIRFOIL LEADING EDGE SLAT USING AN INVERSE AERODYNAMIC CALCULATION METHOD by J.A.van Egmond and B.van den Berg	6
MODELLING CIRCULATION BY BLOWING by M.M.E.Soliman, R.V.Smith and J.C.Cheeseman	7
TURBULENT BUBBLES BEHIND AIRFOILS AND WINGS AT HIGH ANGLE OF ATTACK by V.Losito and G.Torella	8
SESSION 3 –HIGH LIFT SYSTEMS III	
AERODYNAMIC ISSUES IN THE DESIGN OF HIGH LIFT SYSTEMS FOR TRANSPORT AIRCRAFT by B.Dillner, F.W.May and J.H.McMasters	9
AN UPDATE OF THE CANADA/USA AUGMENTOR-WING PROJECT by D.C.Whittley	10
SESSION 4 – DRAG REDUCTION I	
AIRCRAFT DRAG REDUCTION TECHNOLOGY by A.S.W.Thomas	11
APPLICATION DES CRITERES BI ET TRIDIMENSIONNELS AU CALCUL DE LA TRANSITION ET DE LA COUCHE LIMITE D'AILES EN FLECHE par D.Arnal et E.Coustols	12
THEORETICAL STUDY OF BOUNDARY-LAYER CONTROL by E.H.Hirschel	13

DRAG REDUCTION DUE TO BOUNDARY-LAYER CONTROL BY COMBINED BLOWING AND SUCTION
by J.Wiedemann and K.Gersten 14

DESIGN STUDIES OF THICK LAMINAR-FLOW AIRFOILS FOR LOW SPEED FLIGHT EMPLOYING TURBULENT BOUNDARY LAYER SUCTION OVER THE REAR PART
by J.L.van Ingen, J.J.H.Blom and J.H.Goei 15

SESSION 5 – DRAG REDUCTION II

TECHNOLOGY DEVELOPMENT FOR LAMINAR BOUNDARY LAYER CONTROL ON SUBSONIC TRANSPORT AIRCRAFT
by R.D.Wagner, D.V.Maddalon and M.C.Fischer 16

TURBULENT DRAG REDUCTION RESEARCH
by D.M.Bushnell, J.B.Anders, M.J.Walsh and R.McInville 17

ON THE RELAXATION OF A TURBULENT BOUNDARY LAYER AFTER AN ENCOUNTER WITH A FORWARD FACING STEP
by D.I.A.Poll and R.D.Watson 18

FULL SCALE EXPERIMENTS INTO THE USE OF LARGE-EDDY-BREAKUP DEVICES FOR DRAG REDUCTION ON AIRCRAFT
by A.Bertelrud 19

PNEUMATIC TURBULATORS – A DEVICE FOR DRAG REDUCTION AT REYNOLDS NUMBERS BELOW 5×10^6
by K.H.Horstmann, A.Quast and L.M.M.Boermans 20

SESSION 6 – SHOCK WAVE BOUNDARY LAYER INTERACTIONS

L'INTERACTION ONDE DE CHOC-COUCHE LIMITE TURBULENTE ET SON CONTROLE
par J.Delery 21

INTERET DU PIEGE INTERNE POUR LE FONCTIONNEMENT DANS UN DOMAINE ETENDU DU NOMBRE DE MACH (1.8 – 3+), D'UNE PRISE D'AIR BIDIMENSIONNELLE
par G.Laurelle, C.Sans et R.Lefebvre 22

INTERACTION ONDE DE CHOC OBLIQUE – COUCHE LIMITE TURBULENTE SUR PAROI POREUSE AVEC ASPIRATION
par D.B.Lee et R.Leblanc 23

ACTIVE AND PASSIVE SHOCK/BOUNDARY LAYER INTERACTION CONTROL ON SUPERCRITICAL AIRFOILS
by P.Thiede, P.Krogmann and E.Stanewsky 24

TRANSONIC SHOCK INTERACTION WITH A TANGENTIALLY-INJECTED TURBULENT BOUNDARY LAYER
by G.R.Inger 25

SUMMARY AND DISCUSSION D

Reference

RECENT PROGRESS ON DEVELOPMENT AND UNDERSTANDING OF HIGH LIFT SYSTEMS

by

D J Butter
British Aerospace
Weybridge Division
Stockport
Cheshire SK7 1QR

AD-P004 052

1 INTRODUCTION

In aircraft design the constraints between the high speed cruise and the low speed take-off and landing conditions force the designer to incorporate some form of high lift device to improve the lift at low speed. Most aircraft, be they civil or military, have some form of high lift device that is normally used exclusively during take-off and landing, and for many years, apart from a few novel concepts, this has mainly been a mechanical alteration of the wing section shape over the inboard part of the wing. The complications of sweep, be it forward or backward, engine installation, lateral controls, undercarriage installation and high speed wing design have always been accommodated within the configuration of a trailing edge flap and in some cases a leading edge slat. This paper concentrates principally on the mechanical high lift device as it is used on transport type aircraft and examines the design process and recent progress on both the development of high lift device design and on the understanding of the physics of the flows that has been reached. It also suggests the likely future development and the way in which this may be achieved.

2 THE STATE OF THE ART

High lift devices are used on most aircraft during the take-off and landing phases of the flight primarily to reduce the distances used to allow the aircraft to carry its required payload from the design airfield constraints. This is usually given take-off and landing distances with a minimum climb gradient after take-off with an engine failed, although increasingly the effect of the aircraft noise on the community surrounding an airport is being considered as well.

For a take-off as shown in figure 1 the distance is principally proportional to $1/C_L$ and to a lesser extent the L/D of the aircraft, which mainly affects the smaller airborne part of the take-off. To a first order the take-off distance of aircraft can be correlated against a parameter s

$$\text{where } s \propto \frac{W}{T}\frac{W}{S}\frac{1}{\sigma C_L}$$

Similarly the landing distance, as shown in figure 2 depends on the same factors, although the thrust term is not now included, and can be correlated against

$$s \propto \frac{W}{S}\frac{1}{\sigma C_L}$$

Obviously, these two parameters are very broad and the correlation is only generally reasonable for similar types of aircraft with the same number of engines and similar wing aspect ratios. However, they do serve to show the important parameters in aircraft design for take-off and landing.

In an initial project design when all the constraints are considered, the thrust loading, T/W, and the wing loading, W/S, are compromises to satisfy all the constraints as closely as possible and it is only by altering the lift coefficient independently of the overall wing design that the designer has any real freedom to reduce the field lengths without affecting the other flight regimes.

A clean unswept wing with no high lift devices will have a maximum lift coefficient in the region of 1.6 with a stall normally resulting from a region of separated flow progressing forward from the trailing edge. To improve this value so that the field lengths and the take-off speeds can be reduced to sensible values there are three main alternatives:-

a) increase the camber

b) increase the effective wing area

c) boundary layer control to delay the flap stall onset

The effect of these is shown in figure 3 where it can be seen that by increasing the rear camber of the aerofoil with flap deflection the maximum lift of the section initially increases significantly, linearly with flap angle until the flap flow starts to separate when although further increases of flap angle do still produce increases in lift their effect is generally small. By using some form of boundary layer control, be it passively with slotted flaps or actively with some form of internal or external blowing, the 'flap stall' can be suppressed and greater values of lift achieved at a given flap angle with associated reductions in the drag. Lift on the section can be further increased at a given flap angle by designing the flap to extend the wing chord as it deflects, which is a gain not so much in efficiency but by increasing the lifting area.

Most trailing edge devices to a greater or lesser extent reduce the stalling incidence of the basic section because by increasing the circulation they raise the leading edge suctions on the main section which increases the adverse pressure gradient and promotes an earlier stall. This effect can be alleviated by some device such as a slat which modifies the leading edge shape and either directly reduces the leading edge suctions or by introducing a slot spreads the loads to reduce the high peak suctions on the main element. So far all forms of direct boundary layer control, such as augmentor wings, externally or internally blown flaps, upper surface blowing, deflected slipstream and even vectored thrust, which is more a direct lift control replacing the flap function, introduce compromises in the overall aircraft design in terms of weight, engine size, fuel useage and engine failed controllability which are generally unacceptable for aircraft operating from normal airfields. It is only when short field lengths are required, usually for military purposes, that these devices become worthwhile. However, even with mechanical devices the choice is wide; from simple plain flaps to multi-slotted Fowler flaps with some leading edge device which can with careful design increase the aircraft maximum lift by a factor of nearly 2.

The above discussion has principally concentrated on lift and although the take-off and landing field lengths are primarily dependent on the maximum lift, the climb gradient after take-off is dependent on the lift-drag ratio. As shown in figure 4, the climb angle is for small angles

$$\gamma \approx \frac{T - D}{W} \approx \frac{T}{W} - \frac{D}{L}$$

After take-off for civil aircraft all the regulating authorities require that with an engine failed the aircraft must maintain a positive climb angle in excess of 1.38° for a two engined aircraft and 2.06° for a four engined aircraft. Usually the most critical regime is the so called second segment of the climb immediately after take-off when the undercarriage has been retracted but the high lift devices are still deflected. Clearly from the above equation the climb angle is critically dependent on the L/D of the aircraft. For this reason the climb configuration of the high lift system must be very efficient. On landing, however, the situation is somewhat different where the thrust is sensibly zero and the aircraft requires a low L/D to give it a sensibly high approach angle of about 7-9° for manoeuvrability. Consequently, the landing requires a high drag at high lift which can be achieved by having a large flap deflection angle and benefiting from the separated flow which will generally then occur on the flap. One of the shortcomings of the blown flap system is that it reduces the drag at high flap angles and makes it difficult to achieve the high approach angles unless some form of airbrake is used to increase the aircraft drag independently of the high lift system.

Apart from the take-off and landing requirements some military aircraft use part of their high lift system during high speed manoeuvres to increase the margin on the high speed stall and buffet boundary allowing a higher 'g' to be used. Currently this does not tend to be a design case for the high lift system in terms of the aerodynamics although for a fully optimised system it must obviously be included. Civil transport aircraft are normally limited by a combination of gust and manoeuvre margins at the high speed and there may well be scope for improvements in the buffet boundary particularly with some form of active system.

But looking at today's generation of aircraft it is obvious that the high lift systems are in principle very similar to those of the previous generation and there has not been any dramatic improvements in concept. In fact the current trends are towards mechanically simpler systems. The reasons for this are not lack of ideas or natural conservatism amongst aircraft designers but, as the above has indicated, the mechanical flap is a reasonably efficient, good design compromise for achieving the various design requirements and it is only the more specific requirements of very short field operations, for example, which will force the designer to look at alternatives.

However, because there does not appear to have been much development in high lift system design does not mean that the aircraft design is not sensitive to improvements in the performance of the system. Typically it is found that:-

5% improvement in take-off C_{Lmax} ⟶ 12-15% increase in payload

5% improvement in take-off L/D ⟶ 20% increase in payload

5% improvement in landing C_{Lmax} ⟶ 25% increase in payload

which in terms of the normal coefficients for a large twin engined aircraft would mean about 0.15 increase in C_{Lmax} at take-off and 0.20 at landing and a reduction of .006 in C_D at a given C_L, and although there has apparently been little progress in the types of high lift devices there has been a steady improvement in the efficiency and C_{Lmax} of the existing types. Figure 5 shows in a much simplified picture the way that C_{Lmax} has increased between generations of design and although there is unlikely to be such a large step on the next aircraft, there is still room for improvement.

Any change in maximum lift will come from two main sources:-

a) the ability to test and design for high Reynolds numbers and to be able to take advantage of this.

b) an understanding of the three dimensional flow and the ability to optimise devices in 3-dimensions both in terms of the design and the engineering.

There will also be some improvements with a greater understanding of the effects of the engineering excrescences, both large such as flap and slat tracks, and small, such as steps and gaps in the wing surface.

However, the major changes will be in the improvements in the L/D ratio, which is still a much forgotten parameter in the design of the high lift system where it generally takes second place to C_{Lmax}. Figure 6 shows the difference between the ideal achievable L/D and the current practice and the area between the ideal polar of $C_{Do}+C_L^2/\pi A$ and the envelope polar is indicative of the potential for performance improvement. Whilst there are clearly substantial opportunities in reducing the profile drag of leading and trailing edge devices by improving their sectional design and optimisation, major performance improvements particularly at the higher lifts will also come from understanding the 3-dimensional aspects of the wing design. For example, although induced drag can be significantly reduced by eliminating flap cut-outs and extending the span, the trim drag penalty associated with flap span extension, particularly on a swept wing, reduces this benefit and also, whilst the effect of the fuselage can, with careful design of the wing/fuselage junction, be small, there will still be a loss of C_{Lmax} particularly at the higher flap angles. This figure also illustrates the relationship between the operational limit and the envelope polar which is fixed by the operating C_L being a fixed fraction, at least 1/1.44, of the C_{Lmax} and it can be seen that at the higher flap deflection angles that improvements in C_{Lmax} not only give benefits per se but also move the operating limit closer to the envelope polar.

3 CURRENT DESIGN TECHNIQUES

Although the lift required from a high lift system is to a first order independent of the remaining wing design, the field lengths are functions of other parameters as well which are included in the overall optimisation and so the high lift system must be considered in all the stages of the aircraft design. Generally the initial project design phase will select the type of device and the size of the lift increment required and the detailed design phase will result in the optimised 3-dimensional configuration.

3.1 Project Design

At the initial design stage of a project all aspects of the aircraft aerodynamics are considered and the resulting design is clearly a compromise to meet as closely as possible all the design objectives and requirements. In general the design at this stage is based on previous experience and empirical methods. For high lift systems, these empirical methods are based on correlations of a data base of experimental results around a theoretical framework, such as those described in the ESDU and DATCOM Data Sheets, references 1 and 2, and which in many places have been developed to very sophisticated levels based on an increasing database of experimental work. A typical method used in British Aerospace for predicting the trimmed lift curve and drag of aircraft high lift systems is shown schematically in figure 7. As can be seen from this figure the method builds up the various parameters of lift, drag and pitching moment taking into account all the major configurational aspects of the aircraft and the increments in the parameters due to the high lift devices are extracted from a database of information for the different leading and trailing edge devices. The success of the method is illustrated in figure 8 where it can be seen that the L/D of the system is predicted to within 3% across a wide range of aircraft. Variation with flap angle for an individual aircraft, illustrated in figure 9, is also predicted accurately. Basically this method was outlined by McRae 14 years ago, reference 3, and has largely remained unchanged. Over the intervening years the improvement has principally been in the increase of the database and the number of types of devices the method will cater for. The success and lack of development of the method suggests that it is based on a good physical framework and an indication of this is given in figure 10. Here some recent results from tests on a flap system based on a supercritical aerofoil with significant rear loading are plotted on the curve for χ, the flap incremental lift curve, against flap angle and compared with the line published in McRae's report. Apart from the different 'stalling' characteristics of the new flap, the agreement is remarkable.

These empirical methods are obviously a powerful tool in the aircraft design and, when they are combined with the weight and performance prediction methods of typical initial design procedures, allow the type of system most suited to a particular project to be selected. They also give a good degree of confidence in the early estimates of the aerodynamic performance of the flap system. However, such an answer will always be within the current capabilities of the state of the knowledge and, if a general research programme in high lift devices has not been sustained between projects, this will inevitably be at the standard of the last aircraft.

3.2 Detailed Design

What follows is a detailed design in both 2 and 3-dimensions involving theoretical and experimental programmes to optimise the chosen type of device for the aircraft. These designs are usually made within the constraints of the high speed design but may, more generally for the shorter range aircraft, involve iteration with the high speed design. Such a process is illustrated in McRae's paper on the aerodynamic development of the A300 aircraft, reference 4. In this case, the initial project optimisation based on the experiences with the Trident and its development studies resulted in the choice of a tabbed Fowler flap and a slat with a take-off C_{Lmax} of 2.62.

This choice was then followed by the sectional development on a constant chord half model. It is this work which is the foundation of the high lift system design in that it explores the high lift characteristics of the section and optimises the various devices for the design constraints. The extent of this programme is controlled generally by cost and the time available. Ideally models would be tested using a genuinely 2-dimensional technique with a wing spanning the tunnel, or between floor to ceiling end plates, of as high an aspect ratio as possible, 2 or greater on the undeveloped chord, with adequate protection against end wall separation problems and guaranteed 2-dimensionality. This is an expensive test both in terms of the model and the tests. Forces have to be obtained by integration of the pressure distributions and wake traverses and demand lengthy runs for each configuration. As McRae illustrated, one device design optimisation exercise involves the angle, gap and lap of the slat, flap and tab. Each individual optimisation will cover about three variables with four or five values of each. That is about 100 runs for each device before considering the variables of Reynolds and Mach number.

Obviously, it is necessary to reduce the cost and timescale of these tests and whereas some pruning of the parameters tested can be done it is not desirable and so cheaper and quicker ways of testing are sought. These are generally one of two 'pseudo' 2-dimensional tests, namely:-

a) an end plate model: which is a constant chord, unswept model between two endplates and mounted on the tunnel balance. The ability to measure forces on a balance can considerably reduce the testing time and because the model is generally smaller than that for a full 2-dimensional test it is cheaper to make, particularly if the pressures are not required.

b) a half model wing: which is a constant chord wing with full span devices mounted on the tunnel balance. Using a swept wing will, with care, ensure that the stall occurs away from both the root and the tip. An advantage of this method is that the boundary layer on the system will represent the 3-dimensional cross flow more like that on the real wing. Again this is a relatively cheap model and results can be obtained quickly.

The choice between these two experiments is based largely on the experience held in interpreting these 'pseudo' 2-dimensional results in a 3-dimensional design and normally one design organisation would be expected always to use the same approach. Clearly both have shortcomings in relation to a proper 2-dimensional test and it is important to calibrate these simpler techniques against known 2-dimensional cases.

Whichever of these two approaches is adopted more than one model will be required for it is desirable to test at as high a Reynolds number as possible and if full advantage is to be taken for designing at a high Reynolds number then it must approach that of flight. This means a large model tested in one of the pressurised tunnels which will have to be designed to withstand high loads and will consequently be very expensive. Testing in these tunnels will also be expensive and will be kept to a minimum. So a second model will be built for a low speed atmospheric tunnel to be a 'workhorse' for the big optimisation programme and also at a later stage of the programme for investigating the effect of design changes. In the A300 programme testing a combination of two half models was used to optimise the settings for the devices and figure 11 shows a result of the optimisation for the slat which indicates that the aerodynamic optimum cannot in practice be used because the engineering constraints on the mechanism prevented it and the final position is a compromise across the span. After the initial optimisation, the atmospheric tunnel model was also used to investigate the effect of leading edge modifications stemming from improvements in the high speed design. This model had been designed at the outset to allow such changes to be incorporated and tested both quickly and cheaply.

Having designed and optimised the devices in 2-dimensions, it is clearly necessary to test them in 3. Ideally, the optimisation would be repeated in 3-dimensions, but now the variables are increased as the angle, gap and overlap would have to be varied across the span. This is generally a prohibitive experiment and if done at all is only usually done for a very limited range of the parameters. 3-dimensional testing is usually aimed at investigating the high lift characteristics of the complete aircraft and to develop some of the real features on the aircraft such as a stall fixing and slat and flap cut-outs. Again for this work there will be more than one model with most of the development testing being done in an atmospheric tunnel, generally on site, and the final confirmatory testing being done in a large pressurised tunnel.

For the A300 as a result of the tunnel tests at this stage of the design the estimated aircraft C_{Lmax} for take-off was increased to 2.71 from the 2.62 of the early project estimates. Also from these tests a reduced slat angle for the take-off was found to have a beneficial effect on L/D and was included in the final aircraft design.

4 FUTURE DEVELOPMENT

The design procedures described above have not altered much over the last several years and most of the effort has been spent in building up the database of experimental results for the various predictive methods. This has in general led to steady but unspectacular improvements in C_{Lmax} for a wide variety of both leading and trailing edge devices but has largely left the knowledge of the basic physical processes unaltered and it is only recently that a proper understanding of the physics of the flows has been recognised as important and the required investigative research programmes started. Today there are still many problems unanswered but generally work is in hand to lead to a better exploitation of high lift systems. It is essential that the ability to design high lift systems with a better lifting efficiency and the minimum of structural complexity is improved so that the required low speed performance can be obtained as economically as possible without compromising the high speed design. Because, when the aircraft is flight tested the achievement of better than predicted low speed performance may be welcome in that it gives a stretch potential or a better field performance, this over achievement could mean a high lift system that was too extensive or too elaborate and therefore heavier and more expensive than necessary. For these reasons the end result in over-designing for high lift differs from that for high speed where better performance is immediately translatable into better fuel economy and direct operating costs.

From present knowledge in order to be able to remove the inbuilt conservatism of the design procedures it is essential to improve the understanding of the flows both in 2 and 3-dimensions. In 2-dimensions the basic flow phenomena are as shown in figure 12 and the basic features are:-

a) the region of flow is multiply connected with the wakes from upstream elements interacting with the boundary layers of downstream elements.

b) the shear layers over the flap are very thick and the curvature of the flow gives rise to a static pressure variation across the shear layer.

c) the slat and the flap must fit back snugly to form the cruise aerofoil with the result that there are cavities beneath the slat and the shroud in which separation bubbles are formed.

d) if the angle of deflection of the flap is sufficiently large then the flow will separate from the flap. Although the drag is markedly increased the complete aerofoil will not necessarily stall and, in fact, the separated flow on the flap can exist throughout the incidence range.

e) at the leading edge of the aerofoil the suctions on the slat can be high enough to indicate that supercritical flow has developed even through the freestream Mach number is only about 0.2.

However this knowledge does not either give the important parameters for optimising the C_{Lmax}, say, or tell which model results are correct. There are many phenomena on multi-element aerofoils which are the result of the complex interactions of the basic flows illustrated above which have to be fully understood and predicted before the optimum design can be said to have been achieved.

4.1 Slat Performance

Even at low freestream Mach numbers the velocities on the slat can, as the C_{Lmax} is approached, exceed the critical velocity and easily reach M=1.25, with M=1.5 seen in certain configurations. As at low speeds the variation of the critical C_p with freestream Mach number is very rapid, the effects of compressibility can vary noticeably with the freestream Mach number. It is only recently with the pressurised wind tunnels that it has been possible to vary the Mach number independently of the Reynolds number. Whereas previously increasing Mach number meant increasing Reynolds number which tended to mask the effect of compressibility, now, as shown in figure 13, the two effects can be separated and at a given Reynolds number the effect of Mach number is seen to be significant where the presence of shock waves probably thickens the slat boundary layer giving a stronger interaction with the wing boundary layer and a consequent reduction in C_{Lmax}. Correspondingly at constant Mach number there is a strong variation with increasing Reynolds number particularly at the lower Mach numbers where the Reynolds number on the slat, based on the slat chord, is very small.

The variation of C_{Lmax} with Mach number is less researched and probably less well understood than that with Reynolds number, but from the available data, above a freestream Mach number of about 0.2, the flight results give a higher rate of falling off of C_{Lmax} with increasing Mach number than that measured in the tunnel and dC_{Lmax}/dM is some 50% greater.

4.2 Slat Optimisation

Figure 14 is typical for the design study on a slatted section and shows a locus of C_{Lmax} for varying slat trailing edge positions with a given slat and flap deflection. From this it can be seen that at this deflection angle the optimum C_{Lmax} is not very sensitive to the slat position and within an area of ± 1/2% chord will vary by less than 1%. However, looking at the position of the slat the optimum C_{Lmax} from various models of the same sectional geometry, figure 15 shows the disparities for three of the techniques normally used for optimisation studies at essentially the same Reynolds and Mach number. Apart from these model differences, also shown in this figure is the variation of the optimum position with varying Reynolds number at constant Mach number for the 3-dimensional model. From these results, depending on which experiment was used, the optimum could have been within an area of ± 1% chord which could represent a variation of C_{Lmax} nearer to 10% and it has already been shown what this would mean in terms of the design parameters.

4.3 Flap Optimisation

Similar C_{Lmax} loci of positions of trailing edge flaps can be drawn, as shown in figure 16, where it can be seen that not only in general are the results more sensitive to the position but also there is a phenomenon called 'flow recovery'. Shown in the figure are two boundaries outside of which the flow on the flap is always either attached or separated at all incidences but between these two boundaries the flow can be either separated or attached depending on the incidence and is usually such that as the maximum lift is approached the flow on the flap reattaches and the lift curve slope can in some cases increase dramatically as shown in figure 17. The associated flap pressure distributions are shown in figure 18. This flow recovery is thought to be either due to the adverse pressure gradient on the flap boundary layer being alleviated as the incidence increases with the thickening of the wake lying above the flap or possibly due to improving the flow through the flap slot from the flap cove. Clearly the knowledge on this phenomenon is slight and it is important to be able either to exploit or avoid it at full scale and to determine the scale effect on it. As this flow regime appears over a very small gap range it will be sensitive to production tolerances and aeroelastic effects which could easily lead to asymmetric lift variations or significant differences between production aircraft.

4.4 Scale Effect

Apart from the effect of Reynolds number described above the normal scale effect of Reynolds number, which is probably well understood for single element wings, still has to be established for the multi-element wing and the available evidence is limited leading to a divergence of opinion. Figure 19 shows the results for a slatted wing which apart from illustrating the problems of measuring C_{Lmax} in flight, shows a somewhat indeterminate variation with Reynolds number. Whilst there are many differences between flight results and the tunnel such as contamination by excrescences, sideslip, control activity etc. analysis of the available results on scale effect suggest that the higher the freestream Mach number the greater the range of Reynolds number over which scale effect is noticed and that the effect varies with flap (and possibly slat) angle.

Further, model tests, even at a reasonable Reynolds number, will have a Reynolds number based on the slat or flap chords which are very low by normal standards of a single aerofoil and should lead to significant scale effects. An intriguing aspect of this problem is that flaps when tested on models at a mean chord Reynolds number as low as 1×10^6 have consistently yielded normal force coefficients of up to 1.5 based on flap chord at large deflections for a single slotted flap. Under these conditions it could reasonably be expected that the flap boundary layer would have a laminar separation giving a maximum normal force of below 1.0 but the presence of the turbulent wake from the upstream element appears to promote transition to turbulence either directly or by causing a turbulent reattachment after the laminar separation. If this is true the effect of Reynolds number on the flap can be dependent on the development and position of the wakes of the upstream elements as well as the other factors described above.

Added to these effects of increasing Reynolds number in 3-dimensions is the unknown of attachment line transition which can lead to an adverse scale effect as the transition mechanism switches from some laminar/turbulent transition near the suction peak to one where the boundary layer is fully turbulent from the attachment line. The effect of this, as shown in figure 20, is a sudden drop in C_{Lmax} at a given Reynolds number as the flow switches from one type to the other. The Reynolds number at which this occurs is dependent on wing sweep, leading edge design and sources of boundary layer contamination. Clearly for tests across a wide range of Reynolds number for multi-element wings this phenomenon of attachment line transition could occur at different times on the different elements and could easily mask the other scale effects.

4.5 3-Dimensional Effects

The above illustrates some of the complexity and lack of understanding of the flow about multi-element wings but has been largely concerned with 2-dimensional aspects of the flow. It is normal practice in 3-dimensional design to design the high lift system for a section of the outer wing and assume that the optimum conditions there apply across the entire span. Obviously this will not be so, particularly with the large changes in thickness and twist that are now common on civil aircraft, and there will be gains to come from such effects as spanwise grading

of the slat and flap position, angle and size, reduced engine/pylon/wing interference, improved inner wing design and, possibly the most important, the development of the required optimum flow conditions that represent a good design.

Already as we are beginning to obtain more information about testing fully representative models at higher Reynolds numbers, comparisons between these tests and flight are only adding to the confusion that already existed and it is possible to make the following observations:-

a) there is a need for much stricter measurement of drag both in the tunnel and in the flight not only for comparison purposes but also because one drag count, ΔC_D = 0.0001, is equivalent to a payload of one passenger on a large twin engined aircraft.

b) comparisons between flight and tunnel should include the flow mechanisms leading to the stall because unless the same mechanisms exist there is little meaning in the correlations of C_{Lmax}.

c) the effects of stall fixes are strongly dependent on Reynolds number and studies in the tunnel can be questionable unless the tests are at a high Reynolds number.

Figure 21 describes schematically the progression of the stall on a complete model of an A300 type aircraft where the stall patterns were observed with tufts on the wing. On this model the inboard stalled area was reluctant to spread across the inboard wing while an outboard separation developed in front of the outboard flap and spread forward to the leading edge near the slat fence. This onset of the outboard separation appeared to define C_{Lmax}. It is worth noting that the basic stall pattern shown here was largely unaffected by changes of freestream Mach or Reynolds number. This figure illustrates the complexity of a 3-dimensional stall and underlines the problems both in attempting to calculate and in trying to optimise the aircraft maximum lift. It also hints at some of the other 3-dimensional problems adding to the difficulty, where separated flow appears on the inboard aileron and engine nacelle at incidences well below the stall.

5 ANALYSIS AND PREDICTION

The previous section has described some of the flow characteristics about high lift aerofoils and has underlined the lack of understanding in many of them. To date successful flap design has been advanced by small steps using a knowledge of the variations of the various parameters built up over the experimental testing of many configurations. This process will undoubtedly continue but because of the lack of understanding of the high lift flow fields the current techniques are very heuristic in their approach and improvements will be small. Major advances will only arrive when both the experimental and theoretical prediction techniques are improved and the basic physics of the flow understood. To improve on the current position requires a programme of fundamental research largely independent of the pressures of project work.

5.1 Experimental Techniques

Over the years the wind tunnel has undoubtedly played the major role in the advancement of the design of high lift systems and even today its use has not been significantly reduced by the appearance of theoretical methods, as has been the case with the high speed design problems. However, most of the work has been orientated towards project aircraft and has in general not been aimed towards increasing the basic understanding of the flows. Consequently the knowledge gained has been built up piecemeal and provides only limited support for the development of analysis techniques. During this period commercial pressures have led to improvements in the experimental facilities, and wind tunnels and measuring techniques have become bigger and more sophisticated so that now there is the prospect of a cryogenic tunnel in which flight Reynolds numbers can be achieved. Even the simpler, pressurised tunnels of today's technology can give Reynolds numbers approaching flight values for some aircraft at low speed. A typical range of Reynolds and Mach number for 2 and 3-dimensional models in the RAE 5 metre tunnel is shown in figure 22. However, the drawback with high Reynolds number testing is its cost, both of the manufacture of the model and the running of the tunnels and which, with each major advance in tunnel, is probably increasing the cost by an order of magnitude. Because full scale Reynolds number testing is very expensive this tends to re-emphasise the trends of high lift system testing to be aimed primarily at project aircraft design rather than fundamental research. It is certain that this project orientated work will continue and grow in the near future in much the same way as it has done in the past and will continue to be the driving force for better wind tunnels. Lack of confidence in the cheaper 2-dimensional testing techniques and the goal of benefits from designing at a high Reynolds number will also push testing towards full 3-dimensional models. However what none of this will do per se is necessarily to improve the understanding of the flow and the ability to design better and more efficient high lift systems.

To address that problem requires its own programme of research. In such a programme it would be ideal to perform the testing at as high a Reynolds number as possible and as the facilites will permit but because of the large parameter space of the multi-element wing even a 2-dimensional optimisation where only integrated forces are of interest is expensive. If research is also to include flow field measurements both in the boundary layer and the wakes it

is obviously prohibitive and at best will only be undertaken occasionally, possibly as a collaborative project amongst various interested parties. Clearly it is essential that simpler, cheaper tests at low Reynolds number must be formulated if the fundamental research is to progress. In some cases particular flow phenomena can be isolated and 'model' experiments carried out at a fraction of the cost and also sometimes at representative Reynolds number. But, because of the interactive nature of the total flow field, it will always be necessary to test some complete high lift models.

Whether the interest is in 2 or 3-dimensions, it is necessary to choose the type of model to be tested. So far a satisfactory technique has not been developed yet for 2-dimensional tests. Here the choice of model can be broadly split into three different types as shown in figure 23; all of which have their pros and cons. A model spanning the tunnel, figure 23a, should give a 2-dimensional flow but, apart from the structural problems when either the aspect ratio or the Reynolds number is high, the boundary layer on the tunnel wall is usually thick so that the wall boundary layer interference effects can be quite large particularly at high lift causing significant 3-dimensional effects. This can be overcome by applying tunnel wall suction to remove the tunnel boundary layer and create a smooth streamline flow in the junction but this is dependent on the tunnel having such a facility and can add significantly to the cost and time of testing. A simpler approach, figure 23b, is to install large false walls from tunnel floor to ceiling and mount the model between them, here the wall boundary layer will be much thinner and cause less interference. However, the drawback of this technique is that the tunnel is split into three elements and the flow in each of the channels is governed by the resistance there. Consequently, the flow in the centre section where the model is mounted will not necessarily be the same as that in the outer sections and will differ from the mean flow in the tunnel. This difference will also vary with the drag of the model. An improvement can be obtained by fitting dummy wings in the outer sections of the tunnel but here, as the model approaches the stall, the centre and outer sections will stall at different incidences because of the different aspect ratio. The third alternative, figure 23c, is to fit the model with end plates which do not span the tunnel height. With such a model it is easy to produce a chordwise pressure distribution independent of the spanwise position but the lift curve slope will still be a long way from the 2-dimensional value unless a high aspect ratio model is used with large end plates.

This approach has been used by some design teams within British Aerospace as a high lift system development technique principally because its cost is about a third of the full 2-dimensional test. However, here the results have to be corrected for the finite wing effects at the effective aspect ratio in order to give the 2-dimensional values, but as shown in figure 24, uncorrected results show the optimum configuration can be the same in both cases. On the other hand, figure 25 does illustrate the errors in this method where the induced camber due to the trailing vortices alters the load distribution between the elements. So this technique cannot sensibly be used for research testing as such differences must in detail yield different shear layer behaviours.

Consequently for 2-dimensional testing aimed at investigating the detailed flow field as well as the overall characteristics it is essential to mount a fully 2-dimensional test with the model spanning the tunnel and appropriate corrections to the tunnel flow applied at the model/tunnel junctions. However, even this presents problems. As can be seen from figure 26, although a reasonable spanwise variation of C_L can be expected, the drag can vary in an indeterminate manner and by a significant amount. A further difficulty is encountered if the flow field has a region of separated flow in it for which it is very difficult to ensure a constant behaviour across the span.

Another aspect of research work apart from the type of tunnel and model is the measurement techniques. Since it is necessary to measure both the mean and fluctuating parameters in the viscous layers as well as the surface pressures, the number of parameters per case is dramatically increased and because the shear layers are frequently physically small at model scale, sometimes have reverse flow regions and in many configurations are difficult to reach the equipment used must be very sophisticated. Add to all this the number of the parameters to be investigated for one high lift system and it can be seen that the cost of acquiring a thorough knowledge of even the two dimensional flow around high lift systems will be prohibitively expensive unless some more cost effective method can be found.

In 3-dimensions it becomes even more expensive. Apart from all the parameters of 2-dimensional flow there are now those peculiar to the 3-dimensional geometry, such as:-

1) wing sweep, aspect ratio and taper ratio

2) wing root and tip effects

3) effects of fuselages, nacelles and pylons

4) end effects and spanwise cut-outs in flaps and slats

5) spanwise variation of slat and flap gaps, overlaps, chord and section shape

6) effects of ailerons and spoilers

7) slat and flap tracks, mechanisms and leaks

8) locally induced flow fields from engine intakes, exhausts or propeller slipstreams

9) devices such as boundary layer fences, leading edge notches and vortex generators

Clearly not all these are essential to acquiring a fundamental knowledge of 3-dimensional flow field but even concentrating on only the first 6 items still gives an immense task especially when there has been little work in these fields in the past and any 3-dimensional knowledge has been gained from the ad hoc testing for particular aircraft projects.

Basically, the same problems have to be faced as existed in 2-dimensions. Firstly the choice of the tunnel has to be made and now the pressure of achieving a sensible Reynolds number across the whole span will force at least a significant part of the tests to a large pressurised tunnel. Figure 27 shows a typical variation of the Reynolds number across the span of an A300 type aircraft and it can be seen that even in the pressurised tunnel the Reynolds numbers at the tip are low. In an atmospheric tunnel of reasonable size the Reynolds number based on the local chords would be very low outboard and those based on the slat chords would be ridiculous. This highlights the second problem of the choice of the model, for although it is desirable to represent a typical aircraft configuration by only modelling half of the aircraft so that the Reynolds number can be immediately doubled it raises the spectre of incorrect induced and profile drag effects from the tunnel/fuselage/wing junctions; this has not yet been satisfactorily resolved for simple, single element wings. Apart from this, on a half or full model it is difficult to engineer some of the necessary variations on only one model and there is pressure to use a simpler and cheaper model such as the swept panel model either with constant chord or a simple taper. With a constant chord model, as shown in figure 28, this model does show considerable sweep effects on the total forces but the pressure distributions can be normalised and, as illustrated in figures 29 and 30 for a measuring station at the mid semi-span, are remarkably consistent. However, none of the available techniques has a clear advantage and the choice is inevitably made on either the traditional grounds of experience that the particular researcher has in this field, the availability of existing models which can be modified or simply the cost.

Assuming these problems can be successfully resolved, there is still the question of the required measurement techniques. Here the number of parameters is automatically increased by a half as all the velocity fields now have a third spanwise component and the integrated forces also present additional problems because the total drag has contributions from the profile drag and the lift dependent drag of which it is necessary to know the breakdown. Determination of the two components *is only possible* to the required degree of accuracy by means of a wake traverse technique which apart from the shear cost of traversing a flow field at several incidences, still requires development to become a routine tool.

From the above it is obvious that any programme of research to investigate the basic physics of the 3-dimensional flow field about high lift systems will be expensive, require many man years of effort and will even then inevitably not be able to include all the parameters of interest. Therefore, to develop the knowledge to improve the design of high lift systems on aircraft it will be necessary, as in 2-dimensions, to discover an alternative, more cost effective path than simply experimentation. That path must be through the development of a sound theoretical method supported by selected high quality experiments. Once such a method is available, apart from the possible problems of computer cost, it will be possible to investigate the flow fields to a far greater extent and more quickly than can be done experimentally.

5.2 Theoretical Techniques

However, there are currently no available theoretical models which will address the 3-dimensional flow field in anything like the required detail. Present computational capability is largely restricted to 2-dimensional attached flow cases. But even in 2-dimensions it is necessary to have a method which will predict the changes as various parameters are altered and to be able to predict the maximum lift and drag of the section, and today there is no method with that capability on a production basis. Consequently theoretical methods are faced with a long period of development which will be expensive and require a lot of effort but will, when successful, give the basis for the only real technique of systematically varying all the parameters on a high lift wing, and, as has been amply demonstrated with the application of theoretical methods to high speed wing design, will reduce the amount of tunnel testing for project studies. It will also eventually and perhaps more importantly allow the optimum flow conditions to be determined for which the high lift wing should be designed.

With the present knowledge of the flow around 2-dimensional multi-element aerofoils it is possible to identify the major flow features as shown in figure 12 and to construct a theoretical model. Current 2-dimensional methods are capable of calculating the flows about simple configurations but as a recent comparison between theory and a range of experiments has shown, there are still many problems to be overcome. Figure 31 shows the results for an NLR experiment with a two element configuration, shown in figure 32, specifically designed with no flow separations and no merging of the wakes and boundary layers so that it is a simple test case which is a little more complicated in its various effects than a single aerofoil except for the calculation and representation of the wing wake over the flap. Although the effect of the wake is significant and its modelling important, the flow is computed quite successfully and

figure 33 shows the overall agreement between the experiment and the computed pressure distributions is good. Small differences in pressure on the flap upper surface are principally caused by the incorrect modelling of the wing wake which in this particular method is represented by the calculation of a symmetric wake when it is in fact very asymmetric in this region. It is also possible to detect from the lower surface pressures in particular the effects of too much circulation on the flap which together with the incorrect trailing edge pressure suggests an incomplete modelling of the Kutta condition. Figure 34 shows a comparison of the measured and calculated momentum thicknesses for the two elements and it can be seen that the agreement is also good.

For this test case a comparison of 5 different computational methods has been made, only two of which include a specific algorithm for computing the wake/boundary layer interaction, and figure 35 shows the increments at various incidences in both C_L and C_D predicted between two model configurations where the gap between the wing and flap had been halved to give a significant interaction between the two shear layers. Obviously from the results none of the methods can be relied on to predict the correct variations although the methods which compute the wake/boundary layer interaction do give the right sort of change and trends in lift but even they are a long way from predicting the drag changes.

Further problems can be seen with another more realistic two element case where this time there is a cove region under the wing shroud as sketched in figure 36. It can be seen from the pressure distribution that the method is far from satisfactory. For this case the separated flow in the cove region cannot be modelled and has to be represented by a streamline fairing drawn from experience. The shape of this fairing critically controls the flow through the slot and hence the pressures in that region. Better agreement between the calculated and measured pressures can be obtained by adjusting the fairing but the shape to give the best agreement is far from the intuitive shape so that this approach is difficult to use in practice when the required pressures are not known before hand.

Methods again show problems with more complicated three element aerofoil from the RAE which, as shown in figure 37, has a slat and a flap with positions such that there is a moderate interaction between the wakes and the boundary layers. On this model there are now two cove regions, on the slat and on the wing, which have to have approximate streamline fairings incorporated to allow the computer program to execute. Apart from the cove region separated flows, the flow also nearly separates on the flap upper surface with a trailing edge value of 2.47 for the shape parameter H being measured. This indicates a strong interaction between the viscous and inviscid flows which will cause difficulties particularly to the methods which use a direct form of the viscous/inviscid coupling. A further difficulty is the strong compressibility effects on the slat and wing upper surfaces and although there is no shock waves the flow is nearly sonic on the slat at 20° incidence which should be treated with some solution of the compressible flow equations. It can be seen from the pressure distributions in figure 38 that whilst the agreement is reasonable the mathematical model used in this particular method does not adequately represent the effects.

It is interesting to note in this calculation that for the flap the agreement is particularly poor and, while it only contributes a small part to the overall lift, 0.4 C_L in a total 4.2, and maybe considered not to be too important, it must be remembered that it does control the circulation about the whole aerofoil and incorrect predictions can be expected to have a global effect. In the case illustrated, the discrepancies are caused by an incorrect modelling of both the wake over the flap surface and of the Kutta condition which is here complicated by the method predicting a separation towards the rear of the flap upper surface where the experimental flow remains attached to the trailing edge. In terms of the overall integrated forces the agreement in total lift is reasonable as show in figure 39, but the drag is unpredicted. This is not surprising as it is unreasonable to expect the simple Squire and Young method, as used in this particular theoretical method by being applied at the trailing edge of each element and then summed for the total drag, to give the correct answer.

A fourth test case from ONERA, shown in figure 40, is again a three element aerofoil but which has a large deflection angle of the flap with a significant region of separated flow. It also has a merging of the shear layers both between the slat wake and the wing upper surface boundary layer and also the wing wake and flap upper surface boundary layer probably after the latter has separated. The comparisons, figure 41, for this case have been computed by the ONERA method which uses a semi-inverse viscous/inviscid coupling procedure and an inverse boundary layer method capable of predicting separated flow. In general, it produces good predictions of the separated flow region both in terms of the pressure level and the point of separation but it does underestimate the peak suctions. It also underestimates the pressure distributions on the wing suggesting that in spite of a good separated flow model it is not controlling the overall circulation correctly, however, this method does not represent the wake/boundary layer merging and is in the early stages of development. This experiment has a further flow complication in that it exhibits the 'flow recovery' phenomenon described in a previous section, and at 18° incidence, 2° higher than the results shown in figure 41, the flow reattaches which is, not surprisingly, not predicted by this theoretical method.

The results described above have largely been drawn from a recent comparison of several theoretical methods and three experimental test cases, which were carefully chosen to cover the range of flow phenomena likely to occur on multi-element high lift aerofoils. From these comparisons it was possible to make the following general observations about the state of the art of 2-dimensional computational methods:-

1) the drag is poorly estimated by most methods and must be improved for the methods to become useful design tools.

2) the effects of compressibility and sonic flow on the slats and wing leading edges is significant. None of the methods accurately predicted the near sonic flow and there was little agreement between the simple compressibility corrections used. Figure 42 shows a Mach number distribution on a typical slat at a freestream Mach number of 0.20 with a peak local Mach number of over 1.2 and clearly some method which solves the full compressible equations with a modelling of the shock wave is required.

3) it is difficult with the large number of different effects to decide whether the Kutta condition is being satisfied correctly but generally the trailing edge pressures are poorly predicted and there is a need for an improved model of the Kutta condition in the presence of multiple, curved shear layers.

4) the displacement effects of the wakes from upstream elements must be included in the equivalent inviscid flow even when there is no merging of the wake and boundary layer and the size and position of the singularities representing that wake are equally important as shown in figure 43.

5) it is necessary to be able to compute the development of curved wakes from the slat or wing through an adverse pressure gradient including the near wake behind the upstream element in order to be able to predict the drag correctly. Calculating the drag by the Squire and Young method at the trailing edge of each element cannot be expected to give the correct answer, however, as shown in figure 44, correctly applied to the flow conditions at the flap trailing edge can give a reasonable result for a wide variety of configurations.

6) a method for computing the interaction of confluent wakes and boundary layers is needed and that method has to be able to predict separation of the boundary layer and to continue the calculation in the presence of that separation. This obviously requires a very sophisticated shear layer calculation and will demand a finite difference method of solution of at least the boundary layer equations with a sophisticated turbulence model. Figure 45 shows some recent results using a Reynolds Stress model.

7) a model of the separated flow is required both for the 'closed' separation in the slat and wing cove regions and for the 'open' separation on the wing and flap upper surfaces.

8) none of the methods predicts C_{Lmax} or the post stall behaviour of the aerofoil.

From these results it is clear that the state of the art of theoretical modelling even in 2-dimensions does not meet the basic requirements set out earlier but as methods do exist and most of the problems have been identified, it should now be possible to make progress towards improving the current generation of methods.

In 3-dimensions there has been little or no serious development work, save that of one important item at Boeings, which mainly reflects the difficulties experienced with the 2-dimensional methods and the lack of effort that has been available to apply to the problem. It is possible to construct 3-dimensional methods which solve the potential flow for high lift wings in a reasonable manner but, because of the difficulties in representing the 3-dimensional effects of flap ends, cut-outs etc. and the lack of any 3-dimensional viscous method to deal with confluent wakes and boundary layers, no one has yet embarked on attempting a full theoretical method. To date the only serious attempt has been that at Boeings, reference 5, where a 3-dimensional potential flow analysis is used to predict 'critical sections' on the wing. Using these sections, their characteristics can be calculated with a 2-dimensional method and related back to the 3-dimensional case with Lock's equivalence method to account for the effects of sweep, taper and aspect ratio. The 3-dimensional analysis is then adjusted to take account of the viscous effects by using an 'effective camber' surface for the multi-element section in the potential flow method. Obviously this approach relies on a high aspect ratio wing where the section characteristics dominate the wing flow and also assumes that the spanwise effect of the boundary layer can be neglected, but as shown in figure 46 good comparisons of the integrated forces can be obtained. In the Boeing formulation the 3-dimensional analysis is based on a vortex lattice method specifically tailored for high lift applications to multi-element wings with part span flaps, bodies and nacelles and the 2-dimensional method is an 'in house' method based on a panel method including the effects of viscous flows. This quasi-3-dimensional analysis is clearly limited and because of the simplifications used cannot be used for general research interests. But nevertheless it is evidently a powerful tool in project aerodynamics and has been used extensively by Boeing.

A similar approach to this is a simple strip theory where the potential flow method is used to calculate the inviscid onset flow to several sections across the span and with these onset flows the characteristics of each strip can be calculated using a suitable 2-dimensional method which includes the effect of viscosity. At this level it has no iteration between the two calculations and will generally not be expected to give predictions which are any better than the Boeing approach. However, provided that the 2- and 3-dimensional methods are based on singularity type panel methods a more powerful hybrid approach can be used. This concept developed by Jepps, reference 6, is based on a basic iteration algorithm:-

$$(3\text{-d})_n = \left\{(3\text{-d})_{n-1} - (2\text{-d})_{n-1}\right\} + (2\text{-d})_n$$

where one iteration consists of applying this algorithm to each strip of the wing. The n^{th} iteration may be interpreted as computing the 2-dimensional singularities in the presence of the 3-dimensional onset flow U and satisfying the 3-dimensional boundary conditions. U is the 3-dimensional flow induced at that strip by the entire set of 3-dimensional singularities minus the 2-dimensional flow at that strip due to the 2-dimensional singularities, both computed during the previous $(n-1)^{th}$ iteration. The 3-dimensional singularities are taken to be the 2-dimensional singularity strengths, computed in the previous iteration for each strip, applied on the 3-dimensional panels. This method has been previously developed for potential flow applications but could be extended to include viscous effects. Now the restrictions of wing planform of the previous methods have been removed and the only assumption is that the spanwise effects of viscosity can be neglected. Whether this is restrictive remains to be seen, but further developments of the method may well permit some cross flow terms to be included in the viscous flows in the formulation.

Apart from these simplified approaches, some preliminary results are being obtained by extending the 2-dimensional formulations into 3-dimensions. Results, figure 47, are available from a 3-dimensional panel method formulation including the simple effects of viscosity due to the boundary layers on each element, which, although they are encouraging, show that this is only the start of a long road of development. In spite of the 2-dimensional knowledge, there are still many problems to be overcome which are peculiar to 3-dimensional configuration, namely:-

a) the representation of the wakes, both the inviscid trailing vorticity and the viscous wake. It is not now possible simply to place the singularities on an assumed wake profile as it is known that the 3-dimensional wake distorts and rolls up rapidly and the 2-dimensional analysis, figure 43, has illustrated the importance of the wake position.

b) the wake modelling problem extends to the flap and slat ends and the modelling of the flow in this region. It has yet to be shown whether this is just a problem of modelling the inviscid trailing vorticity and its correct deformation or whether there are significant effects due to the viscous layers. Recent NASA work has illustrated that the vortex rolled up behind a part span flap end is quite different in the nature of its total head distribution than that from the wing tip and its mean velocities are significantly lower suggesting the low energy viscous layers are pulled into the vortex core.

c) development of 3-dimensional calculation methods for shear layers which include the wake/boundary layer interaction.

d) interference effects, particularly on the viscous flow, from other lifting surfaces, such as pylons, and bodies, such as fuselages and nacelles, which is not a problem unique to the high lift wing and is common to all 3-dimensional methods, although wing body junctions with high lift devices deflected can present additional problems.

e) effects of compressibility in 3-dimensions needs to be included.

f) the computation of separated flow becomes much more difficult. As shown in figure 21, it is a more complex pattern with parts of the wing stalled and parts not so that the viscous computation has to be very complex. Also in 3-dimensions the flow in the slat and wing cove regions may, depending on the wing sweep angle, be of different character from the 2-dimensional flow in so far as it may form a spanwise vortical flow rather than a closed bubble.

These problems have to be solved before a successful 3-dimensional method is available as a tool for research into high lift flows. There is a basic framework for a 3-dimensional calculation method which, with the successes and failures in the development of 2-dimensional methods, will point the work, at least initially, in the right direction. However it is a prerequisite of starting the development of a 3-dimensional method that it will also be necessary to carry out several high quality experiments to provide the basic data to support the calculations and the development of the various viscous flow algorithms, although these may well, in part, be satisfied with 'model' tests rather than a full 3-dimensional aircraft model.

6 CONCLUDING REMARKS

The previous sections have shown the way high lift systems are designed for aircraft and the techniques used in that work. However, it is clear that the knowledge of the fundamental physics of the flow around even a 2-dimensional multi-element aerofoil is far from complete and will not be advanced with the ad hoc testing associated with project design. Section design by traditional methods has probably reached a plateau and future improvements on the 'cut and try' principal will only yield limited growth. There are many flow phenomena which can be identified at this stage but which are not fully understood and which require further investigation at a detailed level. Whilst some of these can, at least in the first instance, be isolated from the complete high lift configuration and treated by 'model' experiments and calculations, it is nevertheless essential that some major, comprehensive experimental programme be mounted on a fully 2-dimensional model. These tests would require measurements not only of the surface pressures and integrated loads but also detailed measurements of the mean and fluctuating velocities in the boundary layers and wakes. However, principally because of the size of the parameter space and the problems and cost of achieving the representative Reynolds and free-stream Mach number experimentally, theoretical calculations will play an important part in the overall research. But the current generation of 2-dimensional methods are inadequate for this work and, although many of the defficiencies have been identified and are being investigated, it will still be some time before a suitable method is available.

In 3-dimensions there are significant gains to be achieved from improvements to the design in terms of optimising the spanwise grading of the slat and flap gaps, overlaps, chords and section shape, improved inboard wing design, minimising the adverse interference effects of flap ends, cut-outs, body junctions etc. and for designing at the flight Reynolds number. This will require not only to be able to analyse a given geometry but also to be able to describe the optimum flow conditions for which a high lift wing should be designed and how to modify the configuration to achieve them. Obviously, this can only come with a good basic knowledge of the flow field about the high lift system and the shear number of variables makes it impossible that a 3-dimensional design could ever be fully optimised experimentally. Consequently there is a requirement for a comprehensive theoretical method which is capable of predicting the changes due to altering various parameters, the maximum lift of the wing and the L/D at least close to the design condition. Without such a method it will never be possible to take full advantage of a 3-dimensional design and the knowledge gained from ad hoc project type testing will always be partial. However, that is not to say that such a method will ever replace the wind tunnel testing or even reduce the requirement for the expensive high Reynolds number wind tunnel facilites. It will not. To start with there is no suitable theoretical method in existence and it will be a long development to achieve one. During this time there will be a need for extensive experimental support at all levels of sophistication and without a theoretical design capability, there will be a continuing requirement for the project aircraft testing. Even at the end of the road, the theoretical method will not be as complete a model as would be liked and will in practice only give the ability to design nearer to the optimum configuration so that it will always be essential to test the final configuration in a wind tunnel at near flight conditions. But these tests should eventually only be confirmatory tests and the amount of tunnel testing for a given project should be considerably reduced in much the same way as has happened for high speed wing design. To create such a theoretical method will require a significant effort which for efficiency must be marshalled into a organised research programme and would probably represent the main research in high lift aerodynamics for the next decade or so.

However, apart from the progress which will be achieved by the understanding of the high lift flows and the developing of suitable analysis techniques, there will almost certainly be inevitable improvements from new design philosophies but over a much longer timescale. What will be achieved is speculation but as aircraft wings of transport aircraft, at least, will always be directed to the achievement of the best possible cruise and high speed performance, high lift will always be achieved by the use of variable geometry. However in spite of the proven efficiency of the mechanical high lift devices there are definite limits to the ability to engineer variable geometry to deal with some critical areas of the wing and it is probably here that boundary layer control by blowing or suction could be an effective and practical way of dealing with very localised problems. Leading from this proposal, because of the margins required for manoeuvring and for providing protection against the atmospheric disturbances such as strong gusts and wind shear, for most of the time the high lift devices are deployed the demands made in terms of lift are much below that potentially available. This means that high lift devices are deployed to larger deflection angles than are required most of the time and are usually generating more drag than would be the case if these margins did not have to be permanently provided. This could be avoided if active high lift devices were used where the device could be rapidly deployed when the demand arose in which case the drag benefits would be considerable. However, for extending chord devices it seems that active flaps or slats with a high rate of deployment are not likely to be practical. Consequently here it might be possible to use boundary layer control in active form. For this type of boundary layer control it would be attractive to use a reservoir system so that rapid demands could be made without more than a small effect on the engines and thrust performance. For a reservoir system to suffice and not be too large it necessitates that control of the flight path shall be as efficient as possible, and this points to the need for computer control of the flight path. Take-off and landing manoeuvres could then be programmed to be controlled in the most efficient manner with parallel programmed control of the mechanical high lift devices simultaneously to minimise drag and the demands made on the blowing system. Having already invoked computer directed control it is

natural to extend this to c.g. control and relaxed stability which are powerful ways of improving high lift performance and should certainly feature strongly in the search for ways of increasing high lift performance.

Further most present day transport aircraft sacrifice a considerable amount of lift capability in order to generate the stall handling characteristics required to meet the airworthiness requirements. Computer control of aircraft could be developed so that stalling is totally eliminated and with such a control system 'stall fixing' and the associated loss of maximum lift would not be necessary or would at least be much diminished.

The problems of implementing these are obviously very great; a thorough understanding of the complexities of local flows in all the critical regions of 3-dimensional wings is essential so that the boundary layer control by blowing can be employed in the most economical manner. The blowing system would also have to be developed for economy and would be likely to have a variable nozzle area rather than controlling the blowing through a fixed nozzle by a throttle. All of this would have to be done in parallel with the development of computer directed flight path control. To achieve this, very close liaison would be needed between the various disciplines ranging from the fluid dynamic scientists through the structural, mechanical and electronic engineers to the flight dynamicists. But similar liaison has obviously been achieved for the Boeing YC-14 with overwing blown flaps and could be again in the future.

REFERENCES

1	-	ESDU Data Sheets
2	-	USAF Stability and Control DATCom
3	McRae D M	Aerodynamics of mechanical high lift devices AGARD Lecture Series No 43 1971
4	McRae D M	The aerodynamic development of the wing of the A300B RAeS Journal July 1973
5	McMasters J H Henderson M L	Some recent applications of high lift computational methods at Boeing. AIAA-81-1657 1981
6	Jeppe S A	The computation of vortex flows by panel methods VKI Lecture Series 4 1978

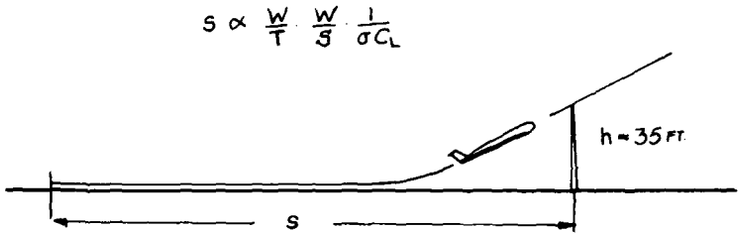


Figure 1 Take-off distance

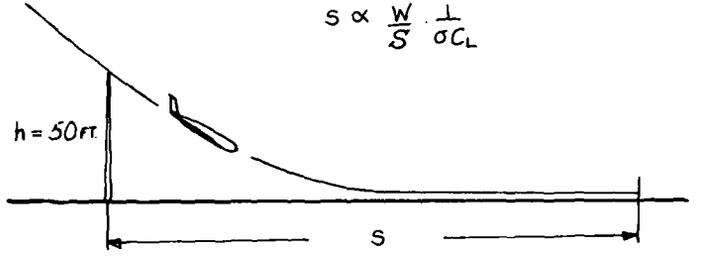


Figure 2 Landing distance

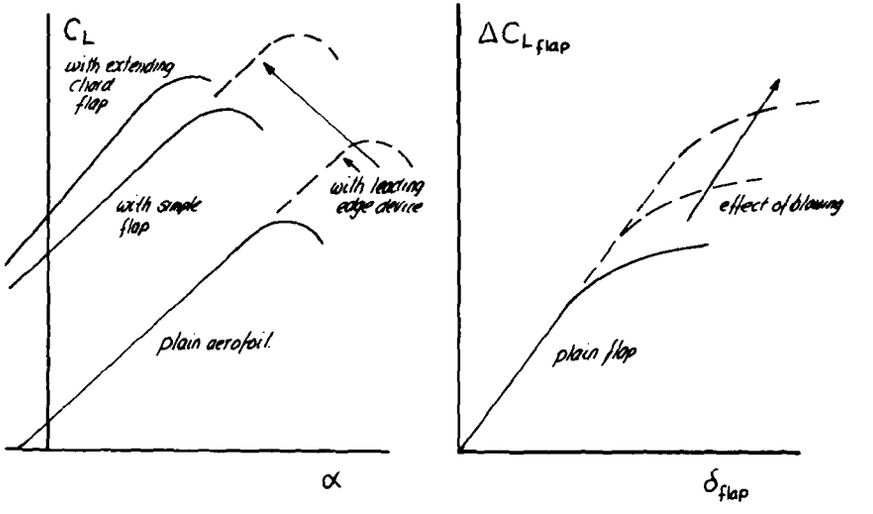


Figure 3 The effect of slats and flaps on the lift of an aerofoil

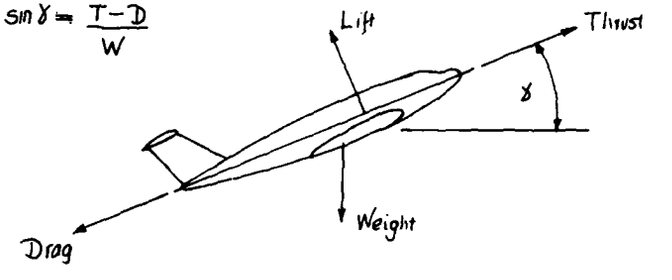


Figure 4 Climb gradient

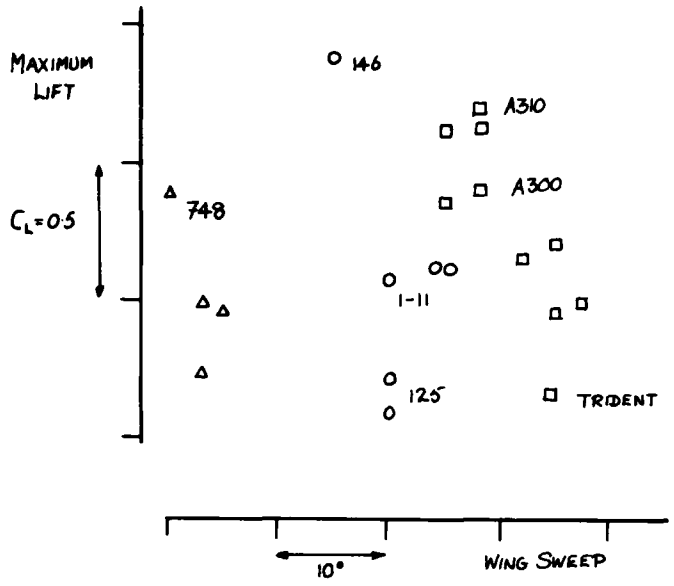


Figure 5 Variation of maximum lift of transport aircraft wings with wing sweep angle

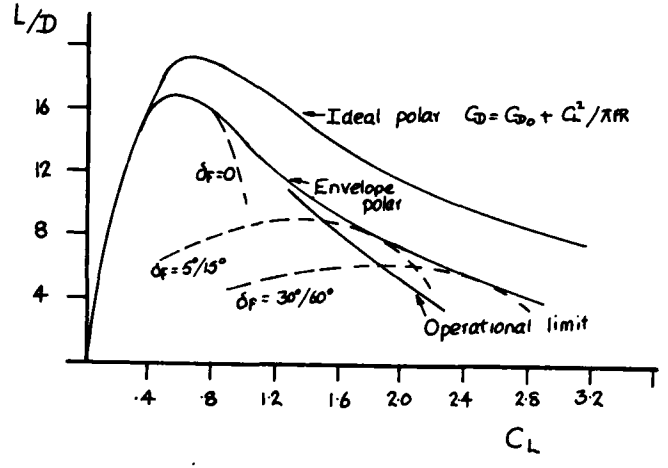


Figure 6 Difference between ideal and envelope drag polars

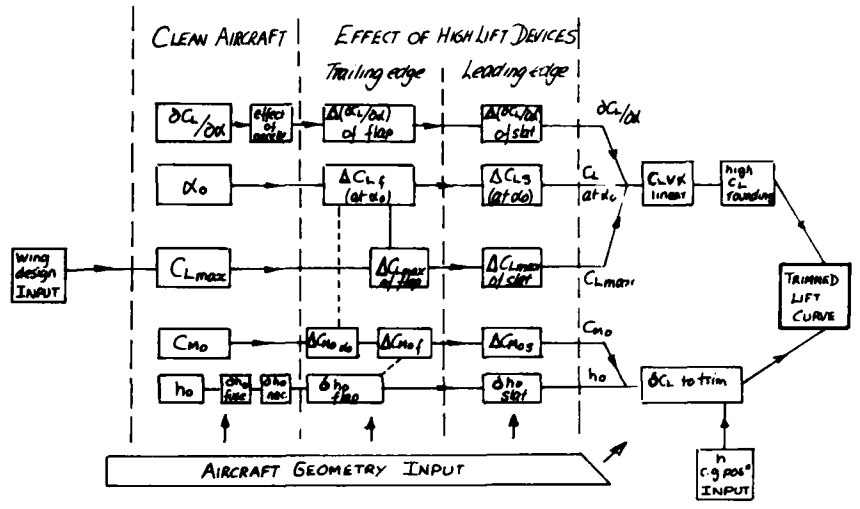


Figure 7 Schematic of an empirical high lift prediction method

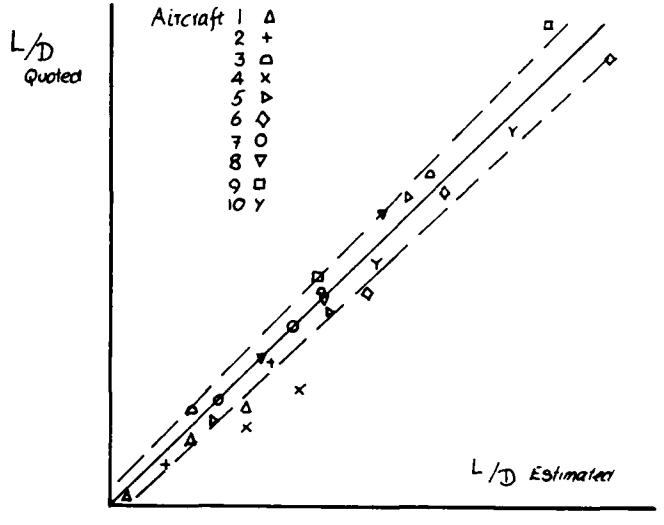


Figure 8 Comparison of the L/D results of the high lift method with published aircraft values

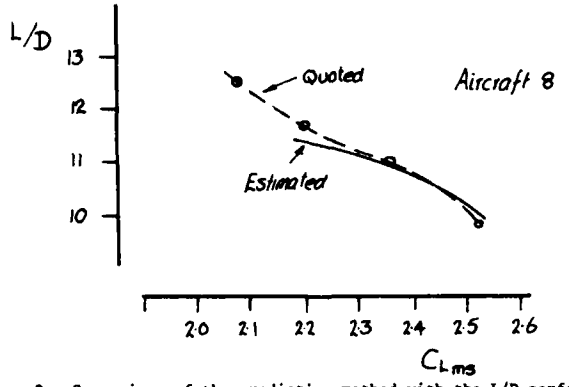


Figure 9 Comparison of the prediction method with the L/D performance for a given aircraft

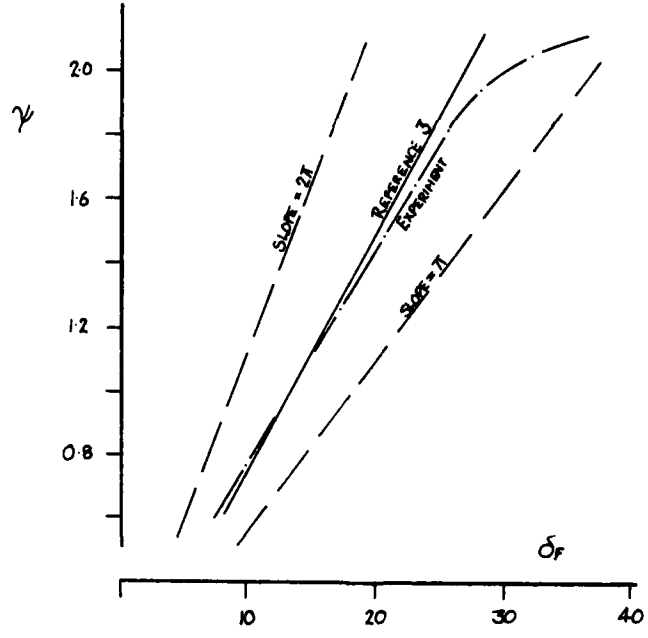


Figure 10 Variation of the flap lift curve parameter with flap angle

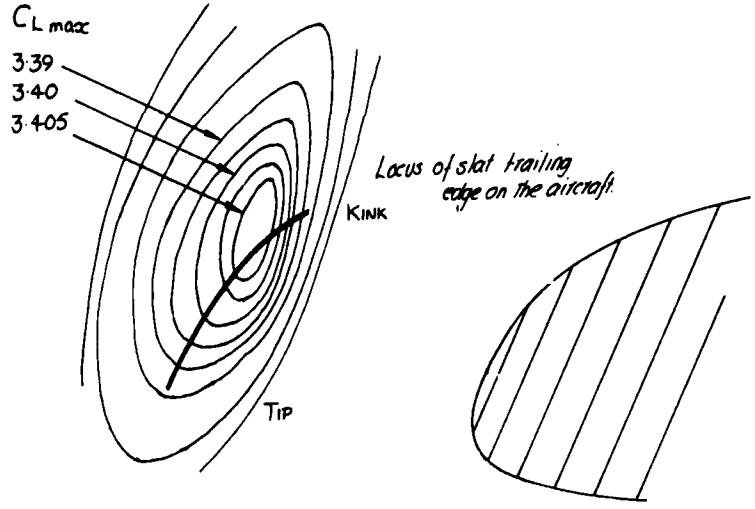


Figure 11 C_{Lmax} locus of the slat trailing edge on an A300 model

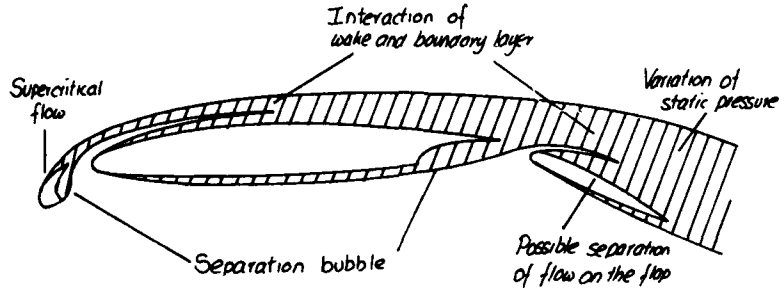


Figure 12 Basic features of the flow about a multi-element aerofoil

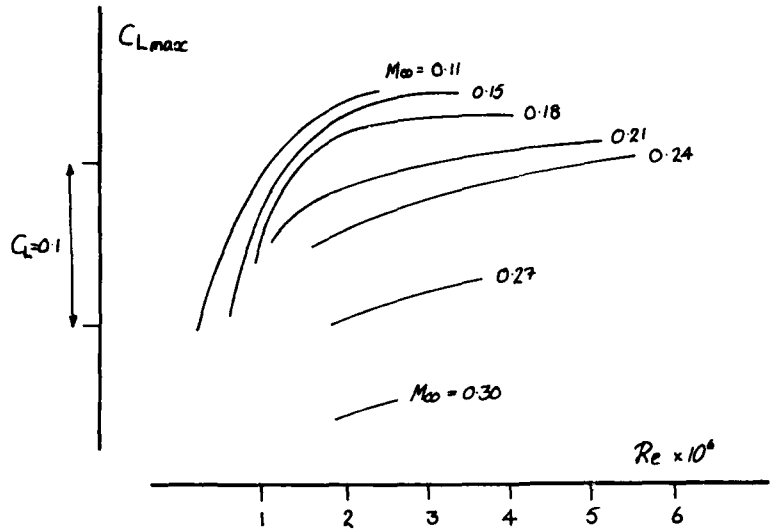


Figure 13 Variation of C_{Lmax} with Reynolds and freestream Mach number

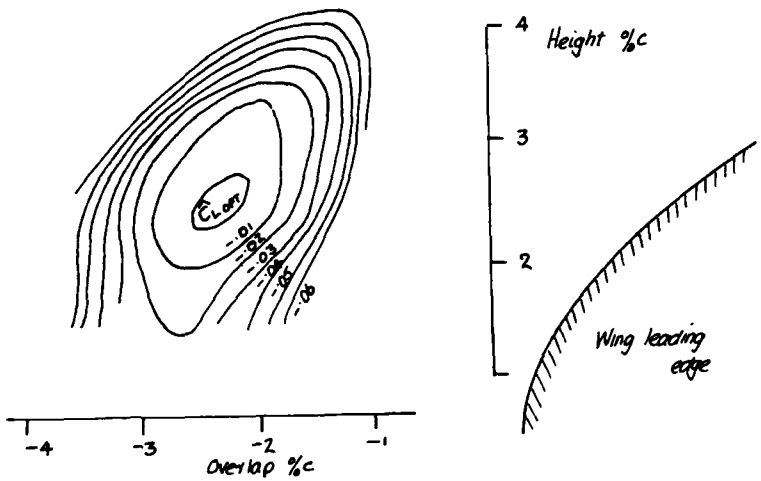


Figure 14 C_{Lmax} locus for the slat trailing edge on a typical multi-element aerofoil

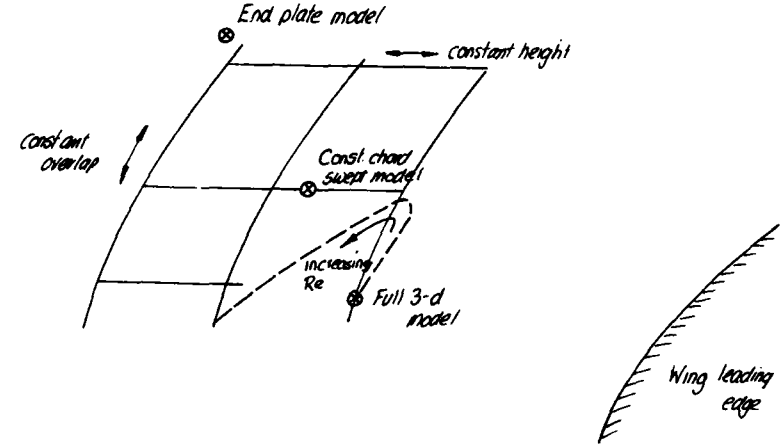


Figure 15 Variation of the optimum slat trailing edge position for different tunnel models and varying Reynolds number

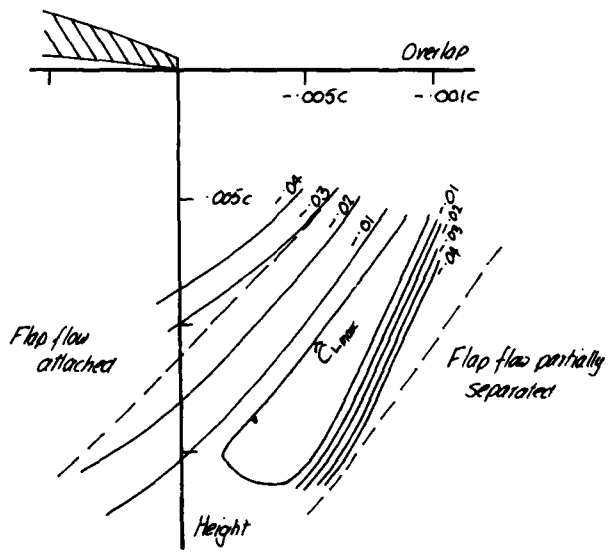


Figure 16 C_{Lmax} locus for the flap leading edge for a typical multi-element aerofoil

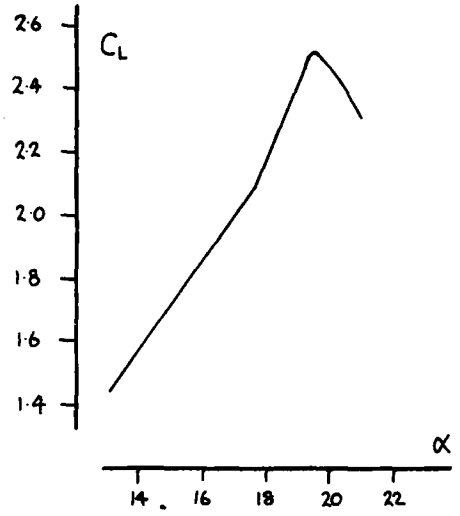


Figure 17 Effect of a flow recovery region on the lift curve of a multi-element aerofoil

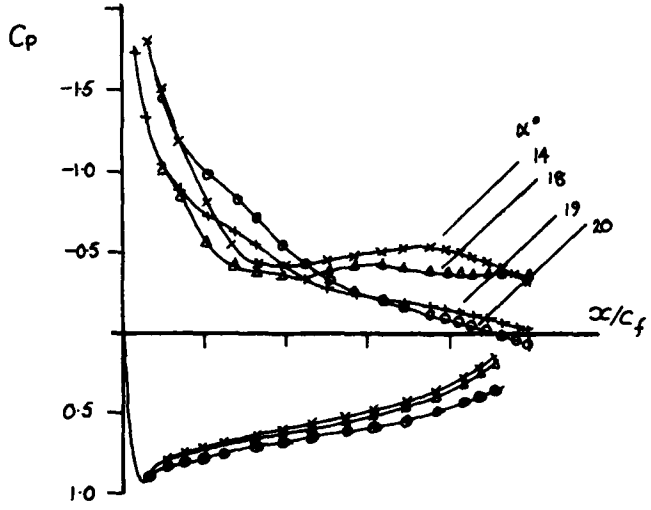


Figure 18 Flap pressure distributions for an aerofoil with a flow recovery region

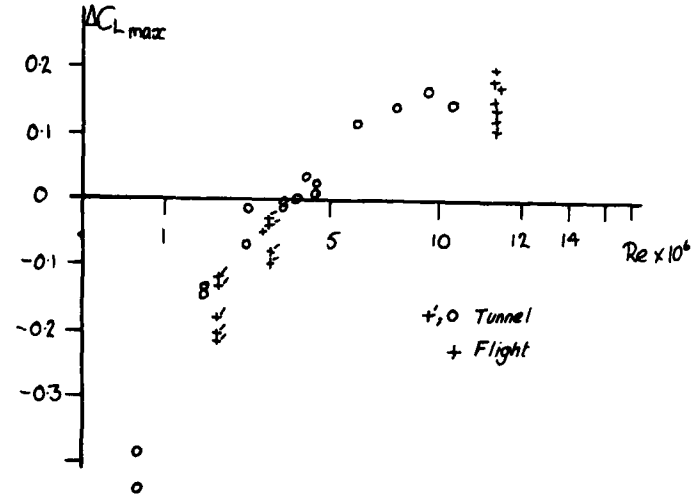


Figure 19 Variation of C_{Lmax} with Reynolds number for tunnel and flight results

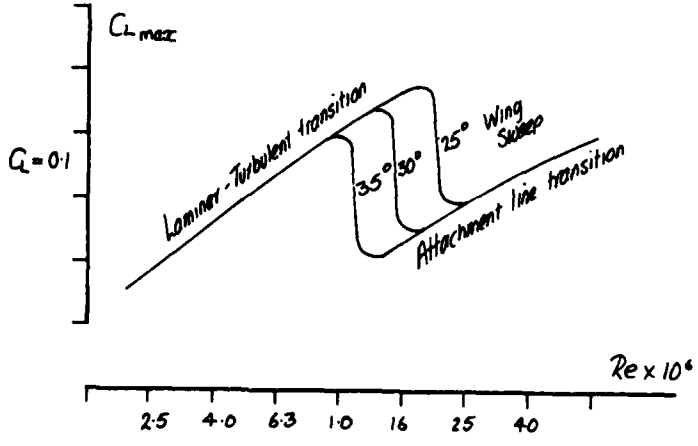


Figure 20 Effect of an attachment line transition on the C_{Lmax}

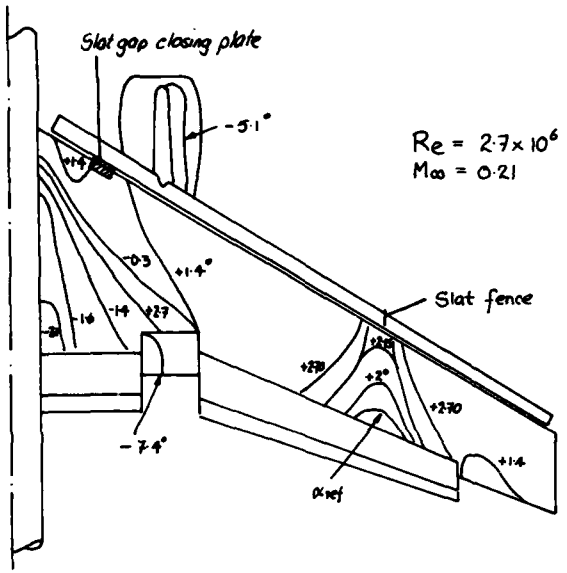


Figure 21 Schematic of the stall progression on a transport aircraft wing

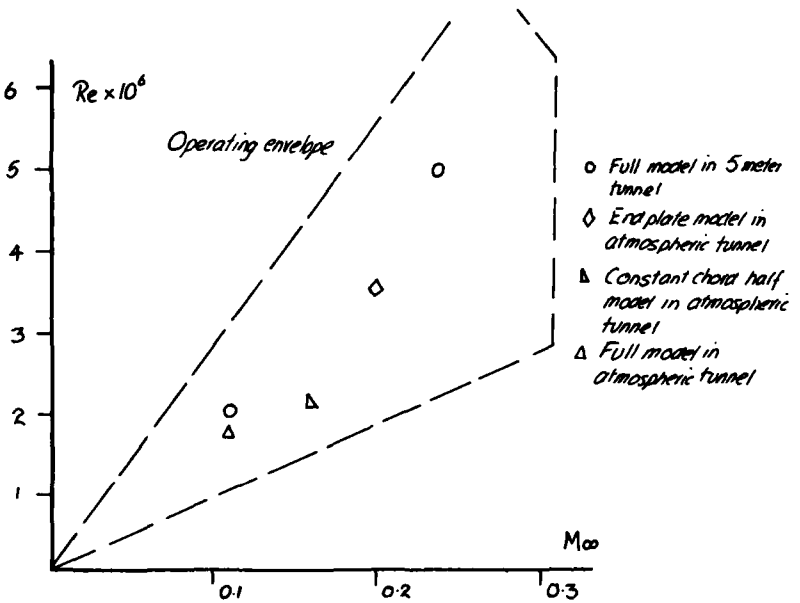


Figure 22 Range of Reynolds and Mach numbers for the RAE 5 metre wind tunnel, including typical values for models tested in other tunnels

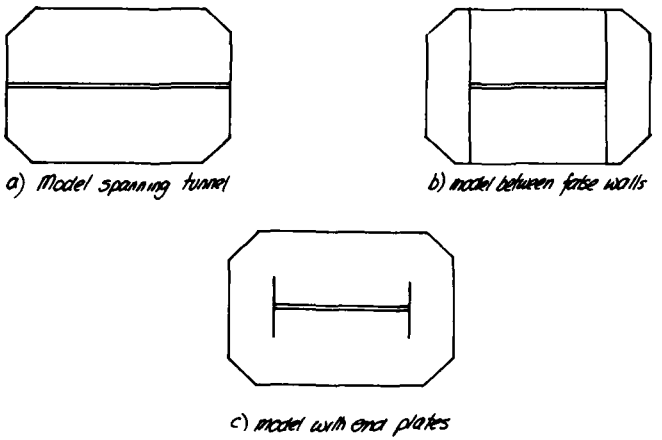


Figure 23 Different techniques of two-dimensional aerofoil testing

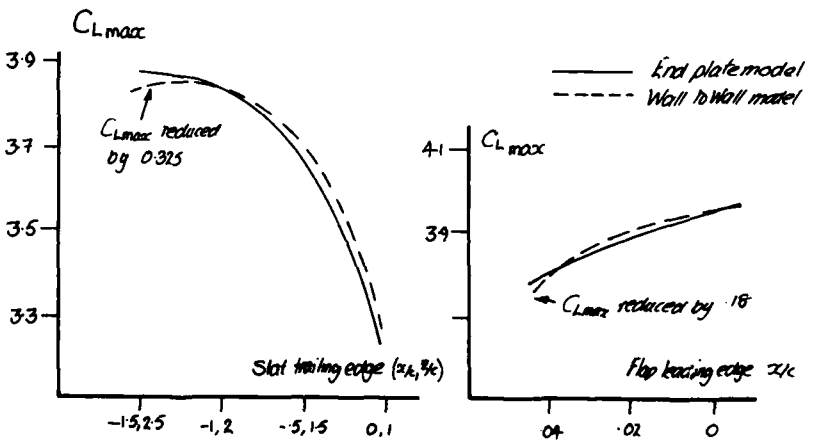


Figure 24 Comparison of the $C_{L_{max}}$ results for an aerofoil using two of the different tunnel testing techniques

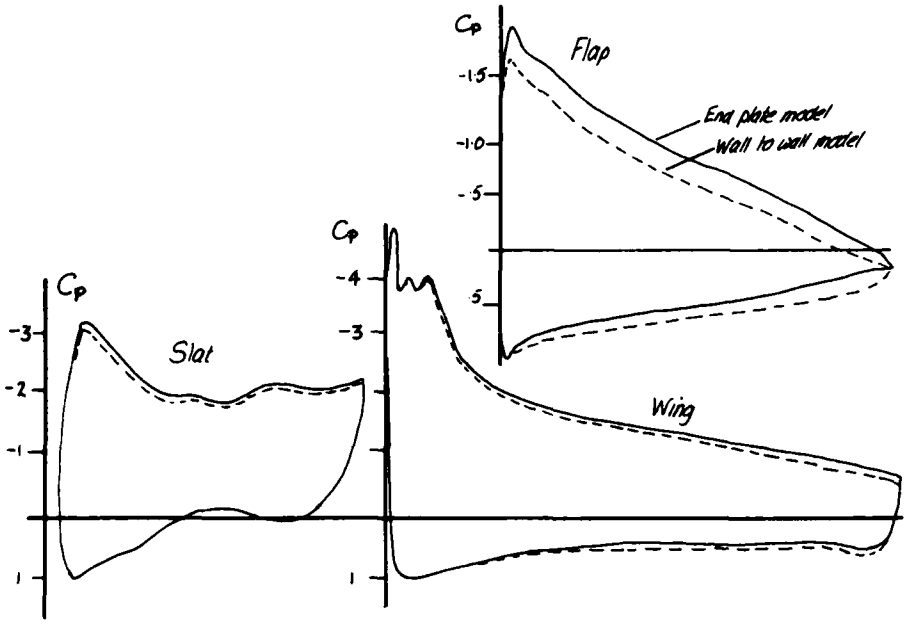


Figure 25 Comparison of the pressure distributions for an aerofoil using two different tunnel testing techniques

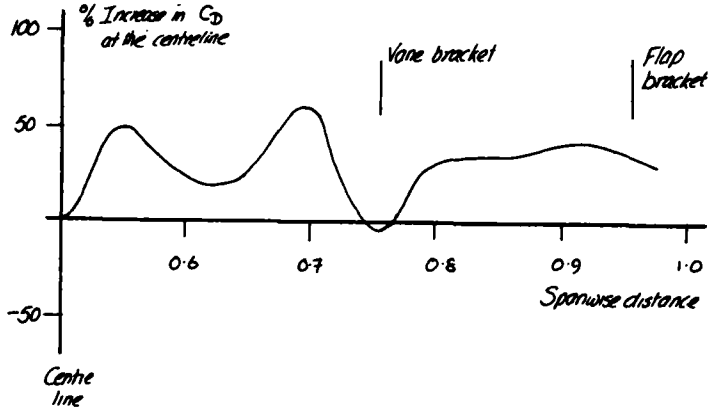


Figure 26 Variation of the drag behind a 2-dimensional aerofoil spanning the tunnel

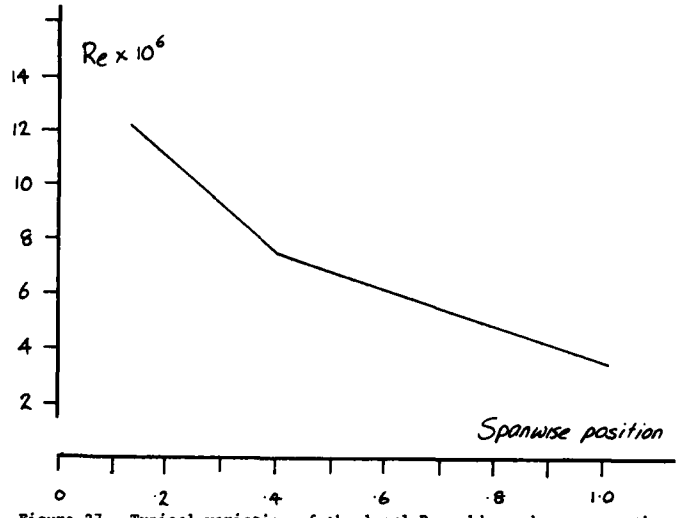


Figure 27 Typical variation of the local Reynolds number across the span of a transport aircraft wing in the RAE 5 metre tunnel

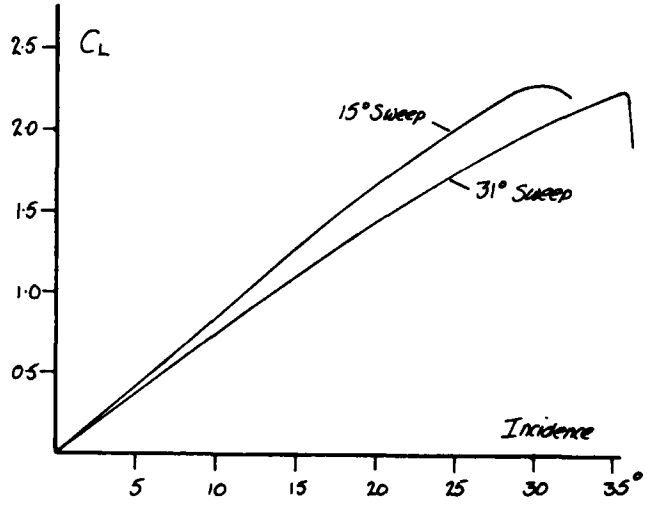


Figure 28 Effect of wing sweep angle on the lift curve for the constant chord half model

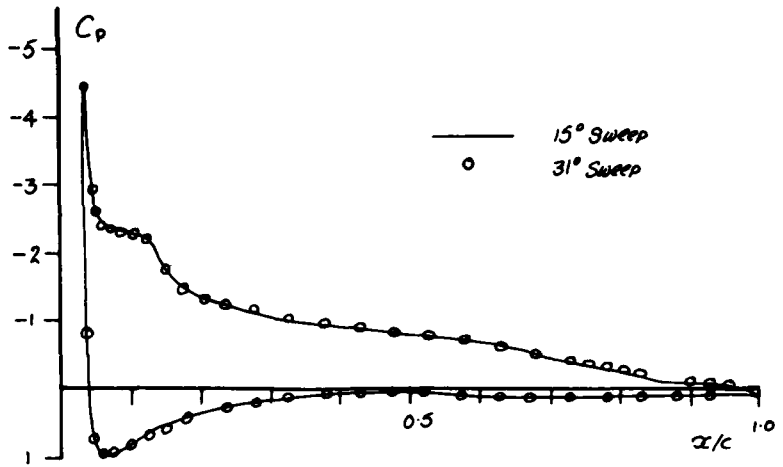


Figure 29 Normalised slat pressure distribution for two wing sweep angles

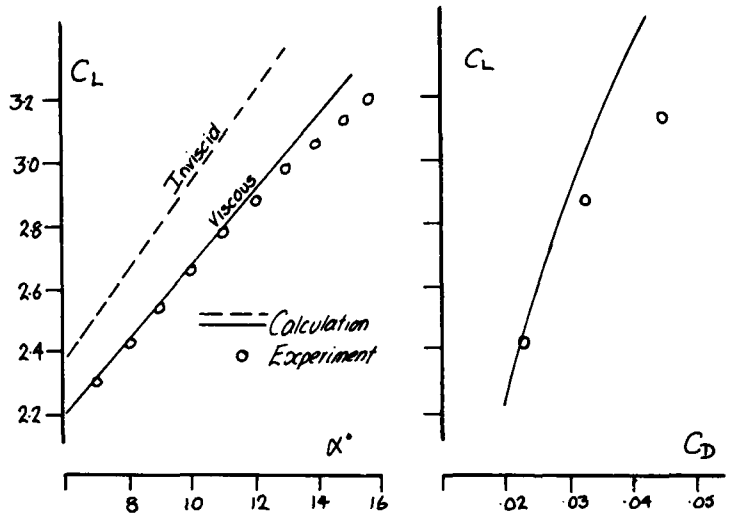


Figure 31 Comparison of the experimental and theoretical lift and drag characteristics for an NLR two element aerofoil

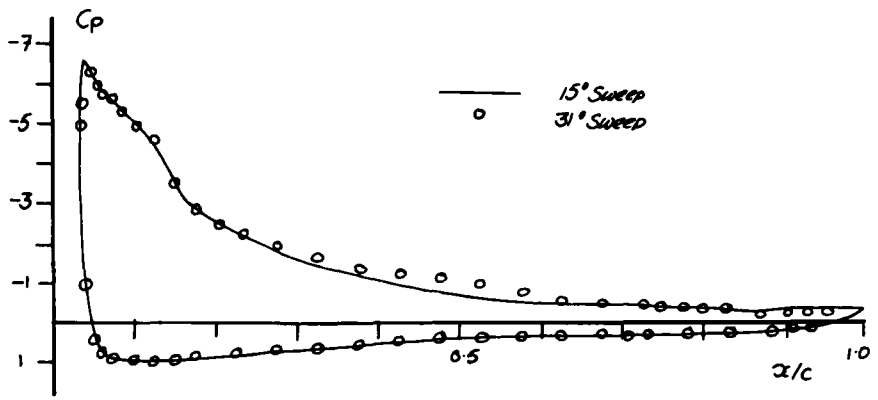


Figure 30 Normalised wing pressure distribution for two wing sweep angles

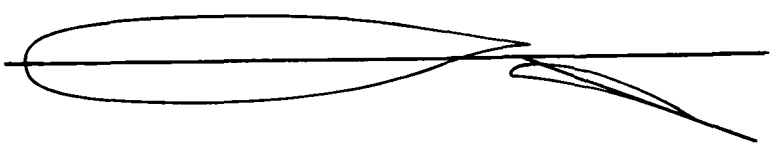


Figure 32 NLR two element aerofoil tested at a Rynolds number of 2.5×10^6

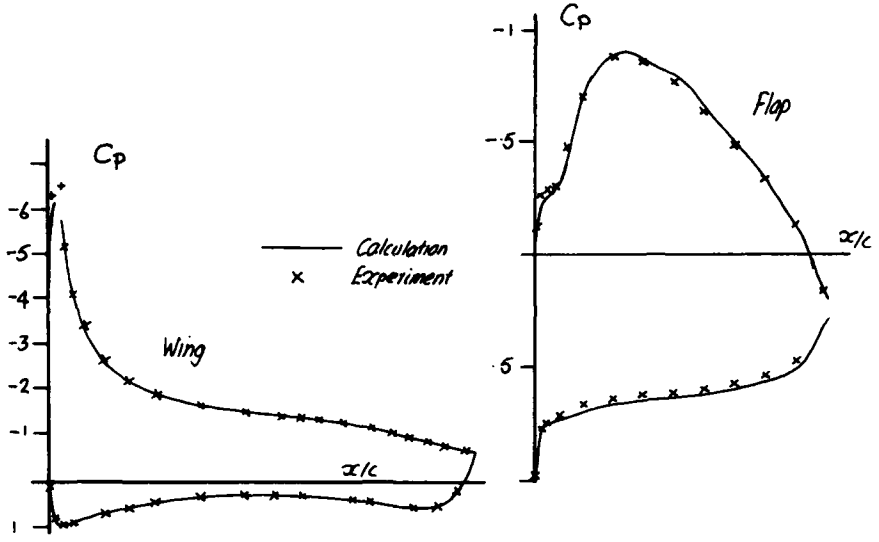


Figure 33 Pressure distributions for the NLR two element aerofoil at an incidence of 6 degrees

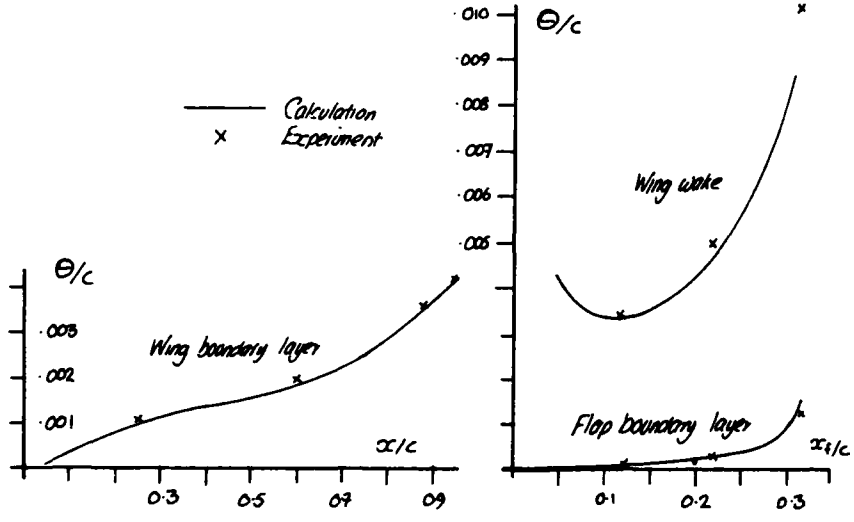


Figure 34 Momentum thickness distributions for the NLR two element aerofoil at an incidence of 6 degrees

Inc.	C_L (gap 1) - C_L (gap 2)					
	Expt.	Calculation				
		Methods:-	1*	2	3	4*	5
6.0°	-.05		-.24	0	+.02	-.11	+.04
10.1°	-.08		-.30	-.01	-	-.11	-
13.1°	-.13		-	+.01	+.05	-.15	-

Inc.	C_D (gap 1) - C_D (gap 2)					
	Expt.	Calculation				
		Methods:-	1*	2	3	4*	5
6.0°	-.0004		-.0018	-.0002	+.0005	+.0056	0.0
10.1°	-.0001		-.0012	-.0023	-	+.0066	-
13.1°	+.0002		-	-.0009	+.0007	-.0003	-

* indicates the methods which include modelling of the confluent wake and boundary layer.

Figure 35 Comparison of 5 theoretical methods for the increments in C_L and C_D between two different flap gaps for the NLR aerofoil

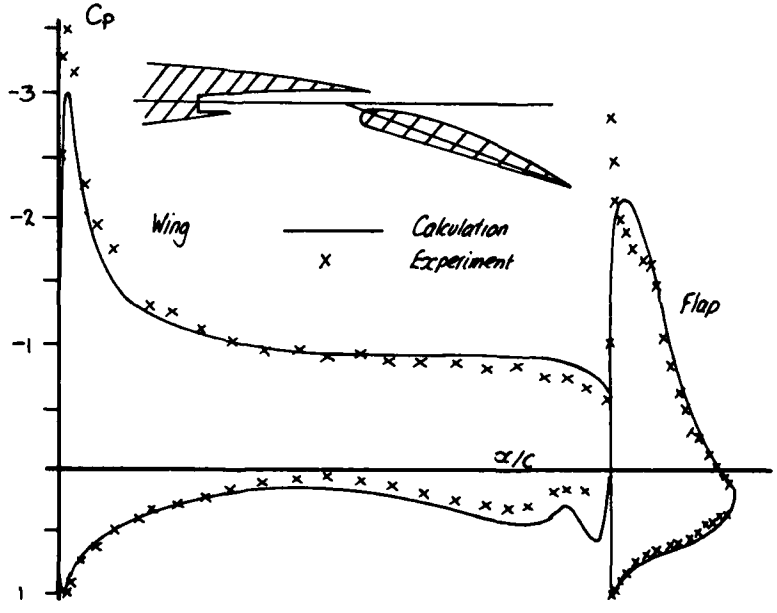


Figure 36 Pressure distributions for a two element aerofoil with a cove region under the wing shroud

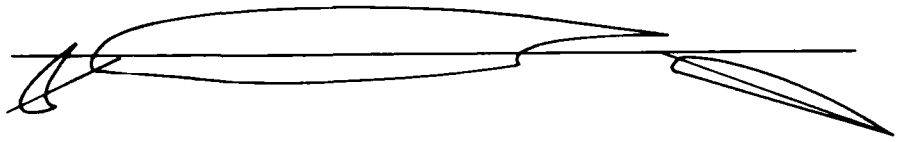


Figure 37 RAE three element aerofoil tested at a Reynolds number of 3.81×10^6

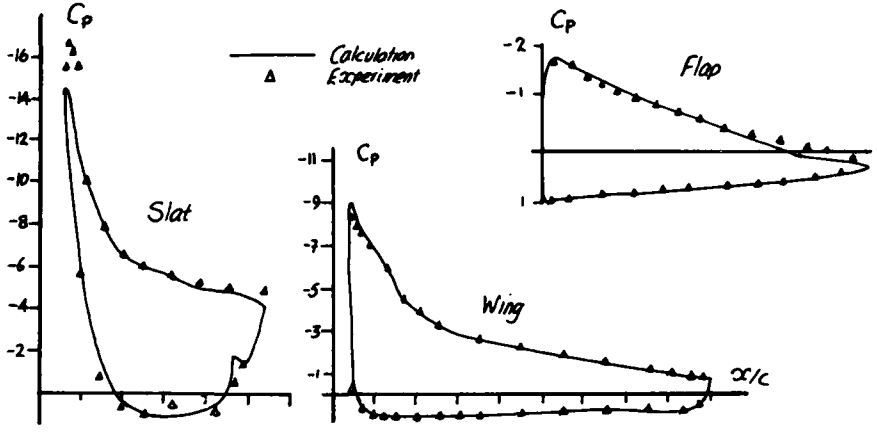


Figure 38 Pressure distributions for the RAE three element aerofoil at an incidence of 20 degrees

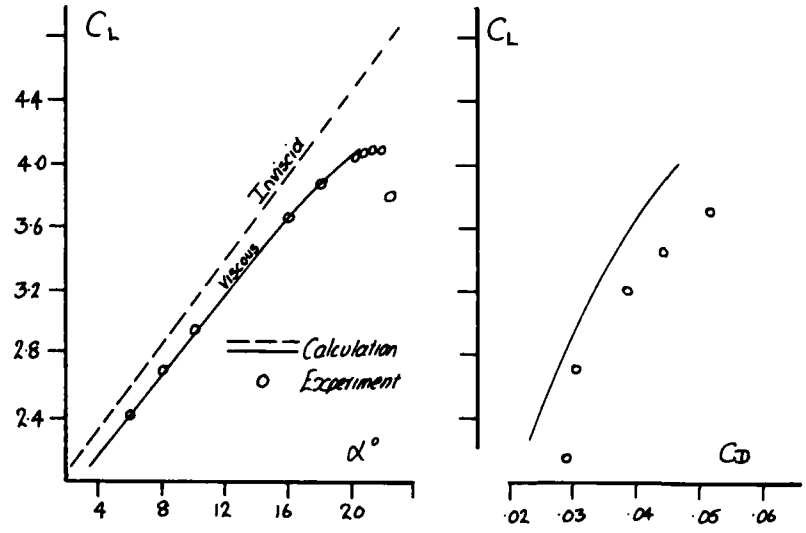


Figure 39 Comparison of the experimental and theoretical lift and drag characteristics of the RAE three element aerofoil



Figure 40 ONERA three element aerofoil tested at a Reynolds number of 1.8×10^6

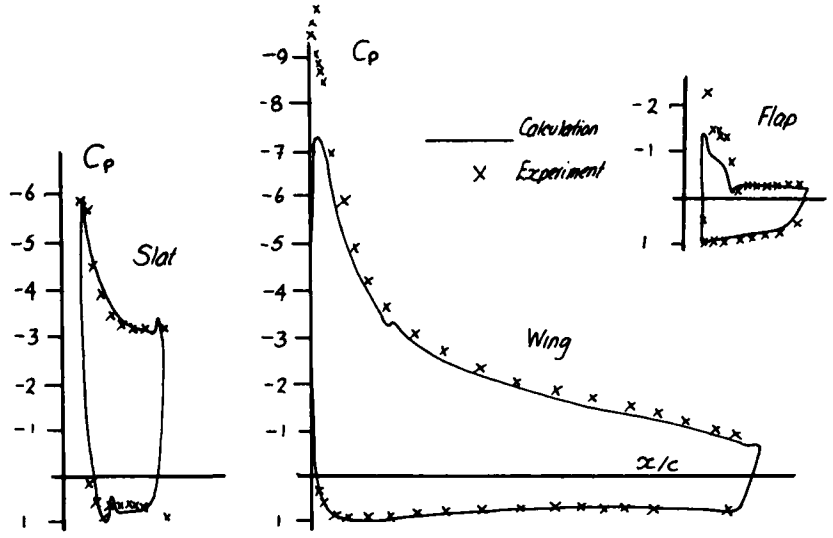


Figure 41 Pressure distributions for the ONERA three element aerofoil at an incidence of 16 degrees

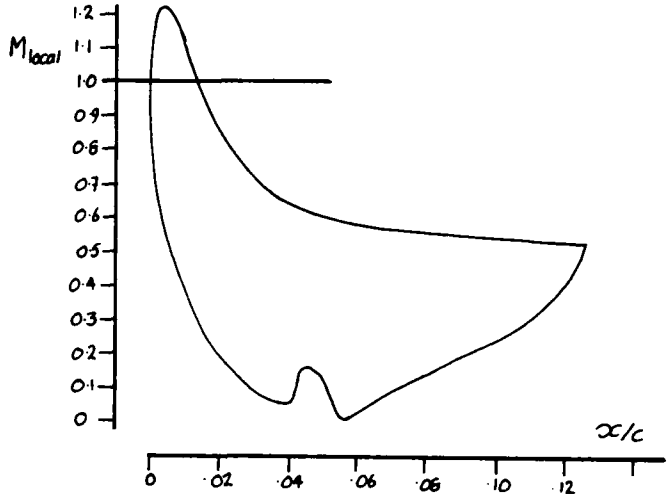


Figure 42 Typical Mach number distribution on a slat of a high lift aerofoil

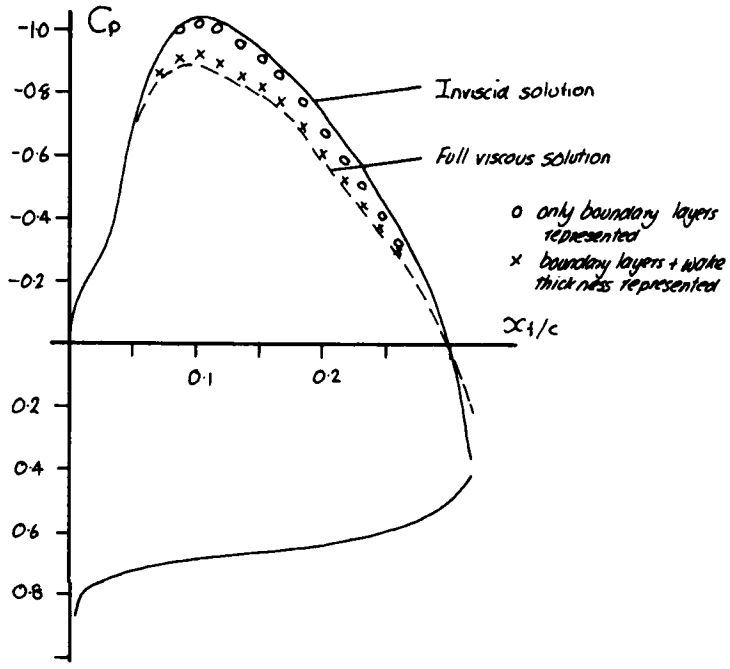


Figure 43 Effect of representing the viscous layers on the calculation of the flap pressure distribution of a two element aerofoil

No. of elements	Angle of incidence	Profile drag Wake traverse	Profile drag Squire and Young
2	0	0.0135	0.0145
2	4	0.0178	0.0189
2	9	0.0310	0.0299
4	17	0.0747	0.0761
4	17	0.0747	0.0725
4	18.5	0.0812	0.0798
5	15	0.0849	0.0810
5	17	0.0922	0.0991

Figure 44 Comparison of the predicted and measured drag coefficients for several multi-element aerofoils

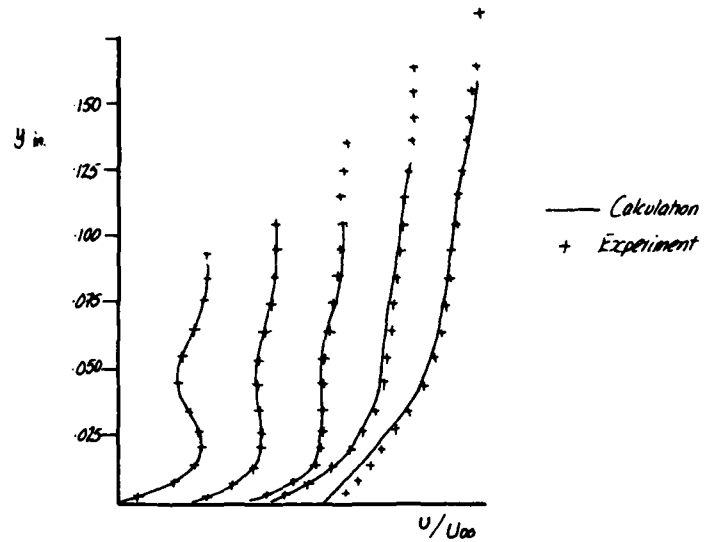


Figure 45 Prediction of the confluent wake and boundary layer using a method of solution including a Reynolds stress turbulence model

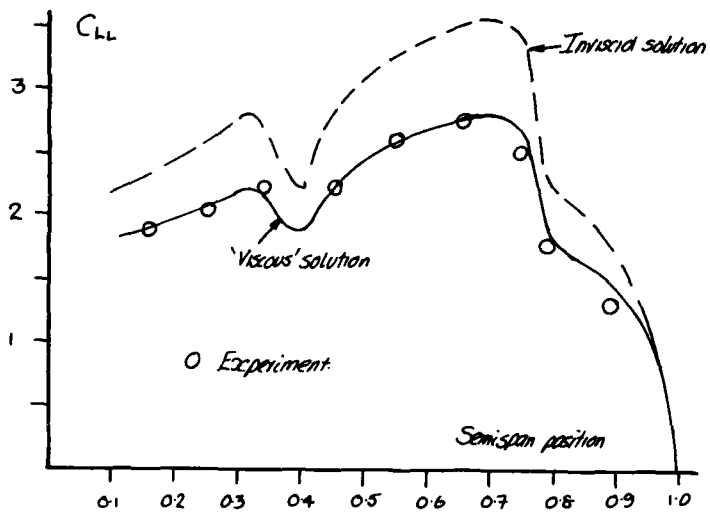


Figure 46 Comparison of the Boeing method for the prediction of the spanwise lift distribution of a transport aircraft wing

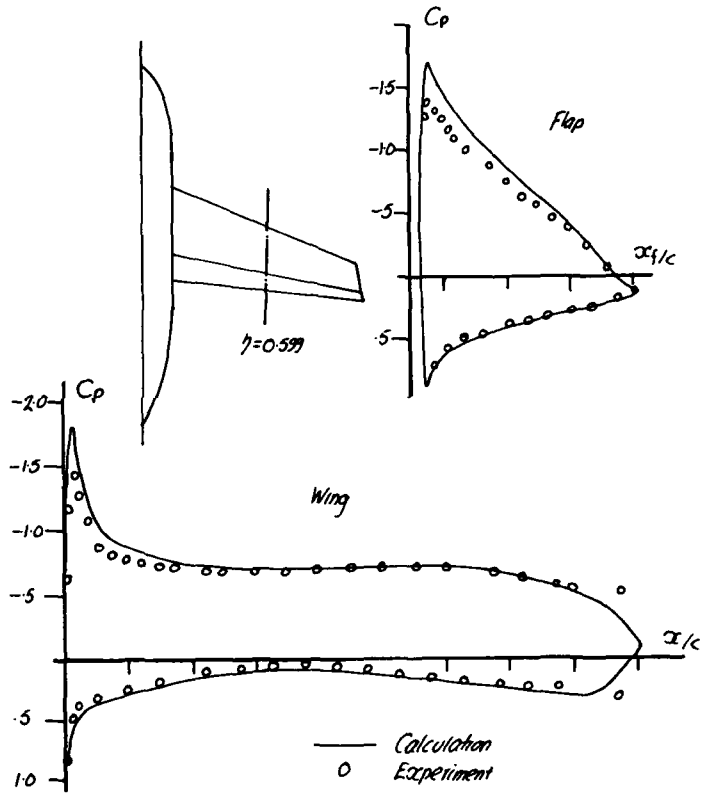


Figure 47 Comparison of the experimental and calculated pressure distribution for a high lift wing at 0.5 degrees incidence

INVESTIGATIONS INTO THE EFFECTS OF SCALE AND COMPRESSIBILITY ON LIFT AND DRAG IN THE RAE 5m PRESSURISED LOW-SPEED WIND TUNNEL

by

S. P. Fiddes, D. A. Kirby, D. S. Woodward and D. H. Peckham
Aerodynamics Department
Royal Aircraft Establishment
Farnborough
Hampshire
GU14 6TD
United Kingdom

AD-P004 053

SUMMARY

A survey is presented of results obtained from experiments in the RAE 5m low-speed pressurised wind tunnel. The tunnel is capable of operation over a range of pressures (from one to three atmospheres) so that the effects of Mach and Reynolds number may be separated. This decoupling of scale and compressibility effects has made possible reliable extrapolation of test results to full-scale conditions (where this is necessary) as well as giving greater insight into the underlying flow mechanisms. The large size of the tunnel, combined with pressurisation to three atmospheres, has enabled some tests, on small combat/trainer aircraft and on bomb-like stores, to be carried out at full scale.

Three facets of the work of the 5m tunnel are described: work aimed at predicting or improving the high-lift performance of specific aircraft; work of a more fundamental nature concerned particularly with the optimisation of high-lift devices on generalised research models, and work on the drag of stores carried externally on combat aircraft.

1 THE EFFECTS OF REYNOLDS AND MACH NUMBER ON THE MAXIMUM LIFT OF MODELS OF THE HAWK AND A300

1.1 Tests on Hawk

To illustrate the capabilities of the 5m tunnel in the study of the stalling characteristics of specific aircraft we present results from tests of two models. The first, that of the Hawk strike/trainer, is an example of the type of small combat aircraft designed for a high subsonic capability with good manoeuvrability but of sufficiently low wing loading that the required field performance can be achieved by a comparatively simple high-lift system with no leading-edge flaps or slats. The photograph, Fig 1 shows the model mounted in the tunnel on the mechanical balance cart using a main central strut support to carry the loads. The model, which is fully representative of the external shape of the Hawk aircraft, is to a scale of 0.315 and consequently since the tunnel can be pressurised to 3 bars we are able to cover, as Fig 2 shows, the correct Reynolds numbers and Mach numbers appropriate to the stall for the whole of the altitude range at which stalling trials are made on the real aircraft. Development work in the tunnel aimed at improving the high-lift performance and studies of the onset and control of the stall can thus be made under natural transition-free conditions.

For the RAF trainer version of the Hawk, that is with the aircraft in the form it has made world-wide appearances in the Red Arrows, the wing meets the required high-lift capability with a double-slotted flap of the fixed-vane type. The main part of the flap extends from the fuselage side to 65% of the semi span but the vane only extends to 57% of the semi span. Suitable buffet warning and stalling characteristics are obtained by using the combination of a wing fence at 67½% semi span and two sharp-edged breaker strips of 4% semi span centred on 34% and 56% semi span respectively. This combination was developed mainly in flight tests on the prototype aircraft, but with the introduction of the 5m wind tunnel it became possible to study the further development of the aircraft and assess the losses in performance associated with such stall control devices under the controlled test conditions provided by a tunnel where, in addition, the separate effects of variations in Reynolds number and Mach number could be examined. Fig 2 shows the changes in Reynolds number and Mach number with altitude for a constant equivalent stalling speed, ie aircraft weight.

The work on the Hawk model covered a number of flap deflections without and with the undercarriage and tailplane fitted. We present some results for the largest flap deflection, 50 degrees, without undercarriage and tailplane. Fig 3 shows the maximum lift coefficient obtained for several Reynolds number/Mach number combinations for the model with

(a) the standard vane,

(b) the vane extended to the end of the main flaps,

(c) the vane extended and the breaker strips removed.

At a Reynolds number of 5.5×10^6 and a Mach number of 0.2, which is a condition appropriate to flight tests of the stalling characteristics, these progressive changes in the model configuration result in an overall increase of about 0.35 in maximum lift coefficient compared with the value of about 0.25 indicated for the unpressurised

tunnel, Reynolds number = 2.5×10^6, and a value of about 0.4 for a Reynolds number higher than full scale, 7.5×10^6. The reasons for these differences and the noticeable difference in the effect of varying Mach number at constant Reynolds number when the breaker strips are removed, becomes more apparent when the individual lift curves are studied in conjunction with the results of some observations of the onset and spread of the stall made using surface tufts. Fig 4 shows the lift coefficients in the region of $C_{L_{max}}$ for varying Reynolds number at a constant Mach number of 0.2 and for varying Mach number at a constant Reynolds number of 5.5×10^6, with and without the breaker strips fitted for the extended vane configuration. When the breaker strips are fitted the variation of $C_{L_{max}}$ with Reynolds number or Mach number is comparatively small and this is consistent with the tuft observations which showed that the breaker strips ensured that flow separation started on the inboard wing at the leading edge at a similar incidence for the various Reynolds number/Mach number combinations. As the angle of incidence was increased the area of separation extended to join up with a further flow separation starting inboard of the fence and the maximum lift coefficient was, except at the lowest Reynolds number, determined by the incidence at which the whole of the wing inboard of the fence was stalled, the flow still being attached on the outboard wing. Only for the lowest Reynolds number, 2.7×10^6, did the outboard wing stall before the inboard indicating that for smaller models in unpressurised wind tunnels the results could be very misleading if used to predict the likely full-scale stalling characteristics.

However, when the breaker strips were removed flow separations on the inboard wing were confined to a small area adjacent to the fence and the maximum lift coefficient was determined by the angle of incidence at which the wing outboard of the fence stalled. Compared with the gradual loss of lift curve slope prior to the incidence for maximum lift coefficient measured for the breaker strips on configuration there was with the breaker strips removed often a very sharp loss of lift as the whole of an outboard wing stalled. This was more noticeable at the lower Mach numbers where the whole outboard wing stalled so suddenly that it was difficult to detect from simple tuft observations where on the wing the flow separation started. At the higher Mach numbers there was evidence of separation at the trailing edge, which resulted in a reduced circulation round the outer wing sections and a more rounded lift curve near the maximum lift coefficient. It is evident that this stall of the outboard wing and consequently the achieved maximum lift is very sensitive to Reynolds number and Mach number variation and that when attempting to develop this type of aircraft by means of model tests to obtain the best high-lift performance compatible with an adequate stall control it is essential that the work be done at full-scale Reynolds number. Furthermore the effects of Reynolds number and Mach number variations need to be determined both to assist in the development and in the understanding of subsequent flight data since the Reynolds number and Mach number at the stall vary considerably with altitude and ambient temperature.

1.2 Tests on A300

The work on the model of the Hawk showed substantial reductions in maximum lift coefficient with increase of free-stream Mach number when the greater lifting potential of the wing was released by removing the breaker strips, a behaviour that is consistent with the achievement of supersonic flow in regions near the wing leading edge. This phenomenon has been examined more closely in tests made on our 1/13th scale model of the A300 airbus, shown in Fig 5 mounted on a sting rig in the 5m tunnel. For this civil transport aircraft the high-lift capability is provided by an extending double-slotted flap and a leading-edge slat. The effect of varying the Reynolds number and Mach number on the maximum lift coefficient for a leading flap configuration is shown in Fig 6. As for the Hawk the effects of increasing Reynolds number and of increasing Mach number are in opposition and the chain-dotted line on the left of the figure demonstrates the misleading information on the variation of the maximum lift coefficient which is obtained in an unpressurised tunnel if an increase of wind speed is used to increase Reynolds number and the Mach number effects are ignored.

In order to advance our understanding of the various effects we have made detailed measurements of the surface pressures on the wing of the A300 model. Analysis of the results showed that there was a marked reduction in the peak suction coefficient recorded as the free-stream Mach number was increased above about 0.25. Fig 7 shows for a constant Reynolds number of 4.9 million the variation in maximum lift coefficient with Mach number and beneath it the peak suction coefficient developed on the wing at two of the outer wing stations for which pressure measurements are available for the A300 model. The Figure also shows the suction coefficients needed to achieve various Mach numbers, sonic and above, as the free-stream Mach number is increased.

For the lower free-stream Mach numbers the peak suction coefficient is nearly constant, as was the maximum lift coefficient, but as the free-stream Mach number is increased beyond about M = 0.22 the peak suctions measured indicate that locally sonic speed has been achieved near the wing leading edge and that speeds as high as $M_{local} = 1.2$ are achieved before the peak suction coefficient, and consequently the maximum lift coefficient fall more sharply with increase of free-stream Mach number. This fall does not occur because of anything dramatic such as a shock-induced separation of the flow, but rather because of the influence of thickened boundary layers affecting the flow further aft on the wing and causing a degradation of the flap performance and hence a reduction in the circulation round the wing sections affected. For the

A300, as for the Hawk, at the higher free-stream Mach numbers the increasing loss of lift as this degradation spread spanwise with increasing angle of incidence determined the maximum lift achieved on the model.

The outboard wing is affected first by this phenomenon because the section lift coefficients are higher over the outer region of a swept back tapered wing. To meet the requirements of the Airworthiness authorities in the certification of transport aircraft it is usually necessary to arrange for the inner wing to stall first with a margin in angle of incidence before the outer wing stalls. Such margins could be substantially eroded by the Mach number effects discussed above and it is therefore advantageous to be able to use a pressurised wind tunnel such as the 5m to identify the separate effects of variations in Reynolds number and Mach number on the stall. This should be done at the early design stage of a new aircraft in order to be able to minimise the performance losses implicit in ensuring the necessary stall margins.

2 THE EFFECTS OF REYNOLDS AND MACH NUMBER ON THE OPTIMUM LOW SPEED PERFORMANCE OF MECHANICAL HIGH-LIFT SYSTEMS

2.1 Background

The design of low-speed high-lift devices for modern transport or combat aircaft is usually constrained by other performance requirements. The wing planform and aerofoil shape, etc, are determined by cruise and manoeuvre conditions, and the designer must develop an efficient high-lift system within these constraints. However, for mechanical high-lift systems the designer has some choice in where to deploy, say, a slat, in terms of its position relative to the main wing and its deflection angle. An obvious design aim is to position the slat where the complete high-lift system develops its maximum lift, or produces minimum drag for a given lift. That such an 'optimum position' exists is the result of at least two competing effects.

As the components of a high lift system (slat, wing and flap) are moved closer together, their mutual aerodynamic interference shares the loading between them in a way that tends either to lower trailing-edge pressures, or decrease suction peaks. This reduces adverse pressure gradients. Furthermore, the 'dumping' of the trailing edge flow from an upstream element into the low pressure region on the upper surface of an adjacent downstream element enables the overall pressure recovery, from slat suction peak to flap trailing edge, to be achieved in a number of steps. This cascade effect allows high suction levels to be achieved, and therefore greater lift, without increasing the likelihood of separation on each element (see Ref 1). However, the suction levels are so great that compressibility effects become important - indeed, a limiting suction level may be reached. Also, by bringing the elements closer together, the wake from an upstream element can impinge upon the boundary layer of a downstream element, and possibly thicken it[2]. The thicker, merged boundary layer is less likely to withstand adverse pressure gradients than an unmerged one, and separation can occur earlier.

The competing effects of favourable inviscid interaction (ultimately limited by compressibility effects) and adverse viscous effects (contamination of downstream boundary layers by upstream wakes) lead to the existence of an optimum position for each element of a mechanical high-lift system; not so close that viscous merging thickens the shear layers too much, or so far apart that the mutual inviscid interaction is too weak. Because of the importance of viscous and compressibility effects in determining the optimum geometry, the optimum can be strongly Reynolds and Mach number dependent.

2.2 Description of models

Results have already been presented for the effects of Reynolds and Mach number on a fixed geometry; the A300 research model. These illustrate generally improved performance with increasing Reynolds number, and the adverse effects of increasing Mach number. In this section, the freedom to change the geometry of the high-lift system on two more general research models is exploited. Results will be presented for RAE Model 477, which has a relatively low sweep (32.5 degrees at the leading edge), aspect ratio 7 transport wing, and for RAE Model 495, a combat aircraft model with a leading edge sweep of 40 degrees, and aspect ratio 3.4. These models are illustrated in Figs 8 to 11. Both models were fitted with a fixed trailing-edge flap, and a movable slat whose position was defined within a 'box' of lap and gap positions, as shown in Fig 14. The slats were positioned to give a constant sectional shape across the wing. Thus the slat position could be described in terms of the relative position of the slat trailing edge, in percentage chord, and its angular rotation from the undeployed position. The models were tested over a range of Reynolds and Mach number, as shown in Fig 12 and 13. For each slat position, within the 'box', the maximum lift coefficient for a given Reynolds and Mach number, from the test conditions, was found.

2.3 Results from Model 477

Fig 15 shows some of the results obtained with Model 477, at a Reynolds number of 5.4 million, and a Mach number of 0.16. The results of the maximum lift tests are shown as a contour plot of maximum achieved lift against slat position. As can be seen, the optimum position for this combination of Reynolds and Mach number lies near the centre of the 'box', at a gap of 2% and a lap of -1.5%. The contours are drawn as percentages of the 'optimum' lift coefficient. It is seen that small changes in slat position away

from the optimum position can produce appreciable reductions in the maximum lift. With the ability of the 5m tunnel to be pressurised, such contour plots can be obtained at a number of Reynolds and Mach numbers, and the optimum position of the slat found for each condition. Fig 16 shows the movement of the optimum position of the slat as the Reynolds number is increased at fixed Mach number and vice versa. As the Reynolds number increases, the slat moves nearer the main wing. This is consistent with the idea that the thinner shear layers at the higher Reynolds numbers allow the slat to be closer to the wing before adverse wake/boundary layer interaction takes place. It should be noted that the optimum position of the slat for the lowest Reynolds number tested lies outside the 'box'. The optimum position and corresponding maximum lift has been obtained by extrapolation of the results from within the 'box' for this case.

As the results for the A300 model show, the effects of Mach number variations on low-speed high-lift flows can be large, even though the free-stream Mach number is only about 0.2 to 0.3. The suction levels associated with high-lift are very great, and the flow can be accelerated to locally supersonic speeds. Fig 17 shows, for a fixed Reynolds number of 3.3 million, the variation of $C_{L_{max}}$ with Mach number, and, at a fixed Mach number of 0.16, the Reynolds number variation of $C_{L_{max}}$. It is seen that increasing the Mach number above about 0.2 has a strongly adverse effect on the maximum lift. Fig 18 shows a typical pressure distribution measured on Model 477. Note that the suction levels on the slat are high enough for the flow to be locally supersonic over part of it. This is the source of the adverse Mach number effects. The slat suction levels can be reduced by moving the slat away from the main wing, partially alleviating the compressibility effects, but only at the expense of raising the suction peak on the main wing, until the main wing suffers from compressibility effects or premature separation.

The movement of the optimum slat position for increasing Mach number is shown in Fig 16. As expected, increasing the Mach number moves the optimum position away from the main wing.

To analyse these results a little further, we pose the following question; what is the penalty, in terms of maximum lift, for operating at an off-optimum position? To make this question more precise, consider the real problem facing the designer of a low-speed high-lift system. It is possible for him to conduct model tests, typically at atmospheric pressure, to find the optimum slat position for the corresponding (low) Reynolds number. If the high-lift system is to be used on a full-scale aircraft, then there will be some gain in maximum lift from operating the same configuration at a higher Reynolds number, even with the slat in the low R optimum position. But what is the further gain to be had by moving the slat to the optimum for the new, higher Reynolds number? Furthermore, where is the optimum postion for the high R case? With some models (eg the Hawk trainer) it is possible to achieve full-scale Reynolds number in the 5m tunnel and answer this question directly. However, with most transport models there is a shortfall in Reynolds number achievable in the 5m tunnel (a factor of 4 for the A300 model) and so some extrapolation is required. The ability of the 5m tunnel to obtain a range of Reynolds number at fixed Mach number allows us to perform this extrapolation with some confidence.

Fig 19 illustrates the potential gain of operating at an optimum condition appropriate to higher Reynolds numbers. The lower line shows the increase in maximum lift with increasing Reynolds number for a slat fixed in a position that is optimum at the lower R . In fact this is the optimum for Model 477 at atmospheric pressure. upper curve shows the increase in maximum lift obtained by increasing the Reynolds number and re-optimising the slat position at each Reynolds number. The fixed slat shows a 7% gain in maximum lift over the Reynolds number range shown, while a further 3% increase is possible by re-optimising the slat for higher Reynolds numbers.

2.4 Results from Model 495

The results described above have been obtained from RAE Model 477. Model 495 has a lower aspect ratio and greater leading-edge sweep. This produces relatively higher suction levels on the forward part of the outboard wing, and it is the stall on this part of the wing that determines the maximum lift. The increased suction levels near the tip are shown in Fig 20, which compares pressures measured on the outboard part of the wing with those measured inboard. A slat optimisation exercise, similar to that conducted using Model 477, has been performed with Model 495, with some important differences in the results. First, the slat deflections needed were higher. For Model 477 a slat deflection, measured normal to the leading edge, of 25 degrees was found to produce a stall of the slat and wing together. With Model 495, a 25 degree slat stalled much earlier than the main wing, and a 45 degree deflection was needed to bring the stalls closer together. The optimum position of the slat was not as sharply defined as on Model 477, as the contour plot in Fig 21 shows. Only a 3% drop in maximum lift was found over the entire 'box' of slat positions. However, the optimum position is much lower, relative to the main wing, than is the case for the higher aspect ratio Model 477.

The effect of Reynolds number variation on the maximum lift performance was not very great. Fig 22 shows the lift-incidence curve for three Reynolds numbers. As the Reynolds number is increased the maximum lift increases - but only slightly (less than 2%). By contrast, the effects of increasing Mach number are very marked, as Fig 23 shows. Increasing the Mach number from 0.16 to 0.28 at a fixed Reynolds number produced

a stall that occurred some 5 degrees earlier, and a reduction in maximum lift of over 4%. These strong Mach number effects can be anticipated from Fig 20, which shows that at a free-stream Mach number of 0.22, both the slat and main wing have locally supercritical flow.

2.5 Discussion

Some insight into the effects of Mach number on the low-speed high-lift flows considered here can be gleaned by considering the expression for the local Mach number on the wing, based on the velocity component normal to a spanwise generator (ie a line of constant x/c for the simply tapered wings considered here). If the sweep of such a line is Λ, then the critical pressure coefficient, C_p^* at which the local 'normal' Mach number is unity is given by:

$$C_p^* = \frac{2}{\gamma M^2}\left[\left(\frac{2}{\gamma+1} + \left(\frac{\gamma-1}{\gamma+1}\right) M^2 \cos^2\Lambda\right)^{\frac{\gamma}{\gamma-1}} - 1\right] \quad . \tag{1}$$

Expanding this expression for small M (which is less than 0.3 for the flows considered here) gives:

$$C_p^* = \left(\left(\frac{2}{\gamma+1}\right)^{\frac{\gamma}{\gamma-1}} - 1\right)\frac{2}{\gamma M^2} + \left(\frac{2}{\gamma+1}\right)^{\frac{\gamma}{\gamma-1}} \cos^2\Lambda + O(M^2 \cos^4\Lambda) \quad . \tag{2}$$

With $\gamma = 1.4$, this becomes:

$$C_p^* \approx -\frac{0.6739}{M^2} + 0.5283 \cos^2\Lambda \quad . \tag{3}$$

This immediately reveals two things:

(i) That C_p^* varies rapidly with free-stream Mach number for low values of M.

(ii) That sweep does not greatly alleviate compressibility effects at low Mach numbers. The second term in equation (3) does not give a great gain in critical pressure coefficient. Raising the sweep from 0 degree to 60 degrees only raises the critical Mach number from, say, 0.280 to 0.287.

If the performance of one of the components of a high-lift system is limited by a maximum achievable Mach number (as the previously described results for the A300 seem to suggest), then equation (3) shows that the product $M^2 C_{p_{min}}$ reaches a limiting value dependent upon the limiting Mach number. Smith, in Ref 3, reports the results of Mayer, who, by examining a wide range of aerofoil results (nearly all at much higher Mach numbers than considered here), found that $M^2 C_{p_{min}} = -1$ was an apparently limiting value for single element aerofoils. Examining our results from Model 495, this limit seems to apply to multi-element wings as well, although the apparent limit on Model 477 is somewhat lower, nearer 0.85.

Examining the product $M^2 C_{p_{min}}$ is thus a rapid way of determining whether a compressibility limit or 'cap' has been reached in the lifting performance of a high-lift wing. Whether Mayer's limit of -1 is reached depends upon whether viscous effects produce separation before the limiting suction level is reached, ie at low Mach numbers, say below 0.2 here, the minimum C_p is limited by viscous effects, and as the Mach number increases $C_{p_{min}}$ is 'capped' by compressibility effects. An important conclusion from this is that the specification of take off or landing Mach number is as important in determining the high-lift performance as specifying the corresponding Reynolds number.

3 THE EFFECTS OF REYNOLDS NUMBER ON THE FORCES ACTING ON ISOLATED STORES

3.1 Introduction

Modern combat aircraft generally carry stores externally, permitting greater operational flexibility and more extensive loads. The presence of external stores can, however, greatly affect an aircraft's performance. As noted by Pugh and Sadler[4], strike radius can be reduced by 25% and maximum sustainable 'g' can be reduced by 50%, due to the incremental drag of the external stores, which can for underwing stores carriage be significantly greater than the zero-lift drag of the clean carrier aircraft.

It would be a time-consuming and expensive task to measure the incremental drags of all possible weapon combinations for each aircraft, and in any case estimates of the effect of a weapons fit on aircraft performance are often needed on a shorter time-scale than a wind tunnel test can be arranged. Thus one often has to rely on semi-empirical prediction methods[5] to estimate the incremental drag of external stores on aircraft, but

such methods are dependent on an accurate knowledge of the aerodynamics of individual stores in free air. This is because the drag of a single store is amplified by mutual interference with other stores nearby, so that the isolated drag of a store assembly is greater than the sum of its components, and in turn the drag of such a store assembly is further increased by aerodynamic interference with the parent aircraft when installed in the carriage position. Thus any initial uncertainty in isolated-store drag can be considerably magnified in the prediction of the installed drag of a group of stores.

The aerodynamic properties of isolated stores for use with existing prediction methods are required over a wide range of both Mach number and Reynolds number. Data over the Mach number range $0.4 < M < 1.4$ is generally obtained from models, where $\frac{1}{4}$ scale is probably the largest feasible scale because of constraints on tunnel size. Such data can be deficient in two respects. Firstly, in general, no systematic measurements are carried out to obtain the effects of Reynolds number, and maximum Reynolds number is usually only about $\frac{1}{4}$ of the full-scale value for flight at low altitudes. Secondly, most stores (with the possible exception of fuel tanks) are far from aerodynamically clean and exhibit many excrescences; even with models as large as $\frac{1}{4}$-scale there remains some uncertainty as to how well excrescences can be represented.

With the availability of the 5m pressurised low-speed wind tunnel[6] there arose the possibility of testing real stores, albeit at low speed, but over a range of Reynolds number representing full-scale values for low-level flight up to sonic Mach number. Also, results from such tests, when compared with those at low-speed from scale-model tests would permit an assessment of the fidelity of representation of the scale models and the efficacy of the method used for transition-fixing, and provide details of Reynolds number effects independent of compressibility effects.

Thus a rig suitable for testing full-scale stores in the 5m wind tunnel has been constructed, along the lines of a similar rig in use at ARA Ltd[7] (Fig 24) which is used for testing isolated stores up to $\frac{1}{4}$-scale.

3.2 Rig details

The full-scale stores rig is shown in Fig 25. The pylon is as near as possible a full-scale representation of the general-purpose pylon used on the ARA $\frac{1}{4}$-scale rig, and has a chord of 1.5 m, a depth of 0.368 m and a thickness/chord ratio of 8.3% (to accommodate the force balance it was necessary to increase pylon thickness/chord ratio to 8.3% from the 6.8% of the $\frac{1}{4}$-scale rig). At present the rig design is such that the pylon is earthed, but simple design changes would allow the pylon to be mounted live to the balance, if required.

The support tube is 0.152 m in diameter and extends some 3.5 m ahead of the foremost extremity of the pylon, such that velocity perturbations induced by the nose profile have decayed sensibly to zero before the foremost store is reached. The 15 degree sting crank between the tunnel sting and the support tube ensures that for typical single stores the store axis coincides with the tunnel centreline at zero angle of incidence, and that sideslip can be achieved with modest roll angles.

Use is being made of an existing 6-component strain-gauge balance, and this is situated in a housing within the lower part of the pylon in order to minimise rolling moment. The maximum permitted loads for this 3 in balance are as follows:

Channel	Load (SI units)	Load (Imperial units)
Normal force (Z)	15.57 kN	3500 lb
Pitching moment (M)	2.71 kN m	2000 lb ft
Side force (Y)	3.11 kN	700 lb
Yawing moment (N)	0.73 kN m	540 lb ft
Rolling moment (L)	0.73 kN m	540 lb ft
Axial force (X)	1.18 kN	265 lb

The balance incorporates weapon-attachment points at standard 0.355 m (14 inch) centres. The method of attachment of weapon to balance can be either bail-lug with fore-and-aft crutching arms, or MACE (minimum area crutchless ejector). When bail-lug mounting is used, the crutching arms are similar in design to those associated with the commonly used No. 119 Mk 1 ejector release unit. With the full-scale stores no artificial boundary layer transition devices were used.

3.3 Test details

At $\frac{1}{4}$-scale, ten configurations were chosen to be tested in order to provide representative coverage of most types of single stores, and some assemblies on carriers. The configurations chosen were:

a triple carrier loaded with 1000 lb bombs;
an air-to-ground guided weapon;
a bluff bomb;
bombs type A, B and C;
a designator pod;
two bombs on a tandem beam mount;
a rocket launcher;
an air-to-air guided weapon.

Boundary layer transition was fixed on these ¼-scale models, and the pylon, using narrow bands of sparsely distributed ballotini, of diameter 0.117 mm to 0.137 mm, set in a thin film of adhesive. Napthalene sublimation tests were performed to confirm transition at the roughness bands.

Four real full-scale stores were tested, two of which had been tested at ¼-scale:

Bomb type A
A rocket launcher
Bombs type D and E

The wind tunnel test conditions, shown in Fig 26, covered the Mach number range 0.2 to 0.34 and a Reynolds number range 4.7×10^6/m to 17.7×10^6/m. This Reynolds number range for the full-scale stores is equivalent to that of sea-level flight from a Mach number of 0.2 upwards to a Mach number of 1.0. Test conditions were arranged to give data at a constant Reynolds number of 11×10^6/m over the Mach number range, and at a constant Mach number of 0.275 over the Reynolds number range.

The drag results for the full-scale stores were corrected for tunnel blockage constraint and wake blockage buoyancy on the basis of Garner et al[8]. The magnitude of the correction to drag due to these effects amounted to about 1%. In the case of the ¼-scale stores corrections to drag values were found to be negligible.

3.4 Results and discussion

Fig 27 shows the measured drags of the ¼-scale stores plotted against Mach number, for approximately the same Reynolds number (11×10^6/m in the 5m tunnel; 13.1×10^6/m in the ARA tunnel). With the exception of one configuration, there is very good agreement between the data from the earlier ARA measurements and the measurements in the 5m tunnel. No suitable explanation for the drag difference in this one case has been found. On some of the lower-drag stores there is little or no increase in drag coefficient with Mach number, at constant Reynolds number; on most stores, however, there is a tendency for drag coefficient to increase with Mach number.

Fig 28 shows the measured drags of the ¼-scale stores plotted against Reynolds number, for the three test Mach numbers of 0.20, 0.275 and 0.34. The most striking aspect of these results is that most of the ¼-scale stores exhibit no significant variation of drag over more than a 3:1 range of Reynolds number, whereas the predicted variation of skin-friction drag indicates that about a 15% reduction might have been expected. In two cases, there are significant drag changes with Reynolds number in which a minimum-drag situation occurs; both these cases are for bluff-nosed stores and it is thought that the drag changes may be associated with variations of the size of a nose separation bubble. The only store configuration which exhibited a reduction in drag with increasing Reynolds number, more or less in line with the predicted reduction of skin-friction drag, was the 2-bomb tandem beam assembly.

It is thought that the lack of drag variation exhibited by several of the ¼-scale stores may, at least in part, be because of the roughness transition bands used, which remained unchanged during the tests. Thus as Reynolds number was increased it is possible that the drag contribution from the 'over-sized' transition material may have masked any fall in skin-friction drag level due to Reynolds number effects. Also, the excrescences on the stores were correctly scaled geometrically, with the result that they would have been immersed in relatively thick boundary layers at low Reynolds number but thinner boundary layers as Reynolds number was increased; here again, this effect would tend to mask any fall in the level of skin-friction drag.

For the full-scale stores (Figs 29 and 30), all drag values fall consistently with increasing Reynolds number as would be expected, by up to 12% over the range of Reynolds number covered. In all cases, free-air drag increases gradually with Mach number over the range $0.2 < M < 0.34$ by up to about 3%. Unfortunately, there are only two cases where direct comparisons can be made between ¼-scale and full-scale tests. For the bomb type B, drag values scaled from the ¼-scale tests are in excellent agreement with the full-scale measurements. For the rocket launcher however, the full-scale drag appears to be about 5% higher; however, there were some differences in pylon geometry between the two cases and it is possible that the results were affected by differing pylon/store interference effects.

The overall conclusion from comparison of the measurements for full-scale and ¼-scale and stores is that the trends observed at full-scale are not always evident from tests on small-scale models. Whether these differences are due to difficulties in representation of small details, or because of experimental difficulties inherent in small-scale testing, is not clear from the present tests. However, these findings suggest that extreme care must be exercised in predictions of the installed drag of stores when only data from scale-model tests are available. Clearly it is best to use a full-scale rig for measuring store drag whenever possible. Such a procedure, although more expensive in direct wind tunnel costs, nevertheless can give considerable time and cost savings in that real stores can be used instead of constructing costly models.

4 CONCLUDING REMARKS

This paper has shown that a large, pressurised low-speed wind tunnel is an essential tool for obtaining measurements of lift and drag appropriate to full-scale

conditions, and for obtaining a physical understanding of the separate effects of scale and compressibility.

Tests on a transport model and a strike/trainer model have both shown that maximum lift is very sensitive to Reynolds and Mach number variation, and that a misleading result would have been obtained in an atmospheric tunnel where an increase of Reynolds number is obtained solely by increasing tunnel speed.

An experimental investigation of the factors determining the maximum lift of both a high- and a low-aspect ratio swept wing equipped with high-lift devices has shown that the optimum slat setting can vary appreciably with Reynolds and Mach number. In particular, for the high aspect ratio wing, worthwhile gains in maximum lift are possible by optimising the slat position for conditions as close as possible to those of full scale.

With regard to the drag of bomb-like stores, it is concluded that the trends observed at full scale are not always evident from tests on small-scale models, and it is suggested that extreme care must be exercised in predicting the drag of stores when only data from scale-model tests are available.

REFERENCES

1 A.M.O Smith. Aerodynamics of high-lift systems in "Fluid Dynamics of Aircraft Stalling". AGARD CP 102 (1972).

2 D.N. Foster, H.P.A.H. Irwin and B.R. Williams. The two-dimensional flow around a slotted flap. RAE Technical Report 70164 (1970).

3 A.M.O. Smith. Remarks on the fluid mechanics of the stall in "Aircraft Stalling and Buffeting". AGARD LS 74 (1975).

4 P.G. Pugh and A.J Sadler. Weapon-aircraft interaction: lecture delivered at Cranfield Institute of Technology, September 1980. RAE Technical Memorandum Aero 1859.

5 A.J. Sadler, P.G. Pugh and M.B. Wood. The prediction of the installed drag of stores. Unpublished RAE Report (1980).

6 J.A. Ross and A.J. Sadler. Reynolds number effects on the forces acting on isolated stores: results of tests in the 5m wind tunnel. Unpublished RAE Report.

7 K.J.C. Eyers and P.G. Hutton. Measurements of the isolated drag of various single stores. Unpublished ARA Report.

8 H.C. Garner et al. Subsonic wind tunnel wall corrections. AGARDograph 109.

Copyright © Controller HMSO London, 1984

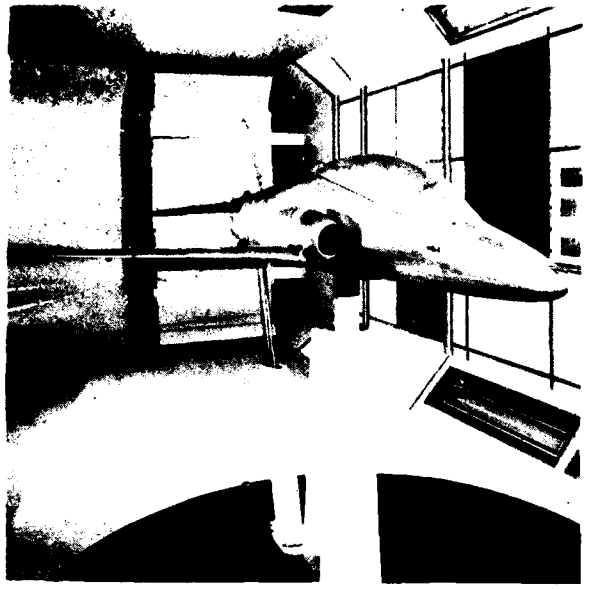


Fig 1 Hawk model in 5 metre tunnel

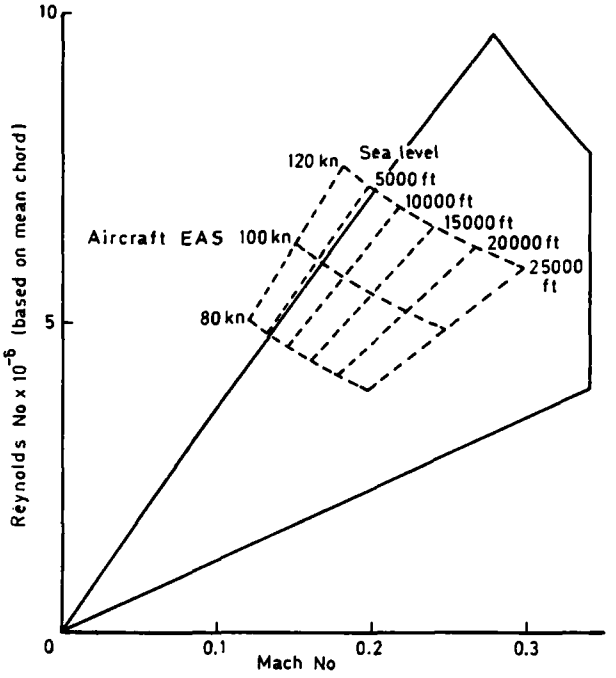


Fig 2 0.315 scale model of Hawk in 5-metre tunnel

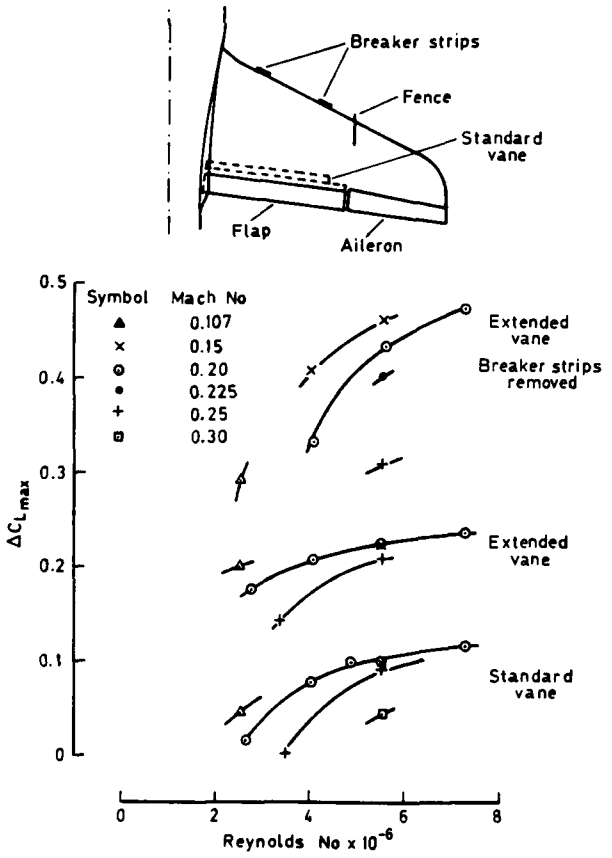


Fig 3 $\Delta C_{L_{max}}$ for Hawk with flaps deflected 50°

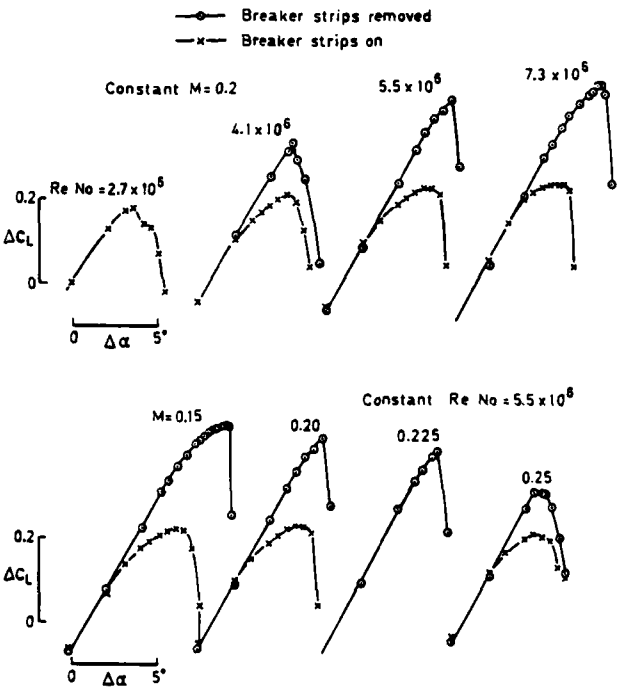


Fig 4 Lift curves near $C_{L_{max}}$ for Hawk with flaps deflected 50°

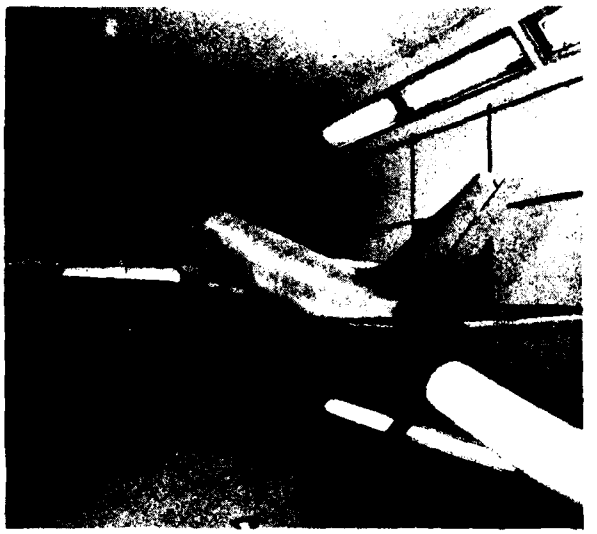


Fig 5 A300 model in 5 metre tunnel

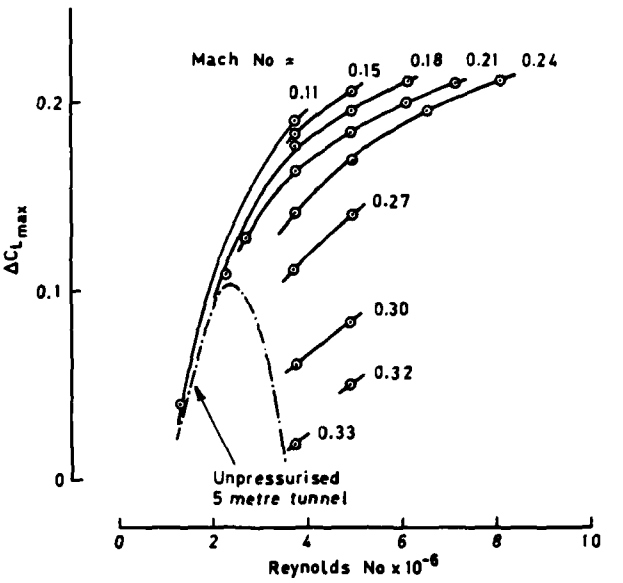
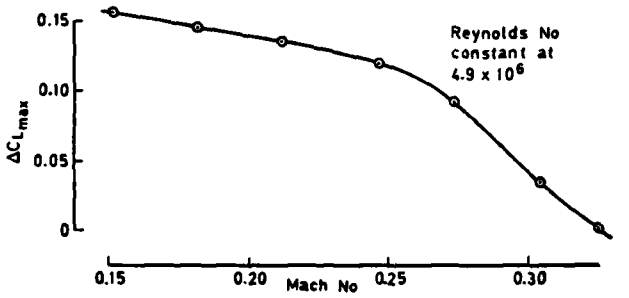


Fig 6 $C_{L_{max}}$ for A300 with flaps deflected 25°



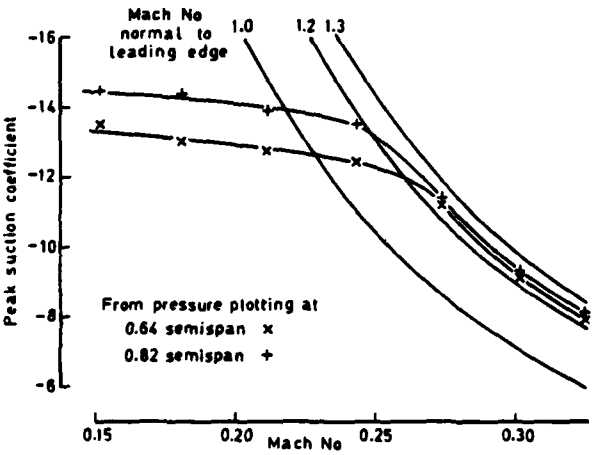
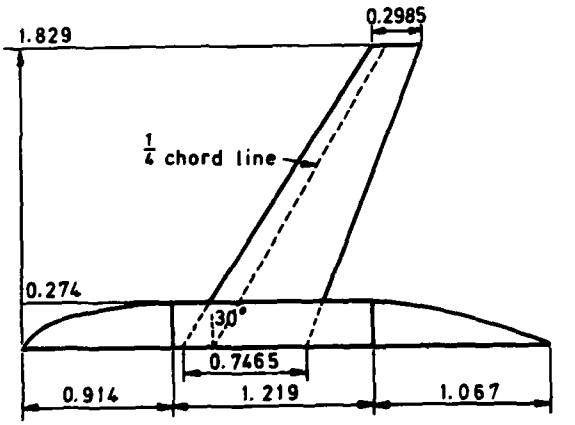


Fig 7 Mach number effects at constant Reynolds number for A300 with flaps deflected 25°



Model 477 Basic planform
All dimensions given in metres

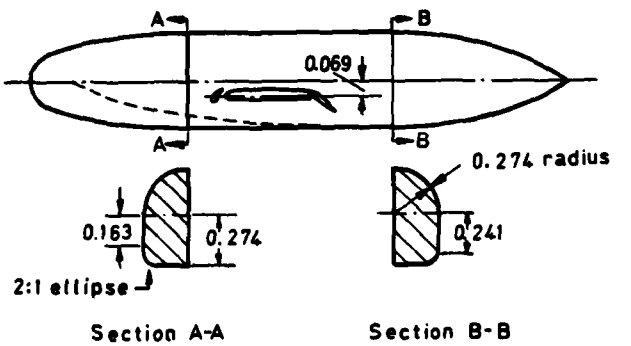


Fig 8 RAE Model 477



Fig 9 RAE model 477

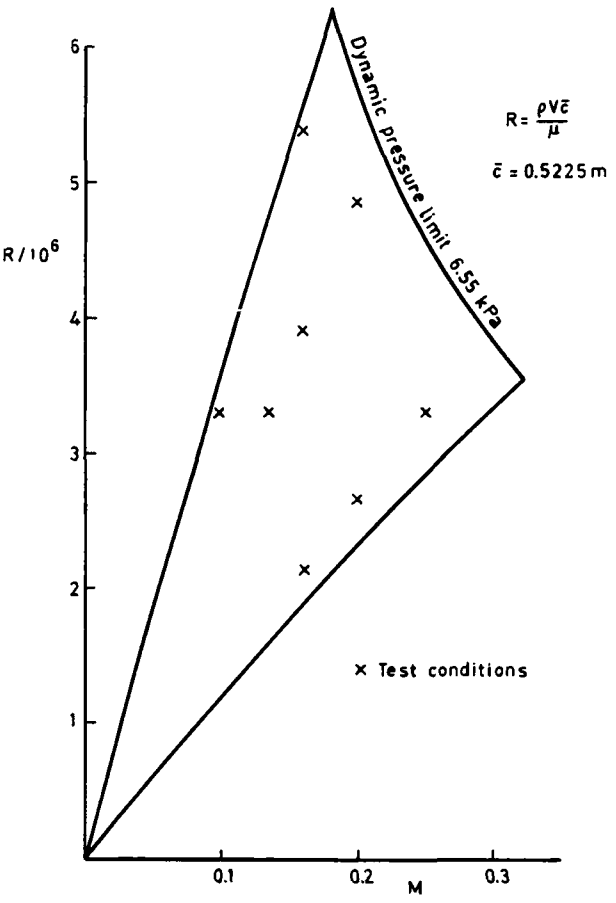


Fig 12 Model 477 tunnel operating envelope

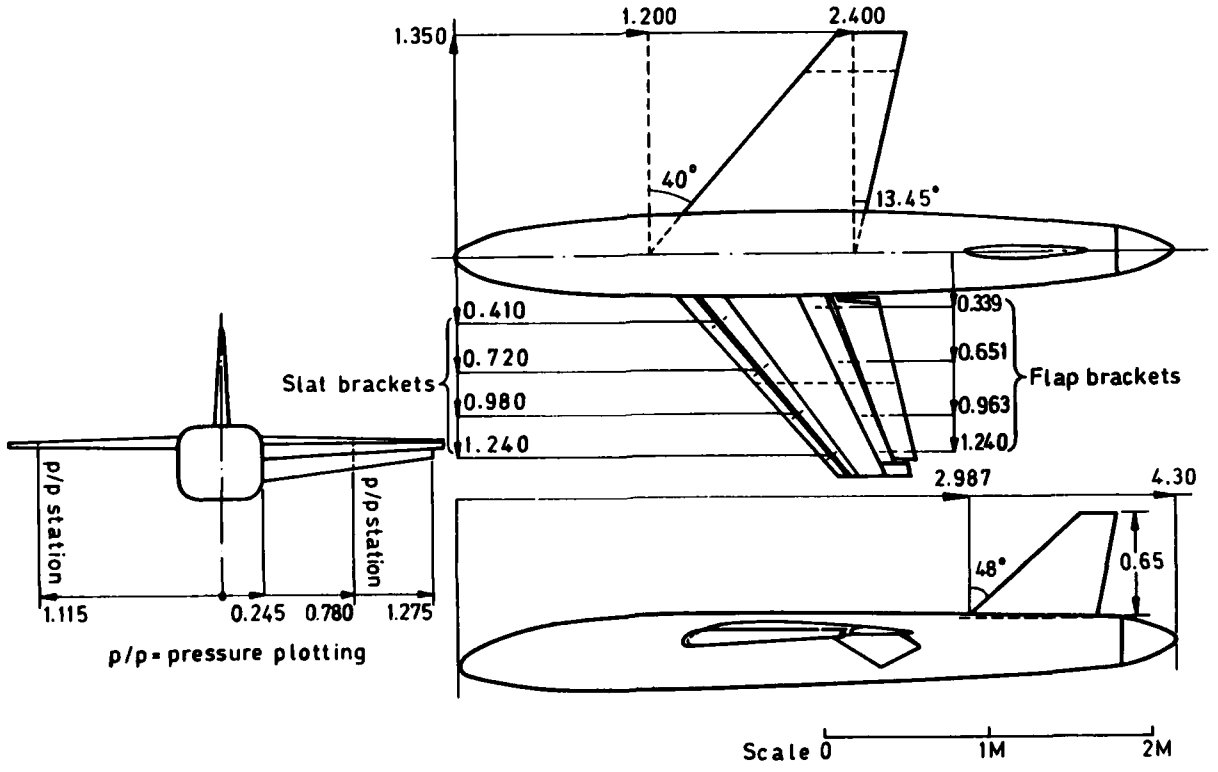


Fig 10 RAE Model 495



Fig 11 RAE model 495

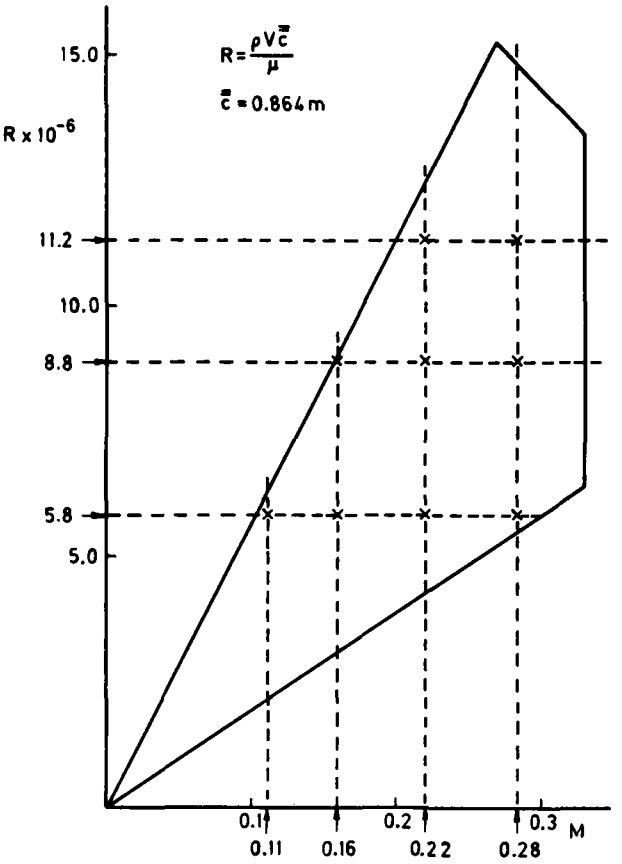
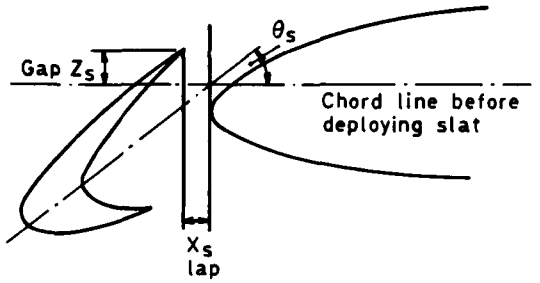


Fig 13 Tunnel envelope and M495 test conditions



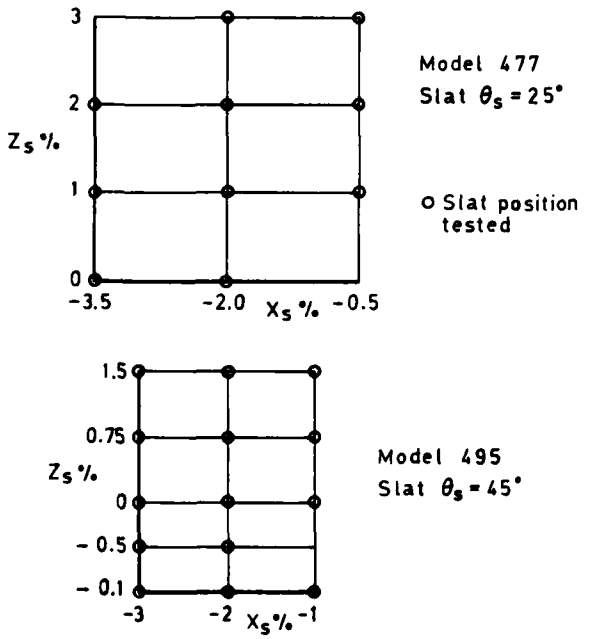


Fig 14 Range of slat lap and gap: Models 477 and 495

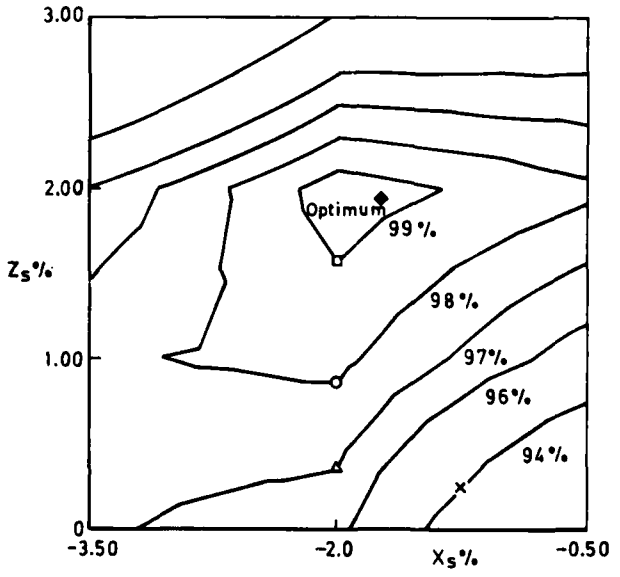


Fig 15 Contour plot of maximum lift for varying slat position (Model 477, R = 5.4 x 10^6, M = 0.16, slat 25°)

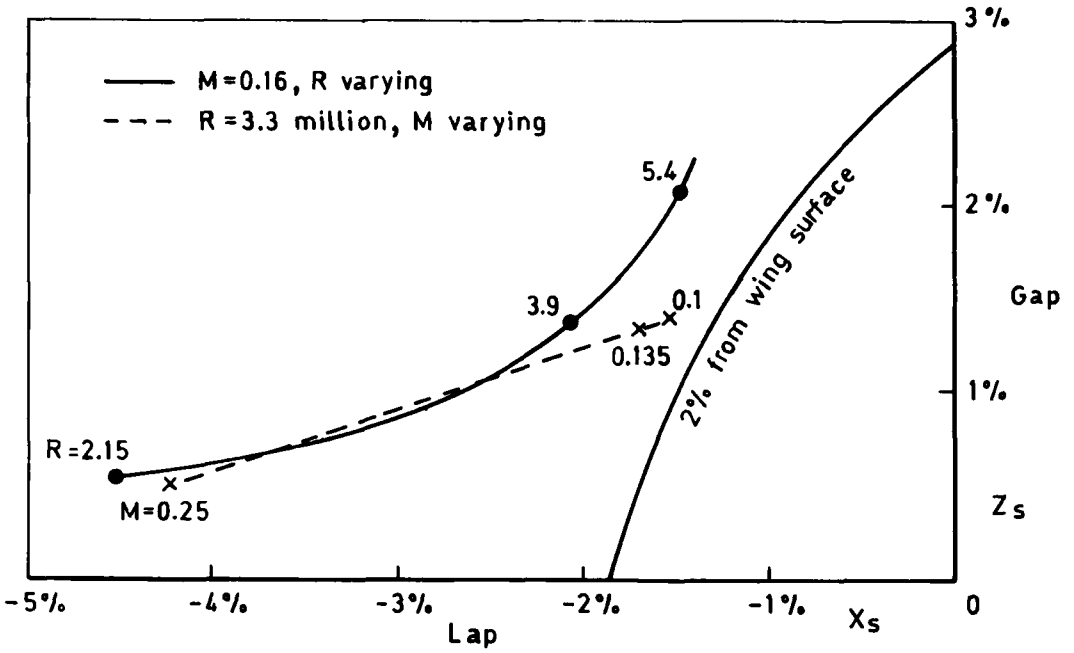


Fig 16 Optimum slat position: Model 477

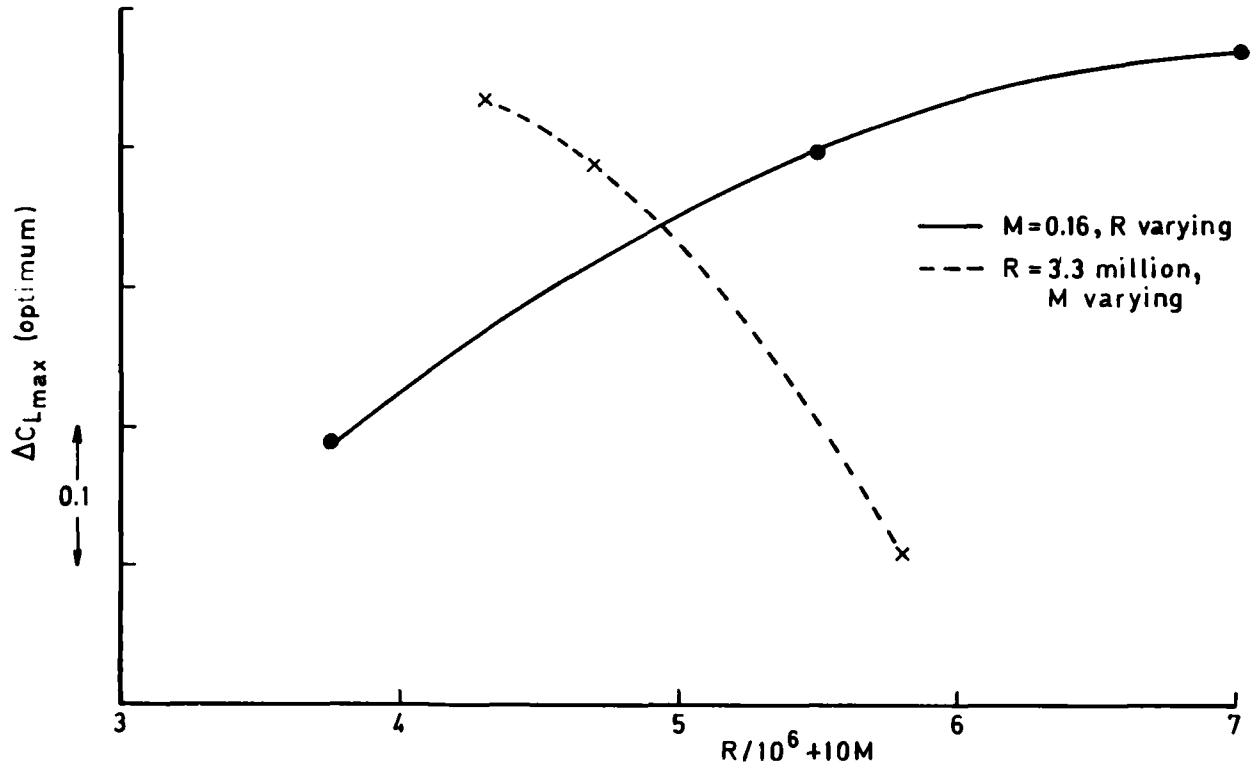


Fig 17 Effect of Reynolds and Mach number on optimum lift for Model 477

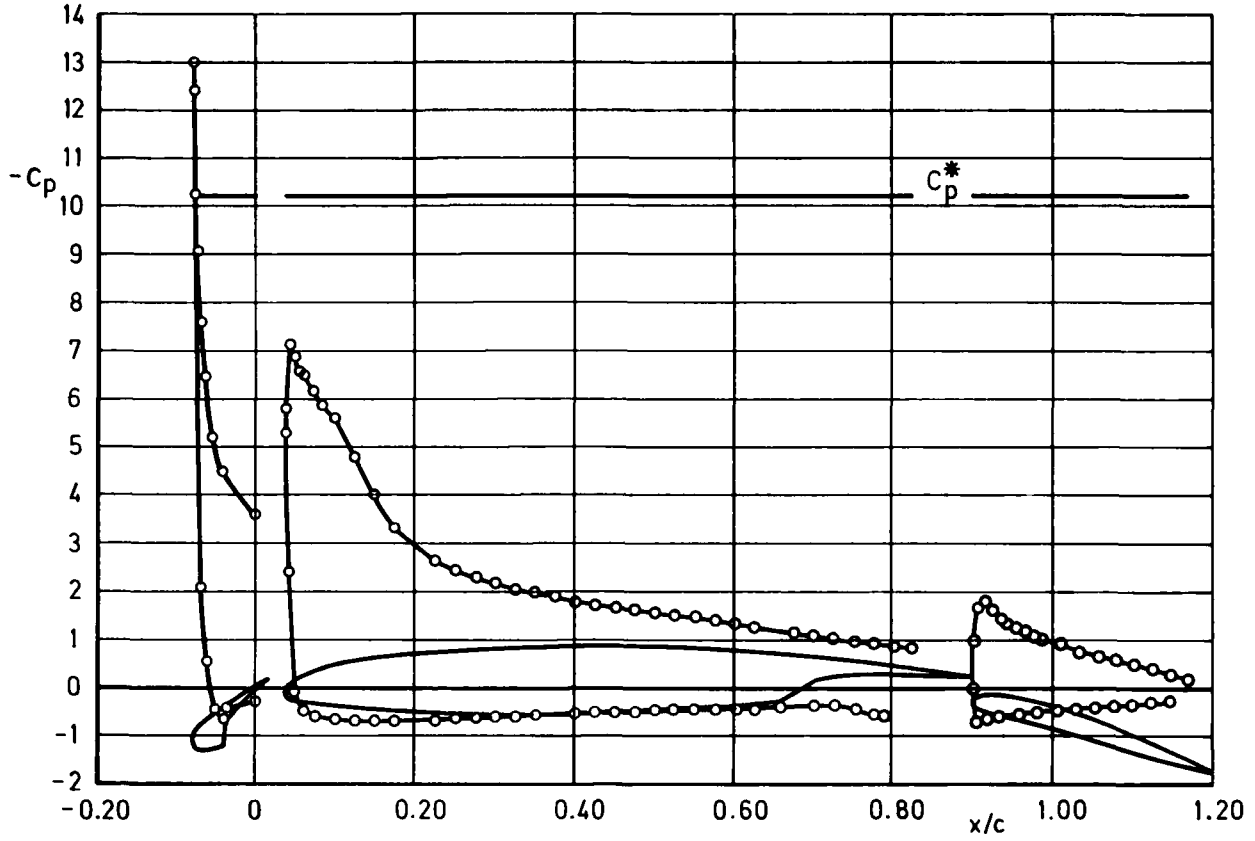


Fig 18 Model 477, M = 0.25, R = 3.3; pressure distribution *near* $C_{L_{max}}$

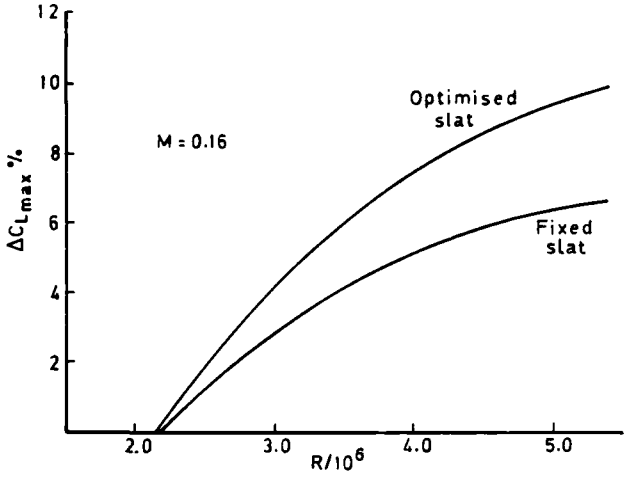


Fig 19 Performance gain from slat optimisation (Model 477)

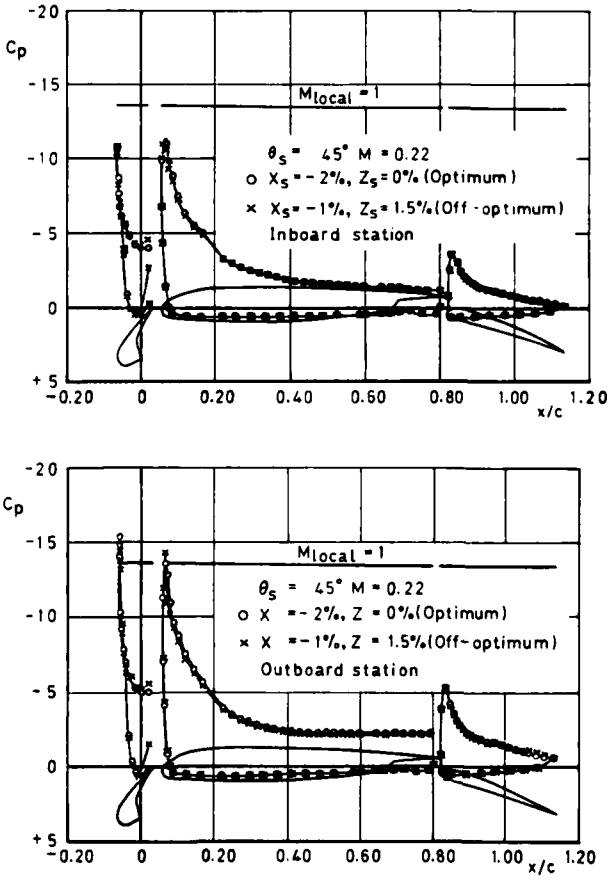


Fig 20 Pressure distributions at optimum and off-optimum slat positions for Model 495 near $C_{L_{max}}$

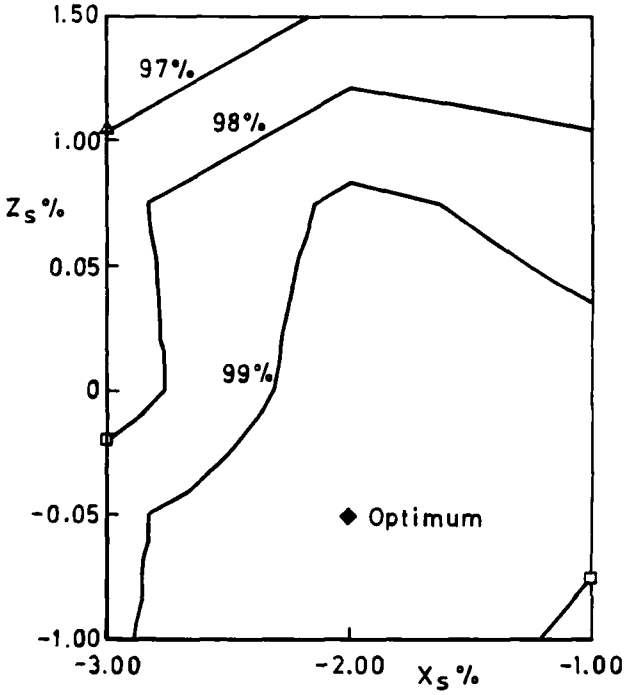


Fig 21 Contour plot of maximum lift for varying slat position (Model 495, R = 11.4 x 10^6, M = 0.22)

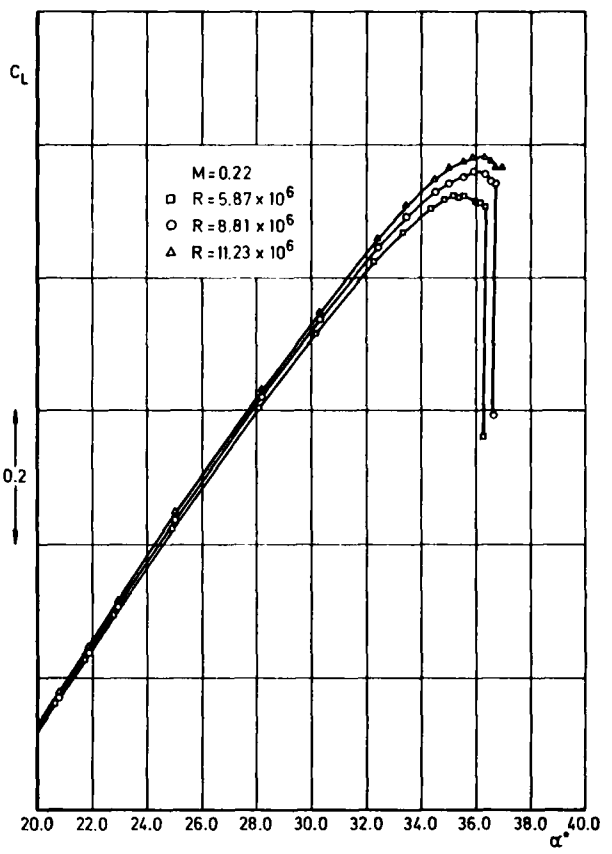


Fig 22 Reynolds number effect, 45° slat: Model 495

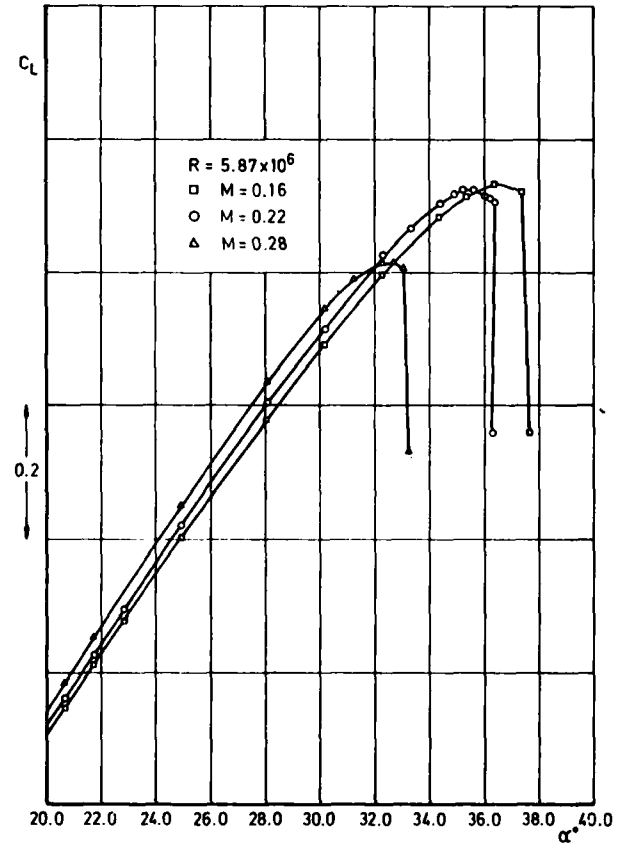


Fig 23 Mach number effect, 45° slat: Model 495

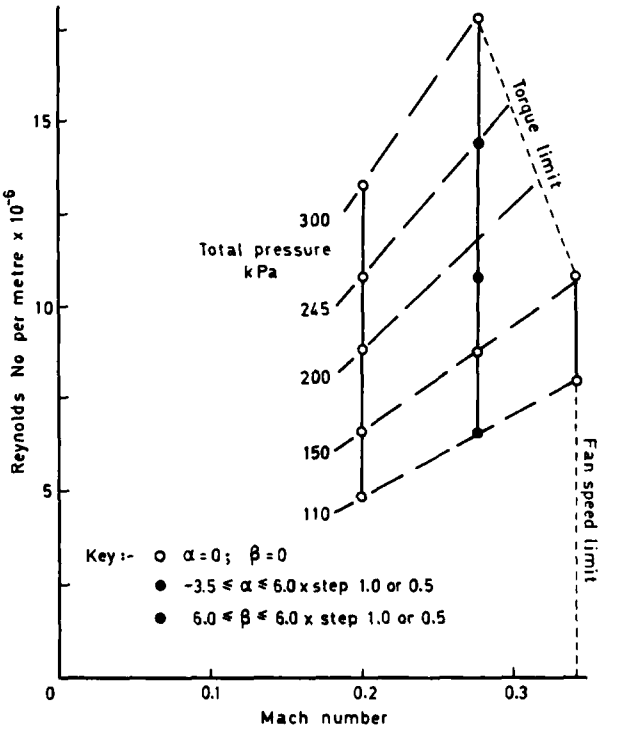


Fig 26 Test conditions for isolated store tests in 5 metre tunnel

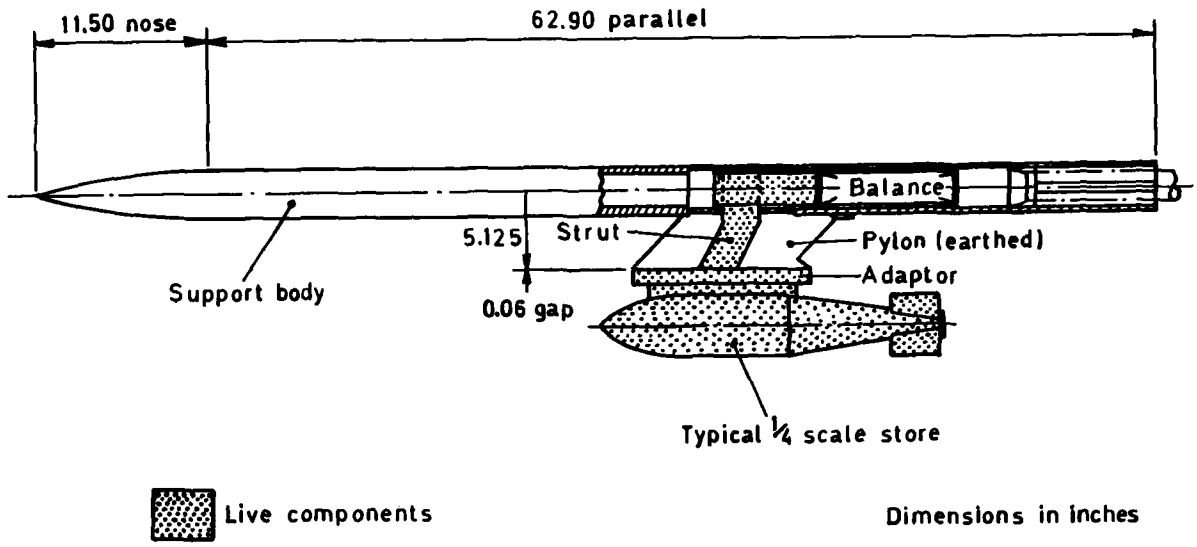


Fig 24 Details of isolated store drag rig (ARA)

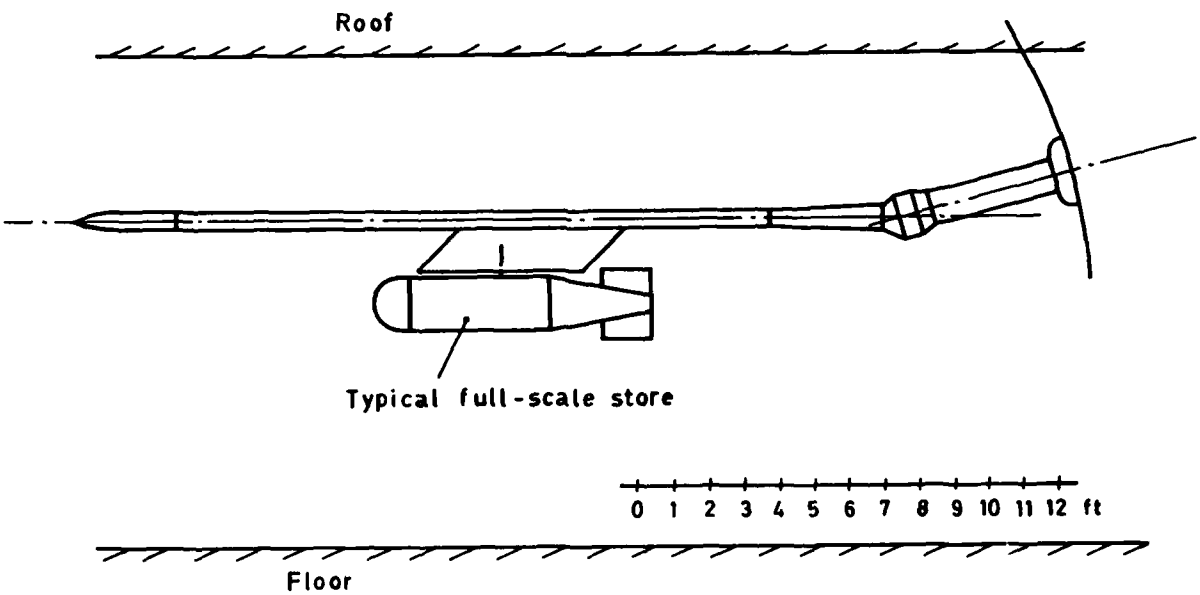


Fig 25 Isolated-store drag rig (5 metre tunnel)

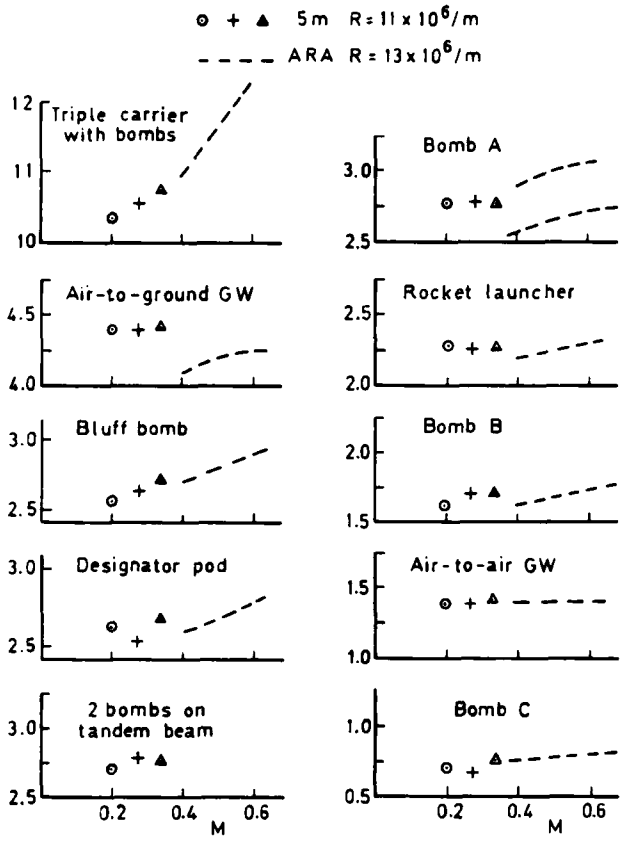


Fig 27 Variation of drag (D/q — nominal units) with Mach number — ¼ scale stores

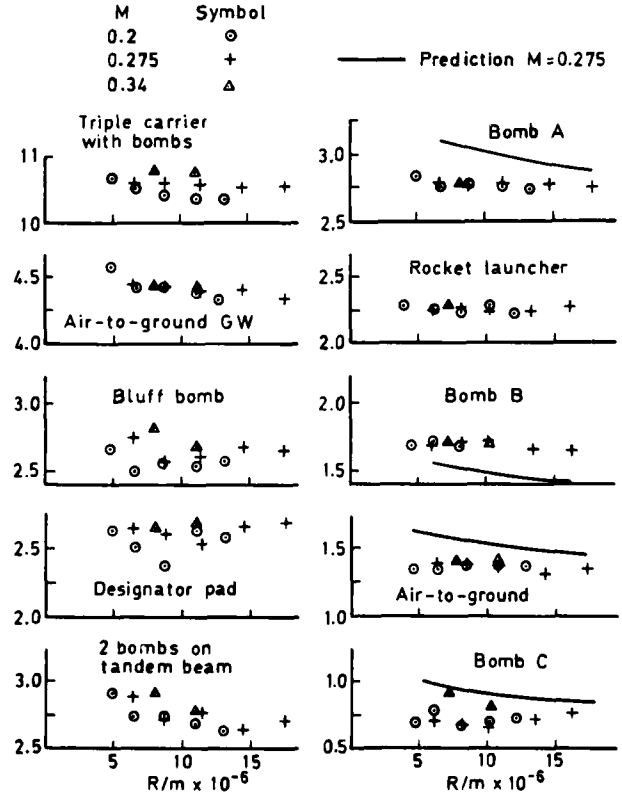


Fig 28 Variation of drag (D/q — nominal units) with Reynolds number — ¼ scale stores

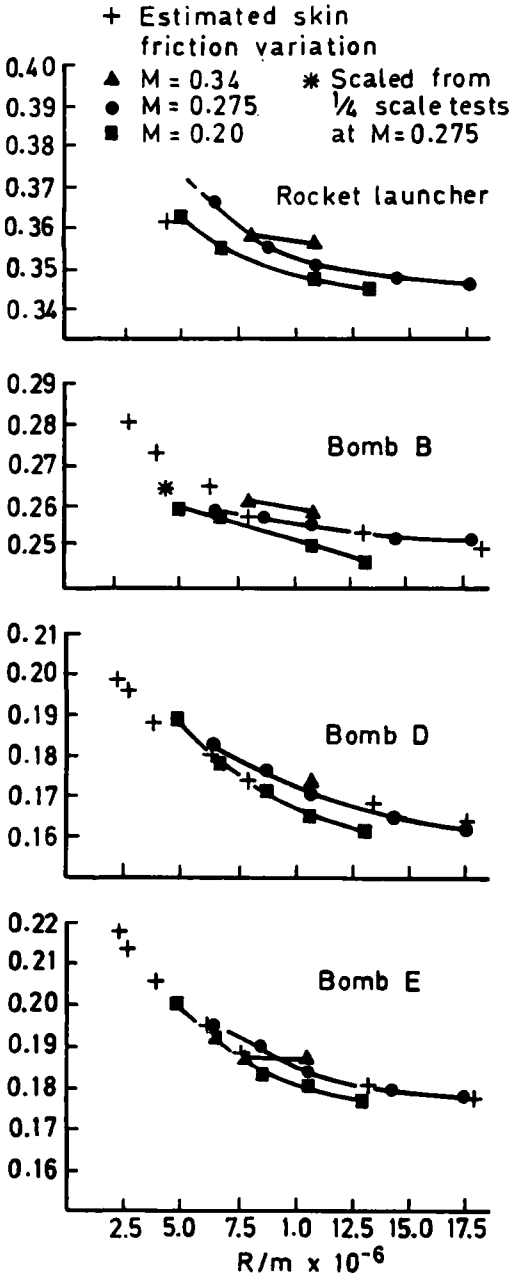


Fig 29 Variation of drag (D/q – nominal units) with Reynolds number – full-scale stores

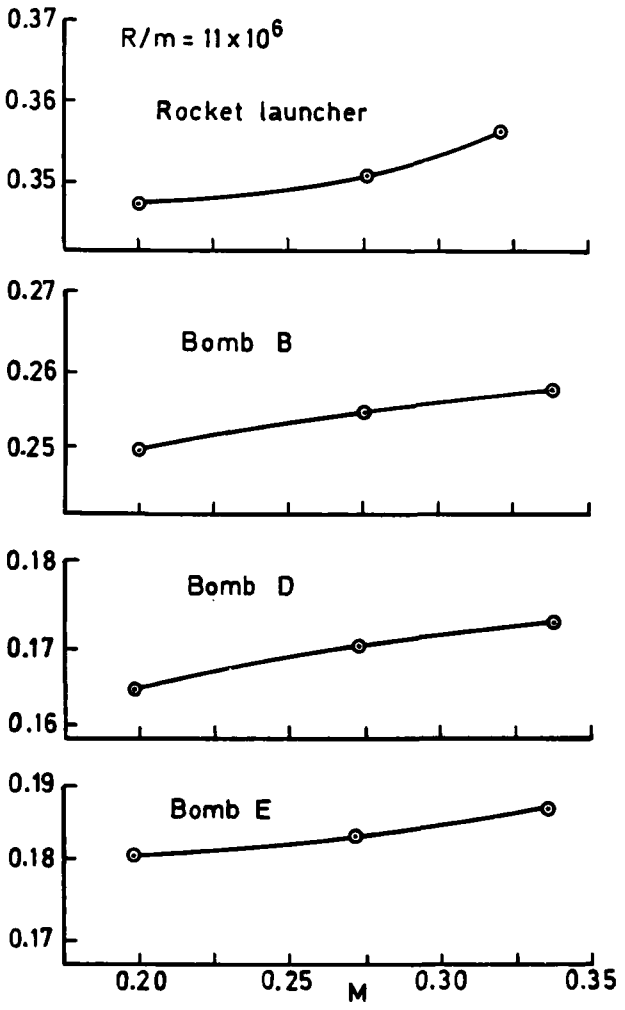


Fig 30 Variation of drag (D/q – nominal units) with Mach number – full-scale stores

RECENT ADVANCES IN COMPUTATIONAL METHODS TO SOLVE THE HIGH-LIFT MULTI-COMPONENT AIRFOIL PROBLEM*

AD-P004 054

by
B. Oskam
National Aerospace Laboratory, NLR
P.O. Box 90502
1059 CM Amsterdam, The Netherlands
and
D.J. Laan and D.F. Volkers
Aerodynamics Department, Fokker B.V.
P.O. Box 7600
1117 ZJ Schiphol, The Netherlands

SUMMARY

Current research in the area of high-lift aerodynamics is directed towards the development of a computational design capability for high-lift systems consisting of flaps and slats. The development of mathematical models to analyze viscous flow over high-lift multi-component airfoil configurations is the first phase in such a research program. This paper describes recent advances made in solving this high-lift multi-component airfoil problem. Two particular aspects of the problem are addressed. The first aspect concerns the calculation of viscous wakes subjected to large adverse pressure gradients. This "off-the-surface" pressure recovery is a flow feature unique to multi-component airfoils, and is not present in the single-component airfoil problem. The second aspect dealt with in the present paper concerns the locally supersonic flow over the slat of a high-lift configuration, with a free stream Mach number of around 0.2. In this "low speed" regime the highest local velocities are found to reach Mach numbers of around 1.6 indicating that in the final analysis of viscous flow over high-lift multi-component airfoil configurations it is imperative to include the nonlinear compressible flow effects.

1. INTRODUCTION

Present methods for computing viscous flow over multi-component airfoils all fall into one of three different categories:

A: Codes solving the time-averaged Navier-Stokes equations with an appropriate turbulence model for closure. These equations unify such physical processes as flow separation, strong viscous-inviscid interactions, nonlinear inviscid phenomena, viscous-viscous interactions between different shear layers and unsteady viscous flows. The computation [1] of viscous flow over a tri-element airfoil falls into this category.

B: Zonal methods based on interactive-type iterative procedures to obtain solutions of the coupled inviscid and viscous flow equations. These methods involve separate calculations of shear layers and of the inviscid flow external to these layers, together with appropriate treatment of the interaction of these flows. The developments reviewed by Melnik [2] form typical examples of this category. A survey of recent work on interactive flows [3] shows a wide recognition of the fact that the steady boundary layer equations can be used to predict small regions of separated flow provided the strong interaction with the outer inviscid flow is accounted for.

C: A third category is formed by the separated-flow airfoil analysis methods. The essential feature which distinguishes these computational methods from the category B is the inviscid character of the separated flow models employed. In a study [4] comparing four computer programs which model large flow separations it was concluded that these codes do have engineering utility. However, no method was capable of accurately predicting all of the cases investigated in that study.

In the present paper we will consider methods in category B which have been applied to multi-component airfoils. Taking a closer look at the methods of this category [5, 6, 7, 8, 9, 10, 11, 12, 13] we find that none of these can deal completely with the viscous flow about a multi-component airfoil at high angles of attack, even in the absence of flow separation, although various models can deal with certain subsets of the complete problem. If one studies in detail all the special problems involved one rapidly arrives at the conclusion that much development work is required.

One of the unsettled problems identified in a previous study [14], and which is still with us, is the computation of turbulent wakes in adverse pressure gradient. This flow process is unique to multi-component airfoils, and is not present in the single-component case. It arises on any multi-component airfoil where a trailing edge pressure is lower than the free stream value. The turbulent wake originating from a trailing edge with a pressure lower than the free stream level is necessarily flowing into a region of higher pressure. This off-the-surface pressure recovery results in an amplification of the displacement thickness of the wake. In case the required off-the-surface pressure recovery exceeds a certain limit we can even have flow reversal near the centerline of the wake, and may expect a substantial interaction between the viscous wake and the inviscid flow. For single-component airfoils the trailing edge pressure, in the absence of flow separation, is invariably higher than the free stream value, excluding the possibility of wake displacement thickness amplification.

Another high-lift problem not investigated in any of the previous studies [5-13] is the occurrence of a pocket of supersonic flow near the leading edge of a high-lift configuration at low free stream Mach numbers. In high-lift testing local velocities can reach Mach numbers of around 1.6 when maximum lift is approached. For such conditions it is quite clear that the compressibility of the inviscid and viscous flow on the slat, or near the leading edge of a high-lift configuration without slat, must be quite significant.

* Part of this investigation has been performed under contract with the Netherlands Agency for Aerospace Programs (NIVR).

These two special questions, the wake flow problem and the local supersonic flow problem, will be addressed in this paper. As far as the first question is concerned we do recall that the theory of turbulent wakes in adverse pressure gradient is not nearly so well developed as the theory of adverse-pressure-gradient boundary-layer flow [15]. At the same time we will assume that the turbulent wake is separated from the adjacent shear layers by a region of potential flow. This means that the influence of boundary-layer wake confluence is assumed to be small. Whether or not this assumption is justified for a given configuration will depend on the size of the gaps between the components, relative to the viscous entrainment of the shear layers. With respect to this point it is comforting to know that for optimum designs various shear layers retain their separate identity up to the flap trailing edge such that confluence of wakes and boundary layers occurs only marginally under these circumstances, as concluded from experimental observation [16].

The outline of the paper is as follows.
First we study in detail the pressure recovery capabilities of nonconfluent turbulent wakes. The turbulence model in the analysis is based on the concept of eddy-viscosity. This turbulent wake analysis procedure is subsequently embedded in a zonal method involving separate calculations of shear layers and of potential flow. The strong interaction between the turbulent wake and the potential flow is treated by solving the viscous and inviscid flow equations simultaneously. Computations show that this analysis method results in improved predictions for high-lift airfoils. At the end of the paper we will discuss the importance of Mach number effects and show a comparison between the computational results of the transonic panel method [17] and some experimental data.

2. TURBULENT WAKES

An interactive-type zonal method cannot be valid unless all its elements, including the off-the-surface pressure recovery, are sound. Although this question about off-the-surface pressure recovery capabilities is vital to high-lift aerodynamics it has not resulted in any published investigations.

We will analyze a turbulent wake while the following simplifying assumptions hold:

- boundary layer approximations are valid,
- two-dimensional, incompressible and nonconfluent flow,
- Reynolds normal-stress gradients are negligibly small in comparison with Reynolds shear-stress gradients.

The momentum and continuity equations may then be written as

$$u \frac{\partial u}{\partial x} + v \frac{\partial u}{\partial y} = U \frac{dU}{dx} + \nu \frac{\partial^2 u}{\partial y^2} + \frac{\partial(-\overline{u'v'})}{\partial y} \tag{1}$$

$$u = \frac{\partial \psi}{\partial y} \quad \text{and} \quad v = -\frac{\partial \psi}{\partial x} \tag{2}$$

where the functions $u(x,y)$ and $v(x,y)$ are the mean flow velocity components, and $U(x)$ represents the inviscid flow velocity outside the viscous wake. The shear stress $\overline{u'v'}$ will be modeled according to

$$-\overline{u'v'}(x,y) = \nu_T(x) \frac{\partial u}{\partial y}(x,y) \tag{3}$$

where the eddy viscosity ν_T is assumed to be constant across the wake. We define a coordinate transformation from (x,y) to (x,η) by

$$\eta(x,y) = \frac{y}{\theta(x)} \tag{4}$$

and a dimensionless stream function $f(x,\eta)$ by

$$f(x,\eta) = \frac{\psi(x,y)}{U(x)\theta(x)} \tag{5}$$

wnere the momentum defect thickness θ of the total wake is used as scaling length. Introducing the transformations into Eqs. (1) - (3) we get

$$\frac{(\nu + \nu_T)}{U\theta} f''' + \frac{1}{U} \frac{d(U\theta)}{dx} ff'' + \frac{\theta}{U} \frac{dU}{dx} [1 - (f')^2] - \theta[f' \frac{\partial f'}{\partial x} - f'' \frac{\partial f}{\partial x}] = 0 \tag{6}$$

Primes denote differentiation with respect to η.
Note that Eq. (6) still represents the exact boundary layer equations, combined with the shear stress Eq. (3). A very useful concept in studying the exact solutions of Eq. (6) is the idea of similarity, i.e. special cases in which the velocity profile u/U depends only on one variable. In such cases Eq. (6) reduces to a set of ordinary differential equations (ODE's). In the similarity analysis we use three ODE's, two of these are given by

$$\frac{d}{dx}(U^2\theta) + \delta^* U \frac{dU}{dx} = 0 \tag{7}$$

$$\frac{d}{dx}(U^3\delta_3) - 2(\nu + \nu_T)\frac{U^2}{\delta^*} H_d = 0 \tag{8}$$

where δ^*, θ, δ_3 and the dimensionless dissipation integral H_d are given by

$$\delta^* = \theta \int_{-\infty}^{+\infty} (1 - f')d\eta \tag{9}$$

$$\theta = \theta \int_{-\infty}^{+\infty} f'(1 - f')d\eta \tag{10}$$

$$\delta_3 = \theta \int_{-\infty}^{+\infty} f'[1 - (f')^2]d\eta \tag{11}$$

$$H_d = \frac{\delta^*}{\theta} \int_{-\infty}^{+\infty} (f'')^2 d\eta \tag{12}$$

Eqs. (7) and (8) are exact integrals of Eq. (6) obtained by integrating from $\eta = -\infty$ to $\eta = +\infty$, and employing the boundary condition

$$\lim_{y \to \pm \infty} [u(x,y)] = U(x) \tag{13}$$

Eq. (7) is a simple form of the boundary layer momentum integral equation, and Eq. (8) is an energy integral equation obtained by multiplying Eq. (6) by f' prior to integration.

Neglecting the molecular viscosity ν, making ν_T dimensionless by $U\theta$ according to

$$\nu_T = H_T U\theta \tag{14}$$

and requiring similarity reduces Eq. (6) to

$$H_T f''' + \frac{(H+1)}{(H+2)} \frac{d\theta}{dx} ff'' - \frac{1}{(H+2)} \frac{d\theta}{dx}[1 - (f')^2] = 0 \tag{15}$$

where the shape factor H is defined by $H = \delta^*/\theta$. A requirement for similarity is that

$$\theta(x) = \theta_o + \frac{d\theta}{dx} (x - x_o) \tag{16}$$

and that the x-dependent factors H_T, H and $\frac{d\theta}{dx}$ are constants and independent of x although these factors may vary from one flow to another. The corresponding free stream velocity U follows from Eq. (7) and reads

$$\frac{U(x)}{U_o} = \left[\frac{\theta(x)}{\theta_o}\right]^{-\frac{1}{2+H}} \tag{17}$$

The values U_o and θ_o are reference values at x_o and are given by $U_o = U(x_o)$ and $\theta_o = \theta(x_o)$. Thus we get a similarity-type solution for the turbulent wake flow when the external velocity U varies with x as prescribed by Eq. (17). In such a flow the x-derivatives in the last term of Eq. (6) are zero, resulting in Eq. (15). If we introduce

$$F = \alpha f \tag{18a}$$

$$Y = \alpha \eta \tag{18b}$$

$$\alpha^2 = \frac{1}{H_T} \frac{(H+1)}{(H+2)} \frac{d\theta}{dx} \tag{19}$$

and

$$\lambda = -\frac{1}{H+1} \tag{20}$$

into Eq. (15), we get

$$F''' + FF'' + \lambda[1 - (F')^2] = 0 \tag{21}$$

where primes of F(Y) denote differentiation with respect to Y. Eq. (21) is the Falkner-Skan equation, well known in laminar boundary-layer theory. In the present analysis it describes turbulent wake flow with an x-dependent eddy viscosity ν_T given by

$$\nu_T = H_T U_o \theta_o \left[\frac{d\theta}{dx} \frac{(x-x_o)}{\theta_o} + 1\right]^{(H+1)/(H+2)} \tag{22}$$

Specification of the constant of proportionality H_T of the eddy viscosity in Eq. (14) completes the problem and determines the pressure recovery capability of the wake. This critical piece of information in the turbulence model may be derived from experimental data as explained in Section 3.

3. TURBULENCE CLOSURE MODEL

Gartshore [18] observed experimentally that pressure gradient significantly lowered the Reynolds shear-stress level in a turbulent wake. He proposed an empirical correlation of this effect by expressing the dimensionless shear stress in terms of the appropriate dimensionless parameter, the ratio of the extra strain rate $\partial u/\partial x$ to the primary rate-of-strain $\partial u/\partial y$

$$\xi = \left[\frac{\partial u}{\partial x} \Big/ \frac{\partial u}{\partial y}\right]_{y = L_o} \tag{23}$$

This ratio, denoted by ξ, is evaluated at $y = L_o$ where L_o is half the width between positions of half maximum deficit, $\frac{1}{2}u_o$, of the wake velocity profile, see Fig. 1. The correlation of the shear stress at $y = L_o$ is given by

$$(-\overline{u'v'})_{y = L_o} = \frac{1}{R_T}\, u_o L_o \left[\frac{\partial u}{\partial y}\right]_{y = L_o} \tag{24a}$$

and

$$R_T = a_o + a_1\, \xi^2 \tag{24b}$$

with

$$a_o = 13 \quad \text{and} \quad a_1 = 4500 \tag{24c}$$

The magnitude of a_1 already shows that even for small ξ we can have a surprisingly large effect on the shear stress.

For small-deficit wakes, $\bar{u}_o \equiv u_o/U \ll 1$, we can linearize Eq. (21) and solve it analytically

$$F'(Y) = 1 - \bar{u}_o \exp(-\tfrac{1}{2}Y^2) \tag{25}$$

Since this solution, Eq. (25), is a good approximation to the experimental velocity profiles of Gartshore [18] we can employ this nondimensional profile to relate the length and velocity scales in Eq. (24a) to those of Eq. (14). This relation between $u_o L_o$ and $U\theta$

$$u_o L_o = \frac{1}{\sqrt{2} - \bar{u}_o} \sqrt{\frac{2 \ln 2}{\pi}}\, U\theta \tag{26}$$

allows us to derive a specification of our eddy viscosity factor H_T by combining Eqs. (3), (14), (24) and (26)

$$H_T = \frac{1}{\sqrt{2} - \bar{u}_o} \sqrt{\frac{2 \ln 2}{\pi}}\, \frac{1}{R_T(\xi)} \tag{27}$$

The turbulent Reynolds number R_T in Eq. (27) is given by Eq. (24b), which expresses the influence of the longitudinal strain rate $\partial u/\partial x$ on the shear stress level.

4. SELF-SIMILAR TURBULENT WAKES

To obtain a wake solution we will have to find an expression for the strain-rate-ratio ξ by introducing Eqs. (4), (5), (18) and (19) into Eq. (23)

$$\xi = -\frac{1}{\alpha}\frac{d\theta}{dx}\left[Y + \frac{1}{(H+2)}\,\frac{F'}{F''}\right]_{Y=Y_o} = \frac{-1}{\alpha}\frac{d\theta}{dx}\, B_2 \tag{28}$$

where Y_o is the Y position of half maximum deficit, or

$$F'(Y_o) = \tfrac{1}{2} + \tfrac{1}{2}F'(Y = 0)$$

This expression, Eq. (28), shows that the strain-rate-ratio ξ is a constant for similarity-type solutions, which is consistent with the requirement that H_T be constant. So the turbulence model given by Eqs. (14) and (27) can be used to predict the exact pressure variation of self-similar turbulent wakes.

To find the actual solution we rewrite Eqs. (7) and (8), using Eq. (14) and neglecting ν,

$$\frac{d\theta}{dx} = 2\frac{(H+1)}{(H-1)}\,\frac{H_d}{H_{31}H^2}\, H_T = B_o H_T \tag{29}$$

where the shape factor H_{31} is defined by $H_{31} = \delta_3/\delta^*$. Introducing Eq. (27) into Eq. (29) yields the following cubic equation

$$\left(\frac{d\theta}{dx}\right)^3 + a_2\,\frac{d\theta}{dx} + a_3 = 0 \tag{30a}$$

with

$$a_2 = \frac{a_o}{a_1}\,\frac{(H+1)}{(H+2)}\,\frac{B_o}{B_2{}^2} \tag{30b}$$

and

$$a_3 = -\frac{1}{a_1}\,\frac{(H+1)}{(H+2)}\,\frac{1}{\sqrt{2} - 1 + F'(0)}\sqrt{\frac{2 \ln 2}{\pi}}\left(\frac{B_o}{B_2}\right)^2 \tag{30c}$$

Analysis of Eq. (30) shows that its discriminant is positive resulting in one root being real. This one root is our self-similar turbulent wake solution.

Because we have not distinguished between upper and lower halves of the wake in Eq. (28) we are actually dealing with symmetric velocity profiles. The symmetric solutions of Eq. (21) are plotted in figure 2 for a range of values of H, which is equivalent to a range of λ, see Eq. (20). The behavior of the centerline velocity F'(0) is plotted in figure 3, where we can see that reversed flow sets in when the shape factor H goes beyond a value of 4. For larger values of H the centerline velocity F'(0) reaches a minimum value of -.184 at H = 27.4, and subsequently increases and approaches zero as H tends to infinity, see figure 2.

The other part of the solution, the root of Eq. (30), is also plotted in figure 3, giving the momentum thickness gradient as function of H. The associated rate-of-strain ratio ξ, given in figure 4, shows the magnitude of the effect of the longitudinal strain rate $\partial u/\partial x$. We see that ξ reaches a minimum of around -0.11, implying a shear stress level reduction of 81 percent in comparison with a zero-pressure-gradient, small-deficit wake ($\xi = 0$). This is indeed a surprisingly large effect, which deserves our attention.

The pressure recovery capabilities of these self-similar turbulent wake flows can be seen in figure 5 where the dimensionless pressure gradient

$$\frac{\theta}{U}\frac{dU}{dx} = -\frac{\theta}{\rho U^2}\frac{dp}{dx}$$

is shown to reach a peak value of about -.011 at H = 2.3. This means that a self-similar turbulent wake flow with a shape factor of H = 2.3 can withstand an adverse pressure gradient which cannot be withstood by self-similar wake flows with higher or lower values of H.

These new wake solutions may be compared with equilibrium turbulent boundary layer solutions [19] as is done in figure 5. In this comparison we have doubled the momentum thickness of the turbulent boundary layer because we consider a turbulent boundary layer to be equivalent with one half of the total wake. The equilibrum family of boundary layers is shown for $Re_\theta = 10^6$, which is equivalent with a flat plate Reynolds number of 850 million. Mellor and Gibson [19] found the separation point of this turbulent boundary layer branch at

$$2\left(\frac{\theta}{U}\frac{dU}{dx}\right)_{T.B.L.} = -.0081 \qquad \text{for} \qquad H = 2.35$$

At this limit point the dependence on Reynolds number vanishes. From the comparison of wake and boundary layer results one observes that

i) the maximum adverse pressure gradient in equilibrium turbulent wakes is approximately 30 percent larger than the equivalent maximum in equilibrium turbulent boundary layers; both maxima are found at H = 2.35 approximately,

ii) equilibrium turbulent boundary layers separate at H = 2.35, while equilibrium turbulent wakes can go up to H = 4.0 (λ = -0.1988) before reversed flow sets in.

The answer to the question about pressure recovery, Eq. (17), of equilibrium turbulent wakes is plotted in figures 6a and 6b. The results show that the amount of pressure recovery possible, U/U_o, depends only on the distance available in terms of the inital momentum thickness, $(X_L - X_o)/\theta_o$. The recovery is independent of the Reynolds number. For short distances the associated optimum shape factor H equals 2.3, which is identical with the peak in figure 5. Optimum pressure recovery over larger distances is achieved with lower values of H (< 2.3) because low values of H have a favorable effect on the exponent of Eq. (17).

Before going to the viscous-inviscid interaction method let us summarize the results of our wake analysis:

- the self-similar wakes presented are exact solutions of the boundary layer equations, subject to a turbulence model specified by Eqs. (3), (14) and (27),
- the effect of the longitudinal strain rate $\partial u/\partial x$ is surprisingly large,
- the pressure recovery capability of a turbulent wake is large in comparison with that of an equivalent turbulent boundary layer, in spite of the adverse effects due to the longitudinal strain rate.

5. VISCOUS-INVISCID INTERACTION

One of our recent advances in high-lift computations concerns the viscous-inviscid analysis of wake flows. This progress has been achieved by adding a new wake procedure to an existing calculation method [10, 14] for viscous flow around multi-component airfoils. This calculation method [10] is an interactive-type procedure solving incompressible potential flow and boundary layer problems iteratively, i.e. a zonal method of category B, see Introduction.

In the new wake procedure we have represented the effect of the viscous wakes in the potential flow by implementing viscous boundary conditions on each wake centerline

$$\phi_n^+ - \phi_n^- = \frac{1}{\rho}\frac{d}{ds}(\rho U \delta^*) \tag{31a}$$

$$\phi_s^+ - \phi_s^- = -\kappa U(\delta^* + \theta) \tag{31b}$$

$$\phi_n^+ + \phi_n^- = 0 \tag{31c}$$

$$U = \tfrac{1}{2}(\phi_s^+ + \phi_s^-) \tag{32}$$

where s, n are curvilinear coordinates along and normal to the wake centerline (n = 0). Matching condition (31a) specifies a jump across the wake centerline in the normal component of the potential flow velocity,

Φ_n, and represents an outflow due to the displacement effect of the viscous wake. The jump in the tangential component $\phi_s^+ - \phi_s^-$, specified in Eq. (31b), results from normal pressure gradient considerations [2]; κ is the curvature of the wake centerline. Eq. (31) requires the outflow to be equal on both sides of the wake, making the wake centerline a dividing streamline of the flow. Of course the position of this dividing streamline is part of the problem to be solved.

The iteration procedure to solve the nonlinear incompressible potential flow problem is depicted in Diagram 1.

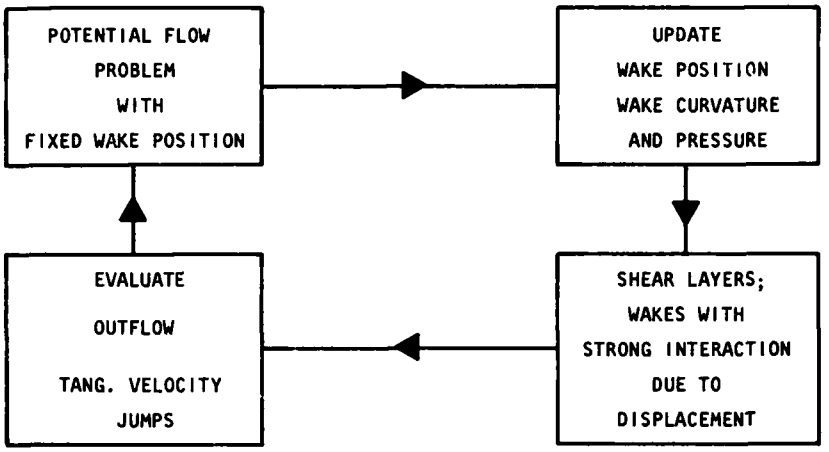


Diagram 1. Wake computation with strong inviscid-viscous interaction embedded in global iteration procedure

The iteration procedure includes all the elements of the existing method [10], such as laminar boundary layer, turbulent boundary layer, near wake and trailing edge treatment. The new element is the viscous wake analysis in which the viscous-inviscid interaction between the pressure in the wake and the viscous displacement of the wake itself is regarded as "strong", while the effects of wake position and curvature, and inviscid interaction between the pressure in one wake and the displacement of other wakes, are regarded as "weak". Thus the strong interaction solution of the viscous wakes, which is itself a nonlinear problem solved by iteration, will be determined repeatedly to obtain a converged solution which accounts for all viscous effects, including the "weak" ones. In this respect it should be recalled that the existing calculation method [10] treats the viscous-inviscid interaction of the boundary layers as a "weak" effect. Although such treatment is not satisfactory in case of boundary layer separation, we will accept this for the time being and will not pay further attention to this separation problem at this time.

The strong interaction problem of each wake is formulated as follows

$$U^{(n+1)}(s) = \tfrac{1}{2}(\phi_s^+ + \phi_s^-)^{(n)} + \frac{1}{2\pi}\int_{\xi=s_o}^{\xi=\infty} \frac{\frac{d}{d\xi}\left[\tfrac{1}{2}(\phi_s^+ - \phi_s^-)^{(n)}\,(\delta^{*(n+1)} - \delta^{*(n)})\right]d\xi}{s-\xi} \tag{33}$$

$$F_2(U^{(n+1)}, \delta^{*(n+1)}, H^{(n+1)}) = 0 \tag{34}$$

$$F_3(U^{(n+1)}, \delta^{*(n+1)}, H^{(n+1)}) = 0 \tag{35}$$

In these expressions the superscript n indicates the iteration index of the global iteration procedure (Diagram 1). The integral in Eq. (33) is actually the perturbation velocity due to symmetric thickness effects in thin airfoil theory. In the strong interaction procedure Eqs. (33), (34) and (35) are solved giving the functions $U^{(n+1)}(s)$, $\delta^{*(n+1)}(s)$ and $H^{(n+1)}(s)$, while the variables with superscript n are fixed and known from the previous global iteration cycle. The magnitude of the integral in Eq. (33) is merely a measure of convergence of the global iteration procedure. Once the global iterates have converged this integral in Eq. (33) becomes zero, and Eq. (33) reduces to Eq. (32) exactly. Thus the genuine solution of the global iteration cycle does not depend on the integral in Eq. (33) at all.

Eqs. (34) and (35) are a symbolic representation of Eqs. (7) and (8), two first order ordinary differential equations. The initial conditions for Eqs. (34) and (35), i.e. $\delta^*(s = s_o)$ and $H(s = s_o)$, follow from the turbulent near wake of course. The precise form of Eqs. (34) and (35) is based on the assumption that the velocity profiles in the wake may be approximated by the family of solutions of the Falkner-Skan equation, displayed in figure 2. This model of the mean velocity profiles is substituted in Eqs. (7), (8) and in the definition of the strain-rate-ratio, Eq. (23), to yield two first order ordinary differential equation in which the function $U(s)$, $\delta^*(s)$ and $H(s)$ are the only unknowns. This type of integral technique, in combination with strong inviscid-viscous interaction, was first used by Lees and Reeves [20] in a study of boundary-layer/shock-wave interaction in 1964. For a recent discussion of integral techniques in turbulent boundary layers the reader is referred to the proceedings of the 1980-81 Stanford Conference on complex turbulent flows [21]. Further details of the present method will be given in [22].

The boundary value problem defined by Eqs. (33) through (35) is discretized [22] and solved by Newton's method, i.e. exact linearization of all terms including the turbulence model. The linearized equations are

viewed as a large matrix inversion problem which is solved at each Newton step by a relaxation scheme based on approximate factorization [23]. This idea of viewing the strong interaction numerically as a large matrix inversion problem has not been used before in interacted boundary layer theory, as noted in [3]. Most of the standard approaches are based on spatial forward marching [3]. The discriminatory features of the present scheme are its computational efficiency (integral technique) and its quadratic convergence termination property (Newton's method).

Before finishing this section it should be remarked that when the shear layer equations in the wake, Eqs. (1) and (2), are solved subject to an imposed free stream velocity, U(s), a Goldstein type of singularity occurs as soon as the maximum velocity deficit becomes large due to adverse pressure gradients. The integral technique by itself, i.e. without strong interaction, does not remove the singularity. The presence of such a singularity can be demonstrated by viewing Eqs. (34) and (35) as two equations in two unknowns, $d\delta^*/ds$ and dH/ds, and evaluating the determinant of the two by two coefficient matrix. This determinant turns out to be a function of H only [22] and is plotted in figure 7. The singularity (D=0) is found at H = 3.2, which is equivalent with a maximum velocity deficit of 92 percent of U, i.e. before reversed flow occurs (H=4). The implicit treatment of Eqs. (33), (34) and (35) removes this classical singularity.

6. VISCOUS DRAG

One of the reasons that drag calculations for high-lift airfoils usually have poor accuracy can be attributed to improper treatment of the viscous wakes. Often used procedures such as calculating the drag by the Squire and Young formula at the trailing edge of each component are a source of large errors. In the present calculations we have handled this problem by calculating the wakes through adverse pressure gradients and sufficiently far downstream, 3 to 7 chord lengths, such that the momentum balance can be evaluated directly [22], without resorting to empirical formulas.

7. HIGH-LIFT AIRFOIL RESULTS

7.1 WING WITH FLAP

A suitable test case for the new method is the NLR7301 airfoil with a 32 percent chord trailing edge flap [24] shown in figure 8. Calculations reported previously [10, 14, 25] showed good agreement between experimental data and calculated results at 6 degrees incidence, but at higher angles of attack, 10 and 13 degrees, no converged solutions could be obtained due to the occurrence of a Goldstein-type singularity in the wing wake calculation procedure, as alluded to in the last paragraph of Section 5. The new wake procedure, i.e. the implicit treatment of the pressure in the wake, removes this singularity. Converged viscous flow solutions showing the development of the wing-wake displacement body as function of incidence are presented as figure 9.

We are now in a position to answer a question posed in [26]: Does the wing-wake displacement development with incidence, shown in figure 9, have an inviscid effect on the flap surface pressure? The converged results of the viscous theory, presented in figure 10 for α = 6°, 10° and 13°, show that the pressures at the flap upper surface are indeed affected significantly, reducing the lift of the flap as the wing wake grows with incidence. Inviscid theory (zero wing wake displacement) predicts the lift of the flap to be largely independent of incidence, see figure 10. The explanation of the inviscid wake effect in the viscous theory is as follows. First we observe that the initial momentum thickness of the wake increases steadily with increasing angle of attack. This deterioration of the wing-wake initial conditions reduces its pressure recovery capability over a fixed distance, see figure 6, and causes the wing-wake displacement to grow such that the imposed pressure gradient is reduced. This reduction of the adverse pressure gradient at the wing wake centerline, with increasing angle of attack, can be seen in figure 11. The observed variations in the pressure with incidence are induced by the displacement of the wing wake itself, other effects being of smaller magnitude. The resultant effect on the flap upper surface pressure distribution merely reflects the self-induced interaction of the wing wake. The comparison between experimental data and viscous theory in figure 12 shows that the inviscid wake effect on the flap pressures is also observed experimentally.

The experimental and theoretical C_l-α and C_l-C_d curves are shown in figures 13 and 14. In contrast to the previous method [10] the new viscous theory provides converged solutions up to an angle of attack of 15.6 degrees. This last solution at α = 15.6° exhibits a region of turbulent boundary layer separation over the last 3 percent chord of the wing upper surface; this result is displayed in figure 15a where the skin friction coefficient C_f is plotted over the last 15 percent chord of the wing, for α = 14.6, 15.1 and 15.6 degrees. These results indicate that the stall is initiated by trailing-edge separation at the wing upper surface leading to a progressive deterioration of wing-wake initial conditions. The load on the flap upper surface turbulent boundary layer is diminishing with increasing angle of attack, see figure 15b. This increase in skin friction over the last portion of the flap is a direct result of the inviscid wake effect on the pressure shown in figure 10.

In Section 4 we mentioned that the longitudinal strain rate does have a surprisingly large effect on the development of the wake. To see how the longitudinal strain-rate term in the turbulence model does affect the lift-drag curve, of the wing with flap configuration, we have repeated the calculation of the theoretical lift-drag curve of figure 14. This second set of calculations is identical with the first except for the turbulence model; in the second set we have neglected the longitudinal strain-rate term; i.e. $a_1 = 0$ in Eq. (24b). Figure 16 shows the results and indicates that the longitudinal strain-rate term in the turbulence model does have a significant adverse effect on the lift-drag curve; this term causes a loss of lift and additional drag. These findings lead us to the conclusion that there is a substantial interaction between the wing-wake turbulence model and the flow field, such that the calculated maximum lift is affected directly by the turbulence model.

The conclusion above asks for a closer examination of the wing-wake turbulence model. If we look at the calculated wing-wake displacement distribution and compare it with the experimental value at the flap trailing edge location, see figure 17, we find that the present turbulence model, including Eq. (24), does not exag-

gerate the wing-wake effect. As a matter of fact the predicted maximum displacement in figure 17 is still 10 percent low in comparison with experimental data, for an angle of attack of 13 degrees. Further study has revealed that these remaining differences between viscous theory and experimental data as found in figure 17, and also in figures 13 and 14, are mainly due to compressibility effects in the flow near the wing nose; these effects have not been taken into account in the viscous theory as yet.

7.2 WING WITH DOUBLE-SLOTTED FLAP

A second test case for the new wake calculation procedure is a wing with double-slotted flap which is shown in figure 18 and denoted by configuration 2. A comparison between the experimental C_l-α, C_l-C_d curves and the theoretical results is shown in figures 19 and 20. Taking a close look at the pressure distribution of the flap in figure 21, and the results of the corresponding boundary-layer computations, reveals a region of turbulent boundary layer separation over the last part of the flap upper surface. This turbulent boundary layer separation extends over the last 10 percent of the local flap chord, and is found to be largely independent of the angle of attack. Calculations with a separated flow free-streamline model of inviscid character, see Introduction, indicate that such a separation in the rear causes a loss of lift of $\Delta C_l = 0.12$ independent of the angle of attack. In the present viscous theory we neither take this boundary layer separation nor the compressibility effects into account. As a result we may expect some differences between viscous theory and experimental data, see figures 19 and 20.

The behavior of the wing wake of configuration 2 is particularly interesting. The theoretical C_l-α curve in figure 19 already shows a drop in lift at $\alpha = 10°$, caused by the wing wake. The convergence characteristics of the global iteration procedure for $\alpha = 0°$ and $\alpha = 10°$ are shown in figures 22a and 22b. As a rule the global iterates, lift and drag, will converge to a steady level after about 10 iterations with a relaxation factor of $\omega = 0.3$, as is the case for $\alpha = 0°$ in figure 22a. Higher angles of attack show similar behavior. However, if we approach $\alpha = 10°$ the convergence slows down, and at $\alpha = 10°$ the global iteration procedure fails to converge because the strong-interaction wake procedure suddenly predicts a very large region of reversed flow in the wing wake, see figure 22b. This sudden occurrence after 12 global iterations at $\alpha = 10°$ causes a 800-count-increase in C_d and a steadily decreasing lift C_l.

The development of the wake displacement thickness with increasing angle of attack can be found in figure 23 for $\alpha = 0°$, 6°, 9.5° and 10°. This last case, $\alpha = 10°$ with a global iteration index of 15, is beyond maximum lift. In these calculations the wakes extend up to 7.5 chords downstream of the wing. A larger portion of the wakes is shown in figure 24 where one can observe the shape of the displacement bodies in the wake obtained after nine global iterations just before wing-wake reversed flow sets in, and at an incidence of $\alpha = 10°$.

The good qualitative agreement between the viscous theory and the experimental data in figures 19 and 20 supports the validity of the present viscous theory. This theory predicts an abrupt stall due to the occurrence of reversed flow in the wing wake of a wing with double-slotted flap (figure 18). The critical flow process initiating the stall is the pressure recovery capability of the wing wake, see the end of Section 4 above. The initial conditions of the wing wake deteriorate and reduce the pressure recovery capability of the wake, as the angle of attack increases. As soon as this pressure recovery capability falls short of the pressure rise required, in spite of favorable inviscid-viscous interaction effects, stall is initiated.

7.3 WING WITH FLAP AND SLAT

In all the results presented in the sections above we have neglected the compressibility effects. In this section we will pay some attention to the effect of compressibility in the inviscid flow. For this purpose we have solved the full potential equation, employing the transonic panel method [17], for a wing with flap and slat, see figure 25. One of the questions that arise concerns the pocket of supersonic flow near the leading edge of the slat, and the possible interaction between a shock wave and the slat boundary layer. In order to be able to investigate these "local" viscous effects we have modified the experimental geometry to take care of "global" viscous effects such as the wakes.

The geometry considered in the full potential problem is identical with the experimental geometry, except for two modifications:

i) the cove of the slat is redesigned to obtain a region of constant pressure simulating the turbulent separation in the cove, see figure 26

ii) the flap angle is reduced to simulate "global" viscous effects such as the wakes. The magnitude of this flap angle reduction is determined by matching the total lift of the full potential solution and the corresponding total lift in the experiment at the same free stream Mach number and angle of attack.

The comparison between the resultant full potential solution and the experimental data is shown in figures 27 and 28, for free stream Mach numbers of 0.225 and 0.255 respectively. These last two figures show the Mach number distribution on the slat upper surface plotted as function of the distance from the heel of the slat, see figure 27.

The results show that the highest local velocities correspond with Mach numbers of around 1.6 at a free stream Mach number of 0.225. The measurements at a Reynolds number of 6.9 million also displays this high Mach number region. This agreement between the full potential solution and the experimental data leads to the conclusion that the interaction between the shock, terminating the supersonic flow, and the slat boundary layer does not cause separation to any significant extent, in spite of the rather strong shock wave involved. As a matter of fact we observe good agreement some distance downstream of the shock indicating that the experimental data is close to isentropic recompression. Near the trailing edge of the slat we see a larger difference which is due to the strong inviscid-viscous trailing-edge interaction. From these findings we conclude that the full potential equation as model for the inviscid flow does hold some promise, although further work is required in this area of high-lift compressible-flow aerodynamics.

8. CONCLUDING REMARKS

The research in high-lift computational methods described in this paper has brought several advances in the capability to analyze the viscous flow over high-lift multi-component airfoil configurations. Development of a computational method for turbulent wakes in adverse pressure gradient, including strong inviscid-viscous interaction, has improved the understanding of such phenomena as the off-the-surface pressure recovery capability of viscous wakes. The example of a wing with double-slotted flap shows that the wake, flowing into a region of higher pressure, may play a critical role that, to the authors' knowledge, has not been recognized before. Moreover it is found that there is a substantial interaction between the wing-wake turbulence model and the flow field, such that the calculated maximum lift is affected directly by the turbulence model.

Another aspect dealt with in the present paper concerns the locally supersonic flow over a slat. Results of the transonic panel method, solving the full potential equation, and the experimental data both show high local velocities reaching Mach numbers up to 1.6 at a free stream Mach number of 0.225. The good agreement suggests that the transonic potential flow model may be useful in the computational analysis and design of high-lift devices. The examples given illustrate improved capabilities in the analysis of high-lift systems. However, it is also obvious that much remains to be done, such as the unified treatment of all relevant flow processes.

REFERENCES

[1] Lasinski, T.A., Andrews, A.E., Sorenson, R.L., Chaussee, D.S., Pulliam, T.H., and Kutler, P., "Computation of the Steady Viscous Flow Over a Tri-Element Augmenter Wing Airfoil", Paper AIAA-82-0021, Januari 1982, Orlando, Florida.

[2] Melnik, R.E., "Turbulent Interactions on Airfoils at Transonic Speeds - Recent Developments", Paper 10, AGARD-CP-291, Sept.-Oct. 1980.

[3] McDonald, H. and Briley, W.R., "A Survey of Recent Work on Interacted Boundary Layer Theory for Flow with Separation", Proc. of Second Symposium on Numerical and Physical Aspects of Aerodynamic Flows, January 1983, Long Beach, California.

[4] Blascovich, J.D., "Characteristics of Separated Flow Airfoil Analysis Methods", Paper AIAA-84-0048, January 1984, Reno, Nevada.

[5] Stevens, W.A., Goradia, S.H. and Braden, J.A., "Mathematical Model for Two-Dimensional Multi-Component Airfoils in Viscous Flow", NASA CR-1843, July 1971.

[6] Callaghan, J.C. and Beatty, T.D., "A Theoretical Method for the Analysis and Design of Multielement Airfoils", Journal of Aircraft, Vol. 9, No. 10, Dec. 1972, pp. 844-848.

[7] Seebohm, T. and Newman, B.G., "A Numerical Method for Calculating Viscous Flow Round Multiple-Section Aerofoils", Aeronautical Quarterly, Vol. 26, August 1975.

[8] Jakob, H., "Erweiterung eines 2D Panelverfahrens auf Profile mit dicken Hinterkanten und Kopplung des Verfahrens mit einem Grenzschichtverfahren", VFW Bericht Ef 612, 1976.

[9] Brune, G.W. and Manke, J.W., "An Improved Version of the NASA/Lockheed Multi-Element Airfoil Analysis Computer Program", NASA CR-145323, March 1978.

[10] Oskam, B., "A Calculation Method for the Viscous Flow Around Multi-Component Airfoils", NLR TR 79097 U, 1979.

[11] Butter, D.J. and Williams, B.R., "The Development and Application of a Method for Calculating the Viscous Flow about High-Lift Airfoils", Paper 25, AGARD-CP-291, Sept.-Oct. 1980.

[12] Olsen, L.E. and Orloff, K.L., "On the Structure of Turbulent Wakes and Merging Shear Layers of Multi-Element Airfoils", Paper AIAA 81-1238, June 1981, Palo Alto, California.

[13] Le Balleur, J.C., "Numerical Viscid-Inviscid Interaction in Steady and Unsteady Flows", Proc. of Second Symposium on Numerical and Physical Aspects of Aerodynamic Flows, Januari 1983, Long Beach, California.

[14] Oskam, B., "Computational Aspects and Results of Low Speed Viscous Flow about Multi-Component Airfoils", Paper 19, AGARD-CP-291, Sept.-Oct. 1980.

[15] Smith, A.M.O., "High-Lift Aerodynamics", Journal of Aircraft, Vol. 12, No. 6, June 1975.

[16] Ljunström, B., "Experimental High-Lift Optimization of Multiple Element Airfoils", Paper 13, AGARD-CP-143, April 1974.

[17] Oskam, B., "Transonic Panel Method for the Full Potential Equation Applied to Multi-Component Airfoils", Paper AIAA-83-1855, July 1983, Danvers, Massachusetts (to appear in AIAA J.).

[18] Gartshore, I.S., "Two-Dimensional Turbulent Wakes", J. Fluid Mech. (1967), Vol. 30, part 3, pp. 547-560.

[19] Mellor, G.L. and Gibson, D.M., "Equilibrium Turbulent Boundary Layers", Journal of Fluid Mechanics (1966), Vol. 24, part 2, pp. 225-253.

[20] Lees, L. and Reeves, B.L., "Supersonic Separated and Reattaching Laminar Flows: I. General Theory and Application to Adiabatic Boundary-Layer / Shock-Wave Interactions", AIAA Journal, Vol. 2, No. 11, Nov. 1964, pp. 1907-1920.

[21] Cousteix, J., "Integral Techniques", Proceedings of the 1981 AFOSR-HTTM-Stanford Conference on Complex Turbulent Flows, Volume II, Edited by S.J. Kline, et al., pp. 650-671, Published by Stanford University, California, 1982.

[22] Oskam, B., "Calculation of Turbulent Wakes in Adverse Pressure Gradients", NLR Report to be published.

[23] Oskam, B. and Fray, J.M.J., "General Relaxation Schemes in Multigrid Algorithms for Higher-Order Singularity Methods", Journal of Computational Physics, Vol. 48 (1982), pp. 423-440.

[24] Van den Berg, B., "Boundary Layer Measurements on a Two-Dimensional Wing with Flap", NLR TR 79009 U, 1979.

[25] Van den Berg, B. and Oskam, B., "Boundary Layer Measurements on a Two-Dimensional Wing with Flap and a Comparison with Calculations", Paper 18 of AGARD-CP-271, September 1979.

[26] Moser, A. and Shollenberger, C.A., "Inviscid Wake Airfoil Interaction on Multielement High-Lift Systems", J. Aircraft, Vol. 10, No. 12, Dec. 1973, pp. 765-767.

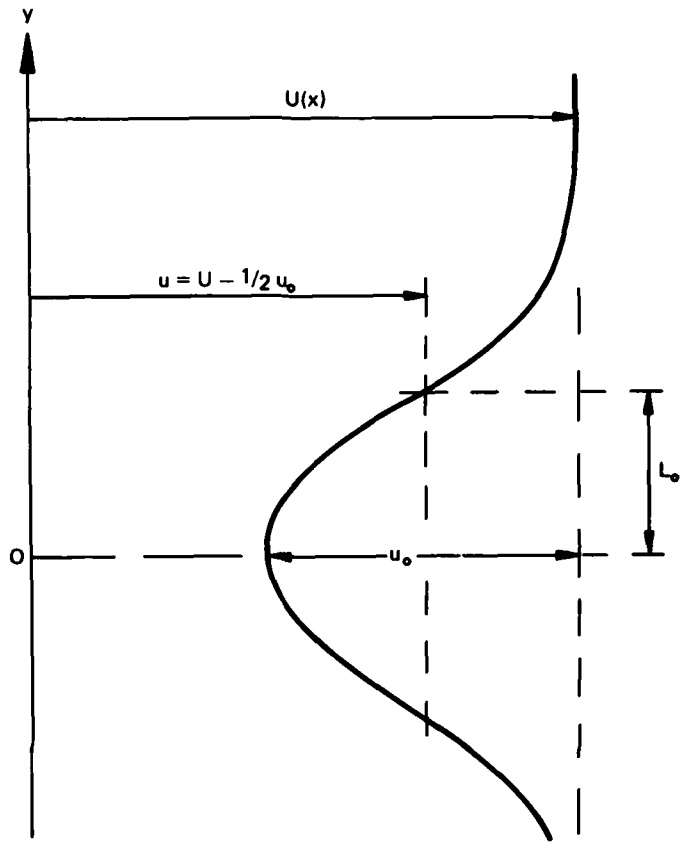


Fig. 1 Mean velocity profile of turbulent wake defining maximum deficit u_o

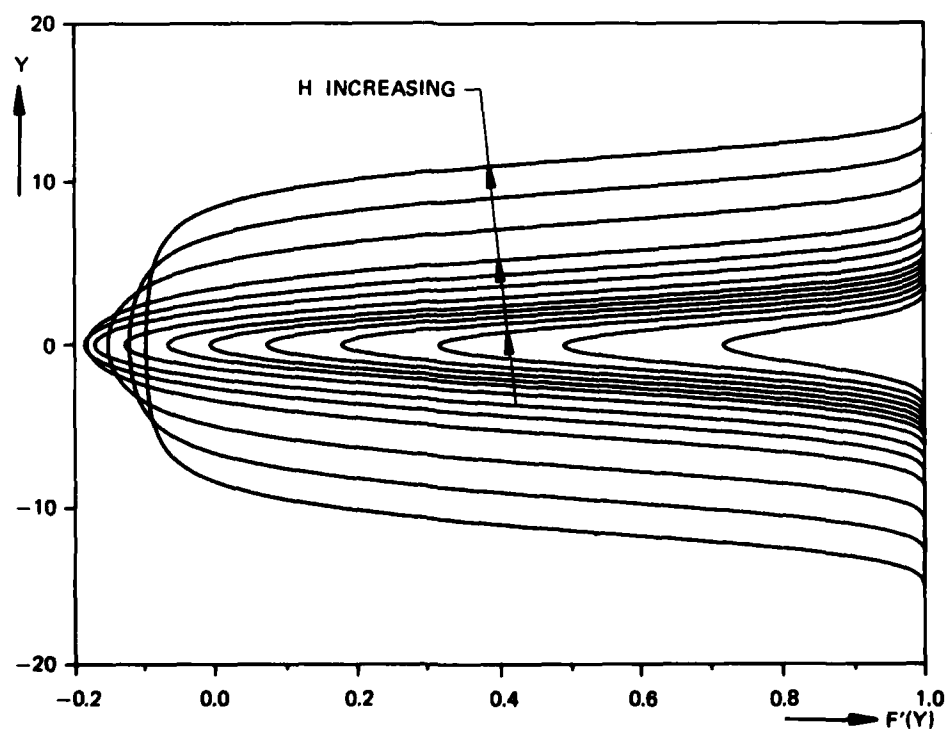


Fig. 2 Symmetric velocity profiles of turbulent wake obtained by solving Falkner-Skan equation for various values of λ

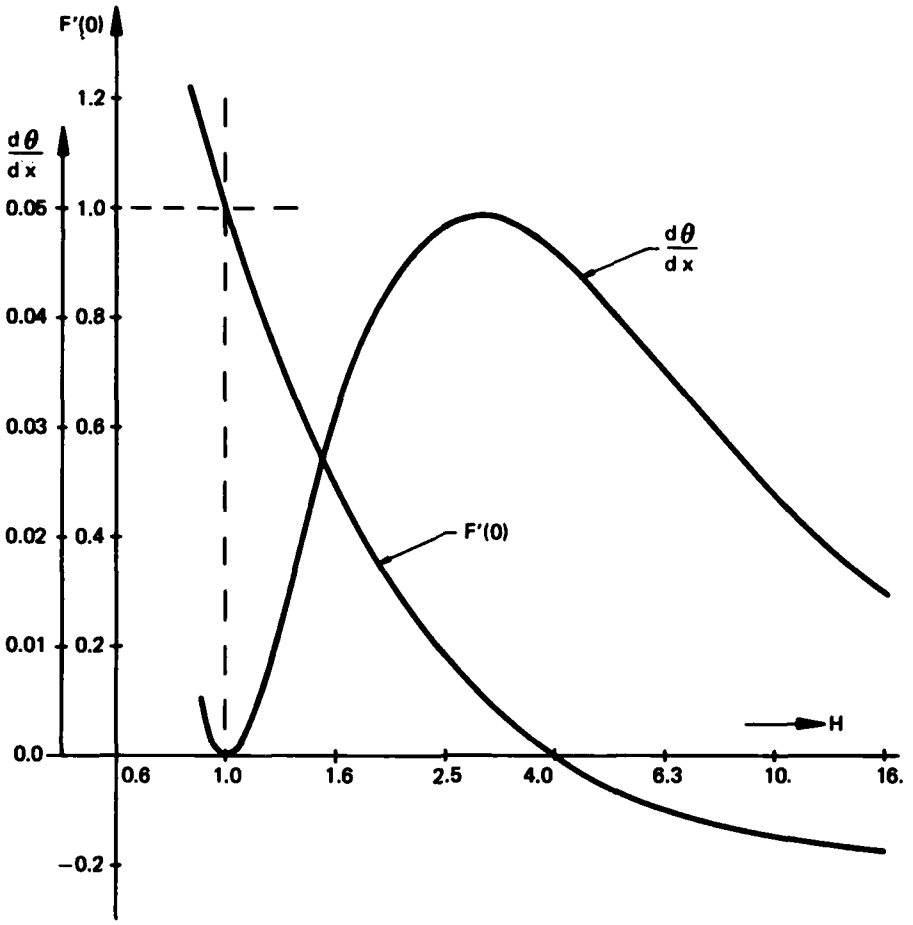


Fig. 3 Self-similar turbulent wake solution; centerline velocity F'(0) and momentum thickness gradient as function of shape factor H

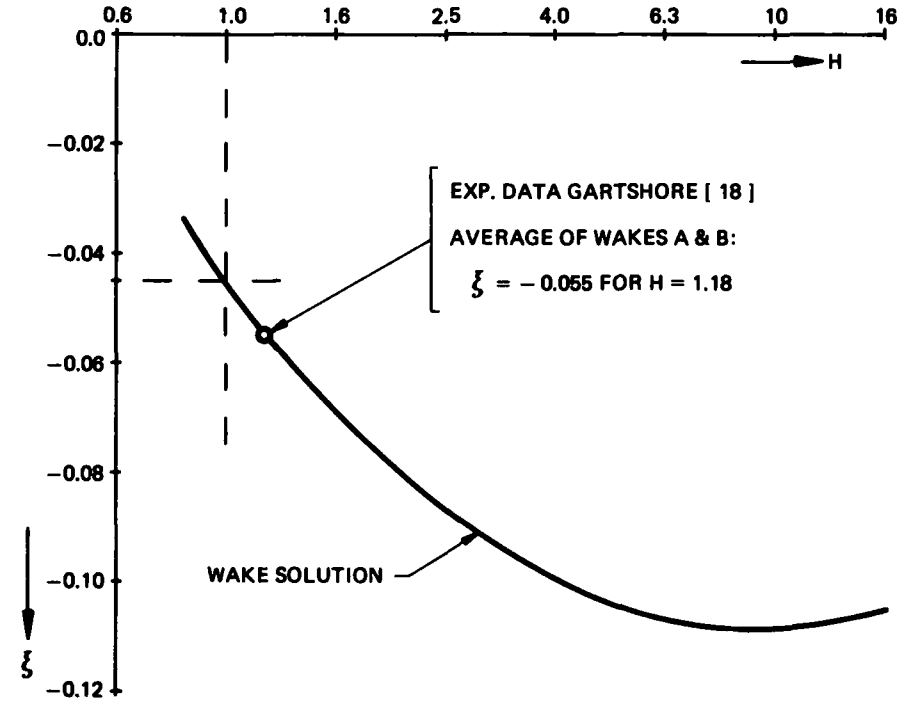


Fig. 4 Self-similar turbulent wake solution; rate-of strain ratio ξ as function of shape factor H

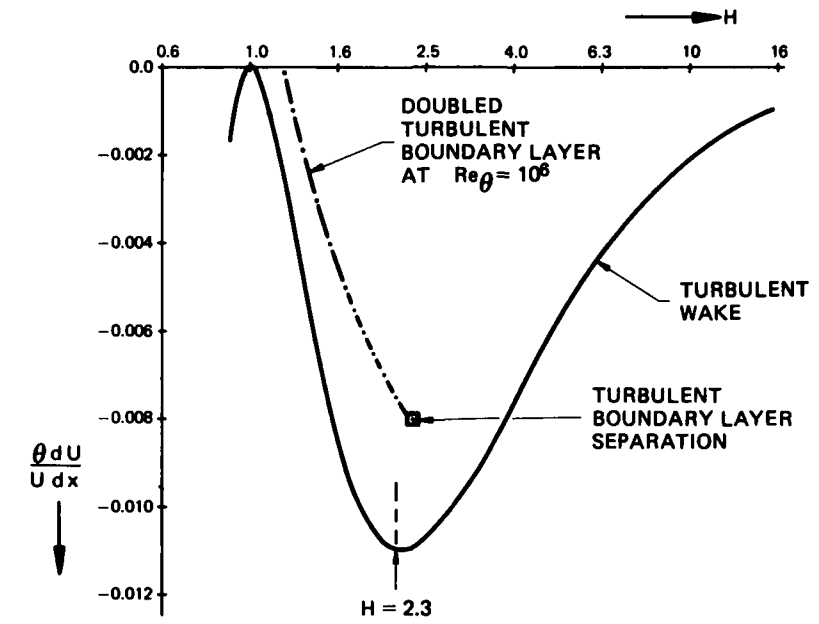


Fig. 5 Self-similar turbulent shear layer solutions; dimensionless pressure gradient parameter as function of shape factor H

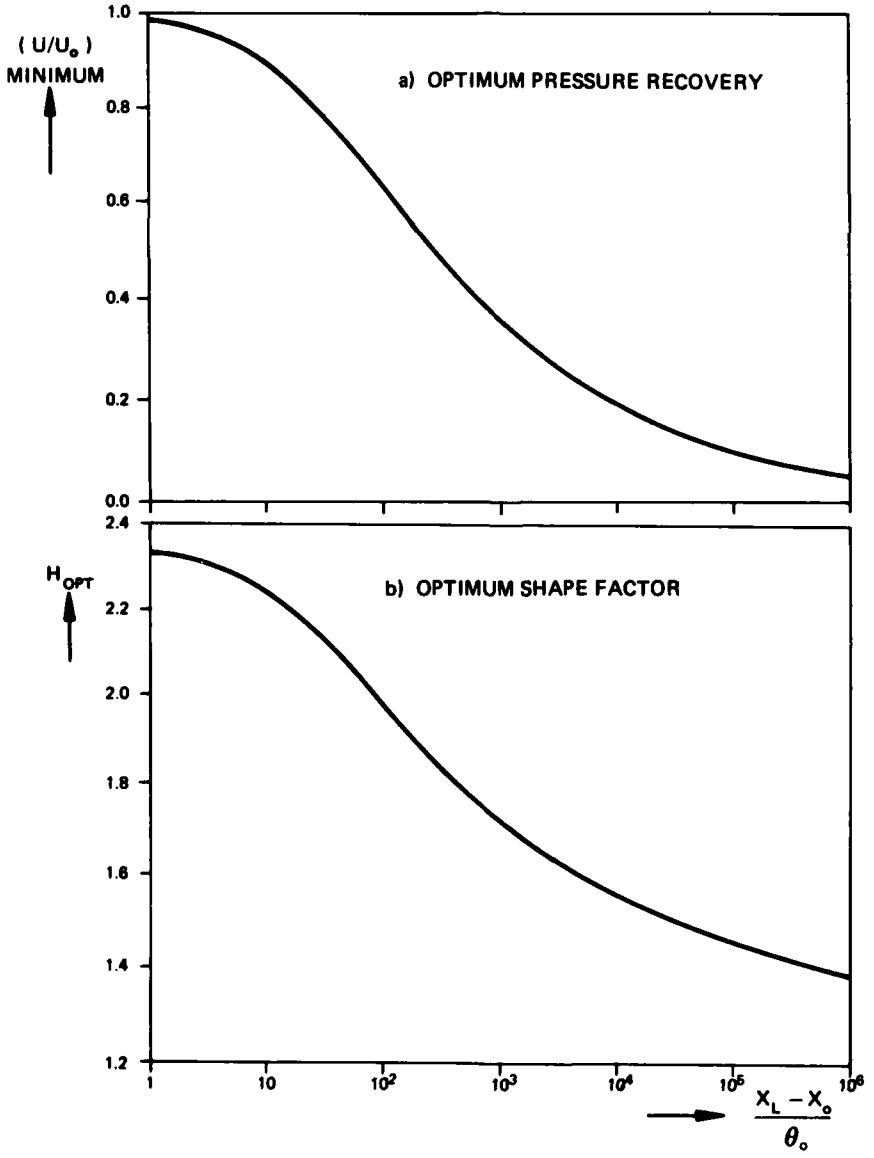


Fig. 6 Self-similar turbulent wake flow; optimum pressure recovery, in terms of U/U_o, and optimum shape factor H_{opt} as function of recovery distance, $(x_L - x_o)/\theta_o$

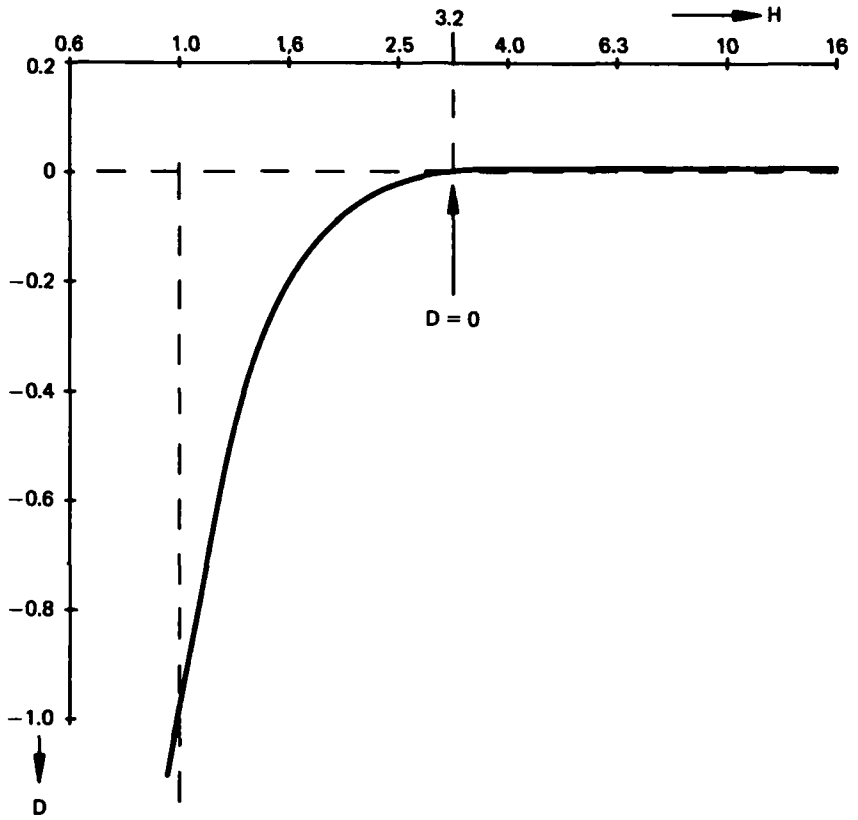


Fig. 7 Determinant of boundary layer integral equations (34) and (35) as function of the shape factor H

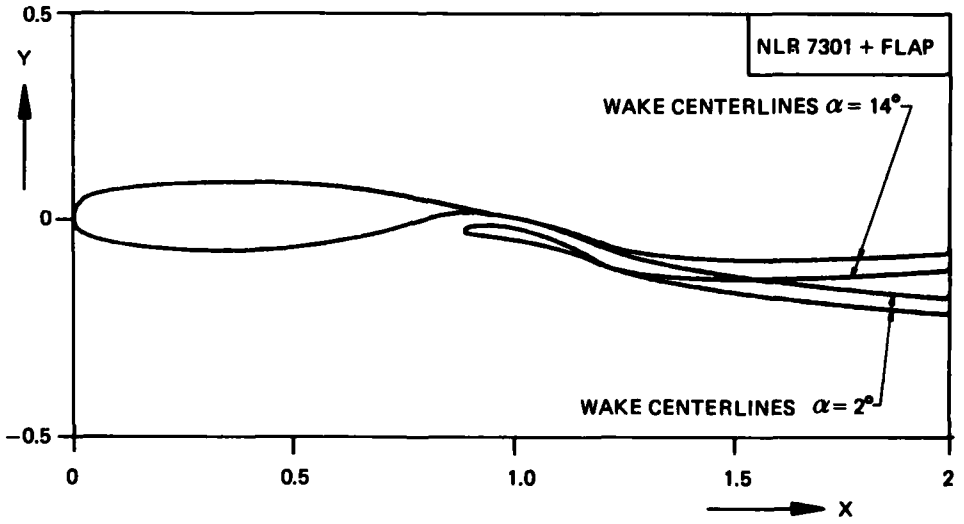


Fig. 8 NLR7301 airfoil with flap of 32 percent chord; wake centerlines for angles of attack α of 2 and 14 degrees

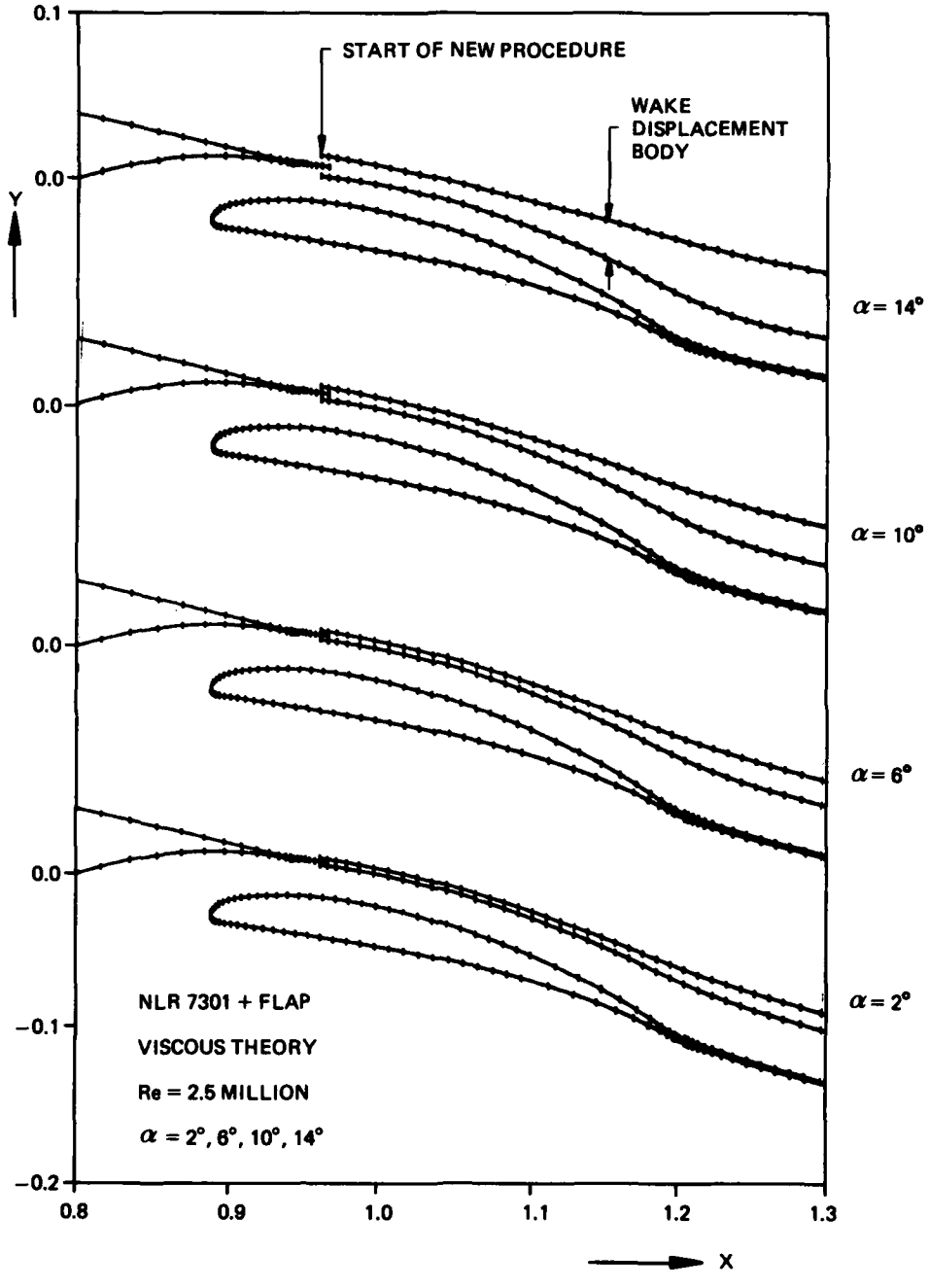


Fig. 9 Converged viscous flow solutions showing development of wing-wake displacement bodies as function of incidence

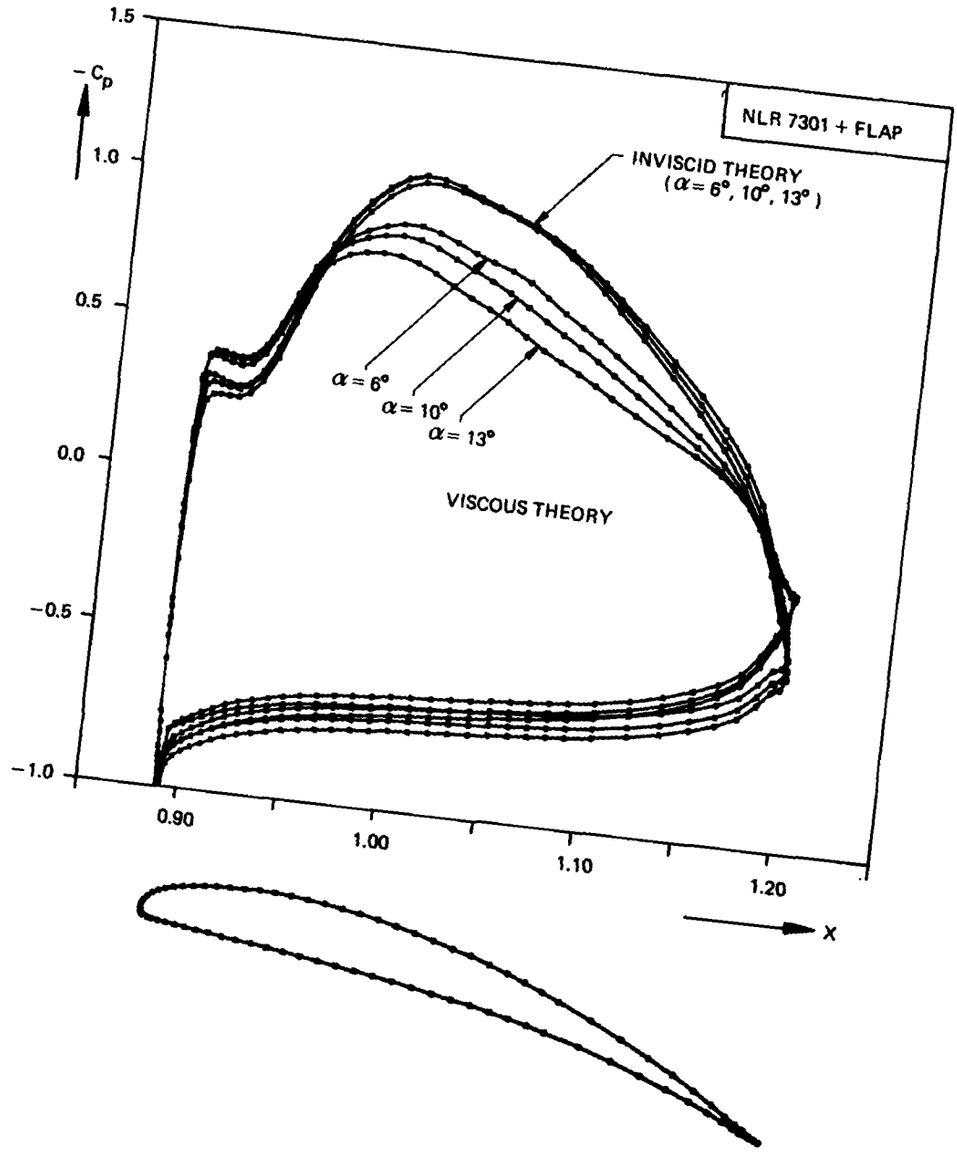


Fig. 10 The flap pressure distribution predicted by inviscid theory and viscous theory; three angles of attack $\alpha = 6°$, $10°$ and $13°$

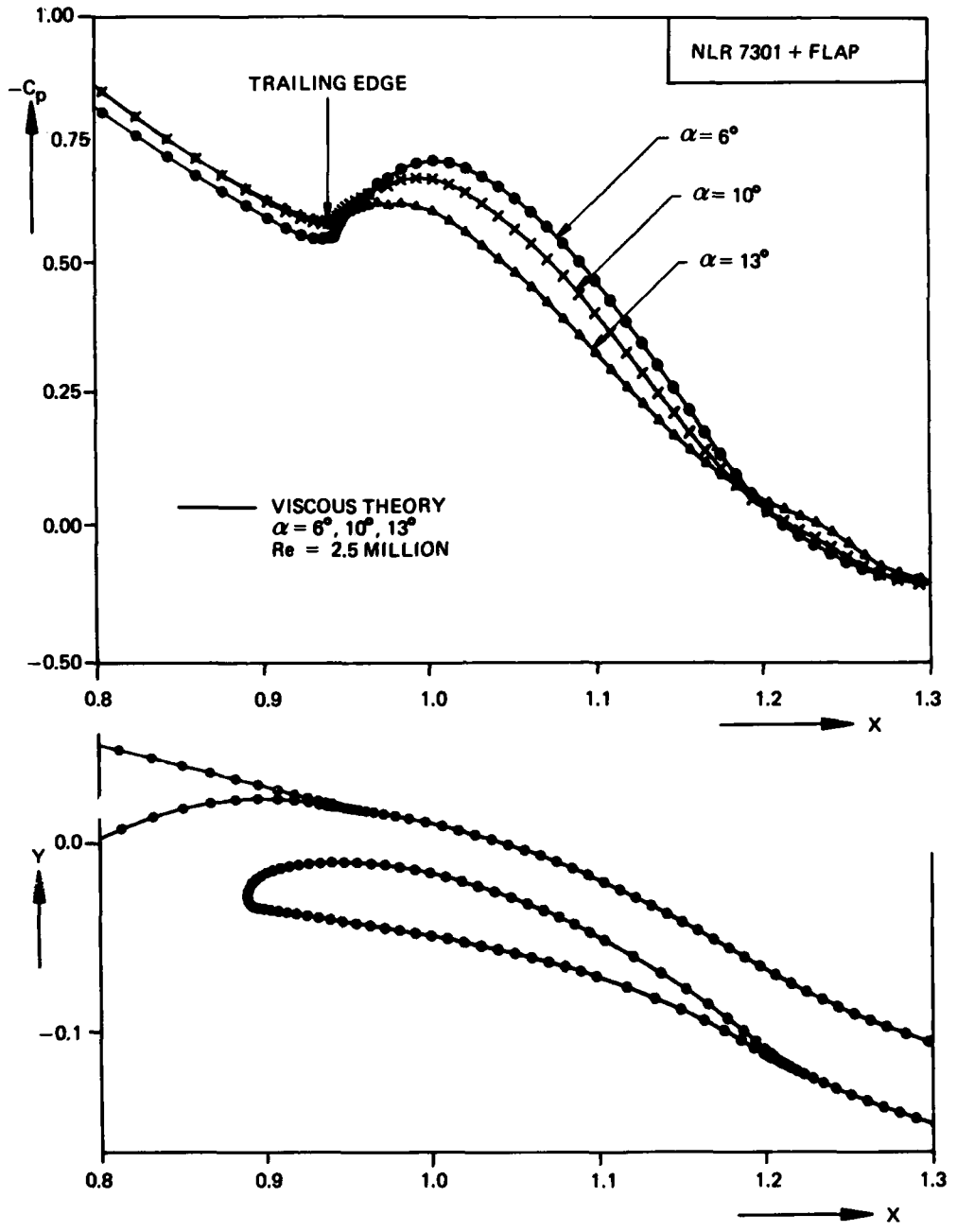


Fig. 11 Pressure distribution at wing wake centerline predicted by viscous theory for three angles of attack, α = 6°, 10° and 13°

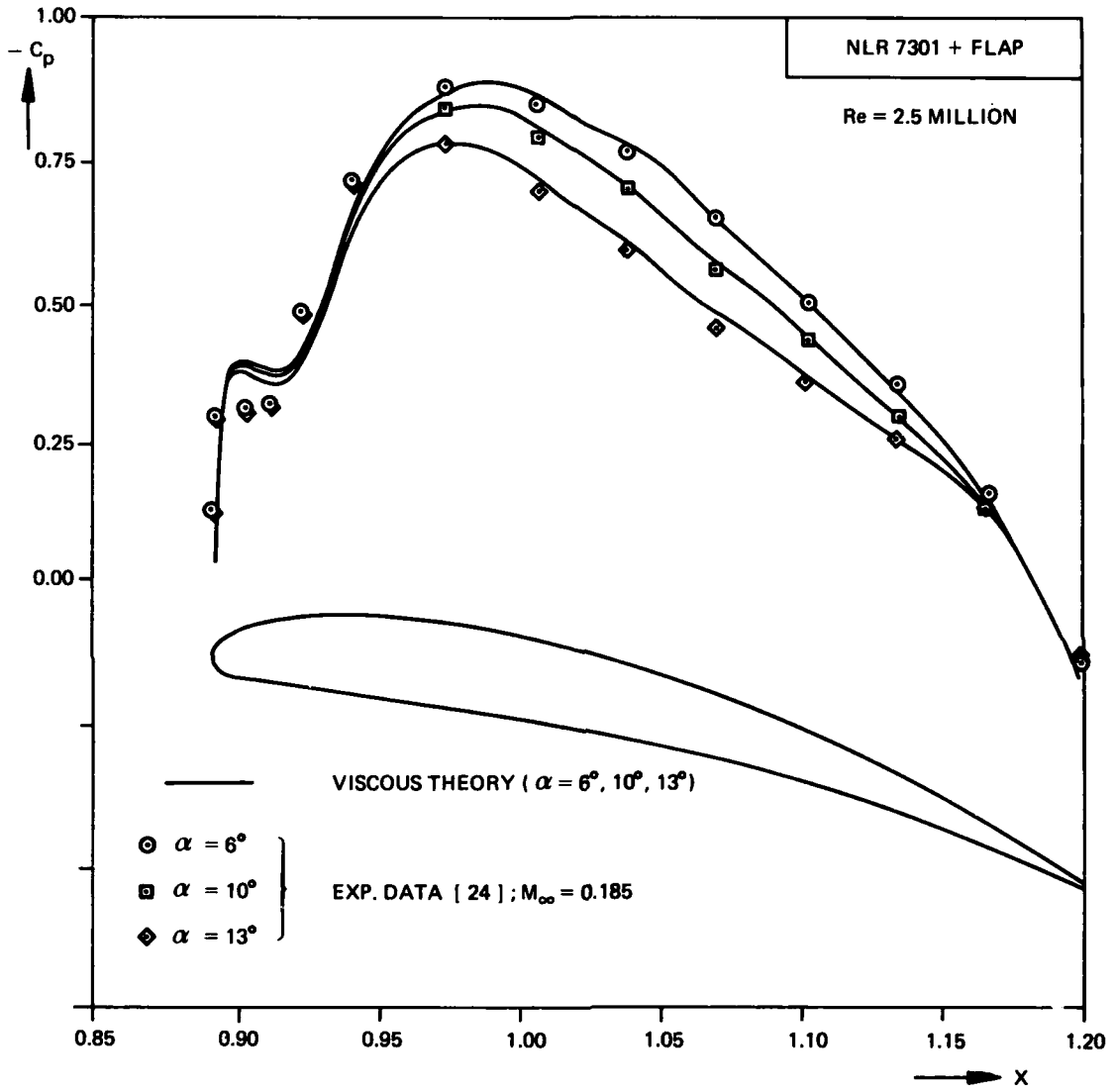


Fig. 12 Comparison between viscous theory and experimental data of the pressure distribution at the flap upper surface

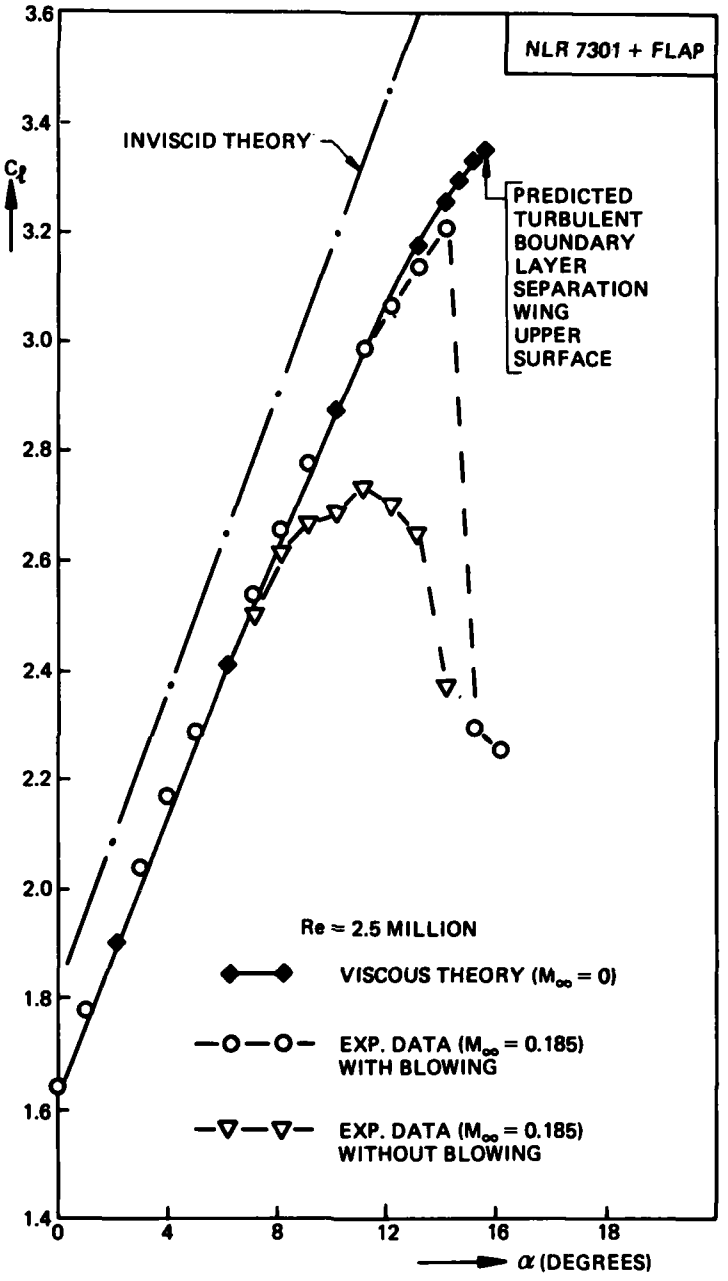


Fig. 13 Comparison of lift coefficient versus angle of attack between viscous theory and experiment for NLR7301 plus flap

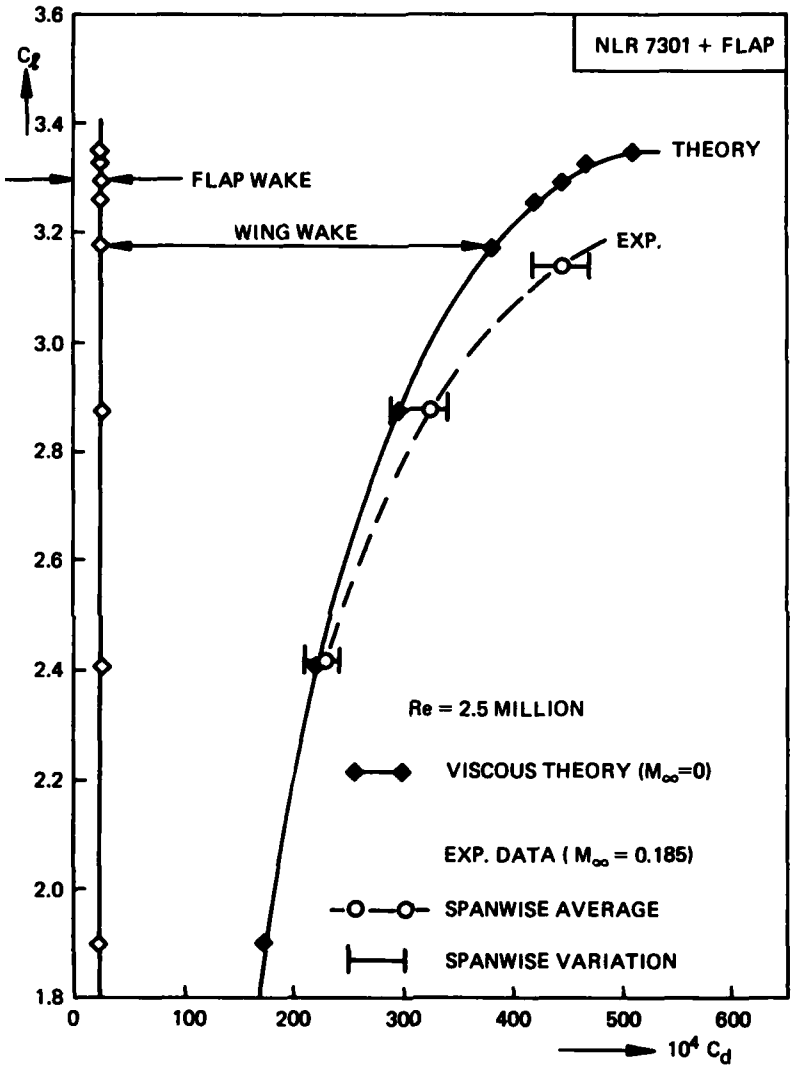


Fig. 14 Comparison of lift-drag curves between viscous theory and experiment for NLR7301 plus flap

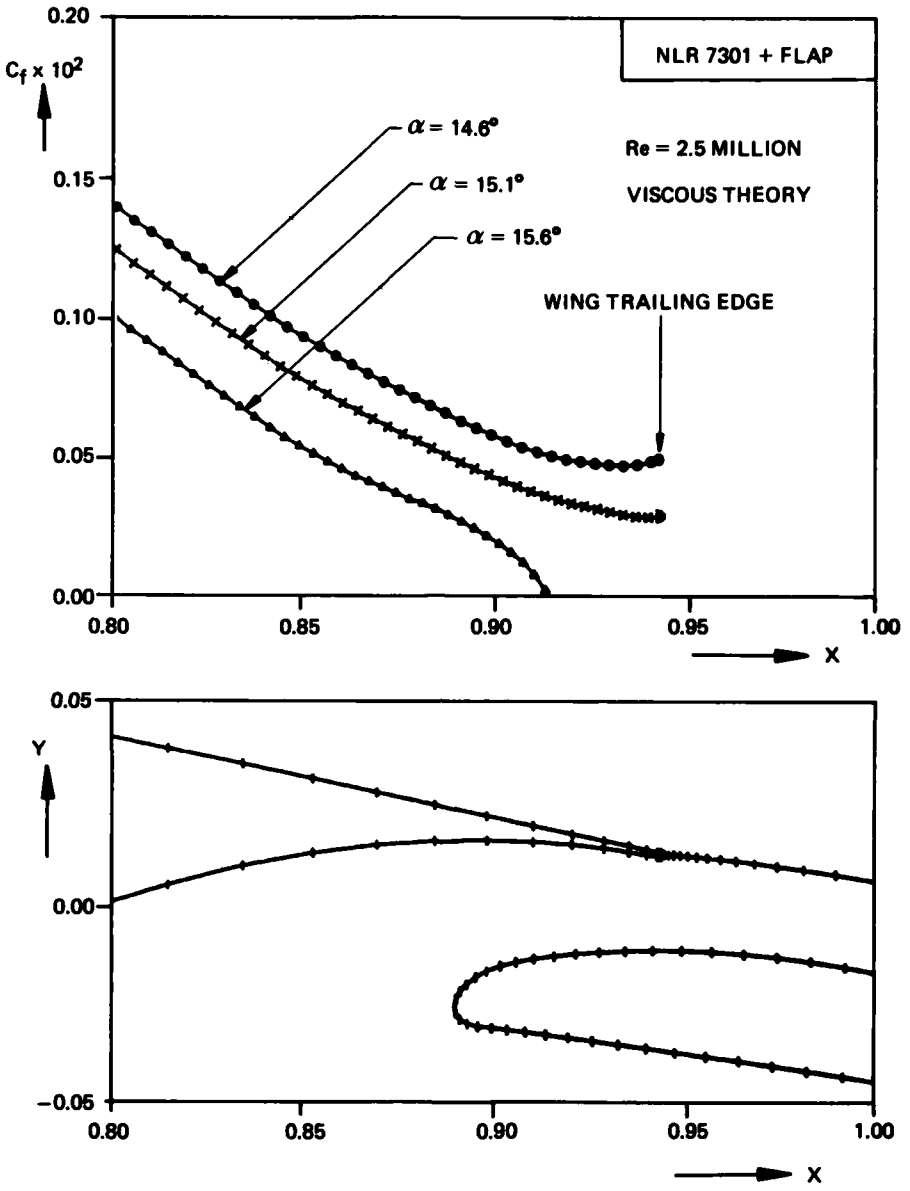


Fig. 15a Skin friction coefficient of wing upper surface turbulent boundary layer predicted by viscous theory for α = 14.6°, 15.1° and 15.6°

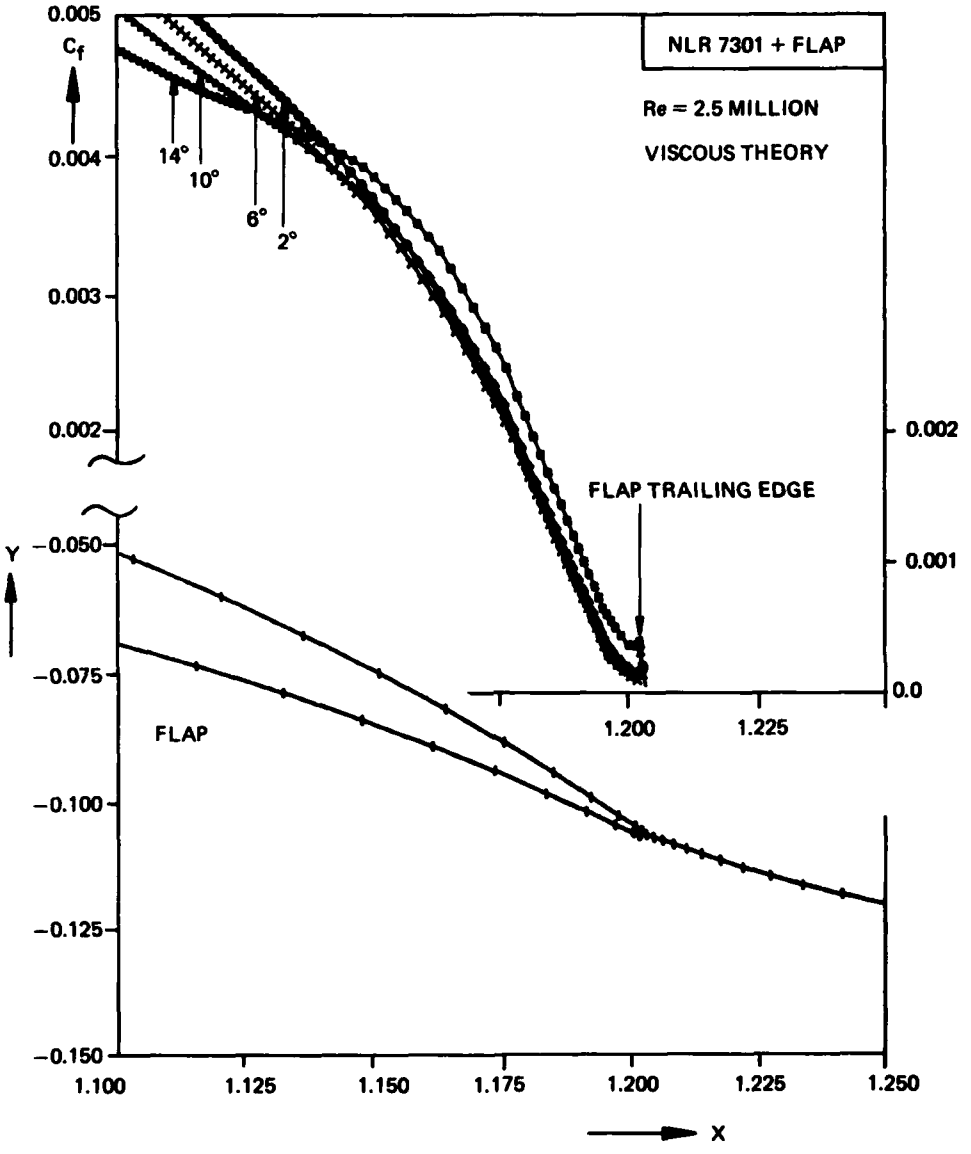


Fig. 15b Skin friction coefficient of flap upper surface turbulent boundary layer predicted by viscous theory for α = 2°, 6°, 10° and 14°

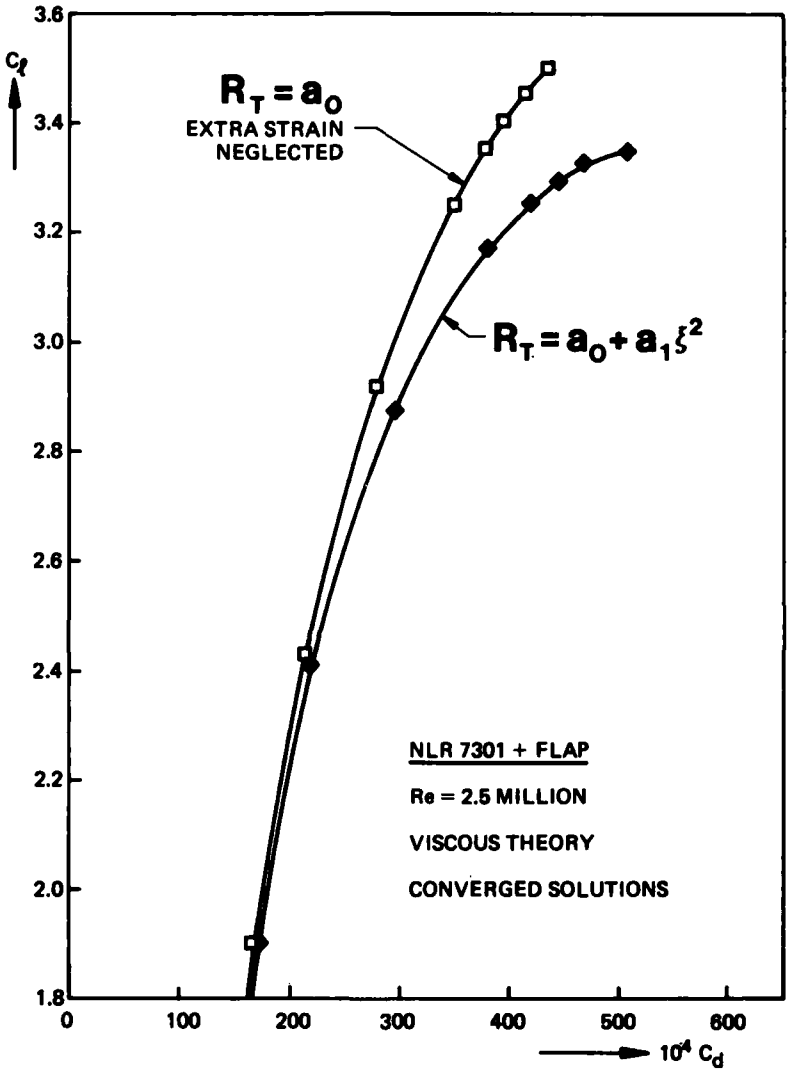


Fig. 16 Effect of longitudinal strain-rate term, in turbulence model, on the lift versus drag curve of NLR7301 plus flap

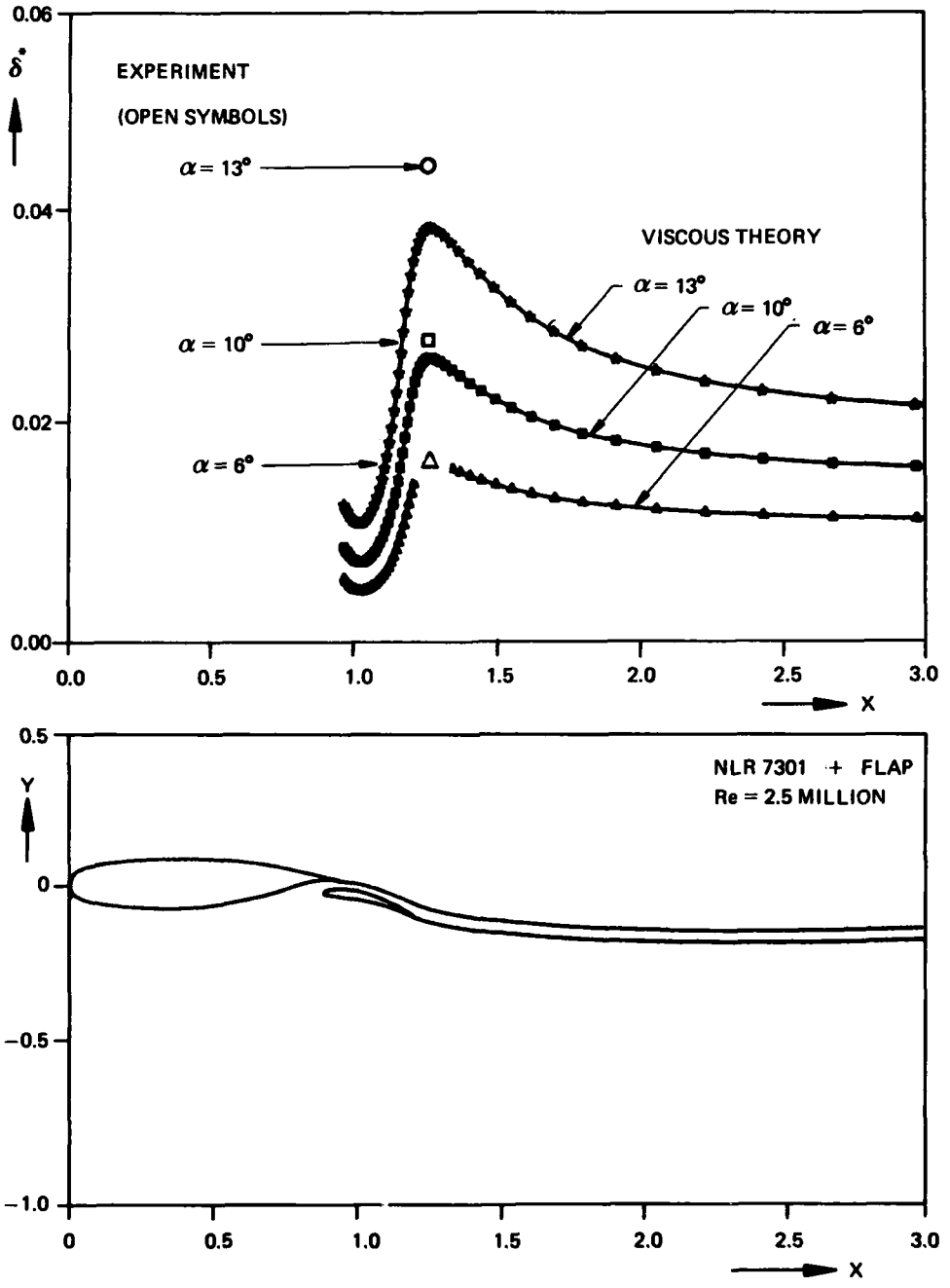


Fig. 17 Wing-wake displacement development downstream of NLR7301 plus flap; three angles of attack, α = 6°, 10° and 13°

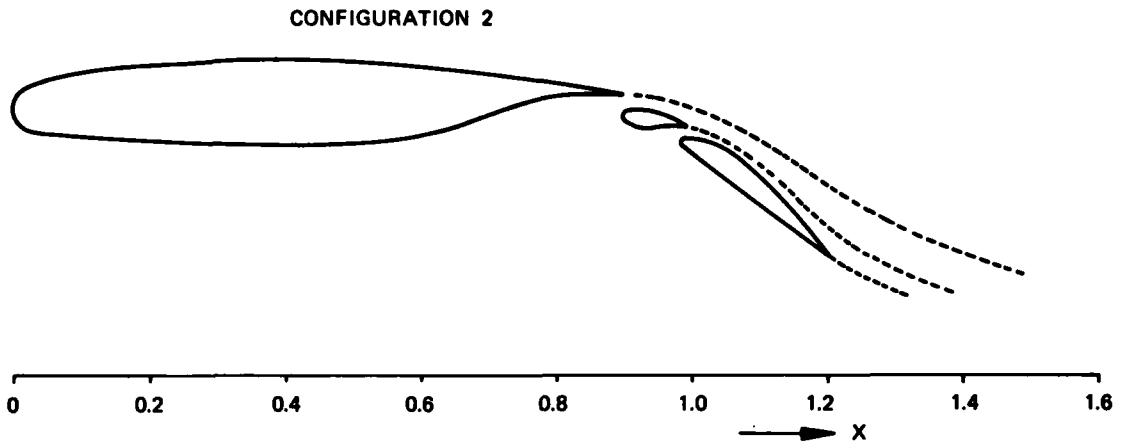


Fig. 18 Wing with double-slotted flap; denoted by configuration 2

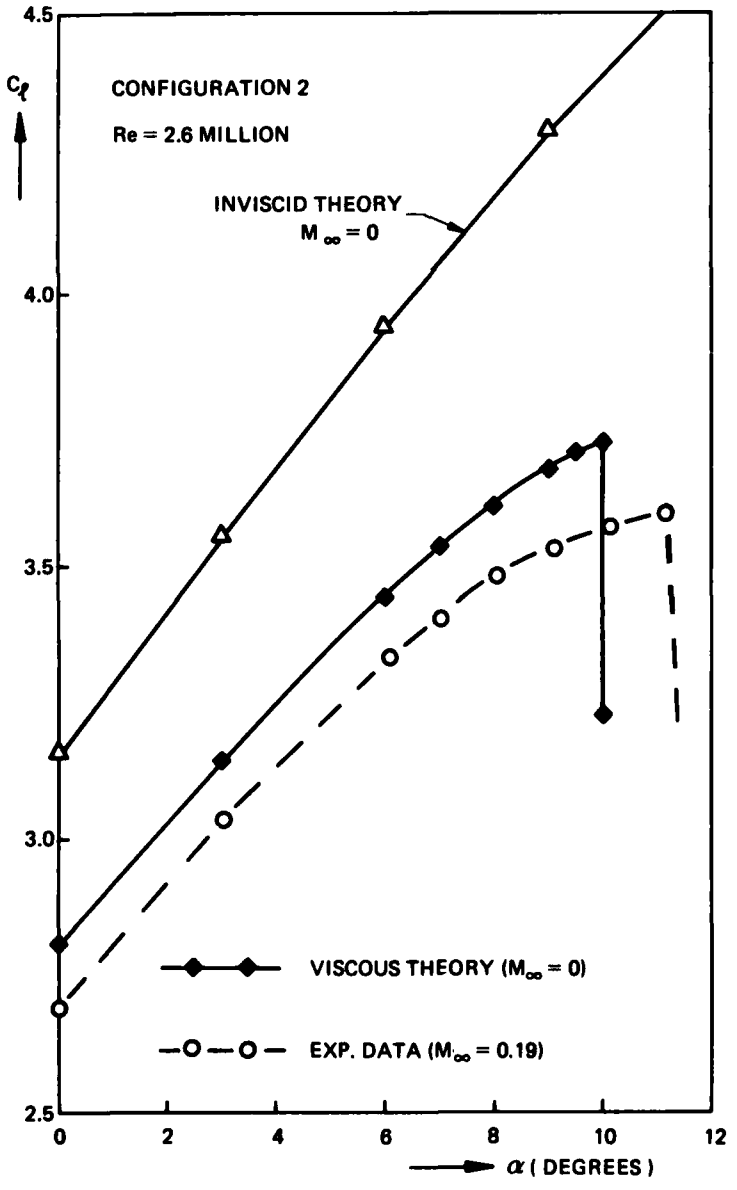


Fig. 19 Comparison of lift versus angle of attack between viscous theory and experimental data for configuration 2

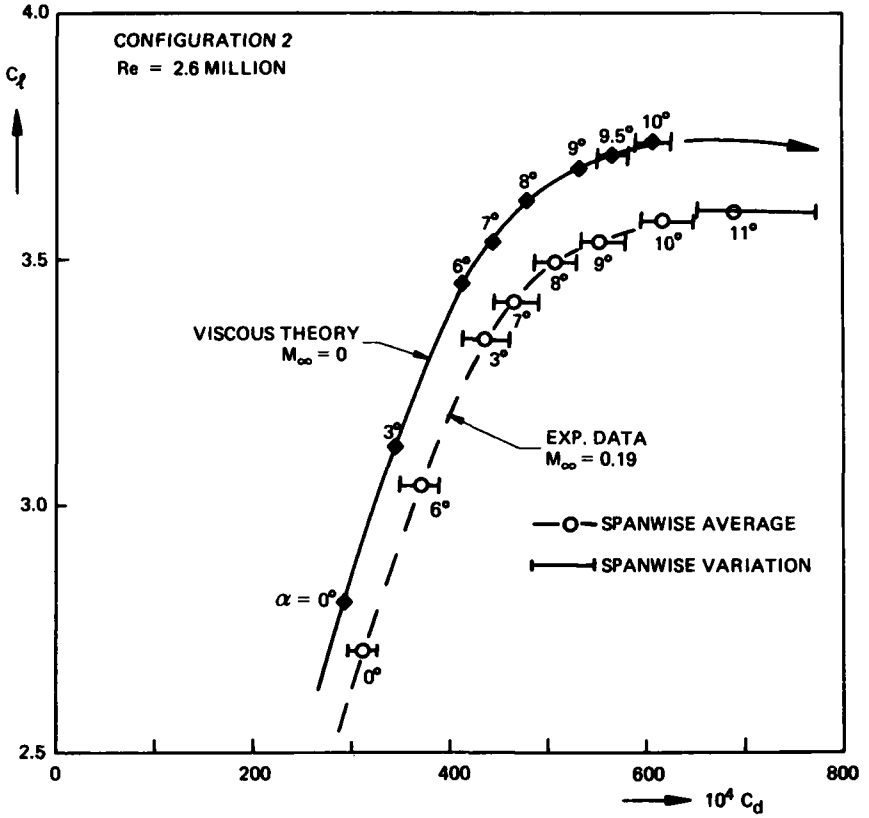


Fig. 20 Comparison of lift-versus-drag curve between viscous theory and experimental data for configuration 2

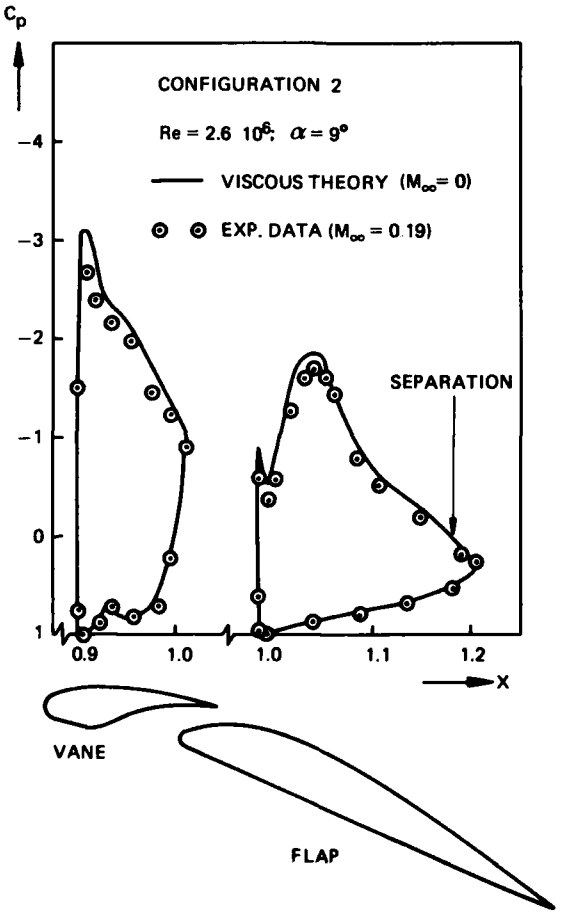


Fig. 21 Pressure distribution on vane and flap of configuration 2

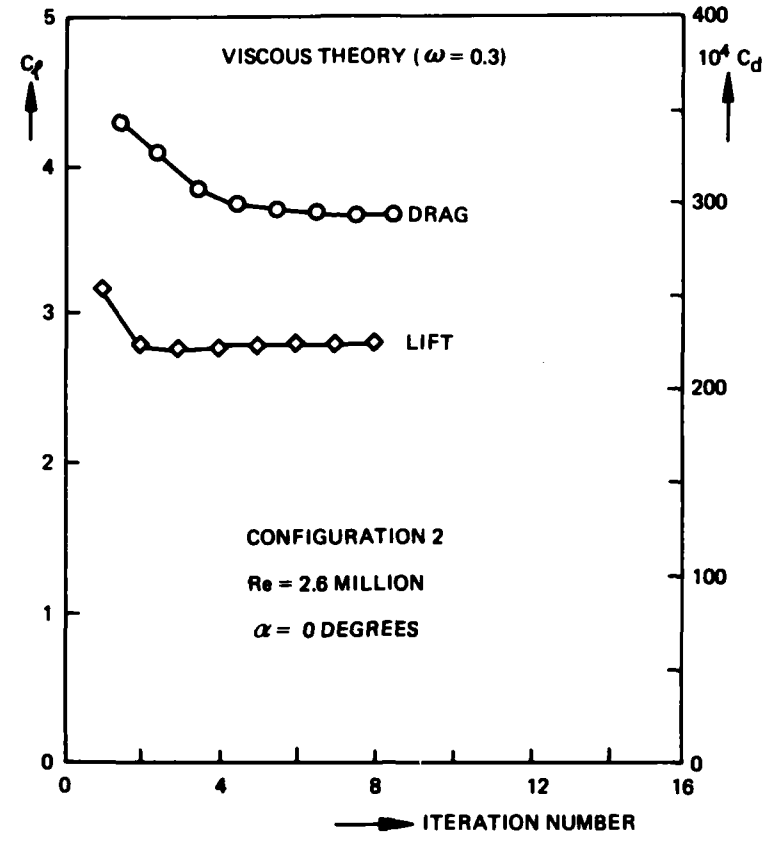


Fig. 22a Convergence characteristics of global iteration procedure applied to configuration 2 at zero degrees incidence

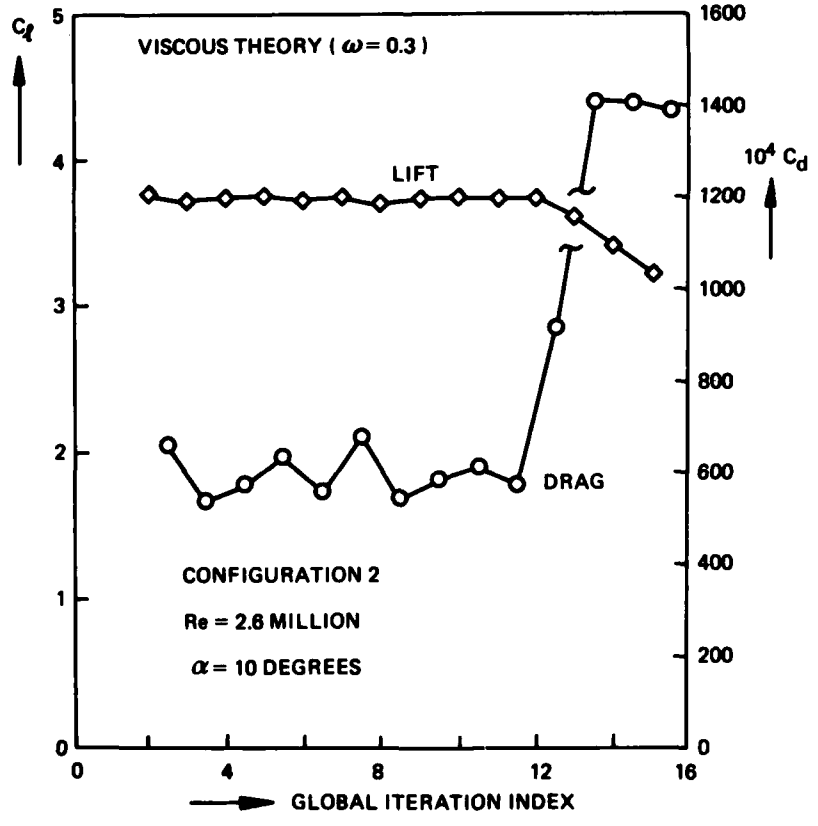


Fig. 22b Convergence characteristics of global iteration procedure applied to configuration 2 at 10 degrees incidence

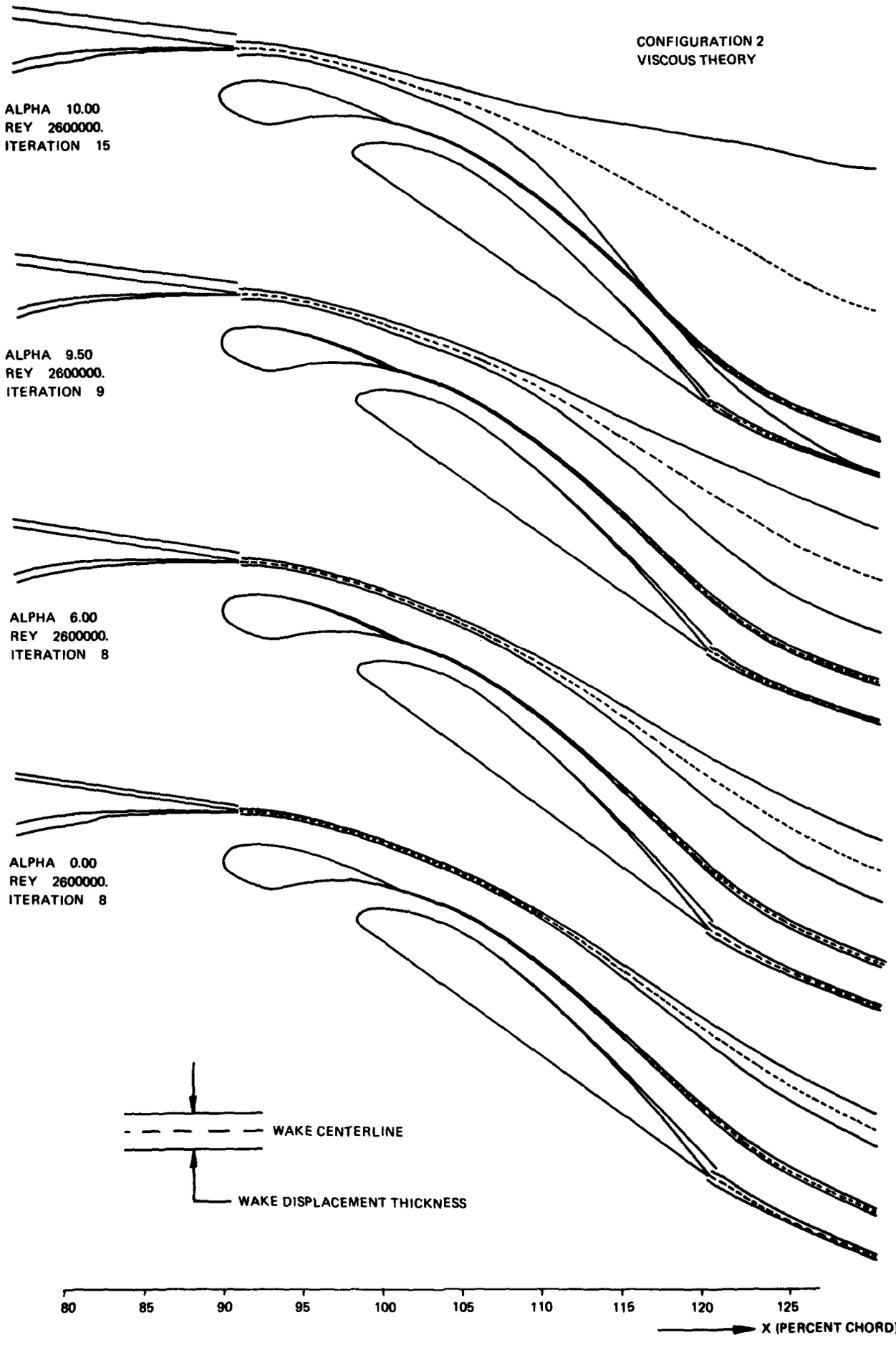


Fig. 23 Development of wake displacement bodies as function of incidence for configuration 2

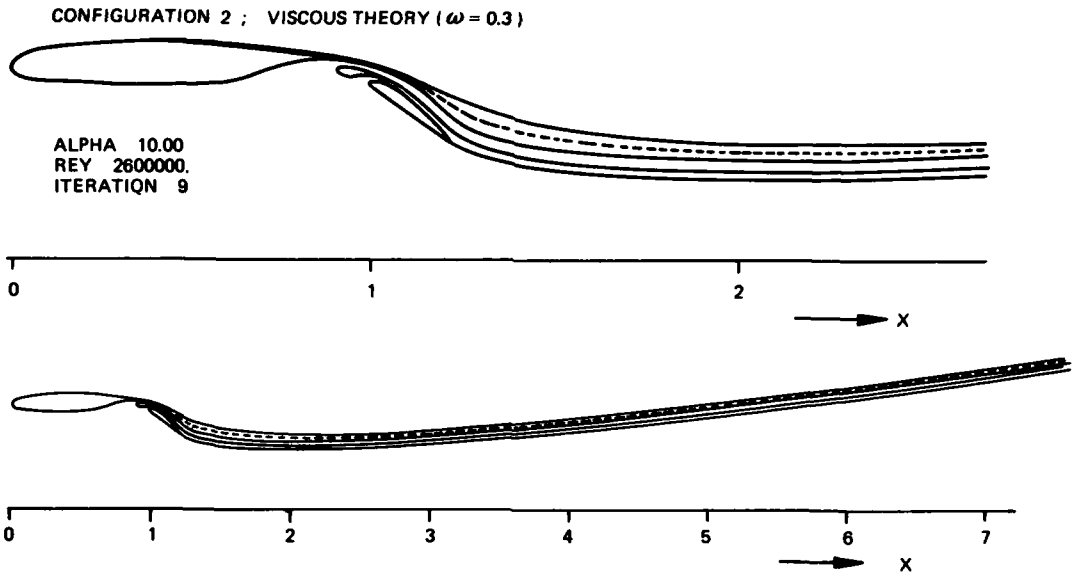


Fig. 24 Wake displacement body predicted by viscous theory for configuration 2 at 10 degrees incidence

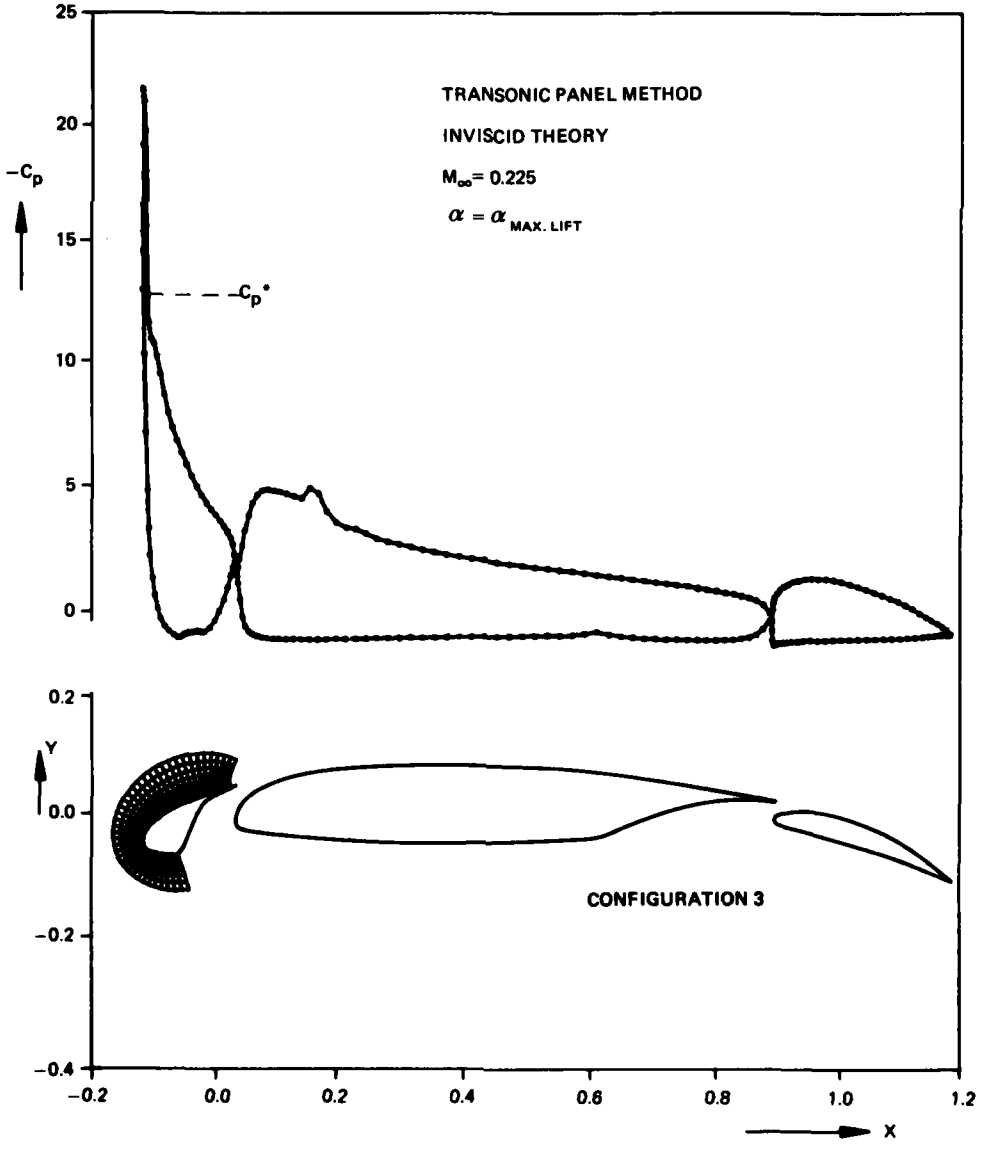


Fig. 25 Potential flow pressure distribution computed by transonic panel method [17]; maximum lift conditions at free stream Mach number of 0.225

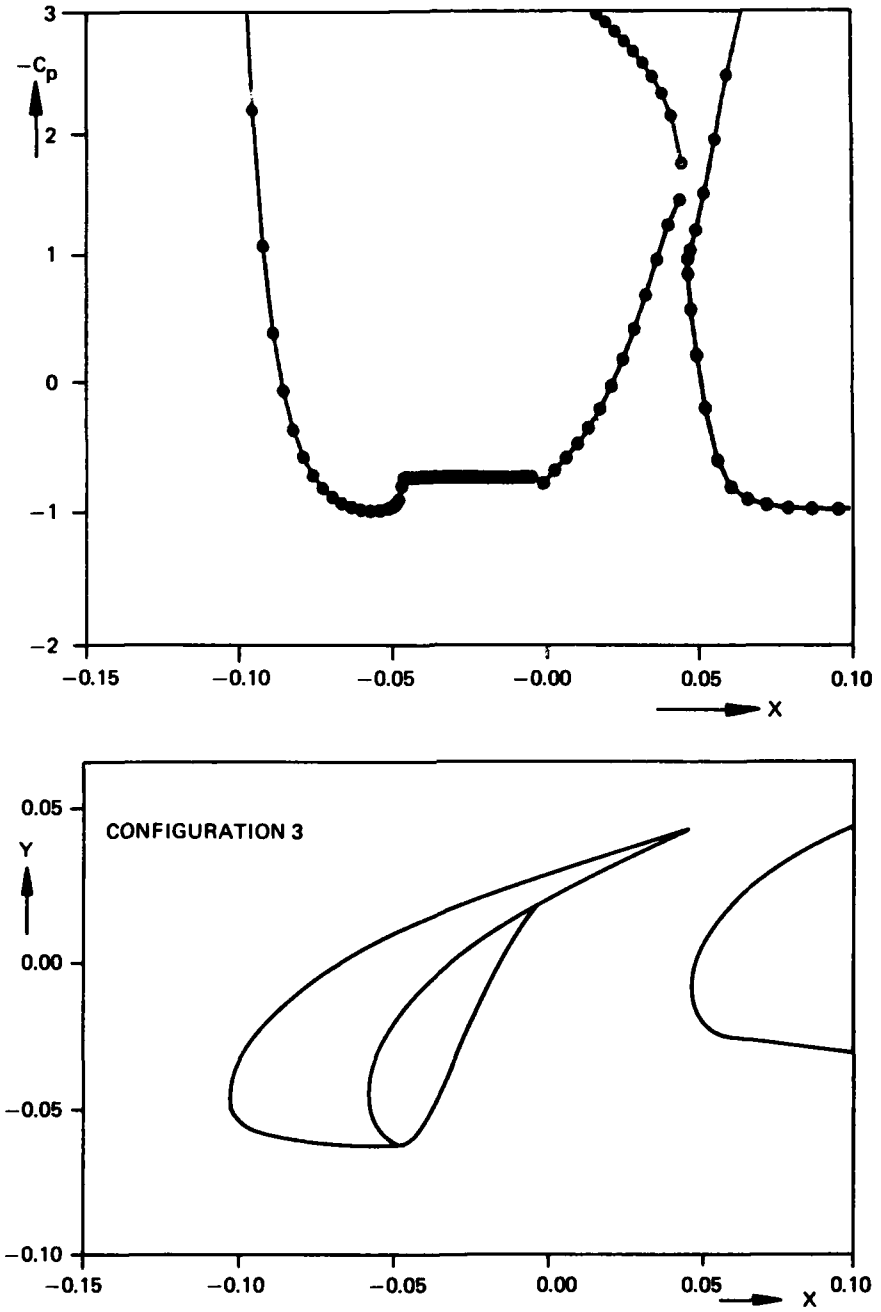


Fig. 26 Designed fairing in the slat-cove of configuration 3; slat pressure distribution showing a region of uniform pressure simulating turbulent separation

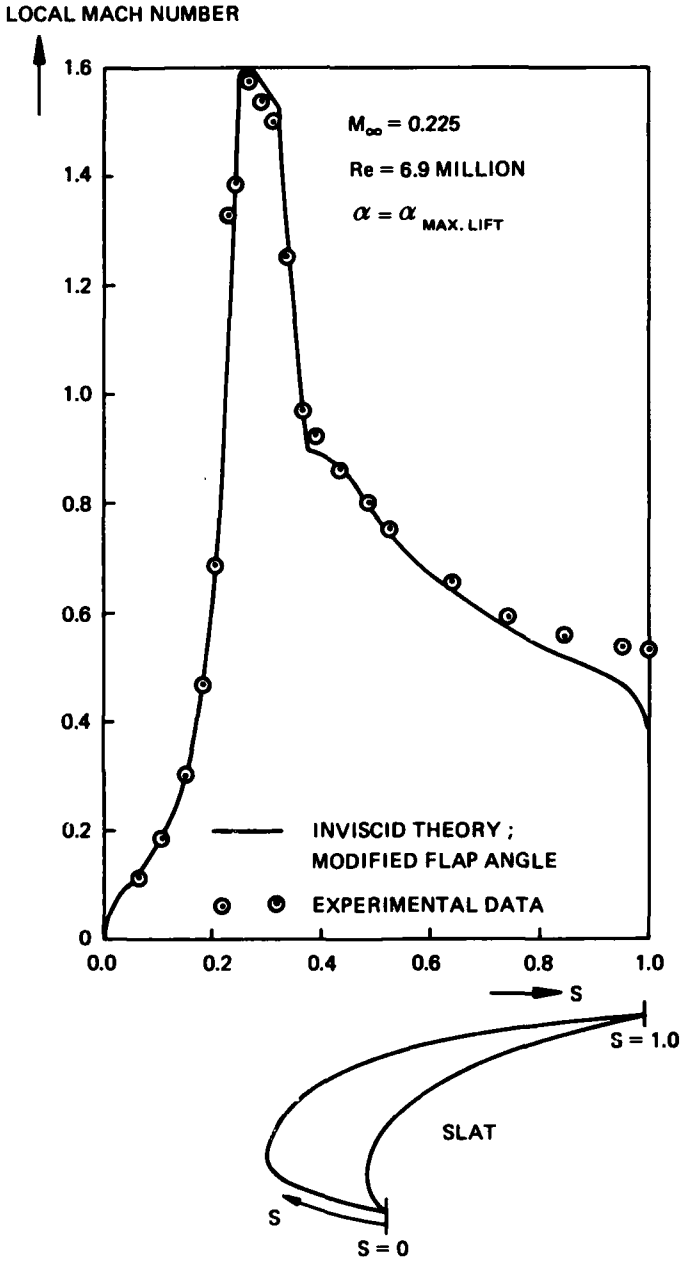


Fig. 27 Comparison of Mach distribution on slat of configuration 3 between full potential solution and experimental data for a free stream Mach number of 0.225

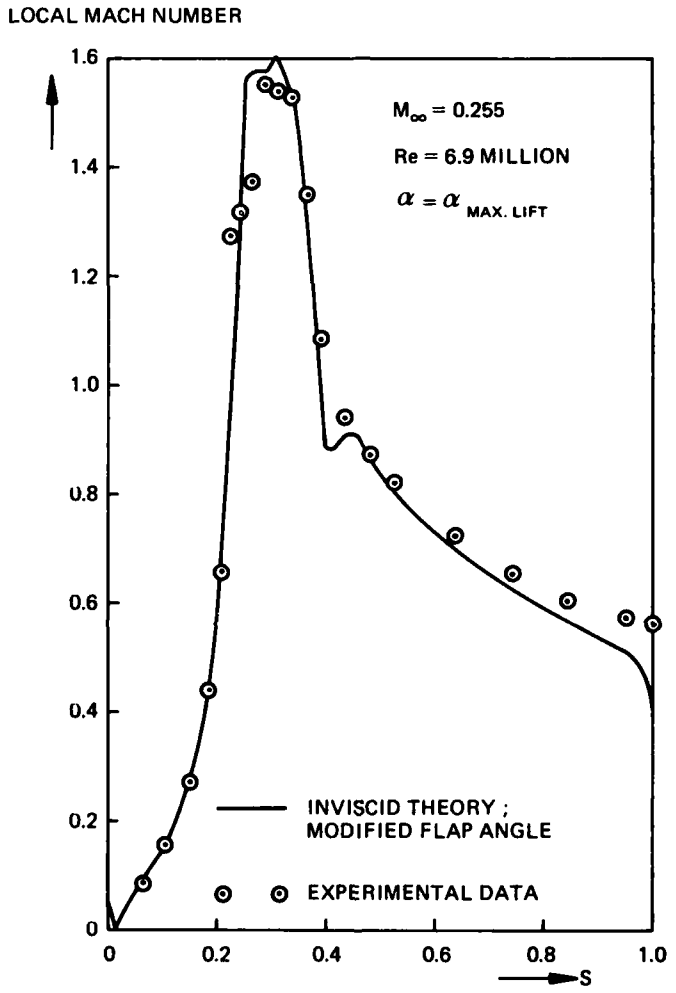


Fig. 28 Comparison of Mach distribution on slat of configuration 3 between full potential solution and experimental data for a free stream Mach number of 0.255

ETUDE DETAILLEE DE L'ECOULEMENT AUTOUR D'UN PROFIL HYPERSUSTENTE. COMPARAISONS AVEC LES CALCULS

par

Mme B.Porcheron et M. J.J.Thibert
Office National d'Etudes et de Recherches Aérospatiales
29 Ave de la Division Leclerc
92320 Châtillon, France

RESUME

L'ONERA a entrepris il y a quelques années, le développement d'une méthode de calcul de l'écoulement visqueux autour de profils hypersustentés et l'étude expérimentale détaillée de l'écoulement autour de telles configurations. Ces études théoriques et expérimentales ont pour but de disposer à terme d'un outil capable de prédire de façon précise les performances de systèmes hypersustentateurs mécaniques et par conséquent de les optimiser. Cet exposé présente les principaux résultats obtenus à ce jour tant au niveau expérimental que théorique. Les mesures de vitesse en valeur moyenne et fluctuations effectuées autour d'une configuration triple corps mettent bien en évidence l'influence mutuelle des zones visqueuses (sillages et couche limite) même lorsqu'il n'y a pas confluence et ont permis de dresser des cartographies précises de l'écoulement. La méthode de calcul de l'écoulement autour de telles configurations, basée sur une méthode de singularités de type mixte pour le fluide parfait avec prise en compte des effets visqueux par couplage fort donne des résultats très encourageants même en présence de plusieurs zones décollées simultanées. Les comparaisons calcul expérience présentées montrent cependant qu'il est nécessaire d'améliorer la modélisation utilisée dans la zone située au dessus du volet.

SUMMARY

A few years ago, ONERA undertook the development of a theoretical method computing the viscous incompressible flow around multi-element airfoils and at the same time the detailed experimental study of the flow around such configurations. The aim of these theoretical and applied studies is to set up a computing method able to give accurate prediction of mechanical high-lift systems performances in order to be able to optimize such devices.

This paper presents the main results we have got up to now experimentally, as well as theoretically. The velocity profiles and the turbulence measurements around a multi-element airfoil clearly show the interaction between boundary-layer and wakes even when these are not merging and they have been used to draw accurate maps of the flow. The computing method of the flow around these configurations is based upon a panel method (both sources and vortices) for the inviscid part of the flow and a method providing calculation and coupling for boundary layers and wakes, under strong viscous interaction conditions. This method has given quite good results even when there are several simultaneous separated flow regions. The comparisons between computation and experiment described here underline the necessity of improving the computing method in the region located above the flap.

1 - INTRODUCTION -

Un des problèmes importants pour les avionneurs est de définir des systèmes hypersustentateurs mécaniques capables de founir des portances élevées conjointement avec de faibles niveaux de trainée spécialement dans les configurations de décollage. Pour définir de tels systèmes il est nécessaire de disposer de méthodes de calcul capables de prédire de façon précise leurs performances. Or du fait de la complexité de l'écoulement autour de telles configurations, il n'est pas envisageable à moyen terme de disposer de méthodes exactes mais il est possible de développer des méthodes approchées, suffisamment précises, prenant en compte par des modèles appropriés ses principales caractéristiques.

C'est dans ce but que l'ONERA a entrepris il y a quelques années, conjointement, le développement d'une méthode de calcul de l'écoulement incompressible visqueux autour des profils multicorps et l'étude expérimentale détaillée de l'écoulement autour de telles configurations.

L'objet de ce papier est de présenter les principaux résultats obtenus dans ces deux domaines. Dans une première partie le support expérimental et l'analyse des sondages détaillés de l'écoulement autour d'une configuration triple corps seront décrits. Dans une seconde partie la méthode de calcul en cours de développement sera brièvement présentée et les résultats obtenus avec cette méthode seront comparés aux résultats expérimentaux.

2 - ANALYSE DE L'ECOULEMENT AUTOUR D'UN PROFIL HYPERSUSTENTE -

2.1 - Description des essais -

Le support expérimental est un profil supercritique (profil RA16SC1) équipé d'un volet de bord de

fuite à braquage variable et d'un bec à fente fixe. La maquette a une envergure de 1m, le bec de 0,12m de corde est braqué à 30°, le volet de 0,145m de corde est braqué à 20° ou à 40° selon la configuration étudiée. La corde de référence est celle du profil de base et est égale à 0,5m. Les essais ont été effectués dans la veine courant plan de la soufflerie F1 de l'ONERA [1] . La maquette est montée entre deux panneaux verticaux dans lesquels sont aménagées des zones d'aspiration des couches limites latérales permettant de maintenir un écoulement quasi-bidimensionnel jusqu'au décrochage(Fig.1). Les essais ont été effectués pour une vitesse de l'écoulement de 40m/s et une pression génératrice de 1,3 bar soit un nombre de Reynolds de $1{,}8\times10^{6}$.

La maquette est équipée de 104 prises de pression permettant par intégration d'obtenir la portance et le moment. La traînée est déduite des mesures de pressions effectuées à une corde en aval du profil dans le sillage.

Des sondages détaillés de l'écoulement ont été obtenus pour deux braquages du volet (δ = 20° et 40°) et plusieurs valeurs de l'incidence en plusieurs stations autour des différents éléments (Fig. 2). Pour ces sondages l'utilisation de sondes à fils chauds "DISA" a permis de mesurer la vitesse moyenne de l'écoulement ainsi que ses fluctuations. Pour les stations situées à l'extrados du volet, dans le sillage et au voisinage du bord de fuite du corps principal, une sonde à fils croisés a été choisie, par contre pour les autres stations les sondages ont été effectués avec une sonde à fil droit moins encombrante permettant des mesures plus proches de la paroi.

2.2 - *Résultats expérimentaux* -

2.2.1 - *Efforts globaux - Répartitions de pressions* -

Les évolutions du coefficient de force normale CN avec l'incidence pour les deux braquages de volet sont présentées Fig. 3. L'analyse des résultats expérimentaux présentée dans ce papier concerne la configuration braquage 20° pour les incidences α = 16°, 18° et 20° et la configuration braquage 40° pour une incidence de 16°. Les répartitions des pressions sur les différents éléments pour un braquage de 20° du volet sont tracées Fig. 4. L'incidence a peu d'influence sur le volet, l'écoulement autour de cet élément étant essentiellement imposé par la géométrie de la fente qui fixe la position du point d'arrêt.

Sur le bec l'augmentation d'incidence se traduit par une augmentation des survitesses à l'extrados et par une diminution du niveau de pression dans la zone décollée à l'intrados alors que pour le corps principal seul le pic de survitesse au voisinage du bord d'attaque s'accroît légèrement.

2.2.2 - *Sondages détaillés de l'écoulement* -

2.2.2.1 - *Profils de vitesse moyenne*

Les profils de vitesse moyenne tracés Fig. 5 permettent de décrire finement l'écoulement. Ainsi les sondages à l'intrados du bec (station 3B') mettent nettement en évidence la réduction de la taille de la bulle de décollement lorsque l'incidence augmente, réduction qui s'accompagne d'une diminution de la vitesse extérieure et de son gradient transversal. En sortie de fente bec/corps principal (station 2B) les vitesses augmentent légèrement aussi bien du côté extrados qu'intrados. Sur le corps principal (stations 1C, 2C, 5C) les profils de vitesses montrent le fort gradient transversal près du bord d'attaque (1C), l'augmentation de la vitesse dans le champ avec l'incidence (stations 1C et 2C), la réduction de la partie inférieure du sillage du bec due à la diminution du décollement à l'intrados, le déplacement en altitude et l'élargissement du sillage du bec entre les stations 1C et 5C. On notera également qu'il n'y a pas de mélange entre la couche limite de l'aile qui s'épaissit lorque l'incidence augmente et le sillage du bec.

Sur le volet en sortie de fente (station 1V') les profils de vitesses font apparaître le gradient transversal dans l'écoulement potentiel entre la couche limite du volet et le sillage de l'aile et l'épaississement du sillage du bec avec l'incidence. Pour ce qui est du sillage du corps principal, la partie inférieure provenant de l'intrados n'est pas modifiée avec l'incidence, par contre la partie supérieure qui provient de l'extrados s'épaissit et se mélange avec le sillage du bec. On notera également le développement important du sillage du corps principal entre les stations 1V' et 3V dû à la recompression de l'écoulement extérieur. A l'aval du bord de fuite du volet (stations 1S et 2S) l'épaisseur de la couche visqueuse constituée des sillages des différents éléments atteint 120mm soit environ le quart de la corde de référence.

2.2.2.2 - *Fluctuations de vitesse* -

Les sondages au fil chaud ont permis de mesurer les fluctuations de la vitesse pour les différentes stations (Fig. 6).

Dans la zone décollée à l'intrados du bec (station 3B'), les fluctuations sont élevées et atteignent 20% de la vitesse extérieure. Les profils de turbulence longitudinale mettent nettement en évidence la diminution de la bulle de décollement avec l'incidence.

Sur le corps principal (stations 1C, 2C) les profils de fluctuations au sein du sillage du bec varient peu avec l'incidence et le maximum diminue lorsqu'on s'éloigne du bord de fuite du bec.

Au bord de fuite du corps principal (station 5C) la zone turbulente atteint 50mm soit 10% de la corde de référence et il y a confluence entre la couche limite de l'aile et le sillage du bec.

Au niveau du sillage du bec, en tenant compte des mesures de $\overline{w'^2}$ et en admettant que $\overline{v'^2} = \overline{w'^2}$ on obtient pour l'énergie cinétique de turbulence une valeur relative $(\sqrt{k}/u_e)_{max} \sim 5\%$ à $\alpha = 20°$. Pour ce qui est de la couche limite de l'aile, le niveau de turbulence est également élevé $(\sqrt{k}/u_e)_{max} \sim 13\%$ et varie peu avec l'incidence.

En sortie de fente sur le volet (station 1V') on retrouve une zone d'écoulement faiblement turbulente entre la couche limite du volet et le sillage de l'aile, zone qui disparaît au bord de fuite du volet (station 3V) où les fluctuations sont très élevées $(\sqrt{k}/u_e)_{max} \sim 10\%$).

Pour ce qui est de la tension de Reynolds les profils mesurés au bord de fuite du corps principal, sur le volet et dans le proche sillage sont tracés Fig. 7. Ces profils présentent des pointes correspondant aux régions à fort gradient transversal et sont peu influencés par l'incidence.

2.2.3 - *Influence du braquage du volet* -

Pour une incidence de 16° l'influence du braquage du volet sur les répartitions de pressions, les profils de vitesse moyenne et ses fluctuations sont présentées Fig. 8, 9 et 10.

2.2.3.1 - *Distributions de pressions* -

Les distributions de pressions (Fig. 8) mettent en évidence une augmentation de la charge avec l'augmentation du braquage du volet sur le bec et le corps donc une augmentation des survitesses au bord d'attaque. A l'intrados du bec, l'étendue du décollement diminue quand le braquage augmente. Sur le bec et sur le corps, les variations d'incidence et de braquage du volet ont les mêmes effets. A l'extrados du volet compte tenu de la variation de géométrie de la fente avec le braquage, les répartitions des pressions sont très différentes avec un décollement sur le volet pour $\delta = 40°$.

2.2.3.2. - *Ecoulement* -

a) Bec :

L'influence du braquage est très nette aux deux stations de sondages sur le bec (2B et 3B') : l'augmentation du braquage accroît la survitesse en sortie de fente à la station 2B de 30% environ, ainsi que l'épaisseur du sillage (Fig. 9). Les écarts sur les minima de vitesse au sein du sillage et sur la position en altitude de ces minima sont dûs à un léger écart de l'abscisse de sondage pour les deux braquages. En 3B', l'épaisseur de la zone décollée diminue avec le braquage, ainsi que la vitesse extérieure. Pour ces deux stations, l'intensité des fluctuations longitudinales $\sqrt{\overline{u'^2}}$ varie peu avec le braquage du volet (Fig. 10).

b) Corps :

L'augmentation des survitesses avec le braquage est très marquée au voisinage de la sortie de fente (stations 1C et 2C). On remarquera également un déplacement en altitude de la position du sillage par rapport au corps principal entre les deux valeurs de braquage. La fluctuation $\sqrt{\overline{u'^2}}$ est plus forte à 20° dans le sillage du bec en 1C et 2C tandis qu'en 5C l'augmentation de l'épaisseur de couche limite sur le corps principal s'accompagne d'une augmentation des fluctuations longitudinales de la vitesse (Fig 10).

d) Volet :

Les figures 9 et 10 ne montrent pas de différences essentielles entre les deux braquages pour la première station du volet à l'exception de la vitesse en sortie de fente. Il faut remarquer que les deux stations ne sont pas rigoureusement à la même abscisse ce qui explique que l'on ne retrouve pas dans le sillage les écarts constatés en 5C sur la couche limite du corps principal.

e) Sillage :

La présence d'un décollement pour le braquage à 40° du volet conduit à un sillage plus étendu pour cet élément. De plus la différence du champ de pression au-dessus du volet provoque un décollement très différent du sillage du corps principal. Les écarts constatés au niveau des profils de vitesse se retrouvent sur les fluctuations (Fig. 10) avec une forte augmentation de celles-ci pour 40° de braquage.

3 - *COMPARAISON CALCULS-EXPERIENCE* -

3.1 - *Description de la méthode de calcul* -

La méthode de calcul de l'écoulement visqueux incompressible autour de profils multicorps est decrite en détail dans [2]. Nous rappellerons ici son principe.

3.1.1 - *Fluide parfait* -

L'écoulement de fluide parfait est calculé par une méthode de singularités de type sources à caractère mixte aux bords de fuite. Chaque élément de profil, comme chaque sillage est figuré par une répartition de densités de source variant linéairement sur chaque segment joignant deux points de définition. Les points de contrôle où sont imposées les conditions sur la vitesse normale sont situés au milieu de chaque segment (Fig. 11a). Pour assurer la condition de Joukowsky un terme tourbillonnaire réparti sur tout l'élément, d'intensité variant linéairement avec l'abscisse x, maximale au bord d'attaque et nulle au bord de fuite est utilisé. En outre pour améliorer la qualité de la répartition de vitesse dans les zones de faible épaisseur au voisinage des bords de fuite des différents éléments, des termes tourbillonnaires ont été rajoutés dans ces régions. A chacun des termes tourbillonnaires correspondent deux distributions de densité tourbillonnaire, l'une à l'intrados, l'autre à l'extrados, construites à partir de densités élémentaires de même géométrie que les sources élémentaires et de profils $f_k(x)$ linéaires par morceaux en fonction de l'abscisse x (Fig. 11b). Ces termes tourbillonnaires supplémentaires sont déterminés par des conditions de régularité imposées à l'écoulement fictif à l'intérieur du profil. Les conditions choisies consistent à imposer l'égalité des vitesses tangentielles de cet écoulement intérieur à la paroi en des couples de points de contrôle extrados et intrados situés à la même abscisse que les densités tourbillonnaires.

3.1.2 - *Fluide visqueux*

Les couches visqueuses (couches limites et sillages) sont calculées au moyen des équations intégrales de continuité, de quantité de mouvement et d'une équation de moment (entraînement ou énergie cinétique). Les relations de fermeture sont obtenues dans le cas laminaire à partir des solutions de similitude avec ou sans courant de retour ; dans le cas turbulent les profils de vitesse sont modélisés par une loi composite rappelant celle de Coles et un modèle de turbulence algébrique est utilisé. Dans les équations intégrales, les grandeurs non visqueuses (ρ,u,w) et leurs dérivées partielles sont relevées à la paroi. Une formulation déficitaire est utilisée pour la définition des épaisseurs intégrales permettant de prendre en compte un gradient de pression normal.

Le système différentiel visqueux est résolu en mode direct pour les faibles valeurs du paramètre de forme et en mode inverse dans les autres cas.

3.1.3 - *Couplage*

Le couplage est réalisé à la paroi par itérations successives sur des résolutions découplées du fluide parfait et des couches visqueuses. Les itérations sont de type direct lorsque le paramètre de forme est inférieur à 1,8 et de type semi-inverse lorsque le paramètre de forme est supérieur à 1,8.

3.2 - *Résultats de calcul* -

Les coefficients globaux (Cz, Cx, Cm) calculés sont comparés aux résultats expérimentaux Fig.12 . Pour les deux braquages du volet, le calcul surestime les effets visqueux ce qui conduit à des Cz plus faibles que ceux mesurés, les écarts étant de l'ordre de 5% pour le braquage de 20° et de 10% pour le braquage de 40°. On notera l'importance des effets visqueux notamment pour le braquage de 40° du volet. Pour ce qui est de la traînée, elle est très bien estimée paradoxalement pour la configuration la plus difficile (volet à 40°) et surestimée d'environ 25% pour la configuration volet à 20°. Les répartitions de pression calculées pour une incidence de 16° et les deux braquages de volet sont comparées aux mesures Fig. 13 et 14. Pour le braquage de 20° du volet (Fig. 13) le calcul prévoit un petit décollement au bord de fuite du volet qui n'existe pas expérimentalement. Sur le corps principal les pressions sont bien estimées sauf au voisinage du bord d'attaque, les écarts étant dûs pour une partie à l'hypothèse d'incompressibilité mais aussi au fait que dans son état actuel le programme ne traite que des bords de fuite pointus ce qui a conduit à modifier la géométrie réelle du bec mais aussi en conséquence celle de la fente. Sur le bec le niveau de pression calculé dans le décollement intrados est surestimé et la mauvaise prévision de la circulation sur le volet conduit à une surestimation de la charge du bec. Pour le braquage de 40° (Fig. 14) le décollement expérimental sur le volet est bien prévu par le calcul, on retrouve comme dans le cas précédent une sous évaluation des vitesses en sortie de fente bec/corps principal, par contre la charge sur le bec et le niveau de pression dans la zone décollée à l'intrados sont bien estimés.

Pour ce qui est des couches limites au voisinage du bord de fuite du corps principal (Fig. 15), les écarts de survitesses au voisinage du bord d'attaque conduisent à des épaisseurs intégrales calculées plus faibles que celles mesurées notamment dans le cas du braquage 40°.

Les résultats des comparaisons calcul-expérience, bien que non totalement satisfaisants, sont très encourageants et montrent l'intérêt d'une telle approche pour le calcul de configurations multicorps présentant simultanément plusieurs zones décollées. Les écarts constatés au niveau du calcul sont dûs pour une large part à une mauvaise prévision de l'écoulement sur le volet. Ceci est dû au fait que dans la méthode utilisée la couche limite du volet et le sillage du corps sont traités indépendamment or les résultats expérimentaux mettent nettement en évidence que la

présence du sillage du corps qui s'épaissit rapidement dans le gradient de vitesse dû au champ du volet conduit à une zone visqueuse fortement turbulente qui influence le développement de la couche limite sur le volet même s'il n'y a pas mélange entre ces deux couches visqueuses. Il semble donc important d'améliorer la modélisation de l'écoulement dans cette région. Une des voies possible est le calcul de l'ensemble de l'écoulement au dessus du volet par une technique de différences ou volumes finis, cependant se pose le problème du type d'équations à utiliser. Une tentative a été effectuée en utilisant les équations de couche limite. Cette méthode développée au DERAT est du type volumes finis et le modèle de turbulence à 2 équations pour l'energie cinétique de turbulence k et sa dissipation $\mathcal{E}$ est voisin de celui de Jones et Launder. Le calcul a été effectué entre les stations 1V' et 3V et en utilisant comme données de départ les épaisseurs intégrales (mesurées dans le sillage du corps en 1V' et calculées pour la couche limite du volet). Le profil de vitesse au départ est construit selon la méthode de Whithield. Pour ce qui est de l'énergie cinétique de turbulence k le profil théorique au départ est calculé en utilisant le modèle de longueur de mélange. Dans le calcul il n'a pas été tenu compte du sillage du bec ce qui explique l'écart entre le profil de $\sqrt{k}$ calculé et le profil expérimental de $\sqrt{\overline{u'^2}}$ pour des valeurs de z comprises entre 40 et 60mm. A la station 3V les comparaisons calcul expérience (Fig. 16) montrent que le profil de vitesse moyenne est assez bien estimé avec toutefois un léger décalage en altitude du sillage du corps et une surestimation des vitesses entre la couche limite du volet et le sillage du corps. Pour ce qui est de la turbulence longitudinale (assimilée à k dans le calcul) elle est sous-estimée surtout dans une zone située juste au dessus de la couche limite du volet. Enfin la tension de Reynolds $\overline{u'w'}$ est elle aussi assez mal prédite dans la zone du sillage du corps principal.

L'intégration des profils de vitesse calculés permet d'obtenir les évolutions des épaisseurs intégrales du sillage du corps et de la couche limite du volet (Fig. 17). Les évolutions obtenues montrent un accord satisfaisant avec les valeurs expérimentales au bord de fuite du volet (station 3V).

4 - CONCLUSION -

Les études effectuées sur une configuration triple corps ont montré qu'au niveau expérimental il était indispensable de disposer de mesures détaillées et complètes permettant de comprendre les phénomènes et par conséquent de construire des modèles théoriques susceptibles de représenter correctement l'écoulement. A cet égard les sondages au fil chaud effectués en de nombreuses stations autour des différents éléments répondent à cette exigence bien qu'ils n'aient pas permis d'obtenir des informations précises dans les zones visqueuses de faible épaisseur. Cette étude expérimentale sera donc poursuivie pour obtenir un dossier expérimental plus complet. Pour ce qui est des études théoriques, l'approche effectuée a donné des résultats encourageants puisque une convergence des calculs a été obtenue dans des conditions extrêmement difficiles avec plusieurs zones de décollement simultanément présentes. Les résultats obtenus sont encore trop éloignés des valeurs expérimentales pour que cette méthode soit réellement utilisable pour l'optimisation de profils hypersustentés. Toutefois un certain nombre d'améliorations notamment pour le calcul de l'écoulement en sortie de fentes (traitement des bords de fuite épais) et au-dessus du volet (prise en compte de l'influence du sillage du corps principal) permettront sans doute d'améliorer nettement les prévisions théoriques.

REFERENCES -

1 J.M. CARRARA et A. MASSON - Trois ans d'exploitation de la soufflerie subsonique pressurisée de l'ONERA - 12th Congress of the International Council of the Aeronautical Sciences - Munich - 12-17 octobre 1980. T.P. ONERA 1980-129.

2 M. NERON - J.C. LEBALLEUR - Calcul d'écoulements visqueux décollés sur profils d'ailes par une approche de couplage - Agard /FDP Symposium on Computation of Viscous - Inviscid Interactions - Colorado Springs (U.S.A.) - 29 septembre-1er octobre 1980.

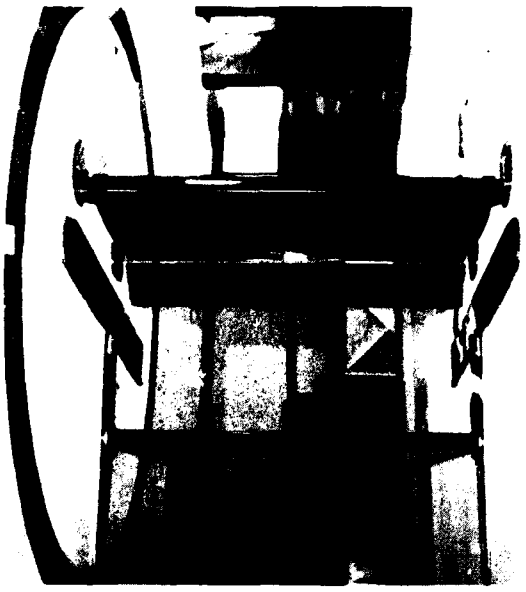
LISTE DES SYMBOLES -

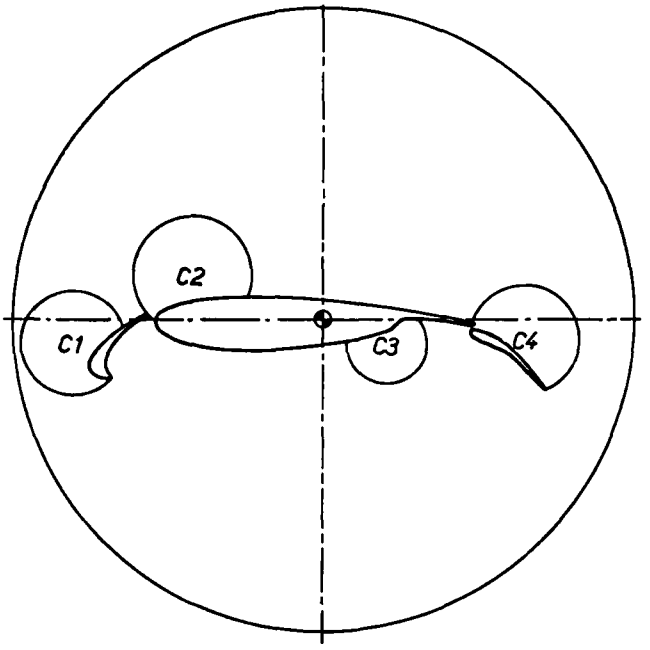
C	corde de référence du profil
Cm	coefficient de moment à 25% de la corde
Cn	coefficient de la force normale
Cx	coefficient de trainée de sillage
Cz	coefficient de portance
Kp	coefficient de pression
po	pression statique de référence
Re	nombre de Reynolds rapporté à la corde de référence
u	composante longitudinale de la vitesse moyenne

w	composante normale de la vitesse moyenne
$\sqrt{\overline{u'^2}}$	moyenne des fluctuations de la composante u de la vitesse
$\sqrt{\overline{w'^2}}$	moyenne des fluctuations de la composante w de la vitesse
$\overline{u'.w'}$	tension de Reynolds
x,z	coordonnées liées au profil
α	angle d'incidence
δ	angle de braquage du volet
δ_1	épaisseur de déplacement de la couche limite
δ_2	épaisseur de quantité de mouvement de la couche limite
k	énergie cinétique de turbulence
ε	taux de dissipation
ρ	masse volumique de l'air

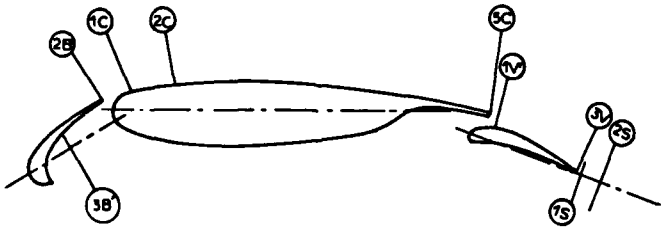
FIGURES -

1	Photo de la maquette dans la veine courant plan de F1 et disposition des zones d'aspiration
2	Stations de sondage
3	Evolution du coefficient CN avec l'incidence
4	Influence de l'incidence sur les répartitions de pression (volet 20°)
5	Evolution de la vitesse en fonction de l'incidence (volet 20°)
6	Evolution de $\sqrt{\overline{u'^2}}$ en fonction de l'incidence (volet 20°)
7	Evolution de $\overline{u'.w'}$ en fonction de l'incidence (volet 20°)
8	Influence du braquage du volet sur les répartitions de pression (α = 16°)
9	Evolution de la vitesse en fonction du braquage du volet (α = 16°)
10	Evolution de $\sqrt{\overline{u'^2}}$ en fonction du braquage du volet (α = 16°)
11	a : Discrétisation de chaque élément de profil b : Densités tourbillonnaires supplémentaires et conditions associées
12	Coefficients globaux : comparaison calcul-expérience
13	Répartitions de pression calculées et expérimentales - volet 20° (α = 16°)
14	Répartitions de pression calculées et expérimentales - volet 40° (α = 16°)
15	Couches limites à l'extrados du corps - comparaison calcul - expérience
16	Profils u, $\sqrt{\overline{u'^2}}$, $\overline{u'.w'}$ à l'extrados du volet : comparaison calcul - expérience
17	Couches limites à l'extrados du volet et dans le sillage du corps principal : comparaison calcul - expérience



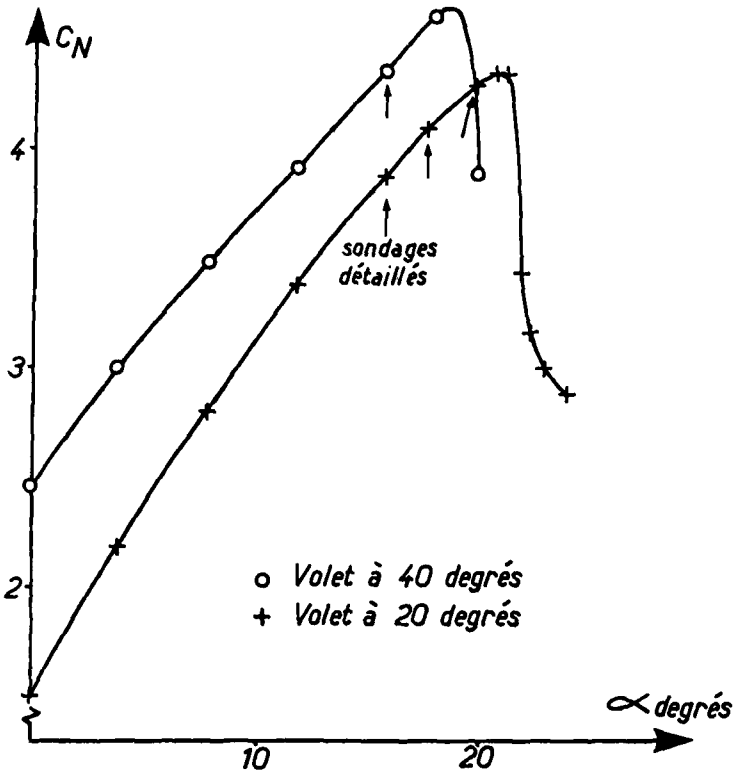


1 - Photo de la maquette dans la veine courant plan de Fl et disposition des zones d'aspiration

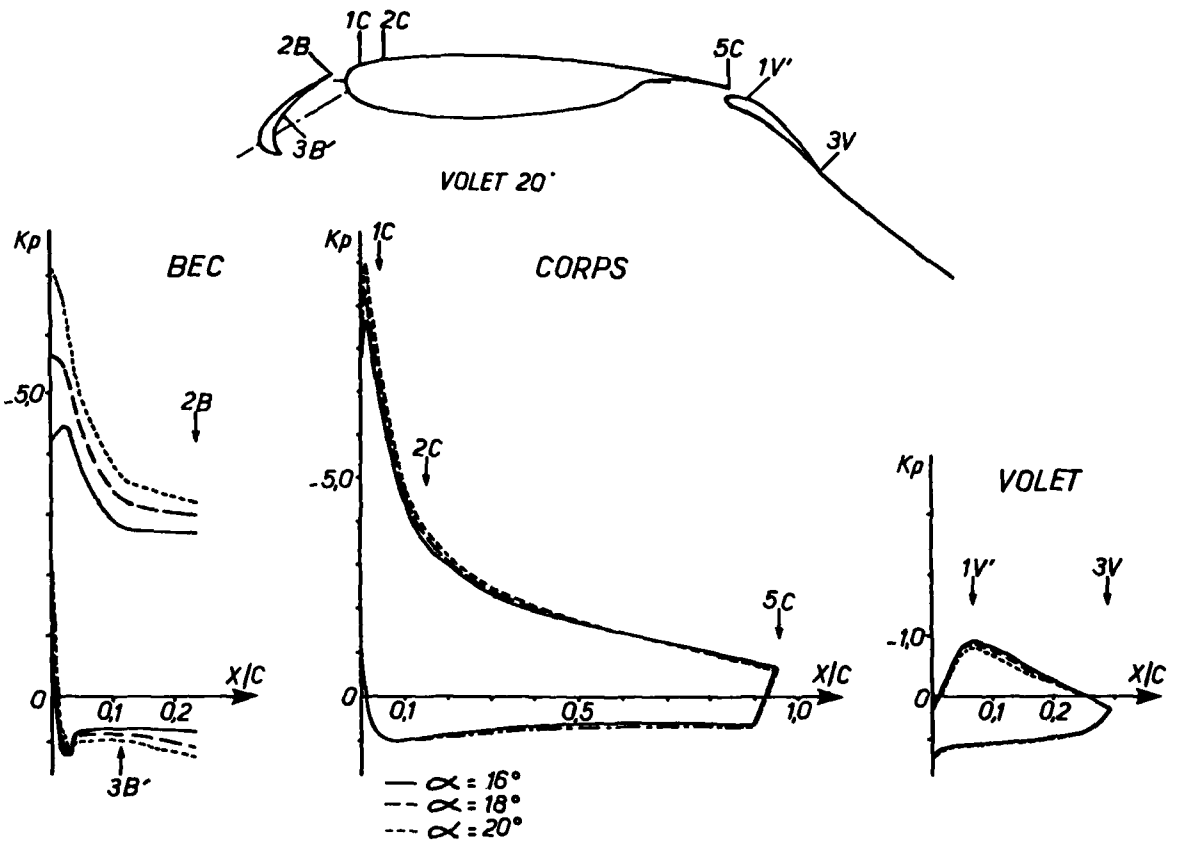


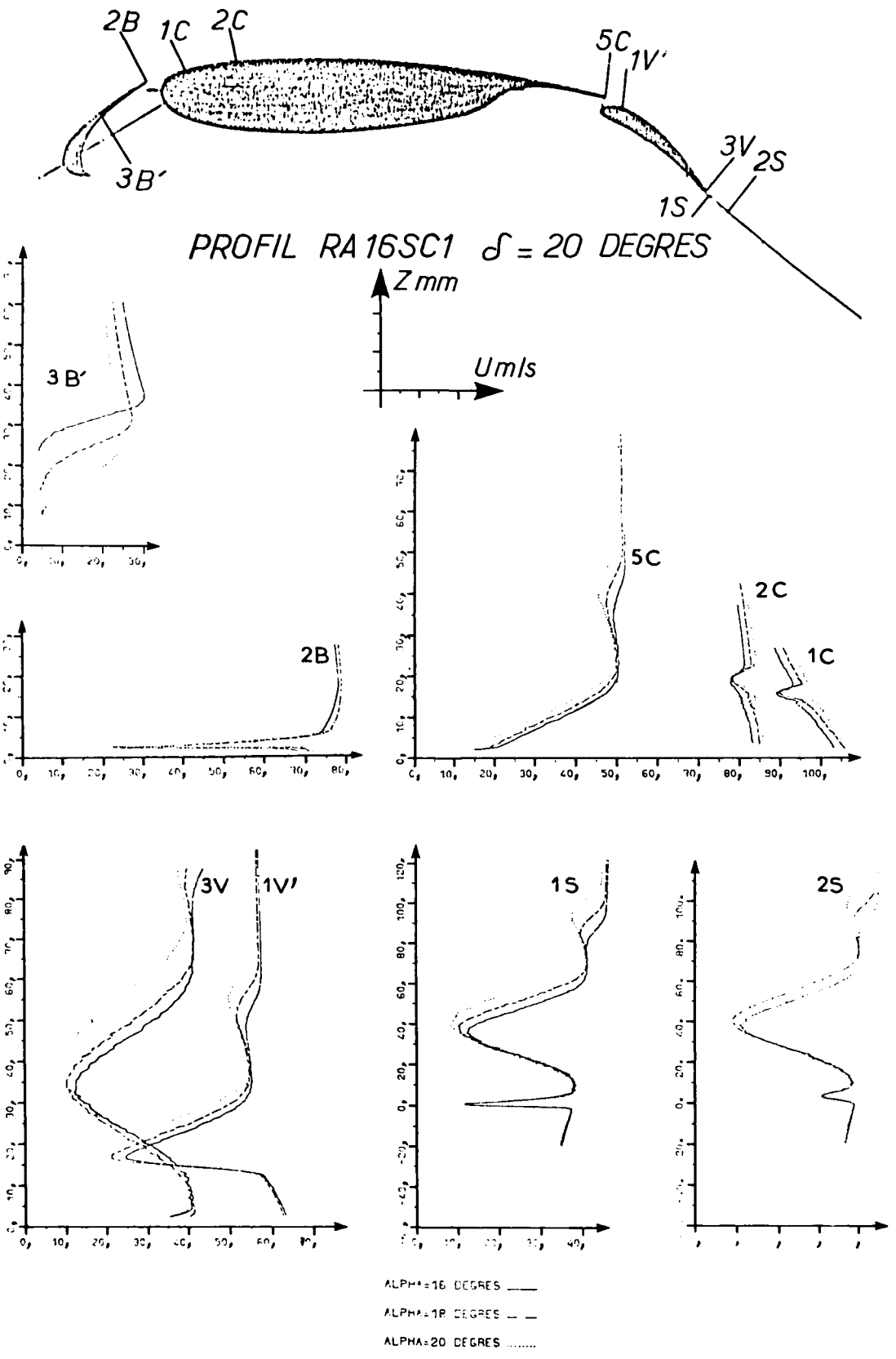
nature sondage	couche limite							sillage	
element	bec		corps principal			volet			
face	extrados	intrados	extrados			extrados			
station	2B	3B'	1C	2C	5C	1V'	3V	1S	2S
x/c	,24	,118	,04	,15	,96	068	,29	014	,06

2 - Stations de sondage

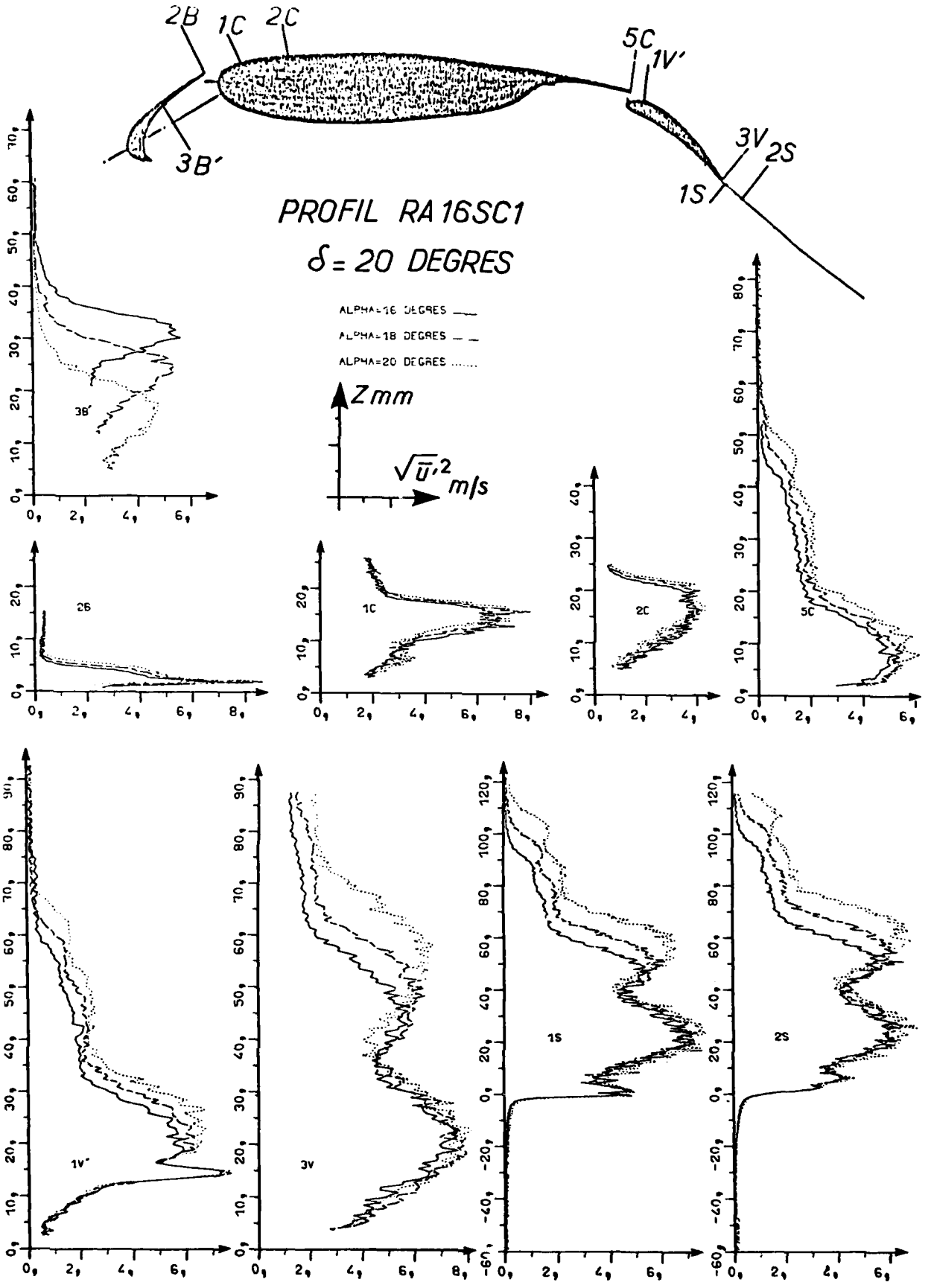


3 - Evolution du coefficient CN avec l'incidence

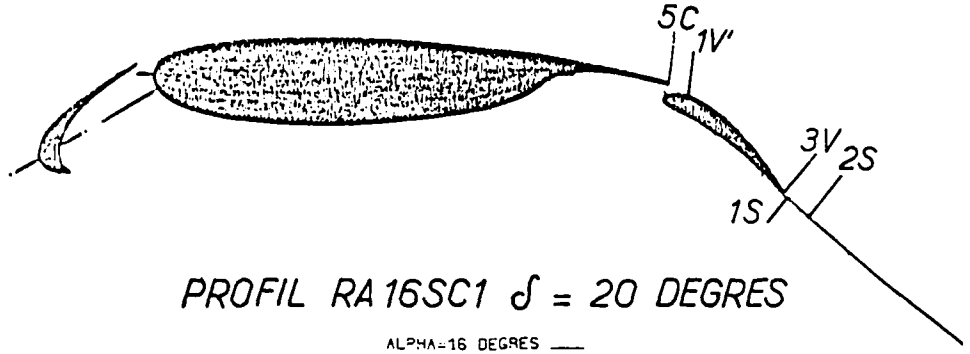




5 - Evolution de la vitesse en fonction de l'incidence (volet 20°)



6 - Evolution de $\sqrt{\overline{u'^2}}$ en fonction de l'incidence (volet 20°)

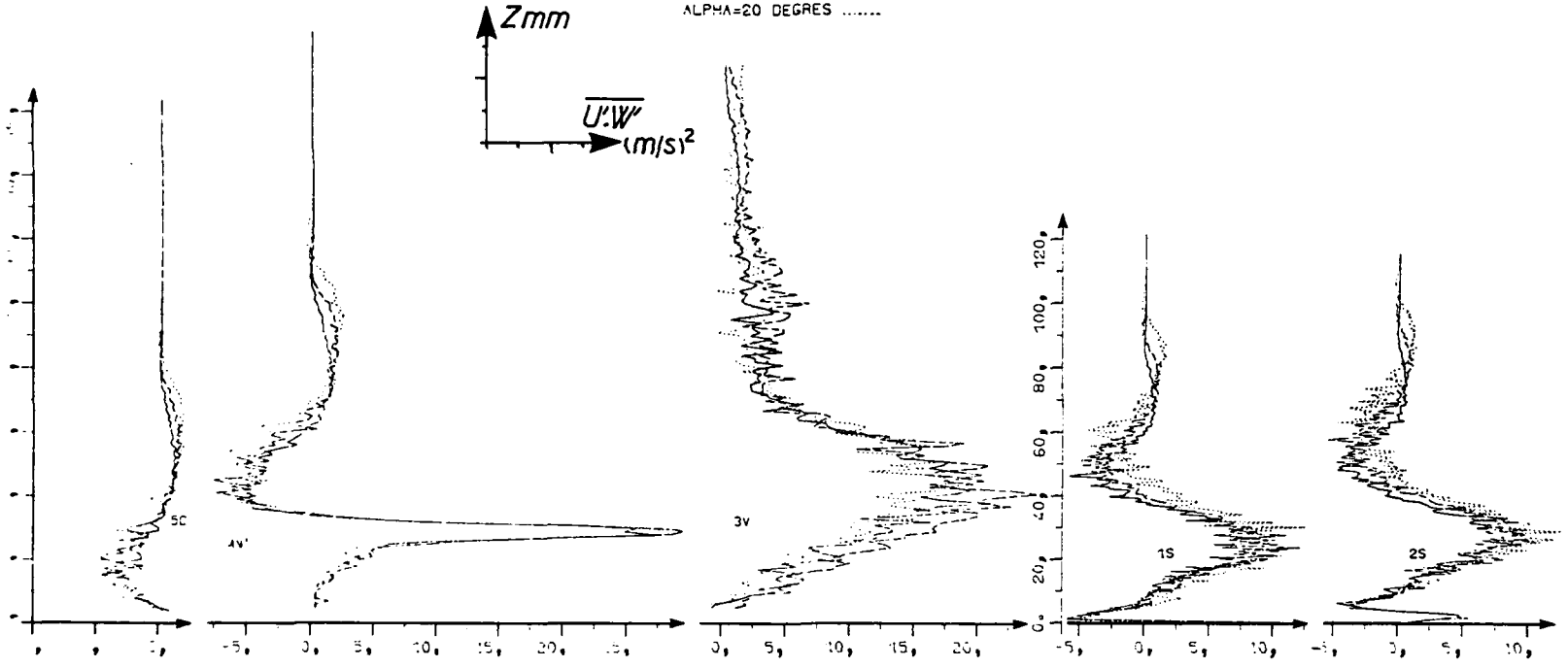


PROFIL RA 16SC1 δ = 20 DEGRES

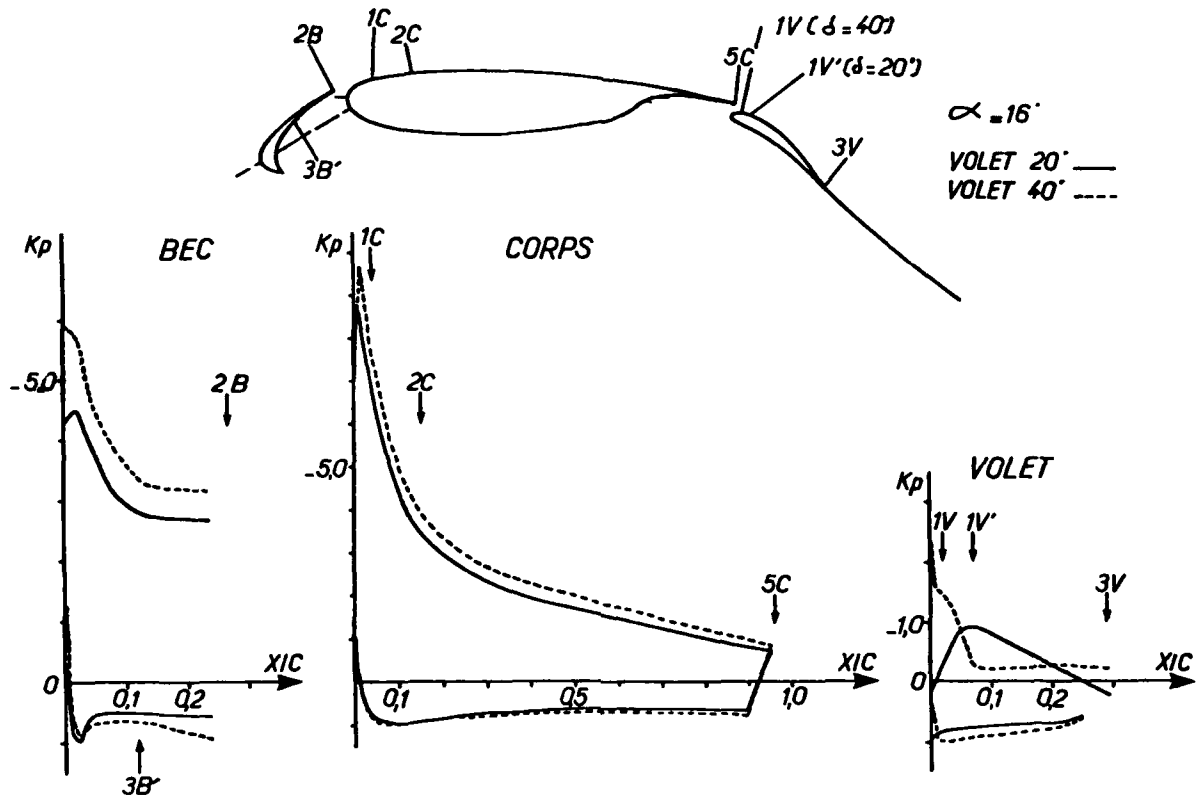
ALPHA=16 DEGRES ——

ALPHA=13 DEGRES – –

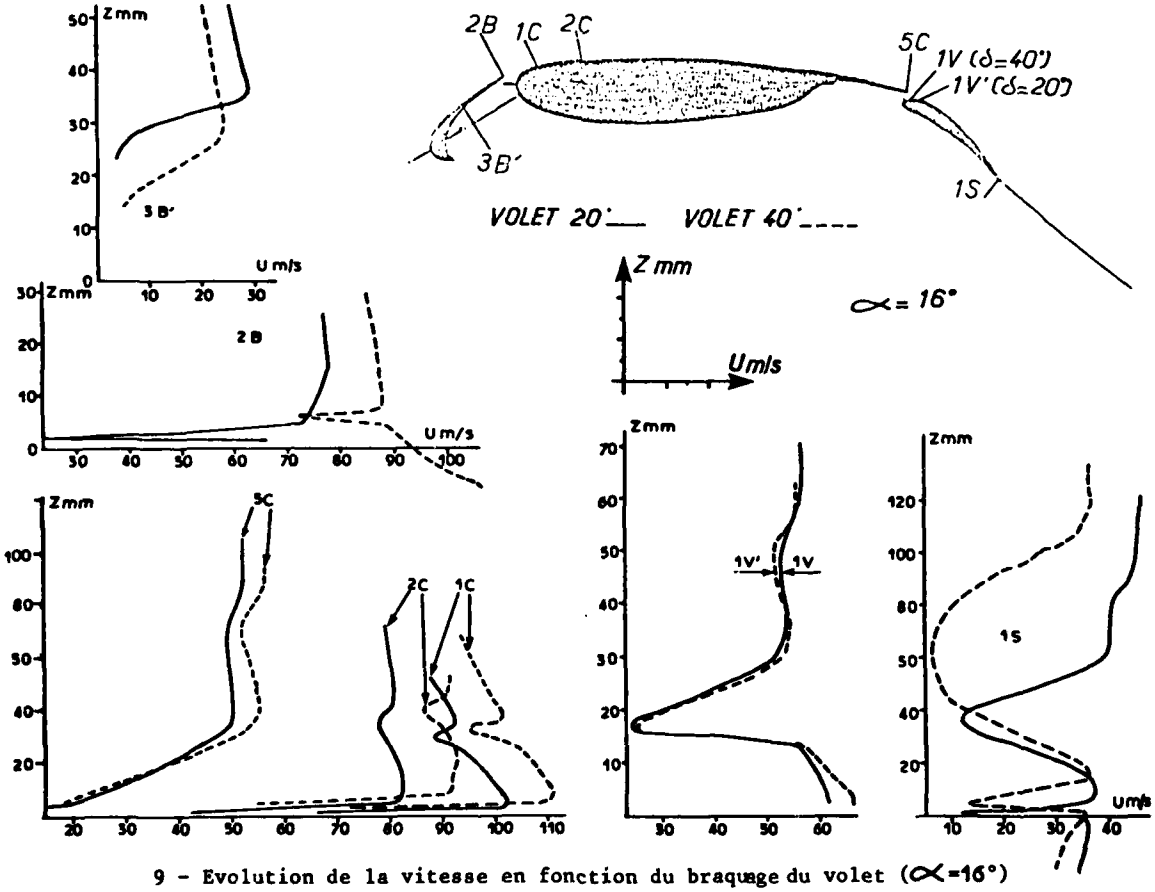
ALPHA=20 DEGRES .....



7 - Evolution de $\overline{u'.w'}$ en fonction de l'incidence (volet 20°)



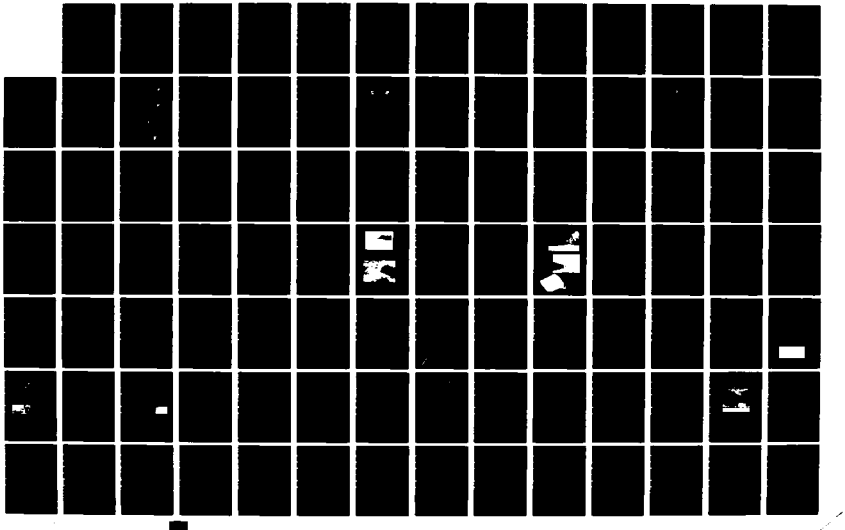
8 - Influence du braquage du volet sur les répartitions de pression (α=16°)

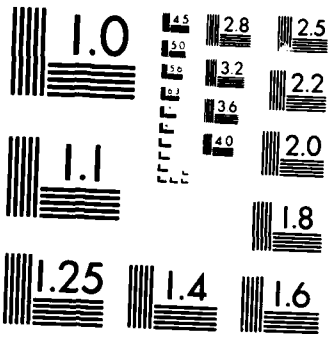


9 - Evolution de la vitesse en fonction du braquage du volet (α=16°)

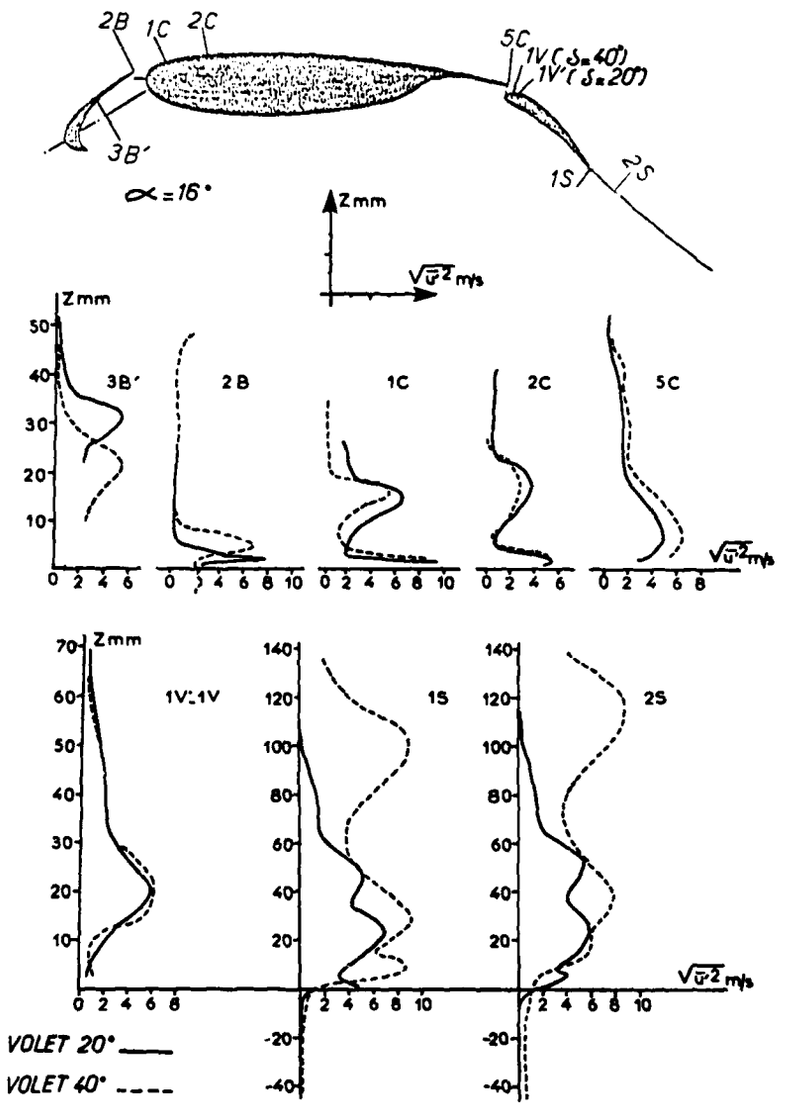
AD-A147 396 PROCEEDINGS OF THE CONFERENCE ON IMPROVEMENT OF AERODYNAMIC PERFORMANCE T..(U) ADVISORY GROUP FOR AEROSPACE RESEARCH AND DEVELOPMENT NEUILLY.. AUG 84

UNCLASSIFIED AGARD-CP-365 F/G 20/4 NL

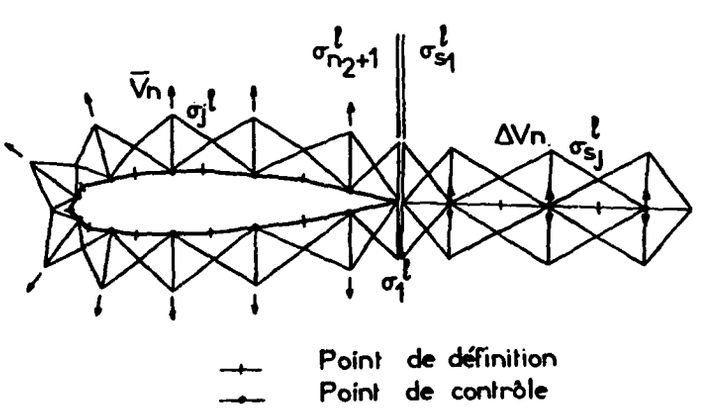




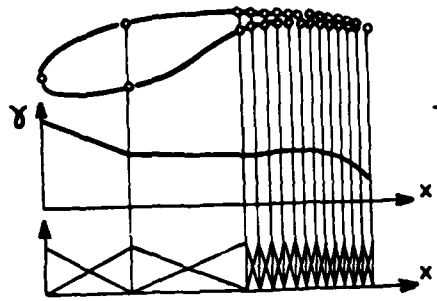
MICROCOPY RESOLUTION TEST CHART
NATIONAL BUREAU OF STANDARDS-1963-A



10 - Evolution de $\sqrt{\overline{u'^2}}$ en fonction du braquage du volet (α=16°)

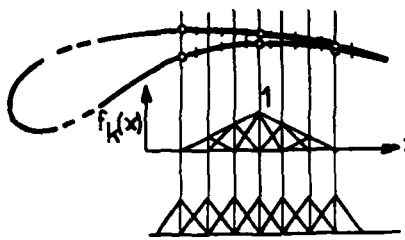


11 - a : Discrétisation de chaque élément de profil



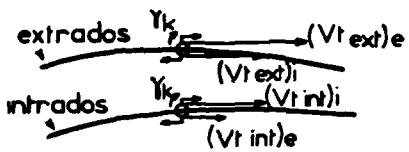
PROFIL GLOBAL DE DENSITÉ TOURBILLONNAIRE

profils $f_k(x)$



densités tourbillonnaires correspondant à un même terme γ_k

densités tourbillonnaires élémentaires

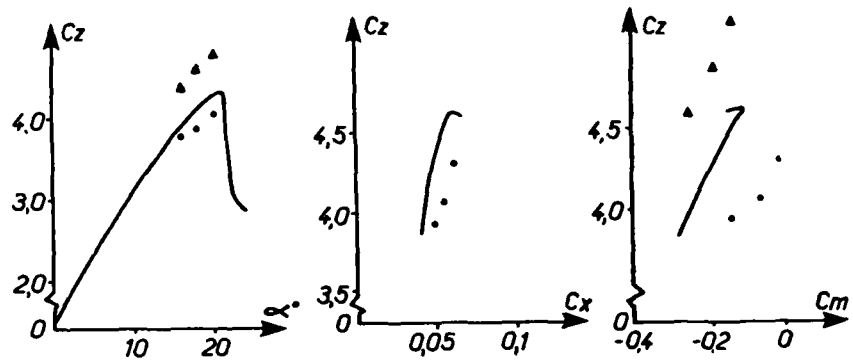


conditions supplémentaires pour les γ_k

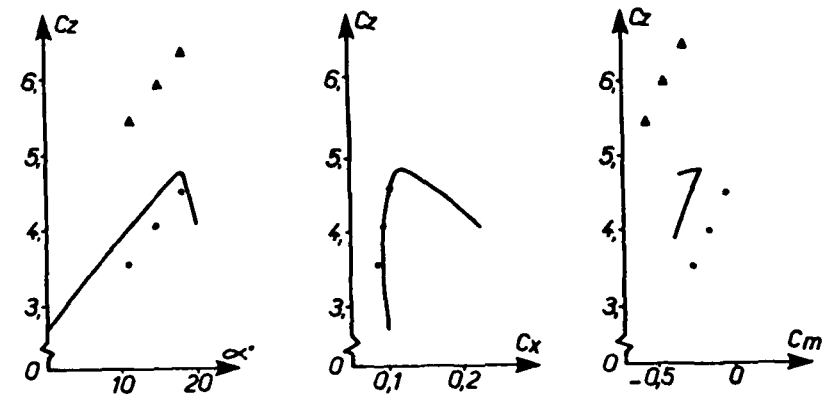
11- b : Densités tourbillonnaires supplémentaires et conditions associées

PROFIL RA 16 SC1 HYPERSUSTENTE

▲ *calculs fluide parfait*
• *calculs fluide visqueux*
— *expérience*

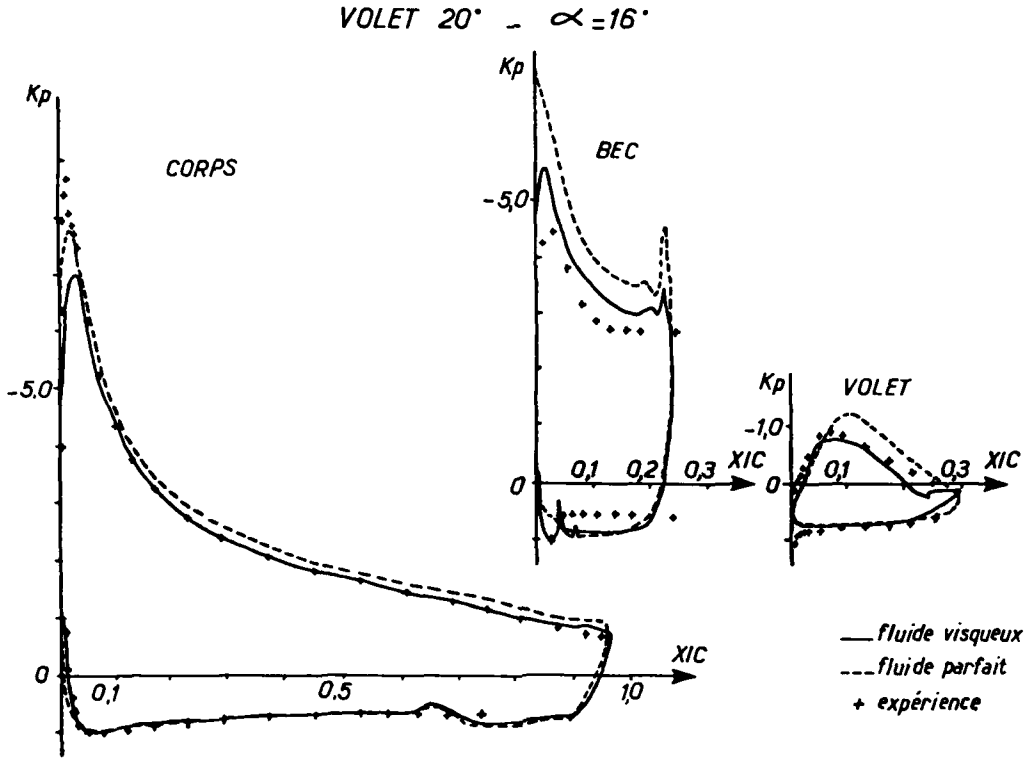


VOLET 20°

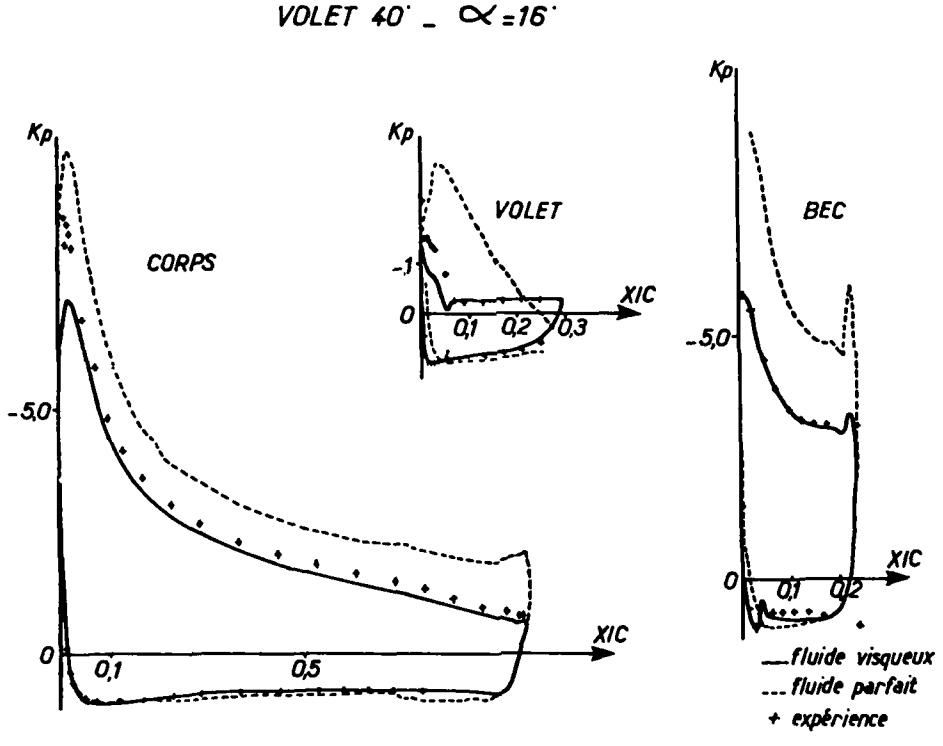


VOLET 40°

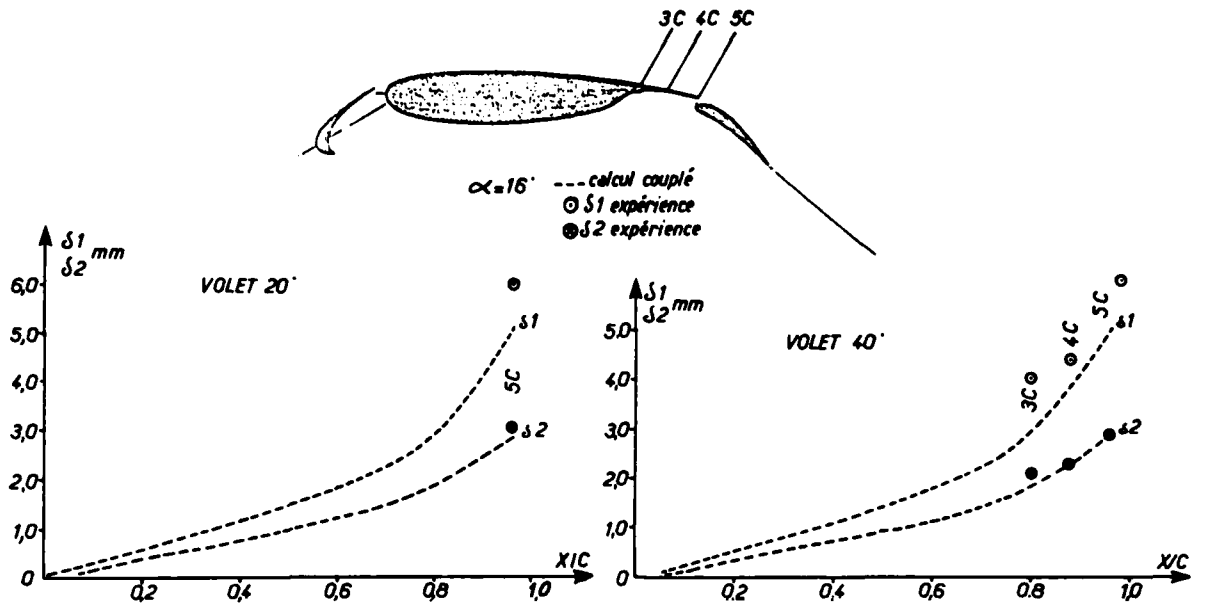
12 - Coefficients globaux : comparaison calcul-expérience



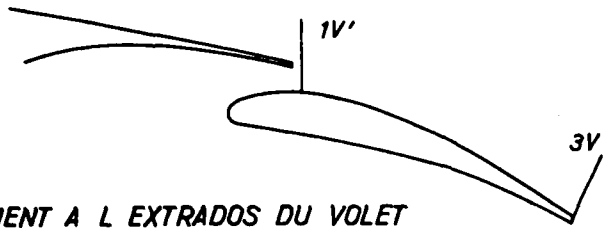
13 - Répartitions de pression calculées et expérimentales - volet 20° (∝=16°)

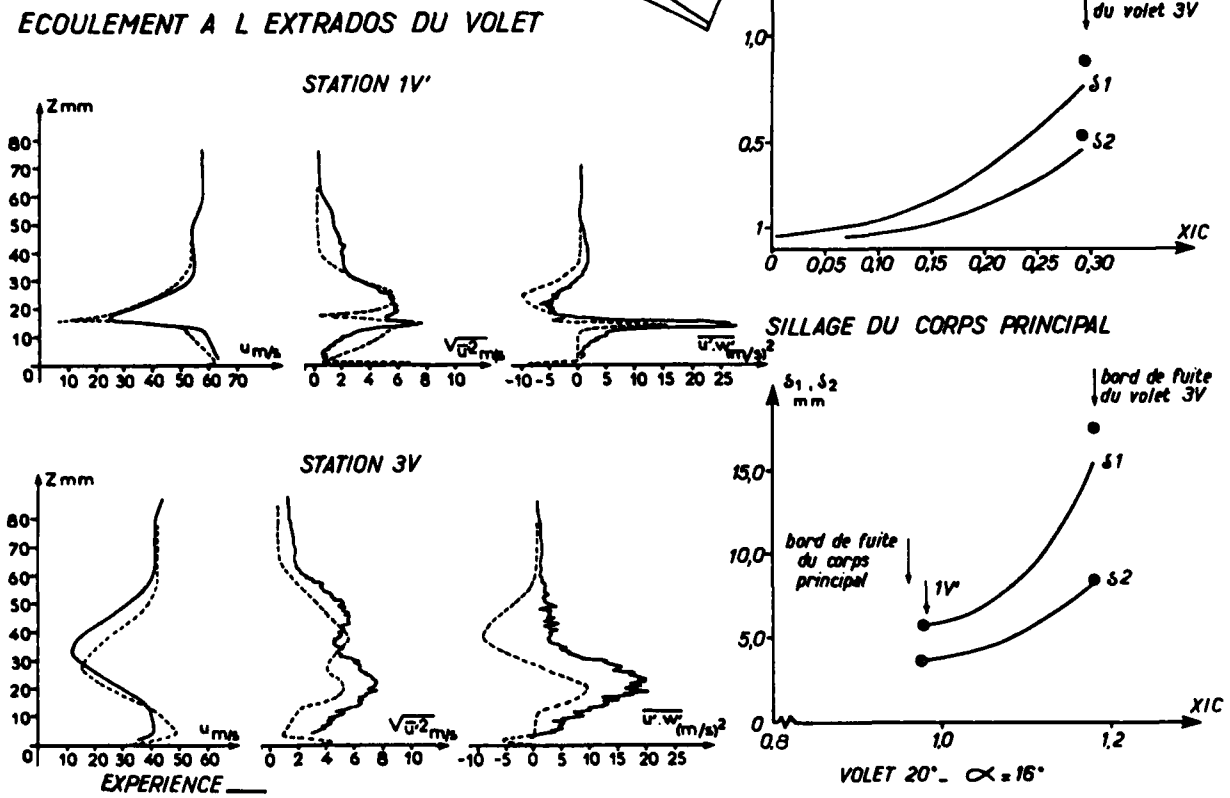


14 - Répartitions de pression calculées et expérimentales - volet 40° (∝=16°)

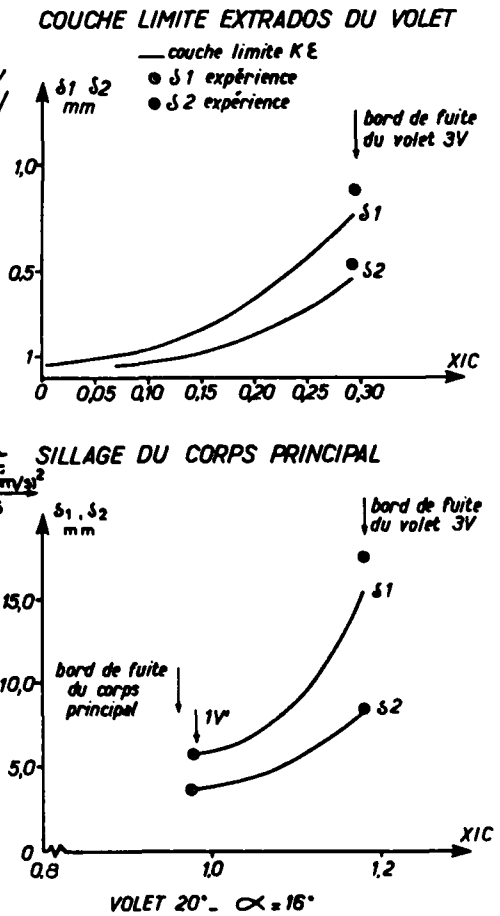


15 - Couches limites à l'extrados du corps
- Comparaison calcul – expérience





16 - Profils u, $\sqrt{\overline{u'^2}}$, $\overline{u'.w'}$ à l'extrados du volet
: comparaison calcul – expérience



17 - Couches limites à l'extrados du volet et dans le sillage du corps principal comparaison calcul – expérience

INVISCID COMPRESSIBLE FLOW PAST A MULTI-ELEMENT AEROFOIL

by

I.M. HALL and A. SUDDHOO
Department of the Mechanics of Fluids
University of Manchester, Manchester M13 9PL, England

AD-P004 055

SUMMARY

A conformal transformation method is used to generate an orthogonal curvilinear grid for two- and three-element configurations. The compressible potential flow equations are solved by finite difference methods. The solution could serve as a starting point for an iterative solution of the full viscous compressible flow case.

INTRODUCTION

Without high lift devices the maximum lift coefficient attainable by a high aspect ratio wing is about five times the incidence at incidences up to the stall. Typical values of $C_{L_{max}}$ are commonly in the range 1.0 to 1.5. The addition of high lift devices such as flaps and slats can more than double $C_{L_{max}}$ with consequent improvement in take off and landing performance.

Flaps and slats can take many forms but slotted flaps and simple leading edge slats are quite common. Several such configurations are shown in Fig.1. In practice the final requirement is for a satisfactory three-dimensional configuration but it is usual for the high lift devices to extend over a significant proportion of the span and therefore consideration of two-dimensional configurations is relevant.

A powerful method for the calculation of incompressible flows past multi-element configurations has been developed by Williams and Butter[1]. This depends on the use of panel methods to calculate the inviscid flow coupled with boundary layer calculations based on the inviscid flow pressure distribution as outlined in Fig.2. When the flow is attached, which is usually desirable, this approach has proved satisfactory.

However, experiments have shown that compressibility effects could be significant even at quite low free stream Mach numbers. Although compressibility effects can be estimated by applying the Prandtl-Glauert law to the incompressible results obtained by panel methods this is not entirely satisfactory because it essentially scales the incompressible results and cannot show any trend towards a change in the form of the pressure distribution. A more precise compressible flow calculation seems desirable.

An alternative approach to the incompressible case has been given by Ives[2]. For a two element configuration he used conformal transformations to map the flow region into the region between two concentric circles. He states that the solution obtained by Lagally[3] may be used to calculate the flow but no results are given. A modification to Ives's approach is used in the present paper and the sequence of transformations is shown in Fig.3. A detailed description of this sequence is given later.

Williams[4] used simple conformal transformations to map two circles into two aerofoils, analogous to the transformation of a circle into a Zhukowski aerofoil, and thus obtained an exact solution for a particular two element configuration. He did this for two cases, known as Williams configurations A and B, Fig.4, which serve as important test cases against which other incompressible flow methods can be assessed.

For the single aerofoil case, inviscid flows at freestream Mach numbers up to and slightly in excess of the critical Mach number can be accurately calculated by the method devised and developed by Sells[5], Garabedian and Korn[6], Jameson[7] and others. In essence this method depends on transforming the flow region onto the inside of a circle so that a uniform polar grid in the circle plane corresponds to a convenient orthogonal grid in the aerofoil plane. After subtraction of the singularities a numerical solution can easily be obtained using finite difference methods. For slightly supercritical flows the modified difference scheme introduced by Murman and Cole[8] is used.

It is relatively easy to extend this method to a two-element aerofoil. Following the general approach of Ives[2], described above, the outer flow region can be transformed onto the region between two concentric circles. Using the grid in the aerofoil plane corresponding to a uniform polar grid in the circle plane the compressible flow equations can be solved numerically as in the single aerofoil case. There are two new factors which cause additional difficulties. Firstly, the necessity to subtract out additional singularities before solving numerically results in considerable algebraic complexity. Secondly, the solution is very sensitive to small changes in the circulation. Although the total circulation, and hence the total lift, seems to be relatively easily obtained, the distribution between the two elements is more difficult to determine accurately. Grossmann and Melnik[9] used a grid stretching technique in the circle plane to regulate the coordinate grid in the aerofoil plane.

Thompson and Mastin[10] approached the transformation problem in a different way. They introduced a cut between the elements and transformed the cut plane into a rectangular region. In the present paper, a similar approach is used to deal with the three element case. A cut is introduced between two of the elements reducing the triply-connected region to a doubly-connected region. This can then be conformally transformed into the region between two circles as in the two-element case. A detailed discussion of the problems involved is given below.

GRID GENERATION FOR A TWO-ELEMENT AEROFOIL

The two main criteria governing the choice of a method to generate a curvilinear, orthogonal grid about a given number of bodies are firstly, the surfaces of the bodies must themselves be grid lines and secondly, the grid must extend to regions at infinity. These two conditions then respectively allow accurate implementation of the surface and far-field boundary conditions. For the case of a single aerofoil, Sells[5] showed that such a grid is produced by conformally transforming the region exterior to the aerofoil onto the interior of a circle. Considerable advantages are obtained by using a uniform polar grid which results in a non-uniform grid in the aerofoil plane with mesh density greatest in the most important regions.

The method adopted herein for a two-element aerofoil also makes use of conformal mapping. Through subsequent transformations, described below, the two aerofoils are mapped onto two concentric circles, whereby the annular region between the circles represents the external region about the aerofoils. Thus a system of polar coordinates in the annular region corresponds to an orthogonal grid in the plane of the aerofoils. Such a transformation was first introduced by Ives[2]. However his approach involves a laborious mapping procedure whereas the present scheme is much simpler and computationally more efficient.

Fig.3 shows the intermediate stages of the transformation. As an example the case of a main aerofoil and flap is sketched. First the flap in the physical (z) plane is mapped onto a near circle in the z_1-plane by using the corner removing Karman-Trefftz transformation given by

$$\frac{z_1 - s}{z_1 + s} = \left(\frac{z - z_T}{z - z_N} \right)^{1/k} \quad ; \quad k = 2 - \frac{\tau}{\pi} \quad ; \quad s = \frac{z_T - z_N}{2k} \qquad (1)$$

and τ is the trailing edge angle of the flap. The transformation is singular at the points z_T and z_N and these are respectively placed at the trailing edge and at a point midway between the nose of the flap and its radius of curvature. Since the above mapping function involves a fractional power, enforcing the continuity of the argument of the bracketed term in Eq.(1) as the aerofoil's contour is traversed ensures that the correct root is taken. The mapping of the flap onto a near circle distorts the main aerofoil. A second application of the Karman-Trefftz transformation, this time to the image of the main aerofoil, produces a near circle in the z_2-plane while the image of the flap although slightly distorted, remains a near circle.

The third step is to translate the coordinate system of the z_2-plane to the centroid of the near circle representing the main aerofoil. This improves the convergence of a mapping series used in the next stage. However, in many cases, the Karman-Trefftz transformation as given by Eq.(1) produces a near circle whose centroid lies close to the origin of the mapped domain and thus this translation is not absolutely necessary. The fourth step is to map the near circle representing the main aerofoil in the z_2-plane onto a unit circle in the z_3-plane. This transformation is effected using the Theodorsen[11] mapping series given by

$$z_2 = z_3 \exp\left[\sum_{j=0}^{N} \left(A_j + i B_j \right) z_3^{-j} \right] \qquad (2)$$

A practical method of carrying out this mapping using Fast Fourier techniques is given by Ives although it appears that some of his equations are printed incorrectly. Theodorsen's transformation also distorts the flap image and this distortion is calculated iteratively from Eq.(2) using a suitably large value of z_3 to initiate the process.

The next step is an inverse bilinear transformation of the z_3-plane whereby the external region is mapped onto the annular region in the z_4-plane bounded by a unit circle representing the main aerofoil and a near circle representing the flap. This transformation is carried out using the mapping function

$$z_4 = \frac{1}{|z_c|} \left(\frac{|z_c|^2 - z_3 \bar{z}_c}{z_3 \bar{z}_c - 1} \right) \qquad (3)$$

where z_c is a complex constant. A large contour taken at infinity in the z_3-plane maps

onto the point denoted by '∞' in the z_4-plane and given by

$$z_{4\infty} = -\frac{1}{|z_c|} \tag{4}$$

It is essential for the convergence of the mapping series to be used for the final transformation that the image of the near circle under the above transformation is centrally positioned inside the unit circle by determining the constant z_c as follows:

(a) Set z_c^n equal to the approximate centre, e.g. the mid-point of a diameter, of the near circle in the z_3-plane.

(b) Carry out the transformation using Eq.(3) and determine the approximate centre, say z_{4c}, of the resulting near circle in the z_4-plane.

(c) By reversing Eq.(3), a new value of z_c^{n+1} is then given by

$$z_c^{n+1} = \frac{|z_c^n|}{\bar{z}_c^n}\left(\frac{|z_c^n| + z_{4c}}{z_{4c}|z_c^n| + 1}\right) \tag{5}$$

(d) Using the latest value of z_c, repeat steps (b) and (c) until z_{4c} is approximately equal to zero.

The last step is to map the near circle representing the flap in the z_4-plane onto an exact circle of radius $\hat{R}$ in the σ-plane while the image of the main aerofoil is kept a unit circle. This is accomplished by using the Garrick[12] transformation

$$z_4 = \sigma \exp\left[ib + f(\sigma)\right]$$

where

$$f(\sigma) = \sum_{j=1}^{N}\left[(-C_j + i D_j)(\hat{R}\sigma)^j + (C_j + i D_j)\left(\frac{\hat{R}}{\sigma}\right)^j\right] \tag{6}$$

By using a method analogous to that of Theodorsen's mapping series, the coefficients and the radius $\hat{R}$ of the above series may be determined. The real constant b is chosen such that the image of the trailing edge of the main aerofoil lies on the real positive axis of the σ-plane. The image of infinity and that of the trailing edge of the flap are obtained iteratively from Eq.(6).

The above intermediate transformations thus effectively map the surfaces of the two-element configuration and the external region of the physical plane respectively onto the circumferences of two concentric circles and the annular region between them. A large contour taken at infinity in the physical plane maps onto the point denoted by '∞' in the σ-plane. Superimposing a polar grid in the annular domain and tracing its image backwards through the transformations, we obtain an orthogonal grid that extends to infinity about the two aerofoils, whose surfaces are themselves grid lines. Typical grids for an aerofoil-flap and an aerofoil-slat configurations are shown in Figs.5 and 6 respectively.

FLOW EQUATIONS FOR A TWO-ELEMENT AEROFOIL

The steady, inviscid and compressible flow is assumed to be isentropic and irrotational. In cases when the flow is transonic these assumptions remain valid provided only weak shock waves occur. Strong shock waves would in any case tend to cause boundary layer separation and buffeting, calling for an altogether more elaborate analysis including shock wave boundary layer interaction and unsteady flow. Also a configuration on which there were strong shock waves would be undesirable because of the accompanying loss of lift and drag rise.

The equations of the flow in the physical (aerofoil) plane are expressed in curvilinear coordinates (r,θ) corresponding to the polar coordinates in the circle (σ) plane. If B represents the modulus of the mapping derivative, i.e.

$$\mathcal{B} = \left|\frac{dz}{d\sigma}\right| \tag{7}$$

the curvilinear metrics h_1 and h_2 are

$$h_1 = \mathcal{B} \quad \text{and} \quad h_2 = \mathcal{B}r \tag{8}$$

The continuity equation is therefore

$$\nabla.(\rho \underline{q}) = \frac{1}{r}\frac{\partial}{\partial r}\left(\rho r \frac{\partial \phi}{\partial r}\right) + \frac{1}{r}\frac{\partial}{\partial \theta}\left(\frac{\rho}{r}\frac{\partial \phi}{\partial \theta}\right) = 0 \tag{9}$$

where

$$|\underline{q}|^2 - (\nabla\phi)^2 - \frac{1}{B^2}\left[\left(\frac{\partial\phi}{\partial r}\right)^2 + \left(\frac{\partial\phi}{r\partial\theta}\right)^2\right] \tag{10}$$

and

$$\rho = \left[1 + \frac{\gamma-1}{2} M_\infty^2 \left(1 - |\underline{q}|^2\right)\right]^{\frac{1}{\gamma-1}} \tag{11}$$

where ϕ is the velocity potential and ρ and q respectively denote the density and velocity vector, γ being the specific heat ratio and M_∞ the free stream Mach number.

The above three equations govern the flow and the unknowns of the problem are the velocity potential and the density. Eqs. (9) and (11) are two coupled non-linear equations for ϕ and ρ and their solutions require an iterative process. Given an approximation of ρ, Eq. (9) may be solved for ϕ and using Eq. (11) the density can then be adjusted and the process repeated.

The velocity potential must satisfy the far-field boundary condition in the physical (z) plane. Ludford[13] showed that for a large contour taken at infinity in the z-plane, the expansion for the velocity potential is of the form

$$\phi = R\cos(\psi-\alpha) - \left(\frac{\Gamma_M + \Gamma_F}{2\pi}\right)\tan^{-1}\left[\beta\tan(\psi-\alpha)\right] \tag{12}$$

where (R,ψ) are polar coordinates of the physical plane, Γ_M and Γ_F are respectively the circulations about the main aerofoil and the flap as shown in Fig.3, α is the free stream incidence and β is given by

$$\beta = \sqrt{1 - M_\infty^2}$$

In order to apply the far-field boundary condition in the transformed (σ) plane, a net relationship between the z and σ planes must be deduced first. This is initiated by considering a large contour in the z-plane and tracing its image through the transformations onto the point (σ_∞). It can be shown that the relationship is given by

$$z \sim \left[\frac{\sigma_\infty\left(1-|z_c|^2\right)e^{A_0+iB_0}}{\bar{z}_c\left\{1+\sigma_\infty f'(\sigma_\infty)\right\}}\right]\left[\frac{1}{\sigma-\sigma_\infty}\right] \tag{13}$$

which may be abbreviated to

$$z \sim \frac{c_1 e^{ic_2}}{\sigma-\sigma_\infty}$$

where the real constants c_1 and c_2 are completely defined by constants from the intermediate transformations. Using Eq.(12) and the above asymptotic relation, the corresponding expansion for ϕ near the point (σ_∞) reveals that the overall transformation effectively maps a uniform flow in the physical plane onto a doublet located at the point (σ_∞) in the σ-plane. Thus the velocity potential contains a singularity and this may be subtracted by introducing a reduced potential, G. Fig.7(a) shows the distribution of the circulations in the σ-plane. Taking into account that of the flap, the expansion for the velocity potential in the σ-plane becomes

$$\begin{aligned}
\phi = {} & C_1\left(\frac{r\cos(\theta+\alpha_N) - r_\infty\cos(\theta_\infty+\alpha_N)}{r^2 + r_\infty^2 - 2rr_\infty\cos(\theta-\theta_\infty)}\right) && \text{(Doublet at } \sigma_\infty\text{)} \\
& + (E_M+E_F)\tan^{-1}\left[\beta\tan\left\{\alpha_N + \tan^{-1}\left(\frac{r\sin\theta - r_\infty\sin\theta_\infty}{r\cos\theta - r_\infty\cos\theta_\infty}\right)\right\}\right] && \text{(Vortex at } \sigma_\infty\text{)} \\
& - E_F\theta && \text{(vortex at origin)} \\
& + G(r,\theta) && \text{(Reduced potential)}
\end{aligned} \tag{14}$$

where

$$\alpha_N = \alpha - C_2 \;;\quad E_M = \frac{\Gamma_M}{2\pi} \;;\quad E_F = \frac{\Gamma_F}{2\pi} \;;\quad \sigma_\infty = r_\infty e^{i\theta_\infty} \;;\quad E_T = E_M + E_F$$

For the sake of brevity the above equation is written as

$$\phi = W(r,\theta) + (E_M + E_F)\,X(r,\theta) - E_F\,\theta + G(r,\theta) \qquad (15)$$

In the above form, the singularity of the velocity potential is subtracted, leaving a finite and single-valued reduced potential. Thus instead of solving for the singular velocity potential, we now treat the regular reduced potential as one of the unknowns of the problem. We therefore express the governing Eqs.(9) and (10) in terms of G and these respectively become

$$r^2\frac{\partial^2 G}{\partial r^2} + r\left[1 + \frac{r}{\rho}\frac{\partial \rho}{\partial r}\right]\frac{\partial G}{\partial r} + \frac{\partial^2 G}{\partial \theta^2} + \left[\frac{1}{\rho}\frac{\partial \rho}{\partial \theta}\right]\frac{\partial G}{\partial \theta} + g(r,\theta) = 0 \qquad (16)$$

where

$$g(r,\theta) = r^2\left(W_{rr} + E_T X_{rr}\right) + r\left(1 + \frac{r}{\rho}\frac{\partial \rho}{\partial r}\right)\left(W_r + E_T X_r\right) + \left(W_{\theta\theta} + E_T X_{\theta\theta}\right) + \frac{1}{\rho}\frac{\partial \rho}{\partial \theta}\left(W_\theta + E_T X_\theta - E_F\right)$$

and

$$|q|^2 = \frac{1}{B^2}\left[\left(W_r + E_T X_r + \frac{\partial G}{\partial r}\right)^2 + \frac{1}{r^2}\left(W_\theta + E_T X_\theta - E_F + \frac{\partial G}{\partial \theta}\right)^2\right] \qquad (17)$$

where W_r, X_θ, W_{rr}, and $X_{\theta\theta}$ denote partial derivatives. The partial differential Eq.(16) is elliptic for subsonic flow and is mixed elliptic and hyperbolic when the flow is transonic. It can also be shown that Eq.(16) reduces to the Laplacian of G in the incompressible case when derivatives of the density disappear.

The boundary condition of zero normal velocity on the surfaces of the aerofoils implies that on the grid line (r=1) of the σ-plane,

$$\left[\frac{\partial G}{\partial r}\right]_{1,\theta} = -E_T\left[X_r\right]_{1,\theta} - \left[W_r\right]_{1,\theta} \qquad (18)$$

Similarly on the flap's surface, represented by the grid line ($r=\hat{R}$), we have

$$\left[\frac{\partial G}{\partial r}\right]_{\hat{R},\theta} = -E_T\left[X_r\right]_{\hat{R},\theta} - \left[W_r\right]_{\hat{R},\theta} \qquad (19)$$

The circulations about the aerofoils are determined by satisfying the Kutta condition at the trailing edges. In order to have finite velocities at the trailing edges, we must impose the condition of zero velocity at their images in the σ-plane. Thus at these two points, in addition to the normal velocity being zero, the tangential velocity must also vanish. By satisfying the latter condition, two linear equations are obtained from which the circulation constants are given by

$$E_F = \frac{\left[X_\theta\right]_{1,0}\left[W_\theta + \frac{\partial G}{\partial \theta}\right]_{\hat{R},\hat{\theta}} - \left[X_\theta\right]_{\hat{R},\hat{\theta}}\left[W_\theta + \frac{\partial G}{\partial \theta}\right]_{1,0}}{\left[X_\theta\right]_{1,0} - \left[X_\theta\right]_{\hat{R},\hat{\theta}}} \qquad (20)$$

$$E_M = \frac{E_F\left(1 - \left[X_\theta\right]_{1,0}\right) - \left[W_\theta + \frac{\partial G}{\partial \theta}\right]_{1,0}}{\left[X_\theta\right]_{1,0}} \qquad (21)$$

where $(\hat{R},\hat{\theta})$ and (1,0) are respectively the locations of the trailing edges of the flap and main aerofoil in the σ-plane.

FINITE DIFFERENCE SCHEMES

The numerical solution of the flow equations is carried out using finite difference methods. For this purpose it is convenient to perform the calculations on a rectangular projection of the σ-plane as shown in Fig.7(b). The two horizontal sides of the computational grid represent the two aerofoils' surfaces while the two vertical sides are topologically identified because of the periodicity of θ. The mesh spacing is Δr and Δθ.

For subsonic flow, the partial derivatives of the reduced potential G, occurring in the governing Eqs.(16) and (17) are approximated using central differences such that

$$\frac{\partial G}{\partial r} = \frac{G(i+1,j) - G(i-1,j)}{2\Delta r} \qquad \frac{\partial G}{\partial \theta} = \frac{G(i,j+1) - G(i,j-1)}{2\Delta\theta}$$

$$\frac{\partial^2 G}{\partial r^2} = \frac{G(i+1,j) - 2G(i,j) + G(i-1,j)}{(\Delta r)^2} \qquad \frac{\partial^2 G}{\partial \theta^2} = \frac{G(i,j+1) - 2G(i,j) + G(i,j-1)}{(\Delta\theta)^2} \tag{22}$$

and similarly for the derivatives of the density. Substituting the above approximations into Eq. (16) and assuming a given set of density values at the mesh points, a linear equation for G(i,j) in terms of its neighbouring values is given by

$$-PG(i,j) + QG(i+1,j) + SG(i,j+1) + TG(i-1,j) + VG(i,j-1) + f = 0 \tag{23}$$

where P, Q, S, T, V and f involve the density and its derivatives and are evaluated at the point (i,j). Applying the above equation at every interior mesh point of the grid, gives a set of linear equations which in matrix form may be written as

$$[C][G] = [D] \tag{24}$$

where the coefficient matrix [C], is of block tridiagonal form. A direct solution for the unknown column vector [G] requires an inversion of the coefficient matrix and in general this is not practicable because of its large size even when dealing with a coarse grid. Since the density values are not yet known, the determination of [G] at this stage only represents one cycle of a main iterative process and thus a direct inversion of the coefficient matrix is not necessary.

The method adopted herein is an iterative process akin to the point Gauss-Siedel scheme with successive relaxation and is based on the fact that the coefficient of G(i,j) is comparatively larger than those of the neighbouring points. Given an approximate set of values G^n at the mesh points, a better value G^{n+1} is obtained by rewriting Eq.(23) as

$$G^{n+1}(i,j) = G^{n}(i,j) + \frac{w}{P}\left\{ QG^{n}(i+1,j) + SG^{n}(i,j+1) + TG^{n+1}(i-1,j) + VG^{n+1}(i,j-1) + f - PG^{n}(i,j)\right\} \tag{25}$$

where w is a relaxation factor. As the whole of the interior grid is swept through column by column, the above equation updates the value of G at every interior mesh point. On the horizontal sides of the grid where boundary conditions of zero normal velocity given by Eqs.(18) and (19) apply, second order one-sided differences are used to approximate the r-derivatives. Consequently the boundary values of G on the grid lines (i=1) and (i=I) are respectively related to the interior values by

$$G(1,j) = \frac{1}{3}\left\{4G(2,j) - G(3,j) + 2\Delta r\left(E_r[X_r]_{1,j} + [W_r]_{1,j}\right)\right\} \tag{26}$$

$$G(I,j) = \frac{1}{3}\left\{4G(I-1,j) - G(I-2,j) - 2\Delta r\left(E_r[X_r]_{I,j} + [W_r]_{I,j}\right)\right\} \tag{27}$$

where a relaxation factor may again be used.

The Kutta condition given by Eqs.(20) and (21) then allows the evaluations of new values of the circulation constants. Since the trailing edge of the flap does not lie at a grid point, interpolation is required to evaluate the derivative of G occurring in Eq.(20).

For a starting approximate set of values of G and ρ together with a starting approximation of the circulation constants, the above procedure yields better values of G and the circulation constants. These new values are then used to readjust the density at every mesh point. First the velocity is calculated using Eq.(17), then new values of the density are obtained from Eq.(11). The latest values of the density can now be used to repeat the process until both the reduced potential and the density converge to a set tolerance.

In the transonic case, information propagates through the supersonic zone in the streamwise direction. Thus it is important to simulate the directional bias of the flow in the numerical calculation. The computational grid is therefore subdivided into sweep directions, reminiscent of those used by Grossman and Melnik[9], as shown in Fig.7(b). The line ($r = r_\infty$) represents the radial coordinate of the image of infinity in the σ-plane.

The horizontal lines interior to r_∞ surround the flap whereas those exterior surround the main aerofoil. The transonic difference scheme used is essentially that of Murman and Cole[8]. Marching in the prescribed sweep directions, the velocity at each interior mesh point is calculated using central differences of frozen values of G of the previous iteration. At subsonic points the governing equation is discretized using central differences as previously described. At supersonic points, first derivatives of G are approximated using central differences and backward differences are used for all second derivatives of G in the θ-direction, such that

$$\frac{\partial^2 G}{\partial \theta^2} = \frac{G(i,j) - 2G(i,j-1) + G(i,j-2)}{(\Delta\theta)^2} \quad , \quad \frac{\partial^2 G}{\partial r \partial \theta} = \frac{G(i+1,j) - G(i+1,j-1) - G(i-1,j) + G(i-1,j-1)}{2\Delta r \Delta\theta} \tag{28}$$

with appropriate changes when the sweep direction is in the θ-decreasing sense. Also, at supersonic points derivatives of the density occurring in the governing equation are evaluated by first expanding them in order to reveal their dependences on the derivatives of G which are then approximated as above. For example from Eq.(11), we have

$$\frac{\partial \rho}{\partial \theta} = \left[1 + \frac{\gamma-1}{2} M_\infty^2 \left(1 - |\underline{q}|^2\right)\right]^{\frac{2-\gamma}{\gamma-1}} \left[-M_\infty^2 |\underline{q}| \frac{\partial |\underline{q}|}{\partial \theta}\right] \tag{29}$$

where the derivatives of the velocity can be expressed in terms of derivatives of G using Eq.(10). The finite difference scheme effectively yields, for every interior mesh point, an equation relating G(i,j) to its neighbouring values. This equation depends on whether the flow at the point (i,j) is subsonic or supersonic. The boundary and the Kutta conditions and the density readjustment are analogous to the entirely subsonic case.

RESULTS FOR TWO-ELEMENT AEROFOILS

Using the method of images, analytical solutions for the incompressible flow past two particular configurations (Fig.4) were presented by Williams[4]. The incompressible case in the present method is obtained by fixing the density at all mesh points to the free stream value. Comparisons of pressure distributions for one of the test cases are given in Fig.8. The agreement with the exact solution is good although small discrepancies are present due to a grid size effect. The variation of the reduced potential G, on the grid line (r = 1) which represents the main aerofoil's surface is shown in Fig.9. Due to the smoothness of the curve coupled with the fact that it is defined pointwise at small equal intervals, interpolation of high order can be used to obtain solution at non-grid points. For example by fitting a cubic spline through the curve of the interpolated region shown in Fig.9, which corresponds to a region near the leading edge of the main aerofoil, derivatives of G may be evaluated to give the pressure at corresponding points on the main aerofoil. Comparison of the interpolated result with the exact solution is shown in Fig.10. Again the agreement is good.

The incompressible solution is a good starting approximation for subsonic calculations. Over relaxation is used in Eq.(25) during the iterative process. The solution is obtained when both the density and the reduced potential converge to a tolerance of 5×10^{-5}. The pressure distributions for the slat and main aerofoil case in an entirely subsonic flow are given in Fig.11. It is noted that there is a significant decrease in the lift-coefficient of the slat compared to the incompressible case while there is little change on the surface of the main aerofoil except for a marked drop in the pressure peak near the leading edge. Since the reduced potential remains a smoothly varying function and since all of the flow parameters may be calculated from the derivatives of G, interpolation as described earlier can again be used to obtain more details in regions of mesh sparcity. The Mach number effect on Williams's Test Case (B) is shown in Fig.12 and the corresponding effect on the lift-coefficient is given in Fig.13.

In the transonic case, for slightly supercritical flow in the absence of shock waves, the program developed works without difficulty. However, as the supersonic zones that develop on the surfaces of the aerofoils grow larger and stronger due to an increase in the free stream Mach number, the iterative process showed signs of oscillation when over relaxation was used. In order to achieve convergence under relaxation was used at supersonic points. The pressure distributions for a transonic flow past Williams's configuration (B) are shown in Fig.14, where Cp* denotes the critical pressure coefficient. Supersonic zones occur on both the main aerofoil's and flap's surfaces and in the former case, a shock wave is also formed.

GRID GENERATION FOR A THREE-ELEMENT AEROFOIL

Whereas for a two-element aerofoil, it was possible to initialise the grid generation process by transforming the two aerofoils onto two concentric circles, a direct extension of this approach for a three-element configuration, such as a mapping onto three concentric circles, is not possible because of the multiple connectivity of the

physical domain. A method based on conformal mapping was introduced by Halsey[14]. His approach essentially uses branch cuts to string together the components of the configuration. The resulting body is then treated as a single body and mapped onto a circle. However in cases where the components of the given configuration overlap each other, Halsey's scheme tends to generate grids that are extremely sparse in the regions between overlapping elements. Since overlapping is a very common feature from the practical point of view, this is a serious drawback.

The present method also makes use of string mapping, but ideas from the two-element transformation are employed to ensure that the generated grid is well defined in the overlapping regions. Fig.15 shows a sketch of the transformation of a three-element aerofoil. The intermediate transformations, as described below, effectively introduces a branch cut to string together two of the components of the configuration thus reducing the degree of connectivity of the domain. The stringed components may be regarded as a single body and therefore a three-element configuration is reduced to a two-element case. Consequently, following a method analogous to that described previously, the resulting two bodies are mapped onto two concentric circles.

The first step is to map the three aerofoils onto three near circles in the z_1-plane, by a triple application of the Karman-Trefftz transformation given by Eq.(1), once for each aerofoil. The second step uses the two-element mapping procedure to transform the images of the main aerofoil and the flap onto two concentric circles in the σ-plane except that this time the image of the slat is carried through. The third step is a bilinear transformation of the σ-plane such that the point representing infinity maps onto the origin of the σ_1-plane. This transformation also keeps the shape of the image of the main aerofoil a unit circle and is given by

$$\sigma_1 = \frac{\sigma e^{-i\theta_\infty} - r_\infty}{\sigma r_\infty e^{-i\theta_\infty} - 1} \qquad (30)$$

where $(r_\infty, \theta_\infty)$ denotes the polar coordinates of the image of infinity in the σ-plane. A straight line branch cut as shown in the σ_1-plane is then introduced to string together the near circle representing the slat and the circle representing the flap. The branch cut passes close to the image of infinity and this is a vital feature which determines the length of the cut in the physical plane. The stringed body is treated as a single body by storing its coordinates in a continuous manner. The fourth step is to stretch-open the stringed configuration. This may be visualised by imagining the two ends of the branch cut to extend in both directions to points inside the near circle and the circle. Then by placing the two singularities of Eq.(1) at the two imaginary ends of the cut, the Zhukowski transformation which is a special case of Eq.(1) when τ is zero, can be used to map the two sides of the branch cut onto two circular arcs as shown in the σ_2-plane. This step is necessary in order to ensure and improve convergence of the Theodorsen mapping series to be used later, and it also distorts the image of the unit circle of the σ_1-plane. The resulting configuration has four corners. These discontinuities in slope are removed by applying the Karman-Trefftz transformation once at each corner. Theodorsen's mapping series can now be used to map the smooth body onto a unit circle in the σ_4-plane. Finally the Garrick transformation produces the final configuration of two concentric circles by mapping the outer near circle representing the main aerofoil onto a circle of radius $\hat{r}$ while the shape of the inner unit circle is preserved. The surfaces of the slat and the flap together with the two sides of the branch cut are now represented by the circumference of the unit circle in the ξ-plane.

Since the external region about the three-element aerofoil is now confined to the annular domain of the ξ-plane, a system of polar coordinates in this annular region corresponds to an orthogonal grid in the physical plane. Also the surfaces of the aerofoils and the sides of the branch cut are grid lines in the transformed plane. Fig.16 shows the type of grid generated by the above scheme. We note the desirable high concentration of grid points in the overlapping regions. Contrary to Halsey's method, we also note that the branch cut is well defined in terms of grid points. This is an important factor which enhances the implementation of the reentrant boundary conditions when considering the flow problem.

OUTLINE OF METHOD OF SOLUTION FOR A THREE-ELEMENT AEROFOIL

The formulation of the flow problem for the three-element case is similar to that of the two-element configuration. The overall transformation of the three-element aerofoil is summarised in Fig.17 which also shows the representations of the individual circulations in the ξ-plane. An expansion for the velocity potential and also the definition of the reduced potential become

$$\phi(r,\theta) = W(r,\theta) + (E_m + E_F + E_s)\chi(r,\theta) - (E_F + E_s)\theta + G(r,\theta) \qquad (31)$$

where E_s represents the circulation constant for the slat. The above equation then leads to a similar analysis to that of the two-element case. However two major differences arise. Firstly, the Kutta condition to be satisfied at all three trailing edges yields

three non-linear equations for the three circulation constants. These may be solved using a three-dimensional Newton-Raphson iteration process. Secondly, because of the introduction of the branch cut, reentrant boundary conditions must be applied on the two sides of the cut in the computational plane shown in Fig.17. This condition can be implemented in the numerical procedure by requiring the velocities at grid points on one side of the cut to be equal to the velocities at corresponding points on the other side of the cut. This scheme will require some measure of interpolation since grid points on one side of the cut do not correspond to grid points on the other side. The finite difference schemes, the choice of suitable sweep directions for the transonic case and the numerical method of solution are analogous to the two-element case.

CONCLUSIONS

For the two-element aerofoil case, the grid generation method based on conformal mapping and applicable to two aerofoils of arbitrary shapes, becomes a simple scheme resulting from modifications made to Ives's method. The compressibility effects in the flow are fully implemented in the formulation of the flow problem. The type-differencing used in the numerical calculation which are performed on a rectangular grid, leads to an iterative process. A working computer program has been developed which gives reliable results for the incompressible, subsonic compressible, and transonic cases. The method of solution has also proven capable of predicting weak shock waves in the solution. In regions of relative sparseness of the grid, the smoothness of the converged solution for the reduced potential in the transformed plane, allows interpolation of high order to be used to obtain solution at non-grid points. One of the long term aims of this work is to include the viscous effects of the flow. This may be initiated by modifying the present program to include a preliminary calculation of the boundary layer thickness and wakes from the inviscid results.

For the three-element configuration, the grid generation method emerges from ideas used for the two-element case together with Halsey's concept of string mapping. The result is a grid that is well defined in the overlapping areas of the configuration and is possibly the best that may be obtained from conformal mapping methods without coordinate stretching. There is some scope for extending the present approach to configurations of more than three components although this would require extra effort in terms of intermediate transformations involved. The analysis of the flow problem is analogous to that of the two-element case and a program is currently being developed.

REFERENCES

1. Williams, B.R. 1980. The finite element method for subsonic compressible flow around multiple aerofoils. Num. Meths. in Appl. Fluid Dynamics. (Hunt, B. Ed.) Associated Press.

2. Ives, D.C. 1976. A modern look at conformal mapping including multiply-connected regions. AIAA Journal 14, 1006-1011.

3. Lagally, M. 1929. Die reibungslose Stromung in Aussengebiete zweir. Kreise. ZAMM 9, 209-305.

4. Williams, B.R. 1973. An exact test case for the plane potential flow about two adjacent lifting aerofoils. ARC Reps. and Memo. 3717.

5. Sells, C.C.L. 1968. Plane subcritical flow past a lifting aerofoil. Proc. Roy. Soc. A 308, 377-400.

6. Garabedian, P.R. and Korn, D.G. 1971. Analysis of transonic aerofoils. Comm. Pure and App. Maths. 24, 841-851.

7. Jameson, A. 1974. Iterative solution of transonic flows over airfoils and wings, including flows at Mach 1. Comm. Pure and Appl. Math. 27, 283-309.

8. Murman, E.M. and Cole, J.D. 1970. Calculation of plane steady transonic flows. AIAA Journal 9, 114-121.

9. Grossman, B. and Melnik, R.E. The numerical computation of the transonic flow over two-element airfoil systems. Fifth Conf. on Numerical Methods in Fluid Dynamics. Enschede, Netherlands. 1976.

10. Thompson, J.F. and Mastin, C.W. 1980. Grid generation using differential systems techniques. NASA CP 2166.

11. Theodorsen, T. 1932. Theory of wing sections of arbitrary shape. NACA Rep. 411.

12. Garrick, I.E. 1936. Potential flow about arbitrary biplane wing sections. NACA Rep. 542.

13. Ludford, G.S.S. 1951. The behaviour at infinity of the potential function of a two-dimensional subsonic compressible flow. J. Math. Phys. 30, 117-130.

14. Halsey, D. 1982. Conformal grid generation for multi-element airfoils. Appl. Math. and Comp. 10/11, 585-599.

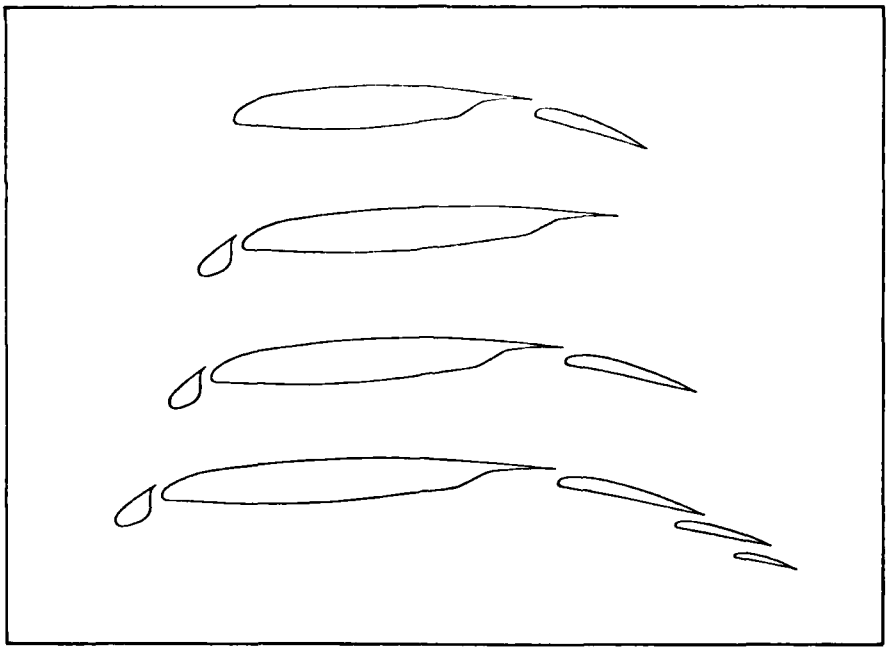


Fig. 1 Examples of slotted high-lift devices.

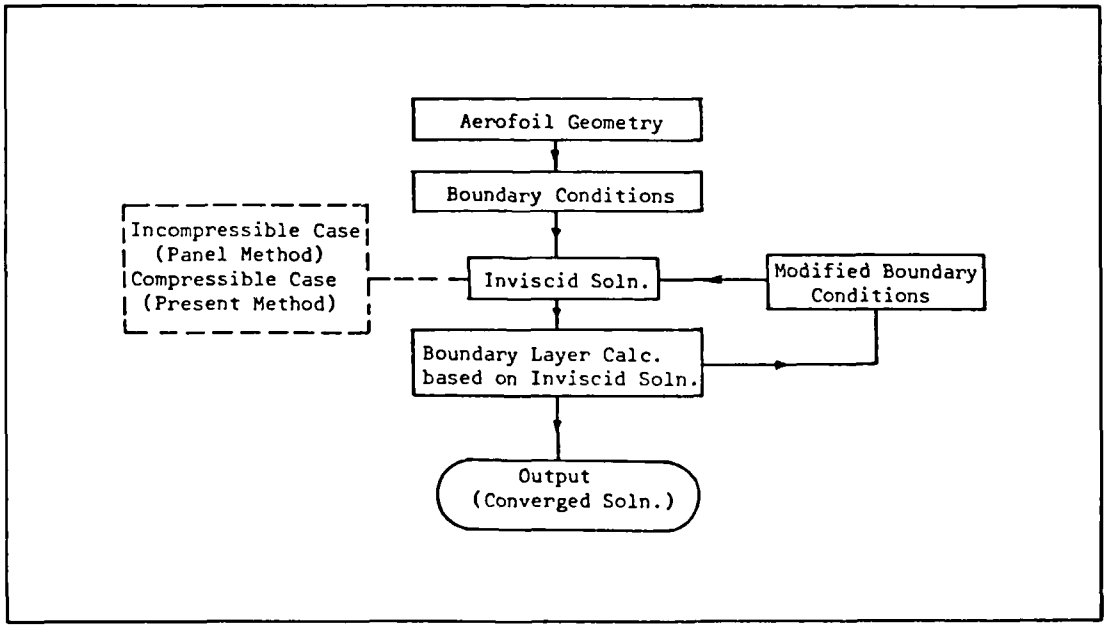


Fig. 2 Flow chart for inviscid-viscous iterative calculation.

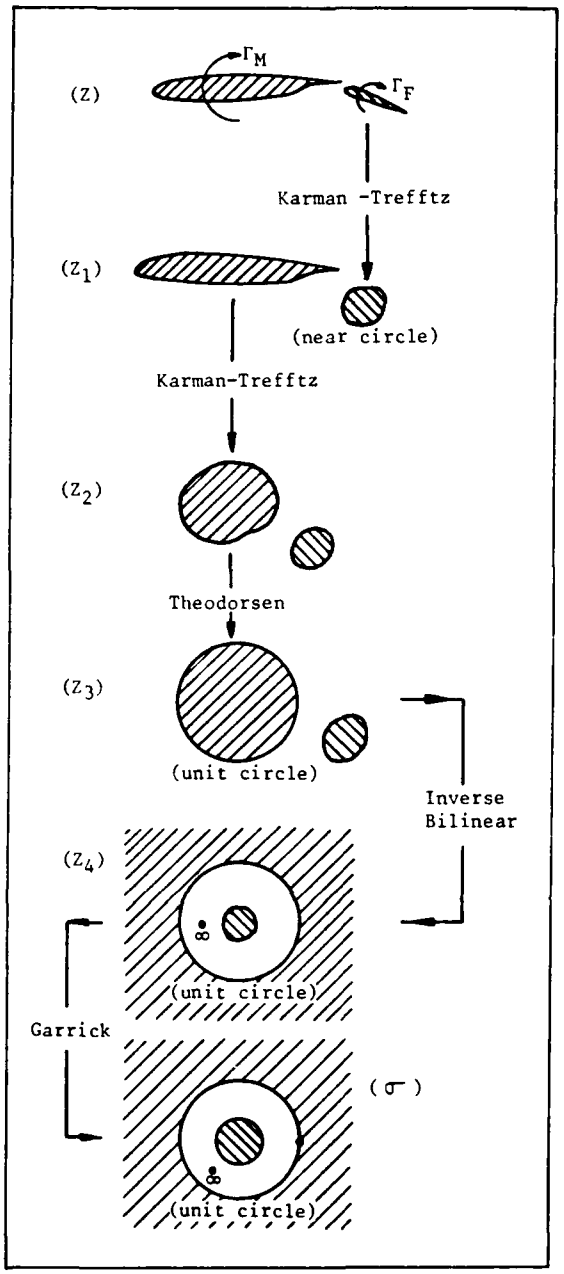


Fig. 3 Conformal transformation of two-aerofoils onto two concentric-circles.

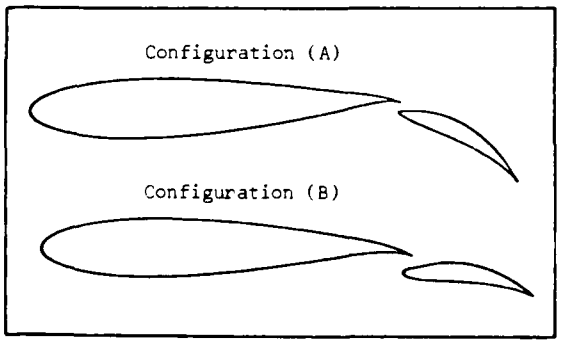


Fig. 4 The two-element test cases investigated by B.R. Williams.

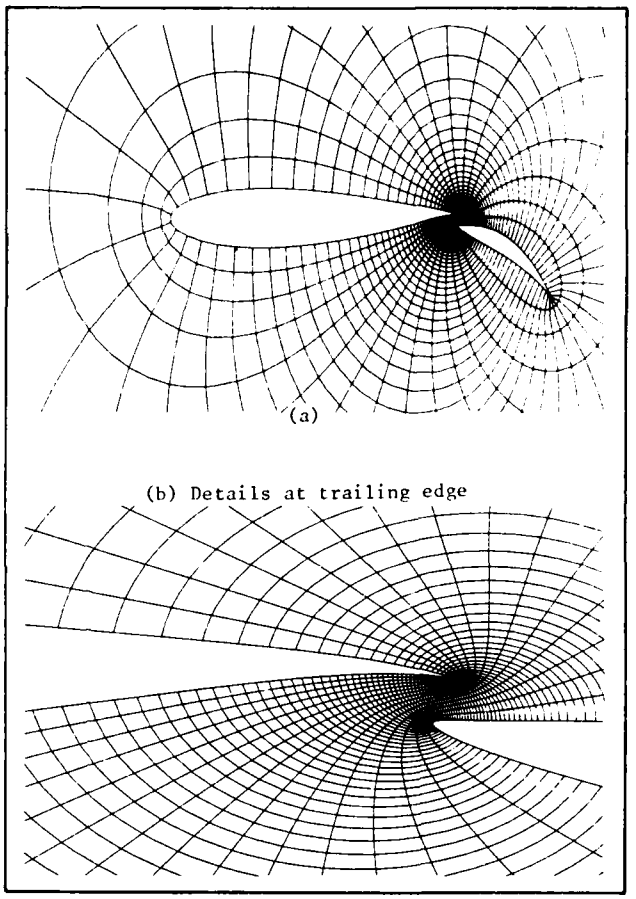


Fig. 5 Grid for an aerofoil-flap configuration

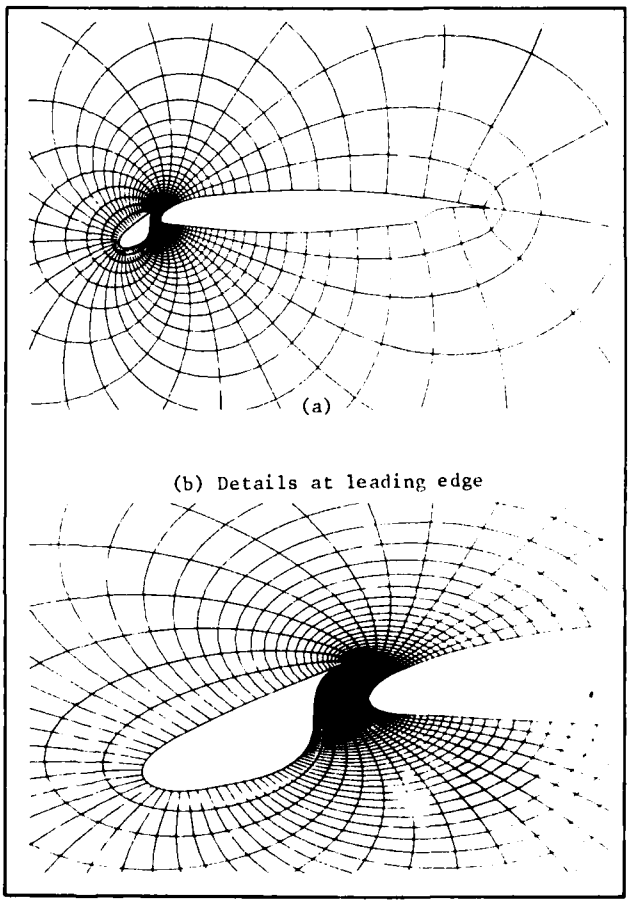


Fig. 6 Grid for a slat-aerofoil configuration

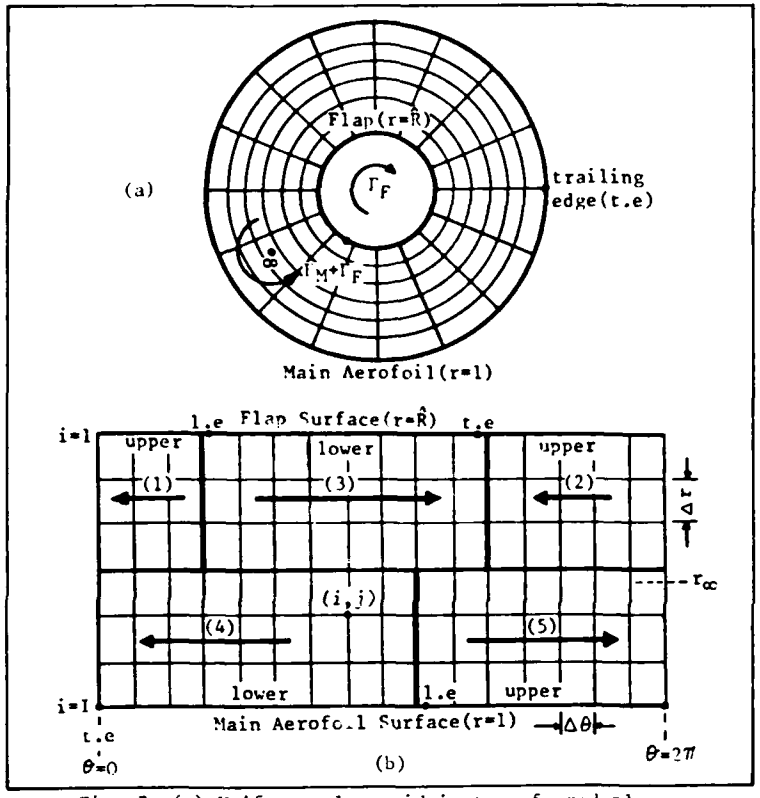


Fig. 7 (a) Uniform polar grid in transformed plane.
(b) Computational plane.
Sweep directions for transonic flow.
(l.e, leading edge)

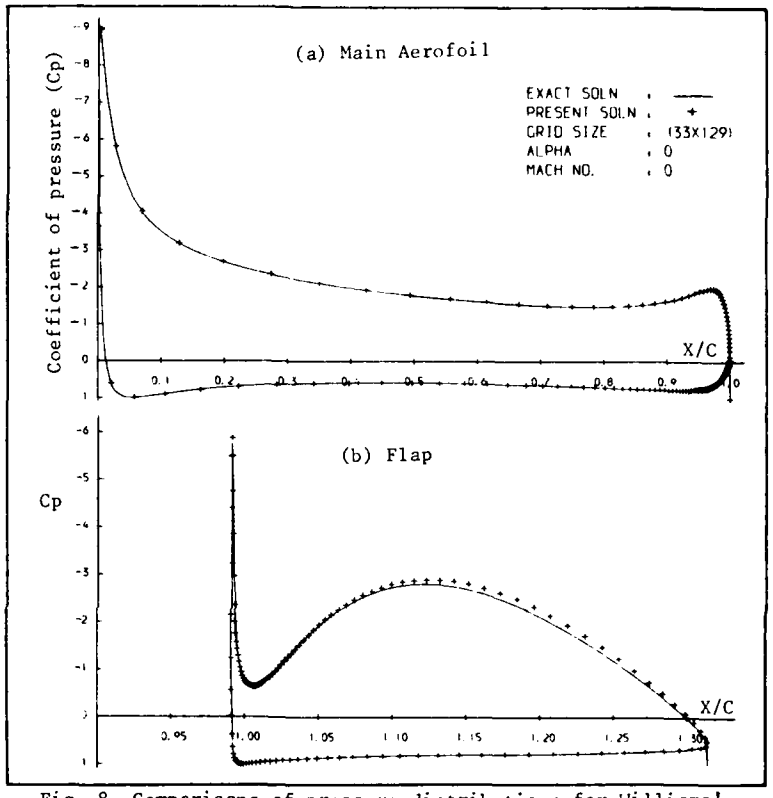


Fig. 8 Comparisons of pressure distributions for Williams' configuration (A). Incompressible Flow.

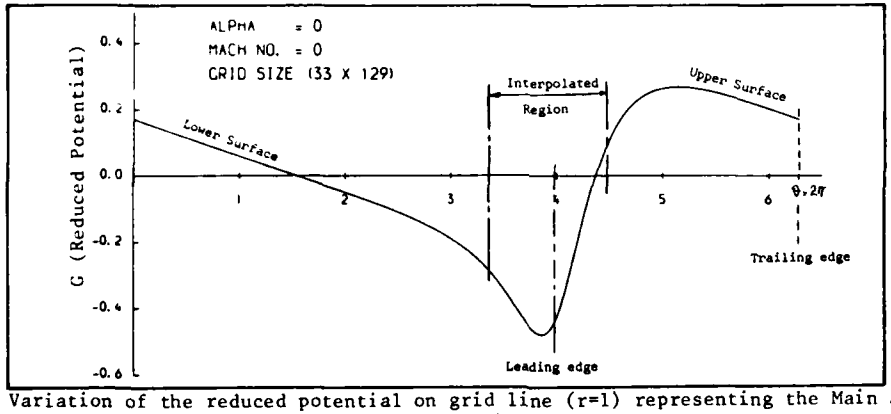


Fig. 9 Variation of the reduced potential on grid line (r=1) representing the Main Aerofoil. Williams' configuration (A). Incompressible flow.

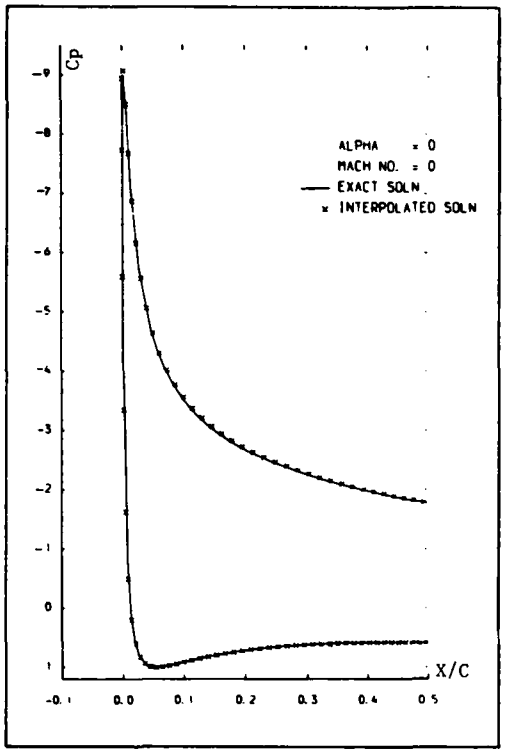


Fig. 10 Comparison of interpolated result with exact solution near the leading edge of Williams' configuration (A).

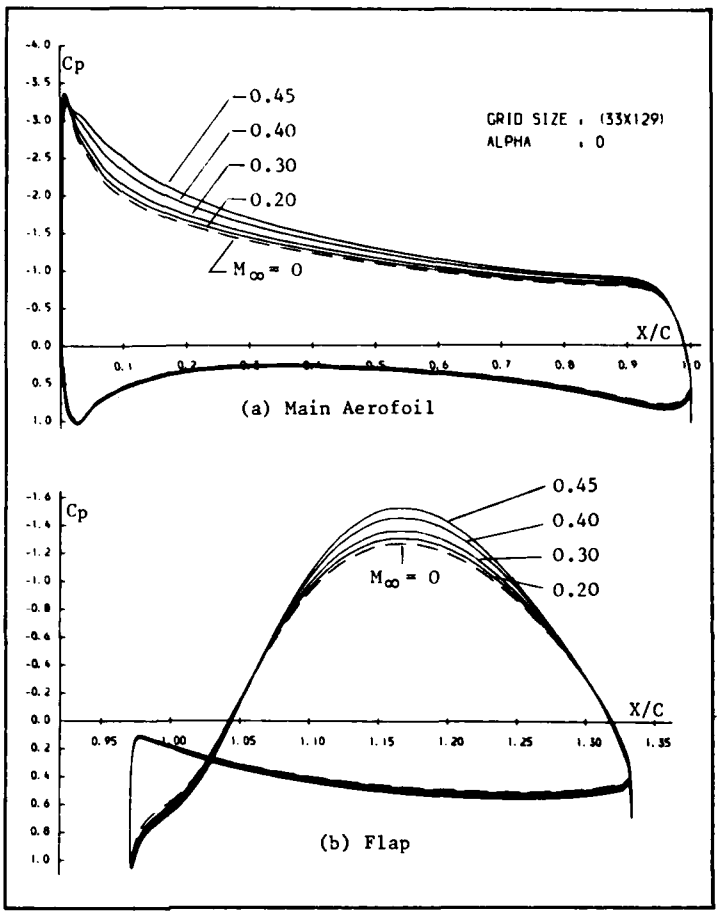


Fig. 12 Mach number effect on pressure distributions of Williams' configuration (B).

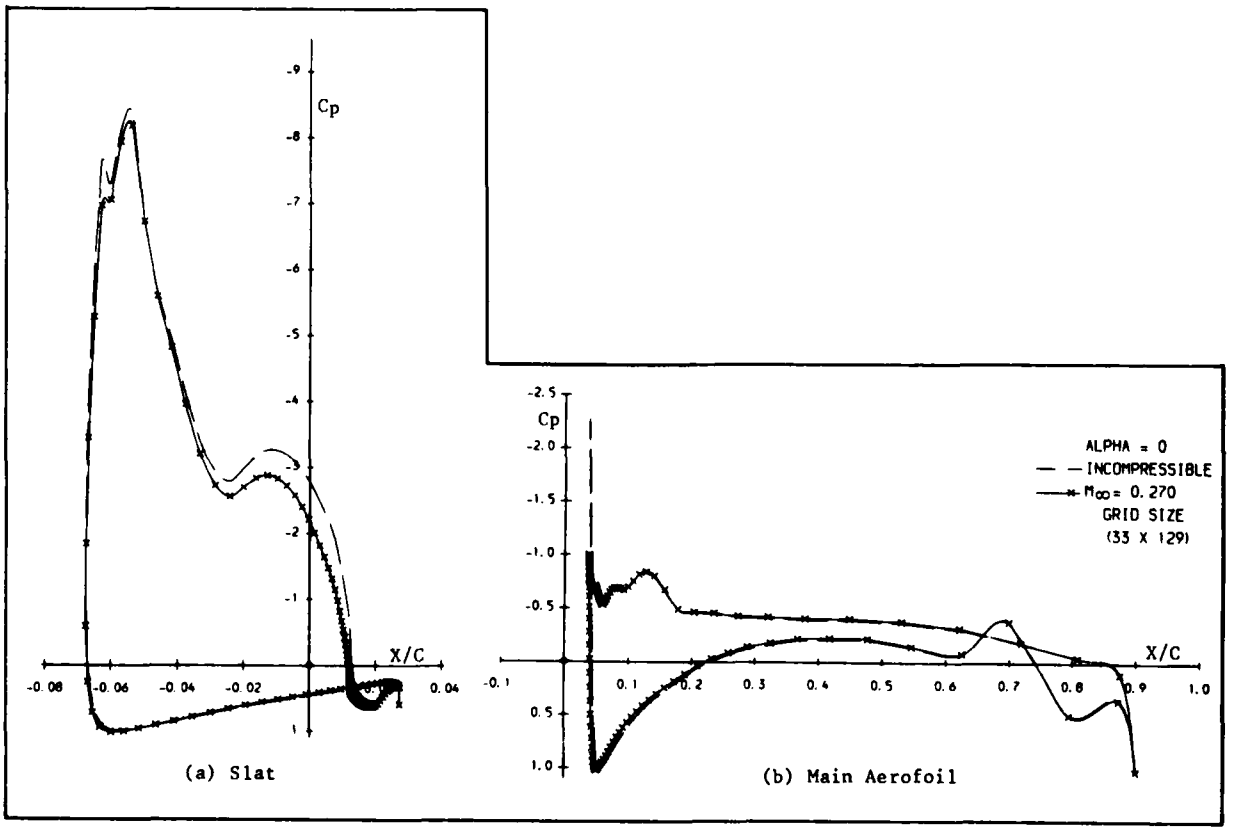


Fig. 11 Pressure distributions for Slat-Aerofoil configuration in subsonic flow.

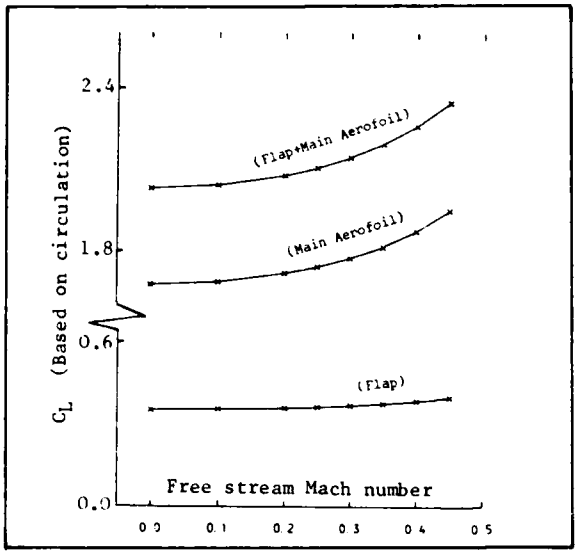


Fig. 13 Mach number effect on Lift coefficient. Williams' configuration (B) at zero incidence.

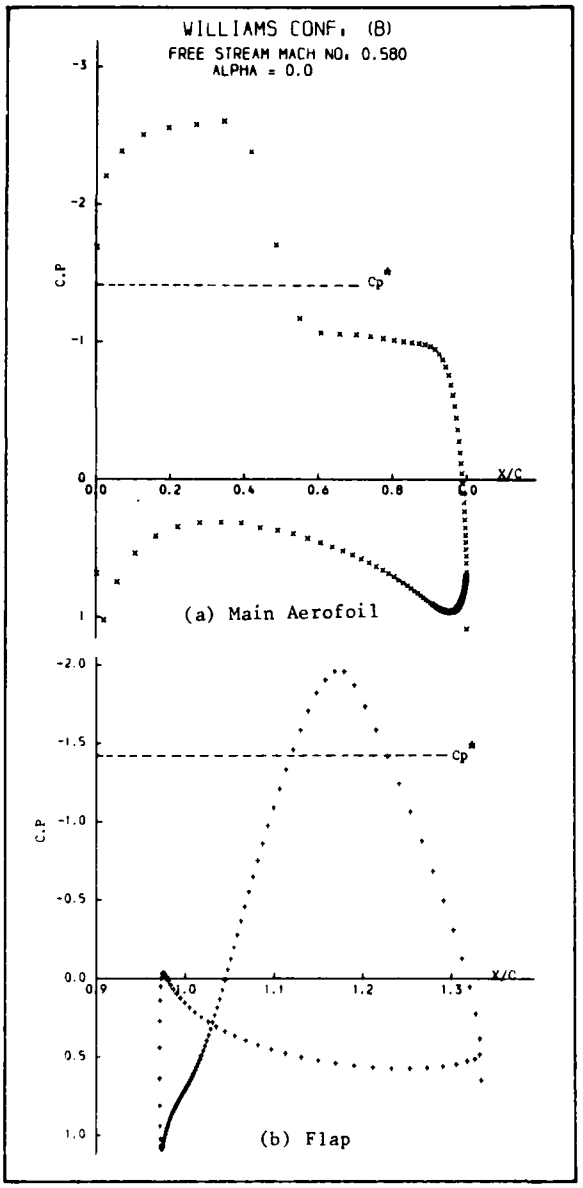


Fig. 14 Transonic flow past Williams'configuration (B).

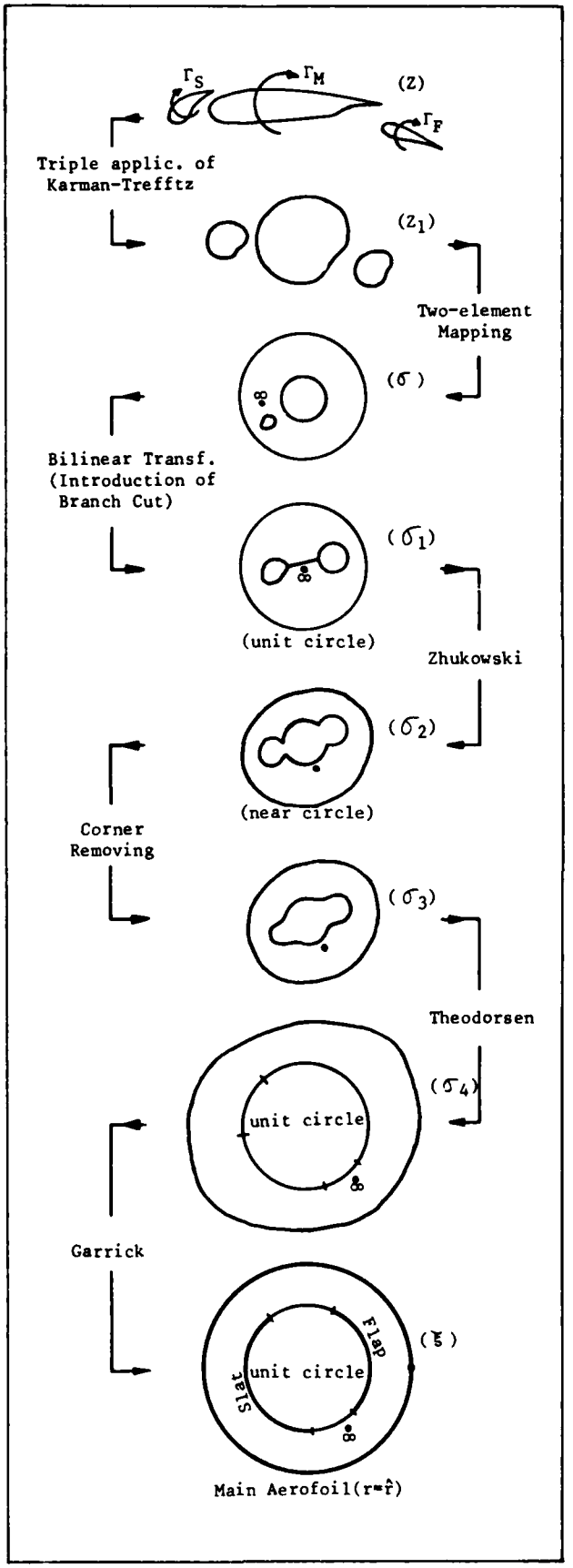


Fig. 15 Conformal transformation of a three-element aerofoil onto two concentric circles.

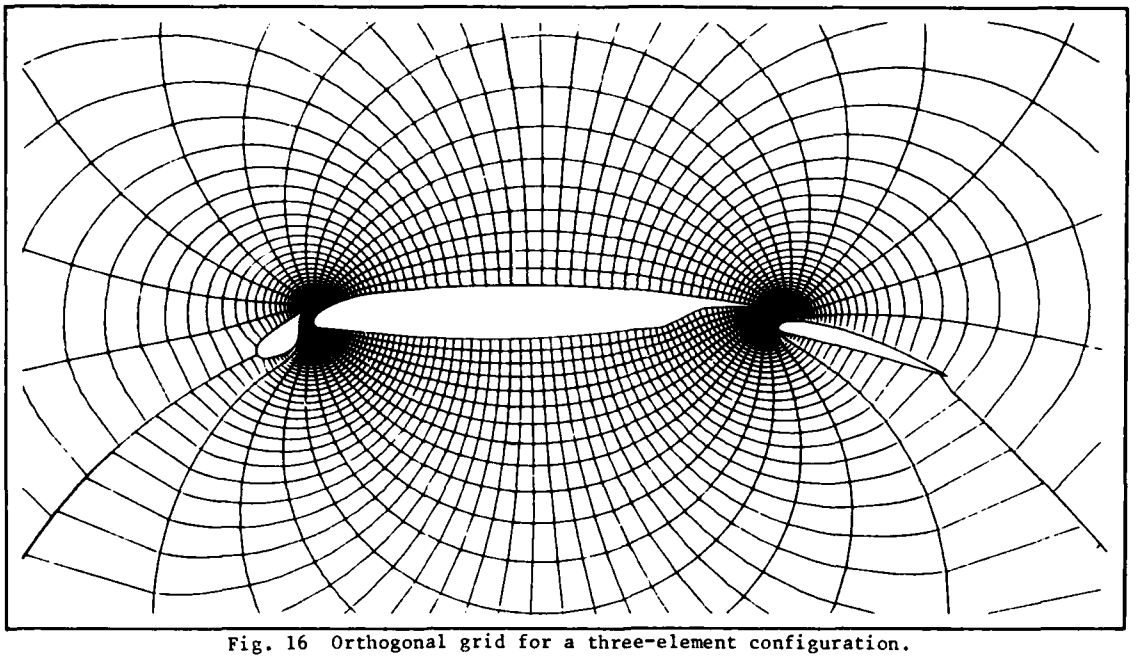


Fig. 16 Orthogonal grid for a three-element configuration.

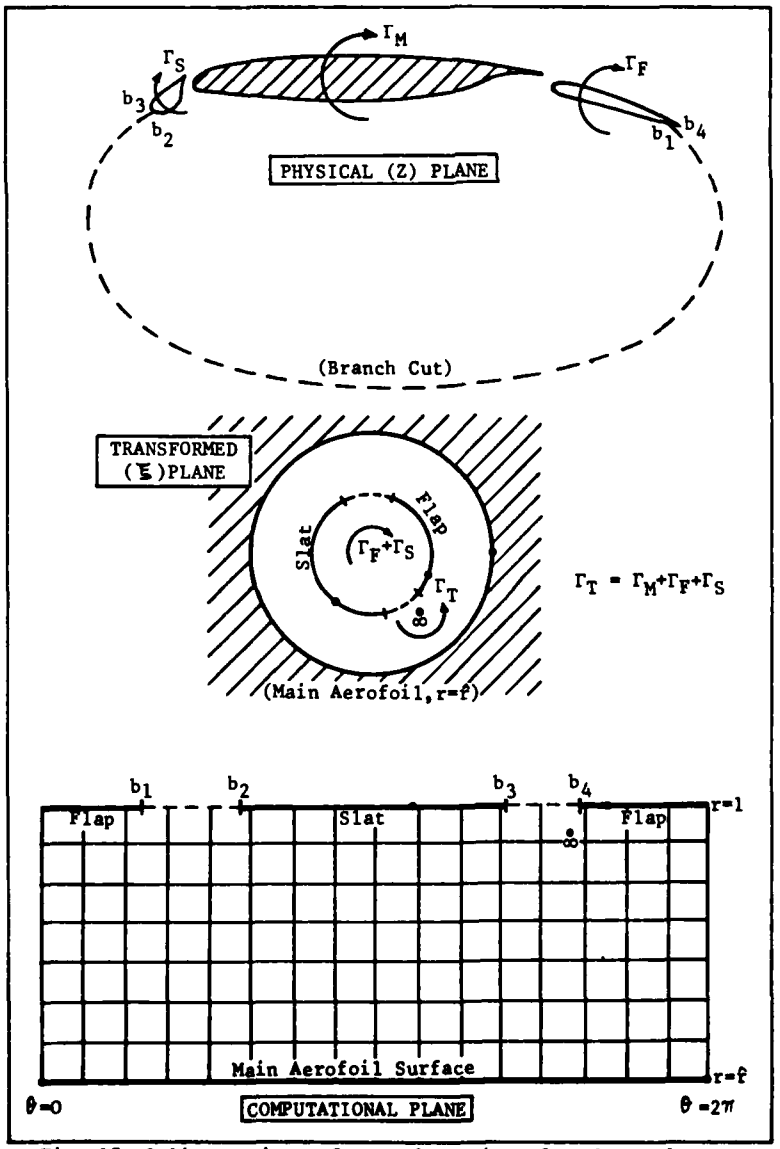


Fig. 17 Salient points of transformation of a three-element aerofoil.

DESIGN OF AN AIRFOIL LEADING EDGE SLAT USING AN INVERSE AERODYNAMIC CALCULATION METHOD

by
J.A. van Egmond and B. van den Berg
National Aerospace Laboratory, NLR
P.O. Box 90502
1059 CM Amsterdam, The Netherlands

AD-P004 056

SUMMARY

With the objective to evaluate the capabilities of a computer program system for the aerodynamic design of multi-element airfoils, a two-element airfoil design study has been performed. In the present study a two dimensional wing-slat combination, tested earlier in the wind tunnel, was selected as the starting configuration. From these tests, the "takeoff condition" for this configuration appeared to suffer from an early turbulent boundary layer separation on the main wing upper surface resulting in high drag values. To improve the drag characteristics, a new slat-wing configuration has been designed. The design was focussed on the main wing nose geometry at the slat-wing intersection.

Both, the original and the new slat-wing configuration have been tested in the NLR low speed wind tunnel LST 3 x 2 at M_∞ = 0.19 and Rec = 3.1 x 10^6. The tests showed a substantial improvement in the drag characteristics for the new configuration and unchanged maximum lift properties (in takeoff condition).

1. INTRODUCTION

The design of the high lift system of an airplane is perhaps one of the most complicated aerodynamic design problems. Strong mutual interferences, large viscous effects and rigid geometry constraints have to be dealt with. In the past, the high lift design process relied largely on empiricism and wind tunnel testing procedures. More recently computational methods for both the analysis and design of high lift configurations have become increasingly important.

Nowadays several computational methods for the design and/or analysis of high lift configurations can be found in the literature (see e.g. Refs. 1-6). Based upon an aerodynamic design philosophy which involves the use of inverse methods to generate shapes that will produce desired pressure distributions (Fig. 1), Labrujère at NLR has developed the design system MAD (Multi-element Airfoil Design). Like most of the existing methods, MAD has been based upon an integral equation method (panel method) for incompressible potential flow. A possibly unique feature of the code is that it contains means for explicit control of the geometry. The computer program system is based on a method which solves the inverse aerodynamic problem in an approximate way subject to geometric constraints. A priori specified aerodynamic requirements (surface pressure distribution) and geometry requirements are both fulfilled approximately. The deviations from the requirements are minimized in a least-squares way, introducing weight factors to emphasize locally either the aerodynamic - or the geometry requirements.

To evaluate the applicability of the design system MAD, it was decided to perform a design study for a two-dimensional wing with leading edge slat. The problem is representative for that of a transport airplane operating out of high altitude airfields (Refs. 7, 8) requiring a high lift-to-drag ratio at takeoff. A two-dimensional high lift configuration tested earlier in the NLR low speed wind tunnel LST 3 x 2 m was selected as the starting configuration.

In chapter 2 of the present paper, a brief description is presented of the design system MAD. The actual leading edge slat design is described in chapter 3. The new slat-wing configuration was tested in the wind tunnel and some of the test results are presented in chapter 4 together with some results of the baseline configuration.

2. DESIGN PROCEDURE

"MAD" stands for an interactive computer aided design system for two-dimensional (multi-element) airfoils in incompressible potential flow*). The system is based on the use of, alternating, direct and inverse second order panel methods utilizing the surface doublet distribution formulation. Both the doublet distribution and the airfoil contour are approximated by means of quadratic functions (Ref. 9).

Labrujère solves the design problem for multi element airfoil configurations by formulating the object functional:

$$F = \int_0^s (F_t^2 + F_n^2 + F_g^2)ds$$

with

$F_t = W_t(\phi_t - N_t)$ = weighted deviation from a prescribed target velocity

$F_n = W_n \cdot \phi_n$ = weighted deviation from zero normal velocity

$F_g = W_g(Z - Z_o)$ = weighted deviation from starting (target) geometry

*) The system has recently been extended with possibilities for viscous flow analysis (MADV). However, this option was not yet available at the time of the present design study.

Minimizing this object function results in an (multi element) airfoil configuration fulfilling approximately a priori specified aerodynamic and geometric requirements. The object function is minimized by varying the doublet strengths and, as far as admitted by the designer (by prescribing W_g) the coordinates of the geometry. By taking W_n large in comparison with W_t and W_g, the solution approximates the boundary condition of zero normal velocity at the airfoil contour sufficiently close. The aerodynamic designer chooses initial geometry, target design pressure distribution and the weight functions. The latter may be adjusted during the design process to relax or enforce geometric constraints. The system involves a data base in which all data generated during the design process are stored such that the user can recall previous results at will. Options for interactively modifying the design parameters (weight functions, geometry, target pressure distribution) and an interactive geometry routine (smoothing, interpolation) form part of the design system.

A general view of the iterative design process is presented in figure 2. It proceeds as follows:

1. The user chooses a starting geometry and a target design pressure distribution. These are fed into the system either from file or by means of a graphical tablet or from the data base saved from an earlier session.
2. Additional design requirements, such as possible constraints on the geometry are selected and a new configuration is determined by means of the design calculation method
3. Review of the resulting configuration may lead to changing the design requirements and determining a new starting configuration. However, in general the flow properties of the new configuration will first be analyzed by means of the analysis method. Then the user may proceed with a next design iteration or;
4. if the user is satisfied with the degree of fulfillment of the design requirements, the flow properties can be analyzed for off design conditions (e.g. another angle of attack, different mutual positions of the airfoil elements) also by means of the analysis method.
5. The whole design process can be concluded by presentation of the results by means of off-line plots and tables.

3. DESIGN OF THE NEW CONFIGURATION

3.1 General

As mentioned above, the aim of the present design study is to re-design a two dimensional slat-wing configuration with the objective to improve the drag characteristics at takeoff condition, without affecting the maximum lift. The starting configuration has been depicted in figure 3 (slat in takeoff position). The wind tunnel tests of this configuration (see also chapter 4) gave a maximum lift coefficient $Cl_{max} \approx 3$ (Rec = 3.1×10^6). The design liftcoefficient of the present study was therefore chosen as $Cl_{des} \approx 2.1$, being the "takeoff" liftcoefficient commonly defined at $Cl \approx 0.7\ Cl_{max}$.

The measured pressure distribution for the starting configuration at $Cl \approx 2.1$ ($\alpha = 20.2°$) is presented in figure 4. From this pressure distribution it can be seen that turbulent boundary layer separation must have occurred on the main wing upper surface at about 70 % chord (this has been confirmed by oil flow visualization tests). This suggests that a substantial drag reduction might be obtained when this separation region could be reduced.

Because the MAD system utilizes potential flow methods, the first step in the design process was to perform some analysis calculations for the starting configuration. The purpose of this was to determine the potential flow angle of attack at which the suction peak levels (and C_l) for the potential flow are in reasonable agreement with the experimental design condition. This was found to occur at $\alpha = 17°$ (see figure 4).*)

In performing these calculations, the effect of the separation bubble in the slat lower surface cavity was simulated through an "effective bubble geometry". This effective bubble geometry was determined by means of the MAD system by prescribing measured pressure distributions for the slat lower surface. Strictly speaking, this bubble geometry ought to be adjusted for each flow condition. However, it was found that the required bubble geometry varied little within a certain range of flow conditions. Therefore, the bubble geometry used for these analysis calculations (covering only a limited C_l range) has been kept constant. The bubble geometry used is indicated in figure 3.

To start the actual design computations, a set of design requirements has to be defined, concerning both the geometry and the aerodynamics. The aerodynamic requirements were chosen with the aim to reduce the drag of the baseline configuration (without affecting maximum lift properties) and from the analysis presented above. The aerodynamic requirements result in the choice of a design target pressure distribution, which will be discussed in more detail in paragraph 3.3. The geometry is, to a large extent, determined by the geometry of the basic airfoil. In practice, detailed geometry requirements follow from the structural wing design. Because of the fact that the present design study is not directed towards a specific practical wing design, the geometry constraints were mainly based on wind tunnel model manufacturing requirements. These geometry constraints are discussed in the next paragraph.

3.2 Geometry requirements

For a conventional slat-wing configuration, the slat geometry is largely determined by the basic airfoil geometry and only a few degrees of freedom in geometry are left, viz.

- slat position
- the intersection between main wing and slat
- the slat chord; to a limited extent (see below)

The geometry was redesigned subject to the following constraints

- the slat traling edge angle should be sufficiently large for model manufacturing reasons
- the slat chord may not exceed 18 % of the basic airfoil chord, as the original wind tunnel-model is built up by parts with partition at 18 % chord.

*) The irregularities in the calculated suction peaks for the main wing are due to local curvature peaks in the geometry, showing up somewhat clearer in the calculations than in experiment.

Although these constraints have been dictated by wind tunnel model manufacturing requirements one may expect that similar geometry constraints apply in a practical wing design.

3.3 Aerodynamic requirements and target pressure distribution

Under the given circumstances, the main aerodynamic requirements are rather simple and can be summarized as follows:

- To reduce drag, the extent of the separation region on the main wing upper surface near the trailing edge must be reduced. With the main wing nose shape as the unconstrained part of the geometry, this reduction can be obtained most effectively by trying to reduce the suction peak level on the main wing nose.
- Decreasing this suction peak means, in general, decreasing the lift contributed by the main wing. So, preferably, the slat should contribute more lift. Then, to prevent early slat flow separation (and possibly decreasing Cl_{max}), the dumping velocity at the slat trailing edge must be increased.

Because, as mentioned before, the design code MAD neglects viscous effects the design target pressure distribution must be prescribed in potential flow. Except for the slat lower surface, the target pressure distribution has been defined by means of alterations in the potential flow pressure distribution for the baseline configuration (α = 17°, GA = 2.5 %, ov = 0, DS = 10°). The slat lower surface target pressure distribution has been related to the measured pressure distribution on the basic configuration. The target pressure distribution, for the theoretical design condition (α = 17°), was chosen as indicated in figure 5. The four domains of main interest are (see Fig. 5):

(i) a decreased velocity peak on the main wing upper surface, to improve the boundary layer characteristics and delay the separation

(ii) a more rapid expansion around the main wing nose, resulting in higher velocities in the region where the slat trailing edge is situated (see also next item)

(iii) an increase of the slat dumping velocity, to increase the lift contribution of the slat, without increasing the risk of early flow separation on the slat upper surface.

(iv) an increase of the slat lower surface pressure level (compared with the measured level at α = 17°), again to increase the slat lift contribution but at the same time because of possibly favourable effects on the drag. It has to be emphasized that the latter is highly speculative because the slat lower surface pressure level will be determined mainly by the viscous effects in the slat cavity.

The magnitude of the "modifications" has been chosen rather arbitrarily. However, adjustments can easily be made during the design proces.

3.4 Design computations

First it should be mentioned that the design computations do not optimize automatically for chord length. For this reason, different design runs were performed for different slat- to wing chord ratios.

In defining - and adjusting the weight functions, some care must be taken to prevent the system of equations to become underdetermined by too much freedom in both geometry and target velocity at the same location. Potential problem areas are stagnation regions and nose regions when large geometry changes occur. In stagnation regions, the geometry weight function Wg must be $\neq 0$ in order to satisfy the so-called regularity condition (Ref. 10). On the other hand, the geometry should not be kept too rigid because this would jeopardize the possibility to obtain an improved pressure distribution. When large geometry changes occur, the regularity of the panel distribution may be disturbed locally, resulting in numerical problems. These are prevented by rearranging the panel distribution from time to time during the iteration process.

The final results of the design computations are presented in figures 6 and 7. Figure 6a shows the new geometry, together with the original one. The main wing nose has become quite blunt. The slat chord has increased slightly. In order to prevent the slat trailing edge region from becoming too thin, the main wing chord had to be decreased a little. In figure 7 the potential flow design pressure distribution for the new configuration is compared with the target pressure distribution. As can be seen, a fairly close agreement has been achieved. The slat position (GA = 2.7 %, ov = 0, DS = 8.8°) differs only slightly from that of the original configuration, although the slat position was kept free during the design computations. The design computations indicated that the pressure distribution is not very sensitive to (small) changes in slat position. It should be noted, however, that the computations also showed that the pressure distribution is very sensitive to small changes in the main wing nose geometry.

4. EXPERIMENTAL VERIFICATION

The aerodynamic properties of the new configuration have been verified experimentally in the NLR LST 3 x 2 wind tunnel. The tests comprised measurement of surface pressure distributions, wake traverses, boundary layers and flow visualization tests for several slat-wing configurations. Full results of this experimental study are to be published elsewhere (Ref. 11). However, the results pertaining to the present design study are discussed below. The test results to be shown have been obtained with natural boundary layer transition, at a Reynolds number $Re_c = 3.1 \times 10^6$ and Mach number $Ma_\infty \approx 0.2$.

Several slat positions have been investigated both for the original - and for the new configuration. Mainly on the basis of optimum lift to drag ratio, a gap of GA = 2.5 % c, zero overlap (ov = 0) and a relative slat angle DS = 10° was selected as the takeoff condition for the original configuration. Subsequent tests with the new design indicated a slightly different optimum situation viz. a gap of 2 % c, 1 % c overlap at the same relative slat angle of 10° (see Fig. 6b). This differs from the theoretically determined design position (see previous chapter). The effects of this difference are, theoretically as well as experimentally of minor importance at the design condition ($Cl \approx 2.1$). The reason to choose yet a slightly different slat position for the new design is because of a favourable influence on the maximum lift (the latter was not addressed directly in the theoretical design process).

Figure 8 shows the lift curve measured for both configurations. The new design exhibits higher lift at the same angle of attack, indicating reduced viscous losses particularly in the range $1.8 < C_l < Cl_{max}$. This is clearly reflected in the C_l-C_d curves (Fig. 9). At the design condition ($C_l \approx 2.1$), a drag reduction is found of approximately 30 %.

Some typical measured pressure distributions around the design condition are presented in figures 10a and b for the slat, and in figures 11a and b for the main wing (pressure coefficient plotted against arc length along airfoil contour, with the origin at the upper surface trailing edge). On the slat, as expected, both the peak velocities and dumping velocities are higher for the new configuration. On the main wing, a substantial reduction of the peak velocities is obtained, which is also in agreement with the design goal. The latter has resulted in a rearward shift of the separation position. This can be seen from the pressure distributions and was confirmed by flow visualization tests. The rearward shift of the separation point on the main wing is very likely the main reason for the lift increase and drag decrease (at constant angle of attack) of the new configuration.

Finally, figures 12a and b present some typical boundary layer velocity profiles measured at $\alpha = 21.2°$. For the slat these were obtained near the trailing edge and for the main wing in a position close to the separation point of the original configuration. The higher velocities in the wall region for the new configuration indicate improved boundary layer conditions both for slat and main wing (more remote from separation). A small drawback of the higher mean velocities on the slat upper surface appears in the slat wake (Fig. 12b) as a somewhat larger velocity defect, with consequently a somewhat larger drag contribution from the slat. However, this is more than compensated by the improvements in the main wing upper surface boundary layer flow.

5. CONCLUDING REMARKS

A two-element airfoil design study has been performed with the primary aim to evaluate the applicability of the interactive design system MAD for the design of multi-element airfoil configurations. An attractive aspect of MAD is the possibility to balance aerodynamic- and geometric requirements by means of weight functions.

The study concerned the improvement of the drag characteristics of a slat-wing configuration at "take-off" condition. Subject to certain geometric constraints, a new slat-wing configuration has been generated exhibiting approximately 30 % lower drag than the original configuration at the design lift coefficient ($Cl \approx 2.1$) in the wind tunnel ($Re_c = 3.1 \times 10^6$), while the maximum lift remained unchanged.

During the design computations it was found that the flow around the main wing nose is very sensitive to small geometry changes; in the authors' opinion the detailed design of the main wing nose geometry would not have been possible without inverse design computations.

Acknowledgement

The authors would like to thank mr. Th.E. Labrujère for his co-operation, and the Netherlands Agency for Aerospace programs (NIVR) for the permission to publish the presented results.

REFERENCES

1. Callaghan, J.G.; Beatty, T.D. — A theoretical method for the analysis and design of multielement airfoils. J. Aircraft, Vol. 9, No. 12, Dec. 1972, pp. 844-848

2. Narramore, J.C.; Beatty, T.D. — An inverse method for the design of multi-element high lift systems. AIAA paper No. 75-879, June 1975

3. Kennedy, J.L.; Marsden, D.J. — A potential flow design method for multicomponent airfoil sections. J. Aircraft, Vol. 15, No. 1, Jan. 1978, pp. 47-52

4. Bristow, D.R. — A new surface singularity method for multi-element airfoil analysis and design. AIAA papaer 76-20, January 1976

5. Bristow, D.R. — Development of panelmethods for subsonic analysis and design. NASA CR 3234, 1980

6. Lind, I.A. — An airfoil with single-slotted flap designed for maximum lift. KTH Aero rapport FI49, The Royal institute of Technology, Stockholm, 1979

7. Henderson, M.L. et al — High lift selected concepts NASA contractor report 159093 Boeing, August 1979

8. McMasters, J.H.; Henderson, M.L. — Some recent applications of high-lift computational methods at Boeing. J. Aircraft, Vol. 20, No. 1, January 1983, pp. 27-33

9. Labrujère, Th.E. — MAD, a system for computer aided analysis and design of multi-element airfoils. NLR TR 83136 L, 1983

10. Slooff, J.W. — Computational methods for subsonic and transonic aerodynamic design. AGARD Rep. 712, Special course on subsonic/transonic interference for aircraft, 1983

11. Van den Berg, B. — Experimental investigation into some details of the flow around a two-dimensional wing with slat. NLR Report to be published

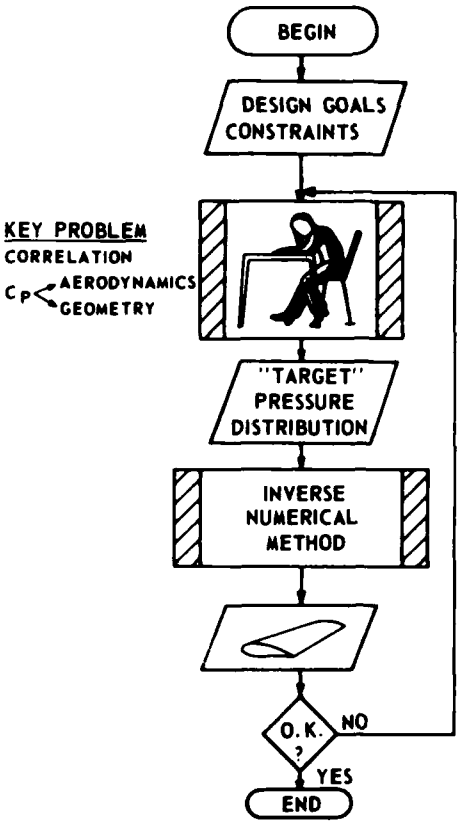


Fig. 1 Aerodynamic design procedure based on "inverse" method

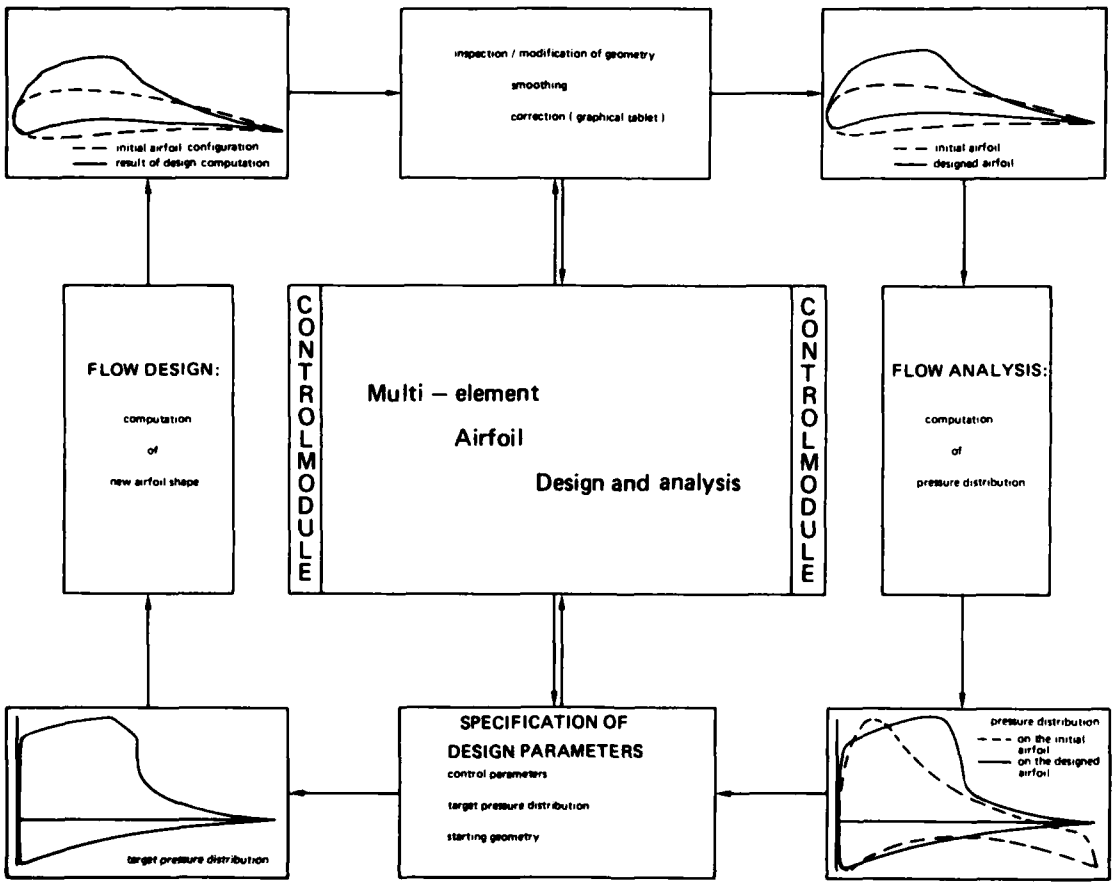
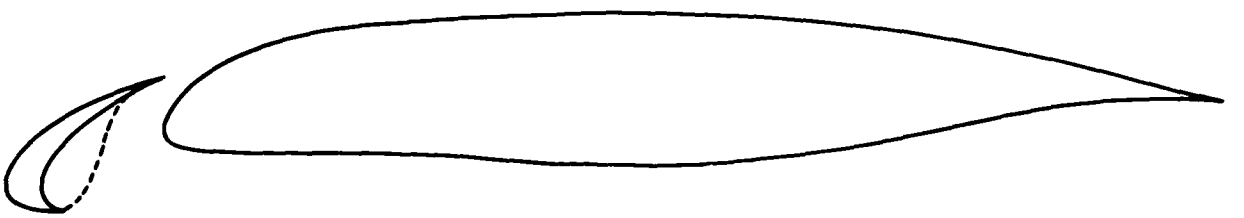


Fig. 2 The iterative design process



SLAT POSITION : OV = 0
GA = 0.025
DS = 10°

----- BUBBLE SIMULATION ; USED IN COMPUTATIONS

Fig. 3 Sketch of the original wing-slat configuration

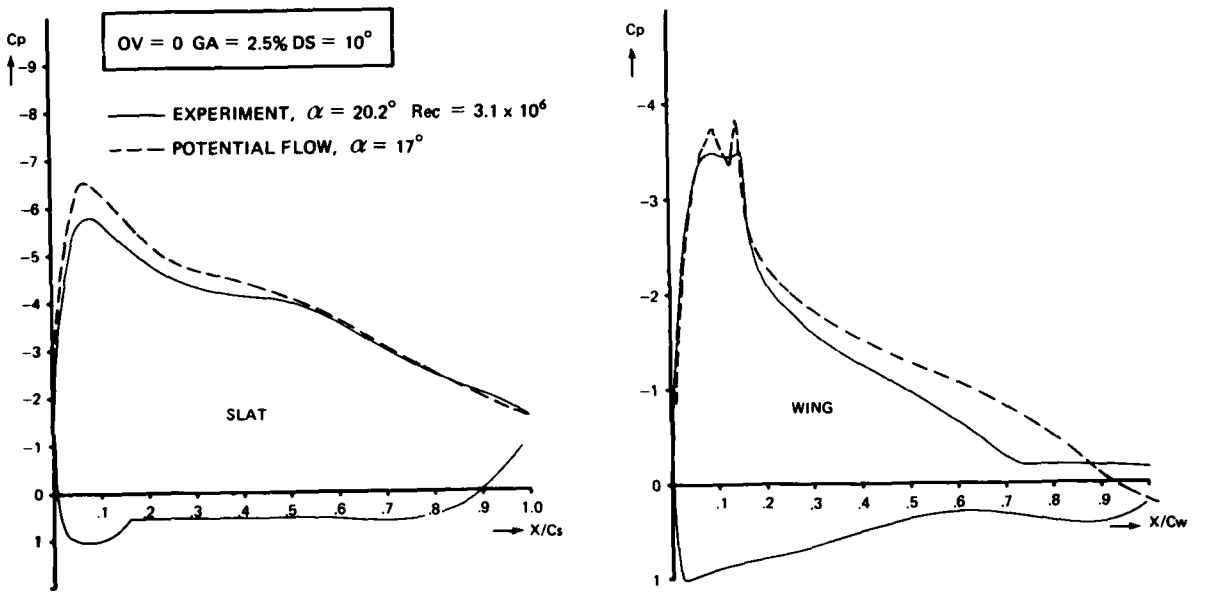


Fig. 4 Measured- and potential flow design condition for the original configuration

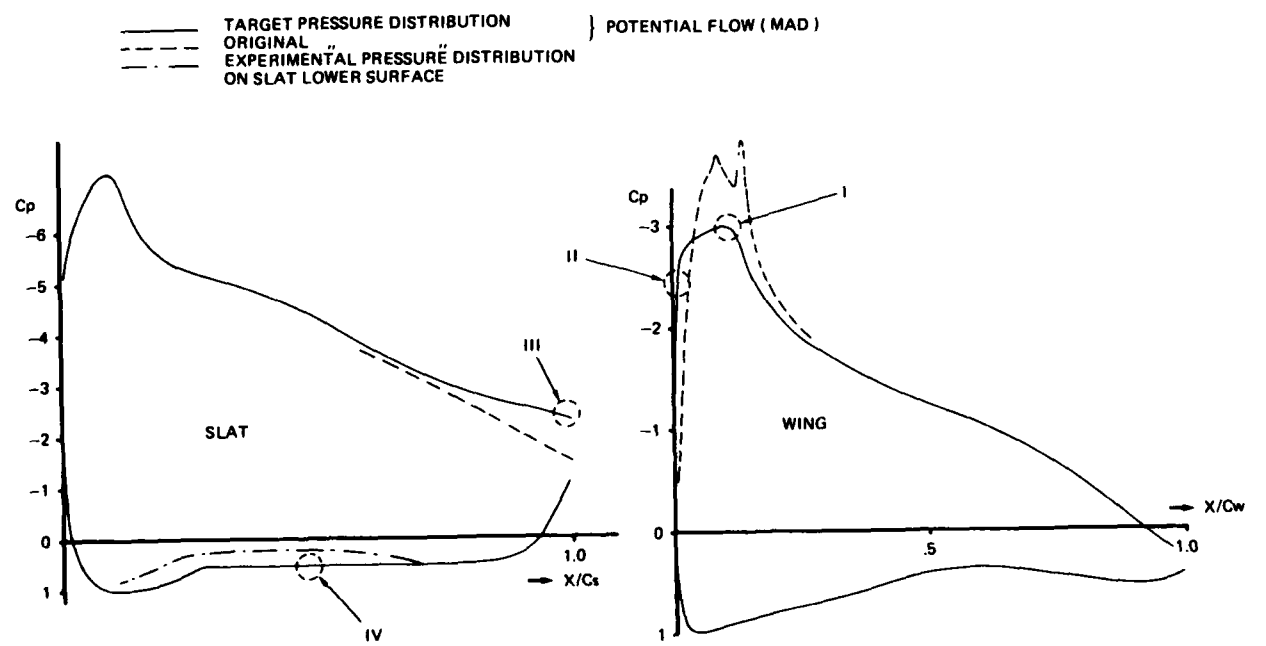


Fig. 5 Target pressure distribution for new wing-slat configuration α = 17°

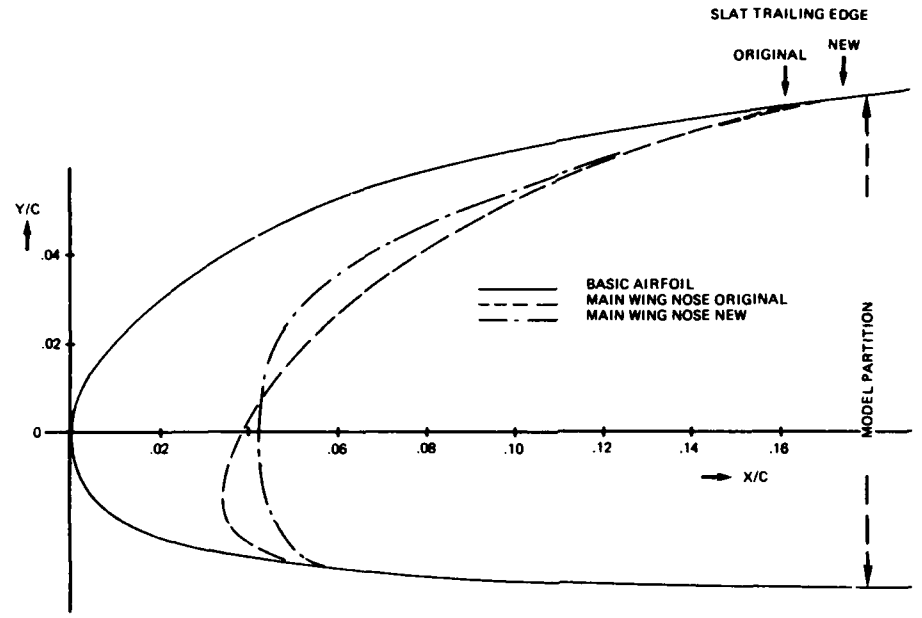


Fig. 6a Sketch of the original and newly designed wing nose

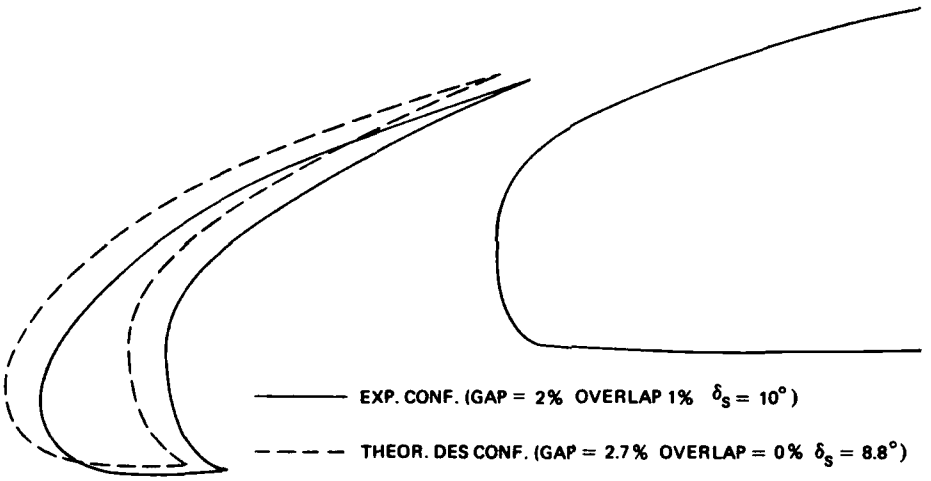


Fig. 6b Sketch of the new configuration in experimental design condition

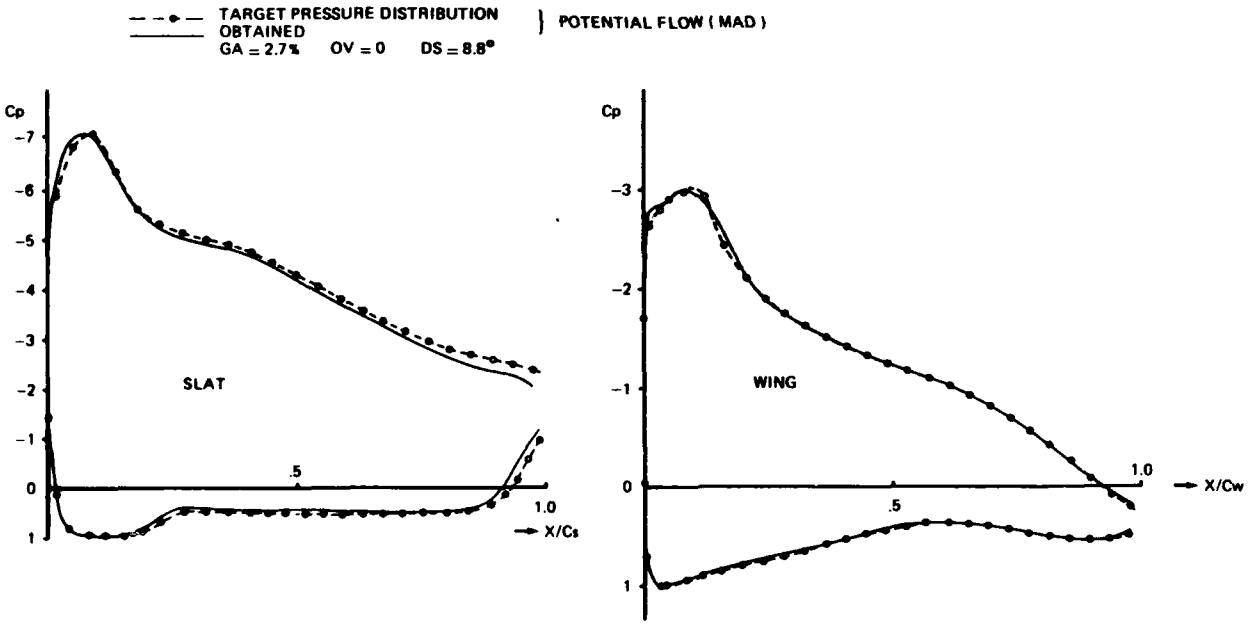


Fig. 7 Comparison of target pressure distribution and pressure distribution obtained with the new wing-slat configuration $\alpha = 17°$

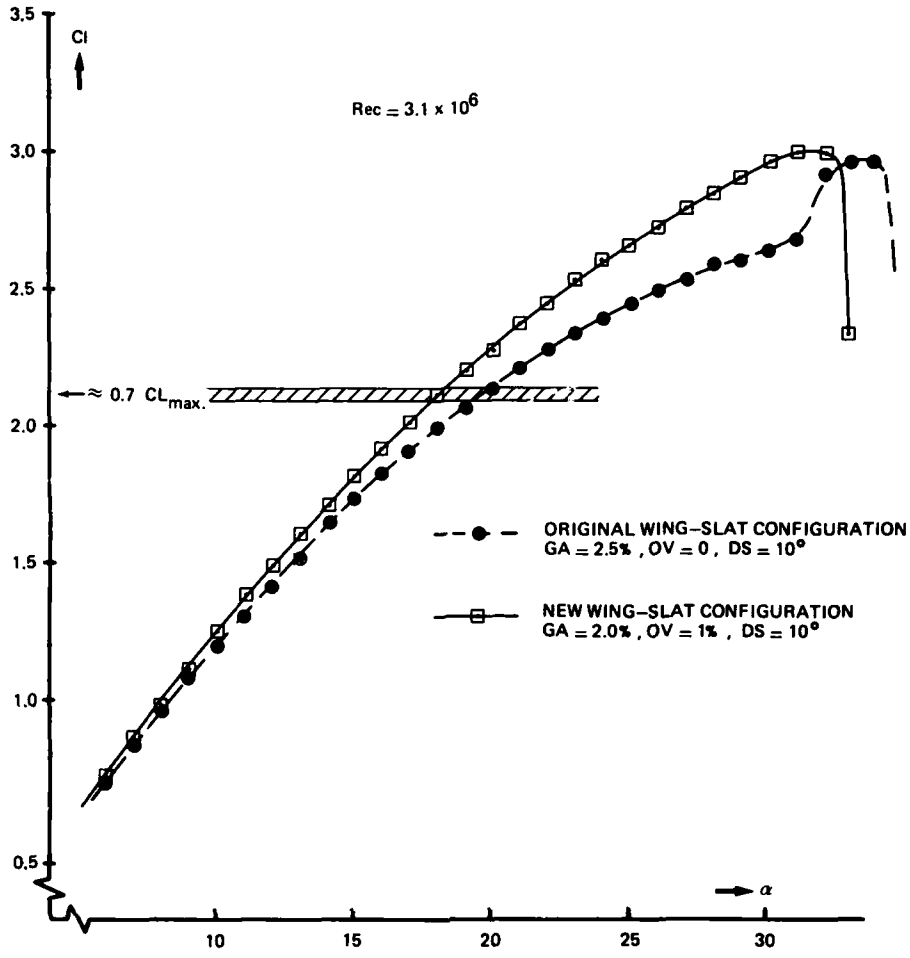


Fig. 8 Measured C_ℓ-α curves for both wing-slat configurations

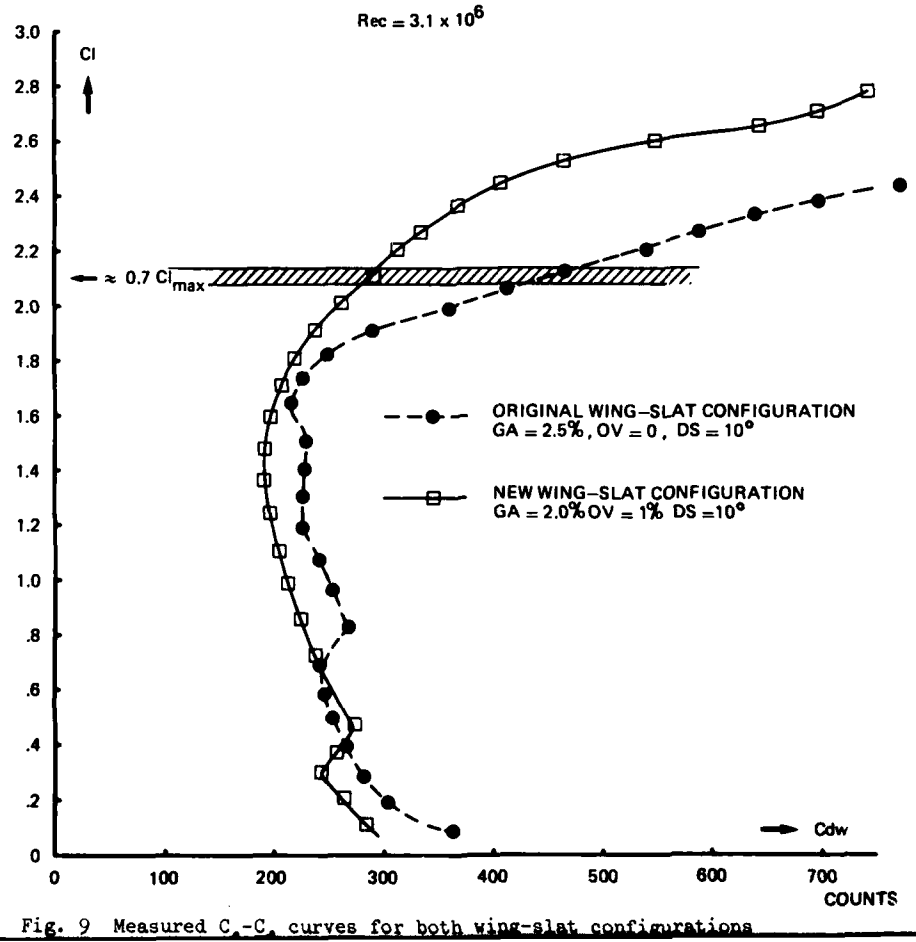


Fig. 9 Measured C_ℓ-C_d curves for both wing-slat configurations

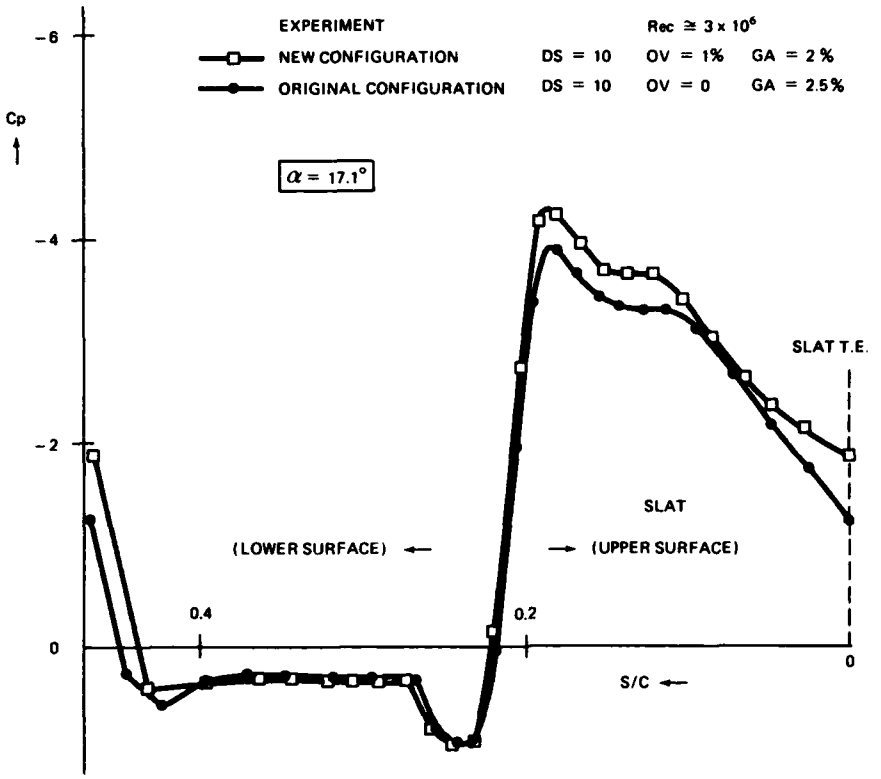


Fig. 10a

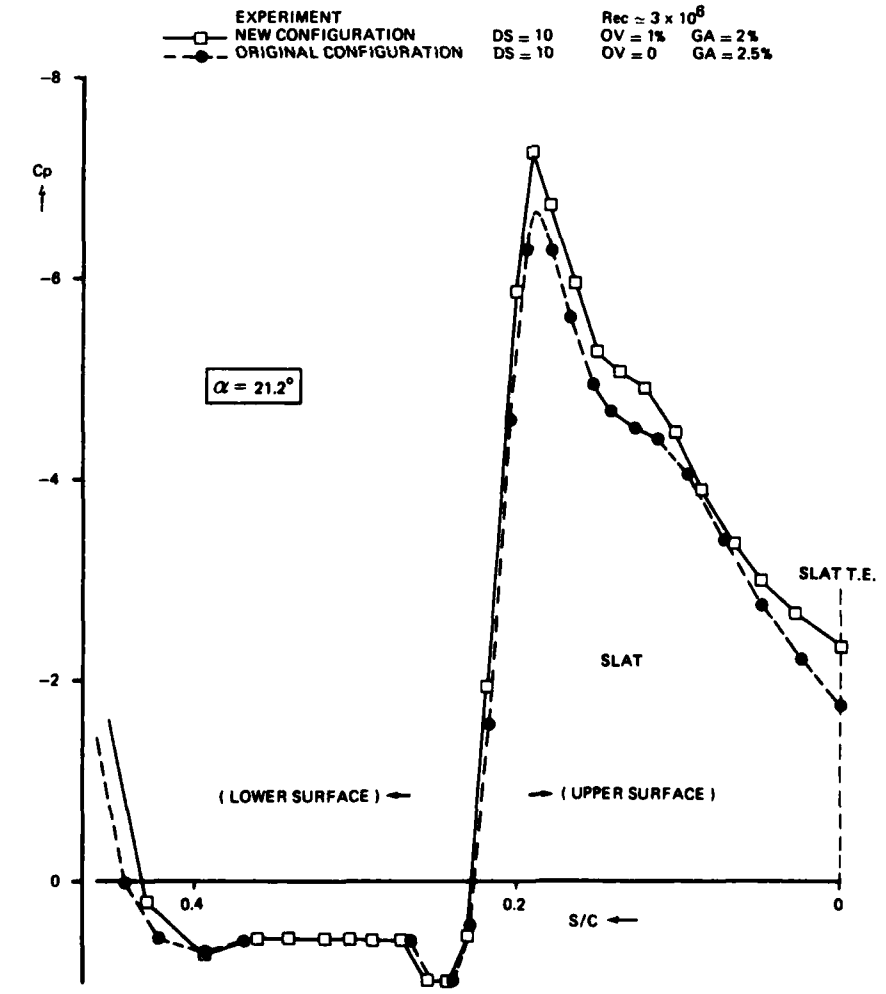


Fig. 10b Measured pressure distributions on the slat for both wing-slat configurations

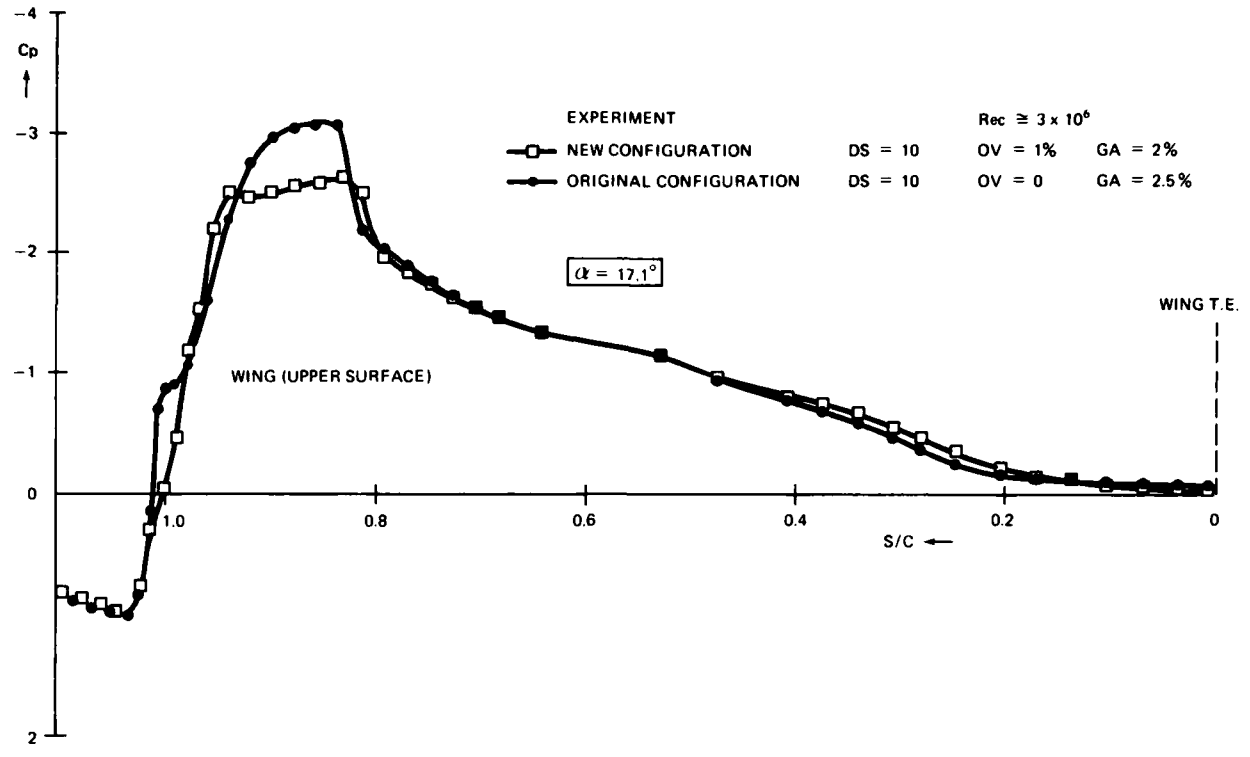


Fig. 11a

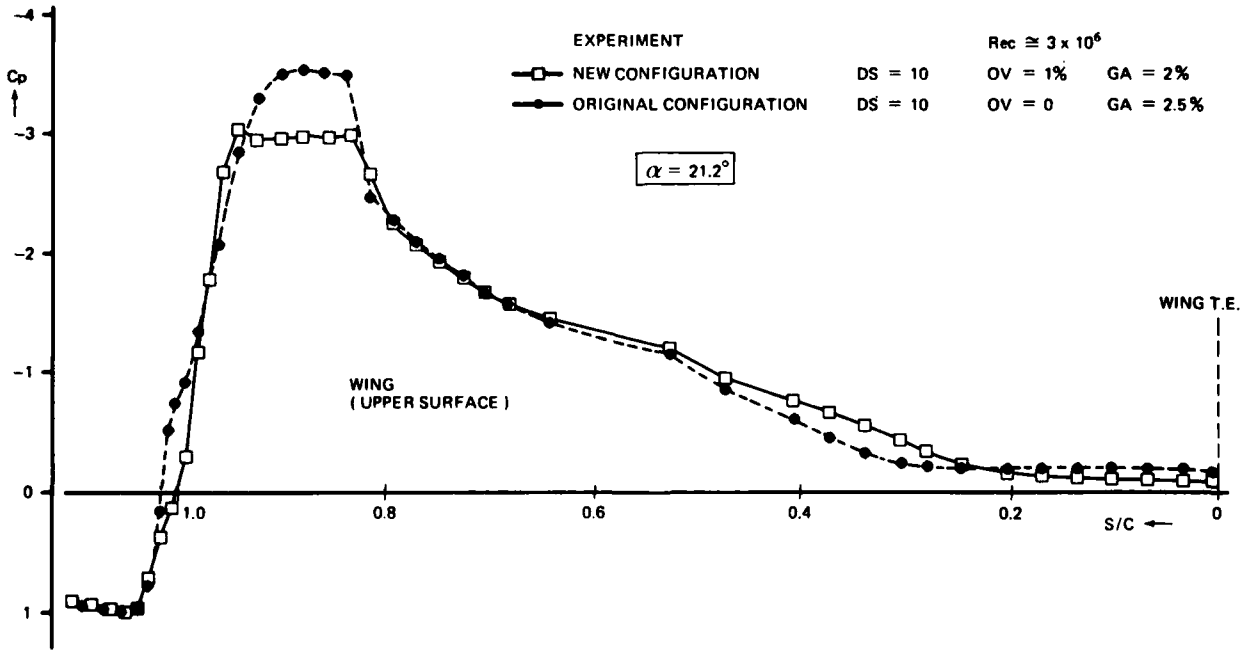


Fig. 11b Measured pressure distribution on the wing upper surface for both wing-slat configurations

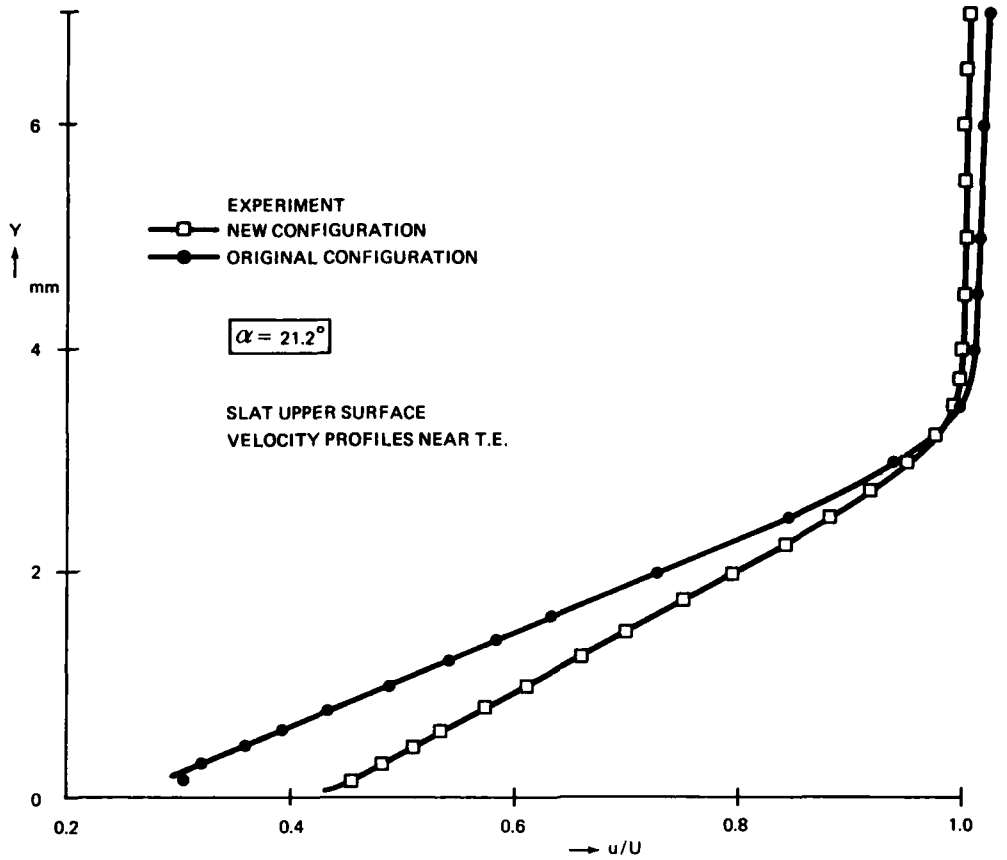


Fig. 12a Measured boundary layer velocity profiles on the slat upper surface near the trailing edge

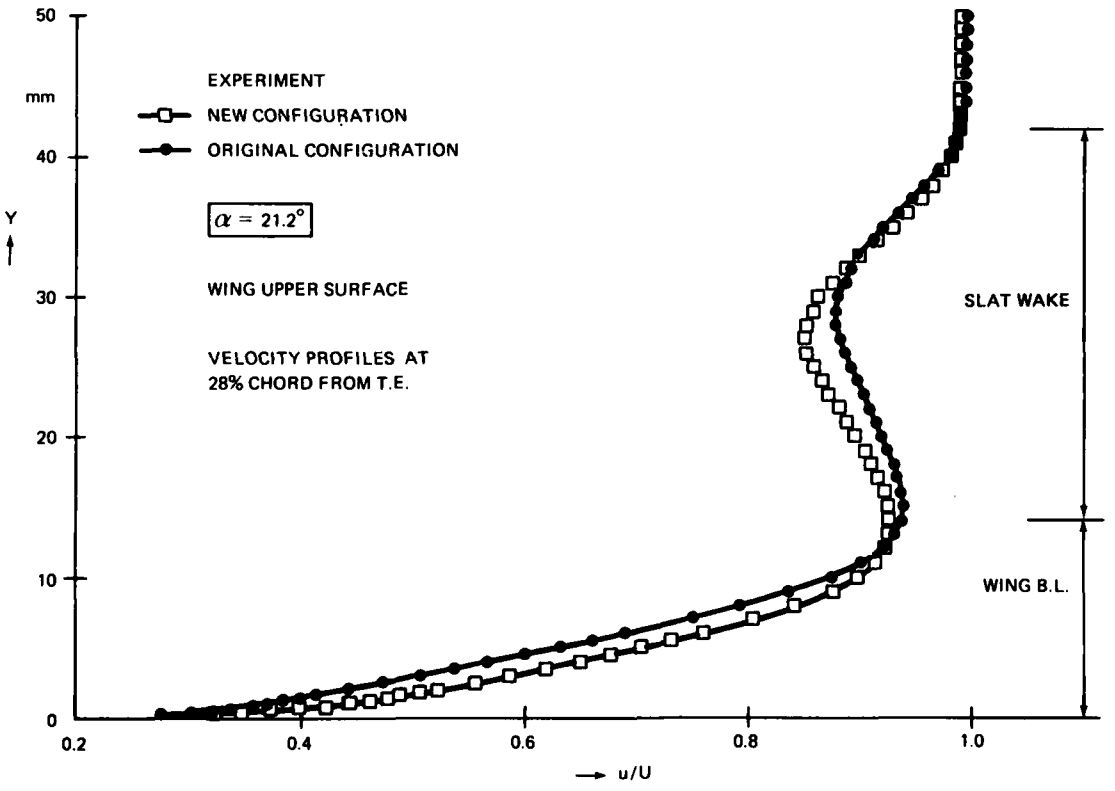


Fig. 12b Measured velocity profiles on the wing upper surface at s/c = 0.28 (a short distance upstream of separation)

AD-P004 057

MODELLING CIRCULATION CONTROL BY BLOWING

M.M. Soliman, Research Fellow, Southampton University
R.V. Smith, Chief Project Engineer, Westland Helicopters, Yeovil
I.C. Cheeseman, Professor of Helicopter Engineering, Southampton University, UK.

SUMMARY

This paper describes a new theoretical representation of circulation control based on discrete vortex modelling techniques. The application of discrete vortex modelling to the prediction of circulation control is initially presented for the Coanda flow of a wall jet around a circular cylinder in a free stream. The decay in the jet momentum, due to viscous and entrainment effects, has been represented in the model by decaying the strength of each vortex as it flows downstream from the slot. The model's application has then been extended to predict the effect of circulation control on other shapes of aerofoil. The paper includes the application of the model to an elliptic section as an example of any aerofoil section that can be represented in a potential flow. The model has had considerable success in predicting the lift produced from such bodies due to the jet, but information about the drag requires additional modelling of the surface boundary layer. A similar technique has been used to represent the boundary layer by discrete vortices and doublets. The model's prediction has been compared with the experimental data of an unblown circular cylinder.

C	:	Chord
C_L	:	Lift coefficient
C_D	:	Drag coefficient
C_J	:	Jet momentum coefficient
d	:	Vortex distance
K	:	Arbitrary decay constant
q	:	Tangential velocity
R_o	:	Radius of the cylinder
R_v	:	Radial position of a vortex
R_i	:	Radial position of an image vortex
R_b	:	Radial distance of the outer edge of boundary layer
R_d	:	Radial distance of the outer edge of displacement thickness
t	:	Age of a vortex
t_j	:	Slot thickness
U_∞	:	Free stream velocity
γ	:	Vortex strength
γ_o	:	Initial vortex strength
δ_d	:	Displacement thickness

1. INTRODUCTION

The concept of circulation control for high lift generation was developed in the early 1960's at the National Gas Turbine Establishment and has since been investigated by a number of researchers. Early work in the subject had investigated the lift and drag characteristics of two-dimensional circular and elliptic cross-sections with circulation control (References 1-4). Later work extended the application of circulation control concept to helicopter rotors (References 5-6). The main current research effort is the X-wing, being developed for the US Navy and DARPA (References 7-9).

Circulation control relies for lift generation on the ability of a wall jet to control the separation point at the bluff trailing edge of an aerofoil. Conventional aerofoils feature a sharp trailing edge which effectively determines the location of the rear stagnation point. The rear stagnation point of an aerofoil with a non-sharp trailing edge is not constrained in this manner, and its location can be controlled by a wall jet. Control of the aerofoil circulation results in, what is known as, "circulation control by blowing".

The relationship between the lift generated by a circulation control aerofoil and the wall jet momentum supplied reflects a complex interaction of the aerofoil design parameters. Factors influencing performance include the aerofoil shape, leading and trailing edge design, blowing slot width and the number of slots as well as slot(s) position. The performance of an arbitrary circulation control aerofoil is determined by the interaction of these design parameters. If a theoretical model does not correctly represent the effects of those parameters, it will fail to model an arbitrary circulation control aerofoil. The lack of a generalized performance prediction method has restricted circulation control development and applications despite its promising performance.

2.1 CONVENTIONAL CIRCULATION CONTROL MODELLING

There have been several efforts to predict the performance of an arbitrary circulation control aerofoil, all based on a conventional boundary layer approach to the problem. This approach was developed initially by Dunham (Reference 10) to predict the flow about a circular cylinder fitted with a wall jet exhausting near tangentially to its surface. Dunham's method relied on the conventional boundary layer and wall jet calculations to decide the pressures at the separation points on the upper and lower surfaces. A solution was reached when a certain jet strength satisfied Thwaites condition (Reference 11) of equal separation pressures at the upper and lower surfaces.

The model's accuracy of prediction depended on the assumptions made regarding the wall jet representation, flow entrainment from the outer flow to the jet, and the separation criterion. Dunham's model satisfactorily predicted circulation control performance trends at low momentum coefficients (Figure 1). However, the numberical accuracy became poor at high momentum coefficients with small slot widths or when analysing single slot models. This accuracy reflected the sensitivity of the model to the treatment of separation and entrainment. These became significant considerations when the length of the surface between the blowing slot(s) and the separation point was large, either at high momentum coefficient, or when only one slot was employed at a position far from the separation point.

Similar methods have been developed (References 12-13), but all these methods relied on successful development of semi-empirical expressions to treat turbulent boundary layers and wall jets over curved surfaces in the presence of an arbitrary pressure gradient. Although encouraging results have been obtained using this technique, a more fundamental approach is desirable. It is desirable that such an approach should be sufficiently general to allow treatment of the many applications of boundary layer control and Coanda flows in contemporary aerodynamics. A new model is developed, and described below, which is based on a discrete-vortex approximation to the shear layer external to a wall jet under an external stream.

2.2 DISCRETE VORTEX MODELLING OF CIRCULATION CONTROL

Discrete-vortex modelling consists of the representation of a shear layer, by a number of discrete vortex filaments surrounded by an inviscid, irrotational flow. Deformation of the sheet is calculated by evaluating the velocity induced at each element by the remaining elements and satisfying the boundary conditions of the initial flow. Discrete-vortex modelling has been applied to a wide range of flows which include shear layer(s). Rosenhead (Reference 14) applied this technique to the shear layer formed between two uniform streams of flow with equal speed in opposite directions. The same technique was used to represent the two shear layers separating a stream from an exterior stream flowing with equal speed in the opposite direction (Reference 15). Gerrard (Reference 16) adapted this approach to model the wake shed by a bluff body, the shear layer at the wake boundary being represented by discrete vortices introduced into the flow at successive time steps.

The application of this technique to circulation control was developed initially for circular cylinders (Reference 17), then extended later for other forms of aerofoils (Reference 18). Several modifications and developments have been introduced since, and the latest form of the models is presented below.

3.1 MODEL DESCRIPTION

Initially, the flow about a circular cross-section in a uniform stream is modelled with zero circulation. The circular boundary is formed by introducing a doublet into the uniform stream. The shear layer formed at the edge of the jet is represented by a series of discrete vortices. The shear layer is formed as the jet emerges from the slot, so the vortices are introduced progressively to simulate the growth of the jet as it leaves the slot and flows downstream. The first vortex is introduced at a point above the circular boundary where the slot is located. The distance of this point from the boundary is the slot width. The vortex is accompanied by an image vortex inside the boundary, with the same strength but opposite sense of rotation. The position of the image vortex is decided by the equation:

$$R_v R_i = R^2_o \qquad (1)$$

where R_v : Radial distance of the vortex
R_i : Radial distance of the image vortex
R_o : Radius of the circular boundary

The reason for introducing the image vortex is to preserve the shape of the circular boundary by ensuring the absence of any normal velocity at the circular boundary. The external vortex moves a specified distance step after calculating the induced velocities on this vortex by all elements of the flow field, including its image. The image vortex position is readjusted according to equation (1), while a new vortex is introduced at the slot lip with its new image. The process is repeated, allowing each vortex to move a distance proportional to the time taken by the initial vortex to move over the fixed distance-step, and also to the local velocity of the vortex in question. After each step, a new vortex/image is introduced at the slot lip. The process leads eventually to a sheet of discrete vortices as shown in Fig.2.

3.2 JET DECAY

In the real flow, the jet momentum decays due to viscous and mass entrainment effects. As a segment of the jet mass flow leaves the slot and flows downstream, a gradual loss of its momentum occurs due to viscosity and entrainment from the external flow. This loss in momentum may be represented in the model by the use of a time dependent vortex decay. The rate of loss of momentum is expected to be in proportion to the initial jet momentum and the external flow momentum. Therefore, an arbitrary form of decay has been adopted in the model by reducing the vortex strength as it flows from the slot. Assuming that the initial strength of the vortex is (γ_o), then its strength will be reduced to the value

$$\gamma(t) = \gamma_o . EXP(- K U_\infty \gamma_o t/d) \qquad (2)$$

where U_∞ : Free stream velocity
d : Distance step
t : Time age of the vortex
K : Arbitrary constant

The value(γ_0/d)represents the circulation per unit length of the shear layer when the jet leaves the slot, hence it can be used as a measure of the jet momentum. The value U_∞ is a measure of the momentum of the external flow. The chosen form of decay obeys the observed conditions that the strength of the vortex becomes zero as its age increases indefinitely and that its decay is most rapid, when the vortex age is small and the shear is greatest.

3.3 CALCULATION OF THE LIFT AND JET MOMENTUM COEFFICIENTS (C_L and C_J)

The lift coefficient (C_L) is calculated by integrating the normal local pressure coefficients (C_{p_ℓ}) on the circular boundary, determined as usual from

$$C_{p_\ell} = 1 - (U_\ell/U_\infty)^2$$

where U_ℓ = local velocity induced by all the flow elements.

The jet mass flow rate ($\dot{m}$) is defined as $\rho V_J t_J$, where V_J is the mean jet velocity at the slot exit, t_J is the jet thickness at the slot.V_J is calculated in the model as the surface velocity beneath the slot lip and defined as V_s. The jet momentum is then defined as the product of $\dot{m}$ and the increment in surface velocity beneath the slot(ΔV)due to the presence of the jet. In defining this jet momentum, a primary consideration is that the momentum coefficient predicted should be zero when no air is supplied to the blowing system. Therefore the jet momentum coefficient is calculated as:

$$C_J = (V_s\ \Delta V\ t_j)/(U_\infty^2\ R_O)$$

where V_s is the total surface velocity at the slot and ΔV is the velocity induced at the surface by the vortices only.

4.1 MODEL CONVERGENCE AND SENSITIVITY TO VORTEX SPACING

The lift and momentum coefficients will be reliably predicted when the following conditions are met:-

1) the geometry of the jet sheet should stabilise so that the introduction of additional vortices have no effect on it

2) the vortex spacing used to model the jet sheet should not affect the lift and momentum coefficients.

In the previous sections it has been shown that the process of introducing vortices at the slot lip eventually led to a fixed geometry for the jet sheet which was unaffected by the introduction of further vortices at the slot lip, thus satisfying condition (1) above.

Condition 2 was tested by evaluating C_L and C_J for different values of the vortex-distance ratio (d' = d/R) for appropriate initial vortex strengths γ_0 determined so that γ_0/dU_∞ remained constant. Figures 3 and 4 show that the predicted values of C_L and C_J is strongly dependent on the vortex-distance ratio d'. The curves of both figures suggest that there are unique values of C_L and C_J when d' = O. The curves do not continue to d' = 0 because the effect that one vortex induced on its immediate neighbours became very large at small d' and the resultant motions of the sheet are best described as chaotic. To solve this problem, a vortex splitting process has been adopted, as explained below.

4.2 VORTEX SPLITTING

In order to study the convergence of the model's prediction, further reduction in the vortex distance is needed, without altering the contour of the vortex sheet. Reduction of the vortex distance is possible by splitting the vortices after the sheet's contour has been established. Each vortex in the sheet is divided into a group of sub-vortices. The sub-vortices are spread along the line separating this vortex from the next one. The strength of each sub-vortex is calculated in proportion with the general decay of the sheet as expressed in equation (2), provided that the total strength of a group of sub-vortices equals the strength of the original vortex which was split. This has similarities to Maskew's work (Ref.19).

The splitting process allows an indefinite reduction in the vortex distance without altering the contour of the vortex sheet, or the circulation.

Figures 5 and 6 show the results obtained by introducing the splitting process to the model. The figures show that both C_L and C_J continue to converge towards ultimate values, as suggested before by Figures 3 and 4. A wider range of investigation on different circular cylinders has concluded that if the vortex distance is eventually reduced to 0.1 per cent of the cylinder's radius, the predicted C_L and C_J values will converge to within 0.5 per cent of its ultimate values. The ultimate values are those expected if the vortex distance is reduced to zero, i.e. when the vortex sheet becomes a continuous sheet of vorticity. The model, in this form, has successfully represented a continuous sheet of vorticity by a discrete vortex model.

5.1 COMPARISONS WITH EXPERIMENTAL DATA

The mathematical model has been applied to a wide range of circular cylinders and its predictions compared with the corresponding experimental data. The application has covered different circular cylinder designs and flow conditions. A variety of circular cylinders have been tested and reported in Ref.(2). Two of those models have been chosen to demonstrate the vortex model's prediction capability. Figure 7 shows the comparison for a single slot model (ROMNEY MODEL 2 BUILD 4) at two angles of attack. Figure 7a represents the case when the slot was located at the top dead centre, with the wind tunnel speed at $M_\infty = 0.2$. In Figure 7b the slot was moved 20^0 aft from top dead centre, while the tunnel speed was at $M_\infty = 0.34$. The prediction has been calculated in each case for different

values of the arbitrary constant (K), defined in the decay equation (2). The model gives an excellent prediction of the experimental results when K = 0.165. Despite the differences in free stream velocity and slot position, the same value of K has produced equally good agreement with the experiment shown in the second case (7b).

A different model (ROMNEY MODEL 2 BUILD 2) has been used for further comparison. The model employed two slots, one at top dead centre and the other at 30° downstream, while the wind tunnel speeds were M_∞ = 0.2 and 0.32, as shown in Figure (8). The discrete vortex model has been applied in this case by introducing vortices from the two slots simultaneously. Both sheets have the same intensity of vorticity, the total jet momentum coefficient is the sum of both jet momentum coefficients. The motion of each vortex is decided by the velocity induced on this vortex by all vortices in both sheets. Figure 8 shows that the prediction is consistent with that produced in the single slot model, since the value of K remains virtually unchanged. The comparison of the discrete vortex model's prediction with other circular cylinders has produced the same conclusion. The value of K remains near constant in all cases, regardless of the model's dimension, slot(s) position on free stream velocity. A similar conclusion has been obtained when the model is applied to cross-sections other than circular. An example of this application is shown below.

5.2 APPLICATION OF THE MODEL TO ELLIPTIC-SECTIONS

The discrete-vortex modelling may be used to represent a jet on other cross-sections. The modelling can be applied to any section provided that it can be represented by potential flow elements such as doublets, sinks, sources, etc. This representation is essential because it is used as a starting point for the discrete vortex modelling. However, an alternative method to predict the performance of a specified cross-section is to use the conformal transformation. If the required section can be produced by a suitable conformal transformation from a circular section, then the velocity distribution, as predicted from the model discussed above, can be transformed to predict the performance of the required section. This method has been used to predict the performance of an elliptic-section. The Kutta-Zhukovsky transformation has been used to calculate the velocity distribution on the elliptic boundary which allows the calculation of both lift and jet momentum coefficients of the ellipse.

A comparison with experimental results is shown in Figure 9. The experimental model is Allcock's elliptic section 10/A (Reference 3), the section has a thickness chord ratio of 20%, with the slot located at a position of 0.874C from the leading edge, C being the chord of the ellipse. Figure 9 shows a similar result to that demonstrated for the circular section. A value of K within the range of 0.15-0.165 brings the model's prediction into very good agreement with the experimental data, further supporting the thought that K may be a constant irrespective of section.

6.1 BOUNDARY LAYER MODELLING BY DISCRETE-VORTICES

The previous discussion has shown that the discrete vortex modelling of the jet's shear layer successfully predicts the lift produced from an arbitrary aerofoil section with circulation control. The model in its present form cannot provide a prediction of the drag produced from such an aerofoil. An accurate prediction of the drag requires additional modelling of the surface boundary layer. The surface boundary layer is a shear layer which forms on the aerofoil boundary due to the "non-slip" condition at the surface. The surface shear layer is formed between a zero-velocity surface and an external flow of non-zero velocity, while the jet shear layer is formed between a high velocity jet flow and an external slower velocity flow. Therefore the surface shear layer can be considered as a sheet of vorticity similar to that of the jet but with the opposite sense of circulation. While the jet sheet speeds up the flow at the upper surface, the boundary layer sheet tends to slow the flow down. Therefore the circulation in the two sheets will be opposite. A discrete vortex model of the boundary layer on an unblown circular section has been developed prior to combining it with the jet model in order to predict both lift and drag.

6.2 UNBLOWN CIRCULAR SECTION BOUNDARY LAYER MODEL

A model of discrete vortices, which represent the boundary layer, must satisfy the boundary conditions of the flow in this layer. The velocity profile inside the boundary layer should satisfy the two basic conditions of zero velocity at the surface and a velocity at the outer edge of the profile equal to that of the potential flow. The presence of the vortices should create a velocity field which, when combined with the potential flow field, leads to a velocity profile similar to that measured in the boundary layer. Figure 10 explains how a pair of vortices (vortex + image) create a velocity profile that alters the potential flow profile into one similar to that of a boundary layer. The magnitude of the velocities in the vortex profile depend on the strength and position of the vortex relative to the circular boundary, as well as the angular distance of the vortex from the control point A.

To calculate the strength of the vortex, consider a control area as shown in Figure 11. The area lies between two arbitrary angular positions (θ_1, θ_2), its internal edge is the circular cylinder surface and the outer edge lies in the flow just outside the boundary layer. The total circulation bounded by this area can be calculated as:

$$\gamma = \oint q \, ds$$

where q = the velocity tangential to the area's boundary
and ds = element of distance along the area's boundary

Since q = 0 along the circle surface

$$\gamma = \int_{\theta_1}^{\theta_2} R_b \, q_t \, d\theta - \int_{R_o}^{R_b} q_{n_2} \, dr + 0 + \int_{R_o}^{R_b} q_{n_1} \, dr$$

where q_t : Potential flow tangential velocity
q_n : Normal velocity inside the boundary layer
θ : Angular position measured from the leading edge

Assuming that the change in the normal velocity between positions θ_1 and θ_2 is negligible, i.e. $q_{h_1} = q_{h_2}$

$$\gamma = R_o \int_{\theta_1}^{\theta_2} q_t \, d\theta \qquad (3)$$

The circulation calculated in this way satisfies the conditions of zero surface velocity, and that the velocity outside the boundary layer is that of the potential flow. However, if equation (3) is applied for the vortices at positions of $\theta > 90°$, the calculated circulation will decrease as θ increases because of the reduction in q_t. This is not physically acceptable, since the boundary layer vorticity has to increase because it represents the momentum destroyed by the surface. Therefore it has been assumed that the vortex strength remains constant for the region $\theta > 90°$. The complete modelling of the boundary layer starts by dividing the layer along the surface into (n) control areas of equal angular width. The circulation within each box is calculated according to equation (3) or according to the assumption mentioned above, then each calculated circulation is concentrated in a single vortex at the middle angular position between θ_1 and θ_2 (Fig.11). The distance of each vortex from the circular surface is decided by applying the condition of zero velocity at (n) control points on the circle. The control points are chosen at the intermediate angular positions between the vortices. These points are used as reference points for calculating the velocity profiles across the boundary layer. The application of zero velocity condition leads to (n) algebraic equations which can be solved to calculate the exact positions of the vortices. The model adopts two groups of (n) discrete vortices to represent the boundary layer at the upper and lower surfaces, but only (n) algebraic equations are solved because of the symmetry of the flow on both surfaces. The velocity profile has been calculated at each control point, and the outer edge of the profile (R_b) is considered to be reached when the calculated velocity equals that of the potential flow.

The calculated velocity profile has been used to calculate the displacement thickness at each control point. The displacement thickness is calculated from the equations:

$$\left(\int_{R_o}^{R_d} q_t \, dy \right)_{PF} = \left(\int_{R_o}^{R_b} q_t \, dy \right)_{PF} - \left(\int_{R_o}^{R_b} q_t \, dy \right)_{BL} \qquad \text{where } R_d = R_o + \delta_d$$

where dy : distance element along the radial direction
δ_d : Displacement thickness
PF denotes the original potential flow
BL denotes the boundary layer due to vortex flow

This equation is driven from the definition of the displacement thickness as the distance by which the potential flow streamlines are displaced by the presence of the boundary layer.

The pressure coefficient at this point is then defined as

$$C_p = 1 - (q_{td}/U_\infty)^2$$

where q_{td} is the tangential potential flow velocity at the distance R_d. The pressure coefficient distribution along the surface is used to correlate the model's prediction with the experimental data. To complete modelling the flow around the circular cylinder, it is necessary to model the separated flow region behind the cylinder. The position of the separation point is decided from the calculated velocity profiles by using the definition of separation. The separation point is defined as the point where the surface shear stress vanishes, i.e. when the tangential velocity gradient at the surface becomes zero $(\partial q_t/\partial y)_s = 0$. This gradient has been calculated from the velocity profile at each control point until its value reaches zero. The separation is considered to occur at this position and the separation pressure coefficient is taken as the pressure coefficient of this point. Since the separated flow region has constant pressure, it is simulated by introducing a number of doublets on the surface between the separation points. The strength of these doublets are decided by applying the condition of constant separation pressure at the control points in the separated area.

The model's prediction of the pressure coefficient distribution has been compared with Achenbach's data (Reference 20) for a supercritical flow, i.e. the turbulent boundary layer is fully developed. Figure 12 shows the comparison between experiment, potential flow and model's prediction. The figure shows how the number of vortices has affected the predicted separation position and pressure. It has been found, as suggested by the figure, that the prediction converges rapidly as the number of vortices increases. If the number is increased more than 60, there is little effect on the predicted position and pressure at separation. Apart from the region between $\theta = 85°$ and $105°$, the prediction has produced a very good agreement with the experimental data. The deficiency in the prediction in this region is probably due to the assumption of constant vorticity in the region of $\theta > 90°$. The model's prediction is expected to improve if the vorticity increases in this region rather than remaining constant. Further investigation is required to find a formula governing the growth of vorticity in this region. The drag coefficient C_D has been calculated by integrating the predicted pressure distribution, and compared with the experimental value. The predicted pressure distribution gave a value of $C_D = 0.768$, while the corresponding experimental value was $C_D = 0.755$, that is, an error of less than 2%. The noticable error in the model's prediction of the C_p distribution in the region of $105° > \theta > 85°$ has, as expected, a very small contribution to the calculated value of C_D.

7. CONCLUSIONS

A theoretical model has been developed to predict the performance of an arbitrary aerofoil whose circulation is controlled by blowing. The model relies on representing the existing shear layer(s) by sheet(s) of discrete vortices rather than using the conventional boundary (shear) layer analysis. Initially, a model has been developed to predict the lift and jet momentum coefficients of a section equipped with a slot which discharges a wall jet downstream. The shear layer between the jet and the external flow has been represented by a series of vortices emerging from the slot. The model has employed a form of vortex time decay to simulate the real jet decay due to

viscous and entrainment effects. It has been assumed that the strength of decay is in proportion to the external flow momentum, the jet momentum and an arbitrary constant of decay. In comparison with experimental data, the model's prediction has shown that the value of this arbitrary constant is approximately fixed despite the wide variations in model geometry, number of slots and external flow velocity. In order to predict the drag of the circulation controlled aerofoil, a second model has been developed to represent the boundary layer on an unblown circular aerofoil, as an initial step towards combining the two models for the prediction of both lift and drag. The boundary layer, as a shear layer, has been represented in the model by a series of discrete vortices, while the separated flow region has been simulated by a group of doublets. The strength of vortices/doublets has been calculated using the boundary conditions applicable to the boundary layer and separation criteria. The model's prediction of the pressure distribution around the surface has produced reasonable agreement with the experimental data of the unblown circular section. The experimental drag coefficient is predicted theoretically, with an error of only 2%.

A combination of the jet and the unblown models is expected to result in a generalized representation which predicts both lift and drag coefficients of an arbitrary circulation controlled aerofoil. It is also expected that by combining the jet and the boundary layer sets of vortices, an explanation for the nearly constant value of decay in the jet model may be possible.

REFERENCES

1. I.C. Cheeseman: The lift and drag of a circular cylinder equipped for circulation control by spanwise blowing. August 1964. Unpublished NGTE Note.

2. J. Dunham: Circulation control applied to a circular cylinder. July 1967. NGTE R287.

3. A.W.R. Allcock: Observations on the lift performance of elliptical-section aerofoils with circulation control. May 1969. NGTE NT750.

4. A.R. Osborn and C.N. Sherbourne: Two-dimensional wind tunnel tests on 10 per cent and 40 per cent elliptic section models with tangential blowing slots. June 1968. NGTE PLAND Note No.5.

5. I.C. Cheeseman and A. R. Seed: The application of circulation control by blowing to helicopter rotors. July 1967. Jour. of Roy.Aer.Soc., Vol.71, No.679.

6. I.C. Cheeseman: Circulation controlled rotor aircraft. July 1969, Aircraft Engineering.

7. R.M. Williams, R.T. Leitner and E.O. Rogers: X-wing: A new concept in rotary wing VTOL. Aug. 1976, Amer.Heli.Soc. Symposium on Rotor Technology.

8. J.B. Wilkerson and D.W. Link: A model rotor performance validation for CCR technology demonstrator. 1975 31st Amer. Heli.Soc. Forum.

9. E.O. Rogers: Recent progress in performance prediction of high advance ratio circulation control rotors. 1980 6th European Rotorcraft and Powered Lift Aircraft Forum Paper No.29

10. J. Dunham: A theory of circulation control by slot blowing applied to a circular cylinder. 1968 Jnl. of Fluid Mechanics, Vol.33, Part 3.

11. B. Thwaites: Incompressible Aerodynamics, 1960, Clarendon Press, Oxford.

12. E.S. Levinsky and T.T. Yeh: Analytical and experimental investigation of circulation control by means of a turbulent Coanda wall jet. 1972 NASA CR-2114.

13. E.H. Gibbs and N. Ness: Analysis of circulation control aerofoils. 1976, AIAA Jnl. of Aircraft, Vol.13, No.2.

14. L. Rosenhead: Formation of vortices from a surface of discontinuity. 1931, Proc.Roy.Soc. Series A, Vol.134.

15. F.H. Abernathy and R.E. Kronauer: The formation of vortex sheets. 1961 Jnl of Fluid Mechanics, Vol.13.

16. J.H. Gerrard: Numerical computation of the magnitude and frequency of the lift on a circular cylinder. 1967 Phil.Trans.Roy.Soc., Vol.261, No.118.

17. R.V. Smith: A theoretical and experimental study of circulation control with reference to fixed-wing applications. 1978 Ph.D. Thesis, University of Southampton.

18. M.M.E. Soliman: A theoretical study of circulation controlled aerofoils and experimental application to symmetrical aerofoil. 1980 M.Sc. Thesis, University of Southampton.

19 B. Maskew: Subvortex techniques for the close approach to a discretized vortex sheet. 1977 AIAA Journal of Aircraft, Vol.14, No.2.

20 E. Achenbach: Distribution of local pressure and skin friction around a circular cylinder in cross-flow up to $R_e = 5 \times 10^6$ 1968 Jnl. of Fluid Mechanics, Vol.34, Part 4.

ACKNOWLEDGEMENT

We gratefully acknowledge the support of Westland Helicopters Ltd. and the Procurement Executive, Ministry of Defence, for their financial support of the work reported.

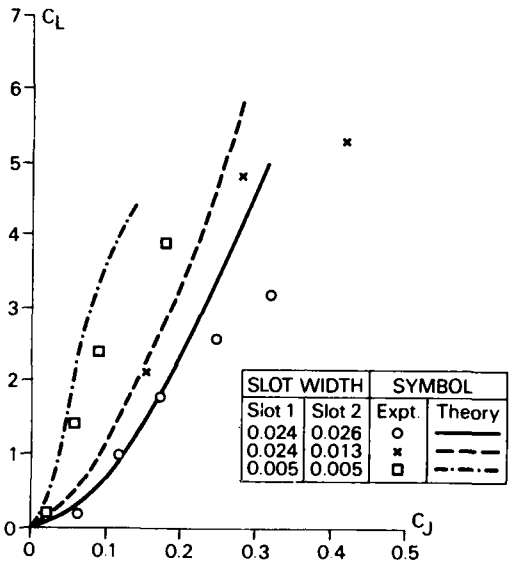


Fig.1. Dunhams prediction of the performance of a circular cylinder with two blowing slots

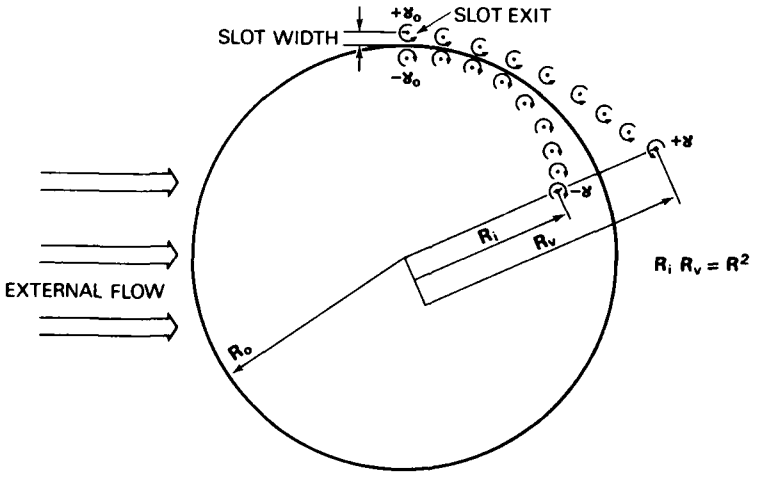


Fig.2. Elements of potential flow model

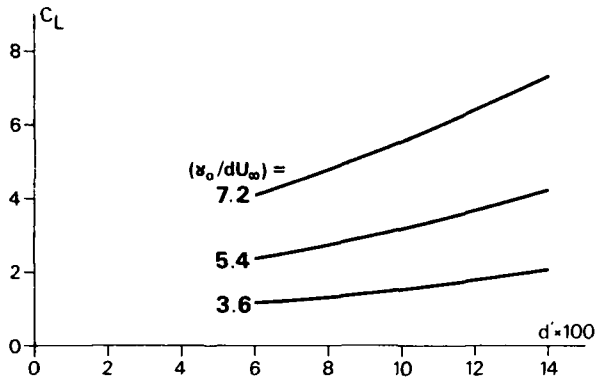


Fig.3. Influences of vortex-distance on the jet momentum predicted

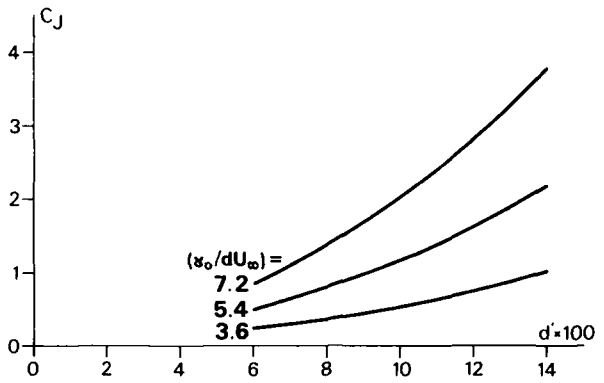


Fig.4. Influence of the vortex-distance on the lift predicted

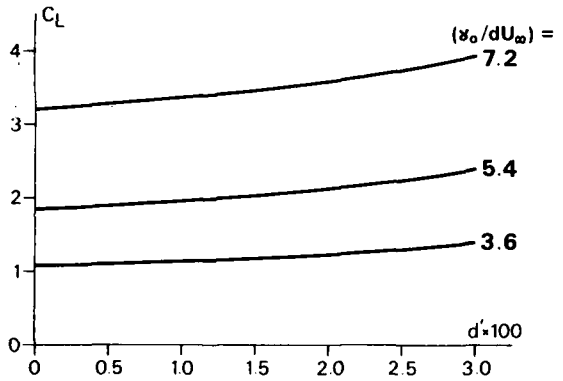


Fig.5. *Convergence of lift coefficient*

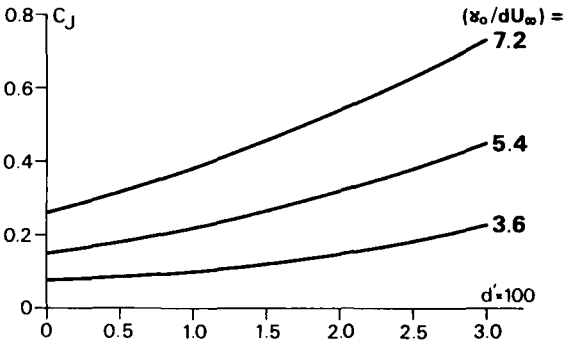


Fig.6. Convergence of jet momentum coefficient

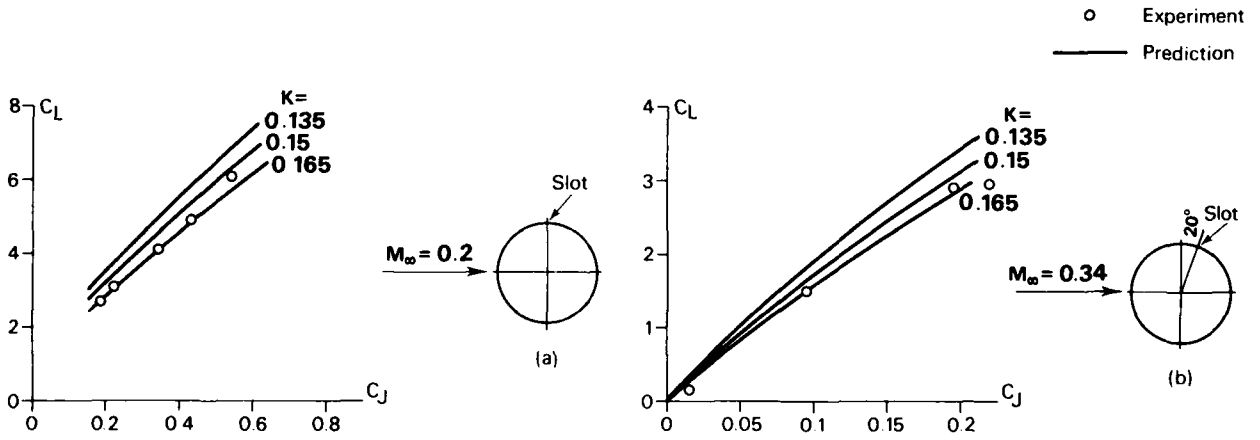


Fig.7. Romney model 2 build 4, single slot

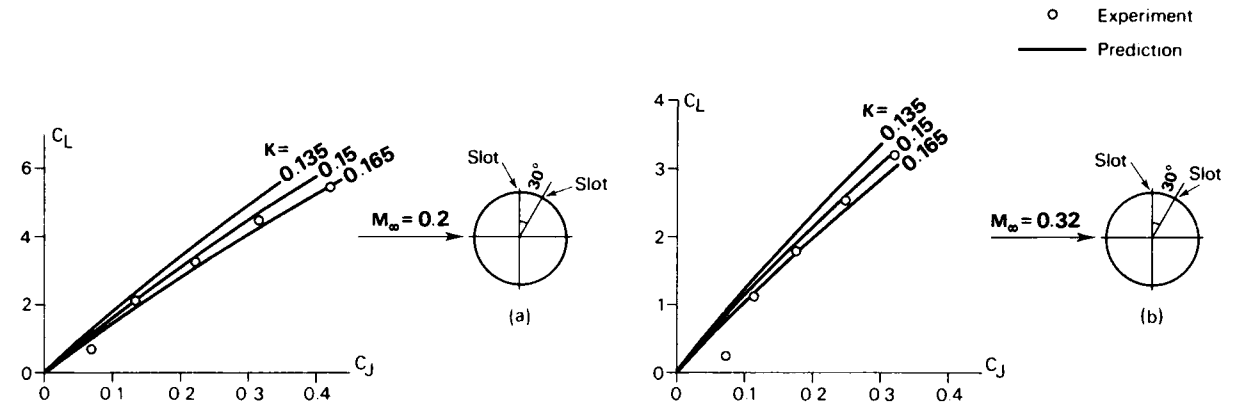


Fig.8. Romney model 2 build 2.double slots

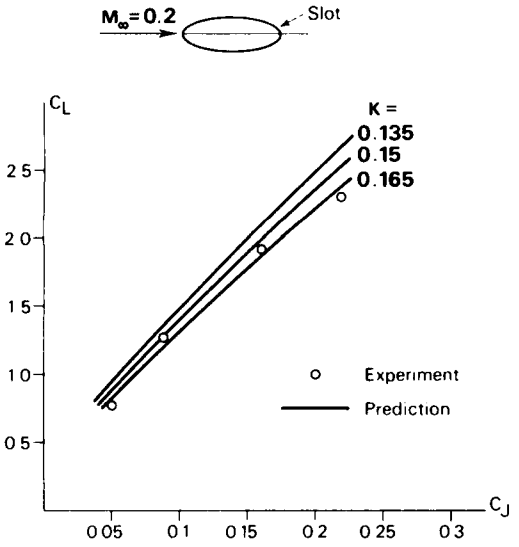


Fig.9. Allcock elliptic model 10/A

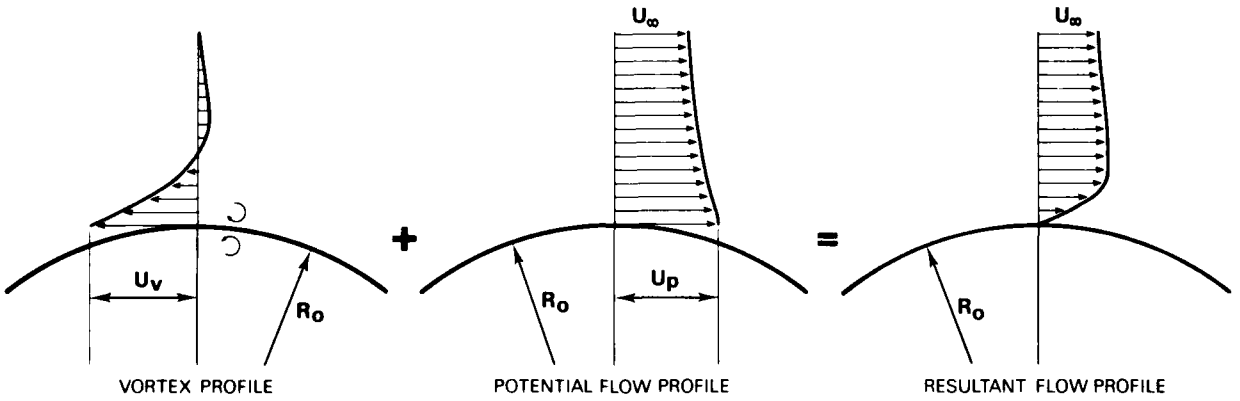


Fig.10. Boundary layer profile formation by vortices

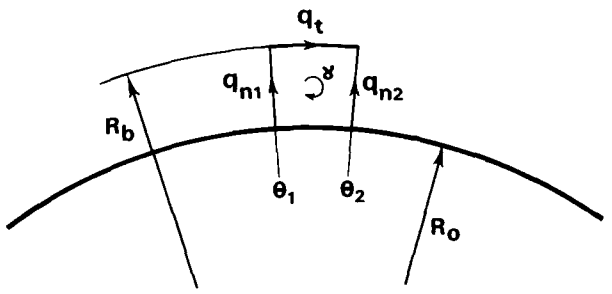


Fig.11. Vorticity inside a boundary layer element

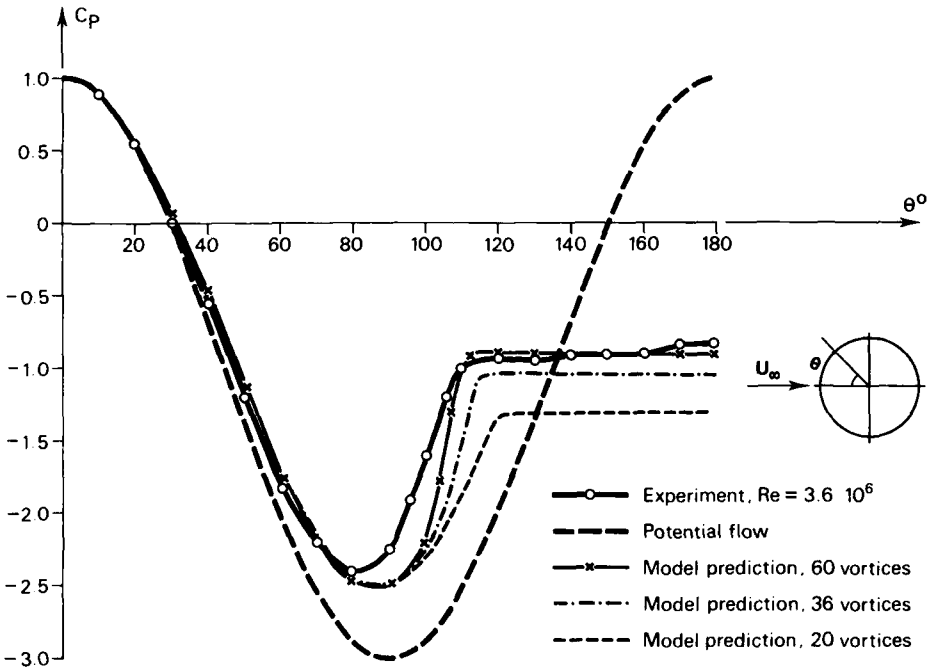


Fig.12. Pressure distributions around circular cylinder, no blowing

AD-P004 058

TURBULENT BUBBLES BEHIND AIRFOILS AND WINGS AT HIGH ANGLE OF ATTACK

by

V. LOSITO
Department of Flight Sciences, Italian Air Force Academy
Institute of Aerodynamics 'U. Nobile', University of Naples

and

G. TORELLA
Department of Flight Sciences, Italian Air Force Academy
Pozzuoli Italy

SUMMARY

More accurate inviscid and viscous flow models are needed for simulating the main features of the turbulent bubbles in the near wakes behind airfoils at high angles of attack.

Descriptions of these flows are not sufficientely detailed to allow accurate modelling for the recirculating flow regions.

Numerical and wind tunnel experiments are required to ensure convergence criteria and wake closure conditions at different Reynolds numbers.

A simple relation is found which correlates the airfoil viscous lift loss with the location of the upper surface separation point and lift predicted in full attached flow conditions.

This simple 2-D model has been extended to 3-D wing flows with embedded turbulent bubbles after a set of wind tunnel experiments and oil-flow visualizations.

A fast and efficient method is given for predicting spanwise load distribution and C_{Lmax} for finite unswept wings.

1. INTRODUCTION

Large turbulent bubbles may be observed in the near wakes behind axysimmetric and 3-D bluff-bodies as well as behind airfoils and wings at high angles of attack.

For axysimmetric bodies detailed experimental mean velocity profiles in the near and far wakes are available (Ref. 1) and furthermore the shape of the turbulent bubbles have been correlated to the boundary layer momentum thickness at the separation points. Since these points may be easily predicted or fixed, an efficient, fast and accurate computational method has been presented in Ref. 2 for iterative calculations of the outer inviscid, turbulent boundary layers and wake regions, which leads to a very good agreement with the experimental data.

For wakes flows behind bluff-bodies like car configurations up to now the complex structure of turbulent bubbles, with and without embedded longitudinal vortices, is studied by qualitative examination of oil-flow patterns on the body surface. Searches are in progress for a better comprehension of the wakes behind road vehicles by visualizations of measurements of total pressure with coloured isopressure maps (Ref. 3), and by some wake surveys conducted with the ultimated goal of the drag prediction e.g. (Ref. 4).

Fig. 1 shows the oil-flow pattern on a notchback car configuration obtained in the small scale test facility at the Italian Air Force Academy. The starting lines of these wakes cannot be accurately predicted by the present abilities of the 3-D boundary layer computational methods.

It is well known from the basic paper of Mc Cullough and Gault (Ref. 5), that infinite unswept wings show a turbulent type of stall which is the representative mechanism of the breakdown of flow for all airfoils at high Reynolds numbers ($Re_\infty > 10^7$) and for thick airfoils at intermediate Reynolds numbers.

In the trailing-edge separation region and in the near wake of these airfoils turbulent bubbles are found at moderate angle of attack α but their effects increase with α.

The upper surface separation region is usually characterized by a constant pressure but in the near wake a recompression region follows up to the rear stagnation point, the closure point of the wake Fig. 2.

Available experimental techniques for measuring mixing process in the separated regions suffers from the basic shortcoming that flow separation from an airfoils is quite sensitive

to small change in the ambient flow even at large distance. The flying hot-wire, which is well usable to measure wake flows behind bluff-bodies, seems to be a difficult tool for airfoil flows since appreciate interference effects became measurable.

Consequently are very few detailed measurements of flow fields associated with low speed turbulent boundary layers and wakes for airfoils; are not extensive the pressure and velocity surveys of the pre and post-separated regions on airfoils with rear separation.

For example Seetharam and Wentz (Ref. 6) have measured for 17% thick GA(W)-1 airfoil section at angle of attack of 10, 14 and 18 deg. steep gradients of displacement and momentum thickness and of the separation streamline. Details of the wake velocity and pressure distributions were obtained at only four stations and it has been observed that the region of flow reversal terminates at the rear stagnation point within a short distance of less than 20% chord downstream from the trailing-edge for the test range of angle of attack.

More recently Mehta and Goradia (Ref. 7) have published new experimental studies of the separated flow always over the NASA GA(W)-1 airfoil. Mean velocity profiles, boundary layer properties and skin friction distributions have been presented but measurements have not been performed behind the trailing-edge.

Furthermore experimental investigations of separating boundary layers and downstream wakes by Laser-Doppler velocimeters have been generally concerned with small regions of separated flow and the consequent wakes (Ref. 8-11).

Computational models based on the solution of Navier-Stokes equations (Ref. 12 to 19) have been developed too for flows when the depths and lenghts of separated regions are small, the downstream wakes are symmetric or weakly asymmetric and the test Reynolds numbers are often not of engineering interest.

In this paper the capabilities of boundary element methods for predicting airfoil type flows at high angle of attack are critically examined in view of their extension to 3-D flows.

Our knowledge and understanding of 3-D separated flows is today poor and computational methods of 3-D boundary layers where strong crossflows are involved are seen to be inadequate for the prediction of wing flows at high angle of attack. The conclusion is that effects of turbulent bubbles behind finite wings can be calculated only by suitable extension of simple 2-D models.

It will be shown that the 2-D viscous lift losses are strictly related to the lenghts of turbulent bubbles and particulary to the distance of separation point from the trailing-edge even when the recirculating flow in the turbulent bubbles change almost abruptly from pre-stall at post-stall conditions.

This result has been extended to 3-D finite unswept wings and justified also with the aid of oil-flow pattern visualizations.

By an efficient and fast procedure based on a modified lifting-line theory and on 2-D viscous calculations at several spanwise stations accurate solutions for high (10.05) and low (3.1) aspect ratio unswept wings have been obtained at pre and post-stall conditions.

2. SIMULATIONS OF SEPARATED FLOWS BY BOUNDARY ELEMENT METHODS

A general computational iterative scheme for predicting inviscid, viscous and wake regions is shown in Fig. 3.

Numerical predictions of pressure and skin friction distributions and the overall aerodynamic characteristics for airfoils and wings are currently very successful in the aerospace industries when the viscous-inviscid interactions are weak, i.e. when small separation regions are very close to the trailing-edges. These engineering solutions can be achieved in a fast and economic way with the today available computers.

At higher angles of attack the viscous-inviscid interaction become more and more severe up to the dramatic behaviour of flow at stall criticalincidence.

In almost all the proposed methods inviscid approximations are introduced for modelling separated boundary-layers and wakes. Separation streamlines or thin vortex-sheet are calculated combining boundary-layer and potential flow codes in an iteration cycle.

In the inviscid problems Neumann and Dirichlet mixed boundary conditions are imposed on the attached regions and on the separated streamlines respectively. The Neumann condition on the outer surfaces of attached flow regions is sometimes imposed as an internal Dirichlet boundary condition as stated by known potential theory. This type of condition is then imposed everywhere on the boundaries.

First-order source panel procedures have been used by Jacob (Ref. 20 and 21), Geller (Ref. 22), Farn and al. (Ref. 23). Finite difference calculations were performed by Barnwell (Ref. 24), Carlson (Ref. 25). First-order vortex panel method has been picked by Dvorak and Maskew (Ref. 26). These last excepted all the other impose the boundary conditions in a linearized form but even in the free vortex sheet model of Dvorak any detail of the flow within the turbulent bubbles are not given.

Convergence criteria and wake closure have not investigated or ensured in many of the above proposed models.

Boundary-layer calculations are carried out by integral methods in order to reduce computing times; therefore predictions of separation points are not often accurate. In many investigations locations of separation points were prescribed according to the experimental measurements or were arbitrary fixed.

Moreover empirical relations have been introduced to obtain appropriate lenghts of the separation streamlines or vortex sheets.

Almost all the mentioned approximations have been introduced in the computational models developed by Gross (Ref. 27), Zumwalt and Naik (Ref. 28) and Zumwalt and Elongaven (Ref. 29), even if an attempt of simulation of turbulent bubbles in the recompression regions has been set up. The mixing process in the outer part of the bubbles, from separation to the rear stagnation point, is computed with an adaptation of the Chapman-Korst turbulent mixing theory (Ref. 30) to the incompressible case. Approximate elliptic velocity profiles are used in the lower part of the recirculating flow regions.

As a consequence of various simplifying assumptions and approximations good correlations with the experimental data for both pressure distributions and lift coefficients have been achieved in very few cases.

Generally the constant pressure level C_{ps} in the separation zone are somewhat lower than experiment; but if C_{ps} values are in close agreement with experimental results the same accuracy has not shown to be attained in the attached flow regions.

Finally it is unusual to see accurate predictions for the pressure drag. It must be pointed out that when weak viscous-inviscid interaction are taken in account the computed airfoil drag characteristics are in very close agreement with experiment for low and intermediate angle of attack Fig. 4 (Ref. 38). Conversely if some procedure, such as, for example the approach used by Dvorak and Maskew (Ref. 26) gives reasonable correlation with experimental data at high incidence there is to be surprised that comparisons of calculated and experimental drag characteristics at lower lifting conditions are worst as in Fig. 4.

Really many detailed phisical aspects of the turbulent bubbles are not yet well Known and the actual processes in the separated region have not been incluted in the models.

Some improvements can be easily introduced in the computational elements and works are in progress to this aim as shown in (Ref. 32).

Computational methods for 3-D wing flows with embedded turbulent bubbles at high angles of attack are very few. With the potential code of (Ref. 26) extended to 3-D flows, Summa and Maskew (Ref. 33) have applied the vortex sheet model to a 10° swept wing at 21° incidence with 3-D separation line prescribed according to experiment (approximately at 6% chord).

Comparison of calculated and experimental pressure distributions are shown only at two stations, but are not reported neither the spanwise lift distributions nor the overall lift and drag caefficients.

In section 4 a simple and fast method for evaluating spanwise load distributions on wings with extended separation within turbulent bubbles will be discussed.

Here it should also be stated some remarks concerning the basic weak point of the prediction of separation at high angle of attack when high adverse pressure gradient can be met even at a very short distance from the airfoil leading-edges.

After extensive experimentations we have come, years ago, to a conclusion that boundary layer calculations by finite difference methods such as the modified Mellor procedure of (Ref. 34), lead to reasonable prediction of separation.

At high angle of attack two basic results stem from our numerical experiments:

1) the interactive flow $w_{int} = \partial/\partial s(U_e \delta^*)$, computed at the separation points, exhibits a maximum value just at the stalling incidence (Ref. 35), Fig. 5. An explanation of this behaviour may be the following: the interactive normal flow w_{int} increases with α at all the airfoil contour points and the shiftings of the separation points (SP) are small at pre-stall conditions. Just at the stall angle of attack the separation points (for airfoils with turbulent stall) shift remarkably towards the leading-edge and there one meets with a lower level of interactive flow;
2) a go-down of lift curves after stall is attained without introducing any wake model, using a "reduced perimeter" in the basic airfoil circulation $4\pi p$ (Ref. 35, 36) Fig. 6.

3. 2-D VISCOUS LIFT LOSS

Global effects of 2-D turbulent bubbles on the airfoil lift could be measured by the two characteristic lenghts of the bubbles, i.e. the distance from the trailing-edges of the upper surface separation points and of the reattachement points in the near wakes.

Experimental observations show that the location of wake closure does not appreciably change with the angle of attack at constant Reynolds number.

The assumption is here made that the lifting capability of an airfoil with an embedded turbulent bubble is reduced in comparison with the full attached flow conditions in direct ratio to the location, in term of chord fraction, of the upper-surface separation point i.e.:

$$\frac{C_{l_{exp.}}}{C_{l_{FA}}} \simeq K \frac{x_{sep.}}{c} \qquad (1)$$

where K is a constant which can be evaluated from experiments.

The simple relation (1) comes from physical resonings as well as from computations of several potential flows and turbulent boundary layers.

Full attached flow solutions have been obtained by higher order panel method (Ref. 7). Boundary layer equations were solved by the finite difference procedure of (Ref. 34).

Fig. 7 shows the calculated results ($C_{l_{FA}}$, $x_{sep.}$) and the experimental data ($C_{l_{exp.}}$) for a standard and laminar airfoil. It can be observed that eq. (1) with $K \simeq 1$ is verified quite well for NACA 63_3-018 and quantitatively in a less fashion for the NACA 0012 airfoil whose behaviour at the stall is abrupt. Eq. (1) will be used in 3-D separated flows for his simplicity and for the good agreement shown in many 2-D flows with turbulent bubbles.

4. CALCULATION OF FINITE WINGS AT HIGH ANGLE OF ATTACK

For finite unswept wings at high lift and at low speed the separation zone is largely two-dimensional except at the wing tips and at wing-body junction.

This conclusion has been confirmed too by the oil-flow visualizations of limiting streamlines on the upper surface of several rectangular wings, with different aspect ratio and thickness.

Fig. 8 to 10 show some oil-flow patterns obtained in the low Reynolds number ($4\text{-}7\cdot10^5$) small scale wind tunnel at Italian Air Force Academy.

Strong 3-D effects are manifest at the wing tip and near the tunnel wall-model junction with intense vortices and 3-D separated flows. In the mean part of the models either in the attached or even in large separation regions the limiting streamlines show 2-D behaviour.

The assumption that for unswept finite wings the potential flows in the streamwise plane of motion are 2-D comes from the Prandtl's genious. The 2-D hypothesis can be extended even for viscous flows once it is known the spanwise distribution of the induced angle of attack in order to obtain the effective spanwise incidence ($\alpha_e = \alpha_g + \alpha_i$).

For small values of α_g this technique has been successfully applied in (Ref. 38) for the calculation of polar drag of finite wings within an integrated computer system.

At higher angles of attack the viscous computations, at different spanwise stations, should include simulations of 2-D wake effects. In any case, once the separation points have been predicted, the lift curve slopes $C_{l_\alpha}(y)$, which are input parameters in the lifting line theory, have been reduced according to:

$$\frac{\left[C_{l_\alpha}(y)\right]_{\text{viscous+wake corrected}}}{\left[C_{l_\alpha}(y)\right]_{\text{full attached flow}}} \simeq \frac{x_{sep.}(y)}{c} \qquad (2)$$

3-D inviscid solutions have been achieved by the Multhopp method as modified by the first author (Ref. 39) with a fast and accurate extension of Prandtl's wing theory to very low aspect ratio unswept wings.

A first set of calculations has been carried out for a 10.05 aspect ratio tapered and twisted wing, experimentally investigated in (Ref. 40).

Locations of separation points at different angles of attack have been obtained by viscous calculations and shown in Fig. 11. Spanwise load distributions in full attached flow and with the viscous correction of eq. (2) can be seen in Fig. 12, representing pre-stall ($\alpha = 16°$), stall ($\alpha = 17°$) and post-stall ($\alpha = 18°$) conditions.

Comparison of calculated lift coefficients with experimental data are quite satisfactory as shown in Fig. 13. At $\alpha = 17°$ the predicted maximum lift coefficient is $C_{L_{max}} = 1.44$ in good agreement with the experimental value 1.43. At $\alpha = 20°$ the calculated $C_{L_{max}}$ is 1.38, lightly lower than the measured value 1.39.

A second set of numerical solutions have been achieved for a 3.1 aspect ratio untwisted rectangular wing at $\alpha = 22.5°$, recently investigated by Jacob (Ref. 41). Jacob's calculations lead to an overprediction of the spanwise load distribution and of the overall lift.

The spanwise load distribution in full attached flow is shown as the upper curve in Fig. 14 and is in very good agreement with the solution of lifting surface theory used by Jacob.

The obtained spanwise separation line has been reported in Fig. 15 and compared with Jacob's solutions and with experimental data from DLR-FB-21-12. With the now known x_{sep}/c new inviscid 3-D lifting line calculations have been performed, assuming for the spanwise

2-D lift curve slopes values corresponding to the proposed equation (2).

The calculated spanwise lift distribution for the given wing with extended separation (α=22.5°) is given in Fig. 14 and is found in a closer agreement with experiment than Jacob's solutions.

It is necessary to point out that our viscous calculations for seven stations in the halfspan need for 21 minutes on an IBM 3032 in comparison with the about 1 hour CPU-time on an IBM 370/158 computer spent in the Jacob's calculations.

A paltry time is obviously required for the inviscid solutions with the modified lifting-line theory.

The present method is very profitable when separation lines are known from experiments or from other viscous computations.

Fig. 16 show shapes of separation lines given in (Ref. 33) and the calculated spanwise load distributions and overall lift coefficients for a 4 apect ratio rectangular wing at 12°, 16° and 18° deg. and Reynolds number Re= $6 \cdot 10^6$. The results state that this wing should have a stalling angle of attack α =16° and a C_{Lmax}=0.887.

5. CONCLUSIONS

The abilities of potential and viscous methods for simulating airfoil type flows at high angle of attack with large turbulent bubbles have been examined in view of their extensions to 3-D flows.

Improvements are needed in the inviscid models to ensure convergence criteria of the iteration cycles and conditions of wake closure at different Reynolds number.

Better velocity profiles have to be introduced in modelling the viscous recirculating flows inside the turbulent bubbles at pre-stall and post-stall conditions.

With these improvements closer agreements with experiment will be attained for the pressure distributions and for lift and drag characteristics for all airfoils with turbulent type of stall.

A simple but efficient correlation between the 2-D viscous lift losses and lengths of turbulent bubbles has been introduced after computations of several potential flows and turbulent boundary layers.

The proposed correlation has been extended for 3-D unswept wing flows when the separation zone is largely 2-D.

Intensive experimental tests have been carried out by the oil-flow technique to obtain confirmations of the 2-D behaviour of large separated flows far from wing tips and from wing-body junction even at post-stall angle of attack.

By the proposed correlation a computational method has been presented which leads to fast and accurate predictions of spanwise lift distributions and maximum lift coefficient of high and low aspect ratio unswept wing.

The present method can be easily applied to wings with spanwise and chorwise blowing once are known blowing effects on x_{sep}/c (y).

6. REFERENCES

1 - Delerey,J. and Sirieix,M. "Encoulements de Culot", AGARD LS-98 Feb. 1979, pp. 6.1-6.78

2 - Losito,V. and de Nicola,C. "An Improved Method of Computing the Wake Effects on Aerodynamic Characteristics of Road Vehicles", Int. Jour. of Vehicle Design, pp. 441-450 1983

3 - Cogotti,A. "Wake Surveys of Different Car-Body Shapes with Coloured Isopressure Maps" SAE Paper 840299, 1984

4 - Onorato,M.,Costelli,A.F.,Garrone A. "Drag Measurement Through Wake Analysis", SAE Paper 840302, 1984

5 - Gault,D.E. "A Correlation of Low-Speed Airfoil Section Stalling Characteristics with Reynolds Number and Airfoil Geometry", NACA TN 3963, 1957

6 - Seetharam,H.C. and Wentz,W.H. "A Low-Speed Two-Dimensional Study of Flow Separation on the GA(W)-1 Airfoil with 30% Chord Fowler Flap", NASA CR 2844, 1977 see also "Experimental Investigation of Subsonic Turbulent Separated Boundary Layers on an Airfoil" Jour. of Aircraft Vol. 14 N. 1, Jan. 1977

7 - Mehta,J.M. and Goradia, S. "Experimental Studies of the separated Flow over a NASA GA(W)-1 Airfoil", AIAA Journal Vol.22 n. 4, Ap. 1984, pp. 552-554

8 - Young,W.H. and al. :NASA TP 1266, 1978

9 - Bachalo,W.D. and Johnson,D.A. :AIAA Paper 79-1479, 1979

10 - Solignac,J.L. : Rech. Aerosp. N. 1980/3,65,1980

11 - Johnson,D.A. and Spaid,F.W. : AIAA Paper 81-1242,1981

12 - Murphy,J.D. :AIAA Journal Vol. 15 p. 1307, 1977

13 - Thomson,J.F. and al. :NASA CP 2045, 1979

14 - Sugavanam,A. and WU,J.C. : AIAA Journal Vol. 20, p. 464, 1982

15 - Rhie,C.M. and Chow,W.L. :AIAA Paper 82-0998, 1982
16 - Andreopulos,J. and Bradshaw,P. :J. Fluid Mech. Vol. 100, p. 639
17 - Yu,J.C. "Mean-Flow and Turbulence Measurements in the Vicinity of the Trailing-Edge of a NACA 63_1-012 Airfoil", NASA TP 1845, 1981
18 - Hah,C. and Lakshminarayana,B. :J. Fluid Mech. Vol. 115, p. 251, 1982
19 - Baker,A.J. and al. :AIAA Journal Vol. 20, p. 20, 1982
20 - Jacob,K. "Berechnung der Potentialstromung un Profile mit Absaugung und Ausblasen", Ingenieur Archiv. Vol. 32,N. 1, pp. 51-65, 1963
21 - Jacob,K. "Berechnung der Abgelosten Incompressiblen Stromung un Traflugelprofile und Maximalen Afttriebs", Zeit fur Flugwiss, 17 Jahrgung, Heft7, pp. 221-230, 1969
22 - Geller,W. "Incompressible Flow Through Cascades With Separation", AGARDograph 164 1972
23 - Farn,C.L.S., Goldschmied,F.R., Whirlow,D.K. "Pressure Distribution Prediction for Two-Dimensional Hydrofoils with Massive Turbulent Separation", J. of Hydronautics, Vol. 10, N. 3, pp. 95-101, 1976
24 - Barnwell,R. "Two Inviscid Computational Simulation Of Separated Flow about Airfoils", AIAA Paper N. 379, 1976
25 - Carlston,L.A. "A Direct-Inverse Technique fir Low Speed High Lift Airfoil Flowfield Analysis", AGARD CPP 291, 1980
26 - Dvorak,F.A. and Maskew,B. "Application of the AMI C_{Lmax} Prediction Method to a Number of Airfoils", NASA CP 2045, 1978
27 - Gross,L.W. "The Prediction of Two-Dimensional Airfoil Stall Progression", AIAA Paper 78-155, 1978
28 - Zumwalt,G.W. and Naik,S.N. "A New Flow Model for Highly Separated Airfoil.Flow at Low Speeds", NASA CO2045, 1978
29 - Zumwalt,G.W. and Elangovan,R. "Computation of Low Speed Past Multi-Element Airfoils with Large Flow Separation", ICAS Paper 82-6.2.2, pp. 342-352, 1982
30 - Korst,H.H. "A Theory of Base Pressures in Transonic and Supersonic Flow", J. of Applied Mech., Vol. 23, Transaction of ASME Vol. 78, pp. 593-600, 1956
31 - Maskew,B. and Dvorak,F.A. "The Prediction of C_{Lmax} Using a Separated flow Model", J. Amer. Hel. Soc., April 1978
32 - Amendola,A., de Nicola,C., Losito,V., Vitiello,D. "Un Metodo di Tipo Misto per Flussi Separati", to be published in Atti del VII° Congresso AIMETA, Ottobre 1984
33 - Summa,J.M. and Maskew,B. "Predicting Automobile Characteristics Using an Iterative Viscous/Potential Flow Technique", SAE Paper 830303, 1983
34 - Losito,V. and de Nicola,C. "A New Viscous-Inviscid Interaction Method", Proc. of 1st Int. Conf. on Laminar and Turbulent Flow Swansea, U.K. July 1978 (Penthec Press)
35 - Losito,V., Riviello,V.P., de Nicola,C. "A Viscous-Potential Interaction Method by Direct Superposition", III° Congresso AIMETA 1976
36 - Losito,V., de Nicola,C. "Un metodo di Predizione dello Stallo Turbolento dei Profili Alari", Atti del VII° Congresso AIDAA pp. 231-243, 1983
37 - Losito,V., Napolitano,L.G. "Calculation of Flow Fields by Source-Panel Method-A Proposal of an Higher Order Panel Tecnique", Euromech Colloquium 75-Braunschweig/Rhode May 10-13 1976; see also Napolitano,L.G., Losito,V. "The Closed Spline Functions" Computer Methods in Applied Mechanics and Engineering, Vol 13, pp. 335-350, 1978
38 - Losito,V. and Riviello,V.P. "Un Programma Integrato di Calcolo delle Polari di Ali Finite per Velivoli dell'Aviazione Generale", l'Aerotecnica Missili e Spazio N. 1 1977
39 - Losito,V. "Estensione della Teoria della Linea Portante alle Ali di Basso Allungamento", l'Aerotecnica Missili e Spazio, N. 2/3, pp. 134-138, 1971
40 - Neely,R.H.,Bollech,T.V.,Westrick,G.C. and Graham,R.R. "Experimental and Calculated Characteristics of Several NACA 44-Series Wings with Aspect Ratio of 8, 10 and 12 and Taper Ratios of 2.5 and 3.5", NACA TN 1270, 1947
41 - Jacob,K. "Computational of the Flow Around Wings with Rear Separation", J. of Aircraft Vol. 21, N.2, pp. 97-98, Feb. 1984

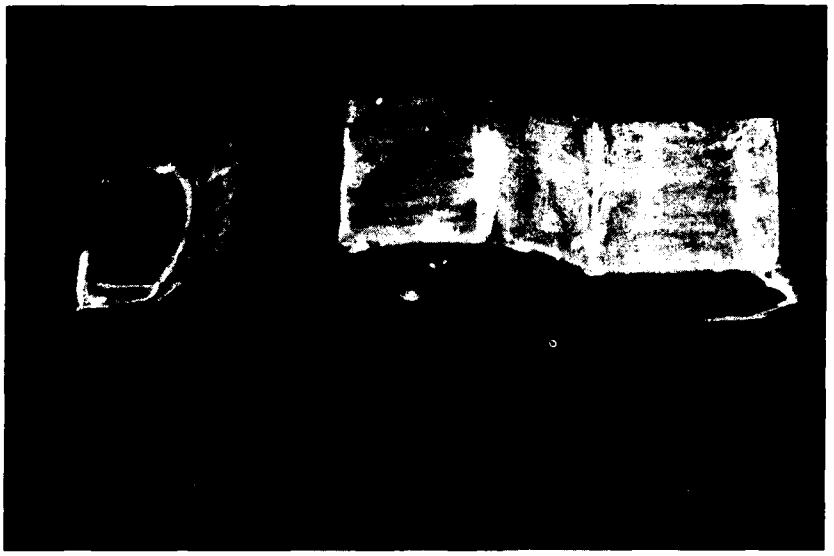


Fig. 1 Oil-Flow Pattern on a Notchback Car Model



Fig. 2 Turbulent Bubble Visualization Behind Airfoil at High Angle of Attack

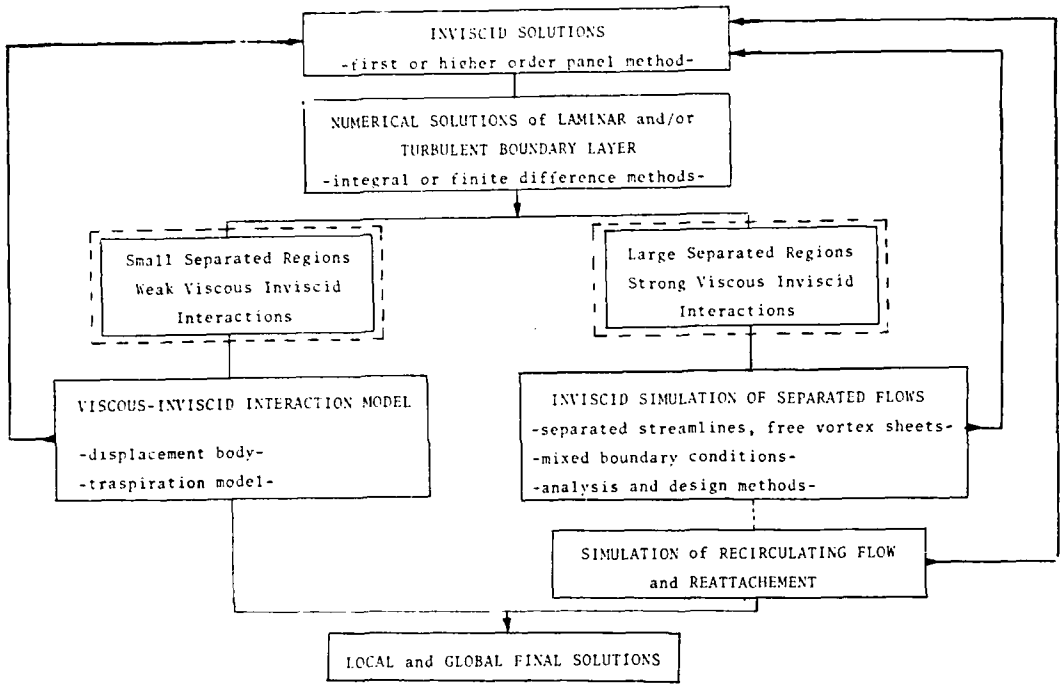
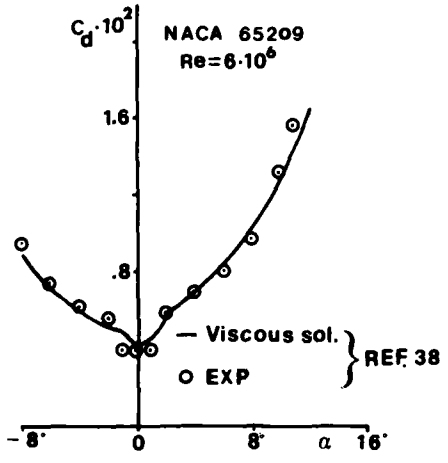
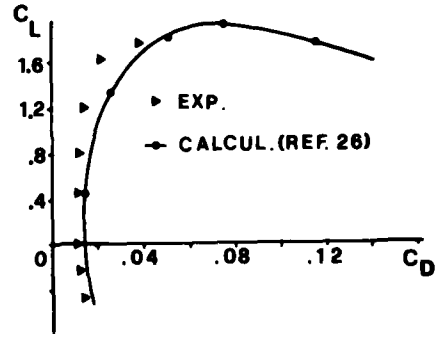


Fig. 3 General Iterative Scheme for Predicting Inviscid, Viscous and Wake Regions



a) weak viscous-inviscid interactions



b) strong viscous-inviscid interactions

Fig. 4 Comparison of Calculated Airfoil Drag Coefficient with Experiments

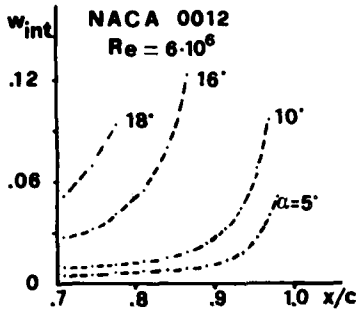


Fig. 5 Distribution of Interactive Flow at Various Incidences $\alpha_{stall} = 16°$

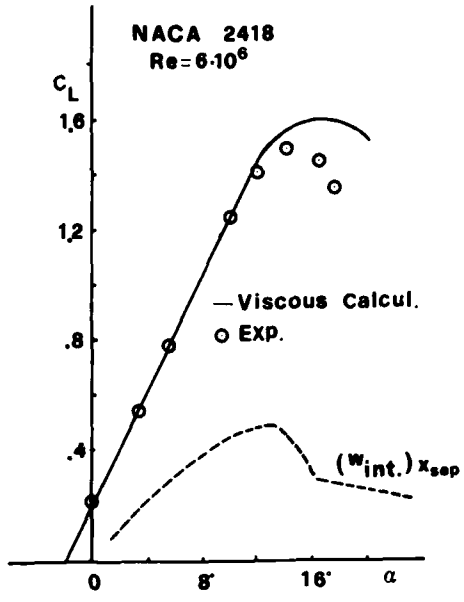
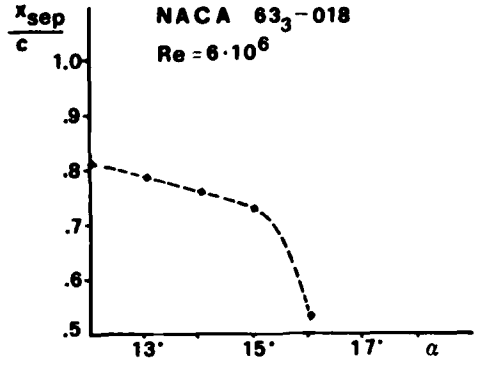
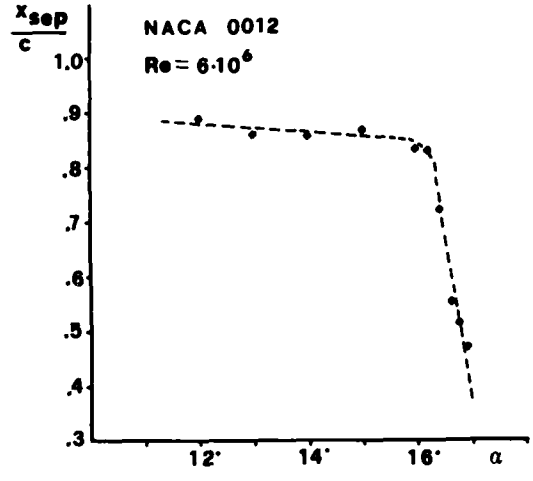
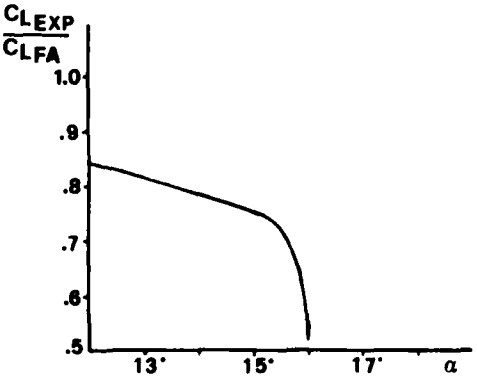


Fig. 6 Calculated Lift Without Wake Model but With "Reduced Perimeter"







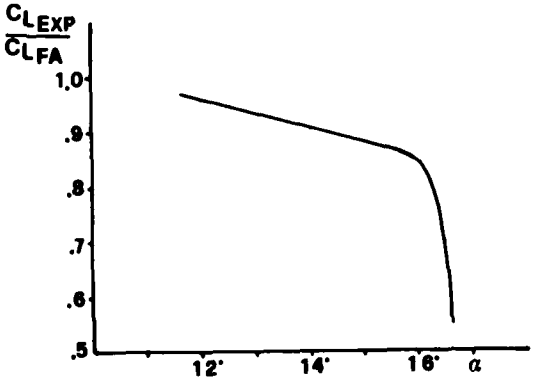


Fig. 7 Computed Correlation of Viscous Loss with x_{sep}.

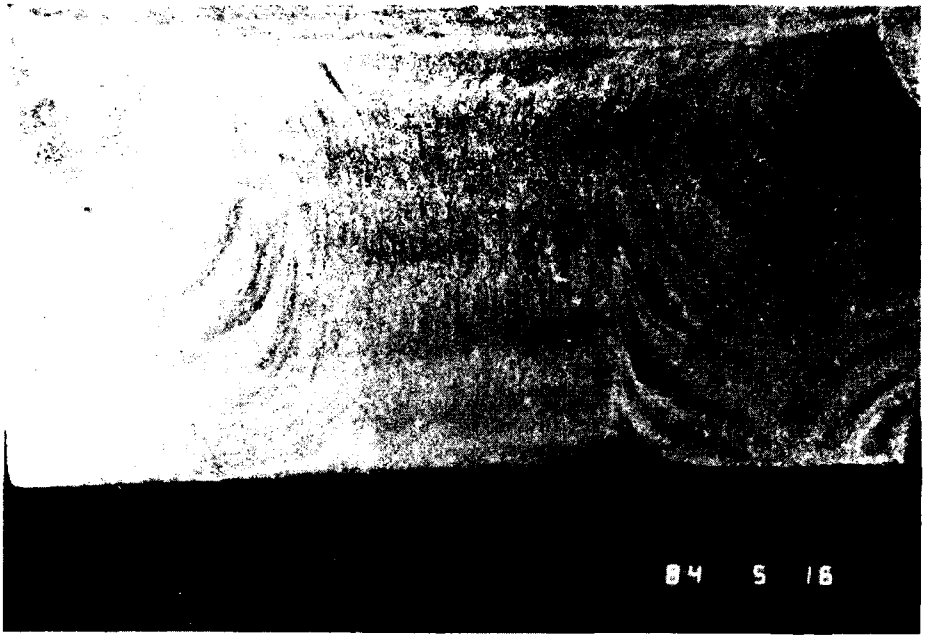


Fig. 8-9 Oil-Flow Pattern (Titanium Dioxide Technique)



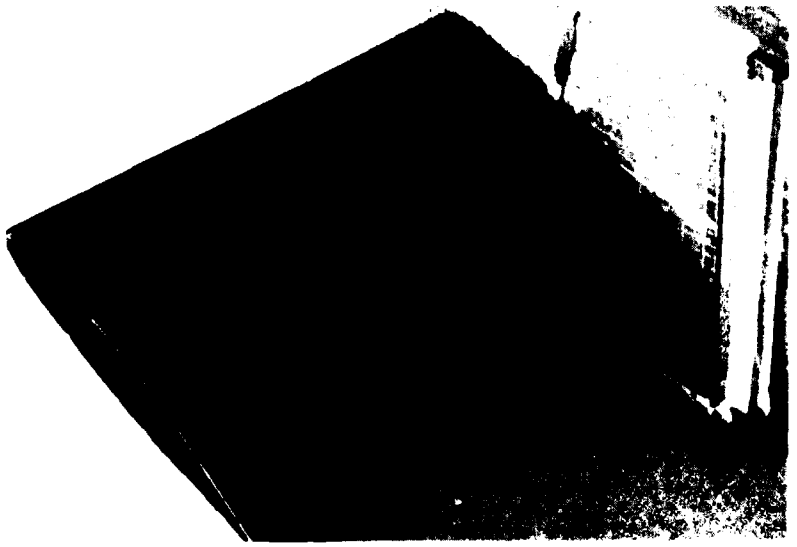


Fig. 10 Oil-Flow Pattern
(Saturn Yellow Pigment)

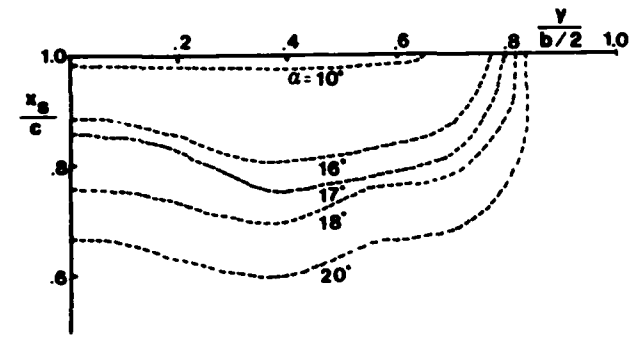


Fig. 11 Separation Lines on a 10.05 Aspect Ratio, Tapered (λ=o.4), Twisted Wing - Root Section NACA 4420 - Tip Section NACA 4412

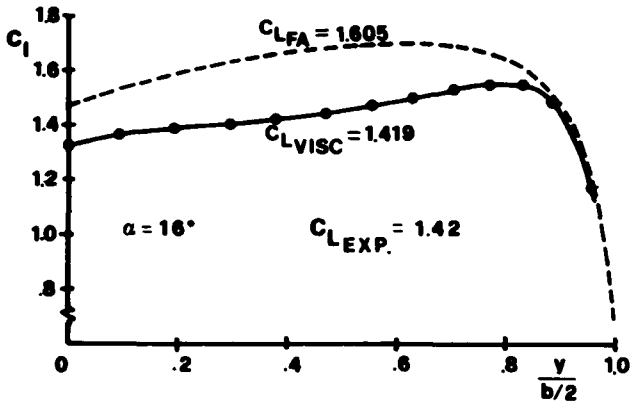
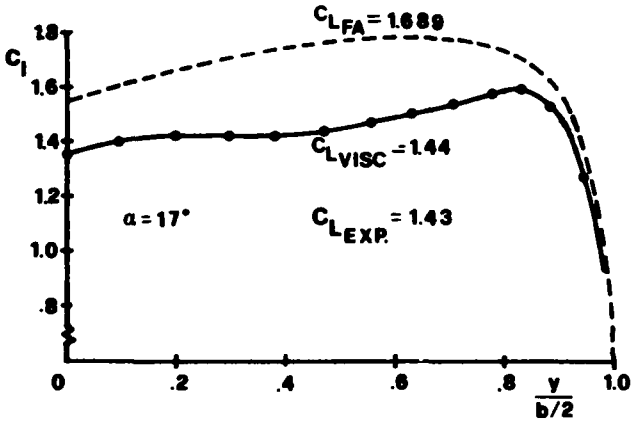
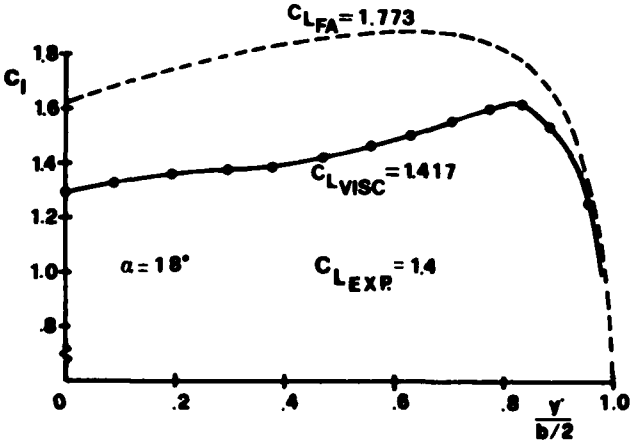


Fig. 12 Spanwise Load Distribution on a 10.05 Aspect Ratio, Tapered (λ=0.4), Twisted Wing - Root Section NACA 4420 Tip Section NACA 4412, at High Angles of Attack





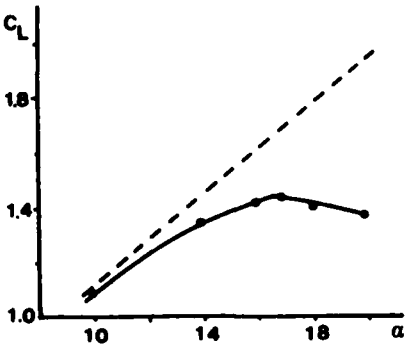


Fig. 13 Comparison of Calculated and Experimental Wing Lift Coefficient at High Anles of Attack

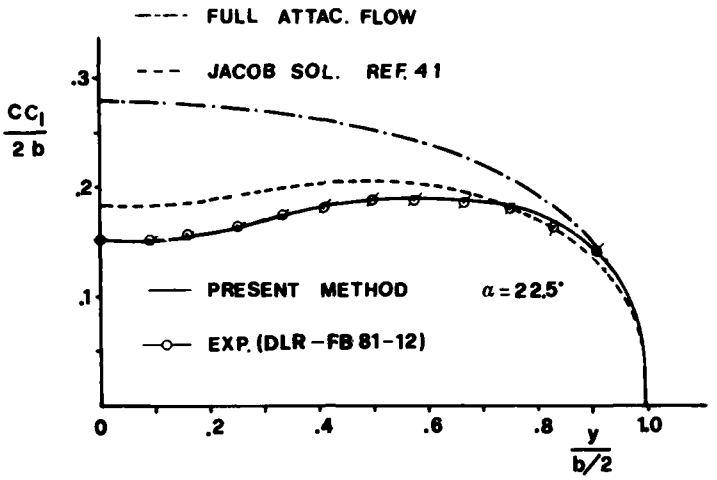


Fig. 14 Comparison of Computed Lift Distribution with Experiment and Jacob's Solutions for a Rectangular Wing at High Angle of Attack

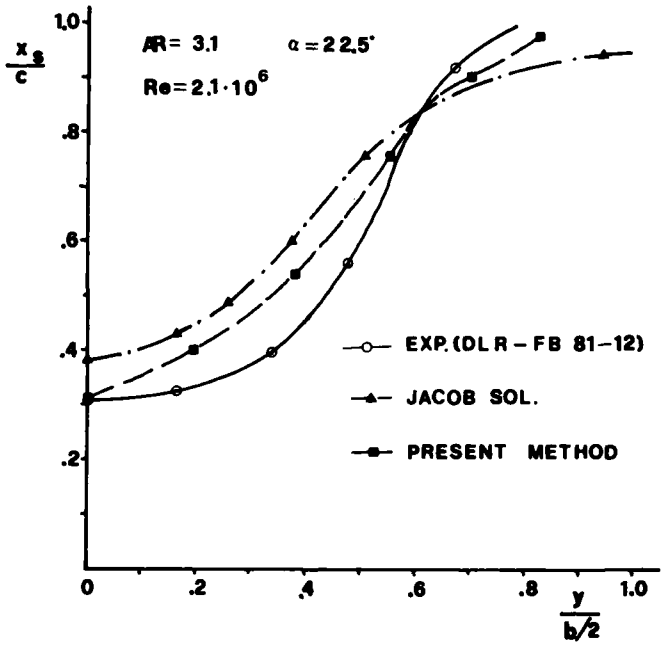
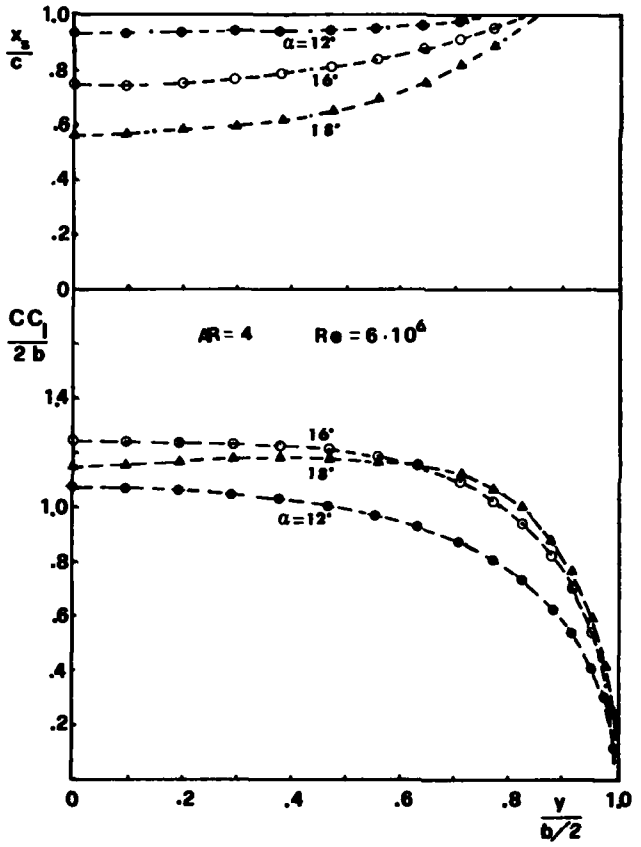


Fig. 15 Separation Lines on the Upper Surface of Rectangular Wing (α=22.5°)



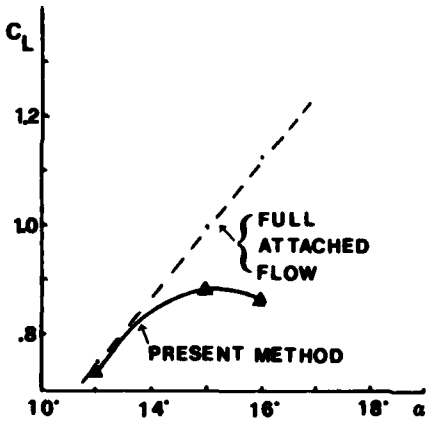


Fig. 16 Load Distribution and C_{Lmax} for a 4 Aspect Ratio Rectangular Wing with Given Separation Lines

AD-P004 059

AERODYNAMIC ISSUES IN THE DESIGN OF HIGH-LIFT SYSTEMS FOR TRANSPORT AIRCRAFT

by

Bertil Dillner
Chief Engineer, Aerodynamics

Fred W.May
Aerodynamics Staff

MS 43—77
Boeing Military Aircraft Company
Box 370, Seattle, WA 98124
USA

and

John H.McMasters
Senior Specialist Engineer, — Aerodynamic Staff
Boeing Commercial Airplane Company
Box 370, Seattle, WA 98124
USA

SUMMARY

The design of the high lift system has a profound effect on the sizing and total performance of transport aircraft, both civil and military. ~~The purpose of~~ this paper ~~is to~~ first review the fundamentals of high-lift system design and the phenomena that govern their performance. A review of the computational methods available to the high lift designer, with examples of their validity, is then presented. New developments in flow diagnostic techniques are reviewed. Finally, examples of several Boeing high-lift design efforts are presented. Emphasis is placed on the use of computational aerodynamic methods and the synergistic effect of using those methods in parallel with testing. Finally a list of todays ten most important issues is presented.

NOMENCLATURE

AePP	=	Aerodynamic Prediction Program
AR	=	aspect ratio, b^2/S
b	=	wing span
c	=	basic cruise wing or airfoil chord
c	=	average wing chord S/b
c_d, c_l, c_m	=	two-dimensional (section) drag, lift and pitching moment coefficients, force/qc and moment/qc^2
C_D, C_L, C_M	=	three-dimensional configuration drag, lift and pitching moment coefficient, force/qS and moment/qSc
C_μ	=	blowing coefficient $M_j V_j / q_\infty S$
C_p	=	pressure coefficient, $\Delta p/q_\infty = (P_{local} - P_\infty)$
DVM	=	Distributed Vorticity Method
H	=	boundary layer form parameter, δ^*/θ
L/D	=	ratio of lift to drag
M	=	Mach number
M_j	=	jet mass flow rate
p	=	static pressure
q	=	dynamic pressure
Re	=	Reynolds Number
SASS	=	Subsonic Analysis Section System
S	=	Wing area
T	=	Thrust
t	=	airfoil thickness
V	=	Velocity
V_j	=	jet velocity
W	=	Weight
x	=	longitudinal coordinate
y	=	lateral coordinate
α	=	angle of attack
Δ	=	differences (residuals)
δ_f	=	flap deflection
δ^*	=	boundary layer displacement thickness
θ	=	boundary layer momentum thickness
η	=	non-dimensional spanwise wing station 2y/b
Λ	=	sweep angle measured at wing quarter chord

Subscripts

eff	=	"effective" viscous condition
exp	=	experimental value
f	=	flap
geo	=	geometric value
max	=	maximum
min	=	minimum
∞	=	free stream conditions
r	=	point at which pressure recovery to freestream conditions begin on an airfoil
visc	=	viscous

Superscripts

$(\hat{})$	=	adjusted or scaled quantity
$(*)$	=	critical section

INTRODUCTION

It has been a decade since A.M.O. Smith, then of the McDonnell-Douglas Aircraft Corporation, presented his Wright Brothers Lecture[1] entitled "High-Lift Aerodynamics" (based on an earlier AGARD Lecture[2]) to the American Institute of Aeronautics and Astronautics. In the flood of technical papers which have documented the extraordinary progress of aeronautical science over the past forty years, A.M.O. Smith's paper stands as a true classic. In addition to greatly clarifying the physics of important aspects of high-lift aerodynamics, Smith clearly set the stage for much of the subsequent work in this discipline.

The history of high-lift technology can be traced in the application of high lift devices on Boeing aircraft over the past forty years shown in Figure 1. Since the authors have been involved in at least part of this development at Boeing, we necessarily approach our subject from that somewhat parochial viewpoint. As will be described in later sections of this paper, much of the progress demonstrated in Figure 1, was achieved by a process best characterized as "enlightened cut-and-try." This was aided in its later phases by slowly improving but still fairly elementary analytical methods. Testing was conducted almost universally in wind tunnels operating at Reynolds numbers at least an order of magnitude lower than actual flight conditions. Such has been the general state of affairs until very recently throughout the industry.

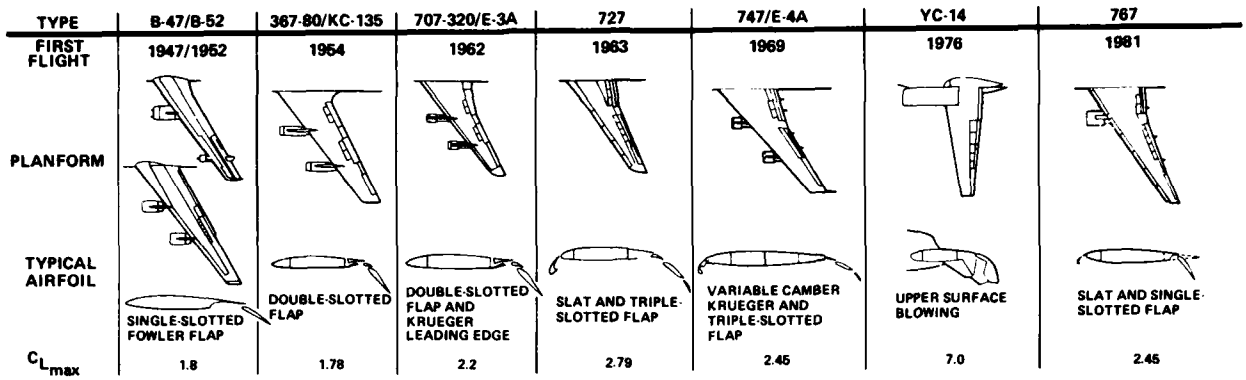


Figure 1. Trends in Boeing Transport High-Lift System Development

Advances over the past fifteen years in both computational methods, including use of inverse methods, and experimental flow diagnostic technology, have made possible a high lift system design process quite different than that which has relied largely on experience, intuition and experimentation alone. The further development and enhancement of this modern high-lift design process is one of the major issues referred to in the title of this paper.

There were several objectives in preparing this paper. These include:

- A review of some of the factors which influence the design of modern transport aircraft (both civil and military) and the effect of high-lift system performance on the overall design of such aircraft.
- The assessment of progress in the understanding and methodology development which has occurred in the decade since A.M.O. Smith presented his classic AIAA Wright Brothers Lecture.
- The demonstration of a modern approach to the solution of selected practical high-lift system design problems.
- To list the major issues, both practical and theoretical, which still confront the high-lift aerodynamicist as perceived by the authors.

As numerous authors have pointed out, the topic of high-lift aerodynamics covers an enormous range of flight vehicle types operating under a wide range of Mach and Reynolds number condition. While the entire topic holds a fascination for the authors, it is necessary to limit the scope of this paper to high-lift issues relating specifically to transport aircraft during "normal" take-off and landing.

HIGH-LIFT AERODYNAMIC ISSUES

The fundamental issues to be addressed in this paper are:

- Recognizing that maximizing the maximum lift coefficient is a simplistic view of the high-lift system design problem, what are the appropriate high-lift system aerodynamic design criteria for the anticipated range of moderate-to-large sized transport aircraft?
- In the light of our present theoretical understanding, how much practical performance, in terms of maximum lift coefficient, remains to be extracted from a truly optimized "conventional" high-lift system i.e. one which relies on passive boundary layer control based on geometry alone?
- What tools are available to design practical, efficient high-lift systems, and what additional tools do we need?

Before addressing any of the questions listed above, it is useful to compare and contrast the general design objectives and constraints of military and civil transport aircraft, particularly as these factors may influence the designer's options regarding high-lift system design. A partial summary listing of these design objectives/constraints is presented in Table 1.

In reviewing the criteria listed in Table 1, it should be noted that the general civil transport aircraft design problem is driven largely by economic considerations with an equally strong concern for safety. Thus, the design is generally optimized first and foremost for cruise efficiency. The objective of the complementary high-lift design effort is to produce a system which will allow a cruise optimized configuration to adequately meet take-off and landing requirements safely and reliably. It should also be noted that in normal commercial operations, the operating environment is relatively benign (aside from meterological considerations) involving paved runways, adequate to excellent air traffic control and landing aides, and well established maintenance facilities.

The military transport airplane designer appears to face a somewhat different problem. In principle, the dominant design criterion is successful mission accomplishment. While basic economic criteria such as range, payload and cruise speed, as an index of productivity, play important roles in layout and sizing, mission accomplishment simultaneously places very heavy demands on the high-lift system designer. In this case, mission accomplishment may require that the aircraft be able to operate

Issues	Civil	Military
Dominant design criteria	• Economics and safety	• Mission accomplishment and survivability
Performance	• Maximum economic cruise • Minimum off-design penalty in wing design	• Adequate range and response • Overall mission accomplishment
Airfield environment	• Moderate-to-long runways • Paved runway • High-level ATC and landing aides • Adequate space for ground maneuver and parking	• Short-to-moderate runways • All types of runway surfaces • Often Spartan ATC, etc. • Limited space available
System complexity and mechanical design	• Low maintenance—economic issue • Low system cost • Safety and reliability • Long service life	• Low maintenance—availability issue • Acceptable system cost • Reliability and survivability • Damage tolerance
Government regulations and community acceptance	• Must be certifiable (FAA, etc.) • Safety oriented • Low noise mandatory	• Military standards • Performance and safety • Reliability oriented • Low noise desirable • Good neighbor in peace • Detectability in war

Table 1. Transport Aircraft Design Objectives and Constraints

from battle damaged and/or primitive airfields, sometimes in a hostile environment. In exchange for these more demanding criteria, the military high-lift systems designer has more system options at his disposal in that presently "difficult to certify" powered lift schemes become viable - if they can be shown to be sufficiently reliable, maintainable and insensitive to battle damage.

It is perhaps ironic that in the extended "peacetime" environment, many of the civil aircraft design criteria play a larger role in military design requirements than may be fully appropriate. As examples one may cite budgetary constraints which demand low initial cost biasing the design in favor of minimum size and weight and low fuel burn to minimize routine operating and training flight costs. Also increasing concern for community acceptance carries potential performance penalties in terms of concessions for noise reduction and engine emissions. The longer military transport aircraft serve the function of contributing to maintaining peace, the more civil type design criteria become important in the overall balance.

The discussion so far indicates that while the basic design criteria for civil and military aircraft are somewhat dissimilar, the high-lift system design problem still resolves into several common issues. Fundamentally, the high-lift system must allow the aircraft to achieve adequate performance - both at landing and take-off (Fig. 2 & 3). Experience indicates that for CTOL aircraft the dominating factor for take-off is climbout L/D and for landing, C_{Lmax}. As shown in Fig. 4, approach speed has a value in itself, not only as a performance variable, but as an important safety factor. Even though the level is dependent on the operational environment and level of technology the general trend holds true.

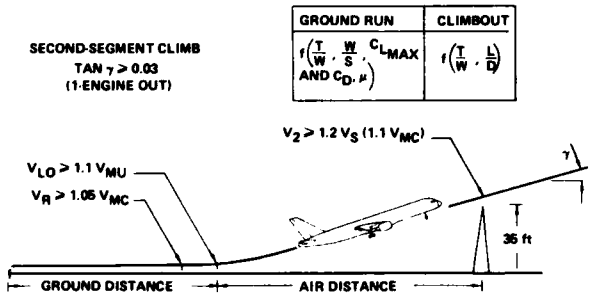


Figure 2. Takeoff Profile

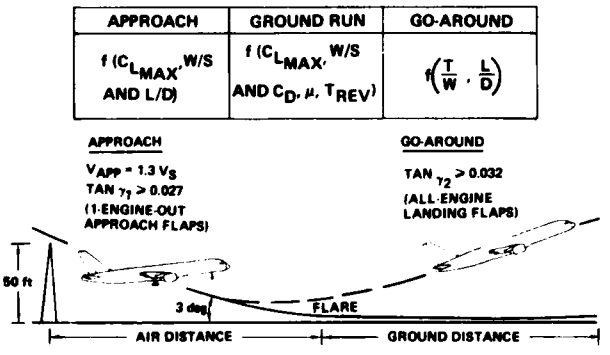
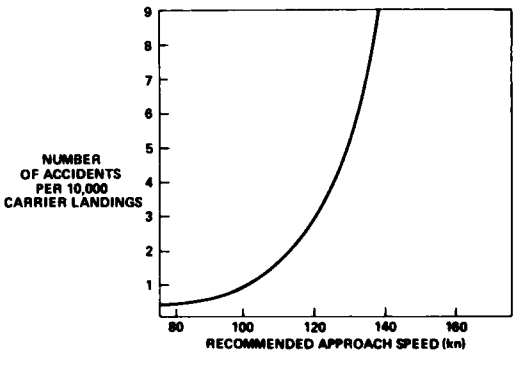


Figure 3. Landing Profile



SOURCE: AIRCRAFT RECOVERY BULLETIN NO. 26-12A NAEL-SE-731

Figure 4. Influence of Aircraft Approach Speed on Carrier-Landing Accidents

Finally, it is obvious that whether the primary concern is safety and certifiability, or mission accomplishment, the high-lift system must be reliable. Thus the strongest bias must be in favor of simplicity. In both the civil and military case, maintainability implies availability, and simplicity has a very strong leverage on these factors. Vulnerability to battle damage is intrinsic in mechanically complex systems, and the attraction of a very large number of mechanically complex augmented/powered lift schemes begins to vanish despite the potentially large increments in lift achievable with such systems under benign conditions.

THE INFLUENCE OF HIGH-LIFT SYSTEM PERFORMANCE ON TRANSPORT AIRCRAFT SIZING

Having discussed in general terms the objectives and constraints on civil and military transport aircraft design, it now remains to demonstrate in more detail how high-lift system performance may influence the sizing of such aircraft. While a comprehensive discussion of this topic is far beyond the scope of this paper, two examples, one civil and one military, will serve to illustrate the complex trades to be made in selecting an appropriate high-lift system for such aircraft.

An Energy Efficient Transport

The first example selected is based on work for the NASA Energy Efficient Transport EET program (ref 3 & 4). Most of the analysis and design methods used in this study were developed under Boeing Independent Research and Development (IR&D) funds and will be described in some detail in later sections of this paper. The intent of the present discussion is to demonstrate the dominant high-lift system requirements which emerge in the course of a typical preliminary design exercise for a modern commercial transport airplane.

Typically the wing for a new design is sized to satisfy cruise considerations, including initial cruise altitude, cruise Mach, buffet margin, etc., and low-speed, high lift considerations such as approach speed and takeoff field length.

The results of a typical "thumb print" analysis of the Boeing baseline EET configuration (Fig. 5) is summarized in Fig 6. In the study, size consequences of three discrete optimization indicies were explored. These were:

- Minimum take-off gross weight which would presumably result in an aircraft of minimum airframe acquisition cost.
- Minimum block fuel burned; of major interest to the EET program.
- Minimum direct operating cost (DOC); the traditional index of interest to airline operators.

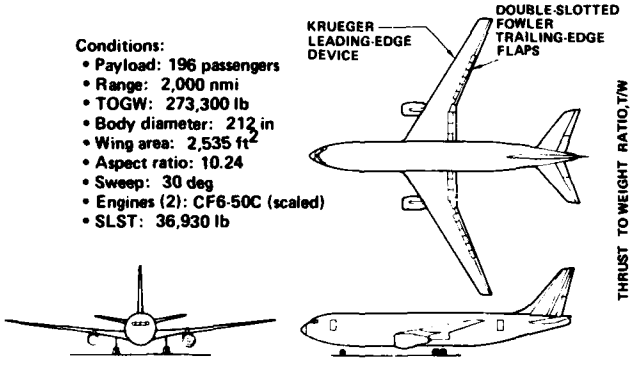


Figure 5. Baseline Airplane

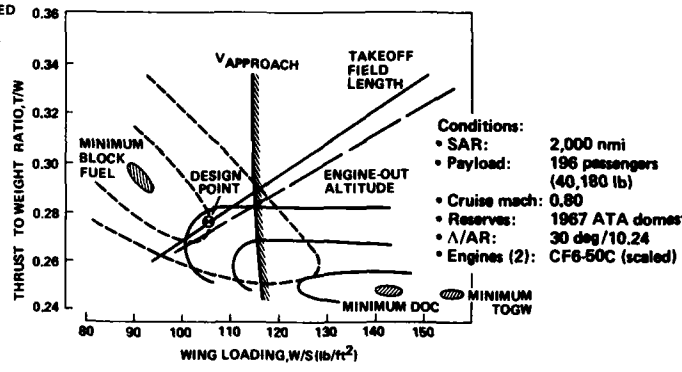


Figure 6. EET Baseline Design Selection Chart

The conclusions drawn from the results shown in Figure 6 were:

- Both the minimum weight and minimum DOC design points were very far away from the minimum fuel burn design point. The minimum block fuel airplane required a much larger wing and engines than either the minimum DOC or minimum weight designs.
- A conservative, state-of-the-art double-slotted flap/variable camber Krueger leading edge high-lift system more than adequately met approach speed and landing field length requirements.
- The dominant constraint on sizing, leading to a compromise design point skewed in favor of the minimum block fuel condition, was take-off field length (and hence take-off lift-drag ratio) followed very closely by a nominal 12,000 ft. engine-out altitude constraint.

From this study it is clear that a priori assumptions regarding high lift system performance requirements for a new design are inappropriate. Care must be taken to evaluate the range of conditions (take-off, landing, initial climb, etc.) in which high lift system performance may be critically important before investing much resource in developing a high lift system.

A Military Short-Haul Transport (MST)

This example will use results from a feasibility study for a Medium STOL Transport (MST) which led to the Advanced Medium STOL Transport (AMST) program under which the Boeing YC-14 and McDonnell-Douglas YC-15 were developed. The fundamental performance requirements were that the airplane fly a radius mission with a 28,000 pound payload operating into and out of a 2,000 foot long airfield at the mission midpoint. The field was assumed to have an elevation of 2500 feet and an ambient temperature of 93°F. Operation had to consider failure of the most critical engine during takeoff and landing. In addition, the aircraft had to carry 38,000 pounds of payload for 2600 nmi while operating from longer runways.

One of the fundamental considerations was selection of a high-lift system concept. Figure 7 shows a map of airplane design solutions for the design radius mission for a four engine airplane using a high lift system having a maximum lift coefficient of 4.0. Superimposed on this map are takeoff and landing field length and engine-out climb gradient limits. The selected design is the lowest takeoff gross weight solution satisfying all of the design constraints.

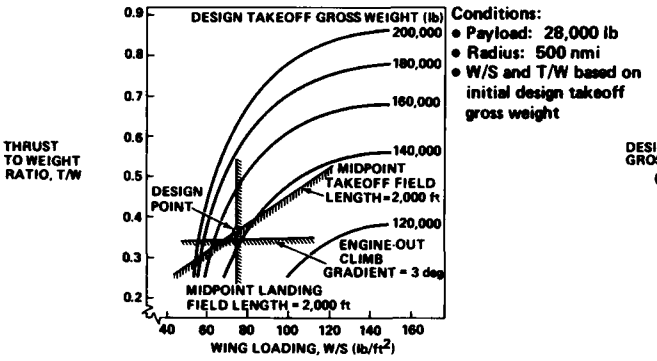


Figure 7. MST Design Sizing

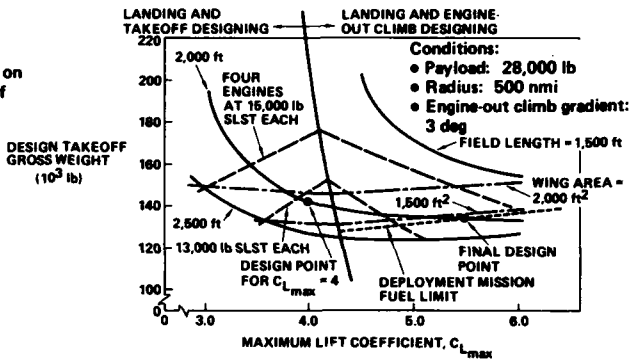


Figure 8. Effect of Lift Capability on MST Design

This process can be repeated for high lift systems having varying lift capability accounting for the obvious fact that the weight of a high lift system increases as its maximum lift increases. These results are shown in Figure 8. The design point determined from Figure 7 is noted. Airplane size for a 2000 foot mid-point field length continues to decrease as maximum lift coefficient is increased up to $C_{L\ MAX}$ of about 6.0. However, the wing volume available for fuel tankage to fly the deployment mission now becomes a limit. The selected design had a $C_{L\ MAX}$ of 5.5 and a design gross weight of 235,000 pounds. This study was conducted in 1976 with the propulsion and aerodynamics technology available at that time. If it were repeated today the results would differ but the process by which the airplane was sized and the high lift system selected would remain the same.

THE LIMITS OF HIGH LIFT

Before assessing the state of high lift aerodynamics, it is useful to establish an "upper bound" against which one can compare the "practical" limits in design. A.M.O. Smith discussed these limits a decade ago and it is merely necessary to summarize his discussion with the inclusion of Figure 9.

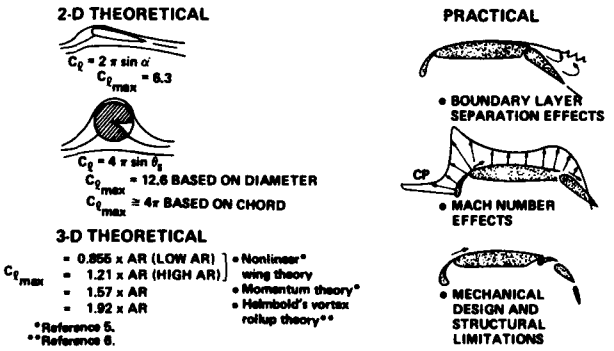


Figure 9. $C_{\ell_{max}}$ Limits

The left hand side of Figure 9 shows a number of theoretical two- and three-dimensional bounds which have been developed for maximum lift generating capability of "ideal" configurations. The right hand side shows several of the practical factors which may severly limit achievable performance. In addition to obvious limits imposed by viscosity, compressibility and mechanical constraints on two-dimensional sections, further losses are incurred in applying such sections to three-dimensional configurations. These effects include the adverse influence of wing sweep, the fact that the entire wing span of most practical configurations cannot be taken up with idealized high-lift systems, and the existence of necessary supporting structures which may produce local interference and boundary layer contamination effects. Besides reducing the lift these factors also tend to increase drag, and the effects on achieved lift-to-drag ratio for a typical transport are demonstrated in Figure 10. The influence of wing sweep on the achieved maximum lift performance of a variety of modern transport aircraft with conventional high-lift systems is shown as a function of high-lift system complexity in Figure 11.

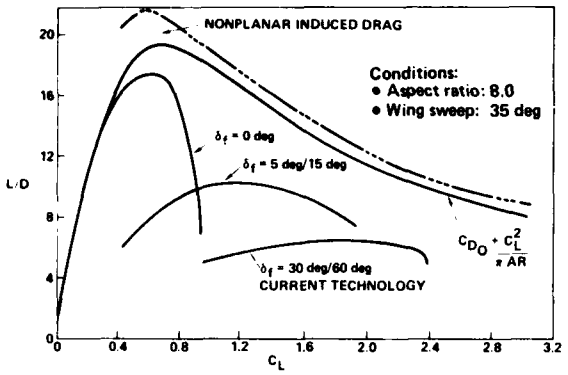


Figure 10. Potential Performance Improvement for Mechanical High-Lift Systems

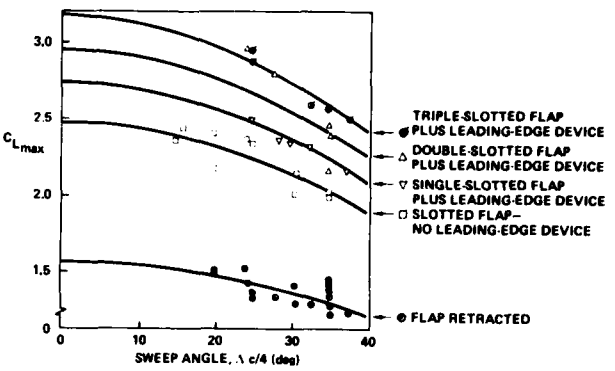


Figure 11. Statistical Analysis of Maximum Lift Coefficient for Transport Aircraft

If one now plots (Figure 12) the theoretical limits specified in Figure 9 and identifies the region of maximum lift coefficient achieved with unpowered high-lift systems, one sees the huge gap between achieved levels and the theoretical limits. It is here that powered lift schemes have application. A very useful discussion of this range of powered lift schemes is presented by Foster[7] as a companion piece to A.M.O. Smith's discussion. A recent paper by Loth & Boasson[9] provides an update on Foster's discussion in addition to providing a description of practical STOL aircraft operational requirements vis-a-vis powered lift system performance characteristics.

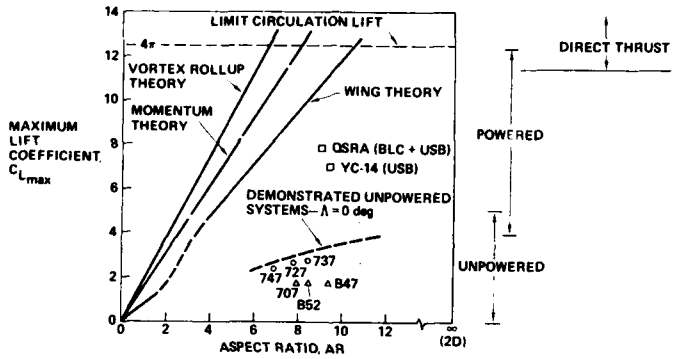


Figure 12. Limits of Maximum Lift Coefficient

Having noted the approximate boundaries of the feasible in terms of maximum lift coefficient as shown in Figures 9 and 12, it has been shown that the practical limits of maximum lift demonstrated for unpowered high-lift systems is far below the theoretical limit, even when systems of considerable mechanical complexity are employed. Of the practical reasons for this huge discrepancy noted earlier, by far the dominant factors limiting maximum lift are viscous effects and flow separation.

In view of the design space available within Figure 12 it is possible to describe a hierarchy of ways to control the boundary layer on a wing surface.
These are:

- Passive Boundary Layer Control by Contour Shaping and Variable Geometry. This approach is the most subtle; so much so that one sometimes forgets that it is a form of boundary layer control. The limits of boundary layer/circulation control for both single and multielement airfoils has been greatly clarified in the past two decades, perhaps foremost by A.M.O. Smith and his co-workers at Douglas, specifically R. H. Liebeck[9]. The full extensions of this work to three dimensional flows remains to be accomplished however.

- Power Augmented Boundary Layer/Circulation Control. Once one has approached the limit of maximum lift achievable by passive boundary layer circulation control through contour shaping including the mechanical complexity of multielement airfoils and wings, the next level of performance increase is achieved by using small amounts of auxiliary power to (1) increase the energy of the boundary layer by blowing or (2) remove all or part of the boundary layer by suction. As shown in Figures 13 & 14 there are a wide variety of schemes to accomplish either of these objectives. In all cases the objective is to delay the onset of separation and thus produce an increase in maximum lift.
  The particular application under study and the indices of merit by which the overall configuration will be judged will determine when substitution of a simple blowing/suction system would be preferable to adding yet another flap element to an already complex passive/mechanical system. At the other extreme, when does one reach a blowing/suction limit and one of the more powerful jet flap/circulation control schemes (Figure 15) becomes a better way to produce still higher lift coefficients.

- Powered Lift. As the required lift coefficients increase, we again pass through a transition region to the powered lift concepts involving the propulsion system as an integrated part of the high-lift system (Fig 16). Two types of powered lift concepts may be identified. The first separates the propulsion and circulation lift system and provides only direct jet lift, e.g., vectored thrust or lift engines. The second combines the propulsion and circulation

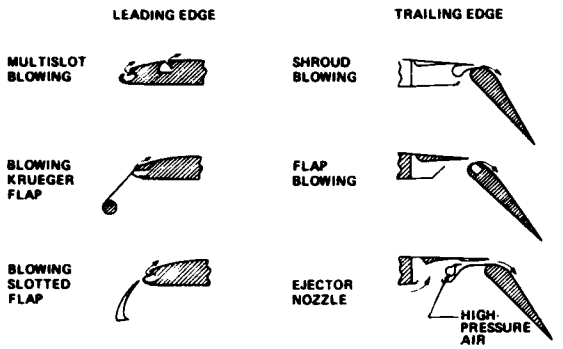


Figure 13. Blowing BLC Concepts

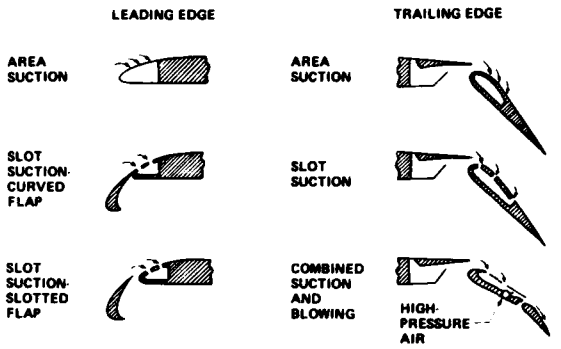


Figure 14. Suction BLC Concepts

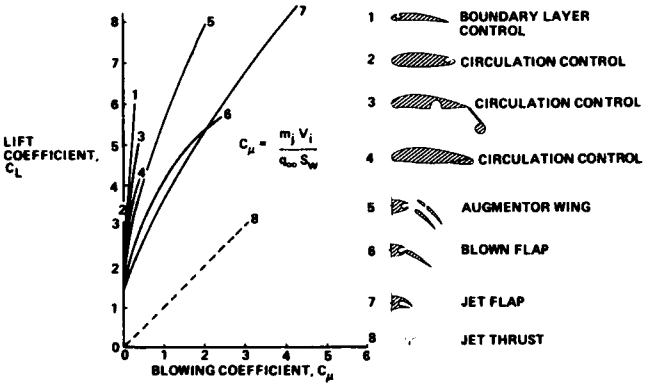


Figure 15. Powered High-Lift Performance for Various Wing Configurations (ref. 8)

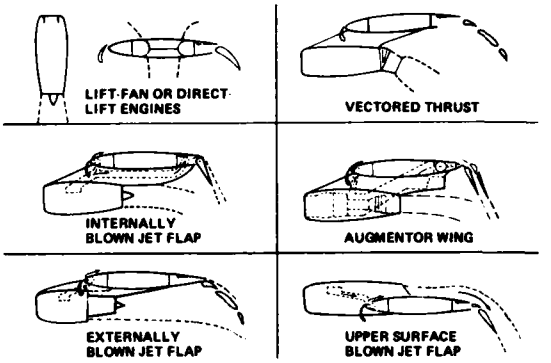


Figure 16. Powered Lift Concepts

lift system into a jet-flap type powered lift system. The augmentor wing, *externally blown* flap, and upper surface blown flap can all be considered subsets of the jet-flap concept.

While identifying the various lift enhancing schemes aids in discussing the multitude of possibilities and gives some flavor for the general level of lift performance achievable, it still does little to establish which is "best" for a particular application. This will depend on the payoff function, (e.g., DOC, LCC, Trip Fuel, etc;), the payload range of the airplane, and off design mission requirements.

While the probable trends in high-lift system development for long field-length transports can be described with some assurance, the same cannot be said for the case of STOL transport aircraft. What does emerge from the preceeding discussion is that there are a number of promising ways to achieve the high lift performance required for any reasonable STOL mission. All of the powered lift systems mentioned previously have been incorporated into flight hardware. The pure jet flap on the Hunting 126, the augmentor wing on a Boeing/NASA modified Buffalo, the externally blown flap on the McDonnell-Douglas YC-15, and the upper surface blown flap on the Boeing YC-14 and Boeing/NASA QSRA are some examples.

Passive/mechanical BLC high-lift systems are likely to be the norm for long range, moderate to long field length transport aircraft into the forseeable future. It must continue to form a major element of a discussion of high-lift technology. There is still progress to be made in the design of such systems.

The design of powered lift aircraft requires that more variables be considered than in the design of more conventional airplanes since STOL airplanes encounter control and handling qualities problems more severe than conventional airplanes. It must be noted that solutions to these problems have been found in specific design applications.

An example of one practical limit is the angle of attack of a particular configuration required to generate a given lift level. Here the coupling between approach speed, glide slope angle, and angle of attack as it influences pilot visibility and hence decision time, is shown schematically in Figure 17.

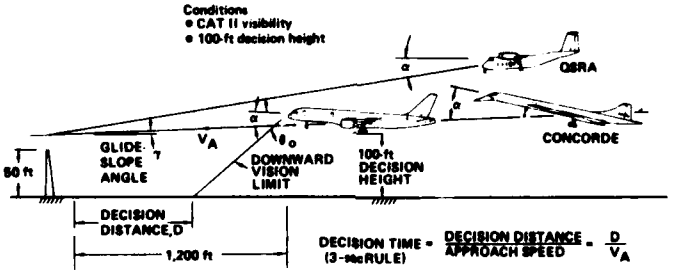


Figure 17. Effects of Glideslope and Angle-of-Attack on Decision Time

In view of the factors discussed, it is the authors' present opinion that of the many powered lift schemes presently available to choose from, relatively few offer the prospect of satisfactorily meeting the performance requirements and many constraints of practical STOL transports. Experience with the upper surface blowing (YC-14, QSRA) and externally blown flap (YC-15) indicates that these approaches could be developed into satisfactorily reliable and economical vehicles for both civil and military applications.

With the overview discussion of practical issues in high-lift technology provided above, it is now possible to discuss the state-of-the-art in methodology available to the high-lift system designer.

BOEING RESEARCH IN HIGH-LIFT TECHNOLOGY

A comprehensive survey of the industry-wide research devoted to solution of the theoretical problems in high-lift technology identified by AMO Smith a decade ago is a prohibitive task. Instead we choose to outline Boeing research devoted to this topic in the past decade and cite limited examples of related significant work by others. Further, the majority of the discussion is limited to mechanical systems since little theoretical work has been done at Boeing in recent years on powered lift systems.

While fully realizing that the approach taken here represents a rather parochial view of a very broad topic, it is the authors' opinion that the Boeing research effort is representative of the current state-of-the-art.

The Boeing Company research effort has been directed at developing a range of powerful tools for the design and analysis of transport type aircraft operating in low-speed/high-lift conditions. The basic objectives of this, largely company-funded, long term effort have been:

- To develop computational methods for the analysis and design of high-lift configurations.
- To provide improved flow diagnostic techniques and experimental data bases to support computational methods development.
- To apply these new tools to practical design problems to assess their capabilities and to guide further basic method development.

Thus over the past decade, the basic approach has been a balanced one encompassing theory, experiment and applications.

POTENTIAL FLOW SIMULATION OF THREE DIMENSIONAL MULTIELEMENT WINGS

Potential flow simulation of transport aircraft with hign-lift devices deployed is an essential step in the evolution of a rational analytic design capability and also serves as the foundation for viscous/vortex flow simulations of these configurations. In addition, until a full three-dimensional viscous analysis capability becomes available, a three-dimensional potential flow analysis/design capability remains an essential cornerstone of an analytic high-lift design procedure. The work has been devoted largely to two computer programs: A Distributed Vorticity Lifting Surface Theory, and extension of the PAN AIR code to the modeling of high lift configurations.

Computational methods for the analysis and design of three-dimensional wing and wing-fuselage configurations have evolved over the years from simple lifting line techniques which made very restrictive assumptions about the geometry of the configuration and the flow conditions, to very sophisticated and general panel methods. The most sophisticated of the newer methods (e.g. PAN AIR, ref. 10) offers the designer a very powerful potential flow analysis tool. However the difficulty in using these methods because of the very precise geometric definitions required especially for multielement high-lift configurations, coupled with the expense of running such codes, has precluded their wide spread use in high-lift applications. Only in cases where detailed pressure distribution information is required are they being used. Parenthetically we note that in our opinion the concern with computer costs is overstated. The actual machine costs of obtaining a solution are substantially less than the cost of the engineering labor required to prepare the problem for input to the computer. In may cases the money spent in the search for computer efficiency might be better spent in making the code more user friendly.

In many practical problems the analyst/designer primarily requires accurate information on items such as net lift, pitching moment, induced drag and span loading - items available in principle from a potential flow analysis of less sophistication than a full higher order panel method.

In 1975, M. I. Goldhammer began to develop the elements of an advanced lifting surface method (ref. 11). Goldhammer developed a very powerful version of his program aimed specifically at the multielement wing/body problem and possessing a great deal of automation aimed at easing the burden on the user of the code.

Two different lifting-surface theories are included in Goldhammer's computer program. A non-planar, non-linear distributed vorticity method (DVM) is the primary method while a simpler vortex lattice approach is available as a user option. The primary technique represents the thin wing by a continuous sheet of distributed vorticity which lies on the mean camber surface. The vorticity distribution used is continuous in the chordwise direction and is piecewise constant in the spanwise direction (Fig 18). Special treatment is given to the chordwise vorticity distribution. The loading at the wing leading edge is modeled to be infinite, which is consistent with the thin wing approximation. The DVM technique also explicitly satisfies the Kutta condition by forcing each trailing edge loading to zero.

Full provision is made for multielement wings with part span flaps. A two-dimensional algorithm is used by the program to specify the downstream path of shed vorticity. The program is highly automated, and the user need specify only gross geometric parameters for multielement wings (e.g. planform, twist, camber, flap deflection) the program then generating its own detailed vorticity networks.

In addition the overall method includes a modified slender-body theory representation of the fuselage, which is adequate for modeling wing lift carry-over effects and the body contribution to pitching moment.

The program also includes three-dimensional design (inverse) capabilities. An induced drag minimization technique is included, for example, based on the Lagrange multiplier technique.

Since release of the production version of the basic code in 1978, the program has achieved widespread acceptance within the Boeing Company. As part of the code development and subsequent validation effort a number of test-theory comparisons have been made, with the results shown in Fig. 19 being typical of those obtained.

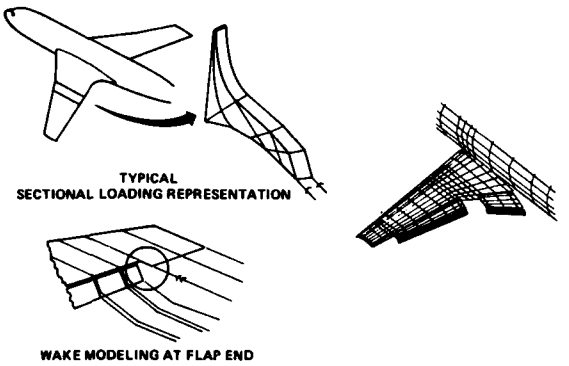


Figure 18. DVM Lifting Surface Analysis for High-Lift Configurations

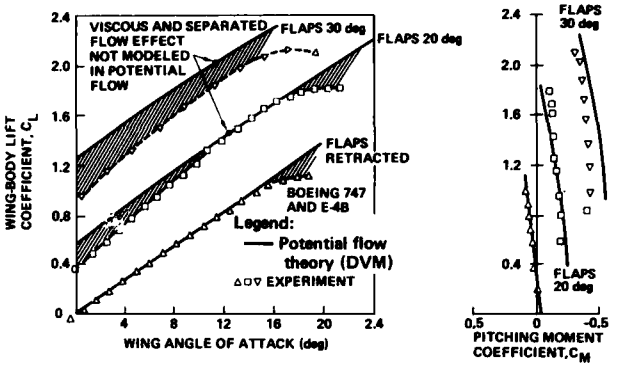


Figure 19. Typical Distributed Vorticity Method (DVM) Results

The excellent agreement in both lift curve slope and lift level demonstrate the satisfactory nature of the thin wing approximation when no separation occurs. The usual explanation for these good results is that neglect of both thickness effects and boundary layer build-up ("viscous decambering") are counter effects which approximately cancel each other. This mutual cancellation effect deteriorates at higher flap deflections and most particularly when there is significant partial separation of the flow.

The DVM Lifting Surface Theory program does a remarkably good job of predicting net lift, pitching moment, induced drag and span loadings for a wide class of high-lift configurations. However, it does not provide two important capabilities. It cannot give detailed potential flow pressure distributions and it does not have the ability to model details of the configuration such as wing/body junctions or nacelle/strut combinations.

To obtain such additional detailed information, one must resort to more sophisticated methods such as PAN AIR. While application of panel method technology to the cruise configuration has been widely successful, its extension to high-lift configurations has not. Early attempts to model multielement wings using panel methods led to major discrepancies in prediction of both lift level and lift curve slope. These difficulties have generally been attributed to deficiencies in the way early panel methods handled the Kutta condition and uncertainties in proper modelling of multiple wakes and vorticity shed from part-span flap edges.

With final production release of the Lifting Surface Theory, attention turned to the problem of adapting the lessons learned regarding wake modelling to the advanced panel method codes. In addition, the difficulty of paneling the complex geometries of multielement wings has been solved. A typical result compared with experimental data from ref. 12, is shown in Fig. 20.

The central purposes of this work with PANAIR have been:

- To extend the power of the full panel method to include high-lift configurations.
- To provide potential flow pressure distribution data essential to future development of a full three-dimensional viscous flow analysis capability for multielement wings.
- To provide a theoretical tool which provides some insight into the inviscid aspects of large scale vortex/airframe interaction problem.

An early PANAIR test-theory comparison for the case of a swept wing with part-span, triple-slotted flaps and leading edge slat is shown in Fig. 21.

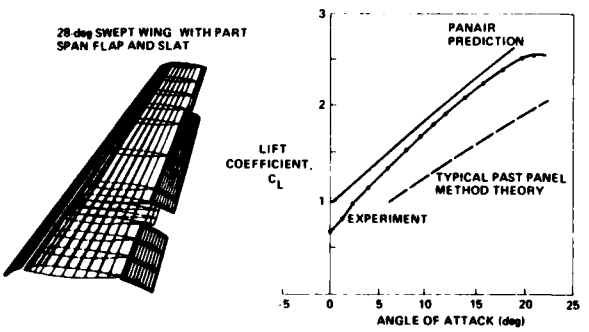


Figure 20. PANAIR Modeling of Wings With High-Lift Devices

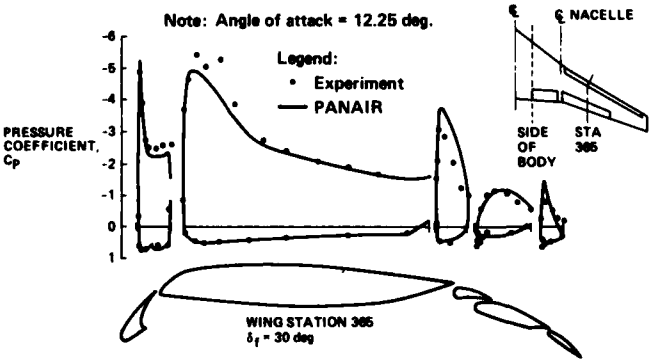


Figure 21. Test-Theory Comparison of PANAIR Modeling of a Boeing 737-300 Wing

ANALYSIS AND DESIGN OF MULTIELEMENT HIGH-LIFT SYSTEMS IN A VISCOUS FLOW

The performance of high-lift systems is largely limited by viscous flow phenomena and subsequent separation. Because of the inordinate difficulty of computing viscous flows in three-dimensions, particularly those which may occur on complex multielement wings, the bulk of past effort has been devoted to the development of a full viscous flow analysis and design (inverse) capability for two-dimensional, multielement airfoil sections. It was in the clarification of the physics of multielement airfoils that A.M.O. Smith made one important contribution to high-lift technology.

The flow around high lift airfoils is characterized by many different inviscid and viscous flow regions as illustrated in Figure 22. In particular, the existence of confluent boundary layers and the regions of separated flow distinguish the high lift airfoil problem from the aerodynamic problem of airfoils at normal operating conditions. The characteristics of the various flow regions must all be calculated. Futhermore, the prediction of transition from laminar to turbulent boundary layer flow, the prediction of the onset of boundary layer separation and the effects of large scale separation from one or more airfoil elements are a necessary part of any general high-lift analysis computer program.

In addition to allowing a pure analysis of a given geometry, a truly utilitarian code should also contain an inverse capability, which allows one to extract an airfoil shape from a specified pressure distribution. In addition methodology should exist which would allow the design/optimization of this pressure distribution in a viscous flow.

The development of this full capability has been a central objective of the Boeing high lift research effort since 1975. The outcome has been the development of two basic computer programs each of which possess unique capabilities which are not presently fully duplicated in the other.

As pointed out earlier, the most striking viscous phenomena which distinguish the flow around high-lift systems from the flow at cruise conditions are the possible existence of confluent boundary layers and of significant regions of separated flow at normal operating lift levels. The dual problems of separation and confluence have generally been approached separately in the course of developing analysis schemes for multielement airfoils, although the existence of a strong confluent boundary layer flow may have a substantial influence on the point(s) at which the flow may separate. A large body of experimental two-dimensional multielement airfoil data indicates that optimum high lift performance is obtained when gap and overlap conditions on the airfoil elements are set such that no regions of strong confluence exist (Fig. 23). However, any general multielement airfoil analysis should have the capability of accounting for merging shear layers in addition to its other capabilities. Without this capability it is impossible to properly perform analytical gap-overlap optimization studies, to account properly for boundary layer characteristics in the presence of even weak confluence which may effect both drag and separation location.

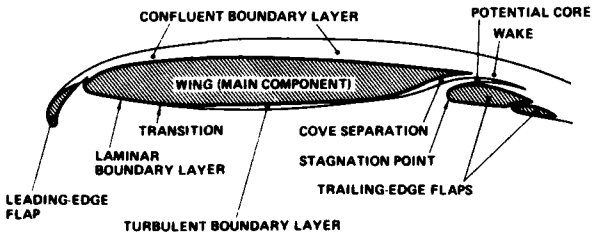


Figure 22. 2-D Viscous Flow Analysis and Design

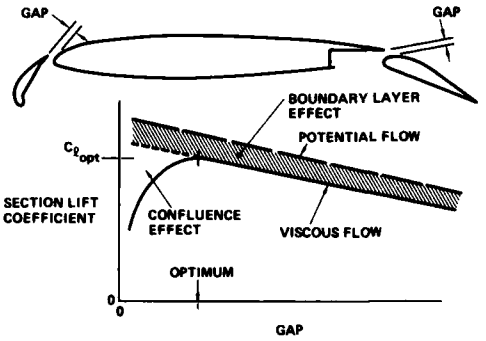


Figure 23. Influence of Airfoil Element Gap on Optimum Lift Performance

One approach to multielement airfoil analysis was originally developed by Goradia and his coworkers (ref. 15) at Lockheed-Georgia under the sponsorship of the NASA-Langley Research Center. This program was among the first attempts at analyzing the complex viscous flow about slotted airfoils and received worldwide distribution and usage. A unique feature of this multielement airfoil program was the model of the confluent boundary layer flow.

Over the years , the original version of the program was modified extensively to improve its predictions for different types of high lift airfoils. Many improvements, mainly in the area of the potential flow calculation, were made by researchers at the NASA-Langley Research Center. For this reason, the code generally has been referred to as the NASA-Lockheed multielement airfoil program.

This program has since been further developed by Brune et al (ref 16 & 17) partly under contract with NASA-Langley.

In many respects, this program, (with the Boeing modifications) is an excellent tool for the analysis of multielement airfoils with fully attached boundary layers. It remains useful both as a research tool and for those cases where its assumptions and limitations are non-restrictive in project use. It suffers from two major shortcomings, however. It is incapable of analyzing separated flows and it has no inverse capability. A typical analysis result is shown in Fig. 24.

In the course of modifying the NASA-Lockheed code, Brune found the original confluent boundary layer analysis method to be inadequate. Therefore a new confluent boundary layer scheme was developed. (ref 16). It is a finite difference technique which solves the turbulent boundary layer equations and a two-equation model of turbulence due to Jones and Launder (ref. 17) known as the Kappa-epsilon model.

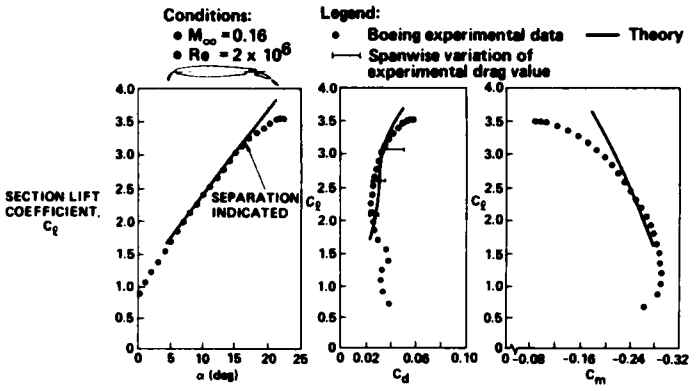


Figure 24. Lift, Drag, and Pitching Moment of a Boeing Four-Element Airfoil

One of the central difficulties in validating confluent boundary layer methods and viscous flow analysis methods for multielement airfoils in general, is the very sparse set of complete experimental data which exist in the literature for realistic airfoil sections. Thus a comprehensive test was conducted to acquire the data necessary to fully validate the new theory. In addition to force, moment and pressure distribution data, detailed information on mean velocity profiles and turbulence properties in the boundary layer at several chordwise stations was required.

Prior to conducting the test however, a survey of available instrumentation showed that existing equipment was inadequate to provide the high quality, detailed data required. Thus, an improved mechanical traversing mechanism was designed which would provide minimum disruption to the flow being measured and high position accuracy.

This new traversing mechanism and flow sensors are shown in figure 25. The traverse is self-propelled and is normally mounted on the side of the model opposite to the surface on which measurements are being taken. The traverse mechanism is equiped with four flow sensors: a pitot probe, two X-hot wires and a dual split film. Data from all sensors is acquired simultaneously. A description of this probe and samples of the very high quality data obtained are discussed in ref. 18 and 19. Sample data are shown in Fig. 26. The test-theory comparison of this data with the new confluent boundary layer program is shown to be excellent.

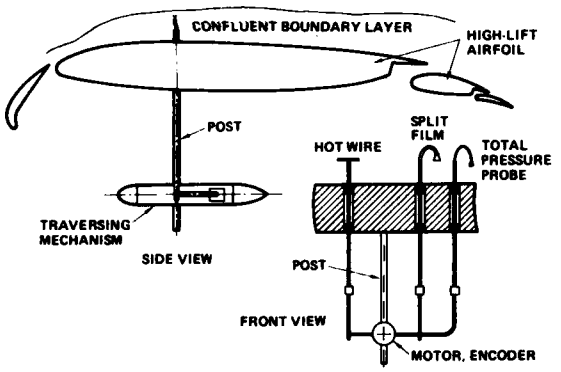


Figure 25. Sketch of Boundary Layer Traversing Mechanism Configuration for Minimum Flow Disturbance

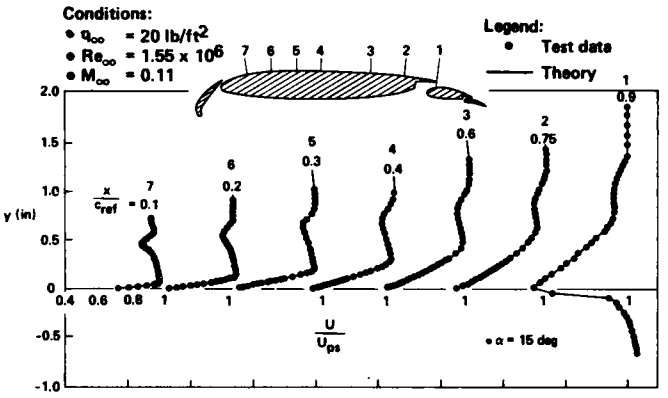


Figure 26. Confluent Boundary Layer Experiment

In most realistic applications, knowledge of section maximum lift coefficient is important, if not crucial, in airfoil design/optimization. In the absence of a computational capability to predict the effects of large scale flow separation, and hence maximum lift coefficient, heavy reliance must be placed on wind tunnel testing which has traditionally been conducted at Reynolds numbers an order of magnitude lower than actual flight conditions. This has generally led to substantial conservatism in the design, in efforts to reduce risk. In addition, the usual approach to computational design has been conducted by an iterative analysis process, wherein one begins with a baseline geometry and a desired performance goal and by analyzing the characteristics of the baseline geometry, obtained either experimentally or computationally, attempts to determine "intuitively" how the initial geometry ought to be modified to meet performance goals. Whether conducted in the wind tunnel or on the computer, the process remains largely one of "cut-and-try."

It has long been realized that a more rational approach to the aerodynamic design problem would be to begin with a realistic set of performance objectives and constraints, and derive the pressure distributions and other flow characteristics necessary to meet these objectives based on boundary layer theory. With the desired flow characteristics established, one can then extract by computation the geometry necessary to produce these desired flow characteristics. This "inverse" or synthesis process, while conceptually simple and desirable has only become practical with the advent of large digital computers.

With these considerations in mind, M. L. Henderson developed a versatile computer program system (ref. 20) which would allow both the analysis and design of multielement airfoils with inclusion of the effects of separation in the analysis mode and inverse boundary layer techniques for pressure distribution synthesis in the design mode.

The Subsonic Analysis Section System (SASS) is based on two-dimensional higher order panel method algorithms for potential flow and integral boundary layer methods for viscous flow computations. The two important components of the separation modeling are the determination of the separation point(s), and and the streamline displacement caused by the separated wake. This latter problem is handled by introducing a separation cavity whose contours may be determined without recourse to detailed calculations of the complex interior physics. This wake displacement body is added to the bare airfoil geometry, and the whole "equivalent body" may then be analyzed in potential flow to predict separated flow airfoil section performance. This procedure is described in detail in refs. 3 and 20. Some typical test-theory comparisons are shown in Figure 27.

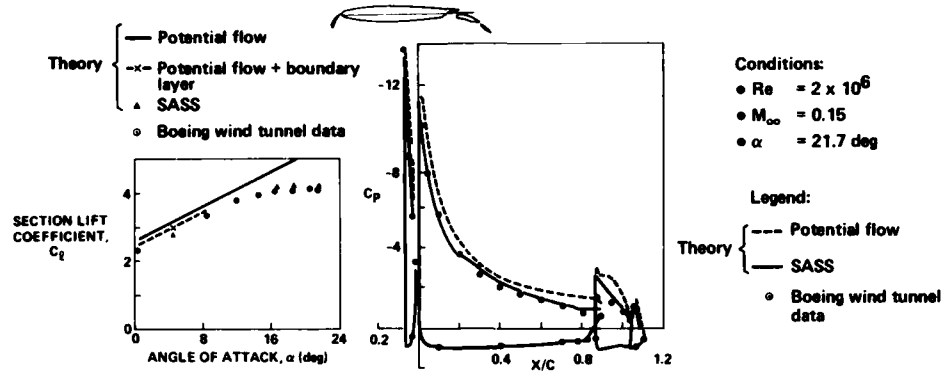


Figure 27. Predicted Airfoil Data From Subsonic Analysis Section System (SASS)

The overall program system also incorporates provision for a separate inverse boundary layer method for the design and evaluation of pressure distributions for input to the design mode of the program. This inverse boundary layer method, (ref. 21 and 22) is also a valuable tool in its own right.

HIGH-LIFT FLOW CORRELATION AND PREDICTION TECHNIQUES

At present there is no analytic method capable of solving the three-dimensional viscous flow about wings, let alone full aircraft, in high-lift configurations. Even if or when this capability is developed it will likely be time-consuming and expensive to use on a production basis. Tnus there will always be a need for:

- Correlation methodology for two-and three-dimensional flows which allow (where appropriate) the use of simpler, more economical two-dimensional viscous methods loosely coupled to three-dimensional potential flow techniques.

- Semi-empirical techniques for the prediction of full-scale aircraft high-lift performance from wind tunnel data and from the performance of previous aircraft of similar geometry.

- Techniques for the prediction of both wind tunnel and flight level high-lift performance of preliminary design configurations for which no specific wind tunnel data exists.

The problem of establishing rational methods for connecting the results of three-dimensional potential flow with two-dimensional viscous flow analyses has been an important part of the high-lift research effort. As a major part of this effort it has been necessary to establish the correlation between two-dimensional multielement section characteristics with the corresponding sections on three-dimensional wings as influenced by sweep, induced angle-of-attack and camber effects, and spanwise components of boundary layer flow.

As an example of early correlation methodology work, it was found that "simple sweep theory" type corrections to two-dimensional results, which are rigorously valid only for thin wings of constant chord and infinite aspect ratio, should be replaced by the more theoretically correct method due to R. C. Lock (ref. 23) which explicitly accounts for taper and finite aspect ratio effects.

With the advent of the DVM Lifting Surface Theory program, Goldhammer was able to achieve a substantial advance in correlation/prediction methodology. For the first time it became possible to reliably obtain potential flow results for high-lift configurations representative of actual transport aircraft.

An example of what Goldhammer was able to achieve with combined use of programs DVM and SASS (corrected for sweep), to predict high-lift wing/body characteristics beyond the linear portion of the lift curve is demonstrated here. The assumptions made in this example are that airfoil section characteristic dominate the lift behavior of the wing; and that even in cases where the flow may be locally separated, spanwise boundary layer flow effects can be neglected.

As demonstrated earlier, use of the DVM program for cases of highly deflected part- or full-span flaps, with separation at normal operating conditions, leads to a substantial overprediction of lift. However, by analyzing "critical 2D sections" of the wing (located at "peaks" in the span loading distribution) using the SASS program with its separated wake modeling capability, an "effective" viscous flap deflection angle can be determined as shown in Figure 28.

When this new effective viscous flap deflection is input to the potential flow analysis (DVM) the result is a dramatic improvement in the test-theory comparison of span loading shown in Figure 28.

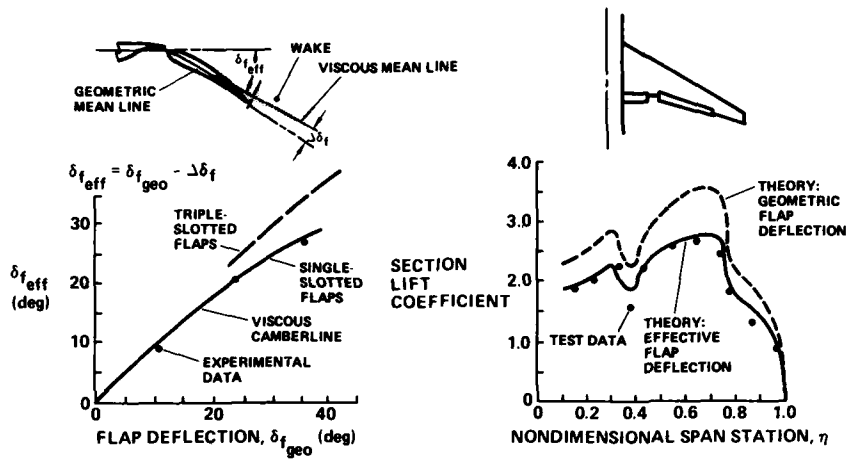


Figure 28. Effective Flap Deflection—Influence on Span Loading

Perhaps a more remarkable outcome of this sort of analysis was the fact that applications of the DVM program to a variety of other transport type configurations showed a repeatable (to first order) correlation between effective and geometric flap deflections for a given number of elements in the high lift system. This led to the tentative construction of the graph relating effective and geometric flap deflections shown in the figure. These relations hold only for standard wind tunnel level Reynolds number, although a comparable set could be constructed for flight levels.

It should be noted that the work reported so far has been largely directed toward providing computational tools to project level engineers for use during the detail design phase of an airplane development program. This goal continues to be important and has been remarkably successful. As reported in ref. 24, the combined progress in 3D potential flow analysis and 2D viscous flow analysis and design when coupled with progress in 2D-to-3D correlation methodology has lead to a quasi-3D viscous flow analysis and design capability for multielement wings. This design process which relies heavily on the use of 2D inverse methods is shown diagramatically in Fig. 29, and will be demonstrated in more detail later in this paper.

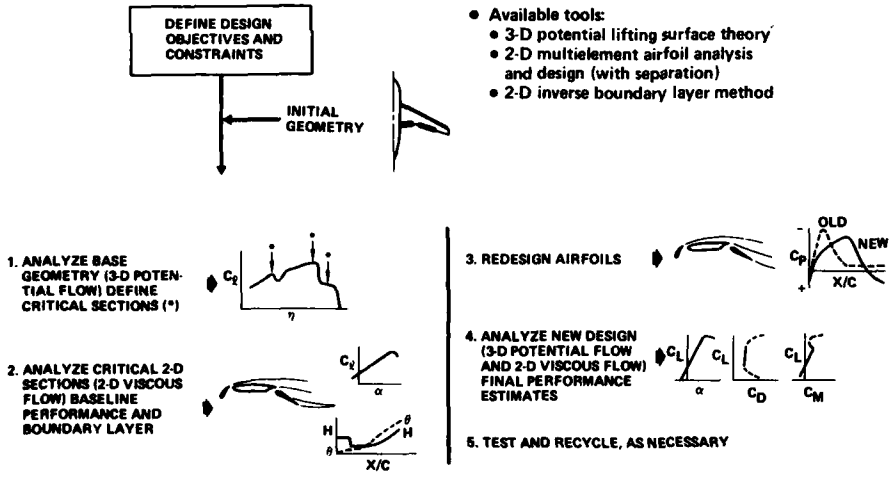


Figure 29. High-Lift Analytical Design Procedure

As shown in the overview diagram (Figure 30), at the detail design level, computational methods intended to complement extensive testing must be highly accurate. Thus costs may be high, although fully justified if an enhanced design process results.

Design level	Accuracy required	Turnaround time	Cost	Method
Conceptual	Approximate (±10-20%)	Negligible	Negligible	Handbook and calculator
Preliminary	Good (±5-10%)	Rapid	Low	Semiempirical
Detail (project group)	High (±2-5%)	Reasonable	Moderate	Full analysis and design Viscous 2-D Inviscid 3-D

Figure 30. Low-Speed Aerodynamic Prediction Methods

In a preliminary design phase of aerodynamic configuration development, computational methods are also of major importance. In this case, however, where many continually changing configuration variables must be considered and their effects on the global aerodynamic characteristics readily evaluated, the conflicting requirements of computational accuracy and ease of use, rapidity of turnaround and low cost make the development of appropriate computational methodology challenging.

The need for modern predictive methodology appropriate to preliminary design level aerodynamic analyses remains, however. Recognizing the limitations of existing theoretical tools, better computationally based predictive methodology can be devised if one accepts certain underlying assumptions, as discussed in ref. 25.

A method devised to fill the block for a preliminary design level predictive tool in Figure 30 is semi-empirical and relies on two computer programs. The new method is made possible and practical by the existence of the DVM potential flow computer program specifically developed for the analysis and design of multielement high lift configurations described previously.

The second program in the system, is identified as AePP (Aerodynamic Prediction Program). AePP is a highly automated system of bookkeeping, interpolation/extrapolation, scaling and post-processor routines which produce the predictions of global aerodynamic characteristics of a configuration in a subsonic viscous flow.

The structure is based on a framework in terms of potential flow lift curve, pitching moment, induced drag and span loading provided by independent runs of the DVM program, as shown in Figure 31, and provides the engineer with two options:

Option 1: By numerically comparing DVM lifting surface theory predictions on a baseline configuration for which experimental data exists with experimental data, using AePP, the effects of changes in the baseline geometry (e.g., flap span, flap chord, number of flap elements) can be estimated with good accuracy. In this case the full procedure shown in Figure 31 is used.

Option 2: In the case where no explicit baseline experimental data exists, combining generic empirical data stored in AePP with DVM lifting surface theory results for the geometry of the configuration to be evaluated, provides estimates of global aerodynamic characteristics of adequate accuracy for preliminary design purposes.

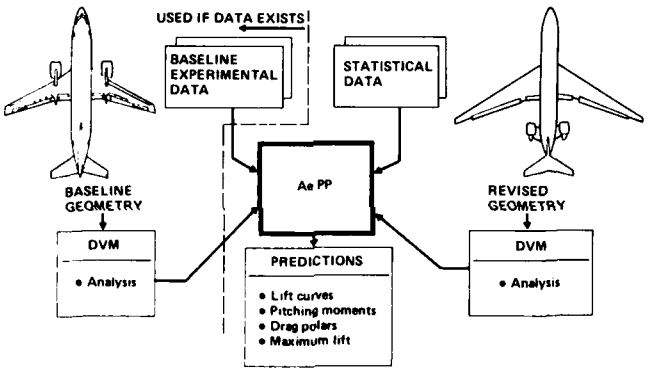


Figure 31. Aerodynamic Prediction Procedure (Low-Speed)

An outline of the overall method and its program elements is shown in Figure 31. How the method works is shown in Figure 32. A complete discussion of the assumptions made and how the empiricism described above is incorporated in the method together with several examples of application are described in ref. 25.

One example from this reference is reproduced here to demonstrate the capability of the basic approach. In this example, Figure 33, wind tunnel data from a Boeing 767 was used to predict the lift, drag and pitching moment (tail-off) characteristics of a Boeing 737-300. The quality of the predictions appear quite acceptable for preliminary design purposes.

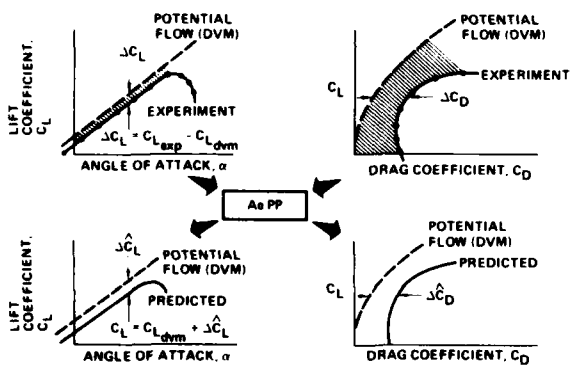


Figure 32. Low-Speed Aerodynamic Prediction Procedure

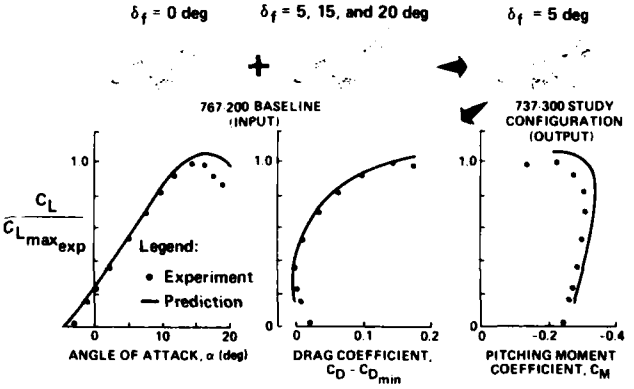


Figure 33. Prediction of a Boeing 737-300 From a 767-200

WAKE VORTICES AND VORTEX/BOUNDARY LAYER INTERACTIONS

An important high-lift problem is that associated with the lift-induced trailing vortices that roll up in the wake of large airplanes and are persistent and sufficiently powerful to be hazardous if other airplanes encounter them before they decay. The problem is most acute in the traffic patterns of

airports, where both aircraft congestion and vortex intensity are greatest and where maximum air traffic control is required. Although it is important to predict such phenomena, and a good deal of research has been devoted to the problem, wake vortex alleviation has up to now not been a factor in high lift system design.

In addition to the classic wake vortex problem, a number of other practical high lift problems associated with the formation and shedding of large scale vortices from various components of an aircraft have been identified. Among these are the effect of large vortices shed from nacelle/strut combinations, strakes, etc., on the aerodynamic characteristics of the wings and empennage, and most particularly the interaction of such vortices with the boundary layer flow on the wing. While in some cases these vortices may be beneficial, in other important cases they may seriously degrade high-lift performance.

The approach to vortex research at Boeing has been the development of predictive technology, and experimental techniques for the measurement of vortex flows. The general objective is to understand and predict the formation, growth and decay of a wide range of large scale vortex flows as they interact with other components of the airframe itself and/or subsequently influence other aircraft in proximity to shed vortex wakes. The ultimate objective is to find means of either controlling the formation or intensity of large scale vortices so that they interact favorably or with minimum penalty with other components of the generating airframe.

Since the state-of-the-art in modeling realistic vortex flows (c.f. Fig 34) is still primitive, particularly in the case where vortices interact strongly with a boundary layer, the majority of the work done so far in this area has been experimental. The emphasis has been on:

- Development and exploition of a number of flow field visualization techniques for the diagnosis of complex viscous/vortex interactions and shed vortex wakes.
- Development of experimental data bases for transport aircraft configurations in high-lift/high angle-of-attack conditions. These efforts have been conducted to:
  - Provide necessary data to validate the extension of codes like PANAIR to analyses of multielement wings.
  - Clarify the physics of vortex formation and interactions as generated by high-lift configurations.
  - Establish an experimental data base with which to compare current efforts to model three-dimensional separated flow.
  - Provide data for wake/downwash prediction at the plane of the empennage, particularly during operation at high-lift/high-angle-of-attack conditions.

A great deal of flow field visualization and diagnostic work has been done ranging from tests in water tunnels to subsonic wind tunnels. The conclusion from tests conducted in water tunnels has been that, while yielding useful results for certain types of configurations (e.g., fighters with wings with sharp leading edges), the low Reynolds numbers typical of such testing make such experiments nearly useless for transport type configurations. A far better approach has been to use flow field visualization techniques recently developed for conventional wind tunnels. These techniques include:

- The Boeing developed Wake Imaging System (WIS) described in ref. 26. Typical WIS total pressure survey data is shown in figure 34 in a black-and-white reproduction. The actual result, obtained in about four minutes of survey time and available immediately, are in the form of color polaroid photographic prints.



Figure 34. Wake Image System (WIS) Survey Behind a High-Lift Wing

- The five port probe (ref.27) which can give survey data similar to the WIS, with the additional advantage that fully quantitative data, three velocity components and total pressure are provided in minimum post run time. This latter technique has been used very effectively to map wakes as shown in Fig 35, and a full discussion of recent test results using this technique is reported in refs. 27 and 28. These experiments have shown good correlation between WIS and five port probe data, both of which also correlate reasonably well with limited laser velocimetry measurements.

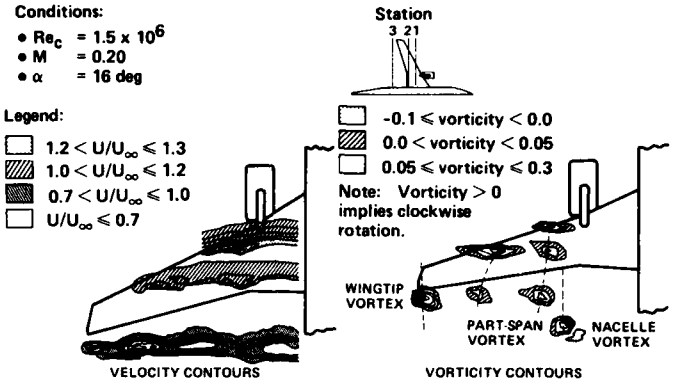


Figure 35. Five-Port Probe Survey Data

The cited references give further details on these flow visualization techniques and some additional results will be discussed in the next section on practical applications.

In an appropriate experimental approach to complex viscous/vortex, separated flow and/or wake problems, it is important to recognize that a "full set" of data is usually necessary, and such a full data set includes forces, surface pressures and both surface flow and flow field visualization. It has been our experience in diagnosing complex flows that given a number of equally experienced interpreters evaluating the same surface flow pattern, one often gets as many interpretations as there are evaluators.

To evaluate the surface flow in a systematic way mathematical topology ("critical point theory") as developed by several investigators has been of considerable value. Critical point theory has the virtues of rapid application, and it clearly establishes which flow interpretations are kinematically feasible.

The technique is well described by Peake and Tobak (ref. 29) and Dallmann (ref 30). A typical result of work due to Brune (so far unpublished) of extensions to high-lift and multielement wing configurations is shown in Fig. 36.

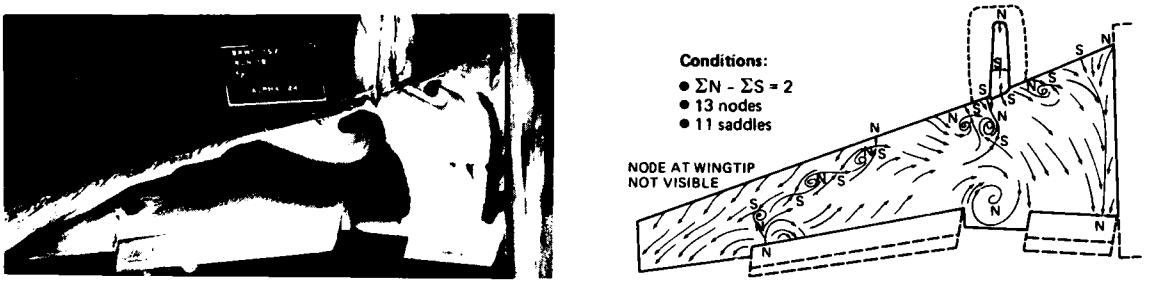


Figure 36. Interpretation of Separated Flow Pattern, Using Critical-Point Theory

SOME APPLICATIONS OF BOEING HIGH-LIFT DESIGN METHODOLOGY

In the preceding sections of this paper a great deal of progress has been reported in the development of improved methodology, both computational and experimental, for the design and analysis of transport aircraft high-lift systems. In order to complete the discussion and to clarify several of the issues raised earlier, two examples of applications of this improved methodology to practical design problems have been selected.

A Redesign of the Boeing 747 High-Lift System

The first example was selected because it demonstrates the way in which the general quasi-three dimensional viscous flow design methodology (Fig 29) with its strong reliance on the use of inverse methods, was used to evaluate a complex design problem. The problem posed was: Given the wing of the existing Boeing 747, is it possible to simplify the triple slotted flap/variable camber Krueger high-lift system without degrading the approach speed. Further constraints were:

(1) The cruise aerodynamic configuration must remain unaltered.
(2) Major structural modification outside the flaps would not be allowed.
(3) Handling characteristics should not be degraded.

As shown in Fig. 37, the baseline geometry was first analyzed in potential flow using the DVM Lifting Surface Theory. This yielded the span loads at various values of lift coefficients. From the span loads, the "critical 2D sections" were selected and evaluated using the 2D multielement airfoil code SASS. These results corrected for sweep are shown in Fig. 38. Additional information obtained from these analyses are viscous flow pressure distributions and details of the boundary layer characteristics. At this point one has the basic data necessary to begin the redesign effort.

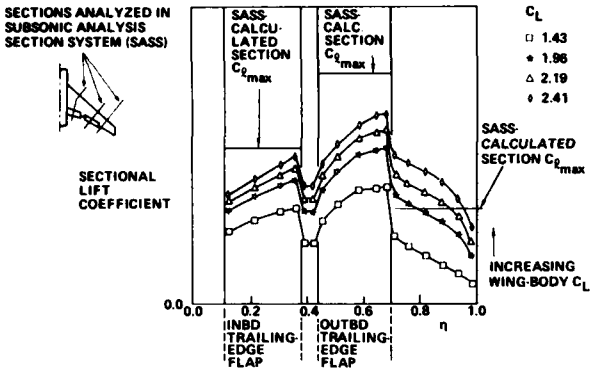


Figure 37. Spanloading on Baseline 747-200, Flaps 30, Calculated With SASS

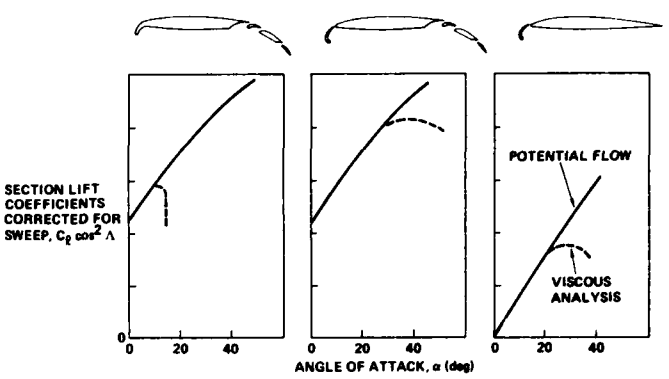


Figure 38. SASS-Calculated Sectional Lift Curves, $\delta_f = 30$ deg

Using the 2D inverse boundary layer method, improved viscous flow pressure distributions are derived for the various elements of the multielement airfoil ensembles. These design point pressure distributions are then used in the inverse mode of the SASS program to generate new airfoil geometries. These new geometries are a combination of revised surface contours and/or modified flap gap, overlap and deflection relationships.

With the new geometry established, these sections are analyzed in the SASS program to obtain full section lift curves, including the effects of flow separation from one-or more airfoil element. Typical final results are shown in Figures 39.

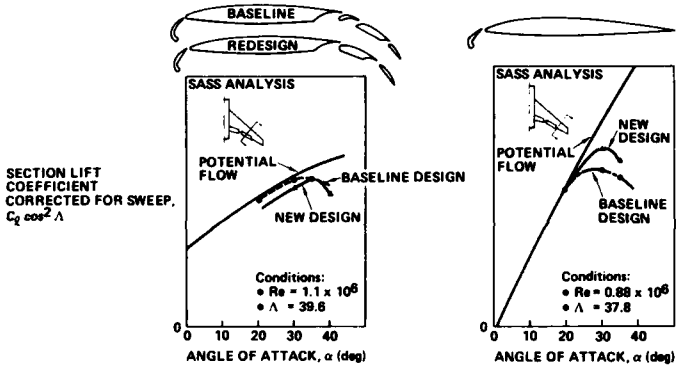


Figure 39. SASS Analysis of Baseline and Redesigned Flaps

As a final step, if the resulting new geometry differs substantially from the baseline case, a reevaluation of the total high lift systems in the DVM program can be conducted to assure that a "converged" design solution has been achieved and this data can be used to estimate the new wing/body maximum lift coefficient and/or lift-drag ratio.

An interesting result of the present example is shown in Fig. 39. The new double slotted flap does indeed yield the same section maximum lift coefficient as the baseline triple slotted system but more important however, at a given angle of attack the lift coefficient is lower for the redesigned system than for the baseline. This means that the net result of integrating this revised section into the system would be that the aircraft would have to approach at higher angles-of-attack to maintain the same approach speeds. In practice this is not possible due to tail strike limitations. For this reason, the results of this particular exercise remain of largely academic interest and the new configuration was not tested. The example does demonstrate clearly, however, the power of the new analytic approach to high-lift design.

Transport Aircraft Maximum Lift Performance Improvement

The second application example to be discussed is of interest for several reasons.

1. Both wind tunnel and flight test validation results exist.
2. The full computational methodology previously described was applied to a difficult flow problem involving a complex airplane geometry.
3. While the computational methods alone were inadequate to cope with the full problem, when used to augment and guide the wind tunnel testing, they provided the crucial element in achieving a difficult aerodynamic goal.
4. An approach to partially circumvent some major limits of conventional low Reynolds number testing in high-lift system development was demonstrated. This approach can only be pursued efficiently by application of computational techniques.

The objective was to retrofit the basic Boeing 707 airframe with four large diameter high-bypass ratio turbofan engines with minimum modification to the remainder of the airframe and without an off-design (i.e., low-speed) performance penalty. The new nacelles were compatible with the baseline airframe, provided the nacelle struts of the new installation were shorter than those of the baseline, resulting in the nacelles being placed in closer proximity to the wing. Wind tunnel tests comparing the baseline and retrofit airplanes showed no low-speed performance penalty. Corresponding flight tests showed a 10

percent loss in airplane maximum lift capability. The comparison results are shown in Figure 40. Further, based on low Reynolds number wind tunnel force data alone, there appeared to be no obvious experimentally derivable aerodynamic fix.

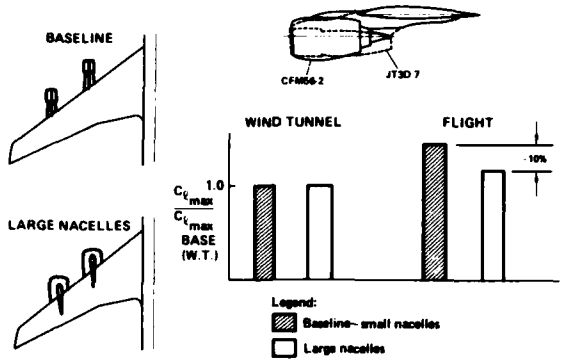


Figure 40. Nacelle Influence on $C_{\ell_{max}}$

The puzzle regarding the cause of the lift loss was solved by additional wind tunnel testing with particular emphasis placed on carefully documented flow visualization. Nacelle-on and -off tests clearly showed (Fig. 41) that flow separation occured on the sides of the large diameter nacelles at high angles of attack and high flap deflection conditions, leading to the formation of large vorticies which flowed streamwise over the wing. While the section characteristics of the wing were very strongly Reynolds number scale dependent, the paths and strength of the nacelle shed vortices were almost scale independent as a comparision with flight test showed (fig 42). Further, under certain conditions, the vorticies interacted in an unfavorable way with the boundary layer on inboard sections of the wing downstream. As a result, at wind tunnel Reynolds numbers, the maximum lift characteristics of the wing were dominated by the outboard section characteristics. At flight level Reynolds numbers, the outboard wing sections benefited from the increased Reynolds number so that maximum lift was limited by the unfavorable inboard wing boundary layer/nacelle vortex interaction. Thus, the two configurations, both with identical wings and high-lift systems, exhibited almost equal maximum lift performance in the wind tunnel, but not at flight conditions. Subsequent analysis of the wing using the quasi-3D viscous analysis approach described earlier further validated and clarified this diagnosis.

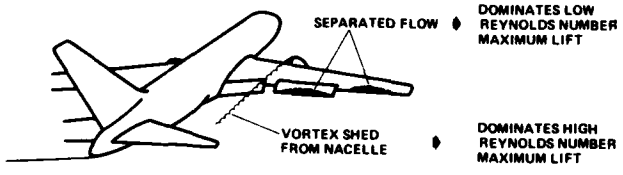


Figure 41. Stall Mechanisms at High and Low Reynolds Number



Figure 42. Nacelle Vortices

Thus, the puzzle was solved, but the problem was not. Having observed that the wind tunnel, using a model which carefully simulated the full scale geometry of the proposed configuration, could not duplicate the necessary flow phenomena, the traditional approach would be to embark on an expensive and time consuming flight test program, with the fear that a substantial revision of the baseline high-lift system might prove to be the only satisfactory solution. However, with the availability of computational tools, a quite different approach became feasible.

This approach was to simulate the full scale aerodynamics, rather than the full scale geometry in defining the parts of the wind tunnel model. While conceptually appealing, this course is almost impossible to follow unless one has sufficiently powerful computational tools with design capability.

In the case under discussion, the full scale simulation was rather crude but extremely effective. Having determined both by flow visualization and analysis that the low Reynolds number stall characteristics were driven by outboard wing section characteristics, it was a straightforward procedure to design an alternate, non-standard, leading edge device (Fig. 43) which could be fitted to the outboard wing of the wind tunnel model. In this way, the outboard wing behaved at wind tunnel Reynolds number very much like the full scale wing did in-flight, i.e., nacelle vortex/wing boundary layer interactions determined the stall in the wind tunnel.

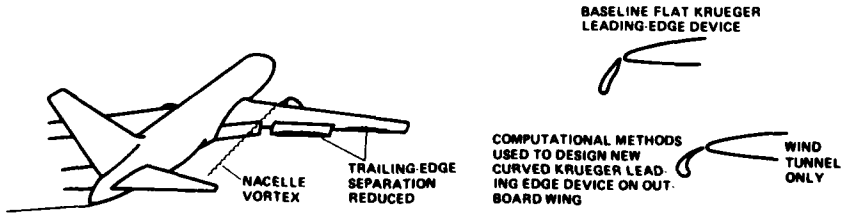


Figure 43. Wind Tunnel Test To Find Solution

Having adjusted the wing's stall patterns in the wind tunnel, attention turned to the necessary modifications of the nacelles to improve the maximum lift performance. Additional reliance on flow visualization utilizing the wake imaging system lead to development of a set of nacelle mounted vortex control devices (VCDs) which finally solved the problem without further change to the baseline high-lift system. These devices were subsequently flown on the full scale airplane with satisfactory results, as shown in Figure 44.

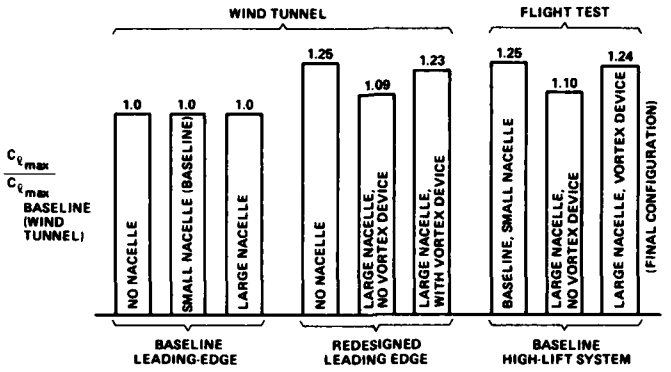


Figure 44. Maximum Lift Comparisons

CONCLUDING COMMENTS

An outline of low-speed/high-lift aerodynamic research at Boeing, and the quasi-3D viscous flow computational methodology developed for the analysis and design of transport high-lift systems was presented. To demonstrate the overall utility of this methodology, two examples of its application to practical, project oriented design/analysis problems were described. The important conclusions to be drawn from these examples are:

1. Modern high-lift computational methods have become sufficiently well developed to allow a designer to use these new methods in a greatly improved (compared to experimental/analytical cut-and-try) design process.

2. Since, in the forseeable future, management cannot be expected to make decisions which risk millions of dollars based solely on "analytic wind tunnel" results, the objective of a practical research effort must be to derive computational tools which will both augment and improve the efficiency of what remains an experimental process. With the parallel development of improved flow visualization techniques, the experimental process has been advanced as well.

3. The role of the wind tunnel will change as computational methods of increasing power become available. Much routine parametric evaluation can now be conducted with the computer, with the wind tunnel acting as both the vehicle for visualization of complex flows and the final arbiter of predicted results. Thus theory and experiment form a necessary complementary pair.

4. Modern computational methods now allow the high-lift system designer to do many of the things that were once conceptually possible, but impractical due to either lack of physical understanding or budget limitations. Both computational exercises described and the modeling of "full scale" aerodynamics rather than full scale geometry in the wind tunnel, are examples of these emerging capabilities.

5. Most of the work described in this paper has related to transport aircraft with unpowered high-lift systems. Much of the technology described (most particularly the improved flow visualization techniques) is fully applicable to military aircraft and powered lift concepts. As the methodology described matures, attention will logically be devoted to extending these kinds of capabilities to the full range of future high-lift schemes.

It would be satisfying to be able to say that we limited ourselves to unpowered high-lift systems due to the large volume of material available and that a comparable paper could be written on powered-lift systems. Unfortunately this has not been the case. Despite the flurry of activity in powered-lift in the early to mid-1970's, as evidenced by the flight of four different powered lift airplanes only limited analytical development has been undertaken. This is still a largely virgin territory awaiting the inspired researcher.

While the above comments are specific to the Boeing high-lift effort, it remains to make some more general observations relating to the issues identified in the introduction of this paper. Central of these was the question of the tools available to the high-lift designer and those which remain to be developed. Many of the aspects of this question have been addressed in previous sections of the paper and need not be summarized again here. One matter of interest does deserve attention here however.

At the conclusion of his Wright Brothers Lecture A.M.O. Smith left us with his list (circa 1974) of the ten pressing theoretical problems in high-lift aerodynamics. In light of the progress reported in this paper, it is of interest to review these ten issues and comment on the progress made on each in the intervening period. We may then propose a new list of our own.
A.M.O. Smith's list was as follows:

1. Very general calculation of three-dimensional laminar and turbulent flows.
   This must stand as an important on-going effort despite years of effort and advance. It should be noted that success in this area is still strongly coupled to our ability to solve the inviscid flow portion of the problem and here the complexity of the geometry of practical

aircraft high-lift systems still presents major obstacles both aerodynamically and in geometry definition. The capability to predict trailing edge separation on three-dimensional configurations is also emerging, but the capability to predict vortex/boundary layer interactions remains very primitive.

2. Calculation of flows involving partial separation in the rear.
   Here great progress has been made in 2D flows (c.f. Henderson, ref. 20, Bristow, ref. 31, and Mani, ref. 32). This is an area where much progress may be made in the near term in three dimensional flow without recourse to solution of the full Navier-Stokes equations.

3. Practical calculation of flows involving forward separation bubbles.
   Much detail work remains to be done in this area. While apparently a mere footnote to the overall high-lift problem, as long as wind tunnel tests continue to be conducted at "low" Reynolds numbers, the capability to predict the formation and effect of laminar separation bubbles remains an important, imperfectly developed, capability.

4. Practical calculation of flows involving shock-boundary layer interactions.
   Slow, but steady progress has been made on this fundamental problem (ref. 33) but its relevance to the low-speed high-lift problem would seem obscure. "Supercritical" leading edge devices on transport aircraft are items to be avoided in our experience.

5. Calculations of viscous flow around the trailing edges of wings and bodies.
   Despite the work of, for example, Melnik (ref. 34) this problem remains to be fully resolved and remains, as it did for Smith a decade ago, a major annoyance.

6. Further development of inverse methods.
   Substantial progress has been made for 2-D cases. For 3-D the PANAIR technology has great promise. It may also be noted that development of such methods is less than half the problem. Teaching engineers, accustomed to "design by repetitive analysis" to use inverse methods effectively is as large a problem and requires a great deal of further understanding and education.

7. Drag of multielement airfoil systems.
   Squire and Young still reign in this area and progress of real substance remains to be made.

8. Practical calculation of merging boundary-layers, wall jets and wakes.
   With the completion of the combined theorical/experimental work by Brune (ref 16 & 19) reported here, this problem seems to have reached the state-of-the-art in overall 2D viscous flow computational capability. Having done the work we observe that it may have been a problem of limited priority in retrospect. Analytic gap/overlap studies are nearly as expensive to perform computationally as experimentally, and aside from evaluating the adverse effects of imperfectly sealed slats, etc, the analysis capability is of rather limited utility.

9. The analysis of flows over swept wings on which a leading-edge vortex is developed.
   This is a major area of interest and substantial progress has been made for highly swept wings with sharp leading edges. For moderately swept wings with rounded leading edges where vortices are less well defined much work remains to be done.

10. Three-dimensional transonic calculations, particularly for arbitrary wing and wing body conbination.
    Very great progress has been made here, largely with reference to cruise configurations. This topic is not within the scope of the present paper and it seems to us of less relevance for transport type high lift systems.

In quick summary then we see a decade's progress. It remains only to propose a menu of our own for further work. Our shopping list is as follows:

1. Very general calculation of three-dimensional laminar and turbulent boundary layers.
2. Computation of three dimensional separation,
3. Drag of multielement wings.
4. Further development of inverse methods.
5. Wake and downwash prediction from 3D multielement configurations.
6. Vortex/boundary layer interactions.
7. Propulsive lift analysis.
8. 3 D flow visualization and measurement techniques.
9. Modeling of swept wing leading edge flow with separation
10. Analytical buffet prediction

Further comments on the above list seems superflous in light of the preceding discussions and the authors want to end this paper with the hope that the coming ten years will show as spectacular progress as the last ten.

REFERENCES

1. Smith A.M.O., "High Lift Aerodynamics", Journal of Aircraft, June 1975, pp. 501-30.

2. Smith A.M.O., "Aerodynamics of High-Lift Airfoil Systems", in Fluid Dyanmics of Aircraft Stalling, AGARD CP-102, April 1972.

3. "High Lift Selected Concepts", NASA CR 159093, August 1979.

4. Sullivan, R.L., "The Size and Performance Effects of High Lift System Technology on a Modern Twin Engine Jet Transport", AIAA Paper 79-1795, August 1979.

5. Lissaman, "Applied Aerodynamics of V/STOL", Short Course Notes, presented at Washington University, St. Louis Missouri, April 1970.

6. Helmbold, H.B., "Limitations of Circulation Lift"., Journal of Aeronautical Sciences, Vol. 24, No.3, March 1957.

7. Foster, D.N., "A Review of the Low-Speed Aerodynamic Characteristics of Aircraft With Powered Lift Systems", in Prediction Methods for Aircraft Aerodynamic Characteristics , AGARD-LS-67, May 1974.

8. Loth, J.L. and Boasson, M., "Circulation Controlled STOL Wing Optimization", Journal of Aircraft, February, 1984, pp. 128-34.

9. Liebeck, R.H., "Design of Airfoils for High Lift", AIAA Paper 80-3034, March 1980

10. Johnson, F.T., "A General Panel Method for the Analysis and Design of Arbitrary Configurations in Incompressible Flow", NASA CR-3079, 1980.

11. Goldhammer, M.I., "A Lifting Surface Theory for The Analysis of Non-Planar Lifting Systems", AIAA Paper 76-18, Jan. 1976.

12. Lovell, D.A., "A Wind Tunnel Investigation of the Effects of Flap Span and Deflection Angle, Wing Planform and a Body on the Performance of a 28^{o} Swept Wing", RAE Report CP No. 1372, 1977.

13. Steven, W.A., Goradia, S.H. and Braden, J.A., "Mathematical Model for Two-Dimensional Multicomponent Airfoils in Viscous Flow", NASA CR-1843, July 1971.

14. Brune, G.W. and Manke, J.W., "An Improved Version of the NASA/Lockheed Multi-Element Airfoil Analysis Computer Program", NASA CR-145323, March 1978.

15. Brune, G.W. and Manke , J.W., "Upgraded Viscous Flow Analysis of Multi-Element Airfoils", NASA CP2045, Pt. 1, March 1978.

16. Brune, G.W., "Theoretical Predictions of Confluent Boundary Layers," Proc. Third Symposium on Turbulent Shear Flows, Davis, Calif. Sept. 1981.

17. Jones, W.P. and Launder, B.E., "Prediction of Low-Reynolds Number Phenomena with a Two-Equation Model of Turbulence, "International Journal of Heat and Mass Transfer, Vol. 16, 1973.

18. Brune, G.W., Sikavi, D.A., Tran, E.T. and Doerzbacher, R.P., "Boundary Layer Instrumentation for High-Lift Airfoil Models," AIAA Paper 82-0592, March 1982.

19. Brune, G.W. and Sikavi, D.A., "Experimental Investigation of the Confluent Boundary Layer on a Multielement Low Speed Airfoil", AIAA Paper 83-0566, Jan. 1983.

20. Henderson, M.L., "Two-Dimensional Separated Wake Modeling and its Use to Predict Maximum Section Lift Coefficient," AIAA Paper No. 78-156, January 1978.

21. Henderson, M.L., "Inverse Boundary Layer Technique for Airfoil Design", NASA CP 2045, Vol. I, March 1978.

22. McMasters, J.H. and Henderson, M.L., "Single Element Airfoils Synthesis," NASA CP2086, Vol. 1, June 1979.

23. Lock, R.C., "Equivalence Law Relating Three-and Two Dimensional Pressure Distribution," ARC R&M 3346, May 1962.

24. McMasters, J.H. and Henderson, M.L., "Some Recent Applications of High-Lift Computational Methods at Boeing", Journal of Aircraft, January 1983, pp 27-33.

25. Murillo, L.E. and McMasters, J.H., "A Method for Predicting Low-Speed Aerodynamic Characteristics of Transport Aircraft", Journal of Aircraft, March 1984, pp. 168-74.

26. Crowder, J.P., "Quick and Easy Flow Field Surveys", Aeronautics and Astronautics October 1980.

27. Hallstaff, T.H. and Brune, G.W., "An Investigation of Civil Transport Aft Body Drag Using a Three-Dimensional Wake Survey Method", AIAA Paper 84-0614.

28. Sunseri, M.C., Seetharam, H,C., and Mack, M.D., "Flow Field Studies of a Transport Airplane", AIAA Paper 84-0012, January 1984.

29. Peake D.J. & Tobak, M., "Three-Dimensional Interactions and Vortical Flows with Emphasis on High Speeds", AGARDograph No. 252, 1980.

30. Dallmann, U., "Topological Structures of Three-Dimensional Vortex Flow Separation", AIAA Paper 83-1735, July 1983.

31. Bristow, D.R., "Development of Panel Methods for Subsonic Analysis & Design", NASA Contractor Report 3234, February 1980.

32. Mani, K.K., "A Multiple Separation Model for Multi-Element Airfoils"AIAA Paper 83-1844, July 1983.

33. Oskam, B., "Transonic Panel Method for the Full Potential Equation Applied to Multi-Component Airfoils", AIAA Paper 83-1855, July 1983.

34. Melnik, R.E., "A Survey of Turbulent Viscid/Inviscid Interaction Theory in Aerodynamics", AIAA Paper 84- Presented at AIAA Aerospace Sciences Meeting, Reno, Nevada, January 1984.

AD-P004 060

An Update of the Canada/U.S.A. Augmentor-Wing Project

by

D. C. Whittley

Program Manager: Advanced Research and Technology

the de Havilland Aircraft of Canada, Limited
Downsview, Ontario, Canada M3K 1Y5

1.0 INTRODUCTION

According to the published guidelines "it is intended that this symposium bring together the practioners of various applications of boundary layer control with those interested in the underlying fluid mechanics for the purpose of mutual learning". This paper presents some views of a practitioner from the perspective of powered lift in which a substantial proportion of engine thrust is devoted to augmentation of wing lift. As such, control of the boundary layer takes place in rather a macroscopic way due largely to entrainment of secondary flow into a powerful jet or jet sheet.

The Augmentor-Wing powered lift concept has been the subject of investigation jointly by Canada and the United States since the late sixties. Following extensive tests of a half scale model in the NASA, Ames 40' x 80' wind tunnel, a decision was made to design and build a minimum cost flight demonstrator based on the de Havilland Buffalo airframe. (Figure 1). This technology demonstrator aircraft first flew in 1972 and subsequently underwent trials at NASA, Ames accumulating a total of 650 flying hours.

Following completion of the NASA trials in 1980, work has continued in Canada covering four main areas of interest:

- additional flight trials on the technology demonstrator aircraft,
- propulsion system development,
- experimental investigation of a new compound supercritical airfoil,
- project definition studies.

The paper touches briefly on these four topics expanding more so in areas likely to be of interest to the Fluid Dynamics Panel.

2.0 DESCRIPTION

A powered lift STOL transport differs from one which relies solely on passive lift (such as the de Havilland Dash 7) in four fundamental ways, all of which relate to steep gradient approach at low speed:

(1) Power for approach is set at 50 to 60% of maximum thrust available as compared to idle approach power with a passive flap.

(2) Forward components of thrust are nullified (by vectoring, by variable pitch fan or by bucket type reversers) to achieve a steep gradient approach.

(3) Restoration of forward thrust (e.g. by vectoring) becomes an essential part of the wave-off manoeuvre.

(4) A large imbalance in roll is likely to occur in the event of engine failure.

Wave-off following engine failure represents a particularly difficult combination (Figure 2).

Generally, in the case of External Blown Flap (EBF) or Upper Surface Blowing (USB), integration of engine thrust and flap serves both to augment wing lift by supercirculation and to vector thrust for steep gradient approach. However, since the entire thrust of the engine is devoted to flap blowing, it follows that the flap must be partially retracted to re-vector thrust for wave-off and a substantial transient loss of wing lift is unavoidable. Again, wave-off with one engine failed is difficult, especially in combination with a large roll imbalance: in the case of the YC-14, flap retraction on the "live wing" is necessary to achieve roll balance causing a further lift loss. Such issues are important when considering the airworthiness of powered lift aircraft.

The Augmentor-Wing internally blown system attends to some of these issues by having separate control over the propulsive and blowing components of thrust and by introducing cross-ducting to eliminate roll upset in the event of engine failure. Thus, at constant engine speed, lift of the blown flap may be considered as equivalent to that of a passive flap, whereas thrust vectoring (or V.P. fan) can be used to modulate forward thrust in lieu of the throttle. Hence the characteristics and mode of flight can be related to the conventional and thereby correlated directly with existing airworthiness rules.

The Augmentor-Wing concept is comprised of four elements in all:

- A propulsion/blowing engine (Figure 3) which delivers about one third of total thrust for wing lift augmentation.

- An effecient ejector flap (Figure 4) which generates high lift by supercirculation and which serves also to augment nozzle thrust. Thus, in combination with thrust recovery, thrust margin for takeoff is substantially increased (this being especially important for climb-out with one engine inoperative).

- Ducting which supplies blowing air to the wing to maintain roll balance in the event of engine failure and to enhance control power at low flight speeds by means of the augmentor choke (Figure 5).

- A thick supercritical compound airfoil otherwise known as a cruise augmentor flap (Figure 6).

3.0 FLIGHT TRIALS

Early in 1980, a team from the National Aeronautical Establishment assumed operational control of the Buffalo/Spey research aircraft at NASA, Ames and in 1981 flew the aircraft to their own laboratory located in Ottawa. A new central data computer was installed by NAE to replace the Sperry STOLAND unit which had been retained by NASA for other use.

The new computer unit restored the longitudinal SAS, the speed hold system and the controls integration capability. In broad terms, speed hold is achieved by modulation of (Pegasus type) nozzle angle whereas glide path tracking can be improved by controls integration, such as throttle into choke or pitch attitude into choke with a transient wash-out. Important handling qualities experiments were carried out in Canada but are considered outside the direct interest of the Fluid Dynamics Panel.

Following check-flights by NAE in the summer of 1982, the aircraft was handed over to de Havilland for further evaluation. Two series of tests each of 2½ months duration have taken place at Canadian Forces Base, Mountain View, Ontario. Some of this work is reviewed in Reference 1. Three subjects have been selected for comment, one relating to powered lift stalling characteristics, another to the maximum effort takeoff performance with vectored thrust and a third to no-flare landing techniques.

3.1 Powered Lift Stall

Suction generated by the augmentor flap serves to establish a spanwise line of low pressure at about 60% of the chord. This acts as a powerful means to prevent flow separation in a macroscopic fashion since an entire layer of upper surface flow is accelerated and ingested by the ejector. Half scale model tests in the NASA Ames 40' x 80' wind tunnel showed that onset of stall occurs at the wing/fuselage junction at about $\alpha = 20^{o}$ and is confined to that general region well beyond peak lift at an angle of attack in excess of 30^{o}. The model was equipped with a blowing slot across the upper surface of the fuselage located at about 10% chord: this was designed to suppress flow separation at the wing root and encourage lift "carry-over". In the wind tunnel,tests were conducted with and w ithout body blowing on both straight and swept wings. Results were as follows:

- On the straight wing at high C_J, body blowing gave a small increase in lift for $\alpha > 20^{o}$, a small increase in $C_{L_{max}}$ of order 0.3 and generally a smoother lift curve at high α. The wing and body was tufted liberally: at a yaw angle of 10^{o} (say) and body blowing off, the tufts became quite agitated whereas with body blowing, the tufts remained smooth generally over the whole model.

- On the swept wing, body blowing was shown to have no effect. Lift curves were smooth to high α, and the lift peak was quite flat: maximum lift was slightly greater for the swept wing at the same level of blowing coefficient.

To minimize risk, it was decided that body blowing (accounting for 7% of the blowing flow available) would be fitted to the research aircraft. If, as suspected, the benefit is indeed quite small, it follows that this flow could be put to better use in a future design. Thus it became important to determine the effect of body blowing by flight test. Accordingly, modifications were made to remove this flow from the fuselage and discharge it through a plain propulsion nozzle at the rear. Stalls and steady sideslips were performed both with and without body blowing. At a weight of about 43,000 lb., tests were conducted at 8000 to 10,000 ft. with flaps 65^{o}, nozzle angle 80^{o} and engines at 94% rpm. Minimum speed occurred at 43 to 45 kt. depending upon weight. In the same configuration, steady sideslips were performed at 65 kt. to a maximum of 15^{o}. It was found that removal of body blowing had no discernible effect on stalling speed or handling qualities in steady sideslip.

3.2 MAXIMUM EFFORT TAKEOFF

Flight trials at NASA Ames focussed upon glide path tracking for a steep gradient $7\frac{1}{2}^{o}$ STOL approach followed by flare and touchdown so that the effect of thrust vectoring on takeoff performance remained enexplored. Tests were planned to determine the optimum combination of flap and vector angle to minimize takeoff ground roll.

Standard takeoff flap is 20^{o} with a thrust vector angle of 6^{o}: ground roll is in the order of 750 ft. and distance to 50 ft. is about 1250 ft. It was found that flap 40^{o} with nozzles at 36^{o} gave a minimum ground roll of 350 ft. to lift-off and about 850 ft. at the 50 ft. screen height. In this latter case, speed at the start of rotation was 50 kt. EAS, lift-off speed was 53 kt. EAS with a peak rotation rate of nine degrees/second. Figure 7 presents a time history of this particular takeoff.

3.3 LANDING

Performance and technique for landing without flare were explored in the Canadian trials. At W = 40,000 lb, flaps 70^{o} and nozzles at 60^{o}, it was possible to capture a $4\frac{1}{2}^{o}$ glide slope at $\alpha = 6^{o}$ giving a slight nose-up attitude for nose wheel clearance at touchdown: the corresponding $C_{L_{app}} = 3.9$.

For a given wing loading, approach speed is a good indicator of the degree of powered lift. It is of interest to determine the levels of blowing thrust loading ($TB/_S$) and blowing thrust to weight ratio ($TB/_W$) for the above case and then to extrapolate to a value of wing loading more in keeping with an advanced tactical transport while holding wing area and blowing coefficient constant, at 865 sq.ft. and 0.59 respectively.

In the table below, line one relates to the experimental flight case, line two to a transformation of the research aircraft in which lift coefficient is adjusted to account for changes in wing geometry and removal of body blowing, and line three to an increase in weight to raise (or to increase) wing loading to 90 lb./sq.ft. as for a typical advanced STOL transport. It can be seen that for W/S=90, an approach speed of 78 kt. requires that TB/W = 0.136 and TB/S = 12.23. The former ratio provides some measure of powered lift efficiency whereas the latter, the relative ease of duct accommodation in the wing.

	DESCRIPTION	AR	t/c	W lb.	Vapp kt	$TB/_S$	$TB/_W$
1	Experimental Case	7.2	0.16	40,000	60	7.17	.155
2	New wing less body blowing	12	0.21	45,600	60	7.17	.136
3	Increase in weight	12	0.21	77,850	78	12.23	.136

4.0 PROPULSION

Control of boundary layer for high lift is generally achieved not by suction but by blowing - for wing flaps, for leading edge devices or for control surfaces. Even for supplementary purposes, the quantity of flow is generally such that it cannot be removed from the HP compressor without a significant loss in engine performance (especially for high bypass ratio). Thus it becomes advantageous to consider an engine having an oversize intermediate compressor to generate a blowing source at a pressure ratio of about three.

For high lift systems such as jet flap (requiring a significant proportion of total thrust) it is possible to separate the hot and cold streams of a low bypass engine as was done for the Buffalo/Spey research aircraft. This procedure may find application for a high performance powered lift fighter aircraft but is less well suited for transport type aircraft on account of high noise level and poor fuel consumption at low altitude. Again, the need arises for a high bypass engine which generates blowing air as part of the basic engine cycle.

To meet the need, Rolls-Royce has proposed the RB419 series of propulsion/blowing engines. Furthermore, it has been shown possible to synthesize one such engine using existing components with the Spey 202 as core, the TF-41 fan as intermediate compressor and the Dowty/Rotol variable pitch fan as a single stage LP compressor. This engine, known as the RB419-03, generates three streams:

(1) low pressure bypass stream
(2) intermediate pressure blowing stream
(3) residual hot core stream.

Tabulated data for the RB419 are given below,whereas Figure 8 shows the variation of non-blowing thrust versus blowing thrust: growth potential is of the order 20% based on uprating of the core.

The engine provides separate thrust for propulsion and blowing with the ability to modulate the propulsive or forward thrust while maintaining constant blow, as described earlier. In the overall, it does appear that the propulsion/blowing engine will become the generic type for powered lift transport aircraft just as the vectored thrust Pegasus engine has become for combat aircraft.

RB419-03 LEADING PARTICULARS

Parameter	Takeoff ISA SLS	Cruise 36,000 ft Mach 0.7
Thrust (lb)	18,200	3,930
Sfc (lb/hr/lb)	0.425	0.700
Mass flow (lb/sec)	671	280
Overall pressure ratio	18.4	21.7
Blowing mass flow (lb/sec)	147	59
Blowing pressure ratio	2.6	3.8

5.0 THE CRUISE AUGMENTOR FLAP

The cruise augmentor flap is a supercritical compound section designed to operate at high subsonic speed with ejector blowing. Interest in the configuration arose from a desire to simplify the Augmentor-Wing STOL concept by eliminating the need both to divert blowing flow and close down the flap elements for cruise while, at the same time, to gain some aerodynamic advantage. In particular, it was thought that drag rise Mach number could be delayed by achievement of aft loading on the upper shroud (by virtue of the powerful mid-chord control of boundary layer) and that propulsion efficiency could be improved on account of boundary layer ingestion by the ejector itself. Also it was thought that the compound section would operate satisfactorily for quite large values of thickness/chord (say 20% or more) and provide an improvement in buffet boundary due to blowing (jet flap effect). Recovery of pressure toward the trailing edge of the upper surface (with consequent thickening of the boundary layer) is of special concern in the design of supercritical airfoils (Figure 6). This concern is alleviated somewhat for the compound section in that recovery takes place in two stages, first to the ejector throat where pressure is substantially less than that at the trailing edge and secondly within the ejector itself where the remaining pressure rise takes place in a controlled manner. A family of compound airfoils is shown in Figure 9.

Experimental work was undertaken,both 2-D (NAE 5' x 5' tunnel) and 3-D (NASA, Ames 11' x 11' tunnel), on an 18% $t/_c$ section. Test results confirmed the expectations listed above and provided further understanding as follows:

- The compound airfoil operates well with or without blowing.
- The section is very tolerant to off-design operation having a very flat C_D vs C_L characteristic.
- Tight control of the boundary layer at mid-chord ameliorates drag creep with Mach number as M_D is approached.
- Pressures on the shroud upper surface remain essentially constant throughout the α range,thus shroud shape can be determined to satisfy requirements at the design point with no fear of flow separation or shock wave formation at higher α. Similarly in the region of drag rise, shock waves form first on the main body, not on the shroud.
- A thickness increase from 0.18 to 0.24 resulted in essentially no drag penalty (at the corresponding design point and below drag rise).

- Leading edge devices are not needed at low speed/high lift on account of the large leading edge radius of these thick sections.

Based on in-house test data, some comparisons are presented between a 16% $t/_c$ plain supercritical airfoil and the compound section at 18% and 24% $t/_c$.

5.1 BUFFET BOUNDARY

Wing buffet was found to correlate well with "drag break". The latter was more readily available and could be defined more precisely and was therefore taken as the limit of useable lift. Figure 10 shows a substantial advantage for the 18% $t/_c$ compound section as compared to the 16% plain foil. The flight boundary improves further with ejector blowing.

Taking M = 0.66 as the design speed for the 24% $t/_c$ section, it displays an advantage of $\Delta C_L = 0.15$ as compared to the corresponding compound foil at 18% $t/_c$.

5.2 DRAG

Interest surrounds level of drag and the point of drag rise. Drag creep characteristics of the plain and compound sections differ substantially so that conventional methods for defining drag rise Mach number are of little value; therefore comparisons have been made on the basis of drag level at the cruise design point which is more meaningful in any event.

Both 2-D and 3-D test data are available in-house for airfoils with C_L (design) = 0.35 whereas for C_L (design) = 0.6, only 2-D data exist. The variation of design Mach number with thickness was taken as follows:

Thickness/chord ratio	0.16	0.18	0.24
Design Mach number	0.725	0.70	0.66

5.2.1 Two-Dimensional Test Data

The NAE 5' x 5' wind tunnel is equipped with wall inserts to form a two-dimensional working section for testing at high subsonic speed. Typically, the model Reynolds number is about 20×10^6.

On the left, Figure 11 shows the variation in drag at $C_L = 0.6$ for three foils with the corresponding design Mach number shown for each. At low Mach number without blowing, the compound sections exhibit a higher level of drag (compared to a conventional foil) but show less drag creep at high Mach number. At the respective cruise design points, the drag 'evel of all three airfoils is essentially the same: this point is examined in more detail in Figure 12 where drag (at design point) is plotted versus thickness/chord ratio. It is shown that increase in drag with thickness is very small for the compound section which implies that the boundary layer has been controlled effectively even at 24% $t/_c$.

Blowing has been shown to reduce effective drag where $C_{D_{eff}} = C_{D_{measured}} + C_J$ (nozzle) and C_J (nozzle) = measured nozzle static thrust (shrouds off) ÷ qS,
for example, Figure 11 shows that the skin friction penalty of the compound foil is partially offset in the mid-Mach number range, whereas for $M < 0.5$, a net benefit results.

Figure 13 illustrates the off-design tolerance of the 24% $t/_c$ compound section. Although designed for M = 0.66 and $C_L = 0.6$, drag increase is very small even at $C_L = 0.75/0.80$. On a typical aircraft of aspect ratio 12,this equates to a cruise $L/_D$ correspondingly higher by about 10%.

5.2.2 Three-Dimensional Tests

Test data were available for a reflection plane model having a compound section (18% $t/_c$ root to tip) and a full span model having a conventional section (16% $t/_c$ at the root, 13% $t/_c$ at the tip). Design lift coefficient in each case was 0.35.

Equivalent profile drag for the 3-D tests was obtained in the usual manner by subtracting the "ideal" level of lift dependent drag ($C_L{}^2/\pi A$) from balance drag. This procedure results in a level of profile drag somewhat higher than the true 2-D value. On the right of Figure 12 it is again shown that drag of plain and compound foils are comparable at the design point. The figure illustrates once more the off-design tolerance of the compound section with the attendant opportunity to cruise at higher C_L for improved $L/_D$.

6.0 PROJECT STUDIES

A substantial experimental data base has been established as a result of the joint Canada/USA powered lift research program. De Havilland is currently under contract to the Canadian government (Department of Industry, Trade and Commerce) to conduct application studies and to carry out additional experiments. In particular, project studies have been undertaken on a powered lift STOL transport and a sea based support type aircraft capable of short takeoff and vertical landing.

6.1 POWERED LIFT STOL TRANSPORT

Consideration has been given to transport aircraft powered by two, three and four RB419 propulsion/blowing engines. A comprehensive parametric/trade-off study has been undertaken on the twin engined variant encompassing a range of wing aspect ratio (8, 10, 12), section thickness/chord ratio (0.18, 0.21, 0.24) and wing sweep (0^o, 20^o, 27.5^o).

Details of the basis for the study are quite complex and not discussed here except to point out that each combination of wing sweep and thickness/chord ratio was explored over a range of wing loading so that aircraft were derived covering a wide spectrum of STOL capability.

It is postulated that a military transport of this kind would serve a dual purpose: in time of peace for routine transport duties and in time of emergency in a tactical role for supply into a remote site or battle damaged runway (Figure 14). In drawing up a transport aircraft specification, the director of operational requirements is generally aware that some penalty would result if field performance demands were too stringent or cruise speed set too high; therefore he requires trade-off data in order to make a sensible compromise. For example, he may wish to trade transport fuel efficiency in routine duty against field performance at the mid-point of the tactical supply mission. Figures 15 and 16 show the form of such a trade-off for the twin-engined variant of aspect ratio ten.

Payload-range for the strategic supply mission is determined by an interactive procedure. Each aircraft has payload equal to 25% of design gross weight and wing area derived first* such that fuel capacity of the wing equals the fuel required for the mission and then exceeds it by 10%, 20% and 30% increments. Each such aircraft is then exercised in the radius mission and STOL performance is determined on arrival and departure at the mid-point. In Figure 15, payload miles per pound of fuel for the strategic supply mission is plotted versus takeoff ground roll at the mid-point of the tactical mission. Figure 16 shows a cross plot at a ground roll of 900 ft. to illustrate the trade-off of fuel efficiency against cruise speed. Observations are as follows:

- A choice of 900/1100 ft. as takeoff ground roll incurs a relatively moderate penalty in fuel efficiency for regular transport duty (Figure 15).
- This degree of STOL performance at the mid-point is compatible with takeoff field size of about 8000 ft. at DGW for regular transport duty and is therefore well matched for the dual role.
- Figure 16 shows that choice of a lower cruise speed provides a clear advantage in fuel efficiency.
- For a given cruise speed, the choice of a thick wing in combination with some degree of sweep angle provides for greater fuel capacity and thereby the ability to exchange payload for greater range.
- Thick wing sections make possible the low speed/high fuel efficient option by providing for necessary fuel capacity without unduly large wing area.

The parametric study data base has been used to predict the performance of various point designs: in particular consideration has been given to a twin-engine, powered lift version of the C-130 Hercules (Figure 17). For the same payload-range, this powered lift variant would reduce ground roll by 50% or more, increase cruise speed by 100 kt. and display a much smaller radar signature.

Propfan technology has the potential for improvement in specific fuel consumption. In Ref. 2, Coplin has suggested a hybrid engine described as a turbofan-prop which combines turbofan and propfan propulsion: in fact, it is a three-stream engine similar to the RB419. This leads to the possibility of a propulsion/blowing engine with propfan and an energy efficient powered lift STOL transport of the future as shown in Figure 18. Power to the propeller would be substantially less than for the conventional propfan and therefore gearbox development presents less of a problem.

6.2 POWERED LIFT STOVL SUPPORT AIRCRAFT

The Augmentor-Wing concept lends itself readily to a twin engine layout capable of vertical landing such as might be required for sea based operation in AEW & ASW roles. The developments in thick supercritical sections permit containment of ducting in the wing for ejector blowing and for engine-out balance. Two layouts are depicted, one based on the Pegasus engine (Figure 19) the other on the projected RB419 engine (Figure 20). The excellent buffet boundary characteristics of thick wing make it well suited for AEW surveillance at high altitude.

7.0 REFERENCES

1. Augmentor-Wing: Testing Toward Operational Goals.
   M. P. Rose'Meyer, the de Havilland Aircraft of Canada, Limited
   CASI Flight Test Symposium, Hull, Quebec, 1983.

2. The Accelerating Pace of Advancing Aero-Engine Technology.
   J. F. Coplin, Rolls-Royce, U.K.
   R.Ae.S. Lecture, London, November 1983.

* This first case is the one having maximum transport capacity (PR) but no flexibility to exchange payload for fuel and thereby extend range (without addition of external tanks).



FIGURE 1

THRUST MANAGEMENT FOR WAVE-OFF

D⁴H

- ALL ENGINES
- 80% POWER LEVEL
- BLOWN FLAP FOR HIGH LIFT (LOW SPEED)
- MODULATE LIFT AND/OR DRAG FOR GLIDESLOPE TRACKING
- ONE ENGINE OUT
- MAXIMUM POWER ON LIVE ENGINE(S)
- BLOWN FLAP FOR HIGH LIFT (WING LIFT RETAINED OEI)
- CONTROL ROLL/YAW/PITCH DUE TO THRUST ASYMMETRY

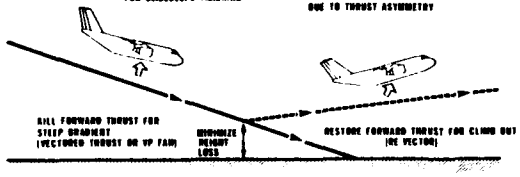


FIGURE 2

EFFICIENT BLOWN WING WITH EJECTOR FLAP FOR STOL

(STATIC THRUST AUGMENTATION APPROXIMATELY 1.5)

D⁴H

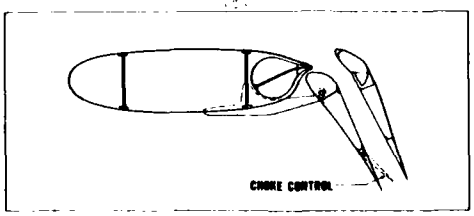


FIGURE 4

PROPULSION/BLOWING ENGINES

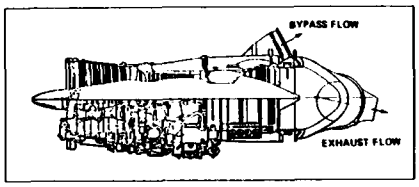
ROLLS-ROYCE SPEY Mk 801 SF

WITH VECTORING NOZZLES

D⁴H

ROLLS-ROYCE RB-419

BASED ON V.P. FAN AND SPEY CORE



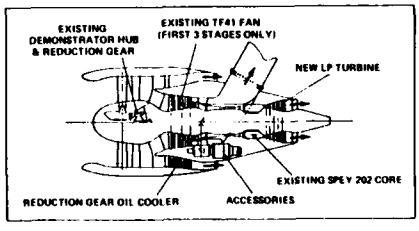


FIGURE 3

CROSS-DUCTING SCHEMATIC

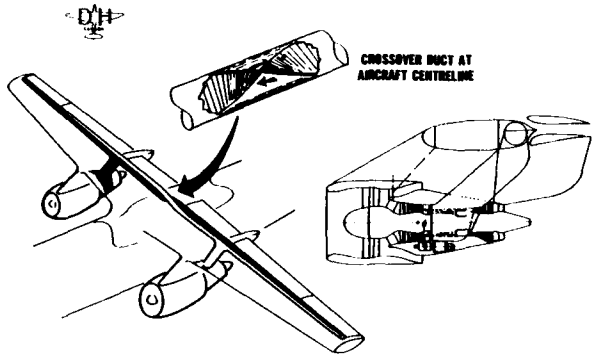


FIGURE 5

SUPERCRITICAL AIRFOIL DEVELOPMENT

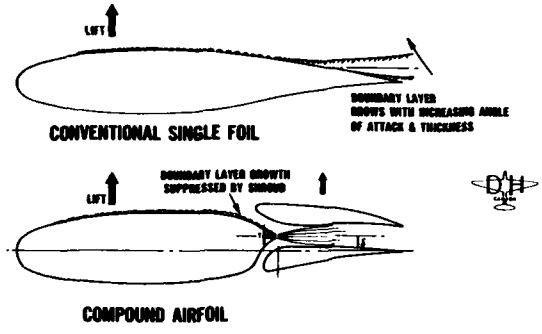


FIGURE 6

AWRA MAXIMUM EFFORT TAKEOFF 42,000 LB

FLAP 46° NOZZLES 38° HEADWIND 5.4 KT : 20°C

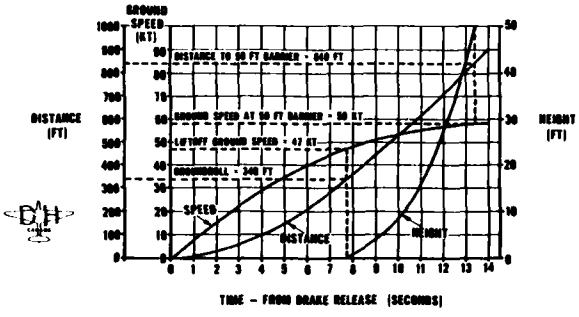


FIGURE 7

RB419-03 ENGINE APPROACH PERFORMANCE

ASSOCIATED CONDITIONS:
1. ISA
2. SPEED = 70 KNOTS
3. HEIGHT = 500 FEET

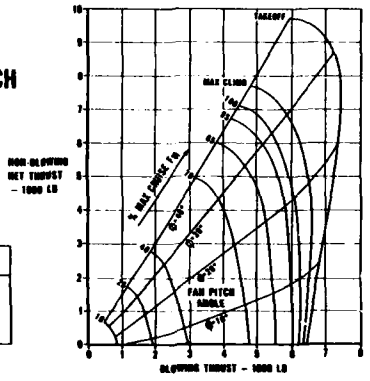


FIGURE 8

A FAMILY OF SUPERCRITICAL COMPOUND AIRFOILS

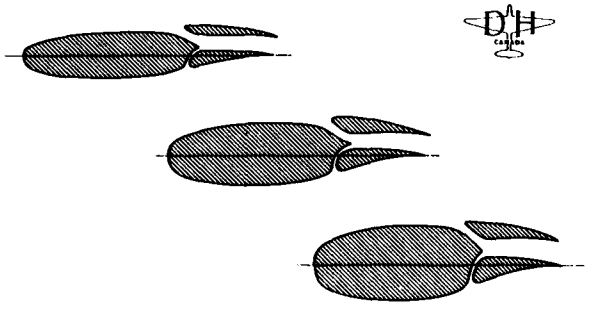


FIGURE 9

FLIGHT BOUNDARIES FOR COMPOUND AIRFOIL

YIELDS:
HIGH ALTITUDE FOR:
• CRUISE EFFICIENCY
• AIRCRAFT EARLY WARNING

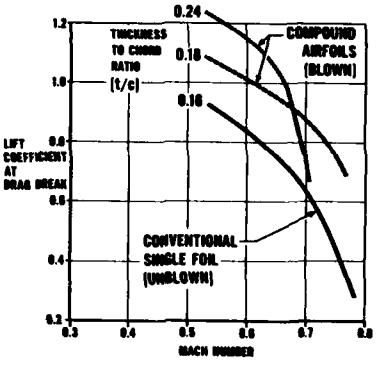


FIGURE 10

DRAG CHARACTERISTICS OF COMPOUND AIRFOIL

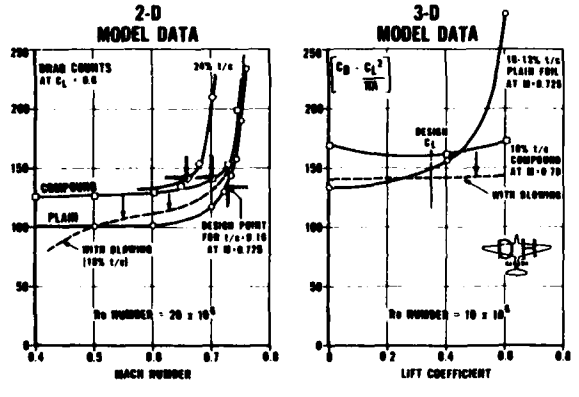


FIGURE 11

DRAG vs THICKNESS/CHORD FOR $C_{L\,DES}$ = 0.6

O PLAIN FOIL
△ COMPOUND UNBLOWN

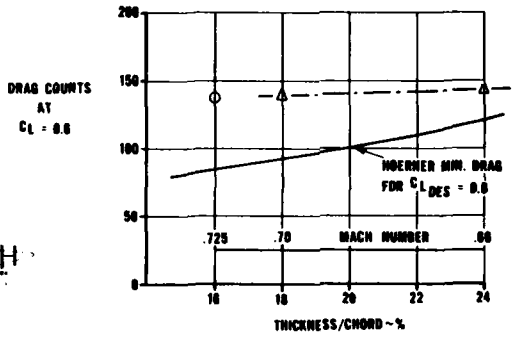


FIGURE 12

DRAG POLARS: t/c = 0.24

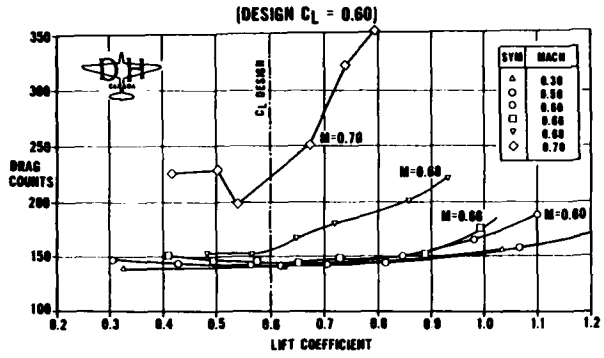


FIGURE 13

MILITARY TRANSPORT MISSIONS

(TRADE-OFF STUDY: PAYLOAD = 0.25 DESIGN GROSS WEIGHT)

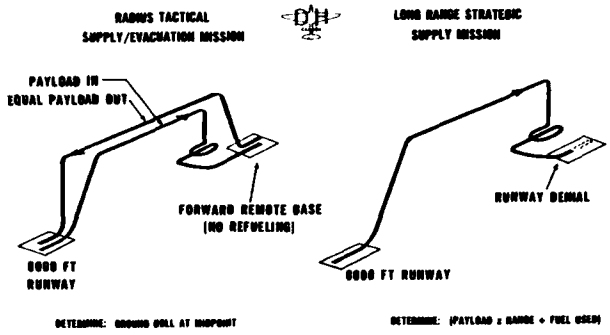


FIGURE 14

TRANSPORT FUEL EFFICIENCY vs REMOTE BASE GROUND ROLL

ASPECT RATIO = 10

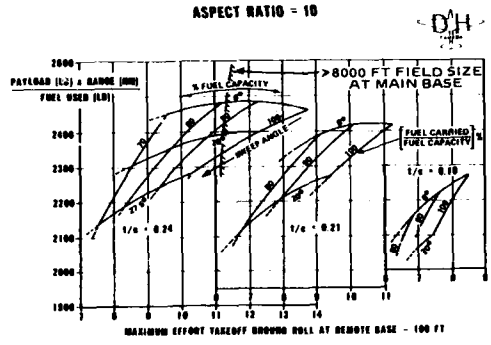


FIGURE 15

TRANSPORT FUEL EFFICIENCY vs CRUISE MACH NUMBER

ASPECT RATIO = 10; TAKEOFF ROLL = 900 FT

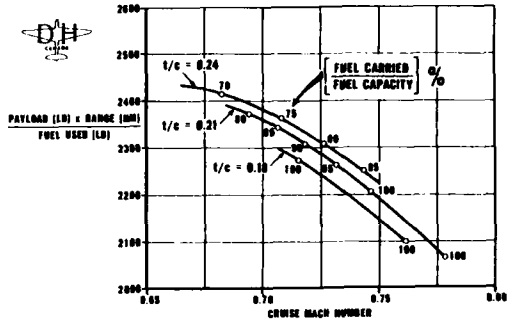


FIGURE 16

ADVANCED STOL TRANSPORT: C-130 FUSELAGE

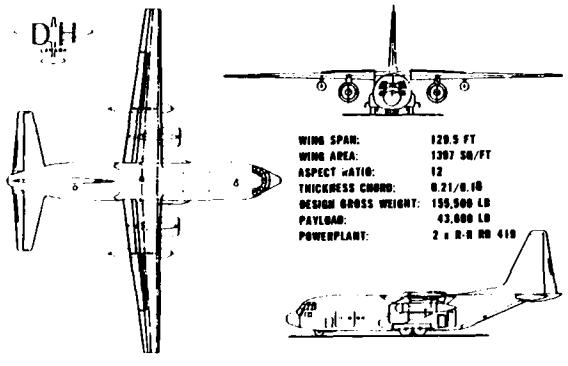


FIGURE 17

ADVANCED POWERED LIFT TRANSPORT WITH TURBOFAN-PROP

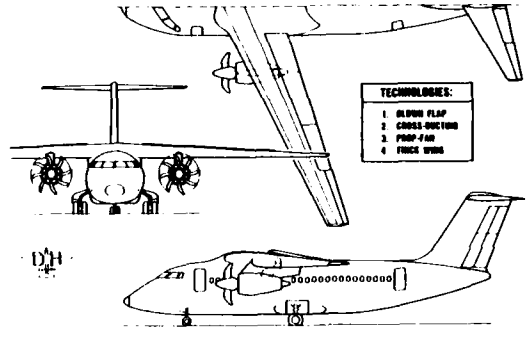


FIGURE 18

STOVL SUPPORT TYPE AIRCRAFT
WITH SHOULDER MOUNTED ROLLS-ROYCE PEGASUS ENGINES

POWERPLANT:	2 x RR PEGASUS II
WING AREA:	700 SQ FT
ASPECT RATIO:	6
TAPER RATIO:	0.5
t/c:	25%

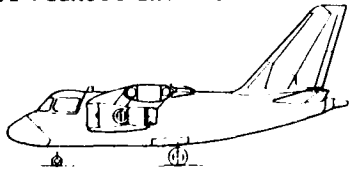




FIGURE 19

STOVL SUPPORT AIRCRAFT
TILT WING/VECTORED THRUST COMBINATION

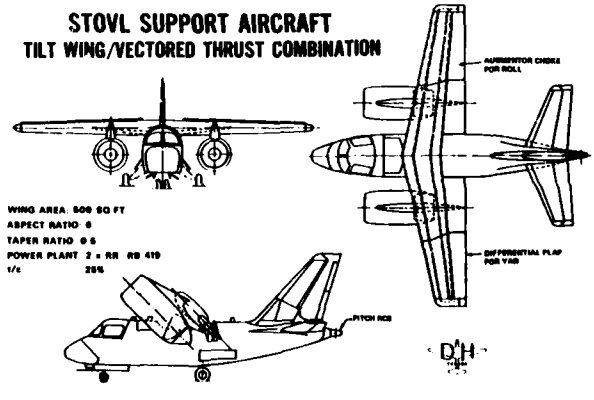


FIGURE 20

AIRCRAFT DRAG REDUCTION TECHNOLOGY

Andrew S. W. Thomas

Advanced Flight Sciences
Lockheed-Georgia Company
Marietta, Georgia, 30063
U.S.A.

AD-P004 061

SUMMARY

This paper presents a review of the current techniques of aircraft viscous drag reduction and some of the more recent developments that have taken place in this technology. The various sources and relative contributions of aircraft drag are described including skin friction drag, pressure drag, interference drag and lift induced drag. In the discussion, emphasis is given to the physical processes that lead to these drag contributions, followed by a discussion of methods of reducing the impact of these drag sources. Finally some brief discussion is presented to show how innovative and optimized aircraft configurations can lead to drag benefits.

1. INTRODUCTION.

Since the early seventies and the subsequent trend in world fuel prices (Figure 1), aircraft drag reduction technology has become of prime importance to military and civilian operators. For example, a 10% drag reduction on a large military transport aircraft is estimated to have the potential to save up to 13 million gallons of fuel per aircraft over the lifetime of the aircraft. Considering also that US domestic operators spent a staggering 2.1 billion dollars on fuel in 1976 alone, it is clear that enormous benefits are to be derived from drag reduction technology. Additionally, with the very high cost of aquisition of new aircraft, existing fleet lifetimes are being extended and derivative designs are now coming on to the marketplace. Thus, retrofittable drag reduction technologies are critically important.

The aerodynamic forces experienced at the surface of an aircraft may be either tangential to the surface or normal to the surface and both will contribute to the total drag on the body. The interrelation and development of these forces is shown in Figure 2. The only tangential force that is present is the viscous skin friction due to the development of boundary layers over the surfaces. The development of the normal forces, i.e. pressures normal to the surface, is more complex and, as Figure 2 shows, these can arise from a number of contributions. Firstly, there is the pressure field modification due to the displacement thickness of the boundary layers and possible formation of regions of separation (and which, with the skin friction, constitutes the profile drag). Next, there are pressure forces that arise from the formation of vortices in the wake and which may further modify the flow around the body. This is termed vortex drag. If compressibility effects are present, then there are additional pressure forces due to the compressibility effects and the presence of waves in the flow.

The non-zero integrated streamwise component of these pressure forces constitutes the pressure drag on the aircraft. Because lifting conditions are present, there is a strong component of the lift-dependent vortex drag which in conjunction with a smaller amount of lift-dependent profile drag gives rise to the so-called induced drag.

Although the relative importance of different drag sources varies for each aircraft type and mission that is flown, a representative breakdown is shown in Figure 3. The important contributors to the total drag are the following:

(1) Skin friction drag due to viscous boundary layer formation.
(2) Lift induced drag due to the conserved circulation developed around the wings.
(3) Pressure drag due to the open separation in the afterbody and other regions.
(4) Interference effects between aerodynamic components.
(5) Wave drag due to compressibility effects at near-sonic flight conditions.
(6) Miscellaneous effects such as roughness effects and leakage, etc.

All these drag sources contribute to the total drag by different relative amounts for different types of aircraft and the breakdown in Figure 3 corresponds to the case of a large subsonic transport of the type flown by most major airlines. The greatest contribution arises from turbulent skin friction drag, a fact that has provided the impetus for most of the friction drag reduction work that will be described. The next most significant contribution arises from the lift induced drag and this, added with the friction drag, accounts for about 85% of the total aircraft drag. Interference drag, wave drag, trim drag to balance the aircraft, and miscellaneous effects account for the remainder. In drag reduction studies, it might be argued that it is more worthwhile to address only the more significant drag contributions. However, this is not necessarily the case because very often it is easier to obtain much greater percentage reductions in the smaller drag sources than in the larger contributions. For example a 50% reduction in afterbody drag is feasible and might represent a 5% total drag reduction. To achieve the same total drag reduction through skin-friction reduction alone may be a much more difficult task.

The purpose of this paper is to review and summarize the various aircraft drag reduction technologies that are currently being explored. Compressibility effects and transonic wave drag reduction will not be discussed explicitly and instead, emphasis will be given mostly to the drag sources associated with viscous flows. This is because viscous flow drag reduction technology is the area that has advanced most rapidly in recent years and which is currently receiving the greatest attention. The discussion will therefore concentrate on skin friction reduction, afterbody drag reduction, induced drag reduction and interference drag reduction. Finally, some brief discussion will be given to show how innovative aerodynamic configurations can be exploited to achieve low drag characteristics.

2. SKIN FRICTION DRAG REDUCTION.

For the reduction of skin friction drag, either of two different philosophies may be followed. The first is to capitalize on the low friction characteristics inherent to laminar boundary layers and to delay transition on the

wetted surfaces as much as possible. This is the approach that has been followed in the laminar flow control programs that were undertaken in England (summarized in Ref. 1) after the second war and later in the United States at Northrup (Ref. 2) and more recently at NASA Langley (Ref. 3). An alternative philosophy for friction reduction that has recently emerged is to accept the inevitability of turbulent flow and to attempt to modify or interact with the turbulent structures to reduce the friction (Ref. 4).

2.1 Laminar Flow Control (LFC).

Although laminar flow control is a generic term, it has, by association, come to mean the maintenance of laminar flow through the use of wall suction. The suction may be in the form of distributed porosity over the surface (Refs. 5 and 6) or in the form of a series of spanwise-running slots (Refs. 5, 7 and 8). The suction is not sufficient to suppress any existing turbulence, but serves to modify the curvature of the laminar velocity profile which in turn reduces the amplification of any instability waves in the boundary layer that grow and lead to the formation of turbulence. As depicted in Figure 4, local friction can be reduced to about 20% of its turbulent value and with sufficient care, laminar flow can be maintained up to Reynolds numbers of the order of 60 million. An extensive bibliography of the literature describing LFC can be found in Reference 2.

The current Lockheed concept for an LFC aircraft is shown in Figure 5 taken from Ref. 9. Control is only exercised on the wing surfaces because of the greater difficulty of maintaining laminar flow at the high fuselage Reynolds numbers as well as the problems of surface discontinuities at the windows. The suction units for this configuration are mounted in the lower fuselage at the wing root and the propulsion engines are mounted in the tail to minimize noise and vibration on the wings. The real benefits of such a configuration must be evaluated against the performance of an equivalent advanced turbulent aircraft and, as Figure 6 (from Ref. 9) shows, these benefits are greater for long stage lengths and represent a 27% performance improvement. Whether or not this is sufficient to justify the higher aquisition and maintenance costs of a new fleet of such aircraft will depend largely on future fuel price developments.

While the feasibility of LFC has been known for a long time, the system does suffer from a number of design, manufacturing and maintainability problems as depicted in Figure 7. An essential problem with any laminar flow condition is its susceptibility to dirt and other particulates, such as insect debris accumulating near the leading edge during low altitude flight. These can trip the flow to turbulence which will then spread over a wide area of the wing. To avoid this, close manufacturing tolerances must be followed and some kind of in flight cleaning system (Ref. 9) or leading-edge protection must be employed (Ref. 10).

From an aerodynamic viewpoint, probably the greatest difficulty lies in being able to confidently predict where transition will occur. The design procedure requires that the boundary-layer characteristics, with suction, first be accurately determined using a boundary-layer analysis of the type in Ref. 11. This is followed by a stability analysis to determine the amplification of the instability waves in the flow (Ref. 12).

A fundamental difficulty is that the stability analysis is based upon a set of linearized small-disturbance equations so that the actual amplitudes cannot be calculated, but the amplification can. Furthermore, the receptivity of the flow to the free stream disturbances that drive the instabilities is also not well known (Ref. 13). The problem, therefore, is analagous to predicting the output of an amplifier given its gain, but knowing nothing of its input signal level.

To circumvent these difficulties, empirical transition criteria must be used, such as the e^N criterion (Ref. 14), which assumes that transition takes place once the amplification ratio (or system gain) exceeds some critical threshold given by the value of e^N. The critical values of N are typically 11-12 for the mid-chord regions dominated by quasi-two-dimensional Tollmien-Schlichting instability (Ref. 15), and 10-11 for the crossflow instability that originates most severly near a swept-wing leading edge (Ref. 14).

In order to derive the optimal efficiency of the LFC system it is best to minimize the suction quantities that are required and this generally requires a careful iteration of the design procedure that has been described. Furthermore, the way that the suction is achieved can have a bearing on the overall system efficiency both from an aerodynamic and a structural weight penalty viewpoint. One approach is to use discrete slots as in Figure 5, or through the use of strips of porous material as an integral part of the wing surface. The porous strips have been studied in References 16 and 17, and it has been demonstrated that discrete suction through porous strips can be as effective as suction distributed continuously over a greater streamwise length. Both the suction approaches have been critically evaluated in work that has been undertaken at Lockheed-Georgia (K.C. Cornelius, private communication). As Figure 8 shows, it has been demonstrated through stability measurements that the suction slots have a greater stabilizing influence, for a given suction flow rate, than do the porous strips. Naturally, other parameters such as skin structural integrity must also be considered before a final choice of surface type can be made.

2.2 Natural Laminar Flow (NLF).

The simplest technique for maintaining laminar flow over a suface is to capitalize on the stabilizing effect that favorable pressure gradients have on laminar boundary layers (Ref. 18). In order to implement NLF on a wing, it is necessary to bring the point of maximum thickness as far aft as possible so as to create extensive regions of favorable pressure gradient over the wing surface as depicted in Figure 9. The concept can be employed without the need for considering the attendant weight and structural penalties associated with the LFC suction system and, from an aerodynamic point of view, the design procedures are similar to those used in LFC (including the inherent empiricisms).

A number of low-speed aircraft are currently flying with NLF (Ref. 19), although in some cases this has been fortuitous. In a high-speed application where good transonic cruise is needed, additional design considerations arise. For example, permissible wing sweep is limited by the onset of crossflow instability at the leading edge. Also, in order to rise to the correct pressure at the trailing edge after a large region of favorable gradient, large adverse gradients are necessary and these can lead to strong shocks and a wave drag penalty or the possibility of separation. Careful design studies are needed to minimize these detrimental effects.

2.3 Hybrid Laminar Flow Control (HLFC).

A compromise LFC system that avoids some of the problems associated with LFC and NLF is the Hybrid Laminar Flow Control System (HLFC) shown in Figure 10. This is a mix of the other two systems and suction is applied only at the leading edge to minimize crossflow instability. Control of the instabilities in the mid-chord region is achieved with tailoring of the pressure gradient as with NLF. In this way a larger wing sweep can be achieved for transonic flight than with NLF, and the weight penalties are not as great as for LFC. Also, the suction orifices at the leading edge can double as a leading-edge-cleanser discharge system to prevent accumulation of dirt and insects during the low-altitude climbout.

2.4 Wall Cooling.

Another favorable physical effect that could conceivably be exploited in a drag reduction scheme is by the use of wall cooling (Ref. 20). As Figure 11 (adapted from Ref. 22) shows, a reduction in surface skin temperature can lead to significant increases in the minimum critical Reynolds number. This is not because the kinematic viscosity goes up (the reverse is true), but arises because the heat transfer modifies the viscosity distribution across the boundary layer which causes the mean profiles to become more full, thereby increasing their stability. This has been substantiated by the flat plate experiments of Ref. 20 for Tollmien-Schlichting type disturbances. However, the calculations in Ref. 21 have shown that while the same is true for crossflow-type instabilities, the effect is much smaller as depicted by the growth curves in Figure 12.

In order to implement such a concept, a very large heat sink is needed. One possibility would be to use liquid hydrogen in the cryogenic state to fuel the aircraft (Refs. 22 and 23). To maintain the laminar flow, the fuel would be circulated just below the wing surface as a preheater to the combustion process. The same effect could be achieved if liquid methane was used.

2.5 Active Wave Suppression (Wave Cancellation).

The transition control concepts that have been described are passive and do not require a dynamic interaction with the flow. A new transition control concept that has been suggested and tested under laboratory conditions (Refs. 24, 25, 26 and 27) is by the use of active wave suppression or wave cancellation. The idea is to detect any low amplitude pre-transitional instability waves in the flow and then to introduce a control disturbance that is of equal amplitude and 180 degrees out of phase with the original disturbance. In principle, superposition should then remove the primary disturbances from the flow.

To date, the concept has only been evaluated under low speed conditions but significant increases in the transition Reynolds numbers have been reported. An example of the streamwise amplitude history of an instability wave, with and without the control disturbance is shown in Figure 13, and a smoke-wire visualization of the corresponding flow conditions is shown in Figure 14 (from Ref. 27). These demonstrate that while an impressive degree of control of the two-dimensional disturbances is possible, some residual three-dimensional disturbances remain in the flow and that these bring about transition.

The reason for this is that transition arises from complex wave interactions between a primary disturbance and three-dimensional disturbances that have their origins with the free stream (Ref. 28). Thus, while the control disturbance removes most of the energy of the primary disturbance, the now amplified three-dimensionalities still remain. Therefore, any real implementation of the concept will probably require a complex three-dimensional control system, even for two-dimensional flow. Whether or not this is possible at the very high instability growth rates characteristic of flight Reynolds numbers remains to be determined.

3. TURBULENT SKIN FRICTION REDUCTION.

An alternative approach to the reduction of skin friction is based not upon trying to maintain laminar flow, but instead on attempting to modify the turbulence in some way so as to reduce friction. Possible approaches may be passive, as in the case of the riblets and large eddy breakup devices etc., or active as in the case of the synthetic boundary layer. These efforts are still quite new and arose largely from a series of ongoing tests that were begun at NASA Langley during the late seventies (Ref. 4).

3.1 Riblets.

Because it is known that the near wall structure of a turbulent boundary layer is dominated by streaks of streamwise vortices with an average spacing of $z^+=100$, it has been argued that changing the surface geometry with micro-grooves should spatially lock the structures which may alter the momentum transport characteristics and reduce the skin friction. Studies have therefore been made of the friction characteristics of a boundary layer that develops over surfaces with various geometries of small streamwise grooves carved into them (Ref. 29). As shown in Figure 15, it has been demonstrated that local drag reductions of the order of 10% are indeed possible, despite the increase in wetted area. The optimized groove spacing is of the order of ten wall units. Also, sharp pointed grooves tend to perform better than grooves with rounded peaks (Ref. 29).

Because the optimized groove spacing is about an order of magnitude less than the streak spacing, it is difficult to picture them as interacting with the streaks and experimental studies have been made to look at the characteristics of the turbulence that develops over the grooved surfaces (Refs. 30, 31). These studies have attempted to measure the mean turbulent bursting frequency and conditional averages of the velocity fluctuations during the bursting process, since this activity is a measure of the turbulence production mechanism. One example, that of the mean turbulence bursting frequency is shown in Figure 16 taken from Reference 30. Some apparent change is indicated due to the presence of the riblets. Unfortunately, there is a fundamental difficulty in objectively defining the turbulence activity thresholds that are used to measure when a turbulent burst is taking place. Therefore, whether or not the changes in Figure 16 accurately represent flow structure changes associated with the drag reduction is difficult to say.

An alternative model for the drag reduction is proposed in Reference 31 and is based upon the idea that the drag reduction does not arise from a direct interaction with the turbulence structure, but arises instead because of the way the viscous fluid flows over the ribbed surface. The flow in the valley of the grooves is at low Reynolds number

and is creeping in character and the local wall shear is low. Because of the mean velocity gradient, the wall shear is higher at the top of the rib as found in the data of Ref. 30. If the geometry is right, the low shear dominates and, even though the wetted area is increased, and a net drag reduction results. In this model, any turbulence changes are then merely a passive attendant to the wall shear change, rather than a direct cause. This would also serve to explain why the sharp groove tips have better drag reducing characteristics since they minimize the surface area exposed to high shear.

The multi-colored dye visualizations shown in Figure 17, from Ref. 31, show the inhibited lateral spreading of the flow in the grooves and its creeping nature. By themselves they do not prove the proposed model, but they are certainly consistent with that view. More detailed experimental studies of the flow field within the grooves as well as numerical simulations are needed to resolve this question.

3.2 Large Eddy Breakup Devices, Manipulators (LEBU).

Another very promising concept for the reduction of turbulent skin friction is by the use of plates or fences inserted into the boundary layer flow. Friction reductions of the order of 20% have been recorded downstream of the devices (Refs. 32-36) and because it has been suggested that the devices break up the large scale structures of the flow, they have been referred to as large eddy breakup devices (LEBU). The term turbulence manipulator may be more appropriate.

The boundary-layer development downstream from a set of thin plates immersed in a flow is depicted in Figure 18 taken from Ref. 4. The change in slope of the curve of momentum thickness development is representative of friction changes by virtue of the momentum integral equation. There is a device drag penalty that must be paid before a break-even point is reached, but thereafter a net drag reduction can be achieved. The best drag reduction configuration for these devices appears to be thin airfoil shapes to minimize the device drag. They should be of the order of the local boundary layer thickness in streamwise extent and located at about 80% of the boundary layer thickness from the wall. Tandem devices also appear to perform well and the geometrical characteristics of the devices are critically important for good performance (Ref. 34).

At present there is some controversy over the mechanism behind the observed drag reductions. The first investigations suggested that the devices serve to break up the large eddies of the flow and the smoke-wire visualizations in Figure 19 (from Ref. 35) show that while large eddy structures are clearly visible in the uncontrolled flow, they are not apparent in the controlled flow. This is perhaps surprising in view of the fact that logarithmic behavior is still evident in mean flow measurements of the controlled flow (Ref. 33). However, conclusions about structural features should not be based on streakline data alone and measurements of correlations and length scales are needed to clarify this issue.

An alternative description for the behavior of the devices has recently been proposed in Ref. 36. In that model, the large eddies are viewed as conglomerations of smaller scale hairpin vortices and the wake eddies of the manipulator interact with these hairpins in such a way so as to inhibit wallward motions. Thus, it is the introduction of new structures into the flow rather than the destruction of existing ones that is important. Flow visualization data seem to support this interpretation and it is consitent with the continued existence of logarithmic behavior in the velocity profiles. However, the examination was based on manipulators that were quite thick and which consequently had large wakes.

An important fundamental issue with the devices is how long the drag reduction effect will persist in the downstream direction. The indications from Ref. 34 are that the flow does indeed return to an uncontrolled state after about 150 boundary layer thicknesses downstream of the device. Whether or not further devices can be used to reimplement control is an issue that remains to be examined.

3.3 Other Surface Geometry Effects.

In addition to the riblets, a number of other surface geometry effects are recieving attention as possible friction reduction concepts. Among these are streamwise surface curvature, transverse surface waves and transverse micro-grooves.

While concave curvature increases near wall turbulence intensities through the Görtler instability, convex curvature appears to reduce intensities and skin friction (Ref. 37). The mechanism for this is not clear and Ref. 4 suggests that the effect is mostly due to a change of the outer eddies. An alternative and quite plausible possibility, is that if the near wall streaks themselves arise from a Görtler rotational instability due to local streamline curvature as suggested by Ref. 38, then it is possible that the convex wall curvature changes the streamline curvature to suppress these structures. Whatever the case, it does appear that there is a very long relaxation distance of low drag after regions of convex curvature which can be exploited in a drag reduction scheme.

If the scale of the curvature is reduced and made periodic, transverse surface waves result. This has been suggested as a possible drag reduction scheme since measurements over surfaces with low amplitude waves and wavelengths of the order of the boundary layer thickness have shown friction reductions (Ref.39). Unfortunately, the static pressure distribution over the wall shifts in phase relative to the surface wave and there is an attendant pressure drag (Refs. 40 and 41). NASA Langley experiments on non-symmetric surface waves have attempted to minimize this effect, but no net drag reductions have yet been reported and the wall shear reductions appear to be diminished (Ref. 40) For the case of moving (compliant) sinusoidal wavy walls beneath turbulent boundary layers the situation is not clear and is curently under investigation. Numerical simulations suggest that there may be drag reductions for the case of wave speeds approaching the free stream velocity (Refs. 42 and 43), but for passive compliant surfaces, careful experiments have shown no net drag reductions in air (Ref. 44).

Another transverse surface geometry that is recieving attention is to use closely spaced transverse cavities (D type roughness, Ref. 45) of small scale to reduce drag (Ref. 4). These have been referred to as micro-air bearings with an implication that small vortices recirculate in the cavities providing low shear stress to the external flow at the lip of the cavity. As with wavy walls, there is an attendant pressure drag, and the vortex structures, if they do form at these low Reynolds numbers, will not be stable and will periodically burst out of the cavities giving rise to pulses in the pressures drag. This may explain why no net drag reductions have been achieved. Ref. 4 suggests that these cavities in conjunction with some other device (LEBU's, streamwise vortex generators etc.) to minimize the eruptions may be a viable approach.

3.4 The Synthetic Boundary Layer.

In a unique series of experiments, Coles and Savas (Ref. 46) have shown that it is possible to create turbulence with large scale structures that are spatially and temporally periodic. This was achieved using an array of turbulent spot generators in a laminar boundary layer driven at the appropriate frequency and relative phase. This is a form of controlled transition and has been suggested as a possible means of creating stable turbulent flows of reduced skin friction. This is currently under examination at Lockheed-Georgia (Ref. 47) and tests at NASA Langley (Ref. 48) have shown local friction modifications. As with the LEBU's, a fundamental issue that remains to be resolved is whether or not the flow will remain in the modified state ad infinitum, or whether it will ultimately relax back to some uncontrolled state.

Although the concept is dynamic in character, it could conceivably be implemented by a purely passive means. This is because periodic disturbances are not necessarily the only way to produce periodic arrays of spots. Indeed, it has been found that an array of periodic spots will arise from a small non-moving pin placed on the wall beneath a laminar boundary layer. Thus, an appropriately spaced (streamwise and spanwise) array of such pins could be used to produce the desired phase and frequency of spots. Since the pins are small (<0.3 d) and in a region of low velocity laminar flow, their device drag might also be quite low.

4. AFTERBODY DRAG REDUCTION.

4.1 Separation Control as a Means of Drag Reduction.

For the reduction of the drag associated with the separated flow of generic streamlined shapes, concepts such as the use of vortex generators have been in use for many years. Recently, however, a number of novel flow control methods have been developed. For example, Ref. 49 describes a technique whereby it is possible to use a disk mounted in the wake region of a bluff body (Fig. 21) to lock a vortex in the wake. This gives rise to some pressure recovery on the afterbody which in turn reduces the total drag. The same technique has also been used with considerable success to reduce forebody drag (Ref. 50). Likewise, tests at NASA Langley have shown that transverse grooves on a tapered afterbody can reduce drag (Ref. 51, Figure 21,22) as can large streamwise grooves (Ref. 52, Figure 23). In each case the vortex structure set up within the grooves changes the near wall momentum transfer to modify the separation point. In one case the vortex structure is transverse to the flow, while in the other a streamwise vortex system is present. Control of separated flows can also be achieved by periodic re-energizing of the near wall flow using, for example, the embedded rotating cam devices suggested in Ref. 53.

Direct base suction has been suggested as a drag reduction scheme since it does reduce the wake region. However, as shown in Ref. 54 high drag inevitably results due to the low pressure created at the base of the body. In any case prodigious amounts of suction are invaribly required.

If the geometry of the body allows the flow in the afterbody region to be attached, then these kinds of flow control concepts are not necessary. Instead, inverse design procedures can be used to devise shapes that have a prescribed low skin friction from which the required body shape can be determined. This approach is based upon a Stratford type (Ref. 55) flow that has low wall shear, but a penalty is paid in the higher pressure drag that can result with the thicker boundary layers. Some optimization is therefore necessary. Ref. 56 describes the procedures and resulting shapes for axisymmetric flows and Ref. 57 describes similar calculations for 3-D wings with prescribed skin friction. More work in the area of 3-D flows would be useful since it may be possible to define optimized shapes by minimizing the drag producing streamwise component of skin friction while allowing the cross-stream component to vary as needed to keep the flow attached.

4.2 Upswept Fuselages - The Real Problem.

In order to meet operational requirements and take-off rotation, it is necessary that the aircraft aft fuselage have upsweep as depicted in Figure 24. This gives rise to a flowfield that is fundamentally different from the closed separations typical of bluff bodies and limits the applicability of some of the separation control methods that have been described. In order to implement any drag reduction scheme, it is important that the physics of this flowfield be correctly understood.

The important characteristics of the flow field typical of upswept fuselages are also shown in Figure 24. It is characterized by a 3-D boundary layer with significant crossflow regions on the fuselage. This boundary layer separates into a pair of counter rotating-vortices trailing downstream. The flow is analagous to the flow abou a missile at high angle of attack or the flow over a delta wing, although in the present case a hard separation line does not exist.

The total drag associated with this kind of flow can be split into two components. First, there is the pressure drag that arises because of the reduced pressures on the lower surface of the fuselage. In addition, there is a considerable loss of flow energy in the form of rotational kinetic energy of the vortex structures and this is manifested as a vortex drag component. (This loss is analagous to the lift induced drag that can be related to the tip vortex structures behind a wing.) Depending upon the geometry of the aircraft, the relative contributions of each may vary.

An important point to be made is that the other aerodynamic components can interfere with this flow and compound, or possibly relieve the drag problem. Wing downwash is the most severe contributor to this effect since it changes the effective upsweep angle. Externally mounted gear pods, if present, can also feed vorticity to the trailing vortex structure. Accurate drag definition therefore requires testing and optimization of complete aircraft configurations.

A survey of the wake structure behind a fuselage with large upsweep and large drag is shown in Figure 25. The wake vortex structure is clearly in evidence. These data were recorded with 5-hole pressure probes and the corresponding data for a low upsweep fuselage with much less drag are shown in Figure 26. The reduction in the intensity of the wake vortex system is evident. These kinds of data are very useful for drag reduction studies since integration of the crossflow velocities enables the vortex drag to be determined and integration of the wake total pressure enables the pressure drag to be found (Ref. 58). This information is therefore of much greater utility than force measurements alone.

For reducing the drag associated with this kind of flowfield, the best approach is to attempt to optimize the geometry of the configuration at the design stage. Thus, high upsweep angles should be avoided. Also, slender fuselages with little or no flatness in cross-section should be used since these minimize the area exposed to the low pressure. An example of the importance of the geometry is shown in Figure 27 where a tail cone was added to a blunt fuselage to reduce its drag (Ref. 59). As can be seen a significant drag reduction is obtained, presumably through a reduction in the size of the separation region.

In many applications it is not possible to optimize the geometry due to the need to meet structural and operational requirements and significant amounts of vortex drag can sometimes result. One very good approach for reducing the drag, and one which is finding application as a retrofit to existing aircraft, is by the use of strakes. These were first fitted to a Short-Belfast strategic transport (Ref. 60) and are shown in Figure 28 for a Lockheed C-130 Hercules aircraft. Essentially these are small vertical plates or fins placed beneath the fuselage and embedded in the vortex flow. They act to reduce the intensity of the swirl of the vortex structures and so reduce the vortex drag. To be effective the devices must be optimized since they carry a skin friction and weight penalty. It might be added that the same devices can be used to control the vortex flow over forebodies (Ref. 61).

The utility of some of the other separation control concepts that were mentioned previously has not yet been evaluated for these kinds of fuselages and this would appear to be an area for fruitful research. Also, modification of the structure of the incoming boundary layer that separates and feeds vorticity to the vortices is an area that warrants examination.

5. LIFT-INDUCED DRAG REDUCTION.

Lift induced drag arises primarily because the lift producing circulation around the airfoil leads to a sheet of trailing vorticity in the wake which rolls up into a pair of counterrotating vortices. This vortex structure is concentrated at the tips and induces a downwash over the wing which reduces the effective angle of attack. Therefore, to achieve the same lift, it is necessary to tip the wing back which rotates the lift vector away from the vertical thereby producing a component of drag force (Ref. 62). As in the case of the afterbody flow, this drag is manifested in the wake as rotational kinetic energy. The minimum induced drag is achieved for an elliptical lift distribution across the span which also corresponds to the case of constant wing downwash.

To reduce the induced drag, wings of large aspect ratio should be used since these enable the tip vortex structures to be separated which reduces the strength of the average induced flow between them. However, a point that is not well appreciated is that for the same chord, this will also lead to a weight penalty that may offset the drag reduction. In fact, the selection of optimal aspect ratio is intimately tied to the criteria used to define aircraft geometry. This is discussed in Ref. 9 and as Figure 29 from that reference shows, optimal wing aspect ratio for a transport aircraft varies from 7.5 for minimum aquisition cost, to 9.8 for minimum gross weight, to 12.0 for minimum direct operating cost, and to 15.2 for minimum fuel. At present aspect ratios as large as 15.2 are not structurally feasible but the importance of aspect ratio is clear.

Other techniques for the reduction of induced drag include various wing tip devices, tip blowing, span extension and active controls for load relief.

5.1 Wing-Tip Devices.

Winglets.

It has long been recognized that the addition of tip mounted surfaces to a wing can reduce and diffuse the vortex structures arising from the tips. Induced drag reductions result, but these may be offset by unfavorable interference and viscous effects. The winglet concept shown in Figure 30 is one of the most promising of these concepts and can be thought of as a device to increase the effective span of the wing. As shown in the Figure, the winglet is a small wing mounted in the swirling flow at the wing tip. The lift on the winglet acts as a sideforce and, with proper positioning of the winglet, it will have a thrust component in the stream direction. As with the afterbody strakes, the structure of the vortices is somewhat diffused due to the winglets. Most of the development work for these kinds of devices has been undertaken at NASA Langley and is described in References 64 and 65.

The computed spanwise lift and drag distributions for a wing with and without winglets are shown in Figure 31 (from Ref. 63). As can be seen , there will be an increase in wing root bending moment due to both the increased wing loading and the winglet loading. This may limit the utility of winglets as retrofittable devices. A nose down pitching moment can also occur due to the above center thrust location and this can lead to a trim drag penalty. In addition there are attendant increases in other forms of drag such as skin friction drag and interference drag at the junction region. Thus, while typical total drag reductions of the order of 3-6% may result, comparable performance can in some cases be achieved by a simple tip extension (Ref. 63).

For best performance, proper design of the winglets is clearly very important and some specific design details are discussed in References 63, 65, 66 and 67. These may be summarized as follows:

(1) For good supercritical performance, the winglet should be tapered and swept aft. It should be mounted behind the region of lowest pressure of the main wing to minimize interference effects.
(2) Some outward cant is desirable and helps to minimize interferences at the junction.
(3) As Figure 32 shows (from Ref. 63), smooth fillets should be used between the wing tip and the winglet or smaller drag reduction benefits might result.
(4) From Ref. 65, some toe-out of the winglet is needed due to the inflow angles at the wing tip. This is also desirable since it reduces the likelihood of winglet stall during sideslip.
(5) Although the drag reduction increases with winglet span, it is less than linear (Ref. 66). Therefore, the optimal winglet height must be a trade-off between the improved aerodynamics and the increased moments due to the larger moment arms.
(6) In principle winglets can be mounted above or below the wing, but operational requirements and ground clearances favor upper mounts. A smaller winglet below and ahead of the main winglet is desirable for preventing stall on the main winglet at high lift conditions (Ref. 65).

It might also be mentioned that winglets confer other favorable characteristics, besides drag reductions, which might

be important. Among these are the better control of the spreading and dispersal of particulates behind agricultural aircraft and improved hanger and ground maneuvering clearances for large aircraft. In certain integrated aircraft designs they can also act as control surfaces (see, for example some of the configurations in Ref. 20).

Vortex Diffuser Vanes.

Another concept that is similar to the winglet and which attempts to extract some of the rotational energy from the tip vortices are the vortex diffuser vanes devised at Lockheed-Georgia (Ref. 68). The device is shown schematically in Figure 33 and operates on the same principles as winglets. The advantage of these devices is that the aft mount places them in a region of more intense vortex flow with the possibility of greater energy recovery. Figure 34 shows the reduction in crossflow kinetic energy that can be achieved using a two-vane version of the device. The total integrated reduction for this test condition was 19%.

Another advantage to the rear mount of the vanes is that unfavorable wing interference effects are minimized. Furthermore, unlike for winglets, some inward cant appears to be desirable for optimal aerodynamic performance and as Figure 35 from Ref. 68 shows, this can, under certain circumstances, lead to a reduction in wing-root-bending moment rather than an increase.

Wing-Tip Sails.

A logical extension of the tip devices that have been described is the use of multiple winglets or vanes as suggested by Spillman (Ref. 69). These are shown in Figure 36. These are referred to as sails and are mounted in a spiral array around the wing tip. They are similar to the tip feathers of some species of soaring birds. Induced drag reductions of up to 30% have been reported and for best performance, the array should be essentially horizontal rather than vertical and rearward mounts seem to be preferable. The angle between each successive vane should be about 15 to 20 degrees and four vanes with spans no more than 30% of the wing chord are recommended (Ref. 69). A larger number of vanes is to be avoided, presumably due to the increased interference and viscous losses.

Wing-Tip Devices versus Wing-Tip Extensions.

A fundamental issue with the devices that have been described is whether or not it is better to fit some kind of wing tip device in preference to merely extending the wing tips. This question can not be answered in generality and each configuration must be examined for its weight penalty, bending moment increases, structural integrity as well as the likely vortex drag reductions.

The example described in Ref. 65 has shown that winglets were to be preferred over tip extensions but that case was for quite short tip extensions. The example quoted in Ref. 63 indicates that in order to get 5% drag reduction with tip extensions then a 12% increase in aspect ratio is needed. Such an increase is likely to be heavier than the use of winglets optimized for the same drag reduction. This is because the winglets generally have a smaller chord than the wing tip. From Ref. 68 it is shown that an important correlating parameter is the lift coefficient at the tip. Thus, wings that carry considerable outboard loading are good candidates for wing tip devices.

Comparative analyses of wing tip extensions, winglets, vortex diffusers and tip sails are given in Ref. 63, and the findings are summarized in Figure 37. The even trade lines are for an equal percentage reduction in drag and in bending moment at the wing root and correspond closely to the lines of constant lift coefficient. The added area for each device was kept equal in all cases. The data do not show a clear preference for winglets over tip extensions and overall, the sails showed the best drag reduction for a given area increase. These data apply, however, only to a low aspect ratio wing, and similar data for large aspect ratio, tapered wings may yield differing results.

5.2 Wing-Tip Blowing.

Because of the poorer performance that is obtained from devices such as winglets at off-design conditions, an alternative that has been suggested is to use spanwise-blown jets of air at the tips to increase the effective span (Ref. 70). The idea may have originated with tip blowing as a means of vortex wake hazard alleviation where improvements in L/D were also observed (Ref. 71). Increases in the normal force coefficient of about 0.1 have been reported for quite modest blowing rates. The main advantage of the concept lies in being able to vary the blowing and to be able to select the desired blowing ports in order to get the best performance at any particular flight condition. System studies are needed to determine whether or not the weight of ducting and the effect of the bleed from the engine are sufficient to outweigh the benefits of the concept.

An alternative form of blowing that has been suggested is described in Ref. 63 and is to blow the jets of air in the streamwise direction so as to breakup the tip vortex structure. Measurements of the vortex structure in the wake do show structural changes (Ref. 63), but it does appear that the benefits of the concept level off at higher blowing rates and a tradeoff must be made between blowing energy requirements and the drag reduction.

A logical development of this concept is to mount engines at the wing tips and to use the fan exhaust to break up the tip vortex structure. Whitcomb (Ref. 65) has reported induced drag reductions of the order of one-third with such a configuration on a wing that has significant outboard loading. A large part of this arises from the end-plate effect of the nacelle itself and would be less for a tapered wing. Also, there would be flutter and other structural problems associated with such an installation.

5.3 Active Controls for Load Alleviation

Installation of any wing-tip device, including direct wing-tip extensions, leads to the possibility of undesirable increases in the wing-root-bending moments. Indeed, this essentially limits the amount of tip extension that can be fitted to an aircraft to reduce its induced drag. One possible way to avoid this is to use controlled aileron deflections to off-load the outer wing panels during certain critical phases of the flight when large bending moments are present. To do this requires a sophisticated active control system and three possible applications can be considered (Ref. 72):

(1) Use of symmetric aileron deflections to reduce wing loads during maneuver,
(2) Use of aileron deflections to reduce the wing elastic respose to gust loads, and,

(3) Use of the horizontal stabilizer to reduce the overall airplane response to gusts.

Concepts such as these enable the peak wing loadings to be reduced which enable tip extensions to be added to an aircraft for the same cruise loadings. Alternatively, they enable the weight of the wing structure to be reduced so that the lift (and hence the drag) may be reduced.

The active control concept is currently finding application on the Lockheed L-1011 and has enabled 4.5 foot wing-tip extensions to be added to the aircraft (Figure 38) with no change to the fundamental wing structure. Appropriately distributed accelerometers are used to provide the required inputs to the control systems which in turn drive the aileron servos. The consequent reduction in the induced drag represents about a 3% increase in fuel efficiency for the aircraft.

6. INTERFERENCE DRAG REDUCTION.

Detrimental interference effects usually arise when aerodynamic components are mated together to complete a configuration such that the configuration drag is may be greater than the sum of the drag of the individual components. Very often however, it is possible to capitalize on interference effects to get favorable drag benefits. A very simple example of a favorable interference is given in Ref. 73 where it is shown that the drag of two disks in tandem is less than that for a single disk. For aircraft, the important drag producing interferences are the regions of juncture flow at the wing-root, empennage and pylon junctions etc., and the interferences between the engine mounting and the wing flows.

6.1 Juncture Flow Interferences.

The juncture regions of the various aerodynamic components of an aircraft all lead to a drag penalty and various examples are cited in Refs. 73 through 79. This juncture drag is due to the occurrence of an unfavorable modification of the local pressure field and the additional rapid straining of the vorticity of the incoming boundary layer that usually leads to the formation of vortices in the juncture regions. The flowfield in an unfilleted juncture region is shown in Figure 39 and has long been known to be characterized by the formation of a horseshoe vortex structure ahead of the junction. Careful filleting can reduce these effects, and Ref. 73 gives an example of reducing the drag at the juncture of two struts by more than an order of magnitude with careful fairing. Even with fairings, however, a vortex structure may still ultimately form in the downstream corner regions with its attendant energy loss.

The importance of the geometry to these kinds of flows is also shown by the examples in Figure 40 (from Ref. 59) that correspond to a wing root and an externally mounted gear pod. It is evident that significant drag reductions can be obtained from careful design. At present, the optimized design of these kinds of juncture regions must rely heavily on the use of wind tunnel evaluations and empirical engineering methods. This is because computational methods are not yet sufficiently advanced to correctly account for the complex three-dimensional viscous and transonic effects that are present. Indeed, in many cases only a 3-D Navier-Stokes simulation will provide sufficient accuracy to enable favorable designs to be developed theoretically.

6.2 Engine Installation Effects.

Interferences between the engine/nacelle flow and the wing flow can represent a major souce of interference drag and some specific examples are given in Refs. 80-83. Part of this drag is due to juncture of the pylon, but a large contribution also arises from the presence of the pressure field of the nacelle and the suction and exhaust flows. This is especially true for some of the large fan engines that are now being used (Refs. 84, 85). As a consequence, the positioning of the engine installation can lead to either favorable or unfavorable influences and each installation configuration may have its own merits. For example, Ref. 65 gives two examples where optimizing the engine installation can reduce drag. In one case, that of an underwing mount, careful positioning of the pylon inhibits the spanwise flow induced by the tip vortex system and reduces the induced drag. In the other case, that of a forward-overwing mount, the entrained flow of the exhaust accelerates the upper surface air to enhance the lift. As Figure 41 from that reference shows, induced drag reductions can be obtained through the reduced loadings on the other regions of the wing. Some recent work has also shown that, an aft-slung-underwing mount (Ref. 86) might be a particularly promising concept because the engine is in a region of lower velocity and has less unfavorable interference with the lift producing flow over the wing than does a forward lower mount.

The work in Refs. 87 and 88 has shown, however, that for conventional configurations, the geometry of the installation, the capture ratio and the exhaust velocity all have a bearing on the problem. Subtle variations in these parameters can lead to either beneficial or detrimental effects. Computational methods are currently being developed by industry and government agencies (Refs. 87 and 88) which will enable more optimized engine installations to be developed and some of the recent developments in the area of propulsion system design and installation can be found in Ref. 89.

7. INNOVATIVE AIRCRAFT CONFIGURATIONS.

Because drag reduction techniques are providing drag decreases in smaller and smaller increments, an additional area that warrants some mention is the use of innovative aerodynamic configurations (as opposed to aerodynamic concepts) to reduce the drag penalty and fuel consumption associated with transporting a given amount of load over a given flight mission. This is not a viscous flow drag reduction problem per se, but novel configurations do have the possibility of reducing fuel consumed per tonnage of load carried.

A number of these concepts are shown in Figures 42 through 44, and each is designed with some specific aerodynamic or structural advantage in mind. Thus, the spanloader in Figure 42 (from Ref. 9) is designed to have large aspect ratio and reduced fraction of afterbody drag. The control surface at the wing tips provide an added advantage as winglets. Unfortunately, the operation of such a configuration will require much larger runways and taxi areas than currently available and the high aquisition cost of the system would limit its application under current airline economics.

An alternative method for achieving high span that is receiving considerable interest at the present is to use tandem fuselages as shown in Figure 43 (from Ref. 9). The advantage of this configuration is that because the load is concentrated at two points rather than one, then it is possible to significantly reduce the wing-root bending moment

and consequently the structural weight of the wing box over that of an equivalent large single-body aircraft. The studies in Ref. 9 suggest that this may be as great as a 7% reduction.

The configuration shown in Figure 44 (from Ref. 90), is less extreme and utilizes over-the-wing engines to enhance the wing circulation. The engines are mounted on canards to avoid pylon/wing interferences and because the canards can also act as an auxiliary control surfaces, the empennage size can be reduced.

Use of full canard control surfaces, rather than tail mounted surfaces is also desirable from a drag point of view, because, for static stability and balance, conventional configurations require a download on the horizontal control surface at the tail. This must be balanced by higher wing lift and an attendant drag. For the canard configuration, the canard control surface produces an upload, but the aircraft will be inherently dynamically unstable. Application of an active control system to provide stability will eliminate this problem and the induced drag will be lessened than that for the aft-control surface configuration. The problem is that control system failure may lead to an unflightworthy condition. (The original Wright Flyer flew in this mode, but the instability responses were so slow that the pilot could correct for them.)

Use of active controls on conventional configurations has already been mentioned in the context of load relief, but there is an additional benefit to be derived with relaxed static stability (RSS). If appropriate dynamic and active control surface deflections are available, it is possible to allow the center of gravity to be moved further aft and relax the stability of the aircraft. Smaller control surface sizes are then permissible and the skin- friction drag can be reduced. Figure 45 (from Ref. 70) shows that for the L-1011 aircraft, the benefits that can be derived by utilizing relaxed static stability amount to a 40% reduction in the size of the horizontal stabilizer.

ACKNOWLEDGEMENTS.

The author is indebted to Dr. Joe Vadyak, Dr. J.E. Hackett, Mr. Geoff Webber, Mr. Roy Lange and Prof. Spiro Lekoudis for advice and guidance in the preparation of this paper. Thanks are also due to Ms. Shelby Christophers for the typing of the manuscript.

REFERENCES

1. Head, M.R., History of Research on Boundary Layer Control for Low Drag in U.K., in Boundary Layer and Flow Control, Vol 1, G.V. Lachmann (Ed.), Pergamon Press, 1961, p 104.

2. Pfenninger, W., Laminar Flow Control Laminarization, AGARD Report No. 654, Special Course on Concepts for Drag Reduction, 1977, Paper No. 3.

3. Wagner, R.D., Maddalon, D.V. and Fischer, M.C., Technology Development for Laminar Boundary Layer Control on Subsonic Transport Aircraft, presented at the AGARD symposium on Improvement of Aerodynamic Performance Through Boundary Layer Control and High-Lift Systems, Brussels, Belgium, May 21-23, 1984.

4. Bushnell, D.M., Turbulent Drag Reduction for External Flows, AIAA Paper No. 83-0227, 1983.

5. Gregory, N., Research on Suction Surfaces for Laminar Flow, in Boundary Layer and Flow Control, Vol 2, G.V. Lachmann (Ed.), Pergamon Press, 1961, p104.

6. Thelander, J.A., Allen, J.B., and Welge, H.R., Aerodynamic Development of Laminar Flow Control on Swept Wings using Distributed Suction Through Porous Surfaces, ICAS Paper No. 82-5.1.2, 1982.

7. Lange, R.H., Design Integration of Laminar Flow Control for Transport Aircraft, AIAA Paper No. 83-2440, 1983.

8. Thomas, A.S.W. and Cornelius, K.C., Investigation of a Laminar Boundary Layer Suction Slot, AIAA Journal, Vol 20, No. 6, p790, 1981.

9. Lange, R.H., Trends in Very Large Aircraft Design and Technology, AIAA Paper No. 80-0902, 1980.

10. Pearce, W.E., Progress at Douglas on Laminar Flow Applied to Commercial Transport Aircraft, ICAS Paper No. 82-1.5.3, 1982.

11. Cebeci, T., Kaups, K. and Ramsey, J., A General Method for Calculating Three-Dimensional Compressible Laminar and Turbulent Boundary Layers on Arbitrary Wings, NASA CR-2777, 1977.

12. Srokowski, A.J. and Orszag, S.A., Mass Flow Requirements for LFC WIng Design, AIAA Paper No. 77-1222.

13. Reshotko, E., Boundary Layer Stability and Transition, Annual Review of Fluid Mechanics, Vol. 8, p311, 1976.

14. Malik, M.R. and Orszag, S.A., Comparison of Methods for Prediction of Transition by Stability Analysis, AIAA Paper No. 80-1375.

15. Van Ingen, J.L., Transition, Pressure Gradient, Suction, Separation and Stability Theory, AGARD Conference on Laminar-Turbulent Transition, AGARD-CP-224, p20.1, 1977.

16. Reynolds, G.A. and Saric, W.S., Experiments on the Stability of the Flat-Plate Boundary Layer with Suction, AIAA Paper No. 82-1026, 1982.

17. Reed, H.L. and Nayfeh, A.H., Stability of Flow over Plates with Porous Suction Strips, AIAA Paper No. 81-1280, 1981.

18. Saric, W.S. and Nayfeh, A.H., Nonparallel Stability of Boundary Layers with Pressure Gradients and Suction, AGARD Conference on Laminar-Turbulent Transition, AGARD-CP-224, p6.1, 1977.

19. Holmes, B.J. and Obara, C.J., Observations and Implications of Natural Laminar flow on Practical Airplane Surfaces, ICAS paper No. 82-5.1.1, 1982.

20. Kachanov, Y.S., Koslov, V.V. and Levchenko V. Ya., Experimental Study of The Influence of Cooling on The Stability of Laminar Boundary Layers, Isvestia Sibirskogo Otdielenia Ak. Nauk SSSR, Seria Technicheskikh Nauk, Novosibirsk, No. 8-2, p75, 1974.

21. Lekoudis, S.G., The Stability of a Boundary Layer on a Swept Wing with Wall Cooling, AIAA Paper No., 79-1495, 1979.

22. Reshotko, E., Drag Reduction by Cooling in Hydrogen Fueled Aircraft, Journal of Aircraft, Vol. 16, No. 9, p584-590, 1979.

23. Brewer, D.G., The Case for Hydrogen Fueled Transport Aircraft, Astronautics and Aeronautics, Vol. 12, No. 5, p40-51, 1974.

24. Liepmann, H.W., Brown, G.L. and Nosenchuck D.M., Control of Laminar-Instability Waves Using a New Technique, J. Fluid Mech., Vol 118, p187, 1982.

25. Liepmann, H.W. and Nosenchuck D.M., Active Control of Laminar-Turbulent Transition, J. Fluid Mech., Vol 118, p201, 1982.

26. Milling, R.W., Tollmien-Schlichting Wave Cancellation, Physics of Fluids, Vol. 24, p979, 1981.

27. Thomas, A.S.W., The Control of Boundary-Layer Transition Using a Wave Superposition Principle, J. Fluid Mech., Vol. 137, p233, 1983.

28. Saric, W.S. and Thomas, A.S.W., Experiments on the Subharmonic Route To Turbulence in Boundary layers, Proceedings of the International Symposium on Transition (to be published), Kyoto, Japan, Sept., 1983.

29. Walsh, M.J. and Lindemann, A.M., Optimization and Application of Riblets for Turbulent Drag Reduction, AIAA Paper No. 84-0347, 1984.

30. Hooshmand, A., Youngs, R.A., Wallace, J.M. and Balint, J.-L., An Experimental Study of Changes in The Structure of Turbulent Boundary Layer Due to Surface Geometry Changes, AIAA Paper No. 83-0230, 1983.

31. Gallagher, J.A. and Thomas, A.S.W., Turbulent Boundary Layer Characteristics Over Streamwise Grooves, AIAA Paper No. 84-2185, 1984.

32. Corke, T.C., Nagib, H.M. and Guezennec, Y.G., A New View on Origin, Role and Manipulation of Large Scales in Turbulent Boundary Layers, NASA CR No. 165861, 1982.

33. Bertelrud, A., Truong, T.V. and Avellan, F., Drag Reduction in Turbulent Boundary Layers Using Ribbons, AIAA Paper No. 82-1370, 1982.

34. Anders, J.B., Hefner, J.N. and Bushnell, D.M., Performance of Large-Eddy Breakup Devices at Post-Transitional Reynolds Numbers, AIAA Paper No. 84-0345.

35. Corke, T.C., Guezennec, Y.G. and Nagib, H.M., Modification of Drag of Turbulent Boundary Layers Resulting from Manipulation of Large-Scale Structures. In Viscous Flow Drag Reduction, edited by Hough G.R., Vol 72, Progress in Astronautics and Aeronautics, 1980.

36. Mumford, J.C. and Savil, A.M., Parametric Studies of Flat Plate Turbulence Manipulators Including Direct Drag Results and Laser Flow VIsualization, presented at the ASME Fluids Engineering Symposium, Feb. 12-16, New Orleans, 1984.

37. So, R.M.C. and Mellor, G.L., An Experimental Investigation of Turbulent Boundary Layers Along Curved Surfaces, NASA CR No. 1940, 1972.

38. Brown, G.L and Thomas, A.S.W., Large Structure in a Turbulent Boundary Layer, Physics of Fluids, Vol. 20, No. 10, Pt. 2, ps243, 1977.

39. Kendall, J.M., The Turbulent Boundary Layer Over a Wall With Progressive Surface Waves, J. Fluid Mech., Vol. 41, p259, 1970.

40. Lin, J.C., Walsh, M.J., Watson, R.D. and Balasubramanian, R., Turbulent Drag Characteristics of Small Amplitude Rigid Surface Waves, AIAA Paper No. 83-0228, 1983.

41. Sengupta, T. and Lekoudis, S.G., Calculation of Turbulent Boundary Layers Over Moving Wavy Surfaces, AIAA Paper No. 83-1670, 1983.

42. Sengupta, T., Turbulent Boundary Layers Over Rigid and Moving Wavy Surfaces, Ph.D Dissertation, School of Aerospace Engineering, Georgia Institute of Technology, in preparation, 1984.

43. Kuhn, G.D., Moin, P., Kim, J. and Ferziger, J., Turbulent Flow in a Channel with a Wall with Progressive Surface Waves, in Symposium on Laminar and Turbulent Boundary Layers Control, Modification and Marine Applications, New Orleans, February, 1984.

44. McMichael, J.M., Klebanoff, P.S. and Mease N.E., Experimental Investigation of Drag on a Compliant Surface. In Viscous Flow Drag Reduction, edited by Hough G.R., Vol 72, Progress in Astronautics and Aeronautics, 1980.

45. Mulhearn, P.J., Turbulent Flow Over a Periodic Rough Surface, Physics of Fluids, Vol 21., p1113, 1978.

46. Coles, D. and Savas, O., Interactions for Regular Patterns of Spots in a Laminar Boundary Layer. In Laminar-Turbulent Transition, Eppler, R. and Fasel, H. (Editors), Springer-Verlag, Berlin, 1980.

47. Chambers, F.W., Preliminary Measurements of a Synthetic Turbulent Boundary Layer, Lockheed-Georgia Research Report No. LG82RR0009, 1982.

48. Goodman, W.L., Attempts to Alter Turbulent Large Eddy Structure Through Emmons Spot Modification, Washington Drag Reduction Symposium Abstracts, p65, 1982.

49. Little, B.H. and Whipkey, R.R., Locked Vortex Afterbodies, Journal of Aircraft, Vol. 16, No. 5, p296, 1979.

50. Roshko, A. and Koenig, K, Interaction Effects on the Drag of Bluff Bodies in Tandem. In Aerodynamic Drag Mechanisms of Bluff Bodies and Road Vehicles, Sovran, G., Morel, T. and Mason, W.T., (Editors), Plenum Press, 1978.

51. Howard, F.G., Goodman, W.L. and Walsh, M.J., Axisymmetric Bluff-Body Drag Reduction using Circumferential Grooves, Presented at the AIAA Applied Aerodynamics Conference, Danvers, Mass., July, 1983.

52. Quass, B., Howard, F.G., Weinstein, L. and Bushnell, D., Longitudinal Grooves for Bluff-Body Drag Reduction, AIAA Journal, Tech. Notes, Vol. 19, No. 4, p535, 1981.

53. Viets, H., Piatt, M. and Ball, M., Boundary Layer Control by Unsteady Vortex Generation, Proceedings of ASME Symposium on Aerodynamics of Transportation, p223, ASME, New York.

54. Brogna, S.J. and Hawkes, R.J., Effect of Base Suction on Subsonic Drag of Bluff Bodies, Journal of Aircraft, Vol. 15, No. 7, p443, 1978.

55. Stratford, B.S., The Prediction of Separation of the Turbulent Boundary Layer, J. Fluid Mech., Vol. 5, No. 1, p1, 1959.

56. Smith, A.M.O., Stokes, T.R. and Lee, R.S., Optimum Tail Shapes for Bodies of Revolution, J. Hydronautics, Vol. 15, No. 1, p67, 1981.

57. Lekoudis, S.G., Radwan, S.F., and Sankar, N.L., A Method for Designing Three-Dimensional Configurations with Prescribed Skin Friction, AIAA Paper No. 84-0526.

58. Hackett, J.E., Phillips, C.G. and Lilley, D.E., Three-Dimensional Wake Flow Measurements for a Wing and a Bluff Car-Like Body, Lockheed-Georgia Engineering Report, LG81ER0201, 1981, (prepared under NSF Grant No. ENG-7900891).

59. Webber, G.W., Aerodynamic Development for Efficient Military Cargo Transports, AIAA Paper No. 83-1822, 1983.

60. McCluney, B., Improving the Belfast, Flight International, 3 Aug., 1967.

61. Polhamus, E.C. and Spreemann, K.P., Effect of High Subsonic Speeds on the Static Stability and Vertical-Tail-Load Characteristics of a Complete Model Having a Delta Wing, NACA RM L157k15a, 1958.

62. Perkins, C.D. and Hage, R.E., Airplane Performance Stability and Control, John Wiley and Sons, New York, 1953.

63. Webber, G.W. and Dansby, T., Wing tip Devices for Energy Conservation and Other Purposes - Experimental and Analytical Work in Progress at Lockheed-Georgia Company, Canadian Aeronautics and Space Journal, Vol. 29, No. 2, p105, 1983.

64. Whitcomb, R.T., A Design Approach and Selected Wind-Tunnel Results at High Subsonic Speeds for Wing-Tip Mounted Winglets, NASA TN D-8260, 1976. (See also NASA TN D-8624,8627,8473,8474,8478 for specific details of winglet development.)

65. Whitcomb, R.T., Methods for Reducing Subsonic Drag Due to Lift, Paper No. 2 of AGARD Special Course on Concepts for Drag Reduction, AGARD Rept. No. 654, 1977.

66. Darel, I., Eliraz, Y. and Barnett, Y., Winglets Development at Israel Aircraft Industries, ICAS Paper No. 80-12.5, 1980.

67. Gifford, R.V. and van Dam, C.P., The Design Integration of Wingtip Devices for Light General Aviation Aircraft, ICAS Paper No. 82-1.4.4, 1982.

68. Hackett, J.E., Vortex Drag Reduction by Aft-Mounted Diffusing Vanes, ICAS Paper No. 80-13.4, 1980.

69. Spillman, J.J., The Use of Wingtip Sails to Reduce Vortex Drag, Aeronautical Journal, Paper No. 618, p387, 1978.

70. Wu, J.M., Vakili, A. and Chen, Z.L., Wing Tip Jets Aerodynamic Performance, ICAS Paper No., 82-5.6.3, 1982.

71. Poppelton, E.D., Effect of Air Injection Into Core of Trailing Vortex, Eng. Notes, J. of Aircrft, Vol. 8, No. 8, 1971.

72. Foss, R.L. and Lewolt, J., Use of Active Controls for Fuel Conservation of Commercial Transports, AIAA Paper No. 77-1220, 1977.

73. Hoerner, S.F., Fluid Dynamic Drag, published by the author, New Jersey, 1958.

74. Küchemann, D., Some Remarks on the Interference Between a Swept Wing and a Fuselage. In Aerodynamic Interference, AGARD-CP-71-71, Paper No. 1, 1971.

75. Weber, J., Interference Problems on Wing-Fuselage Combinations, Part 1, RAE-TR-69130, 1969.

76. Weber, J. and Joyce, M.G., Interference Problems on Wing-Fuselage Combinations, Part 2, RAE-TR-71179, 1971, Part 3, RAE-TR-73189 and Part 4, RAE-TR-73190, 1974.

77. Yoshino, F., An Experimental Investigation of the Effect of Fuselage on Wing Characteristics, Princeton University Rept. No. AMS-TR-1151, Prepared for the Office of Naval Research, 1975.

78. Gersten, K., Corner Interference Effects, AGARD Rept. No. 299, 1959.

79. Sopher, R., Design of a Fairing fo the Junction of Two Wings, J. Aircraft, Vol. 4, No. 4, p379, 1967

80. Patterson, J.C., Wind Tunnel Studies of Nacelle Interference Drag at High Subsonic Speeds Including the Effect of Powered Jets, NASA SP-124, Paper No. 18, p259, 1966.

81. Runckel, J.F., Aerodynamic Interference Between Exhaust System and Airframe, AGARD CP-71-71, Paper No. 15, 1971.

82. Ewald, B., Airframe-Engine Interaction for Engine Configurations Mounted Above the Wing, AGARD CP-150, 1975.

83. Hess, J.L. and Faulkner, S.M., Determination of Low Speed Interference Effects by Superposition, AGARD CP-71-71, Paper No. 24, 1971.

84. Aldridge, S.E. and Nye, J.L., Experimental Results of High Bypass Ratio Turbofan and Wing Aerodynamic Interference, AGARD CP-71-71, Paper No. 23, 1971.

85. Swan, W.C. and Sigilla, A., The Problem of Installing a Modern High Bypass Engine on Twin Jet Transport Aircraft, AGARD CP-124, Paper No. 17, 1973.

86. The Effect of Underwing Aft-Mounted Nacelles on the Characteristics of a High-Wing Transport, NASA-Langley Rept. No. 1-15664, 1984, to be published.

87. Atta, E.H. and Vadyak, J., A Grid Embedding Transonic Flow Analysis Computer Program for Wing/Nacelle Configurations, NASA-CR-166529, 1983.

88. Vadyak, J. and Atta, E.H., A Computational Program for the Calculation of Three-Dimensional Transonic Nacelle/Inlet Flowfields, NASA-CR-166528, 1983.

89. Aerodynamics of Power Plant Installation, AGARD-CP-301, 1981.

90. Krenz, G. and Hilbig, R., Aerodynamics Concepts for Fuel-Efficient Transport Aircraft, ICAS Paper No. 82-1.5.2, 1982.

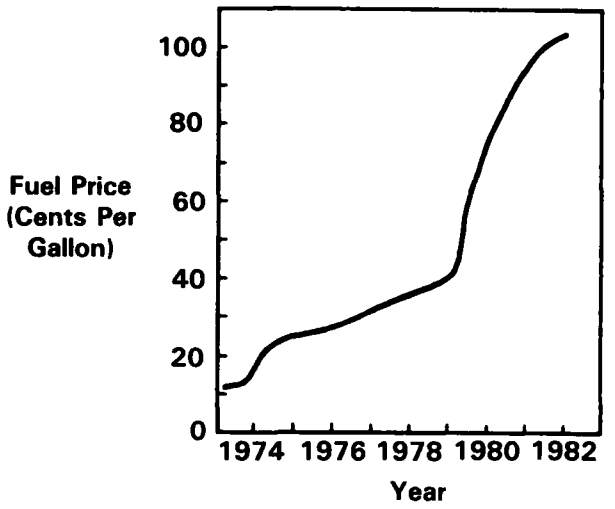


Figure 1. Trend in world fuel prices.

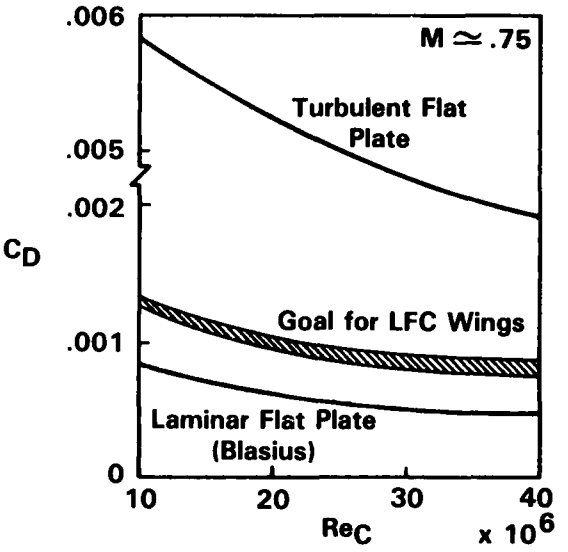


Figure 4. Skin friction goal for LFC surfaces.

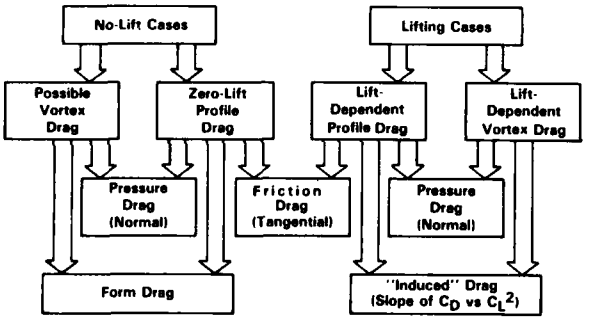


Figure 2. Sources and terminology of drag contributions.

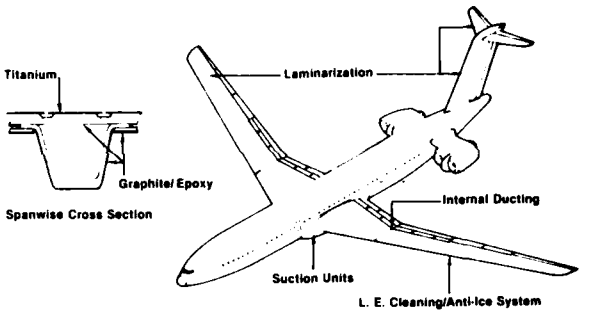


Figure 5. The Lockheed LFC aircraft concept (Ref. 9).

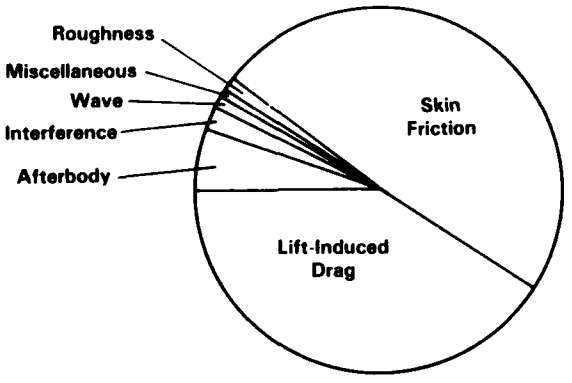


Figure 3. Contributions of different drag sources for a typical transport aircraft.

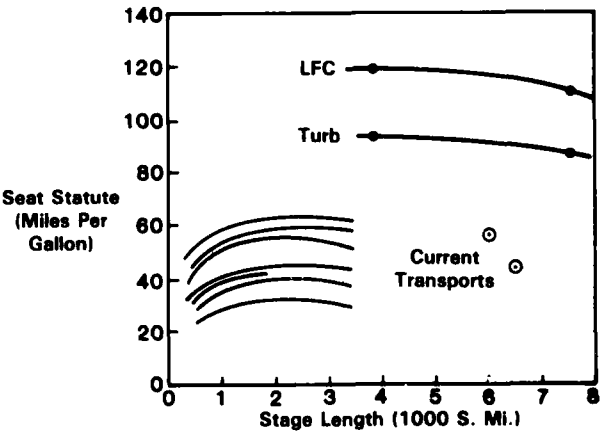
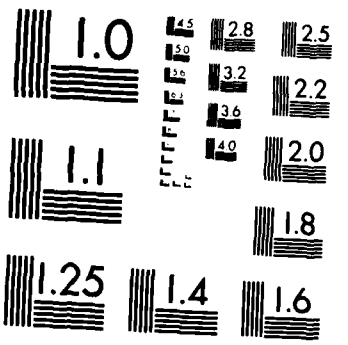


Figure 6. Fuel efficiency - current transports versus an advanced LFC aircraft and an advanced turbulent aircraft (Ref. 7).

AD-A147 396 PROCEEDINGS OF THE CONFERENCE ON IMPROVEMENT OF AERODYNAMIC PERFORMANCE T..(U) ADVISORY GROUP FOR AEROSPACE RESEARCH AND DEVELOPMENT NEUILLY.. AUG 84 3/5

UNCLASSIFIED AGARD-CP-365 F/G 20/4 NL





MICROCOPY RESOLUTION TEST CHART
NATIONAL BUREAU OF STANDARDS-1963-A

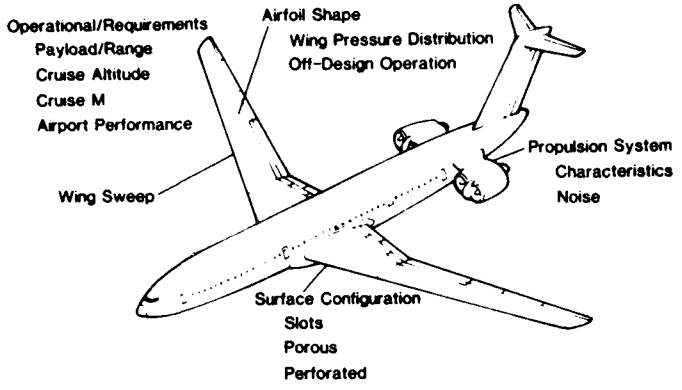


Figure 7(a). Factors affecting LFC design (Ref. 7).

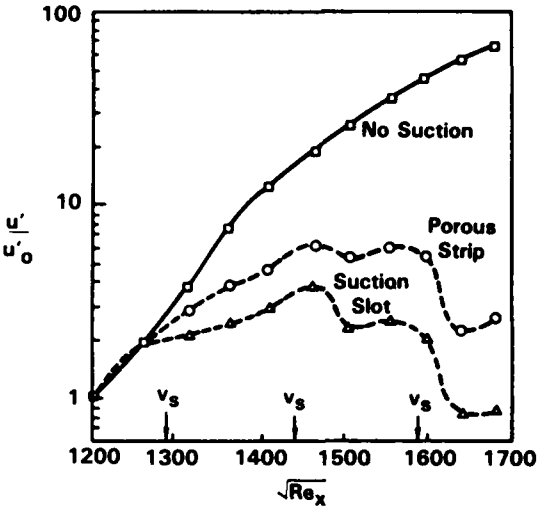


Figure 8. Instability wave growths for suction through a slot or through a wide porous strip.

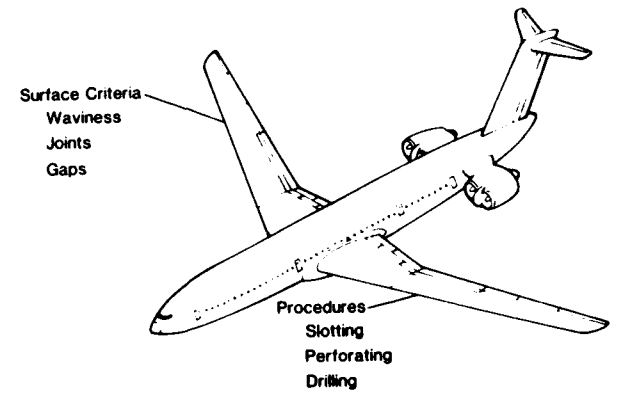


Figure 7(b). Factors affecting LFC manufacturing (Ref. 7).

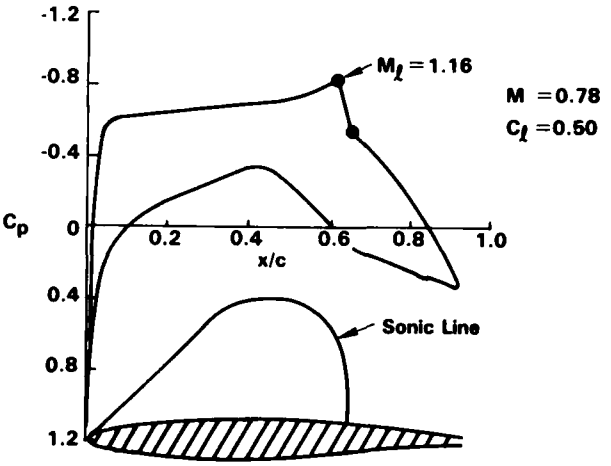


Figure 9. Wing geometry and surface pressures characteristic of a Natural Laminar Flow wing.

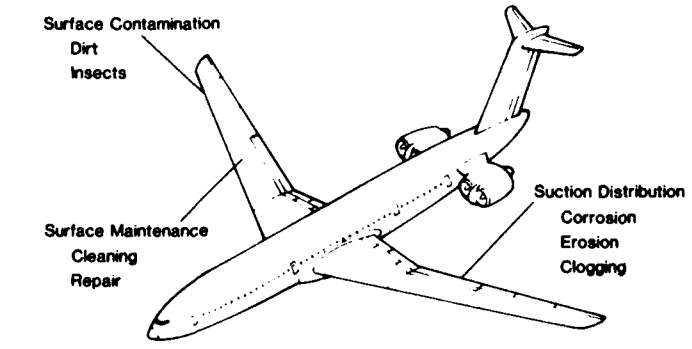


Figure 7(c). Factors affecting LFC operations (Ref. 7).

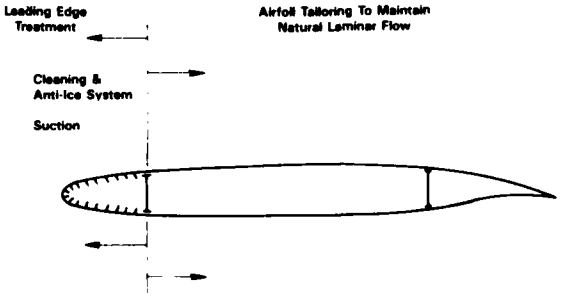


Figure 10. The Hybrid Laminar Flow Control concept.

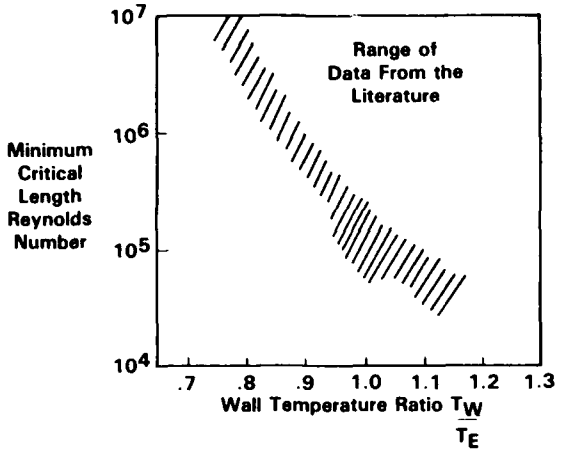


Figure 11. The effect of wall cooling on transition Reynolds numbers (Ref. 21).

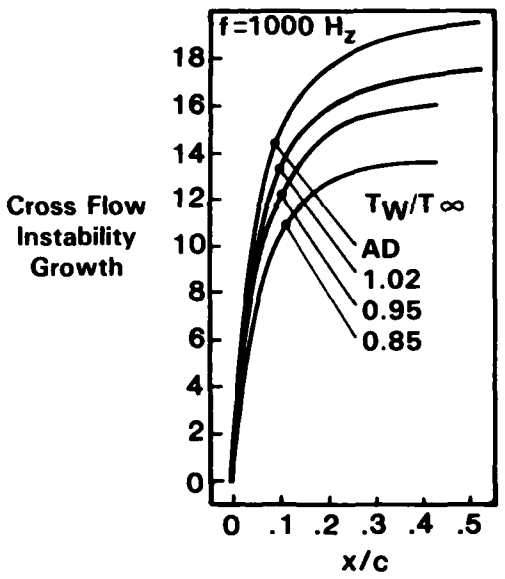


Figure 12. Crossflow instability growth for different wall temperatures (Ref. 22).

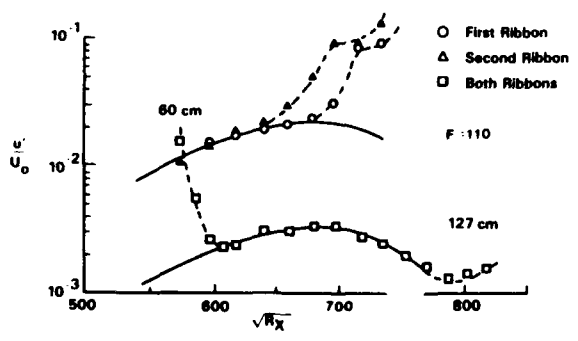


Figure 13. Instability wave growth with and without a control disturbance being present (Ref. 28).

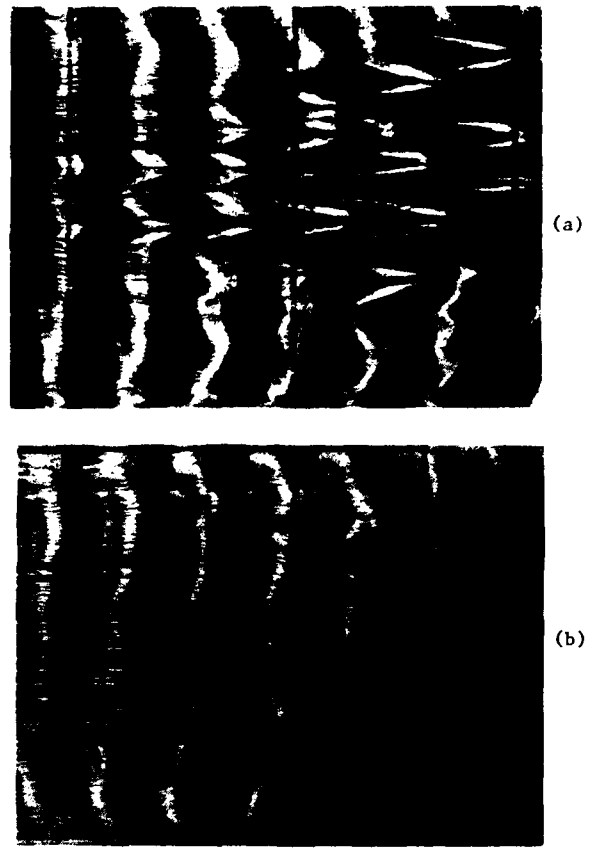


Figure 14. Smoke wire visualization of (a) uncontrolled and (b) controlled instability waves (Ref. 28).

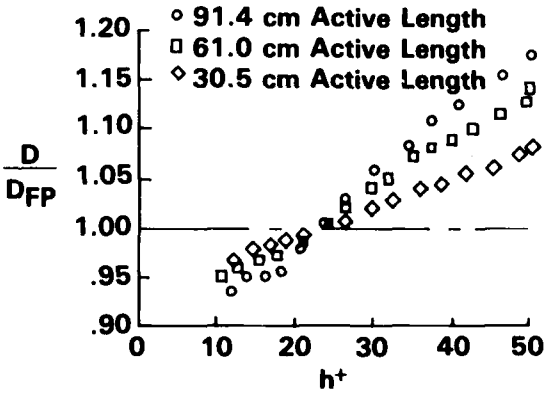


Figure 15. Drag reduction over riblet surface (Ref. 30).

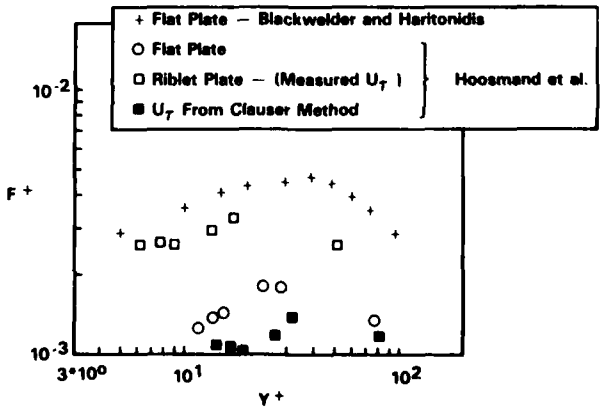


Figure 16. Turbulent bursting frequency over riblet surface (Ref. 31).

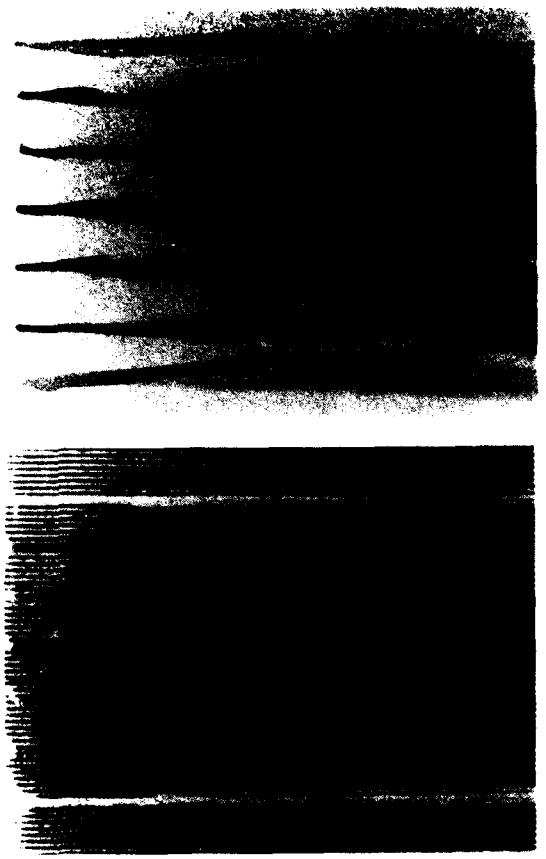


Figure 17. Multi-colored dye visualization of the flow over (a) a flat plate surface and (b) a riblet surface. Flow is from left.

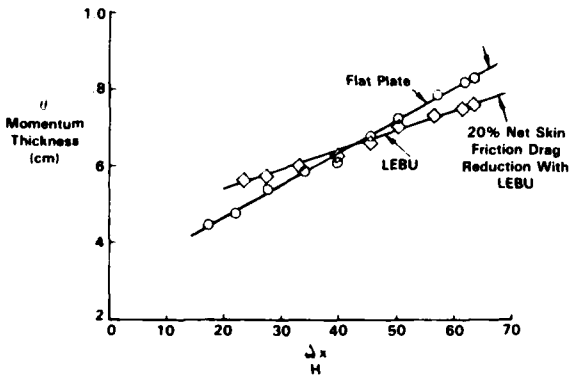


Figure 18. Boundary layer development downstream of a LEBU (Ref. 36).

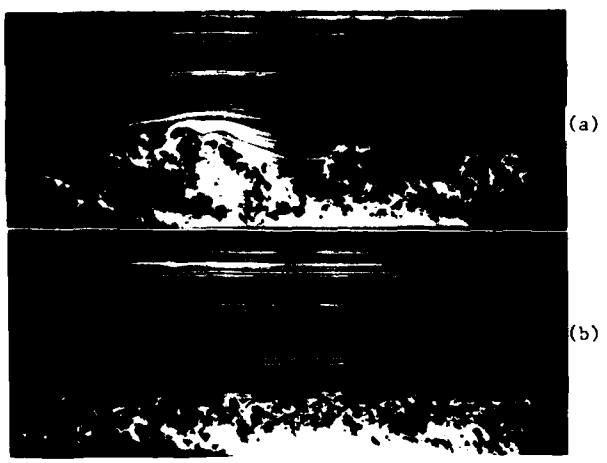


Figure 19. Smoke wire visualizations of (a) controlled and (b) uncontrolled turbulent boundary layer structure (Ref. 36). Flow is from right to left.

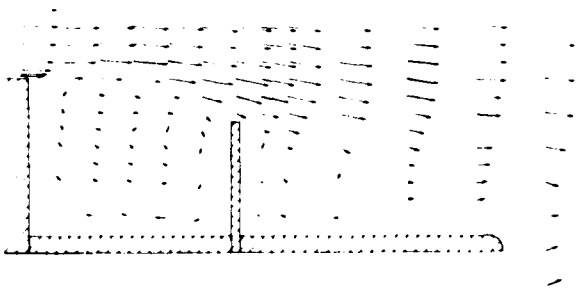


Figure 20. Locked vortex afterbody flow control (Ref. 49).

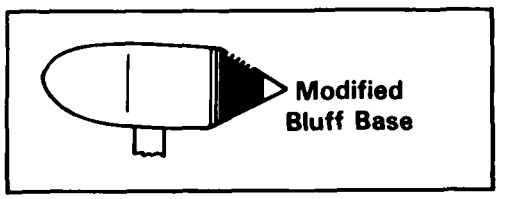


Figure 21. Transverse grooves for afterbody drag reduction (Ref. 51).





Figure 22. Flow visualization of the flow over an afterbody (a) with and (b) without transverse grooves (Ref. 51).

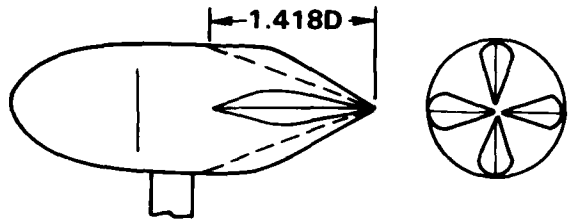


Figure 23. Streamwise grooves for afterbody drag reduction (Ref. 52).

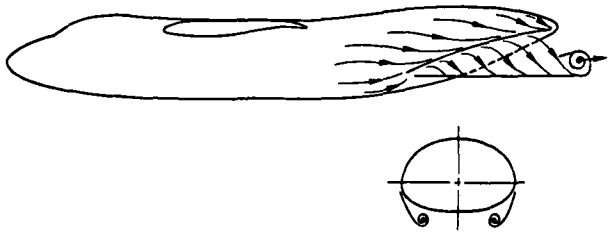


Figure 24. The vortex wake behind an upswept afterbody.

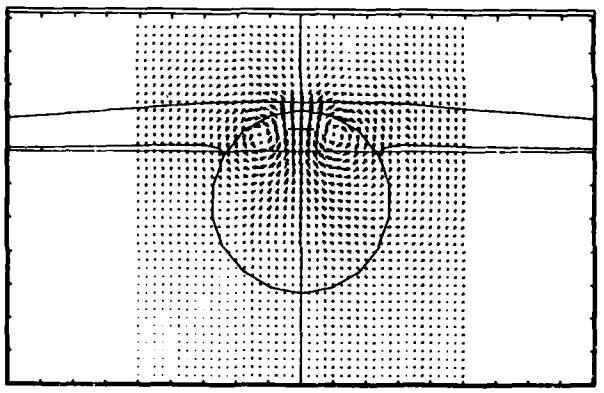


Figure 25. Crossflow velocities in the wake of a highly upswept fuselage.

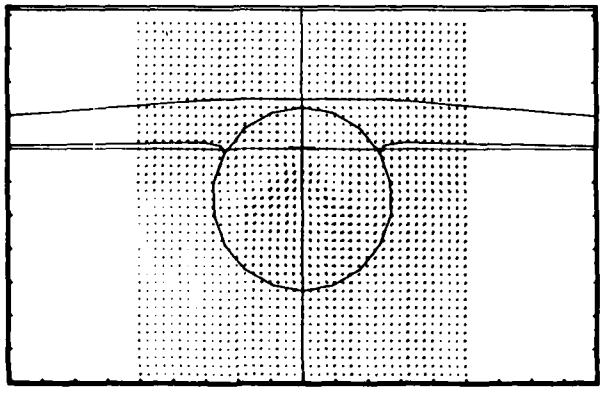


Figure 26. Crossflow velocities in the wake of a fuselage with low upsweep.

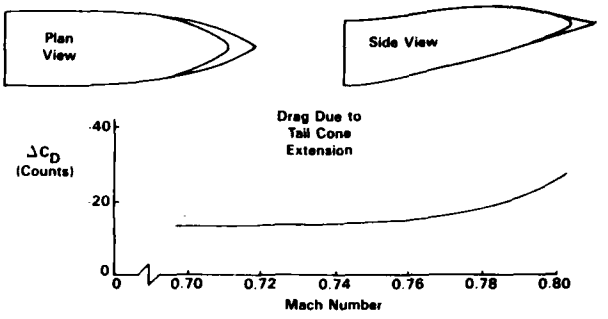


Figure 27. The use of a tail cone to reduce afterbody drag (Ref 59).

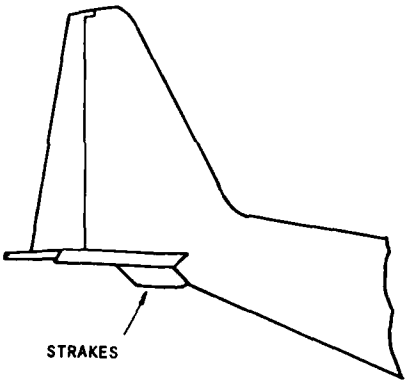


Figure 28. The drag reducing strakes on the C-130 aircraft.

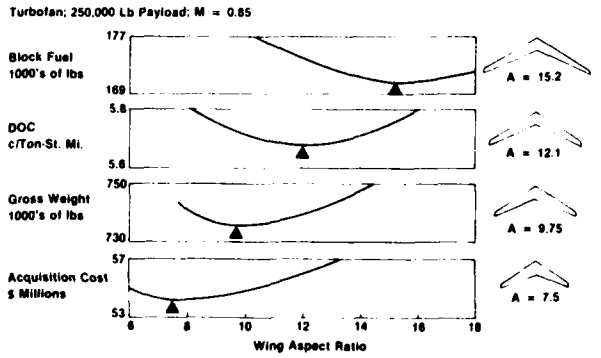


Figure 29. Effect of wing aspect ratio (Ref. 9).

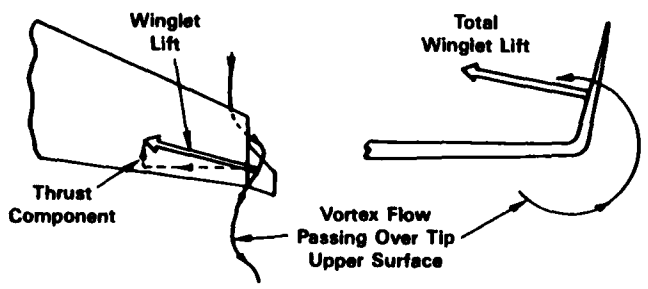


Figure 30. Winglets for drag reduction (Ref 63).

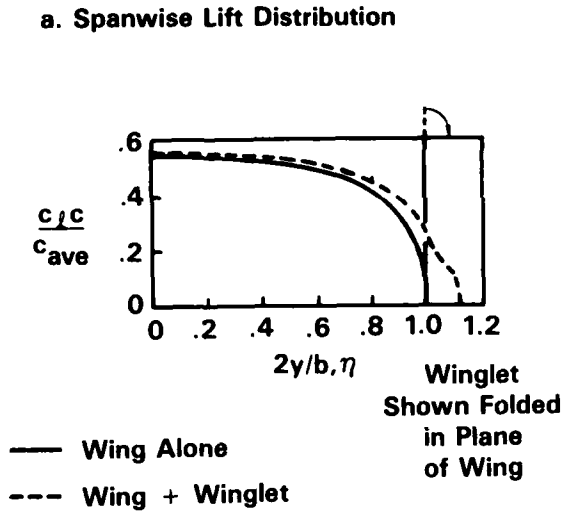


Figure 31. Spanwise lift and drag components for a wing with and without winglets.

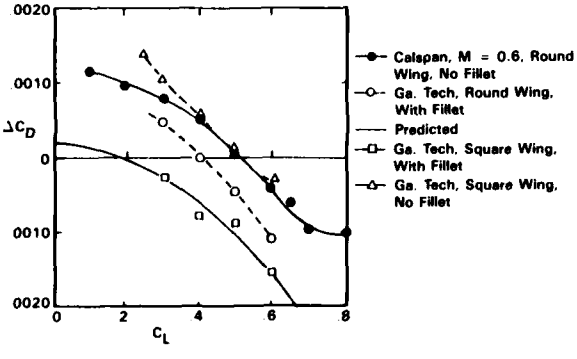


Figure 32. Winglet performance with and without appropriate filleting.

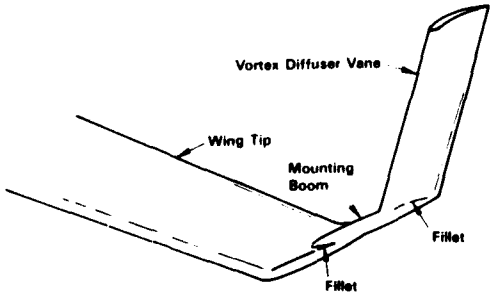


Figure 33. The vortex diffusing vane (Ref. 68).

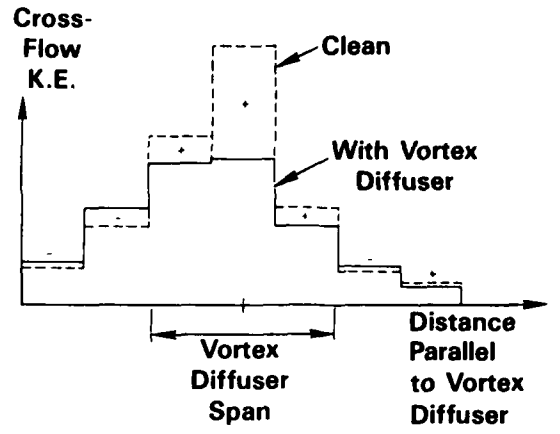


Figure 34. The reduction in crossflow kinetic energy available from vortex diffusing vanes (Ref. 68).

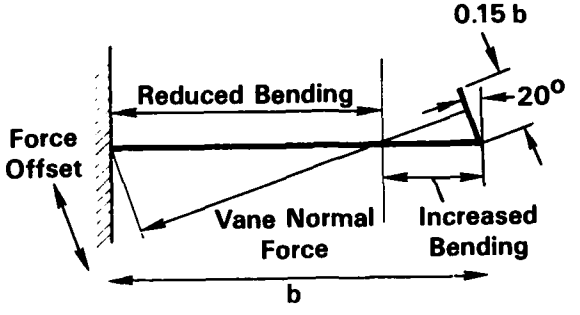


Figure 35. Possible reduction in wing-root bending with vortex diffusing vanes (Ref. 68).

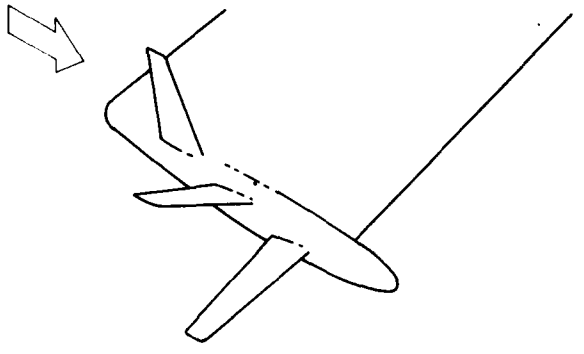


Figure 36. Wing-tip sails for drag reduction.

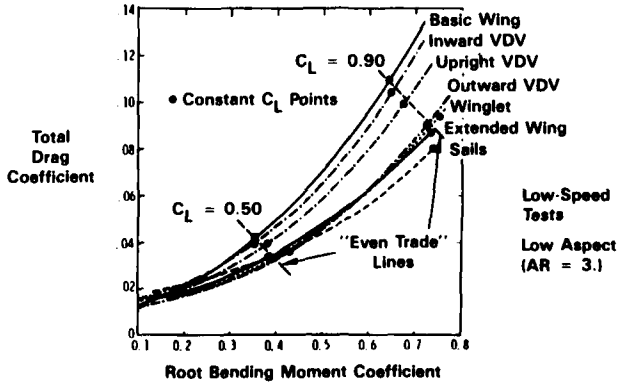


Figure 37. Comparitive performance of various wing-tip devices and tip extensions (Ref. 63).

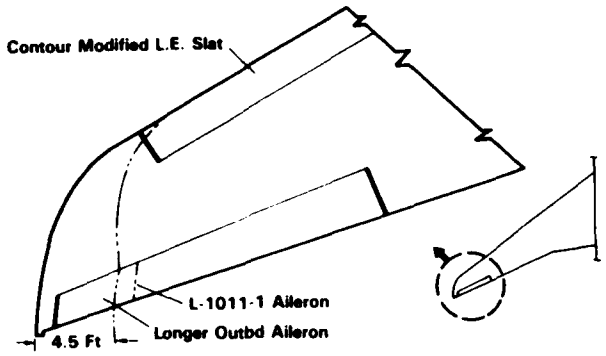


Figure 38. Wing-tip extensions for the L-1011 aircraft with active controls (Ref. 70).



Figure 39. The horseshoe vortex structure ahead of an unfilleted junction.

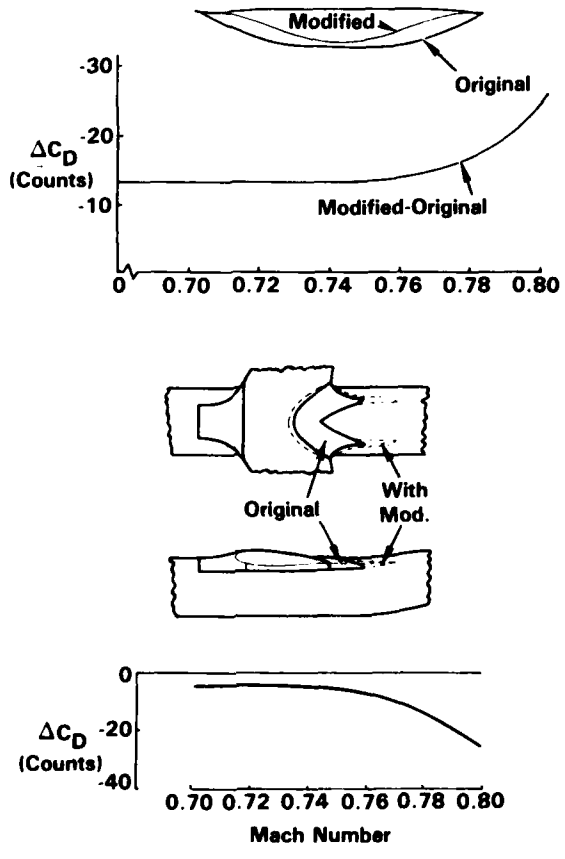


Figure 40. Reduction of juncture drag with filleting.

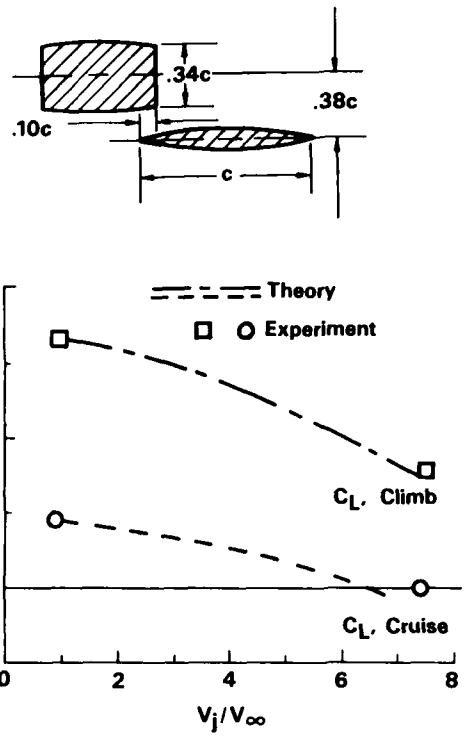


Figure 41. Induced drag reduction with an over wing engine mount (Ref. 65).

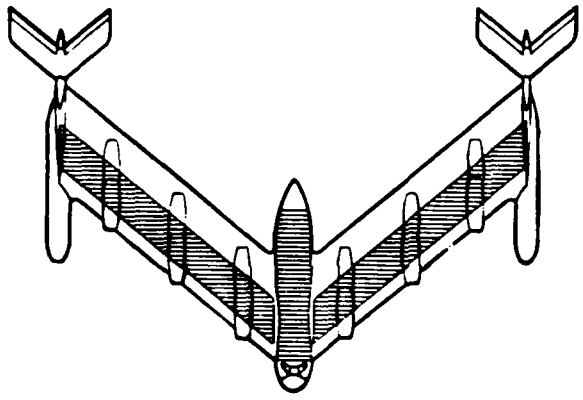


Figure 42. The spanloader concept (Ref. 9).

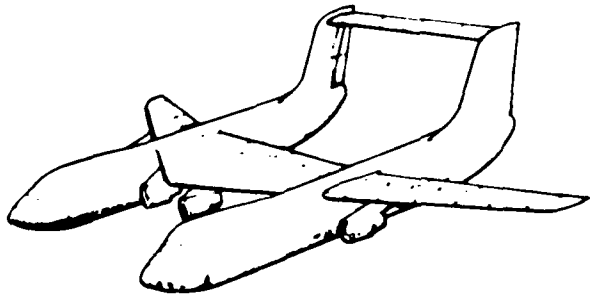


Figure 43. The tandem fuselage concept (Ref. 9).

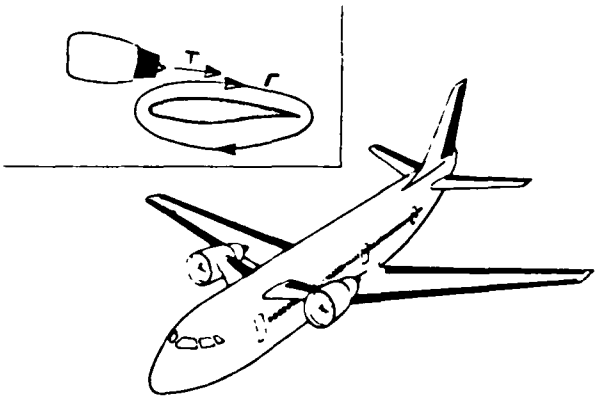


Figure 44. Canard mounted engines for performance improvements (Ref. 90).

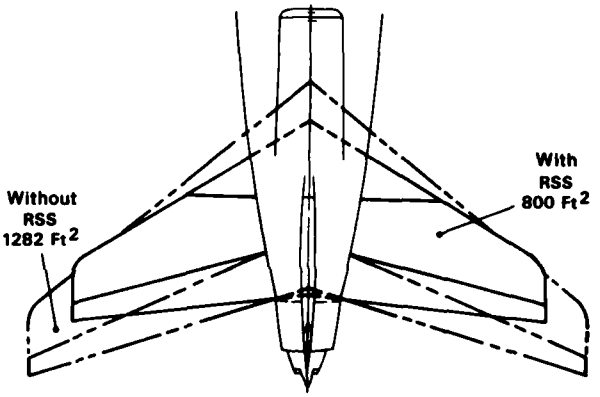


Figure 45. Reduction in control surface size through relaxed static stability (Ref. 70).

APPLICATION DE CRITERES BI ET TRIDIMENSIONNELS AU CALCUL DE LA TRANSITION ET DE LA COUCHE LIMITE D'AILES EN FLECHE

D. ARNAL et E. COUSTOLS

Office National d'Etudes et de Recherches Aérospatiales (ONERA)
Centre d'Etudes et de Recherches de TOULOUSE
2 avenue Edouard Belin
31055 TOULOUSE Cedex - FRANCE

RESUME

Après avoir rappelé les différentes formes d'apparition de la turbulence sur une aile en flèche infinie, on propose une méthode de prédiction de la transition pour ce type d'écoulement tridimensionnel, ainsi qu'une modélisation simple de la région de transition. On étudie ensuite de façon théorique l'influence de la mise en flèche d'un profil d'aile sur la transition et, par conséquent, sur la traînée de ce profil. L'efficacité d'une aspiration à la paroi est aussi discutée.

APPLICATION OF TWO AND THREE-DIMENSIONAL CRITERIA FOR CALCULATING TRANSITIONS AND BOUNDARY LAYERS OVER SWEPT WINGS

SUMMARY

The possible origins of turbulence on an infinite swept wing will be, at first, recalled. A method for calculating the beginning of transition, as well as the transition region itself, is suggested for that kind of three-dimensional flow. Then, from a theoretical point of view, we look at the influence of sweep angle on transition and on drag coefficient of the considered airfoil. Efficiency of wall suction is also discussed.

NOTATIONS

(x, z, y) (x1, z1, y)	repères cartésiens orthonormés
Q	vitesse totale
U,W, V	composantes de la vitesse dans (x, z, y)
U1,W1, V	composantes de la vitesse dans (x1,z1, y)
Vp	vitesse d'aspiration à la paroi
c	corde du profil dans la direction orthogonale au bord d'attaque
Cf	coefficient de frottement pariétal suivant x1
Cp	coefficient de pression
Cx	coefficient de traînée totale
Tu	taux de turbulence extérieure
α_n	incidence normale
β_o	angle entre les lignes de courant extérieure et pariétale
ε	angle avec la direction normale à la ligne de courant extérieure
φ	angle de flèche
δ	épaisseur physique de couche limite
$\tilde{\delta 1} = \int_o^\delta (1 - \frac{W}{W_e})\, dy$ $\theta = \int_o^\delta \frac{W}{W_e}(1 - \frac{W}{W_e})\, dy$	épaisseurs intégrales sur la ligne d'arrêt
$\theta = \int_o^\delta \frac{U}{U_e}(1 - \frac{U}{U_e})\, dy$	épaisseur intégrale bidimensionnelle
$\delta 1 = \int_o^\delta (1 - \frac{U1}{U1_e})\, dy$ $\delta 2 = \int_o^\delta - \frac{W1}{U1_e}\, dy$ $\theta 11 = \int_o^\delta \frac{U1}{U1_e}(1 - \frac{U1}{U1_e})dy$	épaisseurs intégrales tridimensionnelles

$H = \delta 1/\theta$ — paramètre de forme bidimensionnel

$H1 = \delta 1/\theta 11$ — paramètre de forme longitudinal

$R\theta = \frac{U_e\ \theta}{\nu}$

$R\tilde{\theta} = \frac{W_e\ \tilde{\theta}}{\nu}$

$R\theta 11 = \frac{U1_e\ \theta 11}{\nu}$

$R\delta 2 = \frac{U1_e\ \delta 2}{\nu}$

$Rc = \frac{Q_\infty\ c}{\nu \cos\varphi}$

— nombres de Reynolds

ν — viscosité cinématique

Indices

cr	critique
e	extérieur à la couche limite
t	régime turbulent
BF	bord de fuite
T	début de transition
∞	infini amont
ϵ	dans la direction définie par l'angle ϵ

1 - INTRODUCTION

Il est bien connu que la position de la transition sur une aile d'avion se répercute directement sur l'épaisseur de la couche limite au bord de fuite, elle-même liée au coefficient de traînée de l'aile. Le problème consiste à réduire l'étendue de la région turbulente, où la couche limite épaissit très rapidement, donnant lieu à des coefficients de frottement pariétaux bien plus élevés qu'en régime laminaire. Tant que l'on reste en écoulement bidimensionnel, l'allure de la distribution de vitesse extérieure suffit pour donner une bonne idée de l'emplacement de la transition : dans les distributions de type "laminaire", où l'écoulement est accéléré sur une longue portion de la corde, la transition se produira aux alentours du maximum de vitesse extérieure ; dans les cas où il existe une pointe de survitesse près du bord d'attaque, elle aura lieu dans le gradient de pression positif immédiatement en aval, souvent dans un bulbe de décollement.

Le problème est de savoir ce que deviennent ces tendances lorsque l'aile est mise en flèche. Il se crée alors un écoulement transversal qui conduit à des formes d'instabilité inconnues en bidimensionnel, dont il importe de pouvoir préciser les effets sur la transition. Le but de cet article est d'évaluer ces effets de façon théorique, en calculant le développement de la couche limite sur une aile placée à divers angles de flèche et d'incidence ; avant d'aborder les applications proprement dites, on décrira les éléments nécessaires au calcul complet de la couche limite depuis le bord d'attaque jusqu'au bord de fuite : technique numérique, critères de transition, modélisations de la région de transition et du régime turbulent établi.

La majeure partie des calculs effectués concerne des couches limites se développant sur une paroi imperméable. On présentera en outre quelques résultats obtenus en imposant une aspiration pariétale uniforme ; cette technique est certainement la plus fiable pour contrôler l'écoulement laminaire, mais son efficacité est moins bien connue en tridimensionnel qu'en bidimensionnel ; on s'attachera donc à décrire son influence, aussi bien sur l'écoulement transversal que sur l'écoulement longitudinal.

2 - CALCUL DE LA COUCHE LIMITE LAMINAIRE SUR UNE AILE EN FLECHE INFINIE

2.1. Repères et notations - Généralités

La figure 1 montre le schéma d'une aile en flèche, sur lequel sont reportées les principales notations. φ désigne l'angle de flèche. La vitesse à l'infini amont Q_∞ donne une composante normale au bord d'attaque U_∞ et une composante parallèle au bord d'attaque W_∞. On définit deux repères : l'un (x, z, y) est lié à l'aile, l'autre (x1, z1, y) est lié à la ligne de courant extérieure ; y désigne la normale à la paroi, dirigée vers l'écoulement.

La vitesse locale sera notée Q(y). U(y) et W(y) désignent les projections de Q(y) suivant x et z, tandis que U1(y) et W1(y) -appelés respectivement profil longitudinal et profil transversal- sont les projections de Q(y) suivant les axes x1 et z1.

A l'extérieur de la couche limite, U et W atteignent respectivement les valeurs U_e et W_e ; par contre, W1 s'y annule et U1 se raccorde à la vitesse résultante $U1_e = (U_e^2 + W_e^2)^{1/2}$.

2.2. Equations - Méthode de résolution numérique

L'hypothèse d'aile en flèche infinie permet de simplifier les équations de couche limite écrites pour des écoulements tridimensionnels incompressibles : elle se traduit par une invariance des pressions et des vitesses suivant l'envergure. On en déduit en particulier que $W_e(x) = W_\infty$ et que la distribution de vitesse $U_e(x)/U_\infty$ est celle que l'on aurait sur la même aile, à flèche nulle, pour la même incidence normale.

2.2.1. Equations de base

Le calcul de l'écoulement moyen se fait par résolution des équations locales de continuité et de quantité de mouvement écrites dans le repère (x, z, y) :

$$\begin{cases} \dfrac{\partial U}{\partial x} + \dfrac{\partial V}{\partial y} = 0 \\ U \dfrac{\partial U}{\partial x} + V \dfrac{\partial U}{\partial y} = U_e \dfrac{dU_e}{dx} + \nu \dfrac{\partial^2 U}{\partial y^2} \\ U \dfrac{\partial W}{\partial x} + V \dfrac{\partial W}{\partial y} = \nu \dfrac{\partial^2 W}{\partial y^2} \end{cases} \qquad (1)$$

Le système des équations à résoudre (1) étant de type parabolique dans la direction x, la méthode numérique utilisée nécessite la connaissance des profils U(y), V(y) et W(y) à la station initiale du calcul, qui coïncide, dans les écoulements étudiés ici, avec la ligne d'arrêt où $U_e = 0$ et $Ul_e = W_e = W_\infty$.

2.2.2. Solutions au voisinage de la ligne d'arrêt

Au voisinage de cette ligne d'arrêt, il est possible d'obtenir des solutions de similitude à partir des considérations suivantes :

- la vitesse extérieure $U_e(x)$ est linéaire : $U_e(x) = kx$ où $k = \left(\dfrac{dU_e}{dx}\right)_{x=0}$;
- on recherche les profils semblables sous la forme $\dfrac{U}{U_e} = f'(\eta)$ et $\dfrac{W}{W_e} = g(\eta)$, où η est la variable de similitude $y(k/\nu)^{1/2}$.

Une tabulation des fonctions $f'(\eta)$ et $g(\eta)$ est donnée, par exemple, dans ROSENHEAD /1/. Connaissant $f'(\eta)$, l'équation de continuité fournit par intégration $V(\eta) = -(k\nu)^{1/2} f(\eta)$.

On remarquera que sur la ligne d'arrêt proprement dite ($x = 0$), on a $U_e = 0$. $Ul/Ul_e = Wl/W_e = W/W_e$ n'est autre que le profil $g(\eta)$. Introduisant la longueur caractéristique $\tilde{\eta} = (\nu/k)^{1/2}$ et le nombre de Reynolds $\tilde{R} = W_\infty \tilde{\eta}/\nu$, l'intégration du profil $g(\eta)$ fournit les relations suivantes /2/ :

$$\tilde{\delta 1} = 1{,}026\ \tilde{\eta}\ ;\ \tilde{\theta} = 0{,}404\ \tilde{\eta} \quad \text{d'où } H = 2{,}54$$

$$\text{et} \quad R\tilde{\theta} = 0{,}404\ \tilde{R} \qquad (2)$$

Sur la ligne d'arrêt, le profil longitudinal est en fin de compte très voisin du profil de plaque plane en écoulement bidimensionnel (profil de BLASIUS).

2.2.3. Méthode de résolution numérique

Pour résoudre le système (1) de type parabolique en x, à partir des profils initiaux, nous avons utilisé une méthode inspirée des travaux de PATANKAR et SPALDING /3/. L'intérêt essentiel de cette méthode est sa rapidité, due au caractère non itératif du calcul.

La méthode dite par "volumes finis" utilisée pour résoudre (1) consiste à intégrer les divers termes sur un domaine, composé de mailles rectangulaires et situé dans le plan (x, y). Le maillage peut être variable au fur et à mesure de l'avancement du calcul. Toutes les grandeurs sont supposées connues à la station amont $x = x_U$; on veut maintenant les calculer à la station aval $x = x_D$.

Des hypothèses sont faites pour traduire l'évolution des grandeurs à calculer suivant les deux directions du maillage ; de manière générale, on tiendra à avoir un schéma le plus implicite possible, c'est-à-dire à exprimer le plus grand nombre de facteurs à la station aval (indice D).

Pour chaque grandeur A (U ou W), on aboutit après discrétisation à l'équation :

$$a_j A^D_{j+1} + b_j A^D_j + c_j A^D_{j-1} = d_j \qquad (3)$$

(j : indice dans la direction y)

La forme discrétisée des coefficients peut être trouvée dans /2/. Il reste alors à inverser une matrice tridiagonale ; la méthode utilisée introduit une relation de récurrence entre A_j et A_{j+1} et un simple balayage suivant la direction y permet d'obtenir les profils de vitesse U(y) et W(y).

2.3. Evolution générale de la couche limite laminaire sur une aile en flèche infinie

Les profils U(y) et W(y) étant calculés, on en déduit par projection les profils de vitesse longitudinaux Ul(y) et transversaux Wl(y). La pente à l'origine de ces deux profils donne l'angle β_o que fait la ligne de courant à la paroi avec la ligne de courant extérieure :

$$\operatorname{tg} \beta_o = \lim_{y \to 0} \frac{Wl}{Ul} = \left.\frac{\partial Wl/\partial y}{\partial Ul/\partial y}\right|_{y=0}$$

L'équation de la ligne de courant extérieure s'écrit : $dx/U_e = dz/W_\infty$.

Elle présentera donc un point d'inflexion à l'abscisse où la distribution de vitesse extérieure $U_e(x)$ passe par un maximum. Jusqu'à cette abscisse, l'écoulement transversal est dirigé vers la partie concave de la ligne de courant extérieure (figure 2). Le gradient de pression longitudinal change ensuite de signe, mais la réponse de la couche limite à cette variation de gradient n'est pas immédiate, si bien que l'abscisse correspondant à $\beta_Q = 0$ sera située en aval du point d'inflexion et que le profil de vitesse transversale Wl(y) s'inversera d'abord à la paroi. On observe alors des profils transversaux en forme de "S". Remarquons que le retournement complet du profil Wl(y) pourra s'obtenir si le gradient de pression positif est suffisamment intense, à moins que la distribution de vitesse extérieure ne possède d'autres extrema !

3 - CRITERES DE TRANSITION SUR UNE AILE EN FLECHE INFINIE

CALCUL DE LA REGION DE TRANSITION

Le problème abordé dans ce chapitre concerne d'une part la prédiction du début de transition et d'autre part le calcul de la région de transition.

Afin de déterminer l'abscisse de début de transition sur une aile en flèche, la démarche théorique la plus rigoureuse consiste à traiter les équations de stabilité laminaire pour rechercher les directions de propagation et les fréquences des ondes les plus instables. Outre le fait que de tels calculs restent longs et coûteux et que leur exploitation n'a rien d'évident, il faut faire appel à l'expérience pour décider, par exemple, que tel ou tel niveau d'amplification des ondes sera dangereux pour la stabilité de la couche limite. C'est pourquoi l'utilisation de critères empiriques de début de transition présente un intérêt pratique certain. De façon générale, ils corrèlent des paramètres caractéristiques de la couche limite au point de début de transition.

Pouvant déterminer l'abscisse de transition par application de tels critères, un calcul de la région de transition sera proposé de façon à pouvoir connaître l'évolution de la couche limite tout le long de l'aile.

3.1. Critères de transition

3.1.0. La figure 3, relative à un cas expérimental étudié par BOLTZ, KENYON et ALLEN /4/, illustre l'aspect le plus important de la transition en écoulement tridimensionnel. A côté de la distribution de vitesse extérieure normale au bord d'attaque, est portée l'évolution de l'abscisse de transition en fonction d'un nombre de Reynolds de corde Rc, c'est-à-dire de la vitesse d'essais Q_∞ puisque les paramètres géométriques restent fixés ($\Psi = 20°$, $\alpha_n = 0°$).

Aux faibles nombres de Reynolds, la transition a lieu sur l'arrière du profil, dans la région de gradient de pression positif. Son évolution ressemble à celle que l'on aurait sur le même profil à flèche nulle. Elle est régie par les propriétés du profil longitudinal et on l'appellera "transition (par instabilité) longitudinale".

A partir de $Rc = 20\ 10^6$, la transition se déplace rapidement vers l'avant, venant se fixer assez près du bord d'attaque dans un gradient de pression longitudinal négatif. Un tel mouvement ne peut se concevoir en bidimensionnel, où les zones accélérées stabilisent la couche limite laminaire. Cette transition, propre aux écoulements tridimensionnels, sera appelée "transition (par instabilité) transversale".

Une troisième forme d'apparition de la turbulence peut se rencontrer sur une aile en flèche : c'est le phénomène de "contamination de bord d'attaque". Lorsque l'aile est en contact avec une paroi (fuselage, par exemple), la couche limite turbulente de cette paroi risque de contaminer l'écoulement sur l'aile dès la ligne d'arrêt. Il existe toujours une valeur de Rc pour laquelle la contamination entre en jeu ; dans l'exemple présenté sur la figure 3, cette valeur se situe au-delà de la gamme des nombres de Reynolds d'étude. Le plus souvent, un écoulement turbulent, sur une aile en flèche, ne redevient pas laminaire mais, exceptionnellement, une rapide accélération (c'est le cas dans la région proche du bord d'attaque) peut provoquer une relaminarisation, phénomène que nous considèrerons également.

De façon générale, l'utilisation de critères simples repose sur la règle de jeu suivante : on suppose que la turbulence apparaît soit par instabilité longitudinale, soit par instabilité transversale, soit par contamination de bord d'attaque. On applique des critères pour chacun de ces mécanismes et on admet que la couche limite cessera d'être laminaire dès que l'un d'entre eux sera vérifié.

3.1.1. Critère longitudinal

Nous utiliserons un critère, développée à l'ONERA/CERT /5/, /6/ pour des écoulements bidimensionnels, dont nous formulerons une extension pour les écoulements tridimensionnels. Il tient compte d'un certain nombre de résultats déduits de la théorie de l'instabilité laminaire.

Etabli à partir de calculs de stabilité effectués pour la famille de profils de FALKNER-SKAN et de la relation de MACK /7/, le critère bidimensionnel se présente sous la forme analytique suivante :

$$R\theta_T - R\theta_{cr} = -206 \exp(25{,}7\ \bar{\Lambda}_{2T}) \left[\ln(16{,}8\ \tau_u) - 2{,}77\ \bar{\Lambda}_{2T}\right] \qquad (4)$$

où

$$\bar{\Lambda}_{2T} = \frac{1}{x_T - x_{cr}} \int_{x_{cr}}^{x_T} \frac{\theta^2}{\nu} \frac{dU_e}{dx}\, dx$$

$R\theta_{cr}$ est défini dans la théorie de l'instabilité laminaire : c'est le nombre de Reynolds "critique", basé sur l'épaisseur de quantité de mouvement, en dessous duquel toutes les perturbations, quelle que soit

leur fréquence, sont amorties. $R\theta_T$ est la valeur de $R\theta$ au point de transition. $\bar{\Lambda}_{2T}$ représente la valeur moyenne du paramètre de POHLHAUSEN calculée entre l'abscisse critique, à laquelle correspond $R\theta_{cr}$, et le point de début de transition.

Une représentation du réseau de courbes, construit à partir de (4), est donnée sur la figure 4. Est également reporté le critère de GRANVILLE /8/ qui recoupe assez bien le critère proposé aux faibles Tu (entre 0,05 % et 0,1 %). Le critère bidimensionnel est en fait une extension du critère de GRANVILLE, dans laquelle on prend en compte le paramètre turbulence extérieure Tu.

La détermination du nombre de Reynolds critique et de l'abscisse critique s'effectue comme suit : on trace les évolutions longitudinales du $R\theta$ de la couche limite laminaire et du $R\theta_{cr}$ "fictif" ($R\theta_{crf}$) obtenue à chaque pas de calcul. Si $R\theta < R\theta_{crf}$, l'écoulement est stable ; par contre, si $R\theta > R\theta_{crf}$, l'écoulement est instable. C'est au point d'intersection $R\theta = R\theta_{crf}$ que l'on définit le véritable nombre de Reynolds critique de la couche limite, ainsi que l'abscisse critique correspondante.

D'un point de vue pratique, $R\theta_{crf}$ est calculé par la formule de LEES, déduite de considérations mathématiques sur les équations de stabilité /9/ :

$$R\theta_{crf} = \frac{25\ U_o'^2}{U_c'\ c^4} \qquad (5)$$

où $\quad U' = \dfrac{\partial(U/U_e)}{\partial(y/\theta)} \quad ; \quad U'' = \dfrac{\partial^2(U/U_e)}{\partial(y/\theta)^2} \quad ; \quad U_o' = U'\big|_{y=0} \quad ; \quad U_c' = U'\big|_{y=y_c} \quad ; \quad U_c'' = U''\big|_{y=y_c}$

$U_c = c \quad ; \quad y_c = y(U = c)$, c solution de $-\pi\ U_c''\ U_o'\ c = 0{,}58\ U_c'^3$

Nous supposerons que le critère longitudinal, établi pour les écoulements bidimensionnels, reste valable en tridimensionnel à condition de l'appliquer le long d'une ligne de courant extérieure. Par conséquent, dans l'équation (4), θ sera remplacé par $\theta 11$, U_e par Ul_e et x par s, abscisse curviligne le long de la ligne de courant extérieure.

3.1.2. Critère transversal

Comme pour le cas précédent, nous avons utilisé les résultats de la théorie de l'instabilité laminaire pour élaborer avec le plus de rigueur possible une méthode de prévision des transitions transversales.

Pour un nombre de Reynolds de corde Rc et une abscisse fixés, les propriétés de stabilité des profils de vitesse U_ε, projetés dans une direction ε, sont étudiées depuis $\varepsilon = 0$ (direction de l'écoulement transversal) jusqu'à $\varepsilon = 90°$ (direction de l'écoulement longitudinal). On définit pour ces profils une épaisseur de déplacement $\delta 1_\varepsilon$ et le nombre de Reynolds $R\delta 1_\varepsilon$ correspondant :

$$U_\varepsilon(y) = Ul(y)\ \sin\varepsilon + Wl(y)\ \cos\varepsilon \ ; \ U_{\varepsilon e} = Ul_e\ \sin\varepsilon \ (\text{si } \varepsilon \neq 0)$$
$$\delta 1_\varepsilon = \int_o^\delta \left(1 - \frac{U_\varepsilon}{U_{\varepsilon e}}\right) dy \quad \text{et} \quad R\delta 1_\varepsilon = \frac{U_{\varepsilon e}\ \delta 1_\varepsilon}{\nu} \qquad (6)$$

On définit alors la fonction $g(\varepsilon)$, rapport du nombre de Reynolds critique $R\delta 1_{\varepsilon ci}$ du profil U_ε au nombre de Reynolds $R\delta 1_\varepsilon$ de ce même profil. A une abscisse fixée, g dépend non seulement de ε, mais aussi du nombre de Reynolds de corde R_c. La position de g par rapport à 1 nous renseigne sur la stabilité du profil projeté considéré : si $g(\varepsilon)$ est supérieur à 1, le profil $U_\varepsilon/U_{\varepsilon e}$ sera stable ; si $g(\varepsilon)$ est inférieur à 1, il sera instable. Lorsque Rc augmente, la fonction $g(\varepsilon)$ diminue et la plage des directions instables s'élargit. Les valeurs de ε rendant minimale la fonction g correspondent aux directions les plus instables /2/ et /6/.

La figure 5 schématise l'évolution de g en deux abscisses typiques sur un profil d'aile, pour un nombre de Reynolds de corde donné. A la première abscisse, située dans une zone de gradient de pression négatif intense, les angles définissant le domaine instable sont petits mais non nuls ; par contre, l'écoulement longitudinal reste très stable. Cet exemple illustre la notion d'instabilité quasi-transversale. A la deuxième abscisse située dans la zone de gradient de pression positif, la fonction $g(\varepsilon)$ présente deux minima, proches des directions transversale et longitudinale, le second étant minimum absolu. Il s'agit dans ce cas d'instabilité longitudinale. Ces courbes montrent le passage de l'instabilité longitudinale à l'instabilité quasi-transversale. Mais la détermination rigoureuse de l'évolution de g, à différentes abscisses, nécessite des calculs extrêmement longs. En conséquence, on a mis au point une méthode approchée du calcul du nombre de Reynolds critique $R\delta 1_{\varepsilon cr}$, supposé ne dépendre que de l'altitude du point d'inflexion du profil projeté $U_\varepsilon/U_{\varepsilon e}$ et de la dérivée du profil en ce point. Lorsque le profil ne possède pas d'inflexion, $R\delta 1_{\varepsilon cr}$ est simplement fonction d'un paramètre intégral tel que le facteur de forme.

On observe que la direction de l'écoulement transversal ($\varepsilon = 0°$) est toujours plus stable que la direction ε_{min} ($= \varepsilon |\ g(\varepsilon)$ soit minimal) voisine de quelques degrés (1° à 5°) (figure 5). Le critère de transition proposé est obtenu par une corrélation empirique entre d'une part, le nombre de Reynolds formé avec l'épaisseur de déplacement du profil de vitesse projeté dans la direction ε_{min} et d'autre part, le facteur de forme du profil longitudinal Hl et le taux de turbulence extérieure, Tu. Signalons que ce dernier paramétrage est difficile car les résultats expérimentaux qui ont permis l'établissement de ce critère "quasi-transversal" donnaient uniquement quatre valeurs de Tu, dont deux très voisines /2/.

Le réseau de courbes obtenu est représenté sur la figure 6. Une formulation paramétrique peut en être donnée :

$$R\delta 1_{\varepsilon T}\ (\varepsilon = \varepsilon_{min}) = (-\ 86{,}901\ \mathrm{Ln}\ Tu - 379{,}45)\ \exp\left(\frac{7{,}657\ 10^{-4}}{Tu^{1{,}552}}\ (H1 - 2{,}4)^{4{,}5}\right)$$

$$\text{pour } 2{,}4 \leq H1 \leq 2{,}7 \qquad (7)$$

Pour des valeurs de H1 inférieures à 2,4 -cas où la transition se produit dans la région de gradient de pression négatif intense- on considère que $R\delta 1_{\varepsilon T}\ (\varepsilon = \varepsilon_{min})$ n'est fonction que du paramètre Tu ; son expression est donnée par les asymptotes des courbes précédentes. D'autre part, il est inutile de donner une représentation pour des H1 supérieurs à 2,7 car, dans ce cas, l'expérience montre que l'instabilité longitudinale est prépondérante.

3.1.3. Contamination de bord d'attaque

Le phénomène de contamination de bord d'attaque a été largement étudié par POLL /10/. Un paramètre important est le nombre de Reynolds défini sur la ligne d'arrêt (il s'agit en fait de $R\theta 11$) :

$$\tilde{R\theta} = \frac{W_\infty}{\nu} \int_0^\delta \frac{W}{W_\infty}\left(1 - \frac{W}{W_\infty}\right) dy$$

Les solutions de similitude (cf 2.2.2.) permettent d'exprimer $\tilde{R\theta}$ comme suit :

$$\tilde{R\theta} = 0{,}404\ \frac{Q_\infty \sin\varphi}{(\nu k)^{1/2}}$$

$$\text{avec} \quad k = \left(\frac{dU_e}{dx}\right)_{x=0} \qquad (8)$$

Lorsque l'aile est en contact avec la paroi, la couche limite prenant naissance sur l'aile peut être contaminée par l'existence de grosses structures dues à la couche limite turbulente de paroi. Il n'existe pas de théorie rigoureuse pour prévoir une éventuelle contamination ; il faut faire appel aux résultats expérimentaux qui montrent que :

- si $\tilde{R\theta} < 100$, l'écoulement le long du bord d'attaque aura tendance à rester laminaire ou à redevenir laminaire dans le cas où il serait devenu localement turbulent ; la couche limite sera laminaire sur l'aile jusqu'à la transition "naturelle" ;

- si $\tilde{R\theta} > 100$, il y a contamination et l'écoulement sur l'aile devient turbulent dès le bord d'attaque.

Remarquons que la relation (8) nous montre que pour avoir des valeurs importantes de $\tilde{R\theta}$, il est nécessaire d'avoir d'importants angles de flèche, de fortes vitesses à l'infini amont ou un grand rayon de bord d'attaque, c'est-à-dire une faible valeur du gradient de vitesse extérieure sur le bord d'attaque.

3.1.4. Relaminarisation

Le paramètre caractéristique, défini le long de la ligne de courant extérieure, est :

$$K = \frac{\nu}{(Ul_e)^2}\ \frac{dUl_e}{ds} \qquad (9)$$

où s représente l'abscisse curviligne le long de la ligne de courant extérieure.

Des études réalisées par LAUNDER et JONES /11/ en écoulement bidimensionnel et BEASLEY /12/ en écoulement tridimensionnel montrent que pour des valeurs de K supérieures à $5\ 10^{-6}$, un écoulement turbulent peut redevenir laminaire.

D'un point de vue pratique, K tend vers un maximum très près de la ligne d'arrêt et, de ce fait, la relaminarisation semble possible uniquement dans la zone de gradient de pression négatif, lorsque la turbulence est due au phénomène de contamination de bord d'attaque.

3.2. Calcul de la région de transition

Nous disposons donc de trois critères simples de localisation du point de début de transition, sur des ailes en flèche infinies, ainsi que d'un critère de relaminarisation. Il nous faut maintenant calculer la région de transition elle-même, par résolution des équations locales de couche limite.

Dans le repère (x, z, y), les équations de couche limite pour un écoulement sur une aile en flèche d'envergure infinie s'écrivent :

$$\begin{cases} \dfrac{\partial U}{\partial x} + \dfrac{\partial V}{\partial y} = 0 \\ U\dfrac{\partial U}{\partial x} + V\dfrac{\partial U}{\partial y} = U_e\dfrac{dU_e}{dx} + \dfrac{\partial}{\partial y}\left(\nu\dfrac{\partial U}{\partial y} - \overline{u'v'}\right) \\ U\dfrac{\partial W}{\partial x} + V\dfrac{\partial W}{\partial y} = \dfrac{\partial}{\partial y}\left(\nu\dfrac{\partial W}{\partial y} - \overline{v'w'}\right) \end{cases} \qquad (10)$$

. En régime laminaire, les tensions de Reynolds $-\overline{u'v'}$ et $-\overline{v'w'}$ sont nulles. Le système (10) est identique au système (1) dont la méthode de résolution numérique est donnée en 2.2.3..

. En régime turbulent établi, nous utiliserons le modèle de longueur de mélange de PRANDTL, appliqué et testé par MICHEL et al dans des conditions variées de gradient de pression /13/ :

$$-\overline{u'v'} = \nu_t \frac{\partial U}{\partial y} \quad \text{et} \quad -\overline{v'w'} = \nu_t \frac{\partial W}{\partial y} \tag{11}$$

où la viscosité tourbillonnaire ν_t s'exprime sous la forme :

$$\nu_t = F^2 \ell^2 \left(\left(\frac{\partial U}{\partial y}\right)^2 + \left(\frac{\partial W}{\partial y}\right)^2\right)^{1/2} \tag{12}$$

ℓ, longueur de mélange est une fonction donnée de y :

$$\frac{\ell}{\delta} = 0{,}085 \text{ th } \left(\frac{0{,}41}{0{,}085} \frac{y}{\delta}\right) \tag{13}$$

F est une fonction correctrice de sous-couche visqueuse :

$$F = 1 - \exp\left[-\frac{\ell}{10{,}66\ \nu}(\nu + \nu_t)\left(\left(\frac{\partial U}{\partial y}\right)^2 + \left(\frac{\partial W}{\partial y}\right)^2\right)^{1/2}\right] \tag{14}$$

La méthode de résolution numérique est identique à celle développée précédemment, en considérant toutefois pour les termes de diffusion $\partial((\nu + \nu_t)\ \partial U/\partial y)/\partial y$ et $\partial((\nu + \nu_t)\ \partial W/\partial y)/\partial y$.

. Dans la région de transition, nous utiliserons une méthode dite "d'intermittence". Les résultats expérimentaux montrent que dans cette région se succèdent, au cours du temps et à une abscisse donnée, des spots turbulents et des régions laminaires.

Le principe de la méthode de calcul utilisée consiste à exprimer les tensions de Reynolds sous la forme suivante :

$$-\overline{u'v'} = \varepsilon_i \nu_t \frac{\partial U}{\partial y} \quad \text{et} \quad -\overline{v'w'} = \varepsilon_i \nu_t \frac{\partial W}{\partial y} \tag{15}$$

Le coefficient ε_i qui ne dépend que de x peut être assimilé au facteur d'intermittence, en ce sens qu'il doit croître de 0 en laminaire à 1 en régime turbulent établi.

A partir de résultats expérimentaux obtenus pour des écoulements bidimensionnels, avec et sans gradient de pression longitudinal, on a pu remarquer qu'entre le début et la fin de la région de transition, l'épaisseur de quantité de mouvement est à peu près multipliée par un facteur 2 /14/. Cette remarque suggère alors de faire dépendre ε_i du rapport $(\theta/\theta_T - 1)$. L'extension aux écoulements tridimensionnels est réalisée en remplaçant simplement θ par $\theta 11$.

Le modèle régi par les équations (15), mis au point d'abord pour les écoulements bidimensionnels, a donné également des résultats en bon accord avec l'expérience pour des écoulements tridimensionnels /2/ et /15/. La courbe utilisée pour la variation du paramètre ε_i en fonction de l'épaisseur de couche limite, est représentée sur la figure 7. On remarquera que l'on a dû imposer un "overshoot" au-dessus de 1 ; ainsi, ε_i ne représente pas en fait seulement le facteur d'intermittence. L'analyse conditionnelle de la région de transition justifie cet overshoot en montrant qu'une différence entre les vitesses de passage des spots turbulents et des régions laminaires donne lieu à un terme supplémentaire, correspondant à une augmentation du frottement $-\overline{u'v'}$ /16/.

4 - APPLICATION : ETUDE PARAMETRIQUE DE L'ECOULEMENT SUR UNE AILE EN FLECHE

On est donc en mesure de procéder à un calcul complet de la couche limite, depuis le bord d'attaque jusqu'au bord de fuite, en localisant la transition grâce à des critères empiriques. Les méthodes de calcul exposées précédemment seront appliquées à la mise en flèche d'un profil donné (OAP 01), afin d'estimer la traînée de ce profil pour différents angles d'incidence.

4.1. Profil considéré - Distributions de vitesse extérieure

Le profil OAP 01 étudié est un profil d'aile de planeur ; il est dissymétrique avec un maître-couple situé à environ 35 % de corde. On a utilisé comme données, pour les calculs de couche limite, les distributions de pression théoriques déterminées à la Direction d'Aérodynamique de l'ONERA par un calcul en fluide parfait.

Trois incidences normales (α_n = 0°, 1° et 2°) et trois angles de flèche (φ = 0°, 20° et 30°) ont été considérés. Les distributions du coefficient de pression, à flèche nulle, aux trois incidences étudiées, sont représentées sur la figure 8. La mise en flèche du profil se fait à incidence normale constante ; par conséquent, les distributions de vitesse $U_e(x)/U_\infty$ sont conservées.

A l'extrados, ces distributions sont de type "laminaire" avec de forts gradients de pression positifs sur l'arrière du profil. A l'intrados, une pointe de survitesse apparaît près du bord d'attaque à incidence nulle, puis se résorbe lorsque l'incidence augmente pour disparaître à α_n = 2°. De façon générale, on observe qu'à l'intrados, la vitesse potentielle est quasiment constante entre 10 et 60 pour cent de corde.

4.2. Evolution de la position de transition

L'application des critères longitudinal et transversal décrits au paragraphe 3 nécessite la connaissance du taux de turbulence extérieure Tu, que nous prendrons arbitrairement égal à 0,1 pour cent. Pour cette étude comparative, l'évolution de l'abscisse de début de transition sera portée en fonction d'un nombre de Reynolds de corde, Rc, calculé à partir de grandeurs évaluées dans la direction de la vitesse à l'infini amont :

$$Rc = \frac{Q_\infty \; c}{\nu \cos\varphi}$$

4.2.1. $\varphi = 0°$

La figure 9.a présente les résultats obtenus à l'extrados. La longue portion de gradient de pression négatif stabilise l'écoulement, si bien que la transition ne se produit jamais avant l'abscisse correspondant au maximum de vitesse extérieure. La transition avance lentement vers le bord d'attaque lorsque Rc augmente. Pour des nombres de Reynolds inférieurs à 10 millions, la couche limite reste laminaire jusqu'au décollement qui se produit à environ 45 % de corde. On peut penser que la transition a lieu dans le décollement, mais la méthode numérique utilisée ne peut calculer ce phénomène.

Par contre, à l'intrados, la transition se rapproche rapidement du bord d'attaque, essentiellement à incidence nulle, où la portion de survitesse déstabilise la couche limite laminaire (figure 9.b). Cette avancée rapide s'atténue aux plus grandes incidences.

4.2.2. $\varphi = 20°$ et $\varphi = 30°$

A l'extrados, les résultats sont qualitativement comparables pour les deux angles de flèche considérés : $\varphi = 20°$ (figure 10.a) et $\varphi = 30°$ (figure 11.a). Le gradient de pression longitudinal négatif retarde en effet la transition longitudinale, mais crée un écoulement transversal important ; la transition se rapproche rapidement du bord d'attaque. A incidence nulle, l'instabilité transversale est prépondérante à partir de nombres de Reynolds de l'ordre de 20 millions pour $\varphi = 20°$ et de 10 millions pour $\varphi = 30°$. Il est intéressant de noter que, pour un Rc donné, la transition recule vers l'arrière du profil, lorsque l'incidence augmente, à des abscisses où l'écoulement transversal est plus faible. Ce phénomène va en sens inverse de ce que l'on observe en bidimensionnel ou par application du critère longitudinal.

Remarquons que le critère longitudinal fournit pratiquement les mêmes positions de transition que dans le cas de la flèche nulle ; en effet, les lignes de courant extérieures font un angle faible (inférieur ou égal à 5°) avec la direction de l'écoulement à l'infini amont. De façon générale, la gamme de Reynolds conduisant à des transitions par instabilité longitudinale est très réduite.

Pour $\varphi = 20°$, lorsque Rc atteint 38 à 43 millions (suivant la valeur de α_n), la couche limite laminaire de bord d'attaque est contaminée par la turbulence de paroi (figure 10.a) et la couche limite se développant sur l'aile est entièrement turbulente. A un angle de flèche plus élevé, ce phénomène de contamination de bord d'attaque apparaît, bien sûr, à des nombres de Reynolds plus faibles : 18 à 20 millions (figure 11.a). Pour tous les cas de contamination rencontrés, l'accélération de l'écoulement en aval de la ligne d'arrêt n'a pas été suffisante pour provoquer une relaminarisation de l'écoulement.

Les figures 10.b et 11.b présentent les résultats obtenus à l'intrados pour des angles de flèche égaux respectivement à 20° et 30°. Bien sûr, les nombres de Reynolds de corde de contamination sont les mêmes qu'à l'extrados puisque ceux-ci ne dépendent, à une flèche et une incidence données, que de $(dU_e/dx)_{x=0}$. Pour des incidences normales égales à 0° ou 1°, la zone de gradient de pression longitudinal négatif, favorable à l'instabilité transversale, est très réduite si bien que la mise en flèche du profil ne crée qu'un écoulement transversal minime. Par conséquent, en augmentant Rc, on passe directement de l'instabilité longitudinale à la contamination de bord d'attaque et ce pour les deux angles de flèche.

Pour une incidence plus élevée ($\alpha_n = 2°$), l'écoulement transversal reste également faible, mais on observe néanmoins une petite zone d'instabilité transversale pour $\varphi = 30°$ (figure 11.b).

4.3. Calcul complet de la couche limite

Le point de début de transition étant connu, par application des critères avec un taux de turbulence extérieure de 0,1 pour cent, des calculs complets de couche limite (laminaire-transition-turbulent) ont été réalisés. Nous présenterons les évolutions de certains paramètres caractéristiques de la couche limite, depuis le bord d'attaque jusqu'au bord de fuite, pour une configuration donnée ($\varphi = 20°$, $\alpha_n = 1°$) et deux nombres de Reynolds de corde : Rc = 10 et 30 millions, à l'extrados du profil OAP 01.

Pour Rc = 10 millions, la transition causée par instabilité longitudinale se produit juste avant le décollement laminaire, à environ 44 pour cent de corde. Par contre, à un nombre de Reynolds de 30 millions, la transition due à l'instabilité transversale est proche du bord d'attaque, à une abscisse voisine de 17 pour cent de corde.

On observe dans la zone de transition une décroissance assez rapide du paramètre de forme longitudinal H1 jusqu'à une valeur pouvant atteindre 1,3 lorsque Rc vaut 30 millions (figure 12). Cette faible valeur résulte du fait que l'écoulement est encore accéléré à la sortie de la région de transition. H1 tend ensuite lentement vers 1,4, indiquant que les gradients de pression mis en jeu sont faibles pour le régime turbulent.

La longueur de la région de transition -qui peut être définie, par exemple, entre les deux extrema du coefficient de frottement longitudinal Cf- est assez faible : 5 pour cent de corde pour Rc = 30 millions et 10 pour cent de corde pour Rc = 10 millions (figure 13).

Les résultats relatifs aux épaisseurs de déplacement ($\delta 1$) et de quantité de mouvement ($\theta 11$) longitudinales, sont reportés sur la figure 14. Ces épaisseurs intégrales restent faibles dans la région laminaire puis augmentent assez nettement en régime turbulent. Pour un nombre de Reynolds de 30 millions, la

valeur de θ11 au bord de fuite de l'aile est supérieure à celle obtenue pour Rc = 10 millions, puisque le début de la région de transition est situé plus en amont.

4.4. Etude comparative de l'épaisseur de quantité de mouvement au bord de fuite

En écoulement bidimensionnel, le coefficient de traînée totale d'un profil d'aile peut être déterminé à partir des caractéristiques de la couche limite et de la vitesse potentielle au bord de fuite, par application de la formule de SQUIRE et YOUNG :

$$Cx = 2\frac{\theta}{c}\left(\frac{U_e}{U_\infty}\right)^{\frac{H+5}{2}}$$

relation s'appliquant séparément à l'intrados et à l'extrados.

Dans le cas tridimensionnel étudié ici, les lignes de courant potentielles sont pratiquement alignées avec la direction de l'écoulement à l'infini amont ; on peut donc appliquer la relation précédente en remplaçant θ par θ11, U_e par Ul_e, U_∞ par Q_∞ et H par H1. De plus, les paramètres de forme de la couche limite turbulente au bord de fuite sont suffisamment voisins à l'extrados et à l'intrados pour que la somme des épaisseurs de quantité de mouvement, que l'on désignera simplement par θ_{BF}, soit directement représentative du coefficient de traînée totale.

Précisons cependant que l'on a toujours utilisé les distributions de pression de fluide parfait et qu'on n'a donc pas tenu compte du couplage fluide parfait-fluide visqueux, qui modifierait en fait la vitesse au bord de fuite, donc le coefficient de traînée. Une variation de 5 pour cent sur la vitesse potentielle Ul_e entraînerait, par l'exposant (H+5)/2, une variation d'environ 15 % sur le Cx.

La figure 15 présente à l'incidence $\alpha_n = 1°$, les variations de θ_{BF} en fonction du nombre de Reynolds Rc, pour les trois angles de flèche considérés. Pour $\varphi = 0°$, θ_{BF} est pratiquement constant lorsque Rc varie de 10 à 40 millions ; la diminution de l'épaisseur de quantité de mouvement lorsque le nombre de Reynolds augmente est compensée par l'avancée progressive de la transition vers le bord d'attaque. Pour $\varphi = 20°$ et 30°, le brusque accroissement de θ_{BF} pour Rc = 24 millions et 12 millions respectivement, correspond à l'apparition à l'extrados de transitions causées par instabilité transversale. Remarquons pour $\varphi = 30°$, la portion de courbe verticale à Rc = 19 millions, nombre de Reynolds correspondant à la contamination de bord d'attaque. Au-delà, la couche limite est complètement turbulente sur toute l'aile et l'épaisseur de quantité de mouvement θ_{BF} diminue avec une augmentation de Rc.

La figure 16 traduit l'évolution de θ_{BF} avec l'incidence, pour un angle de flèche donné $\varphi = 20°$. Pour $\alpha_n = 2°$, les transitions sont causées par instabilité longitudinale tant que Rc reste inférieur à 30 millions ; θ_{BF} décroît car "l'effet Reynolds" est prépondérant devant le lent déplacement de la transition vers le bord d'attaque. Les augmentations rapides de θ_{BF} sont liées, bien sûr, à l'apparition de transitions dues à l'instabilité transversale.

5 - INFLUENCE DE L'ASPIRATION

5.0. Le moyen le plus efficace pour maintenir sur des ailes un écoulement laminaire et pour diminuer ainsi la traînée est certainement un contrôle de cette laminarité par une aspiration de la couche limite à travers la paroi.

On considère ici simplement les effets d'une aspiration continue de vitesse verticale fixée. De nombreuses études ont fourni dans ce cas des résultats complets et cohérents en écoulements bidimensionnels.

Les informations disponibles sont plus rares pour les écoulements tridimensionnels. Des calculs de stabilité relatifs à des profils de vitesse de couche limite tridimensionnelle, effectués notamment par MACK /17/, SROKOWSKI et ORSZAG /18/ ont mis en lumière l'influence stabilisatrice de l'aspiration.

On cherchera à utiliser les critères précédemment décrits (cf paragraphe 3) pour analyser l'influence de l'aspiration sur la transition elle-même.

5.1. Effet de l'aspiration sur les caractéristiques de la couche limite laminaire

Des calculs ont été effectués pour la distribution de vitesse extérieure de l'extrados du profil OAP 01 ; les configurations choisies sont 20° et 30° d'angle de flèche pour 1° d'incidence normale. L'aspiration, supposée constante dans la direction de l'écoulement, commence depuis la ligne d'arrêt ; Vp désignant la vitesse d'aspiration à la paroi, on considère le paramètre S défini par :

$$S = -\frac{Vp}{Q_\infty}\,Rc^{1/2}$$

(S est constant dans les solutions semblables de couche limite laminaire avec aspiration).

Différents essais ont été réalisés pour des taux d'aspiration, S, variant entre 0 et 0,8. Notons pour fixer les ordres de grandeurs que, pour un avion volant à une altitude de 10 km à un nombre de Mach de 0,8, le débit correspondant à une aspiration telle que S = 0,8 est légèrement inférieur à 2 kg/s pour une surface d'aspiration de 150 m^2.

Pour une flèche de 20° et un nombre de Reynolds de 20 millions, les profils longitudinaux Ul et transversaux Wl -rendus sans dimension par la vitesse potentielle résultante Ul_e- sont tracés sur la figure 17 pour deux abscisses, respectivement x/c = 0,145 et x/c = 0,416. Les comparaisons sont effectuées entre l'aspiration nulle et S = 0,8.

A la première abscisse, située dans la zone de gradient de pression négatif, le profil Wl a un signe constant dans la couche limite. Le taux d'aspiration S = 0,8 amincit la couche limite et diminue la valeur maximale de Wl. De plus, le point d'inflexion du profil transversal est amené plus près de la paroi. Le profil longitudinal Ul ne subit pas de grande modification.

Par contre, à l'abscisse x/c = 0,416 -située dans la portion d'écoulement décéléré- une telle aspiration (S = 0,8) élimine le point d'inflexion du profil U1, détruisant ainsi, à cette station, la possibilité d'une instabilité inflexionnelle. Le profil de vitesse transversale W1 change de signe à la paroi ; il possède deux points d'inflexion qui sont également rapprochés de la paroi.

Ainsi, les profils longitudinaux et transversaux peuvent être tous les deux stabilisés par l'aspiration qui change leurs formes. Il est aisé d'éliminer le point d'inflexion sur le profil U1, ce qui est impossible pour W1. Il semblerait donc qu'en gradient de pression positif, il soit plus commode de contrôler l'instabilité longitudinale que l'instabilité transversale.

Remarquons qu'une aspiration augmente $\partial U1/\partial y|_{y=0}$ et diminue par contre $\partial W1/\partial y|_{y=0}$ car l'effet de diminution de W1 max est prépondérant devant l'amincissement de la couche limite laminaire. Par conséquent, l'angle β_o est réduit sous l'effet d'une aspiration et les lignes de courant pariétales sont moins déviées par rapport à la direction de l'écoulement extérieur.

Les variations du rapport $R\delta 2/(R\delta 2)_{S=0}$ avec S sont reportées sur la figure 18 pour différentes abscisses ; $R\delta 2$ et $(R\delta 2)_{S=0}$ désignent respectivement les nombres de Reynolds transversaux avec et sans aspiration. On peut démontrer que pour une aile en flèche infinie et à incidence normale constante, ce rapport ne dépend pas de la flèche. La figure 18 s'applique donc aussi bien à $\varphi = 20°$ qu'à $\varphi = 30°$. Pour un taux d'aspiration S = 0,8, le nombre de Reynolds $R\delta 2$ diminue d'environ moitié à l'abscisse x/c = 0,427, située dans la région de gradient de pression positif. Par contre, à la première station x/c = 0,074, où l'écoulement transversal est le plus intense, il ne diminue que de 20 % par rapport au calcul effectué sans aspiration.

Il est à noter que l'abscisse correspondant à $R\delta 2 = 0$ ne varie pratiquement pas avec l'aspiration. L'effet stabilisant de l'aspiration sur le nombre de Reynolds transversal, donc sur le profil transversal, est plus important lorsqu'on est en présence d'un faible écoulement transversal. Ce résultat est en accord avec les résultats de MACK /17/.

Sur la figure 19 est représentée l'évolution de $R\theta 11/(R\theta 11)_{S=0}$ avec S, pour $\varphi = 20°$. Contrairement à $R\delta 2$, ce rapport varie avec l'angle de flèche, pour une aile en flèche infinie maintenue à incidence normale constante. Toutefois, pour $\varphi = 30°$, les résultats concernant les variations de $R\theta 11/(R\theta 11)_{S=0}$ sont très voisins du cas $\varphi = 20°$. On constate que le nombre de Reynolds du profil longitudinal $R\theta 11$ décroît lorsque S augmente mais, à l'abscisse située la plus en arrière sur le profil, la diminution (de l'ordre de 20 %) est beaucoup plus faible que pour l'écoulement transversal. En conséquence, l'effet de l'aspiration sur le nombre de Reynolds longitudinal est moindre.

5.2. Influence de l'aspiration sur la position de la transition

La prédiction de la transition utilise les critères employés précédemment ; néanmoins, ceux-ci doivent être adaptés pour tenir compte de l'influence de l'aspiration sur la forme des profils de vitesse et, en conséquence, sur la stabilité de la couche limite laminaire et sur la transition.

Critère longitudinal

On a vu dans le cas sans aspiration que le critère de transition fait intervenir un paramètre de gradient de pression moyen :

$$\bar{\Lambda}_2 = \frac{1}{s - s_{cr}} \int_{s_{cr}}^{s} \frac{\theta 11^2}{\nu} \frac{dU1_e}{ds} \, ds$$

Avec aspiration, la forme des profils de vitesse n'est plus seulement fonction de ce paramètre de gradient de pression mais dépend aussi directement de l'aspiration par l'intermédiaire du paramètre $(v_p/U1_e)\, R\theta 11\, (Cf/2)\, R\theta 11$.

Ainsi, le critère longitudinal avec aspiration est conservé sous la forme :

$$R\theta 11_T - R\theta 11_{cr} = f(\bar{\Lambda}^*_{2_T}, Tu)$$

mais $\bar{\Lambda}_{2_T}$ est remplacé par un paramètre modifié :

$$\bar{\Lambda}^*_{2_T} = \frac{1}{s_T - s_{cr}} \int_{s_{cr}}^{s_T} \left(\frac{\theta 11^2}{\nu} \frac{dU1_e}{ds} + \frac{v_p}{U1_e} \, R\theta 11 \, \frac{Cf}{2} \, R\theta 11 \right) ds$$

Critère transversal

On admet que l'aspiration intervient essentiellement par son action sur la forme des profils de vitesse projetés dans la direction la plus instable. On est ainsi amené à utiliser le critère $R\delta 1_{\varepsilon_T}$ (H1, Tu), représenté sur la figure 6, étant entendu que l'aspiration diminue $R\delta 1_\varepsilon$ et H1 et que la transition s'en trouve retardée.

Contamination de bord d'attaque

Nous supposerons que le phénomène de contamination de la couche limite laminaire de bord d'attaque peut être évité lorsque l'aspiration est effective sur la ligne d'arrêt ou du moins repoussé à des nombres de Reynolds beaucoup plus importants.

L'évolution de la position de la transition en fonction du nombre de Reynolds de corde Rc est portée pour différents taux d'aspiration S ; les configurations choisies sont $\varphi = 20°$ (figure 20) et $\varphi = 30°$ (figure 21) pour une incidence normale de 1°. La gamme de Rc étudiés peut s'étendre jusqu'à 60 millions.

Il est à noter que l'abscisse de décollement laminaire évolue sensiblement avec S. Ceci est dû à la présence d'un fort gradient de pression positif sur l'arrière du profil ; il faudrait en fait augmenter l'aspiration dans cette région pour mieux contrôler le décollement. Au début de la région d'écoulement décéléré, on supprime bien le point d'inflexion, mais il finit quand même par apparaître, ce qui se traduit par un effet finalement minime sur la position du décollement.

Pour $\varphi = 20°$, à un nombre de Reynolds de corde donné, les transitions longitudinales se déplacent progressivement vers l'arrière du profil, lorsque le taux d'aspiration augmente (figure 20). Par exemple, pour Rc égal à 20 millions et pour S = 0,8, la transition se situe à 13 % de corde en aval de l'abscisse correspondant au calcul effectué sans aspiration. D'autre part, pour des nombres de Reynolds supérieurs, il n'y a plus de transitions transversales dès que le taux d'aspiration est suffisamment important : pour Rc = 40 millions, une valeur de S au moins égale à 0,8 recule l'abscisse de transition de près de 40 % de corde. La longue portion d'écoulement laminaire ainsi contrôlée nous permettra de diminuer l'étendue de la région turbulente ; l'épaisseur de quantité de mouvement au bord de fuite du profil sera alors plus faible et, par conséquent, la traînée sera réduite.

Remarquons que pour des nombres de Reynolds de vol classiques, de l'ordre de 40 millions, il est possible de n'obtenir que des transitions dues à des instabilités longitudinales, pour un taux d'aspiration suffisamment fort.

Pour un angle de flèche de 30° (figure 21), les résultats sont qualitativement comparables en ce qui concerne l'influence de S. Néanmoins, l'aspiration est plus efficace à 20° qu'à 30° car, pour un Reynolds de 30 millions et un S de 0,8, il subsiste toujours des transitions causées par instabilité transversale. Pour $\varphi = 30°$, un taux d'aspiration important est nécessaire pour reculer les transitions transversales ; en effet, bien que $R\delta 2/(R\delta 2)_{S=0}$ soit indépendant de l'angle de flèche, le nombre de Reynolds transversal $R\delta 2$ et, par conséquent, l'écoulement transversal, augmentent avec φ, rendant ainsi plus délicat le "contrôle" de l'écoulement laminaire.

Il faut néanmoins garder à l'esprit que des aspirations trop importantes peuvent conduire à une couche limite très mince, qui deviendrait alors très sensible à la rugosité des parois ; ce phénomène pourrait déclencher prématurément une transition que l'on essaie de contrôler.

6 - CONCLUSION

L'étude paramétrique sur le profil OAP 01 mis en flèche a conduit à quelques conclusions pratiques importantes. Il apparaît que les distributions de vitesse du type "laminaire" sont effectivement intéressantes pour retarder les transitions longitudinales. Mais la longue zone d'accélération crée un écoulement transversal important et une flèche de 20° à 30° suffit à amener la transition près du bord d'attaque. Avec des distributions de vitesse extérieure plus "plates", avec pointe de survitesse éventuelle, l'écoulement transversal se développe beaucoup moins et a peu de chances de conduire à une transition prématurée. Cette transition prématurée se rencontre quand même, mais elle est causée ici par l'écoulement longitudinal. Les façons de lutter contre les deux formes de transition sont donc antagonistes ; ce qui empêche l'une favorise l'autre. Il s'agit alors de trouver un compromis. Quant à la contamination de bord d'attaque, on peut la rencontrer à des nombres de Reynolds de corde voisins de 20 millions, même pour des angles de flèche modérés.

Les calculs effectués avec aspiration à la paroi montrent que cette technique est effectivement très efficace pour retarder la transition. Elle agit de deux façons sur l'écoulement longitudinal : d'une part, elle réduit le nombre de Reynolds local, d'autre part, elle peut modifier les propriétés de stabilité des profils de vitesse longitudinaux, en supprimant par exemple les points d'inflexion dont l'effet déstabilisant est bien connu ; en fait, il est plus exact de dire que l'apparition de ces points d'inflexion est simplement retardée ; la suppression du décollement laminaire exigerait en réalité des taux d'aspiration beaucoup plus importants. En ce qui concerne l'écoulement transversal, l'aspiration modifie très peu la forme des profils de vitesse moyenne, mais la réduction de l'épaisseur de couche limite suffit pour reculer la transition de façon appréciable. Ces résultats extrêmement encourageants ne doivent pas faire oublier qu'une aspiration continue tout le long du profil est très délicate à mettre en oeuvre du point de vue technologique ; les études expérimentales récentes /19/, /20/ montrent que des aspirations discontinues par bandes poreuses discrètes peuvent également s'avérer efficaces. Quoiqu'il en soit, qu'il y ait aspiration ou non, les calculs présentés dans cet article montrent qu'il est dangereux de négliger les effets transversaux et de considérer que la transition ne s'écartera pas de sa position bidimensionnelle pour des angles de flèche aussi modestes que 20 ou 30 degrés.

REFERENCES

/1/ ROSENHEAD L. — "Laminar boundary layers" - OXFORD University Press (1963)

/2/ COUSTOLS E. — "Stabilité et transition en écoulement tridimensionnel : cas des ailes en flèche" - Thèse de Docteur-Ingénieur soutenue à l'ENSAE (1983)

/3/ PATANKAR S.V. SPALDING D.B. — "A calculation procedure for heat, mass and momentum transfer in three-dimensional parabolic flows" - Int. J. Heat and Mass Transfer Vol. 15, p. 1787-1806

/4/ BOLTZ F.W. KENYON G.C. ALLEN C.Q. — "Effects of sweep angle on the boundary layer stability characteristics of an untapered wing at low speeds" - NASA Technical Note D-338 (May 1961)

/5/ HABIBALLAH M. — "Analyse de l'instabilité des couches limites laminaires et prévision de la transition du régime laminaire au régime turbulent" - Thèse de Docteur-Ingénieur soutenue à l'ENSAE (1981)

/6/ ARNAL D., HABIBALLAH M., COUSTOLS E. — "Théorie de l'instabilité laminaire et critères de transition en écoulement bi et tridimensionnel" - La Recherche Aérospatiale N° 1984-2

/7/ MACK L.M. — "Transition and laminar instability" - Jet Propulsion Laboratory Publication 77-15 PASADENA, CALIFORNIA (1977)

/8/ GRANVILLE P.S. — "The calculation of the viscous drag of bodies of revolution" - David Taylor Model Basin Report 849 (1953)

/9/ LEES L. — "The stability of the laminar boundary layer in a compressible flow" - NACA Report N° 876 (1947)

/10/ POLL D.I.A. — "Some aspects of the flow near a swept attachment line with particular reference to boundary layer transition" - CRANFIELD Institute of Technology, College of Aeronautics, Report N° 7805 (1978)

/11/ LAUNDER B.E., JONES W.P. — "On the prediction of laminarisation" A.R.C. CP 1036 (1968)

/12/ BEASLEY J.A. — "Calculation of the laminar boundary layer and the prediction of transition on a sheared wing" - A.R.C. R and M 3787 (1973)

/13/ MICHEL R., QUEMARD C., DURANT R. — "Application d'un schéma de longueur de mélange à l'étude des couches limites d'équilibre" - ONERA Note Technique N° 154 (1969)

/14/ ARNAL D., JUILLEN J.C., MICHEL R. — "Analyse expérimentale de la transition de la couche limite avec gradient de pression nul ou positif" - ONERA T.P. N° 1979-8

/15/ ARNAL D., COUSTOLS E., JUILLEN J.C. — "Etude expérimentale et théorique de la transition sur une aile en flèche infinie" - A paraître dans La Recherche Aérospatiale

/16/ ARNAL D., JUILLEN J.C., MICHEL R. — "Analyse expérimentale et calcul de l'apparition et du développement de la transition de la couche limite" - ONERA T.P. N° 1977-54

/17/ MACK L.M. — "On the stabilization of three-dimensional boundary layers by suction and cooling" - Communication au Symposium IUTAM, STUTTGART, GERMANY (1979)

/18/ SROKOWSKI A.J., ORSZAG S.A. — "Mass flow requirements for LFC wing design" - AIAA Paper 77-1222

/19/ REYNOLDS G.A., SARIC W.S. — "Experiments on the stability of the flat plate boundary layer with suction" AIAA Paper 82-1026

/20/ SARIC W.S., REED H.L. — "Effect of suction and blowing on boundary layer transition" - AIAA Paper 83-0043

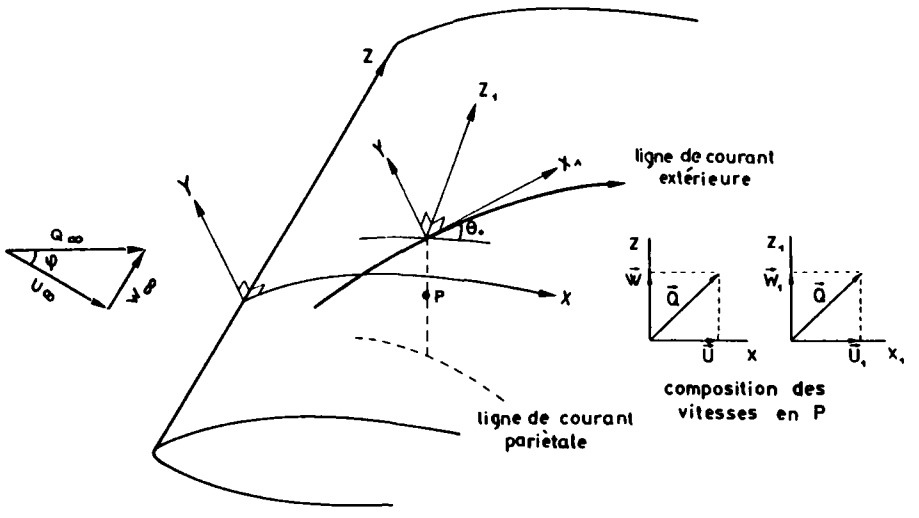


Fig. 1 - Schéma d'aile en flèche - Principales notations

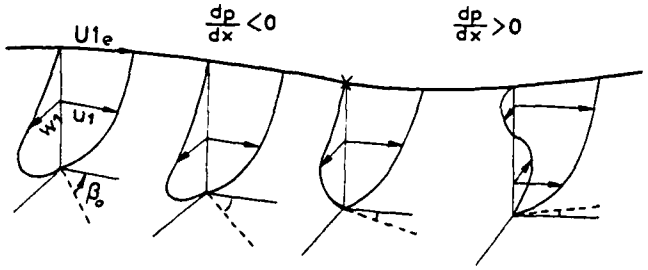


Fig. 2 - Evolution des profils de vitesse dans un repère lié à la ligne de courant extérieure

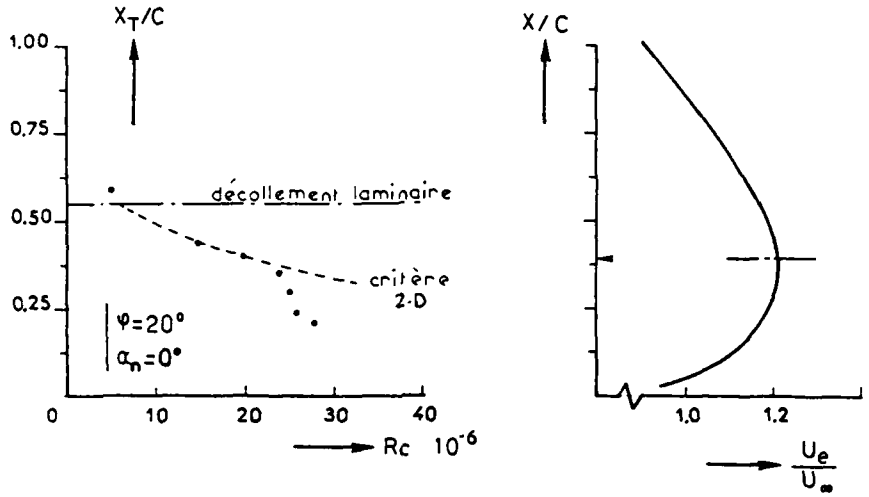


Fig. 3 - Mouvement de la transition en écoulement tridimensionnel ; position du problème

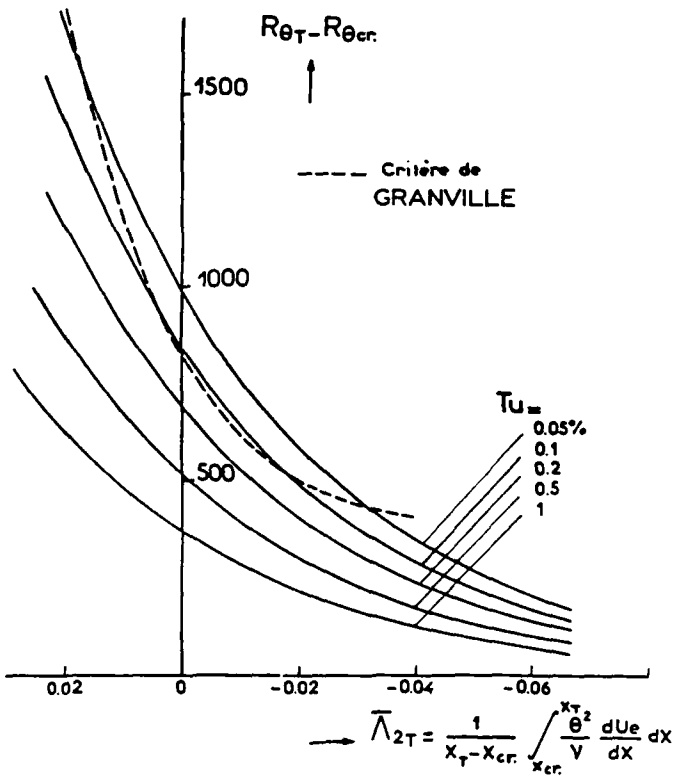


Fig. 4 - Critère de transition bidimensionnel

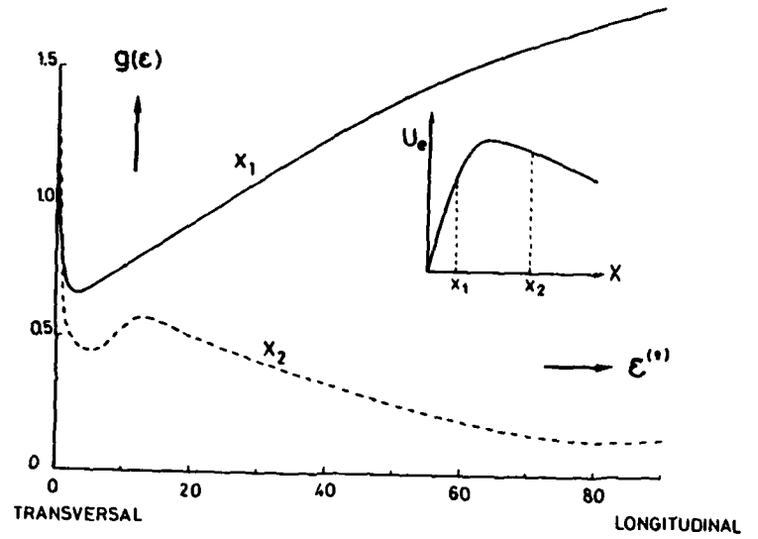


Fig. 5 - Evolution de la fonction g(ε) pour un nombre de Reynolds de corde et une configuration donnés

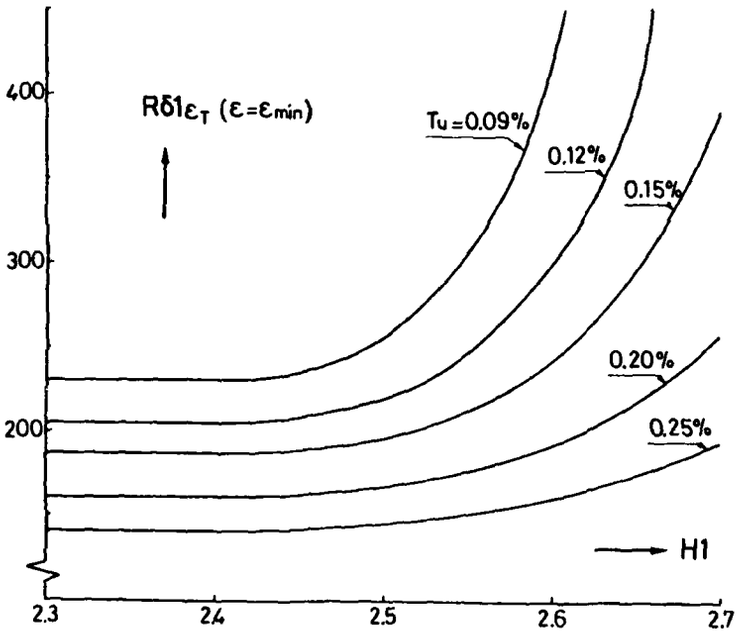


Fig. 6 - Critère de transition transversal

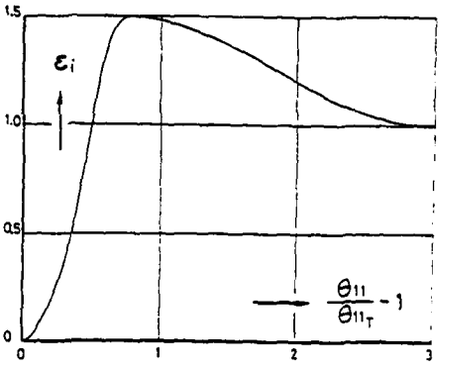


Fig. 7 - Fonction adoptée pour le coefficient ε_i intervenant dans le modèle de calcul de la région de transition

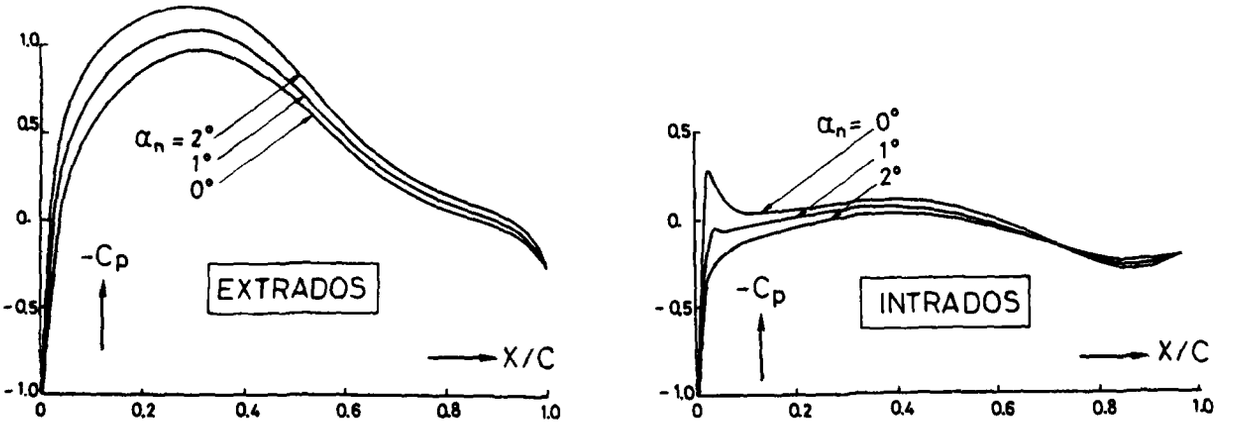


Fig. 8 - Distribution des coefficients de pression à l'extrados et l'intrados du profil OAP 01 pour trois incidences normales

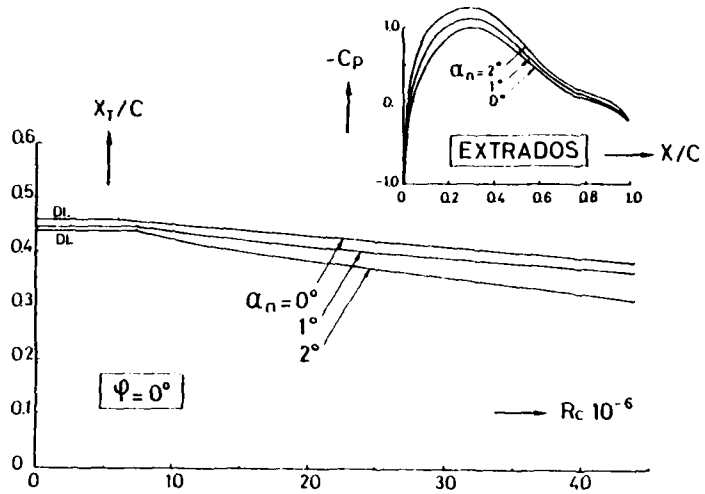


Fig. 9a. - Evolution de l'abscisse de transition en fonction du nombre de Reynolds de corde pour $\varphi = 0°$. DL : décollement laminaire - Profil OAP 01 extrados $\alpha_n = 0°$, 1° et 2°

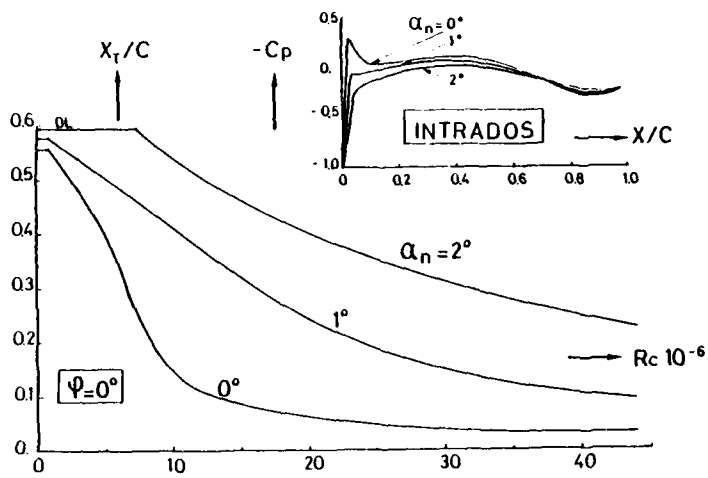


Fig. 9b. - Evolution de l'abscisse de transition en fonction du nombre de Reynolds de corde pour $\varphi = 0°$. DL : décollement laminaire - Profil OAP 01 intrados $\alpha_n = 0°$, 1° et 2°

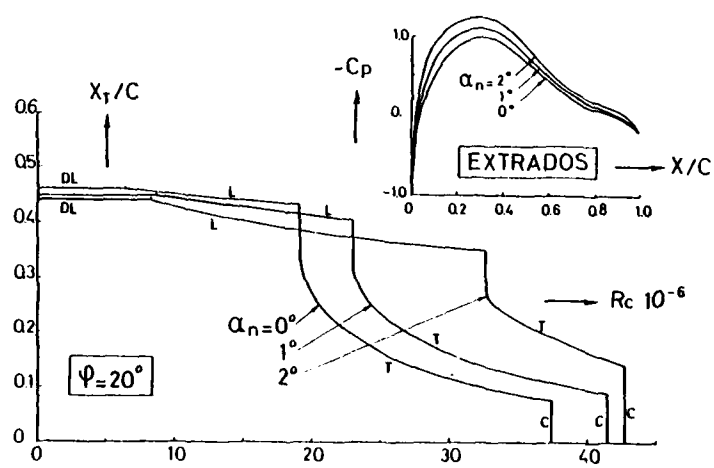


Fig. 10a. - Evolution de l'abscisse de transition en fonction du nombre de Reynolds de corde pour $\varphi = 20°$. DL : décollement laminaire. L : longitudinal. T : transversal. C : contamination de bord d'attaque - Profil OAP 01 extrados $\alpha_n = 0°$, 1° et 2°

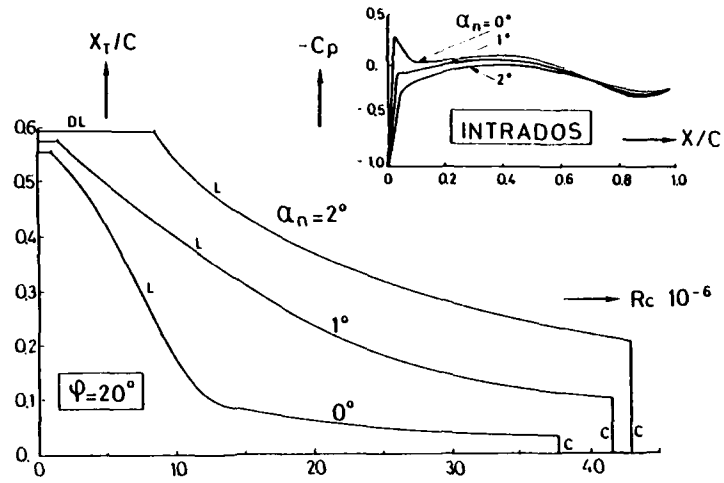


Fig. 10b. - Evolution de l'abscisse de transition en fonction du nombre de Reynolds de corde pour $\varphi = 20°$. DL : décollement laminaire. L : longitudinal. T : transversal. C : contamination de bord d'attaque - Profil OAP 01 intrados α_n = 0°, 1° et 2°

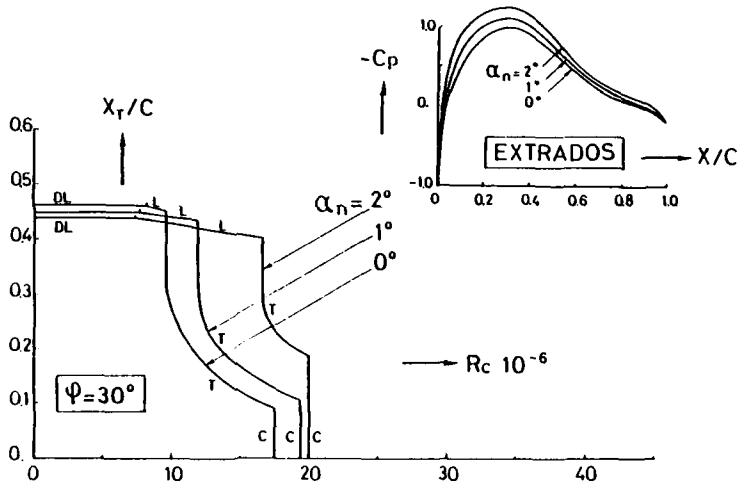


Fig. 11a. - Evolution de l'abscisse de transition en fonction du nombre de Reynolds de corde pour φ = 30°. DL : décollement laminaire. L : longitudinal. T : transversal. C : contamination de bord d'attaque - Profil OAP 01 extrados α_n = 0°, 1° et 2°

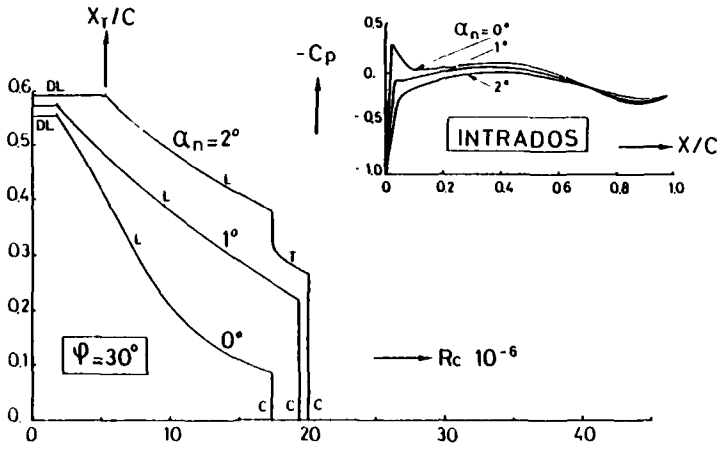


Fig. 11b. - Evolution de l'abscisse de transition en fonction du nombre de Reynolds de corde pour φ = 30°. DL : décollement laminaire. L : longitudinal. T : transversal. C : contamination de bord d'attaque - Profil OAP 01 intrados α_n = 0°, 1° et 2°

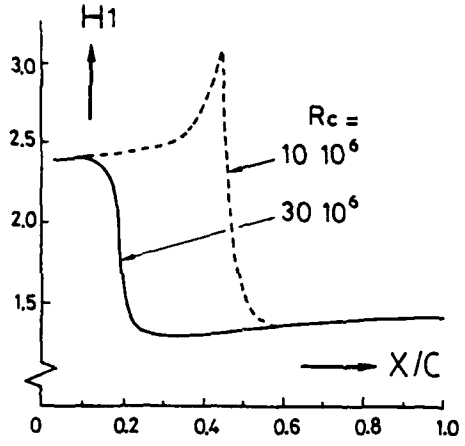


Fig. 12 - Calcul de la région de transition. Evolution de H1 avec x/c pour deux nombres de Reynolds. Profil OAP 01, extrados, $\varphi = 20°$ et $\alpha_n = 1°$

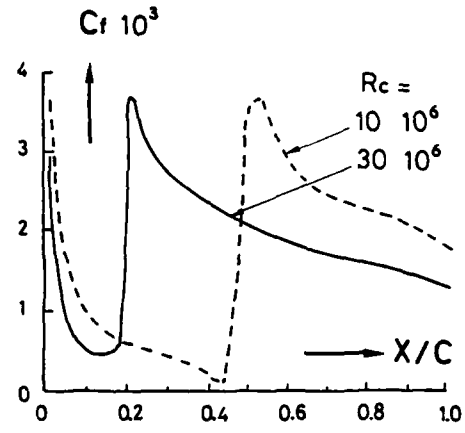


Fig. 13 - Calcul de la région de transition. Evolution de Cf avec x/c pour deux nombres de Reynolds. Profil OAP 01, extrados, $\varphi = 20°$ et $\alpha_n = 1°$

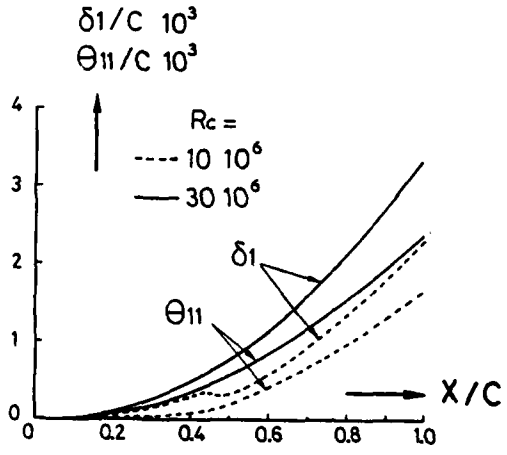


Fig. 14 - Calcul de la région de transition. Evolution de $\delta 1/c$ et $\theta 11/c$ avec x/c pour deux nombres de Reynolds. Profil OAP 01, extrados, $\varphi = 20°$ et $\alpha_n = 1°$

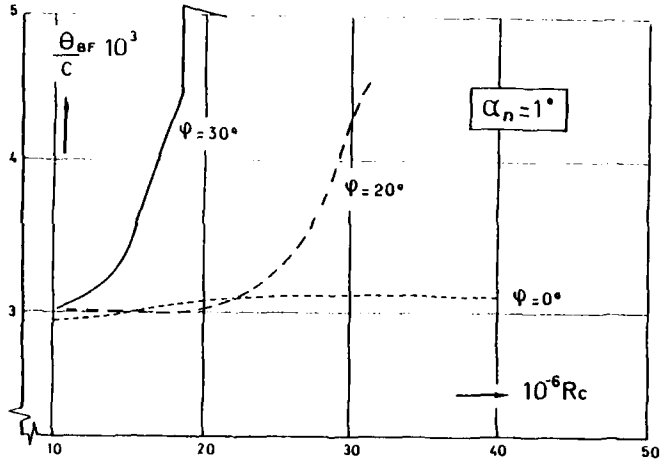


Fig. 15 - Epaisseur de quantité de mouvement totale (extrados et intrados) au bord de fuite en fonction du nombre de Reynolds de corde et de l'angle de flèche. Profil OAP 01 $\alpha_n = 1°$

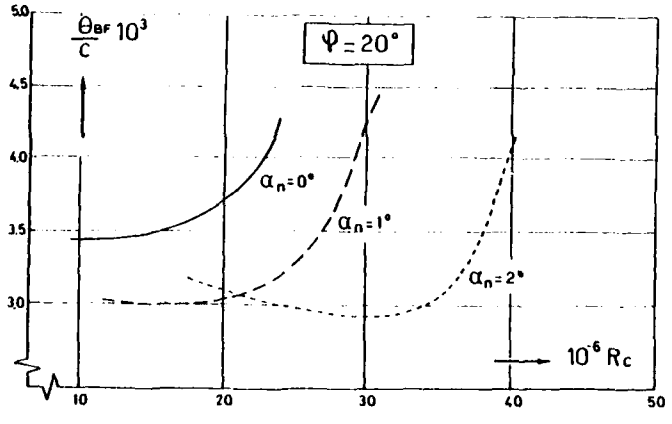


Fig. 16 - Epaisseur de quantité de mouvement totale (extrados et intrados) au bord de fuite en fonction du nombre de Reynolds de corde et de l'angle d'incidence normale. Profil OAP 01 $\varphi = 20°$

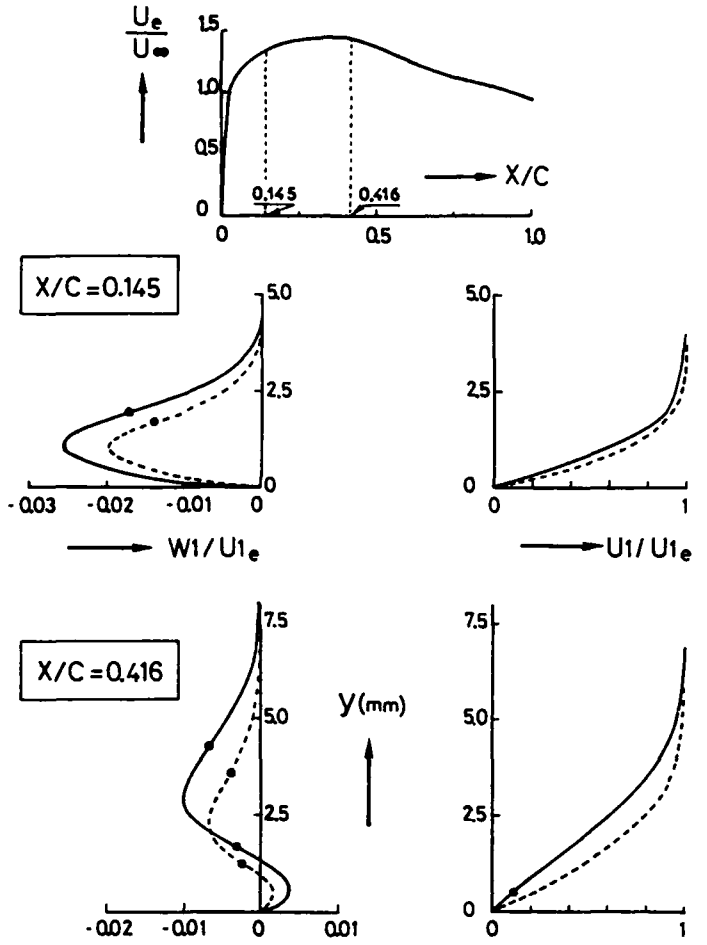


Fig. 17 - Influence de l'aspiration sur les profils longitudinaux et transversaux, à deux abscisses. Profil OAP 01, extrados, $\varphi = 20°$ $\alpha_n = 1°$ Rc = 20 millions.

—— S = 0 ---- S = 0,8 • point d'inflexion

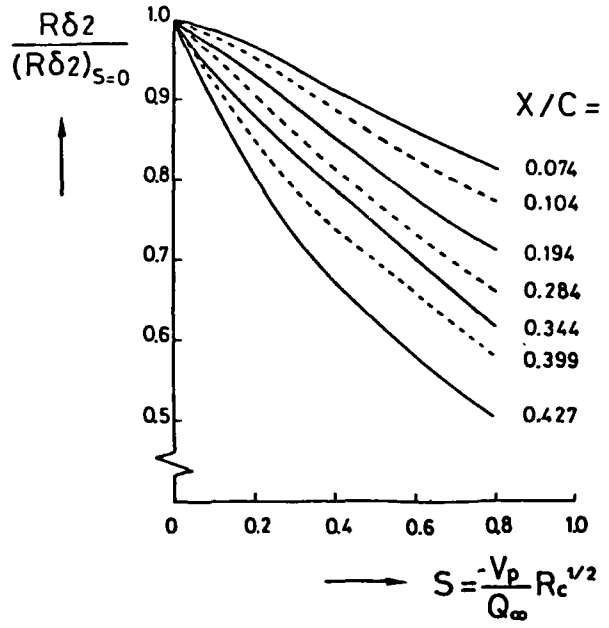


Fig. 18 - Evolution de $(R\delta 2)/(R\delta 2)_{S=0}$ avec S pour différentes abscisses. Profil OAP 01, extrados, $\alpha_n = 1°$

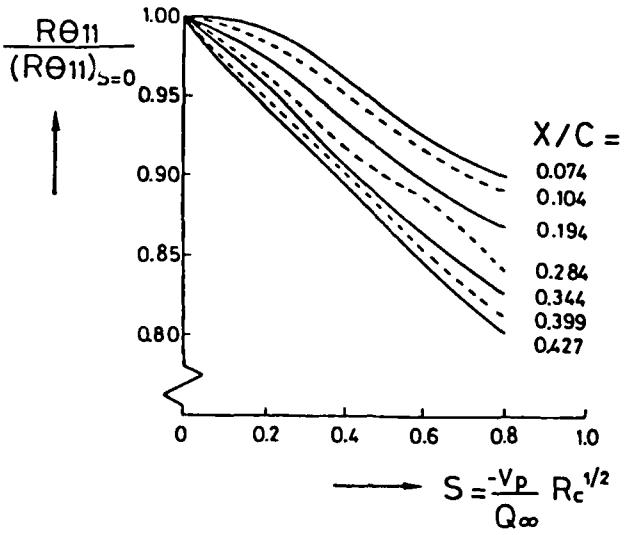


Fig. 19 - Evolution de $(R\theta 11)/(R\theta 11)_{S=0}$ avec S pour différentes abscisses. Profil OAP 01, extrados, $\varphi = 20°$, $\alpha_n = 1°$

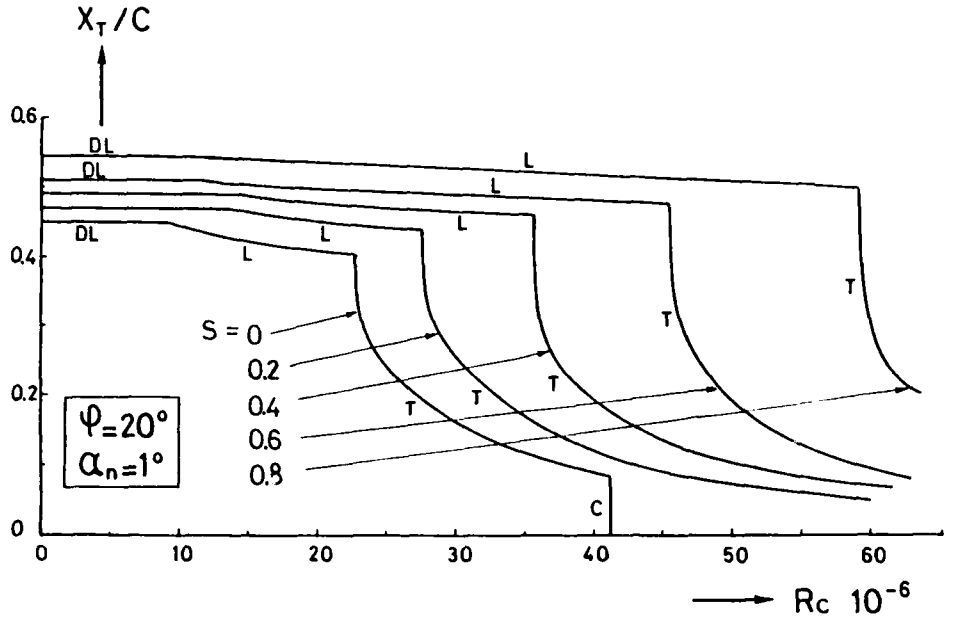


Fig. 20 - Evolution de l'abscisse de transition en fonction du nombre de Reynolds de corde pour différents taux d'aspiration S. Profil OAP 01, extrados, φ = 20° α_n = 1° - DL : décollement laminaire. L : longitudinal. T : transversal. C : contamination de bord d'attaque.

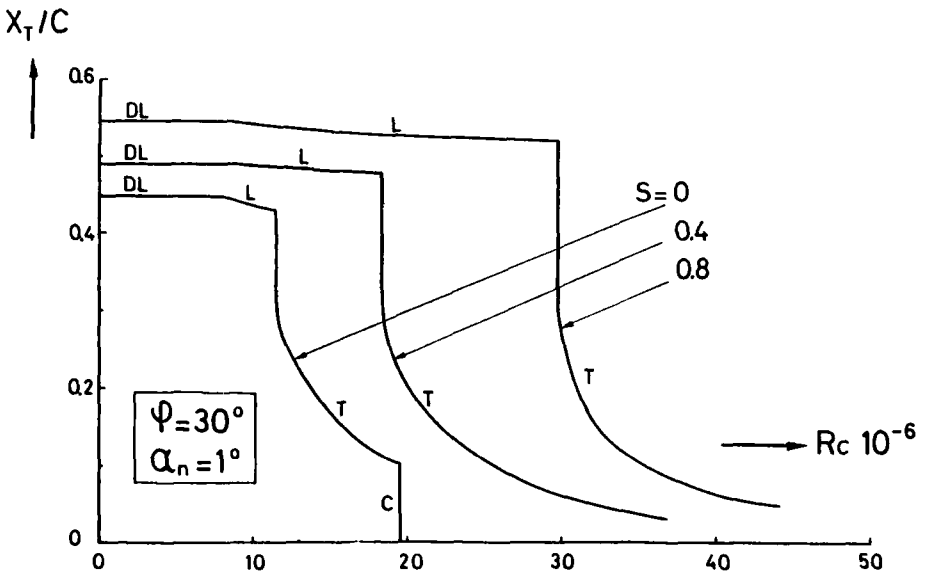


Fig. 21 - Evolution de l'abscisse de transition en fonction du nombre de Reynolds de corde pour différents taux d'aspiration S. Profil OAP 01, extrados, φ = 30° α_n = 1° - DL : décollement laminaire. L : longitudinal. T : transversal. C : contamination de bord d'attaque.

THEORETICAL STUDY OF BOUNDARY-LAYER CONTROL

by
E.H. Hirschel
Messerschmitt-Bölkow-Blohm GmbH
Postfach 801160
8000 München 80, FRG

AD-P004 062

SUMMARY

The inviscid flow past the upswept rear part of a fuselage is directed beneath the fuselage. This leads to an accumulation of boundary-layer material at the lower side of the fuselage which might be prone to separation. In the present study the cross-sections of the rear end of a typical transport airplane fuselage were modified from the original circles to rounded triangles, in this way shifting downward the centers of gravity of the cross-sections. The side-view contour and the width of the fuselage remain unchanged; the same holds roughly for the volume. Three different configurations without wing and tail unit were studied, the original and two modified ones. The inviscid flow was computed with the MBB-panel method, the boundary-layer development with the integral method of Cousteix and Aupoix for three-dimensional turbulent, compressible flow. The results show that less boundary-layer material is transported under the rear part of the fuselage in the modified cases. The tendency of the skin-friction lines to converge is reduced. The whole flow pattern at the base is improved. In the frame of boundary-layer theory, however, no statement can be made about possible pressure drag reductions. An improvement of the elevator performance appears to be probable. The study shows that the upsweep of the fuselage is the main factor in the boundary-layer development. The addition of the wing and the tail unit will only modify the picture.

1. INTRODUCTION

The flow past the upswept rear part of a fuselage is marked by an accumulation of boundary-layer material on its lower side. This can influence adversely the performance of an APU, of the elevator unit, and can lead to premature separation in the base area.

The main reason for this flow behaviour lies in the fact that the upswept rear part directs already the inviscid flow beneath the fuselage, which is enhanced to a certain degree by the presence of the wing and the tail unit.

In the present study it is investigated how much changes in the cross-section of the fuselage will affect the boundary-layer development especially on the lower side of the fuselage. The changes in the cross-sections are made in such a way that the side-view contour, and the from-above-view contour remain the same for the whole fuselage. Only the centers of gravity of the cross-section areas are shifted downward.

The inviscid flowfields for three different configurations were computed with the MBB-panel method [1], and the boundary layers with the MBB-3-D boundary-layer package (see e.g. [2]), which uses an integral method [3] for the solution of the boundary-layer equations.

The fuselage considered is a typical transport-airplane fuselage without wing and tail unit. The computations were made for a free-stream Mach number $M_\infty = 0.8$, a Reynolds number with respect to the fuselage length of $Re = 7 \cdot 10^8$. The angle of attack was $\alpha = 0°$ in all cases.

2. MODIFICATIONS OF THE FUSELAGE

Fig. 1 shows the side-view of the fuselage in the Cartesian reference coordinates $x^{i'}$ ($i' = 1, 2, 3$). In direction of the fuselage axis the surface coordinate parameter x^1 ($0 \le x^1 \le 1$) is defined, and in circumferential direction the surface coordinate parameter x^2, with $x^2 = 0$ in the upper, and $x^2 = 0.5$ in the lower symmetry line [4,5]. The part of the fuselage, where the changes are made in the cross-sections, begins at $x^1 = x^1_B = 0.6$, the end of the cylindrical part.

The fuselage part $x^1 > x^1_B$ of the original configuration (MO) has circular cross-sections. The modification M1 leads to a rounded triangle with roughly the same cross-section area as the original configuration. The modification M2 keeps the original circular shape in the upper half, but makes the lower half to a rounded rectangle, thus enlarging the cross-section area. For both the modifications M1 and M2 the centers of gravity of the cross-section areas lie lower than for the original configuration MO.

The modifications begin at x^1_B, where the modification coordinate parameter ξ starts with $\xi = 0$, and end at the base, where $\xi = 1$:

$$(1) \qquad \xi = \frac{x^1 - x^1_B}{1 - x^1_B} \quad .$$

In Fig. 2 schematically the cross-sections M1 and M2 are given which evolve linearily from the circular cross section at x^1_B with the radius $r_o(x^1_B)$. The radius $r_o(x^1)$

of the original contour, however, does not change linearily with x^1, Fig.3a (note that all lengths given are non-dimensionalized with the length L of the fuselage).

The modification parameters, see Fig.2, for M1 read:

$$(2) \qquad a_1 = \frac{r_o}{2}\,\xi \ ,$$

$$(3) \qquad a_2 = \frac{r_o}{\sqrt{2}}\,\xi \ ,$$

$$(4) \qquad r_1 = r_o\left(1 - \frac{1}{2}\,\xi\right) \ ,$$

and for M2:

$$(5) \qquad a_3 = \frac{3\sqrt{2}}{4}\,r_o\,\xi \ ,$$

$$(6) \qquad r_2 = r_o\left(1 - \frac{3}{4}\,\xi\right) \ .$$

Their graphs are given in Fig.3a, too.

In Fig.3b the cross-section circumferential length ratio, and the cross-section area ratio of M1 and M2 are given as function of ξ. These ratios are referred to the values of the original circular cross-section (lower index o). The configuration M1 has a wetted surface slightly larger than that of the original configuration MO, the volume is smaller. The configuration M2 has both a larger wetted surface and volume compared to MO. Fig.4 finally shows the changes of the shapes by means of the panel models of the three configurations.

3. DISCUSSION OF RESULTS

The panel-method computations were made with approximately 430 panels on one half of the fuselage. The boundary-layer computations were started at $x^1 = 0.08$, where the external flow still is accelerated, with approximated initial data. The step size in x^1-direction was $\Delta x^1 = 0.03$, and in circumferential direction $\Delta x^2 = 0.02$.

Both the computed inviscid surface streamlines, and the skin-friction lines are given in Fig.5 for the three configurations in the parameter plane (x^α-plane, $\alpha = 1, 2$). The flow past the original configuration is marked by a strong convergence of the inviscid streamlines near the lower symmetry line close to the base. To this a divergence pattern near the upper symmetry line corresponds. On the modification M1 the flow in the vicinity of the lower symmetry line is nearly parallel to it, whereas for M2 a weak convergence pattern exists. For this modification the divergence near the upper symmetry line is the smallest, for M1 it is the largest of all three cases, which intuitively could be expected by considering the cross-section shapes, Fig.4.

The skin-friction line patterns of the boundary layer are accordingly. On the original fuselage near the lower symmetry line close to the base the inviscid surface streamlines are appreciably bent due to a lateral pressure gradient. This is a consequence of the strong convergence toward the symmetry line, which finally must give way to a flow asymptotically parallel to it. Because the boundary-layer streamlines, and especially the skin-friction line, always react stronger to a lateral pressure gradient than the inviscid external streamline - this is due to the lower flow momentum of the boundary layer - these are curved more strongly. On the original fuselage thus the whole boundary layer on the lower side is affected rather strongly. On the modified fuselage M1 clearly the two skin-friction lines closest to the lower symmetry line are almost parallel to it, whereas for M2 even a convergence pattern is present.

The inviscid external streamlines and the skin-friction lines on the real surface are given in Figs.6 to 8. The side-view pictures, Fig.6, show that the accumulation of the inviscid streamlines and the skin-friction lines in the lower-side region is reduced for the configurations M1 and M2. On the upper side of the fuselages, Fig.7, the divergence of inviscid streamlines and skin-friction lines around the upper symmetry line is strongest for configuration M1, which was already indicated in Fig.5. On the lower side of the fuselage, Fig.8, finally the different convergence patterns - strongest for MO and weakest for M2 - are discernable.

Before an attempt is made to interprete these patterns with regard to separation, other indicators for separation [6] must be investigated. One of these is the development of the boundary-layer thickness δ and the displacement thickness δ_1 distributions, especially in circumferential direction. In Fig.9 for cross-section A (see Fig.1) these distributions (δ and δ_1 are non-dimensionalized with the fuselage length L) are seen to be very similar for all three configurations. For all of them a slight bulging of the thickness contours around the lower symmetry line is present, which is largest for the original fuselage MO. The bulging is due to the accumulation of boundary-layer material because of the flow beneath the rear part of the fuselage, which here already is present.

In Fig.10 the distributions are given for cross-section B, where already strong dif-

ferences in the configurations are present. The boundary-layer thickness on the original configuration MO is bulging out very strongly on the lower side, which is true also for the displacement thickness. Remarkable is the peak in the immediate vicinity of the lower symmetry line. The thickness distributions on the configurations M1 and M2 exhibit the pattern typical for imminent vortex-sheet separation [2,6]: a peak of the boundary-layer thickness, a sharp peak together with a nearby dip into negative values of the displacement thickness. The peak feature at $x^2 \approx 0.45$ is, however, also present on the original configuration.

The magnitude of the wall shear-stress coefficient c_f in the x^α-plane in Fig. 11 reveals on the original fuselage MO the existence of a singular point, most certainly a saddle point, on the lower symmetry line at $x^1 \approx 0.92$. This point is indicated by the dip of the wall shear-stress coefficient, together with the strong divergence of the skin-friction lines (Fig. 5a). The peaks both of the boundary-layer thickness and the displacement thickness, Fig. 10a, don't really fit into the picture, probably because of the violation of the boundary-layer assumptions in this area. Up to $x^1 \approx 0.85$ boundary-layer material accumulates according to Fig. 5a and then is swept away very suddenly from the lower symmetry line.

On the modified fuselages M1 and M2 no dip of the wall shear-stress coefficient appears on the symmetry line in the region considered. The peak of the boundary-layer thickness in Fig. 10b and Fig. 10c at $x^2 \approx 0.45$ corresponds to the dips of the wall shear-stress coefficient at the same location in Figs. 10a to 10c. This dip is strong for the configurations MO and M1, and weak for M2. The rise of the wall shear-stress coefficient near and on the upper symmetry line up to $x^1 \approx 0.9$ observed on all configurations is due to the divergent inviscid and boundary-layer flow pattern here (Fig. 5), and is strongest for the fuselage M1, where the divergence is the largest, Fig. 5b.

The formal shape parameter $H_{tt} = \delta 1_t / \delta 2_{tt}$ (t is the local direction of the inviscid external streamline, $\delta 1_t$ and $\delta 2_{tt}$ are the displacement thickness, and the momentum-loss thickness, respectively of the boundary-layer profile in this direction, the main-flow profile) in Fig. 12 completely reflects the result found so far: on the lower side of the fuselage the boundary-layer development near the rear end seems to be the least critical on configuration M2.

In Figs. 13 and 14 the inviscid streamline and skin-friction line patterns near the base on the original fuselage MO, and on the modification M2 are enlarged in order to discuss the possible separation patterns, Fig. 15. The strong divergence of the boundary-layer flow around the lower symmetry line on the configuration MO (Fig. 14a), together with the upwash (Fig. 13a) most probably indicates kind of a closed separation [7], as sketched in Fig. 15a. The singular point is indicated by the dip of the wall shear-stress coefficient, Fig. 11a, on the lower symmetry line, as well as other features of the solution, as discussed above.

In contrary to this on the configuration M2, Fig. 15b, and similarly on M1, an open separation [7] seems to exist, with, of course, a closed separation near the very base. This feature cannot be found from the present solution because of the limitations of boundary-layer theory. Around the lower symmetry line the boundary layer at $x^1 \approx 0.9$ moves in near parallel fashion toward the base, whereas vortex-sheet separation lines on the flanks seem to be approached. This is supported by the boundary-layer thickness distributions, Fig. 10c, and the wall shear-stress and shape parameter distributions, as discussed above, too.

Fig. 16 finally shows a comparison of the accumulated friction drag $R^{1'}$ in x^1-direction. Up to $x^1 \approx 0.7$ no differences are discernable for the different configurations. Then a slightly larger friction drag ensues for the configuration M2, which might partly be due to the larger wetted surface (see C/C_2 | M2 in Fig. 3b).

4. CONCLUSIONS

In the present study it is shown that changes in the cross-section of fuselage aft ends can lead to flow improvements. The limitations of boundary-layer theory allow only an approximative description of separation behaviour of three-dimensional boundary layers because neither the local (elliptical properties of the flow near separation) nor the global (change of the inviscid flowfield due to the ensueing vortex sheets and/or vortices) interactions can be taken into account. However, experience shows that in many cases quite reliable predictions of the separation pattern can be made [2,6].

If this is accepted, the present results indicate a better separation behaviour of the boundary layer on both the modified fuselages compared to that on the original fuselage. This could lead to a smaller total drag of the modified configurations. Of course, the larger cross-section area at the base of the configuration M2 could lead to a larger base drag. The flow at the root of the elevator unit as well as the flow with regard to an APU might also be affected positively because less boundary-layer material is washed downward into this area.

It appears from the results as a whole that on the configuration M2 the best flow pattern exists. In any case the geometrical configuration M2 appears to be better suited for realization. However, both the modified configurations M1 and M2 are in no sense optimized, especially because no wing and no tail unit was taken into account. These will change, at least locally, the flow behaviour.

A complete assessment of the value of the changes in geometry and in the subsequent changes in the flow pattern can only be made by means of wind-tunnel experiments. Solutions of the Navier-Stokes equations might give to a certain extent answers regarding the total drag of the fuselages.

REFERENCES

[1] Kraus,W. and Sacher,P.: "Das Panelverfahren zur Berechnung der Druckverteilung von Flugkörpern im Unterschallbereich", Zeitschrift für Flugwissenschaften (ZFW), Vol.20 (1973), pp. 301-311.

[2] Hirschel,E.H.: "Computation of Three-Dimensional Boundary Layers on Fuselages", J. of Aircraft, Vol.21, No.1, 1984, pp. 23-29.

[3] Cousteix,J.: "Theoretical Analysis and Prediction Method for a Three-Dimensional Turbulent Boundary Layer", ESA TT-238 (1976).

[4] Hirschel,E.H., and Kordulla,W.: "Shear Flow in Surface-Oriented Coordinates", Vol.4 of Notes on Numerical Fluid Mechanics, Braunschweig, Vieweg Verlag, 1981.

[5] Hirschel,E.H.: "Boundary-Layer Coordinates on General Wings and Bodies", Zeitschrift für Flugwissenschaften und Weltraumtechnik (ZFW), Vol.6 (1982), pp. 194-202.

[6] Hirschel,E.H.: "Three-Dimensional Boundary-Layer Calculations in Design Aerodynamics". Proc. IUTAM-Symposium on Three-Dimensional Boundary Layers (H.H. Fernholz, E.Krause, eds.), Berlin-Heidelberg-New York, Springer Verlag, 1982, pp. 353-365.

[7] Wang,K.C.: "New Developments in Open Separation". Proc. IUTAM-Symposium on Three-Dimensional Boundary Layers (H.H. Fernholz, E.Krause, eds.), Berlin-Heidelberg, New York, Springer Verlag, 1982, pp. 94-105.

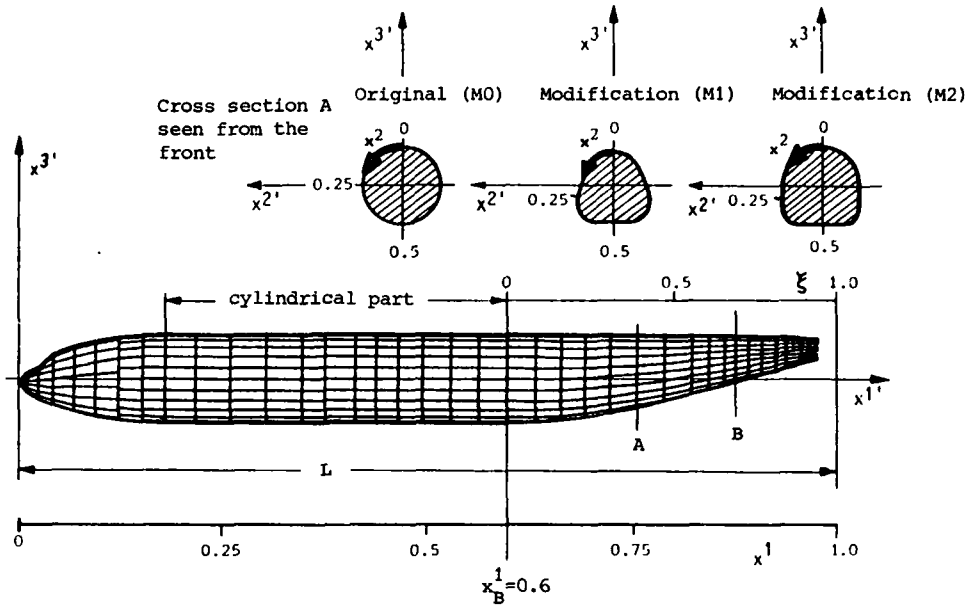


Fig. 1 Schematic of fuselage, coordinate systems and the two modifications of the rear-end part M1 and M2

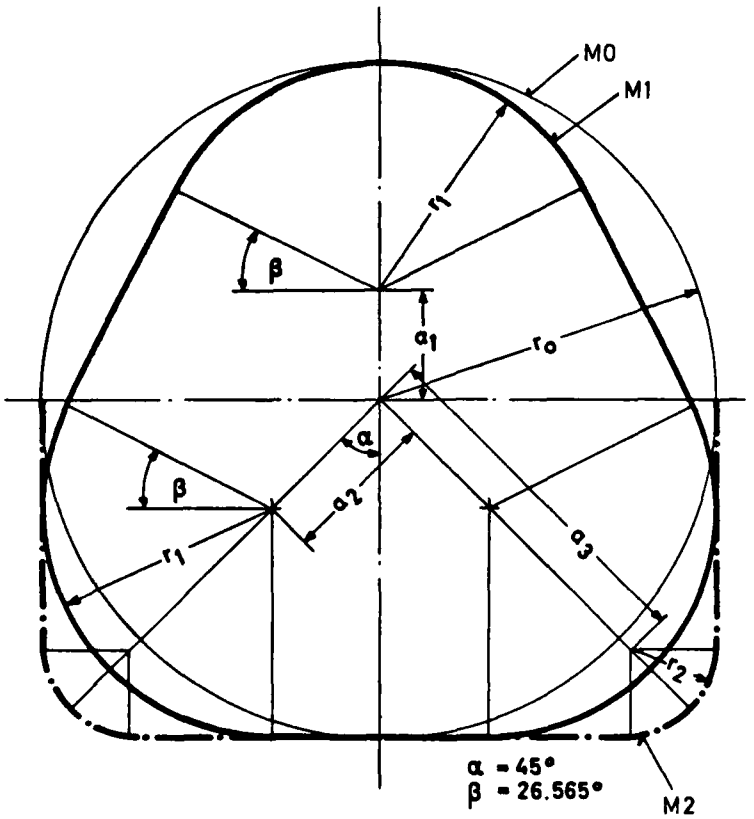


Fig. 2 Schematic of fuselage modifications

——— original contour (M0)
——— modified contour (M1)
—·— modified contour (M2)

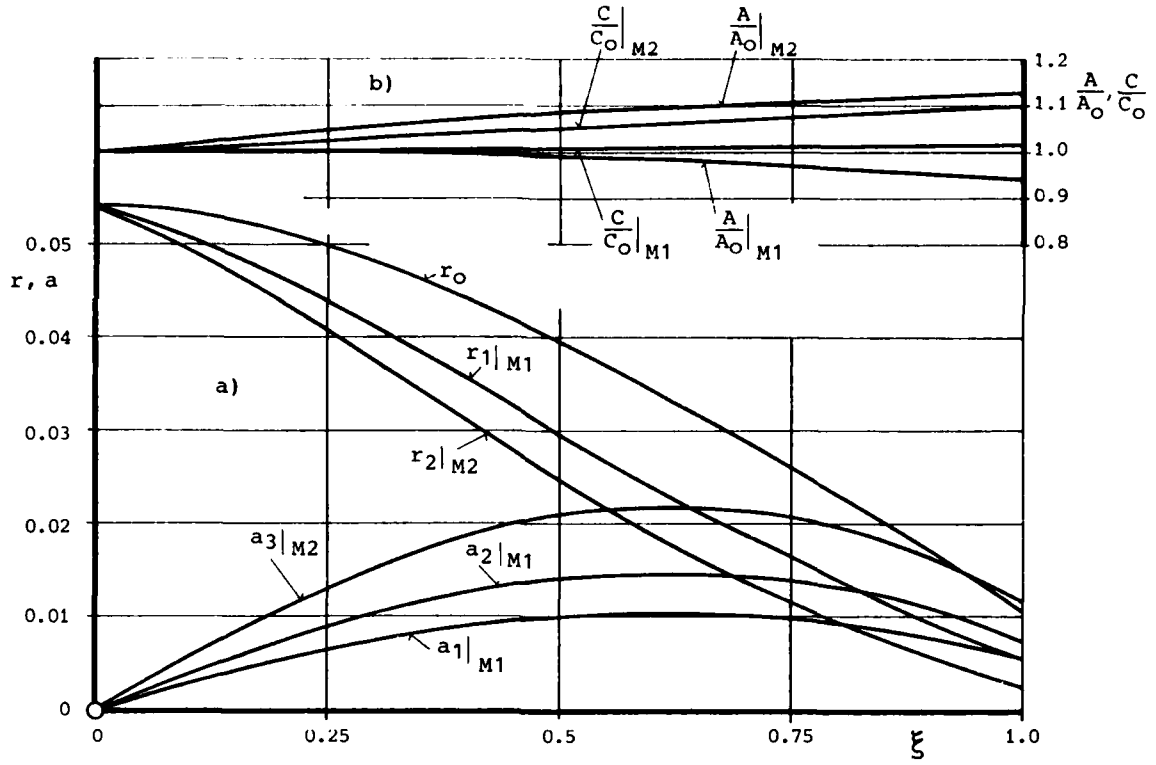


Fig. 3 Distribution as function of ξ of a) the radius r_o of the original cross sections, and the parameters a and r, b) of the circumferential length ratio C/C_o, and the area ratio A/A_o for the modifications M1 and M2

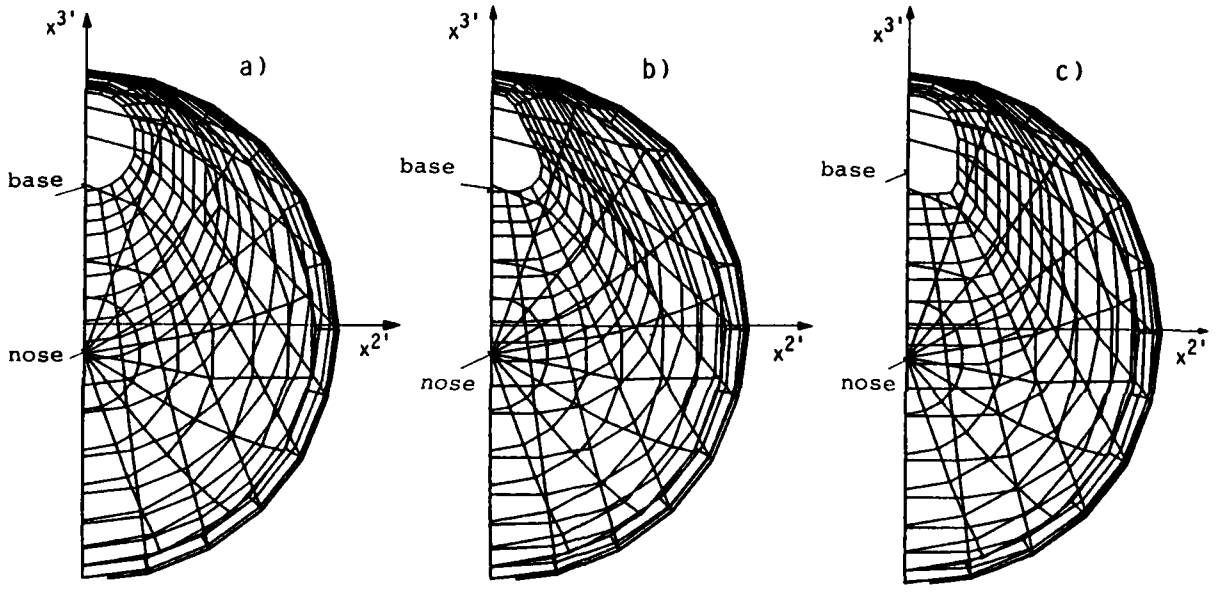


Fig. 4 Panel model of the right half of the fuselage seen from behind: a) original fuselage M0, b) modification M1, c) modification M2

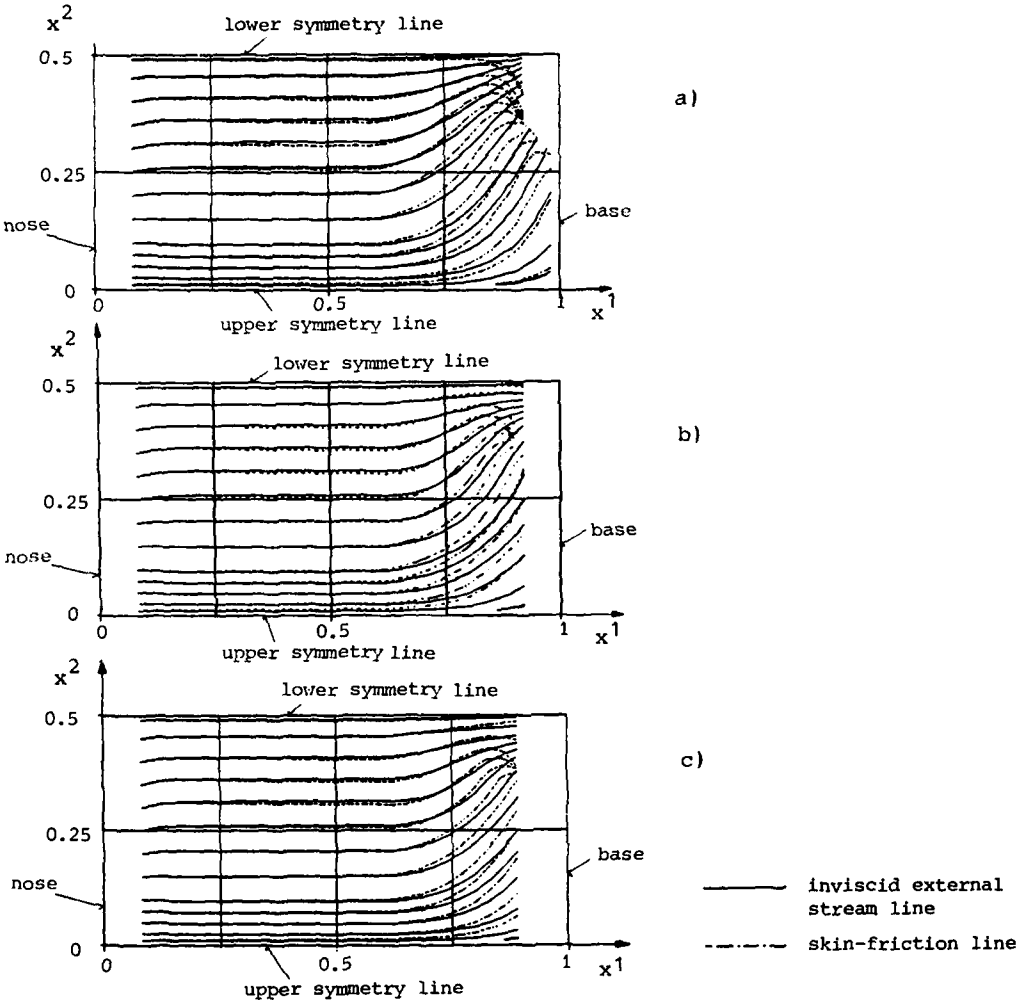


Fig. 5 Inviscid external stream lines and skin-friction lines in the x^{α}-plane (right half of fuselage)
a) original fuselage M0, b) modification M1, c) modification M2

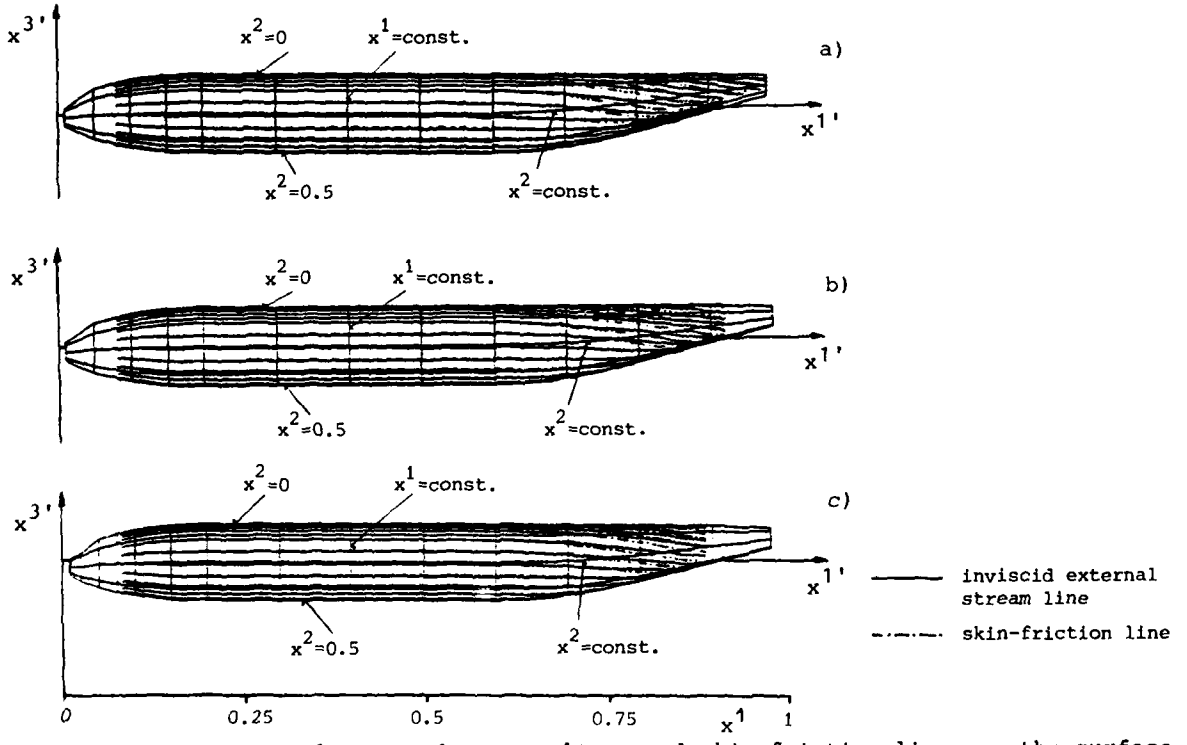


Fig. 6 Inviscid external stream lines and skin-friction lines on the surface (side view)
a) original fuselage M0, b) modification M1, c) modification M2

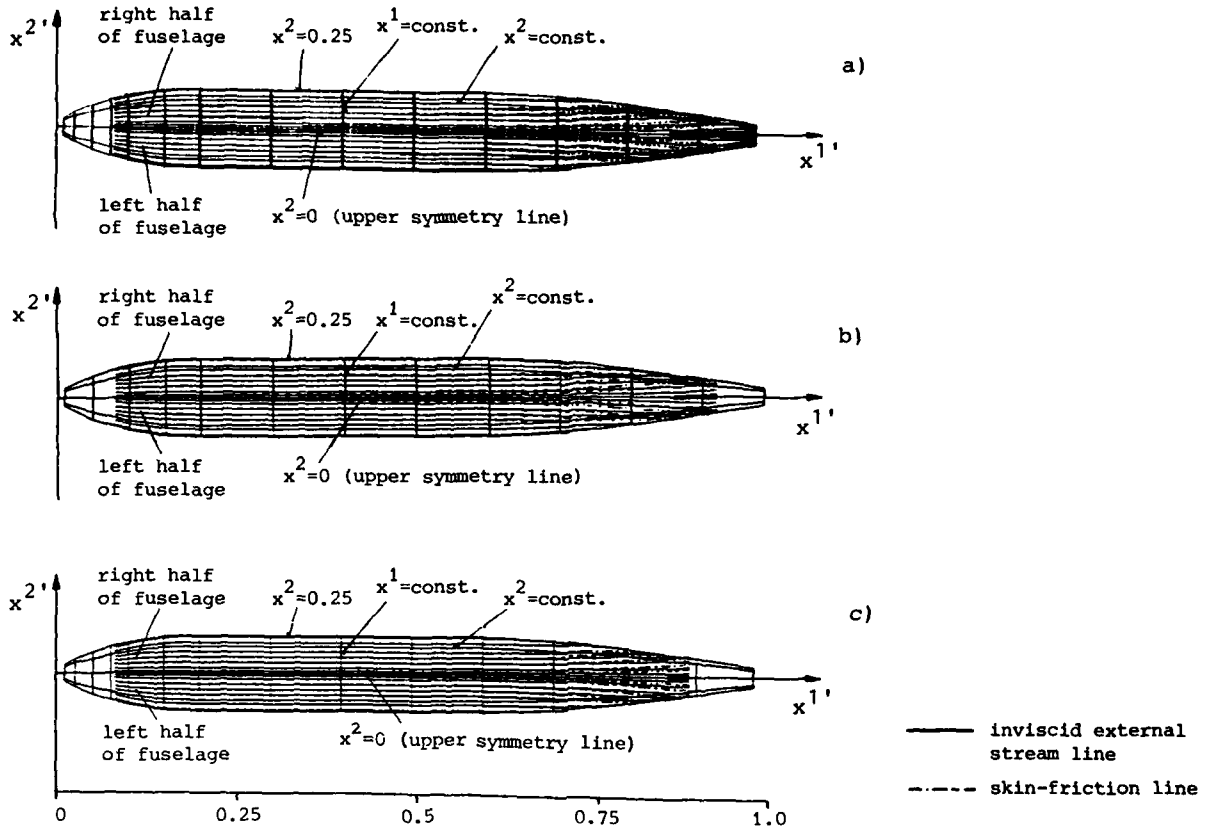


Fig. 7 Inviscid external stream lines and skin-friction lines on the surface of the fuselage (view from above)
a) original fuselage M0, b) modification M1, c) modification M2

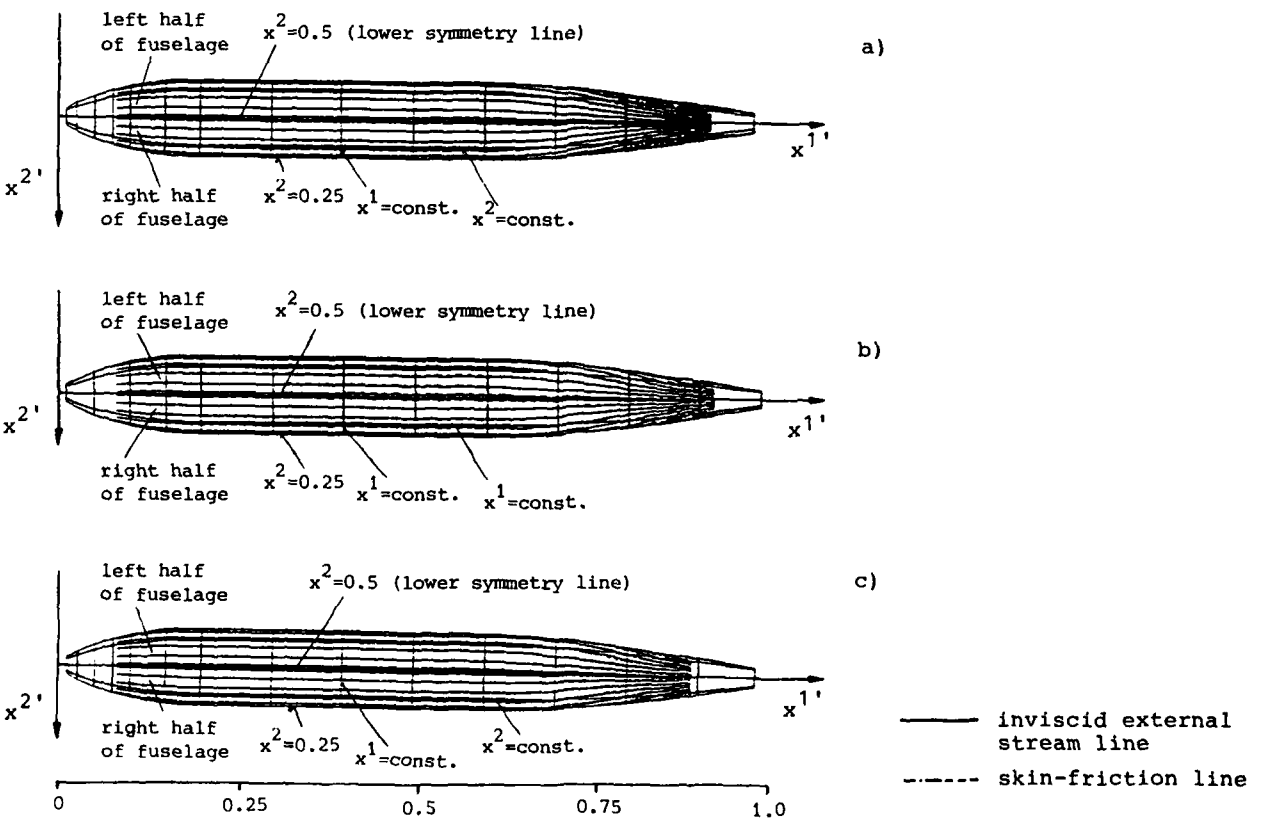


Fig. 8 Inviscid external stream lines and skin-friction lines on the surface of the fuselage (view from below)
a) original fuselage M0, b) modification M1, c) modification M2

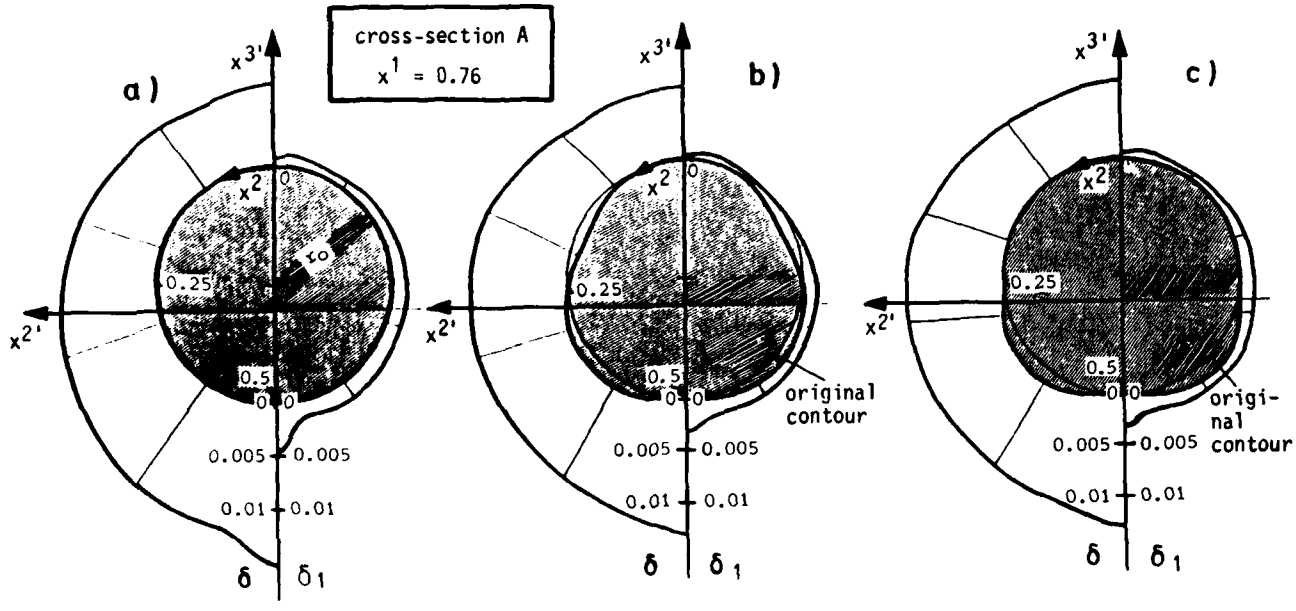


Fig. 9 Boundary-layer thickness δ and displacement thickness δ_1 at cross-section A: a) original fuselage MO, b) modification M1, c) modification M2

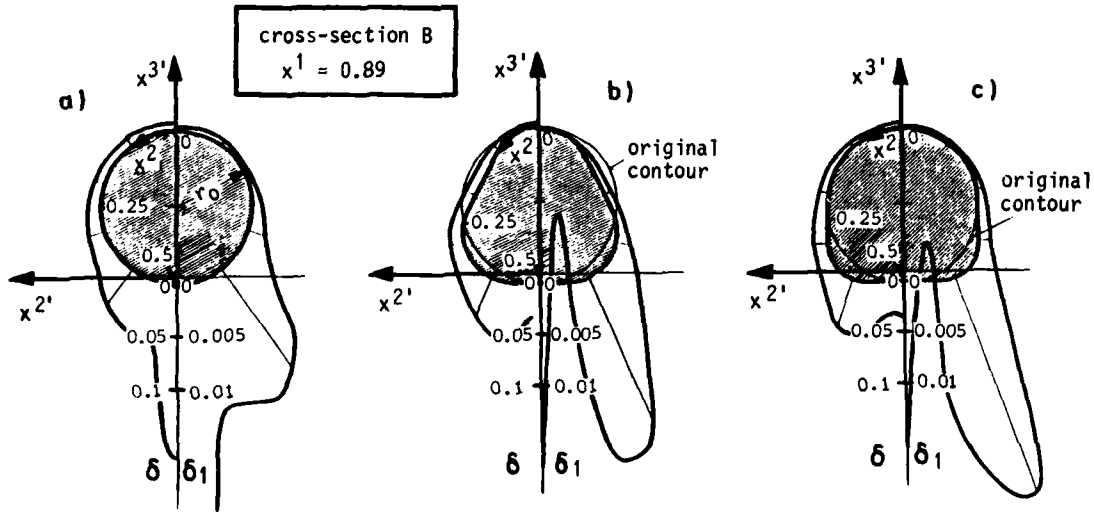


Fig. 10 Boundary-layer thickness δ and displacement thickness δ_1 at cross-section B: a) original fuselage MO, b) modification M1, c) modification M2

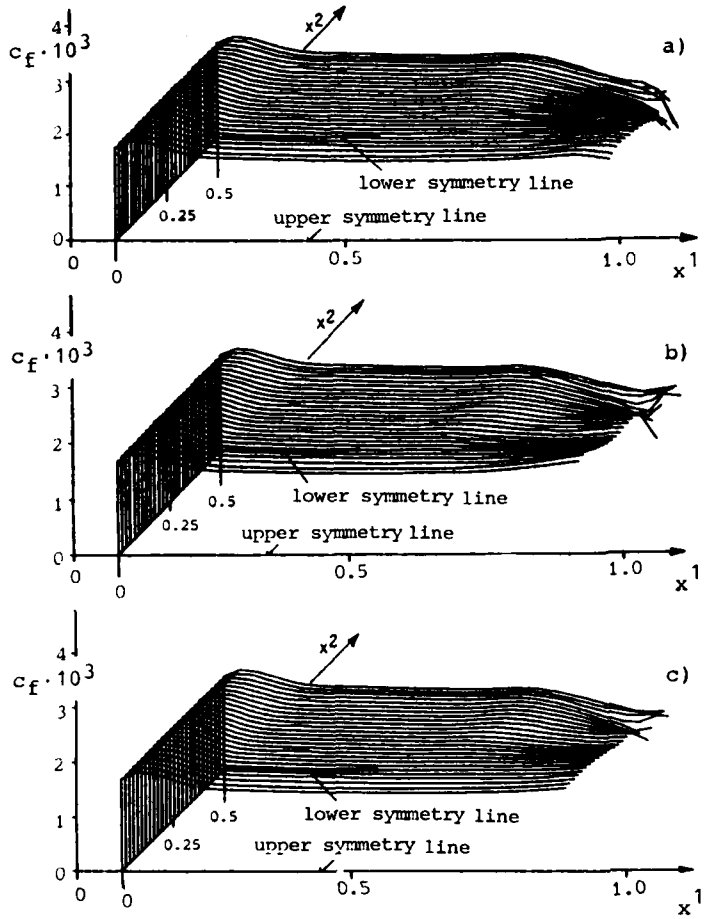


Fig. 11 Magnitude of wall-shear stress coefficient $c_f(x^a)$ (right half of fuselage)
a) original fuselage M0
b) modification M1
c) modification M2

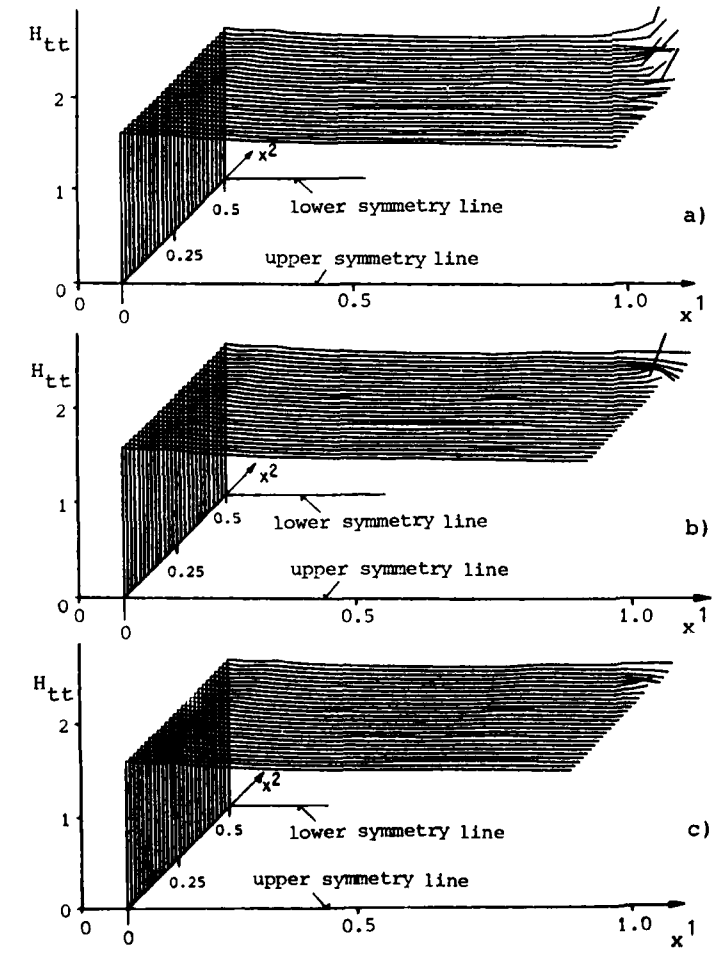


Fig. 12 Formal shape parameter $H_{tt}(x^a)$ (right half of fuselage)
a) original fuselage M0
b) modification M1
c) modification M2

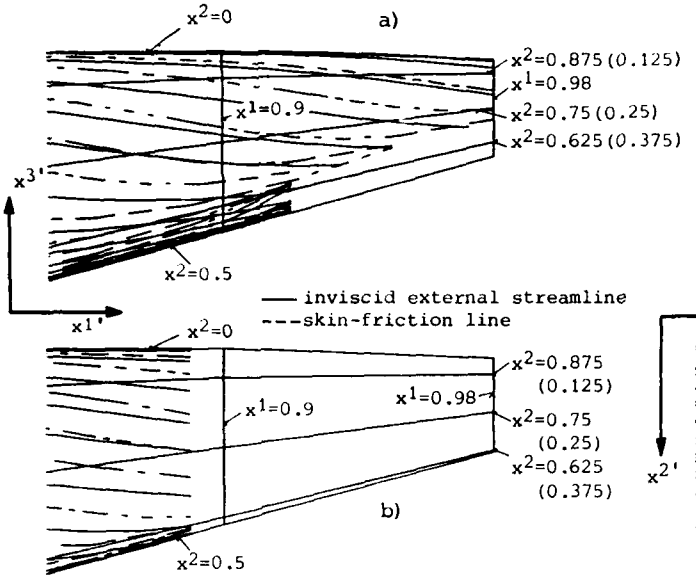


Fig. 13 Inviscid external streamlines and skin-friction lines on the surface of the fuselage near the base (side view):
a) original fuselage M0
b) modification M2

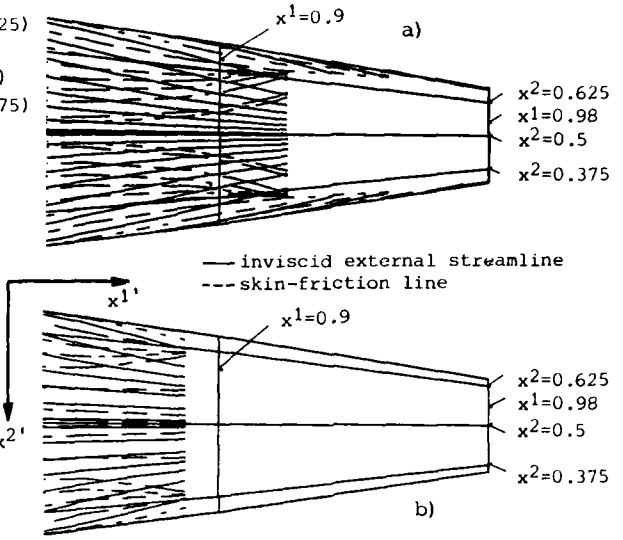


Fig. 14 Inviscid external streamlines and skin-friction lines on the surface of the fuselage near the base (view from below):
a) original fuselage M0
b) modification M2

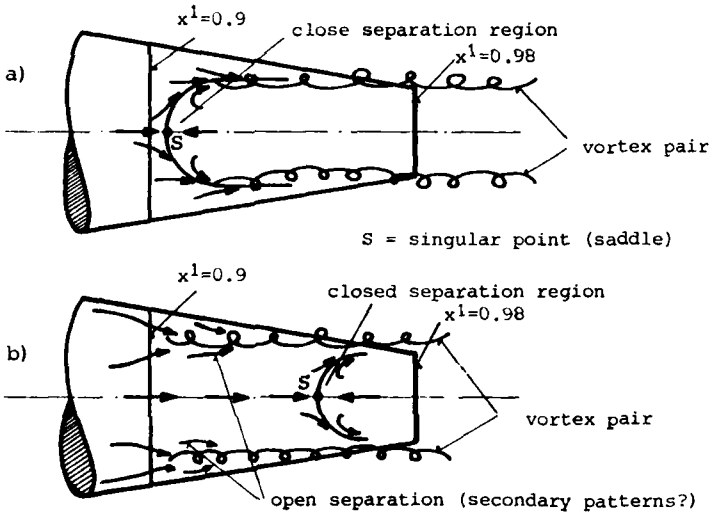


Fig. 15 Schematic of possible separation pattern (view from below):
a) original fuselage M0
b) modification M1 and M2

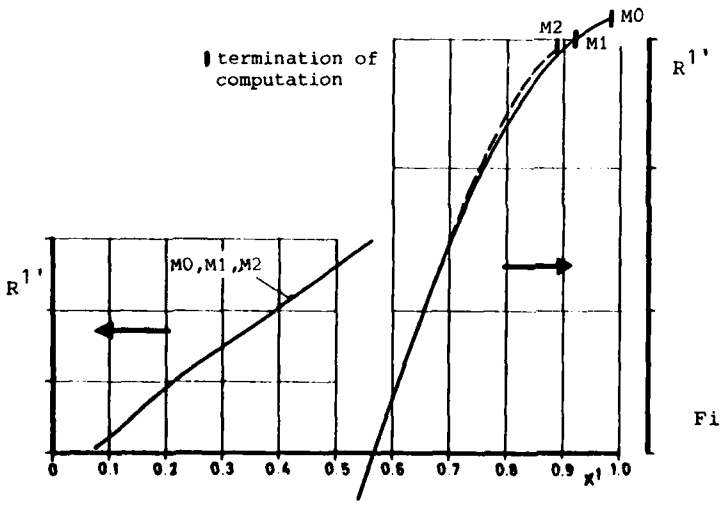


Fig. 16 Cumulated friction forces $R^{1'}(x^1)$:
original fuselage M0
modification M1 and M2

DRAG REDUCTION DUE TO BOUNDARY-LAYER CONTROL BY COMBINED BLOWING AND SUCTION

by

J. Wiedemann, K. Gersten

University Bochum
Institut für Thermo- und Fluiddynamik
Postfach 10 21 48
D-4630 Bochum 1

AD-P004 063

SUMMARY

A boundary control system of combined blowing and suction is investigated. Blowing is applied in the front part of the body where the pressure gradient is favourable, whereas suction is applied in the rear part of the body where adverse pressure gradients exist. In order to avoid the "sink drag" the volume rate of suction should be equal or smaller than the blowing volume rate.

Theoretical investigations of laminar flows include optimization of the blowing velocity distribution as well as second-order boundary layer effects such as pressure drag and displacement effects on friction drag.

Experimental results (mean velocities and shear stresses) of turbulent boundary layers with very strong blowing velocities near the stagnation point of a circular cylinder are used as a basis of a simple prediction method. Experiments on a circular cylinder show considerable drag reductions due to the combined blowing and suction boundary layer control system.

1. INTRODUCTION

The drag of an immersed body can be determined by integrating the forces acting on the body surface. It consists of two parts: the pressure drag due to the pressure (normal) forces and the friction drag due to shear (tangential) forces.

In subsonic flow the pressure drag is originated mainly by boundary-layer separation. It is well-known that boundary-layer separation can be suppressed by boundary-layer control due to suction. The application of continuous suction on the body surface where usually boundary-layer separation may occur makes it possible to reduce the pressure drag of the body.

On the other hand, continuous blowing perpendicularly into the boundary-layer leads to a reduction of the wall shear stresses and hence to a reduction of the friction drag. Figure 1 shows the wall shear stress near the stagnation point of an immersed body in incompressible flow as a function of the blowing velocity. This result of Prandtl's boundary-layer theory leads to the conclusion, that the wall shear stress can be reduced to any value wanted if the blowing rate is chosen strong enough.

Reductions of both drag components, the pressure drag as well as the friction drag, could be achieved by a combination of boundary-layer control due to blowing and due to suction in such a way that blowing is applied on the surface area with accelerated flow where high wall shear stresses can be expected and suction on surface areas with decelerated flow with the danger of boundary-layer separation.

In this paper theoretical as well as experimental investigations will be discussed which refer to systems of boundary-layer control by combined blowing and suction. Laminar as well as turbulent flow will be considered.

2. LAMINAR FLOW

2.1. Prandtl's Boundary Layer Theory for Strong Blowing (and Suction)

When the boundary layer along a permeable body is controlled by blowing and/or suction, the solutions of Prandtl's boundary-layer equations lead to limiting solutions for very large blowing and/or suction rates. In Figure 1 the skin friction near the stagnation point in two-dimensional incompressible flow is shown as function of the blowing velocity v_w (negative v_w corresponds to suction). There are two asymptotes for the skin-friction curve corresponding to the two limiting solutions of the boundary layer equations. In the limit of strong suction the skin friction increases with growing suction velocity. The skin friction is equivalent to the so-called "sink drag" due to momentum loss by suction. In order to avoid this sink drag the air sucted in has to be blown out again at a proper area. This leads to another limiting solution for large blowing velocity, sometimes called the "blowhard problem", see [1]. As Figure 1 shows, in this limit the skin friction is inversely proportional to the blowing velocity v_w, in other words, it can be reduced as much as desired, if the blowing velocity v_w is chosen large enough. For the given outer-flow velocity distribution $U(x)$ and the blowing velocity distribution $v_w(x)$ the wall shear stress is given by the simple formula:

$$\tau_w(x) = \frac{\rho \nu U(x)}{v_w(x)} \frac{dU}{dx} \tag{1}$$

This formula, originally derived for blowing ($v_w > 0$ and $dU/dx > 0$) can also be applied for suction, if the combination $(1/v_w(x))(dU/dx)$ stays positive, i.e. when suction is used at adverse pressure gradients ($v_w < 0$, $dU/dx < 0$). As the formula shows the wall shear stress is inversely proportional to the blowing velocity $v_w(x)$. In this limit of strong blowing the flow field has a three-layer structure as shown in Figure 2 for the example of a circular cylinder with $v_w \sim \cos \phi$, i.e. when blowing is applied on the front part of the cylinder and suction on the rear part of the cylinder. The viscosity is not essential for satisfying the no-slip condition at the wall and plays a role only in a thin free shear layer along the dividing streamline detached from the wall.

The drag coefficient of the circular cylinder (d: diameter; b: span; R: radius; $Re = U_\infty d/\nu$) is in this limit

$$c_D = \frac{D}{\frac{\rho}{2} U_\infty^2 \, b \, d} = \frac{8 \pi}{c_M \sqrt{Re}} \tag{2}$$

where

$$\frac{v_w(x)}{U_\infty} \sqrt{Re} = c_M \cos \frac{x}{R} \quad . \tag{3}$$

The mass-transfer coefficient c_M is connected with the volume rate coefficient

$$c_Q = \frac{Q}{U_\infty \, b \, d} \tag{4}$$

by

$$c_M = c_Q \sqrt{Re} \tag{5}$$

where Q is the volume rate of the recirculating flow inside the dividing streamline (see Figure 2).

In Figure 3 the drag reduction of a circular cylinder by two different boundary-layer control systems is shown for the Reynolds number $Re = U_\infty d/\nu = 4 \cdot 10^4$. Curve I refers to the combination of blowing and suction according to Eq. (3), whereas curve II corresponds to the case of homogeneous suction with the total suction rate Q. The asymptote of curve I, given by Eq. (2), shows clearly that the drag can become as small as desired if the circulating flow rate is large enough. On the contrary, curve II shows a drag reduction down to a value of $c_D \approx 0.2$, but further suction will increase the drag due to the sink drag, see also Figure 1. The comparison shows very clearly that the system of combined blowing and suction is much more effective than the system of homogeneous suction.

For bodies other than the circular cylinder the Eqs. (2) and (5) will also be valid with just different coefficients. For a symmetrical Joukowsky airfoil (4.4 % relative thickness) the drag coefficient as function of the volume rate coefficient is shown in Figure 4. In this example the distribution of the blowing velocity v_w was chosen $v_w \sim dU/dx$ in order to make sure that the combination $(1/v_w)(dU/dx)$ is always positive. As a consequence, the blowing rate Q_{Blow} is larger than the suction rate Q_{Suc}, namely $Q_{Blow} = 9.1 \, Q_{Suc}$. The excess of blowing rate is equivalent to a thrust of the airfoil similar to the sink drag in the case of suction. But Prandtl's boundary-layer theory is not able to cover this thrust effect, which, as will be shown later, is a higher-order boundary-layer effect.

2.2. Optimization

For a given body geometry and a given velocity distribution U(x) the following optimization problem can be formulated:

> An optimal distribution $v_w(x)$ has to be found such that the drag becomes a minimum under the additional condition of equal blowing and suction volume rates.

Figure 5 shows the result for such an optimization of the circular cylinder. Curves I correspond to the case shown in Figure 2 and given by Eq. (2). Due to optimizing the v_w-distribution (curves II) the drag could be reduced by 44 % from $c_D \, c_Q \, Re = 25$ down to $c_D \, c_Q \, Re = 14$.

A similar optimization of the symmetrical Joukowsky airfoil (4.4 % relative thickness) led to the minimum value $c_D \, c_Q \, Re = 1.0$. Each body has its minimum value $c_D \, c_Q \, Re$ depending on the velocity distribution U(x).

2.3. Second-Order Boundary-Layer Theory.

When in the system of combined blowing and suction the blowing rate is larger than the suction rate, a negative drag, i.e. thrust, is produced. This force against the oncoming

flow direction must be a pressure force. This, however, cannot be predicted by Prandtl's boundary layer theory. This thrust due to blowing is a second-order boundary layer effect. Second-order boundary layer theory will also yield information about the displacement effects of the fairly thick boundary layers due to blowing.

The second-order boundary-layer effects for the circular cylinder ($v_w \sim \cos\phi$, see Figure 2) have been investigated in [2]. The drag formula, Eq. (2), has been extended to

$$c_D = \frac{8\pi}{c_M\sqrt{Re}} + \frac{2\pi^2}{Re} \qquad (6)$$

It is worth mentioning, that the second-order term is independent of c_M.

Figure 6 shows the second-order effects on the drag of the Joukowsky airfoil ($v_w \sim dU/dx$, see Figure 4) at Reynolds number $Re = U_\infty c/\nu = 10^4$ (c = chord length of airfoil). The blowing rate $c_{Q\,Blow}$ is larger than the suction rate $c_{Q\,Suc}$, therefore thrust due to blowing occurs, $c_D = -1.78\, c_{Q\,Blow}$. As in the example of the circular cylinder an additional friction drag due to second-order effects (displacement effects) exists, which reaches a finite value of $c_D \approx 0.0052$ (independent of $c_{Q\,Blow}$) for infinitely large blowing rates. Contrary to the circular-cylinder example where second-order effects on drag were only friction drag, here also a pressure drag (curve IIb) exists, which unfortunately has the same order of magnitude as the friction-drag reduction due to blowing.

3. TURBULENT FLOW

3.1. Experiments of the Flow Field Near Stagnation Point

So far, laminar flow was assumed. But in the area where blowing is applied, turbulent flow has to be expected, because blowing has a strong destabilizing effect on the boundary layer. Therefore, detailed measurements of the flow characteristics (mean velocities, turbulence intensities, turbulent shear stresses) within the boundary layer with blowing have been undertaken by using Laser-Doppler anemometry, [4]. The experiments have been carried out at the stagnation point area of a porous circular cylinder (see Figure 2) with extremely large blowing rates (up to $v_w/U_\infty = 0.18$) which have not yet been reported in the literature.

Figures 7 and 8 show the mean velocities and the turbulent shear stresses at different positions over the front part of the circular cylinder. Turbulent boundary layers along impermeable walls have usually a two-layer structure with the "wall" layer and the "defect" layer, where the friction velocity $u_\tau = \sqrt{\tau_w/\rho}$ is the characteristic velocity.

Turbulent boundary layers with strong blowing still have the two-layer structure, but with a few important differences.
Firstly, the basic characteristic velocity is

$$u_{\tau\,max} = \sqrt{\frac{\tau_{max}}{\rho}} \qquad (7)$$

i.e. based on the maximum shear stress τ_{max} within the boundary layer (see Figure 8) rather than based on the wall stress τ_w.
Secondly, the boundary layer thickness is growing with the blowing velocity, but the defect layer is growing relatively faster than the wall layer, in other words, the defect layer plays an increasing role compared to the wall layer when the blowing rate is increasing.

As a consequence, all velocity distributions shown in Figure 7, will approximately collapse into one universal curve (except close to the wall) if represented as defect laws according to

$$\frac{U - u}{u_{\tau\,max}} = g\left(\frac{y}{\delta}\right) \quad , \qquad (8)$$

see for details [4]. This law can be interpreted as an extension of the law of the wake by McQuaid [5]. The function $g(y/\delta)$ is identical with the one found by McQuaid for blowing rates up to $v_w/U = 0.008$. It should be mentioned that McQuaid used a characterstic velocity different from $u_{\tau\,max}$. In [4] however it is shown by asymptotic arguments why $u_{\tau\,max}$ is the proper velocity scale.

In Figure 9 the experimental results are shown as defect laws according to Eq. (8) and compared with McQuaid's defect law. Particularly the results for $\phi = 30^\circ$ show that the defect law covers most of the boundary layer for cases of strong blowing.

3.2. Prediction of Turbulent Boundary Layers with Strong Blowing.

Turbulent boundary layers with strong blowing are very well represented by the defect layer governed by Eq. (8) . This result was used as a basis for a simple prediction method of such boundary layers. The following equations have been applied:

a) Momentum integral equation for the defect layer (neglecting the small wall shear stress):

$$\delta_1 \, U \, \frac{dU}{dx} + \frac{d}{dx} \, (\delta_2 \, U^2) = v_w \, U \, . \tag{9}$$

b) Velocity distribution according to defect law of Eq. (8):

$$\frac{u}{U} = 1 - \frac{u_{\tau \, max}}{U} \, g(\frac{y}{\delta}) \, . \tag{10}$$

This leads to

$$\frac{\delta_1}{\delta} = f_1(\frac{u_{\tau \, max}}{U}) \quad , \qquad \frac{\delta_2}{\delta} = f_2(\frac{u_{\tau \, max}}{U}) \, . \tag{11}$$

There are two unknowns $\delta(x)$ and $u_{\tau \, max}(x)$ for given $U(x)$ and $v_w(x)$. In addition to Eq. (9) an entrainment relationship has been used:

$$\frac{dQ}{dx} = \frac{d}{dx} \, [U \, (\delta - \delta_1)] = v_E + v_w \tag{12}$$

where

$$\frac{v_E}{u_{\tau \, max}} = c_E \approx 0.08 \quad , \tag{13}$$

a value typical of entrainments of wakes.
The Eqs. (9) to (13) are a complete set to predict $\delta(x)$ and $u_{\tau max}(x)$ for given $U(x)$ and $v_w(x)$. Figure 10 shows the results of such a prediction and the comparison with the experiments described in Chapter 3.1. The wall shear stress depicted in Figure 10c has been determined from $u_{\tau \, max}(x)$ by a simple estimation given in [4].

The prediction method presented here can be used for a good estimation of the behaviour of turbulent boundary layers with very strong blowing.

4. EXPERIMENTS ON DRAG REDUCTION OF A CIRCULAR CYLINDER

The combination of boundary layer control by blowing and suction has been applied to a circular cylinder in incompressible flow. In Figure 11 a typical arrangement is shown. The front quarter of the cylinder periphery was used for blowing, whereas the rest of the periphery was used for suction. The suction velocity was one third of the blowing velocity to make sure that the net volume rate was equal to zero. Typical results for the pressure distributions at $Re = 9 \cdot 10^4$ are shown in Figure 12. Due to boundary-layer control the pressure drag could be reduced considerably from $c_D = 1.04$ without control down to $c_D = 0.52$ for $v_{w \, suc} / U_\infty = 0.03$. From the comparison with the pressure distribution of potential theory it can be concluded that even better results might be possible by further refinement of the combined boundary layer control system.

5. REFERENCES

[1]: J. D. Cole, J. Aroesty: The blowhard problem - Inviscid flow with surface injection. Int. J. Heat Mass Transfer Vol. II, 1968, 1167-1183.

[2]: K. Gersten: Second-order boundary-layer effects for large injection or suction. In: U. Müller, K.G. Roesner, B. Schmidt (Editors), Recent Developments in Theoretical and Experimental Fluid Mechanics. Springer, Berlin 1979, pp. 446-456.

[3]: K. Gersten, J. Wiedemann: Widerstandsverminderung umströmter Körper durch kombiniertes Ausblasen und Absaugen an der Wand. Forschungsbericht Nr. 3103 des Landes Nordrhein-Westfalen, Westdeutscher Verlag, Opladen 1982.

[4]: J. Wiedemann: Der Einfluß von Ausblasen und Absaugen an durchlässigen Wänden auf Strömungen bei großen Reynoldszahlen, Doctoral Thesis, University of Bochum, 1983.

[5]: J. McQuaid: A velocity defect relationship for the outer part of equilibrium and near-equilibrium turbulent boundary layers, ARC CP No. 885, 1965.

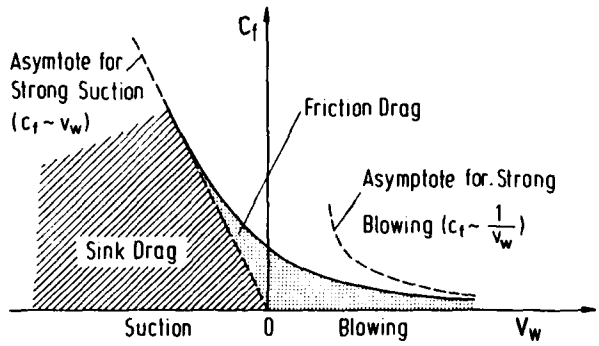
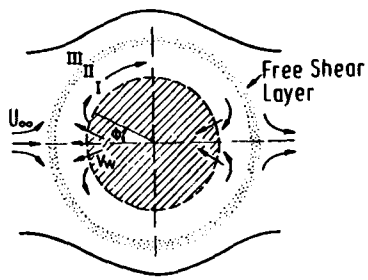


Figure 1: Skin Friction near the Stagnation Point in Two-dimensional Incompressible Flow

Figure 2: Flow past a Circular Cylinder
Blowing in the Front Part
Suction in the Rearward Part



Three Layer Flow
I : Inviscid Outer Flow (Potential Flow)
II : Free Shear Layer
III: Inviscid Inner Layer with Vorticity

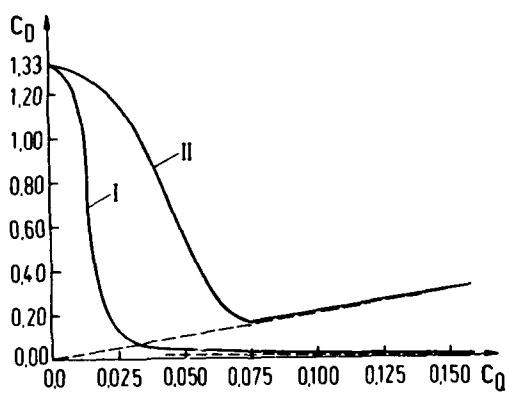


Figure 3: Drag Reduction of a Circular Cylinder by Two Different Boundary-Layer Control Systems.
$Re = 4 \cdot 10^4$

I : Combined Blowing and Suction $v_W \sim \cos \phi$,
c_Q : Volume Rate Coefficient of Recirculating Flow. Asymptote: $c_D = 6.25 \cdot 10^{-4}/c_Q$

II: Homogeneous Suction, v_W = const.
c_Q : Suction Coefficient
Asymptote: $c_D = 2 \cdot c_Q$ (Sink Drag)

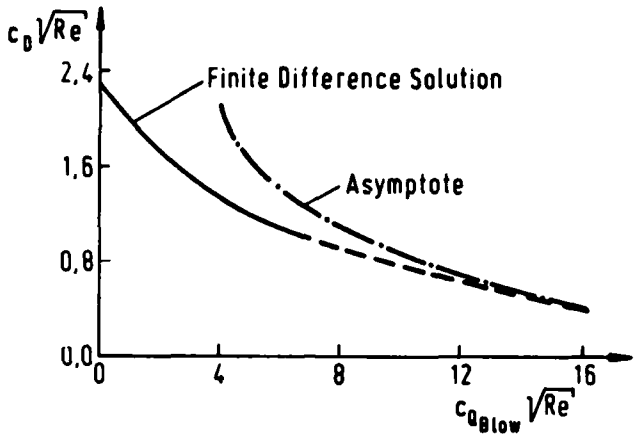


Figure 4: Friction Drag of a Symmetrical Joukowsky Airfoil (4,4 % Relative Thickness) as Function of the Blowing Rate. $v_W \sim dU/dx$, $Q_{Blow} = 9.1\ Q_{Suc}$
Asymptote: $c_D\sqrt{Re} = 8.8/c_{Q\,Blow}\sqrt{Re}$

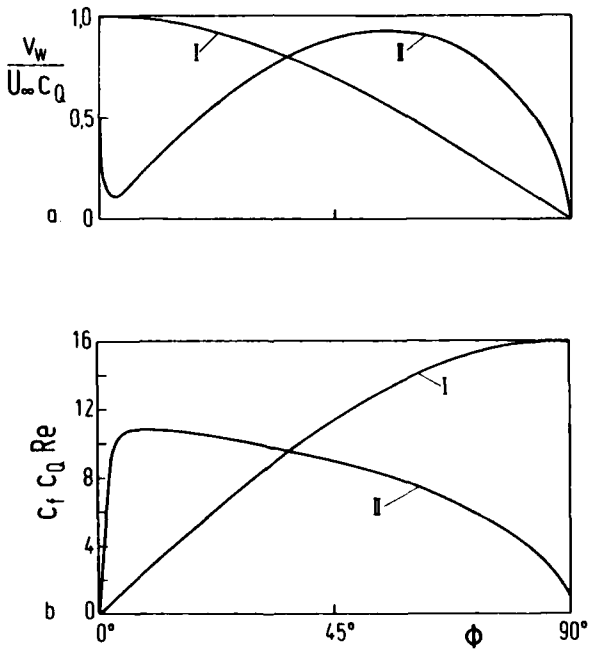


Figure 5: Effect of Distribution of Blowing-Suction Velocity on Drag Reduction. Circular Cylinder in Laminar Flow for the Limit of Strong Blowing and Suction.
a. Blowing-Suction Velocity Distribution
(The same blowing rate for both curves)
b. Shear Stress Distribution

I : $v_W \sim \cos\phi$, $c_D \cdot c_Q \cdot Re = 25$

II: Optimal v_W-Distribution, $c_D \cdot c_Q \cdot Re = 14$

c_Q : Volume Rate of Recirculating Flow

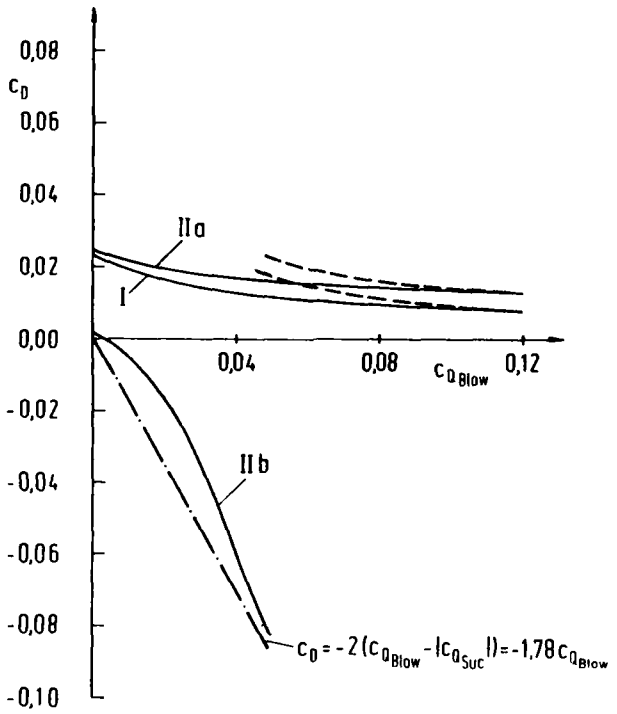


Figure 6: Drag Reduction of Joukowsky Airfoil by Combined Blowing and Suction.

I : Prandtl's (first order) Boundary-Layer Theory.
Asymptote for Friction Drag: $c_D = 9.1 \cdot 10^{-4} / c_{Q\,Blow}$
$c_{Q\,Blow}$: Blowing Rate Coefficient = 9.1 $c_{Q\,Suc}$

II: Second Order Boundary-Layer Theory.
IIa: Friction Drag
IIb: Pressure Drag
----- Thrust due to Blowing, $c_D = -1.78\ c_{Q\,Blow}$

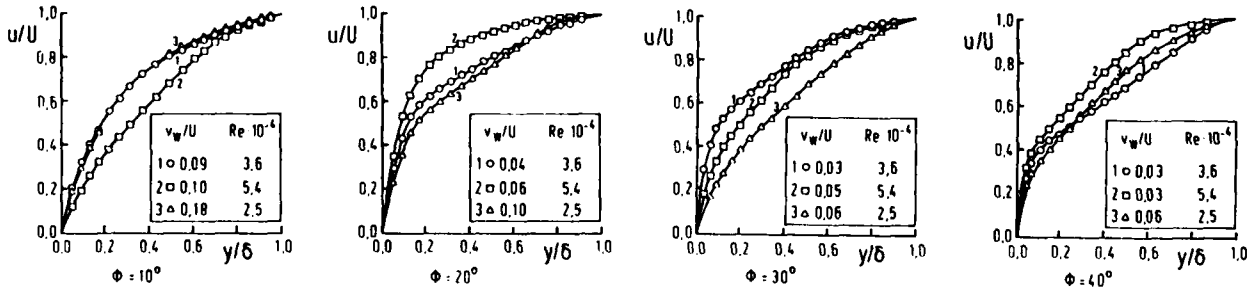


Figure 7: Mean Velocities in the Boundary Layer in the Stagnation Region of a Circular Cylinder with Strong Blowing (LDA Measurements) Re = $U_\infty d/\nu$, U = U(x) : Local Outer Flow Velocity.

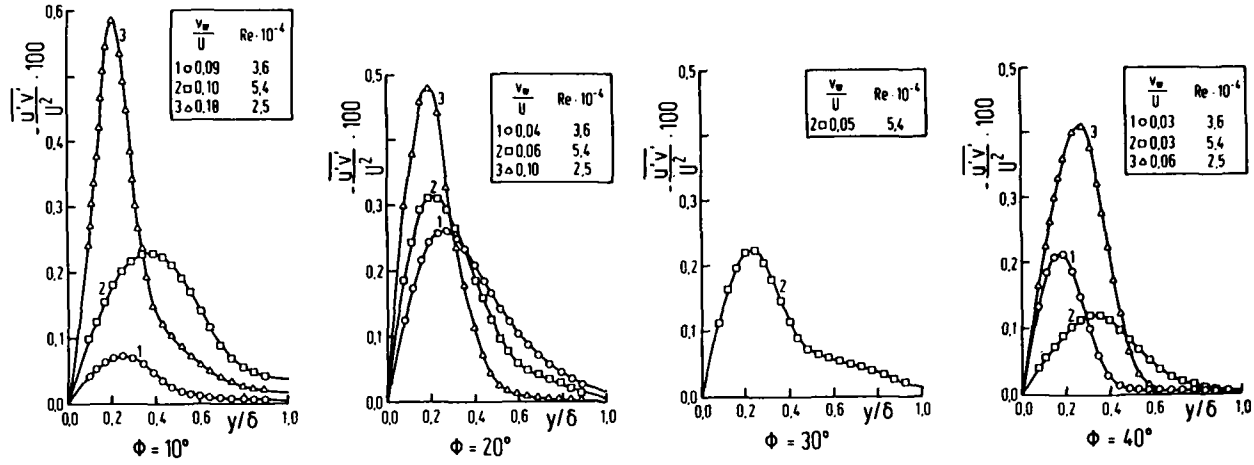


Figure 8: Turbulent Shear Stresses in the Boundary Layer with Strong Blowing, See Figure 7.

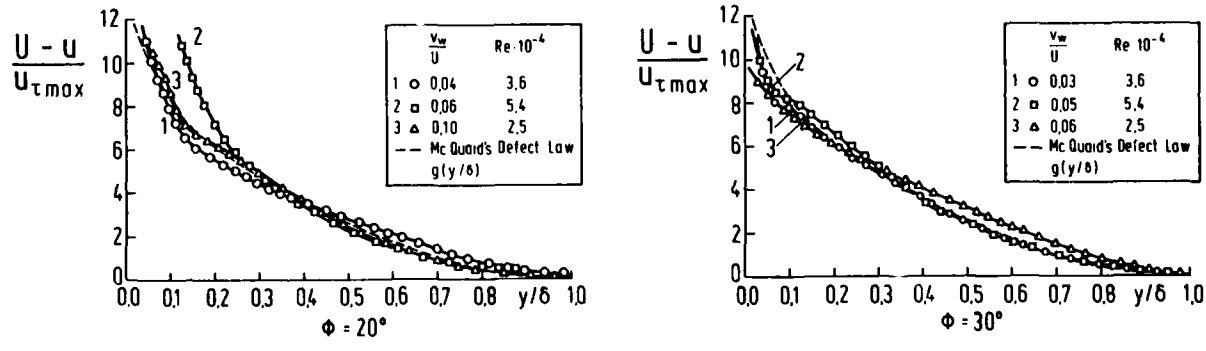
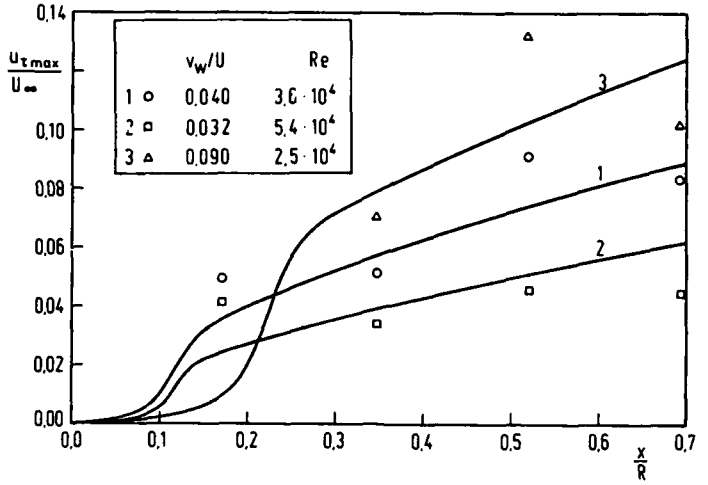
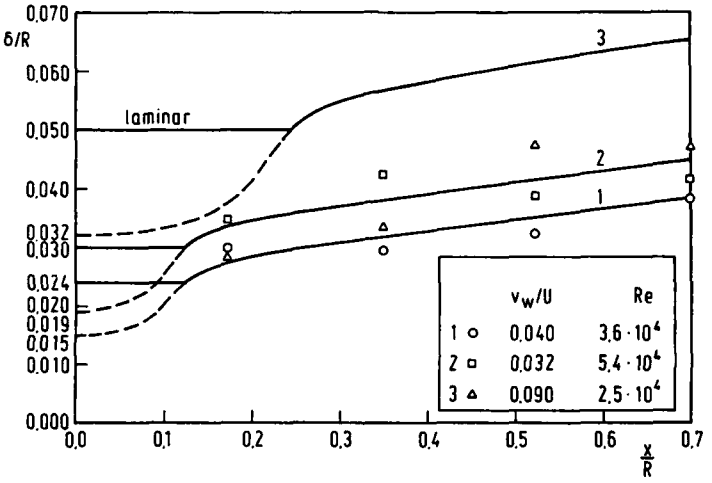


Figure 9: Defect Law in the Boundary Layer with Strong Blowing. See Figures 7 and 8.

a



b



c

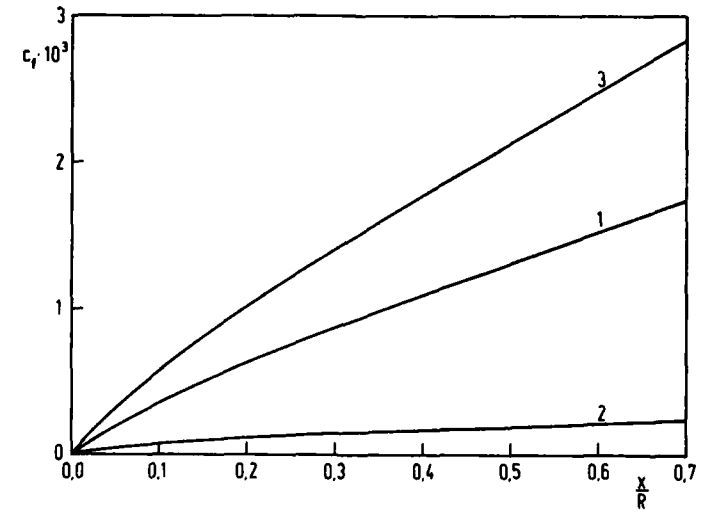


Figure 10: Prediction of Maximum Shear Stress $u_{\tau\,max}$, Boundary Layer Thickness δ, and Skin Friction Coefficient c_f in the Boundary Layer in the Stagnation Region. Comparison of Theory and Experiment.

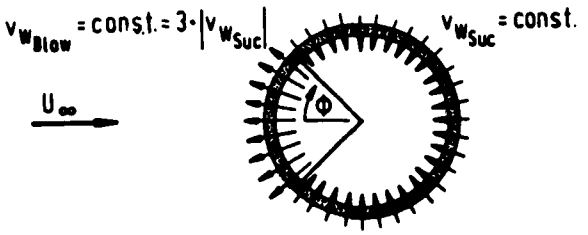


Figure 11: System of Combined Blowing and Suction Applied to a Circular Cylinder, $Q_{Blow} = Q_{Suc}$ $v_{W\,Blow} = 3\ v_{W\,Suc}$

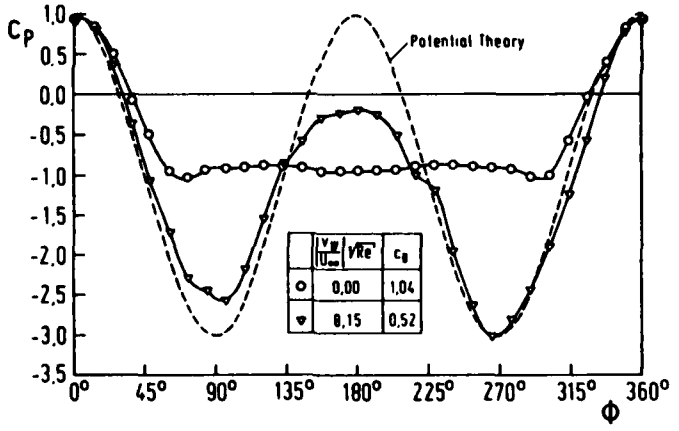


Figure 12: Pressure Distribution on a Circular Cylinder at Re $\cdot$ $9 \cdot 10^4$, $c_p = 2(p-p_\infty)/\rho\ U_\infty^2$.

o No Boundary Layer Control
Pressure Drag: $c_D = 1.04$

▽ Combined Blowing and Suction Boundary Layer Control According to Figure 11, $v_{w\,Suc}/U_\infty = 0.03$
Pressure Drag: $c_D = 0.52$

DESIGN STUDIES OF THICK LAMINAR-FLOW AIRFOILS FOR LOW SPEED FLIGHT EMPLOYING TURBULENT BOUNDARY LAYER SUCTION OVER THE REAR PART

J.L. van Ingen, J.J.H. Blom and J.H. Goei
Department of Aerospace Engineering, Delft University of Technology,
Kluyverweg 1, 2629 HS Delft, the Netherlands.

AD-P004 064

SUMMARY

First the paper briefly reviews some computational tools, used at the author's institute, to analyse and design airfoils for low speed flight (prediction of potential flow pressure distributions, laminar boundary layer flows, transition prediction using the e^n-method and Head's entrainment method for the calculation of turbulent boundary layers). These tools are used in this paper to design pressure distributions and corresponding airfoil shapes producing long runs of natural laminar flow. Inevitably this results in airfoils with the maximum thickness far backwards, eventually leading to separation of the turbulent boundary layer over the rear part of the airfoil. This turbulent boundary layer separation is prevented by selecting a proper pressure distribution over the rear part and/or suction of the turbulent boundary layer through slots or distributed perforations. Design charts are presented which help to select the required pressure distributions for laminar and turbulent flow.

SYMBOLS

The symbols used in this paper are the usual ones. Most of them have been defined in the text where they first occur. Some of them are explicitly mentioned below.

c airfoil chord
c_{d_w} (or $c_{d_{wake}}$) wake drag coefficient
c_{d_s} "suction" drag coefficient, section 7
$c_{d_{tot}}$ $c_{d_w} + c_{d_s}$, total drag coefficient
$c_f = \frac{\tau_o}{\frac{1}{2}\rho U^2}$ skin friction coefficient
c_{pp} suction pressure loss coefficient; Eq.(34)
$c_q = \frac{Q}{U_\infty c}$ suction flow coefficient; $c_q = \frac{\Delta R_\theta}{R_c}$ for a single slot
$"c_q" = \frac{\Delta R_\theta}{R_c}$ safety margin against separation for $\frac{\Delta R_\theta}{R_c} < 0$
$H = \frac{\delta^*}{\theta}$ shape factor
k height of roughness
m exponent in Eq.(7)
Q suction flow per unit span
$R_c = \frac{U_\infty c}{\nu}$
$R_\theta = \frac{U\theta}{\nu}$
$R_{\theta_{lam}}$ R_θ at end of laminar region
$R_{\theta_{turb}}$ permissible value of R_θ at beginning of limiting pressure recovery region
ΔR_θ $R_{\theta_{lam}} - R_{\theta_{turb}}$
U velocity at edge of boundary layer
U_∞ free stream speed
v_o normal velocity at wall, negative for suction
x for boundary-layer calculations: coordinate along surface; otherwise distance along chord
α angle of attack w.r.t. zero lift
α_c angle of attack w.r.t. chord
β Hartree form parameter (Eq.(8))
γ angle between bi-sector of trailing edge angle δ and chord
δ trailing-edge angle
θ momentum loss thickness, Eq.(14)
$\bar{\theta}$ non-dimensional θ for Hartree flows
τ_o wall shear stress

Subscripts
tr : transition
TE : at trailing-edge
w : wake
s : suction

Abbreviations
NLF : natural laminar flow
b.l.c. : boundary layer control

1. INTRODUCTION

Throughout the history of airfoil design, many attempts have been made to reduce skin-friction drag through laminarisation of the boundary layer. As a first example the well-known NACA 6-series airfoils may be mentioned, where through placing the maximum thickness of the airfoil far backwards, long runs of laminar flow were obtained. Although this scheme proved to be fully feasible, the practical construction materials and -methods at that time were not yet sufficiently advanced, that it could be used in commercial applications. Reference [1] provides an account of the development of these airfoils. It should be noted that they have been used extensively with turbulent flow because of other advantages (low critical Mach-number for instance).

The ultimate application of this principle has led to the design of very thick airfoils where, through proper shaping and the addition of a suction slot, the flow was designed to remain laminar all the way back to the trailing-edge. As an example the well-known Griffith airfoils may be mentioned [2, 3, 4]. Although, due to the appearance of Taylor-Görtler vortices over the concave downstream part, full-chord laminar flow was not established, these airfoils showed a great promise if only the surface could be produced and maintained in a smooth condition. The very low critical Mach-number has ended the development of these airfoils.

Laminarisation by suction through porous surfaces or narrow slots can be used on thin airfoils with high critical Mach-numbers. Extensive studies of this scheme have been made in the fifties and early sixties; for a review see the book edited by Lachmann [4]. Also at the author's institute work was done in this field; it was shown for instance that the e^n-method for transition prediction is also valid in the case of distributed suction [5]. Structural and weight problems, the still not completely solved problem of maintaining smooth surfaces and the still comparatively low fuel prices have put an end to these earlier attempts of laminarisation by suction.

In the mean time the supercritical airfoil has been developed for efficient cruising flight at transonic Mach numbers. It should be noted that often the usable maximum thickness of these airfoils is limited through unfavourable shock-wave boundary-layer interaction in off-design situations.

In the past decades, airfoil shaping to obtain extensive regions of laminar flow has been applied with great success to sailplanes. Well-known are the investigations by Wortmann and Eppler. Also at the authors institute work on the analysis and design of low speed airfoils has been performed. Applications have been

made to sailplanes and modern windturbines [8, 9, 10, 11] .
Due to the explosive increase of fuel prices in the last decade, laminarisation through active laminar flow control by suction has gained a new interest. The next paper in this Symposium will discuss the NASA-program on laminar boundary layer control. Recently it has been realised that not only for sailplanes but also for general aviation aircraft laminarisation through shaping ("natural laminar flow , NLF") is worth while. It has been found that, due to modern construction methods and -materials, the achievement of NLF is not such an utopistic idea as has been thought for a long time. Recent NASA studies have revealed extensive regions of laminar flow on certain aircraft, even in propellor slipstreams [12 and 13]. A recent article in Aviation Week [14] entitled "Laminar flow tests pass expectations" gives a summary of these findings.
Another ecouraging example may be quoted from experiences at the authors institute. In a study of the possible application of modern airfoil designs to windturbine rotors, it was decided to do a full scale transition test on the blades of the 25 meter diameter rotor of the windturbine at Petten in the Netherlands. The blades, having the classical NACA 230 series section; are covered with the same anti-erosion paint as was used on earlier versions of the Fokker F-28 aircraft. The turbine is located near the North Sea coast, 50 km north of Amsterdam. It was found that, after two years of operation and without prior cleaning, the flow remained laminar as far back as is compatible with the airfoil pressure distribution at the chord Reynolds number of the investigation [15].
The above mentioned observations gave the authors a new interest in laminar flow. It is their strong belief that the first practical results will be obtained through NLF which does not require a delicate suction surface. To obtain an extensive region of laminar flow at high chord Reynolds numbers through favourable pressure gradients, the resulting airfoils will have a relatively great maximum thickness, located far downstream. Therefore limitations of the degree of laminarisation may be due to different factors. On the one hand the critical Mach number will be lowered; on the other hand the danger for separation of the turbulent boundary layer over the rear part of the airfoil may increase. It is suggested in the present paper that laminarisation through shaping should be combined with passive and/or active control of the turbulent boundary layer. In the first place of course the airfoil shape should be designed such that the behaviour of the turbulent layer is improved. Moreover, vortex generators or suction and blowing may be considered.
For general-aviation or short-haul aircraft with their relatively low cruise Mach numbers the maximum wing thickness might thus be increased leading to a lower construction weight and/or a larger aspect ratio. Maximum thickness would of course be limited eventually by reaching critical flow conditions. But even then, and this also holds for aircraft already employing supercritical airfoils, turbulent boundary layer control might be used to increase the usable maximum thickness by suppressing unfavourable shock-wave boundary layer interactions. It should be noted that this design-tool could be used even without the achievement of laminar flow over the forward part of the airfoil.
In the present paper we will limit the discussions to the low cruise Mach number applications such as for general aviation and short-haul aircraft. The analysis will be for incompressible flow; if necessary the relation between the pressure distribution and the critical Mach number can be determined using the von Kármán-Tsien rule. It will be assumed that turbulent boundary-layer control is by suction, because this is relatively easy to calculate. The purpose of the paper however, is to point out the potential improvement in airfoil design through the combination of NLF and turbulent boundary layer control. The best practical way of achieving turbulent b.l.c. should be determined later on through specific design studies.

2. THE DELFT AIRFOIL ANALYSIS AND DESIGN PROGRAM

Since a number of years work is in progress at the Low Speed Laboratory (LSL) of the Department of Aerospace Engineering of the Delft University of Technology on the development of a computer program for the analysis and design of low speed airfoils. A description of this program may be found in [8, 9, 16, 17] ; some early applications of the program up till 1980 can be found in these references. Some later applications are described in [10,11].
In the present section we will point out only those features of the program which are explicitly needed for the discussions in the remainder of the present paper.
For single-element airfoils use is made of the conformal transformation of a circle into the airfoil as described by Timman [18]. The airfoil with chord c is in the z-plane, the circle with radius R is in the ζ-plane (fig. 1); the transformation is chosen in such a way that the point $\theta_c = 0$ on the circle is transformed into the sharp trailing-edge ($z = 0$). Hence the Kutta-Joukowski condition requires that the point $\theta_c = 0$ is a stagnation point. Then the lift coefficient of the airfoil is given by

$$c_l = 8\pi \frac{R}{c} \sin \alpha \qquad (1)$$

where α is the angle of attack w.r.t. the zero lift direction. For thin airfoils R/c is about 1/4, leading to the familiar value 2π for the lift curve slope. Due to viscous effects the actual lift coefficient will be less than follows from Eq.(1). In the program this is simulated by letting the rear stagnation point on the circle move upwards to $\theta_c = \theta_{st}$; then Eq.(1) has to be modified into

$$c_l = 8\pi \frac{R}{c} \sin (\alpha - \theta_{st}) \qquad (2)$$

The value of θ_{st} follows from the empirical relation:

$$\theta_{st} = 5.0 \tan(\delta) \, (\alpha_c + \gamma) \sqrt{c_{d_w}} \qquad (3)$$

In Eq.(3) δ denotes the trailing-edge angle; α_c is the angle of attack with respect to the chord and γ is the slope of the trailing-edge bisector w.r.t. the chord. It has been found that this empirical correction gives good results for airfoils resembling the NACA 4- and 5-digit series; for airfoils where the trailing-edge is more or less cusped an "effective"value for δ has to be used. We will come back to this problem in section 9.3 when discussing a specific example.
It is easy to invert the conformal transformation method such that airfoils with improved pressure distributions are obtained; examples may be found in the references mentioned above.
The laminar boundary layer is calculated by a method which is a combination of Thwaites' method for the

determination of the momentum loss thickness θ and Stratford's method for the prediction of the laminar separation point. In addition we will use in the present paper a simplified analysis, based on the Hartree similar boundary layers. This will be discussed separately in section 4. Special attention is given in the program to laminar separation bubbles. It has been found that the program predicts the drag coefficient too low when laminar separation bubbles occur. We will neglect this effect in the present paper because it is easy to avoid the bubbles by tripping the boundary layer. Paper no. 20 at this Symposium [21] will discuss this in some detail.
For transition prediction the e^n-method is used, where n is a function of the "effective" free stream turbulence level. This will be discussed in some more detail in section 3.
The turbulent boundary layer is calculated using Head's entrainment method; see section 6.
Finally the wake drag coefficient is determined from the Squire-Young formula

$$c_{d_w} = 2 \frac{\theta_{TE}}{c} \left(\frac{U_{TE}}{U_\infty}\right)^{\frac{H_{TE}+5}{2}} \tag{4}$$

In addition to these standard tools we will need in the present paper computational methods for turbulent boundary layer control; these will be discussed in subsequent sections.

3. TRANSITION PREDICTION

In the Delft airfoil program the e^n-method is used for transition prediction. The exponent n is determined from the "effective" free stream turbulence level Tu (in %) according to

$$n = 3.565 - 6.18\,^{10}\log Tu \tag{5}$$

The choice of Tu depends on the flow quality of the windtunnel; it has been found that good predictions are obtained if Tu is chosen according to the following table

Facility	Tu (%)	n
NACA LTT and similar tunnels	0.10	9.75
Advanced low turbulence tunnels such as at LSL	0.06	11.2
Free flight of gliders	0.014	15.0

In the present paper we will sometimes simplify the laminar boundary layer calculation by approximating the pressure distribution over the forward part of the airfoil by one of the similar flows (see section 4). In this case the transition prediction can also be simplified, because the stability diagram from which the amplification of unstable disturbances has to be calculated, is independent of the streamwise coordinate x. Then a short-cut method due to Wazzan et al [22] can be used. Here the value of $\frac{Ux}{\nu}$ at transition is correlated with the value of the shape factor H by the following formula*) (valid for $2.1 < H < 2.8$):

$$^{10}\log \left(\frac{Ux}{\nu}\right)_{transition} = -40.4557 + 64.8066\,H - 26.7538\,H^2 + 3.3819\,H^3 \tag{6}$$

Wazzan et al claim that Eq.(6) corresponds to an amplification factor $n = 9$; comparing its result for the flat plate boundary layer ($H = 2.5911$) to the results of the Delft program, suggests that in the latter $n = 11$ would be more appropriate. In practice the difference between the results for $n = 9$ and $n = 11$ is not so large that we have to bother about this point.

4. THE HARTREE BOUNDARY LAYERS

Similar solutions of the laminar boundary layer equations are obtained for

$$U = u_1\, x^m \tag{7}$$

where u_1 and m are constants. This flow occurs near the vertex of a wedge with angle $\pi\beta$ where m and β are related by

$$\beta = \frac{2m}{m+1} \quad ; \quad m = \frac{\beta}{2-\beta} \tag{8}$$

Introducing a non-dimensional wall distance η and streamfunction ψ by

$$\eta = y \sqrt{\frac{(m+1)}{2} \frac{U}{\nu x}} \tag{9}$$

$$\psi = \sqrt{\frac{2\nu u_1}{m+1} x^{m+1}}\, f(\eta) \tag{10}$$

the boundary layer equation is reduced to the well-known Falkner-Skan equation

$$f''' + ff'' + \beta(1-f'^2) = 0 \tag{11}$$

where primes denote differentiation w.r.t. η. Boundary conditions for Eq.(11) are

---

*) Note that [22] contains an obvious misprint in the coefficient of H in Eq.(6) as is shown by other references of these authors.

$$\left.\begin{array}{lll} \eta = 0 & f = 0 & f' = 0 \\ \eta = \infty & & f' \to 1 \end{array}\right\} \tag{12}$$

The velocity profile follows from Eq.(11) with

$$\frac{u}{U} = f'(\eta) \tag{13}$$

Since the boundary conditions (12) are given at two ends of an interval a shooting method is often used starting with a trial value for $f''(0)$. In the present paper we can determine the required velocity profiles from Eq.(11) without iteration because the required values of $f''(0)$ can be taken from literature; we use [23].
Some further relations for the Hartree flows which will be used in the present work are:

$$\begin{aligned} \theta &= \int_0^\infty \frac{u}{U}\left(1 - \frac{u}{U}\right) dy \qquad R_\theta = \frac{U\theta}{\nu} = \theta\sqrt{\frac{2}{m+1}}\sqrt{\frac{Ux}{\nu}} \qquad R_x = \frac{Ux}{\nu} \\ \Theta &= \int_0^\infty \frac{u}{U}\left(1 - \frac{u}{U}\right) d\eta \qquad E = \frac{2}{m+1}\Theta^2 \qquad\qquad R_\theta = \sqrt{E\, R_x} \end{aligned} \tag{14}$$

Table I contains some results from the solutions of Eq.(11) taken from [23] which will be needed in the present paper. Also the values of $\left(\frac{Ux}{\nu}\right)_{tr}$ according to Eq.(6) are included. To facilitate interpolation in the table, it contains the values of $\{f''(0)\}^2$ instead of $f''(0)$; we used a quadratic interpolation.

5. PERMISSIBLE ROUGHNESS IN THE LAMINAR FLOW REGION

For the Hartree constant $-\beta$ flows it is rather easy to obtain the permissible roughness height as a function of x, as soon as a criterion for transition due to roughness has been assumed. The shape of the velocity profile is independent of x, only the thickness is different. Hence, when stepping through the boundary layer profile from the wall outwards during the numerical solution of Eq.(11), at each value of η there is a corresponding value for x at which the criterion for transition due to roughness is met. In all examples to be discussed in this paper we used the criterion that transition occurs as soon as $\frac{uk}{\nu}$ exceeds 600, where k is the roughness height. In the general version of the program where no similar flow is assumed this calculation is performed for the actual velocity profile at regular intervals in x-direction.

6. HEAD's ENTRAINMENT METHOD

In the entrainment method the momentum integral relation

$$\frac{d\theta}{dx} + (2+H)\frac{\theta}{U}\frac{dU}{dx} = \frac{1}{2}c_f \tag{15}$$

is used in combination with a skin-friction formula and the "entrainment" equation:

$$\frac{1}{U}\frac{d}{dx}\left[U(\delta-\delta^*)\right] = F(H_1) \tag{16}$$

where

$$\begin{aligned} H_1 &= \frac{\delta-\delta^*}{\theta} & H &= 0.7 + \left(\frac{1.535}{H_1-3.3}\right)^{0.3683} \\ H_1 &= 1.535\,(H-0.7)^{-2.715} + 3.3 & F(H_1) &= 0.0306(H_1-3)^{-0.653} \end{aligned} \tag{17}$$

The starting value for θ is taken equal to the value obtained at the end of the laminar flow region. A difficult point in this type of method is always the specification of the starting value of H. In order to avoid numerical difficulties, in cases where the turbulent boundary layer starts right at the beginning of a region with a steep pressure rise, the starting value of H was always determined sucht that equations (15) through (18) resulted in $\frac{dH}{dx} = 0$ at the start. It should be understood that this is a rather arbitrary choice, which however is thought to be acceptable for the design studies reported in this paper.
The skin-friction formula which is used in the present paper is the one due to Felsch [24]:

$$c_f = \frac{0.058(0.93 - 1.95^{10}\log H)^{1.705}}{\left(\frac{U\theta}{\nu}\right)^{0.268}} \tag{18}$$

The value of c_f resulting from this formula is only a little different from the well-known Ludwieg-Tillman result:

$$c_f = \frac{0.246\ 10^{-0.678\,H}}{\left(\frac{U\theta}{\nu}\right)^{0.268}} \tag{19}$$

An advantage of Eq.(18) over Eq.(19) is that the former predicts zero skin-friction at a finite value of H, namely H = 2.9986.
A solution of Eqs.(15) through (18) which is very useful in airfoil design, is that one for which the skin-

friction is everywhere zero. For this case H is constant and equal to 2.9986 or say 3. Then from (7) we find that $H_1 = 3.4602$ and $F(H_1) = 0.05081$. Eq.(15) can then be integrated between x_1 and x, resulting in:

$$\theta\, U^{2+H} = \text{constant} = \theta_1 U_1^{2+H} \tag{20}$$

The entrainment equation (16) then gives

$$\left(\frac{U_1}{U}\right)^{2+H} = 1 + \frac{F(H_1)(2+H)}{H_1(1+H)}\,\frac{x-x_1}{\theta_1} \tag{21}$$

or with the given values of H, H_1 and $F(H_1)$:

$$\left(\frac{U_1}{U}\right)^{5} = 1 + .01835\,\frac{x-x_1}{\theta_1} \tag{22}$$

For a first example we assume a turbulent flat plate boundary layer from $x = 0$ to $x = x_1$ with constant velocity U_1, the momentum loss thickness θ_1 at x_1 follows from:

$$\frac{\theta_1}{x_1} = .036\left(\frac{U_1 x_1}{\nu}\right)^{-1/5} \tag{23}$$

Using this result we can write Eq.(22) as:

$$\left(\frac{U_1}{U}\right)^{5} = 1 + .5097\,\frac{x-x_1}{x_1}\left(\frac{U_1 x_1}{\nu}\right)^{1/5} \tag{24}$$

This equation describes the maximum adverse pressure gradient which a turbulent boundary layer can negotiate downstream of an initial flat plate without separation. In fig. 2 this result is compared to the well-known Stratford distribution. It follows that Head's result is somewhat conservative as compared to Stratford's. For applications to airfoil design, we non-dimensionalise Eq.(22) with the chord length c and the free stream velocity U_∞, resulting in:

$$\left(\frac{\bar{U}_1}{\bar{U}}\right)^{5} = 1 + 0.01835\,\frac{(\bar{x}-\bar{x}_1)R_c\bar{U}_1}{R_{\theta_1}} \tag{25}$$

At the trailing-edge ($\bar{x} = 1$) we get:

$$\left(\frac{\bar{U}_1}{\bar{U}_{TE}}\right)^{5} = 1 + .01835\,\frac{(1-\bar{x}_1)R_c\bar{U}_1}{R_{\theta_1}} \tag{26}$$

If, in the design case, R_c, $\bar{x}_1$, $\bar{U}_1$ and $\bar{U}_{TE}$ are given, Eq.(26) determines the permissible value of R_{θ_1} at the start of the pressure rise. Eq.(25) then, determines the critical pressure distribution, which for this R_{θ_1} just gives the border-case between separation and no-separation. If R_θ at the start of the pressure rise is higher then R_{θ_1}, local suction can be used to reduce R_θ to this critical value. For $R_\theta < R_{\theta_1}$, there is still some safety margin against separation.
From the Squire-Young relation Eq.(4), using H = 3, together with Eq.(20) in the form

$$\theta_1 U_1^{5} = \theta_{TE} U_{TE}^{5}$$

the wake drag coefficient follows from

$$c_{d_{wake}} = 2\,\frac{R_{\theta_1}}{R_c}\,\frac{\bar{U}_1^{4}}{\bar{U}_{TE}}$$

or with Eq.(26)

$$c_{d_{wake}} = \frac{.0367\,\bar{U}_{TE}^{4}\,(1-\bar{x}_1)}{1-\left(\frac{\bar{U}_{TE}}{\bar{U}_1}\right)^{5}} \tag{27}$$

Since, in general $\left(\frac{\bar{U}_{TE}}{\bar{U}_1}\right)^{5} \ll 1$, Eq.(27) shows that for the case where R_{θ_1} equals the critical value (suction may be needed to limit R_θ to this value), the wake drag coefficient becomes virtually independent of $\bar{U}_1$.

7. TURBULENT BOUNDARY LAYER CONTROL BY SUCTION

To calculate the effect of suction on a turbulent boundary layer we use the momentum integral equation Eq.(15) with an extra term representing the normal velocity at the wall v_o (note that v_o is negative for suction):

$$\frac{d\theta}{dx} + (2+H)\,\frac{\theta}{U}\,\frac{dU}{dx} - \frac{v_o}{U} = \frac{1}{2}\,c_f \tag{28}$$

First we will integrate this equation for a porous region which becomes vanishingly small in x-direction while $|v_o|$ may become large. This will provide a useful approximation for the case of suction through a narrow slot. Integrating Eq.(28) from x_o to $x_o + \Delta x$; assuming H, $\frac{\theta}{U}\frac{dU}{dx}$ and c_f to remain finite; letting $\Delta x \to 0$ and $-v_o \to \infty$ such that $-v_o\Delta x = Q$ = the suction flow per unit span, we find

$$Q = U(\theta_{x_o} - \theta_{x_o} + \Delta x) \tag{29}$$

Introducing the suction flow coefficient $c_q = \frac{Q}{U_\infty c}$ and the reduction in R_θ over the slot $\Delta R_\theta = \frac{U}{\nu}(\theta_{x_o} - \theta_{x_o} + \Delta x)$; it follows from (29) that

$$c_q = \frac{\Delta R_\theta}{R_c} \tag{30}$$

In what follows we will use slot suction to reduce R_θ to the permissible value at the beginning of the pressure rise according to Eq.(26).

An interesting method to design surfaces for distributed suction has been developed by Raspet [25, 26]. The method uses the momentum integral equation for suction Eq.(28). It is assumed that separation is prevented when $v_o(x)$ is chosen such that R_θ is maintained at a constant and not too large value. A difficult point in this respect is the specification of c_f in the case of suction. There are indications that c_f increases due to suction above the values following from the Felsch or Ludwieg-Tillman formula. This effect has been neglected however in practical applications of the method. It has been shown in numerous applications by Raspet and also at Delft University [27] that suction surfaces which have been designed according to this procedure, are satisfactory and even somewhat conservative. The wake drag may be somewhat underestimated by this method. It has been shown by Tennekes that an optimum (constant) value of R_θ over the suction surface maybe obtained by placing a suction slot at the beginning of the region with distributed suction [27]. When R_θ is kept constant by suction, it is also a reasonable approximation to take H and c_f constant. Then equation (28) can be rewritten as:

$$-\frac{v_o}{U_\infty} = \frac{1}{2} c_f \bar{U} - (H+1) \frac{R_\theta}{R_c} \frac{1}{\bar{U}} \frac{d\bar{U}}{d\bar{x}} \tag{31}$$

Integrating Eq.(31) from the beginning of the porous region (x_1) to the end (x_2) we find

$$c_q = \int_{\bar{x}_1}^{\bar{x}_2} \frac{-v_o}{U_\infty} d\bar{x} = \frac{1}{2} c_f \int_{\bar{x}_1}^{\bar{x}_2} \bar{U}\, d\bar{x} + \frac{(H+1)R_\theta}{R_c} \ln\left(\frac{\bar{U}_1}{\bar{U}_2}\right) \tag{32}$$

If there is a suction slot just upstream of x_1 we have to add the slot c_q, from Eq.(30) to Eq.(32). The momentum loss in the wake is strongly reduced by suction; the wake drag is still determined from the Squire-Young relation. However, we have now to take into account the power needed for the suction pump. It is customary to convert this suction power to the so-called "suction-drag" as follows. Assume that the sucked air is reenergised and expelled in stream direction with velocity U_∞ and free stream static pressure p_∞; then no "sink-drag" occurs. The suction power then follows from

$$P_s = \frac{Q(p_{t_\infty} - p_i)}{\eta_s} \tag{33}$$

where p_i is the pressure in the suction plenum chamber and η_s is the efficiency of the pump. Neglecting, in first approximation, the pressure drop through the suction surface, then $p_i = p_b$ where p_b is the lowest static pressure occurring at the suction surface; usually this will be at the beginning of the suction region. Expressing the total-pressure rise over the pump in a pump pressure coefficient c_{pp} according to

$$c_{pp} = \frac{p_{t_\infty} - p_b}{\frac{1}{2}\rho U_\infty^2} = 1 - c_{p_b} = \left(\frac{U_b}{U_\infty}\right)^2 \tag{34}$$

then the suction power per unit span is

$$P_s = \frac{c_{pp}\, c_q}{\eta_s} \frac{1}{2} U_\infty^3 c \tag{35}$$

The power needed to overcome the wake drag is (per unit span)

$$P_w = \frac{c_{d_w} \frac{1}{2} \rho U_\infty^3 c}{\eta_T} \tag{36}$$

where η_T is the efficiency of the propulsing unit.
The total power needed then becomes (per unit span)

$$P_s + P_w = \left(\frac{c_{pp}\, c_q}{\eta_s} + \frac{c_{d_w}}{\eta_T}\right) \frac{1}{2} \rho U_\infty^3 c \tag{37}$$

The total drag coefficient is then defined as

$$c_{d_{tot}} = \frac{\eta_T}{\eta_s} c_{pp}\, c_q + c_{d_w} \tag{38}$$

In what follows we will make the further assumption that $\eta_T = \eta_s$ so that

$$c_{d_{tot}} = c_{pp}\, c_q + c_{d_w}$$

The pressure loss coefficient c_{pp} as defined by (34) is an ideal case. For practical applications we may have to add further pressure losses such as through ducting. In some examples we will do this by increasing the ideal c_{pp} with 0.2. It should be understood that the present paper is only meant to survey the possibilities

of turbulent b.l.c. Extensive design studies will be needed to arrive at a practical realisation. To get an idea about the duct losses we make the following rough estimate of the duct velocity. Assume a twin-engined airplane with a suction pump in each nacelle; allowing the flow to enter from both sides. The two nacelles will not devide the span in equal parts. We will assume that a maximum of 1/3 of the total flow will enter a pump from one side. This amounts to

$$\frac{1}{3}\, c_q\, U_\infty\, c^2\, A \tag{39}$$

where A is the aspect ratio. Assuming an airfoil with maximum thickness t at 75% of the chord and assuming that the interior of the wing downstream of 75% chord is available for the duct, then the duct cross section is about $\frac{1}{8}$ t c (fig. 3). Together with Eq.(39) this leads to the following ratio of maximum duct velocity to flight speed:

$$\frac{V_{duct}}{U_\infty} = \frac{8A}{3}\,\frac{1}{t/c}\, c_q \tag{40}$$

Assuming A = 10 the following results for $\frac{V_{duct}}{U_\infty}$ are obtained

	V_{duct}/U_∞ for c_q =		
t/c	$c_q = 10^{-4}$	$c_q = 10^{-3}$	$c_q = 2.5\ 10^{-3}$
.2	0.013	0.13	0.33
.3	0.009	0.09	0.22

It will follows from examples discussed in the remaining part of the paper, that $c_q = 2.5\ 10^{-3}$ is high enough to obtain useful results. Thus the duct velocities may be expected to remain reasonably small.

8. A DESIGN CHART FOR CHOOSING PRESSURE DISTRIBUTIONS

Before embarking on the detailed design of a laminar flow airfoil, according to certain specifications, we obtain a first impression of the required pressure distribution from a design chart for the chord Reynolds number at which the airfoil has to operate.

In an $\bar{x}$, $\bar{U}$ plane we choose a point $\bar{x}_1$, $\bar{U}_1$ at which a laminar flow with constant β (section 4) has to change-over in a turbulent pressure recovery according to the limiting distribution discussed in section 6. For this the trailing-edge velocity $\bar{U}_{TE}$ has to be specified (fig. 4). The value of β follows from the requirement that $\frac{U_1 x_1}{\nu} = \frac{U_1}{U_\infty}\frac{x_1}{c}\frac{U_\infty c}{\nu} = \bar{U}_1 . \bar{x}_1 . R_c$ just equals the transition value according to Wazzan's short-cut method (Eq.(6) and table 1). For low values of R_c even a slightly adverse pressure gradient with negative β may result. At the same time we obtain from table 1 the corresponding values of f''(0) and Θ. This allows us to obtain the shape of the velocity profile with the corresponding critical roughness height and the value of R_θ at $\bar{x}_1$; this value will be denoted by $R_{\theta_{lam}}$. From Eqs. (25) through (27) in section 6 we can find the limiting pressure distribution between $\bar{x}_1$, $\bar{U}_1$ and $\bar{U}_{TE}$ together with the permissible value of R_θ at the start of the pressure rise ($R_{\theta_{turb}}$). The difference

$$\Delta R_\theta = R_{\theta_{lam}} - R_{\theta_{turb}} \tag{41}$$

indicates whether suction is needed. For $\Delta R_\theta > 0$ a suction coefficient

$$c_q = \frac{\Delta R_\theta}{R_c} \tag{42}$$

with a suction slot at $\bar{x}_1$ will reduce $R_{\theta_{lam}}$ to the permissible value $R_{\theta_{turb}}$. This eliminates turbulent separation. When ΔR_θ is negative it means that the combination of $R_{\theta_{lam}}$, $\bar{x}_1$, $\bar{U}_1$ and $\bar{U}_{TE}$ still has some safety margin against separation. The safety margin is conveniently expressed in a negative c_q as:

$$"c_q" = \frac{\Delta R_\theta}{R_c} \tag{43}$$

It should be noted that a negative c_q means that some blowing would be allowed before separation would occur. In our design chart we do not, of course, use up the safety margin for blowing. Instead, the actual development of the turbulent boundary layer, starting with $R_\theta = R_{\theta_{lam}}$ at $\bar{x}_1$, is calculated. In a final design, the safety margin may be used by the designer to satisfy other requirements, for instance the pressure distribution over the rear part may be altered to improve the stalling behaviour of the airfoil.

The design chart contains further information such as the wake drag coefficient c_{d_w}; suction drag c_{d_s}, normal force coefficient c_n and moment coefficient around the quarter chord point $c_{m_{0.25}}$. For $c_q > 0$ the value of c_{d_w} follows from Eq.(27); for "c_q" < 0 first we obtain θ_{TE} from Head's method and then c_{d_w} from Eq.(4).

In the ideal pressure loss coefficient Eq.(34), we now have to use $U_b = U_1$, resulting in the following suction drag coefficient $c_{d_s} = c_{pp}\, c_q$:

$$c_{d_s} = \bar{U}_1^{\,2}\,\frac{\Delta R_\theta}{R_c} \tag{44}$$

Since the design chart deals with the upper- or lower surface pressure distribution only, the values of c_d, c_n and $c_{m_{0.25}}$ are also for one side only. This means that an arbitrary zero-level for the surface pressure

is needed. In our charts we use free stream total pressure as a reference. This means that the c_d values for both surfaces have to be added while the c_n and $c_{m_{0.25}}$ values for the lower surface have to be subtracted from those for the upper surface.
The normal force coefficient for one surface then follows from

$$c_n = \int_0^1 \frac{(p_{t_\infty} - p)}{\frac{1}{2}\rho U_\infty^2} \, d\frac{x}{c} = \int_0^1 \bar{U}^2 d\bar{x} \tag{45}$$

Using Eqs.(7) and (25) for the laminar and turbulent part respectively, the resulting expressions for c_n are

$$c_{n_{lam}} = \frac{\bar{U}_l^2 \bar{x}_l}{2m+1} \tag{46}$$

$$c_{n_{turb}} = \frac{\bar{U}_l^2 (1-\bar{x}_l)}{0.6} \frac{\left[\left(\frac{\bar{U}_l}{\bar{U}_{TE}}\right)^3 - 1\right]}{\left[\left(\frac{\bar{U}_l}{\bar{U}_{TE}}\right)^5 - 1\right]} \tag{47}$$

$$c_{n_{tot}} = c_{n_{lam}} + c_{n_{turb}} \tag{48}$$

It should be remarked that boundary-layer calculations should be made taking the x-coordinate along the surface of the airfoil. Of course we do so in our complete airfoil analysis and design program. In the present design chart we approximate this coordinate by the distance x along the chord.

When computing a design chart all information on β, c_l, "c_q", c_{d_w}, c_{d_s}, c_n and $c_{m_{0.25}}$ is calculated on a number of grid points of an $\bar{x}_l$, $\bar{U}_l$ plane. The mesh-size and extent of the grid can be chosen arbitrarily. The results may be plotted in various ways. As an example fig. 5 shows the $c_q = 0$ limits for $\bar{U}_{TE} = .707$ ($c_{p_{TE}} = 0.5$) and various values of R_c. Included are the pressure distributions for some selected design points. The critical roughness height for these cases is shown in fig. 6. Fig. 7 shows some more details for $R_c = 9 \times 10^6$; here also some curves for constant non-zero c_q are shown. Fig. 8 shows c_{d_w} for constant values of $\bar{U}_l$ and c_q. Note that c_{d_w} increases rather rapidly when the $c_q = 0$ limit is approached from the left hand (e.q. no-suction-required) side. When suction is applied the wake drag is nearly independent of $\bar{U}_l$ (see section 6, Eq. (27)). It follows that some safety margin ($c_q < 0$) should be maintained if we want to achieve a low drag without suction. Of course, if we are willing to apply suction, this should be started already before reaching the $c_q = 0$ limit to obtain an optimum total drag. When designing airfoils for maximum lift without suction, it may be advisable to select a design point on the $c_q = 0$ curve. (The well-known Liebeck airfoils are in fact based on this concept.)
Values of c_n and $c_{m_{0.25}}$ are shown in fig. 9. It should be noted that all values in the charts are for one surface; hence they get their true meaning only when the designer combines an upper- and a lower surface pressure distribution to meet the design specifications. Similar remarks apply to the values of $c_n/c_{d_{tot}}$ which are also obtained in the calculation, but not plotted here. Very often it will not be difficult to choose a pressure distribution for the lower surface ensuring an extremely low cd for that surface at positive lift coefficient. In practice the required $c_{m_{0.25}}$ may dictate the conditions on the lower surface.

It is stressed again that the pressure distributions obtained from the design charts can only be regarded as guide lines for the designer. In the first place not all pressure distributions guarantee a suitable closed airfoil shape [8]; in the second place the designer will want to tune the airfoil for different angles of attack.
In the charts we assume suction through one slot only, placed at $\bar{x}_l$. In the detailed design it may be found that optimal results would require multiple-slot-suction or a combination of slot suction and distributed suction.

9. SOME APPLICATIONS

In this section we will review some NLF airfoil designs with and without suction. Some of the examples were designed without using the charts; in these cases an a posteriori comparison with the chart can be made.

9.1. Analysis of the NACA 6-series basic thickness forms

Fig. 10 shows the pressure distribution (we will $\bar{U}(\bar{x})$ also indicate by "pressure distribution") at $\alpha = 0$ for the NACA 664-021 basic thickness form. It is shown that the forward part can be approximated by a constant -β flow. The downstream part is essentially a straight line. From results, not shown here, the values for β for all 6-series basic thickness forms with thickness 12, 15, 18 and 21%, have been determined. Hence a good approximation for the laminar boundary layer can easily be obtained from the Hartree flows. The turbulent boundary layer over the downstream part was calculated using Head's method. The resulting drag coefficient for $R_c = 9 \times 10^6$ is compared in fig. 11 with the experimental results from [1]; it follows that a good approximation is obtained. It is known that lower drag coefficients may be obtained if $\bar{U}(\bar{x})$ over the downstream part is concave as in our design charts. An additional curve in fig. 11 shows the improvement resulting from applying the limiting pressure distribution. In all cases a safety margin ("c_q" < 0) was found. It should be noted that the influence of the airfoil thickness is negligible in this case. Fig. 12 shows some results for $R_c = 6 \times 10^6$ indicating the effect of early transition at 5% chord due to roughness. It should be noted that the NACA standard roughness is so severe, that it causes a much higher drag than calculated. Furthermore it is observed that for the smooth airfoils, even at 21% thickness ratio, the drag still decreases with rearward movement of the position of minimum pressure. For the early transition case turbulent separation occurs at 18 and 21% thickness for $\bar{x}_l > .5$; here slot suction might give an improvement.

9.2. Some new basic thickness pressure distributions

Fig. 13 and 14 show $\bar{U}_l$ and $\bar{U}_{TE}$ for the 6-series basic thickness forms together with some "daring" extrapolations up till 30% thickness and positions of minimum pressure up till $\bar{x}_l = 0.9$. In a later investigation these relations will be improved through explicit calculations. The resulting values of $\bar{U}_l$ and $\bar{U}_{TE}$ have been used to design some basic thickness pressure distributions using the design chart. Some results are given in fig. 15; fig. 15a shows that a small amount of suction would already be sufficient to obtain non-separated flow for thick sections with the position of minimum pressure as far downstream as $\bar{x}_l = 0.9$. Fig. 15b shows that very small total drag coefficients can be realised in this way.

9.3. The NLF(1) - 416 airfoil

A well-known example of an NLF airfoil design without suction has been given by Somers in [28]; the airfoil is known as NLF(1) - 416. It has been designed to obtain low drag in cruising flight ($c_l = 0.4$) as well as in climb ($c_l = 1.0$) for Reynolds numbers typical for general aviation aircraft. The maximum extent of laminar flow which was aimed at, was only 30% chord. We will use this design and the experimental results in [28] to show the capabilities of our airfoil analysis and design program. Fig. 16 shows the airfoil shape and the potential flow pressure distribution at various angles of attack. From the published coordinates it follows that $\delta = 5.2^o$ and $\gamma = 12.8^o$ (see also the insert in fig. 16). If we define an effective trailing-edge angle by

$$\delta_{eff} = \text{ATAN} \frac{y_{upper} - y_{lower}}{c - x}$$

we find $\delta_{eff} = 9.35^o$ for $\bar{x} = 0.95$ and $\delta_{eff} = 9.80$ for $\bar{x} = 0.90$.
Fig. 17 shows a comparison between the calculated c_l and c_d values as compared to the experiment results from [28]. If we use the actual values of δ and γ in Eq.(13) for the viscous correction on lift, the resulting c_l is about .06 too high at $R_c = 4 \times 10^6$ (fig. 17b).
Since in Eq.(3) only two parameters occur (δ and γ), we might determine effective values of δ and γ such that at two values of α_c the experimental result of c_l is reproduced. Using $\alpha_c = -2^o$ and $\alpha_c = +6^o$ results in $\gamma_{eff} = 12.7^o$ and $\delta_{eff} = 11^o$; these "effective" values have been used in all other calculations for this airfoil. It follows that lift and drag are predicted well, except for the drag at the low R_c value of 1×10^6. It may be expected that in the experiments laminar separation bubbles have occurred at this R_c.
Fig. 18 and 19 show typical examples of predictions for the pressure distribution and transition position respectively.

9.4. The design of a flapped NLF airfoil with suction

At the Department of Aerospace Engineering at Delft a design study was made by Goei [29] of laminar flow airfoils for application to low-subsonic transport aircraft. This work served the third author of the present paper as a thesis to obtain the degree of aeronautical engineer at Delft University. The design specification for the airfoil was similar to the one used by Somers for NLF(1) - 416, namely low drag at $c_l = 0.4$ (cruise) and 1.0 (en-route climb).The Reynolds numbers were, however, increased to typical values for short-haul aircraft (9×10^6 at $c_l = 1.0$; 18×10^6 at $c_l = 0.4$). Furthermore it was allowed to use a cruise flap and turbulent boundary layer control by suction through a slot and through distributed perforations. The designs were made by a trial and error method, before we developed the design chart. We will briefly review the main results for one of the various airfoils which were designed; the airfoil will be designated by NLAD-1 (Natural Laminar flow Airfoil Design). Fig. 20 shows the airfoil shape with flap deflections of 0 and 10 degrees; the potential flow pressure distributions at various angles of attack are also shown. Note that the flap is very effective in increasing c_l without the penalty of large adverse pressure gradients on the upper surface. It should also be observed that the pressure distribution over the downstream part is nearly independent of the angle of attack. An irregularity occurs in the pressure distribution at the lower surface; in a final design this could, of course, be eliminated by fine-tuning the fairing between flap and main contour. The suction distribution for the airfoil was designed such that first for zero flap deflection at $\alpha_c = 0$ an optimum continuous suction distribution was obtained by varying the starting position for the suction; this resulted in a starting position of 80% chord. The starting value of R_θ (R_θ suction) obtained in this way was kept constant for all other cases. Slot suction at 80% chord was used to reduce R_θ to this value (R_θ suction) when α_c was increased and/or early transition due to roughness occurred. Although the $c_q = 0$ limit in fig. 20 crosses the pressure distributions, there is no early transition; the forward part of $c_p(\bar{x})$ differs too much from a constant β-flow to be comparable with our charts.
Lift and drag for various cases are shown in fig. 21. It follows that a large lift-loss due to viscosity (Eq.(3)) occurs in the no-suction case. The effectiveness of the flap both with and without suction is clearly visible. It should be observed that, even in the case of early transition due to roughness, suction is very effective to achieve low drag. From fig. 22 it follows that the required suction coefficients remain reasonably small. Hence, even if no smooth surfaces can be guaranteed, the application of turbulent b.l.c. might be considered.
The permissible roughness height for $R_c = 9 \times 10^6$ and 18×10^6 follows from fig.23; these results show an increase in permissible roughness near the stagnation point in contrast to the results for constant β ($\neq 1$) in fig. 6. This is due to the fact that the constant $-\beta$ approximation is not valid near the stagnation point (see fig. 10); right at the stagnation point we should find $\beta = 1$.
Some amplification calculations for various α_c and R_c are shown in fig. 24.

9.5. Mask's low drag airfoil design

After the work, reported in [29] was finished, we got access to [30] in which Mask reports on low drag airfoil design using passive laminar flow and an active diffusion b.l.c. concept, using blowing by a wall-jet, together with surface/pressure-gradient shaping. Fig. 25 shows one of the pressure distributions designed by Mask, together with the result of our design chart for the same values of R_c, $\bar{x}_l$, $\bar{U}_l$ and $\bar{U}_{TE}$ as used by Mask. It follows that Mask's design has still some safety margin.

10. CONCLUSIONS

It has been shown that laminarisation by shaping, together with turbulent boundary layer control, is an attractive scheme for performance improvement. Further investigations are considered to be worth while.

REFERENCES

1. Abbott, I.H. and von Doenhoff, A.E.: Theory of wing sections. Dover, New York (1959).
2. Nonweiler, R.: The design of wing sections. Aircraft Eng. July 1956.
3. Thwaites, B. (Ed.): Incompressible aerodynamics (chapter VI), Oxford, Clarendon Press, 1960.
4. Lachmann, G.V. (Ed.): Boundary Layer and Flow Control /olume 1 and Volume 2. Pergamon Press, 1961.
5. Ingen, J.L. van: Theoretical and experimental investigations of incompressible laminar boundary layers with and without suction. Report VTH-124, Delft University of Technology, Dept. of Aerospace Engineering (1965).
6. Ingen, J.L. van: A suggested semi-empirical method for the calculation of the boundary layer transition region. Delft University of Technology, Dept. of Aerospace Engineering, report VTH-74 (1956).
7. Ingen, J.L. van: Transition, pressure gradient, suction, separation and stability theory. In AGARD CP-224: Laminar-Turbulent Transition, Copenhagen (1977).
8. Ingen, J.L. van, Boermans, L.M.M. and Blom, J.J.H.: Low speed airfoil section research at Delft University of Technology. ICAS-80-10.1, Munich, October 1980.
9. Ingen, J.L. van: On the analysis and design of low speed airfoils using potential flow methods and boundary layer theory. Rept. LR-365, Dept. of Aerospace Engineering, Delft University of Technology, August 1982.
10. Boermans, L.M.M. and Selen, H.J.W.: Design and tests of airfoils for sailplanes with an application to the ASW-19B. ICAS-paper 82-5.5.2, 1982.
11. Boermans, L.M.M. and Oolbekkink, B.: Windtunnel tests on an outer wing segment of the ASW-19X sailplane. Report LR-369, Delft University of Technology, Dept. of Aerospace Engineering, 1983.
12. Holmes, B.J. and Obara, C.J.: Observations and implications of natural laminar flow on practical airplane surface. ICAS Paper 82-5.1.1, 1982.
13. Holmes, B.J., Obara, C.J., Gregorek, G.M., Hoffmann, M.J. and Freuhler, R.J.: Flight investigation of natural laminar flow on the Bellanca Skyrocket II. SAE Paper 830717, 1983.
14. North, D.M.: Laminar flow tests pass expectations. Aviation Week & Space Technology, June 21, 1982, p. 56-57.
15. Groenewoud, G.J.H. van, Boermans, L.M.M. and Ingen, J.L. van: Investigation of the laminar-turbulent transition on the rotorblades of the 25 m HAT windturbine. Report LR-390, Dept. of Aerospace Engineering, Delft University of Technology, 1983 (in Dutch).
16. Ingen, J.L. van: Advanced computer technology in aerodynamics: a program for airfoil section design utilizing computer graphics. Lecture notes for Von Karman Institute of Fluid Dynamics (1969), AGARD Lecture Series no. 37: "High Reynolds-number subsonic aerodynamics", p. 8.1 - 8.33 (1970).
17. Ingen, J.L. van: On the design of airfoil sections utilizing computer graphics. De Ingenieur, jrg. 81 no. 43, p. L110-L118 (1969).
18. Timman, R.: The direct and inverse problem of aerofoil theory. A method to obtain numerical solutions. National Aerospace Laboratory NLR, Amsterdam, report NLL-F16 (1951).
19. Dobbinga, E., Ingen, J.L. van, Kooi, J.W.: Som research on two-dimensional laminar separation bubbles. AGARD-CP-102, paper nr. 2, Lisbon (1972).
20. Ingen, J.L. van: On the calculation of laminar separation bubbles in two-dimensional incompressible flow. In AGARD-CP-168:"Flow Separation", Göttingen (1975).
21. Horstmann, K.H., Quast, A. and Boermans, L.M.M.: Pneumatic turbulators - A device for drag reduction at Reynolds numbers below 5 x 10^6. Paper no. 20 of this Symposium.
22. Wazzan, A.R., Gazley, C.Jr., and Smith, A.M.O.: Tollmien-Schlichting waves and transition. Prog. Aerospace Sci., Vol. 18, pp 351-392.
23. Smith, A.M.O.: Improved solutions of the Falkner and Skan boundary layer equation. S.M.F. Paper, FF-10,1954.
24. Felsch, K.O., Geropp, D. and Walz, A.: Method for turbulent boundary layer prediction. Proceedings Computation of Turbulent Boundary Layers, 1968. AFOSR-IFP-Stanford Conference, Vol. I, p. 170.
25. Cornish, J.J.: A simplified procedure for calculating boundary layer control systems for unflapped airfoils. Aeroph.Dept. of Miss.State Univ., Research Rept. 15, 1958.
26. Cornish, J.J.: Practical high lift systems using distributed boundary layer control, Aeroph. Dept., Miss. State Univ., Research Rept. 19, 1958.
27. Tennekes, H.: High lift Boundary Layer Control. TH Delft, Report VTH-114, 1962.
28. Somers, D.M.: Design and Experimental Results for a Natural Laminar Flow Airfoil for General Aviation Applications. NASA-TP-1861, 1981.
29. Goei, J.H.: Design study of laminar flow airfoils for application to low-subsonic transport aircraft. Thesis to obtain the degree of Aeronautical Engineer at Delft University of Technology, May 1983 (in Dutch).
30. Mask. R.L.: Low Drag airfoil design utilizing Passive laminar flow and coupled Diffusion Control. AIAA-conference 1980, Dallas Texas "Viscous Drag Reduction" (1980).

β	$\{f''(0)\}^2$	θ	H	$10_{\log}\left(\frac{Ux}{\nu}\right)_{tr}$ (*)
-.198838	0.000000	0.58543	4.02923	(3.00)
-.195	0.0030439	0.58136	3.64153	(3.13)
-.19	0.0073445	0.57652	3.48079	(3.26)
-.18	0.0165472	0.56771	3.29673	(3.52)
-.16	0.0363970	0.55219	3.09067	4.1237
-.14	0.0574733	0.53856	2.96327	4.6570
-.10	0.1019333	0.51504	2.80111	5.4856
-.05	0.1602585	0.49046	2.67575	6.1908
0	0.2205242	0.46960	2.59110	6.6764
.05	0.2820991	0.45147	2.52894	7.0294
.10	0.3446101	0.43546	2.48089	7.2967
.2	0.4715679	0.40823	2.41079	7.6730
.3	0.6002453	0.38574	2.36171	7.9235
.4	0.7300352	0.36669	2.32521	8.1011
.5	0.8605902	0.35027	2.29694	8.2330
.6	0.9916893	0.33591	2.27435	8.3344
.8	1.2550004	0.31185	2.24047	8.4794
1.0	1.5192732	0.29234	2.21623	8.5775

Table 1: Some characteristic quantities for the Hartree velocity profiles.

(*) : Values for $-.16 \leq \beta \leq 1.0$ according to Eq.(6); values for $\beta < -.16$ have been extrapolated.

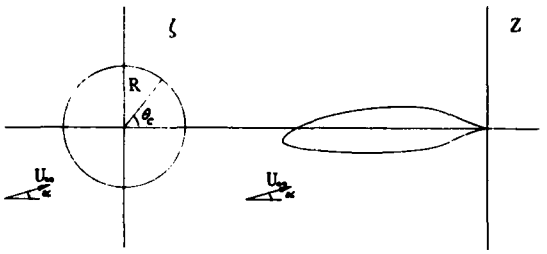


Fig. 1: Conformal transformation according to Timman

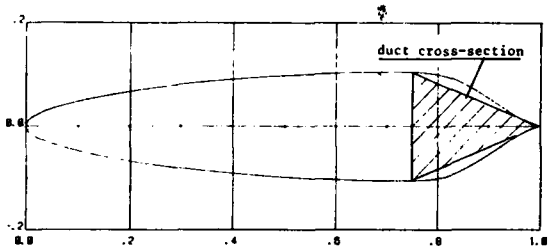


Fig. 3: A typical suction airfoil

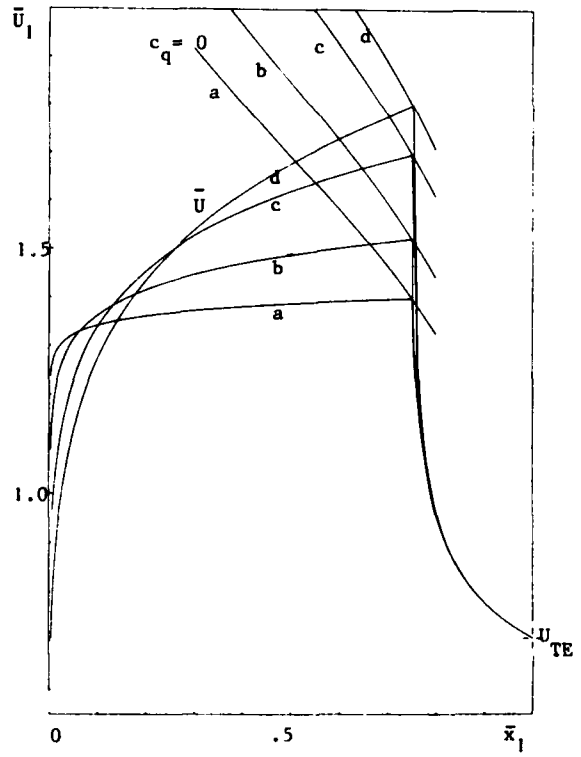


Fig. 5: Examples of limiting curves (c_q = 0) for $\bar{U}_{TE}$ = .707 and corresponding pressure distributions at $\bar{x}_1$ = 0.75.

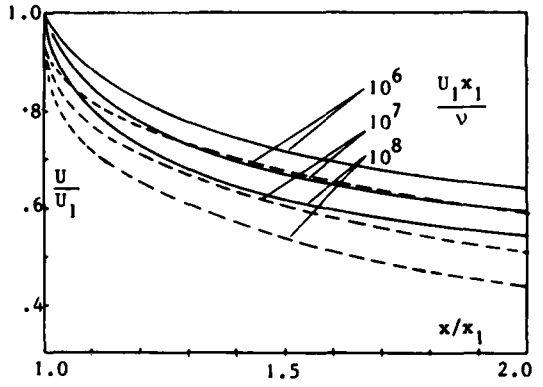


Fig. 2: Limiting pressure distributions for turbulent flow according to Head (———) and Stratford (---)

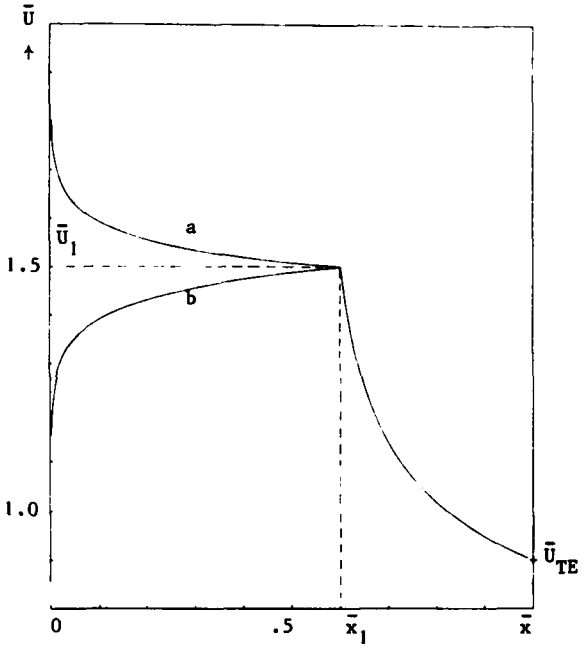


Fig. 4: Typical design pressure distributions for $\bar{x}_1$ = 0.6; $\bar{U}_1$ = 1.5 and $\bar{U}_{TE}$ =0.9
(a): $R_c = 1 \times 10^6$; (b): $R_c = 18 \times 10^6$

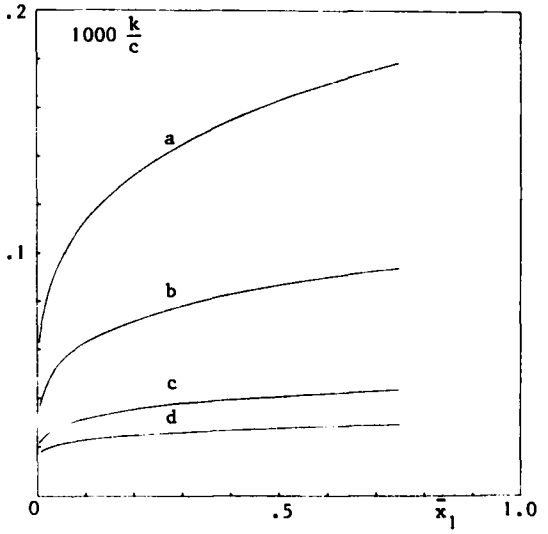


Fig. 6: Permissible roughness height for the examples of fig. 5.

(a): $R_c = 9 \times 10^6$ (b): $R_c = 18 \times 10^6$ (c): $R_c = 40 \times 10^6$ (d): $R_c = 60 \times 10^6$

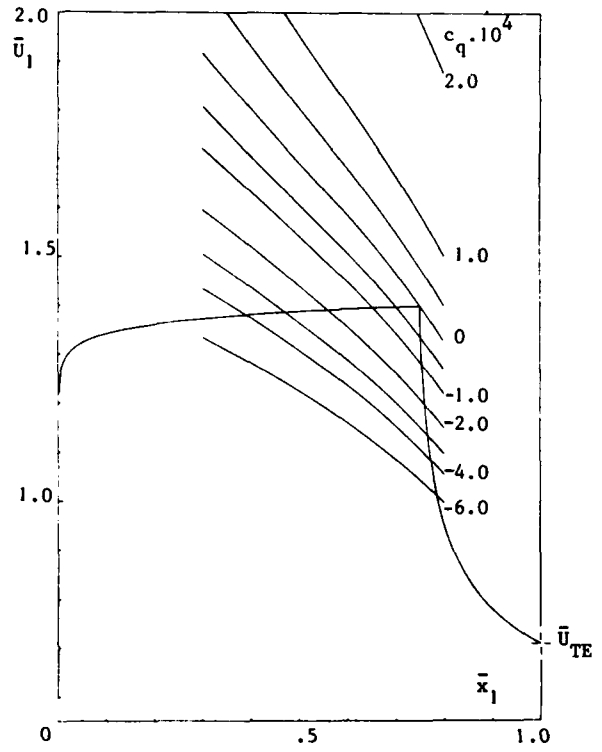


Fig. 7: Design chart for $R_c = 9 \times 10^6$ and $\bar{U}_{TE} = .707$; c_q (one surface) = constant curves and typical pressure distribution ($c_q = 0$; $\bar{x}_1 = 0.75$)

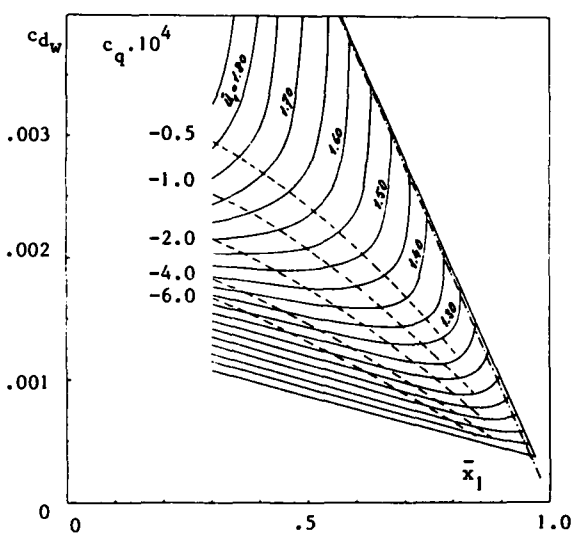


Fig. 8: Design chart for $R_c = 9 \times 10^6$ and $\bar{U}_{TE} = .707$; c_{d_w} (one surface) for constant values of c_q and $\bar{U}_1$

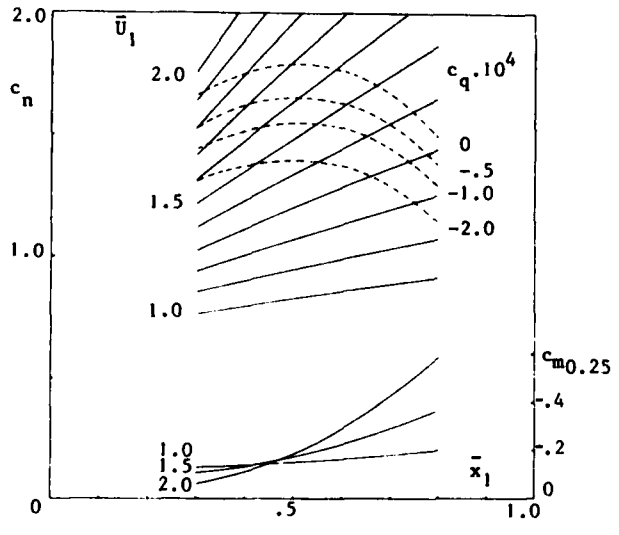


Fig. 9: Design chart for $R_c = 9 \times 10^6$ and $\bar{U}_{TE} = .707$; c_n and $c_{m_{0.25}}$ for one surface at constant values of $\bar{U}_1$ and c_q

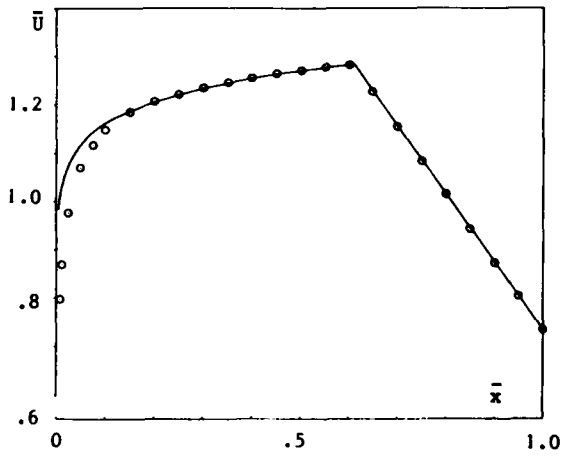


Fig. 10: The pressure distribution for the NACA 66_4-021 airfoil; approximation of the forward part by a constant $-\beta$ flow; o o according to [1]

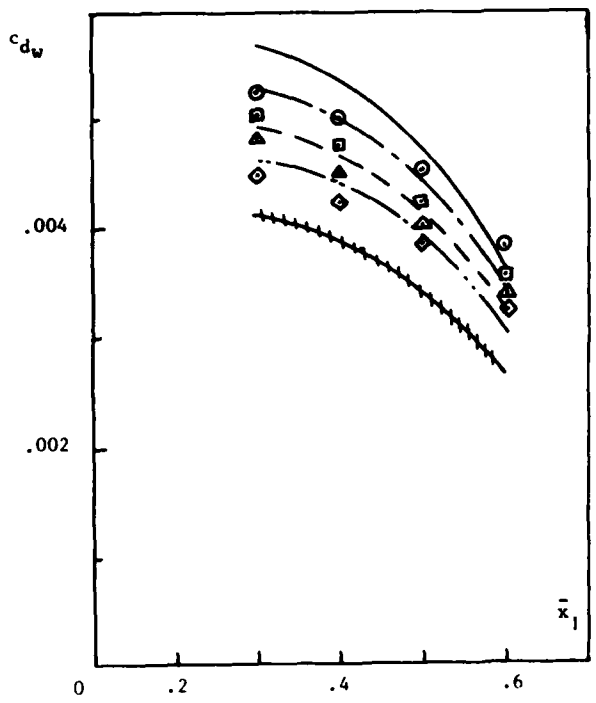


Fig. 11: Calculated c_{d_w} for the NACA 6-series basic thickness forms ($R_c = 9 \times 10^6$)
~~~~~~~~ improved result due to concave $\bar{U}(\bar{x})$ over the rear part

Legenda for figs 11 and 12

Calculation	experiment [1]	t/c
———	⊙	0.21
— — —	⊡	0.18
— — — —	△	0.15
— — — — —	◇	0.12

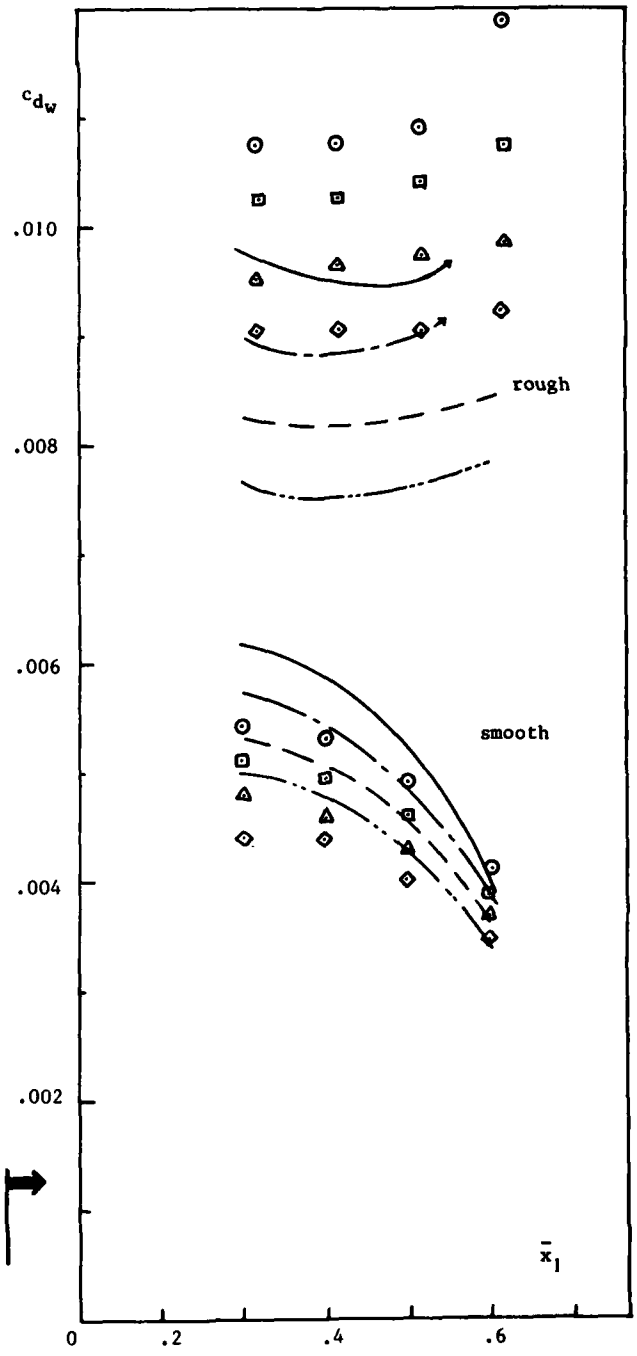


Fig. 12: Calculated drag for the NACA basic thickness forms at $R_c = 6 \times 10^6$; smooth and rough condition (transition assumed at 5% chord) .

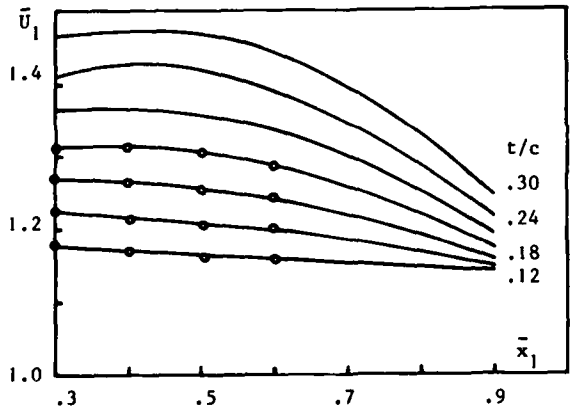


Fig. 13: Maximum speed ratio $\bar{U}_1$ for basic thickness forms at different $\bar{x}_1$ and t/c;
⊙ = NACA 6-series; ——— = extrapolated

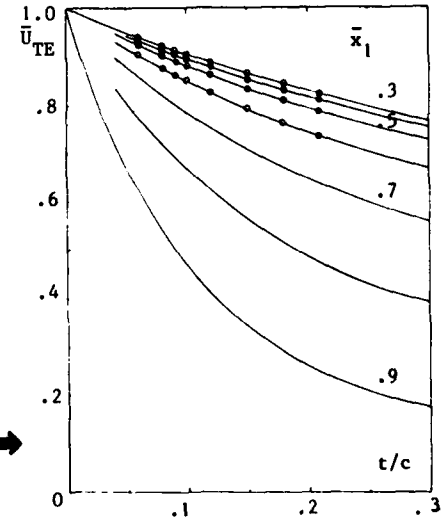


Fig. 14: Non-dimensional trailing-edge velocity $\bar{U}_{TE}$ for basic thickness forms at different $\bar{x}_1$ and t/c; ⊙ = NACA 6-series; ——— = extrapolated
~~~~~~~~

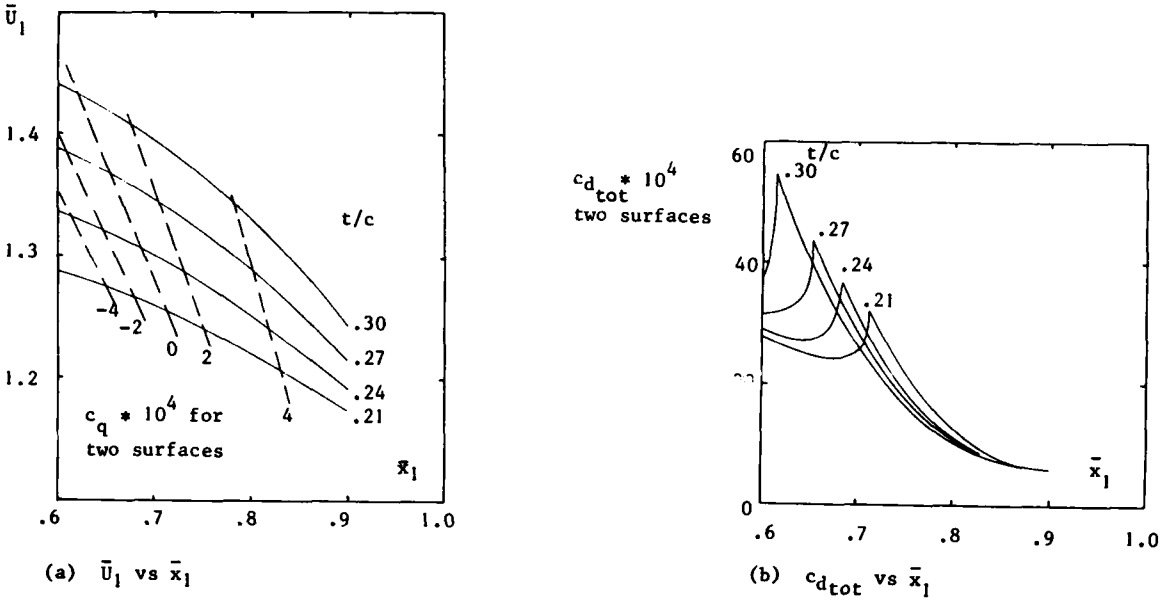


Fig. 15: Some newly designed basic thickness pressure distributions for $R_c = 9 \times 10^6$

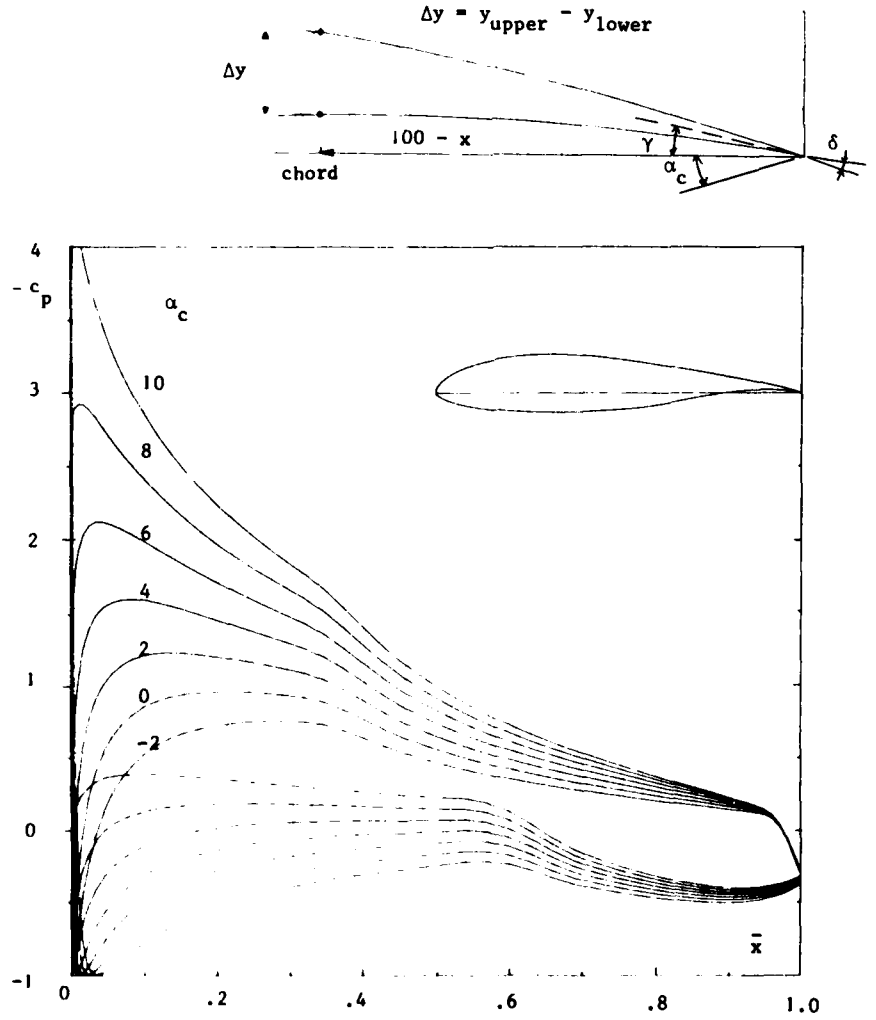


Fig. 16: The NLF(1) -416 airfoil with potential flow pressure distributions as calculated with the Delft program

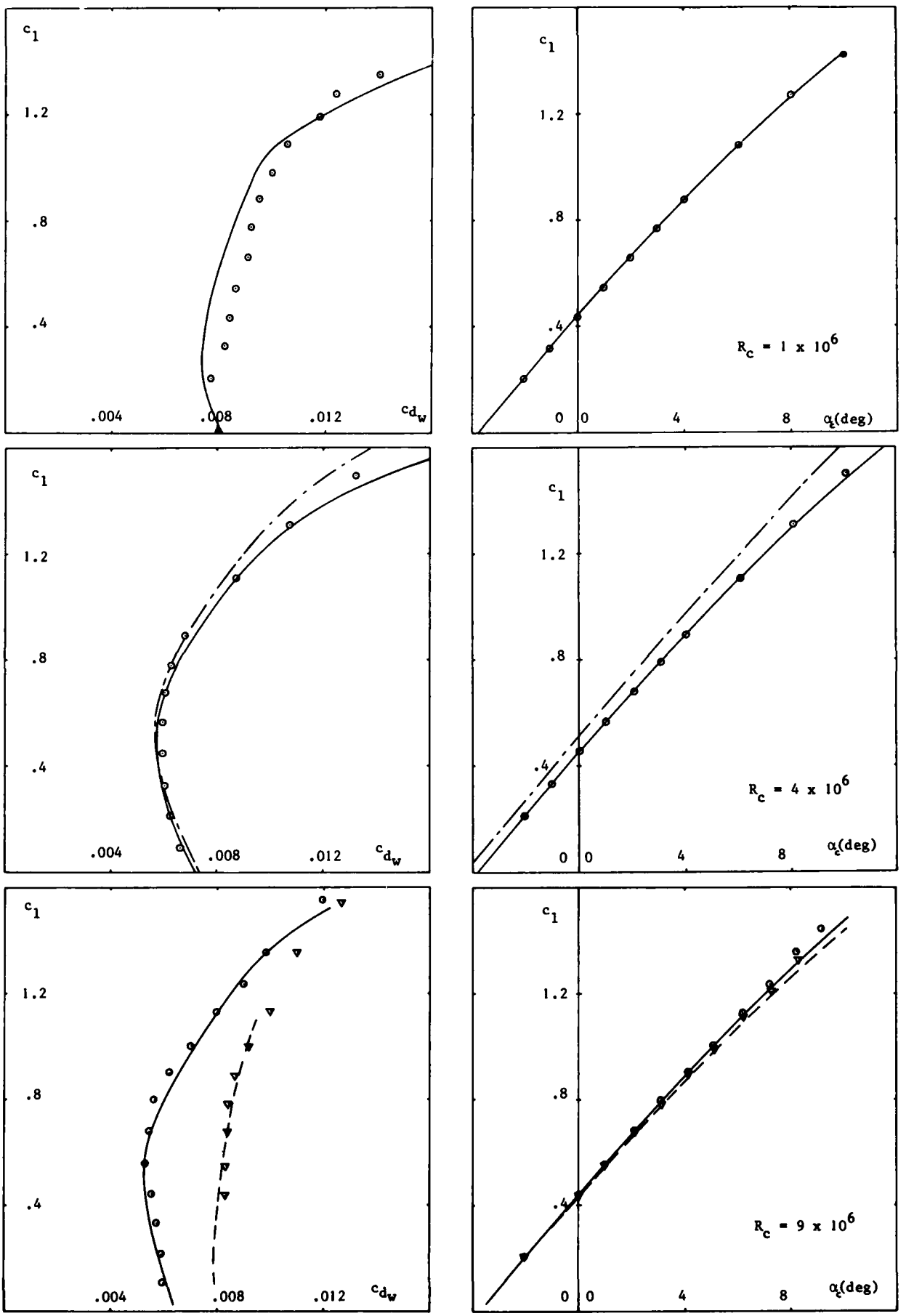


Fig. 17: Calculated lift and drag for the NLF(1) - 416 airfoil; ⊙ (smooth) and ▽ (transition at 5% chord) denote experimental results [28]. —— - —— exact δ and γ; ——— "effective" values of δ and γ, determined from ●

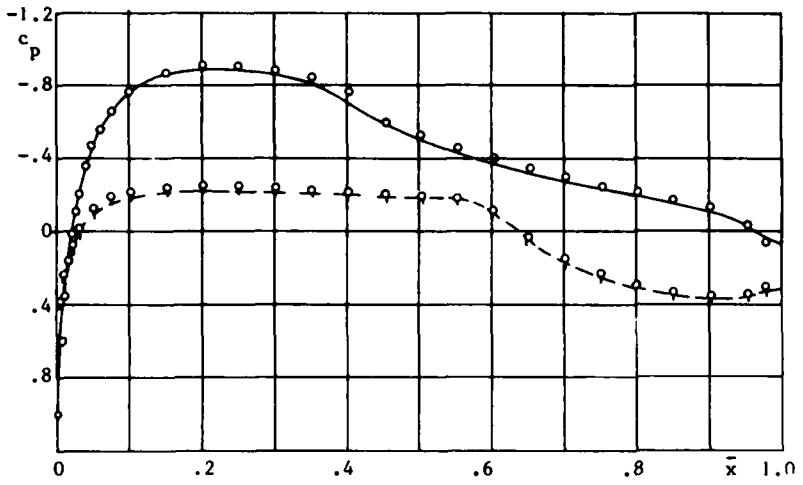


Fig. 18: Calculated pressure distribution for NLF(1) - 416 at $\alpha_c = 0.01^o$ and $R_c = 4 \times 10^6$; ⊙(upper surface) and ♀(lower surface) denote the experimental results [28]

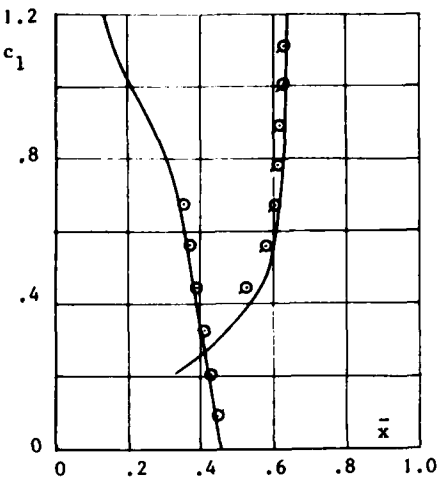


Fig. 19: The predicted transition position for NLF(1) - 416 at $R_c = 4 \times 10^6$; ⊙(upper surface) and ♀(lower surface) denote the experimental results [28]

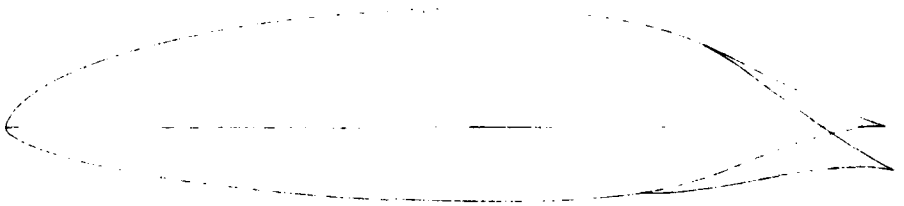


Fig. 20a: Airfoil shape

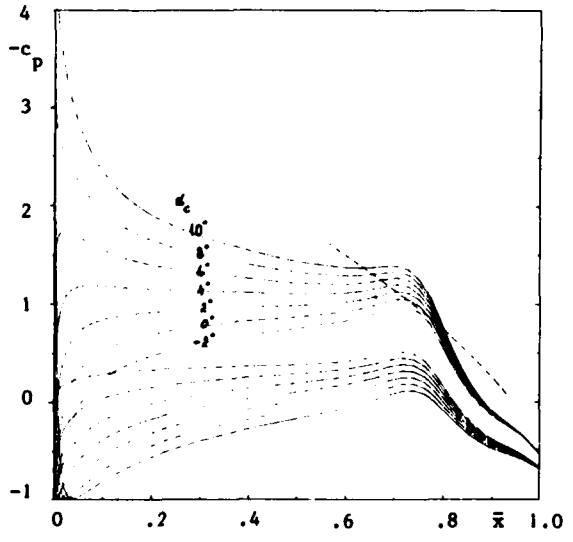


Fig. 20b: Potential flow pressure distributions; zero flap detection

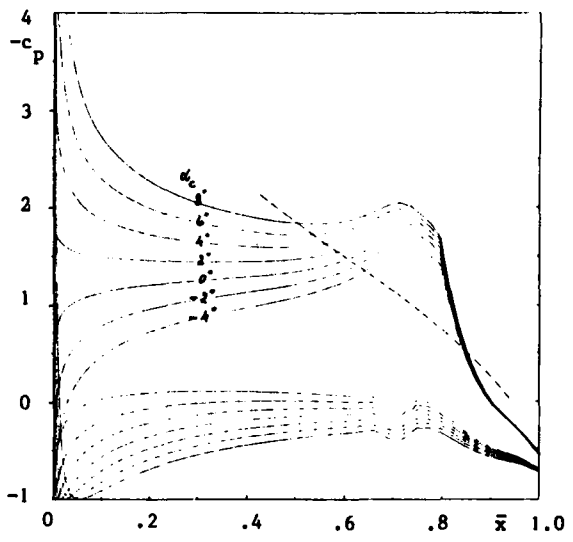


Fig. 20c: Potential flow pressure distributions; flap deflected 10 degrees

Fig. 20: The NLAD-1 airfoil without flap deflection and with flap deflected + 10^o;

— — — $c_q = 0$ limit for $R_c = 9 \times 10^6$

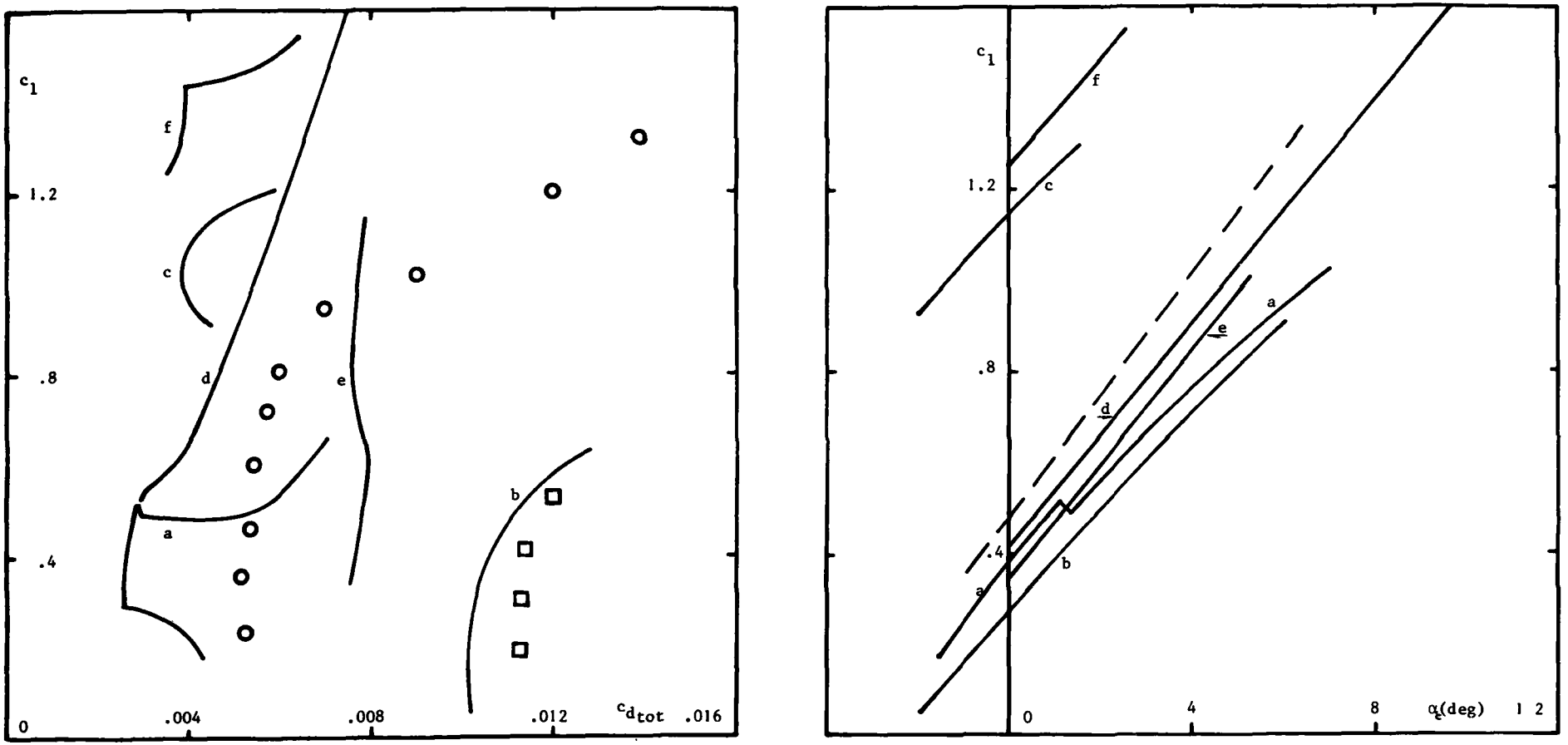


Fig. 21: Calculated lift and total drag for the NLAD-1 airfoil with and without flap deflection and with and without suction. R_c variable from 9 x 10^6 at c_l = 1.0 to 18 x 10^6 at c_l = 0.4; – – – potential flow lift coefficient. Experimental results for NACA 64_4-421 according to [1] : O smooth, □ standard roughness.

Curve	Flap deflection	Suction	Surface condition
a	0	-	smooth
b	0	-	transition at 5% chord
c	10°	-	smooth
d	0	+	smooth
e	0	+	transition at 5% chord
f	10°	+	smooth

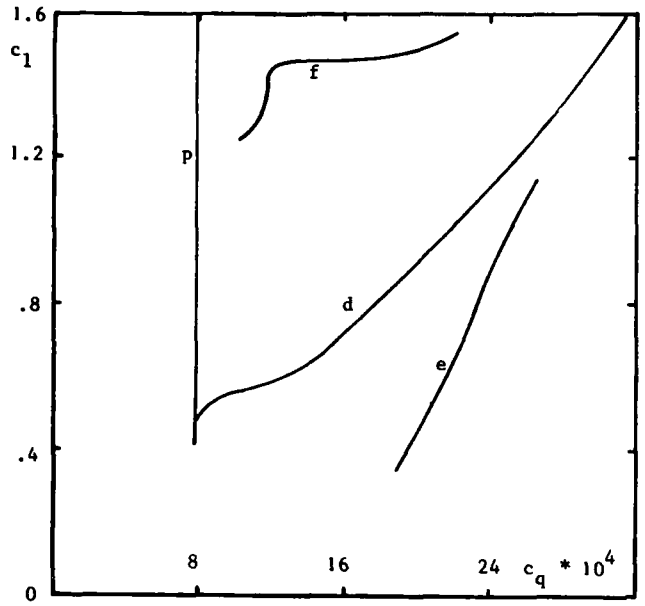


Fig. 22: Suction requirements for the NLAD-1 airfoil; (p) c_q for the distributed suction; the other curves give the total suction requirement.
(d): smooth, $\delta_f = 0$; (e) transition at 5% chord, $\delta_f = 0$; (f): smooth, $\delta_f = 10^o$

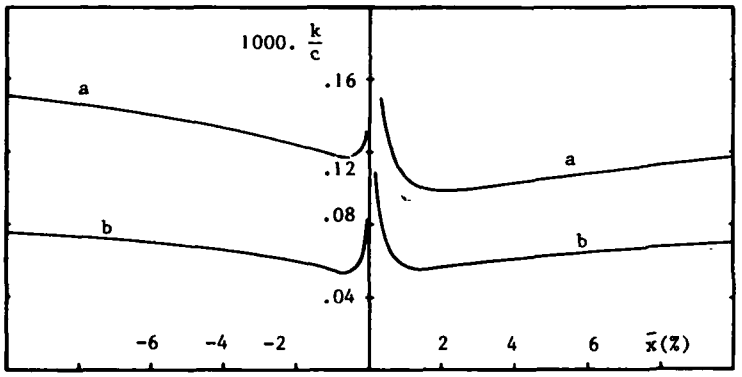


Fig. 23: Permissible roughness height for the NLAD-1 airfoil; (a): $R_c = 9 \times 10^6$;
(b): $R_c = 18 \times 10^6$

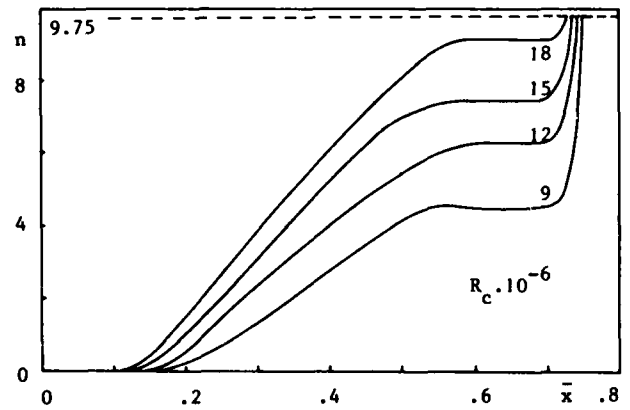


Fig. 24a: Amplification calculation for the NLAD-1 airfoil at $\alpha_c = 0$ and various R_c

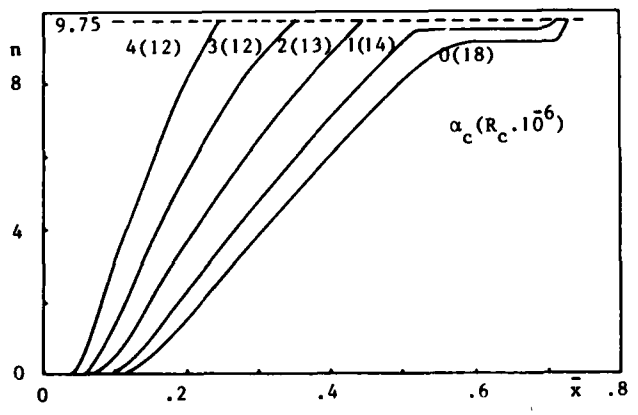


Fig. 24b: Amplification calculation for the NLAD-1 airfoil at various α_c - R_c combinations

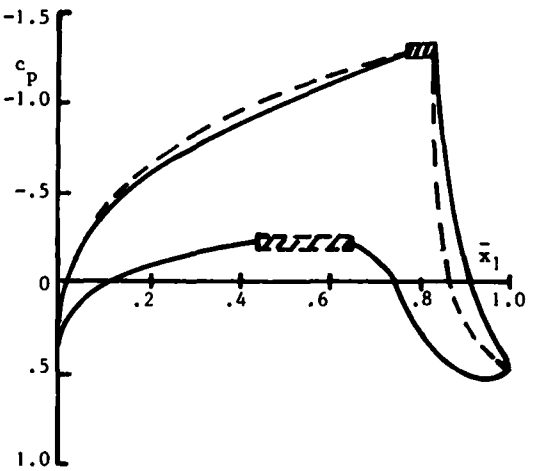


Fig. 25: Pressure distribution design by Mask [30]; $R_c = 40 \times 10^6$; ▨ "transition" region defined by Mask; – – – according to the present design chart

TECHNOLOGY DEVELOPMENTS FOR LAMINAR BOUNDARY LAYER CONTROL ON SUBSONIC TRANSPORT AIRCRAFT

Richard D. Wagner, Dal V. Maddalon, and Michael C. Fischer
NASA Langley Research Center
Hampton, Virginia 23665

AD-P004 065

SUMMARY

Since the beginning of the NASA Aircraft Energy Efficiency (ACEE) program in 1976, significant progress has been made in the development of laminar flow technology for commercial transports. Exploitation of new materials, fabrication methods, analysis techniques, and design concepts is providing convincing evidence that practical laminar flow control (LFC) systems for future transports could become a reality. Other ACEE program studies indicate that extensive laminar flow might be achieved on small transports with natural laminar flow (NLF) wings or hybrids of NLF and LFC (i.e., leading-edge suction on an NLF type of wing). This paper presents an overview of these laminar flow technology developments and describes future efforts in a broadened NASA program to explore the potential and evaluate the practicality of different laminar flow concepts for commercial transports.

NOMENCLATURE

ACEE	Aircraft Energy Efficiency
c	chord
c_ℓ	section lift coefficient
C_p	surface pressure coefficient
DFRF	Dryden Flight Research Facility
EBP	electron beam perforated
G/E	graphite epoxy
HLFC	hybrid laminar flow control
LEFT	leading-edge flight test
LFC	laminar flow control
M	free-stream Mach number
$M_\perp$	Mach number component perpendicular to leading edge
NLF	natural laminar flow
R_c	Reynolds number based on chord
t	wing thickness
TACT	Transonic Aircraft Technology
α	angle of attack
$\delta_{L.E.}$	leading-edge flap angle, deg
$\delta_{T.E.}$	trailing-edge flap angle, deg
λ	wing sweep angle, deg

INTRODUCTION

Laminar flow control (LFC) is a technology with great potential for drag reduction and, hence, fuel savings. The concept dates back to the 1930's when early applications of stability theory for laminar boundary layers led to the observation that laminar boundary layers can be stabilized by either favorable pressure gradients or small amounts of wall suction. Research was performed in many countries to explore approaches for achieving extensive laminar flow with these concepts. Stabilization by pressure gradient became known as natural laminar flow (NLF), and NACA research led to the development of the six-series natural laminar flow airfoils. International research on stabilization by suction, referred to as laminar flow control, was intensive at the same time and culminated in the United States with the flight tests of an unswept suction glove on an F-94 aircraft (Ref. 1) and the X-21 flight tests (Refs. 2, 3, 4, and 5) of a totally new swept LFC wing on a reconfigured WB-66 aircraft in the 1960's.

These flight experiments removed any doubt that extensive laminar flow could be achieved in flight. After the flight tests, however, unresolved concerns prevented serious consideration of LFC as a design option for future aircraft. A principal concern was the practicality of producing, with the technology then available, wing surfaces sufficiently smooth and wave-free to meet laminar-flow criteria and maintaining this wing surface quality in normal service operations.

In 1976 NASA initiated the Aircraft Energy Efficiency (ACEE) program to develop aircraft fuel conservation technology for commercial transports. One element of the ACEE program was to develop the technology for viscous drag reduction through application of laminar flow control. The decision to include LFC as part of the ACEE program was based on a number of considerations. The success of the previous programs in achieving laminar flow and the large potential fuel savings were strong motivations, but the impact that rising fuel prices have upon operating economics overshadow the fuel savings. Finally, developments in materials, fabrication, and airfoil technology offer to resolve the practicality concerns. In the ACEE program, NASA has worked closely with industry and significant progress has been made, notably in the development of transonic airfoils, practical wing construction, and practical leading-edge systems. These developments have also spawned new ideas, and rekindled some old ones, that could lead to near-term applications of LFC technology.

LAMINAR FLOW CONTROL AIRFOIL DEVELOPMENT

Airfoil development has received attention because of a desire to achieve laminar flow without compromising the performance gains of advanced supercritical airfoils. Industry studies have shown LFC and advanced airfoil designs to be compatible (Refs. 6, 7, and 8); however, NASA research indicates that the two technologies can be synergistically combined. At the Langley Research Center (LaRC), an advanced LFC airfoil (Ref. 9) has been developed that incorporates the latest supercritical airfoil technology and features intended to simplify the achievement of laminar flow. The airfoil (Fig. 1) has supercritical flow on both the upper and the lower surface and a drag divergence Mach number comparable to advanced turbulent supercritical airfoils, but, with laminar flow, nearly an order of magnitude higher lift-to-drag ratio. The small leading-edge radius provides a rapid acceleration through the leading-edge crossflow region on the upper surface such that suction is not required in the leading-edge region to stabilize crossflow. The undercut region on the lower surface improves the lift distribution and eliminates suction requirements in the immediate lower leading-edge region. The latter feature, with the lower local velocities (and thus greater laminar-flow tolerance to discontinuities) enhances the prospects for installation of a high-lift device for improving low-speed performance. A test program has been initiated to evaluate the performance of this airfoil at both high and low speeds.

Low speed high-lift wind tunnel tests are being conducted in the Langley 4 × 7 Meter Tunnel on a 3 m semispan, 1 m chord wing (Fig. 2). The model has a constant section, the advanced LFC airfoil, with full-span 10 percent or 12 percent chord leading edges and 25 percent chord trailing-edge flaps. Surface pressures are measured near mid-span. Figure 3 (Ref. 10) presents the measured pressure distribution for a representative configuration (0.12 chord leading-edge flap, $\delta_{LE} = -55°$, $\delta_{TE} = 30°$, $\alpha = 16°$) at a lift coefficient of 2.3; a theoretical pressure distribution at the same lift is also shown. The test indicates that the leading-edge device is required for adequate low-speed high-lift performance. Cursory design studies (Ref. 11) indicate that stowage would be possible in the volume available in the leading edge.

High-speed tests are currently underway in the Langley 8-Foot Transonic Pressure Tunnel (TPT) on a large swept wing utilizing the advanced LFC airfoil section (Ref. 12). The primary objective of the tests is to evaluate the effectiveness of suction through slots or perforated surfaces in extensive supercritical flow regions. The model (designed and fabricated at the Langley Research Center) has a constant section with 23° of sweep, a 7.07-ft chord, and a thickness ratio of 13 percent. At the design point the chord Reynolds number is 20 million; the lift coefficient and Mach number (normal to the leading edge) is 0.55 and 0.755, respectively. Tests up to a chord Reynolds number of 40 million will be performed. With a 10 percent chord trailing-edge flap, the pressure distribution will be controlled to explore off-design performance.

Extensive modifications of the 8-Foot TPT have been made for the test (Fig. 4). These include modifications to reduce tunnel turbulence level to much lower values, installation of a honeycomb and five screens in the settling chamber and a sonic choke ahead of the diffuser. A contoured liner has been installed in the test section to produce an infinite swept-wing flow over the model surface.

The model currently installed in the tunnel (see Fig. 5) has an aluminum surface with spanwise slots for boundary layer suction. Presently, in the tests of the slotted suction model, laminar flow has been achieved with extensive supercritical flow at conditions approaching the design point. Operating conditions are being cautiously increased to avoid potential model damage and to gain further experience with the test apparatus.

Under a NASA contract, the Douglas Aircraft Company has fabricated three panels to replace the upper wing surface panels of the model. The suction surface of these panels (see Fig. 6) is electron beam perforated (EBP) titanium sheet. The titanium sheet is bonded to a fiberglass sandwich panel with a corrugated core forming flutes for

subsurface airflow transfer. The impervious bond areas divide the panel surface such that suction through perforated strips occurs at the surface. Instrumentation is currently being installed in the three panels, and tests will begin after completion of the slotted model tests. The results will provide a direct comparison of the slotted and perforated strip suction approaches. A Douglas Aircraft Company LFC aircraft wing structure concept, to be discussed later, employs outer surface panels virtually identical in construction to these model panels. Fabrication of the model panels (see Fig. 7) has been a demonstration of practical production hardware, since the fabrication methods and panel layups used to meet the demanding laminar flow surface smoothness, waviness, and contour accuracy requirements are believed to be readily adaptable to production processes.

The EBP process produces finely spaced, elliptical or circular perforations. Holes as small as 0.0025 in. in diameter at the surface of the 0.025-in. thick titanium sheet can be produced. The holes taper to about twice that diameter on the opposite surface. Figure 8 shows the remarkable regularity and circularity of the holes produced. These perforations are over an order of magnitude smaller than the smallest perforations that were believed producible with practical manufacturing methods during the time of the X-21 program. At that time, perforated suction surfaces had been dismissed in favor of slotted surfaces. Wind tunnel and flight tests had shown that unless the suction holes were extremely small, suction through the holes induced flow disturbances that caused premature transition. Low-speed wind tunnel tests (Fig. 9) at the Douglas Aircraft Company (Ref. 7) indicate that the electron beam perforations are small enough to allow the use of EBP titanium as a suction surface. These low-speed tests were performed as part of an evaluation of a number of candidate suction surfaces; the two primary ones were a finely woven stainless steel wire mesh surface (Dynapore) and an electron beam perforated titanium surface. The Dynapore surface (Fig. 10) consists of an outer 80 × 700 wire mesh layer diffusion bonded to an inner 80 × 80 wire mesh layer for structural support. The weave is calendered to produce a smooth flat surface. For the wind tunnel test, the model had a constant section with 30° of sweep, a 7-ft chord, and 4.5-ft span width. Interchangeable leading-edge panels allowed testing either type of surface. The airfoil section and the tunnel wall liner were designed to provide a surface pressure distribution representative of a future laminar flow transport. With a nonporous surface (no suction), boundary-layer transition occurred at about 8 percent chord. With suction applied on a Dynapore, or an EBP titanium leading edge (with elliptical perforations, 0.004 in. by 0.008 in.), and Dynapore aft surface, laminar flow was maintained to 80 percent chord, even though the suction region only extended to 70 percent chord (Fig. 9). Tests with an EBP titanium suction surface with 0.0025 in. diameter holes indicated even better performance. Based on these aerodynamic tests and other structural and impact tolerance tests, the EBP titanium surface was considered to be superior to Dynapore.

WING SURFACE PANEL DEVELOPMENT

A central problem in the definition of a practical production LFC transport is the wing structure design. The emergence of composites, milled aluminum skins, and bonded skins as practical design options has changed the outlook since the X-21 program for resolving concerns about practical LFC wing structures meeting stringent LFC surface smoothness and waviness criteria. Although many options have been explored in the ACEE program (Refs. 6, 7, and 8), two design concepts were selected to evaluate their feasibility. One approach has an LFC ducting network integrated into the primary structure and the wing surface suction is through spanwise slots. The other uses a perforated suction surface with less ducting integration into the primary structure.

A Lockheed-Georgia Company (Refs. 6 and 13) design is the integral approach and it employs extensive use of graphite epoxy (G/E) composite materials (Fig. 11). The primary load carrying structure is thick G/E wing skin stiffened with G/E hat section stiffeners. Titanium sheet is bonded to the G/E wing skins and presents a tough, damage tolerant, noncorrosive surface and lightning protection to the substructure. After the bonding process, spanwise slots are cut in the titanium sheet with a high-speed steel jeweler's saw. Suction air passes through the slots into small plenums molded into the G/E skins and through metering holes to spanwise ducts formed by the hat stiffeners. At every other rib station, the suction air is metered into ducts formed by rib caps of truss ribs. The rib cap ducts penetrate the front spar web to transfer the suction air into trunk ducts in the leading-edge box. The trunk ducts collect the suction air into suction pumps. The suction pumps are driven by independent gas turbine power units; both the pumps and power units are located under the wing roots.

To evaluate the design, an extensive fabrication and testing program has been undertaken that examined materials, adhesives, cure process variables, structural characteristics, and fabrication techniques. No significant problems were uncovered. Manufacturing studies, based in part upon the experience gained in the structural specimen fabrication, have allowed an assessment of manufacturing costs and performance benefits in a comparison of features of a Lockheed LFC aircraft with a Lockheed advanced turbulent aircraft. With each aircraft designed to carry 400 passengers for a 6500 nautical mile flight, the LFC aircraft has a gross take-off weight that is 8.5 percent lower than the turbulent aircraft and burns 21.7 percent less fuel. While the acquisition cost is $1.9 million higher per LFC aircraft, fuel usage per year (at $1.5 per gallon) indicates that the LFC system's cost would be offset in the first 6 months of operation with annual fuel cost savings thereafter of nearly $4 million per aircraft.

	Adv. Turbulent	LFC
TOGW (lb)	645,073	590,496
Fuel burn (lb)	274,073	214,711
Acquisition cost ($M)	79.2	81.1
Incremental fuel cost ($M/yr.)	3.9	0

A Douglas (Ref. 14) LFC wing design is illustrated in Figure 12. The main wing box covers are internal blade stiffened G/E skin panels. Suction panels are gloved to the main wing box and suction air collection is external to the wing box. The suction panel construction is virtually identical to the EBP titanium suction panel construction for the Langley wind-tunnel model described earlier (Fig. 6). The suction panels are attached to generally chordwise oriented blades on the outer surface of the wing box cover. These blades also form shallow ducts for suction air collection into trunk ducts in the leading-edge box. This collection scheme is advantageous, over for example spanwise air collection, because the quantity of air flow and collection distance is such that the ducts can be very shallow and wing structural depth loss is a minimum. Behind the rear spar and in the leading-edge box, air collection is in spanwise ducts.

In the Douglas concept, suction is applied only on the wing upper surface and a leading-edge Krueger flap is used. Acceptable low-speed aircraft performance is achieved with a small trailing-edge flap system which allows laminar flow to 85 percent chord on the wing upper surface in cruise. If suction is desired on the lower surface to achieve laminar flow, the Krueger flap would not be used (because of Douglas concerns about maintaining surface smoothness in the stowed condition) and a powerful 30 percent chord trailing-edge flap and larger wing is required to meet acceptable low-speed performance. The larger trailing-edge flap limits the laminar flow to 70 percent chord and the larger wing degrades cruise performance. Douglas trade studies show that laminarization of the upper surface is the most effective application of LFC suction. Since about two-thirds of the wing friction drag is due to the upper surface, the aerodynamically more efficient wing (sized for cruise) and more extensive laminar flow achievement yields an advantage for the upper surface only suction concept.

The upper surface suction design also provides practical solutions to potential manufacturing and maintenance concerns. The wing assembly can be made from the lower surface using internal fasteners that do not penetrate the upper wing surface. All maintenance access can be done through the lower surface, and since most of the ducting is in the leading-edge box, it would be accessible by Krueger flap deployment on the ground. Finally, LFC maintenance for impact damage would be minimized since the upper surface is least exposed to foreign object damage. Another asset is that the Krueger flap can be used to shield the leading edge from insects and debris on take-off and landing.

LFC LEADING-EDGE SYSTEMS DEVELOPMENT

The most difficult problems of achieving laminar flow on commercial transports appear to be associated with the leading-edge region. Solutions to these problems will remove many concerns about the ultimate practicality of laminar flow.

A principal concern in the leading edge is residue from insect impacts on the wing. Sufficient surface roughness can be deposited to prevent the attainment of laminar flow during cruise at altitudes and speeds of subsonic transport operations. Although the need for an active "anti-contamination" system is not clear, in the NASA program we selected the prudent course of developing potential systems and assessing their need in actual operations. Two approaches for insect protection have been developed. A Lockheed concept consists of injecting a cleaning fluid through slots above and below the attachment line (Refs. 6 and 15). Lockheed verified the feasibility of this concept during wind tunnel tests in their low-speed wind tunnel facility (Ref. 6). A partial-span full-scale leading-edge section (Fig. 13) was subjected to insects injected in the free stream at number densities much higher than expected in actual flight at take-off or landing conditions. Cleaning fluid injected through leading-edge slots completely covered and protected the upper and lower surfaces; the insects did not adhere to the wet surface. Douglas utilizes the Krueger high-lift device as a protective shield against insect impact. Tests were conducted (Ref. 7) in the NASA Lewis Icing Research Tunnel (Fig. 14) to evaluate the effectiveness of a Krueger shield in protecting the leading edge from insect contamination. These tests (supported by trajectory analysis) demonstrated that the Krueger flap serves as an effective line-of-sight shield for heavy insects, but suggest that a supplemental spray may be necessary to protect against possible impingement of lighter insects in some areas of the wing. In particular, wing twist can result in direct impacts in the outboard regions, and the high lift induced in the inboard region can deflect lighter insects into the wing.

Clearly the integration of either of the above systems with the anti-icing and suction systems in the leading edge represents a formidable design challenge. A flight program is currently underway within NASA to evaluate the effectiveness of these integrated leading-edge systems developed by Douglas and Lockheed over the past few years. Under NASA contracts both companies have designed and fabricated a leading-edge test article to be installed on a Jetstar (see Fig. 15) to demonstrate that the required systems can be packaged into a leading-edge section representative of future LFC

commercial transport aircraft, and that these systems can operate reliably with minimum maintenance in an airline flight environment.

The Lockheed leading-edge concept is illustrated in Figure 16. The leading-edge box structure is a sandwich construction. A 0.016-in. thick titanium outer sheet is bonded to a sandwich substructure of graphite epoxy face sheets with a Nomex honeycomb core. Suction is accomplished through fine spanwise slots (0.004 in. in width) on both the upper and lower surfaces to the front spar. The suction flow is routed through the structure by a combination of slot ducts, metering holes and collector ducts embedded in the honeycomb. The Lockheed insect protection system is integrated with the anti-icing protection system. It consists of dispensing a cleaning/anti-icing fluid over the surface through slots above and below the attachment line. These slots are purged of fluid during climbout and provide suction to achieve laminar boundary layer flow at cruise conditions.

The Douglas leading-edge concept (Fig. 17) consists of an EBP titanium sheet bonded to a fiberglass sandwich substructure which forms a suction panel. This removable suction panel is attached to a ribbed supporting substructure. The areas where the EBP skin bond to the corrugated substructure are impervious to flow; thus, suction is through perforated strips. Alternate substructure flutes are used for suction air collection. Suction is applied only on the upper surface from just below the attachment line to the front spar. A Krueger-type flap serves as a protective shield against insect impact. Supplemental spray nozzles on the underside of the Krueger shield coat the leading edge with a fluid freezing point depressant to guard against impingement of lighter insects in some areas of the wing. In icing conditions, the Krueger serves as the primary anti-icing protection of the leading edge, supplemented as required with the spray nozzle system. The shield leading edge is equipped with a TKS (commercially available) ice protection system (Ref. 16). A system for purging fluid from the suction flutes and surface perforations is provided if required.

Flight acceptance testing began in late 1983 at the NASA Dryden Flight Research Facility; Figure 18 shows the aircraft in flight. Reference 17 contains a detailed description of this program. After an evaluation of the individual performance of all the systems, a simulated airline service phase of flight testing will be performed wherein the modified Jetstar will operate out of "home base" areas throughout the United States (Fig. 19). Two or more flights daily will be made. The condition of the test articles and achievement of laminar flow will be fully documented after each flight. These simulated airline service flights are designed to provide operational experience. The LFC systems will be operated in a "hands off" mode, to establish a maintenance and reliability data base. A potential operational problem identified during the X-21 program could be the effect of high altitude ice particles.

HIGH ALTITUDE ICE PARTICLE EFFECTS

During flight testing with the X-21 LFC aircraft, it was observed that laminar flow was temporarily lost whenever the aircraft penetrated cirrus clouds, concentrations of ice crystals at high altitude. Given this possibility, a program was initiated to determine the probability of encountering clouds along various airline routes and how cloud frequency varies with altitude, latitude, longitude, and season (Ref. 18). Cloud-encounter data were available from the NASA Global Atmospheric Sampling Program (GASP) archive (Ref. 19). In the GASP program, meteorological and trace-constituent measurements of ambient atmospheric conditions were taken worldwide aboard four Boeing 747's during routine commercial service to obtain detailed measurements of the upper troposphere and the lower stratosphere. These measurements (made during 1975-79 on some 3,000 flights) included some 88,000 cloud encounters. Using this data base, an analysis of LFC loss on major airline routes was made (Fig. 20). The calculations assumed that all cloud encounters result in laminar flow loss and that no cloud avoidance measures (flight management) are taken. Using these conservative assumptions, the results presented in Figure 20 show that laminar flow should be lost at most for about 8 percent of the flight time (world wide). Hence, although infrequent, cloud encounters are not negligible and do occur frequently enough to make further study of cloud-encounter effects desirable. As part of the leading-edge flight program, a Knollenberg probe will be flown on the fuselage (Fig. 20) to monitor ice particle concentrations to correlate with the achievement of laminar flow.

NEW DIRECTIONS

Recent NASA research (Ref. 20) is encouraging with regard to the prospects of obtaining significant amounts of laminar flow on small commercial transports with either natural laminar flow or a hybrid of natural laminar flow and laminar flow control. In 1980 the TACT-F111 aircraft at the NASA Dryden Flight Research Facility was flown with a full chord, partial span airfoil glove designed to achieve natural laminar flow (Ref. 21). In these flight tests extensive laminar flow was observed at moderate wing sweeps suggesting that NLF could be a design option provided wing sweep is not excessive. NASA has also sponsored a recent evaluation by the Boeing Company (Ref. 20) of a hybrid laminar flow control concept, HLFC, which shows attractive gains from combining LFC suction in the leading-edge region with NLF over the wing box (Fig. 21). The suction in the leading-edge box controls the strong crossflow disturbances that occur initially on swept wings; over the wing box the pressure distribution is tailored to provide favorable gradients to stabilize the two-dimensional disturbances. Laminar flow

to 60 percent chord might be achieved; the extent will depend upon the leading-edge sweep, chord Reynolds number, and amount of suction. However, significant performance benefits appear to be achievable without the wing sweep compromise required of natural laminar flow or the structural complications of LFC ducts embedded in the wing in-spar structure.

At present, transition data applicable to this type of wing pressure distribution (Fig. 21) is limited and is needed in order to make valid assessments of the potential of NLF or HLFC wings for transports of various sizes and speeds. A flight program has been initiated to provide a transition data base for such wing designs. An F-14 aircraft with variable wing sweep capability will be modified with up to three full-span gloves to produce a range of upper wing surface pressure distributions (Fig. 22). The gloves will be constructed of foam and fiberglass with no provisions for suction and scabbed onto the existing wing surface. The gloves will extend from below the attachment line over the upper surface to the rear spar location (≈60 percent chord). The first glove will be a simple fiberglass cover of the basic wing which was a strong favorable pressure gradient over the wing box. The fiberglass cover will give the wing a smooth, nearly wave-free surface which meets laminar flow disturbance criteria. Current plans are to begin flight testing of the basic wing glove in early 1985.

CONCLUDING REMARKS

Future NASA efforts will extend the current research to explore the practicality of the achievement of extensive laminar flow in routine flight operations. Currently envisioned is a DC-9 class transport as a test bed aircraft (Fig. 23). LFC, NLF, or hybrid gloves would first be flown to perform flight research in crucial problem areas. Reliability and maintenance would then be evaluated and experience gained with actual flight operations. The ultimate objective will be to establish a technology base for future industry exploitation of laminar flow technology. The potential benefits of extensive laminar flow achievement on commercial transports are enticing, and accomplishments to date indicate that they may be achievable.

REFERENCES

1. Groth, E. E.; Carmichael, B. H.; Whites, R. C.; and Pfenninger, W.: Low Drag Boundary Layer Suction Experiments in Flight on the Wing Glove of a F94-A Airplane-Phase II: Suction Through 69 Slots. NAI-57-318, BLC-94 (Contract AF-33 (616)-3168), Northrop Aircraft, Inc., February 1957.

2. Antonatos, P. P.: Laminar Flow Control - Concepts and Applications. Astronautics and Aeronautics, July 1966.

3. Nenni, J. P.; and Gluyas, G. L.: Aerodynamic Design and Analysis on an LFC Surface. Astronautics and Aeronautics, July 1966.

4. White, R. C.; Sudderth, R. W.; and Wheldan, W. G.: Laminar Flow Control on the X-21. Astronautics and Aeronautics, July 1966.

5. Pfenninger, W.; and Reed, V. D.: Laminar-Flow Research and Experiments. Astronautics and Aeronautics, July 1966.

6. Sturgeon, R. F.; et al.: Evaluation of Laminar Flow Control System Concepts for Subsonic Commercial Transport Aircraft. NASA CR-159253, September 1980.

7. Anon, Douglas Aircraft Co. Staff, Evaluation of Laminar Flow Control System Concepts for Subsonic Commercial Transport Aircraft. NASA CR-159251, June 1983.

8. Anon, Boeing Commercial Aircraft Co. Staff, Evaluation of Laminar Flow Control System Concepts for Subsonic Commercial Transport Aircraft. NASA CR-158976, December 1978.

9. Pfenninger, W.; Reed, H. L.; and Dagenhart, J. R.: Design Considerations of Advanced Supercritical Low Drag Suction Airfoils. AIAA Technical Papers (A81-26501), 1980, Vol. 72 of Progress in Astronautics and Aeronautics, pp. 249-271.

10. Applin, Z. T.: Private Communication to authors, February 27, 1984.

11. Applin, Z. T.: Status of NASA Advanced LFC Airfoil High-Lift Study. NASA CP 2218, September 1981, pp. 43-61.

12. Harvey, W. D.; and Pride, J. D., Jr.: NASA Langley Laminar Flow Control Airfoil Experiment. NASA CP 2218, September 1981, pp. 1-42.

13. Anon: Laminar Flow Control. Lockheed-Georgia Company (NAS1-16219 and NAS1-16235). Presented at the NASA-Dryden Flight Research Facility, September 1981.

14. Pearce, W. E.: Progress at Douglas on Laminar Flow Control Applied to Commercial Transport Aircraft. NAS1-16234, Douglas Aircraft Company. Presented at NASA-Dryden Flight Research Center, September 1981.

15. Etchberger, F. R.: Laminar Flow Control Leading Edge Glove Flight - Aircraft Modification Design, Test Article Development, and Systems Integration. NASA CR-172136, November 1983.

16. McNay, D.; and Allen J.: Laminar Flow Control Leading Edge Glove Flight Test Article Development (NAS1-16220). Presented at the NASA-Dryden Flight Research Facility, September 1981.

17. Fischer, M. C.; Wright, A. S., Jr.; and Wagner, R. D.: A Flight Test of Laminar Flow Control Leading-Edge Systems. NASA TM-85712, December 1983.

18. Davis, R. E.; and Fischer, M. C.: Cloud Particle Effects on Laminar Flow and Instrumentation for Their Measurement Aboard a NASA LFC Aircraft. AIAA Paper No. 83-2734, November 1983.

19. Jasperson, W. H.; Nastrom, G. D.; Davis, R. E.; and Holdeman, J. D.: Cloud Encounter Statistics in the 28.5-43.5 kft Altitude Region from Four Years of GASP Observations. Proceedings of the Ninth conference on Aerospace and Aeronautical Meteorology (American Meteorological Society), Omaha, NE, June 6-9, 1983, pp. 159-164.

20. Anon, Boeing Commercial Aircraft Company Staff, Hybrid Laminar Flow Control Study. NASA CR-165930, October 1982.

21. Montoya, L. C.; Steers, L. L.; Christopher, D.; and Trujillo, B.: F-111 TACT Natural Laminar Flow Glove Flight Results. NASA CP 2208, September 1981.

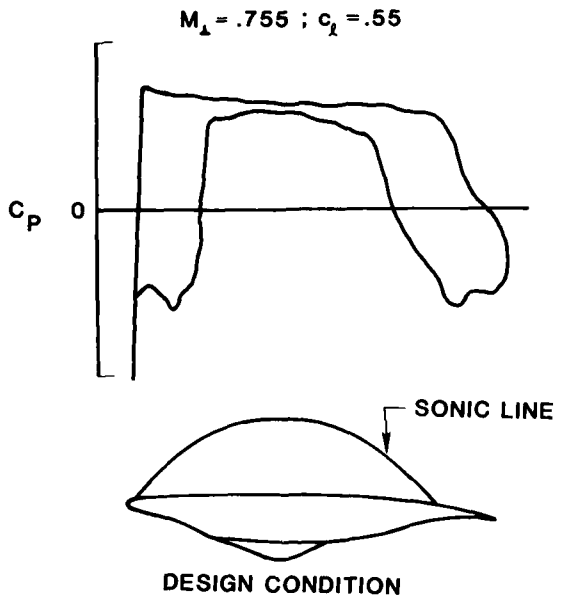


Figure 1. Advanced LFC supercritical airfoil



Figure 2. High-lift advanced LFC airfoil installed in Langley 4 X 7 meter tunnel

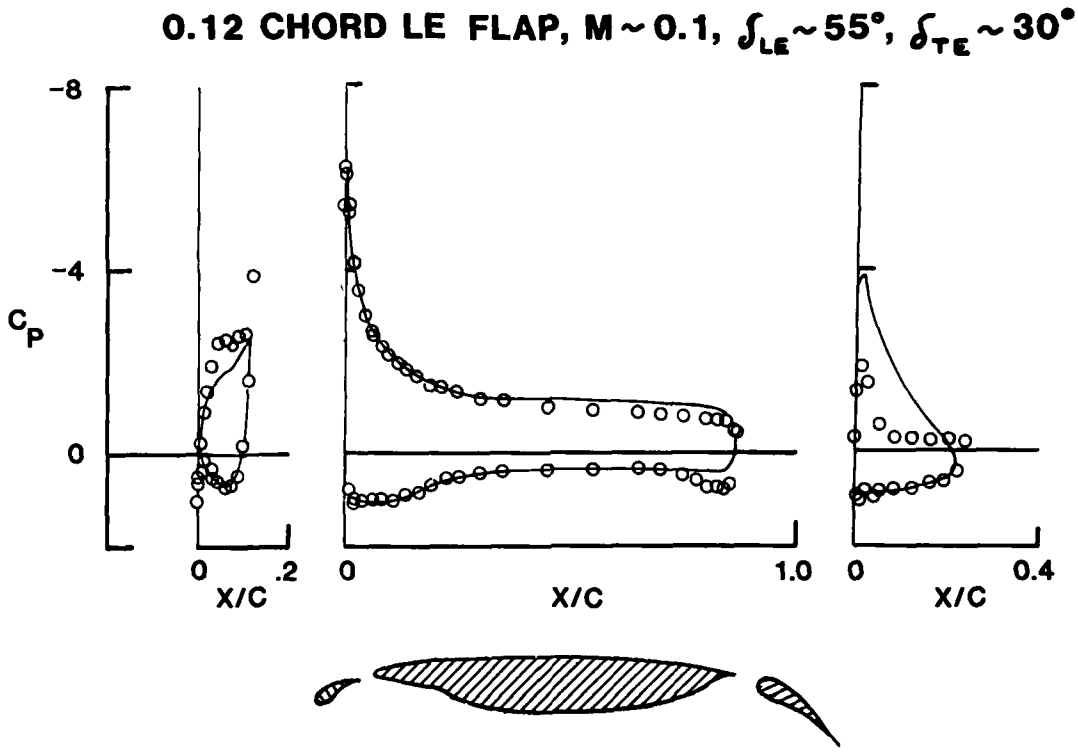


Figure 3. Wind tunnel measurements of high-lift characteristics for the advanced LFC airfoil

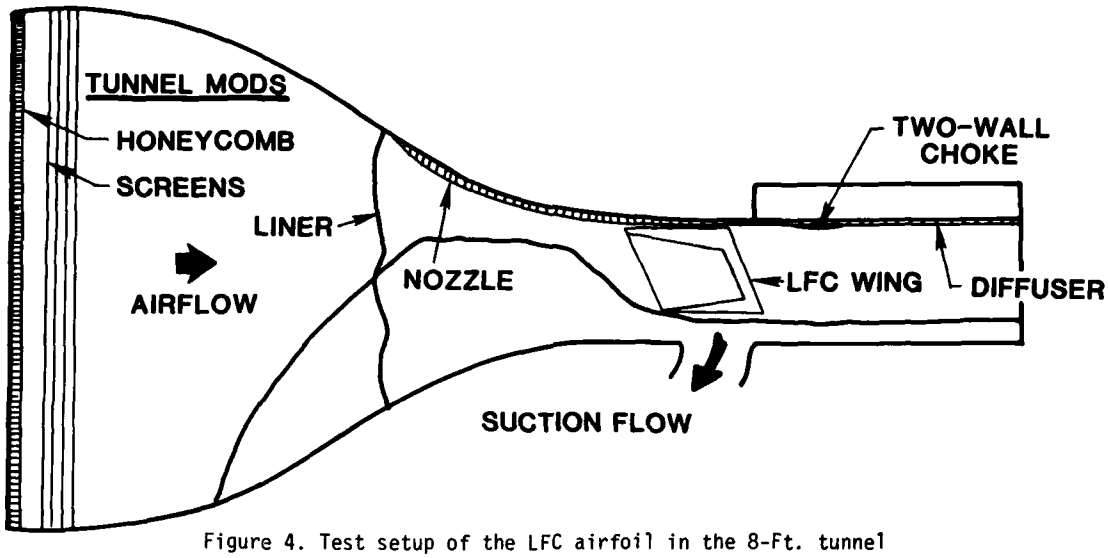


Figure 4. Test setup of the LFC airfoil in the 8-Ft. tunnel

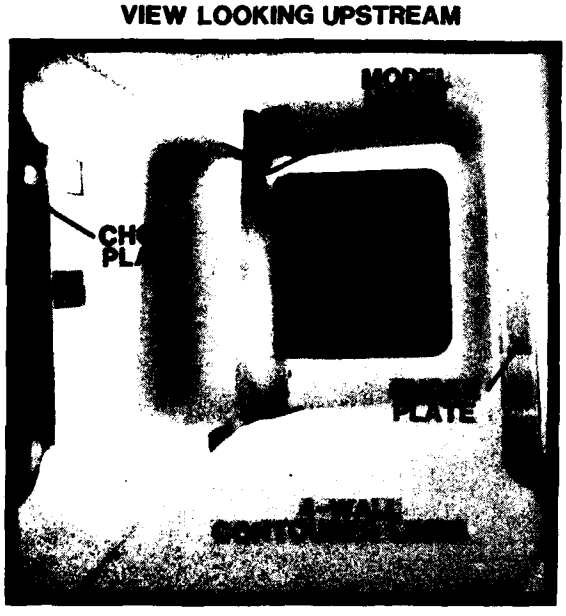


Figure 5. Advanced LFC airfoil installed in the 8-Ft. tunnel

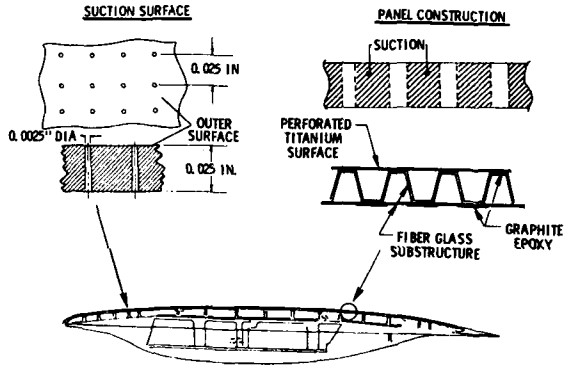


Figure 6. Details of the electron beam perforated titanium panels for the LFC airfoil

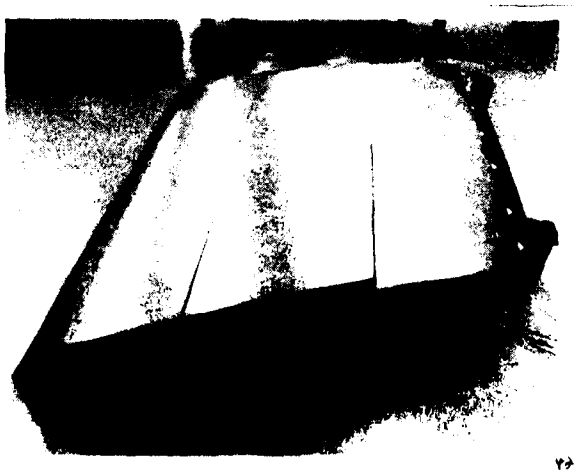


Figure 7. Photograph of electron beam perforated titanium panels

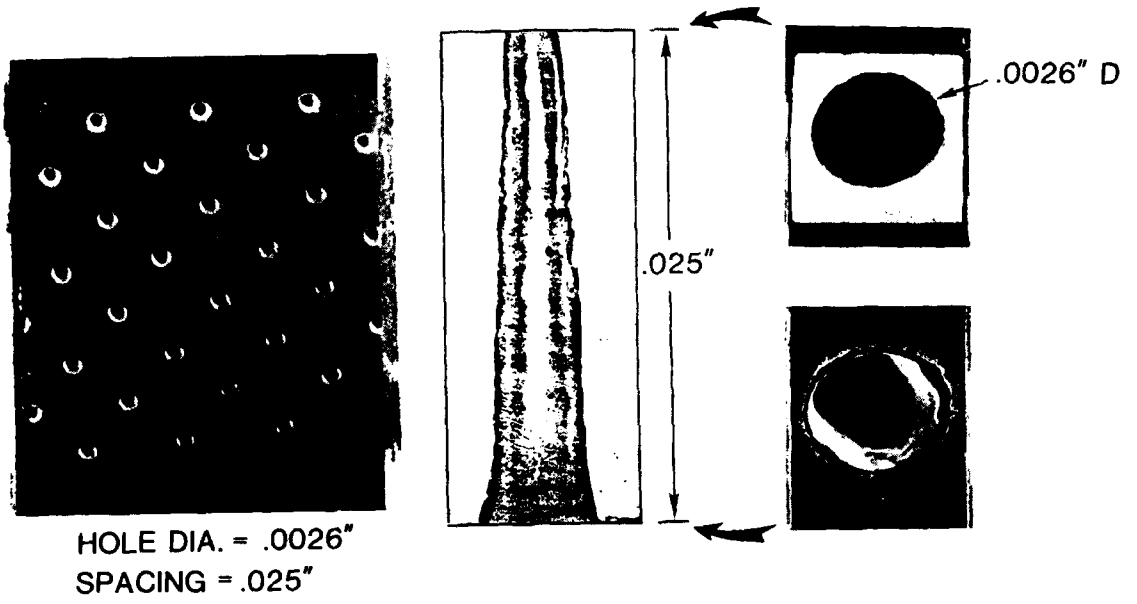


Figure 8. Microphotograph illustrating details of electron beam perforated holes

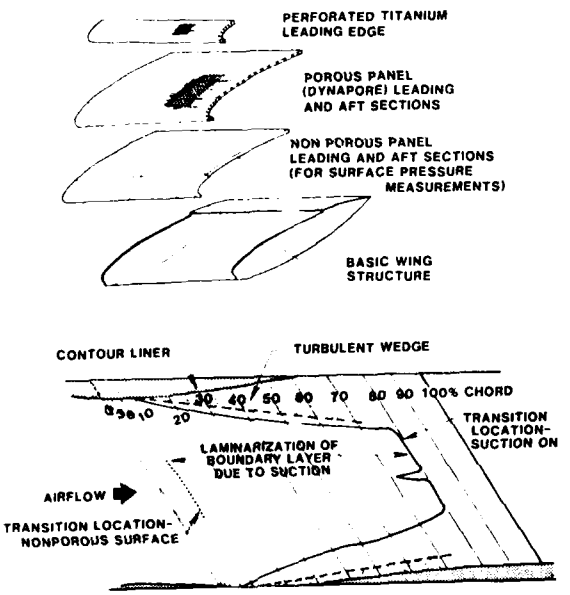


Figure 9. Douglas low-speed wind tunnel tests to evaluate suction surfaces



Figure 10. Microphotograph illustrating details of the dynapore suction surface

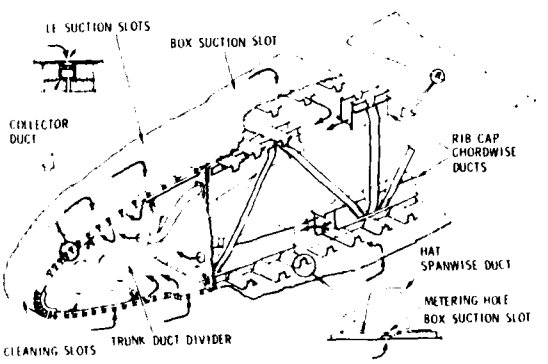


Figure 11. Lockheed LFC wing structural concept

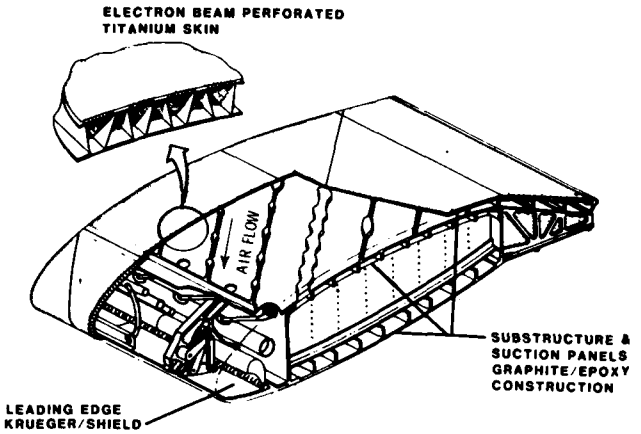


Figure 12. Douglas LFC wing structural concept



Figure 13. Lockheed leading edge wind tunnel test

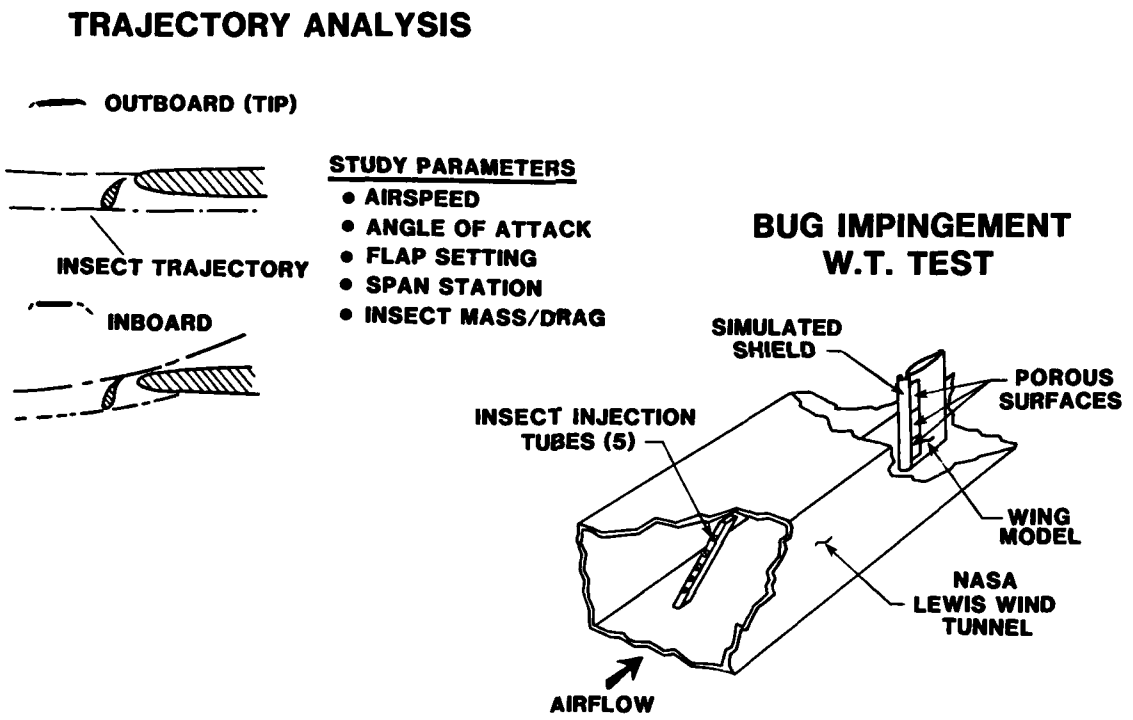


Figure 14. Douglas Krueger shield insect trajectory analysis and wind tunnel test

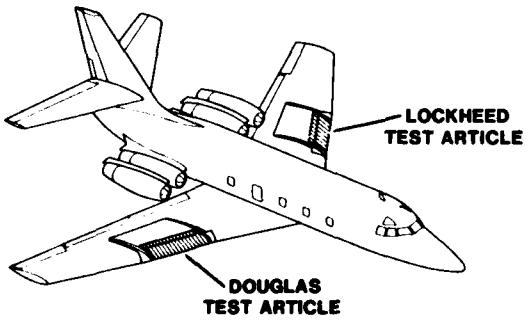


Figure 15. Leading edge flight test JetStar configuration

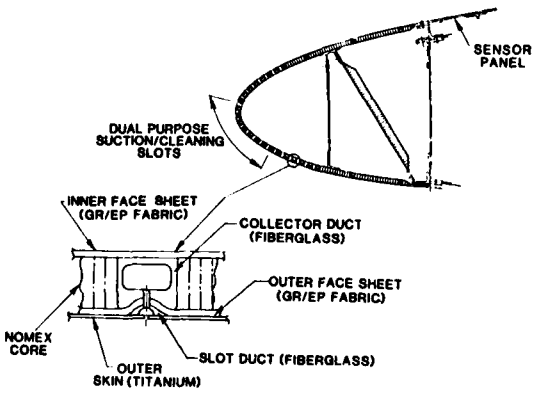


Figure 16. Lockheed leading edge flight test article

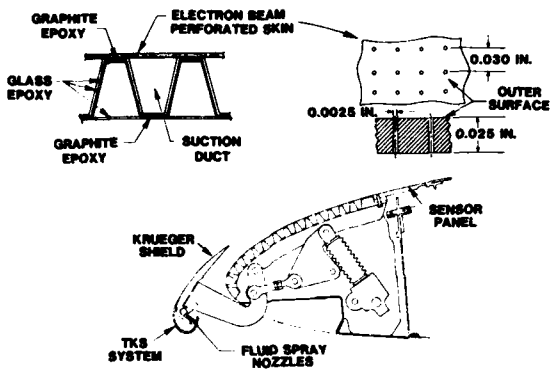


Figure 17. Douglas leading edge flight test article

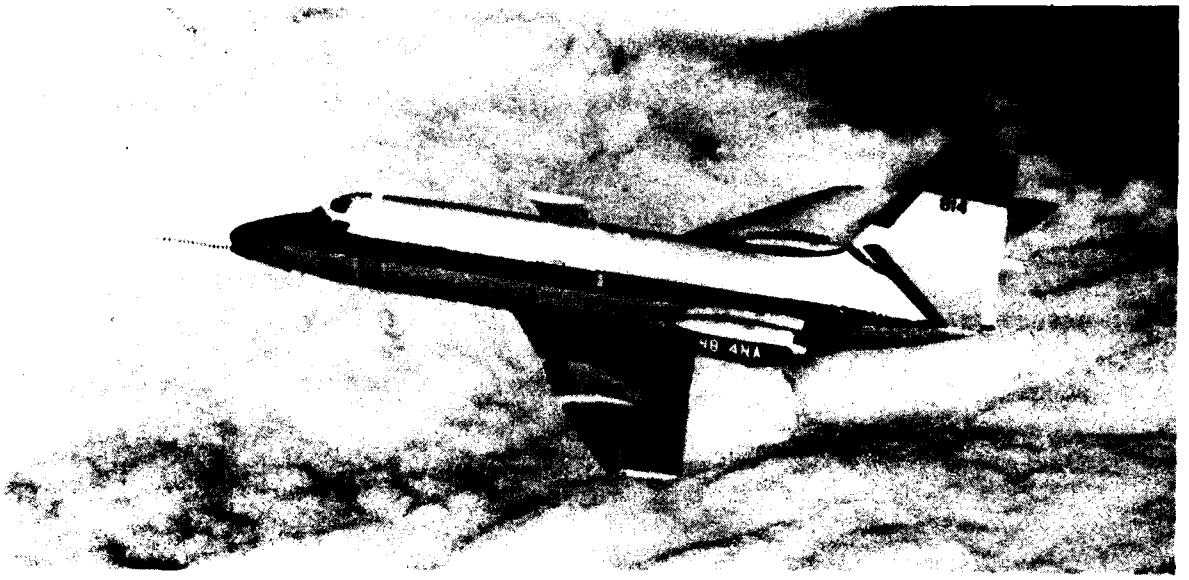


Figure 18. NASA DFRF LFC JetStar in flight

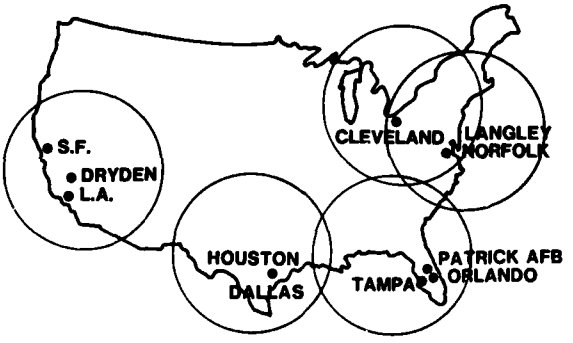
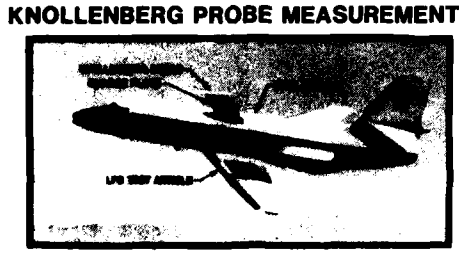
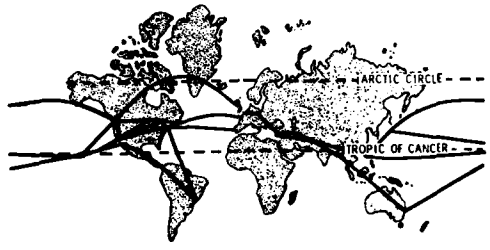


Figure 19. Simulated airline service home bases





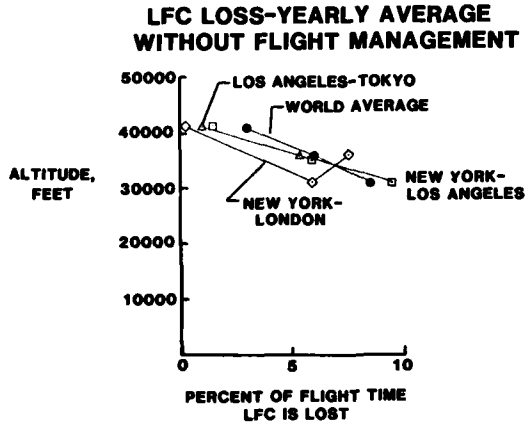


Figure 20. Instrumentation for measurement of cloud particles and estimates of their effect on LFC loss

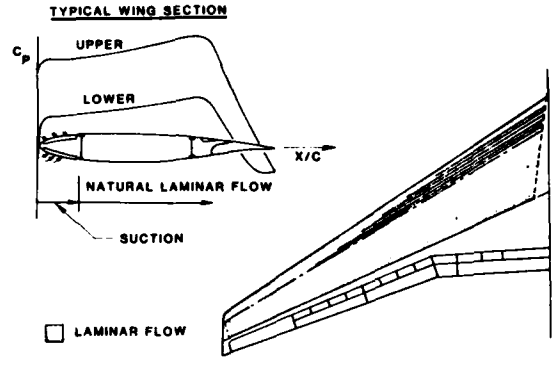


Figure 21. NLF/HLFC wing concept

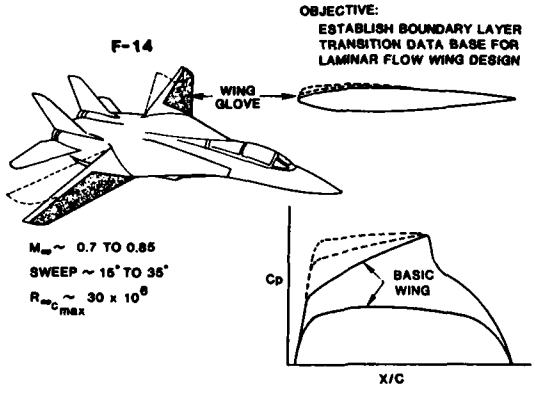


Figure 22. F-14 variable sweep transition flight experiment

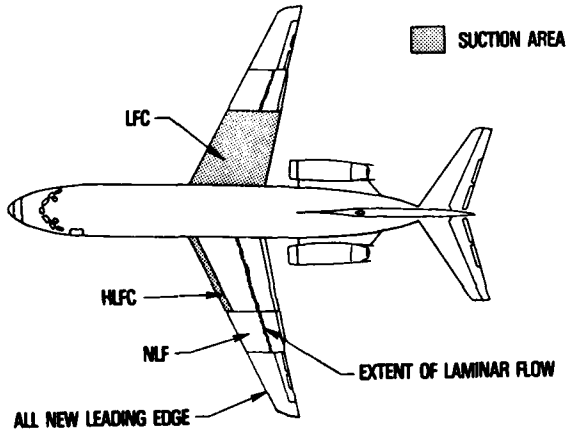


Figure 23. Laminar flow wing flight research aircraft

TURBULENT DRAG REDUCTION RESEARCH

D. M. Bushnell,* J. B. Anders,** M. J. Walsh,+ and
R. V. McInville++

NASA Langley Research Center
Hampton, Virginia 23665

AD-P004 066

ABSTRACT

Paper summarizes recent NASA research in the area of turbulent drag reduction for attached flows. The most promising passive techniques utilize non-planar geometry and indicate a possible combined net performance, the order of 20 percent. Of particular interest is the suitability of these devices for retrofit of existing vehicles. Research to optimize an active system involving tangential slot injection of low momentum (LFC) air indicates that free shear layers which are initially turbulent can be favorably controlled through use of rigid plates (large eddy-breakup devices). More conventional flow control approaches, such as narrow-band acoustic inputs, are evidently not effective for free mixing regions imbedded in thick turbulent layers. Experiments indicate that high frequency forcing of Emmons spots in the initial transition region to create small scale motions provides localized drag reductions, but net reductions are not yet available due to the high levels of forcing energy required.

NOTATION

C_D	total drag coefficient
C_f	local skin friction coefficient
D	total drag
h	device height in physical plane
h^+	riblet height in law-of-the-wall coordinates
ℓ	device chord
R	Reynolds number based upon device chord and local conditions
S	riblet spacing in physical plane
ΔS	longitudinal spacing for tandem LEBU devices
s^+	riblet spacing in law-of-the-wall coordinates
t	device thickness
u,v	longitudinal and normal velocity components
x	streamwise coordinate
y	coordinate normal to surface
∞	yaw angle
δ	boundary layer thickness
θ	momentum thickness

Subscripts

∞	free stream
FP	flat plate
HF	high frequency
o	device location
w	wall
1,2,3	device number

INTRODUCTION

Previous research on pressure drag reduction and roughness control decreased the zero-lift drag coefficient of most air and underwater bodies to the very low values typical of attached turbulent shear flow. Reduction of this residual skin friction drag is a major barrier to further optimization of cruise performance for most aerodynamic and hydrodynamic bodies. Typical benefits from a sizable reduction in viscous drag include design options for (a) increased range, (b) increased speed, (c) decreased size/cost, (d) decreased fuel usage, and/or (e) greater acceleration/maneuverability.

The present paper deals primarily with the problem of reducing turbulent skin friction drag on bodies (as opposed to wings) for conditions where conventional laminar flow control is either not feasible or inordinately difficult. Much of the background and status in the area of turbulent drag reduction is documented in Reference 1. Due to the absence of any sensible "theory" of "shear flow turbulence" the research in this area is, of necessity, primarily empirical (particularly in regard to actual performance to the nearest percent). The Turbulent Drag Reduction Research Program at NASA Langley currently includes a total of 12 different approaches. The present paper summarizes the status of five of these approaches: (1) large-eddy breakup devices, (2) riblets, (3) slot injection optimization, (4) control of Emmons spot generation, and (5) relaminarization through massive suction. Except for the Emmons spot work these methods all indicate the possibility of sizable net reductions in skin friction for laboratory conditions. Further tests and optimization at conditions approaching flight (higher R_ℓ, q_∞, u_∞) are still required before these approaches can be applied, either to new designs or as a retrofit.

It should be noted that the viscous flow control offered by drag reduction devices is also of interest for several other purposes including (1) increased sensor accuracy, (2) reduced wall pressure fluctuations, and (3) decreased size/drag of boundary layer diverters.

LARGE-EDDY BREAKUP DEVICES

Large-eddy breakup devices (LEBU's or turbulence manipulators or ribbons, as they are variously called) have demonstrated large reductions in local skin friction and net drag in air for some laboratory conditions. The early initial experiments at Langley[2] and the Illinois Institute of Technology[3] were followed by the dramatic results of Corke, et al[4] showing a 30 percent reduction in skin friction

*Head, Viscous Flow Branch, High-Speed Aerodynamics Division
**Leader, Turbulence Structure and Modeling Group, Viscous Flow Branch, High-Speed Aerodynamics Division
+Leader, Turbulent Drag Reduction Group, Viscous Flow Branch, High-Speed Aerodynamics Division
++North Carolina State University

with a 20 percent reduction in net drag over a downstream distance of 50-60 boundary-layer thicknesses. Follow-on experiments by Hefner, et al[5] at similar conditions produced smaller net reductions (6 percent) and indicated an apparent sensitivity to the details of the transition process. Bertelrud[6] also measured a smaller net reduction (5 percent) but with local skin-friction reductions of up to 40 percent. More recent works by Takagi,[7] Nguyen, et al,[8] and Mumford and Savill[9] have obtained maximum skin-friction reductions of 20 percent, 35 percent, and 33 percent, respectively, downstream of various large-eddy breakup devices.

Except for the experiments of Reference 8, which were conducted at a Reynolds number $R_\theta \sim 6000$ at the position of the large-eddy breakup device, all of the other LEBU experiments were conducted at relatively low device location Reynolds numbers ($R_\theta < 2300$). In addition, all of these experiments limited their downstream measurements to less than 100 boundary-layer thicknesses ($R_\theta < 6500$). These low Reynolds-number boundary layers probably still contain remnants of transition-related structures[10] and have not yet reached an "asymptotic" state. Therefore, the optimum large-eddy breakup configuration for these reported experiments might be dependent on this remnant of the transitional structure and consequently upon the details of the transition process peculiar to the individual tests. The most recent work at Langley extends the data base for large-eddy breakup devices to intermediate Reynolds numbers ($R \sim 3300$ at the device) with downstream effects measured to 330 boundary-layer thicknesses ($R \sim 17 \times 10^3$). Although such Reynolds numbers do not approach levels expected in actual flight application, they do bring the data closer to the "asymptotic" turbulent boundary-layer state. Additionally, these measurements, over the relatively large area downstream of the large-eddy breakup devices, permitted a determination of the relaxation behavior and skin-friction reduction effectiveness of the altered-turbulent boundary layer. This is extremely important because sufficiently long relaxation regions of reduced skin friction are necessary to compensate for the device drag of the candidate large-eddy breakup devices.

Optimization of the drag reduction performance of large-eddy breakup devices requires that the mechanisms involved in the drag reduction process be determined. A number of mechanisms have been proposed by the various experimentors. Reference 2 suggests that the large-eddy breakup devices "unwind" the large outer scales in the turbulent boundary layer. Corke, et al[4] suggest four possible mechanisms including: (1) restriction of the vertical velocity components by the horizontal elements of the large-eddy breakup devices; (2) suppression of the large scales due to the unsteady circulation around the elements of the large-eddy breakup devices (similar to the "unwinding" of Ref. 2); (3) generation of new scales in the outer part of the turbulent boundary layer by the vortices formed in the wakes of the large-eddy breakup devices; and (4) transfer and redistribution of energy from the turbulence to the mean flow. The more recent work of Reference 9 suggests a combined mechanism; i.e., the elements of the large-eddy breakup devices cut through the large-scale structures (hairpin vortices), as a result of the $v = o$ boundary condition at the surfaces of the LEBU elements, and introduce into the resulting disturbed layer a wake composed of closely-packed vortices which retain their identity downstream to 60 boundary-layer thicknesses. According to Reference 9, the interaction of these wake vortices, particularly the "counter vorticity" components, with the large-scale structure remnants ("chopped" hairpin vortices) provides the primary mechanism for reducing skin friction. In an attempt to determine and verify which of these mechanisms may be valid, Reference 11 employed a variety of large-eddy breakup devices with thin, flat, rectangular elements mounted either alone, in tandem, or in stacked arrays within a turbulent boundary layer. Device drag, local skin friction, net drag, and downstream relaxation lengths were obtained for each of the geometries investigated. A brief summary of this work is presented herein and a number of critical questions relating to the practical application of large-eddy breakup devices will be addressed. These include: the aforementioned effect of higher Reynolds numbers on the performance of the LEBU devices; the extent of the relaxation process downstream of the LEBU devices (Do the large-scale structures, once altered or destroyed, recur? If they do recur, how far downstream? When, if ever, does the local skin friction begin to increase?); the reduction of device drag and the mechanisms involved in the large-eddy breakup process.

Apparatus and Tests Conditions

The experiments were conducted on a splitter plate mounted horizontally in the test section of the Langley 2' x 3' Low-Speed Boundary Layer Channel. The plate was a 3.1 cm thick aluminum-honeycomb sandwich which spanned the 0.91 m width of the test section and extended from a point 0.3 m downstream of the test section entrance to the diffuser entrance, for a total length of 5.8 m. The leading edge of the splitter plate was a 6:1 ellipse. Smoke-wire flow-visualization studies were used to ensure that the leading-edge stagnation streamline was located on the working side of the plate and that no leading-edge separation was present. The boundary layer was tripped using a 5 cm wide strip of 30 grit, open-coat sandpaper postioned 5 cm downstream of the plate leading edge. Measurements with a surface pitot tube indicated boundary-layer transition occurred on the sandpaper itself. The general arrangement of the test plate is shown in Figure 1.

All of the various LEBU configurations were tested at a fixed station on the test plate ($x_0 = 61$ cm). The boundary-layer thickness at this station was 1.27 cm and the momentum thickness Reynolds number was 3300. The devices themselves consisted of thin, ribbon-like strips suspended parallel to the test surface within the turbulent boundary layer. The chords of the devices used in the present experiment were 1.27 cm ($\ell/\delta_0 = 1$) and 1.09 cm ($\ell/\delta_0 = 0.86$) with a thickness of 0.25 mm ($t/\delta_0 = 0.02$), although a limited number of tests were conducted with 0.508 mm thick devices ($t/\delta_0 = 0.04$). A tensioning mechanism was mounted outside the test section to hold the LEBU devices (which passed through holes in the test section wall). The devices experienced single-mode vibration when unsupported over the entire 0.91 m width of the test section, even at near yield-point tension. For this reason 0.5 mm thick vertical struts were placed between the test plate and the devices at positions 15 and 43 cm on each side of the tunnel centerline. Spanwise surveys $70\delta_0$ downstream showed no evidence of these supports.

The local skin-friction coefficients were obtained using the momentum balance technique. The boundary-layer surveys were made using a flattened pitot probe referenced to local freestream static pressure and driven by a streamlined, 3-axis traverse mechanism mounted to the roof of the test sec-

tion. The vertical position of the probe was determined to within ±0.5 mm using a 500 line optical encoder mounted on a traverse lead screw. A 40-60 point velocity survey was performed at each x-station to obtain the integral properties of the boundary layer. The repeatability of the momentum thickness measurements were determined to be ±0.5 percent. The tunnel freestream velocity was measured by a free-stream pitot-static probe at the entrance to the test section and was held constant at 40 m/s (±0.25 percent) for all tests. The spatial nonuniformity of the freestream velocity over the central 30 cm of the test section core, 1.0 m downstream of the test plate leading edge, was measured to be less than ±0.5 percent.

The flexible top wall of the test section was adjusted to give a nominally zero pressure gradient down the length of the splitter plate. The edges of the plate were sealed to prevent any mass transfer to the lower pressure channel under the plate. The two-dimensionality of the flow was checked by performing boundary layer surveys at several spanwise stations on the test plate. The results indicated a typical spanwise nonuniformity in momentum thickness of approximately ±5 percent. This variation, as a percentage of the mean, was constant from front to rear of the test plate.The variation of the local skin-friction coefficient down the plate was determined by graphically differentiating the growth in momentum thickness with x (i.e., $C_f = 2\, d\theta/dx$); both the pressure gradient and the convergence terms in the momentum equation were ignored. The results compared favorably with the familiar Ludwieg-Tillmann relation[12] for a zero pressure gradient, flat-plate boundary layer.

Results and Discussion

Stacked, multi-element arrays, tested extensively in Reference 4, were shown to dramatically alter and reduce the large-scale structures at low Reynolds numbers ($R_\theta \leq 5000$). As a starting point for the present intermediate Reynolds numbers ($3.3 \times 10^3 \leq R_\theta \leq 17 \times 10^3$) experiments, one-two-, and three-element devices were tested. The device drag in these initial experiments increased significantly with the number of elements in the stacked array. A corresponding decrease in the local skin-friction coefficient (lower θ-x slope) occurred immediately downstream of the devices. The local skin-friction reductions were found to persist downstream to a region $50\,\delta_0 \leq x \leq 120\,\delta_0$ depending on the number of elements. Permutations of this arrangement, such as omitting certain elements or translating the entire stack higher or lower in the boundary layer gave essentially the same results and none of the arrangements produced a net drag reduction (i.e., $\theta > \theta_{ref}$). The high device drag of the thin, rectangular plate elements in this initial study prompted an investigation of their drag characteristics. Figure 2 shows the drag coefficients measured (by wake surveys) for two different element thicknesses at several chord Reynolds numbers. The data of Reference 2 (which reported device drag as essentially laminar skin friction) are also shown for comparison. The present data indicate that the element drag is thickness dominated at the higher chord Reynolds numbers, except for the t = 0.102 mm ($t/\delta_0 = 0.008$) case which gave a level near laminar skin friction. These thinner devices, however,, tended to oscillate in single mode vibration unless additional vertical supports were installed and could not be used in the present experiment. Reference 9 concluded from flow visualization studies that devices with $t/\delta_0 = 0.01$ and 0.025 produced the same downstream effects on the visualized turbulence structure, and Reference 2 showed that devices with $t/\delta_0 = 0.02$ produced large increases in device drag. Apparently, then, the structure-altering-effectiveness of the devices is still present even when the device drag is low (the order of laminar skin friction) and higher device drag imposes an unnecessarily large penalty to be overcome in achieving a net drag reduction. Obviously, there must be some compromise between the competing requirements of structural rigidity and low device drag. However, data exist[13] which indicate that the levels of device drag associated with flat, rectangular plates can be reduced by a factor of almost three by using the proper low Reynolds number airfoil shape, even in flows of high turbulence. To assess the possible benefits of airfoil-like shapes, several of the flat elements were machined to have a thin, tapered trailing-edge shape as shown in Figure 3. The device drag for this shape was indeed reduced by more than 12 percent, but the local C_f (i.e., $d\theta/dx$) values immediately downstream of the devices were approximately 5 percent greater than that for the flat elements. Thus, the reduced device drag was also accompanied by a slightly reduced effectiveness in reducing local skin friction, indicating that the momentum defect produced by the devices does indeed contribute to the local C_f reduction although it is not the entire mechanism. Of course, the tapered trailing-edge elements are only a crude approximation of an airfoil shape and further tests using carefully designed, low Reynolds numbers airfoils are planned for the future.

Reference 14 indicates that the circulation around vertical, flat-plate stacks (cascades with a stagger angle of 0°) is less than that for a single flat plate, but increases with increasing stagger angle. Since circulation may be important in the drag-reducing effectiveness of the LEBU device, a staggered array (leading edges of each element swept downstream relative to the element below it) was tested with a stagger angle of 52°. No improvement over the vertical stack was found (data not shown). Since device circulation may also be changed by placing the elements at an angle to the flow, the effect of small positive and negative angles of attack on the momentum thickness growth was examined. Typical results for a tapered, three-element vertical stack indicated that small positive angles of attack gave roughly the same local C_f reduction as $\alpha = 0^0$, with no net drag reduction and small, negative α gave essentially no C_f reduction over the reference case and resulted in a large net drag increase (see Fig. 11, Ref. 11). In the negative α case the device wake is dominated by eddies rotating in the same direction as the large eddies in the natural boundary layer, thus reinforcing the large scales instead of suppressing them. Reference 4 presented smoke pictures of single elements at positive and negative angles of attack that clearly demonstrated an enhancement of the large-scale structures at negative α . The effect of positive α in the visualizations of Reference 4 appeared to be minimal, in agreement with the present measured data. It is unclear as to why an "unwinding" of the large scales did not occour for the $+\alpha$ case, especially in view of the dramatic change with $-\alpha$.

All of the configurations described thus far either produced large net drag increases or, at best, "broke even" by just balancing C_f reduction against device drag. In general, those devices that were most successful in reducing skin friction possessed a large device drag penalty. Of course, only modest C_f reductions will eventually yield a net drag reduction if continued downstream far enough, but the present data indicated that the downstream extent of lower skin friction seldom exceeded $100\delta_0$, not far enough to recoup the high device drag penalty. One configuration which was successful in reducing

device drag while enhancing C_f reduction at low Reynolds numbers was the tandem arrangement.[2-7,9,15] The downstream device is immersed in the wake of the upstream one and hence pays a lower device drag penalty. Figure 4 shows the downstream momentum thickness growth behind a series of tandem spacings. A net drag reduction is achieved within 60 δ_o for the 10 δ_o tandem spacing. Figure 5 shows the variation of the local C_f for the data of Figure 4. The local skin friction remains low for approximately 100 δ_o (a maximum of 26 percent lower for the 10 δ_o spacing), overshoots the reference plate values briefly, and then undershoots the reference value for the remainder of the test plate. One may infer from these data that if, indeed, large-scale suppression is responsible for the reduced skin friction the suppression is not permanent and the large scales return in the neighborhood of $x = 100\delta_o$. Dr. Robert Falco of Michigan State University has recently observed a similar effect using smoke flow visualization and in unpublished work has noted a strong return of the large scales at about $120\delta_o$. The overshoot, and subsequent undershoot with no apparent trend toward relaxation to flat plate values up to 330 δ_o indicate an area for further research. These variations in mean wall shear, if real, must indicate large quasi-permanent structural changes in the turbulent boundary layer.

The data in Figures 4 and 5 were obtained with the tandem devices at 0.8 δ_o. To investigate the effect of element height for tandem LEBU device performance the 10 δ_o tandem spacing devices were also tested at 0.55 δ_o and 0.30 δ_o heights. The integrated total drag is shown in Figure 6. The maximum net drag reduction occurs for the 0.8 δ_o height, even though a larger downstream region of skin-friction reduction was required to offset the higher device drag for this configuration. Within the limits of the available data, the optimum tandem configuration had a height of 0.8 δ_o and a spacing of 10 δ_o and produced a maximum net drag reduction of approximately 7 percent.

RIBLETS

Another effective drag reduction technique employs longitudinally-grooved surfaces having groove depths and spacings on the order of the turbulent wall-burst dimensions.[16-20] When the spacing (s^+) in law-of-the-wall variables was less than 30, References 18 and 20 reported maximum drag reductions of 8 percent for symmetric v-groove surfaces. This section examines the optimization and application of the riblet surfaces as well as the combined drag reduction performance of a riblet surface and a large-eddy breakup device (LEBU).

Micro-photographs of the cross section of four riblet surfaces are shown in Figure 7. The micro-photographs were obtained using a microscope which gave a 30 x magnification of the riblet cross section. Model 13R is an aluminum groove model; whereas, the grooves of Models DA3015B, 13M and 7M were formed on a thin vinyl sheet having an adhesive backing. Models 13R, DA3015B, and 13M had nominal dimensions of 0.18 mm. The exact riblet dimensions will be presented and discussed later in this section. The machined aluminum grooves as shown for Model 13R were typical of the riblet grooves manufactured and tested in References 16-18. The vinyl riblet manufacturing process, which has only recently become available, produced riblets with better dimension and geometry fidelity than the previously machined aluminum riblet models, especially for riblet dimensions less than 0.5 mm. The vinyl riblets with the adhesive backing are extremely interesting from an application point of view since these riblets could be applied as a retrofit on existing aircraft.

The drag data obtained for the symmetric v-groove riblets indicate that their drag reduction performance scales with groove height (h) and spacing (s) in law-of-the-wall variables (h^+, s^+). Figure 8 presents typical drag measurements for three of the riblet surfaces shown in Figure 7. The drag reduction performance is measured by D/D_{FP} which is the ratio of the net drag of the riblet surface to that of a flat plate. This drag reduction performance is shown as a function of s^+ where variations in s^+ were obtained by varying the freestream velocity. The smallest s^+ value for each model is obtained at the lowest operating velocity of the wind tunnel. As shown in Figure 8, Model 13R exhibits the best drag reduction performance, 7-8 percent drag reduction for $s^+ = 10\text{-}15$. It was found that the maximum drag reduction was quite sensitive to the value of h^+ for a value of $s^+ = 15$. All three of the models shown in Figure 8 were designed to have the height of the riblet equal to the spacing. As the dimensions indicate, the manufacturing process always gave a riblet height somewhat smaller than the spacing. This was particularly true for vinyl riblet Models 13M and 7M. As a result of the height reduction for Models 13M and 7M, the value of h^+ at $s^+ = 15$ was smaller than that for Model 13R. As the value of h^+ decreased for fixed s^+ the riblet drag reduction performance decreased. Therefore, the drag data in Figure 8 indicates that a maximum drag reduction of 7-8 percent would have been obtained for a vinyl riblet surface of $h^+ = s^+ = 15$.

The data on Figure 8 indicate that the high velocity data of Model 7M will give the same drag reduction as Model 13R at low velocity if $h^+ = s^+ = 15$ for both models. The highest stream velocity for the data shown on Figure 8 was 43 m/sec. Future plans include tests in a large subsonic tunnel at Reynolds numbers and speeds typical of CTOL aircraft application.

When considering possible aircraft applications, the sensitivity of the riblet drag-reduction performance to angle of yaw or misalignment with the local stream direction must be determined. Initial tests presented in Reference 18 indicated that a riblet with $h = 0.25$ mm was relatively insensitive to 15° yaw. These tests were conducted with machined aluminum models where the surface finish could vary between models. With the availability of the vinyl riblets, the yaw sensitivity of the riblets could be examined without the possible contamination of varying surface finishes. Figure 9 presents data for vinyl Model 13M where the vinyl film was applied to the test plates at three different angles of yaw, 0°, 15°, and 30°. The results show that the riblet drag reduction is relatively insensitive to angles of yaw up to 15°; however, when the yaw angle was increased to 30°, no drag reduction was measured. Also shown in Figure 9 is the drag data for aluminum Model 63 which had approximately the same physical dimensions as Model 13M but with the grooves machined at 15° angle of yaw. These data further confirm the insensitivity of the riblet drag reduction for yaw angles up to 15°.

All the riblets discussed so far in this section have been symmetric v-grooves. Various modifications of the symmetric v-groove riblet geometry have been tested in an attempt to improve the riblet drag reduction performance. Figures 10 and 11 indicate the effect of peak curvature and valley curva-

ture. The models used for comparisons in Figures 10 and 11 have the same height and spacing. Figure 10 shows that the peak curvature of Model DA3015B had little effect on the maximum riblet drag reduction, but it did seem to extend the operating s^+ or u_∞ range for drag reduction. Figure 11 shows th + valley curvature did increase the amount of drag reduction obtained previously with symmetric v-groove riblet Model 29. As indicated in Figure 11 the maximum drag reduction of Model 19 was 4 percent, which is smaller than that obtained for Model 13R with height more equal to the spacing. A model was machined with design dimensions approximately the same as Model 13R but with valley curvature. Due to the height-spacing ratio of 1, there was not enough room to put in significant valley curvature. As a result, the valleys of the model were flat instead of being curved. This demonstrates a practical problem with modifications to the physically small riblets required for drag reduction. Since the riblet dimensions will be even smaller in a flight application, it would be expected that modified v-groove geometries would be impractical and that a basic v-groove geometry with a height-to-spacing ratio of one (or perhaps greater) would be at least a locally optimum practical configuration.

An alternative approach to improve the riblet drag reduction performance is to combine the riblet concept with another approach. In the present study a riblet surface has been combined with a large-eddy breakup (LEBU) device. Reference 5 showed that the LEBU modifies the large scale outer structure and gives downstream local skin-friction reductions. A three-element LEBU was placed upstream of the riblet test surface. The elements were placed at y/δ= 0.211, 0.42, and 0.84. This is not an optimum LEBU configuration, but was utilized merely to oscertain if the riblet and LEBU local skin-friction reduction would be additive. Figure 12 presents drag data for a riblet surface with and without a LEBU mounted in front of the surface as well as a flat plate (sans riblet) with a LEBU, i.e., the standard LEBU case. Since the LEBU was mounted in front of the test plates, the drag levels for the LEBU configurations do not include the device drag of the LEBU. The area averaged drag data indicate that the riblet drag reduction is nearly additive to the drag reduction downstream of the LEBU. This result is probably reasonable since the LEBU operates on the large-scale outer structure and only indirectly upon the wall structure (see Ref. 4); whereas the riblet operates directly on the wall region. In fact, flow visualization studies in Reference 19 found that smoke lingered for an inordinately long time in the riblet valleys. The turbulence data of Reference 20 and the flow visualization of Reference 19 seem to indicate that the riblets thicken the sublayer but do not modify the bursting process.

OPTIMIZATION OF SLOT INJECTION DRAG REDUCTION THROUGH FREE SHEAR LAYER CONTROL

A technique which has proven effective in reducing skin friction drag is the injection of low-momentum fluid, through a rearward facing slot, into the near-wall region of a turbulent boundary layer flow.[21,22] A typical device configuration is shown in Figure 13. The lower fluid velocity (relative to the incoming flow) downstream of the injection plane produces a region of decreased surface drag. At the interface of the slot and boundary layer flows a mixing layer develops and begins to spread as it evolves downstream. Once this region reaches the wall, viscous drag levels return monotonically to their original values. Thus, if the spread rate of the mixing layer could be inhibited so that its point of contact with the wall is shifted downstream, greater drag reductions could be realized.

Experimental studies[23-27] have shown that such mixing regions are characterized by the presence of large scale vortical structures formed by the roll-up of the developing shear layer. The growth and interaction of these entities can determine, to a large extent, the spatial and temporal evolution of the flow field. Specifically, the coalescence of two or more of these relatively discrete vortices into a single larger structure has been found to be the primary source of mixing layer growth in some case.[25,27] If these vortex mergings can be inhibited, or if smaller vortices can be produced initially, the growth rate can be decreased.

Several techniques have been found to be effective in altering the vortex formation and interaction processes. The size of the vortical structures formed initially can be decreased by making the splitter plate separating the two flows as thin as possible.[28] The introduction of small scale turbulence into the flow field can also interfere with the large scale interactions.[29] Broad-band noise from rotor blades has been significantly reduced by placing serrations on the leading edge of the blades.[30] Since the major source of this noise is vortex shedding, the serrations obviously must have had some effect on this process. A shear layer can also be extremely sensitive to periodic disturbances, especially near its origin. The ability of acoustic radiation to alter the downstream evolution in certain circumstances has been demonstrated conclusively.[31-39] Perturbations near the characteristic roll-up frequency of the shear layer tend to produce very rapid growth near the origin while those an order of magnitude higher in frequency tend to suppress the growth rate.[31-36]

The present work investigates the applicability of these various techniques to the manipulation of the mixing layer growth rate in a practical slot injection configuration. In addition, large-eddy breakup devices (LEBU's) were placed in the incoming boundary-layer flow in order to assess their effect in altering the mixing rate of a turbulent free shear layer.

Experimental Procedures

All experimental work was conducted in the 15-inch low turbulence wind tunnel of the Viscous Flow Branch, High-Speed Aerodynamics Division, NASA Langley Research Center. This tunnel is an open-loop system with a maximum velocity of 36.5 m/s. The test section has a 38.1 cm square cross section which is 91.4 cm in length and is located approximately 183 cm from the end of the upstream contraction. The pressure gradient in this region can be adjusted by means of a moveable upper wall.

For the present work, the tunnel was modified to accommodate the slot flow as shown in Figure 13. The floor upstream of the test section was raised by means of a 1.59 cm plexiglas slab. A manifold box was constructed of 0.638 cm plexiglas and positioned underneath the test section floor to provide a means of introducing the slot flow uniformly across the span. Compressed air was brought into the bottom of this chamber through two 2.54 cm diameter stainless steel tubes. This air then passed through two plexiglas baffle plates, several layers of metal screening, and an aluminum two-dimensional nozzle with a 4.8 to 1 contraction ratio. Slot flow velocity was controlled by a pressure regulator on the

supply lines. A 0.159 cm thick aluminum plate was attached to the upper half of the nozzle to form the slot lip. This plate was interchangeable to allow variations in the geometry of the slot lip trailing edge. The slot height was kept constant in all cases at 1.59 cm.

To provide acoustic excitation, two 45-watt horn drivers were mounted underneath the test section floor with their outputs channeled through a 0.159 cm slot directly beneath the injection plane.

The large-eddy breakup (LEBU) devices were formed from 0.025 cm thick blue steel stretched across the tunnel span at a point 16-inches upstream of the slot lip. Openings were cut through the plexiglas tunnel walls to accommodate these devices and an aluminum framework was constructed around the tunnel to hold them in tension.

All experiments were conducted at a free stream velocity of 18.3 m/s and a slot velocity of 5.5 m/s. A spanwise survey of the incoming boundary layer along a line 5.1 cm upstream of the slot lip showed no more than a 10 percent (peak to valley) variation in momentum thickness. A similar survey of the slot flow along the injection plane showed no more than a 5 percent spanwise variation. The test section pressure gradient for these flow velocities was checked by means of a series of static pressure taps located halfway up one sidewall. These taps were located 2.54 cm apart for the first 15.2 cm downstream and 15.2 cm apart for the next 76 cm. While it was not possible to totally eliminate this pressure gradient, its maximum value was reduced to about 0.15 percent of free stream dynamic pressure per inch of streamwise distance.

To determine the spread rate of the mixing region formed by the merging boundary layer and slot flows, velocity profiles were taken at several locations downstream of the slot exit plane. These profiles were obtained using a 0.152 cm diameter pitot-static probe.

Results and Discussion

The first area of investigation concerned the effects of geometry modifications to the slot lip trailing edge. The base case, for comparison purposes, was taken to be a plain flat trailing edge with square corners. The various modifications tested are shown in Figure 14. These consisted of a trailing edge with rounded corners, a tapered trailing edge, and trailing edges with slots, serrations, and perforations ranging in size from 0.159 cm to 0.635 cm. In none of these cases was there found to be any significant differences in the spread rate of the mixing layer.

The effects of acoustic input to the mixing layer origin was next explored. Frequencies in the range from 80 Hz to 1000 Hz were used, corresponding to Strouhal numbers, based on initial momentum thickness and mean flow velocity, in the range from 0.034 to 0.286. Sound pressure levels at the slot lip were the order of 105 dB. In all cases, a plain flat trailing edge with square corners was used. Again, no significant differences in downstream spread of the mixing layer was detected at any forcing frequency (flapping trailing edges were also tried, also without any apparent success).

The lack of any noticeable effects for the techniques considered thus far is attributed to the dominating influence of the fully turbulent incoming boundary layer. These results tend to confirm the observations of some investigators[37-39] that the suppression of the mixing layer growth rate by acoustic excitation occurs only for initially laminar flows. If this is indeed the case, it would appear that the only way to alter the downstream evolution of the mixing region in the usual slot injection case would be to change the turbulent structure of the incoming turbulent boundary layer itself.

To investigate the effectiveness of such an approach, three LEBU device configurations were separately placed into the flow upstream of the slot lip. As mentioned previously, these consisted of lengths of 0.025 cm thick blue steel stretched across the span of the tunnel 41 cm upstream of the slot exit. The boundary-layer thickness δ at this point was 2.54 cm. Three device configurations were tested -- a tandem arrangement with both LEBU's 0.8 δ above the floor and positioned 6.5 δ apart in the streamwise direction; a stacked configuration with two LEBU's located 0.6 δ and 0.8 δ above the floor; and a stacked configuration with three devices placed at 0.4δ, 0.65δ, and 0.9δ. All LEBU's had a 2.54 cm chord. These configurations are shown in Figure 15. Velocity profiles for each case, taken at a point 41 cm downstream of the slot exit (corresponding to 13 slot exit δ boundary layer thicknesses) are shown in Figure 16. As can be seen, all three produced noticeable decreases in the velocity near the wall with the three stacked devices giving the most pronounced effect. Thus, it would appear that the use of LEBU's in the boundary-layer upstream of the slot injection location could make this technique more effective. However, more work is needed to confirm this speculation and to assess/reduce the penalties involved in the device drag of the LEBU's themselves. The observation that a boundary layer device (LEBU) can be used (indeed is required) to alter free mixing rates for flows with thick external boundary layers may have important technological implications far beyong the present slot injection case.

SKIN FRICTION REDUCTION THROUGH EMMONS SPOT FORCING

The various results from the large-eddy breakup device research indicates that reduction in size of the outer eddies reduces wall skin friction. For the region immediately downstream of transition an alternate technique can be employed to produce the requisite smaller sized eddies. Rather than allowing the large outer eddies to form and then breaking them up with a suitable device, this alternative technique seeks to alter their initial formation process through control of the production of Emmons spots.

From the relaxation studies downstream of large-eddy breakup devices, this alternative approach would only be expected to reduce drag the order of 100 δ downstream of the end of transition. Since the δ scale in this case is the relatively small value at the nominal end of transition; the physical distance over which the drag would be reduced would be quite small for most engineering applications. However, the technique may be of interest for certain low Reynolds numbers or specialized applications. The basic concept is to restrict the usual Emmons spot growth by forcing nearly "instantaneous transition." If a large enough disturbance is introduced near the beginning of transition at high fre-

quency (Strouhol number the order of 1) through discrete but closely spaced spanwise sites, a continuous train of small scale Emmons spots should be produced. Due to the close packing imposed by the forcing there is no longer a "laminar sea" in which the spot can grow and develop large scale motions. The friction drag is increased initially due to the foreshortening of the transition process but a compensating lower drag region would be expected further downstream (at least over a distance the order of 100δ). It should be noted that stationary spanwise disturbances (e.g., roughness elements) would not be expected to produce the same phenomena, due to the well-known "calming effect" in the wake of an Emmons spot. A high intensity dynamic trigger is probably required.

The existing data for this alternative large-eddy drag reduction approach (closely spaced high frequency exciters placed at the beginning of the nominal transition process) is documented in Reference 40. Emmons spots were forced using high intensity acoustic drivers acting through a spanwise row of closely spaced (O(δ)) small holes located near the nominal beginning of transition. The measured average skin friction (measured with a large drag balance downstream of the driver section) is shown on Figure 17 as a function of the forcing frequency. The maximum drag reduction (area averaged) is obtained at a Strouhol number the order of 2 based upon boundary layer thickness at the forcing location. Flow visualization using a horizontal (spanwise) smoke wire indicated smaller outer scales for the forced case compared to the standard case (holes taped over). The level of the observed drag reduction (O(15%)) is reasonable considering that a sizable portion of the 20 percent to 30 percent local skin friction reduction measured downstream of large-eddy breakup devices is due to the momentum deficit of the device. Such a momentum deficit is absent, at least to first order, in the acoustic (wall) forcing case.

Unfortunately, the energy required to force the Emmons spots in the drag reduction mode is much larger than the estimated "return on investment" (downstream net drag reduction) and therefore, unless low loss dynamic Emmons spot triggers can be developed/invented this alternative large-eddy reduction approach is of possible interest only for viscous flow control purposes other than net drag reduction.

RELAMINARIZATION USING MASSIVE WALL SUCTION

This method is of particular interest to the CTOL fuselage drag problem. The forward portion of the fuselage is typically characterized by a host of excressences, including windshield wipers, bugs, probes, attachment points and access hatches. The basic concept is to "writeoff" this forward portion of the flow as transitional/turbulent and subsequently relaminarize the boundary layer downstream of the cockpit using massive suction. Maintenance suction and/or wall cooling would be required further downstream to maintain the laminar condition.

Pfenninger[41] successfully carried out a series of relaminarization experiments applicable to this concept but found it necessary to ingest more than the entire mass flow in the boundary layer (up to 1.5δ) to capture all of the "superlayer" fluctuating vorticity. Suction of less than this amount compromised and complicated the downstream maintenance LFC problem. The key ingredients to maximizing the overall system efficiency of this approach are (1) ingesting the minimum mass flow consistent with downstream maintenance LFC and (2) obtaining maximum pressure recovery in the suction inlet.

There exist several possibilities for optimizing fuselage relaminarization. The most obvious is to place the massive suction forward of the minimum pressure region on the fuselage. This placement performs two functions: (a) places the initial (thin and tender) laminar flow region in a stabilizing favorable pressure gradient and (b) should lower the required pumping power (and possibly allow for selfbleed to the side of the fuselage where slot injection might be utilized in regions where laminar flow could not readily be maintained, such as the wing juncture contamination zone). Another optimization possibility is to design the aircraft for minimum disruption of fuselage LFC from the wing-induced pressure field (providing this could be accomplished without unduly altering the wing efficiency). Historically, alterations in the wing and fuselage design for interference have been in favor of the wing. As a "blue sky" possibility, the maintenance laminar flow could be made somewhat easier on passenger aircraft by replacement of the windows with a smooth skin and providing the passengers with a small video screen giving a pilot's-eye-view (or a view in any other direction) using the recent advances in micro-electronics.

A final optimization possibility is to "preprocess" the fuselage boundary layer through a large-eddy breakup device which should, by altering the superlayer structure and thickness, reduce the suction mass flow requirements and therefore possibly increase the overall system efficiency. Research on this last possibility is currently underway at NASA Langley. Closing arguments in favor of downstream fuselage relaminarization include (a) possibility for use of cooling (from liquid H_2 fuel) as a maintenance-LFC technique (not feasible for swept wings (Ref. 42)), (b) greatly reduced problems from "insect remains," and (c) reduced roughness sensitivity compared to the swept wing case (Ref. 43).

CONCLUSIONS

Continuing studies of five methods for reducing turbulent skin friction drag on bodies/fuselages indicate the following (for small pressure gradient, low speed boundary layers):

(1) Large eddy-breakup devices can reduce local skin friction up to 33 percent for downstream distances the order of 100 δ.

(2) Langley experiments indicate overall or net drag reductions the order of 8 percent using tandem arrangements. Larger net reductions are contingent upon reduction of device drag.

(3) V-groove riblets produce net drag reductions the order of 8 percent when the height is approximately equal to the spacing and the spacing is the order of 15 law-of-the-wall units.

(4) The riblet performance (drag reduction) scales on law-of-the-wall variables, and is apparently insensitive to boundary layer transition history and yaw (up to 15°).

(5) Self-adhesive thin vinyl sheets with the riblet geometry molded into the surface perform as well as metal models and offer the possibility of a simple, relatively inexpensive means of retrofitting existing vehicle surfaces.

(6) Limited tests indicate that the performance of riblets and LEBUs is nearly additive.

(7) Tests employing dynamic control of Emmons spot formation indicate local drag reductions the order of 15 percent. However, the energy to trigger/control the flow is, up to this point in time, far larger than any "savings" due to the drag reduction.

(8) Tangential slot injection or a wall wake (using a "low-loss" air source such as LFC suction air from the wings) can be optimized for greater local drag reduction performance using large-eddy breakup devices inserted into the external boundary layer. Attempts to control the slot mixing layer using acoustic or fixed geometric inputs at the slot lip were not successful, presumably due to dominance of the slot mixing process by the external turbulent boundary layer flow structures.

REFERENCES

1. Bushnell, D. M.: Turbulent Drag Reduction for External Flows. Presented at the AIAA 21st Aerospace Sciences Meeting, Reno, Nevada, January 10-13, 1983. Paper No. 83-0227.
2. Hefner, J. N.; Weinstein, L. M.; and Bushnell, D. M.: Large-Eddy Breakup Scheme for Turbulent Viscous Drag Reduction. Viscous Flow Drag Reduction, Vol. 72. Presented at the Symposium on Viscous Drag Reduction, Dallas, Texas, November 1979.
3. Corke, T. C.; Guezennec, Y.; and Nagib, H. M.: Modification in Drag of Turbulent Boundary Layers Resulting from Manipulation of Large-Scale Structures. Viscous Flow Drag Reduction, Vol. 72. Presented at the Symposium on Viscous Drag Reduction, Dallas, Texas, November 1979.
4. Corke, T. C.; Nagib, H. M.; and Guezennec, Y. G.: A New View on Origin, Role and Manipulation of Large Scales in Turbulent Boundary Layers. Illinois Institute of Technology, NASA CR-165861, February 1982.
5. Hefner, J. N.; Anders, J. B.; and Bushnell, D. M.: Alteration of Outer Flow Structures for Turbulent Drag Reduction. Presented at the AIAA 21st Aerospace Sciences Meeting, Reno, Nevada, January 10-13, 1983. Paper No. 83-0293.
6. Bertelrud, A.; Truong, T. V.; and Avellan, F.: Drag Reduction in Turbulent Boundary Layers Using Ribbons. AIAA 9th Atmospheric Flight Mechanics Conference, San Diego, California, August 9-11, 1982. Paper No. 82-1370.
7. Takagi, S.: The Structure of Turbulent Boundary Layer Controlled by the Plates. Proceedings of the 15th Turbulence Symposium, Tokyo, Japan, July 1983.
8. Nguyen, V. D.; Dickinson, J. L.; Anderson, J.; Haeberle, D.; Larose, G.; Boisvert, L. M.; Chalifour, Y.; and Jaen, Y.: Paper presented at the AIAA 22nd Aerospace Sciences Meeting, Reno, Nevada, January 9-12, 1984. Paper No. 84-0346.
9. Mumford, J. C.; and Savill, A. M.: Parametric Studies of Flat Plate, Turbulence Manipulators Including Direct Drag Results and Laser Flow Visualization. Paper presented at ASME Symposium on Laminar/Turbulent Boundary Layers: Control, Modification and Marine Applications ETCE Conference, New Orleans, Lousiana, February 1984.
10. Zilberman, M.; Wygnanski, I.; and Kaplan, R. E.: Transitional Boundary Layer Spot in a Fully Turbulent Environment. IUTAM Sumposium, 1976. Physics of Fluids, Vol. 20, No. 10, Pt. II, October 1977, pp. S258-S271.
11. Anders, J. B.; Hefner, J. N.; and Bushnell, D. M.: Performance of Large-Eddy Breakup Devices at Post-Transitional Reynolds Numbers. Paper presented at the AIAA 22nd Aerospace Sciences Meeting, January 9-12, 1984, Reno, Nevada. Paper No. 84-0345.
12. Ludwieg, H.; and Tillmann, W.: Investigations of the Wall Shearing Stress in Turbulent Boundary Layers. NACA TM 1285, 1950.
13. Miley, S. J.: A Catalog of Low Reynolds Number Airfoil Data for Wind Turbine Applications. Report No. RFP-3387, UC-60, Dept. of Aerospace Engineering, Texas A&M University, College Station, Texas, February 1982.
14. Klein, A.: Aerodynamics of Cascades. AGARDograph No. 220, 1977. Translated and revised from the original German, Aerodynamik Der Schaufelgitter by Prof. Dr.-Ing N. Scholz.
15. Sandborn, V. A.: Aerodynamics-Control of Surface Shear Stress Fluctuations in Turbulent Boundary Layers. Report No. CER-80-81-VAS-46, Dept. of Civil Engineering, Colorado State University, Fort Collins, Colorado, April 1981.
16. Walsh, M. J.; and Weinstein, L. M.: Drag and Heat Transfer on Surfaces With Small Longitudinal Fins. AIAA 11th Fluid and Plasma Dynamics Conference, Seattle, Washington, July 11-12, 1978. AIAA Paper No. 78-1161.
17. Walsh, M. J.: Drag Characteristics of V-Groove and Transverse Curvature Riblets. Viscous Drag Reduction, Progress in Astronautics and Aeronautics, Vol. 72, Gary R. Hough, Editor, 1980.
18. Walsh, M. J.: Turbulent Boundary Layer Drag Reduction Using Riblets. AIAA 20th Aerospace Sciences Meeting, Orlando, Florida, January 11-14, 1982. AIAA Paper No. 82-0169.
19. Hooshmand, A.; Youngs, R. A.; Wallace, J. N.; and Balint, J. L.: An Experimental Study of Changes in the Structure of a Turbulent Boundary Layer Due to Surface Geometry Changes. AIAA 21st Aerospace Sciences Meeting, Reno, Nevada, January 10-13, 1983. AIAA Paper No. 83-0320.
20. Walsh, M. J.; and Lindemann, A. M.: Optimization and Application of Riblets for Turbulent Drag Reduction. AIAA 22nd Aerospace Sciences Meeting, Reno, Nevada, January 9-12, 1984. AIAA Paper No. 84-0347.
21. Hefner, J. N.; and Bushnell, D. M.: Slot Injection for Skin Friction Drag Reduction. Special Course on Concepts for Drag Reduction, AGARD-R-654, June 1977, pp. 3.1-3.12.
22. Howard, F. G.; Hefner, J. N.; and Srokowski, A. J.: Multiple Slot Skin Friction Reduction. Journal of Aircraft, Vol. 12, No. 9, 1975, pp. 753-754.
23. Brown, G. L.; and Roshko, A.: On Density Effects and Large Structure in Turbulent Mixing Layers. Journal of Fluid Mechanics, Vol. 64, 1974, pp. 775-815.
24. Dimotakis, P. E.; and Brown, G. L.: The Mixing Layer at High Reynolds Number: Large Structure Dynamics and Entrainment. Journal of Fluid Mechanics, Vol. 78, 1976, pp. 535-560.

25. Winant, C. D.; and Browand, F. K.: Vortex Pairing: The Mechanism of Mixing Layer Growth at Moderate Reynolds Number. Journal of Fluid Mechanics, Vol. 63, 1974, pp. 237-255.
26. Browand, F. K.; and Weidman, P. D.: Large Scales in the Developing Mixing Layer. Journal of Fluid Mechanics, Vol. 76, 1976, pp. 127-145.
27. Ho, C. M.; and Huang, L. S.: Subharmonics and Vortex Merging in Mixing Layers. Journal of Fluid Mechanics, Vol. 19, 1982, pp. 443-473.
28. Matthews, L.; and Whitelaw, J. H.: Plane Jet Flow Over a Backward Facing Step. Proceedings of the Institution of Mechanical Engineers, Vol. 187, 38/73, 1973, pp. 447-454.
29. Browand, F. K.; and Latigo, B. O.: The Growth of the Two-Dimensional Mixing Layer From a Turbulent and Non-Turbulent Boundary Layer. The Physics of Fluids, Vol. 22, 1979, pp. 1011-1019.
30. Arndt, R. E. A.; and Nagel, R. T.: Effect of Leading Edge Serrations on Noise Radiation From a Model Rotor. AIAA Paper No. 72-655, 1972.
31. Rockwell, D. O.: The Macroscopic Nature of Jet Flows Subjected to Small Amplitude Periodic Disturbances. Sonochemical Engineering, Vol. 67, No. 109, 1971, pp. 99-107.
32. Vlasov, Ye . V.; and Ginevskiy, A. S.: Bilateral Character of Acoustic Action on Free Turbulent Jets. Turbulentnyye Techeniya, Nauka Press, 1974, pp. 149-153.
33. Vlasov, Ye. V.; and Ginevskiy, A. S.: Generation and Suppression of Turbulence in an Axisymmetric Turbulent Jet in the Presence of an Acoustic Influence. Izvestiya Akademiya Nauk SSSR, Mekhanika Zhidkosti i Gaza, No. 6, 1973, pp. 37-43.
34. Borisov, Yu. Ya.; and Rozenfel'd, E. J.: Action of Acoustic Oscillations on Flow Stability and Structure. Akusticheskii Zhurnal, Vol. 17, No. 2, 1971, pp. 179-198.
35. Vlasov, Ye. V.; and Ginevskiy, A. S.: Acoustic Effect on Aerodynamic Characteristics of a Turbulent Jet. AN SSSR, Izvestiya Mekhanika Zhidkosti i. Gaza, 1969.
36. Istaev, S. J.; and Tarasov, S. B.: On the Effect of an Acoustic Field, Directed Along a Jet Axis, on the Jet. Izvestiya Akademii Nauk SSSR, Mekhanika Zhidkosti i Gaza, No. 2, 1971, pp. 164-167.
37. Roffman, G. L.; and Toda, K.: A Discussion of the Effects of Sound on Jets and Fluidic Devices. Journal of Engineering for Industry, November 1969, pp. 1161-1167.
38. Zaman, K. B. M. Q.; and Hussain, A. K. M. F.: Turbulence Suppression in Free Shear Flows by Controlled Excitation. Report FM-7, Dept. of Mechanical Engineering, University of Houston, November 1979.
39. Pavel'ev, A. A.; and Tsyganok, V. I.: Influence of Acoustics and the Flow Regime in the Boundary Layer on Nozzle Walls on the Mixing Layer of an Immersed Jet. Izvestiya Akademii Nauk SSSR, Mekhanika Zhidkosti i Gaza, No. 6, 1982, pp. 36-42.
40. Goodman, W. L.: Emmons Spot Forcing for Turbulent Drag Reduction. Acceped for publication in the AIAA Journal.
41. Pfenninger, W.; and Bacon, John W., Jr.: Investigation of Methods for Re-Establishment of a Laminar Boundary Layer from Turbulent Flow. Prepared under Navy, Bureau of Naval Weapons, Contract No. 63-0762-c, Report Number NOR 65-48, February 1965.
42. Lekoudis, S.: The Stability of the Boundary Layer on a Swept Wing With Wall Cooling. AIAA 12th Fluid and Plasma Dynamics Conference, Williamsburg, Virginia, July 23-25, 1979. AIAA Paper No. 79-1495.
43. Pfenninger, Werner: Laminar Flow Control Laminarization. AGARD Report No. 554. Special Course on Concepts for Drag Reduction. June 1977, pp. 3.1 - 3.75.

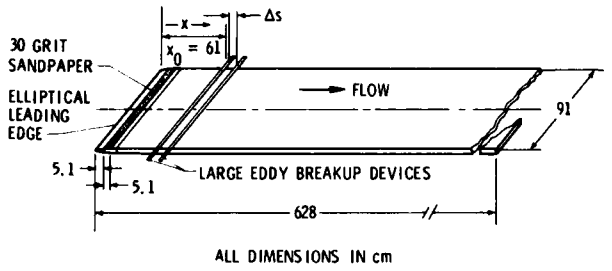


Fig. 1 LEBU test configuration.

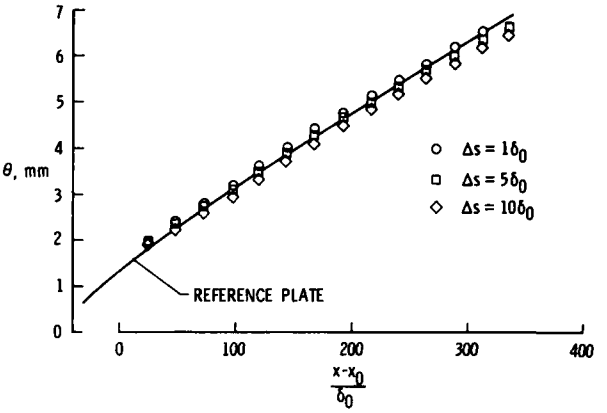


Fig. 4 Performance of tandem LEBU elements.

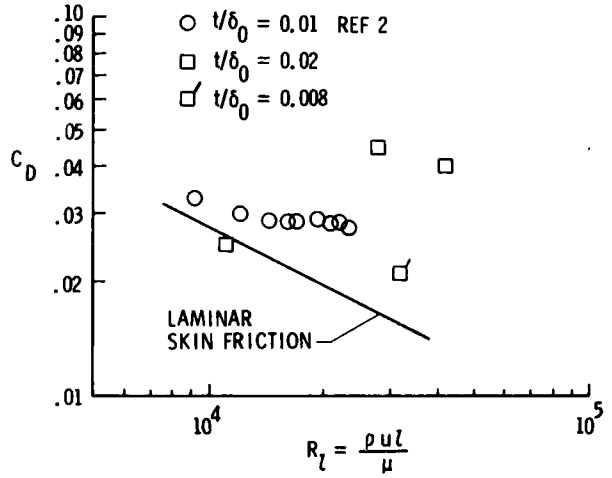


Fig. 2 LEBU element-device drag

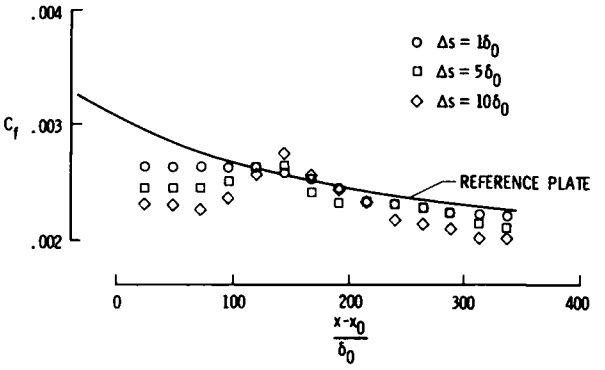


Fig. 5 Local skin friction distribution downstream of tandem LEBU arrays.

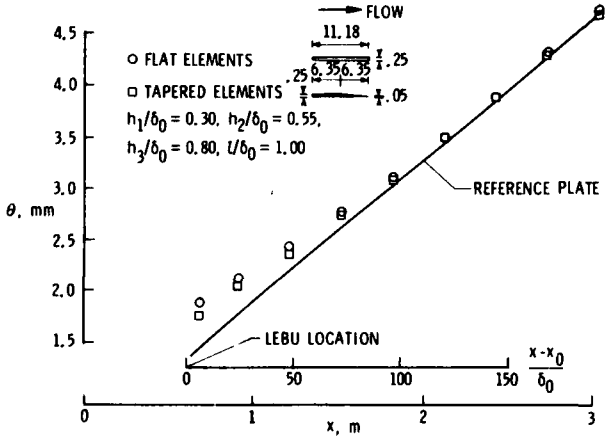


Fig. 3 Drag reduction performance of stacked LEBU elements for bluff and tapered trailing edges.

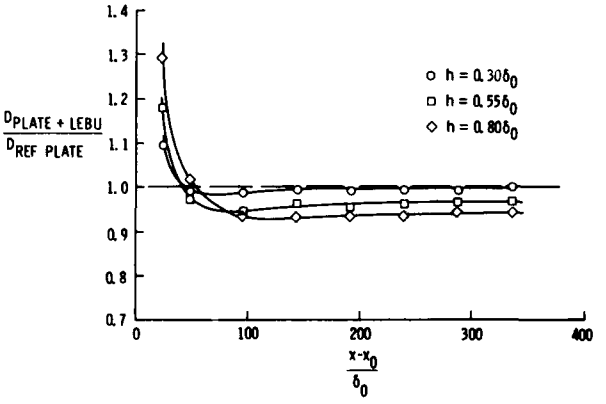


Fig. 6 Net drag performance for tandem LEBU arrays.

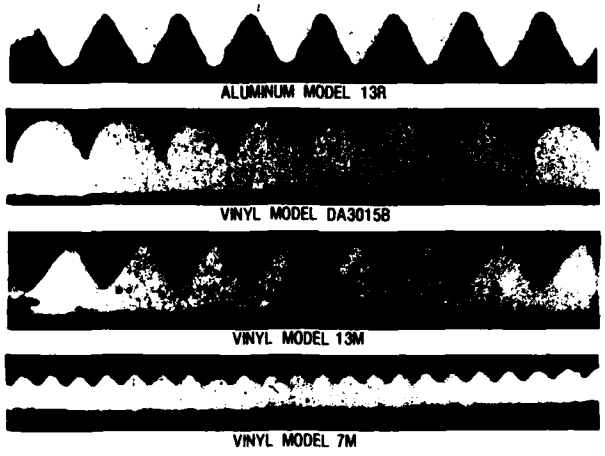


Fig. 7 Micro-photographs of model surfaces.

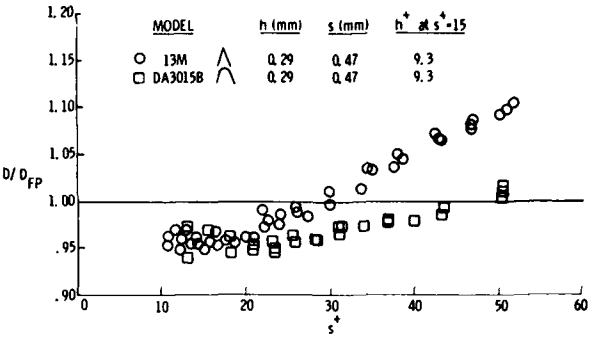


Fig. 10 Effect of peak curvature on riblet performance.

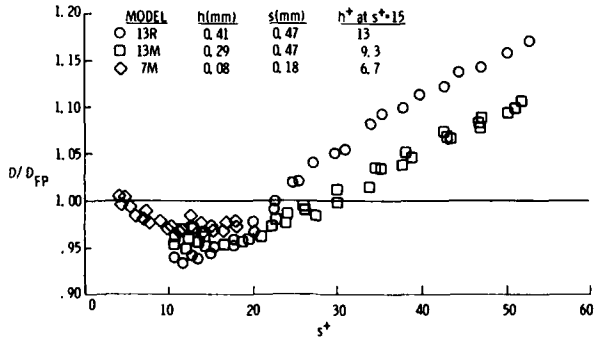


Fig. 8 Law-of-wall scaling for v-groove riblets.

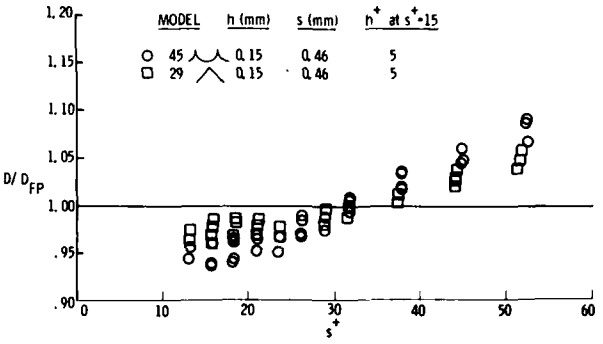


Fig. 11 Effect of valley curvature on riblet performance.

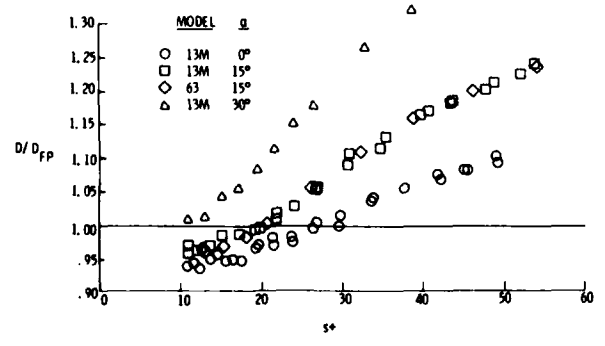


Fig. 9 Effect of yaw on riblet performance.

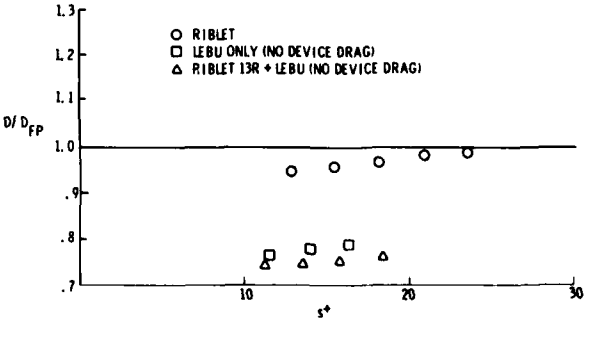


Fig. 12 Results of combined LEBU - riblet experiments.

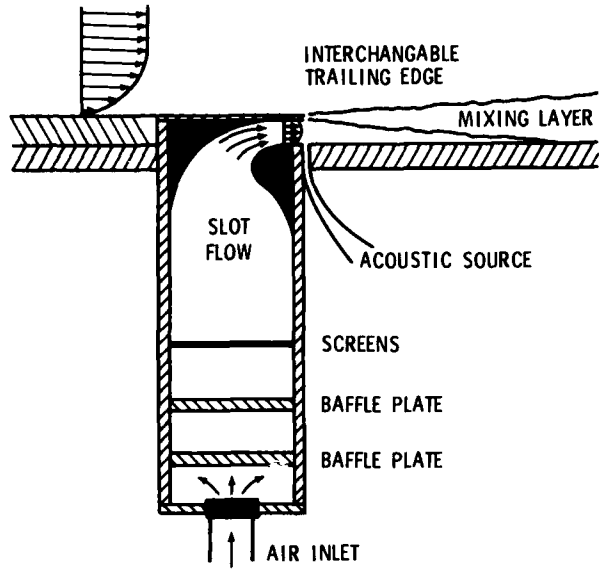


Fig. 13 Schematic of experimental setup - slot injection drag reduction experiment.

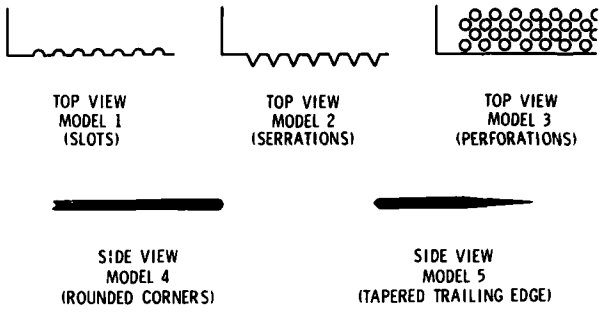
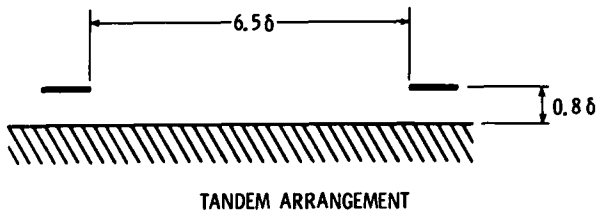


Fig. 14 Interchangeable trailing edge configurations.



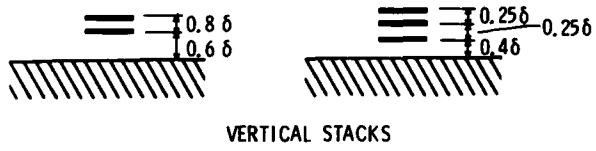


Fig. 15 LEBU arrays inserted into upstream turbulent boundary layer.

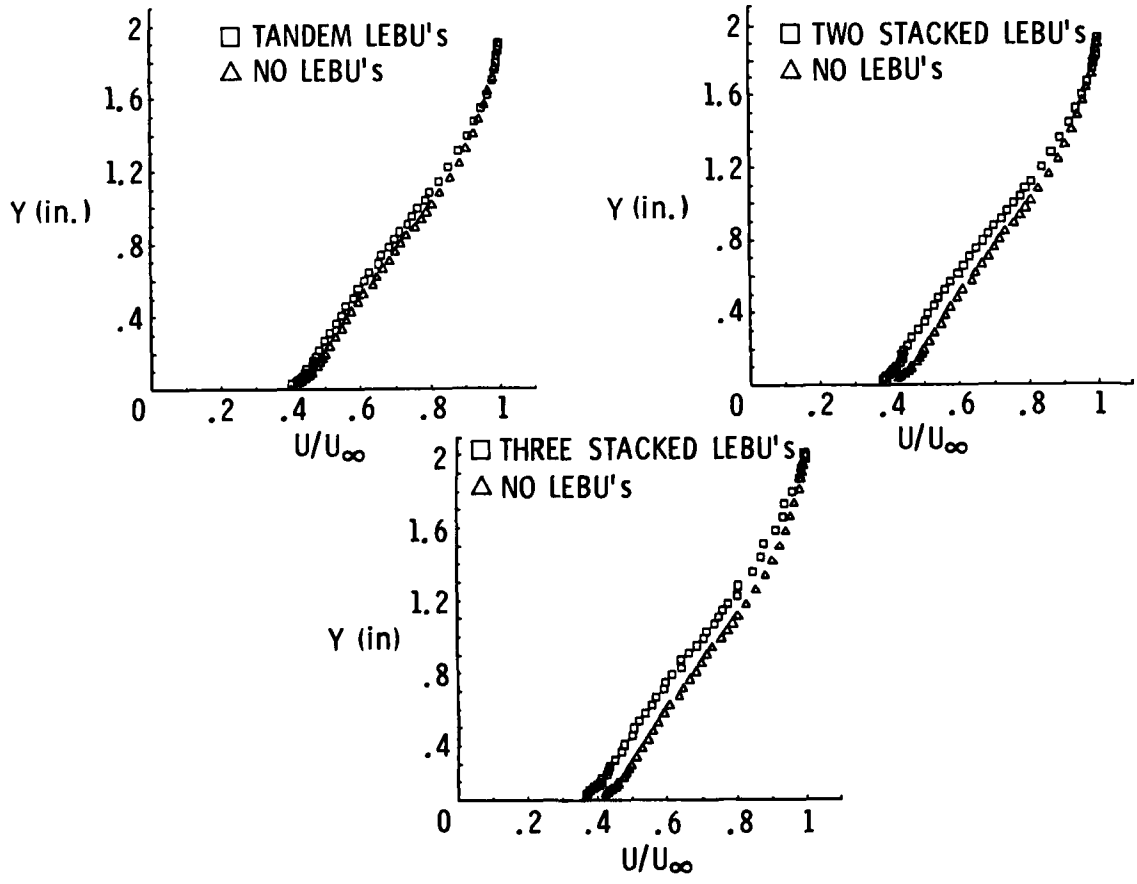


Fig. 16 Influence of LEBU devices upon slot mixing process.

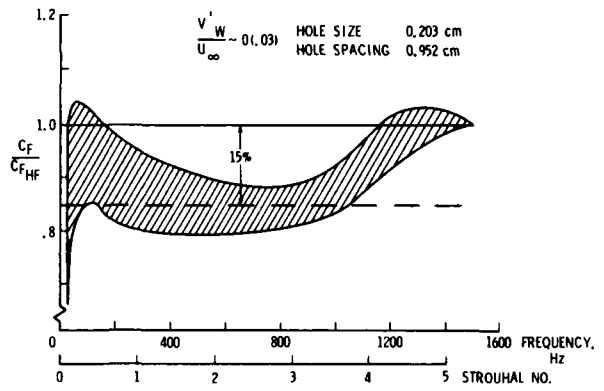


Fig. 17 Effect of high frequency Emmons spot forcing upon wall friction drag.

AD-P004 067

ON THE RELAXATION OF A TURBULENT BOUNDARY LAYER AFTER AN ENCOUNTER WITH A FORWARD FACING STEP

by

D.I.A.Poll

Aerodynamics Division, College of Aeronautics,
Cranfield Institute of Technology,
Cranfield, Bedford, MK43 OAL, England.

and

R.D.Watson

Viscous Flow Branch, High Speed Aerodynamics Division,
NASA Langley Research Center, Hampton, Virginia, 23665, U.S.A.

SUMMARY

An experiment has been performed in a low speed wind-tunnel to determine the mean flow relaxation characteristics for a zero pressure gradient turbulent boundary layer which encounters a small forward facing step. Of primary interest is the behaviour of the local wall shear stress downstream of the step, and this has been determined by the use of a series of buried hot-wire gauges. The mean velocity profiles downstream of the step have been measured using a traversing Pitot tube, and these have indicated that a step produces very marked changes in the distribution for both the inner and outer regions of the flow. The results shed new light upon the variation of wall shear stress downstream of a severe perturbation and also indicate that the use of Preston tube or Clauser chart methods for the determination of wall shear may lead to very large errors. As a consistency check on the data, estimates of the step drag, based upon force-momentum conservation considerations, have been compared with previously published drag balance measurements. The agreement between the data sets is very good.

NOTATION

A,B	constants in the semi-logarithmic inner region	u	velocity in the x direction
		U_τ	friction velocity $(\tau_w/\rho)^{\frac{1}{2}}$
$\bar{A},\bar{B}$	constants in the buried wire gauge calibration	x,y	coordinate system with the origin at the step location - see figure 1
C_D	drag coefficient of the step based upon step frontal area and free-stream dynamic pressure $(\frac{1}{2}\rho U_\infty^2)$	δ	height above the wall at which u reaches 99.5% of the free-stream speed
C_f	skin friction coefficient $(\tau_w/\frac{1}{2}\rho U_\infty^2)$	θ	boundary layer momentum thickness
C_p	pressure coefficient $(p-p_\infty/\frac{1}{2}\rho U_\infty^2)$	ν	kinematic viscosity
E	output voltage from hot-wire bridge	ρ	density
H	boundary layer shape factor	τ	shear stress
h	step height	Subscripts	
p	static pressure	w	at the wall
R	Reynolds number	∞	in the undisturbed free-stream
T	temperature		
ΔT	difference between hot-wire operating temperature and the flow reference temperature		

INTRODUCTION

In recent years there has been considerable interest in the possibility of direct manipulation of the structure of turbulent boundary layers with a view to reducing the overall drag of a given surface. So far two methods, which have potential aeronautical applications and which have been shown to produce modest but repeatable drag reductions for attached fully turbulent boundary layers, have been identified. The first involves the use of small streamwise wall ribs, or riblets (Walsh[1]) whilst the second involves the use of single transverse devices which locally break up the large eddies in the outer part of the boundary layer (Hefner et al[2]). These latter devices are collectively known as LEBUs - standing for Large Eddy Break Up. It appears that, used in conjunction, these turbulence modifiers could produce overall drag reductions of order 5 - 20% for typical civil aircraft configurations. This level of reduction may appear to be rather small but in a review paper Bushnell[3] has estimated that a 20% reduction in fuselage skin friction for the whole of the United States CTOL civil aircraft fleet would result in an annual saving of almost one billion dollars in fuel costs alone. A financial incentive of this

magnitude should provide a powerful argument in support of continued research into the fundamental aspects of turbulent boundary layer structure.

It seems that the wall riblets and the LEBUs operate on entirely different principles. In the former case the drag reduction is associated with the riblet and is felt directly by the riblet. Therefore a surface will have minimum drag if it is completely covered with riblets. A LEBU is, however, an isolated disturbance which itself carries a drag penalty. The immediate effect of the LEBU is to reduce the wall shear stress downstream of the device. This perturbed wall shear gradually relaxes with increasing distance downstream and, consequently, a successful LEBU is one for which the device drag plus the integrated wall shear is less than the integrated wall shear for the undisturbed flow. To date, however, much of the LEBU work has served mainly to highlight the generally poor level of understanding of the behaviour of non-equilibrium boundary layer flows. In particular Hefner et al[2] report that there is a dearth of definitive (reliable) data for initially equilibrium turbulent boundary layers relaxing fully to a new equilibrium, or self-preserving, states after having experienced an abrupt change in boundary condition. Clearly such a relaxation process is of key importance in a drag reducing system since this is the region in which the wall shear stress falls below its undisturbed value. It is, primarily, this basic lack of information which has prompted the present investigation.

The experiment to be described in this paper reveals some of the features of the process by which a fully turbulent boundary layer, which has initially developed under conditions of zero pressure gradient, returns to an equilibrium state after it has encountered a small forward facing step. This particular flow is of interest for three basic reasons. In the first instance the step acts as a one parameter LEBU device since it constitutes a 'change in boundary condition' for the flow which results in a highly localised and extremely severe pressure perturbation near the surface. Therefore, in the terms suggested by Hefner, the resulting relaxation process is relevant to physics of LEBUs in general, despite the fact that, in this case, the pressure force on the step is too large for there to be a net reduction in drag. The basic drag of the step forms the second reason for interest in this flow since the forward facing step constitutes a surface imperfection, or excresence, which is commonly found in aeronautical applications. Whilst it has been known for many years that this type of imperfection can produce significant drag increments there is still only a very limited amount of design information available - see Young and Patterson[4]. The results of this experiment will supplement this data base. Finally, in relation to the basic problem of measuring local wall shear stresses, there are now commercially available hot-film gauges which can be fixed directly to the surface under investigation. Since these gauges have finite thickness the upstream edge will constitute a forward facing step which must disturb the flow locally. Therefore, before these gauges can be used with confidence, it is necessary to quantify the effects of the step on the flow at the point at which the measurement of wall shear is made.

THE EXPERIMENTAL ARRANGEMENT AND TEST CONDITIONS

The experimental arrangement and notation are summarised in figure 1. Tests were performed in a low-speed wind tunnel with a working section 11" wide and 7" high. In order to obtain a thick viscous layer the test boundary layer was that generated on the floor of the working section. To smooth out any spanwise non-uniformity introduced by natural transition this boundary layer was tripped by a transverse wire 0.060" in diameter placed 10" upstream of the step. Part of the floor of the wind-tunnel consisted of an aluminium plate 36" long and 15" wide which was held in place by four screw jacks. These jacks could change the level of this section of the floor in relation to the upstream section which was fixed relative to the tunnel contraction cone. Normally these jacks are used to enable the plate to be set flush with the rest of the floor or to be lowered for removal and replacement. However, for the present experiment the side walls and roof were cut so that the portion of the working section normally in contact with the plate could be moved relative to the rest of the tunnel. In this way the upstream edge of the aluminium plate served as the step whose height could be set to any desired level simply by manipulating the jacks. Moreover, since the walls and roof moved with the plate, the geometrical cross-sectional area of the working section was constant at all streamwise locations irrespective of the height of the step. This meant that the dynamic pressure of the free-stream would not change in the vicinity of the step as a result of a continuity constraint imposed by the tunnel walls. An additional feature of this tunnel was that one of the sidewalls could be moved, as indicated in figure 1. Therefore it was possible, by using the wall to balance far upstream and far downstream static pressures, to ensure that flow beyond the step was relaxing under conditions which were the same as those in which the flow ahead of the step had developed.

Reference conditions for the tests were determined by a wall mounted Pitot tube and a static pressure tapping on the floor of the tunnel - these being positioned 4.00" and 2.32" upstream of the step. Static pressures were measured on the test surface at various positions downstream of the reference static tapping. Downstream of the step (i.e. on the removable aluminium plate) a series of flush mounted hot-wire gauges of the type described by Rubesin et al[5] were mounted at the positions indicated in figure 1. These were used to measure local wall shear-stress and were run in the constant temperature mode with power being provided by a bank of conventional hot-wire anemometer bridges. Finally, the tunnel has a traversing mechanism which allowed the measurement of the mean velocity profiles with a small flattened Pitot tube.

The free-stream conditions and the step heights used in these tests are summarised

in table 1.

THE CALIBRATION OF THE FLUSH MOUNTED HOT-WIRES

One of the most significant features of the present investigation was the use of flush mounted,or buried, hot-wire gauges for the measurement of wall shear-stress. Although these devices measure the stress 'indirectly' i.e. through a relation linking stress to convective heat transfer rate, their performance does not require the mean velocity profile to exhibit any special features e.g. a universal law of the wall. Since the profiles under investigation were initially non-equilibrium it was felt that the use of Preston tubes or Clauser charts was essentially unjustifiable and that the hot-wire gauge was the only practical alternative.

The gauges were calibrated 'in situ' using the wall shear-stress distribution for the undisturbed boundary as determined by Preston tubes. A typical calibration is presented in figure 2. As suggested by Rubesin et al[5] the calibration law is of the form

$$\frac{E^2}{\Delta T} = \bar{A}\tau_w^{1/3} + \bar{B}.$$

In figure 2, however, this relation is inverted and presented as τ_w versus $E^2/\Delta T$. This direct form immediately reveals an inherent problem for this type of gauge, namely the extreme sensitivity of the indicated value for shear stress to errors in $E^2/\Delta T$. In the example given it is clear that a 1% error in $E^2/\Delta T$ leads to a 20% error in τ_w. Consequently, it is essential that $E^2/\Delta T$ be known to a high degree of accuracy. In principle, it is possible to measure the E^2 component to within the necessary limits but the evaluation of ΔT possess a more serious problem. In a closed wind-tunnel the temperature of the air tends to increase with time and there is also a variation of the temperature of the aluminium plate. Since the maximum operating temperature of the wire was approximately 60°C (determined by the properties of the substrate) and the ambient temperature of the air within the tunnel was about 20°C, then to guarantee the accuracy of the shear stress to within ±5% requires that the surface reference temperature for the gauge must be known to within 0.1°C. In the present series of tests this surface reference temperature was obtained by using the most downstream hot-wire gauge as a resistance thermometer. Despite this, repeated calibrations indicated that the shear stress accuracy was limited to ±10%. However, it was felt that in future tests this figure could well be improved upon.

EXPERIMENTAL RESULTS

a) Undisturbed Boundary Layer

The variation of skin friction coefficient (Preston tube), momentum thickness and shape factor with position for a fixed free-stream unit Reynolds number are presented in figures 3,4 and 5 respectively. Figures 6 and 7 show the velocity profiles plotted in 'law of the wall' form and in 'velocity defect' form. These results show that the undisturbed boundary layer exhibits the usual mean flow characteristics of a turbulent zero-pressure gradient boundary layer.

b) Surface Pressure Distribution

The surface pressure distributions for various step heights are shown in figure 8 where the streamwise coordinate x has been normalised with respect to the step height, h. Also shown for comparison is the result according to inviscid flow theory - see Milne-Thomson[6]. It is interesting to note that, despite the fact that the pressure at a fixed value of x/h increases slightly with increasing h/θ, the surface pressure distribution closely follows the behaviour of the inviscid solution. These distributions clearly show the strength of the pressure perturbation introduced by the step. However, it should also be appreciated that this perturbation decays very rapidly with distance normal to the surface. The inviscid solution decay rate suggests that the pressure perturbation will have virtually disappeared at the edge of the boundary layer. Therefore, in the vicinity of the step, the assumption that $\partial p/\partial y$ is equal to zero within the boundary layer is not applicable. As a result of this difficulty no skin friction or velocity profile measurements were made at an x/h of less than 6.

c) Wall Shear Stress Distribution

The distribution of wall shear stress for the various step heights, as indicated by the buried hot-wire gauges, is given in figure 9. Perhaps the most notable feature is the complete insensitivity of τ_w to the height of the step. In all cases the wall shear-stress has returned to within ±10% of the undisturbed value by the first measuring station (0.768" downstream of the step).

d) Momentum Thickness Reynolds Number

Figure 10 shows the variation of momentum thickness Reynolds number with downstream position for several step heights. Although the data exhibit a little scatter it is quite clear that, downstream of the area in which the step produces a significant wall pressure perturbation, the development of R_θ is parallel to that for the no-step condition. Far downstream from the step the pressure gradient is very small and tending to zero, therefore, from the two-dimensional momentum integral equation -

$$\frac{dR_\theta}{dR_x} = \frac{C_f}{2} .$$

Hence the parallel trends for R_θ versus R_x indicate that the values of C_f (and hence τ_w) have returned to the undisturbed levels. This is in agreement with the results from the buried hot-wire gauges (figure 9).

e) Mean Velocity Profiles

An overall impression of the effect of the step on the mean velocity profiles may be obtained from a plot of shape factor, H, versus distance downstream of the step. This is given in figure 11. These data show that the greater the step height the larger the distortion suffered by the mean velocity profile. However, the relaxation length does not appear to depend upon step height. The data show that, no matter what the value of h, the shape factor has returned to the undisturbed value approximately 10 inches, or 25δ, downstream of the step. As an example of the actual velocity profiles figures 12 and 13 show the relaxation process for a step height of 0.124" in both 'law of the wall' and 'velocity defect' form. In both these cases the wall shear-stress used for the data reduction is that given by the buried hot-wire gauges. It is clear that, in both figures, the initial deviation from the undisturbed distributions is large but that the relaxation process is complete at 10" from the step.

DISCUSSION

The use of buried hot-wire gauges for the measurement of local wall shear-stress has shed new light on the relaxation process for a boundary layer perturbed by a step. Data presented in figure 9 show that even the largest step considered in this investigation failed to produce a detectable deviation from the undisturbed level even though the first measuring station was only 6.h downstream of the step. Therefore, it appears that any relaxation of the wall shear-stress is very rapid indeed - of the order 1 to 2 boundary layer thicknesses rather than the 20 to 30δ suggested by the survey of Hefner et al[2]. It should be noted, however, that the present findings are in good agreement with the experiments of Kiske et al[7] who measured wall shear-stress distributions downstream of roughness jumps and sudden enlargements in channels. Their results also show that significant changes in τ_w only occur in the immediate vicinity of the perturbation. In the present case we note that the mean boundary layer profiles are considerably altered by the presence of the step and that the relaxation length for both 'inner' and 'outer' regions is of order 25δ. From figure 12 it can be seen that although there is a region close to the wall which is of the form -

$$\frac{U}{U_\tau} = A \text{ LOG } \left(\frac{U_\tau y}{\nu}\right) + B$$

The values of A and B do not correspond to the generally accepted 'universal' values until the relaxation process for the mean profile is complete. Therefore if the wall shear-stress in the vicinity of the step had been determined by the Preston tube or Clauser plot methods then C_f would have been seriously underestimated. For example, using the first measuring station data given in figure 12, these techniques would yield a skin friction coefficient approximately 30% lower than that indicated by the buried hot-wire gauge at the same location. Since the uncertainty of the buried hot-wire gauge is only ±10% it seems unlikely that this difference could be accounted for in terms of measurement error. Moreover, the apparent discrepancies in the use of the Preston tube and Clauser methods in the present case are similar in magnitude to those noted by Kiske et al[7] in their experiments. The clear implication is that, in work on LEBUs or other drag reducing devices, skin friction in the immediate vicinity of the perturbation should not be determined by either standard Preston tube or Clauser chart methods.

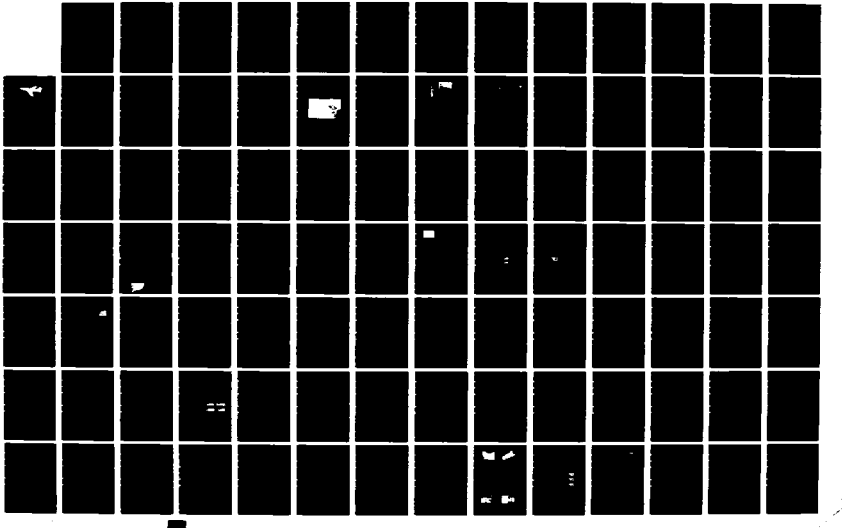
As stated in the introduction there is some interest in the forward facing step as a source of extra drag, i.e. excrescence drag, in aeronautical applications. Previous measurements of the drag of steps have been carried out by mounting steps on a very sensitive drag balance and data have been presented by Gaudet and Johnson[8]. In the present case consideration of the force and momentum balance for a control volume which includes the step but extends sufficiently far upstream, downstream and normal to the test surface for the static pressure to be uniform over those faces of the volume which are in the fluid leads to the conclusion that -

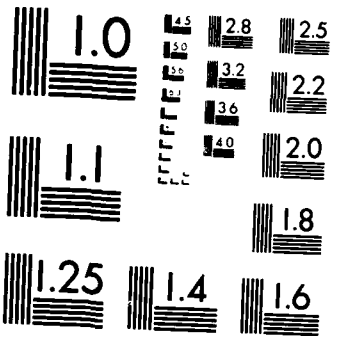
$$\frac{C_D}{C_f} = \frac{2}{C_f}\frac{\Delta\theta}{h}$$

In this relation C_D is the drag coefficient of the step based upon the step frontal area, C_f is the undisturbed skin friction coefficient at the step location, h is the step height and $\Delta\theta$ is the difference between the disturbed and undisturbed momentum thickness at the downstream end of the control volume. The above relation was used to compute the drag of the step from the data presented in figure 10 and the results are presented in figure 14 in the form C_D/C_f versus log $(U_\tau h/\nu)$. Also shown in figure 14 is the empirical relation proposed by Gaudet and Johnson[8] together with the scatter bands for the data upon which this relation was based. The present results lie well within the bounds of the Gaudet and Johnson results and, in general, support the balance data and the suggested empirical relation.

AD-A147 396 PROCEEDINGS OF THE CONFERENCE ON IMPROVEMENT OF AERODYNAMIC PERFORMANCE T..(U) ADVISORY GROUP FOR AEROSPACE RESEARCH AND DEVELOPMENT NEUILLY.. AUG 84 4/5

UNCLASSIFIED AGARD-CP-365 F/G 20/4 NL





MICROCOPY RESOLUTION TEST CHART
NATIONAL BUREAU OF STANDARDS-1963-A

Finally, regarding the use of commercially produced 'glue on' hot-film probes for the measurement of local wall shear-stress, the results presented in figure 9 suggest that, provided the thickness of the substrate is such that -

$$70 < \frac{U_\tau h}{\nu} < 250$$

the indicated τ_w will be equal to the shear-stress of the undisturbed surface (±10%). In view of the considerable convenience of the 'glue on' type probe compared with the flush mounted type used in this experiment this result is of considerable practical importance.

CONCLUSION

This experimental investigation has shown that a small forward facing step produces a significant change in the mean flow characteristics of a zero pressure gradient turbulent boundary layer. The step induces a pressure perturbation in the vicinity of the wall whose strength increases with increasing values of the step height to boundary layer thickness ratio. This pressure perturbation decreases rapidly with increasing downstream distance and, for the step heights considered, undisturbed pressure levels are regained at between 2 and 10 boundary layer thicknesses downstream of the step. The initial distortion of the mean velocity profiles also increases with increasing step height but the relaxation process takes place over a length of approximately 25δ irrespective of the step height. By measuring the wall shear-stress in the relaxation zone with buried hot-wire gauges it has been shown that, when plotted in inner region variables the velocity profile close to the wall exhibits a semi-logarithmic behaviour but this does not correspond to the 'universal' distribution. The data indicate that the universal law of the wall is regained after 25δ. Results obtained from the buried wire gauges also indicate that the wall shear-stress recovers its undisturbed value very rapidly - in this experiment the recovery distance was less than 2δ. This is a disappointing result from the drag reduction point of view. In addition these observations suggest that the use of standard Preston tube or Clauser chart methods for the estimation of wall shear in perturbed boundary layers may lead to very large errors. Consequently, these techniques are not recommended for use in evaluating the performance of LEBU devices. The results of this investigation do, however, indicate that accurate wall shear-stress measurements can be made with 'glue-on' hot-film gauges provided that the substrate thickness is such that it lies within the 'law of the wall' region for the undisturbed boundary layer.

Finally, the detailed measurements of the boundary layer relaxation process have been used to evaluate the drag of the steps from considerations of the force-momentum exchange taking place within a large control volume. The inferred values have been found to be in good agreement with previously published data obtained by an accurate drag balance technique.

ACKNOWLEDGEMENT

This work was performed at the NASA Langley Research Center, Hampton, Virginia, U.S.A. whilst the first author was a visitor with the Joint Institute for the Advancement of Flight Sciences (George Washington University/NASA). Financial support was provided by NASA under contract NAS 1-14605.

REFERENCES

1. Walsh, M.J. — Turbulent boundary layer drag reduction using Riblets. AIAA Paper No 82-0169, 20th Aerospace Sciences Meeting, Orlando, Florida, January 1982. (AIAA Journal, Vol.21, No.4, pp 485-486, April 1983)

2. Hefner, J.N., Anders, J.B., Bushnell, D.M. — Alteration of outer flow structures for turbulent drag reduction. AIAA Paper No 83-0293, 21st Aerospace Sciences Meeting, Reno, Nevada, January 1983.

3. Bushnell, D.M. — Turbulent drag reduction for external flows. AIAA Paper No 83-0227, 21st Aerospace Sciences Meeting, Reno, Nevada, January 1983.

4. Young, A.D., Patterson, J.H. — Aircraft excrescence drag. AGARDograph 264, July 1981.

5. Rubesin, M.W., Okuno, A.F., Matur, G.G., Brosh, A. — Flush mounted hot-wire gauge for skin friction and separation detection measurements. Proceedings of the 6th International Congress on Instrumentation in Aerospace Facilities, 1975.

6. Milne-Thomson, L.M. — Theoretical Hydrodynamics Macmillan and Co., London.

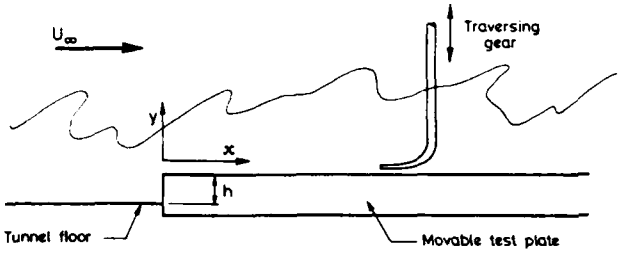
7. Kiske, S., Vasanta Ram, V., Pfarr, K. — The effect of disturbed turbulence structure on the Preston tube method of measuring wall shear stress. The Aeronautical Quarterly,Vol.XXXII, Part 4, pp354-367, Nov.1981.

8. Gaudet, L.
Johnson, P.
Measurements of the drag of various two-dimensional excrescences immersed in turbulent boundary layers at Mach numbers between 0.2 and 2.8.
RAE Technical Report 70190, October 1970.

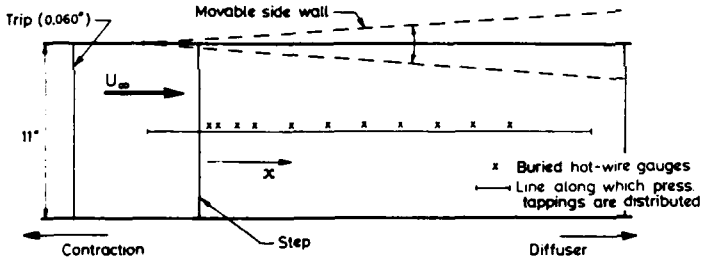
Table 1 - A summary of the test conditions

Free-stream unit Reynolds number	0.444×10^5	(1/ins)
undisturbed boundary layer thickness at step location	0.410	(ins)
undisturbed momentum thickness at step location	0.034	(ins)
undisturbed skin friction coefficient at step location	0.00405	

step height h(ins)	h/δ_{step}	$\left(\frac{U_\tau h}{\nu}\right)_{step}$
0.037	0.090	74
0.070	0.171	140
0.097	0.237	194
0.124	0.302	248



Side view



Plan view

Figure 1. The experimental arrangement and notation.

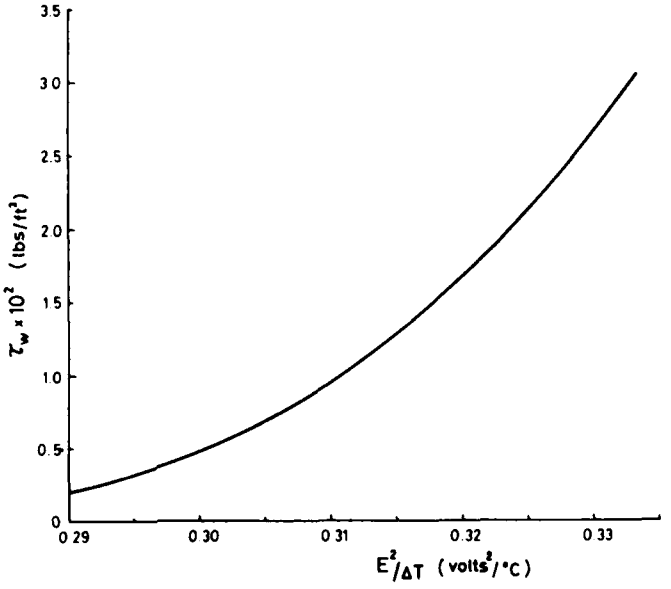


Figure 2. Calibration curve for the buried hot-wire gauge at x = 0.786 inches

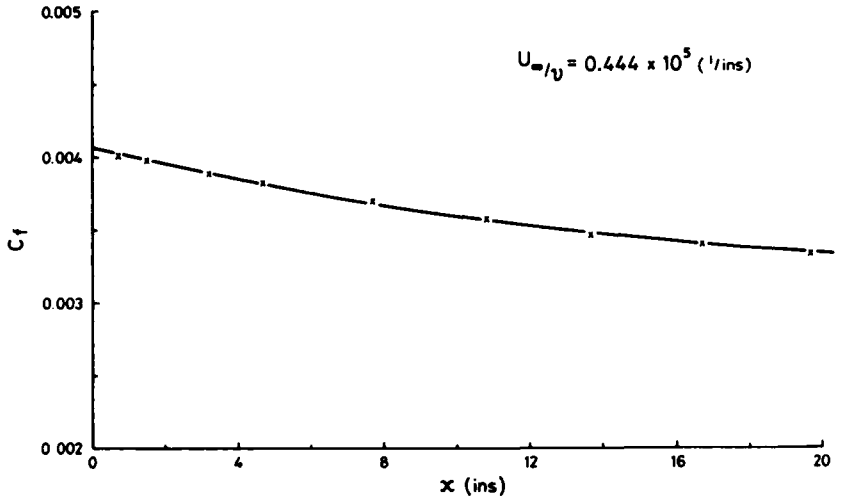


Figure 3. The variation of the skin friction coefficient with position for the undisturbed boundary layer.

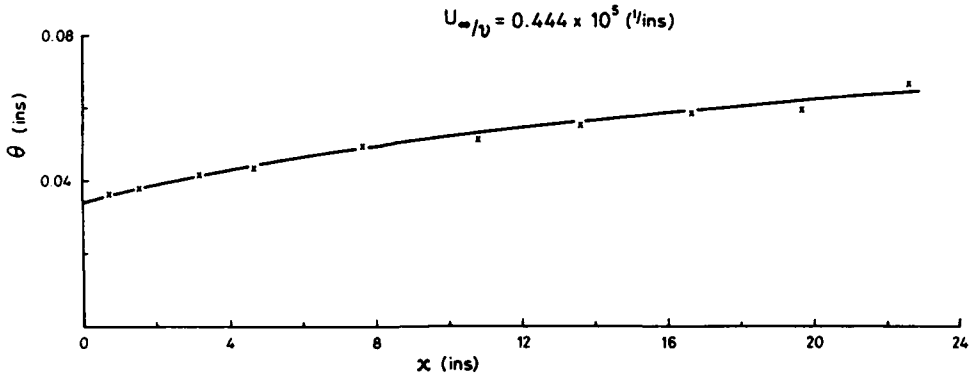


Figure 4. The development of momentum thickness in the undisturbed boundary layer.

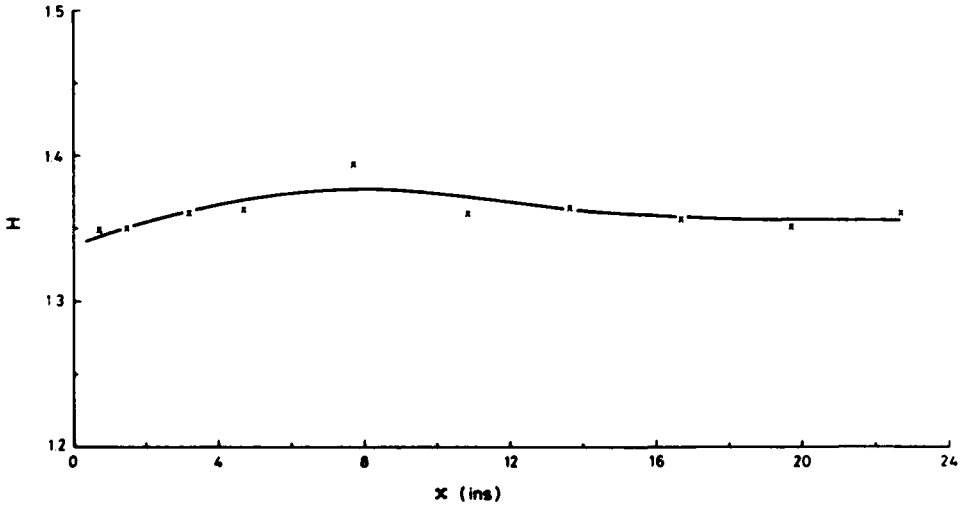


Figure 5. The development of the shape factor in the undisturbed boundary layer.

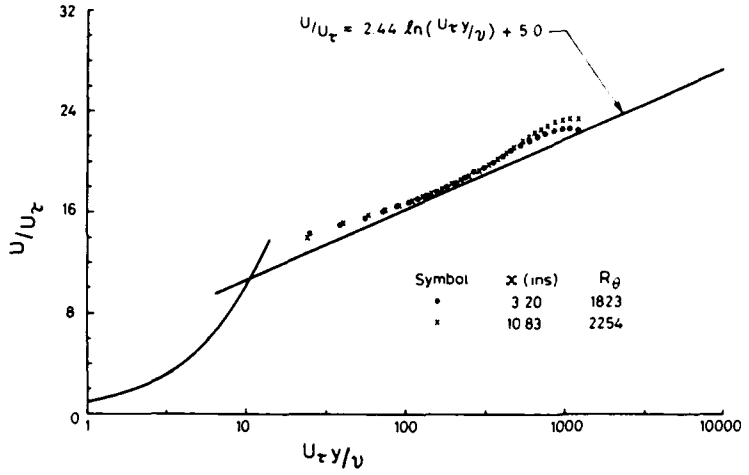


Figure 6. The mean velocity distribution through the undisturbed boundary layer in inner layer coordinates.

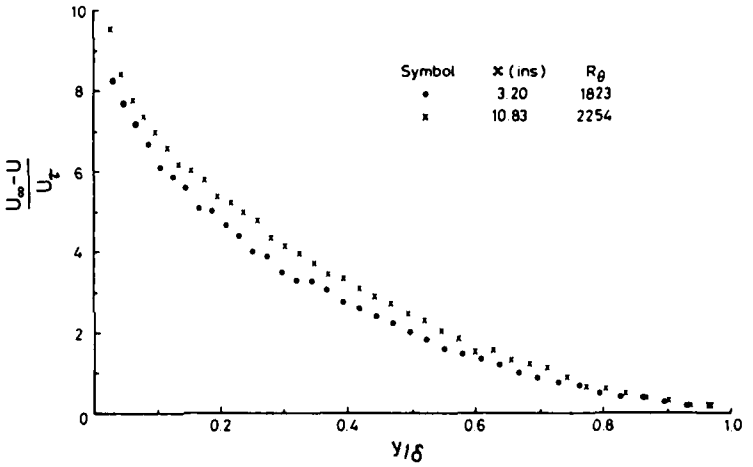


Figure 7. The mean velocity distribution through the undisturbed boundary layer in velocity defect form.

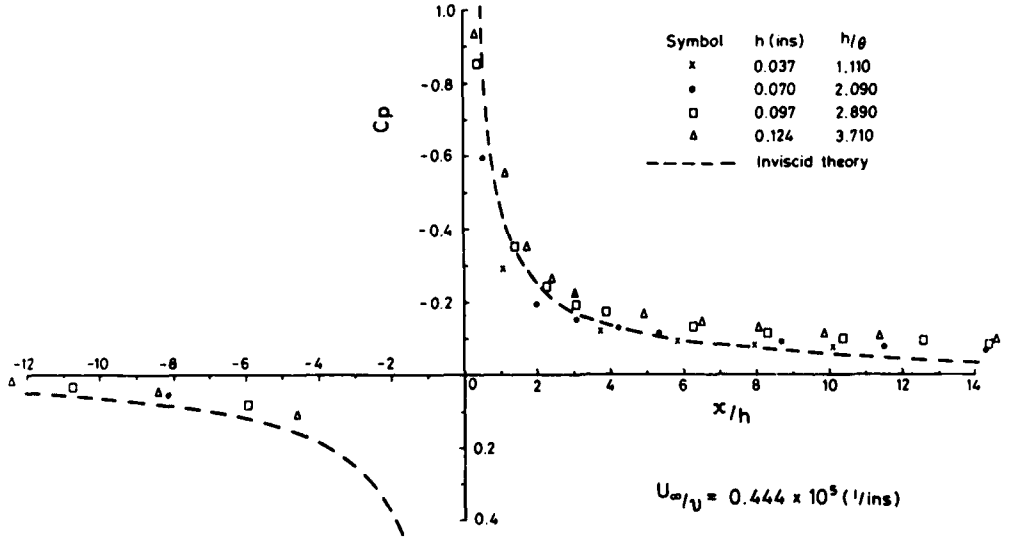


Figure 8. The variation of surface pressure for various step heights at fixed free stream unit Reynolds number.

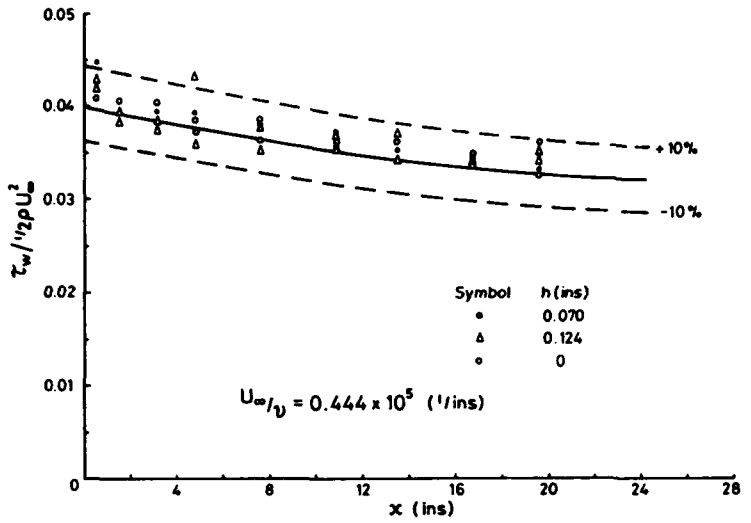


Figure 9. The variation of wall shear stress downstream of the step as indicated by the buried hot-wire gauges.

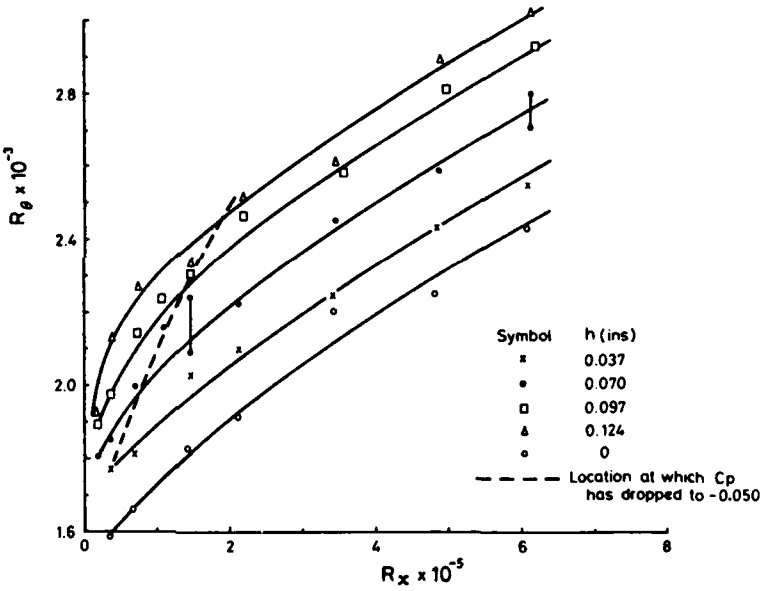


Figure 10. The development of the momentum thickness Reynolds number downstream of the step.

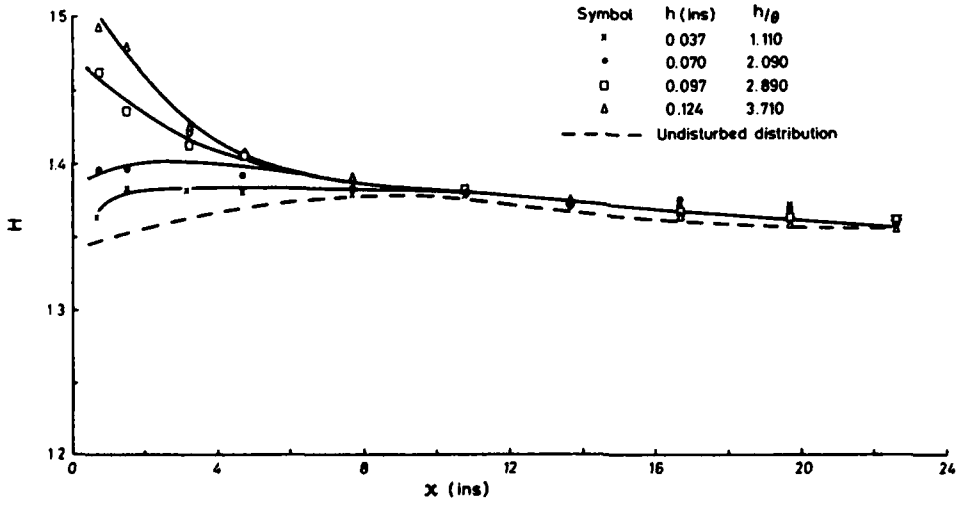


Figure 11. The relaxation of the profile shape factor downstream of the step.

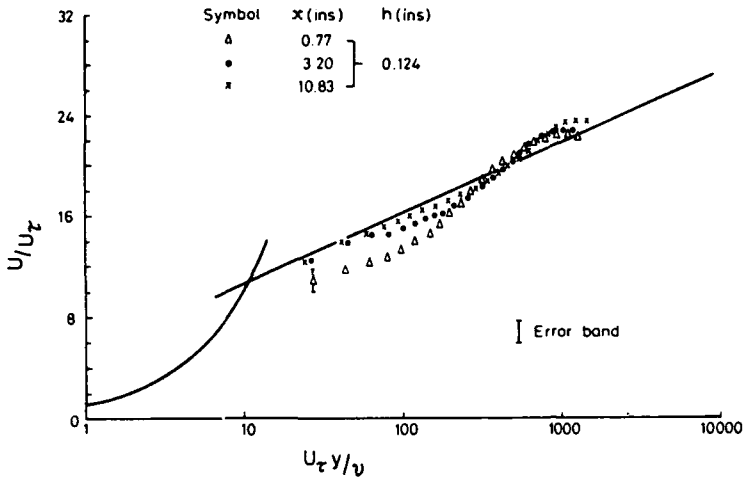


Figure 12. The relaxation of the mean velocity profile in inner layer coordinates.

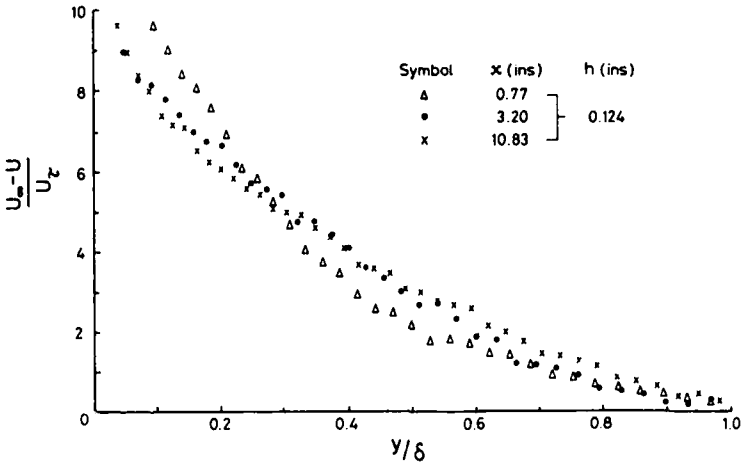


Figure 13. The relaxation of the mean velocity profile in velocity defect form.

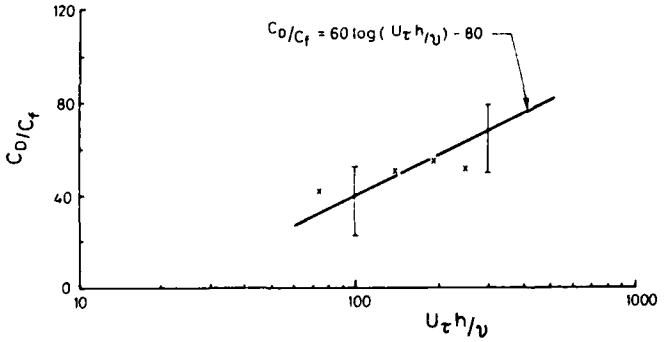


Figure 14. The dependence of step drag upon step height.

FULL SCALE EXPERIMENTS INTO THE USE OF LARGE-EDDY-BREAKUP DEVICES FOR DRAG REDUCTION ON AIRCRAFT

by
Arild Bertelrud
FFA The Aeronautical Research Institute of Sweden
S-161 11 BROMMA, Sweden

AD-P004 068

SUMMARY

An experimental investigation in flight has been performed to explore the feasibility of using LEBU (Large-Eddy-Breakup) devices to reduce the drag of aircraft. Two geometrical shapes of ribbons were used, and the development of local skin friction was monitored downstream. The aircraft was a swept-wing attack aircraft, and the flights covered the entire subsonic regime from M=0.92 down to stall conditions, flight altitudes were 1, 4.5, 7 and 10 km to explore various combinations of angle of attack, Mach - and Reynolds numbers.

An essential part of the study was to learn how to apply the devices, and also to explore the effects the devices might have on the flight characteristics of the aircraft, for example, close to stall or when a shock was present on the wing.

Some information was obtained concerning the turbulence characteristics downstream, and a discussion of the "downstream amplification effect" due to the drag at the device is also done.

1. INTRODUCTION

During the last decade a considerable effort has been put into finding ways of reducing the skin friction drag of vehicles. The reduction is obtained either by keeping the boundary layer laminar or by altering the turbulent boundary layer characteristics. A large number of methods and ideas are pursued for the turbulent drag reduction, as reviewed by Bushnell (Ref. 1). One promising technique is to use Large-Eddy-Breakup (LEBU) devices, consisting of ribbons or profiles inside the boundary layer, mounted transverse to the flow direction. A number of investigations exploring several geometries confirm local reduction of skin friction as well as a net drag reduction (Refs. 2-4). There was an initial inconsistency concerning the amount of skin friction reduction possible, but this appears to have been a result of differences in the turbulent boundary layer at the location of LEBU device. A fully developed turbulent boundary layer with a momentum thickness Reynolds number, Re_θ, larger than 5000 is needed to obtain the wake structure pertinent full-scale conditions.

The work at the FFA started with a cooperative experiment at EPFL, Lausanne, Switzerland, aimed at an independent verification of net drag reduction or increase, as well as obtaining information on optimum geometry. Typical results concerning local skin friction reductions and net drag reductions are shown in Figures 1 and 2. Even with Re_θ reasonably high, a number of extrapolations and answers to many questions are needed before LEBU's can be used in practical applications:

- Reynolds number extrapolation
- Pressure gradient effects
- Three-dimensionality of the mean flow
- Compressibility
- Freestream turbulence (or lack of it)

The Reynolds number extrapolation is uncertain, as no data yet exists at full scale conditions for turbulent boundary layers with LEBU devices. For normal, low-speed boundary layers a variety of formulae may be used to describe the relationship between C_f, Re_θ, H, Re_x, k etc. Using for example Thompson profiles (Ref. 5), the actual shape of the velocity profile is uniquely defined using two out of the three parameters C_f, Re_θ and H. Some success was noted in Ref. 3 using the additional parameters Re_{θ_w} and β_o corresponding to the momentum loss due to the ribbons (Re_{θ_w}) and maximum velocity defect $\beta_o=U_{w_{min}})/U_e$, and assuming a self-preserving wake development downstream.

However, this is a description of one set of experimental results only, and the profiles measured in real, full scale flights, are not easily predicted.

The LEBU devices are assumed to modify large-scale coherent structures, and for some time a discussion has been going on whether these exist at all for the high Reynolds numbers experienced in full scale flight conditions. A recent study by Andrepolous et.al (Ref. 6) seem to confirm their existence at least up to Re_θ=15000 for low speed flows.

Generally the pressure gradient effects should be moderate, as the values of the viscous pressure gradient parameter $\beta=(\theta/\tau_w)\cdot dp/dx)$, indicate local equilibrium profiles.

In the experiments in Switzerland (Ref. 3), some tests were made with a viscous pressure gradient parameter β comparable to those found on the present aircraft at intermediate Mach numbers, and as Figure 3 indicates the local skin friction was reduced even in this case. But generally experiments with large-eddy-breakup devices have been performed in flat plate boundary layers under laboratory conditions only.

The small cross-flow of the mean flow should not matter much as all turbulence is in practice 3D, and trends should not be changed dramatically.

Compressibility and freestream turbulence are also assumed to be second-order parameters.

It was not evident how to mount a device for practical applications, as high dynamic pressure in combination with wing bending and vibration would produce a new environment to the ribbons. Also, they might have an effect on the stall behavior of the aircraft or on the shock location, thus creating problems in flight regimes where they were neither efficient nor needed.

2. EXPERIMENT

Since 1980 the FFA has access to an aircraft (Figure 4) exclusively for aerodynamic and in particular boundary layer studies in cooperation with The Swedish Air Force (FMV:PROV, Malmslätt). This is a swept wing attack aircraft being flown from M=0.95 to stall conditions, and with exceptionally well documented wing flow conditions. It was well suited to give answers to the question; is there any feature in the full scale application of LEBU devices preventing their use?

The aircraft has a straight-tapered wing with a leading edge sweep of 39 degrees. The profile is symmetrical; NACA64A010 normal to the 35 degrees swept 25% chord line. The wing has zero twist.

Practical application of LEBU devices would probably involve retrofitting aircraft alredy in use, and the profile and planform of the SAAB A32 can be seen as a fairly good representative of many commercial swept wing aircraft under cruise conditions.

Flow conditions

The general information concerning pressure distributions etc. for a few cases may be found in Ref. 7, and these may serve as examples on typical conditions. At the FFA the complete database with information from the entire flight envelope and extensive information on boundary layer characteristics is available, and this is utilized in the present analysis.

Figures 4 and 5 show the aircraft, the geometry of the wing and an isobar plot for M=0.8, H=7 km, corresponding to Case C of Ref. 7. The test area for the LEBU experiment is that indicated by the isobar plot. The leading edge flow contains a distinct suction peak for the lower Mach number with a short separation bubble for Mach numbers below 0.35-0.55, depending on flight altitude. At higher Mach numbers the end of acceleration is also in front of the ribbon position, and hence the flow should be considered fully turbulent over the entire region of interest. The ribbons were positioned at 15% chord, and the skin friction was measured back to 80% chord, where boundary layer measurements were performed. The wing type has a leading edge separation at stall, and this is one of the reasons why the cross-flow is small all the way back to more than 80% chord. This allows simplified instrumentation to be used; i.e. boundary layer rakes, Preston tubes etc., whithout significant loss in accuracy. It should be pointed out here that this type of small cross-flow is actually typical for most wings at cruise conditions.

As Figure 5 indicated the isobars are essentially parallel to the generators of the wing, which is important for this type of experiments. To evaluate the data it is also essential to acknowledge the difference in local pressure coefficient at the position of the LEBU device versus the end of the test region. Figure 6 shows that there is a considerable variation, and this is important when discussing the drag of the ribbons and how this drag may be amplified or damped downstream as a result of difference in C_p level. The actual pressure distribution along the chord is shown in Figure 7 for two cases, B and C of Ref. 7, with relatively high Mach number. For both these cases the LEBU device is positioned within a boundary layer with supersonic freestream, although Figure 6 shows that this is an exception rather than a rule through the present experiments. Figure 7a indicates that the spanwise variation in static pressure is very small compared to the streamwise gradients. It also illustrates another typical feature of this wing: an accelerating pressure side flow all the way back to mid-chord. The momentum thickness Reynolds number Re_θ at 20% chord, i.e. close behind the LEBU device, is shown in Figure 8, along with the boundary layer thickness.

To position the LEBU device requires a compromise between local flow conditions throughout the flight envelope. As the present investigation concerned the general features and problems associated with using ribbons in flight, no attempt was made to find an optimum position. Rather the variation of boundary layer thickness should be moderate. This would ensure that the ribbons were always in the outer, intermittent part of the boundary layer. All ribbons were located 8 mm from the surface and hence may have protruded outside the boundary layer for some flight conditions, although it generally meant

an h/δ ratio of 0.8. The use of different flight altitudes allows some information to be obtained about the effect of h/δ, but this is not dealt with in the present paper.

The pressure gradient at the ribbon position was close to zero for most medium or high Mach number flow conditions, and this was considered to be an important feature, as large gradients would have produced unwanted behaviour due to the variation in boundary layer properties at the two ribbons.

Device Mounting

A number of ribbons have been used; all of them located at the same chordwise position and having a tandem configuration with 8 mm wall distance. The chordwise distance between leading edges were 25 mm, total LEBU device length 33 mm, which corresponds to roughly 1.1% chord. (See Figure 9). All ribbons were made of spring steel; initially a rectangular cross-section was used, but the final series of tests were made with profiled leading and trailing edge as it was hoped that this would reduce the device drag (Bushnell, Ref. 8).

For safety reasons the initial ribbons were only 0.5 meters long, and several combinations of ribbon thickness and preloading were required before they would survive a flight. The combination of dynamic aircraft load/ribbon flutter during or after take-off broke the ribbons. Both ribbons were instrumented with strain gages, and their load and interaction in flight has been recorded. Attempts using carbon-fiber ribbons (that would have been suitable for profile development) were abandoned due to strength problems. Also, a stretching mechanism allowing continuous variation of mechanical stress was necessary. The ribbons wre always mounted with the aircraft resting on the landing gear. During flight this meant lowering the stress (as the wings deflected upwards due to lift), but a too low stress also meant risk of flutter. Also, the ribbons and holders had to be designed so that if any part of the device broke off it would be the ribbon, probably not a mid-support and definitely not the end holders. The profiled ribbons were manufactured from rectangular material using grinding and subsequent hardening. The results presented in this paper all concern the final ribbon length of 1 meter with two small, streamlined supports in between.

3. RESULTS

General observations

No adverse effects were observed by the pilot at any speed; neither at high Mach number were shock/ribbon interactions could create problems or at low speeds. The pilot notation of stall occurs, for this aircraft, when this particular part of the wing separates, and no change in behavior was observed. As the ribbons were short, this is not a very strong evidence, but the tufts used on the opposite wing (where the ribbons were also present) did not indicate a premature local separation back to the trailing edge. The loss of ribbons on one side was not noticable in turns, rolls or other maneouvers that were performed.

Static pressure distribution

Figure 10 shows the static pressure coefficient at 50% chord for three different flight altitudes, and no systematic change in local pressure coefficient can be observed. For the low speed cases this agrees with the pilot observations and at high Mach numbers it indicates that no dramatic change in shock position occured.

Local skin friction distribution

This was investigated using modified Preston tubes (Ref. 9), using the compressible calibration of Bradshaw and Unsworth (Ref. 10). These rely on the wall similarity to be valid; a debatable issue. It would have be desireable to determine local C_f through differentiation of the momentum thickness, but due to practical limitations of a real flight experiment as well as complications dealing with 3D, compressible flows with an appreciable pressure gradient, wall similarity techniques were used. In Ref. 3 and 11 there are indications that this similarity is reasonable approximation after some boundary layer thicknesses, and in the present experiment one test was made to show this. At 50% chord a heated film gage (McCroskey, Ref. 11) was located side-by-side with a modified Preston tube and calibrated at the appropriate flight conditions. The heated film gage is based on the heat transfer/momentum transfer similarity and is often claimed to rely on the viscous sublayer law. In the next flight the ribbons were put into position and the change in local C_f indicated by the heated film gage was compared with the change indicated by the modified Preston tube. For H=7 km Figure 11 shows the result, an agreement within the experimental scatter. Admittedly this is no proof of wall similarity but it is an indication that the modified Preston tubes can be used with confidence on the present wing.

It is also of interest to notice that the two gages actually measured an increase in local skin friction as compared to measurements obtained earlier further forward where reductions in local C_f of 10-15% were observed.

To explore the downstream development of C_f (as well as static pressure), a diagonal pattern of probes was used; see Figure 12. Here one extra probe was use in the wake of one of the supports to detect spanwise changes. Figure 13 shows the resulting development of local static pressure C_p and skin friction C_f for M=0.8 and H=7 km, i.e. Case C. The static pressure is seen to repeat within measurement accuracy and the local skin friction indicates 10-15% lower values with the LEBU device. In the Figure results of computations using the boundary layer code of Bradshaw et al. (Ref. 13) finite difference method are shown. The computations are performed with changes in initial Re_θ, which means that the evaluation of C_f corresponds to the effect of lowering C_f through thickening of the boundary layer. As can be seen the measured reduction in C_f cannot be explained by the "thick layer" explanation.

A correlation based upon meaningful flow parameters was difficult to establish. For the cases of constant h/δ ratio a correlation attempt was made of the data as shown in Figure 15, where the findings of Anders et.al (Ref. 4) indicating a region of skin friction reduction 50-80 δ_o long were followed by an "overshoot" between 120-190 δ_o. In the present case, of course, the pressure gradient cause a matter of discussion, but as mentioned earlier the gradients are moderate and the turbulence structure is not necessarily very dependent on it.

The local reduction of C_f was rather small in the present case, as the geometry of the LEBU device had $L/\delta_o \approx 3.5$ or smaller. According to Anders L/δ_o ratios up to 10 should produce lower C_f values.

Mean velocity and turbulence structure

Two boundary layer rakes were located at 80% chord to monitor the downstream result of the LEBU device presence in the leading edge region (15-17% chord). The rakes are shown in Figure 16. The pressure rake had several cobra probes to determine cross-flow in addition to its single total pressure tubes used to obtain the streamwise velocity profile.

To supplement this rake, as well as for independent measurements in the leading edge region of the wing, a miniature rake with 6 hot wires located up to 7 mm from the surface was used to measure the turbulence characteristics. The mean voltages were filtered, digitized and stored with the rest of the reference and pressure information of the test, and the AC amplified turbulent data was recorded on separate tracks on the 14-channel analog tape recorder.

Frequency response was 10 kHz, the wire diameter 5 μ m and wire length 1.5 mm. In the present paper use is made of the direct analog signals to obtain space/frequence information. Both rakes are shown in Figure 16, where also their side-by-side arrangement can be noted. Measurements were made through the entire Mach number region.

Figure 17 shows the boundary layer profiles measured with the pressure rake with and without the ribbons in position for one flight condition (Case C). Here the ribbons create a net drag increase. The cross-flow angle at y=2.8 mm is also indicated, and apparantly the ribbons did not create a higher cross-flow, again confirming the indications that no problems were produced concerning the separation of the flow.

The hot wire rake show more interesting features. Figure 18 exemplifies the results obtained using wires 1, 3 and 5 as well as correlations between these. Two analog signals at a time were fed into an Hewrett Packard Fourier analyzer, where their spectra, cross-spectra, coherence and transfer function was determined. For wires 1 and 3, located 0.2 and 2 mm from the wall respectively, there was a phase shift virtually independent of whether the LEBU device was in position or not. This kmay be seen as a verification that the large-scale structures exist at the present Re_θ values, up to $Re_\theta \approx$ [illegible]. For wires 3 and 5 there was a considerably smaller phase shift with the LEBU device, indicating a change in structure of the turbulence. The data was evaluated up to frequencies where the coherence started disappearing, and the slope in the $d\phi/df$-plane was virtually constant. When this was evaluated as function of flight Mach number, and the time difference corresponding to the phase shift was interpreted as a vertical "phase velocity" in a manner similar to that done by Kreplin and Eckelmann, the results of Figure 19 are obtained. It is seen that close to the wall this velocity is independent of LEBU device presence, whereas the velocity further out in the stream is damped due to the ribbon presence.

It may be of interest to consider the wall distances of the various hot wires expressed in wall units. Wire # 1, at y=0.2 mm has y^+=20-55 when the Mach number varies from 0.8 down to 0.4. Wire # 2 has y^+=110-270 whereas wire # 3 sits at y^+=220-540. It may be noted that Andreupoulous et al. (Ref. 6) in their correlation of the non-dimensional mean bursting interval normalized with outer variables $(T_B \cdot U_\infty)/\theta$, had this interval as approximately 80 from the wall out to $y^+ \approx 100$, a value of 200 for $y^+ > 200$ and an increase from 80 to 200 for intermediate y^+ values.

It should be noted that this velocity is not to be interepreted as a group velocity, as the main energy of the turbulence may not necessarily have this velocity (or angle), but if the horizontal group velocity is approximated by the time-averaged streamwise velocity at that position, the angles of typical turbulent structures may be deduced.

It should be noted that the information on phase shift used has frequencies corresponding to wavelengths larger than the boundary layer thickness.

A couple of additional remarks should be done to the turbulence information described:

The frequencies corresponding to a coherence as well as distinct phase shift between two channels are all in the range of the boundary layer thickness or large. Also no conditional sampling has been performed on the data so far, hence the occurrences like bursts, sweeps etc. can not be identified.

4. CONCLUSIONS

A number of conclusions can be made from the present investigation:

- The present investigation indicates that it is possible to use Large-Eddy-Break-Up devices in flight without deteriorating the performance or handling characteristics of the aircraft in any part of the flight envelope.

- Local reduction in skin friction is found at much higher Reynolds numbers than previously tested.

- The pressure gradients, compressibility and small three-dimensionality of typical aircraft wings do not significantly change the effects of large-eddy-break-up devices.

- The earlier findings indicating an "overshoot" in local skin friction for certain regions behind the ribbons are confirmed.

- The structure of the boundary layer turbulence is altered far downstream, even aft of the skin friction "overshoot" region.

5. REFERENCES

1 Bushnell, D.M.: Turbulent Drag Reduction for External Flows. AIAA Paper 83-0227, 1983.

2 Corke, T.C. et al.: Modification in Drag of Turbulent Boundary Layers Resulting From Manipulation of Large-Scale Structures. Viscous Flow Drag Reduction. Vol. 72. Presented at the Symposium on Viscous Drag Reduction, Dallas, Texas, November 1979.

3 Bertelrud, A., Truong, T.V. and Avellan, F.: Drag Reduction in Turbulent Boundary Layers Using Ribbons. AIAA Paper 82-1370, 1982.

4 Anders, J.B., Hefner, J.N. and Bushnell, D.M.: Performance of Large-Eddy-Breakup Devices at Post-Transitional Reynolds Numbers. AIAA Paper 84-0345, 1984.

5 Thompson, B.G.J.: A New Two-Parameter Family of Mean Velocity Profiles for Incompressible Turbulent Boundary Layers on Smooth Walls. ARC R & M 3463 (1965).

6 Andreopoulos, J. et at. Influence of Reynolds number on characteristics of turbulent wall boundary layers.

7 Bertelrud, A.: Pressure Distribution on a Swept Wing Aircraft in Flight. AGARD AR-138, Addendum, 1984.

8 Bushnell, D.: Private communication. July 1983.

9 Bertelrud, A.: Total Head/Static Measurements of Skin Friction and Surface Pressure. AIAA Journal, March 1977.

10 Bradshaw, P. and Unsworth, K.: A Note on Preston Tube calibrations in Compressible Flow. Imperial College IC Aero Report 73-07, 1973.

11 Nguyen, J. et al.: Some Experimental Observations of the Law of the Wall Behind Large-Eddy Breakup Devices Using Servo-Controled Skin Friction Balances. AIAA Paper 84-0346, 1984.

12 McCroskey, W.J. et al.: Flow Angle and Shear Stress Measurements Using Heated Films and Wires. Trans. of the ASME. J. of Basic Engng. Vol. 74, No. 1, March 1972.

13 Bradshaw, P., Mizner, G.A. and Unsworth, K.: Calculation of compressible turbulent boundlary layers with heat transfer on straight-tapered swept wings. Imperial College of Science and Technology, Dept.Aeron., I C Aero Report 75-04, 1975.

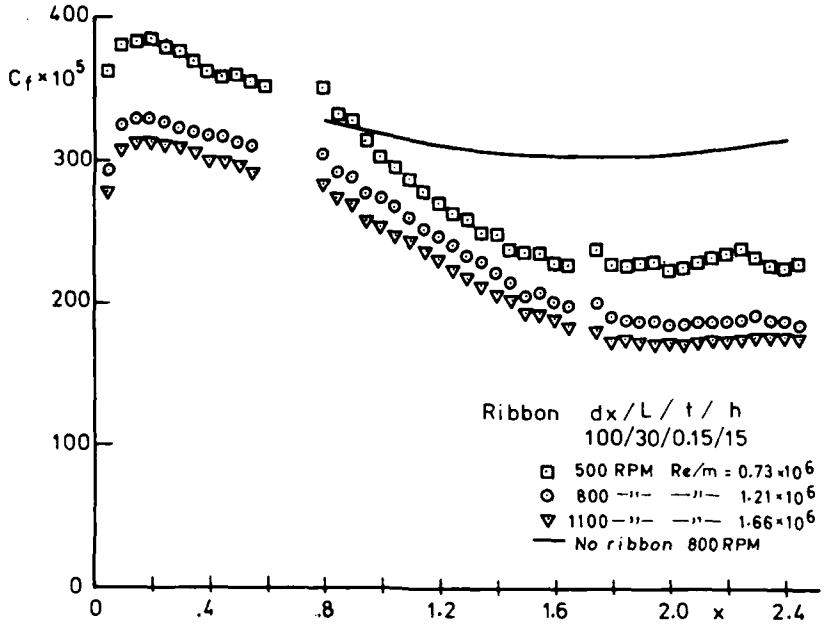


Figure 1. Local skin friction versus streamwise position. LEBU device (two rectangular ribbons in tandem) located at x= 0.8 m. (From Ref. 3.)

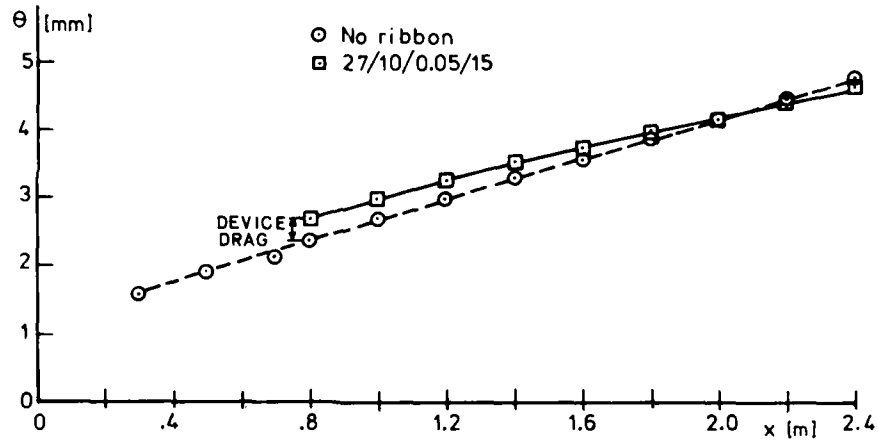


Figure 2. Momentum thickness development with and without LEBU device. Small net drag reduction is indicated. (From Ref.).

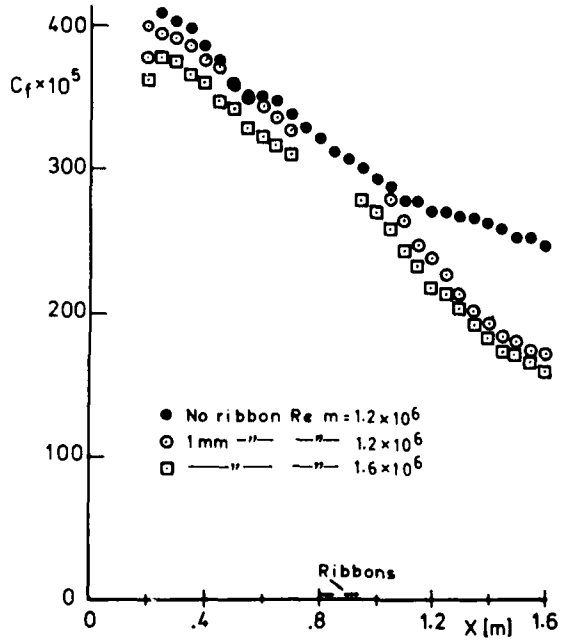


Figure 3.

Local skin friction versus streamwise position. (From Ref. 3.)

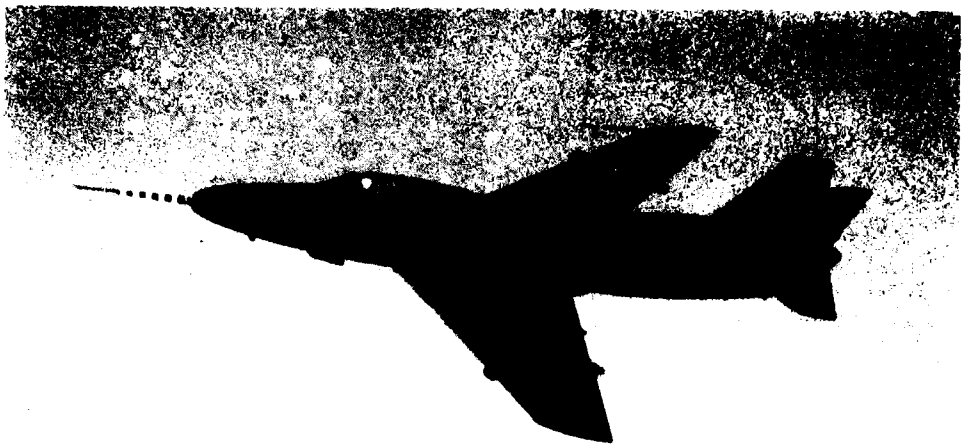


Figure 4. Aircraft used in present study
(SAAB A32 Lansen, serial # 32-209).

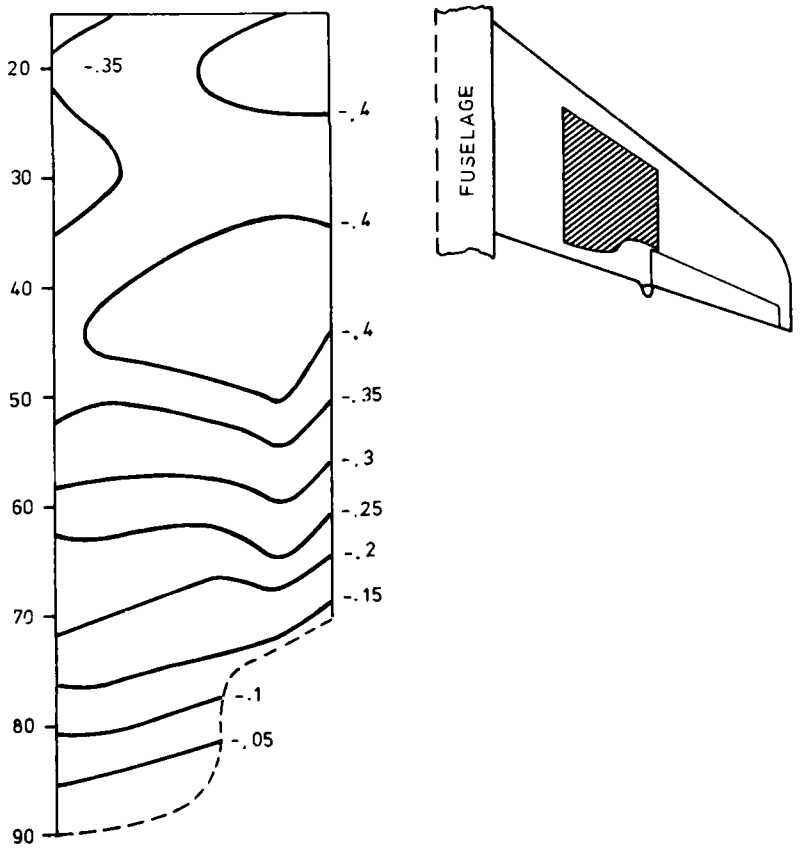


Figure 5. Region of the wing used in the present investigation. Isobar plot of pressure distribution for M=0.8, H=7 km.

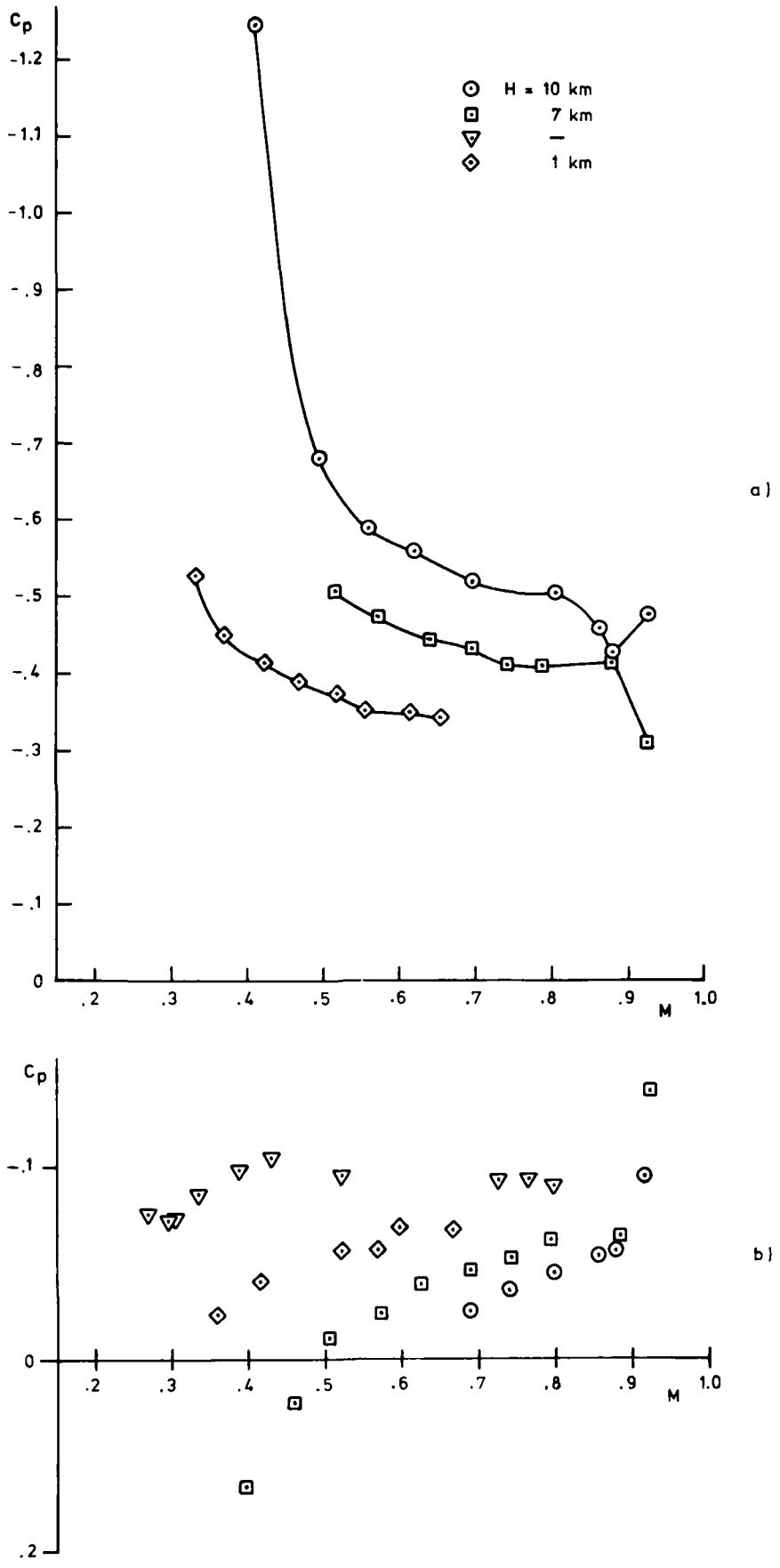


Figure 6. Variation of C_p at front and back ends of test region; ξ= 0.2 and 0.8, η = 0.5.

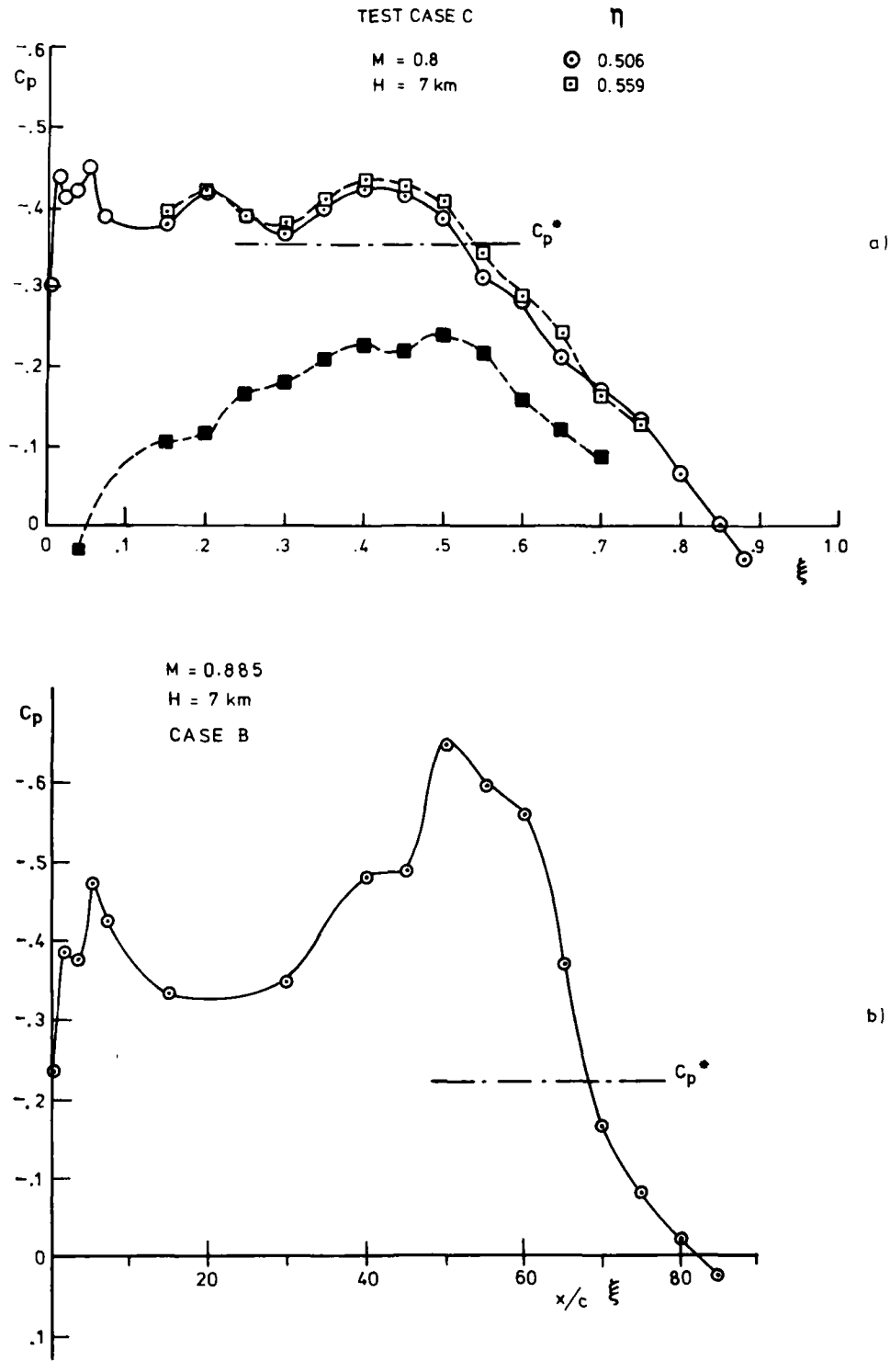


Figure 7. Pressure distributions along chord for two test cases: M=0.885 and M=0.8; H= 7 km.

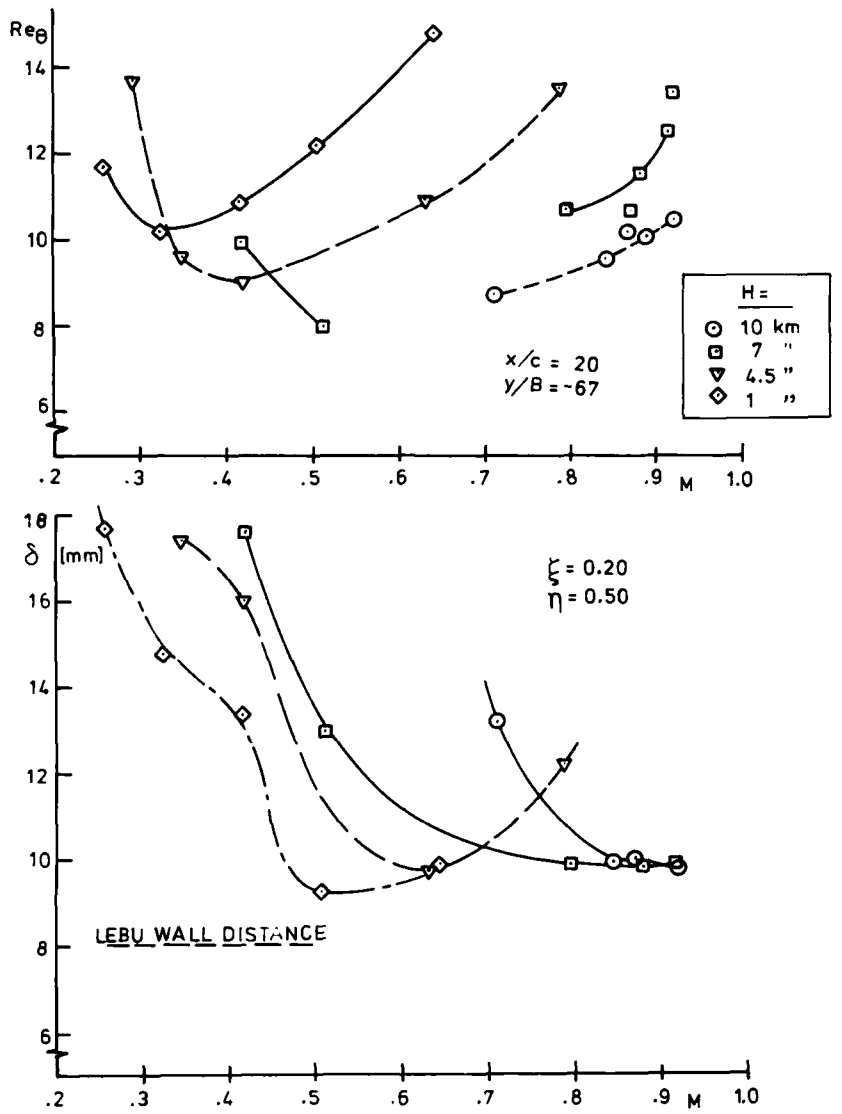


Figure 8. Conditions close behind ribbons; at ξ =0.2. Reynolds number based on momentum thickness, Re_θ, and boundary layer thickness, δ. Variations with flight Mach number and altitude are illustrated.

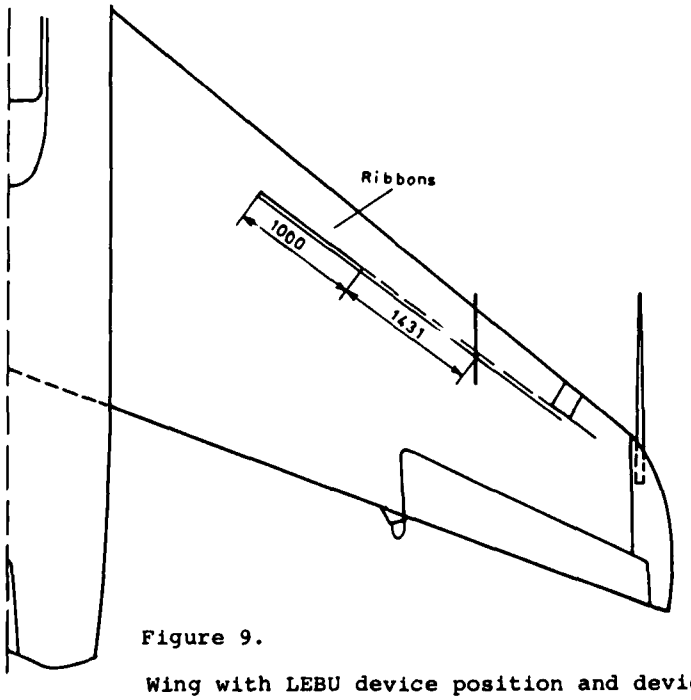


Figure 9.

Wing with LEBU device position and device geometry.

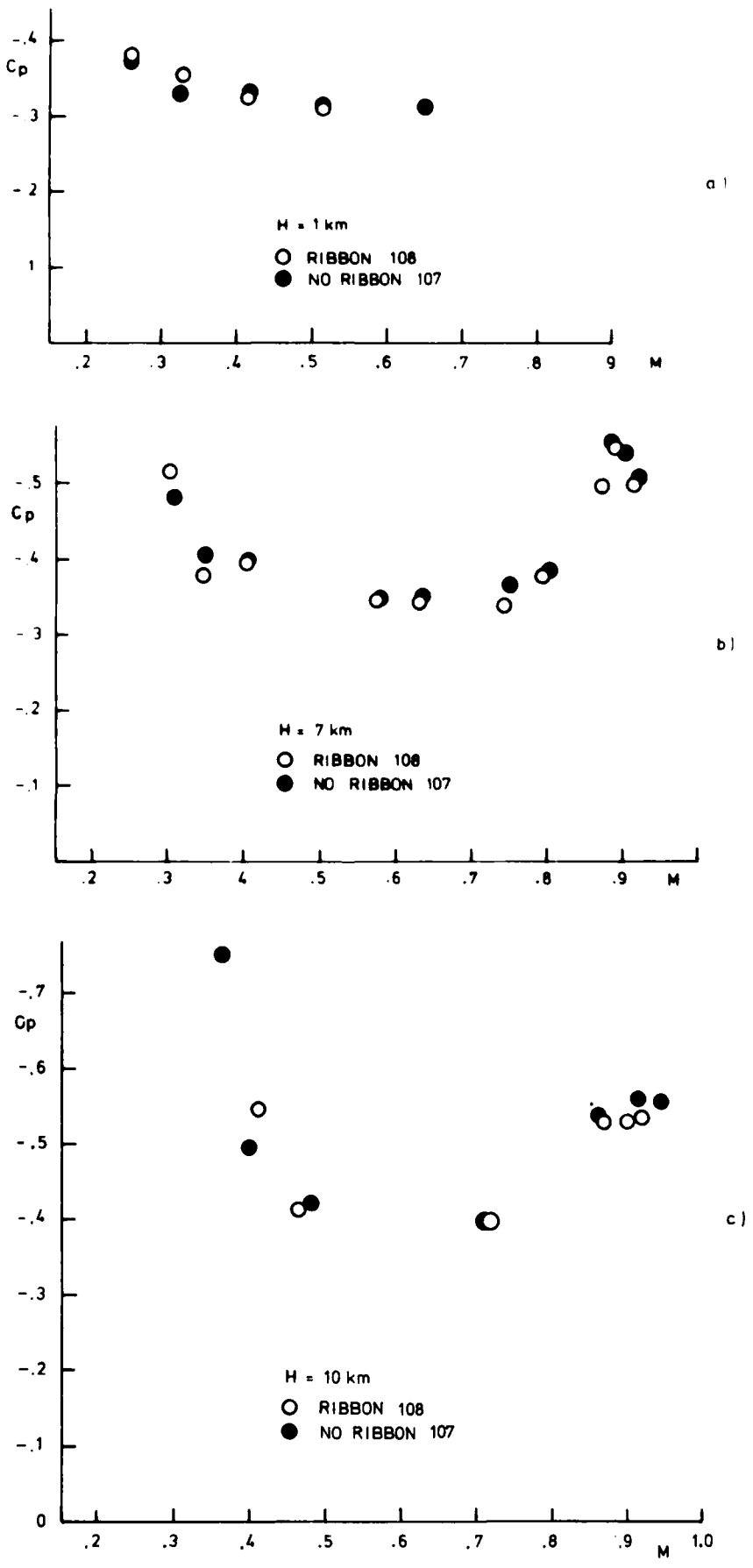


Figure 10. Static pressure C_p as function of Mach number. Open symbols with LEBU device present, filled symbols are baseline.

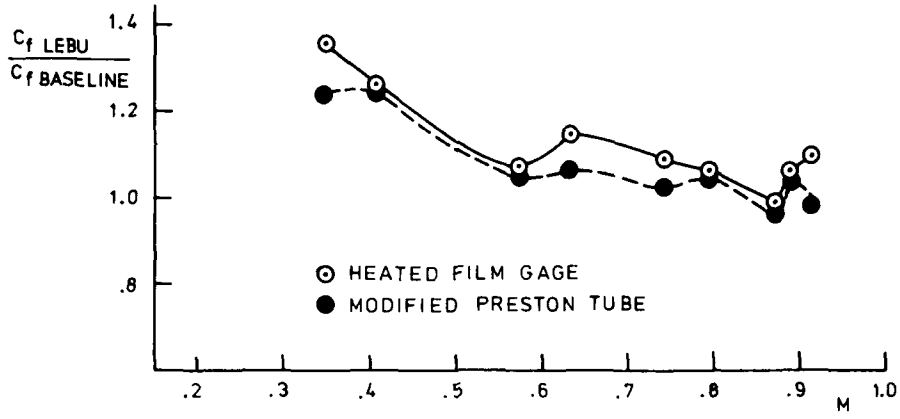


Figure 11. Local skin friction change due to ribbon presence, measured with two different methods.

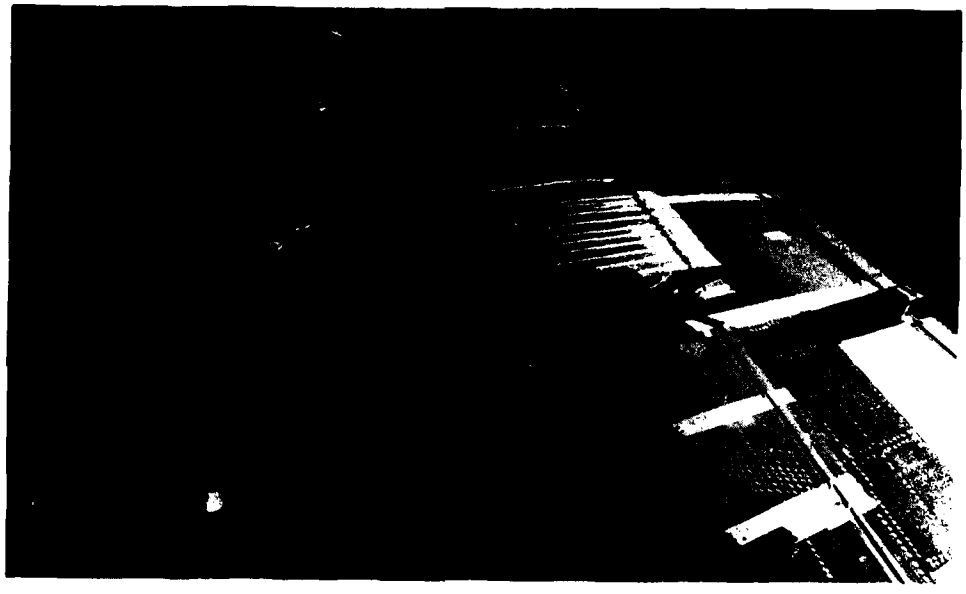


Figure 12. Diagonal array of modified Preston tubes.

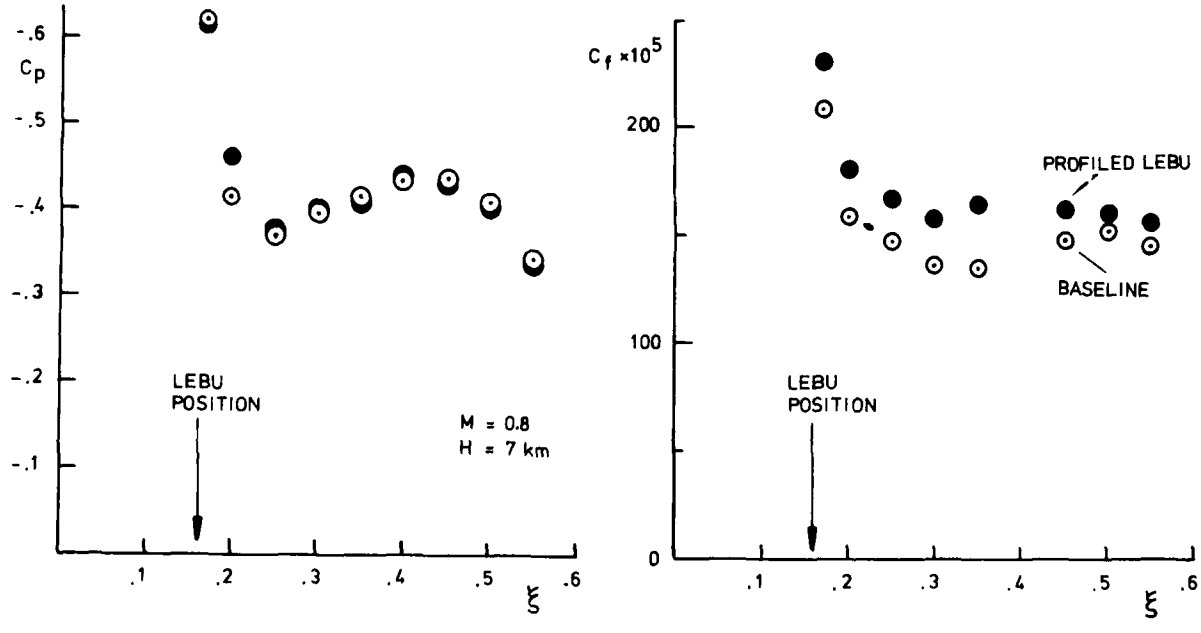


Figure 13. Results from diagonal probe array: local C_f and C_p, compared with baseline values.

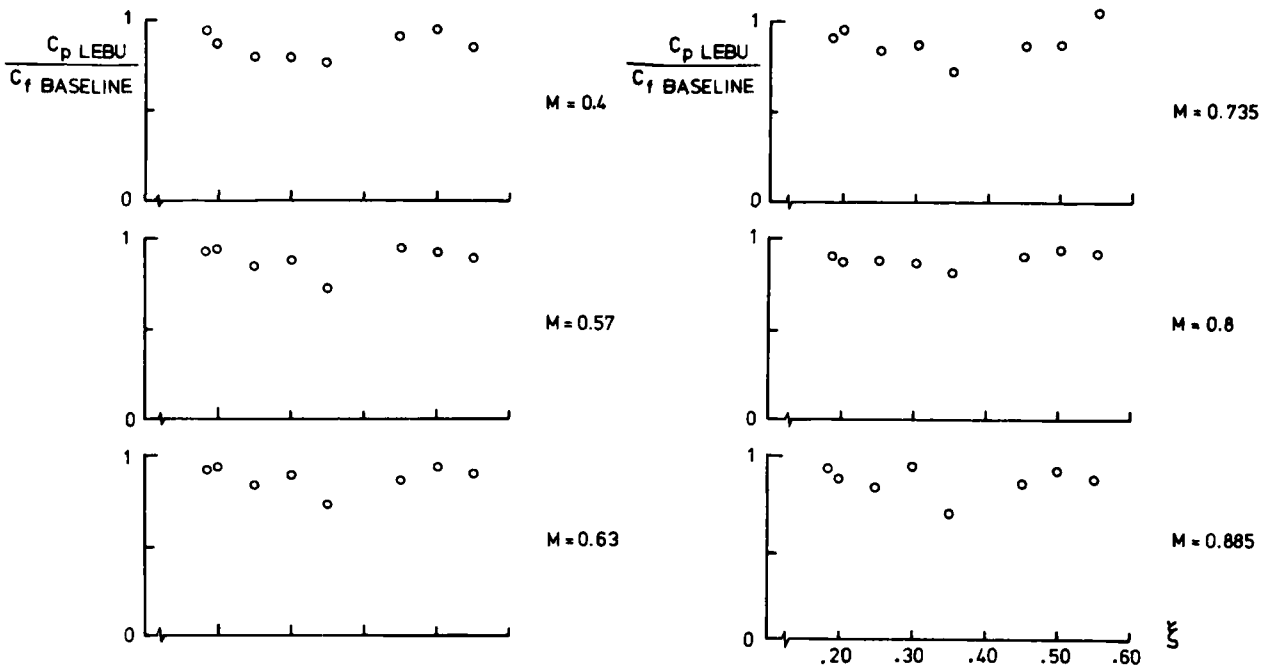


Figure 14. Skin friction reduction/increase along chord at various Mach numbers.

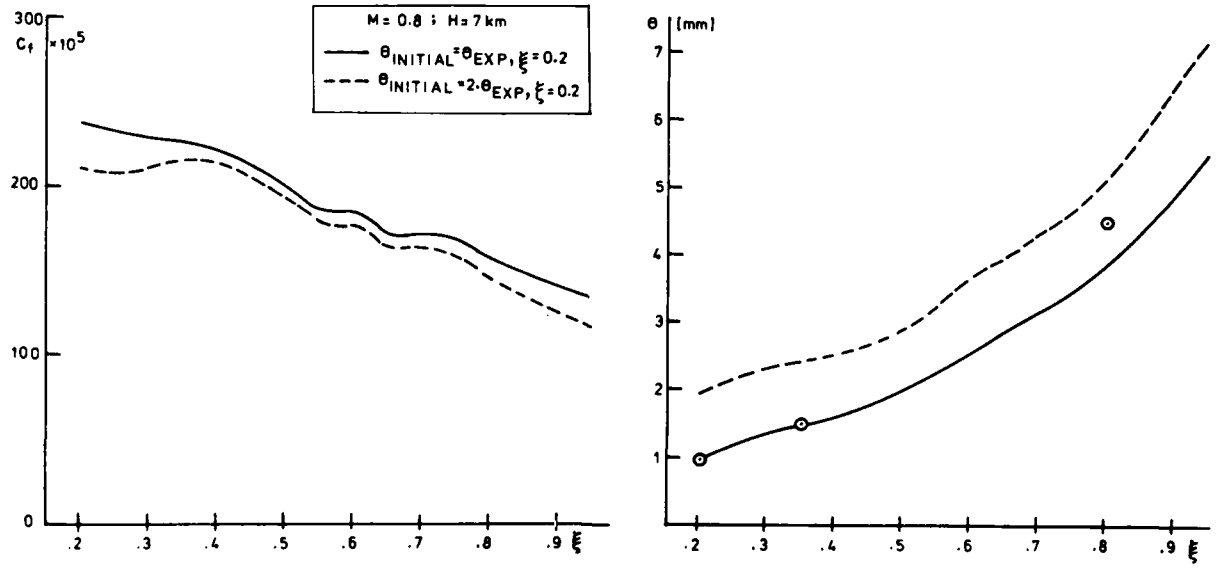


Figure 15. Computed skin friction C_f and momentum thickness θ. M= 0.8 H= 7 km.

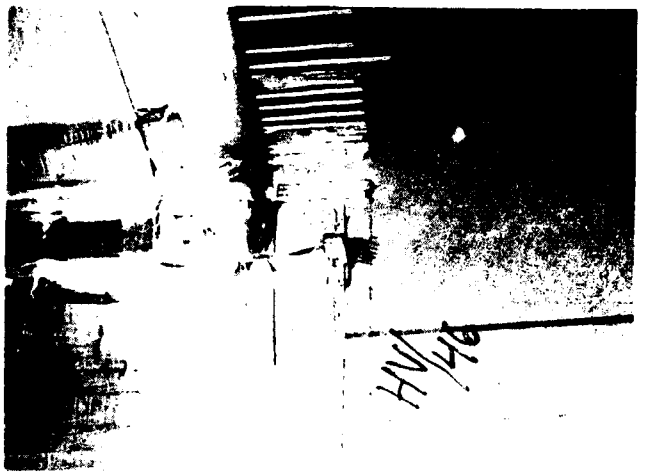


Figure 16. Photography of boundary layer rake and miniature hot wire rake.

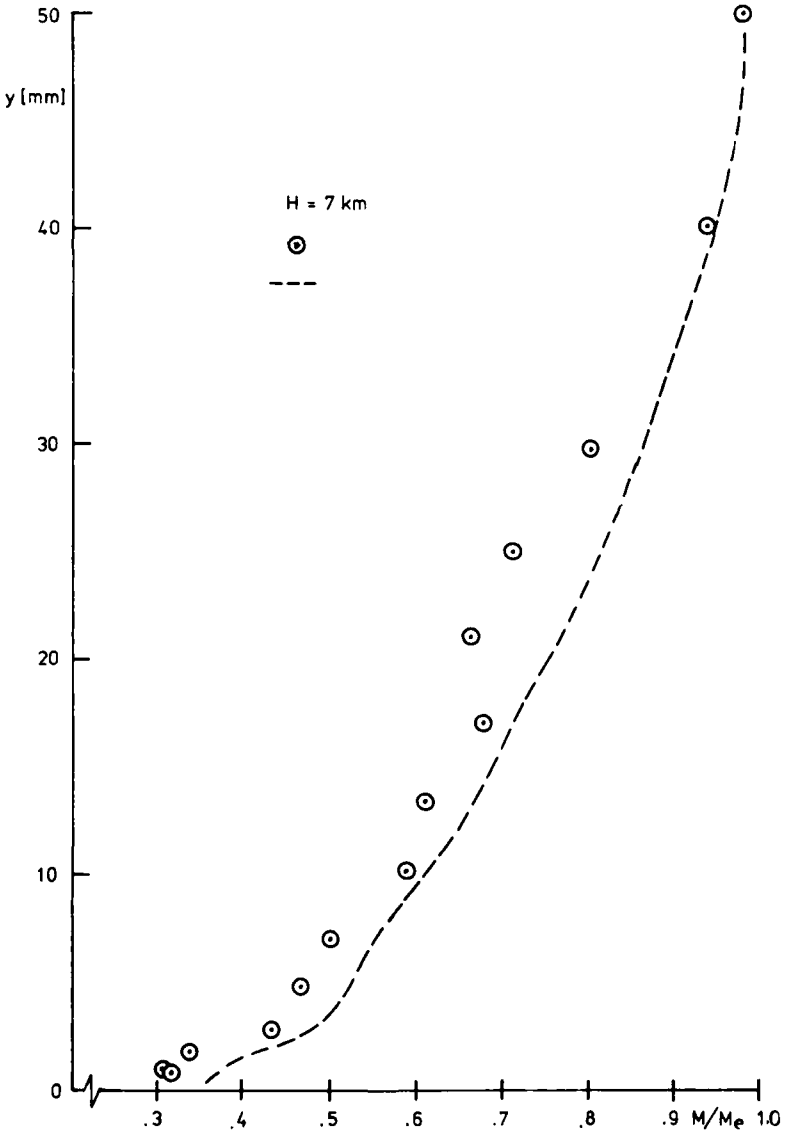


Figure 17. Mean velocity profile at ξ =0.8 with and without LEBU device.

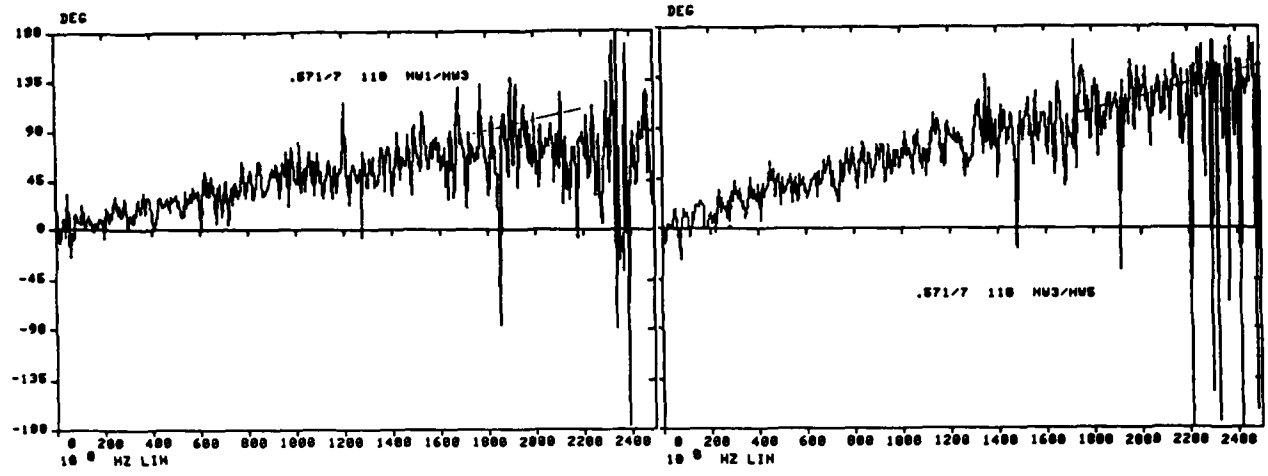


Figure 18. Phase shift between wires in miniature rake at ξ=0.8.
Wire 1 3 5
Wall distance 0.2 mm 2 mm 5 mm

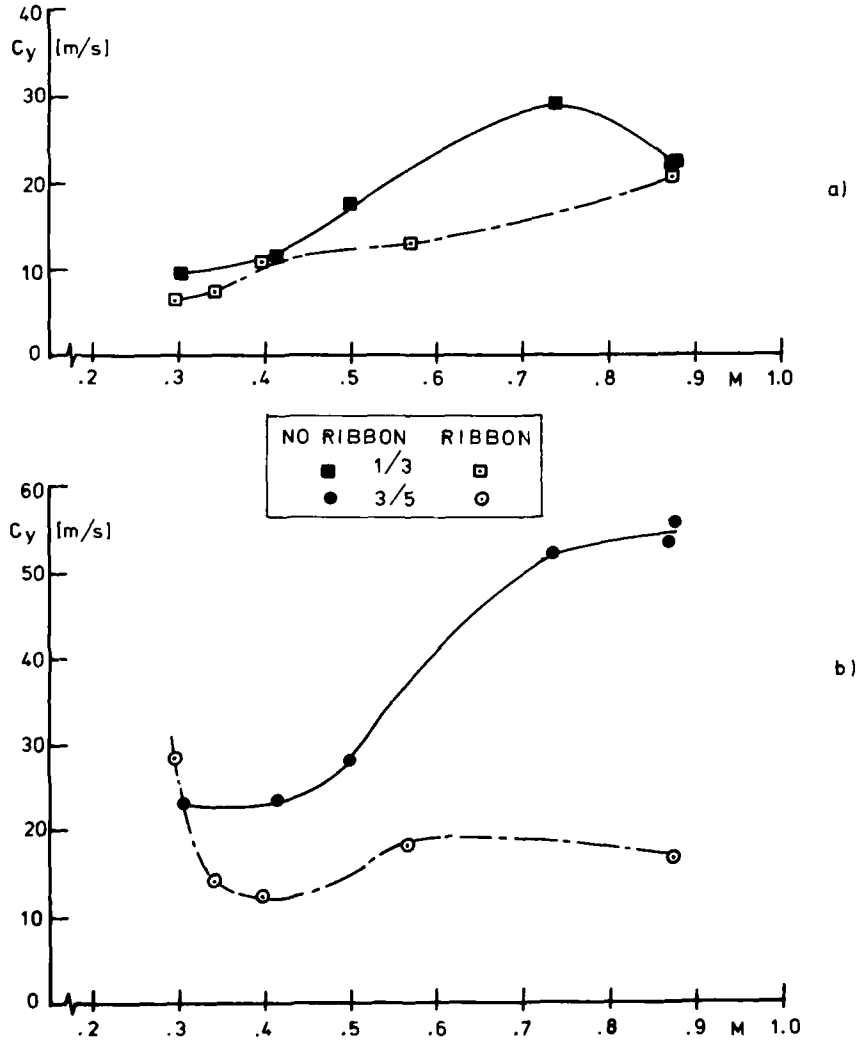


Figure 19. Average phase velocities C_y between wires for cases with and without LEBU device. ξ = 0.8.

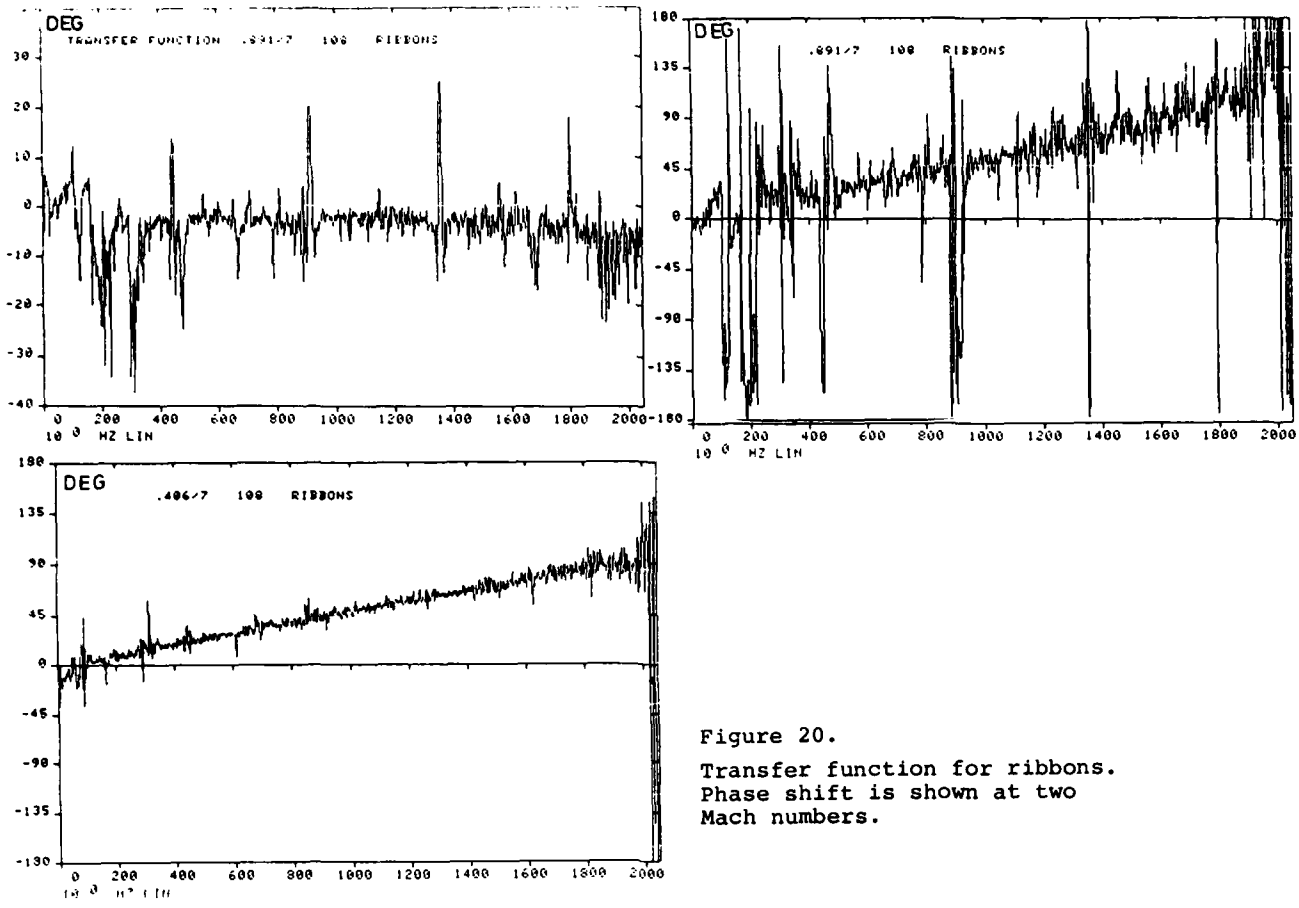


Figure 20.

Transfer function for ribbons. Phase shift is shown at two Mach numbers.

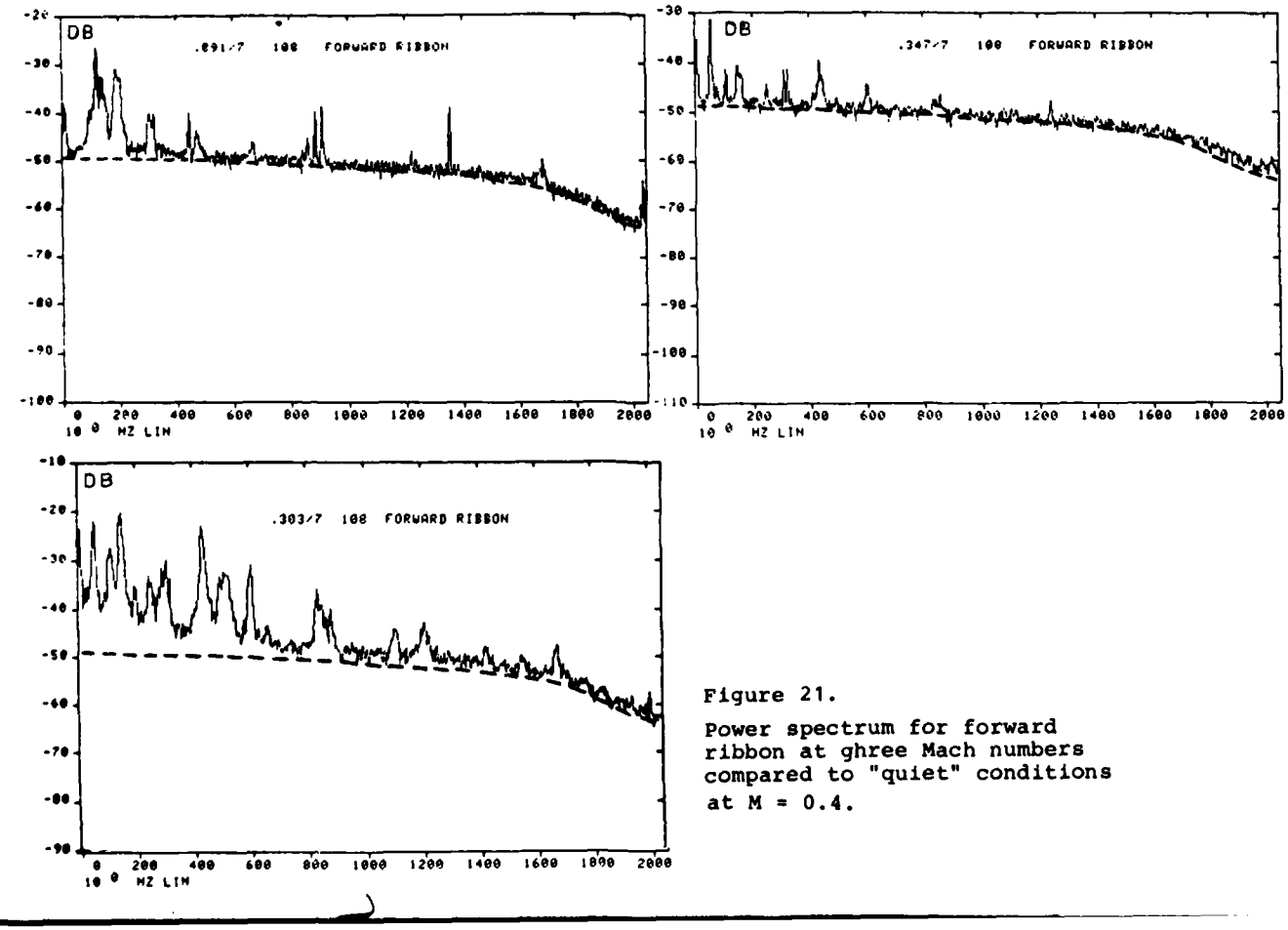


Figure 21.

Power spectrum for forward ribbon at ghree Mach numbers compared to "quiet" conditions at M = 0.4.

PNEUMATIC TURBULATORS - A DEVICE FOR DRAG REDUCTION AT REYNOLDS NUMBERS BELOW 5 × 10^6

K.H. Horstmann
A. Quast
Institut für Entwurfsaerodynamik der DFVLR
3300 Braunschweig, Germany

L.M.M. Boermans
Delft University of Technology
Dept. of Aerospace Eng.
NL 2629 HS Delft, Netherlands

AD-P004 069

SUMMARY

At Reynolds numbers below 5 million, airfoils are affected by laminar separation bubbles which, in many cases, considerably increase the drag. By blowing air from a row of orifices at the beginning of the laminar separation bubble, the bubble can be prevented and the drag can be reduced substantially. This device is called pneumatic turbulator. Free-stream total pressure is sufficient to provide the turbulator bleed air. The additional drag caused by the bleed air and the air jets is negligible. The low drag Reynolds number range of laminar airfoils can be extended by using pneumatic turbulators.

SYMBOLS

c_ℓ		Lift coefficient
c_f'		Local friction coefficient
c_p		Pressure coefficient
c_Q		Turbulator bleed air coefficient $c_Q = \frac{\dot{V}}{U_\infty \cdot S}$
c_d		Airfoil section drag coefficient
dc_d		Drag component of the additional pressure Δc_p due to a laminar separation bubble
H		Shape factor $H = \frac{\delta^*}{\Theta}$
c	m	Airfoil chord
Re		$\frac{U_\infty \cdot c}{\nu}$ Reynolds number based on airfoil chord c
Re_{δ^*}		$\frac{U_x \cdot \delta^*}{\nu}$ Reynolds number based on displacement thickness δ^*
Re_Θ		$\frac{U_x \cdot \Theta}{\nu}$ Reynolds number based on momentum loss thickness Θ
S	m^2	Wing area
u'	m/s	Longitudinal velocity fluctuation
U		Velocity in the viscous shear layer
U_p		(Hypothetical) inviscid flow velocity
U_{po}		Hypothetical inviscid flow velocity at the surface
U_x	m/s	Local velocity calculated from local static pressure
U_∞	m/s	Free-stream flow velocity
$\dot{V}$	m^3/s	Volumetric flow of air jets
x	m	Chordwise distance
x_T	m	Turbulator position
y	m	Distance from the surface
y_o	m	Distance where U = 0; reversed flow region
α	deg.	Angle of attack
γ	deg.	Slope angle of airfoil contour
δ^*	m	Displacement thickness $\delta^* = \int \left(\frac{U_p}{U_{p0}} - \frac{U}{U_{p0}} \right) dy$
Δc_p		Differential pressure coefficient
Δc_d		Additional drag
η_K	deg.	Flap angle
Θ		Momentum loss thickness $\Theta = \int \frac{U}{U_{p0}} \left(\frac{U_p}{U_{p0}} - \frac{U}{U_{p0}} \right) dy$
ν	m^2/s	Kinematic viscosity

Subscript

TE	Trailing edge

1. INTRODUCTION

At Reynolds numbers below about five million, laminar separation bubbles can occur on wings and fuselages. These bubbles are generated by a laminar separation of the flow followed by transition and turbulent reattachment. Laminar separation bubbles are undesirable because they increase the drag by mechanisms which have not yet been fully understood.

The following paper describes the details of laminar separation bubbles and provides a hypothesis of the drag mechanism. Furthermore a device called pneumatic turbulator is presented by which laminar separation bubbles can be avoided, thus leading to a drag reduction. Experimental results on laminar airfoils show the effectiveness of this new device, also in comparison with mechanical turbulators. The application range of the pneumatic turbulators is given.

2. DESCRIPTION OF LAMINAR SEPARATION BUBBLES

Laminar separation bubbles occur, if the laminar boundary layer separates from the surface. Due to the destabilizing effect of the boundary layer velocity profiles with an inflection point the laminar boundary layer rapidly becomes unstable and transition occurs in the free shear layer. Next the turbulent boundary layer reattaches, thus forming a bubble as indicated in figure 1. Figure 1 also shows a typical pressure distribution caused by such a bubble in contrast to a pressure distribution (dashed line) without a separation bubble. The laminar part of the bubble is characterized by nearly constant pressure and the turbulent part by a very steep pressure rise. Due to the change in effective airfoil contour, the pressure in front of and behind the bubble is affected too.

Figure 2 shows a schematic drawing of an oil flow pattern which is frequently observed if the airfoil is vertically mounted in the windtunnel, along with a hypothesis of the internal flow in the bubble. The gradient of the oil flow is an indication of the shear stress: nearly horizontal flow is related to a high shear stress and vertical flow is due to gravity and zero shear.

In the front part of the oil flow pattern the oil flow lines become steeper and finally merge into a vertical line representing the separation line.

In the laminar part of the bubble the oil indicates a slowly moving flow in reversed direction near the surface. The turbulent part of the bubble is indicated by reversed oil flow with high shear stress. In between these rotating flows probably a contrarotating vortex is present. At reattachment there is a fir-tree like flow pattern which is governed by stagnation line flow and shear stress.

It should be mentioned that the oil flow pattern at the end of the bubble frequently indicates a three-dimensional flow character, probably due to three-dimensional waves (originating from the unstable Tollmien-Schlichting waves) or Taylor-Goertler vortices. Accordingly, the drag distribution measured with a wake rake traversing along the model span shows a wavy character.

The size of the laminar separation bubble is related to the stability of the laminar boundary layer which in turn depends on Reynolds number and velocity gradient. By increasing the Reynolds number transition is moving forward and the size of the bubble decreases as shown by the measurements on airfoil HQ 17/14.38 in figure 3. At $Re = 2.5 \cdot 10^6$ there seems to be no bubble anymore. Behind decelerated laminar flow the bubble will be short or non-existent and behind accelerated flow the bubble will be longer. Hence, the bubble dimensions vary with angle of attack, as shown in figure 3 too. It is noted that also in case of transition without a bubble ($\alpha = 4.2^\circ$, $x/c = 0.55$, upper surface), a hump is present in the pressure distribution caused by the change in boundary layer displacement thickness and hence in the effective airfoil contour.

Going into more detail, figure 4 shows results of hot-wire anemometer measurements at several stations on the lower surface of the airfoil. The velocity profiles, longitudinal turbulence intensity profiles (u'), and turbulent frequency spectra (not shown here) were measured perpendicular to the airfoil surface. First the results obtained with the clean surface (continuous line) will be considered. The results obtained with turbulators (broken line) will be discussed in the next chapter.

A laminar separation bubble is present on the lower surface between $x/c \approx 0.73$ where laminar separation takes place, and $x/c \approx 0.81$ where the boundary layer reattaches. Since the hot-wire cannot detect the direction of the flow, the velocities in the lower region of the bubble are misleading. Just behind reattachment, at $x/c = 0.82$, the velocity profile shows a characteristic dint which disappears rapidly downstream as the boundary layer develops into its fully turbulent state. Outside this turbulent boundary layer the velocity shows a slight gradient due to curvature of the flow. Linear extrapolation provides the hypothetical inviscid velocity at the surface U_{po}, which is used as reference in the velocity and turbulence intensity profiles.

Frequency spectra indicate that in the laminar boundary layer several frequencies are amplified, but the turbulence intensity remains very low. In the free shear layer of the bubble, however, the turbulence intensity, in particular the amplitude at 425 Hz, significantly grows. Just in front of $x/c = 0.80$ the pressure distribution shows a sharp corner, generally considered as the position of transition. In the subsequent steep pressure rise both the size of the turbulent region and the intensity of the turbulent motion

drastically grow, as indicated by the profiles at x/c = 0.8 and x/c = 0.82. Frequency spectra show the amplified 425 Hz frequency and its harmonics to be present in the outer flow up to several boundary layer thicknesses from the surface! Hence, the turbulence intensity is not zero at the edge of the boundary layer. Downstream of reattachment the velocity and turbulence intensity near the surface rapidly increase, suggesting a boundary layer velocity profile at reattachment similar to separation, and a large increase of the shear stress thereafter. Downstream of x/c = 0.84 the turbulence intensity decreases, being distributed in the growing boundary layer thickness, and frequency spectra show a regular pattern without peaks. Outside the boundary layer the amplified 425 Hz frequency is present, its power decreases with distance from the surface.

3. ADDITIONAL DRAG OF LAMINAR SEPARATION BUBBLES

It is well-known that laminar separation bubbles can cause additional drag. This additional drag is composed of additional pressure drag and frictional drag on different parts of the surface. Because of the difficulties in calculating the contribution of the pressure drag current profile drag prediction methods compute profile drag by calculating for each surface the development of the momentum loss thickness Θ and applying the well-known Squire-Young relation

$$c_d = 2 \frac{\Theta_{TE}}{c} \left(\frac{U_{TE}}{U_\infty} \right)^{\frac{H_{TE}+5}{2}}$$

in order to correct the momentum defect at the trailing edge (TE) to conditions far downstream. Both pressure drag and frictional drag are incorporated this way.

Following this approach the development of the boundary layer parameters calculated from previous velocity profiles (figure 4) is shown in figure 5. Again, first the results plotted by a continous line will be considered.

Due to the weak pressure gradient the laminar boundary layer development approximates the flat plate case, where H = 2.6. As mentioned earlier, the velocity profiles in the reversed flow region of the laminar separation bubble are misleading. Noting that the velocities in that region are very low, one can write

$$\delta^* = \int_0^\infty \left(1 - \frac{U}{U_x}\right) dy \approx y_o + \int_{y_o}^\infty \left(1 - \frac{U}{U_x}\right) dy$$

$$\Theta = \int_0^\infty \frac{U}{U_x} \left(1 - \frac{U}{U_x}\right) dy \approx \int_{y_o}^\infty \frac{U}{U_x} \left(1 - \frac{U}{U_x}\right) dy$$

which indicates that the reversed flow mainly contributes to the value of δ^*. The increase of δ^* up to the position of transition, and subsequent reduction is evident in figure 5. Contrary, the reattaching and turbulent mixing process involves a sharp increase in momentum loss thickness. Consequently, the shape factor increases to an extremely large value and steeply decreases thereafter. Further downstream a fully turbulent boundary layer develops.

When the boundary layer is artificially disturbed in the vicinity of the laminar separation position, the bubble can be avoided. Figure 4 also shows the pressure distribution and boundary layer profiles measured with a transition strip at x/c = 0.72 (broken line). The strip consists of self-sticking Mylar-film (width 11 mm, thickness 0.25 mm) with digged-in bumps of 1 mm height every 5 mm. Experiments showed that the height of the bumps is just sufficient to trigger the boundary layer.

Behind the strip, at x/c = 0.74, the velocity profile is only slightly affected, however the strip provides turbulence with a primary frequency component of 3600 Hz. Further downstream the boundary layer is much thinner than in the bubble case and the turbulence is concentrated within the boundary layer; the frequency spectra show a regular pattern without peaks.

The corresponding boundary layer parameters in figure 5 also indicate a fully turbulent boundary layer some distance behind the strip.

Applying the Squire-Young relation to the local values of the momentum loss thickness, shape factor and velocity give the development of the equivalent drag values along the surface; the resulting figure is similar to the development of momentum loss thickness. The extrapolated values at the trailing edge indicate that elimination of the bubble reduces the drag contribution of the lower surface by 25% which corresponds to the measured reduction in airfoil drag of 13%.

From these considerations the following tentative conclusions are drawn, illustrated by the schematic sketch in figure 6. In case of a pronounced laminar separation bubble ①,

indicated by the magnitude of the pressure jump for the reattaching transitional shear layer to overcome the increase in momentum loss thickness in this region is the main reason for the drag increase. Triggering the boundary layer in the vicinity of the laminar separation position may easily result in a drag decrease ③ . However, if the bubble is thin or small triggering may be ineffective or even harmful ② . An example of the latter case is given in reference [1].

With respect to profile drag prediction methods, it is clear that the flow mechanism at the rear of the bubble, which define the starting conditions of the turbulent boundary layer, play a crucial role. No method is known to the authors which handles this satisfactorily. As a consequence, drag prediction in case of laminar separation bubbles is not very reliable yet.

Finally, it is noted that there is a lower limit of the Reynolds number Re_ϑ based on the momentum loss thickness below which no turbulent boundary layer flow can exist. For instance, Preston shows that this Reynolds number for a flat plate at zero pressure gradient is 320, reference [2], and that in case of lower values, the drag of the transition device should increase Re_ϑ up to this value.

As mentioned in the beginning of this chapter, the additional drag due to a bubble is composed of additional pressure drag and frictional drag.

While the frictional drag contribution of the turbulent boundary layer can be measured for instance by a pitot-probe (Preston-tube), measurements inside the bubble are difficult. A pitot-probe gives a wrong indication when the flow direction exeeds ±30 degrees and hot wire probes generally do not indicate the flow direction. Probably laser velocimetry will give the answers.

With respect to pressure drag, the next considerations clarify some typical features. Figure 7 shows again the change in pressure distribution due to a bubble, and the resulting additional pressure drag component which can be written as

$$\Delta c_d = \int \Delta c_p \cdot \sin(\gamma + \alpha) d(x/c) \ .$$

$(\gamma + \alpha)$ is the angle of the surface with respect to the oncoming flow. If this angle is zero ($\alpha = -\gamma$), there is no additional pressure drag. Compared to the lift of the airfoil section, the additional lift component is negligible.

The following numerical values illustrate the pressure drag contribution due to a bubble. Assuming that there is no bubble anymore on the lower surface at $Re = 2.5 \cdot 10^6$, the measured pressure distributions of figure 3 can be integrated according to the previous equation, taking

$$\Delta c_p = c_{p\ Re} - c_{p(Re=2.5\cdot10^6)}.$$

The pressure drag values listed in table 1 are of the same order of magnitude as the drag reductions caused by pneumatic turbulators*), indicating that the frictional drag contribution due to the bubble is relatively low. A comparison is given in table 1. The results should be considered with care because integration could only be performed approximately since there were only 5 pressure holes in the region of the laminar separation bubble being not sufficient for an accurate representation of the pressure distribution.

The effect of laminar separation bubbles on the drag polars is shown schematically in figure 8. Figure 8a represents the effect of a laminar separation bubble on the upper surface of an airfoil. A characteristic feature is the increase of the additional drag with increasing lift coefficient (angle of attack), which is in accordance with the previous equation. Another characteristic feature is the reduction of drag at the upper limit of the laminar bucket. This reduction is due to the disappearance of the laminar separation bubble since, at higher angles of attack, suction peaks form at the leading edge and the subsequent pressure rise destabilizes the boundary layer in such a way that a normal laminar-turbulent transition occurs prior to laminar separation.

Figure 8b shows the inverse behaviour due to the additional drag of an airfoil with a lower side bubble. The polar of an airfoil with a bubble on upper and lower side would be as shown in figure 8c. The hatched area indicates the additional drag caused by bubbles on upper and lower surface.

Figure 9 shows a practical example of such a drag polar. The airfoil is the Wortmann FX 66-S-196V1 and the measurements were taken from reference [3]. The drag reduction at the limits of the low drag bucket due to the disappearance of the bubble on either surface is obvious, indicating that an elimination of the bubble on both surfaces by triggering would result in a drag reduction between zero lift and nearly maximum lift.

4. DRAG REDUCTION BY MEANS OF PNEUMATIC TURBULATORS

4.1 Description of bubble avoiding devices

As clarified in the previous chapter, laminar separation bubbles are responsible for

*) pneumatic turbulators are discussed in detail in chapter 4.2

the increased drag of some airfoil sections. To prevent these laminar separation bubbles, different techniques can be used. One of these techniques first used by Wortmann [4] is to shape the airfoil sections with so-called destabilizing regions as shown in figure 10. Destabilizing regions are parts of the airfoil with a slightly adverse pressure gradient which promotes transition without laminar separation. At optimum design of the destabilizing region transition occurs just at the end of the region.

Destabilizing regions, however have the following disadvantages:

- A destabilizing region can only be correct for one particular Reynolds number. As indicated in figure 11, at lower Reynolds numbers a separation bubble forms as a result of insufficient destabilization whilst at higher Reynolds numbers the laminar-turbulent transition occurs too early because of too much destabilization. In both cases, drag is higher than necessary.
- A destabilizing region can only be correct for one particular angle of attack or flap angle. With a higher angle of attack, for instance, the pressure increase is steeper on the upper side and flatter on the lower side.

As a result we can notice, that for an airfoil with only one design point there is no need for turbulators; an optimum design can be performed using only destabilizing regions. As far as there is more than one design point with respect to angle of attack, flap deflection and Reynolds number turbulators are an additional powerful tool to avoid drag originating from laminar separation bubbles.

Other devices are mechanical turbulators consisting of trip wires, steps, artificial roughness of sand grains or wire brackets bonded to the skin. D. Althaus has shown that small strips of tape and tape with digged-in bumps prevent the occurence of laminar separation bubbles [5,6]. Experiments performed by Henningsen [7] showed that porous surfaces covering aluminium honeycomb also acted as "turbulators". With a smooth porous panel, transition from laminar to turbulent flow occured considerably further forward than with a non-porous panel. It was not possible to achieve the original aim of damping out Tollmien-Schlichting oscillations; in the contrary, it appeared that the transition from laminar to turbulent flow was even promoted by the porous surfaces.

4.2 Description of pneumatic turbulators

A transition from laminar to turbulent flow is easily achieved using air jets because the laminar flow is disturbed in three dimensions, thus producing the transition very rapidly. If turbulators are not needed, the air jets can simply be switched off. Experimental techniques frequently make use of these jets of air ejected from a series of holes near the leading edge of an airfoil in order to achieve premature transition from laminar to turbulent flow [8]. In doing this, the aim is to simulate the flow conditions at high Reynolds numbers. Wallis [9] has used air jets practically as a substitute for normal "vortex generators" (but switchable) in order to prevent early turbulent separation. Pfenninger [10] has used rows of air jets in order to prevent laminar trailing edge separation.

In order to prevent laminar separation bubbles, the air jets should operate in the vicinity of the separation line as shown in references [11] and [12]. The jets of air are produced by small tubes with an internal diameter of 0.6 mm which are spaced in spanwise direction at intervals of 1.6 ÷ 3.2% of the wing chord. The air for the jets is supplied by an internal duct with total pressure which if necessary can be reduced by suitable devices, thereby reducing the volume of air emerging from the jet orifices.

Pneumatic turbulators offer the further advantage that they are still active in the region behind laminar separation. A mechanical turbulator submerged within the separated region of the bubble is ineffective. A jet of air, on the other hand, passes through this region and disturbs the laminar flow outside the bubble. This is an important point since the turbulators should remain effective even in the area of the laminar separation bubble (i.e. behind the point of laminar separation) because the bubble can move due to Reynolds number, angle of attack and flap deflection.

In principle, it should be possible to achieve similar results by sucking as well as blowing air through orifices, since a sink in the flow also represents a three-dimensional disturbance. However, there are currently no experimental results available on this subject.

4.3 Results for different airfoils

The effect of pneumatic turbulators can be seen in figure 12, showing the characteristics of airfoil DU-80-176, measured in the windtunnel of the Delft University of Technology. Oil-flow patterns indicated the existence of pronounced laminar separation bubbles downstream of the pressure rise at x/c = 0.65. The air volume flow for the turbulators was adjusted to practical sailplane application: an intake nozzle was dimensioned such that the turbulators worked well at practical combinations of lift coefficient and Reynolds number.

A slightly more cambered version of this airfoil was applied in modifying the wing of an existing high performance sailplane just by adding material to the surface. Flight performance measurements before and after the wing modification showed an improvement of about

5% in glide ratio over the entire flight speed range [13].

Another example which illustrates the effectiveness of pneumatic turbulators is given in figure 13, showing drag and pressure distribution for the airfoil DFVLR-HQ-26/14.82 measured in free flight on the flying testbed sailplane "JANUS" of DFVLR Braunschweig. Turbulators are located at x/c = 0.892 on the lower surface. Again, the drag is reduced by the turbulators. According to chapter 3 the drag reduction decreases with increasing lift coefficient. The pressure distribution without a separation bubble is represented by the dashed line obtained by using pneumatic turbulators. Without these turbulators there is the characteristic pressure increase in front of laminar separation and the pressure flattening thereafter as shown in figure 1. The characteristic steep pressure rise at the rear part of the bubble is missing because it is located behind the trailing edge.

Figure 14 shows results of free flight and windtunnel measurements on the same model with airfoil HQ-17/14.38, mentioned before. The flap was set at $\eta_K = -8°$ and measurements were performed without turbulators, with mechanical turbulators (tape with bums) and with pneumatic turbulators at two different Reynolds numbers. A remarkable drag reduction by turbulators can be seen and furthermore this figure shows that mechanical turbulators nearly have the same effectiveness in this case as pneumatic turbulators.

As in figure 12, in the "no turbulator case" there is a drag reduction at the lower limit of the laminar drag bucket due to the disappearance of the bubble on the lower surface as a result of destabilization of the flow behind a leading edge pressure peak.

The influence of pneumatic turbulators on drag in the Reynolds number region of model airplane is shown in figure 15. The measurements are taken in the small cascade windtunnel of DFVLR Braunschweig [14]. The turbulators are arranged on the upper surface of the airfoil DFVLR-RA-02/K at x/c = 0.445. The drag reduction due to turbulators is strongly increasing with decreasing Reynolds number. A maximum drag reduction of about 40% can be obtained at $Re = 0.1 \cdot 10^6$. At lift coefficients $c_L > 0.8$ the polars with and without turbulators have nearly the same development. In this region the instabilization of the boundary layer is high enough to cause transition upstream of the separation point and thus no bubble is present. It is remarkable that pneumatic turbulators do not cause additional drag, when transition occurs upstream of the turbulator position and hence the turbulators disturb the turbulent boundary layer.

4.4 Parameter investigations

As mentioned before, the size of laminar separation bubbles increase with decreasing Reynolds number. Hence, the drag reduction by turbulators increase too, as shown in figure 16.

In figure 17 the effect of turbulators position on drag reduction at the same airfoil as in figure 15 is shown. There exists an optimum turbulator position close to the laminar separation point. If the turbulators are arranged upstream of the optimum position the drag coefficient increases due to the smaller region of laminar flow. At downstream positions the drag coefficient increases too, due to remaining parts of the bubble between and before the turbulators bleed holes.

The optimum turbulator position is slightly depending on the Reynolds number. With lower Reynolds number the optimum position as well as the laminar separation point is moving upstream. Especially at very low Reynolds number this effect can be seen clearly because the larger laminar separation bubbles (40% of chord at $Re = 0.1 \cdot 10^6$) are more influencing the pressure distribution upstream of the bubble than a smaller one thus inducing a more upstream occuring separation.

Figure 18 shows a typical example of the drag curve with air jet coefficient c_Q (or air volume flow per pneumatic turbulator). As the air volume flow increases, the drag drops initially due to a shrinking of the laminar separation bubble. Next the drag remains at a low level, hardly affected by the amount of air blowing out of the turbulators.

The energy loss (additional drag) as a result of the ram air diverted to the air jets amounts to

$$\Delta c_d = 2\, c_Q \quad .$$

Since the drag coefficient of a laminar airfoil is of the order of 5.10^{-3} this additional drag, being in the order of $5 \cdot 10^{-6}$, is negligible.

As shown in figure 18, a certain minimum amount of air is needed for the pneumatic turbulators to function well. Similarly, a certain minimum height of the mechanical turbulators is needed to trigger the boundary layer. An example of malfunction of mechanical turbulators is shown in figure 19. The airfoil and test techniques are the same as in figure 14, but now the flap is set at $\eta_K = -12°$. At both Reynolds numbers the mechanical turbulators (tape with digged-in bumps, about 0.1% c high and 5% c spacing) do their job if positioned at 72% chord on the lower surface. Due to the flap deflection the pressure distribution changes such that the flow should be triggered just in front of the flap, at 80% chord. As shown, an extra drag reduction of about 10% is obtained at $Re = 3 \cdot 10^6$, however there is a turbulator malfunction at $Re = 1.55 \cdot 10^6$ and c_L below 0.45. Turbulator malfunction of this type was up to now never observed with pneumatic turbulators.

5. THE RANGE OF APPLICATION FOR PNEUMATIC TURBULATORS

It has been shown that pneumatic turbulators prevent laminar separation bubbles and thus extend the low-drag Reynolds number range of airfoil sections.

Pneumatic turbulators can be applied successfully if:

- laminar separation bubbles occur and
- an airfoil section is required with a wide operating range as far as the Reynolds number, lift coefficient and flap deflection are concerned.

There would thus appear to be the following potential applications:

1. cascades in turbomachinery
2. propellers and helicopter rotors
3. gliders and light aircraft
4. RPV and model aircraft.

Experiments with turbine cascades at low Reynolds numbers with different transition devices, conducted at the main cascade test facility in Braunschweig, showed that especially pneumatic turbulators reduce the drag of cascade arrangements in a wide range of Reynolds numbers. Air jets on the suction side were supplied through holes from the pressure side.

6. CONCLUSIONS

At Reynolds numbers below 5 million and if a wide range of operation concerning lift coefficient, flap deflection and Reynolds number is demanded, it is advantageous to implement turbulators in laminar airfoil design. Careful positioning of turbulators near the laminar separation point avoids laminar separation bubbles and reduces the drag. Turbulators enlarge the low drag Reynolds number range of an airfoil giving nearly the same drag which is otherwise obtained by several airfoils designed for minimum drag at different Reynolds numbers.

Therefore the design philosophy for airfoils with turbulators differs considerably from that used up to date in laminar airfoil design: the design of airfoils with turbulators should be based on the maximum Reynolds number for the range of the airfoil and not on average Reynolds number.

Besides well-known mechanical turbulators consisting of bump tape pneumatic turbulators were introduced. Pneumatic turbulators consist of air jets expelled from a row of orifices positioned in spanwise direction close to the laminar separation line simply supplied by total pressure. The energy loss (additional drag) of the air jets is negligible compared to the drag reduction due to the very low air volume flow.

Experimental results of four different airfoils for sailplane and model airplane application taken in windtunnel and free flight tests show that the pneumatic turbulators are very effective, reducing the airfoil drag in the order of 40% at $Re = 0.1 \cdot 10^6$ and 15% at $Re = 1 \cdot 10^6$.

Mechanical turbulators in general give the same results in drag reduction. But they should be used carefully because their height has to be adapted to the flow conditions. Otherwise they may be submerged into the separated flow of the bubble and becoming ineffective.

A very interesting further application of pneumatic turbulator would appear in turbine cascades.

7. REFERENCES

[1] Boermans, L.M.M.
Oolbekkink, B.
Windtunnel Tests on an Outer Wing Segment of the ASW-19X Sailplane.
Report LR-369 (1983), Delft University of Technology, Dept. of Aerospace Engineering.

[2] Preston, J.H.
The Minimum Reynolds Number for a Turbulent Boundary Layer and the Selection of a Transition Device.
Journal of Fluid Mechanics, Vol. 3 (1957), pp. 373-384.

[3] Gooden, J.H.M.
Experimental Low-Speed Aerodynamic Characteristics of the Wortmann FX66-S-196V1 Airfoil.
Ostiv Publication XV, 1980.

[4] Wortmann, F.X. — Experimentelle Untersuchungen an neuen Laminarprofilen für Segelflugzeuge und Hubschrauber.
Z. Flugwiss. 5 (1957), H. 8, pp. 228-243.

[5] Althaus, D. — Profilpolaren für den Modellflug.
Neckar-Verlag, Villingen-Schwenningen, 1980.

[6] Althaus, D. — Influencing Transition on Airfoils.
XVII. OSTIV Congress, Paderborn, Germany, 1981.

[7] Henningsen, A.W. — Versuche zur Dämpfung von Grenzschichtschwingungen mittels poröser Oberfläche.
Studienarbeit DFVLR Braunschweig, Prof. Dr.-Ing. F. Thomas, Januar 1979.

[8] Ashill, P.R.
Weeks, D.J. — An Experimental Investigation of the Drag of Thick Supercritical Aerofoils - A Progress Report.
Lecture Transonic Configuration Symposium, Bad Harzburg, Germany, 13-17 June, 1978.

[9] Wallis, R.A. — The Use of Air Jets for Boundary Layer-Control.
ARL (Australia) Aero. Note 110 (1952).

[10] Pfenninger, W. — Untersuchungen über Reibungsverminderungen an Tragflügeln, insbesondere mit Hilfe von Grenzschichtabsaugung.
Mitt. a.d. Inst. f. Aerodynamik, ETH Zürich Nr. 13, Verlag Gebr. Leeman & Co., Zürich, 1946.

[11] Horstmann, K.H.
Quast, A. — Widerstandsverminderung durch Blasturbulatoren.
DFVLR-FB 81-33 (1981).

[12] Quast, A.
Horstmann, K.H. — Anordnung zur Beeinflussung der Strömung an aerodynamischen Profilen.
Deutsche Patentanmeldung P 30 43 567.7.-53.

[13] Boermans, L.M.M.
Selen, H.J.W. — Design and Tests of Airfoils for Sailplanes with an Application to the ASW-19B.
ICAS-Paper 82-5.5.2, Seattle, USA, 1982.

[14] Voth, M.-A. — Experimentelle Untersuchungen an einem Tragflügelprofil im Reynoldszahlbereich von $1.0 - 2.0 \cdot 10^5$.
Studienarbeit DFVLR Braunschweig, Prof. Dr.-Ing. F. Thomas, 1983.

Re	$\Delta c_d = \Delta c_p \cdot \sin(\gamma + \alpha)\, d(x/c)$	Drag reduction measured as a result of pneumatic turbulators
$0.7 \cdot 10^6$	0.0025	0.0027
$1.0 \cdot 10^6$	0.0019	0.0018
$1.5 \cdot 10^6$	0.0011	0.0012
$2.0 \cdot 10^6$	0	0.0006

Table 1 Comparison of the calculated pressure drag Δc_d of the separation bubble with the measured drag reduction with pneumatic turbulators used on the lower side of airfoil section HQ-17/14.38, $\eta_K = -10^o$, $\alpha = 5^o$.

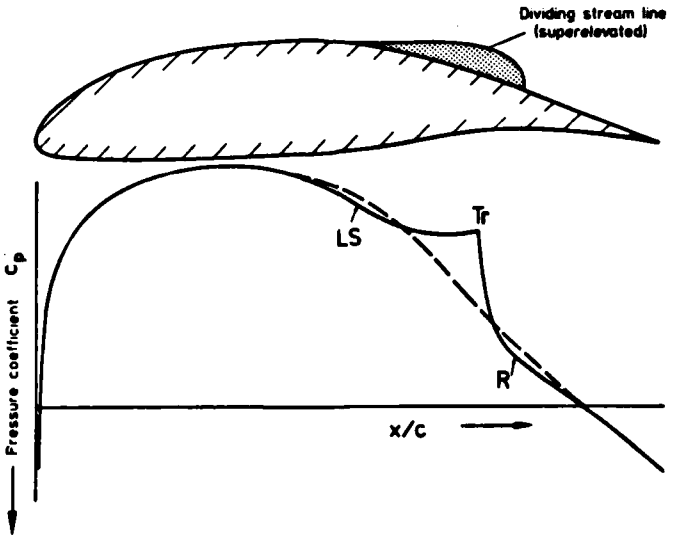


Fig. 1 Characteristic pressure distribution of the upper surface of an airfoil section with laminar separation bubble and assumed dividing streamline
LS = Laminar separation; Tr = Transition;
R = Reattachment

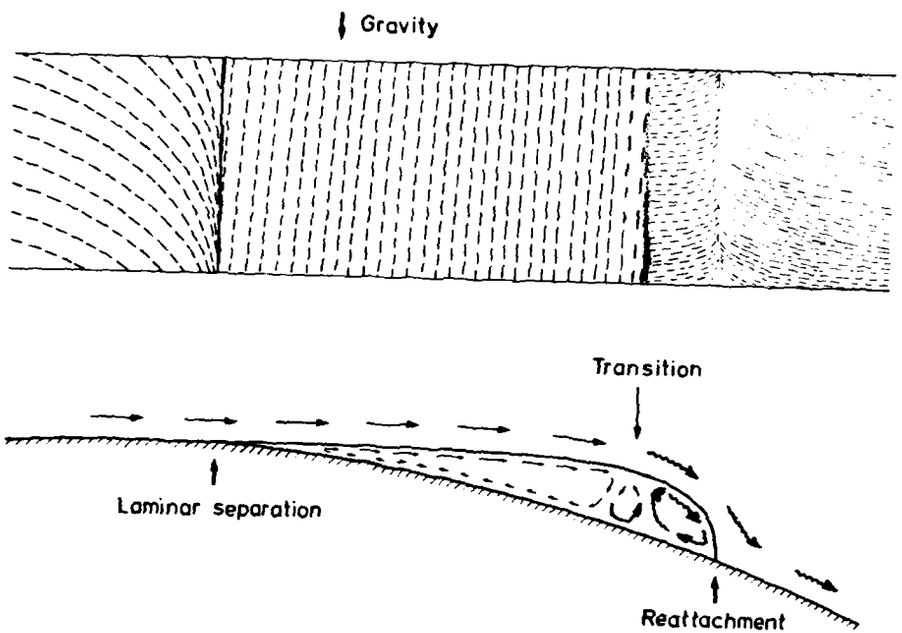


Fig. 2 Schematic view of assumed internal flow in a laminar separation bubble and oil flow pattern on a model vertically installed in the wind tunnel

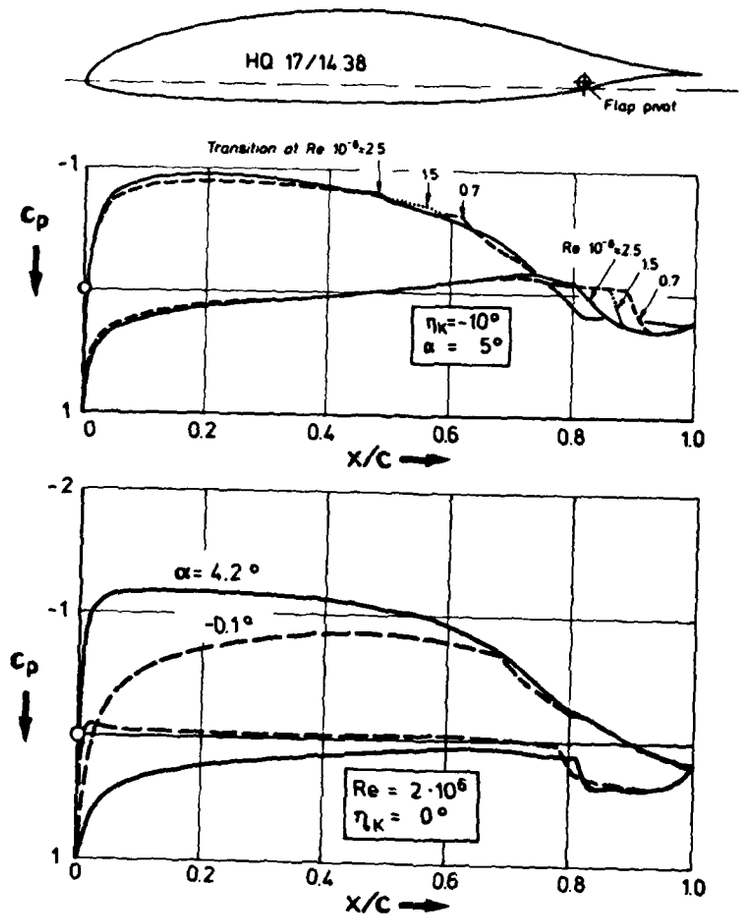


Fig. 3 Size and position of the laminar separation bubble as a function of Reynolds number and angle of attack of airfoil section DFVLR HQ 17/14.38 (Measurements TH Delft)

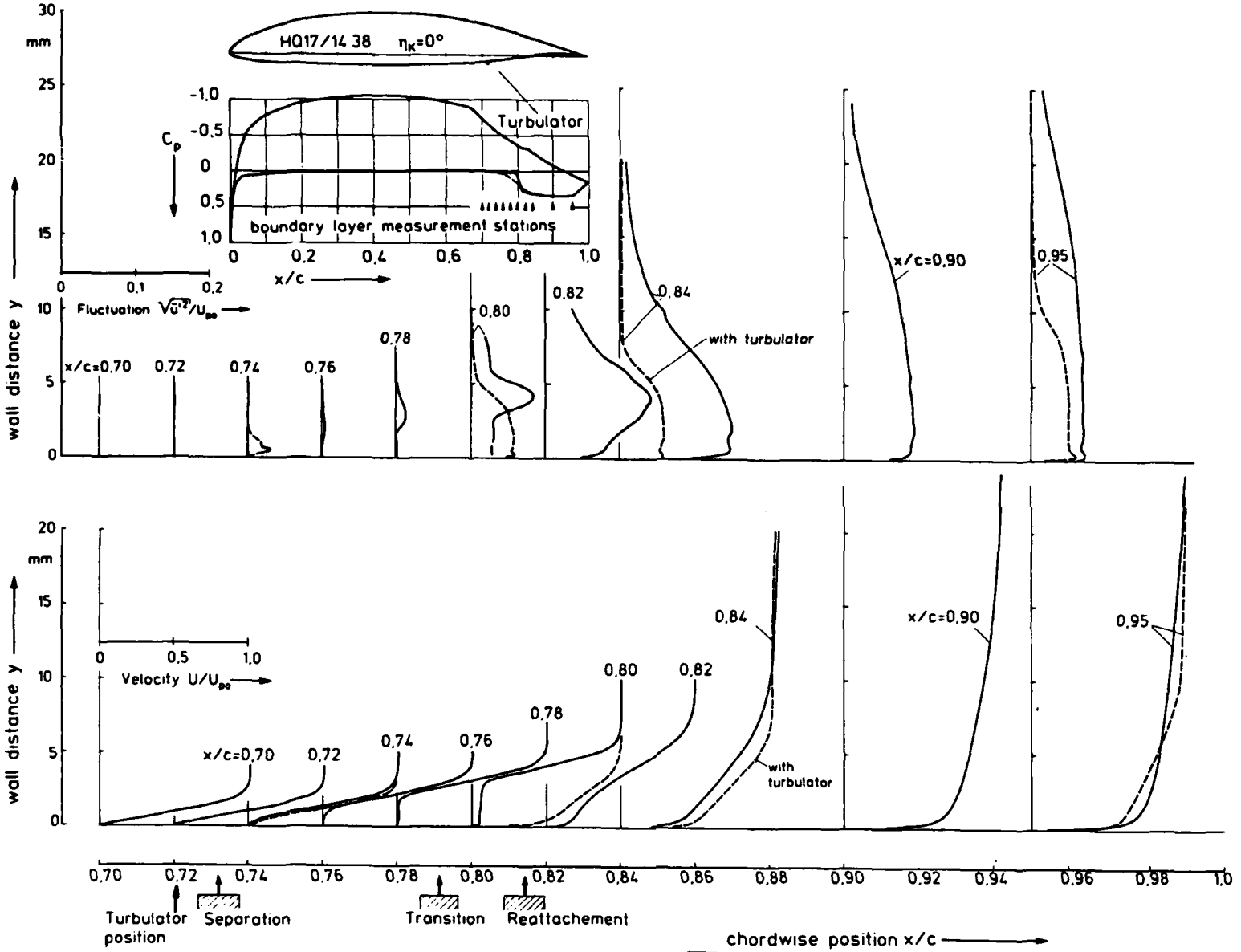


Figure 4 Boundary layer velocity U/U_{po} and fluctuation $\sqrt{\overline{u^2}}/U_{po}$ profiles for lower surface of airfoil HQ 17/14.38 with and without laminar separation bubble, Re = $2 \cdot 10^6$ (Measurements TH Delft)

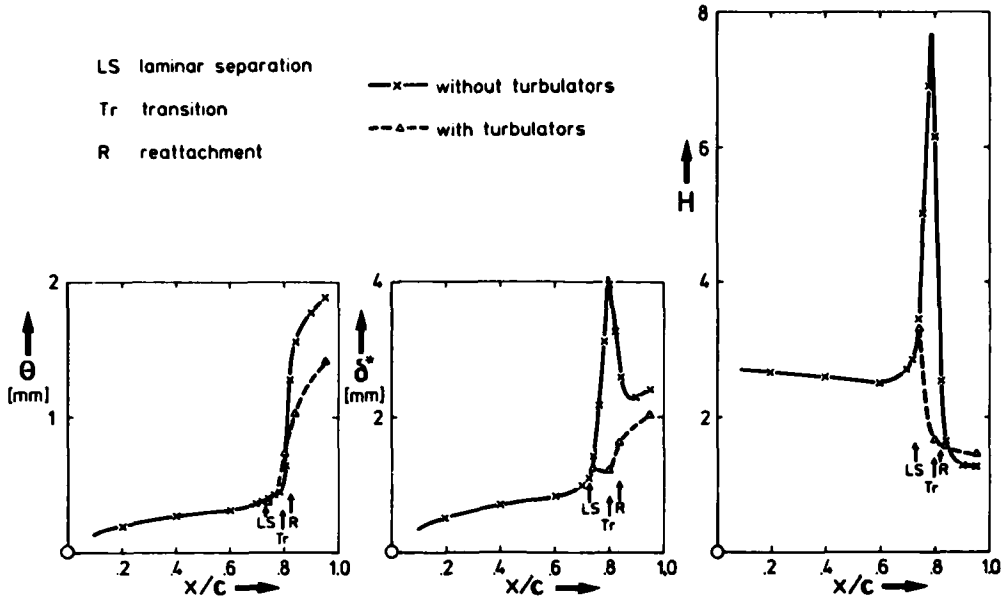


Fig. 5 Development of boundary layer parameters calculated from the velocity profiles in figure 4 (Measurements TH Delft)

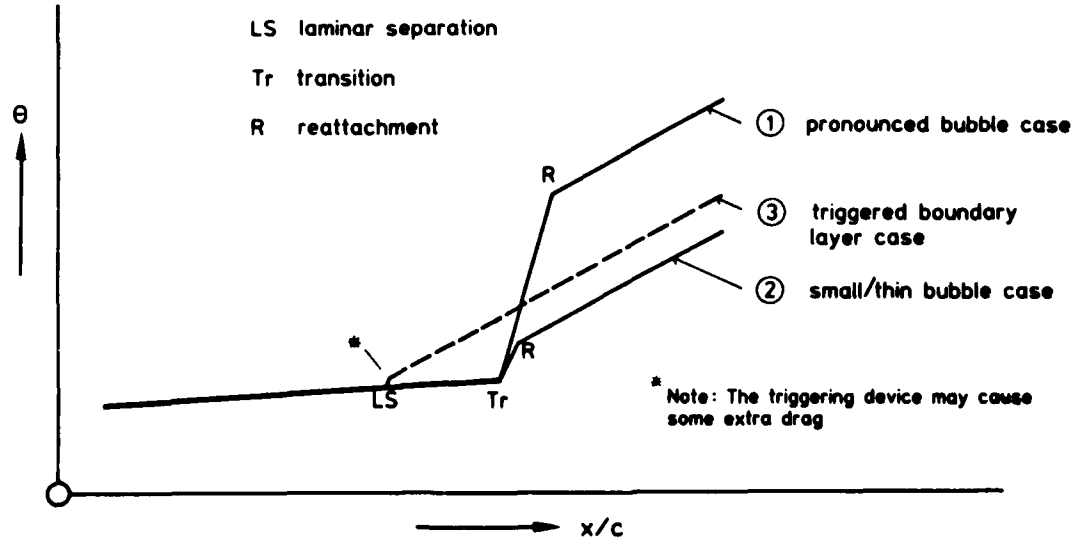


Fig. 6 Schematic sketch of the development of the momentum loss thickness in three typical cases

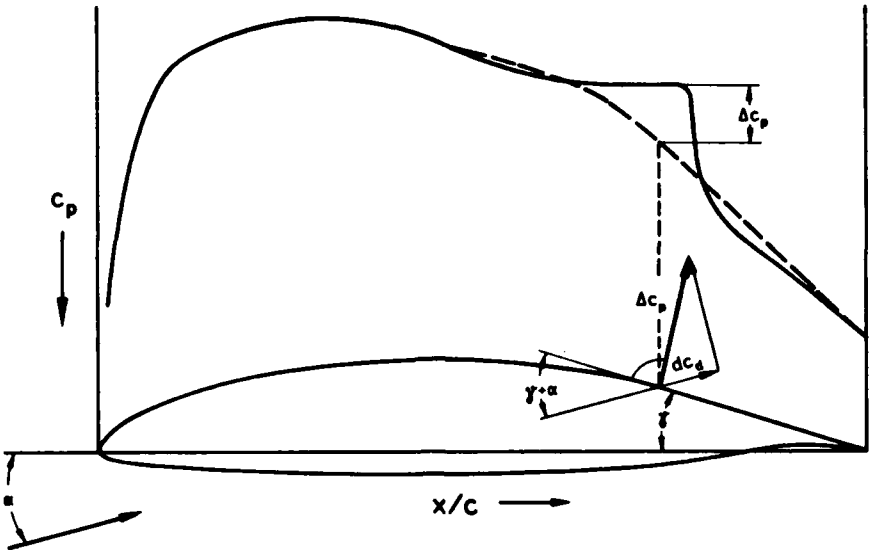


Fig. 7 Schematical representation of the additional pressures Δc_p acting on an airfoil as a result of a laminar separation bubble

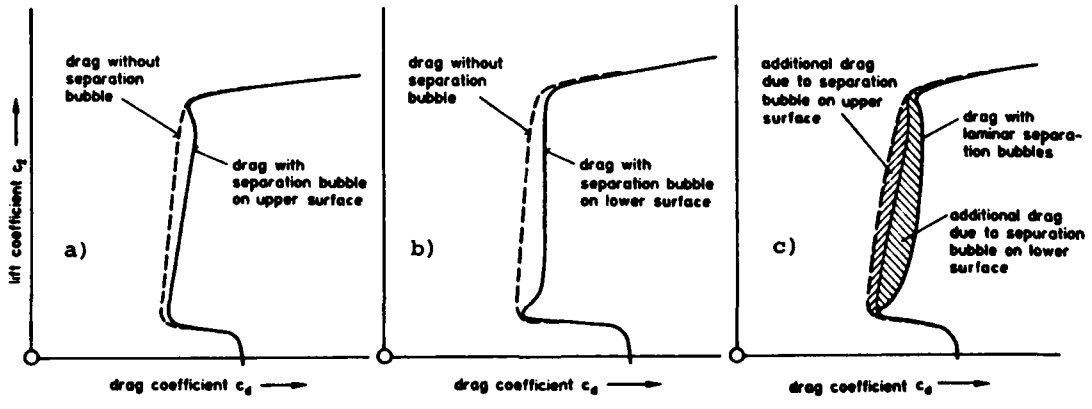


Fig. 8 Assumed development of additional drag caused by laminar separation bubbles on upper and lower surface of an airfoil section

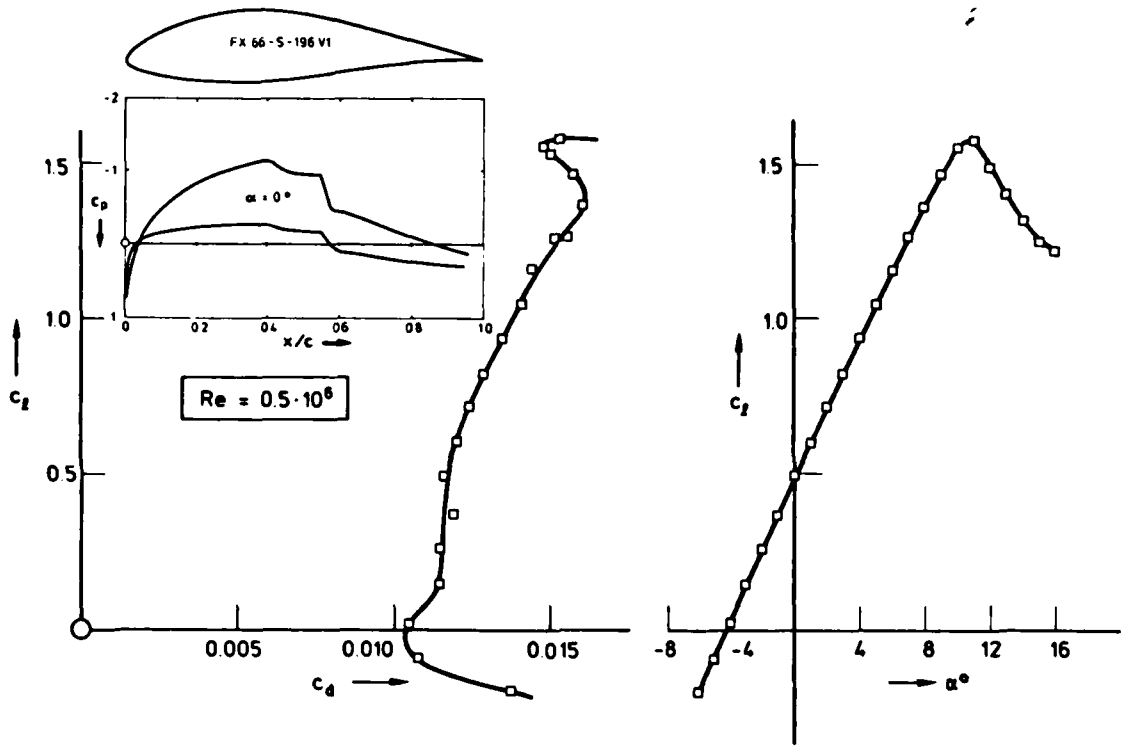


Fig. 9 Characteristics of the FX 66-S-196 V1 Wortmann airfoil section at Re = $0.5 \cdot 10^6$ (Measurements TH Delft [3])

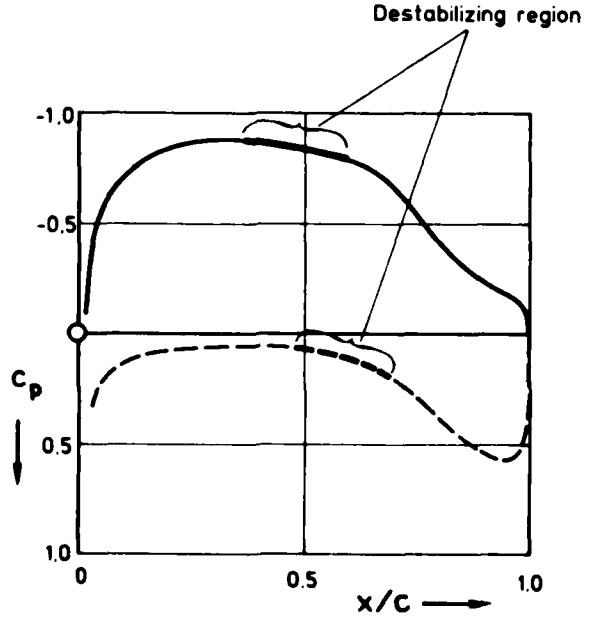


Fig. 10 Airfoil section with destabilizing regions (potential flow calculation of Wortmann airfoil section FX 62-K-131)

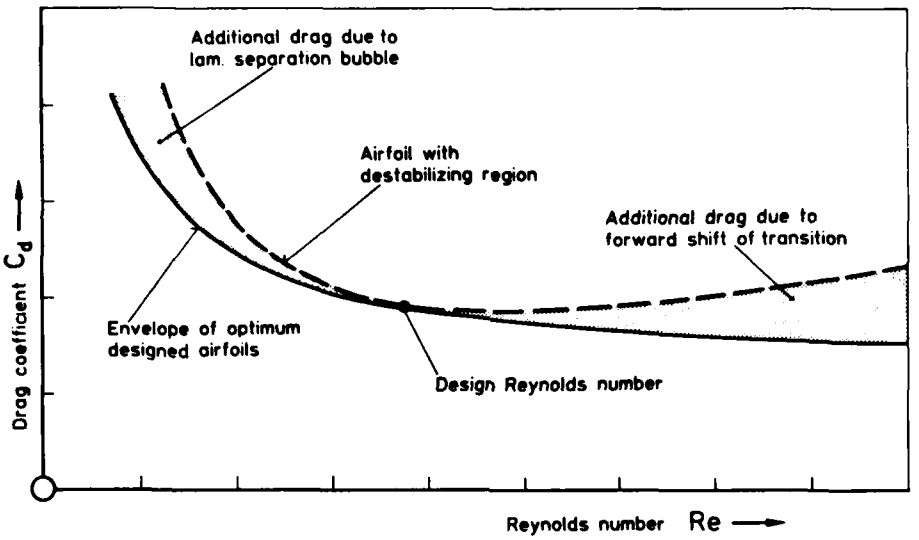


Fig. 11 Diagrammatic representation of the drag curve plotted against Reynolds number for airfoil sections with destabilizing regions

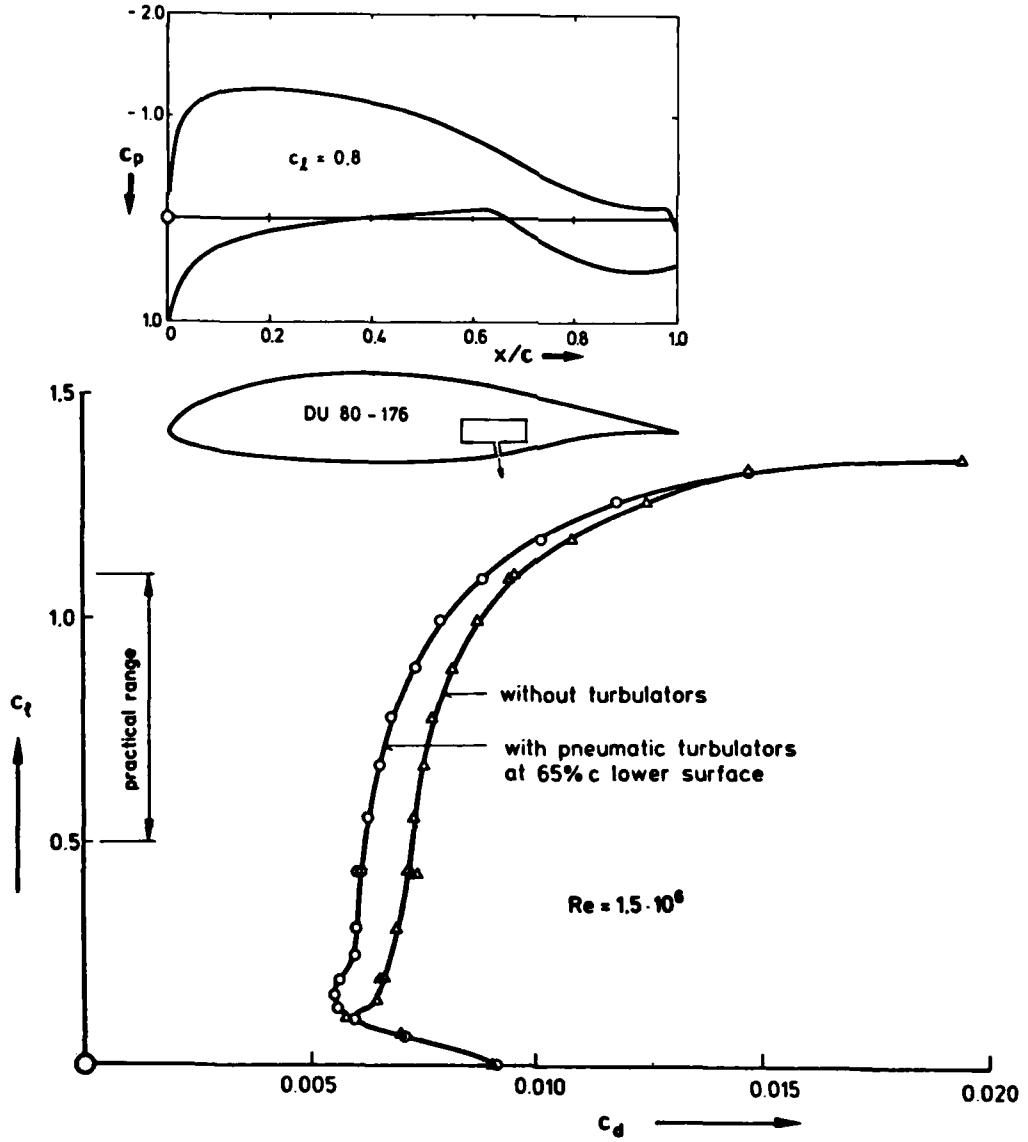


Fig. 12 Drag polar and potential flow pressure distribution of Delft University airfoil DU 80-176

(Measurements TU Delft)

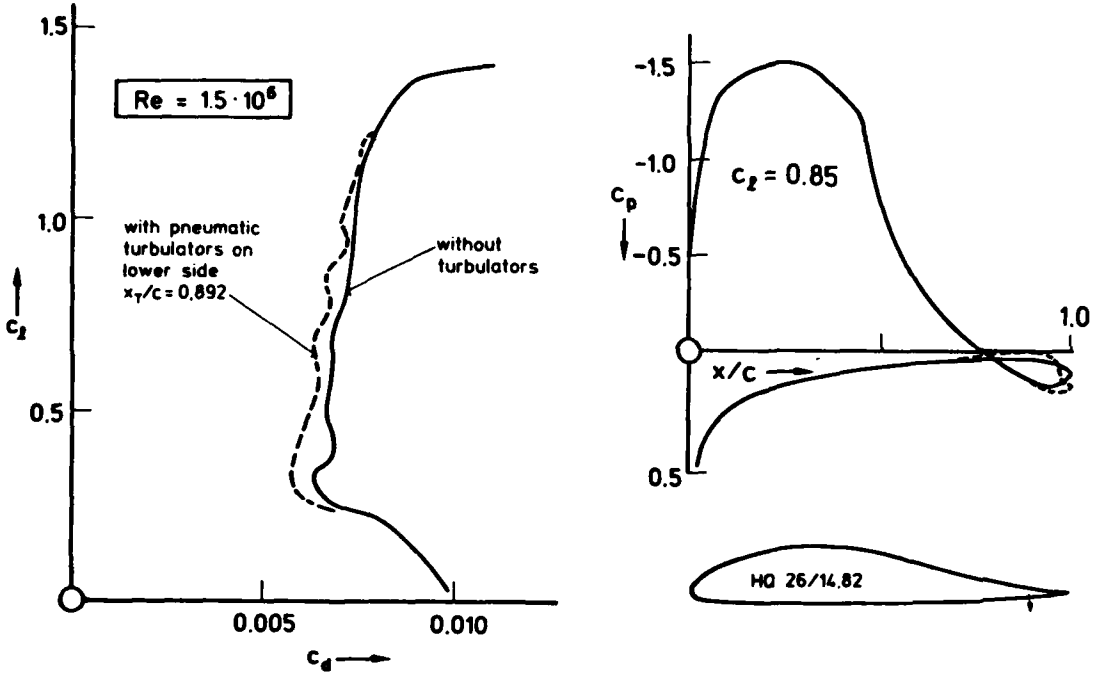


Fig. 13 Drag polar and measured pressure distribution of airfoil DFVLR-HQ 26/14.82 (Free flight measurements DFVLR Braunschweig)

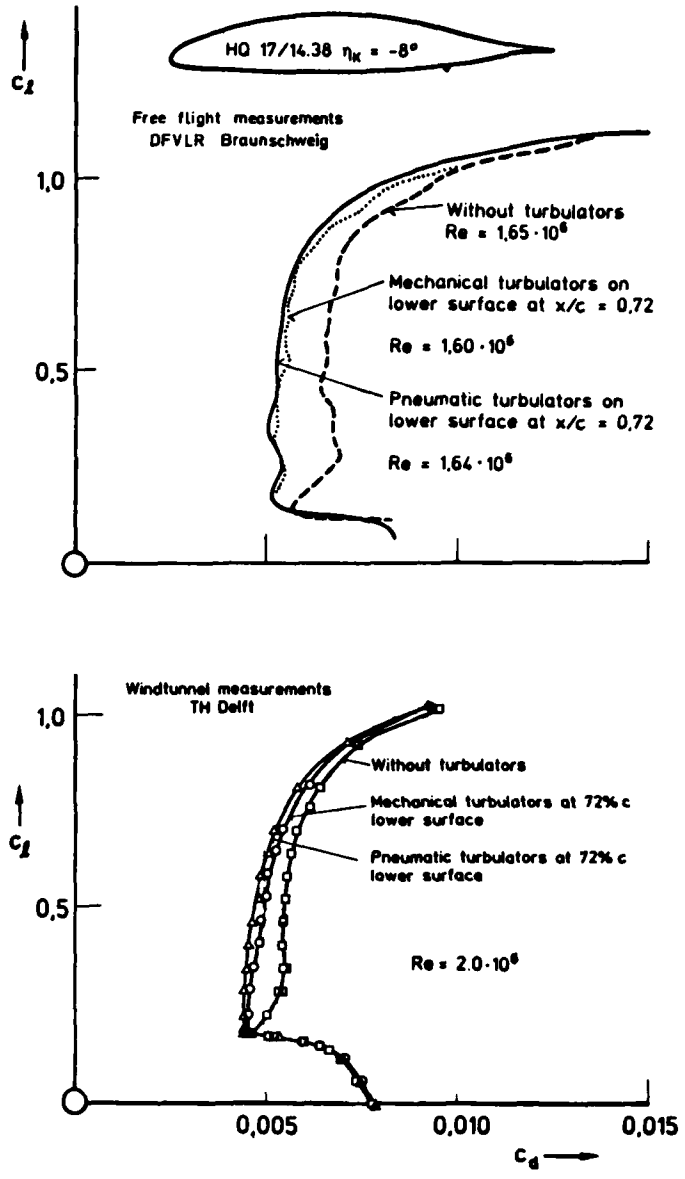


Fig. 14 Results of free flight and windtunnel measurements on HQ 17/14.38 with and without turbulators

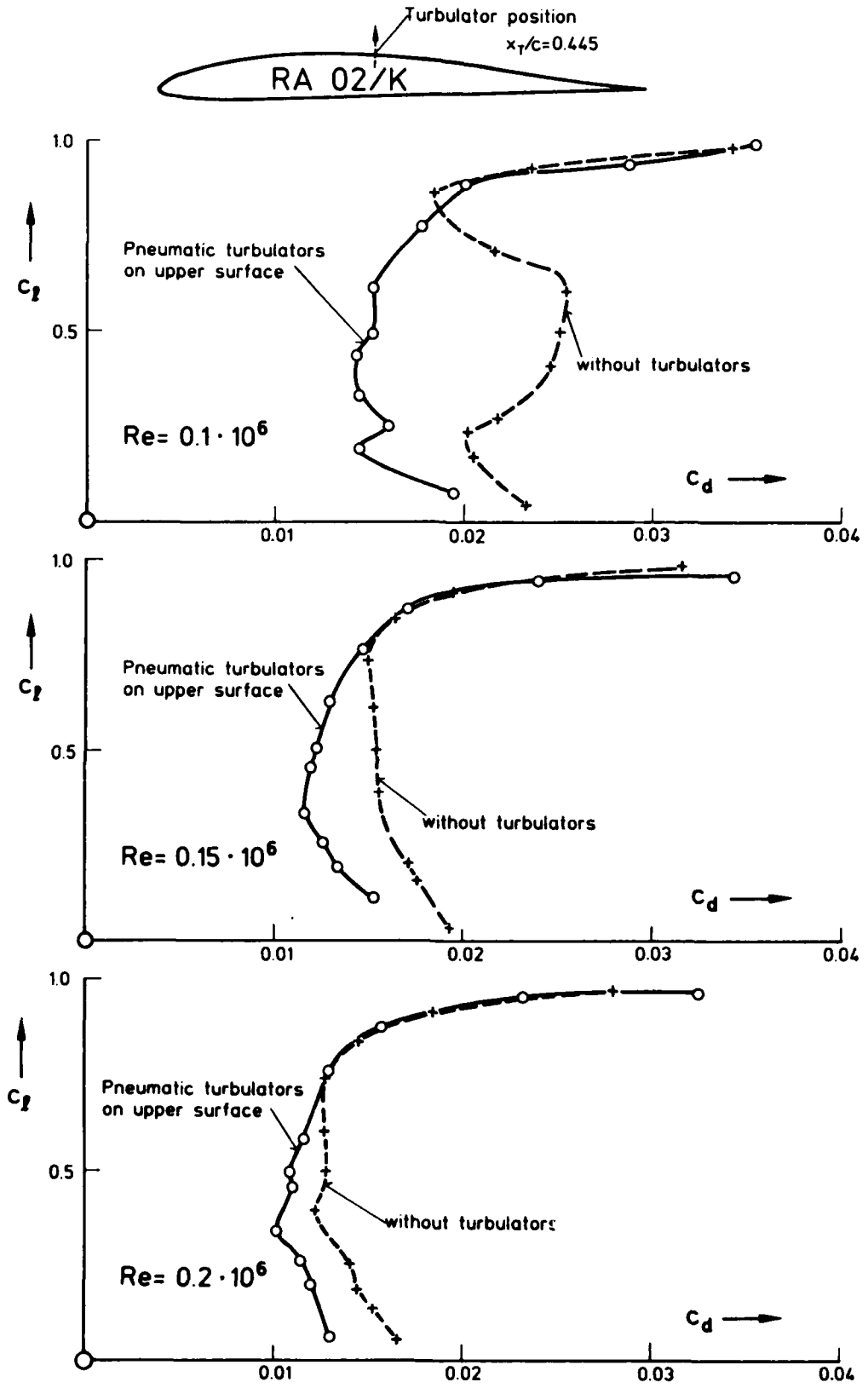


Fig. 15 Drag polars of the airfoil DFVLR RA 02/K with and without pneumatic turbulators (Measured in small cascade windtunnel DFVLR Braunschweig [14])

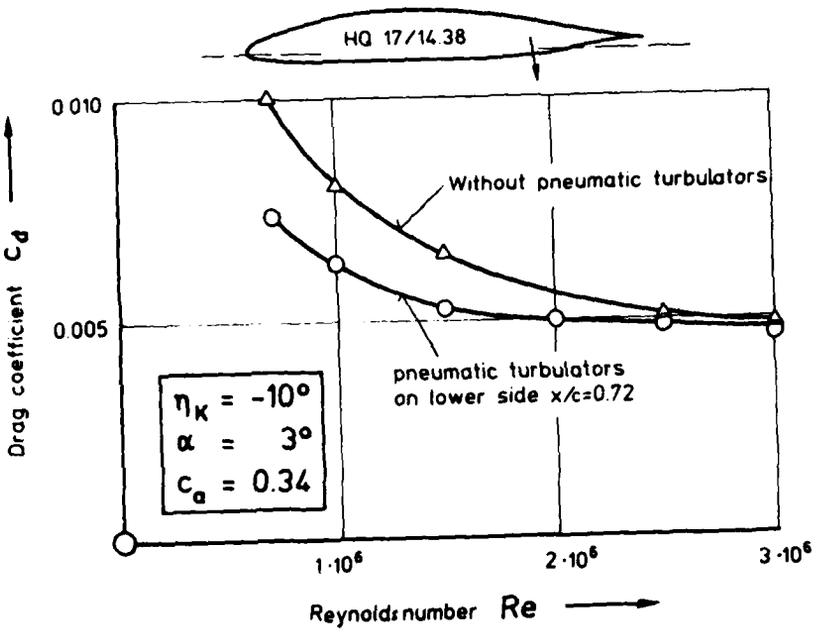


Fig. 16 Drag reduction by turbulators depending on Reynolds number (Measurements TH Delft)

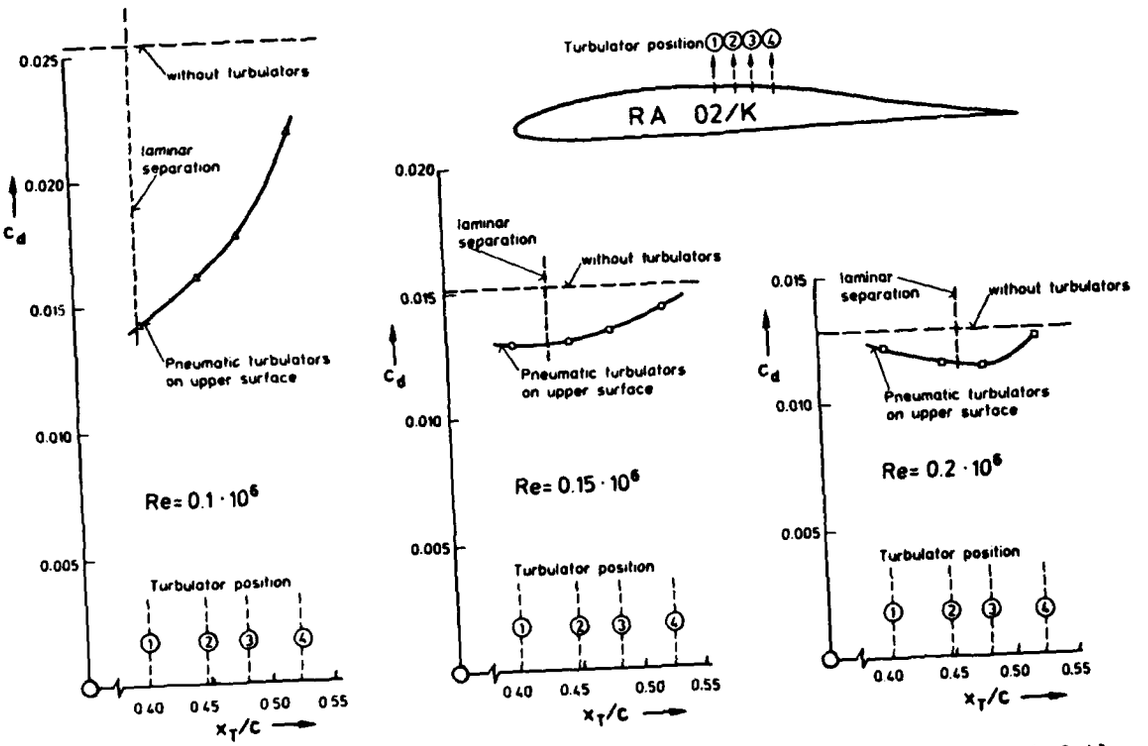


Fig. 17 Drag reduction depending on pneumatic turbulator position of airfoil RA 02/K at c_ℓ = 0.6 (Measured DFVLR Braunschweig [14])

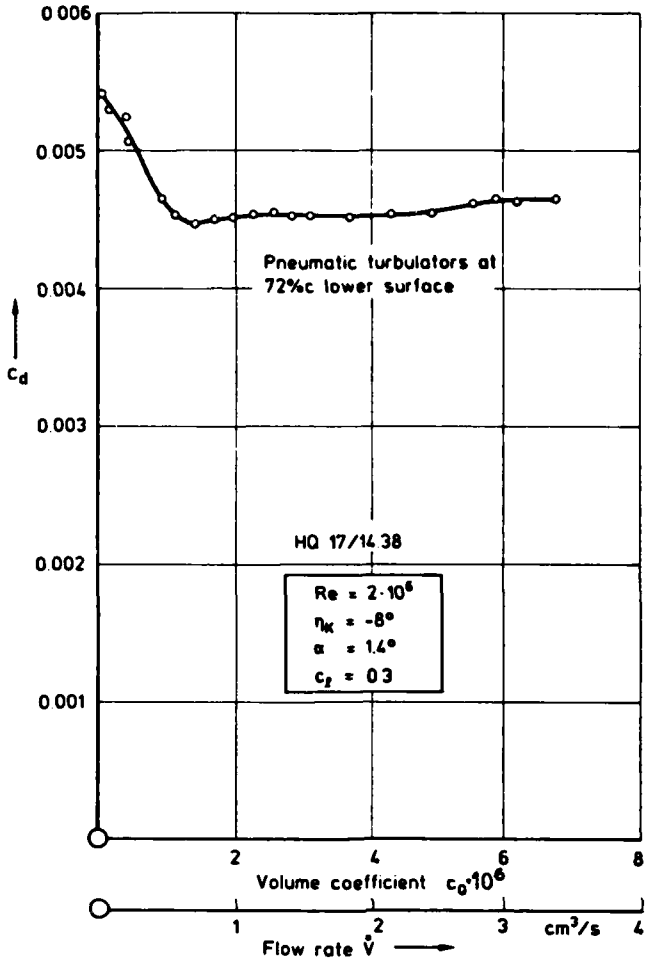


Fig. 18 The drag of airfoil HQ 17/14.38 with various air jet coefficients c_Q and volume flow $\dot{V}$ per hole (Measurements TH Delft)

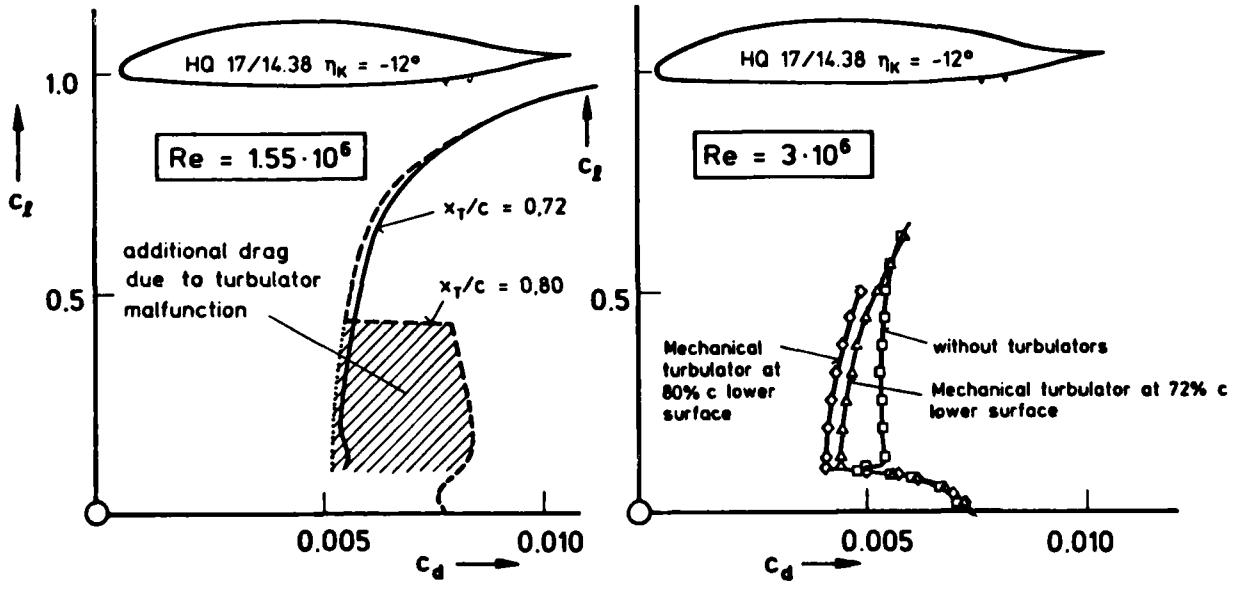


Fig. 19 Results of free flight and windtunnel measurements on airfoil HQ 17/14.38 with and without mechanical turbulators
(Re = 1.55 · 10^6: Free flight measurements DFVLR Braunschweig
Re = 3.0 · 10^6: Windtunnel measurements TH Delft)

L'INTERACTION ONDE DE CHOC-COUCHE LIMITE TURBULENTE ET SON CONTROLE

par

Jean DELERY

Office National d'Etudes et de Recherches Aérospatiales (ONERA)

92320 CHATILLON - FRANCE

RESUME

L'interaction entre une onde de choc et une couche limite a le plus souvent des conséquences extrémement préjudiciables surtout si elle entraîne la formation d'un décollement. Il se produit alors un accroissement très rapide de la taille des zones dissipatives avec intensification considérable des fluctuations turbulentes. Dans cette revue, on rappelle d'abord certaines propriétés fondamentales de l'interaction impliquant une couche limite turbulente dans le cas de base : distances d'influence amont, limites de décollement naissant et effet de destabilisation sur la couche dissipative. Les écoulements transsoniques et supersoniques sont successivement examinés. Ensuite, les procédés de contrôle les plus couramment expérimentés sont décrits en insistant sur la nature des mécanismes physiques mis en jeu. En bref, il est possible de ranger ces procédés en deux catégories : ceux agissant sur les caractéristiques de la couche limite qui va aborder le choc (refroidissement de la paroi, transfert de masse pariétal, soufflage) et ceux ayant une action locale au niveau de l'intéraction (aspiration ou injection par fente ou trous, piège à couche limite). Selon les applications envisagées, l'une ou l'autre de ces techniques sera la plus appropriée. Enfin, quelques méthodes de calcul sont brièvement présentées. Leur domaine d'application est pour la plupart d'entre elles limité au laminaire.

SHOCK/TURBULENT BOUNDARY-LAYER INTERACTION AND ITS CONTROL

ABSTRACT

Most often, the interaction between a shock-wave and a boundary-layer leads to extremely detrimental effects, especially if the shock is strong enough to entail separation of the boundary-layer. Then, there occurs a rapid growth of the dissipative regions along with a dramatic intensifiying of turbulent fluctuations. In the present review paper, some fundamental properties of the interaction are first considered for the basic configuration. The following features are first examined : upstream interaction length, incipient shock-induced separation, evolution of the boundary-layer main characteristics. Both transonic and supersonic flows are considered. In a second part, the most investigated means for controlling shock/boundary-layer interaction are presented, with emphasis on the physical description of the flow phenomena involved in this process. Briefly speaking, control methods can be classified into two categories : those acting on the boundary-layer properties before interaction with the shock (e.g. wall cooling, wall mass transfer, upstream blowing), and those having a local action in the shock foot region (suction or injection, boundary-layer removal). The most appropriate technique depends in fact on the specific application under consideration. Finally, some calculation methods are briefly presented. Most of them are restricted to laminar interactions.

1 - INTRODUCTION -

Les écoulements supersoniques ou transsoniques sont presque inévitablement traversés par des ondes de choc provoqués soit par le changement de pente d'une paroi, soit par une contre-pression obligeant la vitesse à redevenir subsonique. Ces ondes entrent obligatoirement en contact avec des surfaces sur lesquelles se développe une couche limite. Il se produit alors localement un phénomène complexe d'interaction ayant pour conséquence un accroissement des effets dissipatifs en raison de l'action fortement déstabilisatrice du gradient de pression adverse intense auquel la couche limite est soumise. Il s'ensuit une dégradation de sa distribution de vitesse, jusqu'à la formation fréquente d'un décollement.

A titre d'illustration, l'ombroscopie de la figure 1, empruntée à Pearcey [1] ,montre ce qui peut se passer sur un profil en transsonique. Toute la partie de l'écoulement en aval du choc est largement décollée, d'où une évidente chute de performance. Dans de telles circonstances, il peut même se développer des instabilités à grande échelle [2] susceptibles d'induire un tremblement.

Même si ses conséquences ne sont pas toujours aussi graves, l'interaction avec une onde de choc entraîne une amplification des effets visqueux qui fait que l'écoulement réel peut être très éloi[illegible] du modèle non visqueux qui a souvent servi à la définition de la forme aérodynamique. La figure 2 fournit un exemple d'un tel écart entre l'expérience et des calculs de fluide parfait appliqués à un profil supercritique [3] .



Fig. 1 - Interaction avec décollement sur un profil transsonique (d'après [1]).

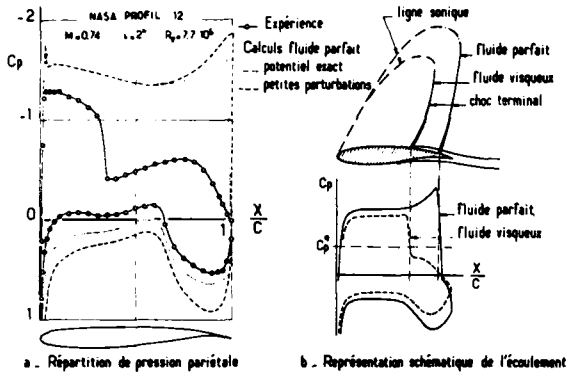


Fig. 2 - Importance des effets visqueux sur un profil supercritique

Les interactions choc-couche limite se rencontrent aussi dans les prises d'air supersoniques. Là, les décollements pouvant en résulter sont susceptibles de diminuer considérablement l'efficacité entraînant ainsi une perte de poussée importante. En outre, l'élévation spectaculaire du niveau de turbulence qu'engendre un décollement est à l'origine de fortes distorsions instationnaires capables de provoquer l'extinction du moteur ou bien d'amorcer un pompage tout aussi néfaste. Les exemples de dispositifs où ce genre d'interaction joue un rôle capital pourraient être multipliés : pales d'hélicoptère, arrière-corps d'avion ou de missile, turbomachines, etc...

L'idée de contrôler le phénomène afin d'en limiter les répercussions les plus dommageables s'est faite jour dès le début des recherches sur les écoulements à grande vitesse autour de profils d'aile. Les premières tentatives se sont tout naturellement inspirées des techniques déjà utilisées pour prévenir le décollement en subsonique. Leur principe de base consite à accroitre l'énergie de la couche limite de façon à lui permettre de franchir le choc avec un minimum de perturbation. Pour cela on peut, soit éliminer tout ou partie de ses zones à plus basse vitesse, soit lui "injecter" de la quantité de mouvement. Ainsi, dès 1941 Regenscheit [4] a étudié l'effet d'une aspiration pratiquée au travers d'une fente à la paroi d'un profil placé dans un écoulement transsonique. Le même procédé a également été envisagé par Fage et Sargent en 1943 [5] . Depuis, ainsi que nous allons le voir, bien d'autres recherches ont été consacrées à cet important problème.

Les deux premières parties de cette revue seront consacrées à un rappel des propriétés les plus marquantes de l'interaction entre une onde de choc et une couche limite en écoulements transsonique et supersonique. Seul le cas turbulent sera considéré en raison de sa plus grande importance pratique actuelle, bien que les recherches actives menées en vue de réduire la trainée de frottement vont certainement redonner de l'actualité au cas laminaire. L'examen portera sur les longueurs d'interaction, les conditions d'apparition du décollement en pied de choc, l'évolution des caractéristiques essentielles de la couche limite. Cet examen concernera ce que nous appellerons l'interaction de base. On se limitera au cas bidimensionnel

Dans une troisième partie, seront présentés les facteurs d'influence en mesure de modifier le phénomène de base dans un sens favorable, c'est à dire de permettre son contrôle. L'attention sera surtout portée sur la description physique de l'interaction en s'appuyant principalement sur des résultats expérimentaux. Bien qu'elles connaissent actuellement une phase de progrès rapides, les méthodes de calcul applicables au cas de base ne seront pas discutées ici. En effet, leur examen nécessiterait des développements trop conséquents pour entrer dans le cadre de cette revue rapide. Le lecteur intéressé trouvera dans les références [6] et [7] un état de l'art dans ce domaine. Egalement, nous laisserons en grande partie de côté les problèmes technologiques posés par la réalisation des moyens de contrôle ainsi que les aspects économiques de leur mise en oeuvre sur un avion. Là encore, la considération de ces questions, pourtant capitales, nous aurait entraînés trop loin.

2 - GENERALITES SUR LE MECANISME DE L'INTERACTION ONDE DE CHOC-COUCHE LIMITE EN ECOULEMENT BIDIMENSIONNEL

Fondamentalement, une couche limite non décollée est une région de faible épaisseur δ à travers laquelle la vitesse passe d'une valeur extérieure u_e élevée à la valeur zéro à la paroi ; le nombre de Mach variant en conséquence de Me à zéro. En dehors des zones de forte interaction, la pression est quasi constante selon une normale à la paroi, si bien que la couche limite peut être vue comme un écoulement quasi-parallèle où l'entropie change d'une ligne de courant à l'autre ou, ce qui est équivalent, comme un écoulement rotationnel. Par ailleurs, quand une onde de choc se propage au travers d'une telle couche limite, les tensions de frottement, résultat aussi bien de la viscosité laminaire que du cisaillement turbulent, sont pratiquement sans effet sur le phénomène sur la plus grande partie de l'épaisseur δ . Ce comportement est parfaitement démontré à la fois par l'expérience [8, 9] et la théorie [10] . Il se conçoit d'ailleurs intuitivement si on réalise que le choc imprime à l'écoulement une décélération si rapide que -à l'échelle macroscopique- les tensions de frottement deviennent temporairement négligeables devant les forces de pression et d'inertie. Ainsi, en première analyse, la pénétration d'un choc à l'intérieur d'une couche limite peut être conçue comme un phénomène de fluide parfait. Une telle schématisation permet d'anticiper certaines tendances sans avoir à prendre en compte, tout au moins en vue d'une interprétation surtout qualitative, les effets dissipatifs. Toutefois, il convient de souligner qu'un modèle d'écoulement entièrement non visqueux conduit à des comportements irréalistes au voisinage immédiat de la paroi où, comme l'a montré Lighthill [10], les termes de viscosité doivent focément être pris en compte pour satisfaire la condition d'adhérence. C'est ainsi qu'une description plus réaliste et cohérente des phénomènes a exigé l'adoption de modèles dits "multi-couches" [10, 11, 12] où l'écoulement en interaction est divisé en une zone externe irrotationnelle ("upper deck"), une couche non visqueuse mais rotationnelle ("main deck") qui, en turbulent, englobe la majeure partie de la couche limite, et au contact de la paroi, un film où les effets visqueux sont prépondérants ("lower deck") et dont l'introduction permet précisemment de satisfaire la condition d'adhérence. De tels modèles ont grandement contribué à la compréhension physique des processus d'interaction forte et, ainsi que nous le verrons plus loin (voir § 3.3), ont servi de

support à des méthodes de calcul [13 -16] économiques et très utiles pour la mise en lumière du rôle joué par les paramètres d'influence principaux. Les discuter en détail serait hors de propos ici.

En turbulent surtout, la sous-couche visqueuse est extrêmement mince si bien que son effet peut en général être considéré comme étant du second ordre et la négliger permet une bonne description des caractéristiques essentielles de l'interaction. Ainsi, selon le schéma de fluide parfait, le choc qui se propage au travers de la couche limite "voit" un écoulement amont dont le nombre de Mach M(y) diminue progressivement au fur et à mesure qu'il s'approche de la paroi. Pour s'adapter à cette situation, il s'incurve et s'affaiblit peu à peu de manière à devenir évanescent lorsqu'il atteint la position où le nombre de Mach local est sonique. Par ailleurs, le signal de pression transporté par le choc est nécessairement transmis en direction de l'amont par le canal de la portion subsonique de la couche limite. Si bien que le saut de pression causé par le choc est ressenti en amont du point où celui-ci rencontrerait la paroi dans un modèle de fluide parfait pur, c'est-à-dire sans couche limite. Par un effet réciproque, l'épaississement de la zone subsonique, dû au ralentissement, induit dans la partie adjacente supersonique des ondes de compression contribuant à l'affaiblissement local du choc. Il résulte de ce mécanisme que le saut de pression que l'on observerait en fluide parfait est remplacé à la paroi par une évolution progressive de la valeur amont p_0 au niveau aval p_1 . D'où la notion de longueur d'interaction (ou encore longueur d'influence amont) qui caractérise l'étalement plus ou moins grand de la compression en fonction de paramètres dont l'influence sera examinée plus loin (voir § 3.1).

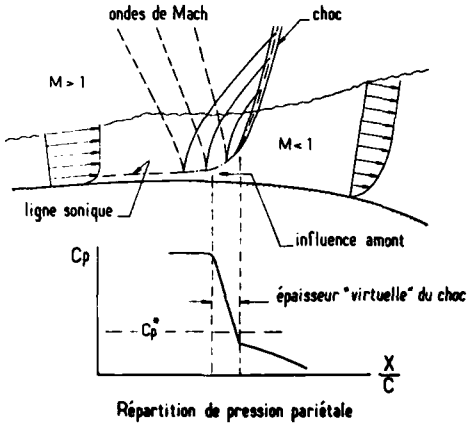


Fig. 3 - Interaction choc-couche limite sans décollement en transsonique. Schéma de l'écoulement.

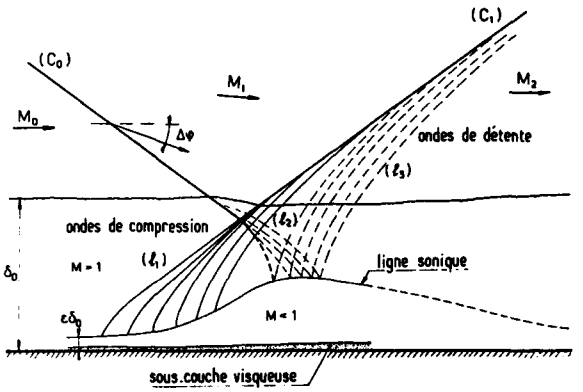


Fig. 4 - Réflexion de choc sans décollement en écoulement supersonique. Schéma de l'écoulement.

La structure du champ associé à des interactions turbulentes sans décollement est représentée Fig. 3 pour un choc normal en transsonique et Fig. 4 pour une réflexion de choc oblique en supersonique [17] . Le deuxième cas montre l'incurvation progressive du choc incident (Co) accompagnant sa pénétration dans la couche limite. La dilatation de la couche subsonique d'épaisseur initiale $\varepsilon\delta_0$ engendre des ondes de compression (ℓ_1) qui contribuent à l'affaiblissement de (Co) et qui, par focalisation, forment le choc réfléchi (C_1). La réfraction des ondes (ℓ_1) et de (Co) au cours de leur propagation dans la couche supersonique rotationnelle $(1-\varepsilon)\delta_0$ induit un système secondaire d'ondes (ℓ_2) qui sont réfléchies par la ligne sonique en ondes de détente (ℓ_3) constituant un pinceau que les visualisations par strioscopie révèlent très bien juste derrière (C_1). Le schéma montre également l'épaississement de la zone subsonique qui en aval de l'impact du choc (Co) doit normalement se contracter en raison de la mise en vitesse des parties inférieures de la couche limite sous l'effet des forces de viscosité qui redeviennent petit à petit prépondérantes. Henderson [18] a proposé de nombreuses variantes au schéma ci-dessus qui donnent des descriptions très détaillées des systèmes d'ondes engendrés par la pénétration d'un choc au sein d'un écoulement parallèle de fluide parfait rotationnel. Nous n'entrerons pas dans ces détails bien que ce travail soit très instructif.

En fait, l'interaction entre une onde de choc et une couche limite met en jeu des mécanismes extrêmement complexes qui sont encore loin d'être entièrement élucidés. Nous nous contenterons donc ici de commenter des tendances dont la considération est essentielle pour bien comprendre le mode d'action des procédés de contrôle de l'interaction.

Compte tenu de ce qui vient d'être dit sur l'influence amont, on conçoit que les distributions de vitesse et de nombre de Mach dans la couche limite qui va aborder la zone du choc contribuent de manière déterminante à l'extension et à la "gravité" de l'interaction. En bref, trois facteurs vont intervenir :

1- l'énergie mécanique transportée par le profil initial qui détermine en grande partie le comportement de la couche limite lors du franchissement du saut de pression. Plus cette énergie sera importante, c'est à dire plus le profil sera "rempli", moins sévère sera la dégradation subie par cette couche limite. Comme on le sait, l'allure d'une distribution de vitesse est bien caractérisée par le paramètre de forme "incompressible" Hi défini par :

$$H_i = \frac{\delta_i^*}{\theta_i} = \int_0^\delta \left(1-\frac{u}{u_e}\right) dy \Big/ \int_0^\delta \frac{u}{u_e}\left(1-\frac{u}{u_e}\right) dy$$

Rappelons que Hi est d'autant plus élevé que le profil est moins rempli. La valeur de Hi en début d'interaction dépend du nombre de Reynolds local R_δ , Hi diminuant quand R_δ augmente ainsi que le montre la figure 5, mais aussi de l'évolution antérieure de la couche limite. Par exemple, si celle-ci a été soumise à une recompression étalée précédant le choc, son Hi sera, à même valeur du nombre de Reynolds, plus élevé que pour une situation de plaque plane.

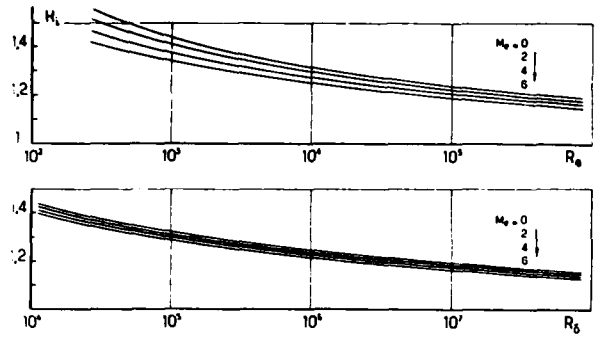


Fig. 5 - Couche limite turbulente de plaque plane. Paramètre de forme incompressible.

2- également, la hauteur y^* de la portion de la couche limite où la vitesse est subsonique doit a priori influer fortement sur la distance de remontée du signal de pression, c'est à dire sur l'étendue de l'interaction. Pour un nombre de Mach Me donné à la frontière δ , la hauteur normalisée y^*/δ est fonction de la distribution de nombre de Mach M(y) qui elle même dépend du profil de vitesse (c'est à dire de Hi) et de l'état thermique à la paroi qui est déterminant pour la distribution de la vitesse du son. Ainsi pour une paroi refroidie (voir Fig. 6), les nombres de Mach dans la partie inférieure de la couche limite seront plus élevés que dans le cas athermane, toutes choses restant égales par ailleurs. A titre d'illustration, la figure 7 indique la position de la ligne sonique en écoulement adiabatique à Me = 2 pour différents profils turbulents typiques représentés par la loi composite de Coles [19] . On y voit l'épaississement très rapide de la couche subsonique quand Hi augmente. L'encart de la figure montre, à même nombre de Mach Me la situation de la frontière sonique pour la couche limite laminaire de plaque plane. La valeur beaucoup plus grande de y^*/δ est un des facteurs qui expliquent l'extension considérable des domaines d'interaction en régime laminaire.

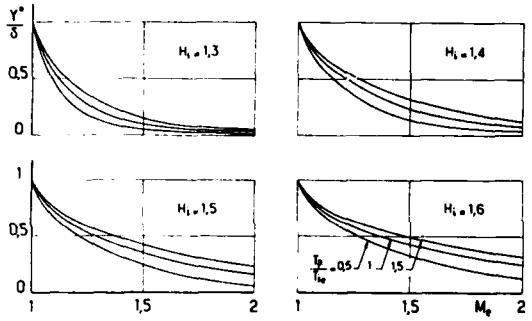


Fig. 6 - Position de la ligne sonique dans une couche limite turbulente. Effet de la température de paroi.

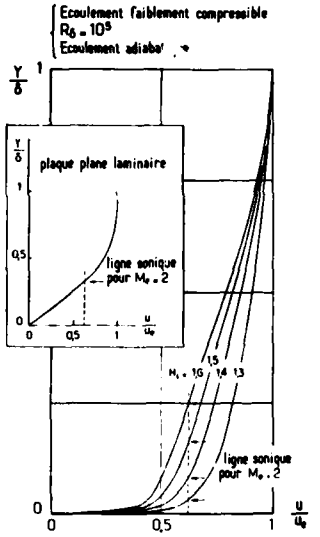


Fig. 7 - Distribution de vitesse dans une couche limite turbulente (d'après la loi de Coles [19]).

3- ainsi que nous l'avons déjà souligné, le mécanisme de l'interaction choc/couche limite ne peut être interprété entièrement dans le cadre d'un modèle de fluide parfait. Il est possible de se faire une idée de l'influence de la viscosité en faisant appel à la théorie de l'interaction libre de Chapman [20] qui repose sur l'écriture d'un bilan de forces exprimé à la paroi. De façon très simple, on établit ainsi que le saut de pression supporté par une couche limite qui décolle est de la forme :

$$\Delta p_0 \propto (M_0^2 - 1)^{-\frac{3}{4}} C_{f_0}^{\frac{1}{2}} q_0$$

où q_0 est la pression dynamique de l'écoulement amont non perturbé de nombre de Mach Mo et C_{f_0} le coefficient de frottement à l'origine Xo de l'interaction. En vertu de cette dépendance, l'aptitude à surmonter une compression par choc augmente avec C_{f_0} , c'est à dire diminue quand le nombre de Reynolds croît pour une valeur fixée du paramètre de forme. On en déduit aussi que l'étendue du domaine d'interaction doit augmenter avec C_{f_0} . La théorie asymptotique de Stewartson et Williams [11] aboutit au même résultat pour le décollement en laminaire. De telles tendances sont évidemment en contradiction avec les arguments précédemment développés selon lesquels la raideur de l'interaction devrait croître avec le nombre de Reynolds

En fait, la réalité est un compromis entre ces deux influences contraires ; c'est à dire que, selon la plage de variation de R_{δ_0} , l'écoulement près de la paroi est régi en priorité soit par la viscosité (grosso modo si $R_{\delta_0} \leq 10^5$ et en régime laminaire), soit par les termes inertiels ($R_{\delta_0} > 10^5$), ces effets étant antagonistes. Le changement de tendance est illustré par les distributions de pression pariétales des figures 8 et 9 qui sont relatives à un décollement turbulent provoqué par une rampe d'angle α . Le premier exemple [20] (voir Fig. 8) correspond à des nombres de Reynolds R_{δ_0} modérés et on voit que l'étendue du domaine d'interaction augmente manifestement avec R_{δ_0} . L'évolution inverse est observée à grands nombres de Reynolds, comme le montre la figure 9 [21] .

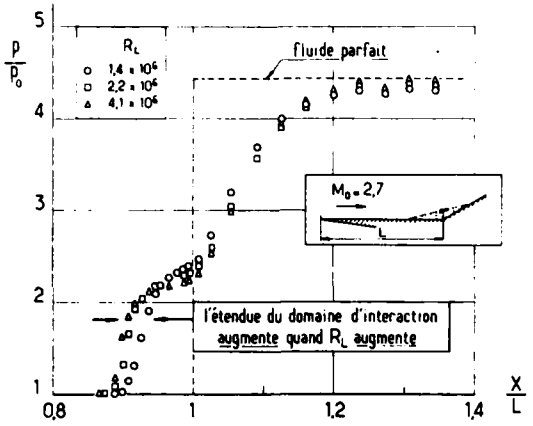


Fig. 8 - Comportement aux nombres de Reynolds faibles ou modérés (d'après [20]).

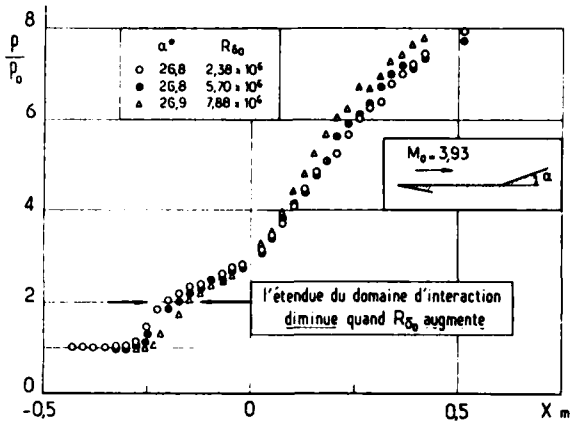


Fig. 9 - Comportement aux nombres de Reynolds élevés (d'après [21]).

L'inversion de tendance observée quand le nombre de Reynolds augmente peut s'interpréter à partir de l'examen des évolutions en fonction de R_δ de la hauteur de la ligne sonique y^* et de l'épaisseur y_{scl} de la sous-couche laminaire. L'exemple présenté Fig. 10 est dû à Settles [22] ; il concerne une couche limite turbulente de plaque plane à un nombre de Mach externe de 3. On y voit que y_{scl} décroît beaucoup plus vite que y^* quand R_δ augmente, ce qui explique le rôle de plus en plus mineur joué par les effets purement visqueux.

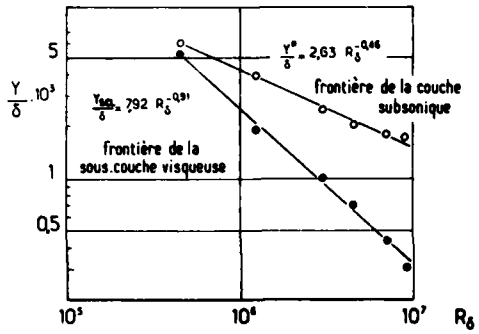


Fig. 10 - Couche limite turbulente de la plaque plane à M_e = 3. Positions des frontières de la couche subsonique et de la sous-couche visqueuse (d'après [22]).

Nous allons maintenant examiner quelques traits essentiels de l'interaction entre une onde de choc et une couche limite turbulente en écoulements transsonique et supersonique. L'attention sera surtout portée sur les lois de comportement des longueurs d'interaction, les changements les plus caractéristiques que la couche limite subit et les conditions d'apparition du décollement sous l'effet du choc. Nous examinerons en premier lieu le cas où la paroi est rectiligne, lisse, imperméable et adiabatique, conditions définissant une interaction qui se sera dite de base. Les modifications de comportement résultant du changement d'une ou de plusieurs de ces conditions seront ensuite envisagées dans la partie consacrée aux méthodes de contrôle.

3 - PROPRIETES DE L'INTERACTION DANS LE CAS DE BASE ECOULEMENT BIDIMENSIONNEL

3.1 - Longueur d'interaction en l'absence de décollement -

Ainsi que nous l'avons déjà souligné, la présence de la couche limite entraîne un étalement de la compression au niveau de la paroi d'où la notion de longueur d'interaction -encore dénommée distance d'influence amont- qui caractérise l'écart de la répartition de pression réelle par rapport à la discontinuité de la solution en fluide parfait. La plus ou moins grande extension de cette longueur est directement liée à l'intensité de l'interaction qui dépend à la fois de la force du choc et de la résistance de la couche limite aux effets destabilisateurs. Dans l'examen qui va suivre de quelques propriétés de la longueur d'interaction nous serons amenés à distinguer le transsonique du supersonique.

- Longueur d'interaction en écoulement transsonique -

La figure 11 montre une visualisation interférométrique d'une interaction se produisant dans un écoulement dont le nombre de Mach Mo immédiatement en amont du choc est voisin de 1,30. La photographie révèle parfaitement la naissance, au sein de la couche limite, d'ondes de compression qui se focalisent en un choc unique quasi-normal (l'épaississement apparent de ce choc loin de la paroi est un effet des interactions avec les couches limites des glaces latérales de la veine d'essai). L'examen attentif de telles visualisations ainsi que des répartitions de pression pariétales correspondantes met en évidence que le domaine d'influence doit être divisé en deux parties, comme indiqué Fig. 11 :

1- d'une part un domaine I où se produit une compression supersonique rapide et continue, du type onde simple, jusqu'à l'état sonique.

2- d'autre part un domaine II, faisant suite à I, où l'évolution de la pression est nettement plus progressive.

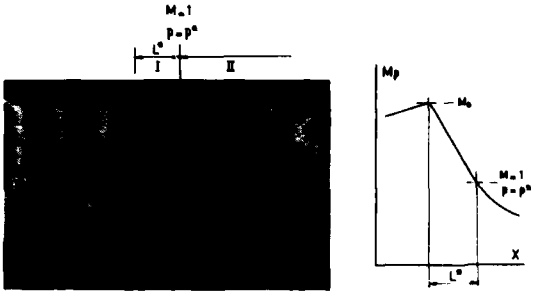


Fig. 11 - Interaction transsonique. Définition de la longueur d'interaction supersonique.

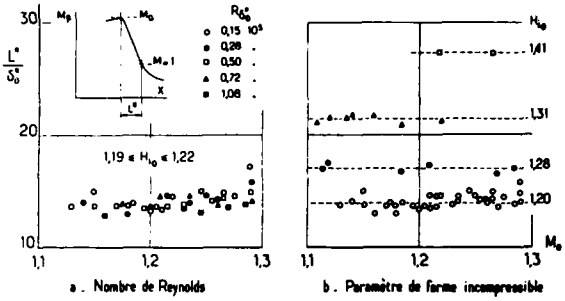


Fig. 12 - Interaction transsonique. Influence des conditions initiales sur la longueur d'interaction supersonique.

Dans ces conditions, il est clair que des propriétés générales intrinsèques du phénomène ne doivent être recherchées que pour le domaine I de nature supersonique. Pour le domaine II subsonique, la structure du champ résulte de l'intégration d'effets qui s'étendent largement en aval et qui tiennent compte de l'ensemble de l'écoulement. C'est ce caractère qui distingue fondamentalement les interactions transsoniques des interactions supersoniques, où d'amont en aval, la plus grande partie du champ obéit à un comportement hyperbolique.

Pour cette raison, une longueur d'interaction caractéristique L^* sera définie comme la distance séparant l'origine amont X_0 du phénomène du point de la recompression où l'état critique (nombre de Mach local égal à un) est atteint. Les corrélations qui vont suivre ont été dégagées de l'exploitation d'un grand nombre de résultats expérimentaux [23] .

Ainsi que le montre la figure 12a, pour une valeur fixe du paramètre de forme amont H_{i_0} , l'influence d'ordinaire très marquée du nombre de Reynolds disparait pratiquement quand L^* est normalisée par l'épaisseur de déplacement δ_0^* en X_0 (δ_0^* a été choisie de préférence à l'épaisseur physique δ_0 dont la définition est souvent imprécise). Etant donné que -toutes choses étant égales par ailleurs- δ_0^* est d'autant plus mince que le nombre de Reynolds est plus élevé, il s'ensuit de la corrélation observée ici que le domaine d'interaction se contracte quand $R_{\delta_0^*}$ augmente, ce qui démontre que pour la plage de $R_{\delta_0^*}$ considérée dans les présents essais les interactions sont dominées par les effets inertiels. De plus, il est manifeste que L^*/δ_0^* ne dépend pratiquement pas du nombre de Mach Mo , sauf lorsque Mo devient proche de 1,30, ce qui correspond à une situation très voisine du décollement naissant en pied de choc comme nous le verrons plus loin (voir § 3.3). Une telle invariance est à première vue paradoxale puisqu'on pourrait s'attendre à une croissance de L^* avec Mo , c'est à dire avec l'intensité du choc. En fait, quand Mo augmente à H_{i_0} fixé, la portion subsonique de la couche limite s'amincit et, en vertu du mécanisme brièvement expliqué plus haut (voir aussi § 3.3), la remontée de l'influence vers l'amont s'effectue sur une distance plus courte ; si bien qu'il y a compensation entre deux effets contraires ce qui contribue à maintenir quasi-constante la longueur d'interaction L^* .

Si la normalisation L^*/δ_0^* est appliquée à un ensemble plus complet de cas expérimentaux mettant en jeu des valeurs nettement distinctes du paramètre de forme H_{i_0} , on observe, comme le montre la figure 12b, un étagement régulier des résultats en fonction de H_{i_0} qui met en évidence l'influence déterminante de ce paramètre. Ainsi, L^*/δ_0^* qui croît régulièrement avec H_{i_0} est pratiquement multipliée par deux quand H_{i_0} passe de 1,2 à 1,4. Une telle évolution était bien sur prévisible puisqu'une augmentation de H_{i_0} entraîne un épaississement de la couche subsonique (toutes choses restant égales par ailleurs). Dans le cas présent, une loi de corrélation simple et tout à fait empirique permet de représenter assez bien à la fois l'influence des nombres de Reynolds et de Mach amont ainsi que celle de H_{i_0} . Elle s'exprime par la relation (voir Fig. 13) :

$$\frac{L^*}{\delta_0^*} = 70\,(H_{i_0} - 1)$$

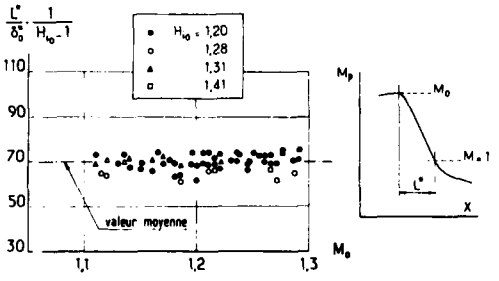


Fig. 13 - Interaction transsonique. Correlation pour la longueur d'interaction supersonique.

- Longueur d'interaction en écoulement supersonique -

En écoulement supersonique, le problème de l'influence amont et de l'étendue de l'interaction a fait l'objet de très nombreuses études expérimentales [22, 24-26] dont nous nous contenterons ici de dégager les conclusions essentielles.

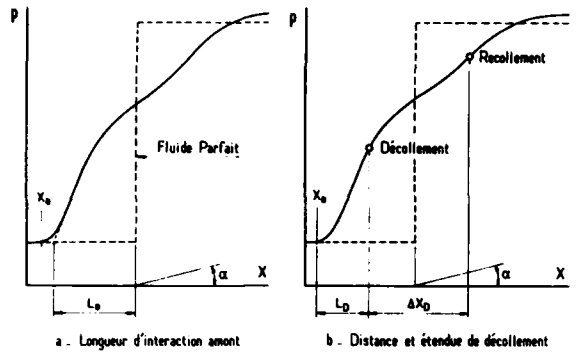


Fig. 14 - Longueurs caractéristiques dans une interaction supersonique.

En supersonique, la longueur d'influence amont L_0 est le plus souvent définie comme la distance séparant le début X_0 de l'interaction du point où le choc rencontrerait la paroi en fluide parfait qui peut être soit l'impact du choc incident dans une réflexion sur paroi plane, soit le sommet du dièdre dans un cas de déflexion brusque (voir Fig. 14). L'origine réelle de l'interaction étant délicate à localiser d'après l'examen des répartitions de pression pariétales, la plupart des auteurs adopte une origine conventionnelle obtenue en extrapolant jusqu'à la paroi la partie quasi-linéaire de la montée de pression au décollement, comme indiqué Fig. 14. Une longueur dont les propriétés sont également intéressantes à analyser est la distance L_D qui, dans le cas de chocs suffisamment intenses, sépare le point de décollement D de l'origine de l'interaction. Toutefois, dans ce qui suit, nous porterons notre attention sur L_0, étant donné que L_D obéit sensiblement aux mêmes lois. Egalement, nous n'envisagerons pratiquement que les écoulements produits par une rampe qui ont donné lieu à des études plus nombreuses et plus systématiques que le cas de la réflexion d'un choc, sans doute en raison de leur plus grande simplicité relative. D'ailleurs, ainsi que l'a souligné Green [27], les deux phénomènes sont en fait très voisins, même s'ils sont à l'origine de champs externes non visqueux dont les structures sont à première vue extrêmement différentes. Cette propriété est mise en évidence Fig. 15 où sont comparées les distributions de pression pariétales mesurées d'une part dans un dièdre, d'autre part dans une réflexion, le saut de pression total étant le même dans les deux cas [28]. Pour qu'il en soit ainsi, il faut que l'angle α de la rampe soit sensiblement le double de la déflexion $\Delta\varphi$ au travers du choc incident.

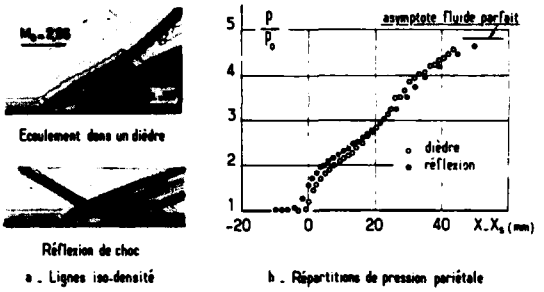


Fig. 15 - Comparaison entre l'écoulement dans un dièdre et une réflexion de choc $M_0 = 2{,}96$, $R_E \simeq 1 \times 10^7$ (d'après [28]).

La figure 16 montre les variations de la longueur d'interaction L_0 en fonction de ce que l'on peut considérer comme les principaux paramètres d'influence ; à savoir : le nombre de Mach amont Mo, le nombre de Reynolds et l'angle du dièdre. L'examen de ces résultats, dûs à Roshko et Thomke [25], met en évidence les tendances suivantes qui rejoignent les observations faites en transsonique :

1- à Mo et nombre de Reynolds R_c fixés (R_c est ici calculé avec les conditions amont et la distance X_c définie Fig. 16) L_0 augmente avec α, c'est à dire avec l'intensité de la perturbation. Il est maintenant clair que cette croissance de L_0 avec la force du choc vient du fait qu'une pression aval plus élevée tend à se propager plus en amont via la partie subsonique de la couche limite.

2- à α et R_c fixés, L_0 décroît quand Mo augmente. Cette tendance s'explique en grande partie par l'amincissement de la couche subsonique quand le nombre de Mach externe est plus élevé (toutes choses restant égales par ailleurs, en particulier H_{i_0} et l'épaisseur δ_0 de la couche limite). Il faut noter qu'elle est également en accord avec la théorie de l'interaction libre, brièvement évoquée plus haut (voir § 2), selon laquelle la dépendance de L_0 à l'égard de M_0 doit être de la forme $(M_0^2 - 1)^{-3/4}$.

3- à α et Mo fixés, L_0 diminue avec le nombre de Reynolds, évolution qui peut aussi s'interpréter par l'amincissement corrélatif de la couche subsonique (voir § 2) mais qui est en contradiction, ainsi que nous l'avons déjà souligné, avec la théorie de l'interaction libre que corroborent les expériences à nombres de Reynolds faibles et modérés [20, 24]. Ce renversement de tendance a déjà été illustré par les distributions de pression représentées Figs. 8 et 9.

Il est à noter que les évolutions ci-dessus se maintiennent quand L_0 est normalisée soit par δ_0 soit par δ_0^*, ce qui prouve que la forme et non seulement l'épaisseur de la couche limite initiale contribue, tout comme en transsonique, à la détermination de l'échelle longitudinale des phénomènes.

Les tendances mises en évidence par les résultats de la figure 16 ont été confirmées par l'étude expérimentale très fouillée de Settles [22] (voir aussi Settles et al. [29]) faite à un nombre de Mach Mo voisin de 3. Ainsi qu'on peut le constater Fig. 17, les résultats de Settles établissent clairement que l'influence du nombre de Reynolds persiste quand L_0 est normalisé par δ_0. La représentation adoptée Fig. 17 montre qu'une corrélation pour L_0 doit être de la forme :

$$\frac{L_0}{\delta_0} \propto R_{\delta_0}^{-1/3} \qquad \text{(à } M_0 \text{ et } \alpha \text{ fixés).}$$

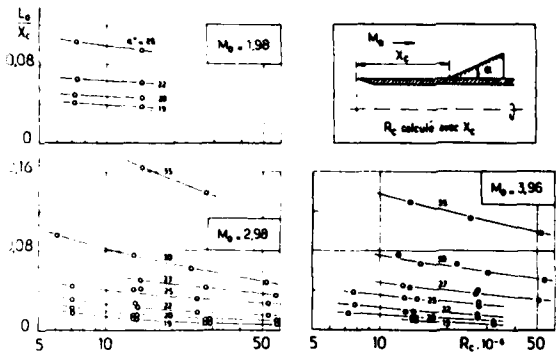


Fig. 16 - Longueur d'interaction amont. Influence des principaux paramètres (d'après [25]).

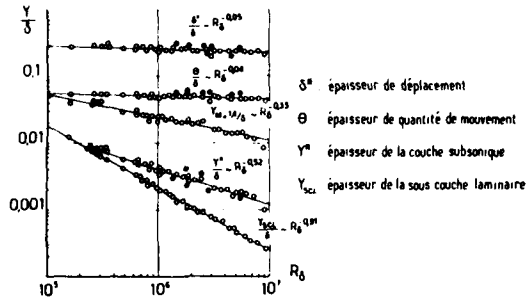


Fig. 17 - Influence du nombre de Reynolds sur certaines échelles à M_O = 3 (d'après [29]).

Or, comme on le voit figure 17, ni les épaisseurs de déplacement et de quantité de mouvement δ^* et θ ni les hauteurs y^* et y_{scL} de la couche subsonique et de la sous-couche laminaire n'obéissent à une loi de dépendance à l'égard de $R\tilde{t}_0$ de la forme $\delta_0 R\tilde{t}_{\delta_0}^{-n}$ qui seule permettrait de normaliser convenablement L_θ . En particulier, y^* qui à première vue semblerait l'échelle la plus représentative pour l'influence amont, n'est pas en mesure de corréler L_θ , comme on avait également pu le constater en transsonique pour L^* .

A notre connaissance, il n'existe pas pour les interactions supersoniques dans la configuration de base de résultats expérimentaux où les effets respectifs du nombre de Reynolds et du paramètre de forme sont nettement dissociés. Mais il est bien évident, ainsi que nous le verrons dans la partie consacrée aux méthodes de contrôle de l'interaction, que H_{i_θ} joue un rôle aussi fondamental qu'en transsonique.

3.2 - *Comportement de la couche limite dans une interaction sans décollement étendu* -

- Interaction en écoulement transsonique -

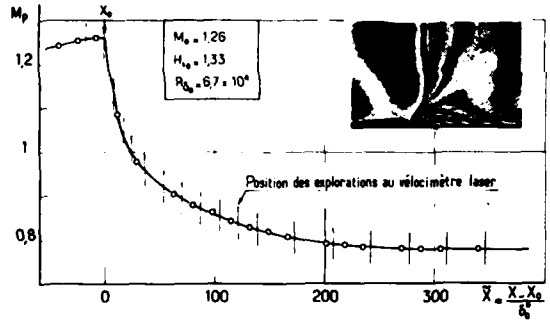


Fig. 18 - Interaction sans décollement en transsonique. Répartition du nombre de Mach "pariétal".

L'effet sur la couche limite d'un choc d'intensité modérée est illustré par les résultats expérimentaux donnés Figs. 18 à 22. Ils sont relatifs à une interaction se produisant dans un canal transsonique pour laquelle le nombre de Mach Mo est égal à 1,26. La répartition correspondante du nombre de Mach "pariétal" M_p est tracée Fig. 18 où sont également indiquées les positions des explorations pratiquées au travers de la couche dissipative par Vélocimétrie Laser (M_p est calculé à partir de la pression mesurée à la paroi en supposant une relation isentropique ; M_p est en fait très voisin du nombre de Mach M_e à la frontière δ de la couche limite). Les distributions verticales représentées Figs. 19, 21 et 22 mettent en évidence les phénomènes suivants :

1- l'interaction produit une distorsion des profils de vitesse moyenne longitudinaux (voir Fig. 19) telle, qu'à l'origine du processus, la décélération est plus forte près de la paroi qu'à l'extérieur, ce qui est un comportement typique de l'action d'un gradient de pression adverse intense. Il en résulte un "vidage" des distributions normalisées $\bar{u}/\bar{u}_e = f(y/\delta)$, que traduit une croissance rapide du paramètre de forme H_i , ainsi que le montre la figure 20. Dans le cas considéré ici, H_i atteint une valeur maximale voisine de 2,4. Plus en aval, l'effet retardateur cesse près de la paroi alors qu'il continue à se faire sentir dans les zones extérieures de la couche limite puisque la pression continue à croître. Ce renversement de comportement est du aux effets d'entraînement turbulent qui opèrent un transfert de quantité de mouvement au profit des parties internes de la couche limite, le mécanisme étant encore amplifié par l'interaction (voir remarques § 3.5 ci-dessous). En conséquence, le paramètre de forme H_i décroît rapidement et tend vers une valeur proche de 1,3 - 1,4 tandis que la couche limite se "relaxe" vers un nouvel état de plaque plane.

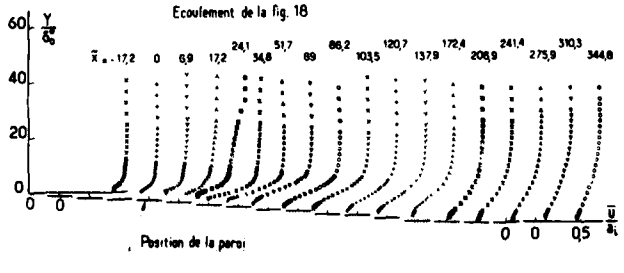


Fig. 19 - Interaction sans décollement en transsonique. Profils de vitesse moyenne longitudinale.

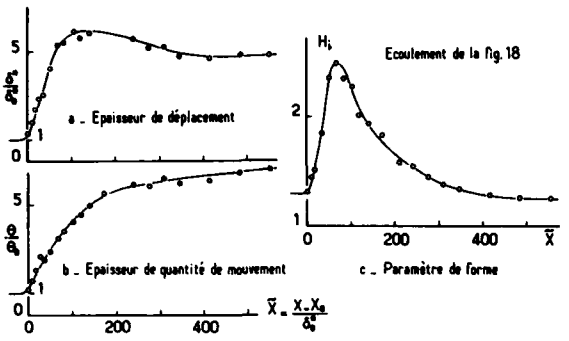


Fig. 20 - Interaction sans décollement en transsonique. Evolution des caractéristiques de la couche limite.

2- en même temps, l'épaisseur physique δ augmente, ce qui en liaison avec la croissance de H_i provoque une augmentation rapide de l'épaisseur de déplacement δ^* (voir Fig. 20). Egalement, l'épaisseur de quantité de mouvement θ subit un accroissement qui est ici plus modéré.

3- les profils d'intensité de turbulence longitudinale sont tracés Fig. 21 ($\sqrt{\overline{u'^2}}$ est normalisé par la célérité du son a_i pour la température génératrice). Ils montrent que l'interaction amplifie la turbulence et on note que le maximum de $\sqrt{\overline{u'^2}}$ dans chaque section s'éloigne progressivement de la paroi en corrélation avec la déformation des profils de vitesse moyenne qui comportent un point d'inflexion pouvant être associé avec le maximum de production de turbulence. Dans le cas présent, le maximum local de $\sqrt{\overline{u'^2}}/\overline{u}_e$ passe de 0,12 -juste en amont du choc- à 0,17 avant de se mettre à diminuer quand commence le processus de relaxation de la couche limite vers un nouvel état d'équilibre.

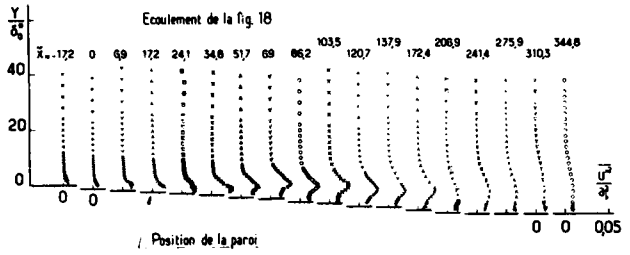
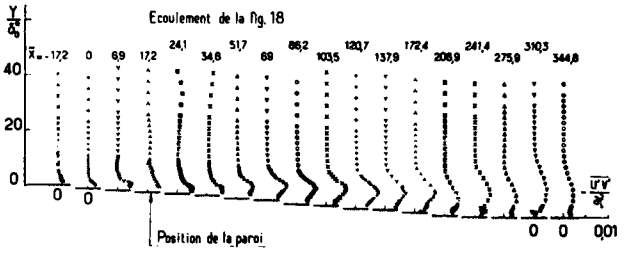


Fig. 21 - Interaction sans décollement en transsonique. Profils de $\overline{u'^2}/a_i^2$.

Fig. 22 - Interaction sans décollement en transsonique. Profils de $-\overline{u'v'}/a_i^2$.



4- la figure 22 montre les distributions de la tension de cisaillement $-\overline{u'v'}$ (normalisée par a_i^2). Qualitativement, ils ont les mêmes caractéristiques que ceux de $\sqrt{\overline{u'^2}}$, avec un maximum très marqué et bien détaché de la paroi. On voit donc que l'interaction entraîne une importante production de turbulence, l'effet croissant rapidement avec l'intensité du choc, spécialement à l'approche du décollement et il devient considérable à partir du moment où un bulbe décollé se forme (voir § 3.3 et 3.4 ci-dessous). Un autre point capital à noter est la lente diminution des niveaux de turbulence au cours du processus de relaxation en aval de l'interaction ; le phénomène étant caractérisé par des effets de non-équilibre très marqués ce qui rend sa modélisation particulièrement difficile [30] .

La valeur du paramètre de forme initial H_{i_0} a également une influence déterminante sur la gravité de la destabilisation que subit la couche limite au cours de l'interaction. Cet effet peut être caractérisé de manière globale par le "saut" amont-aval de grandeurs telles que les épaisseurs de déplacement et de quantité de mouvement. A titre d'illustration, la figure 23 montre les accroissements de δ^* et θ entre l'origine de l'interaction et la station où l'état sonique est atteint (bornes du domaine I défini § 3.1). Ces évolutions ont été calculées par une méthode du type "analyse de discontinuité" [31] fondée sur des lois de corrélation empiriques et reflétant assez bien la réalité comme on le constate Fig. 23. La zone hachurée marque la limite d'apparition du décollement en pied de choc donnée par cette méthode. Les courbes tracées Fig. 23 mettent en évidence les tendances suivantes :

1- l'amplitude du saut de δ^* et θ augmente avec le nombre de Mach Mo , c'est à dire avec l'intensité du choc, la croissance de l'épaisseur de déplacement devenant quasi-"exponentielle" à l'approche du décollement naissant.

2- le "saut" de δ^* ou θ est d'autant plus grand que le paramètre de forme initial H_{i_0} est plus élevé ce qui démontre la plus forte sensibilité d'une couche limite à un facteur de destabilisation quand sa distribution de vitesse est moins remplie.

3- des calculs effectués en faisant varier $R\delta_0$ montrent, qu'à paramètre de forme initiale fixé, l'effet du nombre de Reynolds est faible. La forte dépendance à l'égard de $R\delta_0$ parfois observée est due en fait à une modification de H_{i_0} résultant de la variation de $R\delta_0$ (voir Fig. 5).

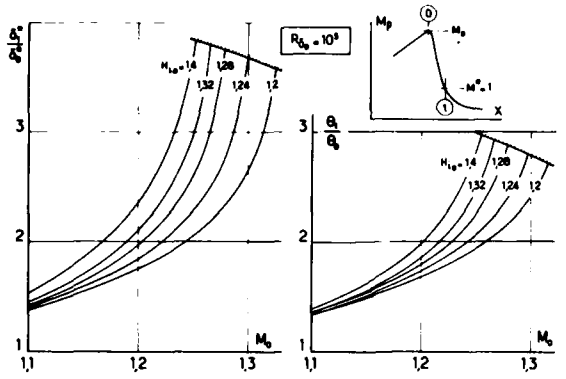


Fig. 23 - Interaction sans décollement en transsonique. Saut des épaisseurs caractéristiques.

- Interaction en écoulement supersonique -

Les évolutions observées en transsonique se retrouvant dans les interactions supersoniques, nous serons ici extrêmement brefs. Les traits essentiels du phénomène sont bien mis en évidence par les résultats d'essais présentés Figs. 24 à 26. Il s'agit de mesures effectuées au Vélocimètre Laser par Ardonceau [32] (voir aussi Ardonceau et al. [33]) dans un dièdre d'angle α , l'écoulement amont uniforme ayant un nombre de Mach égal à 2,25. Trois valeurs de α ont été considérées : α = 8, 13 et 18°. Les répartitions de pression pariétales sont portées Fig. 24 et les distributions de vitesse moyenne Fig. 25. Le cas α = 13° est au bord du décollement et pour α = 18° une zone décollée de dimension encore très réduite se forme, raison pour laquelle nous la considérons dans cette partie. Ces profils exhibent les mêmes tendances que celles déjà notées en transsonique. En particulier, dans les régions les plus aval, l'écoulement est fortement accéléré près de la paroi, ce phénomène étant plus spécialement visible pour la configuration décollée. Les profils ont alors une forme caractéristique présentant trois points d'inflexion.

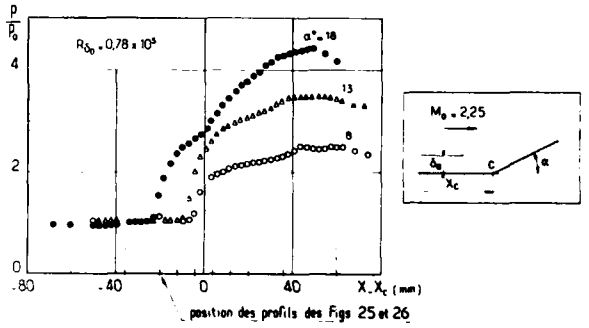


Fig. 24 - Interaction supersonique dans un dièdre (d'après [32]). Répartition de pression pariétale.

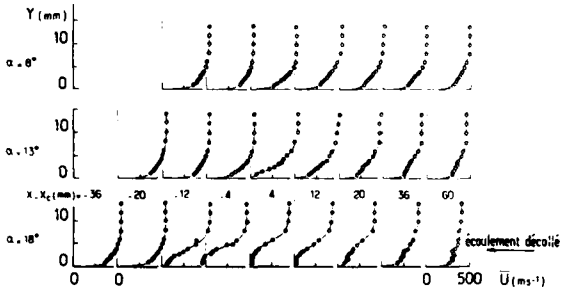


Fig. 25 - Interaction supersonique dans un dièdre (d'après [32]). Profils de vitesse moyenne longitudinale.

Les distributions de la valeur efficace $\sqrt{\overline{u'^2}}$ de la composante fluctuante longitudinale sont donnés Fig. 26. Tout comme en transsonique, elles révèlent l'existence d'un maximum de fluctuation qui se détache de plus en plus de la paroi au fur et à mesure que l'interaction s'intensifie. L'exemple présent montre de manière frappante l'accroissement considérable de la turbulence -donc des effets dissipatifs- qui accompagne l'apparition du décollement.

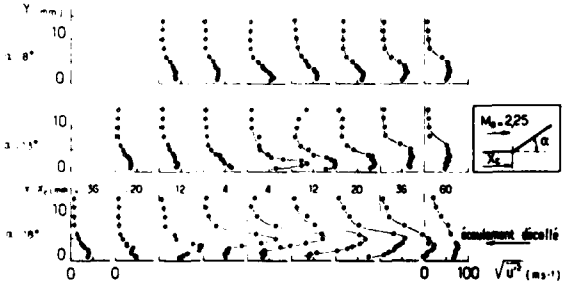


Fig. 26 - Interaction supersonique dans un dièdre (d'après [32]). Profils de $\sqrt{u'^2}$.

3.3 - *Conditions d'apparition du décollement en pied de choc* -

- Le décollement naissant en transsonique -

Traditionnellement, le décollement naissant est défini comme la situation où la valeur minimale atteinte par le frottement pariétal τ_p au cours d'une interaction est juste égale à zéro. Une intensification du choc au delà de cet état conduit à un changement de signe de τ_p , la région où τ_p est négatif étant dite décollée.

Les traits principaux d'une interaction coïncidant pratiquement avec le décollement naissant en pied de choc sont représentés Figs. 27 à 29. Dans le cas présent, le nombre de Mach Mo immédiatement en amont du choc est égal à 1,30. La figure 27 montre les profils de vitesse moyenne mesurés au Vélocimètre Laser

au travers de la couche dissipative en interaction. L'examen de ces seules distributions ne permet pas à vrai dire de détecter le décollement, tant la zone décollée est mince dans cette situation. Il est plus instructif de considérer le tracé dans le plan physique des lignes d'égale valeur de la probabilité $P(u \leq 0)$ pour que la composante de vitesse longitudinale u soit négative ou nulle. Pour un écoulement dans lequel u est constamment positif, cette probabilité est égale à zéro, tandis qu'elle vaut un si u est toujours négatif ce qui peut être le cas dans une région décollée où la vitesse est à contre courant de l'écoulement principal.

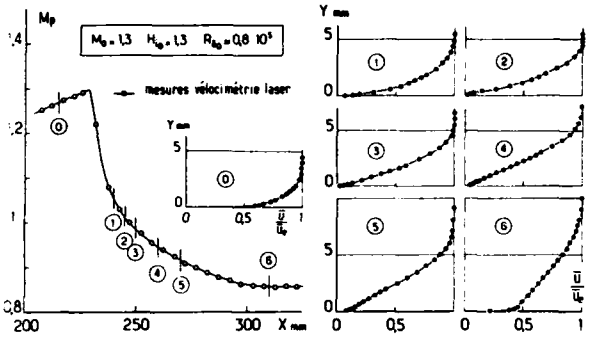


Fig. 27 - Situation de décollement naissant en transonique. Vitesse moyenne longitudinale.

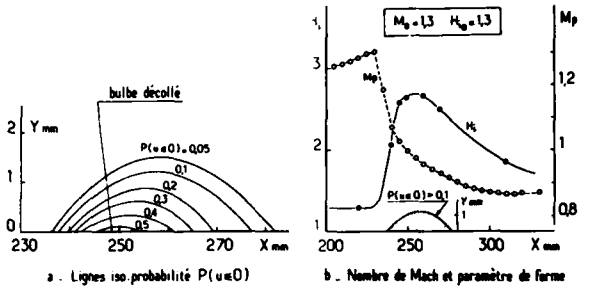


Fig. 28 - Situation de décollement naissant en transonique.

Usuellement, un écoulement turbulent est présumé décollé quand il contient des zones où la vitesse moyenne (au sens de la moyenne de Reynolds) est négative. Selon cette définition $P(u \leq 0) = 0,5$ correspond à $\bar{u} = 0$ et la ligne sur laquelle $P(u \leq 0) = 0,5$ coïncide avec le lieu des points tels que $\bar{u} = 0$ qui joint les points de décollement et de recollement.

Les lignes iso-$P(u \leq 0)$ tracées Fig. 28a révèlent l'existence d'une région où $P(u \leq 0)$ est négative (zone hachurée) si bien que l'écoulement considéré est en fait décollé selon le critère qui vient d'être énoncé. Toutefois, la taille du bulbe de décollement est encore si réduite, que nous nous trouvons pratiquement devant un cas de décollement naissant en pied de choc (par souci de clarté, les distances normales à la paroi ont été fortement dilatées sur la Fig. 28a). Il est à noter que la vitesse instantanée u peut prendre des valeurs négatives dans la région où la moyenne $\bar{u}$ est positive. Cela signifie qu'il existe des instants où l'écoulement près de la paroi est à rebours du flux externe, ce qui peut conduire à des difficultés conceptuelles pour définir la notion de décollement naissant -ou de décollement tout court- en régime turbulent. Ce problème a été discuté en détail par Simpson et al. [34] qui ont suggéré de faire une distinction entre :

1- le décollement pleinement développé ("fully developed separation") qui est défini classiquement par le changement de signe du frottement pariétal moyen et l'existence d'une poche où la vitesse moyenne $\bar{u}$ est négative.

2- le décollement intermittent ("intermittent separation") qui pourrait être défini par la condition que $P(u \leq 0)$ atteigne la valeur 0,2 près de la paroi.

Nous n'entrerons pas plus avant dans cette discussion -très importante sur le plan fondamental- et nous nous en tiendrons désormais à la définition classique formulée en termes d'écoulement moyen.

L'évolution correspondante du paramètre de forme est représentée sur la figure 28b. On y voit que H_i passe par un maximum voisin de 2,6 qui est en bon accord avec la valeur communément admise de $H_i = 2,5$ en un point de décollement turbulent. Par la suite, H_i diminue rapidement et tend vers un niveau représentatif d'un état de plaque plane. Les distributions d'intensité de turbulence longitudinale sont portées Fig. 29. Dans le cas présent, $\sqrt{\overline{u'^2}}/\bar{u}_e$ atteint 0,2, ce qui est un niveau significativement plus élevé que dans le cas d'une interaction sans décollement (voir § 3.2 ci-dessus). Ainsi, l'apparition du décollement donne naissance à des fluctuations turbulentes à grande échelle qui seront ensuite rapidement amplifiées si les circonstances sont telles que le bulbe décollé peut se développer.

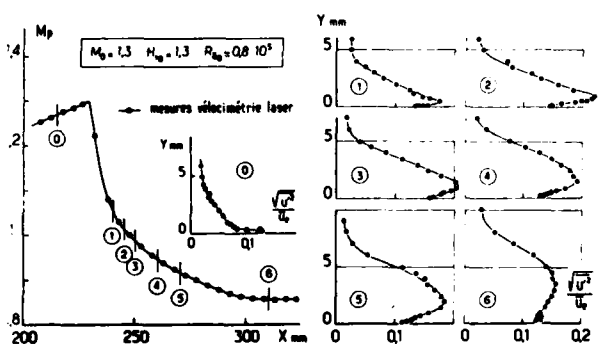


Fig. 29 - Situation de décollement naissant en transonique. Intensité de turbulence longitudinale.

Nous allons maintenant porter notre attention sur une approche plus globale et plus pragmatique du problème en recherchant quels sont les principaux facteurs susceptibles de conduire à une situation de décollement naissant en pied de choc.

Les résultats que nous allons discuter ont été obtenus expérimentalement dans des circonstances très variées (écoulements autour de profils complets ou de "bosses" à la paroi) et en utilisant tout un éventail de méthodes pour détecter l'apparition du décollement (mesures de frottement pariétal, visualisations par enduit déposé à la paroi, explorations au tube de Pitot et au Vélocimètre Laser) [35, 36, 37] L'ensemble de ces mesures a permis de définir la courbe limite de décollement naissant tracée Fig. 30 dans le plan des deux paramètres qui sont apparus comme étant les plus agissants, à savoir : le nombre de Mach Mo en amont du choc (qui en transsonique caractérise à lui seul l'intensité du choc), le paramètre de forme H_{i_0} de la couche limite au moment où elle aborde le choc. Rappelons que le résultat de la figure 30 est uniquement valable pour l'interaction de base, notamment la paroi est imperméable et athermane.

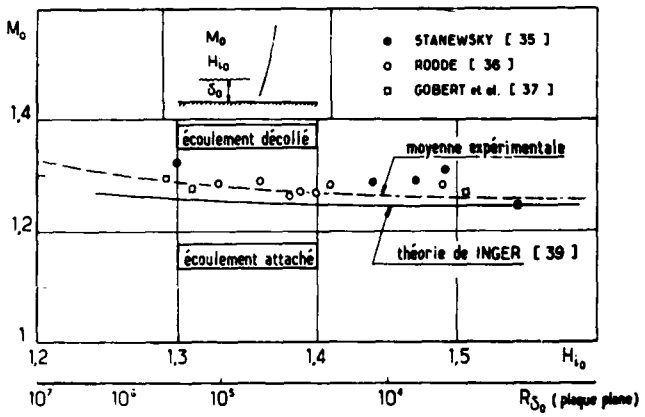


Fig. 30 - Décollement naissant en transsonique. Paroi adiabatique.

L'effet du nombre de Reynolds, plus communément considéré, est en fait pour une large part pris en compte par son influence sur H_{i_0} mais ajoutons que cela n'est vrai en toute rigueur que pour une couche limite de plaque plane (voir Fig. 5 la relation qui existe alors entre H_{i_0} et R_{δ_0}). La corrélation de la figure 30 met en évidence une légère croissance de Mo (c'est à dire de l'intensité du choc) quand H_{i_0} diminue. A grand nombre de Reynolds, lorsque les termes d'inertie prédominent, une telle évolution était prévisible puisqu'à une valeur basse de H_{i_0} correspond un profil de vitesse bien rempli conférant à la couche limite une plus grande résistance au décollement. Toutefois, il est frappant de constater que l'effet est faible, la limite de décollement dépendant peu de H_{i_0} ce qui peut paraître a priori surprenant si l'on considère la grande influence de H_{i_0} sur le "saut" que subissent les propriétés de la couche limite au cours de l'interaction (voir § 3.2 ci-dessus). En fait, ce comportement, également noté par Squire et Smith [38] en supersonique, s'explique par l'augmentation rapide de la longueur d'intéraction L^* avec H_{i_0} (voir § 3.1 ci-dessus). En effet, le décollement de la couche limite est provoqué par le gradient de pression antagoniste auquel elle est soumise. Or, une augmentation de H_{i_0} accroît certes la "fragilité" de la couche limite, mais assi atténue le gradient destabilisateur qu'elle subit par élongation de la zone sur laquelle s'effectue la compression dont l'amplitude demeure elle constante. En définitive, l'augmentation de H_{i_0} produit deux effets contraires qui, dans les circonstances présentes, se compensent presque exactement.

La limite empirique de décollement présentée Fig. 30 est comparée à une prévision donnée par le modèle de Inger [15, 39] . Il s'agit d'une théorie faisant appel à une technique de petites perturbations appliquée au modèle triple couche de Lighthill [10] évoqué § 2. Comme on peut le constater, la théorie de Inger est en assez bon accord avec l'expérience. Même si sa qualité de prévision n'est pas toujours aussi bonne qu'ici, elle a le mérite de permettre la mise en évidence de l'influence spécifique des paramètres agissant sur une interaction choc-couche limite turbulente en transsonique sans avoir à recourir à des calculs beaucoup plus lourds, procédant par exemple par résolution des équations de Navier-Stokes. Pour cette raison, nous serons amenés à utiliser ce modèle dans la seconde partie pour discuter de l'effet de certains facteurs dont la caractérisation expérimentale est difficile, ou douteuse, en raison des incertitudes de mesure.

- Le décollement naissant en supersonique -

Il y a quelques années, un grand nombre d'études expérimentales ont été consacrées à la détermination du décollement naissant en écoulements supersonique et hypersonique. Le plus souvent, les résultats sont représentés dans un diagramme donnant en fonction du nombre de Reynolds R_{δ_0} et avec le nombre de Mach M_0 comme paramètre l'angle α_I de la rampe pour lequel un bulbe de décollement est détecté pour la première fois (il est à noter que α_I peut être aisément traduit en rapport de pression p_I/p_0 de part et d'autre du choc à partir des relations de Rankine-Hugoniot). Une telle représentation implique que α_I ne dépend que de M_0 et de R_{δ_0} . La réalité est probablement plus subtile, et ainsi que nous le savons déjà, le paramètre de forme initial H_{i_0} joue un rôle qui n'est pas forcément pris en compte par le nombre de Reynolds. Toutefois, l'absence de résultats convaincants sur l'influence spécifique de H_{i_0} rend impossible toute corrélation en fonction de ce paramètre. Pour cette raison, nous garderons ici la représentation traditionnelle ne faisant intervenir que R_{δ_0} , étant entendu que les résultats donnés ne sont en toute rigueur valables que pour une couche limite initiale de plaque plane où, dans le cas adiabatique et à nombre de Mach donné, la correspondance entre H_{i_0} et R_{δ_0} est unique (voir Fig. 5).

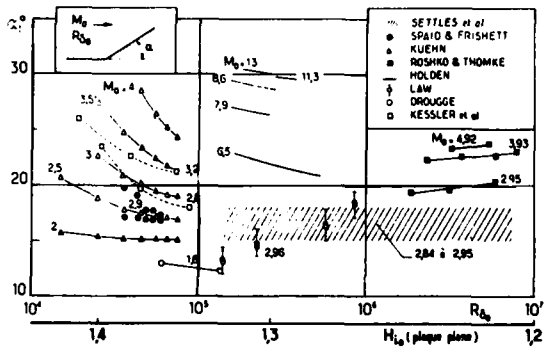


Fig. 31 - Décollement naissant en supersonique. Paroi adiabatique.

La plupart des valeurs de l'angle limite α_I publiées à ce jour sont portées Fig. 31. En dépit d'une dispersion importante, due surtout à l'imprécision dans la détection du décollement naissant, les tendances suivantes peuvent être dégagées :

1- l'angle α_I (ou le saut de pression équivalent p_I/p_0) augmente avec le nombre de Mach amont, ce qui est conforme à la fois avec la théorie de l'interaction libre et avec l'interprétation en termes d'effets inertiels (voir § 2 ci-dessus).

2- à bas nombre de Reynolds, α_I diminue quand R_{δ_0} augmente ce qui est en accord avec la théorie de l'interaction libre, comme nous l'avons vu précédemment.

3- en revanche, à grands nombres de Reynolds, la plupart des expérimentateurs ont observé une inversion de la tendance, c'est-à-dire que α_I croît avec R_{δ_0} .

4- comme la croissance de α_I avec R_{δ_0} est faible et l'incertitude expérimentale souvent grande, selon certains auteurs [40] le décollement naissant serait en réalité indépendant du nombre de Reynolds - tout au moins à grands R_{δ_0} .

Le renversement de la tendance en fonction de R_{δ_0} a donné lieu à de nombreuses discussions, certains chercheurs ayant même mis en doute la signification des résultats obtenus à faibles nombres de Reynolds dans des expériences où la transition est le plus souvent déclenchée artificiellement ce qui peut conférer à la couche limite une structure "anormale". Cependant, le changement dans le sens de la variation de α_I avec R_{δ_0} s'interprète aussi en recourant aux mêmes arguments que ceux avancés pour expliquer l'évolution des longueurs d'influence amont (voir § 3.1 ci-dessus). A savoir, qu'à faible nombre de Reynolds, l'interaction est dominée par les termes de viscosité et alors, tout comme en laminaire, la résistance au décollement diminue quand R_{δ_0} augmente. Au contraire, à grands nombres de Reynolds, le phénomène est contrôlé par une zone de paroi (considérablement plus épaisse que la sous-couche visqueuse) où les effets inertiels sont prépondérants. D'où une plus grande "raideur" de la couche limite quand R_{δ_0} croît.

Plusieurs méthodes simplifiées ont été proposées pour prédire le décollement naissant en supersonique et en hypersonique. Certaines sont dérivées de la théorie de l'interaction libre de Chapman, et s'appliquent donc au cas des écoulements à faibles nombres de Reynolds [41, 42] . D'autres reposent sur des modèles où la viscosité est complètement négligée [43, 44, 45] ; elles ne sont donc en principe valables qu'à grands nombres de Reynolds. Toutefois, parmi ces dernières, la méthode de Elfstrom [45] prédit fidèlement le renversement de tendance qui est attribué en fait à la modification de la structure de la couche limite initiale avec R_{δ_0} et non à un échange d'influence entre les termes de tension et d'inertie. Il existe enfin plusieurs méthodes de prévision du décollement purement empiriques[25, 46] .

3.4 - *Interaction avec formation d'un décollement étendu* -

Quand le choc est assez intense pour faire décoller la couche limite, la situation devient beaucoup plus complexe et, sauf dans une région de dimension très réduite située à l'origine de l'interaction, les phénomènes dissipatifs jouent ici un rôle essentiel.

La figure 32 représente la structure générale de l'écoulement résultant d'une interaction avec décollement en transsonique. Il s'agit d'expériences effectuées dans un canal dont une des parois porte une "bosse" présentant un profil favorisant le développement d'une zone décollée étendue [47] . La répartition du nombre de Mach pariétal M_p est tracée sur la figure 33,qui montre également une visualisation interférométrique de l'écoulement. Les champs externes non visqueux et dissipatifs ont fait l'objet d'analyses détaillées au Vélocimètre Laser qui ont permis de mettre en évidence les caractéristiques suivantes :

1- le décollement s'accompagne d'une montée de pression extrêmement rapide jusqu'à un "plateau" à la frontière duquel le nombre de Mach de l'écoulement de fluide parfait contigu est encore supersonique (voir Fig. 33a). On peut vérifier [47] que ce décollement, de nature en fait supersonique, satisfait parfaitement à la notion d'interaction libre de Chapman [20] , en ce sens qu'il ne dépend pas des circonstances aval l'ayant provoqué mais est entièrement déterminé par la situation de l'écoulement à l'origine de l'interaction. Le plateau de pression est suivi d'une recompression nettement plus progressive qui marque le recollement.

2- dans la partie extérieure du champ non visqueux, se forme un système de chocs en lambda rencontré classiquement dans les décollements transsoniques et ayant fait l'objet d'analyses expérimentales détaillées [47 - 50] . Au décollement est associé un choc oblique "faible" (C_0) (au sens de la solution faible des équations du choc oblique) ; la zone supersonique qui fait suite à (C_0) est terminée par un choc oblique "fort" (C_1), en fait très peu intense. Les chocs (C_0) et (C_1) convergent en un point triple I d'où part le choc oblique "fort" (C_2).

3- la figure 32 montre également les lignes de courant de l'écoulement moyen dans la couche dissipative. Ce tracé révèle que le décollement s'organise en un bulbe de recirculation -ou tourbillon- limité par la ligne de courant limite (s) issue du point de décollement D et aboutissant au point de recollement R. Elle constitue la démarcation entre, d'une part le fluide venant de l'amont et poursuivant son chemin vers l'aval, et d'autre part le fluide, qui faute d'une énergie mécanique suffisante, se trouve emprisonné dans le bulbe. Nous verrons plus loin que ce schéma doit être modifié dans le cas où une injection -ou aspiration- est pratiquée dans la zone d'interaction afin de satisfaire la conservation globale de la masse.

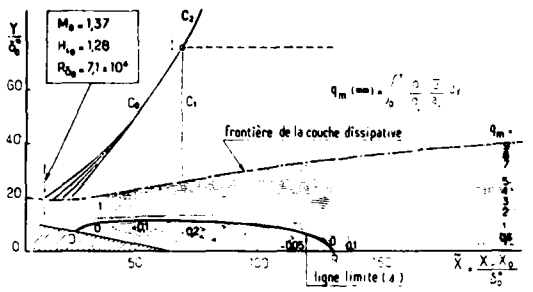


Fig. 32 - Interaction avec décollement en transsonique. Système de chocs et lignes de courant de la couche dissipative.

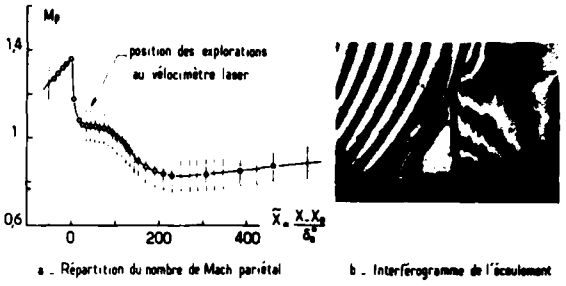


Fig. 33 - Interaction avec décollement en transsonique.

Le cas de la réflexion d'un choc oblique en supersonique est schématisé Fig. 34. La couche limite décolle en un point D situé très en amont de l'impact théorique du choc incident (C_0) en fluide parfait. La compression intense liée au décollement induit dans la partie supersonique de l'écoulement des ondes se focalisant rapidement pour constituer le choc réfléchi (C_1) qui intersecte (C_0) en I. Le choc (C_0) pénètre dans la couche dissipative décollée d'où il est réfléchi en un système d'ondes de détente qui ont un effet de compensation assurant la continuité de la pression dans la zone décollée. Il en résulte une déflexion de l'ensemble de l'écoulement en direction de la paroi sur laquelle le recollement intervient en un point R. Tout comme en transsonique, la compression associée est beaucoup plus étalée que celle accompagnant le décollement. D'une manière générale, la topographie de l'écoulement dissipatif moyen est analogue à celle du cas transsonique, avec notamment la ligne de courant limite (s) frontière du bulbe de recirculation.

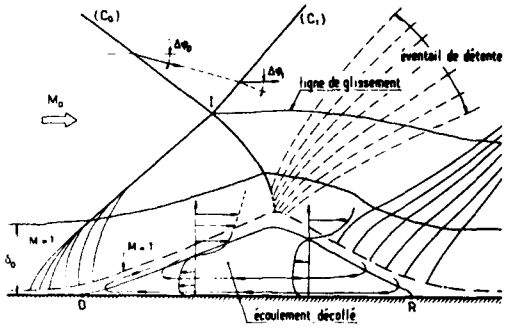


Fig. 34 - Réflexion de choc avec décollement en supersonique. Schéma de l'écoulement.

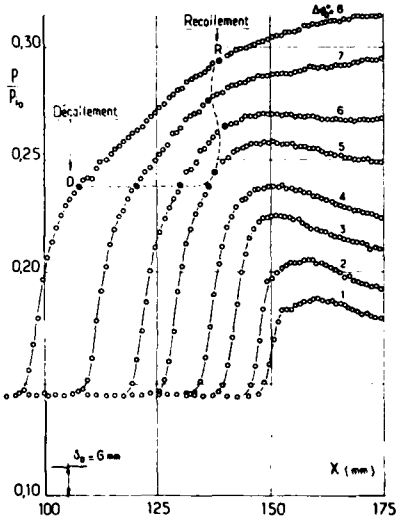


Fig. 35 - Réflexion de choc en supersonique. Répartitions de pression pariétale.

Des répartitions de pression pariétales mesurées dans des réflexions de choc se produisant à un nombre de Mach amont M_0 de 1,93 sont représentées Fig. 35. Elles montrent, en particulier, que l'extension de la zone décollée, caractérisée par exemple par la distance séparant les points de décollement et de recollement, croît avec la déflexion $\Delta\varphi$ au travers du choc incident, c'est-à-dire avec le saut de pression total p_2/p_0 résultant de la réflexion. Or, selon la théorie de l'interaction libre (voir aussi les travaux de Zukoski [51]), la compression Δp_D réalisée au décollement est entièrement déterminée par les conditions amont, qui dans le cas présent sont pratiquement invariables. On constate d'ailleurs que la pression en D demeure quasi-constante quand l'intensité de l'interaction croît. En conséquence, une augmentation du saut total p_2/p_0 ne peut être obtenue que par une montée de pression Δp_R au recollement plus grande. Ceci n'est possible que si les particules fluides s'écoulant sur la ligne limite et qui stagnent au point de recollement R sont à même de négocier une barrière de pression plus haute (pour plus de détail, se reporter aux théories sur le recollement [52]), donc possèdent une énergie mécanique plus grande. Pour qu'il en soit ainsi, il faut que la longueur de la zone décollée s'accroisse de manière telle que les effets d'entraînement aient eu le temps de communiquer un niveau de vitesse suffisant au fluide qui, sur la ligne de courant limite, va aborder le recollement. D'où l'extension de la zone décollée avec l'intensité de l'interaction, comme on le voit Fig. 35.

Le mécanisme qui vient d'être brièvement décrit explique la grande efficacité des techniques de contrôle de l'interaction par effet d'aspiration ou d'injection fluide au sein du bulbe de décollement. Dans les deux cas, un apport ou un prélèvement de débit même très faible est en mesure de produire une forte augmentation de la vitesse u_s sur la ligne de courant qui stagne au point de recollement, ce qui accroît

considérablement la capacité de l'écoulement de négocier un gradient de pression antagoniste. Les méthodes utilisées pour diminuer la traînée au culot des projectiles reposent sur des propriétés identiques [52] .

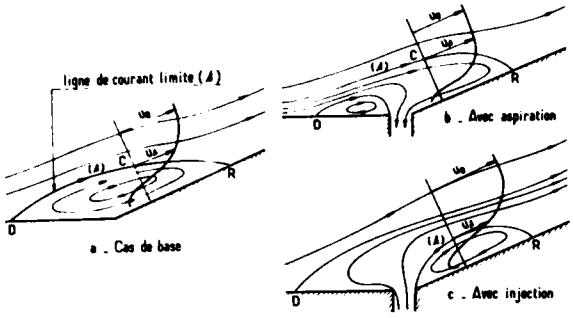


Fig. 36 - Schématisations de l'écoulement dans un bulbe de décollement.

En effet, considérons les schémas de la figure 36 qui représentent, en la simplifiant fortement, l'organisation des lignes de courant de l'écoulement (moyen) décollé dans un dièdre. Pour plus de clarté, le système de chocs associé n'a pas été dessiné. Le schéma ⓐ correspond au cas de base où aucun transfert de masse n'est pratiqué dans l'"eau-morte". Alors, ainsi qu'il a déjà été dit, la ligne de courant *(s)* qui stagne au point de recollement R doit avoir son origine au décollement D afin d'assurer la conservation de la masse en régime stationnaire. Si du fluide est aspiré par la paroi à faible vitesse, des considérations de topologie simples conduisent au schéma ⓑ où c'est maintenant une ligne de courant provenant de l'amont et située dans la couche limite initiale au-dessus de D qui doit stagner en R . Pourvu que l'aspiration soit suffisamment modérée pour ne pas bouleverser complètement la structure de l'écoulement, on peut admettre que la distribution des vitesses dans la couche dissipative en C au moment où le processus de recollement commence n'est pas sensiblement modifiée par rapport au cas de base ⓐ . Si bien que la ligne de courant *(A)* se trouve sur ce profil à une distance plus grande de la paroi et en conséquence la vitesse u_s en C sur *(A)* est plus élevée. D'où une aptitude de l'écoulement à supporter une recompression plus importante au recollement. On devra donc s'attendre à ce qu'une aspiration ait un effet bénéfique, en ce sens qu'elle tendra à réduire l'étendue d'une zone décollée et même, à la limite, à la supprimer totalement.

Le cas d'une injection fluide à très basse vitesse est représenté sur le schéma ⓒ . Maintenant la vitesse sur (A) est plus faible puisque (A) doit être à une position plus basse sur le profil de vitesse en . L'effet résultant sera donc un allongement du bulbe de décollement de manière à ce que u_s ait malgré tout un niveau suffisant pour que la ligne de courant (A) stagne exactement en R . Toutefois, dans le cas présent, si le débit -et donc la vitesse du fluide injecté- deviennent plus importants, il faut s'attendre à un inversion de l'effet puisque les vitesses sur la partie inférieure du profil en C , et en particulier celle sur (A), vont forcément devoir augmenter si le débit apporté dans l'eau-morte croît au delà d'une certaine limite.

Ces remarques nous seront utiles pour interpréter les observations de la deuxième partie.

Les figures 37 à 39 montrent les distributions des grandeurs suivantes pour l'écoulement transsonique largement décollé déjà considéré plus haut (voir Fig. 32) : composante longitudinale moyenne $\bar{u}$ normalisée par $\bar{u}_e$; énergie cinétique de turbulence k , qui se confond pratiquement avec $\overline{u'^2}$; contrainte de cisaillement $-\overline{u'v'}$ (k et $-\overline{u'v'}$ sont rapportées à a_i^2).

Les points les plus notables que révèlent ces distributions sont :

1- l'épaississement très important de la couche dissipative à partir du moment où le décollement se développe (ainsi, dans l'exemple considéré δ est pratiquement multipliée par 6) ;

2- la forte croissance du niveau de turbulence, le maximum maximorum de l'intensité longitudinale étant voisin de 40% ;

3- également, les profils de $-\overline{u'v'}$ mettent en évidence des effets de non-équilibre fortement marqués qui se traduisent, en particulier, par une lente décroissance du taux d'entraînement. D'où des distributions de vitesse qui, en aval du recollement, se "remplissent" très rapidement.

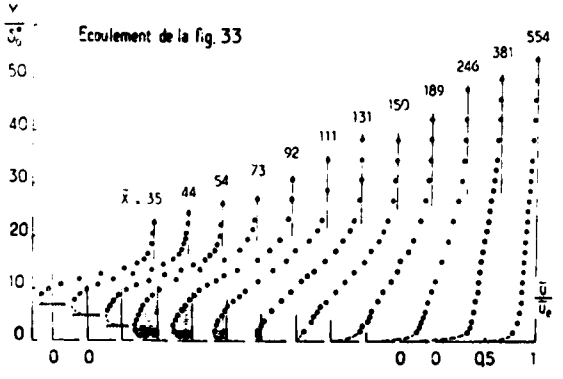


Fig. 37 - Interaction avec décollement en transsonique. Vitesse moyenne longitudinale.

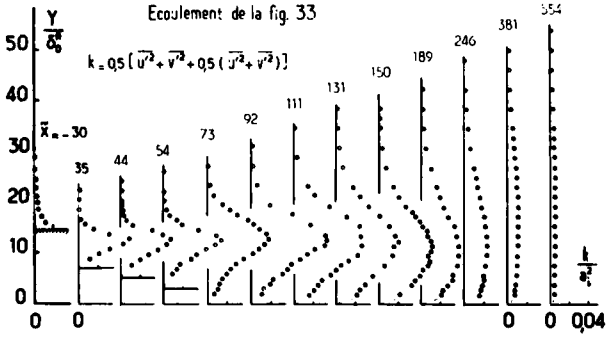


Fig. 38 - Interaction avec décollement en transsonique. Energie cinétique de turbulence.

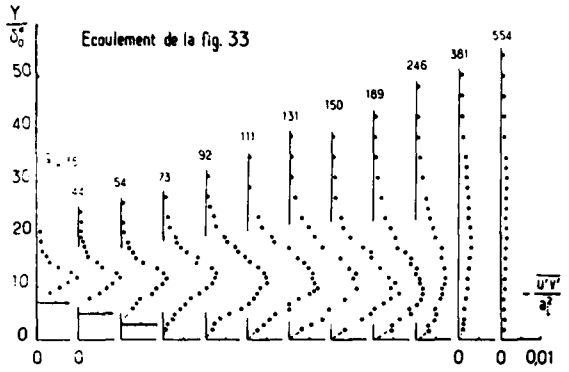
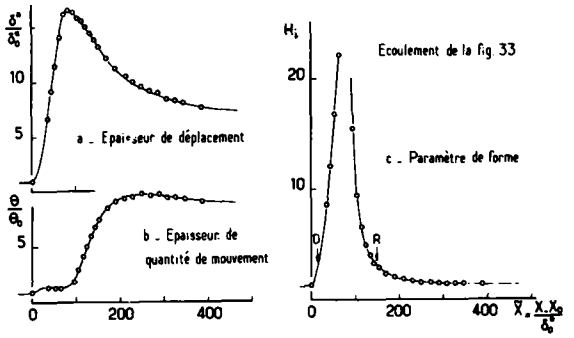


Fig. 39 - Interaction avec décollement en transsonique. Tension de cisaillement.

Les évolutions des épaisseurs de déplacement et de quantité de mouvement ainsi que celle du paramètre de forme H_i sont représentées Fig. 40. Ici la croissance de δ^* est particulièrement importante, δ^*/δ_0^* atteignant une valeur maximale de 16,5. Quant à H_i , il devient pratiquement infini, la couche dissipative acquérant une structure de zone de mélange [53] . Il est à noter que la décroissance de H_i est extrêmement rapide à partir du moment où le processus de recollement commence. En aval de R , H_i tend vers des valeurs basses typiques de distributions de vitesse bien "remplies", l'évolution du phénomène étant analogue à celle observée en écoulement supersonique. Au décollement, la croissance de l'épaisseur de quantité de mouvement est modeste ; elle est beaucoup plus notable lors du recollement.

Fig. 40 - Interaction avec décollement en transsonique. Evolution des caractéristiques de la couche limite.



Nous n'entrerons pas plus avant dans la description de cet écoulement dont les propriétés, celles relatives à la turbulence en particulier, sont analysées plus en détail ailleurs [53] . Comme nous l'avons vu sur un point précis, mais ainsi que le confirment des examens plus complets, le cas supersonique conduit à un comportement voisin quant aux traits principaux de l'écoulement.

3.5 - *Conclusions sur les propriétés de l'interaction* -

En conclusion, en régime turbulent et pourvu que le nombre de Reynolds soit suffisamment élevé, l'apparition du décollement en pied de choc dépend peu des propriétés de la couche limite. En revanche l'effet destabilisateur qui se traduit, en particulier, par l'accroissement des épaisseurs de déplacement et de quantité de mouvement ainsi que du niveau de turbulence dépend fortement de la distribution de vitesse initiale. Ce fait a au moins deux conséquences importantes :

1- si une couche limite est initialement peu remplie, elle ne décollera pas plus facilement, comme nous venons de le voir, mais l'interaction l'amènera dans un état tel qu'un gradient adverse appliqué peu en aval du choc aura sur elle un effet plus néfaste avec comme conséquence éventuelle le décollement. Par exemple, une situation de ce genre se rencontre sur un profil supercritique très chargé dans la région du bord de fuite (interaction du type B selon Pearcey [54]).

2- dans les simulations en soufflerie, les paramètres de forme sont souvent plus grands que dans la pratique en raison de l'insuffisance des nombres de Reynolds d'essai. Une interaction sur maquette ne conduira donc pas forcément à un décollement local prématuré, mais sera la cause d'un épaississement des couches limites plus fort que dans la réalité. Si bien que les effets de gradient, qui sont proportionnels à l'épaisseur relative de la couche limite, seront artificiellement amplifiés sur une maquette de forme donnée. Il s'agit là de ce qu'on appelle les effets d'échelle ("scale effets" ; voir à ce sujet la Réf.[35]).

Il convient toutefois de remarquer que, dans certaines circonstances, l'interaction avec une onde de choc peut avoir des conséquences bénéfiques sur le développement ultérieur de la couche limite. En effet, si le choc destabilise fortement l'écoulement, en même temps et corrélativement ainsi que nous l'avons vu, il intensifie les échanges turbulents. De ce fait, si aucun autre gradient de pression adverse ne succède immédiatement au choc, la couche limite "récupère" extrêmement vite comme en témoigne la rediminution très rapide de son paramètre de forme (voir les exemples des figures 20 et 40). Notamment (voir § 3.4), on a observé que cette intensification de la turbulence contribue à accélerer plus spécialement les régions voisines de la paroi ce qui a pour conséquence de bien remplir le profil dans une zone d'importance capitale. En même temps, les tensions de Reynolds ont des niveaux accrus, la turbulence gardant longtemps la mémoire de l'interaction [53] . Ainsi, comme Rose l'a souligné [55] , cette couche limite a une énergie plus grande qui peut lui permettre de mieux supporter une interaction faisant suite à la première.

4 - FACTEURS D'INFLUENCE DE L'INTERACTION ONDE DE CHOC-COUCHE LIMITE ET TECHNIQUES DE CONTROLE -

4.1 - Généralités -

Nous allons maintenant examiner l'inflence de certains facteurs en mesure de modifier l'interaction par rapport à ce qu'elle est dans le cas de base, le but recherché étant de contrôler le phénomène, c'est-à-dire d'en prévenir les conséquences néfastes. Comme nous l'avons déjà précisé dans l'introduction, le principe de base de ces actions est d'augmenter l'énergie mécanique des zones à faible vitesse. Pour cela, il est possible d'envisager plusieurs procédés dont nous allons analyser le mode de fonctionnement. Les modes d'action retenus seront les suivants :

1- abaissement de la température de la paroi ;

2- aspiration pariétale, soit répartie, soit localisée ;

3- injection de fluide à faible vitesse ;

4- soufflage de la couche limite amont ;

5- générateurs de tourbillons, piège à couche limite.

Ainsi que nous le verrons, ces procédés peuvent également être classés en deux catégories selon qu'ils agissent :

1- en modifiant les caractéristiques de la couche limite amont qui va aborder l'interaction en vue de lui conférer une plus grande résistance ;

2- localement, au niveau et/ou immédiatement en aval de l'onde de choc, par résorbtion de la zone de fluide ralenti.

4.2 - Influence de l'état thermique de la paroi -

Il est bien connu que le comportement d'une couche limite dépend fortement de l'état thermique de la paroi, c'est-à-dire du rapport T_p/T_r de la température de paroi T_p à la température T_r que celle-ci prend à l'équilibre dans le cas adiabatique. Ainsi, un refroidissement énergique a un effet stabilisateur qui retarde la transition laminaire-turbulent, ce qui en fait un procédé envisageable, bien que pour des applications très spéciales, de réductions de la traînée de frottement [56] . Egalement, on sait que refroidir la paroi a une influence bénéfique dans les régions où la couche-limite est soumise à un gradient de pression adverse en empêchant ou retardant le décollement [57] .

Le dernier comportement s'explique si on considère les conséquences d'un flux de chaleur pariétal sur le développement de la couche limite et donc sur ses propriétés au moment où elle va aborder l'agent destabilisateur qui peut être soit une compression étalée, soit une onde de choc. Brièvement, rappelons que refroidir la paroi ($T_p/T_r < 1$) entraînera les changements suivants par comparaison au cas adiabatique et à même valeur du nombre de Reynolds R_δ :

1- le paramètre de forme H_i est diminué, comme le montrent les résultats de la figure 41a déduits d'une famille de profils turbulents proposée par Walz [58] (les figures 41a et 41b sont empruntées à la Réf. [59]) ;

2- à H_i fixé, le coefficient de frottement pariétal est augmenté (voir Fig. 41b) ; la tendance étant fortement accentuée si la dépendance de H_i à l'égard de T_p/T_r est sur-ajoutée ;

3- comme nous l'avons déjà vu § 2 (voir aussi Fig. 6), à H_i et nombre de Mach extérieur M_e donnés, la couche subsonique est amincie en raison de la diminution locale de la vitesse du son qui résulte de l'abaissement de la température. L'amincissement est évidemment plus marqué si l'effet de T_p/T_r sur H_i est aussi pris en considération.

Les comportement ci-dessus sont bien sur inversés dans le cas où la paroi est chauffée ($T_p/T_r > 1$).

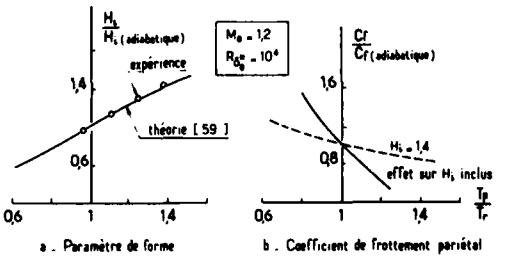


Fig. 41 - Effet de la température de paroi sur certaines propriétés de la couche limite (d'après [59]).

Donc, à la lumière des résultats présentés dans les paragraphes 2 et 3 nous pouvons déjà conclure qu'un refroidissement de la paroi aura des répercussions favorables sur une interaction choc-couche limite par accroissement de la "raideur" de l'écoulement dissipatif. De plus, l'augmentation de C_f qui se produit alors, tendra à retarder le décollement en vertu du mécanisme décrit par la théorie de l'interaction libre (voir § 2 ci-dessus). C'est-à-dire que l'effet agira dans le bons sens à la fois sur les termes inertiels et sur les forces de viscosité.

A notre connaissance, en écoulement transsonique, il existe très peu de résultats expérimentaux vraiment convaincants sur l'influence d'un flux de chaleur sur une interaction choc-couche limite. Toutefois, des renseignements extrêmement instructifs peuvent être tirés du modèle de Inger dont il a déjà été

question (voir § 3.3) et qui donne une représentation réaliste des phénomènes. Ainsi, la figure 42, extraite de la Réf. [59], montre l'influence de la température de paroi sur la distribution de pression réduite $(p-p_0)/(p_1-p_0)$. Si le paramètre de forme amont H_{i_0} est maintenu constant, ce qui revient à appliquer le flux de chaleur uniquement dans la zone d'interaction, l'effet de T_p/T_r est modeste (voir Fig. 42a). Le refroidissement ne provoquant qu'une contraction limitée du domaine d'interaction. Cette tendance est confirmée par les expériences de Padova et al. [60] ainsi que le montre la figure 43. En revanche, l'effet est beaucoup plus marqué si la variation concomitante de H_{i_0} qui doit normalement se produire est prise en compte (voir Fig. 42b).

La figure 44 montre l'accroissement normalisé $(\delta^* - \delta_0^*)/\delta_0^*$ de l'épaisseur de déplacement. Ici, l'effet thermique "pur" est important en raison de sa répercussion sur la distribution de la masse

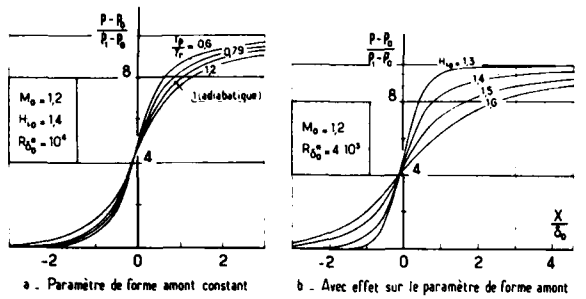


Fig. 42 - Interaction en transsonique . Effet de température de paroi . Répartitions de pression pariétale (d'après [59]).

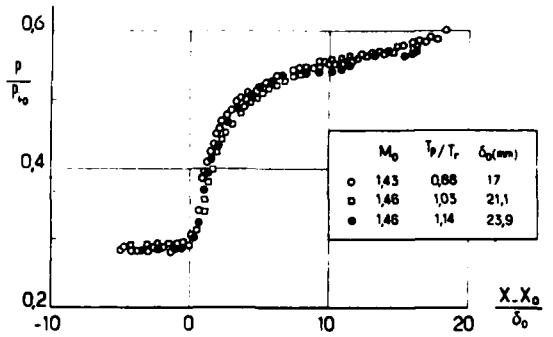


Fig. 43 - Interaction en transsonique - Effet de température de paroi . Répartition de pression pariétale (d'après [60]).

spécifique. Enfin, la figure 45 donne les évolutions du coefficient de frottement pariétal qui sont utilisées pour déterminer l'apparition du décollement en pied de choc. Ainsi, on observe que refroidir la paroi retarde le décollement naissant comme cela apparaît plus nettement sur les courbes limites dans le plan (H_{i_0} , M_0) tracées Fig. 46. Toutefois, si l'influence du flux thermique ne se fait sentir que sur le paramètre de forme initial H_{i_0} , c'est-à-dire si ce flux est appliqué en amont de l'interaction sur une distance suffisante pour lui permettre de modifier les caractéristiques de la couche limite, les conditions de décollement naissant sont peu modifiées en vertu du mécanisme exposé § 3.3. Toutefois, il faut souligner qu'un refroidissement sera quand même bénéfique puisqu'il limitera l'épaississement de la couche limite et fera que le bulbe de décollement sera très restreint.

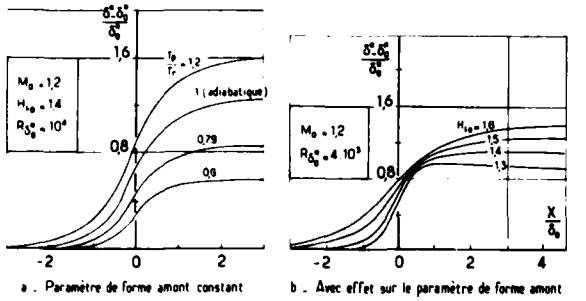


Fig. 44 - Interaction en transsonique . Effet de température de paroi . Evolutions de l'épaisseur de déplacement (d'après [59]).

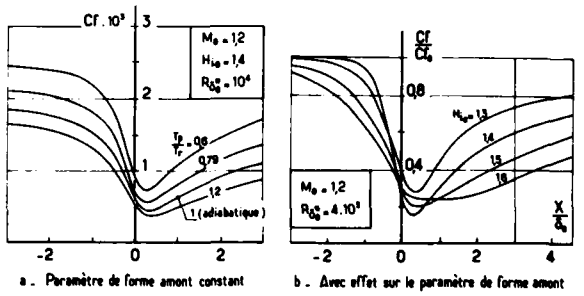


Fig. 45 - Interaction en transsonique . Effet de température de paroi . Evolutions du coefficient de frottement pariétal (d'après [59].

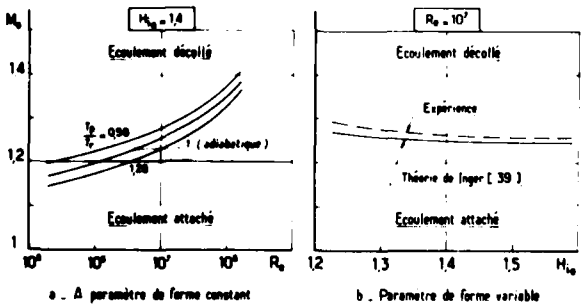


Fig. 46 - Interaction en transsonique. Effet de température de paroi. Limite de décollement naissant.

Réciproquement, chauffer la paroi va amplifier les conséquences néfastes de l'interaction en hâtant l'apparition du décollement et en aggravant le processus destabilisateur. De telles répercussions possibles devront être présentes à l'esprit lors des simulations d'écoulements à grands nombres de Reynolds dans les souffleries cryogéniques [61] .

En écoulement supersonique, les mêmes tendances sont observées, bien que les influences propres des différents paramètres mis en jeu n'aient pas été aussi clairement dégagées qu'en transsonique, faute d'un modèle théorique convenable. A titre d'exemple typique, la figure 47 montre l'effet d'un flux de chaleur sur la longueur de décollement amont L_D (voir schéma de la figure) pour une interaction se produisant dans un dièdre d'angle α à un nombre de Mach M_0 voisin de 3 [24, 62] . La réduction de L_D résultant d'un refroidissement de la paroi apparaît plus nettement Fig. 48 où l'on a représenté le rapport entre la longueur normalisée L_D/δ_0 (ce qui permet de prendre en compte l'influence du nombre de Reynolds)

avec flux et la valeur de L_0/δ_0 dans le cas adiabatique. Dans le même esprit, la figure 49 illustre, par un tracé des lignes de courant, le changement de structure de la zone d'impact d'une onde de choc quand la température de paroi est modifiée. Ces résultats expérimentaux ont été obtenus par Back et Cuffel [63] à un nombre de Mach Mo de 3,5. Ils mettent particulièrement bien en évidence la contraction du bulbe de décollement provoquée par un refroidissement de la paroi. Un tel effet est aussi manifeste sur les répartitions de pression pariétales de la figure 50 qui ont été mesurées dans une réflexion de choc à Mo = 3,18 [64] .

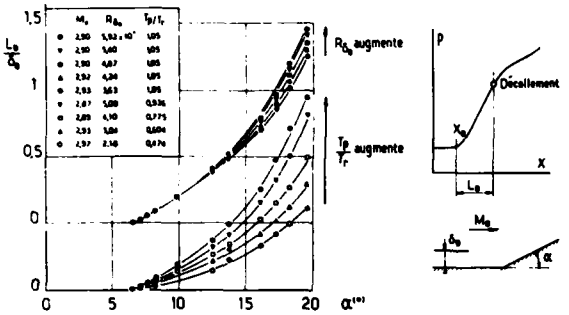


Fig. 47 - Interaction en supersonique. Effet de température de paroi. Longueur de décollement (d'après [24]).

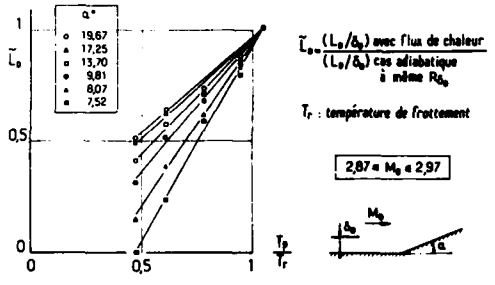


Fig. 48 - Interaction en supersonique. Effet de température de paroi. Longueur de décollement normalisée (d'après [24]).

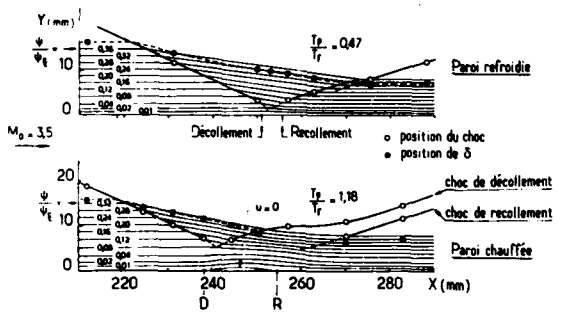


Fig. 49 - Interaction en supersonique. Effet de température de paroi. Organisation des lignes de courant (d'après [63]).

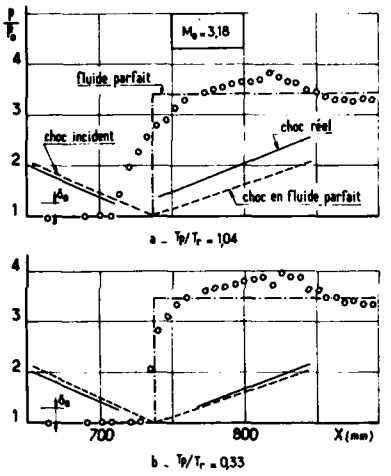


Fig. 50 - Interaction en supersonique. Effet de température de paroi. Répartition de pression pariétale (d'après [64].

On dispose de peu de renseignements concernant la répercussion d'un flux de chaleur sur la limite de décollement naissant en supersonique. Toutefois, ainsi que le montre la figure 51, il est clair que le décollement est retardé sur une paroi froide. La tendance est correctement reproduite par le modèle de Elfstrom [45] , où rappelons le, la couche limite est représentée par un écoulement non visqueux mais rotationnel. Dans ces conditions, le seul effet de la température sera de modifier le profil du nombre de Mach M dans la couche limite, un rapport T_p/T_r inférieur à l'unité élevant les valeurs de M à proximité de la paroi. En conséquence, selon la schématisation de Elfstrom, la couche limite développera une plus grande résistance au décollement, ce que confirme l'expérience, compte tenu d'une assez forte dispersion des mesures.

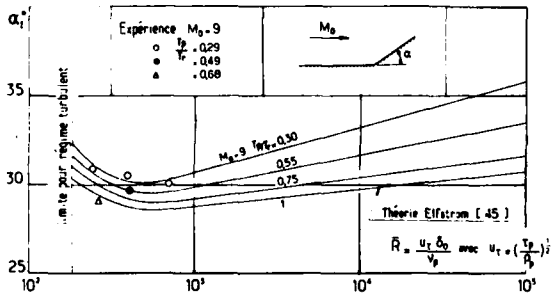


Fig. 51 - Décollement naissant en supersonique. Paroi non-adiabatique (d'après [45]).

4.3 - *Influence de la forme de la paroi* -

Il est bien évident que la forme de la paroi est aussi susceptible d'agir sur une interaction choc-couche limite. Ainsi, en supersonique, un changement de pente convenablement aménagé au poin d'impact d'un choc incident peut en théorie annuler le choc réfléchi par création d'une détente compensatrice. Un tel effet peut également être créé par une injection pariétale, comme nous le verrons § 4.4. D'une manière générale, toute modification de forme entraînant une accélération répartie ou non tendra naturellement à stabiliser la couche limite, en abaissant en particulier son paramètre de forme, c'est-à-dire réduira les risques d'apparition ou d'extension brutale d'un décollement.

En écoulement transsonique, on sait depuis les expériences de Gadd [44] que sur une paroi convexe le décollement est retardé, tendance que prédisent les modèles de Inger et de Bohning et Zierep [16]. En particulier, ces derniers auteurs expliquent un tel comportement par le fait que la détente qui se forme ordinairement juste en aval d'un choc en transsonique ("post shock expansion") est intensifiée par une courbure correspondant à une convexité. A proximité de la paroi, cette détente influe sur le développement de l'écoulement dans un sens qui tend à retarder un possible décollement. Toutefois, d'après les calculs de Inger [39], l'effet serait faible, alors que le modèle de Bohning et Zierep prédit une influence favorable marquée (voir Fig. 52). Ce point mériterait d'être élucidé par des expériences plus systématiques que celles dont on dispose actuellement.

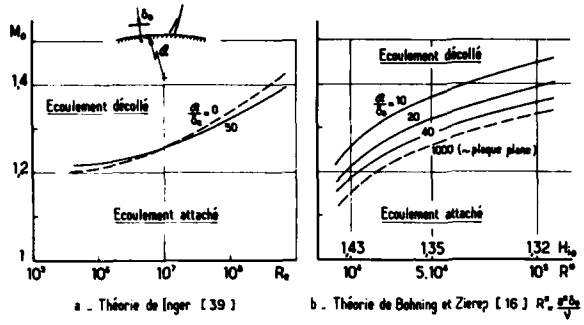


Fig. 52 - Décollement naissant en transsonique. Effet de courbure de la paroi.

4.4 - *Influence d'un transfert de masse à la paroi* -

4.4.1 - *Effet d'un transfert de masse sur les propriétés de la couche limite* -

Comme nous le savons déjà, l'interaction avec une onde de choc dépend beaucoup des caractéristiques initiales de la couche limite, à savoir :

1- son profil de vitesse,

2- sa distribution de nombre de Mach,

3- son frottement pariétal.

Ces trois caractéristiques sont susceptibles d'être profondément affectées par un transfert de masse -aspiration ou injection- pratiqué sur une certaine longueur de paroi. Le but le plus fréquemment recherché est de diminuer la traînée de frottement [56] et aussi d'agir sur les flux thermiques soit pour les intensifier, comme dans les échangeurs, soit au contraire en vue de les diminuer, cas des aubages de turbine par exemple.

La manière la plus naturelle et la plus couramment employée pour modifier les coefficients d'échange pariétaux consiste à pratiquer l'injection (ou l'aspiration) du fluide au travers d'une paroi rendue perméable, une plaque poreuse étant souvent utilisée.

Etant donnée son extrême importance pratique, le développement d'une couche limite en présence d'un effet de transfert de masse a fait l'objet de très nombreux travaux, expérimentaux aussi bien que théoriques; dont l'examen sortirait du cadre de notre sujet. Le lecteur interessé trouvera dans les références [65] à [70] (dont le nombre est loin d'être exhaustif) des renseignements plus complets sur cette question. En fait nous nous limiterons ici à la présentation de quelques exemples typiques dans le seul but d'illustrer l'effet d'une aspiration ou d'une injection sur certaines des propriétés d'une couche limite turbulente.

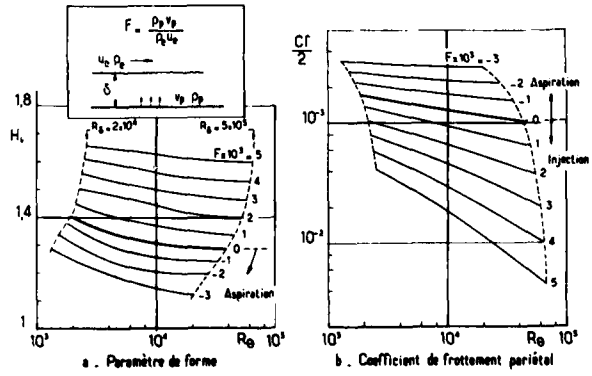


Fig. 53 - Effet d'un transfert de masse sur les propriétés de la couche limite (d'après [69]).

Les résultats présentés Fig. 53 sont empruntés à la thèse de Lili [69]. Le taux d'injection F est ici défini comme le rapport $F = \rho_p v_p / \rho_e u_e$ où v_p est la composante de vitesse normale à la paroi et ρ_p la masse spécifique en $y = 0$. Les courbes tracées mettent en évidence les évolutions suivantes :

1- une injection ($F > 0$) entraîne un "creusement" des distributions de vitesse ; ce qui se traduit par une augmentation du paramètre de forme H_i (voir Fig. 53a). En même temps, le coefficient de frottement C_f diminue (voir Fig. 53b) et la couche limite est épaissie ;

2- une aspiration ($F < 0$) induit les effets inverses ; c'est-à-dire que H_i décroît et C_f croît.

Il est à noter que les tendances ci-dessus vont dans le même sens que celles résultant de l'action d'un gradient de pression positif, dans le cas d'une injection, ou bien négatif, dans le cas d'une aspiration. Aussi, certains auteurs [38, 71] ont proposé d'utiliser ce moyen pour simuler l'interaction d'une onde de choc avec une couche limite initiale destabilisée dans des installations où il est difficile de modeler à volonté le gradient de pression en amont de l'onde de choc. Par cet artifice, on peut aussi envisager de faire varier indépendamment l'un de l'autre le nombre de Reynolds et le paramètre de forme qui ont, comme nous le savons déjà (voir § 3.1 ci-dessus), des influences bien distinctes. Il a été également suggéré de pratiquer une aspiration pariétale pour reproduire sur des maquettes à petite échelle des caractéristiques de couche limite (épaisseur δ comparée à la corde du profil, par exemple) identiques à celles rencontrées sur une aile en vraie grandeur [72, 73] . On aurait ainsi un moyen de s'affranchir des facteurs d'échelle brièvement évoqués § 3.5.

Il convient néanmoins de remarquer que les évolutions de H_i et C_f réalisées par transfert de masse ne se font pas toutes deux dans le sens des variations résultant d'un changement du nombre de Reynolds. En effet, si par exemple R_δ croît, il y a diminution simultanée de H_i et C_f . Simuler des grands nombres de Reynolds par aspiration n'est donc correct que dans les situations où les termes inertiels jouent un rôle prépondérant dans le processus d'interaction (voir § ci-dessus). Même dans ce cas, il conviendra d'être prudent dans l'emploi de tels procédés dont les répercussions sur la structure de la couche limite -sa turbulence en particulier- sont complexes et souvent mal connues. En outre, leur mise en oeuvre sur des maquettes de petite taille peut être délicate.

4.4.2 - Contrôle de l'interaction par aspiration répartie -

Soumettre une couche limite qui va aborder une interaction à un effet d'aspiration pariétale est certainement bénéfique dans la mesure où l'on diminue ainsi son paramètre de forme ce qui a pour conséquence de lui conférer une plus grande résistance à la destabilisation, d'où en particulier :

1- une contraction des longueurs d'interaction,

2- un accroissement moindre des épaisseurs δ , δ^* et θ .

Toutefois, pour ce qui concerne l'apparition du décollement en pied de choc, nous savons déjà (voir § 3.3) que le phénomène dépend peu de H_{i_θ} . Bien plus, des calculs effectués par Inger [74] (voir aussi Inger et Zee [75]), montrent qu'il peut même se produire un renversement de tendance, c'est-à-dire qu'une aspiration trop vigoureuse est susceptible d'entraîner une contraction du domaine d'interaction tellement forte que l'intensification du gradient de pression longitudinal qui en résulte précipite le décollement de la couche limite. Au contraire, une légère injection peut retarder l'apparition du décollement, comme en témoignent les distributions du coefficient de frottement pariétal représentées Fig. 54a. Un tel comportement a également été observé expérimentalement par Squire et Smith [38] en écoulement supersonique pour le cas de la réflexion d'une onde de choc oblique.

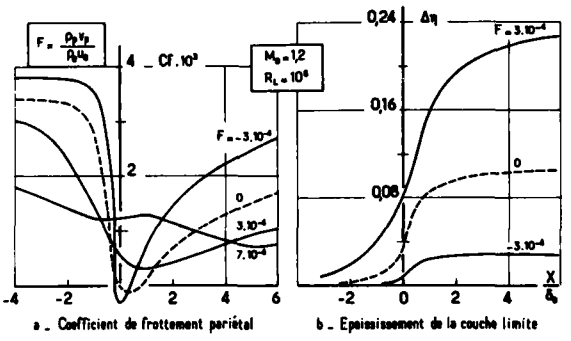


Fig. 54 - Interaction en transsonique. Effet d'un transfert de masse réparti (d'après [74]).

Néanmoins, il convient de souligner qu'une aspiration est en définitive toujours bénéfique dans la mesure où, ainsi que le montre la figure 54a, le décollement qui peut quand même se produire demeure extrêmement localisé et donc sans grand dommage pour l'ensemble de l'écoulement. D'un autre coté, l'épaississement de la couche limite se trouve fortement limité et sa "réhabilitation" en aval du choc notablement accélérée par une aspiration même modeste (voir Fig. 54b).

Dans ces conditions, c'est principalement le contrôle en aval et au pied du choc qui se révèle le plus efficace puisqu'il tend à compenser l'influence destabilisante d'une interaction que l'aspiration pratiquée en amont du phénomène aura eu pour effet d'intensifier.

Sur le plan technologique, une aspiration répartie de manière continue sur un domaine étendu peut être réalisée au moyen d'une paroi perméable -ou poreuse- ce qui assure une bonne qualité de surface et évite donc la formation d'ondes de perturbation dans la partie supersonique de l'écoulement. En outre, ce procédé permet de garder aisément le contrôle d'une interaction pouvant se déplacer en raison d'un changement des conditions amont, par exemple. Enfin, un autre avantage non négligeable de la paroi poreuse est de faciliter -dans une certaine mesure- la modélisation du phénomène en réalisant au mieux une condition aux limites de vitesse normale v_p imposée en tout point d'une région bien définie de la surface de l'obstacle (les problèmes de modélisation sont discutés plus bas § 4.7.1). En contrepartie, cette technique de contrôle comporte un certain nombre d'inconvénients qui font que son emploi est en fait limité :

1- de telles parois sont faites d'un matériau poreux dont la rugosité de surface a pour effet d'épaissir la couche limite et d'accroître son paramètre de forme, c'est-à-dire va à l'encontre de l'effet attendu d'une aspiration dont l'action peut même se trouver annulée.

2- coté écoulement, la pression n'est pas uniforme : elle a en amont du choc une valeur p_0 nettement plus basse que le niveau aval p_1 . En conséquence, pour une pression de cavité p_c uniforme sur l'autre face de la plaque faisant office de paroi, l'aspiration sera forcément moins intense devant le choc là où précisément elle devrait être particulièrement énergique pour l'emporter sur la rugosité. Bien plus, si p_c n'est pas maintenue en permanence à un niveau assez bas il peut arriver qu'elle devienne supérieure à p_0 si les circonstances de l'écoulement changent. Il y a alors effet d'injection en amont du choc avec les conséquences néfastes que l'on imagine.

3- enfin, l'aspiration à travers une paroi qui doit avoir une épaisseur suffisante pour supporter un fort écart de pression sans se déformer se fait au prix d'une perte de charge pouvant être importante ; d'où la nécessité de réaliser des niveaux de p_c souvent très bas.

En raison de son faible rendement, la paroi poreuse n'est donc guère utilisée sur les avions où, à grand nombre de Mach, son refroidissement -qui peut s'avérer indispensable- pose de très difficiles problèmes. En revanche, elle constitue un moyen intéressant pour contrôler et si possible annuler les interactions à la paroi d'une soufflerie où l'on dispose de facilités et d'un "confort" plus grands qu'à bord d'un avion.

En fait, dans une soufflerie, l'objectif le plus souvent visé n'est pas d'éviter un décollement ou de minimiser les conséquences néfastes d'une interaction, mais d'"éteindre" un choc frappant une paroi en empêchant ainsi la formation d'un choc réléchi qui risque d'interactionner une maquette. Ce problème est crucial dans la simulation des écoulements faiblement supersoniques où les ondes font un angle important par rapport au vecteur vitesse. Comme on le sait, quand un choc incident (C_0) produisant une déflexion $\Delta\varphi$ frappe en un point I une paroi plane alignée avec l'écoulement amont, il apparait un choc réfléchi (C_1) créant une déviation $-\Delta\varphi$. Dans ces conditions, l'extinction de (C_1) peut être obtenue de deux manières :

1- soit en donnant à la paroi en I un changement de direction $-\Delta\varphi$ Cette solution, que nous ne faisons que mentionner, a été en particulier étudiée expérimentalement par Chew et Squire [76] .

2- soit en pratiquant immédiatement en aval de I une aspiration telle que la vitesse v_p soit égale à la composante normale v_1 en aval de (C_1). Ce deuxième procédé, qui est plus souple que le premier puisqu'il est facile d'en faire varier la zone d'application et l'intensité, a fait l'objet de nombreuses études que nous ne discuterons pas ici (voir à ce sujet Goethert [77] , Allen [78] , Ramm et Jones [79] , Vayssaire [80]).

En fluide parfait, le problème a donc une solution de principe simple ; mais il est bien sur compliqué par la présence de la couche limite et le fonctionnement de la paroi poreuse. Pour en commenter certains aspects essentiels nous utiliserons les résultats très instructifs obtenus par Lee [81] dans une étude approfondie de la réflexion d'une onde de choc à un nombre de Mach amont Mo égal à 1,43 (voir aussi à ce sujet Fournier et al.[82]). Lee a en particulier observé que -pour le but poursuivi ici- le maximum d'efficacité était obtenu avec un débit aspiré dit "faible". Dans ce cas, l'interprétation des visualisations ombroscopiques et des distributions de pression pariétale permet de mettre en évidence les phénomènes suivants, représentés sur le schéma de la figure 55a :

1- en amont du choc, le débit aspiré est en fait quasi nul, la pression p_0 étant pratiquement égale à celle régnant dans le caisson d'aspiration, p_c . Alors, l'effet de rugosité l'emporte avec les conséquences évoquées plus haut (δ_0 et Hi_0 augmentés) ce qui entraîne une extension du domaine d'interaction et l'atténuation concomitante des gradients de pression adverses longitudinaux.

2- en aval du point d'impact du choc incident, la pression est assez élevée pour que l'aspiration soit effective. Il se produit alors une réaccélération des parties à faible vitesse de la couche limite d'où une contraction de sa portion subsonique. Il s'ensuit, par effet de déflexion dans la région où la vitesse est supersonique, un renforcement de la détente post-choc (ℓ_y) (voir § 2 ci-dessus et Fig. 4) ce qui tend à affaiblir le choc réfléchi. Donc, ainsi que le souligne Lee, ce cas est celui qui se rapproche le plus des modèles de fluide parfait où le choc est compensé par une détente locale en I engendrée par un changement de direction de la paroi.

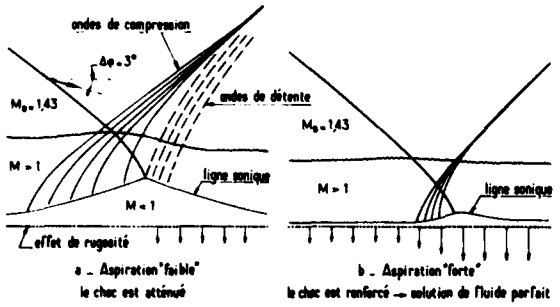


Fig. 55 - Schémas d'interaction sur paroi poreuse selon LEE [81].

En revanche, quand l'aspiration est "forte" (voir Fig. 55b), elle se fait également sentir en amont de l'impact du choc incident et, comme nous l'avons vu, il en résulte un "raidissement" de l'interaction dont l'étendue se contracte,ce qui entraîne une intensification des gradients. La réflexion ressemble alors au modèle de fluide parfait avec un choc réfléchi de force comparable à celle du choc incident. C'est-à-dire,que dans ce cas,on minimise effectivement les effets dissipatifs dans ce qu'ils ont de néfaste mais on va à l'encontre de l'objectif présent.

La réalisation de parois poreuses de qualité posant de délicats problèmes technologiques et leur utilisation ne permettant pas toujours d'aspirer le débit nécessaire pour obtenir l'effet recherché, en raison des pertes de charge importantes qu'elles créent, on leur substitue fréquemment des parois faites d'une tôle perforée. Le comportement local de l'écoulement est ici infiniment plus complexe, en particulier la

condition aux limites à imposer dans les modélisations ne consiste plus -en principe- en une distribution de vitesse v_p uniforme (pour plus de détails, voir § 4.7.1 ci-dessous). En outre, de telles parois peuvent engendrer des fluctuations acoustiques intenses perturbant l'écoulement à analyser, notamment par action sur la transition (voir les Réfs. [83, 84]). Leur fonctionnement et leur définition ont donné lieu à de nombreux travaux dont l'examen sortirait du cadre de notre sujet.

Pour conclure, il apparaît qu'une aspiration pratiquée sur une zone étendue, notamment en amont de l'onde de choc, est d'une efficacité moindre qu'une action plus locale judicieusement dosée au niveau de l'interaction elle-même. Il est en tout cas certain qu'une aspiration effectuée uniquement en amont n'aura que peu d'effet sur le phénomène si le choc est assez intense pour faire décoller franchement la couche limite. Cela ressort des conclusions relatives à l'apparition du décollement (voir § 3.3 ci-dessus) ainsi que des travaux déjà anciens de Sterrett et al.[85] .

Dans un tout autre ordre d'idée, une aspiration pariétale est parfois envisagée pour stabiliser une couche limite laminaire afin de retarder la transition, cette action pouvant être combinée avec un refroidissement de la paroi dont l'effet va dans le même sens. Il est ainsi possible de diminuer considérablement la traînée de frottement.

4.4.3 - *Contrôle de l'interaction par aspiration localisée* -

Nous allons maintenant envisager les dispositifs où l'aspiration est pratiquée dans la région d'impact de l'onde de choc en concentrant d'abord notre attention sur une description des phénomènes qui se produisent alors dans la zone d'interaction. Pour cela nous utiliserons les résultats de l'analyse expérimentale de Mathews [86] . Cette étude a été exécutée sur un montage de révolution dans lequel un choc est engendré par une pointe conique de 1/2 angle $\Delta\varphi$ montée selon l'axe d'une tuyère de révolution donnant un écoulement uniforme de nombre de Mach Mo = 1,99. L'interaction considérée a lieu à l'impact du choc sur la paroi de la tuyère. Une aspiration localisée est pratiquée au travers de trous percés normalement à la paroi dans la zone d'interaction. Les deux paramètres de l'étude sont d'une part l'intensité du choc incident qui est ajustée en changeant $\Delta\varphi$, d'autre part le débit aspiré.

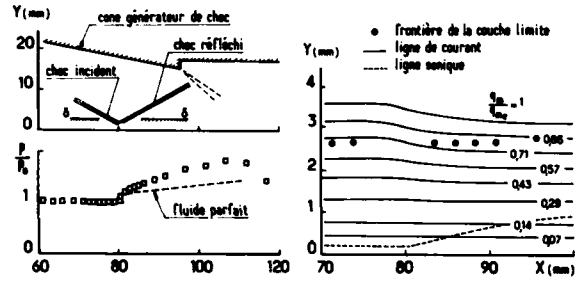


Fig. 56 - Interaction en supersonique (M_o = 1,99) $\Delta\varphi$ = 10°. Réflexion sans décollement, sans aspiration (d'après [86]).

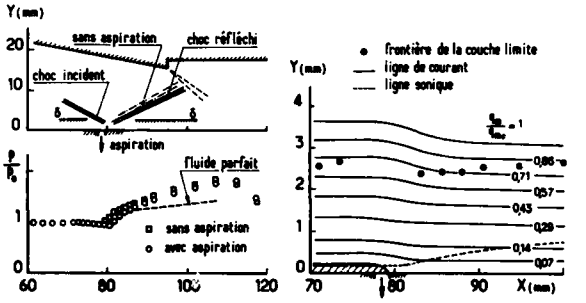


Fig. 57 - Interaction en supersonique (M_o = 1,99) $\Delta\varphi$ = 10°. Effet d'aspiration - $\frac{\dot{m}}{\dot{m}_{CLO}}$ = 0.04 (d'après [86]).

La figure 56 représente les caractéristiques essentielles de l'écoulement , déduites d'explorations à la sonde de pression, pour $\Delta\varphi$ = 10° et en l'absence d'aspiration. Dans ce cas, compte tenu de la valeur du nombre de Mach Mo , la réflexion qui s'opère sans décollement visible, entraîne une contraction des tubes de courant (en fait, comme le montre la figure 58 les épaisseurs de déplacement et de quantité de mouvement augmentent) et un élargissement rapide et important de la partie subsonique de la couche limite. L'aspiration (voir Fig. 57) restreint nettement la décélération dans les parties inférieures de la couche limite dont la portion subsonique se dilate maintenant beaucoup moins. La zone hachurée, en amont des trous d'aspiration, représente symboliquement la part d'écoulement qui est captée. En réalité, au niveau de l'orifice, il se produit une accélération de la partie la plus inférieure de la couche limite ce qui provoque localement un fort "remplissage" de son profil dont la vitesse demeure supersonique pratiquement jusqu'à la paroi.

Les résultats portés Fig. 58 montrent que corrélativement la croissance des épaisseurs de déplacement et de quantité de mouvement a été fortement freinée. En revanche, l'effet sur le coefficient de frottement pariétal est limité. Selon l'auteur, l'élimination de 2 à 4% du débit masse de la couche limite suffit pour provoquer les modifications observées, au delà de 4% le gain devient négligeable.

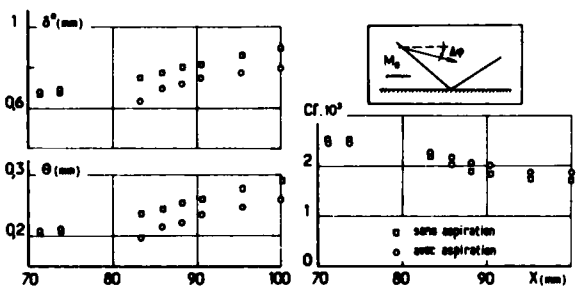


Fig. 58 - Interaction en supersonique (M_o = 1.99) $\Delta\varphi$ = 10°. Effet d'aspiration sur les caractéristiques de la couche limite (d'après [86]).

Pour $\Delta\varphi = 15°$, le choc incident possède une intensité suffisante pour faire décoller la couche limite ainsi que le prouve la structure dessinée Fig. 59 qui révèle l'existence d'un choc de décollement prenant naissance bien en amont du point d'impact théorique du choc incident. Dans ce cas, le "gonflement" de la zone subsonique est spécialement important. L'effet de l'aspiration, représenté Fig. 60, est ici encore plus spectaculaire. Au vu du système de chocs, le décollement a été supprimé et l'épaississement de la couche limite pratiquement annulé. Il en résulte une croissance nettement plus modérée de δ^* et θ, le coefficient de frottement restant maintenant toujours largement positif (voir Fig. 61). L'aspiration a complètement éliminé le fluide à basse vitesse de la partie inférieure de la couche limite qui, pour la paroi imperméable, n'était pas en mesure de franchir le saut de pression imposé par la réflexion et était de ce fait refoulé vers l'amont pour se trouver "piégé" dans un bulbe de recirculation.

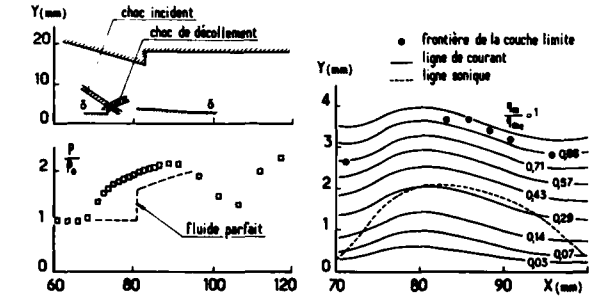


Fig. 59 - Interaction en supersonique (M_o = 1,99) $\Delta\varphi$ = 15°. Réflexion avec décollement, sans aspiration (d'après [86]).

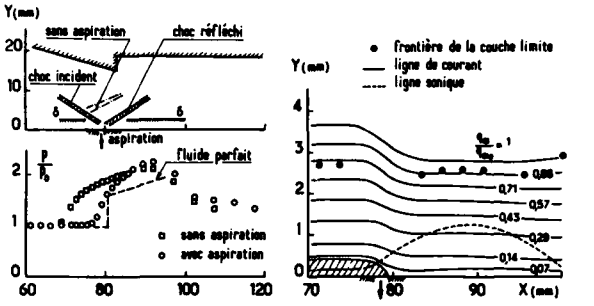


Fig. 60 - Interaction en supersonique (M_o = 1,99) $\Delta\varphi$ = 15°. Effet d'aspiration $\frac{\dot{m}}{\dot{m}_{CLO}}$ = 0,075 (d'après [86]).

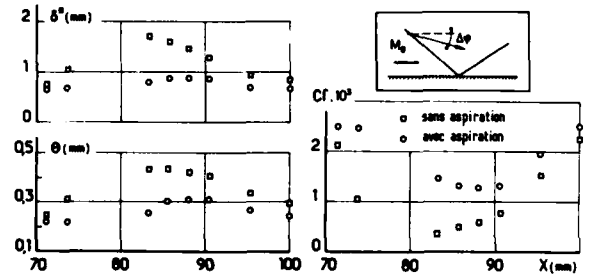


Fig. 61 - Interaction en supersonique (M_o = 1,99) $\Delta\varphi$ = 15°. Effet d'aspiration sur les caractéristiques de la couche limite $\frac{\dot{m}}{\dot{m}_{CLO}}$ = 0.075 (d'après [86]).

Une étude analogue à celle de Mathews a été effectuée par Seebaugh et Childs [87] sur un montage de conception identique et à des nombres de Mach Mo = 2,8 et 3,78. Ces auteurs sont également arrivés à la conclusion que l'élimination -au niveau de la réflexion- d'un débit représentant 2 à 4% de celui de la couche limite amont suffisait à empêcher un décollement. Ils ont aussi constaté qu'aspirer en amont de l'interaction était d'une efficacité beaucoup moindre.

Le contrôle de l'interaction par aspiration au travers de trous a donné lieu à un assez grand nombre de recherches à caractère plus pratique que celles qui viennent d'être évoquées, surtout dans les études de développement des prises d'air supersoniques. Ainsi, Cubbinson et al. [88], à partir d'essais sur une prise d'air de révolution, à compression mixte, placée dans un écoulement de nombre de Mach Mo = 2,5, ont montré toute l'importance d'un choix judicieux de la zone d'aspiration. Selon ces auteurs, le contrôle optimal, en terme d'efficacité de la prise d'air, est obtenu en aspirant immédiatement en aval de la région d'interaction.

Nous allons maintenant considérer plus en détail une étude du même genre effectuée par Fukuda et al [89, 90]. La maquette, représentée schématiquement Fig. 62, est de révolution et dans le cas présent Mo est égal à 2,5 . L'aspiration est pratiquée au travers de rangées de trous en quinconce disposées dans les régions des réflexions successives du choc issu du bord de la carène externe (voir Fig. 62). Les paramètres de l'étude étaient les suivants :

1- géométrie des trous (forme, inclinaison du perçage) ;

2- leur emplacement par rapport aux zones d'interaction ;

3- débit masse aspiré.

Des essais ont également été effectués en aspirant par une écope.

L'efficacité du contôle était caractérisée en examinant le comportement du facteur de forme "transformé" H_{tr} résultant de la transformation compressible-incompressible de la méthode bien connue de Reshotko et Tucker [43] . En fait, H_{tr} se confond pratiquement avec le paramètre de forme usuel H_i . A titre d'exemple, la figure 63 montre pour la position ② , c'est-à-dire en aval de la première réflexion (voir Fig. 62), les évolutions de H_{tr} , δ^* et θ en fonction du débit aspiré $\dot{m}$ normalisé par le débit $\dot{m}_{CLO}$ de la couche limite amont. Les résultats présentés mettent en évidence les tendances suivantes :

1- l'effet maximal, qui se traduit en particulier par la croissance minimale de H_{tr} , est obtenu ici en aspirant en aval de la réflexion. Aspirer dans la zone d'interaction elle-même apparaît comme peu efficace, ce qui est en contradiction avec les constatations de Mathews. En réalité, dans ces essais, il s'établit une recirculation par le canal de la cavité entre l'aval à haute pression et l'amont à

pression plus faible, si bien qu'au niveau du choc la couche dissipative est en fait soumise à une injection.

2- il est confirmé qu'aspirer en amont de la région d'interaction est pratiquement sans utilité, ce qui est particulièrement manifeste pour les épaisseurs de déplacement et de quantité de mouvement.

3- l'effet favorable sur H_{tr} est maximal pour un débit capté représentant 30 à 40% du débit de la couche limite.

4- ces essais ont aussi démontré que la meilleure performance est réalisée avec des trous inclinés vers l'amont.

Les mesures sont comparées à un calcul effectué au moyen de la méthode de "saut" de Seebaugh et al.[91] dont il sera question ci-dessous (voir § 4.7.3)

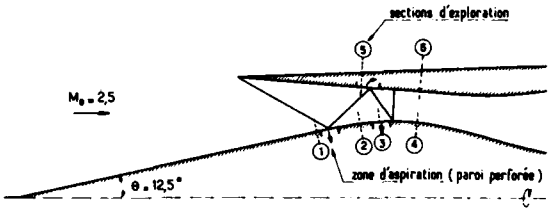


Fig. 62 - Interaction en supersonique. Contrôle par aspiration dans une prise d'air (d'après [89]).

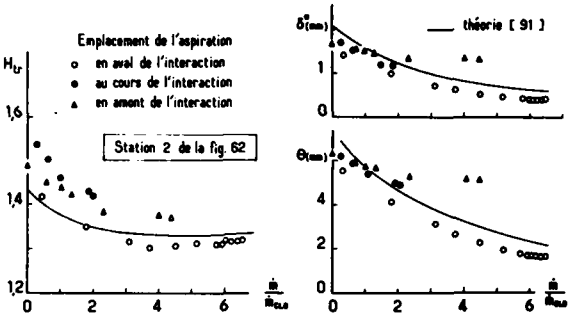


Fig. 63 - Contrôle par aspiration dans une prise d'air. Effet sur les caractéristiques de la couche limite (d'après [89]).

Mentionnons enfin une étude similaire de Wong [92] . Dans ces essais, le but visé est de contrôler l'interaction extrêmement forte se produisant au niveau du choc droit terminal d'une prise d'air à compression mixte. Le nombre de Mach en amont varie, selon les conditions de fonctionnement, entre 1,6 et 1,9. Une très bonne efficacité - avec suppression complète du décollement- est obtenue en aspirant par des portions de paroi perforée situées en amont et au niveau de l'interaction. Toutefois, le bon fonctionnement du système exige que les différentes zones d'aspiration soient en communication avec des cavités séparées de manière à éviter une recirculation du fluide capté. L'auteur propose également un critère simple permettant d'évaluer le débit masse à éliminer en amont de l'interaction.

Le contrôle par aspiration localisée de l'interaction se produisant dans une angle dièdre a été envisagé par Tanner et Gai [93] (voir aussi Gai [94]). Dans ces expériences, le fluide est aspiré par une fente de hauteur h disposée entre la paroi amont -ici rectiligne- et la rampe d'angle α (voir schéma sur la figure 64). Le nombre de Mach amont Mo est égal à 1,93 et trois valeurs de α ont été considérées (α = 8, 12 et 16°). La figure 64a montre l'évolution des distributions de pression pariétales en fonction du débit normalisé $\dot{m}/\dot{m}_{c_{LO}}$ pour le cas α = 16° et h = 2,54 mm,ce qui correspond à $h/\delta_0^* = 1,45$ ou encore $h/\delta_0 = 0,40$. On observe que l'aspiration parvient à résorber complètement le décollement qui est manifeste sur la répartition à $\dot{m} = 0$. De plus, elle provoque une élévation du niveau de pression aval qui peut être rendu pratiquement égal au saut théorique en fluide parfait, c'est-à-dire sans couche limite. La tendance observée s'explique par l'augmentation progressive en fonction de la quantité de fluide aspirée de la vitesse sur la ligne limite de l'écoulement décollé, en vertu du mécanisme décrit au § 3.4 ci-dessus. L'effet de l'aspiration sur la compression totale réalisable est donné par la figure 64b qui met en évidence que la valeur du rapport $\dot{m}/\dot{m}_{c_{LO}}$ nécessaire pour atteindre le niveau fluide parfait a une valeur bien définie pour une hauteur de fente h donnée. En fait, il existe des conditions optimales qui amènent à adopter pour h une valeur représentant environ les 4/3 de l'épaisseur de couche limite à éliminer. Pour les deux angles de rampe envisagés ici (α = 12 et 16°), le débit optimal représente respectivement 12 et 21% du débit de la couche limite amont.

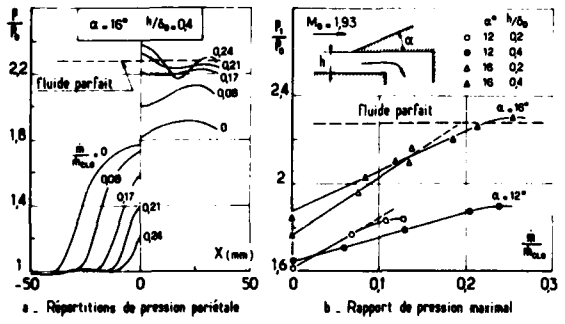


Fig. 64 - Interaction en supersonique. Contrôle par aspiration locale dans le décollement (d'après [93]).

En régime laminaire, le contrôle par aspiration est également très efficace, ainsi que le montrent les expériences de Ball et Korkegi [95] (voir aussi les travaux de Ball [96] et ceux de Rhudy [97]). Ces auteurs ont éxecuté leurs essais en écoulement bidimensionnel plan sur la couche limite se développant à la surface d'un dièdre symétrique. Le décollement est provoqué par le braquage d'un volet et l'aspiration, pratiquée par une fente placée à la charnière du volet, résulte de la dépression "naturelle" entre l'extrados du dièdre et son culot (voir le schéma de la figure 65). La figure 65a, où sont reportées les distributions de pression pariétales, montre clairement la résorption progressive de la zone

décollée au fur et à mesure que la largeur de la fente - c'est-à-dire le débit aspiré- augmente. La figure 65b donne le débit normalisé $\dot{m}/\dot{m}_{cio}$ nécessaire pour éliminer complètement un décollement se produisant à la distance ($X_c - X_0$) de la charnière du volet quand $\dot{m} = 0$. On note que le rapport $\dot{m}/\dot{m}_{cio}$ est pratiquement indépendant du nombre de Mach amont Mo

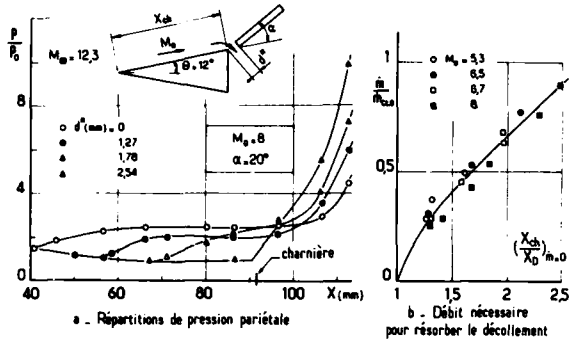


Fig. 65 - Interaction en supersonique. Régime laminaire. Contrôle par aspiration locale dans le décollement (d'après [95]).

Le contrôle d'une interaction en régime transitionnel a été examiné par Pate [98] . Dans son expérience, le décollement a lieu à une jonction cylindre-jupe tronconique et l'aspiration se fait au travers d'une série de fentes disposées juste en amont de la jupe. Les mesures ont été effectuées pour Mo = 2,5 - 3 et 3,5 et deux angles de jupe (α = 7,5 et 15°). L'auteur trouve lui aussi qu'à α fixé le débit normalisé $\dot{m}/\dot{m}_{cio}$ nécessaire pour obtenir une réduction donnée de l'étendue d'écoulement décollé est pratiquement indépendant de Mo .

Pour conclure ce paragraphe, nous dirons un mot des techniques dites de contrôle passif proposées par certains auteurs afin de diminuer la traînée des profils d'aile en transsonique [99, 100] . La méthode consiste à rendre perméable une portion de l'extrados du profil de manière à assurer une circulation naturelle de fluide entre l'aval du choc et son amont (voir schéma Fig. 66). On profite donc ici d'un effet d'injection -considéré jusqu'à présent comme néfaste- pour épaissir la couche limite amont en vue de créer des ondes de compression progressives qui affaiblissent le choc droit d'extrados. En somme, le but est d'étaler la compression ce qui a pour conséquence bien connue de minimiser l'accroissement d'entropie, d'où une traînée d'onde moindre. La situation ainsi réalisée tend à simuler un profil à compression sans choc qui s'adapterait automatiquement à des conditions de nombre de Mach et d'incidence variables sans que sa géométrie ait à être modifiée. La figure 66 montre un exemple de répartition de nombre de Mach "pariétal" qui peut être obtenue par ce moyen [99] . En outre, l'aspiration qui se fait sentir sur la partie arrière du profil limite l'amplification des effets dissipatifs dans la couche limite. Pour juger de la valeur de ce procédé, a priori prometteur, il faut bien sûr tenir compte de la traînée de frottement plus grande d'une paroi rugueuse.

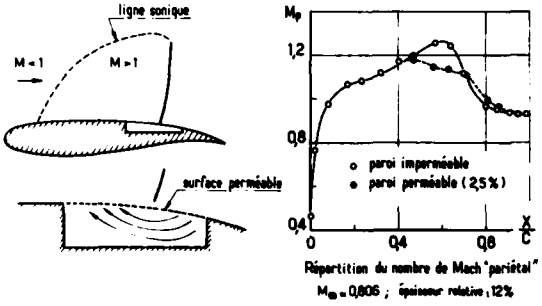


Fig. 66 - Contrôle passif sur un profil supercritique en transsonique (d'après [99]).

4.4.4 - *Optimisation des dispositifs d'aspiration* -

L'optimisation du dispositif d'aspiration est un problème particulièrement complexe que nous ne ferons qu'évoquer ici. Un tel dispositif doit satisfaire non seulement à des critères de bon fonctionnement aérodynamique mais aussi à des contraintes technologiques sévères dans le cas d'une installation sur avion.

Nous avons déjà parlé des avantages et des inconvénients de la paroi poreuse qui permet une aspiration répartie uniformément sur une grande longueur, aussi nous n'y reviendrons pas. Quand il s'agit de réaliser un contrôle local sur une surface continue, une fente disposée transversalement à l'écoulement produit l'effet maximal puisque son action intéresse la couche limite sur tout ou partie de l'envergure. Cependant, si le contrôle doit être maintenu quand le choc se déplace, il convient de mettre en place une succession de fentes parallèles réparties sur la portion de surface balayée par l'onde de choc. Alors, comme nous l'avons déjà mentionné, la meilleure performance est obtenue en reliant chaque fente à un compartiment indépendant dont la pression est ajustée en fonction de la pression p_0 locale extérieur au droit de la fente , ce qui permet en particulier d'éviter une circulation de fluide dans le sens aval-amont dont l'effet est le plus souvent considéré comme désastreux. Un autre avantage d'un dispositif à cavités multiples est de permettre la mise hors service des zones d'aspiration inutiles, par exemple quand elles sont à l'amont du choc ; d'où une économie d'énergie et un gain sur la traînée de captation. L'inconvénient majeur d'un tel agencement est son assez grande complexité technologique, ce qui le rend difficilement utilisable sur un avion.

Une variante consiste à disposer plusieurs fentes dans le sens longitudinal, ce qui assure une distribution plus continue de l'aspiration et permet de garder le contrôle de l'interaction quand le choc se déplace. En outre, on évite de cette façon les perturbations importantes que créent des fentes normales à la direction principale de l'écoulement (d'où une moindre traînée). La contrepartie est qu'il devient alors plus difficile d'empêcher une communication aval-amont.

Dans la plupart des applications sur avion, on s'est plutôt orienté vers l'emploi de parois perforées qui offrent, en quelque sorte, un compromis entre la paroi poreuse et les dispositifs à fentes. La définition d'un système de perforations assurant un fonctionnement optimal est un problème difficile, l'objectif visé étant de parvenir à l'effet voulu tout en minimisant la traînée de captation. Comme on le voit Fig. 67, cette dernière est proportionnelle au débit capté $\dot{m}$ pour une pression de cavité p_c donnée. Il s'agit donc, non seulement de minimiser C_D mais aussi de définir la configuration qui permet d'aspirer ce débit avec la pression p_c maximale. De nombreux paramètres sont impliqués dans ce problème, à savoir :

1- la position de la zone perforée,

2- la géométrie et l'espacement des trous,

3- la pression dans le (ou les) caissons(s) d'aspiration,

4- l'aménagement du dispositif d'évacuation de l'air capté,

5- la tenue aux efforts, à l'échauffement, aux vibrations.....

Nous n'entrerons pas plus avant dans cette délicate question dont la réponse est recherchée par des procédés empiriques ou semi-empiriques [101] .

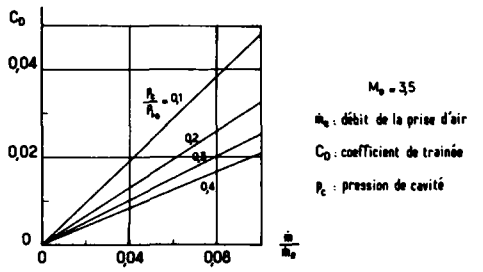


Fig. 67 - Coefficient de traînée de captation d'une paroi perforée. Exemple (d'après [101]).

4.5 - *Action par injection pariétale à faible vitesse* -

Du seul point de vue des pertes par dissipation visqueuse et des instabilités que peuvent créer des décollements étendus, une injection fluide à basse vitesse -qu'il faut distinguer d'une action par jet local à vitesse élevée- a le plus souvent une influence néfaste.

En effet, si l'injection est répartie en amont de l'interaction, elle a pour conséquence d'accroître le paramètre de forme de la couche limite (voir § 4.1.1 ci-dessus et Fig. 53) et par là augmente la sensibilité de cette dernière à l'action destabilisatrice de l'onde de choc.

Pratiqué dans une région décollée, l'apport de masse à basse vitesse entraîne une dilatation du bulbe de décollement et une élévation éventuelle de son niveau de pression en vertu du mécanisme brièvement expliqué au § 3.4. Il y aura donc épaississement des couches dissipatives même si les gradients de pression sont dans une certaine mesure atténués.

Malgré ces aspects négatifs, l'injection pariétale est parfois envisagée pour diminuer la traînée de frottement [56] (voir § 4.4.1 ci-dessus son influence sur le coefficient de frottement C_f) ou bien, comme nous l'avons vu § 4.4.3 à propos du contrôle passif, pour étaler une compression. Toutefois, en écoulement supersonique, elle trouve sa principale application dans la réduction des flux thermiques pariétaux, tels ceux très intenses rencontrés à l'impact d'une onde de choc en hypersonique [45, 102] .

Dans cette optique, Alzner et Zakkay [103] ont étudié expérimentalement l'effet d'une injection d'air puis d'hydrogène sur une interaction avec décollement résultant d'une réflexion de choc à Mo = 6 et à un nombre de Reynolds suffisamment élevé pour garantir un régime naturellement turbulent. L'injection du fluide était pratiquée par une fente débouchant tangentiellement à la paroi dans la zone décollée. Les distributions de pression pariétales sont reportées Figs. 68a et 68b. Elles montrent les tendances suivantes :

1- dans le cas où le fluide injecté est de l'air et lorsque le taux $\lambda = \rho_j u_j / \rho_0 u_0$ est faible (l'indice j désigne les grandeurs relatives au jet pariétal), on observe une croissance d'abord rapide du niveau de pression dans le décollement. Puis il y a renversement de l'évolution, la pression dans la zone décollée diminuant quand λ augmente en même temps que la compression au recollement s'amplifie. Un tel comportement a été qualitativement expliqué au paragraphe 3.4 : on a alors atteint une situation où la quantité de mouvement apporté par le fluide injecté l'emporte sur l'effet d'addition de masse. Le mode d'action s'apparente dans ce cas au contrôle par jet local envisagé ci-dessous.

2- la remontée du décollement vers l'amont observée à λ élevé est dûe à l'effet d'obstacle du jet de gaz.

3- à égalité de taux d'injection, l'augmentation de la pression dans le décollement est beaucoup plus importante avec l'hydrogène. Il est en fait bien connu que la sensibilité d'un bulbe décollé à l'apport de masse est d'autant plus grande que le gaz injecté a une densité plus basse, soit en raison de sa masse moléculaire faible, soit de sa température élevée [52] .

Les répartitions de flux de chaleur $\dot{q}$, normalisé par la valeur $\dot{q}_r$ en l'absence de choc et d'injection, sont représentées Fig. 69a et 69b. L'apport de fluide a pour conséquence de diminuer fortement les niveaux de flux, l'hydrogène se montrant beaucoup plus efficace, comme on pouvait s'y attendre. Dans les présents essais, il y a même un changement de signe de $\dot{q}$ immédiatement en aval de la fente, par suite de la détente que le jet subit à sa sortie.

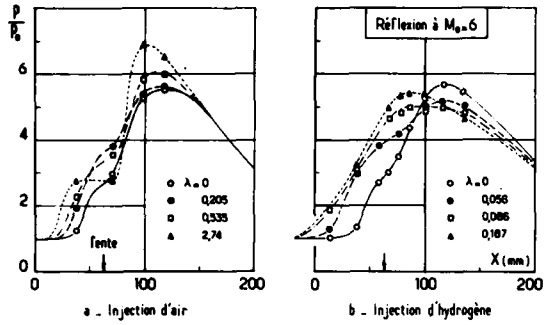


Fig. 68 - Contrôle par injection locale dans la zone décollée. Répartitions de pression pariétale (d'après [103]).

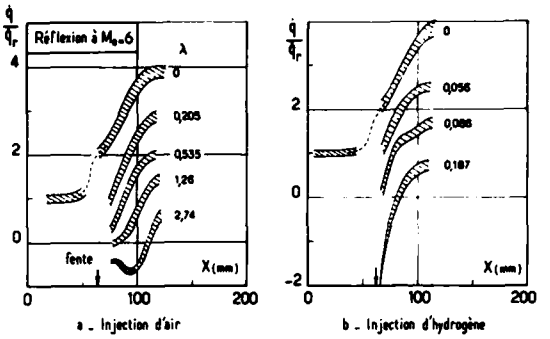


Fig. 69 - Contrôle par injection locale dans la zone décollée. Répartitions de flux de chaleur (d'après [103]).

Le comportement qui vient d'être décrit montre donc qu'il doit être possible d'agir par injection sur un décollement pour en limiter l'étendue, voire le supprimer complètement, à condition de bien doser l'injection qui devra être pratiquée dans la zone décollée elle-même.

En effet, ainsi que nous venons de le rappeler, au-delà d'une certaine valeur du débit $\dot{m}$, le fluide injecté apporte suffisamment de quantité de mouvement à l'écoulement pour lui permettre de négocier une compression plus importante au recollement par accroissement de la vitesse u_s sur la ligne de courant séparatrice (5) (voir § 3.4 plus haut). L'action est bien sûr favorisée si la vitesse u_j est sensiblement orientée dans la même direction que u_s , c'est-à-dire de manière que la composante longitudinale de la quantité de mouvement $\dot{m}\, u_j$ soit maximale, ce qui amène à pratiquer l'injection par une fente faisant face à l'aval et débouchant tangentiellement à la paroi. Dans ces conditions, le procédé peut se révéler extrêmement efficace comme le montrent les expériences de Viswanath et al. [104] . Ces auteurs ont étudié le décollement dans un dièdre d'angle α = 20° placé dans un écoulement bidimensionnel de nombre de Mach Mo = 2,5. Ils ont envisagé deux positions de la fente qui se trouvait à une distance L_j/δ_0 = 0,77 puis L_j/δ_0 = 1,54 en amont de l'origine de la rampe. La figure 70 donne l'évolution des répartitions de la pression pariétale en fonction de la pression génératrice p_{tj} du fluide injecté pour L_j/δ_0 = 1,54. Quand p_{tj} augmente, on observe la diminution progressive de la taille du bulbe décollé, jusqu'à la disparition complète de ce dernier. La figure 71 montre la variation avec le rapport p_{tj}/p_0 de la distance de recollement définie sur le schéma en encart. Elle présente également une comparaison des résultats de Viswanath et al. avec ceux d'autres auteurs ayant utilisé une injection par fente située bien en amont du décollement éventuel. Dans ce dernier procédé, qui va être examiné au paragraphe suivant, l'énergie est communiquée, non pas au fluide décollé, mais à la couche limite amont avant qu'elle n'aborde la région d'interaction. Dans le cas présent, cette deuxième façon de faire est beaucoup moins efficace que la première.

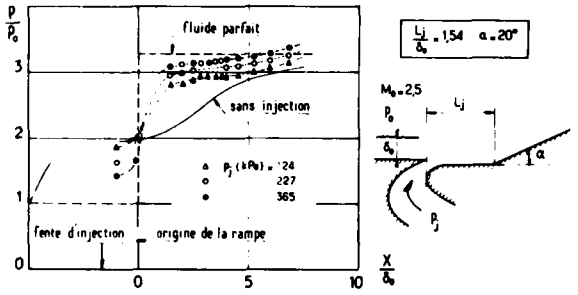


Fig. 70 - Contrôle par injection dans le décollement. Répartitions de pression pariétale (d'après [104]).

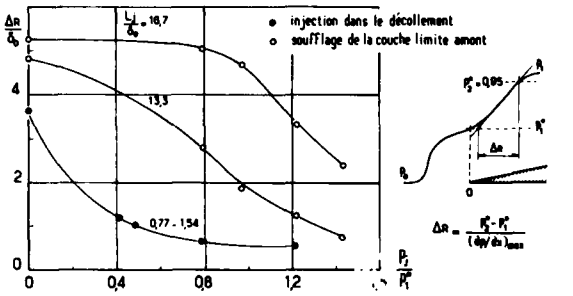


Fig. 71 - Contrôle par injection dans le décollement. Effet sur la longueur de "recollement" ΔR (d'après [104]).

4.6 - *Contrôle par soufflage amont* -

L'aspiration au niveau de l'onde de choc est probablement le moyen de contrôle le plus économique quant au débit à mettre en oeuvre. Néanmoins, extraire du fluide dont la pression est souvent basse puis ensuite l'évacuer n'est pas toujours chose aisée. Pour cela, il faut en effet aménager un ou plusieurs caissons dont l'encombrement peut être inacceptable, comme dans une prise d'air par exemple. En outre, ce procédé, ainsi que celui consistant à injecter de l'air à basse vitesse, perdent toute efficacité si l'onde de choc se déplace ce qui est souvent le cas dans la pratique.

On a donc été amené à envisager un contrôle par soufflage de la couche limite en amont de la région où le choc est susceptible de se placer. Le principe de l'action consiste ici à apporter de l'énergie mécanique à l'écoulement de façon à lui permettre de franchir avec un minimum de dommage le gradient de pression adverse. Il s'agit en fait d'un procédé classique largement employé en subsonique pour prévenir le décollement dans les diffusseurs ou sur les volets de dispositifs hypersustentateurs. Il a donné lieu à de très nombreuses études que nous n'évoquerons pas ici.

Le fonctionnement du soufflage en écoulement supersonique a été plus spécialement analysé par Peake [105] à partir d'expériences à Mo = 1,8 et dans une situation de réflexion d'un choc oblique. Il est démontré que l'efficacité de cette méthode dépend de plusieurs facteurs dont les plus déterminants sont la quantité de mouvement i_j du fluide injecté et la distance L_j séparant la tuyère (ou fente) de soufflage du pied du choc, c'est-à-dire du gradient de pression antagoniste.

A valeur de L_j fixée, la distance L_j la plus appropriée résulte d'un compromis entre deux évolutions qui sont représentées schématiquement Fig. 72. A savoir :

1- d'une part il faut que L_j soit suffisante pour que le processus de mélange (ou d'entraînement) qui assure le transfert d'énergie du jet soufflé vers la couche limite ait eu le temps de faire pleinement son effet en assurant un bon "remplissage" de la distribution de vitesse initialement dégradée. Faute de quoi, le gradient adverse va refouler l'écoulement insuffisamment accéléré. Il y a alors formation d'une poche "décollée" au sein du fluide dans la région où la vitesse (donc aussi la pression génératrice, si les deux écoulements sont à la même température génératrice) passe par un minimum. Ce phénomène appelé par Peake "wake flow reversal", est en fait un éclatement du sillage sous l'effet du choc. Il s'accompagne en général d'un accroissement spectaculaire du niveau des fluctuations turbulentes qui peut être la cause d'instabilités et de pertes d'efficacité si le dispositif est utilisé dans une prise d'air.

2- d'autre part, la nouvelle couche limite se développant entre le jet et la paroi a une épaisseur δ_j qui croît avec L_j . Il peut donc arriver, si la distance L_j est trop longue, que δ_j atteigne une valeur telle que le gradient (dont l'effet est proportionnel à δ_j) fasse décoller cette couche limite (c'est le "boundary layer flow reversal" de Peake). De plus, la vitesse maximale du jet diminue quand L_j augmente, ce qui tend bien sûr à aggraver le processus.

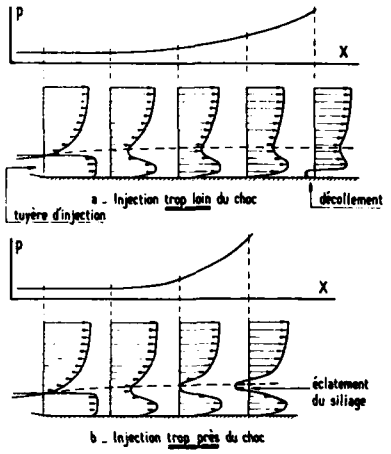


Fig. 72 - Représentation schématique de l'effet de soufflage de la couche limite (d'après [105]).

L'éclatement du sillage est évité si la pression totale dans la zone de mélange reste constamment supérieure à la pression statique locale ; ce qui constitue un critère permettant d'évaluer la distance minimale requise à partir des propriétés de la couche de mélange qui peuvent être déterminées avec une bonne précision en utilisant des modèles classiques. On peut également estimer l'évolution de l'épaisseur δ_j puis, en appliquant un critère de décollement (voir § 3.3 ci-dessus), définir la valeur de L_j à ne pas dépasser. Ainsi, dans ses expériences, Peake trouve que $L_j \sim 6\,\delta_j$ conduit à la meilleure efficacité.

La quantité de mouvement apportée est le plus souvent caractérisée par le coefficient :

$$C_\mu = \frac{\dot{m}\,(u_j - u_{e_0})}{\rho_{e_0}\,u_{e_0}^2\,\theta_0\,b} \qquad (\ b = \text{envergure})$$

qui représente le rapport entre l'excés de quantité de mouvement du fluide injecté (relativement à l'état de vitesse local u_{e_0} dans l'écoulement amont) et le déficit de quantité de mouvement dans la couche limite initiale. Ce coefficient a été utilisé pour la première fois par Kelly [106] pour corréler des résultats de soufflage sur profils. Toujours dans le cas des expériences de Peake, une valeur de C_μ proche de un donne la meilleure performance.

L'utilisation d'un jet pariétal pour contrôler une interaction choc-couche limite en transsonique a été étudiée par Wong et Hall [107] (voir aussi Wong [108]). Ces auteurs ont effectué leurs expériences sur un montage simulant une prise d'air où le nombre de Mach Mo en amont du choc droit terminal est de 1,8. L'air est ici injecté au travers d'une série d'orifices percés dans une petite marche de manière à favoriser le mélange avec l'écoulement externe. La figure 73a montre l'évolution des répartitions de la pression pariétale quand C_μ varie et la figure 73b la variation de l'efficacité de la prise d'air en fonction de son coefficient de débit pour les mêmes valeurs de C_μ . Le décollement étendu observé à $C_\mu = 0$. disparaît dès que $C_\mu \simeq 0{,}9$ et, à partir de $C_\mu = 1{,}5$, la performance rejoint pratiquement le niveau idéal à 1% près. Quand le débit capté diminue, le choc droit se déplace en direction de l'amont si bien qu'il finit par se placer devant le dispositif d'injection. Comme le fait voir la figure 73b, il se produit alors une chute de l'efficacité prouvant qu'un soufflage en aval de l'interaction est d'un faible secours.

Dans le cas présent, il a été observé que ce dispositif de contrôle devenait inopérant pour Mo = 2 [109]. En effet, à ce nombre de Mach, le débit requis est tel que -pour des dimensions de trous inchangées- la pression d'injection p_j devient si élevée que les jets éclatent fortement produisant ainsi un effet d'obstacle faisant lui-même décoller l'écoulement. Il y a donc là un aspect négatif dont il conviendra de se méfier. De fait, en modifiant convenablement le système d'injection, Schwendemann et Sanders [110] sont parvenus à maitriser des interactions jusqu'à Mo = 1,96. Ils ont également mis en évidence qu'employer -à débit $\dot{m}$ égal- de l'air chaud n'apportait pas de gain appréciable contrairement à ce que l'on était en droit d'attendre puisque C_μ se trouve ainsi fortement augmenté (de plus de 350% pour un rapport de températures égal à 2). D'où la conclusion des auteurs selon laquelle seul le coefficient défini à partir de la quantité de mouvement injectée $I_j \simeq \dot{m}\,u_j$ est vraiment significatif.

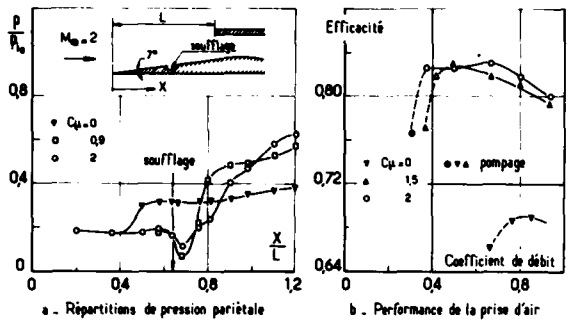


Fig. 73 - Contrôle par soufflage de couche limite dans une prise d'air (d'après [107]).

4.7 - Autres procédés de contrôle -

Il a été également suggéré d'augmenter l'énergie mécanique de la couche limite qui va franchir le choc en mettant en oeuvre des générateurs de tourbillons ("vortex generators"). Il s'agit en fait d'un procédé classique couramment utilisé sur les ailes d'avion en subsonique pour retarder l'apparition des décollements. Il consiste à disposer, en un endroit judicieusement choisi sur le profil, une rangée de petites ailettes en incidence émergeant de la paroi (voir schéma a de la figure 74). Ces ailettes créent une série de tourbillons sensiblement parallèles entre eux qui opèrent un transfert de quantité de mouvement depuis l'écoulement "sain" vers la partie basse de la couche limite. L'emploi de générateurs de tourbillonspour contrôler une interaction choc-couche limite sur un profil transsonique a été envisagé dès 1950 par Donaldson [111] . Ultérieurement, Pearcey [112] s'est livré à un examen plus approfondi de cette technique en cherchant, en particulier, à optimiser la forme des ailettes de manière à maintenir une bonne efficacité dans des conditions de fonctionnement variées. Il a également considéré la possibilité de création de tourbillons au moyen d'une série de jets émis par des orifices inclinés (voir schéma b de la figure 74). L'avantage du procédé serait de produire une augmentation de traînée moindre que les ailettes, le système pouvant en outre être facilement mis hors service quand le contrôle n'est pas utile. Toujours selon Pearcey les générateurs à jets nécessiteraient des débits d'air moins importants que le soufflage de la couche limite. La figure 75, empruntée à Pearcey, montre au moyen de visualisations strioscopiques une comparaison entre divers types de contrôle.

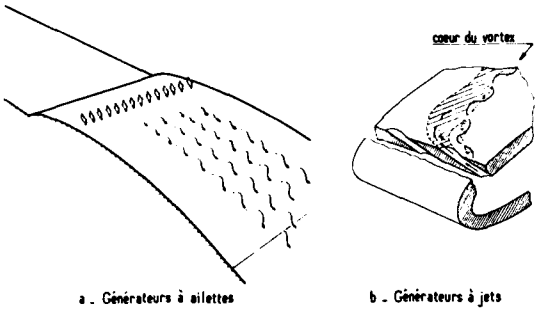


Fig. 74 - Contrôle par générateurs de tourbillons.

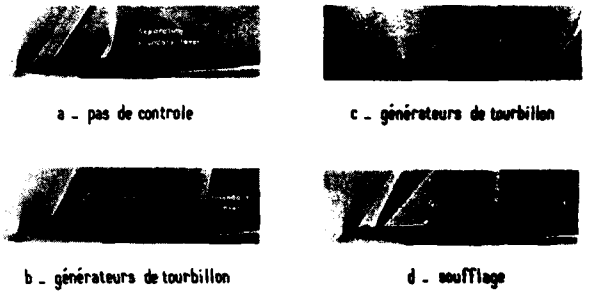


Fig. 75 - Comparaisons des effets de contrôle par générateurs de tourbillons et soufflage de couche limite (d'après [112]).

Une manière extrêmement efficace d'éviter le décollement au niveau du choc droit terminal d'une prise d'air supersonique consiste à éliminer tout ou partie de la couche limite à l'aide d'un piège placé à l'endroit convenable. On peut ainsi améliorer considérablement l'efficacité de l'écoulement principal, le piège ayant en outre pour fonction de stabiliser le choc et d'autoriser une éventuelle variation du débit du compresseur sans pour autant désamorcer la prise d'air. De plus, le débit à éliminer peut être extrait avec un minimum de pénalité en profitant de l'effet d'entraînement du (ou des) jet(s) propulsif(s) par l'aménagement judicieux d'une (ou de) tuyère(s) multi-flux.

Les prises d'air avec piège à couche limite ont donné lieu à de nombreuses études de mise au point lors du développement du projet Concorde. Le fonctionnement aérodynamique d'un tel dispositif est très complexe, nous n'en donnerons ici qu'une description succinte empruntée à une analyse détaillée faite par Leynaert [113] . La figure 76a représente schématiquement l'organisation de l'écoulement dans la zone de captation. On observe que le choc "terminal" (C_0) est en fait un choc oblique incurvé vers le diffuseur à l'approche du piège dans lequel règne une pression de cavité p_c . Suivant les cas, p_c est supérieure ou inférieure à la pression p_0 de l'écoulement amont, ce qui provoque soit une compression soit une détente à l'origine D du piège. Le schéma de la figure 76 correspond à une situation où p_c est égale à p_0 . Le choc (C_0) rencontrant la frontière isobare de l'eau-morte à la pression p_c , une détente se forme à son point d'impact avec déviation de l'écoulement principal qui le long de la frontière conserve la pression p_c , donc sensiblement le même nombre de Mach qu'en amont de (C_0), la perte de pression génératrice à travers de (C_0) étant peu importante. Un choc droit (C_1) met fin à la poche supersonique située en aval de (C_0). L'intensité de ce choc s'atténue progressivement quand on s'écarte de la zone de mélange entre l'écoulement principal et l'eau-morte et s'évanouit sur la ligne sonique. En aval du pied de(C_1), la frontière de l'écoulement subsonique prend une courbure très brusque pour compenser par effet centrifuge le gradient de pression entre l'eau-morte et l'écoulement contigu recomprimé par choc. Le débit aspiré est concentré dans sa quasi-totalité en un jet attaché au bord aval du piège. Il se produit localement un recollement analogue à celui brièvement décrit § 3.4 (voir aussi Fig. 36), c'est-à-dire que seules les particules fluides situées au dessus de la ligne limite ont une énergie suffisante pour s'écouler normalement vers le diffuseur. Les particules plus lentes sont refoulées dans la cavité où elles se détendent pour former un jet étroit pouvant atteidre localement des vitesses supersoniques comme le représente la figure 76b (se reporter à la Réf. [113] pour une description plus complète de ces phénomènes).

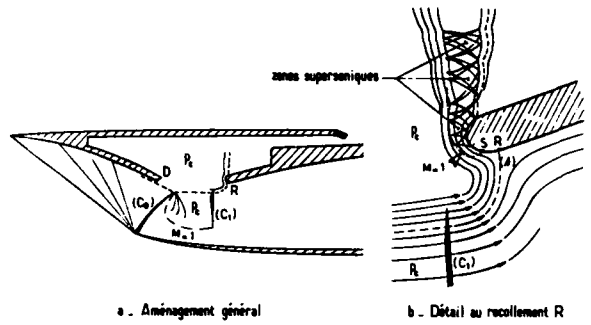


Fig. 76 - Contrôle de l'interaction par piège à couche limite (d'après [113]).

Une étude plus fondamentale du fonctionnement des prises d'air avec piège à couche limite a été effectuée par Meauzé [114] . Cet auteur a exécuté des expériences très détaillées sur un montage de principe et proposé surtout une méthode de calcul simple à caractère global permettant de prédire avec une bonne précision les performances du système.

4. 8 - Modélisations proposées pour une interaction onde de choc-couche limite avec transfert de masse -

4. 8. 1 - Généralités -

Pour s'en tenir au cas d'un écoulement stationnaire, bi- dimensionnel, plan ou de révolution, une des principales difficultés rencontrées par la modélisation réside dans la forme de la conditon aux limites à appliquer à la paroi dans la zone où le transfert de masse est opéré. Dans la plupart des méthodes proposées, cette condition est exprimée en écrivant que la composante de vitesse normale v_p et la masse spécifique ρ_p sont imposées égales à des fonctions de l'abscisse x données. Or, dans la pratique, seule la pression p_c (et éventuellement aussi la température T_c) régnant dans la cavité d'aspiration est commodément accessible si bien que v_p (et ρ_p) doit être déduite de p_c par des relations souvent très approximatives. La difficulté se trouve évidemment considérablement accrue si l'aspiration est pratiquée au travers d'orifices ou de fentes, l'écoulement prenant alors localement une structure tridimensionnelle extrêmement complexe qui devra être fortement schématisée, compte tenu des possibilités actuelles des codes de calcul même les plus performants.

La paroi poreuse réalise assez fidèlement le cas d'une répartition continue de transfert de masse et, pour cette raison, se prête plus aisément à des calculs basés sur des modèles bi-dimensionnels. Toutefois, malgré cette relative simplicité, une première difficulté de taille est rencontrée dans l'évaluation de v_p à partir de la différence de pression ($p_c - p_e$) de part et d'autre de la plaque. Dans ce but, on ne dispose jusqu'à présent que de relations très empiriques fondées sur la loi de Darcy en vertu de laquelle :

$$v_p(x) = k\,(p_c - p_e)/e$$

où le coefficient k dépend, entre autres, de la perméabilité -pas toujours bien connue- du matériau dont la paroi d'épaisseur e est faite.

De plus, dans le cas turbulent -qui est le plus fréquent- il faut tenir compte de l'effet de transfert de masse et aussi de l'influence de la rugosité sur le modèle de turbulence employé, que celui-ci soit du type algébrique ou à équations de transport [69, 115 - 117] . L'examen de ce point -essentiel pour la qualité de la prédiction- nous entraînerait trop loin ; le lecteur intéressé trouvera dans la thèse de Lee [81] , déjà citée, une discussion approfondie de ce problème avec de nombreuses références.

Dans le cas d'une paroi à trous, les informations permettant d'estimer une répartition de v_p réaliste sont encore extrêmement rares. Ce n'est que tout récemment que des renseignements très instructifs ont été publiés par Hingst et Tanji [118] . Ces deux auteurs ont procédé à des mesures du débit traversant les orifices d'une paroi au moyen d'un fil chaud, l'interaction envisagée résultant d'une réflexion de choc à Mo = 2 et 2,5. Les figures 77a et 77b montrent les distributions du débit local $\dot{m}_x$ normalisé par le débit total aspiré pour deux valeurs de l'intensité du choc incident à Mo = 2,5. Comme on pouvait s'y attendre, $\dot{m}_x$ est évidemment plus élevé dans les zones à haute pression ; par ailleurs un accroissement de la force du choc entraîne une augmentation de la pression de cavité p_c d'où une diminution de $\dot{m}_x$ en amont du choc. Pour des sauts de pression encore plus grands, il peut se faire que p_c dépasse p_e d'où un effet d'injection dont les conséquences négatives peuvent annuler le bénéfice de l'aspiration -sauf dans le cas du contrôle passif (voir § 4.4.2 ci-dessus). Il a également été noté, qu'à une abscisse donnée, le débit capté dépendait uniquement des conditons locales régnant dans l'écoulement extérieur et non des valeurs de $\dot{m}_x$ en amont de la station considérée. Cette observation peut aider à la conception de modèles théoriques.

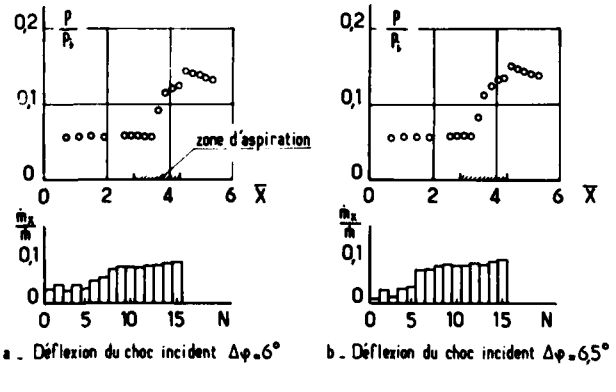


Fig. 77 - Répartitions de débit dans une paroi perforée. Réflexion de choc à M_0 = 2,5 (d'après [118]).

4.8.2 - *Calculs par méthode de couplage et résolution des équations de Navier-Stokes* -

A notre connaissance, les calculs d'interaction avec transfert de masse ont été surtout effectués en laminaire pour des raisons évidentes de simplicité. Par exemple, Don Gray et Mauss [119] ont considéré le cas d'une rampe en écoulement bi-dimensionnel plan et ont utilisé une technique de couplage fluide parfait-fluide visqueux directement inspirée de la théorie bien connue de Lees et Reeves [120]. Rappelons que dans cette méthode, la couche limite est calculée par une méthode intégrale avec des relations de fermeture déduites de solutions de similitude. La compatibilité directionnelle entre le fluide externe irrotationnel et la couche dissipative (équation de couplage) est exprimée à la frontière δ, l'écoulement extérieur obéissant à une relation d'ondes simples. Dans leur version, Don Gray et Mauss utilisent les profils semblables solutions de l'équation de Falkner-Skan dans le cas d'une paroi imperméable en se fondant sur le fait qu'un transfert de masse est assimilable à un effet de gradient de pression, comme l'a montré Stock [121]. C'est-à-dire qu'une couche limite de plaque plane avec injection a la même distribution de vitesse qu'une couche limite accélérée sur paroi imperméable. Nous avons déjà évoqué cette similitude dans le paragraphe 4.4.1 où il s'agissait du cas turbulent. Les interactions modélisées Don Gray et Mauss correspondent à une aspiration pratiquée par une fente située près de l'origine de la rampe. Les résultats qu'ils obtiennent sont en assez bon accord avec les expériences de Ball [96] et celles de Rhudy [97], comme le montre la figure 78.

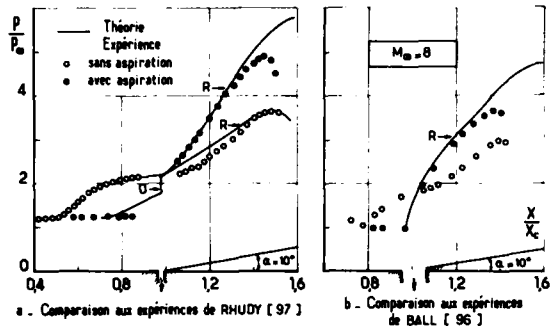


Fig. 78 - Calculs par couplage visqueux-non visqueux de Don Gray et Mauss [119]. Aspiration par fente en laminaire.

Des calculs laminaires ont aussi été exécutés en résolvant les équations de Navier-Stokes par voie numérique. Ainsi, Hanin et al. [122] ont considéré le cas d'une réflexion de choc avec aspiration uniforme sur une portion de paroi d'étendue limitée. Les équations sont résolues par une technique de marche dans le temps utilisant le schéma classique de Mc Cormack. Les auteurs ont de cette façon pu procéder à une étude systématique de l'influence des principaux paramètres : nombre de Mach amont Mo, intensité du choc incident, emplacement et étendue de la zone d'aspiration, valeur de la vitesse d'aspiration. Les figures 79a et 79b montrent, à titre d'exemple, la variation de la longueur de la zone décollée en fonction de ces divers facteurs. On y retrouve les tendances mises en évidence par l'expérience, notamment le calcul confirme que l'efficacité maximale est réalisée en aspirant dans la région où le bulbe de décollement se formerait si la paroi était imperméable, toutes choses restant égales par ailleurs.

La résolution des équations de Navier-Stokes laminaires appliquées au même problème a également été effectuée par Tassa et Sankar [123]. Les figures 80a et 80b donnent les répartitions du frottement et de l'épaisseur de déplacement calculées par eux dans une réflexion à Mo = 2. On voit qu'une aspiration très modérée parvient à supprimer complètement le décollement et prévient l'épaississement de la couche limite.

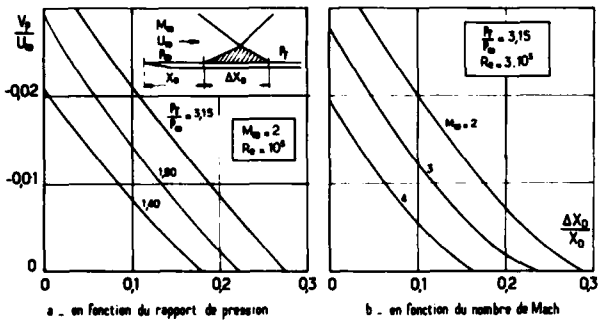


Fig. 79 - Calculs Navier-Stokes de Hanin et Al. en laminaire [122]. Evolution de la longueur du décollement.

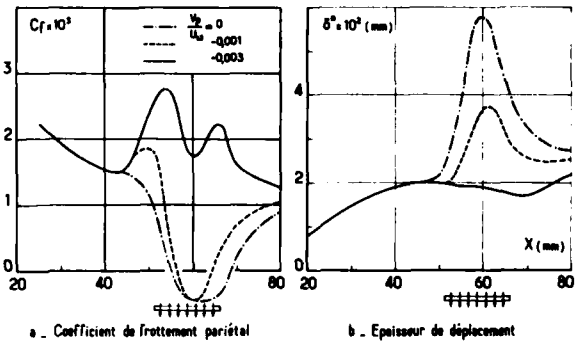


Fig. 80 - Calculs Navier-Stokes de Tassa et Sankar en laminaire [123]. Réflexion de choc pour $M_0 = 2$. $\Delta\psi = 32{,}59°$.

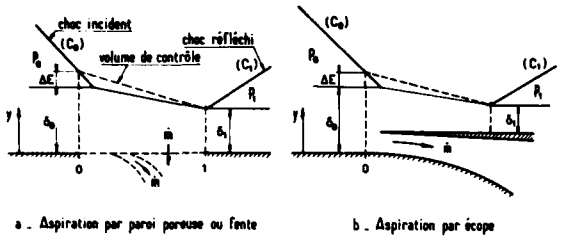
Nous n'avons pas connaissance de calculs analogues pour le cas turbulent. Il convient néanmoins de citer le travail de Lee [81] qui a excécuté des calculs de couche limite "classiques" à partir de distributions de pression mesurées dans une réflexion de choc sur paroi poreuse. Les résultats qu'il a ainsi obtenus fournissent des renseignements précieux sur les problèmes posés par la modélisation de la turbulence dans ces circonstances.

4.8.3 - *Méthodes à caractère global* -

Le principe de base des méthodes globales consiste en l'écriture d'équations de bilan pour le fluide traversant un volume de contrôle entourant l'interaction et qui est limité, en règle générale, par la paroi, une section d'entrée ⓪, une frontière extérieure et une section de sortie ① placée en aval

là où la pression est redevenue uniforme. Sachant que l'objectif est ici de déterminer les caractéristiques globales de la couche limite pour un rapport de pression p_1/p_0 donné entre ⓪ et ① et un débit injecté (aspiré) fixé, en écoulement adiabatique le problème possède trois inconnues qui sont le plus souvent les épaisseurs δ_1 , δ_1^* et θ_1^* en ① . Les bilans de masse et de quantité de mouvement fournissent deux équations, une relation supplémentaire est obtenue en supposant que les distributions de vitesse normalisées $u/u_e = f(y/\delta)$ appartiennent à une famille à un seul paramètre de forme.

Il existe un assez grand nombre de méthodes de ce genre pour l'interaction onde de choc-couche limite aussi bien supersonique que transsonique. Parmi les méthodes prenant en considération un transfert de masse, nous citerons celle de Seebaugh et al. [91] qui traite la réflexion en supersonique et celle de Baker [124] qui s'applique au choc quasi-normal en transsonique.



a . Aspiration par paroi poreuse ou fente b . Aspiration par écope

Fig. 81 - Volume de contrôle pour la méthode globale de Seebaugh et Al. [91].

Le volume de contrôle considéré par le modèle de Seebaugh et al. est dessiné Fig. 81. L'écart ΔE entre la limite (E) extérieure et la frontière δ_0 en ⓪ est introduit pour tenir compte de l'entraînement au détriment du fluide externe. Les équations de bilan sont écrites sous la forme suivante (cas bi-dimensionnel plan) :

1- pour la masse :

$$\int_0^{\delta_1} \rho u \, dy = \int_0^{\delta_0} \rho u \, dy + \dot{m}$$

2- pour la quantité de mouvement :

$$\int_0^{\delta_1} \rho u^2 dy = \int_0^{\delta_0} \rho u^2 dy + p_0 (\delta_0 + \Delta E) - p_1 \delta_1 - \int_{\delta_0 + \Delta E}^{\delta_1} p \, dy - L \bar{\tau}_w + i_x$$

$\bar{\tau}_w$ est le frottement moyen entre ⓪ et ① et i_x la composante de quantité de mouvement selon x du gaz injecté. Les pressions sont fournies par le calcul de fluide parfait et ΔE déterminé en exprimant que le taux d'entraînement le long de (E) est le même qu'en amont de l'interaction.

Dans le cas d'une paroi poreuse ou à trous, on admet que l'aspiration (l'injection) se fait normalement, donc $i_x = 0$. Pour une fente, telle que celle dessinée Fig. 81, i_x est supposée égale à la quantité de mouvement du fluide extrait au moment où il entre dans le volume de contrôle. A l'origine, Seebaugh et al. utilisaient des profils de vitesse u/u_e en puissance. Une première amélioration a été apportée par Mathews [86] qui a introduit une représentation plus réaliste s'inspirant de la loi composite de Coles[19]. Enfin, la méhode a été perfectionnée par Sun et Childs [125] qui ont en outre traité le cas de réflexions successives. Le modèle de Baker est très proche de celui qui vient d'être décrit, aussi nous n'en dirons pas d'avantage à son sujet.

Des méthodes approchées ont également été proposées pour traiter le cas de l'aspiration par fente à la paroi. Ainsi, Pearson [126] donne un procédé prédisant le débit de couche limite à extraire pour prévenir le décollement sous l'effet du choc (voir aussi Kutschenreuter et al. [127]). En bref, ces modèles reposent soit sur l'emploi d'une forme simplifiée de l'équation intégrale de Von Kàrmàn où le frottement pariétal est négligé, soit sur des considérations relatives à la capacité du fluide, près de la paroi, à franchir le saut de pression sans être refoulé ; ce qui met en cause sa quantité de mouvement ainsi que l'effet d'entraînement.

5 - CONCLUSION -

La plupart du temps, l'interaction entre une onde de choc et une couche limite a des conséquences très préjudiciables sur les performances des dispositifs aérodynamiques (profils transsoniques, prises d'air, turbomachines, etc...). Il en résulte toujours un accroissement des pertes par dissipation visqueuse, parfois catastrophiques quand le choc est assez intense pour faire décoller la couche limite. En outre, l'augmentation spectaculaire du niveau des fluctuations turbulentes qui se produit alors est souvent à l'origine de fortes instabilités.

L'interaction choc-couche limite est un phénomène particulièrement complexe dont le mécanisme n'est pas encore entièrement élucidé. En régime turbulent, il échappe pour l'instant à une prévision quantitative réellement satisfaisante, malgré les progrès considérables accomplis par les méthodes de calcul.

Il est néanmoins possible, à partir de l'analyse des nombreux résultats expérimentaux maintenant disponibles et en s'appuyant sur des considérations rationnelles, de dégager des propriétés et des tendances générales pour les distances d'interaction amont, la destabilisation subie par la couche limite et les conditions d'apparition du décollement en pied de choc. Un tel examen préliminaire, limité ici au cas turbulent, permet de mieux comprendre le mode de fonctionnement des moyens employés pour contrôler l'interaction afin d'en prévenir les conséquences néfastes.

Le principe de base de ces techniques est d'accroître l'énergie mécanique de la zone dissipative de manière à lui permettre de franchir le choc en subissant la dégradation minimale et en lui évitant surtout de décoller.

Les procédés utilisés peuvent être classés en deux catégories :

1- ceux agissant en amont de l'interaction par "manipulation" de la couche limite avant qu'elle n'aborde le choc. Il s'agit ici de remplir son profil de vitesse afin d'augmenter sa "raideur". Ce résultat peut être obtenu par refroidissement de la paroi, effet de courbure, aspiration pariétale répartie, apport de quantité de mouvement par soufflage ou activation des échanges turbulents au moyen de "générateurs de tourbillons",... De telles techniques ont en général une efficacité faible mais elles permettent de conserver le contrôle lorsque l'onde de choc se déplace.

2- ceux qui sont appliqués au niveau et/ou immédiatement en aval de l'interaction. Là, on peut agir soit en éliminant par aspiration la zone de fluide "mort" tendant à se former au pied du choc, soit en lui communiquant de la quantité de mouvement par une injection localisée. L'efficacité de ce procédé est très grande, un effet spectaculaire pouvant être réalisé avec des débits fluides extrêmement réduits. En contrepartie, il y a perte de la possibilité de contrôle si le choc vient à se déplacer largement, comme c'est le cas sur un profil, par exemple.

Chacune de ces techniques présente ses avantages et ses inconvénients compte tenu de l'objectif visé et des contraintes d'ordre technologique ou économique. Ainsi le problème se pose en des termes différents dans une soufflerie où l'on cherche l'extinction d'ondes réfléchies -là une aspiration répartie par une paroi perméable peut être une bonne solution- et sur une aile ou dans une prise d'air où c'est la réduction des pertes par effet visqueux et la suppression des décollements qui sont avant tout souhaitées. Dans ces circonstances une aspiration (ou injection) locale semble devoir être préférée en raison de son efficacité et de sa plus grande simplicité de mise en oeuvre. Enfin mentionnons qu'action amont répartie et action locale sont souvent combinées, comme c'est le cas dans le contrôle passif.

Les méthodes de prévision sont encore rudimentaires (sauf dans le cas laminaire), leur développement se heurtant à de difficiles problèmes de modélisation de la turbulence et à la prise en compte réaliste de conditions aux limites complexes. Dans ce domaine, des efforts de recherche sont éminemment souhaitables.

REFERENCES

[1] PEARCEY, H.H.
"Some Effects of Shock-Induced Separation of Turbulent Boundary Layer in Transonic Flow past Aerofoils."
ARC R & M n° 3108 (1955)

[2] SEEGMILLER, H. L., MARVIN, J.G. et LEVY, L., L. Jr
"Steady an Unsteady Transonic Flows"
AIAA Journal, Vol. 16, n° 12, pp. 1262-1270 (Déc. 1978)

[3] MARVIN, J.G.
In "Transonic Viscous Interactions"
AIAA Professional Study Series (1980)

[4] REGENSCHEIT, B.
"Versuche zur Widerstandsverringerung eines Flügels bei hoher Machscher - Zahl durch Absaugung der hinter dem Gebiet unstetiger Verdichtung abgelösten Grenzschicht."
Zentrale für wissenschaftliches Berichtswesen der Luftfahrtforschung des Generalluftzeugmeistens (ZWB). Berlin Adlershof, Forschungsbericht Nr 1424, (juillet 1941), traduction anglaise "Drag Reduction by Suction of the Boundary Layer Separated Behind Shock Wave Formation at High Mach Numbers"
NACA TM n° 1168 (Juillet 1947)

[5] FAGE, A. et SARGENT, R.F.
"Effect on Aerofoil Drag of Boundary Layer Suction Behind a Shock Wave"
ARC R § M n° 1913 (1943)

[6] MARVIN, J.G.
"Turbulence Modeling for Computational Aerodynamics"
AIAA Paper n° 82-0164 (Janv. 1982)

[7] Proc. of the 1980-1981 AFORS-HTTM Stanford Conference on Complex Turbulent Flows :
Comparison of Computation and Experiment.
Stanford University, Sept. 14-18 (1981)

[8] DELERY, J. et MASURE, B.
"Action d'une variation brusque de pression sur une couche limite turbulente et application aux prises d'air hypersoniques."
La Recherche Aérospatiale, n° 129, pp. 3-12 (1969)

[9] ROSHKO, A. et THOMKE, G.J.
"Supersonic Turbulent Boundary Lay r Interaction With a Compression Corner at Very High Reynolds Number."
Mc Donnell-Douglas, Paper 10163 (Mai 1969)

[10] LIGHTHILL, M.J.
"On Boundary Layers Upstream Influence. II Supersonic Flows without Separation".
Proc. Roy. Soc., A 217, pp. 478-507 (1953)

[11] STEWARTSON, K. et WILLIAMS, P.G.
"Self-Induced Separation."
Proc. Roy. Soc., A 312, pp. 181-206 (1969)

[12] SYCHEV, V.Ya
"Concerning Laminar Separation."
Izvestiya Akademii Nauk Armyanskoi SSR, Mekk., Zhidk. Gaza, n° 3, pp. 47-59 (1972)

[13] RIZZETTA, D.P., BURGGRAF, O.R. , et JENSON, R.
"Triple-Deck Solutions for Viscous Supersonic and Hypersonic Flow Past Corner."
J. Fluid Mech, Vol. 89, Part 3, pp. 535-552 (1978)

[14] MELNIK, R.E. et GROSSMAN, B.
"Analysis of the Interaction of a Weak Normal Shock-Wave With a Turbulent Boundary Layer."
AIAA Paper n° 74-598 (Juillet 1974)

[15] INGER, G.R. et MASON, W.H.
"Analytical Theory of Transonic Normal Shock/Turbulent Boundary Layer Interaction."
AIAA Journal, Vol. 14, n° 9, pp. 1266-1272 (Sept. 1976)

[16] BOHNING, R. et ZIEREP, J.
"The Normal Shock at a Curved Wall in the Viscous Case."
Symposium Transsonicum II, pp. 237-243, Springer Verlag (1976)

[17] LIEPMANN, H.W., ROSHKO, A. et DHAWN, S.
"On Reflection of Shock Wave from Boundary Layers."
NACA Report 1100 (1952)

[18] HENDERSON, L.F.
"The Reflexion of a Shock Wave at a Rigid Wall in the Presence of a Boundary Layer."
J. Fluid Mech.,Vol. 30, Part. 4, pp. 699-722 (1967)

[19] COLES, D.E.
"The Law of the Wake in Turbulent Boundary Layer."
J. Fluid Mech. , Vol. 1, Part. 2, pp. 191-226 (1956)

[20] CHAPMAN, D.R., KUEHN, D.M. et LARSON, H.K.
"Investigation on Separated Flows in Supersonic and Subsonic Streams with Emphasis on the Effect of Transition."
NACA TR-1356 (1958)

[21] THOMKE, G.J. et ROSHKO, A.
"Incipient Separation of Turbulent Boundary Layer at High Reynolds Number in Two Dimensional Supersonic Flow over a Compression Corner."
Mc Donnell Douglas, Report DAC 59819 (1969)

[22] SETTLES, G.S.
"An Experimental Study of Compressible Turbulent Boundary Layer Separation at High Reynolds Number."
Ph. D. Dissertation, Aerospace an Mechanical Sciences Dept., Princeton University (Sept. 1975)

[23] SIRIEIX, M., DELERY, J. et STANEWSKY, E.
"High Reynolds Number Boundary Layer Shock Wave Interactions in Transonic Flow."
Lecture Notes in Physics 148, Springer Verlag (1981)

[24] SPAID, F.W. et FRISHETT, J.C.
"Incipient Separation of a Supersonic, Turbulent Boundary Layer, Including Effects of Heat Transfer."
AIAA Paper n° 72-114 (Janv. 1972) ; voir aussi AIAA Journal, Vol. 10, n° 7, p.p 915-922 (Juillet 1972)

[25] ROSHKO, A. et THOMKE, G.J.
"Flare Induced Interaction Lenghts in Supersonic, Turbulent Boundary Layers."
Mc Donnell-Douglas, MDAC Paper WC 2416 (Déc. 1974), voir aussi AIAA Journal, Vol. 14, pp. 873-879 (Juillet 1976)

[26] LAW, C.H.
"Supersonic, Turbulent Boundary Layer Separation."
AIAA Journal, Vol. 12, n° 6, pp. 794-797 (juin 1974)

[27] GREEN, J.E.
"Interaction Between Shock Waves and Turbulent Boundary Layers."
RAE TR-69098 (Mai 1969) ; voir aussi Progress in Aerospace Sciences, Pergamon Press, Vol. 11, pp. 235-340 (1970)

[28] SHANG, J.S., HANKEY Jr., W.L. et LAW, C.H.
"Numerical Simulation of Shock Wave/Turbulent Boundary Layer Interaction."
AIAA Journal, Vol. 14, n° 10, pp. 1451-1457 (Oct. 1976)

[29] SETTLES, G.S., PERKINS, J.J. et BOGDONOFF, S.M.
"Upstream Influence Scaling of 2D and 3D Shock/Turbulent Boundary Layer Interactions at Compression Corners."
AIAA Paper n° 81-0334 (Janv. 1981)

[29] DELERY, J. et VEUILLOT, J.P.
"Recherches expérimentales et théoriques sur la turbulence dans les interactions choc-couche limite en transsonique."
Symposium IUTAM "Structure of Complex Turbulent Shear Flow ." Marseille (Sept. 1982) Springer Verlag (1983) ; voir aussi ONERA T.P. n° 1982-77

[31] DELERY, J.
"Recherches sur l'interaction onde de choc-couche limite turbulente."
La Recherche Aérospatiale, n° 1977-6, pp. 337-348 (Nov. 1977) ; English Translation ESA-TT 476 (1978)

[32] ARDONCEAU, P.
"Etude de l'interaction onde de choc-couche limite supersonique."
Thèse de Docteur ès Sciences Physiques, Université de Poitiers, Juillet 1981

[33] ARDONCEAU, P., LEE, D.H., ALZIARY de ROQUEFORT, T. et GOETHALS, R.
"Turbulence Behaviour in a Shock Wave/Boundary Layer Interaction."
AGARD CP-271 (Janv. 1980)

[34] SIMPSON, R.L., STRICKLAND, J.H. et BARR, P.W.
"Features of Separating Turbulent Boundary Layer in the Vicinity of Separation."
J. Fluid Mech., Vol. 79, Part. 3, pp. 553-594 (1977)

[35] STANEWSKY, E.
"Wechselwirkung Zwischen Aussenströmung und Grenzschicht an Transsonischen Profilen."
Doctor-Engineer Dissertation, D 83, Berlin (Mai 1981)

[36] RODDE, A.M.
"Détermination des conditionsd'apparition du décollement au pied du choc sur le profil LC-100D à bord de fuite modifié."
ONERA RSF-45/1685 AY (Juin 1980)

[37] GOBERT, J.L. SERAUDIE, A. et MIGNOSI, A.
"Etude de l'interaction onde de choc-couche limite sur profil LC-100D de 400 mm de corde dans la soufflerie T2."
ONERA RT-38/7078 AYD (Janv. 1980)

[38] SQUIRE, L.C. et SMITH, M.J.
"Interaction of a Shock Wave with a Turbulent Boundary Layer Disturbed by Injection."
Aeronautical Quarterly, Vol. 31, pp. 85-112 (Mai 1980)

[39] INGER, G.R.
"Transonic Shock/Turbulent Boundary Layer Interaction and Incipient Separation on Curved Surfaces."
AIAA Paper 81-1244 (Juin 1981)

[40] SETTLES, G.S., BOGDONOFF, S.M. et VAS, I.E.
"Incipient Separation of a Supersonic Turbulent Boundary Layer at Moderate to High Reynolds Numbers."
AIAA Paper n° 75-7 (Janv. 1975) ; voir aussi AIAA Journal, Vol. 14, n° 1, pp. 50-56 (Janv. 1976)

[41] ERDOS, J. et PALLONE, A.
"Shock/Boundary Layer Interaction and Flow Separation."
Heat Transfer and Fluid Mechanics Institute Procs., Stanford University Press (1962)

[42] ROSHKO, A. et THOMKE, G.J.
"Correlations for Incipient Separation Pressure."
Douglas Aircraft Co. DAC-59800 (1966)

[43] RESHOTKO, E. et TUCKER, M.
"Effect of a Discontinuity on a Turbulent Boundary Layer Thickness Parameters with Application to Shock-Induced Separation."
NACA TN-3454 (1955)

[44] GADD; G.E.
"Interaction between Normal Shock-Waves and Turbulent Boundary Layers."
ARC R & M n° 3262 (1961)

[45] ELFSTROM, G.M.
"Turbulent Separation in Hypersonic Flow."
Imperial College of Sciences and Technology, I.C. Aero Report 71-16 (Sept. 1971) ; voir aussi
"Turbulent Hypersonic Flow at a Wedge Compression Corner."
J. Fluid Mech, Vol. 53, Part 1, pp. 113-127 (1972)

[46] KORKEGI, R.H.
"Comparison of Shock-Induced Two-and Three-Dimensional Incipient Turbulent Separation."
AIAA Journal, Vol. 13, n° 4, pp. 534-535 (Avril 1975)

[47] DELERY, J.
"Analyse du décollement résultant d'une interaction choc-couche limite turbulente en transsonique."
La Recherche Aérospatiale, n° 1978-6, pp. 305-320 (Nov. 1978) ; English Translation ESA-TT 560 (1979)

[48] SEDDON, J.
"The Flow Produced by Interaction of a Turbulent Boundary Layer with a Normal Shock-Wave of Strength Sufficient to Cause Separation."
ARC R & M n° 3502 (Mars 1960)

[49] KOOI, J. W.
"Influence of Free-Stream Mach Number on Transonic Shock Wave Boundary Layer Interactions."
NLR MP - 78013 U (Mai 1978)

[50] EAST, L.F.
"The Application of a Laser Anemometer to the Investigation of Shock-Wave Boundary-Layer Interactions."
RAE Tech. Memo. AERO 1666 (Fév. 1976) ; voir aussi AGARD CP-193 (1976)

[51] ZUKOSKI, E.E.
"Turbulent Boundary Layer Separation in Front of a Forward Facing Step."
AIAA Journal, Vol. 5, n° 10, pp. 1746-1753 (Oct. 1967)

[52] DELERY, J. et SIRIEIX, M.
"Ecoulements de culot."
AGARD LS-98 (Mars 1979) et ONERA TP n° 1979-14F ; English Translation "Base Flows Behind Missiles."
ONERA TP n° 1979-14 E

[53] DELERY, J.
"Investigation of Strong Shock Turbulent Boundary Layer Interaction in 2D Transonic Flows with Emphasis on Turbulence Phenomena."
AIAA Paper n° 81-185 (Fév. 1983) ; voir aussi AIAA Journal, Vol. 21, n° 2, pp. 180-185 (Fév. 1983)

[54] PEARCEY, H.H., OSBORNE, J. et HAINES, A.B.
"The Interaction Between Local Effects at the Shock and Rear Separation. A Source of Significant Scale Effects in Wind-Tunnel Tests on Aerofoils and Wings."
AGARD CP-35 (1968)

[55] ROSE, W.C.
"The Behavior of a Compressible Turbulent Boundary Layer in a Shock Wave Induced Adverse Pressure Gradient."
NASA TN D-7092 (Mars 1973)

[56] BUSHNEL, D.M.
"Turbulent Drag Reduction for External Flows."
AIAA Paper n° 83-0227 (Janv. 1983)

[57] KEPLER, C.E. et O'BRIEN, R.L.
"Supersonic Turbulent Boundary Layer Growth over Cooled Walls in Adverse Pressure Gradients."
Aeronautical Systems Division, Report ASD TDR-62-87 (Oct. 1962)

[58] WALZ, A;
"Boundary Layers of Flow and Temperature."
M.I.T. Press, Cambridge, Mass. pp. 113 (1969)

[59] INGER, G.R., LYNCH, F.T. et FANCHER, M.F.
"A theoretical and Experimental Study of Non-Adiabatic Wall Effects on Transonic Shock/Boundary Layer Interaction."
AIAA Paper n° 83-1421 (Juin 1983)

[60] PADOVA, C., FALK, T.J. et WITTLIFF, C.E.
"Experimental Investigation of Similitude Parameters Governing Transonic Shock/Boundary Layer Interactions."
AIAA Paper n° 80-0158 (Janv. 1980)

[61] INGER, G.R.
"Transonic Shock-Boundary-Layer Interactions in Cryogenic Wind Tunnels."
Journal of Aircraft, Vol. 16, n° 4, pp. 284-287 (Avril 1979)

[62] FRISHETT, J.C.
"Incipient Separation of a Supersonic Turbulent Boundary Layer Including Effects of Heat Transfer."
Ph. D. Dissertation, University of California, Los Angeles (1971)

[63] BACK, L.H. and CUFFEL, R.F.
"Shock-Wave/Turbulent Boundary Layer Interactions with an without Surface Cooling."
AIAA Journal, Vol. 14, n° 4, pp. 526-532 (Avril 1976)

[64] KILBURG, R.F. et KOTANSKY, D.R.
"Experimental Investigation of the Interaction of a Plane, Oblique, Incident-Reflecting Shock-Wave with a Turbulent Boundary Layer on a Cooled Surface."
NASA CR-66-841 (Oct. 1969)

[65] DORRANCE, W.H. et DORE, F.J.
"The Effect of Mass Transfer on the Compressible Turbulent Boundary Layer Skin Friction and Heat Transfer."
JAS, Vol. 21, n° 6, pp. 404-410 (Juin 1954)

[66] JEROMIN, L.O.F.
"An Experimental Investigation of the Compressible Turbulent Boundary-Layer with Injection."
ARC R & M n° 3526 (1968)

[67] SQUIRE, L.C.
"Further Experimental Investigations of Compressible Turbulent Boundary Layers with Air Injection."
ARC R & M n° 3627 (1970)

[68] JEROMIN, L.O.F.
"The Status of Research in Turbulent Boundary Layers with Fluid Injection."
in Progress in Aeronautical Sciences, Vol 10, Pergamon Press (1970)

[69] LILI, T.
"Couche limite turbulente avec injection à la paroi poreuse d'un même gaz ou d'un gaz différent."
Thèse de Docteur ès Siences Physiques, Université de Poitiers (Sept. 1972) et ONERA Note Technique n° 201 (1972)

[70] THOMAS; G.D.
" Compressible Turbulent Boundary Layers with Combined Air Injection and Pressure Gradient."
ARC R & M n° 3779 (1976)

[71] HAYAKAWA, K. et SQUIRE, L.C.
"The Effect of the Upstream Boundary Layer State on the Shock Interaction at a Compression Corner."
J. Fluid Mech, Vol. 122, pp. 369-394 (1982)

[72] GREEN, J.E.
"A discussion of Viscous Inviscid Interactions at Transonic Speeds."
RAE TR-72050 (1972)

[73] BORE, C.L.
"On the Possibility of Deducing High Reynolds Number Characteristics Using Boundary Layer Suction."
AGARD CP-83-71, Paper 23 (1971)

[74] INGER, G.R.
"Transonic Shock Turbulent Boundary-Layer Interaction With Suction or Blowing."
AIAA Paper 79-005 (Janv. 1979)

[75] INGER, G.R. et ZEE. S.
"Transonic Shock-Wave/Turbulent Boundary-Layer Interaction with Suction or Blowing."
Journal of Aircraft, Vol. 15, n° 11, pp. 750-754 (Nov. 1978)

[76] CHEW, Y.T. et SQUIRE, L.C.
"The Boundary-Layer Development Downstream of a Shock Interaction at an Expansion Corner."
ARC R & M n° 3839 (1979)

[77] GOETHERT, B.H.
"Flow Establishment and Wall Interference in Transonic Wind Tunnels."
AGARD Memorendum, AG 17/P7 (Nov. 1954)

[78] ALLEN, H.J.
"Transonic Wind Tunnel Development of the National Advisory Committee for Aeronautics."
AGARD AG 17/P7 (1954)

[79] RAMM, H. et JONES, M.
"Use of Perforated Walls for Shock Cancellation at Supersonic Speeds."
AEDC TR-59-15 (Aout 1959)

[80] VAYSSAIRE, J.C.
"Absorption d'ondes de choc par des parois poreuses homogènes."
L'Aéronautique et l'Astronautique, n° 47, pp. 85-88 (1974-4)

[81] LEE, D.B.
"Etude de l'interaction onde de choc-couche limite turbulente sur paroi poreuse avec aspiration."
Thèse de Docteur Ingénieur, Université de Poitiers (Mai 1983)

[82] FOURNIER, J. , LEBLANC, R. et VAYSSAIRE, J.C.
"Application de parois perméables aux veines de souffleries transsoniques."
12ème Colloque d'Aérodynamique Appliquée de la AAAF, Poitiers (Nov. 1975)

[83] FREESTONE, M.M. et COX, R.N.
"Sound Fields Generated by Transonic Flows over Surfaces Having Circular Perforations."
AGARD CP-83-71 (1971)

[84] VAUCHERET, X.
"Fluctuations acoustiques engendrées par les parois perméables d'une soufflerie transsonique."
AGARD CP-174 (1975)

[85] STERRETT, J.R., DUNNING, R.W. et BREVOORT, M.J.
"The Use of Suction to Prevent Shock-Induced Separation in a Nozzle."
NACA RM-L50K20 (Janv. 1951)

[86] MATHEWS, D.C.
"Shock-Wave Boundary Layer Interactions in Two Dimensional and Axially-Symmetric Flows Including the Influence of Suction."
Ph. D. Thesis, University of Washington (1969)

[87] SEEBAUGH, W.R. et CHILDS, M.E.
"Conical Shock-Wave Turbulent Boundary Layer Interaction Including Suction Effects."
Journal of Aircraft, Vol. 7, n° 4, pp. 334-340 (Juillet-Août 1970)

[88] CUBBINSON, R.W., MELEASON, E.T. et JOHNSON, D.F.
"Effect of Porous Bleed in a High-Performance Axisymmetric, Mixed Compression Inlet at Mach 2.50."
NASA TM X-1962 (Nov. 1968)

[89] FUKUDA, M.K., HINGST, W.R. et RESHOTKO, E.
"Control of Shock Wave-Boundary Layer Interactions by Bleed in Supersonic Mixed Compression Inlets."
NASA CR - 2595 (1975)

[90] FUKUDA, M. K., HINGST, W.R. et RESHOTKO, E.
"Bleed Effect on Shock/Boundary-Layer Interactions in Supersonique Mixed Compression Inlets."
Journal of Aircraft, Vol. 14, n° 2, pp. 151-156 (Fév. 1977)

[91] SEEBAUGH, W.R., PAYNTER, G.C. et CHILDS, M.E.
"Shock-Wave Reflection from a Turbulent Boundary Layer with Mass Bleed."
Journal of Aircraft, Vol. 5, n° 5, pp. 461-467 (Sept. Oct. 1968)

[92] WONG, W.F.
"The Application of Boundary-Layer Suction to Suppress Strong Shock-Induced Separation in Supersonic Inlets."
AIAA Paper n° 74 - 1063 (Juin 1974)

[93] TANNER, L.H. et GAI, S.L.
"Effects of Suction on the Interaction Between Shock-Wave and Boundary-Layer at a Compression Corner."
ARC C.P. n° 1087 (1970)

[94] GAI, S.L.
"Shock-Wave Boundary Layer Interaction with Suction."
Z. flugwiss Weltraumforsch 1, Heft. 2, pp. 97-101 (1977)

[95] BALL, K.O.W. et KORKEGI, R.H.
"An Investigation of the Effect of Suction on Hypersonic Laminar Boundary-Layer Separation."
AIAA Journal, Vol. 6, n° 2, pp. 239-243 (Fév. 1968)

[96] BALL, K.O.W.
"Further Results on the Effects of Suction on Boundary-Layer Separation."
AIAA Journal, Vol. 8, n° 2, pp. 374-375 (Fév. 1970)

[97] RHUDY, R.W.
"Investigation of Laminar Boundary-Layer Separation on a Flat-Plate-Ramp Combination with and without Mass Removal at Mach Numbers 6,8 and 10."
AEDC TR-69-199 (Mars 1970)

[98] PATE, S.R.
"Experiments on Control of Supersonic Transitional Flow Separation Using Distributed Suction."
AIAA Journal, vol. 7, n° 5, pp. 847-851 (Mai 1969)

[99] BAHI, L., ROSS , J.M. et NAGAMATSU, H.T.
"Passive Shock-Wave/Boundary-Layer Control for Transonic Airfoil Drag Reduction."
AIAA Paper n° 83-0137 (Janv. 1983)

[100] SAVU, G. TRIFU, O. et DUMITRESCU, L.Z.
"Suppression of Shocks on Transonic Airfoils."
14th International Symposium on Shock Tubes and Waves. Svdney, Australie (15-18 Août 1983)

[101] SYBERG, J. et KONCSEK, J.L.
"Bleed System Design Technology for Supersonic Inlets."
AIAA Paper n° 72-1138 (Nov. Déc. 1972) ; voir aussi : Journal of Aricraft, Vol. 10, n° 7, pp. 407-413 (Juillet 1973)

[102] HOLDEN, M.S.
"Shock-Wave/Turbulent Boundary Layer Interaction in Hypersonic Flow."
AIAA Paper n° 72-74 (Janv. 1972)

[103] ALZNER, K. et ZAKKAY V.
"Turbulent Boundary Layer Shock Interaction with and without Injection."
AIAA Journal, Vol. 9, n° 9, pp. 17969-1776 (Sept. 1971)

[104] VISWANATH, P.R., SANKARAN, L., NARASIMHA, R., PRABHU, A. et SAGDEO, P.M.
"Injection Slot Location for Boundary Layer Control in Shock Induced Separation."
AIAA Paper n° 78-1168 (Juillet 1978) ; voir aussi : AIAA Journal, Vol. 20, n° 8, pp. 726-732 (Août 1983)

[105] PEAKE, D.J.
"The Use of Air Injection to Prevent Separation of the Turbulent Boundary Layer in Supersonic Flow."
ARC C.P. n° 890 (1966)

[106] KELLY, M. W.
"Analysis of some Parameters Used in Correlating Blowing Type Boundary Layer Control Data."
NACA RM A 56 F 12 (Sept. 1956)

[107] WONG, W.F. et HALL, G.R.
"Suppression of Strong Shock Boundary Layer Interaction in Supersonic Inlets by Boundary Layer Blowing."
AIAA Paper n° 75-1209 (Sept. 1975)

[108] WONG, W.F.
"Investigation into the Suppression of Strong Shock Induced Boundary Layer Separation in Supersonic Air Injection Systems."
Northrop internal report n° NOR 72-169 (Mai 1974)

[109] WONG, W.F.
"Application of Boundary Layer Blowing to Suppress Strong Shock Induced Separation in Supersonic Inlets."
AIAA Paper n° 77-174 (Janv. 1977)

[110] SCHWENDEMANN, M.F. et SANDERS, B.W.
"Tangential Blowing for Control of Strong Normal Shock Boundary Layer Interactions on Inlet Ramps."
AIAA Paper n° 82-1082 (Juin 1982)

[111] DONALDSON, C. du P.
"Investigation of a Simple Device for Preventing Separation due to Shock and Boundary Layer Interaction."
NACA RM L 50 B 02a (1950)

[112] PEARCEY, H.H.
"Shock Induced Separation and its Prevention by Design and Boundary Layer Control."
in Boundary Layer an Flow Control, Vol. 2, Editeur G.V. LACHMANN, Pergamon Press (1961)

[113] LEYNAERT, J.
"Fonctionnement du piège à couche limite interne d'une prise d'air à compression supersonique externe."
Réunion de Spécialistes AGARD
"Aspects Aérodynamiques de l'Installation des Systèmes Propulsifs."
A.E.D.C. Tullahoma (oct. 1965) et ONERA TP n° 288 (1965)

[114] MEAUZE, G.
"Recompression par choc d'un écoulement interne supersonique en présence d'un piège à couche limite."
Thèse de Docteur Ingénieur, Université de Paris (1967) ; voir aussi ONERA NT n° 1976-8 (1976)

[115] CEBECI, T.
"Calculation of Compressible Turbulent Boundary Layers with Heat and Mass Transfer."
AIAA Journal, Vol. 9, n° 6, pp. 1091-1097 (Juin 1971)

[116] SCHETZ, J.A. et NERNEY, B.
"Turbulent Boundary Layer with Injection and Surface Roughness."
AIAA Journal, Vol. 15, n° 9, pp. 1288-1294 (Sept. 1977)

[117] COLLIER, F.S. et SCHETZ, J.A.
"Injection into a Turbulent Boundary Layer Through Porous Surfaces with Different Surface Geometries."
AIAA Paper n° 83-0295 (Janv. 1983)

[118] HINGST, W.R. et TANJI, F.T.
"Experimental Investigation of a Two-Dimensional Shock-Turbulent Boundary Layer Interaction with Bleed."
AIAA Paper, n° 83-0135 (Janv. 1983)

[119] DON GRAY, J. et MAUSS, J.R.
"Effects of Suction on Ramp Induced Laminar Boundary Layer Interaction."
AIAA Journal, Vol. 19, n° 7, pp. 948-950 (Juillet 1981)

[120] LEES, L. et REEVES, B.L.
"Supersonic Separated and Reattaching Laminar Flows : 1. General Theory and Application to Adiabatic Boundary Layer/Shock-Wave Interactions."
AIAA Journal, Vol. 2, n° 11, pp. 1907-1920 (Nov. 1964)

[121] STOCK, H.W.
"On Laminar Boundary Layers with Blowing and Suction."
Zeitschrift für Flugwissenschaften und Weltraum froschung, 4, Heft 2, pp. 93-100 (1980)

[122] HANIN, M., WOLFSHTEIN, M. et LANDAU, U.E.
"Numerical Navier-Stokes Solution for the Effects of Suction on Shock-Wave - Boundary Layer Interaction".
ICAS Paper n° 74-17 (1974)

[123] TASSA, Y. et SANKAR, N.L.
"Effect of Suction on a Shock-Separated Boundary Layer. A Numerical Study."
AIAA Journal, Vol. 17, n° 11, pp. 1268-1270 (Nov. 1979)

[124] BAKER, C.J.
"The Prediction of Boundary Layer Development through a Normal Shock Wave-Turbulent Boundary Layer Interaction."
Cambridge University, Engineering Department, DUED/A-Aero/TR;10 (1980)

[125] SUN, C.C. et CHILDS, M.E.
"Flowfield Analysis for Successive Oblique Shock Wave-Turbulent Boundary Layer Interactions."
Journal of Aricraft, Vol. 11, n° 1, pp. 54-59 (1974) voir aussi NASA CR-2656 (1976)

[126] PEARSON, L.W.
"Effects of Slot Suction on Turbulent Boundary Layer Separation"
AIAA Paper n° 67.197 (Janv. 1967).

[127] KUTSCHENREUTER, P.H., ZURSCHMEIDE, R.L. et SURBER, L.E.
"An Investigation of Shock-Wave - Boundary layer Interaction with Suction".
Air Force Aeronautical Systems Division Report ASRMDF TM 61-30 (Janv. 1962).

Remerciements :

L'auteur tient à remercier spécialement M. Claude COPY pour sa contribution à la préparation et à l'exécution des figures illustrant ce texte.

INTERET DU PIEGE INTERNE POUR LE FONCTIONNEMENT, DANS UN DOMAINE ETENDU DU NOMBRE DE MACH (1.8 – 3+) D'UNE PRISE D'AIR BIDIMENSIONELLE

par

G.Laruelle, Chef de Subdivision
ONERA
BP 72
92322 Châtillon, France

C.Sans, Ingénieur
ONERA
BP 72
92322 Châtillon, France

et

R.Lefebvre, Chef de Service
Société Nationale Industrielle Aérospatiale
2/18 rue Béranger
92320 Châtillon, France

RESUME

A partir d'une prise d'air bidimensionnelle munie d'un piège à couche limite interne et optimisée vers Mach 2, on cherche à définir, avec le minimum de pièces mobiles, une configuration assurant encore de bonnes performances jusqu'à Mach 3^+. Les principaux paramètres géométriques considérés sont :

- l'inclinaison de la rampe de compression
- la loi de diffusion interne
- la section d'entrée du piège interne.

La première partie rappelle l'intérêt du piège à couche limite interne et les avantages d'une géométrie variable.

La seconde partie présente la maquette à grande échelle utilisée dans la soufflerie supersonique S2 Modane de l'ONERA : motorisation, moyens de mesure et de visualisation interne. Elle comporte la projection d'un film visualisant par ombroscopie l'écoulement au niveau piège interne pour diverses manoeuvres (déplacements de rampe - diffuseur, montée en Mach, mise en incidence, obstruction interne).

La dernière partie analyse quelques résultats ainsi obtenus avec cette maquette de prise d'air. Le choix de deux configurations assurant des fonctionnements corrects dans deux domaines de Mach, par optimisation de la géométrie du piège, est commenté.

INTEREST OF INTERNAL BLEED FOR A TWO-DIMENSIONNAL AIR INTAKE OPERATING IN A WIDE MACH NUMBER RANGE (1,8 - 3+)

SUMMARY

From a two-dimensionnal air intake with an internal bleed and optimized for approximately Mach number 2, a new configuration is sought allowing still good performance up to Mach number 3^+, but with the minimum of movable parts. The main geometrical parameters are :

- the slope of the external compression ramp,
- the internal section law of the diffuser,
- and the inlet section of the internal bleed.

The first part recalls the interest of internal bleed and the advantage of a variable geometry.

The second one presents the model which was built at large scale and its equipments: motorizations, measurement devices and internal visualizations. The tests were performed in the supersonic wind tunnel S2 at ONERA Modane center. A movie shows schadowgraphs of the flow in the air intake geometrical throat, where the internal bleed is located, for several configuration changes (external ramp or diffuser wall rotations, increases of Mach number or angle of attack) and variable internal obstruction.

The last part explains some results, obtained with this air-intake model. The choice of two configurations allowing correct performance in the studied Mach number range, by optimisation of the internal bleed geometry, is commented on.

1 - INTRODUCTION -

Pour aller plus vite ou plus loin, certains missiles des nouvelles générations ont recours à la propulsion aérobie. Le turboréacteur est essentiellement utilisé pour les engins subsoniques à moyenne et longue portée ; pour les vols supersoniques, le statoréacteur est généralement préféré. Dans les deux cas, le missile devra être équipé d'une ou plusieurs prises d'air assurant l'alimentation du moteur pour toutes les attitudes envisagées (incidence, dérapage ou roulis) et parfois dans des domaines de Mach importants.

Si l'on s'intéresse aux missiles supersoniques propulsés par statoréacteur, tous les problèmes liés au fonctionnement à basse vitesse avec des bords d'attaque aigus, et en transsonique, sont évités grâce à l'accélération auxiliaire par propulseur à poudre. Par contre, la sophistication des prises d'air d'avions supersoniques, nécessaire pour l'optimisation aux différents nombres de Mach supersoniques et pour la phase d'accélération, ne peut être acceptée sur un missile tactique. Il en résulte que tout le domaine de Mach supersonique doit être couvert avec des prises d'air "Performantes mais Rustiques", c'est-à-dire avec le minimum de géométrie variable , la géométrie fixe étant bien sur l'optimum pour le devis de masse, le coût et la fiabilité.

Depuis plus de 10 ans, l'ONERA étudie de façon assez systématique, les diverses prises d'air susceptibles d'équiper de tels missiles [1] à [5] . Le positionnement sur le missile, le nombre des entrées et leurs formes font partie des paramètres étudiés. Dans ce cadre, un engin avec deux prises d'air bidimensionnelles adaptées vers Mach 2 avait été essayé en soufflerie. La définition de la prise d'air résultait bien sûr de l'expérience acquise en France sur le programme Concorde [6] à [10] .

Dans le cadre d'un projet de missile de même type, étudié par l'industriel AEROSPATIALE, on a recherché à étendre le domaine de fonctionnement de cette prise d'air bidimensionnelle, jusqu'à Mach 3 environ. Ces essais réalisés en coopération AEROSPATIALE-ONERA constituent l'objet du travail présenté.

2 - CONCEPTION DE LA PRISE D'AIR -

2.1 - Intérêt du piège à couche interne -

On s'intéresse à une prise d'air bidimensionnelle adaptée, à l'origine, à un nombre de Mach voisin de 2. Pour ce faire, la rampe est dessinée de façon que les chocs focalisent juste au voisinage du bord d'attaque de la carène pour ce nombre de Mach d'adaptation. Son profil résulte également d'une optimisation de l'efficacité pour ce même Mach. La première planche présente une strioscopie montrant une compression supersonique externe se terminant par un choc à la limite du détachement, au niveau de la carène.

L'impact de ce choc sur la rampe de compression implique la présence d'un piège à couche limite interne afin de minimiser l'interaction de ce choc avec la couche limite se développant sur la rampe. Deux grandes familles de pièges internes sont envisageables :

- soit avec une paroi localement poreuse ou plus généralement perforée,
- soit avec un trou béant.

La seconde planche montre une application de ce premier principe avec le projet de prise d'air annulaire de l'avion de transport supersonique américain et la suivante une coupe de la prise d'air du Concorde où la paroi présente une discontinuité.

Le fonctionnement de ce piège, rappelé schématiquement sur cette planche a déjà été longuement décrit par ses concepteurs [11] et [12] ; cela ne sera pas repris ici.

On peut noter deux différences quant à l'utilisation de ce piège sur un avion du type Concorde et pour un missile. L'obtention d'un débit secondaire ayant une bonne efficacité pour les fonctions annexes nécessaires au turboréacteur et sa tuyère n'a aucun intérêt pour le missile ; pour ce dernier, le débit capté est évacué à l'extérieur sans être utilisé.

Par contre, un avantage supplémentaire apparait avec l'emploi d'un statoréacteur. Si de façon générale, ce piège permet la régulation et assure une meilleure stabilité de l'écoulement pénétrant dans la prise d'air, avec un statoréacteur, il devient particulièrement avantageux pour atténuer les effets des éventuelles instabilités de combustion qui peuvent remonter dans la manche.

2.2 - *Intérêt de la géométrie variable* -

En partant d'une prise d'air proche de l'optimum à bas nombre de Mach (Mo$\sim$2), on s'intéresse à son fonctionnement jusqu'à Mach 3 environ.

En dépassant le Mach d'adaptation, les chocs issus de la rampe pénètrent sous la carène et provoquent des décollements conduisant à des pertes d'efficacité notables. Si le nombre de Mach amont croît encore, ces décollements subsistent, mais de plus, la recompression choisie à l'origine (déviation imposée par la rampe) devient insuffisante ; le nombre de Mach en fin de compression supersonique externe est trop élevé et le choc final a une efficacité médiocre. Pour une prise d'air bidimensionnelle, le remède à ces deux problèmes est obtenu en redressant la rampe amont. Théoriquement, on peut associer un angle de rotation de cette rampe avec l'augmentation du nombre de Mach pour assurer une certaine optimisation. La faible inclinaison de la carène, pour minimiser la trainée, est une contrainte supplémentaire.

On voit alors l'intérêt d'un piège à couche limite interne obtenu par un trou béant qui isole la rampe amont de la paroi aval placée dans le diffuseur. Toutefois, pour assurer un ralentissement correct de l'écoulement dans cet élément, il est nécessaire d'adapter la position du bord d'attaque de cette paroi à celle de l'extrémité aval de la rampe amont ; ce point sera précisé ultérieurement.

2.3 - *Application à une prise d'air de missile* -

Pour un missile tactique dont la durée de vie s'exprime en secondes, on recherche dans la mesure du possible, des constituants, les prises d'air en particulier, les plus simples possible afin de réduire les coûts et augmenter la fiabilité.

Dans ce but, il est nécessaire de trouver des positions des rampes de compression et de diffusion qui correspondent à un compromis acceptable dans tout le domaine de vol supersonique du missile. Une solution de secours peut être envisagée avec deux positions discrètes des rampes : une première satisfaisant les conditions de vol pour les "bas Mach" et la seconde pour les "hauts Mach". La limite entre ces deux domaines doit résulter des essais en soufflerie. Avec une telle solution, on évite une régulation en continu de la position des rampes avec le nombre de Mach.

C'est dans cet esprit qu'une maquette à grande échelle de la prise d'air bidimensionnelle, avec de nombreuses motorisations, a été réalisée pour être essayée dans la soufflerie supersonique S2 de l'ONERA implantée à Modane Avrieux. Les positions des rampes et les dimensions du piège à couche limite interne sont les paramètres géométriques d'étude.

3 - *MOYENS D'ESSAIS* -

3.1 - *Description de la maquette* -

La maquette correspond à une prise d'air de missile de type bidimensionnel, d'un rapport hauteur (H) sur largeur égal à 2 ; elle est schématisée sur la planche 4.

La rampe de compression, constituée de 3 dièdres, assure une adaptation à Mo = 2,15 en position nominale. Le bord de fuite de cette rampe constitue le début du piège à couche limite interne. Excepté un petit élément fixe à l'amont, elle pivote autour d'un axe situé à 0,35 H du bord d'attaque. Ce débattement angulaire (δ_1) modifie le profil de la rampe de compression qui peut ainsi passer de 3 à 4 dièdres pour $\delta_1 > 0$. La position de l'axe de rotation résulte de la nécessité de fermer l'entrée d'air pendant la phase d'emport du missile sous avion.

A l'aval du piège à couche limite interne, la paroi supérieure du diffuseur est constituée de deux plaques mobiles. Celle située le plus en aval tourne autour d'un axe fixe situé en fin du diffuseur. Son inclinaison par rapport à l'axe longitudinal de la prise d'air est définie par le paramètre δ_3 . La plaque située à l'amont de la précédente à une inclinaison repérée par le paramètre δ_2 ; l'axe de rotation est situé à l'extrémité amont de la plaque précédement décrite. La longueur de ce panneau réglable par position discrète permet de faire varier celle du piège à couche limite interne.

Tous ces paramètres angulaires (δ_1 , δ_2 et δ_3), ainsi que celui qui caractérise la section sonique du piège (Acp) sont variables continuement en cours d'essais grâce à des motorisations implantées dans la maquette. Il en est de même de l'obturation du débit principal qui permet la simulation des divers régimes de la prise d'air.

Des hublots en verre, placés dans les parois latérales de la prise d'air au niveau du piège à couche limite permettent la visualisation ombroscopique de l'écoulement interne. La photographie de la planche 5 les met en évidence.

La carène a une pente interne initiale de 11°.

3.2 - Montage d'Essai -

L'ensemble prise d'air et débitmètre, présenté sur la photographie de la planche 6, est fixé latéralement sur le dard de la soufflerie, au moyen d'un mat situé au niveau de la prise d'air.

Ce dard, relié à un secteur traversant verticalement la veine , permet la mise en incidence ainsi que la mise en roulis de la maquette.

La prise d'air est prolongée, en fin de diffuseur, comme indiqué sur le schéma de la planche 7, par un élément qui comporte un peigne de prises de pression, lui-même suivi d'un obturateur mécanique, composé de deux papillons contrarotatifs, qui assure la variation du régime de fonctionnement de la prise d'air.

En aval de la maquette, le débitmètre est muni de 3 grilles d'homogénéisation afin d'obtenir un écoulement uniforme dans le plan de mesure situé en amont du col sonique permettant la mesure du débit.

3.3 - Equipement de mesure -

Le plan de sondage principal est situé en fin du diffuseur de la prise d'air (Pl. 7). Il comporte 45 prises de pression d'arrêt réparties en 5 rangées de 9 ; les parois sont équipées de 6 pressions statiques : 4 latérales, 1 en haut et 1 bas (planche 8).

Dans le piège interne, l'équipement se compose d'un peigne médian de 6 prises de pression d'arrêt placé en amont du col et de 4 prises de pression statique ; deux sont associées au peigne, les deux autres sont placées dans la cavité sous la rampe amont.

Au culot de chaque col (débitmètre et piège interne), une prise de pression statique permet de contrôler l'amorçage.

Dans le débitmètre, 4 prises de pression statique situées à un diamètre en amont du convergent permettent de s'assurer de l'homogénéisation de l'écoulement et de calculer le débit alimentant le moteur. Le débit total capté est alors obtenu en y ajoutant le débit mesuré au niveau du col sonique du piège interne.

3.4 - Soufflerie -

Les essais ont été effectués dans la soufflerie continue et pressurisée S2 du centre de Modane Avrieux de l'ONERA. La veine supersonique de 1,75 x 1,85 m2 a été utilisée. La température génératrice est toujours voisine de 300°K. La pression génératrice est de 1,6 b pour les nombres de Mach inférieurs et seulement de 1,2 b à Mach 3.

Les cinq motorisations de la maquette associées aux variations des paramètres souffleries (Mach, Incidence, Roulis) ont permis la réalisation d'un essai de près de 7 heures sans arrêt de la soufflerie. Le choix des diverses configurations était possible grâce au traitement en temps quasi réel des mesures de pression, aux tracés des courbes caractéristiques (Efficacité-débit) et à l'enregistrement systématique des ombroscopies avec un magnétoscope.

4 - RESULTATS D'ESSAIS -

4.1 - Prise d'air nominale -

La géométrie de la prise d'air nominale, également dénommée "bas Mach", est schématisée sur la planche 4. Les positions angulaires des diverses rampes sont alors.

$$\delta_1 = 0° \qquad \delta_2 = 5° \qquad \delta_3 = 5°$$

Cette configuration est proche de l'optimum à Mach 2 pour les faibles incidences. Par contre, comme le montre la planche 9, l'efficacité maximale chute très rapidement avec l'augmentation du nombre de Mach. On peut noter une très légère sensibilité à l'incidence, dans la plage 0-6°, pour les grands nombres de Mach.

L'évolution du coefficient de débit à incidence nulle confirme l'adaptation de la prise d'air vers Mach 2,15. A 6° d'incidence, la section de la prise d'air face au vent augmente et le débit capté évolue en conséquence.

Les ombroscopies présentées sur la planche 10, ainsi que celles du film réalisé lors des essais [13] , permettent d'expliquer les performances obtenues.

La première, effectuée à Mach 2 en régime quasi-critique, montre :

- la focalisation des chocs issus de la rampe amont vers le bord d'attaque de la carène ,
- le choc fort interne imposé par cette dernière et limité par la ligne de jet séparant le débit principal de la zone d'eau morte du piège,
- et le choc "droit" limitant le domaine supersonique accroché au bord d'attaque du piège.

A Mach 2,6, sur la seconde ombroscopie, on constate que tous les chocs issus de la rampe amont pénètrent dans la prise d'air et que le jet ne recolle pas à l'aval du piège qui n'a alors plus aucun rôle.

A Mach 3, le décollement a disparu pour ce régime supercritique. Cependant on peut vérifier la faible inclinaison des chocs dans la prise d'air dûe aux nombres de Mach locaux très élevés résultant d'une trop faible compression amont. En régime critique, le choc droit de fin de compression sera intense et l'efficacité sera alors médiocre. On peut également noter un décollement interne sur la carène provoqué par les chocs issus de la compression externe ; le deuxième choc oblique en est la preuve.

Une variante de cette configuration, dont les écarts de performances sont négligeables consiste à réduire l'angle δ_2 et augmenter δ_3 tout en maintenant à la même hauteur le bord d'attaque de la paroi haute du diffuseur. Cette configuration ($\delta_1 = 0°$, $\delta_2 = 0{,}5°$ et $\delta_3 = 9°$) permet de minimiser la divergence initiale du diffuseur à Mach 2 mais également d'obtenir des configurations ayant de meilleures performances à Mach élevé en ne déplacant que le 1er élément de la paroi du diffuseur ($\delta_3 = 9° =$ Constante).

4.2 - *Configuration "haut Mach"* -

Pour les grands nombres de Mach, le missile vole à des altitudes importantes qui peuvent conduire à des incidences d'équilibre supérieures à 5°. Pour des prises d'air montées latéralement sur le fuselage, l'incidence locale croit encore (théoriquement, elle double à la paroi) et une légère survitesse doit être prise en compte.

En conséquence, l'optimisation a été réalisée à grande incidence. La planche 11 compare les efficacités maximales ainsi obtenues, par exemple à 12° d'incidence. On met en évidence un gain atteignant près de 20 % d'efficacité à Mach 3 avec la configuration "Haut Mach" présentée. Il faut noter que ce gain s'atténue lorsque le nombre de Mach décroit et s'annule même vers Mach 2,5. Du point de vue débit, il est bien évident, que la rotation de la rampe amont conduit à une perte non négligeable.

La planche 12 qui définit cette nouvelle configuration ($\delta_1 = 6°$, $\delta_2 = 5°$ et $\delta_3 = 9°$) met en évidence une plus grande sensibilité à l'incidence dans le domaine 0-6° pour l'efficacité maximale et inversement une faible influence en ce qui concerne le débit alimentant le moteur.

Si l'on compare, à faible incidence ($\alpha \sim 0°$), les performances de cette configuration avec celles de la prise d'air nominale, planche 13, on constate un gain d'efficacité, essentiellement vers Mach 2,6 mais qui s'annule vers les nombres de Mach inférieurs et vers Mach 3. Cette configuration ne présente pas d'intérêt pratique à faible Mach à cause de l'importante perte de débit occasionnee par la rampe amont braquée de 6°.

4.2 - *Géométrie de la section d'entrée du piège* -

La géométrie du piège est caractérisée essentiellement par deux paramètres:

- la hauteur relative des deux arêtes limitant la section d'entrée (bord de fuite de la rampe amont - bord d'attaque de la paroi supérieure du diffuseur).
- et la distance entre ces deux arêtes.

Pour la configuration nominale, le dimensionnement résulte de l'expérience de la prise d'air du Concorde. Cette optimisation est traitée dans diverses références [8] à [11]. On se limitera ici à quelques indications relatives au fonctionnement à Mach 3.

Pour une position donnée de la rampe amont, donc de son bord de fuite, on peut faire varier la hauteur relative du bord d'attaque du diffuseur, à une petite variation de la longueur du piège près, en modifiant l'inclinaison δ_2 du premier élément du diffuseur, en conservant par exemple le second fixe ($\delta_3 = 9°$).

La planche 14 présente les caractéristiques (Efficacité, Coefficient de débit) ainsi mesurées à Mach 3 avec la prise d'air placée à 6° d'incidence pour trois inclinaisons du premier élément.

On constate que lorsque le bord attaque du diffuseur est sensiblement à la hauteur du bord de fuite de la rampe amont ($\delta_2 = 9°$), l'efficacité est maximale et une légère perte de débit par le piège est alors mise en évidence. Si ce bord d'attaque est en retrait important, un décollement apparait et le piège ne fonctionne pas comme prévu.

On a constaté par ailleurs qu'en maintenant le bord d'attaque fixe et en réduisant l'angle δ_2 , on peut améliorer légèrement le rendement. Le paramètre essentiel ainsi présenté est bien la position relative des arêtes du piège et non la pente initiale du diffuseur.

La seconde grandeur caractérisant le piège est la longueur de son ouverture ; celle retenue initialement (configuration nominale) est voisine de 0,45 H. Des essais ont été réalisés en réduisant la longueur du premier élément constituant la paroi supérieure du diffuseur afin d'augmenter la section d'entrée du piège. Des exemples de résultats sont présentés sur la planche 15, à Mach 3, avec ces pièges dont la longueur est portée à 0,95 H pour trois positions δ_4 de la rampe amont. Il faut préciser, que les éléments définissant le diffuseur étaient adaptés pour avoir dans chaque cas les meilleures performances de la prise d'air ; en particulier, le bord de fuite de la rampe amont était sensiblement au même niveau que le bord d'attaque du diffuseur.

Pour les deux inclinaisons extrêmes essayées de la rampe amont on constate une perte du débit alimentant le moteur lorsque le piège est long, ainsi qu'un léger gain d'efficacité en régime subcritique. Ces résultats sont cohérents avec un fonctionnement correct du piège qui en absorbant du débit assure une amélioration du rendement de l'écoulement principal.

Si l'on considère la position intermédiaire de la rampe amont ($\delta_1 = 8°$) qui donne avec le piège court d'origine les meilleures performances pour cette attitude et ce nombre de Mach de vol (gain appréciable par rapport aux configurations (δ_1 = 6 ou 9°,7), on constate que l'agrandissement du piège a un effet très défavorable pour l'efficacité et ne conduit pas à une perte de débit en supercritique. Cela résulte du fait, que dans ce cas, l'écoulement ne recolle plus au niveau du bord d'attaque du diffuseur : le piège à couche limite interne ne joue plus son rôle.

On peut donc conclure qu'en général, l'augmentation de la section d'entrée du piège est favorable pour l'efficacité en permettant une aspiration plus importante. Toutefois, pour les configurations optimisées, conduisant à des efficacités élevées, une grande longueur de piège est nuisible.

4.4 - *Autres paramètres d'étude* -

L'optimisation du point de vue de l'aérodynamique interne d'une prise d'air supersonique dépend de très nombreux paramètres, dont certains ont déjà été présentés ci-dessus. Les autres seront seulement cités :

- section de sortie du piège interne,
- angle initial ainsi que profil interne de la carène,
- découpe des flancs (effet du dérapage),
- loi de section du diffuseur...

On peut noter dans cette étude que la contrainte fixant l'axe de rotation de la rampe amont n'a pas permis une bonne optimisation de la compression supersonique externe.

Les diverses modifications apportées à la prise d'air initiale pour définir une configuration "Haut Mach" ont permis d'obtenir les performances souhaitées pour le projet de missile dans tout le domaine de vol. On peut toutefois remarquer que les efficacités obtenues pour les nombres de Mach supérieurs à celui de l'adaptation sont encore loin des maximums possibles. Cela résulte essentiellement de l'interaction des chocs issus de la rampe amont et du choc final de recompression avec la couche limite qui se développe sur la carène. Pour remédier à ce problème, il est possible de créer un nouveau piège au niveau de la carène. Comme indiqué au paragraphe 2,1, il peut être réalisé soit avec une paroi perforée, soit avec une cavité comme le présente la planche 16. Comme précédemment, une optimisation de la position et de la longueur du piège ainsi que du débit à évacuer doit être réalisée.

La planche 17 montre un exemple de gain en efficacité que l'on peut ainsi obtenir, bien sûr au détriment d'une perte en débit.

5 - *CONCLUSION* -

L'étude présentée met en évidence les difficultés rencontrées pour obtenir un compromis, acceptable pour un missile, pour définir une prise d'air bidimensionnelle assurant un bon fonctionnement dans un très large domaine de nombre de Mach sachant qu'il faut minimiser le nombre de pièces en mouvement et éviter a priori les réglages en continu de leur position.

L'étude a été effectuée grâce à une maquette à grande échelle, fortement motorisée, dans la soufflerie supersonique continue S2 de Modane Avrieux. Les essais des divers paramètres géométriques dans tout le domaine Mach 1,8 - Mach 3+et pour diverses attitudes (incidence, dérapage) ont permis d'établir un compromis satisfaisant, malgré la contrainte technologique liée à l'axe de rotation de la rampe amont. Le compromis résulte en particulier de l'optimisation du piège a couche limite interne placé en extrémité de la rampe amont. Les améliorations possibles, qui conduisent à des gains d'efficacité notables nécessitent des pièges complémentaires, sur la carène et éventuellement sur les flancs. Ces pièges ont également une action favorable sur la stabilité de l'écoulement dans la prise d'air, en particulier dans le cas où celle-ci alimente un statoréacteur.

REFERENCES

1 G. LARUELLE
Prises d'air pour missile probatoire de statofusée
Aéronautique et Astronautique n° 98. 1983-1.

2 G. LARUELLE
Comparaison de différentes configurations d'entrée d'air de missiles supersoniques.
Symposium AGARD on Ramjets and Ramrockets for military applications. LONDRES 26-30 October 1981.

3 R. MARGUET, C. HUET et G. LARUELLE
Definition and performance of a one stage rocket ramjet
3th ISABE, MUNICH , 8-11 March 1976.

4 R. MARGUET, C. ECARY et Ph. CAZIN
Etudes et essais de statofusées pour la propulsion des missiles
4th ISABE , ORLANDO (E.U) 1-6 Avril 1979.

5 P. CHAMPIGNY
Problèmes liés à l'aérodynamique externe des missiles aérobies
Symposium AGARD on Missile Aerodynamics TRONDHEIM (Norway) 20-22 September 82.

6 I.H RETTIE and W.G.E. LEWIS
Design and development of an air intake for supersonic transport aircraft.
Journal of Aircraft Nov.Dec 1968.

7 C.S. LEYMAN and D.P. MORRIS
Concorde powerplant development
AGARD CP 91 (1971)

8 J. LEYNAERT
Engine installation aerodynamics
AGARD LS 67 (1974).

9 J. LEYNAERT
Problèmes d'interactions entre la prise d'air et l'avion
AGARD CP 150 (1974).

10 J. LEYNAERT, TW. BROWN, D. COLLARD
A study of the Concorde Air intake in yaw
ICAS paper n° 74-50 (1974) ou Aéronautique et Astronautique n° 58 (1976).

11 J. LEYNAERT
Fonctionnement du piège à couche limite interne d'une prise d'air à compression supersonique externe.
AGARDOGRAPH 103 (1965).

12 J. LEYNAERT, D. COLLARD, et TW. BROWN
Enseignement des prises d'air de Concorde pour un futur supersonique de croisière manoeuvrant.
Symposium AGARD BRUXELLES 1983.

13 Film ONERA n° 968
Prise d'air bidimensionnelle dans la soufflerie S2 du centre de Modane Avrieux de l'ONERA.



FIGURE 1

PRISE D'AIR BIDIMENSIONNELLE

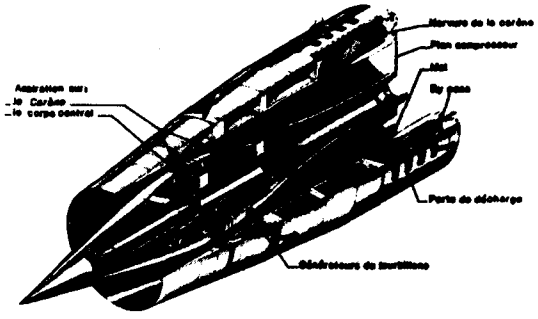


FIGURE 2

PRISE D'AIR DE REVOLUTION (S.S.T.)

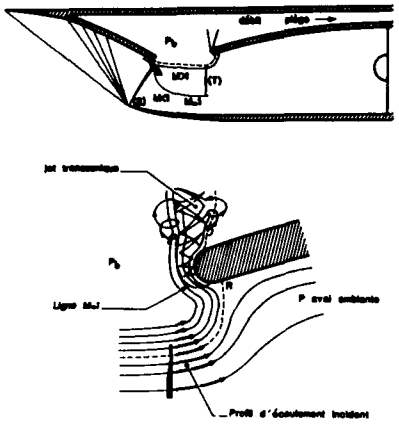


FIGURE 3

PRISE D'AIR CONCORDE.
ECOULEMENT DANS LE PIEGE

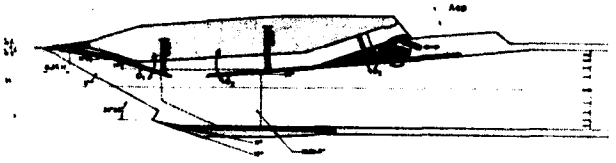


FIGURE 4

DEFINITION DE LA PRISE D'AIR
(CONFIGURATION NOMINALE)



FIGURE 5

VUE DE LA PRISE D'AIR



FIGURE 6

PHOTOGRAPHIE DU MONTAGE EN VEINE

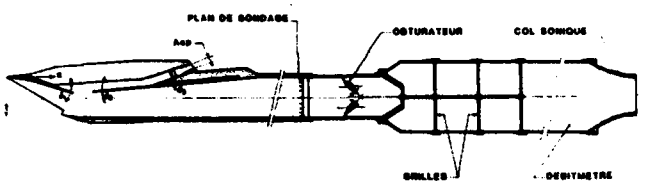
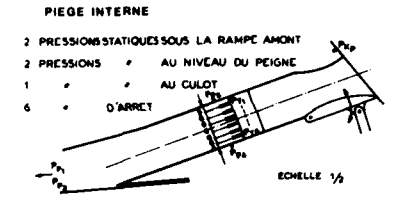


FIGURE 7 - SCHEMA DE LA MAQUETTE



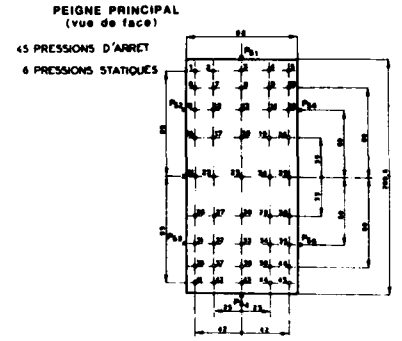


FIGURE 8 - EQUIPEMENT EN PRESSION

$\alpha = 0°$ $\beta = 0°$ $\delta_1 = 0°$

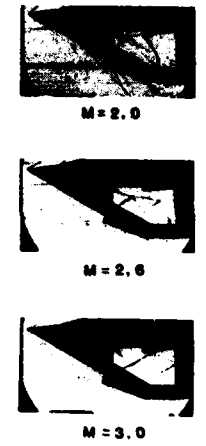


FIGURE 10 CONFIGURATION NOMINALE
OMBROSCOPIES DE L'ECOULEMENT

$\delta_1 = 6°$ $\delta_2 = 5°$ $\delta_3 = 9°$

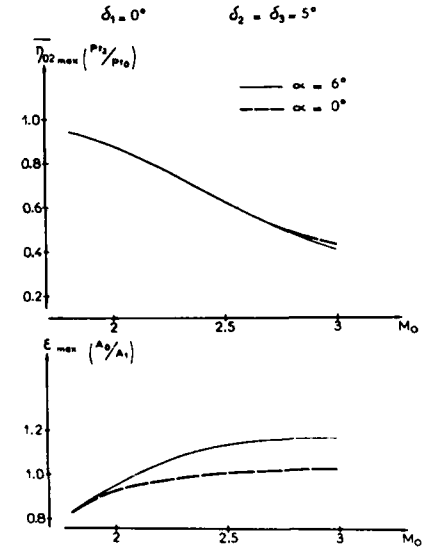


FIGURE 9
CONFIGURATION NOMINALE

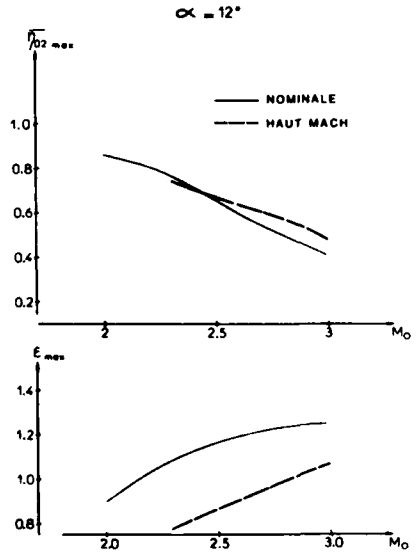


FIGURE 11 - (α = 12°)
COMPARAISON DES DIFFERENTES CONFIGURATIONS

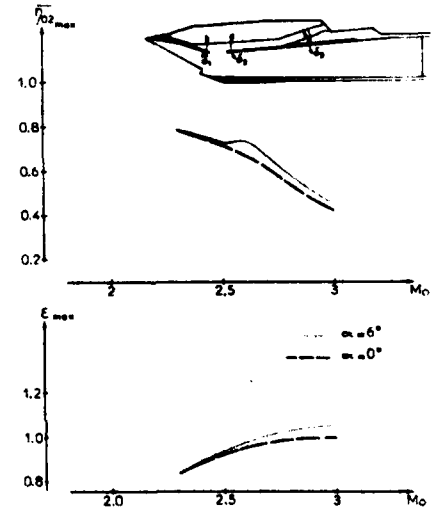


FIGURE 12 CONFIGURATION "HAUT MACH"

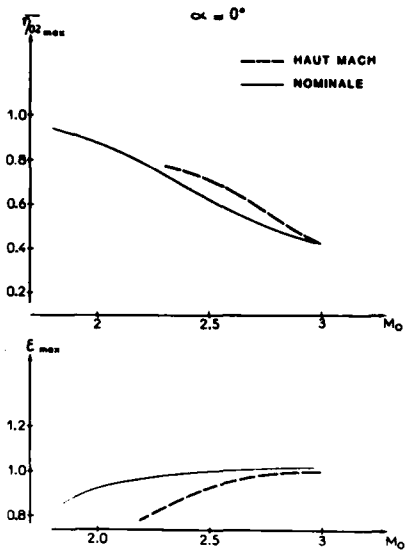


FIGURE 13 - (α = 0°)

COMPARAISON DES DIFFERENTES CONFIGURATIONS

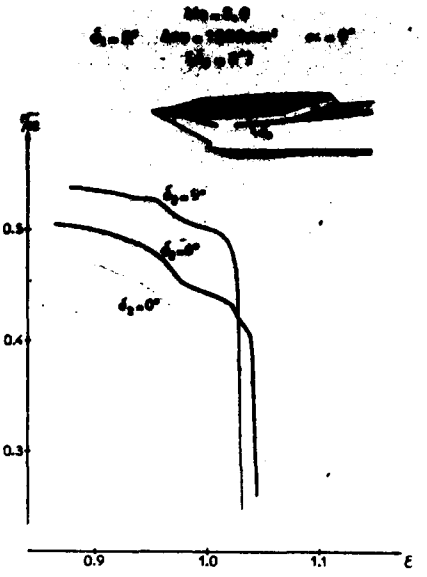


FIGURE 14

INFLUENCE DE LA VALEUR DE δ 2

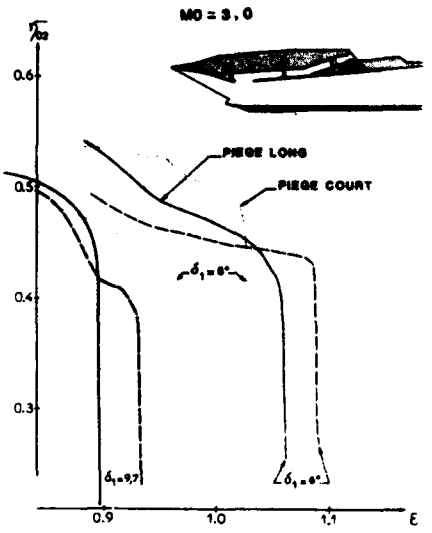


FIGURE 15

INFLUENCE DE LA LONGUEUR DU PIEGE

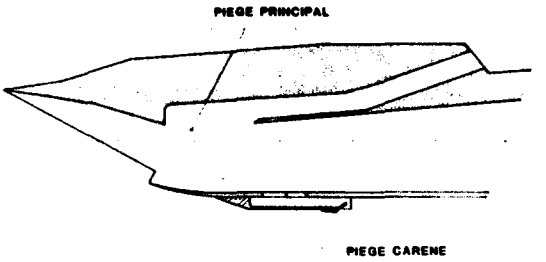


FIGURE 16

PIEGE A COUCHE LIMITE COTE CARENE

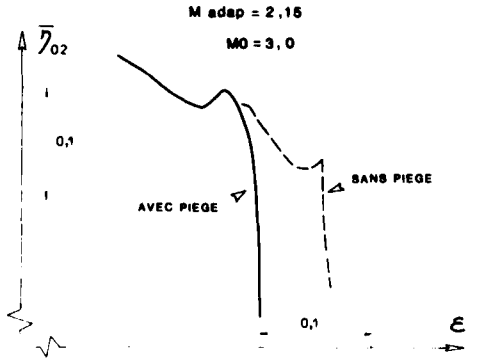


FIGURE 17 - INFLUENCE DU PIEGE COTE CARENE

INTERACTION ONDE DE CHOC OBLIQUE - COUCHE LIMITE TURBULENTE SUR PAROI POREUSE AVEC ASPIRATION

D.B. LEE et R. LEBLANC
Centre d'Etudes Aérodynamiques et Thermiques
(Laboratoire Associé au C.N.R.S.n°191)
43, rue de l'Aérodrome
86000 POITIERS, France

SOMMAIRE

On présente les résultats de l'analyse théorique et expérimentale de l'interaction d'un choc oblique avec une couche limite turbulente soumise à deux taux d'aspiration. Les équations générales sont résolues par une méthode de différences finies. La méthode est directe avec gradient de pression prescrit. Le modèle algébrique de turbulence de Cebeci et Smith est complété pour tenir compte du transfert de masse. Les premières comparaisons avec l'expérience, à M = 1,43, pour une couche limite de paroi plane sans interaction, montre qu'il faut simuler les rugosités, en amont de la zone d'aspiration, par un soufflage correctement adapté. On étudie alors trois cas d'interaction d'un choc oblique créé par une déviation de 3° à M = 1,43 avec la couche limite turbulente de paroi. La méthode expérimentale fournit une description détaillée de la région d'interaction, différente selon qu'il s'agit de la paroi pleine ou de la paroi poreuse et du taux d'aspiration. L'évolution de la couche subsonique, matérialisée par celle de la ligne sonique, joue un rôle essentiel. La méthode de prédiction est satisfaisante pour les deux cas extrêmes (paroi pleine et forte aspiration) mais tombe en défaut quand la couche limite est davantage destabilisée par les rugosités qu'influencée par l'aspiration modérée. On conclut sur la nécessité de mettre en oeuvre un modèle de turbulence prenant en compte à la fois le transfert de masse et les rugosités et d'étudier un couplage qui considère le gradient vertical de pression.

NOTATIONS

A, A^+	fonction d'amortissement de Van Driest et sa forme adimensionnelle (Eq.4)
C_f	coefficient de frottement pariétal
C_p	chaleur spécifique à pression constante
F	paramètre de transfert de masse à la paroi (Eq.1)
H	paramètre de forme
K	paramètre de maillage en η (Eq.7)
$k_{1,2}$	constantes du modèle de turbulence (Eq.4,6)
M	nombre de Mach
P_c, P_t, P_w, P_l	pressions (dans le caisson, génératrice, pariétale et statique à proximité de la paroi)
R_e	nombre de Reynolds
T, T_t	températures
u, v	vitesse selon x,y
u_τ	vitesse de frottement ($\sqrt{\tau w/\rho w}$)
u^*	vitesse généralisée de Van Driest ($u_e/\sqrt{\sigma}$ arcsin $[\sqrt{\sigma}(u/u_e)]$)
x, y	coordonnées cartésiennes (x est mesuré à partir du début de la paroi inférieure interchangeable)
γ	fonction d'intermittence (Eq.6)
γ	chaleur spécifique
δ, δ^*	épaisseur de la couche limite et de déplacement
ε	viscosité tourbillonnaire (Eq. 4,6)
η, ξ	variables transformées de Levy-Lees (Eq.3)
λ	conductivité thermique de l'air
λ	longueur de relaxation (Eq.14)
μ, ν	viscosité dynamique et viscosité cinématique
Π	fonction de sillage ($\frac{k}{2}\{\frac{u_e^*}{u_\tau} - \frac{1}{k} \ln \{R_{e_\delta} (C_f/2)^{1/2} (1-\sigma)^{1.26}\} - 5.1\}$)
ρ	densité de l'air
σ	correction pour la compressibilité ($[(\gamma-1)/2] M_e^2 / \{1+[(\gamma-1)/2] M_e^2\}$)
τ	frottement
Ω	facteur de relaxation (Eq.8)

Indices

e,o	externe
eq	équilibre
i	interne, incompressible
w	en paroi
*	valeur à l'itération précédente
'	valeur fluctuante

1_ INTRODUCTION

Le transfert de masse à travers une paroi a été utilisé intensivement pour contrôler la couche limite qui s'y développe. L'interaction d'un choc extérieur avec la couche limite réduit les performances d'un certain nombre de composants aérodynamiques en vol trans et supersonique (surfaces portantes, entrées d'air..). Si le choc est suffisamment fort la couche limite peut décoller. Il est donc très intéressant d'éliminer ou tout au moins de contrôler les phénomènes secondaires qui résultent de l'interaction (épaississement de la couche limite, transition, décollement,..) et qui engendrent des pertes importantes. Parmi les techniques utilisées, l'aspiration doit permettre à la fois de réduire ces effets mais aussi de minimiser la perturbation réfléchie, ce qui est avantageux également dans les souffleries transsoniques. Cette étude concerne l'analyse théorique et expérimentale de l'interaction d'un choc oblique avec une couche limite turbulente aspirée.

L'effet de l'aspiration sur l'interaction, tant pour éviter le décollement que pour minimiser la réflexion du choc a été peu étudié. Pour atteindre le premier objectif, on a appliqué l'aspiration à une zone limitée au décollement [1]. Pour l'autre, on a essentiellement analysé l'écoulement non visqueux [2]. Quelques approches théoriques ont été faites par la résolution des équations de Navier Stokes pour la couche limite laminaire [3] et par un modèle de triple couche pour le cas turbulent [4]. Mais, du fait des limites de ces modèles, le phénomène d'interaction avec aspiration n'a pu être décrit en détail.

L'étude expérimentale de l'interaction sur paroi poreuse avec aspiration entreprise au C.E.A.T. [5] a été poursuivie et complétée par un calcul du développement de la couche limite [6]. Après une brève description des procédures expérimentales, cette communication présente la méthode théorique mise en oeuvre et appliquée à la couche limite sur paroi pleine et poreuse, sans et avec interaction, et compare les résultats obtenus à ceux des expériences réalisées à M = 1,43.

2_ CONFIGURATION EXPERIMENTALE

La soufflerie transsonique à recyclage (extraction par éjecteur) qui a été utilisée pour l'expérience est schématisée sur la figure 1. La paroi inférieure de la veine d'essai est interchangeable. Ce peut être une paroi pleine ou poreuse. La paroi supérieure est pleine et une rampe de 3° faisant office de générateur de choc peut y être fixée. Une plaque perforée fait suite à la rampe et permet d'aspirer une certaine quantité d'air de la veine pour compenser le blocage provoqué par le déplacement des sondes de pression. Le choc se réfléchit sur la couche limite turbulente de la paroi poreuse inférieure où est pratiquée l'aspiration.

Le caisson d'aspiration, sous la paroi inférieure, est relié à la région basse pression de l'éjecteur par une canalisation rigide sur laquelle est installée une vanne de régulation. Le coefficient local de débit à travers la paroi poreuse, F, est calculé avec la relation :

$$F = \frac{\rho_w v_w}{\rho_e u_e} \qquad (1)$$

w : indice à la paroi
e : extérieur à la couche limite

La détermination d'une valeur moyenne de F n'a de sens que lorsque l'aspiration est homogène à travers la paroi poreuse, ce qui n'est pas le cas, comme nous le verrons, pour la réflexion de choc. On applique alors le loi de Darcy pour calculer le coefficient local F.

Quand le choc se réfléchit sur la paroi poreuse, la différence des pressions statiques entre la veine d'essai et le caisson varie brusquement en amont et en aval du choc. Il peut alors s'y produire un écoulement de recirculation comme schématisé sur la figure 2. Pour le limiter, on fixe une structure en nid d'abeille. Les résultats utilisés pour la comparaison avec le calcul sont ceux obtenus avec nid d'abeille.

Les parois poreuses sont fournies par la Société des Avions Marcel Dassault-Breguet Aviation qui en a développées plusieurs types. Après une série d'essais, on a choisi la paroi référencée 18.09.01 dont on montre la photographie sur la figure 3. Elle est constituée par un empilage croisé de tissus. La chaîne est en tergal et la trame en fils de bore (18 fils par cm) dont le diamètre est égal à 140 µm et la masse volumique à 2,6 gr/cm^3. Le liant est de la résine epoxy dans laquelle est trempé le tissu selon un procédé breveté. L'ouverture de la paroi est environ 8,54% de la surface totale.

Les pressions pariétales sont mesurées à travers des orifices de 0,5 mm de diamètre par l'intermédiaire d'un multimanomètre à mercure. Les tubes sont affleurants pour la paroi pleine et appuyés contre la face inférieure de la paroi poreuse. Dans ce dernier cas, ils sont maintenus en place par collage sur le nid d'abeille.

Les pressions statiques et totales dans la couche limite sont mesurées par deux capteurs à travers une sonde à deux tubes de 0,8 mm de diamètre montés sur un support commun à 10 mm l'un de l'autre. L'extrémité du pitot est applatie. Sa hauteur est 0,2 mm (0,04δ_0). Les mesures sont réalisées tous les 0,5 mm. Les erreurs de mesure ont été analysées en détail [6]. On a montré que leur cumul ne dépasse pas 1,5%. Les pressions génératrices p_t, dans le caisson p_c et de part et d'autre du diaphragme d'aspiration, sont mesurées par trois capteurs et la température génératrice T_t par un thermocouple de chromel-alumel. Les profils de nombre de Mach et de vitesse sont déduits des mesures de pression de façon classique.

On réalise des ombroscopies et des strioscopies de l'écoulement soit en lumière continue (temps de pose égal à 1/250e s) soit avec une étincelle (temps d'exposition égal à 2 µs). Des visualisations pariétales ont été également faites en utilisant un enduit de dibutylphtalate et de noir de fumée.

3. METHODE DE CALCUL

EQUATIONS GENERALES

Les équations d'une couche limite turbulente compressible sont déduites des équations de Navier-Stokes auxquelles on a appliqué la décomposition des variables $V = \bar{V} + V'$, l'hypothèse de Prandtl qui néglige les tensions normales et l'abandon d'un certain nombre de corrélations entre les quantités fluctuantes telles que $v \langle\rho'u'\rangle$ et $\langle\rho'u'v'\rangle$ petites devant $\rho\langle u'v'\rangle$. Le système s'écrit [7] :

$$
\begin{aligned}
&(\rho u)_x + (\rho v + \langle\overline{\rho' v'}\rangle)_y = 0 \\
&\rho u u_x + (\rho v + \langle\overline{\rho' v'}\rangle)\, u_y = \rho_e u_e \frac{du_e}{dx} + (u u_y - \rho\langle\overline{u'v'}\rangle)_y \\
&\rho u (C_p T)_x + (\rho v + \langle\overline{\rho' v'}\rangle)\,(C_p T)_y = -u\,\rho_e u_e \frac{du_e}{dx} + \left(\frac{\lambda}{C_p}(C_p T)_y\right)_y + \mu (u_y)^2 \\
&\qquad\qquad + (-C_p\,\rho\langle\overline{v'T'}\rangle)_y - \rho\langle\overline{u'v'}\rangle u_y
\end{aligned}
\qquad (2)
$$

On transforme alors les équations dans le plan de Levy-Lees pour tenir compte de l'épaississement de la couche limite :

$$
\xi(x) = \int_o^x \rho_e\, u_e\, \mu_e\, dx\,, \qquad n(x,y) = \frac{\rho_e u_e}{\sqrt{2\xi}} \int_o^y \frac{\rho}{\rho_e}\, dy \qquad (3)
$$

Le choix du modèle de turbulence, la loi des gaz parfaits et la relation de Sutherland permettent de fermer le système (2).

Les équations sont paraboliques avec pour conditions aux limites dans le plan physique :

- un profil initial donné,
- à la paroi : $u(x,o) = 0$, $v(x,o) = v_w(x)$, $T(x,o) = T_w(x)$,
- à l'extérieur : $u(x,y_e) = u_e$, $v(x,y_e) = 0$, $T(x,y_e) = T_e(x)$.

la vitesse extérieure u_e est calculée à partir de la distribution de pression pariétale obtenue expérimentalement.

MODELE DE TURBULENCE

On utilise un modèle algébrique pour décrire la turbulence. Il a été montré que ce type de représentation donne de bons résultats pour la couche limite turbulente au voisinage de l'équilibre. On a choisi le modèle à deux couches de Cebeci-Smith. La viscosité tourbillonnaire est exprimée différemment selon que l'on est près ou loin de la paroi :

- Couche intérieure :

$$
\varepsilon_i = \rho (k_1 y)^2\, (1 - \exp(-y/A)^2\, \left|\frac{du}{dy}\right| \qquad (4)
$$

avec

$$
A = A^+ \nu \left(\frac{\tau_w}{\rho}\right)^{1/2} \quad \text{et} \quad k_1 = 0{,}4
$$

L'expression de A^+ pour la couche limite compressible avec transfert de masse à la paroi est donnée par Marvin [8] :

$$
A^+ = 4 + 22 \exp[-0{,}591 - 0{,}0725\, F/C_f + 0{,}00357\, (F/C_f)^2]\, F/C_f \qquad (5)
$$

- Couche extérieure :

$$
\varepsilon_o = k_2\, \rho_e\, u_e\, \delta_i^*\, \gamma(y/\delta) \qquad (6)
$$

avec

$k_2 = 0{,}0168$

$\gamma(y/\delta) = [1 + 5{,}5(y/\delta)]^{-1}$

δ_i^* : épaisseur de déplacement incompressible

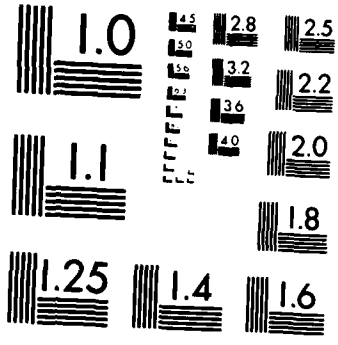
L'ordonnée y_m de la limite entre les deux couches est telle que $\varepsilon_i = \varepsilon_o$.

AD-A147 396 PROCEEDINGS OF THE CONFERENCE ON IMPROVEMENT OF AERODYNAMIC PERFORMANCE T..(U) ADVISORY GROUP FOR AEROSPACE RESEARCH AND DEVELOPMENT NEUILLY.. AUG 84 5/5

UNCLASSIFIED AGARD-CP-365 F/G 20/4 NL



END



MICROCOPY RESOLUTION TEST CHART
NATIONAL BUREAU OF STANDARDS-1963-A

RESOLUTION DES EQUATIONS

La procédure de résolution par différences finies est celle de Harris [7]. C'est une méthode semi-explicite du 2e ordre où les termes non linéaires sont fonction des deux pas précédents.

Le maillage est à pas variable en ξ et η. On obtient un pas en η serré au voisinage de la paroi en prenant une loi en puissance :

$$\Delta\eta_i = K^{i-1}\,\Delta\eta \tag{7}$$

On a choisi les valeurs suivantes :

$$\Delta\eta_1 = 5\times10^{-4}\ ,\quad K = 1{,}08$$

η_{max}, dernière valeur de η, doit être ajustée telle que $F(\eta_{max}) \geq 10^{-7}$.

Les équations de conservation d'énergie et de quantité de mouvement sont résolues simultanément afin de limiter le temps de calcul et l'équation de continuité est ensuite résolue numériquement. La résolution du système tridiagonal est faite par la méthode d'élimination des blocs. Après chaque itération, les coefficients sont recalculés pour l'itération suivante. On utilise une ligne relaxation telle que :

$$[u]_j = [u]_{j-1} + \Omega\,([u]_j^* - [u]_{j-1}) \tag{8}$$

$[u]$ étant un vecteur colonne de solutions, $[u]_j^*$ la solution du système à l'itération j et Ω le facteur de relaxation. L'itération se poursuit jusqu'à satisfaction du critère de précision. Cette relaxation permet la convergence du calcul dans le cas de forts gradients de pression ou de transferts de masse.

La linéarisation est simplifiée en utilisant les relations suivantes pour les termes non-linéaires :

$$\begin{aligned}\theta^2 &= 2\,\theta_j\,\theta_{j-1} - \theta_{j-1}^2\\ F\theta &= F_{j-1}\,\theta_j + F_j\theta_{j-1} - F_{j-1}\,\theta_{j-1}\end{aligned} \tag{9}$$

où les solutions de l'itération j-1 sont utilisées pour la j-ème itération.

La relaxation et la linéarisation des termes non-linéaires sont les deux modifications importantes que nous avons apportées à la méthode de Harris.

PROFIL INITIAL

Le schéma de différences finies de Harris pour le système d'équations paraboliques requiert deux profils initiaux. Ce sont les solutions semblables laminaires issues du système d'équations original en faisant $\xi = 0$, $\partial/\partial\xi = 0$. C'est le profil de Blasius pour le bord d'attaque.

On peut également utiliser un profil initial issu de l'expérience et préalablement lissé. Pour le profil turbulent, la diffusivité de la turbulence le fait rapidement s'adapter aux conditions limites. Une méthode courante est d'engendrer le profil initial turbulent à partir de la loi de Coles. Nous utilisons la loi de paroi-sillage de Mathews et al [9] :

$$\frac{u}{u_e} = \frac{1}{\sqrt{\sigma}}\sin\left\{\arcsin\sqrt{\sigma}\left[1 + \frac{1}{k}\,\frac{u_\tau}{u_e^*}\,\ln(y/\delta) - \frac{\Pi}{k}\,\frac{u_\tau}{u_e^*}\left(1+\cos\frac{\pi y}{\delta}\right)\right]\right\} \tag{10}$$

où σ et Π sont respectivement le facteur de correction de compressibilité et la fonction de sillage de Coles. Cette relation ne dépend que de M_e, C_f et δ. On a également utilisé cette relation pour calculer C_f et δ à partir du profil expérimental (Ref.6).

4_ APPLICATION A LA COUCHE LIMITE DE PAROI PLANE

COUCHE LIMITE SUR UNE TUYERE ET DANS LA VEINE D'ESSAI

On a calculé tout d'abord la couche limite sur la tuyère de la soufflerie utilisée pour les expériences. Le calcul d'une couche limite de tuyère nécessite de connaître ses points d'origine et de transition. On décide de procéder par essais successifs. La distribution de pression extérieure est établie à partir de la forme de la tuyère. Elle est prescrite pour la couche limite.

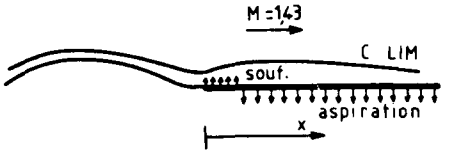
On continue le calcul en aval de la tuyère, sur le plancher de la chambre d'essai. On a représenté sur la figure 4 quatre profils de nombre de Mach pour des distances x de 88, 114, 136 et 150 mm mesurées à partir de la fin de la tuyère. Les résultats sont comparés aux mesures faites avec la sonde double statique/totale [6]. Leur concordance est bonne.

EFFET DE L'ASPIRATION - SIMULATION DES RUGOSITES

On place, en guise de plancher inférieur de la veine d'essai, la paroi poreuse AMD-BA. Deux taux d'aspiration sont appliqués à la couche limite turbulente : F = -0,0056 et -0,008 et on réalise le sondage aux quatre

positions déjà étudiées. On calcule ensuite la couche limite en utilisant comme profils initiaux ceux mesurés à la sortie de la tuyère.

Les résultats du calcul et de l'expérience sont présentés sur la figure 5. L'effet de l'aspiration modéré (F = -0,0056)prédit par la théorie (profil en ligne discontinue, fig.5a) est d'augmenter la vitesse par rapport à celle sur paroi pleine (pointillés). Les résultats expérimentaux montrent un comportement contraire pour les deux premiers profils (x = 88 et 114 mm). On en conclut que l'effet de rugosité de la paroi l'emporte tant que la couche limite n'est pas suffisamment épaisse et que les rugosités ne sont pas noyées dans la sous-couche laminaire, ce qui peut être le cas pour le troisième (x = 136) et surtout le quatrième profil (x = 150). Même avec une aspiration forte (F = -0,008 , fig.5b) le premier profil est encore déstabilisé, Voisinet [10] a montré que l'effet de rugosité était le même que celui du soufflage pour une couche limite supersonique.



Notre programme permet d'appliquer un soufflage, en début de paroi poreuse, et de l'adapter, en intensité et en longueur, de sorte que le profil de nombre de Mach calculé en x = 88 mm soit proche du profil mesuré. C'est ce que l'on obtient avec F = +0,006 et ℓ_{souffl} = 80 mm (profil en ligne continue, fig.5a et b). La correspondance théorie-expérience est remarquable pour les trois premiers profils correspondant à l'aspiration modérée. La différence observée pour le dernier peut être due au fait que l'aspiration est plus importante en aval, dans les expériences, car le caisson sous la paroi est à pression constante et l'écoulement supersonique subissant une recompression vers l'aval, le Δp d'aspiration y est donc plus fort. Les strioscopies révèlent également cette non-uniformité de l'aspiration.

Quand le taux d'aspiration augmente (F = -0,008 , fig.5b), la correspondance théorie (avec rugosités simulées) / expérience est bonne pour les deux premiers profils. Ensuite l'effet de sur-aspiration en aval se produit, plus accentué que dans le cas précédent.

On a comparé sur la figure 5c les profils calculés pour les trois cas F = 0, -0,0056 et -0,0086. Initialement (x = 88) la rugosité l'emporte sur l'aspiration pour déstabiliser le profil. Ensuite (x = 114) les profils "paroi pleine" et "aspiration forte" coïncident sauf au voisinage de la paroi où ce dernier est plus plein, ce qui entraîne un point d'inflexion. Pour x = 136 mm, c'est le cas "aspiration modérée" qui coïncide avec celui de la paroi pleine toujours dans la partie supérieure. Enfin, pour x = 150 mm l'aspiration l'emporte sur les rugosités.

Les résultats de cette première partie permettent de conclure que la méthode de calcul de la couche limite turbulente est opérationnelle tant sur paroi pleine qu'en présence de transfert de masse. Quand la paroi est rugueuse, il faut prendre en compte son état de surface. On y parvient en simulant les rugosités par injection en amont de la paroi poreuse. La distance d'injection et son taux sont ajustés par comparaison avec l'expérience du premier profil obtenu sur la paroi. Moyennant cet empirisme on peut appliquer le calcul au cas de l'interaction choc - couche limite avec aspiration.

5 ANALYSE DE L'INTERACTION ONDE DE CHOC - COUCHE LIMITE AVEC ASPIRATION

STRIOSCOPIES DE L'INTERACTION. PRESSION STATIQUE ET TAUX D'ASPIRATION

Notre objectif est de calculer le développement de la couche limite sur paroi poreuse qui interagit avec un choc oblique. Le couplage n'est pas considéré. On utilise comme donnée la pression statique mesurée sur le plancher. Le taux d'aspiration est également déduit des mesures. Avant d'analyser et d'utiliser ces résultats expérimentaux comme condition limite du calcul, il est utile de faire une description physique des trois cas d'interaction considérée, sur paroi pleine et sur paroi poreuse à un taux modéré et à un taux fort d'aspiration.

Les photographies des strioscopies par étincelle sont montrées sur les figures 6. Le choc oblique interagit avec la couche limite turbulente à une position moyenne de 110 mm. Le taux d'aspiration modéré (fig.6b) est fixé pour n'avoir d'effet qu'en aval de l'impact. Pour cela on ajuste la pression dans le caisson (p_c) égale à la pression à l'infini amont (p_∞). On constate qu'effectivement la couche limite est aspirée en aval, avec un effet croissant jusqu'à x = 150 mm. Les ondes de Mach issues des perturbations dues aux fils de bore révèlent que l'écoulement est supersonique très près de la paroi. Outre la diminution apparente de la couche limite, par rapport au cas de la paroi pleine, on remarque la pénétration plus importante du choc incident et le changement de structure du choc réfléchi et de la détente associée qui le suit. L'aspiration dite forte (fig.6c) est sentie en amont du point d'impact qui, lui-même, semble toucher la paroi. La détente réfléchie est très réduite. Dans les trois cas d'écoulement la détente issue du bord de fuite de la rampe atteint le plancher inférieur entre x = 135 et 150 mm.

Les sondages de pression statique dans la couche limite (fig.7) complètent la description strioscopique des trois cas d'interaction. La pression est généralement constante à l'exception des positions proches de l'impact du choc, x = 97 et 114 mm, où les systèmes d'ondes compression-choc-détente se font sentir.

Les distributions de pression statique sur la paroi pleine p_w et à son voisinage immédiat p_1 (premier point du sondage fig.7) sont représentées sur la figure 8a. Il y a un écart important entre p_w/p_t et p_1/p_t

en aval de l'impact du choc. La détente au bord de fuite de la rampe provoque la décroissance de la pression à partir de x = 136 mm, mais il est difficile actuellement d'expliquer la différence entre la pression mesurée à x = 136 mm par la sonde près de la paroi avec celle relevée sur le plancher au même endroit. Le sondage complet de la couche limite apportera des informations complémentaires.

La pression statique au voisinage de la paroi poreuse est représentée sur les figures 8b, c, pour l'aspiration modérée ($p_c/p_t = 0,3$ c'est-à-dire $p_c \approx p_\infty$) et l'aspiration forte ($p_c/p_t \approx 0.29$ c'est-à-dire $p_\infty - p_c \approx 7\%\ p_\infty$). Rappelons que la pression statique est mesurée sous la paroi poreuse par des tubes collés sur le nid d'abeille et dont l'orifice est au contact de la paroi.

L'aspiration modérée diminue de 40% le niveau de la surpression due à l'impact du choc, par rapport à l'interaction normale. On obtient ainsi l'effet recherché qui est de réduire la perturbation due à l'interaction. L'adjonction du nid d'abeille n'a pas beaucoup d'influence sur la distribution de pression. La pression décroît à partir de x = 136, comme pour la paroi pleine.

L'aspiration plus forte conduit à une distribution de pression statique au voisinage immédiat de la paroi très proche de la pression pariétale sur paroi pleine (inférieure de seulement 3% au point d'impact). L'adjonction du nid d'abeille provoque une décroissance plus rapide de la pression statique après le choc.

Il est difficile de calculer la valeur exacte du taux d'aspiration local, mais on sait qu'il est proportionnel à la différence des pressions de part et d'autre de la paroi poreuse selon la loi de Darcy :

$$\frac{Q}{A} = V_n = \frac{K}{\mu L}\Delta p \qquad (11)$$

où Q = taux d'écoulement volumétrique, de viscosité μ, à travers la surface d'aire A
V_n = vitesse perpendiculaire à la paroi
K = perméabilité de la paroi
L = épaisseur de la paroi
Δp = différence de pression entre les deux côtés de la paroi

Pour la paroi homogène, on peut simplificer cette équation en définissant un coefficient α caractéristique de la paroi :

$$(q_m)_{local} = \alpha(\Delta p)_{local} \qquad (12)$$

Pour la paroi considérée ici, le coefficient de transfert de masse s'exprime par :

$$F_{local} = \frac{\rho_w v_w}{\rho_e u_e} = \left(\frac{p_1(x)}{p_t} - \frac{p_c}{p_t}\right) \times (-2.8 \times 10^{-1}) \qquad (13)$$

Il est représenté sur la figure 9 pour les deux taux d'aspiration (paroi avec nid d'abeille).

PROFILS DE NOMBRE DE MACH. COMPARAISON THEORIE-EXPERIENCE

Les profils de nombre de Mach déduits des sondages de pressions et ceux obtenus par le calcul sont représentés, pour les trois interactions, sur la figure 10. Le profil initial du cas de la paroi pleine est le même que celui qui a été utilisé pour le calcul du chapitre 4. Les distributions calculées de part et d'autre du point d'impact sont moins sensibles à la perturbation de pression due à l'interaction que les mesures. En appliquant une relaxation sur la viscosité tourbillonnaire ε à partir du premier profil selon la relation de Shang et Hankey [11] : $\varepsilon_{eq} - (\varepsilon_{eq} - \varepsilon_o) \exp[-(x-x_o)/\lambda]$ (14)

où ε_o est la viscosité tourbillonnaire amont et λ la longueur de relaxation, on diminue encore la sensibilité de la pression. La méthode de calcul direct de la couche limite turbulente qui est performante quand le gradient de pression est nul ou faible ne prédit donc pas correctement la vitesse au voisinage du point d'impact du choc. La prise en compte du gradient vertical de pression, observé expérimentalement, devrait permettre d'obtenir une meilleure prédiction. Par contre, à environ 10 δ_o en aval de l'interaction (x = 150 mm) la comparaison est à nouveau excellente.

Les profils de nombre de Mach sur paroi poreuse avec aspiration modérée et forte sont représentés sur les figures 10b et c. On a simulé les rugosités par injection comme pour la couche limite de paroi plane sans interaction.

Quand l'aspiration est modérée, les effets de rugosité l'emportent et la couche limite est déstabilisée avant l'interaction : le paramètre de forme Hi calculé à partir des profils mesurés est alors proche de 2 alors qu'il valait environ 1,4 pour l'interaction sur paroi pleine (fig.11a). L'épaisseur de la couche limite et l'épaisseur de déplacement δ^* (fig.11b) décroît de façon continue, l'effet de l'aspiration se faisant sentir en aval d'avantage qu'en amont du fait de la recompression. La comparaison théorie-expérience est médiocre dans ce cas (fig.10b). L'accord est meilleur dans la partie supérieure du profil qu'en paroi où l'aspiration est surestimée en amont et sousestimée en aval par la théorie. On ne prédit pas, au point d'impact près de la paroi la tendance vers le décollement observée expérimentalement. En fait, cet écoulement se rapproche de celui de l'interaction d'un choc avec une couche limite de paroi pleine mais préalablement déstabilisé par soufflage étudié expérimentalement par Leblanc et al [5]. La modélisation d'un tel écoulement passe nécessairement par l'amélioration du modèle de turbulence, la prise en compte du couplage des écoulements visqueux et non visqueux et du gradient de pression vertical dans la couche limite.

Quand l'aspiration est plus forte, la prédiction théorique est très satisfaisante (fig.10c). Le paramètre Hi initialement inférieur à 1 décroît continuement de même que δ^*, même au point d'impact (fig.11). La contrainte imposée à la paroi joue un rôle prépondérant et le ralentissement extérieur dû au choc et imposé dans le calcul se transmet intégralement jusqu'à la paroi (x = 114 mm). La prédiction théorique est alors excellente. Il existe probablement une configuration intermédiaire entre les deux taux d'aspiration qu'il serait intéressant d'analyser comparativement à celle de l'interaction sur paroi pleine.

6_ SYNTHESE DES RESULTATS. PERSPECTIVES FUTURES

On a réalisé avec succès la modélisation de la couche limite turbulente sur une paroi poreuse avec aspiration. Les équations générales établies dans le plan transformé de Levy-Lees sont écrites à l'aide de différences finies et résolues par une méthode semi-explicite du 2e ordre. Le modèle algébrique de turbulence de Cebeci-Smith est modifié pour tenir compte du transfert de masse. La méthode est appliquée à la couche limite de paroi plane à M = 1,43. La distribution de pression statique est imposée. Les résultats sont en très bon accord avec les mesures faites sur un plancher poreux d'une soufflerie à recyclage du C.E.A.T. Pour obtenir cette bonne correspondance, il est nécessaire, dans le calcul, de simuler l'effet des rugosités par un soufflage en amont de la zone d'aspiration. Un modèle de turbulence prenant en compte à la fois les rugosités et le transfert de masse devrait permettre de généraliser la méthode.

On a étudié trois cas d'interaction d'un choc oblique créé par une déviation de 3° à M = 1,43, avec la couche limite turbulente du plancher de la soufflerie équipée de parois pleine et poreuse. Les mesures de pressions et les visualisations peuvent être synthétisées pour fournir une schématisation des écoulements, figure 12. Dans les deux premiers cas, le système des ondes de compression et de détente, de même que le choc incident, pénètrent dans la couche limite jusqu'à la ligne sonique (comparaison des visualisations et de la ligne sonique établie par interpolation des profils de Mach). La différence entre les sytèmes d'ondes figures 12a et b, résulte de l'effet observé et mesuré de l'aspiration sur l'évolution de l'épaisseur de la couche limite, de la vitesse et de la position de la ligne sonique.

Notre interprétation du système d'ondes sur paroi pleine est plus proche de celle de Squire et Smith [12] que celle de Henderson [13]. Par une analyse potentielle de propagation d'ondes dans un milieu de densité variable, celui-ci aboutit à un choc en λ sur la ligne sonique discontinue, ce que nous n'observons pas et semble physiquement peu réaliste. La réfraction du choc conduirait alors à un choc ou une détente réfléchis selon les conditions amont et le gradient de densité. Squire et Smith pensent que le choc se réfléchit sur la ligne sonique comme sur une frontière libre produisant une détente dirigeant l'écoulement vers la paroi qui le redresse et provoque une recompression. Cette description est cohérente. Dans notre cas, la partie subsonique continue à s'épaissir après la réflexion (effet de déstabilisation du choc incident), bien que la couche limite s'amincisse et on ne voit pas nettement l'onde de recompression qui doit suivre l'éventail de détente.

Avec aspiration modérée (fig.12b), les rugosités rendent la couche limite en amont de l'interaction plus épaisse que celle de paroi pleine. On trouve alors une similitude avec les modèles d'interaction destabilisée de Leblanc et al [5] et Squire et al [12]. Ici, la couche limite épaissie n'est pas décollée ($H_i < 2.0$). Le gradient de pression en amont du choc provoque peu d'épaississement et donc peu de compression observable. Le gradient de densité à travers la couche limite est moins fort que celui de la paroi pleine et la courbure du choc incident est donc plus faible. Le choc incident est réfracté en ondes de compression qui se focalisent en choc réfléchi. L'influence amont de l'interaction s'étale d'avantage que dans le cas de la paroi pleine, comme le montre la distribution de pression pariétale. La partie subsonique reste d'épaisseur presque constante, elle tend même à diminuer déjà avant l'impact du choc, dès que l'augmentation de pression statique est suffisante pour augmenter l'effet de l'aspiration. On peut considérer que l'effet de gradient de pression adverse et celui de l'aspiration se compensent et maintiennent l'épaisseur de la couche limite constante. Seule la partie basse montre l'influence de l'aspiration. Comme la couche limite est continuellement aspirée après le point d'impact, l'écoulement est accéléré et l'intensité de la détente est plus forte que sur paroi pleine. La réflexion du choc incident est donc modifiée par l'aspiration. Il y a des points communs avec le cas du choc incident sur une déviation divergente de la paroi étudié par Chew [14]. Cependant, notre modèle, à la différence de celui de Chew, révèle la présence physique des ondes choc-détente réfléchies qui s'annulent.

Avec aspiration forte (fig.12c) la couche limite est déjà aspirée en amont de l'interaction, elle est très mince et le modèle de réflexion ressemble à celui du cas non-visqueux. L'éventail des ondes de compression réfléchies est peu ouvert et convergent rapidement avec la détente pour former le choc réfléchi. La réflexion se fait au voisinage immédiat de la paroi, la partie subsonique de la couche limite étant très mince. Cependant, elle continue à épaissir, même avec l'aspiration. Juste après l'impact, il y a accélération de l'écoulement extérieur et la pression statique décroît très vite. Cependant, du point de vue de la réduction des effets de réflexion de choc, l'aspiration modérée est plus efficace.

La méthode de prédiction de l'interaction qui calcule la couche limite avec gradient de pression imposée est satisfaisante pour les deux cas extrêmes : paroi pleine et aspiration forte. Elle révèle ses défauts quand l'aspiration est modérée. D'une part, les rugosités ont un effet déstabilisateur important et doivent être considérées dans le modèle de turbulence. D'autre part, le gradient de pression à travers la couche limite qui n'est pas négligeable dans la région du point d'impact doit jouer un rôle important sur la couche limite déstabilisée. Il faut aussi prendre en compte le couplage entre les écoulements visqueux et non visqueux. Ces différents points sont actuellement à l'étude [15,16].

REFERENCES

1. Wong,W.F. : The application of Boundary Layer Suction to Suppress Strong Shock-Induced Separation in Supersonic Inlets.
   A.I.A.A. paper No 74-1063, 1974
2. Vayssaire,J.C. : Absorption d'ondes de choc par des parois poreuses homogènes.
   L'Aéronautique et l'Astronautique, No 47, 1974, pp.85-88
3. Tassa,Y. and Sankar,N.C. : Effect of Suction on a Shock-Separated Boundary Layer. A Numerical Study.
   A.I.A.A. J. vol.17, Nov.1979, pp.1268-1270
4. Inger,G.R. and Zee,S. : Transonic Shock-Turbulent Boundary Layer Interaction with Suction and Blowing.
   J. Aurcraft, vol.15, 1978, pp.750-754.
5. Leblanc,R., Antonio ,B. and Lee,D.B. : Interaction avec transfert de masse.
   C.E.A.T. Poitiers, contrat DRET 80/601, rapport final, 1980.

6. Lee,D.B. : Etude de l'interaction onde de choc - couche limite turbulente sur paroi poreuse avec aspiration.
Université de Poitiers, Thèse de Docteur-Ingénieur, avril 1983.
7. Harris,J.E. : Numerical Solution of the Equations for Compressible Laminar, Transitional and Turbulent Boundary Layers and Comparisons with Experimental Data.
NASA TR R-368, 1971.
8. Marvin,J.G. : Turbulent Modeling for Compressible Flows.
NASA TM X-73-188, 1977.
9. Mathews,D.C., Childs,M.E. and Paynter,G.C. : Use of Cole's Universal Wake Function for Compressible Turbulent Boundary Layers.
J. Aircraft, vol.7, No 2, 1970, pp.137-140.
10. Voisinet,R.L.P. : Combined Influence of Roughness and Mass Transfer on Turbulent Skin Friction at M=2.9.
A.I.A.A. paper 79-003,1979.
11. Shang,J.S. and Hankey,W.C. : Numerical Solution of the Navier-Stokes Equations for Compressible Ramp.
A.I.A.A. J., Vol.13, 1975, pp.1368-1374.
12. Squire,L.C. and Smith,M.J. : Interaction of a Shock Wave with a Turbulent Boundary Layer Distrubed by Injection.
Aero. Quat., vol.XXXI, part 2, 1980, pp.85-112.
13. Henderson,L.F. : The Reflection of a Shock Wave at a Rigid Wall in the Presence of a Boundary Layer.
J.M.F., vol.30, 1967, pp.699-722.
14. Chew,Y.T. : Shock Wave and Boundary Layer Interaction in the Presence of an Expansion Corner.
Aero. Quat., 1979, pp.506-527.
15. Stasinopoulos,A. : Etude d'une couche limite turbulente compressible sur une paroi poreuse et rugueuse.
C.E.A.T.-E.N.S.M.A., Poitiers, D.E.A. d'Energétique, Septembre 1982.
16. Aymer de la Chevalerie,D. : Algorithme de couplage inverse pour le calcul d'une interaction onde de choc - couche limite.
C.R.Ac.Sc. Paris, t.297 (26 sept.1983), Série II, pp.189-192.

REMERCIEMENTS

Ce travail a été effectué avec le soutien financier de la Direction des Recherches, Etudes et Techniques du Ministère de la Défense (contrat n°80/601). Les auteurs remercient R. PROUST pour sa contribution au programme de calcul, P. ARDONCEAU, D. AYMER de la CHEVALERIE du C.E.A.T. ainsi que M. VAYSSAIRE, de la Société des Avions Marcel Dassault - Breguet Aviation, pour les discussions intéressantes qu'ils ont eues avec eux.

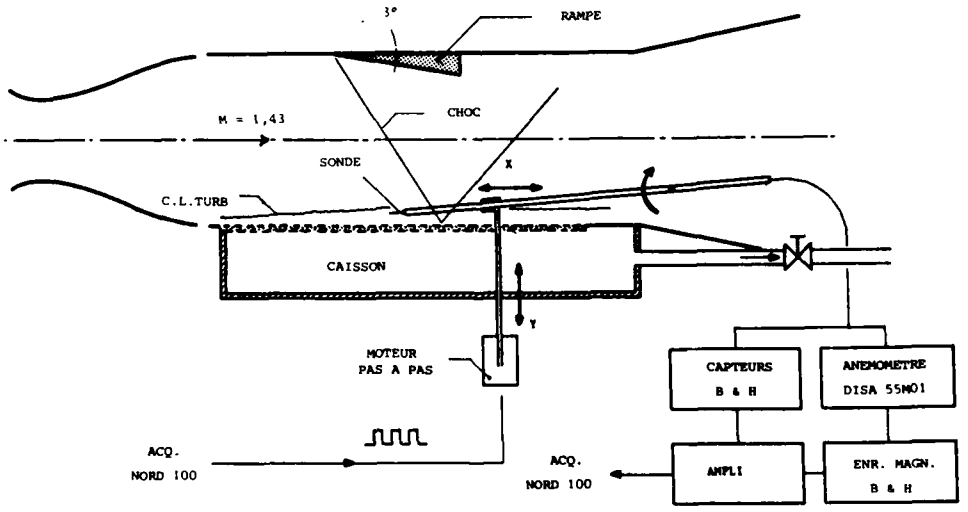


Fig.1 - Schéma du montage en soufflerie

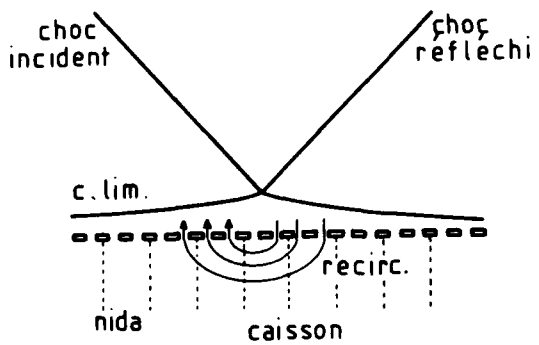


Fig.2 - Problème de la recirculation



Fig.3 - Paroi AMD-BA

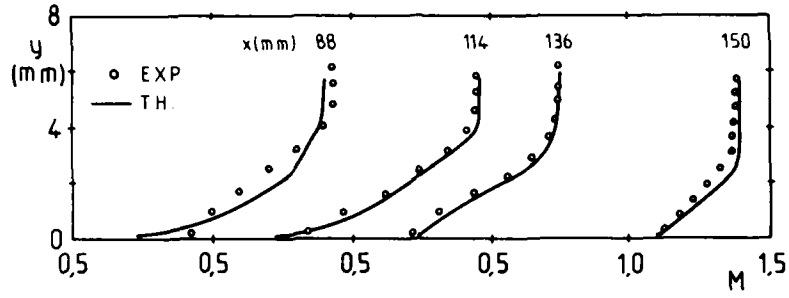
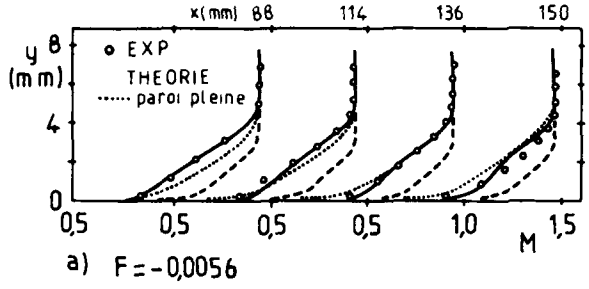
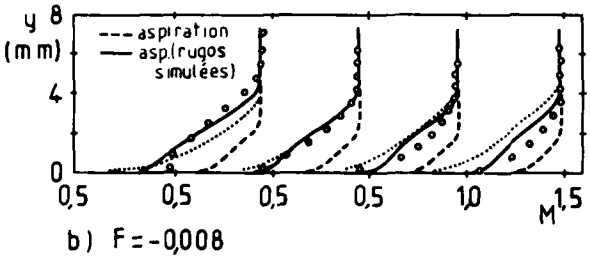


Fig.4 - Profils de nombre de Mach sur paroi pleine





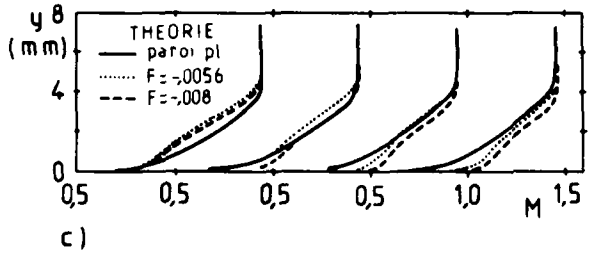
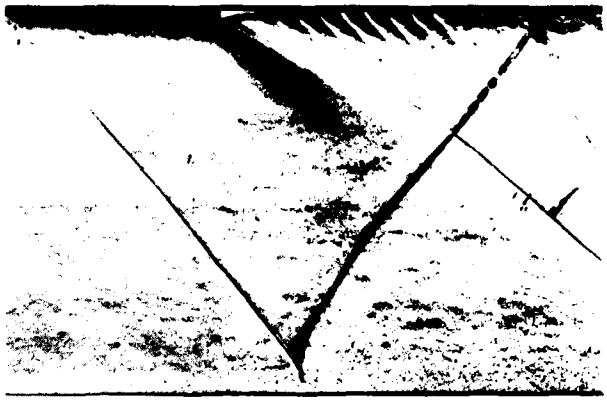
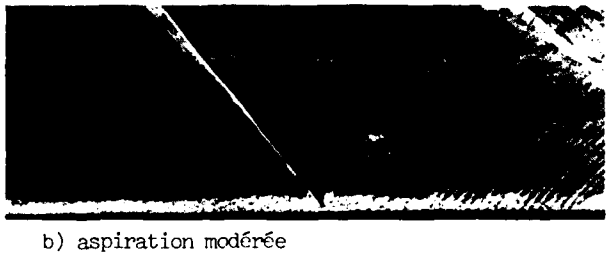


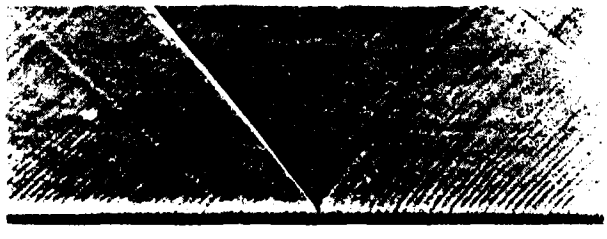
Fig.5 - Effet de l'aspiration sur paroi plane



a) paroi pleine



b) aspiration modérée



c) aspiration forte

Fig.6 - Visualisations strioscopiques

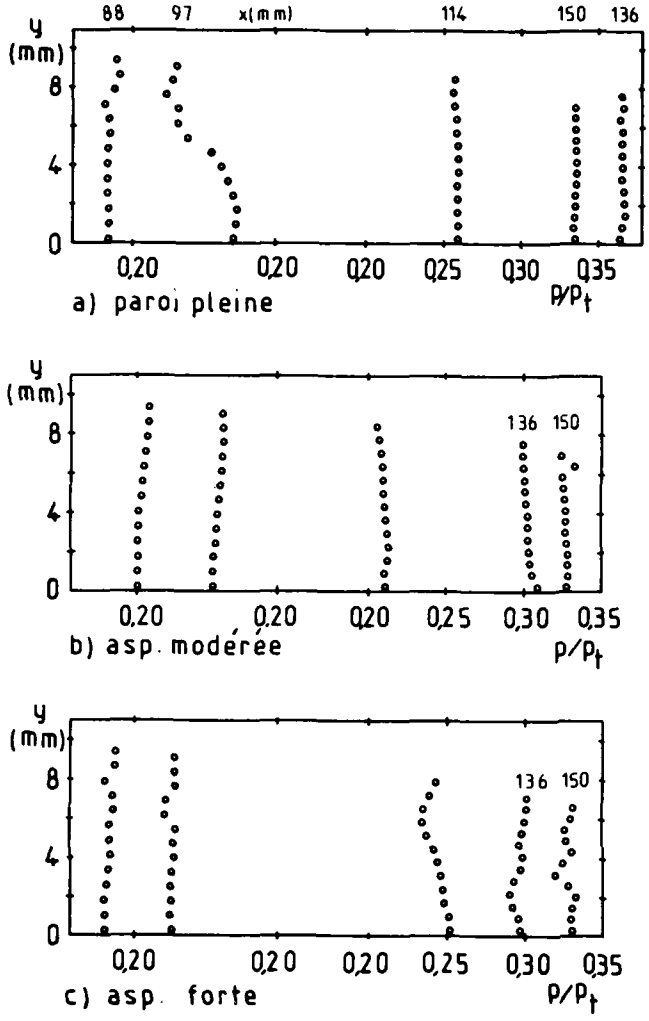


Fig.7 - Sondage de pression statique

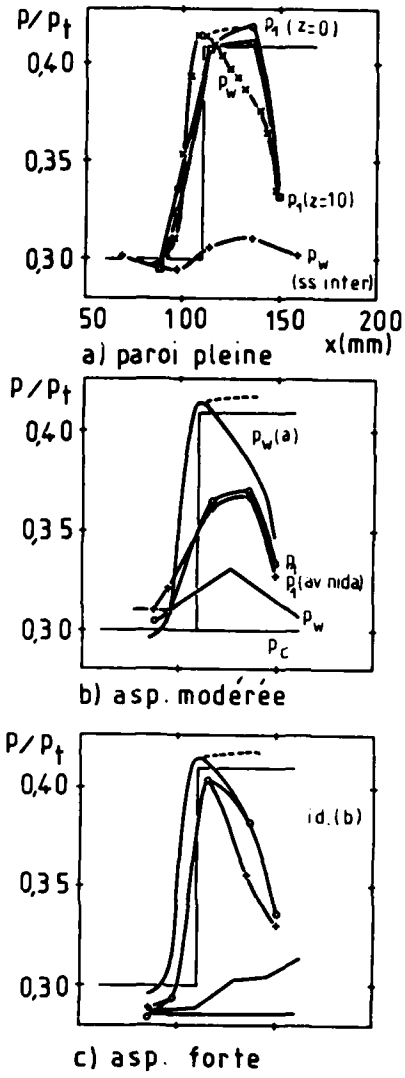


Fig.8 - Pression pariétale

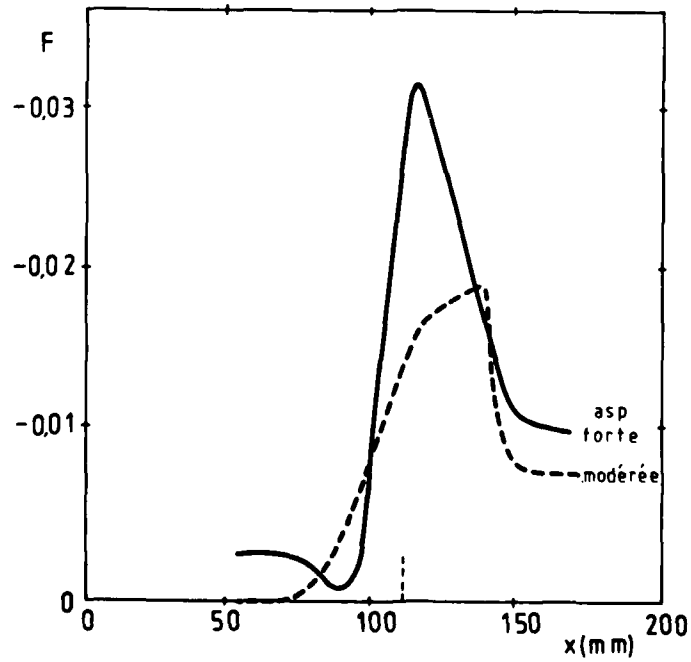


Fig.9 - Taux d'aspiration dans l'interaction

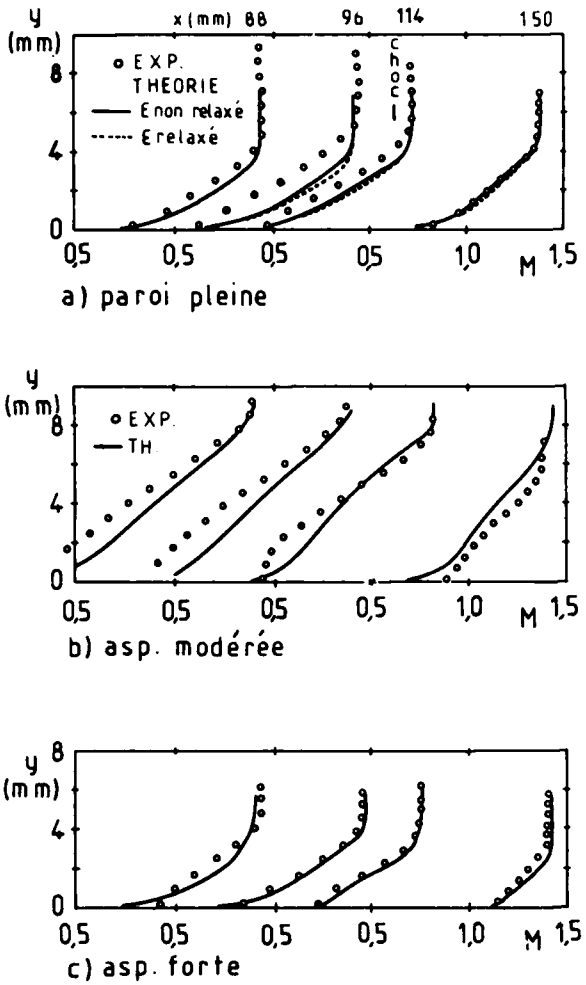


Fig.10 - Profils de nombre de Mach (interaction)

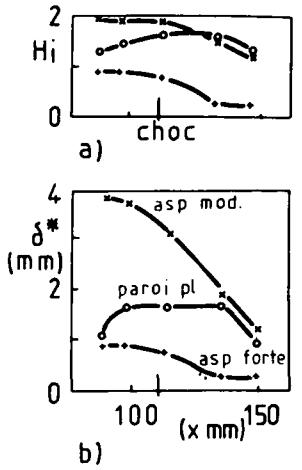
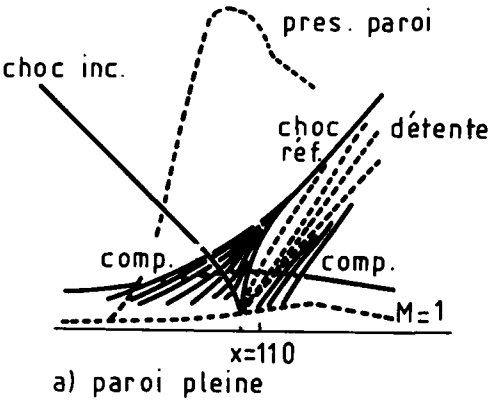
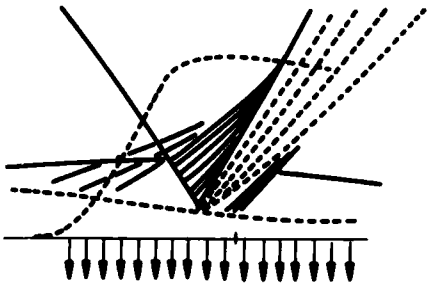


Fig.11 - Paramètre de forme et épaisseur de déplacement





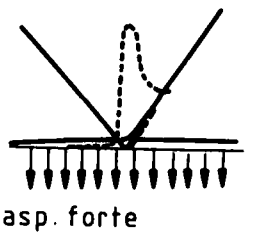


Fig.12 - Schématisation des écoulements

AD-P004 070

ACTIVE AND PASSIVE SHOCK/BOUNDARY LAYER INTERACTION CONTROL ON SUPERCRITICAL AIRFOILS

P. Thiede*
Messerschmitt - Bölkow - Blohm GmbH
Transport Aircraft Division
D-2800 Bremen 1, Hünefeldsstraße 1-5, Germany

P. Krogmann+, E. Stanewsky++
Deutsche Forschungs- und Versuchsanstalt für Luft- und Raumfahrt e.V.
Institut für Experimentelle Strömungsmechanik
D-2400 Göttingen, Bunsenstraße 10, Germany

SUMMARY

Experimental investigations ~~are presented, aiming at the improvement in~~ the off-design performance of supercritical airfoils by active or passive control of the shock/boundary layer interaction (SBLI) through boundary layer suction in the shock region or ventilation respectively.

The experiments were carried out in the DFVLR ~~1m x 1m~~ Transonic Windtunnel Göttingen, ~~(TWG),~~ using the advanced supercritical airfoil VFW VA-2 designed to have a largely fixed shock position at off-design conditions. The basic model was equipped with an exchangeable control device within the shock region to allow measurements with either surface clean, suction through a single slot, double slot or perforated strip or ventilation through a double slot or perforated strip. The effectiveness of the different SBLI control methods is evaluated from surface pressure distribution, wake and boundary layer measurements as well as Schlieren observations.

It is shown that local boundary layer suction in the shock region mainly delays the shock-induced separation to greater shock strength and stabilizes the shock in its rearward position up to higher incidence, resulting in substantial improvements in the airfoil characteristics at off-design conditions. Moreover, without any suction, a favourable passive effect is observed by boundary layer ventilation on the double slot and perforated strip configurations with a plenum underneath. This leads to a weakening of the shock wave, offering a large potential for off-design drag reduction especially.

1. INTRODUCTION

Major improvements in aircraft performance have been reached by the use of supercritical wings characterized by an extended supersonic flow field on the upper surface at subsonic speeds. At design condition, the supersonic flow field is terminated by a nearly isentropic recompression minimizing the airfoil drag. In the off-design case however, e.g. at higher free-stream Mach number or incidence, a compression shock wave occurs at the end of the supersonic zone, resulting in a drag rise due to a higher viscous drag and an additional wave drag. The shock strength depends on the deviation from the design condition.

An important effect of the shock wave arises from the substantial thickening of the boundary layer in the shock region, which increases significantly the boundary layer thickness at the trailing edge too, enhancing the separation tendency there and magnifying the viscous lift loss via the Kutta condition, Fig. 1. At stronger shocks, a shock-induced separation bubble or/and trailing edge separation may occur, altering completely the flow field around the airfoil. Pearcy (Ref. 1) and recently Stanewsky (Ref. 2) have given a detailed description of the complex interaction phenomenon between the shock wave and the boundary layer flow on supercritical airfoils affecting the off-design performance. Furthermore, the shock-induced flow separation occuring with increasing Mach numer or/and incidence leads to rapid drag rise and buffet onset, both restricting the off-design region of supercritical airfoils.

Because of the key role of the shock/boundary layer interaction (SBLI) in the off-design performance, it is nearby to control the shock/boundary layer interaction by active or passive means with the objective to delay the shock-induced flow separation and thus to reduce the shock-induced drag and to extend the off-design boundaries. This may be accomplished

---

* Prof. Dr.-Ing., Head of Viscous Flow Dept.
\+ Dr.-Ing., Research Scientist
\++ Dr.-Ing., Head of High Speed Branch

- either actively by tangentially blowing (Ref. 3) or boundary layer suction through a slotted or perforated wall in the shock region (Refs. 4 to 8)
- or passively by boundary layer ventilation through a slotted or perforated wall with a plenum located underneath.

In this scope, the passive effect is reached by a partial pressure compensation between the sub- and supersonic flow regions causing blowing upstream and sucking downstream of the shock. But the installation of an efficient SBLI control device in a supercritical wing requires a wing section shape with a largely fixed shock position at off-design conditions, as realized in advanced airfoil design (e.g. Ref. 9).

The objective of the present experimental investigations was to study the effects of both active SBLI control by boundary layer suction through either a single slot, a double slot or a perforated strip and passive control by boundary layer ventilation through either a double slot or a perforated strip, positioned in the shock region, on the flow characteristics of a modern supercritical airfoil at off-design conditions.

The present paper summarizes results of active SBLI control, published partially in Refs. 4 to 8, 16 and 17 already, as well as results of passive control obtained more recently.

2. TEST SET-UP

The experimental investigations were carried out in the 1m x 1m Transonic Windtunnel Göttingen (TWG) of the DFVLR, using the two-dimensional supercritical airfoil VFW VA-2 designed for $M_\infty = 0.75$ and $c_L = 0.53$. This airfoil was chosen for the installation of the SBLI control device, because of its small shock shifting at off-design conditions, and furthermore extensive experimental data are available for the basic airfoil without SBLI control (Refs. 10 and 11).

The basic model was equipped with an exchangeable insert in the shock region for measurements with either surface clean (without control), boundary layer suction through a single slot, a double slot or a perforated strip or ventilation through a double slot or a perforated strip, Fig. 3. The insert is placed at the shock position for the off-design Mach number $M_\infty = 0.78$ ($Re_\infty = 2.5 \times 10^6$, transition fixed). Details of the model configuration equipped with the single slot insert are shown in Fig. 4. The slot width s = 0.6 mm was designed for a suction coefficient of $c_Q = 0.0006$. The suction duct within the model, seen in the top view in Fig. 4 with the insert removed, was made conically in order to get a nearly constant duct velocity. Fig. 5 shows details of the model equipped with the perforated strip insert for active and passive SBLI control. The insert, in which a s = 15 mm wide perforated strip is cemented, separates a plenum from the suction duct by a web containing throttling holes. The hexagonal electron-beam drilled perforation, with a d = 0.3 mm hole diameter and a a = 1 mm hole distance, has an opening of 8.16 %.

Fig. 6 shows the general arrangement of the 2-D model in the tunnel for surface pressure distributation, wake traverse and boundary layer probe measurements as well as Schlieren observations. The model with a c = 200 mm chord length and a b = 1 m span was fixed at both ends in rotable plates, embedded in the test section walls in order to change the angle of attack. The part of the model equipped with the SBLI control device has a span of 500 mm. In the symmetry plane, the pressure distribution was measured at 54 positions around the airfoil. The airfoil lift was obtained by integration of the measured pressure distribution. The two-dimensionality of the flow was checked on the upper surface by two additional rows of chordwise pressure taps, each 200 mm of the symmetry plane. The airfoil drag was evaluated from wake measurements two chordlength downstream of the trailing edge. The boundary layer measurements were made in a chordwise plane 50 mm of the symmetry plane by a combined pitot-static-directional probe. The buffet onset was determined from the RMS-value recognizing a steep increase of the model wing root bending moment, and from Schlieren observations of the upper surface flow field. All test and data reduction procedures are described in Ref. 12.

The 1m x 1m Transonic Windtunnel Göttingen (TWG) of the DFVLR is a pressurized closed-circuit continuos working tunnel with 6 % open perforated test section walls, described in Ref. 13, allowing independent Reynolds and Mach number variations. Fig. 7 shows the test set-up in the TWG. In the side view, the suction tube fixed on both sides of the airfoil model is visible. The suction unit is computer controlled. In these tests, the suction coefficient could be varied in the range of $0 \le c_Q \le 0.0012$. The boundary layer probe with the probe drive unit, shown in the front view, was mounted independently of the model at the sting, which usually serves for supporting complete aircraft models.

During the tests, extensive surface pressure distribution, wake traverse and boundary layer probe measurements as well as Schlieren observations were performed on the four model configurations described in Fig. 3. In most active control experiments, the suction coefficient was kept constant $c_Q = 0.0006$, but in some cases it was also varied between $c_Q = 0.00045$ and 0.0012. The SBLI control device was designed for the off-design Mach numbers of $M_\infty = 0.78$, however the Mach numbers covered during the experiments ranged in some cases from $M_\infty = 0.6$ to 0.86. The Reynolds number, based on the chord length, was held approximately constant at $Re_\infty = 2.5 \times 10^6$ for all Mach numbers tested. In order to simulate more realistic flow conditions, boundary layer transition was fixed at 30 % chord on the upper and at 25 % chord on the lower surface.

3. RESULTS AND DISCUSSIONS

From the large number of experiments performed since 1979, only a few typical results of active and passive SBLI control shall be presented and discussed here.

3.1 Active SBLI control by suction

First, the effects of active SBLI control by suction through

- a single slot
- a double slot
- and a perforated strip

in the shock region of the VFW VA-2 supercritical airfoil will be described and compared.

3.1.1 Global effects

Before analysing the flow over the airfoil in some detail, let us begin with the global effects. Fig. 8 shows the influence of boundary layer suction in the shock region of the three model configurations on the lift coefficient of the VFW airfoil at various Mach numbers. In comparison with the basic closed-wall configuration without control, not only pronounced differences can be observed for all suction variants at off-design conditions, but also marked deviations occur between the various suction configurations. On the contrary, at low angles of attack these differences are small. The single slot suction model, tested only at $M_\infty = 0.78$, proves to be most effective. With slot suction the lift rise can be continued beyond the buffet boundary so that a maximum lift increase of about 25 % is obtained at a suction coefficient of $c_Q = 0.0006$. Stronger suction causes only a slightly higher lift increase, not shown here. But the positive single slot suction effects are restricted to a very limited Mach numer range in which shock and slot position match well. This disadvantage can be avoided by double slot suction showing similarly positive effects in the entire Mach number range tested. It is remarkable, that with the exception of $M_\infty = 0.78$ and 0.8 no distinct lift maximum appears in the double slot suction case. In contrast to this, suction through a perforated strip shows to be not as effective as double slot suction in the lower Mach number range but superior to the latter one at higher Mach numbers.

Also the drag of the VFW airfoil is most favourably affected by suction in the shock region, as the comparison of the drag coefficients of the three suction configurations with the basic airfoil without suction demonstrates, Fig. 9. Single slot suction, tested solely at $M_\infty = 0.78$, reduces the drag only at higher angles of attack. On the contrary, double slot suction leads to drag reductions even at low angles of attack. Furthermore, the steep drag rise is largely avoided by double slot suction, and at higher incidence, the drag is reduced drastically up to 40 %. For suction through a perforated strip, the drag coefficients measured only for two Mach numbers and a few angles of attack indicate reductions in the same order as for double slot suction.

Fig. 10 shows the influence of local suction in the shock region of the three configurations on the buffet boundary of the VFW airfoil,determined from the RMS-signals. A strong buffet onset delay was found in the case of single slot suction at $M_\infty = 0.78$, where shock and slot position are well matched, but this positive effect is restricted to a very limited Mach number range. Double slot suction, on the contrary, leads to a smaller but over the entire investigated Mach number range existing delay of buffeting. It is remarkable, that for this suction configuration the buffet intensity was decreased with increasing Mach number, and that at $M_\infty > 0.82$ buffeting couldn't be detected at all. Suction through a perforated strip shows to have not any positive effect on the buffet boundary at low Mach numbers up to $M_\infty = 0.74$, but at higher Mach numbers $0.78 < M_\infty < 0.84$ it even surpasses the double slot suction. However, with suction the buffet intensity of the perforated strip configuration did not vanish.

3.1.2 Local effects

After demonstrating the effects of various active SBLI control methods on the overall aerodynamic characteristics of the VFW airfoil, the influence of local boundary layer suction in the shock region on the flow field structure of the airfoil will be analysed in more detail. Especially, an attempt will be made to give reasons for the strong suction effects on the airfoil characteristics described in the previous chapter.

The preceding figures have shown, that the largest improvements over the basic closed-wall model were gained in the region of the off-design boundaries caused by shock-induced flow separations. Hence, boundary layer measurements were made on the upper surface of the basic and the three suction configurations at $M_\infty = 0.78$, for which the suction device was placed to fit best the shock position.

Some remarks have to be made concerning the quality of the boundary layer probe measurements conducted in a transonic tunnel on an airfoil model of moderate size. In the attached flow region upstream of the shock, the boundary layer displacement thickness is of the same order as the probe used (0.15 mm high flattened pitot tube), resulting in inaccurate results. Further downstream in the shock region, the probe-induced disturbances may be rather large, leading also to incorrect results. Finally, a pitot probe is not able to measure reverse flow velocities within a separation bubble.

The effect of single slot suction on the pressure distribution and the upper surface boundary layer development is shown in Fig. 11 for $M_\infty = 0.78$ and both incidences $\alpha_g = 4°$ and 5° corresponding to the onset of buffeting without and with suction respectively. In the first case, $\alpha_g = 4°$, the measured pressure distributions with and without suction differ only in the shock region, which can be better understood with the measured boundary layer velocity profiles, Fig. 12, and the displacement thickness data. The pressure distribution without suction shows a shock located slightly upstream of the slot, the existence of a shock-induced separation bubble about to expand rapidly, and a still attached trailing edge flow. With suction, the boundary layer thickness is considerably reduced and the separation bubble has disappeared, affecting the entire downstream flow development. As a consequence of the shock/boundary layer interaction, the shock is located further downstream close to the slot with increased strength. Larger shock strength and thinner boundary layer result in additional wave drag and higher friction drag, which are, however, more than compensated by pressure drag reductions, Fig. 9.

At higher incidence, $\alpha_g = 5°$, the upper surface pressure distribution and boundary layer development is completely different in both cases with and without single slot suction, Fig. 11, as is also evident from the measured boundary layer velocity profiles, plotted in Fig. 13. Without suction, the buffet boundary has been clearly exceeded, and the pressure distribution shows the shock far upstream of the slot, while the shock-induced flow separation reaches downstream to the trailing edge, indicated by the negative trailing edge pressure coefficient and the extreme boundary layer thickening at the rear part of the airfoil. With single slot suction applied, the supersonic flow is accelerated to a local Mach number of $M_e = 1.44$ at the slot, causing without suction at that Mach number severe separation behind the shock. But in the suction case, only a local separation bubble is induced similar to that at $\alpha_g = 4°$ without suction; and the trailing edge flow is still attached. The single slot suction effect on the pressure distribution causes corresponding changes in lift, Fig. 8, and buffet onset, Fig. 10; and the reduced flow separation results in a considerable net drag reduction, Fig. 9.

Fig. 14 shows the influence of SBLI control by double slot suction on the pressure distribution and the upper surface boundary layer development for $M_\infty = 0.78$ and $\alpha_g = 4°$ and 5° corresponding to the onset of buffeting without and with control respectively. At $\alpha_g = 4°$, the pressure distribution is affected by double slot suction only in the shock region. In both cases, with and without control, the shock is located immediately upstream of the front slot, and the trailing edge flow is attached. But with control, the measured boundary layer data indicate a significantly stronger boundary layer thickening within and behind the shock region, resulting in a considerably more diffused smearing of the pressure rise across the shock. This behavior is a consequence of the common plenum for both suction slots, leading to different suction rates of the slots due to the pressure gradient in the shock region, and in this case even to blowing instead of sucking of the front slot and increased suction of the rear slot. This additional passive effect will be discussed in more detail in the next chapter. As a result of the weaker shock and the thicker boundary layer over the rear part of the airfoil, wave drag as well as friction drag is reduced to an amount which is not nearly compensated by increased pressure drag, see Fig. 9.

At higher incidence, $\alpha_g = 5°$, SBLI control by double slot suction has a large effect on the upper surface boundary layer development and thus on the pressure distribution. Without control, the upper surface flow is in a condition beyond the buffet boundary and has the typical behavior discussed already in Fig. 11, while in the control case, the measured data indicate indeed a large separation bubble induced behind the shock but attached flow at the trailing edge. The pressure distribution with a shock located immediately upstream of the front slot is very similar to that at $\alpha_g = 4°$ without control. The more rearward shock position with active control is responsible for the increased lift coefficient and the extended buffet boundary, Figs. 8 and 10; and the reduced flow separation leads to drastical net drag reductions, Fig. 9. However, so far it is not completely understood why the buffet intensity decreases when the double slot suction is employed.

Unlike the slot suction, the electron-beam drilled perforated strip provides a distributed suction in the shock region. However, the suction distribution of the perforated strip is not constant in streamwise direction because of the strong pressure gradient in this region, leading to blowing instead of sucking in the forward part of the strip at a suction coefficient of $c_Q = 0.0006$. The SBLI control effect by suction through a perforated strip on the pressure distribution and the upper surface boundary layer is shown in Fig. 15 for $M_\infty = 0.78$ and the angles of attack $\alpha_g = 4°$ and 5° corresponding to buffet onset without and with control respectively. At both incidences, the changes of the upper surface pressure distribution and boundary layer development caused by suction on the perforated strip model are very similar to those obtained with the double slot model, Fig. 14. In comparison with the double slot results, it seems that the shock flattening is more intense and the boundary layer thickening in the shock region is less strong. At lower Mach numbers, $M_\infty < 0.78$, the positive strip suction effects vanish, because the shock is located too far upstream of the perforated strip. At higher Mach numbers, $M_\infty > 0.78$, the airfoil performance improvements by strip suction are sligthly higher due to its better adapted SBLI control than in the double slot suction case.

3.2 Passive SBLI control by ventilation

During the measurements, a strong passive effect was observed on the double slot and perforated strip models without any suction in comparison with the basic closed-wall model. In experiments

of Bahi et al. (Ref. 14) a 30 % chord porous surface with a cavity underneath was used, to reduce the wave drag of a circular arc and a supercritical wall model (without lift) by weakening the shock strength. Preliminary investigations with the objective to suppress completely shocks on a transonic airfoil were made by Savu et al. (Ref. 15) using a perforated upper surface with a cavity underneath reaching nearly from the leading to the trailing edge.

In the following, results of passive SBLI control by ventilation through

- a double slot
- and a perforated strip

in the shock region of the VFW airfoil covering only 7.5 % of the chordlength will be described and discussed.

3.2.1 Global effects

Before analysing details of the complex flow development over the airfoil with passive SBLI control, global effects will be treated. In Fig. 16 lift polars of both models equipped with the double slot and the perforated strip insert are compared at various Mach numbers with the basic model results without ventilation. For the double slot configuration, a favourable passive effect was obtained at off-design conditions at all Mach numbers tested showing no distinct lift maxima. For the perforated strip configuration, on the contrary, the measured lift maxima at low Mach numbers $M_\infty < 0.76$ are lower than without control, but in the higher Mach number range the maximum lift coefficients are considerably increased.

Passive SBLI control by boundary layer ventilation offers a large potential for drag reductions of supercritical airfoils at off-design conditions, demonstrated in Fig. 17 for the double slot and the perforated strip model. Even at low incidence, the drag coefficient is slightly decreased in comparison with the basic model. However, at off-design conditions with strong shock/boundary layer interactions, great drag reductions - about in the same order as measured in Ref. 14 - are obtained for both the double slot and the perforated strip configurations.

Fig. 18 shows substantial improvements of the lift/drag polars of the VFW airfoil, characterizing the aerodynamic quality, by passive SBLI control through boundary layer ventilation in the shock region using both the double slot and the perforated strip at various Mach numbers. Not only in the off-design region with strong shocks, substantial improvements in L/D could be obtained, but also the optimum L/D-ratio could be improved by about 15 %. From the few perforated strip test cases, it seems that this configuration is more effective than the double slot configuration. The results presented show the passive control to be very attractive.

The passive effect of the double slot and the perforated strip devices on the buffet boundary of the VFW airfoil is demonstrated in Fig. 19. The double slot device increases the buffet boundary in the entire Mach number range tested. With perforated strip ventilation applied, at lower Mach numbers $M_\infty < 0.78$ no effect at all on buffet onset was found, whereas in the higher Mach number range $0.78 < M_\infty < 0.84$ even the double slot suction results were surpassed. However, the most striking result of the double slot experiment was, that in the Mach number range investigated, in contrary to the other configurations, neither shock oscillations could be detected in Schlieren observations beyond the buffet boundary, nor severe buffeting was indicated by the RMS-signals. Moreover, buffeting was completely ceased at $M_\infty > 0.82$, although the flow was separated downstream of the shock. It seems that the strong coupling between shock and trailing edge flow behavior is largely suppressed by double slot ventilation.

By comparing the results of passive SBLI control with those of active control, as done in Refs. 16 and 17, it can be established that the passive effects are dominant for the configurations investigated. Compared to active control, only a slightly lower improvement in off-design performance but a clearly smaller extension of the buffet boundary was obtained by passive control.

3.2.2 Local effects

Now, the attempt will be made to interpret the strong passive effects of the double slot and perforated strip devices on the overall aerodynamic characteristics of the VFW airfoil by means of the pressure distribution and boundary layer measurements performed during the experimental investigations. Fig. 20 shows the influence of double slot ventilation on the pressure distribution and the upper surface boundary layer development for $M_\infty = 0.78$ and the angles of attack $\alpha_g = 4°$ and $5°$ corresponding to buffet onset without and with passive control respectively. In the first case, $\alpha_g = 4°$, the pressure gradient in the shock region is definitely flattened and the boundary layer is much more thickened, resulting in considerable airfoil drag reductions.

This passive effect is caused by a partial pressure compensation through the plenum underneath the shock between the sub- and supersonic flow fields. Due to the strong pressure gradient in the shock region, a secondary flow develops leading to blowing of the forward slot and sucking of the rearward slot. As a consequence of the secondary flow, the streamline curvature is changed in the shock region, causing a better matching of both the super- and the subsonic flow fields at off-design conditions, and eventually, a weakening of the shock strength and a reduction of the wave drag. This favourable

passive effect is intensified by an increased boundary layer thickening in the shock region due to the additional passive boundary layer control by combined blowing and suction including the strong influence of blowing on the turbulence structure. Up to now, the understanding of the passive SBLI control mechanism is by no means complete, so that further more detailed investigations about the flow field structure in the shock region are necessary.

The present knowledge of the ventilation mechanism of the double slot model is confirmed as well by the measured pressure distribution and boundary layer data at higher incidence, $\alpha_g = 5°$. Without passive control, severe buffeting was found with the upper surface flow extensively separated as in Fig. 11, while with ventilation, buffeting was not yet observed showing a pressure distribution - like that of $\alpha_g = 4°$ without ventilation - with the shock stabilized immediately upstream of the forward slot and the flow attached at the trailing edge. The more rearward shock position of the double slot configuration is responsible for the lift increase, Fig. 16, and the extension of the off-design region, Fig. 19.

The passive effect of the perforated strip on the pressure distribution and the boundary layer data at $M_\infty = 0.78$ is very similar to that of the double slot, Fig. 21. However, it seems that at both angles of attack $\alpha_g = 4°$ and 5° the shock is more smeared and the boundary layer is less thickened by using the perforated strip than by the double slot. At $M_\infty \geq 0.78$, the perforated strip is somewhat superior to the double slot due to its better adapted passive SBLI control, see Figs. 16 to 19. Again, the gain in lift and buffet onset is caused by the strong passive effect of the perforated strip on the shock location. The net drag reduction is a result, at low incidence, of the thickened boundary layer and the weakened shock, and at high incidence, mainly of the delayed shock-induced separation. At lower Mach numbers, the perforated strip is not as effective as the double slot, because the shock is located too far upstream of the perforation strip.

4. CONCLUSIONS

The present experimental investigations have generally confirmed that the off-design performance of supercritical airfoils can be considerably improved by active and passive shock/boundary layer interaction (SBLI) control.

In detail the results show that active SBLI control through local boundary layer suction in the shock region mainly delays the shock-induced separation to greater shock strength and stabilizes the shock in its rearward position up to higher incidence, resulting in a lift gain and drag reduction at off-design conditions as well as an extension of the off-design boundaries.

The maximum lift increase of about 25 % was obtained by single slot suction, but because of the shock shifting with Mach number this result is restricted to a very limited Mach number range, in which shock and slot position match well. This disadvantage can be avoided by double slot or perforated strip suction showing similarly positive effects in the entire Mach number range tested. However, due to an additional shock weakening effect, double slot and perforated strip suction leads to slight drag reductions even at low angles of attack and to large drag reductions at higher incidence.

During the experiments, a strong passive effect was observed by boundary layer ventilation on the double slot and perforated strip configurations without any suction. The passive effect, caused by a partial pressure compensation between the sub- and supersonic flow fields through the plenum underneath the shock, leads to a weakening of the shock wave. Besides the gain in lift and buffet onset, passive SBLI control offers mainly a large potential for off-design drag reductions up to 40 %. The most striking result of the double slot investigation was that in the entire Mach number range, in contrast to the other configurations, no severe buffeting could be detected beyond the buffet boundary.

So far the understanding of the passive SBLI control mechanism is by no means complete. The present measurements did not allow a detailed investigation of the flow field structure in the shock region. Further more detailed investigations are planned on a larger model, using more sophisticated measuring techniques, to gain deeper insight into this complex flow phenomenon. Finally, with regard to future applications of active or passive SBLI control on supercritical wings, the influence of high Reynolds number and wing sweep will be included in coming investigations.

ACKNOWLEDGEMENT

This investigation was partially supported by the Ministry of Defence of the Federal Republic of Germany under RüFo contracts T/RF41/70021/71429 and T/RF41/90021/91465.

The engagement of the MBB windtunnel model branch in designing and producing the airfoil model as well as of the DFVLR transonic windtunnel team in preparing, conveying and evaluating the measurements is gratefully acknowledged.

REFERENCES

1.	H.H. Pearcey	Some effects of shock-induced separation of turbulent boundary layer on transonic airfoils. ARC TR R&M No. 3108, 1955.
2.	E. Stanewsky	Interaction between the outer inviscid flow and the boundary layer on transonic airfoils. Dissertation TU Berlin, D83, 1981. Also: ZfW 7, Heft 4, pp. 242 - 252, 1983.
3.	K. Finke	Stoßschwingungen in schallnahen Strömungen. VDI-Forschungsheft 580, 1977.
4.	P. Thiede	Supercritical airfoil flow control by slot suction in the shock region. Proc. of USAF/FRG DEA-Meeting on "Viscous and Interacting Flow Field Effects", Annapolis, Md., AFFDL-TR-80-3088, 1980.
5.	P. Thiede G. Dargel	Erweiterung des Einsatzbereiches von transsonischen Profilen durch lokale Grenzschichtabsaugung. BMVg-FBWT RüFo IV T/RF41/70021/71420, VFW, 1980.
6.	E. Stanewsky P. Krogmann P. Thiede G. Dargel	Stoß-Grenzschicht-Interferenz und ihre Beeinflussung durch Grenzschicht-absaugung. 3. DGLR-Symposium "Strömungen mit Ablösung", Stuttgart, 1981.
7.	P. Krogmann	Druckverteilungs- und Grenzschichtmessungen an einem überkritischen Profil mit Grenzschichtabsaugung durch einen Einzelschlitz. DFVLR-IB 222-81 A 06, 1981.
8.	P. Thiede	Erweiterung des Einsatzbereiches von überkritischen Profilierungen durch lokale Grenzschichtabsaugung. BMVg-FBWT RüFo IV T/RF41/90021/91465, VFW, 1982.
9.	K.-D. Klevenhusen R. Hilbig W. Burgsmüller	Entwicklung von superkritischen Profilen und Voruntersuchungen zum superkritischen Flügelentwurf, Teil 1. BMFT-Bericht 523-8891-LFF 34, VFW-Fokker, 1976.
10.	R.D. Boehe	Transsonikmessungen am VFW-F-Profil Va-2 bei der DFVLR Göttingen. ZKP-Flügelsektion -Bericht 8, 1976.
11.	R. Müller	Messungen am superkritischen Profil VFW-F Va-2 im Transsonischen Windkanal Braunschweig, Teil 1: Zusammenstellung der Meßdaten. DFVLR-IB 151-78/13. 1978.
12.	E. Stanewsky P. Thiede	Boundary layer and wake measurements in the trailing edge region of a rear-loaded transonic airfoil. Proc. of USAF/FRG DEA-Meeting on "Viscous and Interacting Flow Field Effects", Meersburg, BMVg-FBWT 79-31, 1979.
13.	T. Hottner W. Lorenz-Meyer	Der Transsonische Windkanal der Aerodynamischen Versuchsanstalt Göttingen. DGLR-Jahrbuch 1968.
14.	L. Bahi, J.M. Ross, H.T. Nagamatsu	Passive shock wave/boundary layer control for transonic airfoil drag reduction. AIAA 21st Aerospace Sciences Meeting, Reno, Nev., Paper 83-0137, 1983.
15.	G. Savu O. Trifu L.Z. Dumitrescu	Suppression of shocks on transonic airfoils. 14th International Symposium on Shock Tubes and Waves, Sydney, 1983.
16.	P. Krogmann P. Thiede	Aktive und passive Beeinflussung der Stoß-Grenzschicht-Interferenz an überkritischen Tragflügeln. 4. DGLR-Symposium "Strömungen mit Ablösung", Göttingen, 1983.
17.	P. Krogmann E. Stanewsky P. Thiede	Effects of local boundary layer suction on shock-boundary layer interaction and shock-induced separation. AIAA 22st Aerospace Sciences Meeting, Reno, Nev., Paper 84-0098, 1984.

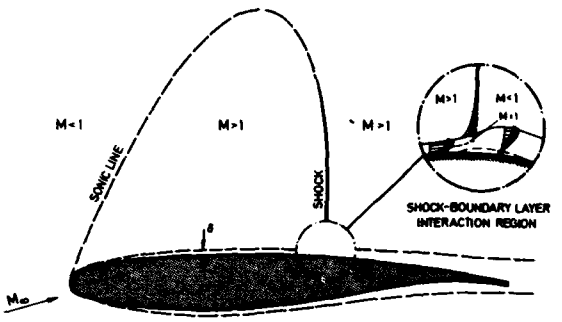


Fig.1 Shock/turbulent boundary layer interaction on a supercritical airfoil in transonic flow

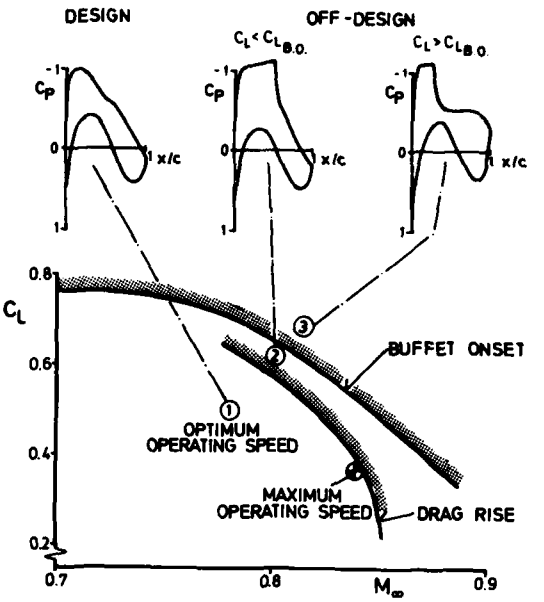


Fig.2 Off-design boundaries as a SBLI consequence

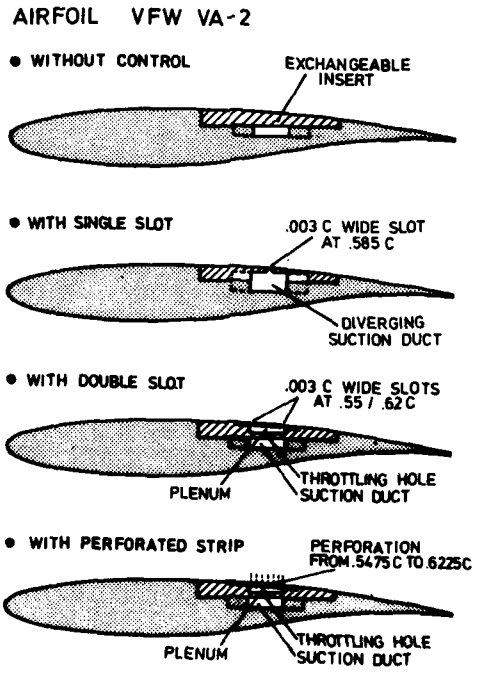


Fig.3 Model configurations tested with active/passive SBLI control devices

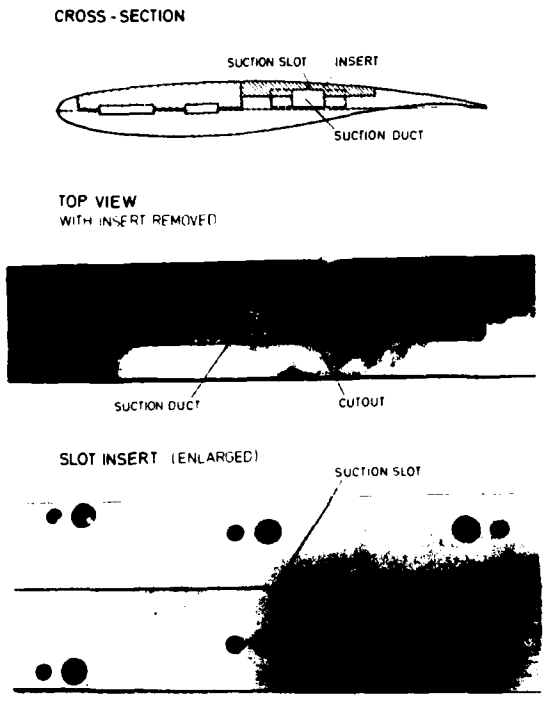


Fig.4 Model with single slot insert

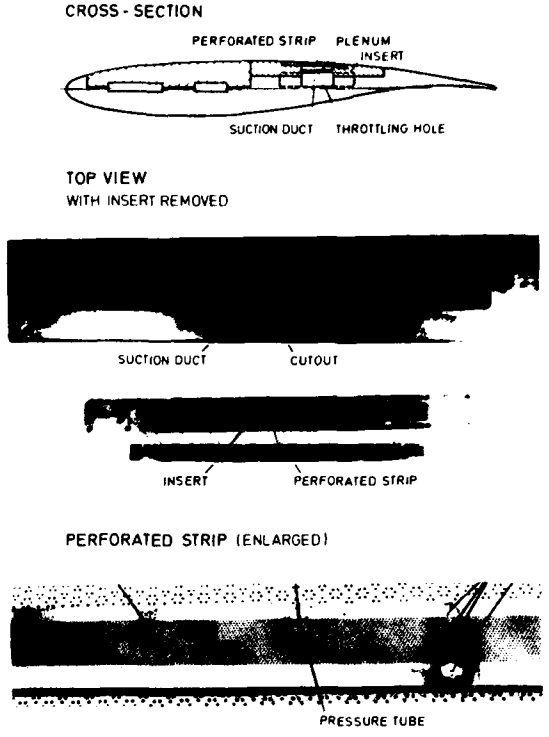


Fig.5 Model with perforated strip insert

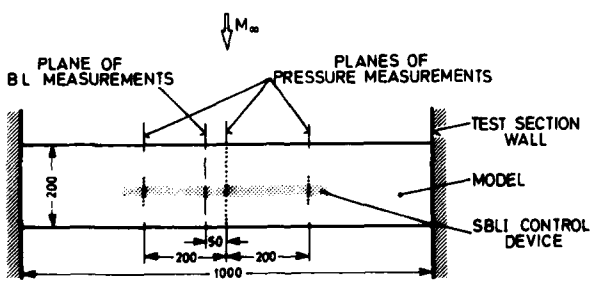


Fig.6 Model arrangement for pressure/b.l. measurements

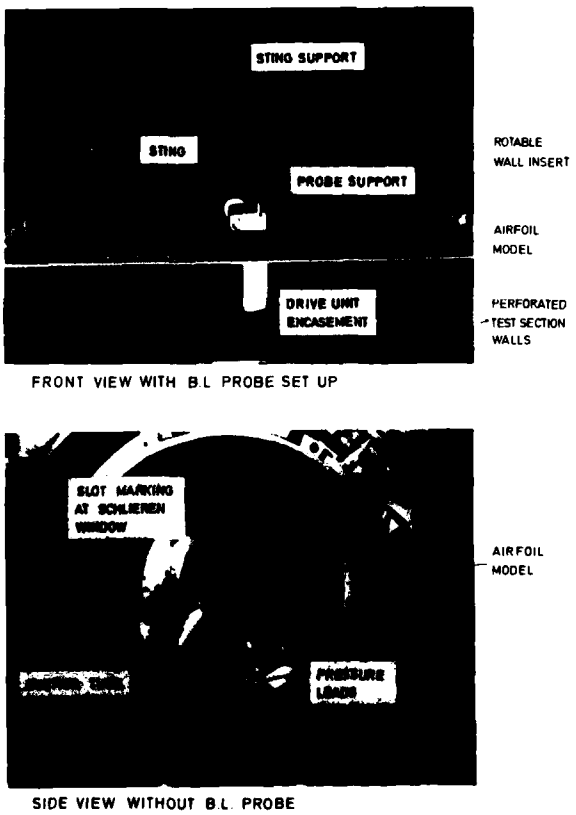


Fig.7 Test set-up in the DFVLR 1m x 1m Transonic Tunnel Göttingen

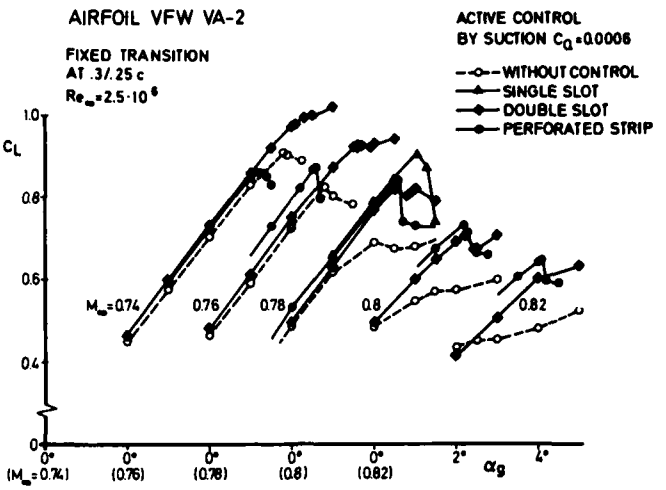


Fig.8 Lift polars with active SBLI control

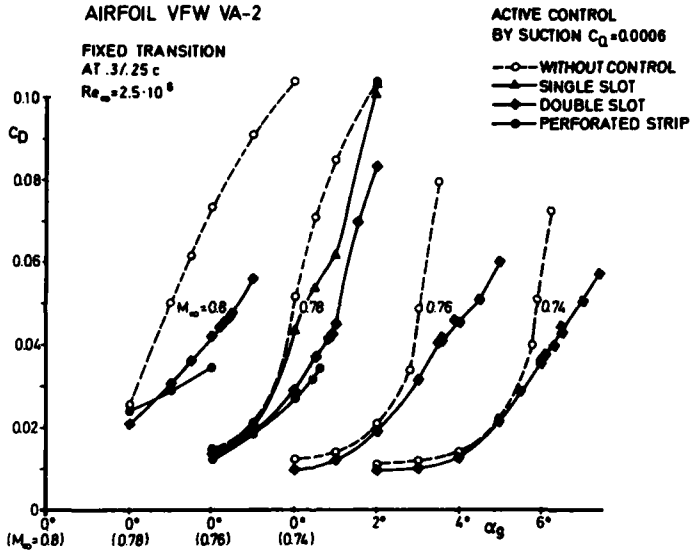


Fig.9 Drag polars with active SBLI control

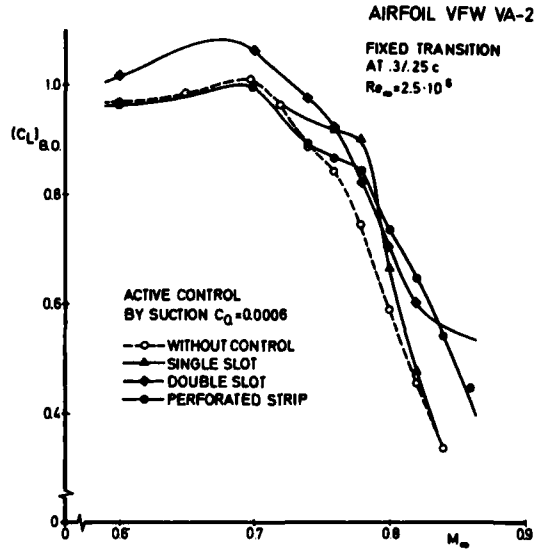


Fig.10 Buffet boundaries with active SBLI control

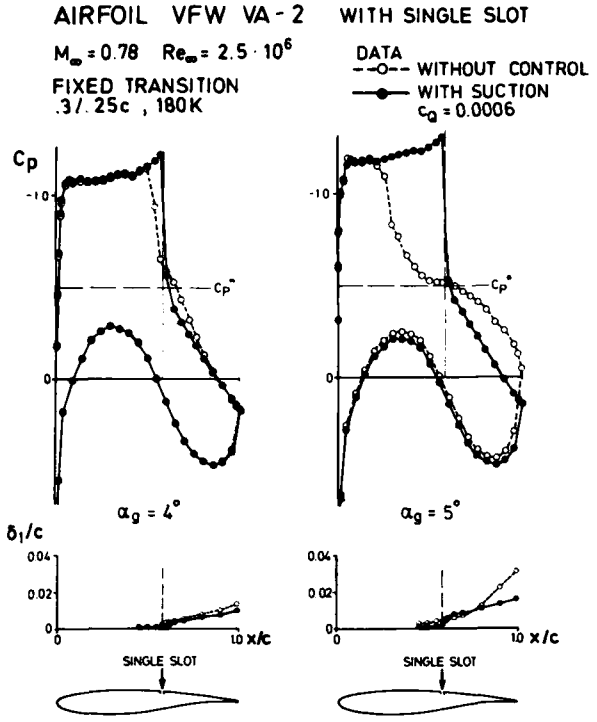


Fig.11 Pressure distribution and b.l. data with/without active SBLI control by suction

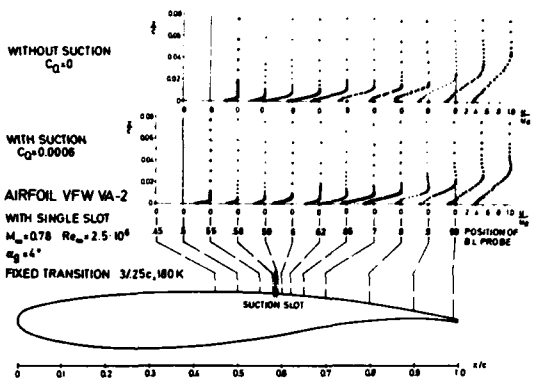


Fig.12 Boundary layer velocity profiles with/without active SBLI control

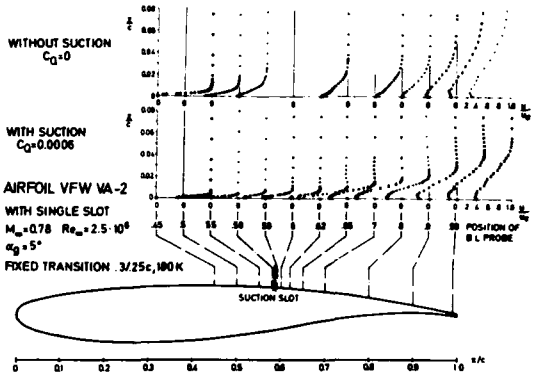


Fig.13 Boundary layer velocity profiles with/without active SBLI control

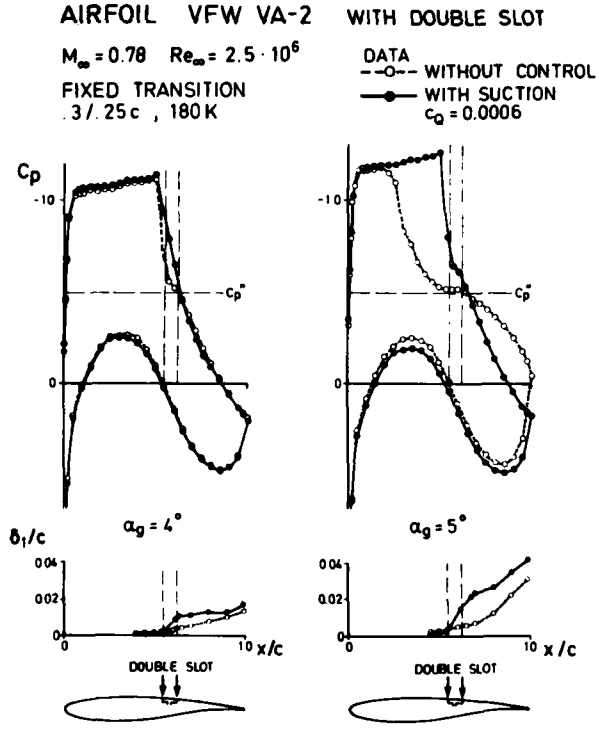


Fig.14 Pressure distribution and b.l. data with/without active SBLI control by suction

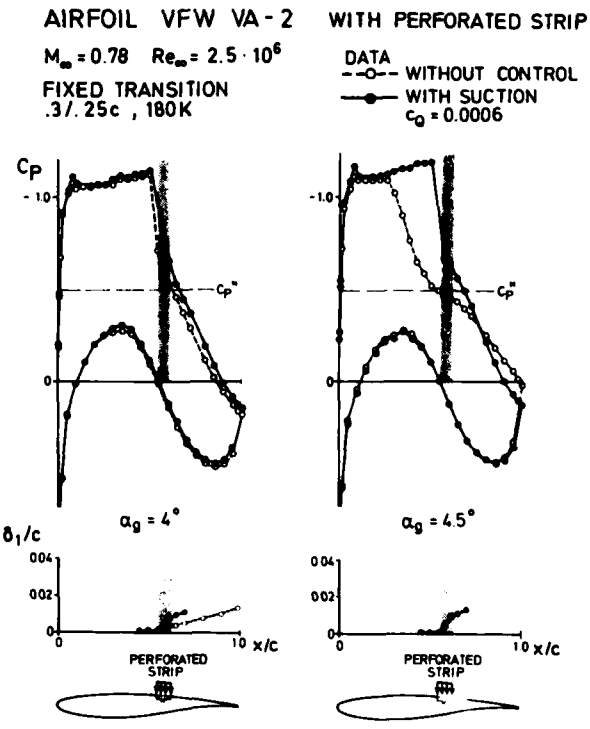


Fig.15 Pressure distribution and b.l. data with/without active SBLI control by suction

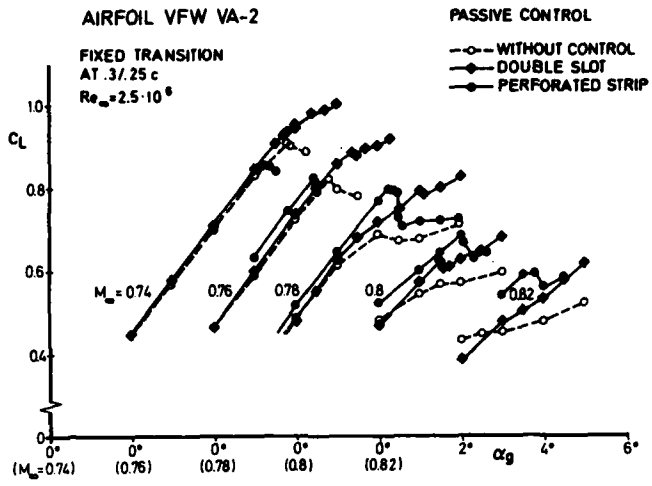


Fig.16 Lift polars with passive SBLI control

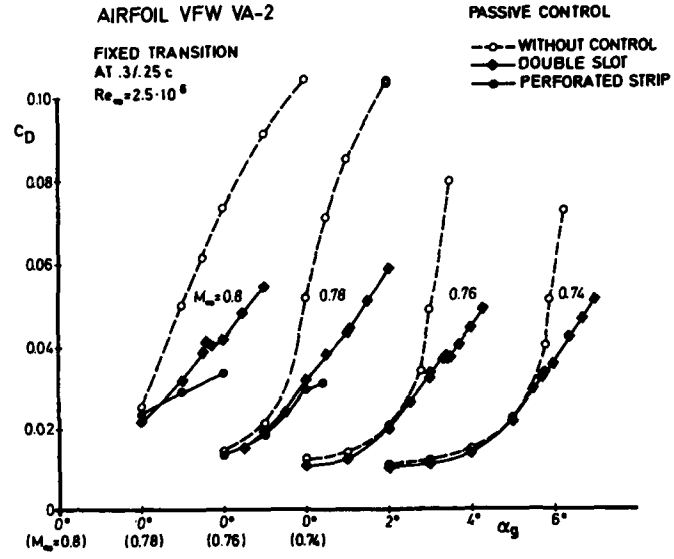


Fig.17 Drag polars with passive SBLI control

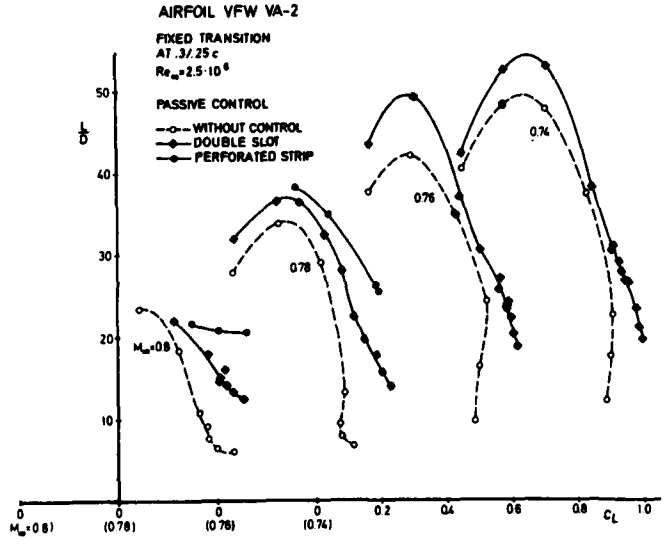


Fig.18 Lift/drag polars
with passive SBLI control

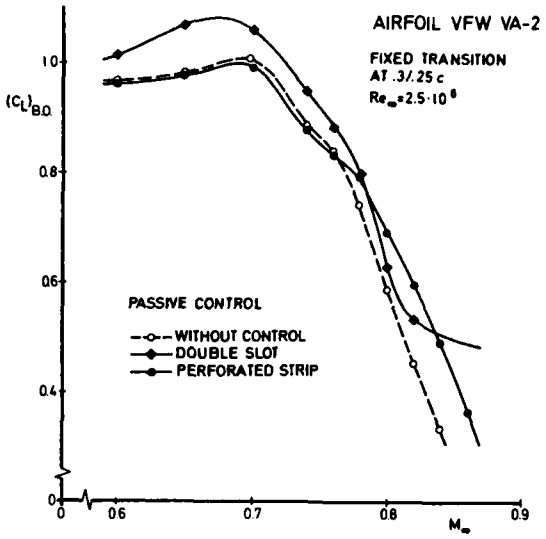


Fig.19 Buffet boundaries
with passive SBLI control

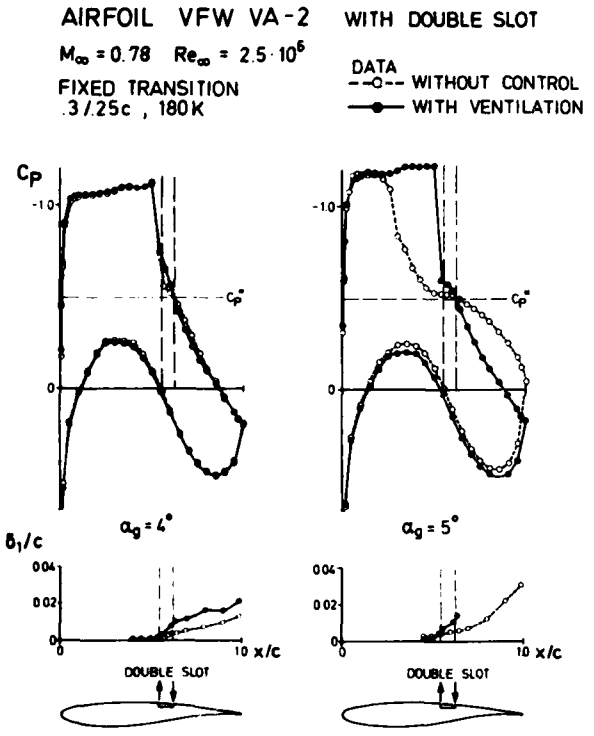


Fig.20 Pressure distribution and b.l. data
with/without passive SBLI control
by ventilation

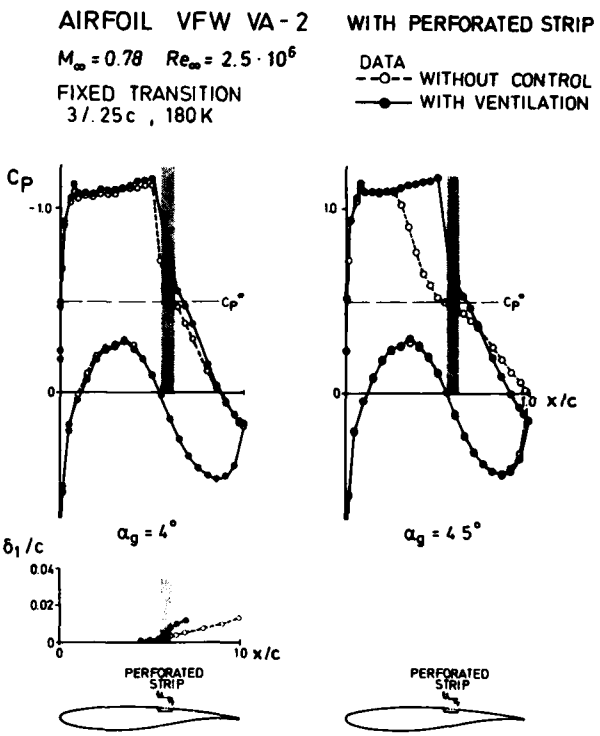


Fig.21 Pressure distribution and b.l. data
with/without passive SBLI control
by ventilation

TRANSONIC SHOCK INTERACTION WITH A TANGENTIALLY-INJECTED TURBULENT BOUNDARY LAYER

by

G.R.Inger†
West Virginia University
Morgantown, West Virginia 26505, USA

AD-P004 071

Abstract

A non-asymptotic triple deck theory of transonic shock/turbulent boundary layer interaction is described which takes into account the influence of upstream tangential injection on a curved wall. In addition to Reynolds number and the shock strength, the theory is parameterized by arbitrary values of the incoming boundary layer shape factor, wall jet maximum velocity ratio and the nondimensional height of this ratio; results of a comprehensive parametric study are then presented. It is shown that the wall jet effects significantly reduce both the streamwise scale and displacement thickening of the interaction zone. While increasing the upstream and downstream skin friction levels, these effects also reduce the minimum interactive Cf and thus actually hasten the onset of incipient separation at the shock foot.

Nomenclature

C_f	skin friction coefficient, $2\tau_w/\rho_{e_o} U_{e_o}^2$
ΔCf	skin friction increment due to wall jet
C_p	pressure coefficient, $2\ p'/\rho_{e_o} U_{e_o}^2$
C_x	lateral spreading factor of wall jet
H	boundary layer shape factor, δ^*/θ^*
H_i	incompressible shape factor
K	curvature of wall in interaction region
M	Mach number
p	static pressure
p'	interactive pressure perturbation, $p-p_1$
$\bar{p}$	pressure jump across incident shock
Re_ℓ, Re_δ	Reynolds number based on length ℓ and boundary layer thickness, respectively
S_w	non-dimensional wall shear function of wall jet
T_w	absolute temperature
T	basic interactive wall-turbulence parameter
u',v'	streamwise and normal interactive disturbance velocity components, respectively
ΔU	wall jet component of total velocity profile
U_o	undisturbed incoming boundary layer velocity in x-direction
x,y	streamwise and normal distance coordinates (origin at the inviscid shock intersection with the wall)
$y_{w_{eff}}$	effective wall shift seen by interactive inviscid flow
y_{max}	location of ΔU_{max}
β	$\sqrt{M_1^2-1}$
γ	specific heat ratio
δ	boundary layer thickness
δ^*	boundary layer displacement thickness
δ_{mix}	wall jet mixing thickness
δ_{SL}	inner deck sublayer thickness
ϵ_T	kinematic turbulent eddy viscosity
ϵ_T'	interactive perturbation of turbulent eddy viscosity
η	y/δ_o
μ	ordinary coefficient of viscosity
ν	μ/ρ
ω	viscosity-temperature dependence exponent, $\mu \sim T^\omega$
ρ	density
θ^*	boundary layer momentum thickness
τ	total shear stress
τ'	interactive perturbation of total shear stress

Subscripts

AD	Adiabatic wall
1	undisturbed inviscid values ahead of incident shock
e	conditions at the boundary layer edge
inc	incompressible value
inv	inviscid disturbance solution value
max	velocity profile maximum due to wall jet
o	undisturbed incoming boundary layer properties

1. Introduction

The use of tangential slot-injection to influence and control turbulent boundary layer behavior has been extensively studied in various types of lowspeed external and internal aerodynamic flow fields (e.g., on circulation-controlled airfoils, slotted flaps, in film cooling applications and for separation control in inlets and diffusers). In recent years, many applications of such injection have arisen in supercritical

† Professor and Associate Chairman , Dept. of Mechanical and Aerospace Engineering

transonic flow fields where local shock wave is present;[1] however, little is presently available to provide a basic understanding of how the resulting shock-boundary interaction ("SBLI") alters the influence of tangential injection. Conversely, in such supercritical flows it may be of interest to know how the effects of SBLI may be altered by the use of injection. The present paper addresses these questions for the case of steady non-separating 2-D turbulent boundary layers on adiabatic surfaces of small-to-moderate longitudinal curvature.

The primary objectives of our work are to develop a fundamental theory of a transonic SBLI region occurring downstream of a tangentially-injected turbulent boundary layer on a curved wall (Fig. 1) and then to present the results of a parametric study of this theory showing the relationship between the dominant physical parameters, the injection and the physics of the SBLI zone. In Section 2, we briefly outline the non-asymptotic triple deck theory of a SBLI zone on a curved surface without tangential injection. Then by taking the SBLI zone sufficiently far downstream of the injection slot for mixing of the wall jet and overlying turbulent boundary layer to have produced a well-defined "jet-bulged" boundary layer profile, the interactive perturbation field caused by normal shock interaction with this profile is analyzed in Section 3 by an extension of the aforementioned SBLI theory. This is followed in Section 4 by presentation and discussion of the results of a parametric study of this extended solution for the interactive pressure, displacement thickness and skin friction effects.

2. Brief Outline of the Basic SBLI Theory

2.1 The Triple-Deck Model

It is well-known that when separation occurs, the disturbance flow pattern associated with normal shock-boundary layer interaction is a very complicated one involving a bifurcated shock pattern, whereas the unseperated case pertaining to turbulent boundary layers up to $M_1 \approx 1.3$ has instead a much simpler type of interaction pattern which is more amenable to analytical treatment (Fig. 2). The flow consists of a known incoming isobaric turbulent boundary layer profile $M_o(y)$ subjected to small transonic perturbations due to an impinging weak normal shock. In the practical Reynolds number range of interest here [$Re_L \approx 10^6$ to 10^8] we purposely employ a non-asymptotic triple-deck flow model[2] that is the turbulent extension of the Lighthill approach that has proven highly successful in treating a variety of other problems involving turbulent boundary layer response to strong rapid adverse pressure gradients and which is supported by a large body of transonic and supersonic interaction data plus detailed formal asymptotic analyses.[3] The resulting flow model, Fig. 2, consists of an inviscid boundary value problem surrounding a shock discontinuity and underlaid by a thin shear stress-disturbance sublayer thatcontains the upstream influence and skin friction perturbations. An approximate analytic solution is further achieved by assuming small linearized disturbances ahead of and behind the nonlinear shock jump, which gives accurate predictions for all the properties of engineering interest when $M > 1.05$. The resulting equations can be solved by operational methods[2], yielding the interactive pressure rise, displacement thickness growth and the skin friction behavior upstream and downstream of the shock foot. This solution contains all the essential global features of the mixed transonic viscous interaction flow and detailed comparisons with experiment[4] and Navier-Stokes numerical solutions have shown that it gives a very good account of all the important engineering features of non-separating interactions over a wide range of Mach-Reynolds number conditions.

An important and unique feature of this interaction theory is that it employs for the incoming turbulent boundary layer velocity profile a very general Composite Law of the Wall-Law of the Wake profile model due to Walz,[5] which is characterized not only by the shock Mach number M_1 and the boundary layer thickness Reynolds number Re_{δ^*} but also by arbitrary nonequilibrium[6] values of the incompressible shape factor H_{i_1}. This model may be combined by the Van Driest transformation[6] (or the equally-accurate Reference Temperature correction method) to account for compressibility effects. The resulting predictions, such as typically illustrated in Fig. 3, show that H_{i_1} has a very large effect on the local and downstream interactive properties that is important to account for in practical applications. By thereby accomodating a wide range of possible upstream histories of pressure gradient, heat and mass transfer, the theory has found wide-spread success as an interactive module in global composite viscous-inviscid flow field analysis programs on supercritical airfoils and projectiles, while also proving adaptable to the accomodation of new effects.

2.2 The Wall Curvature and Shock Obliquity Effects

Since SBLI with tangential injection often arises in flows on curved surfaces, it is desirable to account for wall curvature effects in the foregoing interaction theory. For the small to moderate curvature usually encountered ($K\delta_o \lesssim .02$), analysis[8] of the transonic small disturbance flow in the outer deck shows that while the explicit new curvature terms in the perturbation equations are of the negligible order $K\delta_o$, the interactive viscous displacement effect from the underlying decks eliminates the well-known[9] inviscid shock signularity while slightly altering the shock into an oblique configuration; see Figs. 4-6. Detailed examination of the middle-deck region shows that any new terms in the inviscid rotational disturbance equations are of the negligible order $K\delta_o$; only the curvature effect on the undisturbed boundary-layer velocity and eddy viscosity profiles are of possible significance. Here again, the explicit $K\delta_o$ terms in the governing equations of this incoming flow are all negligible; however, curvature can moderately influence (10-20%) the eddy viscosity terms, with a consequent effect on the boundary-layer profile in the form of a skin friction reduction and shape factor increase as described approximately by the relationships[8]

$$C_{f_o} \approx (1 - 10K\delta_o)[C_{f_o}]_{flat} \tag{1}$$

$$H_{i_1} \approx (1 + 5K\delta_o)[H_{i_1}]_{flat} \tag{2}$$

where to this order of accuracy the corresponding effect on δ_o is negligibly small. Note, for example, that the typical value $K\delta_o \approx 0.01$ yields a reduction and increase in C_{f_o} and H_{i_1} of 10 and 5%, respectively. The use of Eqs. (1) and (2) with the Walz velocity profile model and $K\delta_o$ as an additional input parameter provides a good engineering account of the moderate curvature effects on the middle-deck interaction solution. Within the very thin inner disturbance shear stress deck it is found[8] yet again that explicit curvature effects on the various inertia, pressure gradient, and laminar viscous terms in the disturbance flow equations are altogether negligible. Moreover, because of the extreme inner-deck thinness, the eddy viscosity curvature effect therein may also be safely neglected for the high Reynolds number conditions typifying most practical external aerodynamic flows.

Predictive results for the typical influence of $K\delta_o$ on SBLI properties, which agree with experimental observations, may be found in Ref. 8; they show that it slightly spreads out the interaction, weakening the adverse pressure gradient along the wall, due primarily to the increased shape factor. Since curvature slightly reduces the incoming boundary-layer velocity profile fullness and spreads out the interaction, it further acts to thicken the downstream boundary layer while slightly increasing the local C_f around the shock foot owing the reduced interactive pressure gradient. As regards the slight shock obliquity at the boundary layer edge caused by the interactive displacement thickness effect, detailed investigation[10] has established that it corresponds with a good approximation to the condition of maximum deflection. Hence the pressure rise is equivalent to a normal shock at the effective lower shock Mach number

$$M_{1_{eff}} = M_1 \sin\left(90^o - 37.3\sqrt{M_1 - 1}\right) \tag{3}$$

thereby allowing the obliquity effect to be accurate accomodated in the present theory[11] (Fig. 6).

3. Extension to Include Tangential Injection

We recall that the aforementioned interaction theory feeds upon a known shock strength and an assumed incoming turbulent velocity profile model characterized by the overall parameters H_{i_1}, C_{f_o} and Re_{δ^*}. In the problem at hand we have a new unique shape of velocity profile that exists due to tangential blowing. In this section we will be concerned with modeling the influence of such a profile and its associated wall-region eddy viscosity behavior by a convenient set of parameters that characterize the essential new physical features and allow parametric sensitivity studies.

When air is tangentially injected through a slot of height h into an overlying boundary layer it forms a jet which is entrained by the surrounding flow (Fig. 7a). Immediately downstream of the slot, strong mixing of these flows occurs in a complicated manner which may not be validly treated by boundary layer theory; in any event, the resulting composite velocity profile assumes a unique character with a maximum and a minimum (Fig. 7b). As the flow proceeds further downstream, experimental studies[12] have shown that the minimum is rapidly eliminated by further mixing so that when $x \gg h$, the profile attains a fully-developed "jet-bulged" shape (Fig. 7c) composed of an unblown-type of turbulent boundary layer profile plus a wall jet component containing a velocity maximum near the wall. As this fully-developed shape convects downstream, further mixing gradually decreases and spreads out the jet maximum (Fig. 7d) until the boundary layer ultimately tends toward an ordinary monotone profile shape in which the jet component has been completely eliminated by entrainment. In the present study we deal with with case where the shock interacts with a jet-bulged type of profile (Fig. 7c), since this is the most interesting encountered in practice. (The regions upstream of the slot and very far downstream where the profile maximum has disappeared can of course be handled by the existing "unblown" version of the present SBLI theory).

While possessing a boundary layer profile shape that can be analytically modeled in a manner appropriate to the SBLI solution (see below), this case also permits a simplified treatment of the eddy viscosity aspects of the interactive decks in the boundary layer, as follows. Experimental studies[12-14] have shown that the usual Law of the Wall behavior and its associated mixing length eddy viscosity model applies to the lower portion below the jet maximum when the injection effect is small-to-moderate ($\Delta u_{max}/u_e \lesssim 1.0$). Since the thin disturbance-shear stress inner deck of the SBLI region lies well within this Law of the Wall region, while there are no eddy viscosity-associated perturbation terms in the overlying middle deck owing to the inviscid frozen-turbulence nature of its disturbance flow, it can be shown that the <u>form</u> of all the basic triple-deck Equations in the aforementioned SBLI theory can be carried over to the present problem <u>provided</u> that one fully accounts for the wall jet effects on the undisturbed flow skin friction C_{f_o}, displacement thickness Reynolds number Re_{δ^*} and (especially) incompressible shape factor H_{i_1} as well as on the profile distribution itself.

An appropriate analytical model of the incoming boundary layer profile was developed which accounts for the essential new wall-jet features of the flow while also being well-suited to the Lighthill pressure disturbance equation that is involved in the middle deck solution. It is constructed as the sum of a wall-jet component and an "unblown" component, where to be consistent with earlier work the latter is represented by Walz's Law of the Wall/Law of the Wake composite profile characterized by the three parameters Re_{δ^*}, C_{f_o} and H_{i_1} (see Appendix A). Thus if y_{max} denotes the height of the maximum velocity u_{max} with Δu_{max} denoting the corresponding difference between u_{max} and the unblown velocity due to the wall jet effect (see Fig. 8), the total profile is expressed as

$$u(y) = u_{walz}(y) + \Delta u(y) \tag{4}$$

where the wall jet component $\Delta u(y)$ varies from zero at $y = 0$ (no slip) to its maximum value Δu_{max} at $y = y_{max}$ and then decays outwardly towards zero, becoming negligible beyond some characteristic jet-spread height δ_{mix} above y_{max} (we presume $\delta_{mix} + y_{max} \ll \delta$). Above y_{max}, we have followed the experimentally-based work of Carriere et al[15] and represented Δu by a modified $sech^2$ function whose slope at y_{max} equals $-(dU_{walz}/dy)_{y_{max}}$ such that the <u>total</u> composite profile correctly has a maximum at y_{max}:

$$\frac{\Delta u}{u_e} = \frac{\Delta u_{max}}{u_e}\left\{\frac{SECH^2\left[\left(\frac{y - y_{max}}{\delta_{mix}}\right) + \phi\right]}{SECH^2\phi}\right\} \qquad [y \gtrless y_{max}] \tag{5A}$$

where

$$\phi \equiv \tfrac{1}{2}\left[\ln\left(1 + \frac{C_x}{2}\right) - \ln\left(1 - \frac{C_x}{2}\right)\right] \tag{5B}$$

is a phasing factor insuring the maximum in total velocity at y_{max} and

$$C_x \equiv (\delta_{mix}/\Delta U_{max})[\partial \Delta u/\partial y]_{max} \tag{5C}$$

is a lateral spreading constant (typically ≈ .15 to avoid secondary profile maxima above y_{max}). Below y_{max}, on the other hand, we require a functional representation that gives a reasonable monotonic shape and matches smoothly to Eq. (5) at y_{max}. Furthermore, we desire some control over the wall slope in order to represent injection effects on the local skin friction. The specific constraints on this functional choice are that (a) only one maximum in the total composite profile at $y = y_{max}$, (b) a match with the value and slope of the upper $\Delta u(y)$ function at y_{max}, and (c) positive values of the non-dimensional slope

$$S_w \equiv \left[\frac{d(\Delta u/ue)}{d(y/y_{max})}\right]_{y=0}$$

leading to physically reasonable skin friction increments

$$C_f = S_w \, (\mu_w \delta/\mu_e Re_\delta) \Delta U_{max}/y_{max} \, . \tag{6}$$

Now condition (a) so severely restricts the class of monotone functions it admits that no general solution can be generated to accommodate a completely arbitrary combination of conditions (b) and (c); what can be found, however, are functions which allow either an arbitrary choice of all three parameters S_w, ΔU_{max}, y_{max} within a restrictive range or the choice of a wide range of values for the two key parameters ΔU_{max}, y_{max} with S_w then consequently determined (but still within an interesting range of resulting values). One such function which has proven quite satisfactory for the purposes of this investigation is

$$\frac{\Delta u}{ue} = C_1 \frac{y}{y_{max}} - C_3 \left[\exp\left(C_2 \frac{y}{y_{max}}\right) - 1\right] \qquad (y < y_{max}) \tag{7A}$$

where the aforementioned matching conditions are fulfilled if the constants $C_{1,2,3}$ satisfy the three simultaneous relations

$$C_1 - C_3 \, (\exp C_2 - 1) = u_{max} \tag{7B}$$

$$C_1 - C_3 C_2 \exp C_2 = - y_{max} \tag{7C}$$

$$C_1 - C_3 = S_w \tag{7D}$$

This trio is readily solved numerically during the implementation of the velocity profile model by using a standard non-linear simultaneous root-finder subroutine.

3.2 Implementation of the Extended Theory

The foregoing approach may be implemented by several straightforward modifications to the existing computer program for the zero-blowing SBLI theory, as follows. To include small-to-moderate wall curvature effects ($K\delta_o < .01$), we add $K\delta_o$ as an independent input variable and accordingly modify the input values of H_{i1} and C_{f_o} according to Eqs. (1) and (2); furthermore, we eliminate the inviscid curvature singularity, altering the normal shock to a slightly oblique one at the boundary layer edge, by modifying the input effective normal shock Mach number according to Eq. (3). The influence of tangential injection is accomodated by introducing the two new input parameters $\Delta U_{max}/U_e$ and y_{max}/δ_o, characterizing the magnitude and height, respectively, of the wall jet component effect; in addition, values of the auxillary parameters C_x and S_w can be set within certain restricted ranges. The program subroutine which evaluates the Walz turbulent boundary layer velocity profile model is modified to add the matched upper and lower wall jet-component increments pertaining to these inputs (Eqs. 4-7), using a Reference Temperature-Method compressibility correction of the appropriate parameters. Figure 9 illustrates some typical boundary layer velocity profiles containing these tangential injection effects. Using the adiabatic temperature-velocity relationship

$$T = T_{W,AD} + (T_e - T_{W,AD}) \, U^2/U_e^2 \tag{8}$$

the associated Mach number profile $M_o(y)$ and its derivative dM_o/dy (which are both needed in the interactive pressure solution subroutine) are calculated, the corresponding mass flow and momentum defect distributions $1 - \frac{\rho u}{\rho e Ue}$ and $\left(1 - \frac{\rho u}{\rho e Ue}\right) \frac{u}{ue}$ are also integrated across the boundary layer to obtain the values of δ^*/δ and θ^*/δ, respectively, associated with the wall jet effect. The resulting values of the displacement thickness and shape factor are shown in Figs. 10 to illustrate how the mass and momentum addition to the boundary layer from the wall jet substantially decreases δ^* and produces a greater profile "fullness" reflected in a significantly reduced shape factor. (We note here that while it is formally possible to obtain negative δ^* and θ^* for sufficiently large injection rates, ΔU_{max} say, consistent with our other assumptions, we exclude such cases from this study.) Increasing the height of the jet maximum is seen to have a similar effect, because this enhances the effective strength of the injection effect on the boundary layer profile. Awareness of these overall integral property effects proves helpful in interpreting the predicted interaction properties given below.

Implementation of these wall jet-modifications is quite straightforward, except to note that feedback of the aforementioned modified integral properties into the solution sequence must be properly phased: since the wall jet effect on the incoming boundary layer profile shape is already included in the $M_o(y)$ distribution used in solving the Lighthill interactive pressure equation, the feedback must be done after the pressure is determined. Subsequent use of the jet-altered values of δ^* and C_{f_o} then further influences the local interactive displacement thickening and skin friction solution results.[o] To illustrate the importance of this proper feedback of the jet-influenced profile integral properties a typical set of interactive pressure, displacement thickness and skin friction distributions predicted by the aforementioned extended theory are presented in Fig. 11, showing the various relative effects of tangential injection compared to the zero blowing case. It is seen that the increased boundary layer profile fullness and shape factor reduction due to injection causes a significant streamwise contraction of the interactive pressure rise; this is in agreement with experimental observations.[16] Accompanying this contraction of the interaction zone, the two main

effects of injection on the ratio $\Delta\delta^*/\delta_o^*$ are seen to act with opposite and nearly equal influence: while the profile shape-factor effect of injection reduces $\Delta\delta^*$, the corresponding reduction of δ_o^* is approximately of the same magnitude so that the overall change in $\Delta\delta^*/\delta_o^*$ is small. This implies that the net injection effect on $\Delta\delta^*$ scales approximately with the corresponding effect on δ_o^*. Turning to the interactive skin friction behavior typified in Fig. 11c, it can be seen that the increased Cf level due to the wall jet effect dominates most of the interaction zone both fore and aft of the shock except in the vicinity of the shock foot; in this foot region, the Cf reduction due to the steepened interactive pressure gradient caused by injection becomes the dominant effect and the local value of Cf_{min} is actually reduced. Stated another way, the SBLI effect adversely counteracts the otherwise favorable Cf increase due to injection.

The aforementioned tangential injection effects on SBLI may be readily understood from the overall shape factor and displacement thickness effects shown in Fig. 10: the reduced H and δ^* imply a thinner incoming turbulent boundary layer with a somewhat higher Mach number deep in the layer and a fuller profile shape typical of a favorable upstream pressure gradient history, which in view of the demonstrated sensitivity of SBLI to the shape factor (Fig. 3) have the effect of reducing the streamwise scale and interactive thickening while increasing the corresponding local pressure gradient.

4. Discussion of Parametric Study Results

The present theory has been used to carry out a systematic study of how the key tangential injection parameters influence the essential properties of a subsequent SBLI zone. We now present and discuss the results.

4.1 Interactive Pressure and Displacement Thickening

Typical pressure distributions, showing the strong systematic contraction of the streamwise interactive scale with increasing strength of the wall jet component-effect, are illustrated in Figure 12. A comprehensive summary of such results showing the upstream and downstream influence distances (the distance ahead and behind the shock where the pressure rise is 5% and 95%, respectively, of the overall shock jump value) are presented in Figures 13 and 14 as a function of both the magnitude and location of the jet velocity maximum for a typical supercritical flow of $M_1 = 1.20$. Viewed overall, these results show that tangential injection can significantly reduce the overall upstream influence, and strongly reduce the downstream streamwise scale of the interaction to a degree comparable to, or greater than, the unblown shape factor and/or Mach number effects. When non-dimensionalized in terms of δ_o, the results are not very sensitive to Reynolds number.

The corresponding systematic influence of injection on the relative interactive displacement thickness distribution $\Delta\delta^*(x)/\delta_o^*$ is illustrated in Figure 15, where we see that the effect on $\Delta\delta^*(x)$ and δ_o^* largely cancel over a wide range of wall jet strengths when presented in this ratioed manner. However, there is a significant injection effect on the streamwise slope of $\Delta^*(x)$ at the shock foot, which relates to the effective "viscous wedge" angle sensed by the outer inviscid flow; this effect is illustrated in Fig. 16, where the strong increase of this slope with wall jet strength may be clearly seen.

4.2 Incipient Separation

The present theory, although it breaks down at separation, does yield a useful indication of incipient separation where $Cf_{min} \to 0$, owing to the particular attention paid to the treatment of the local interactive skin friction behavior. Since this indication is of great practical interest, a parametric study of incipient separation conditions from the present theory was carried out.

As a basis for comparison, the results for flow without any tangential injection are shown in Fig. 17a where the shock Mach number above which incipient separation occurs is plotted as a function of the Reynolds number with the shape factor as a parameter; also shown in the figure is the approximate experimental boundary determined by a careful examination of a large number of transonic interaction tests[4], besides the well-known $M \sim 1.30$ criterion for turbulent flow. It is seen that the theoretical prediction of a gradual increase in the incipient separation Mach number value with Reynolds number is in agreement with the trend of this data. The theoretical prediction of only a small influence of shape factor on the incipient separation conditions is also borne out by more recent data,[17] as indicated in Fig. 17b.

Introducing the effect of injection, we first note from the typical behavior of the interactive Cf distribution around the shock foot (see, e.g., Fig. 11c) that the net effect is expected to decrease Cf_{min} (notwithstanding the overall upstream and downstream increase in Cf otherwise due to injection). As shown in Fig. 18, this is indeed found to be the case: the wall jet effect of increasing the local interactive pressure gradient is seen to hasten the onset of incipient separation at the shock foot for a given Reynolds number flow, in the sense that separation occurs at a slightly lower shock number as $\Delta U_{max}/U_e$ is increased. This is of course in sharp contrast to the well-known[16] favorable effect of injection in delaying separation observed by purely subsonic flows with a prescribed adverse pressure gradient, and is due to the fact that the interactive pressure gradient enhancement effect of tangential injection in locally reducing Cf is absent in these flows.

5. Concluding Remarks

Viewed overall, the present study has shown that the usual favorable tangential injection effects of thinning out and delaying the separation of turbulent boundary layers in subsonic flow can be significantly compromised by transonic shock/boundary layer interaction. Conversely, such injection was seen to appreciably reduce the streamwise extent of an SBLI zone albeit with the allied consequence of intensifying the local interactive adverse pressure gradient and thus hastening the onset of shock foot separation. It has further been established that a fundamentally-based triple-deck theory of SBLI with injection is now available to treat these effects in either external or internal supercritical flow fields; moreover, this theory has been constructed to serve as a locally insertable interactive module astride the inviscid shock location, driven by the attendant local boundary layer properties including an arbitrary non-equilibrium shape factor. Consequently it would be possible to investigate in the future interesting problems of blowing in supercritical flow fields, including the use of tangential injection to modify the influence of SBLI upon

the viscous trailing edge effect of supercritical airfoils[18-20] (see Fig. 19), and the inclusion of SBLI effects in viscous-inviscid flow field analysis programs for circulation-controlled airfoils and wings flying at supercritical flight speeds.

Acknowledgement

This work was carried out under the auspices of Office of Naval Research Contract NR-061-274; the resulting support and encouragement of Dr. Robert Whitehead of ONR is sincerely appreciated.

Appendix

Because of its convenient analytical form, accurate blended representation of the combined Law of the Wall - Law of the Wake behavior and generality, we have adopted Walz's model[5] for the incoming turbulent boundary layer upstream of the interaction. For the low Mach number/small heat transfer conditions appropriate to transonic interactions, it may be satisfactorily corrected for compressibility effects by the Eckert Reference Temperature method which under these conditions is, in fact, comparable in accuracy to but far simpler to implement than the Van Driest compressibility transformation approach.[6,7]

Let π be Coles' (incompressible) Wake Function $\eta \equiv y/\delta$ and denote for convenience $R \equiv .41\, Re\delta^*_o/[(1+\pi)(T_w/T_e)^{1+\omega}]$ with $\omega \simeq .76$ and $\gamma \simeq 1.4$ for a perfect gas; then the compressible form of Walz's composite profile may be written

$$\frac{U_o}{U_e} = 1 + \frac{1}{.41}\sqrt{\frac{C_{f_o}}{2}\left(\frac{T_w}{T_e}\right)}\left[\left(\frac{R}{1+R}\right)\cdot\eta^2\cdot(1-\eta) - 2\pi + 2\pi\cdot\eta^2\cdot(3-2\eta) + \ell n\left(\frac{1+R\eta}{1+R}\right) - (.215 + .655R\eta)e^{-3R\eta}\right] \qquad (A\text{-}1)$$

subject to the following condition linking π to C_{f_o} and $Re\delta^*_o$:

$$2\pi + .215 + \ell n(1+R) = \frac{.41}{\sqrt{\frac{C_{f_o}}{2}\left(\frac{T_w}{T_e}\right)}} \qquad (A\text{-}2)$$

Eqs. (A-1) and (A-2) have the following desirable properties: (a) for $\eta \geq .10$ or so U_o/U_e is dominated by a Law of the Wake behavior which correctly satisfied both the outer limit conditions $U_o/U_e \to 1$ and $dU_o/dy \to 0$ as $\eta \to 1$; (b) on the other hand, for very small η values, U_o assumes a Law of the Wall - type behavior consisting of a logarithmic term that is exponentially damped out extremely close to the wall into a linear laminar sublayer profile $U/U_e \simeq R\eta$ as $\eta \to 0$; (c) Eq. (A-1) may be differentiated w.r.t. η to yield an analytical expression for dU_o/dy also, which proves advantageous in solving the middle and inner deck interaction problems (see text) where dM_o/dy must be known and vanish at the boundary layer edge.

The use of the incompressible form of Eq. (A-1) in the defining integral relations for δ_i^* and θ_i^* yields the following relationship that links the wake parameter to the resulting incompressible shape factor $H_{i_1} = (\delta_i^*/\theta_i^*)_1$:

$$\frac{H_{1_i} - 1}{H_{1_i}} = \frac{2}{.41}\sqrt{\left(\frac{T_w}{T_e}\right)\frac{C_{f_o}}{2}}\left(\frac{1 + 1.59\pi + .75\pi^2}{1+\pi}\right) \qquad (A\text{-}3)$$

Eqs. (A-2) and (A-3) together with the defining relation for R enable a rather general and convenient parameterization of the profile (and hence the interaction that depends on it) in terms of three important physical quantities: the shock strength (Me_1), the displacement thickness Reynolds number $Re\delta^*$, the wall temperature ratio T_w/T_e and the shape factor H_{i_1} that reflects the prior upstream history of the incoming boundary layer including possible pressure gradient and surface mass transfer effects. With these parameters prescribed, the aforementioned three equations may be solved simultaneously for the attendant skin friction C_{f_o}, the value of R and, if desired, the π value appropriate to these flow conditions.

REFERENCES

1. Malmuth, N. et al, " Flow Structures Associated with Upper Surface-Blown Airfoils", in Numerical and Physical Aspects of Aerodynamic Flows (T. Cebeci, Ed.), pp. 463-478, Springer-Verlag, N.Y., 1981.
2. Inger, G. R., "Upstream Influence and Skin Friction in Non-Separating Shock Turbulent Boundary Layer Interactions," AIAA Paper 80-1411, Snowmass, Colo., July 1980.
3. Melnik, R. E., "A Survey of Turbulent Viscid-Inviscid Interaction Theory in Aerodynamics," AIAA Paper 84-0264, Jan. 1984.
4. Inger, G. R., "Some Features of a Shock-Turbulent Boundary Layer Interaction Theory in Transonic Flow Field," AGARD CP-291, Symposium on Computation of Viscous-Inviscid Interactions, Colorado Springs, Colo., Sept. 1980, pp. 18-1 to 18-66.
5. Walz, A., "Boundary Layers of Flow and Temperature," M.I.T. Press, Cambridge, Mass., 1969, pp. 113.
6. Van Driest, E. R., "Turbulent Boundary Layers in Compressible Fluids," Jour. of the Aeronaut. Sci. 18, March 1951, pp. 145-160.
7. Burggraf, O. R., "The Compressibility Transformation and the Turbulent Boundary Layer Equation," Jour. of the Aerospace Sci. 29, 1962, pp. 434-439.
8. Inger, G. R., "Transonic Shock-Turbulent Boundary Layer Interaction and Incipient Separation on Curved Surfaces," AIAA Paper 81-1244, Palo Alto, June, 1981. Jour. of Aircraft 20, June 1983, pp. 571-74.
9. Oswatitsch, K., and J. Zierep, "Das Problem des senkrechten Stosses an einer gekrummten Wand," ZAMM 40, 1960, pp. 143-147.

10. Inger, G. R., and H. Sobieczky, "Shock Obliquity Effect on Transonic Shock-Boundary Layer Interaction," ZAMM 58T, 1978.
11. Nandanan, M., Stanewsky, E. and Inger, G. R., "A Computational Procedure for Transonic Airfoil Flow Including a Special Solution for Shock-Boundary Layer Interaction," AIAA Paper 80-1389, Snowmass, Colo., July 1980. AIAA J. Dec. '81, January 1982.
12. M. P. Escudier, W. B. Nicoll, D. B. Spalding, and J. M. Whitelaw, "Decay of a Velocity Maximum in a Turbulent Boundary Layer," Aero Quart. Vol. XVIII, Pt. 2, May 1967, pp. 121-132.
13. Dvorak, F. A., "Calculation of Turbulent Boundary Layers and Wall Jets Over Curved Surfaces," AIAA Jour. 11, April 1973, pp. 517-22.
14. Hubbartt, J. E. and D. H. Neale, "Wall Layer of Plane Turbulent Wall Jets Without Pressure Gradients", J. of Aircraft 9, March 1972, pp. 195-196.
15. Carriere, P., E. Eichelbrenner and Ph. Poisson-Quinton, "Contribution Theoretique et Experimentale a L'Etude du Controle de la Couche Limite par Soufflage," in Advances in Aeronautical Sciences, Vol. 2, Pergamon Press, 1959.
16. Chang , P. Control of Flow Separation, Pergamon Press, N.Y. 1972; p. 330-375, plus 1323.
17. Sirieix, M., J. Delery and E. Stanewsky, "High Reynolds Number Boundary Layer-Shock Wave Interaction in Transonic Flow", Lecture Notes in Physics, Springer-Verlag, 1982.
18. Melnick, R. E., R. Chow and H. R. Mead, "Theory of Viscous Transonic Flow Over Airfoils at High Reynolds Number," AIAA Paper 77-680, June 1977.
19. Lekoudis, S. G., G. R. Inger and M. Khan, "Computation of the Viscous Transonic Flo" Around Airfoils with Trailing Edge Effects and Proper Treatment of the Shock-Boundary Layer Interaction", AIAA Paper 82-0989, St. Louis, June, 1982.
20. Inger, G. R., "Application of a Shock-Turbulent Boundary Layer Interaction Theory in Transonic Flowfield Analysis", Ch. 17 of Transonic Aerodynamics, Vol. 81, Progress in Astronautics and Aeronautics, AIAA, 1982.
21. Jau, W. H., and E. Murman, "A Phenomenological Model for Displacement Thickness Effects of Transonic Shock Wave - Boundary Layer Interactions," Paper 15-1, AGARD Conference on Viscous-Inviscid Interactions," Colorado Springs, Colo., Sept. 1980.
22. Tai, T. C., "Theoretical Calculation of Viscous-Inviscid Transonic Fows," DWTNSRDC Report 80/104, Bethesda, Md., Aug. 1980.

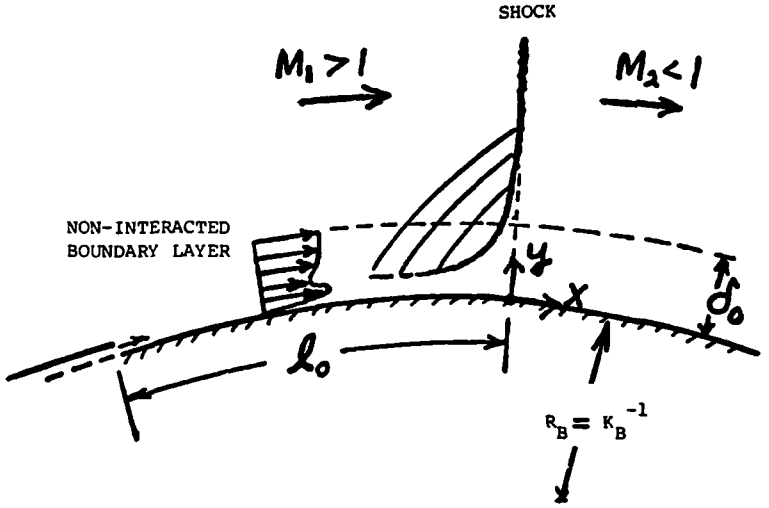


Fig. 1 Interaction Problem Configuration

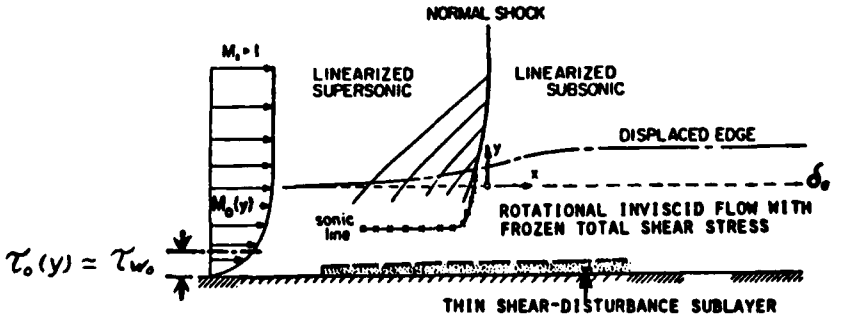


Fig. 2 Triple-Deck Structure of Interaction Field (Schematic)

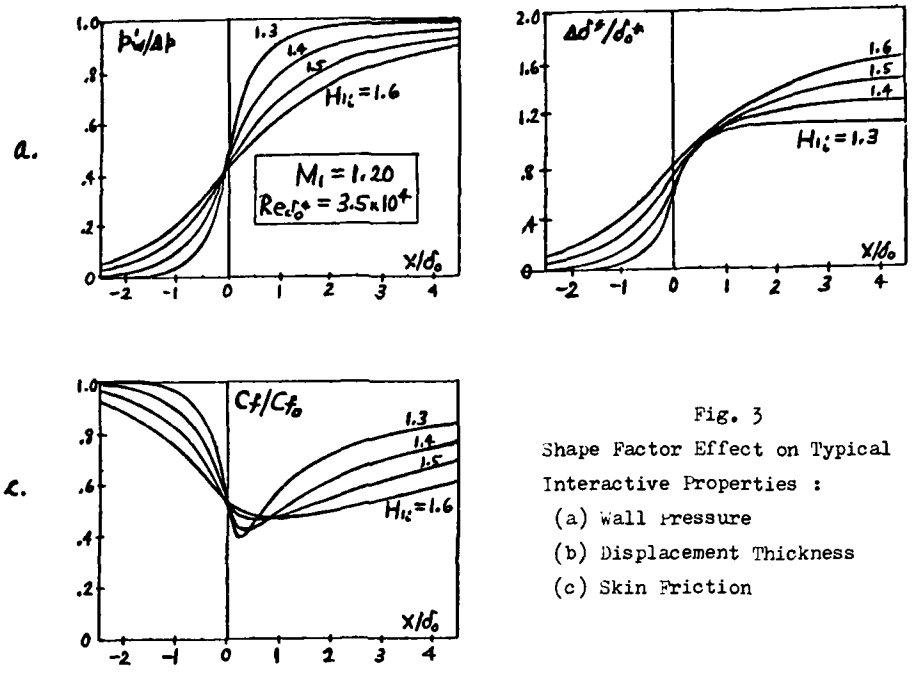
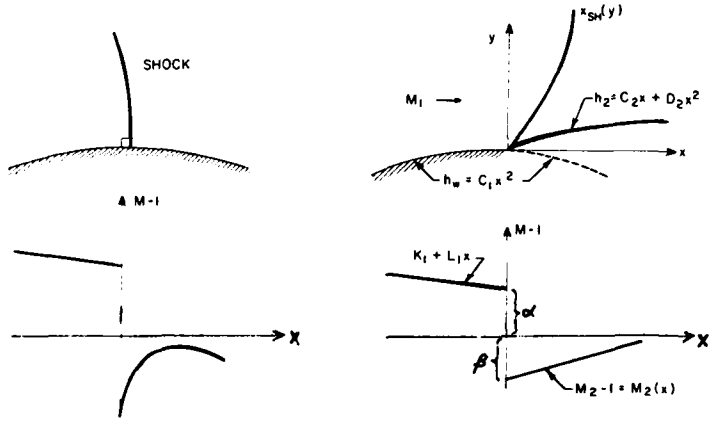


Fig. 3
Shape Factor Effect on Typical Interactive Properties :
(a) Wall Pressure
(b) Displacement Thickness
(c) Skin Friction



A. Singular: Viscous Displacement Effect Neglected.

B. Regular: Viscous Displacement Effect Included.

Fig. 4 Two Possible Inviscid Solutons on a Curved Surface

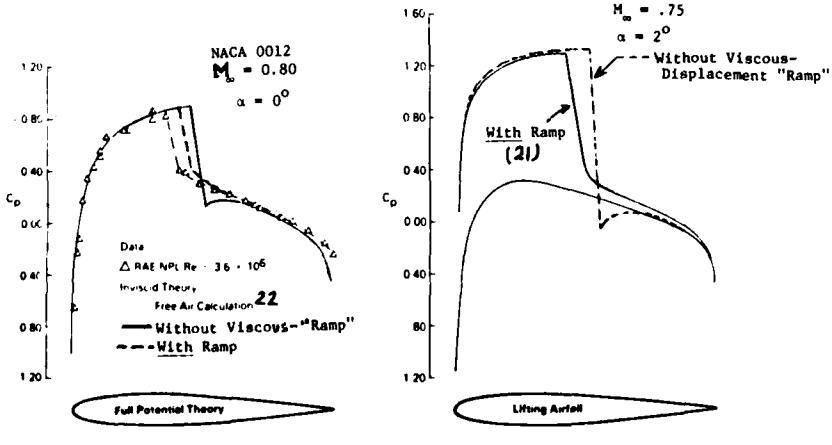


Fig. 5 Elimination of the Post-Shock Curvature Singularity by the Interactive Displacement Thickness - Supercritical Airfoil Calculations



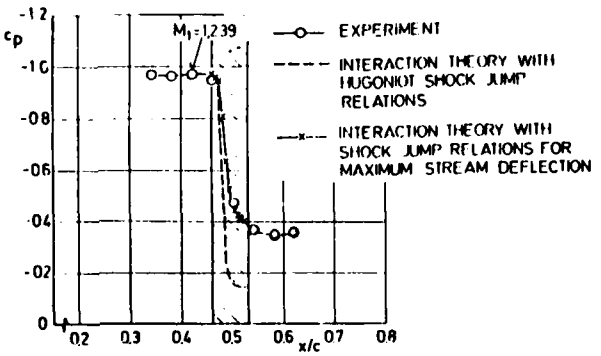


Fig. 6
Shock Obliquity due to Viscous Interaction Displacement Effect

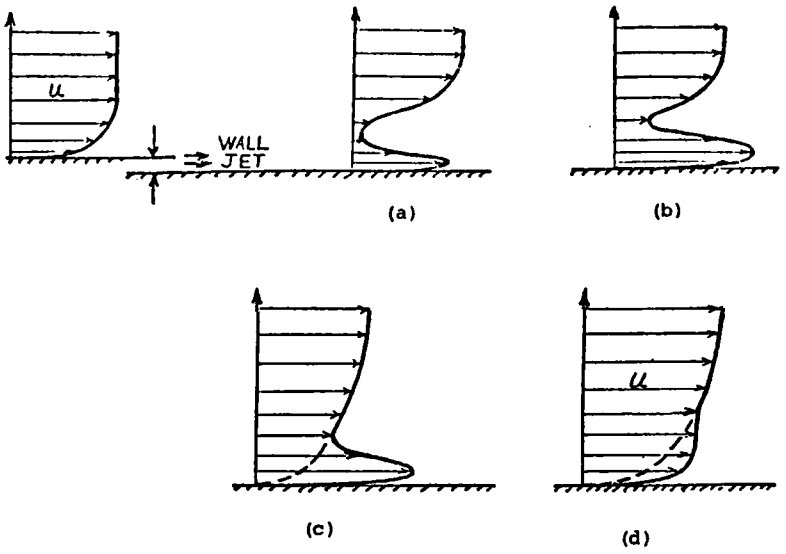


Fig. 7 Schematic of Turbulent Boundary Layer Development Downstream of a Wall Jet

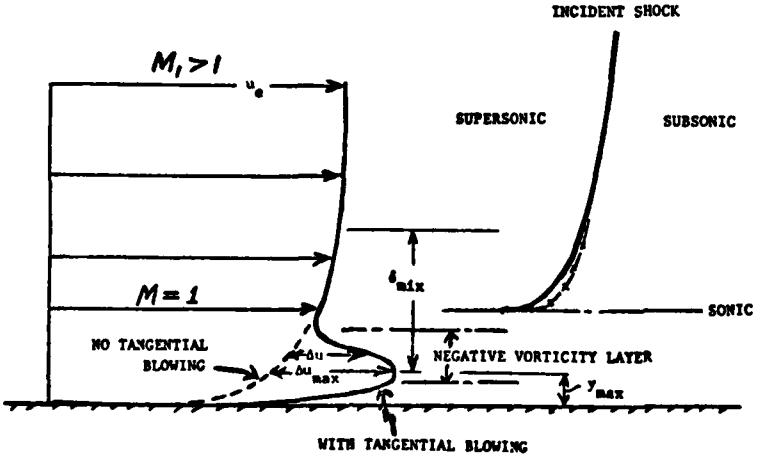


Fig. 8
Model of the Wall Jet- Effect on the Turbulent Boundary Layer Velocity Profile

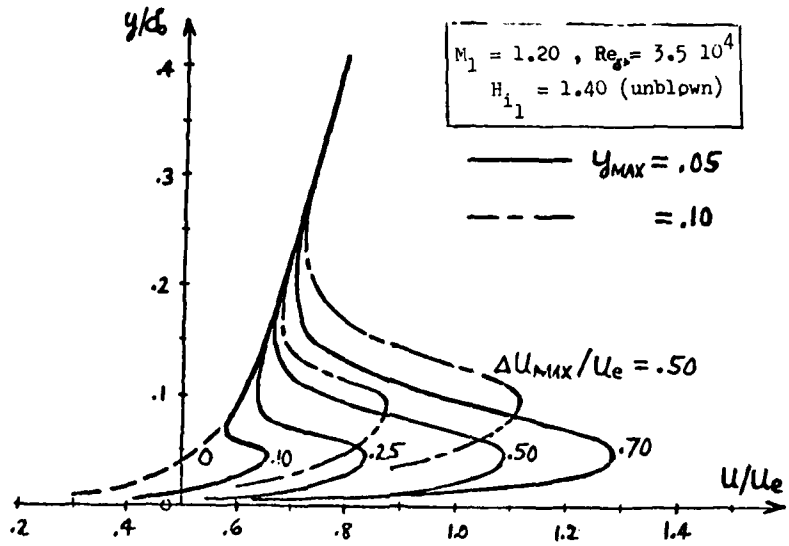


Fig. 9 Typical Turbulent Boundary Layer Profiles with Injection

(a) Displacement Thickness

(b) Shape Factor

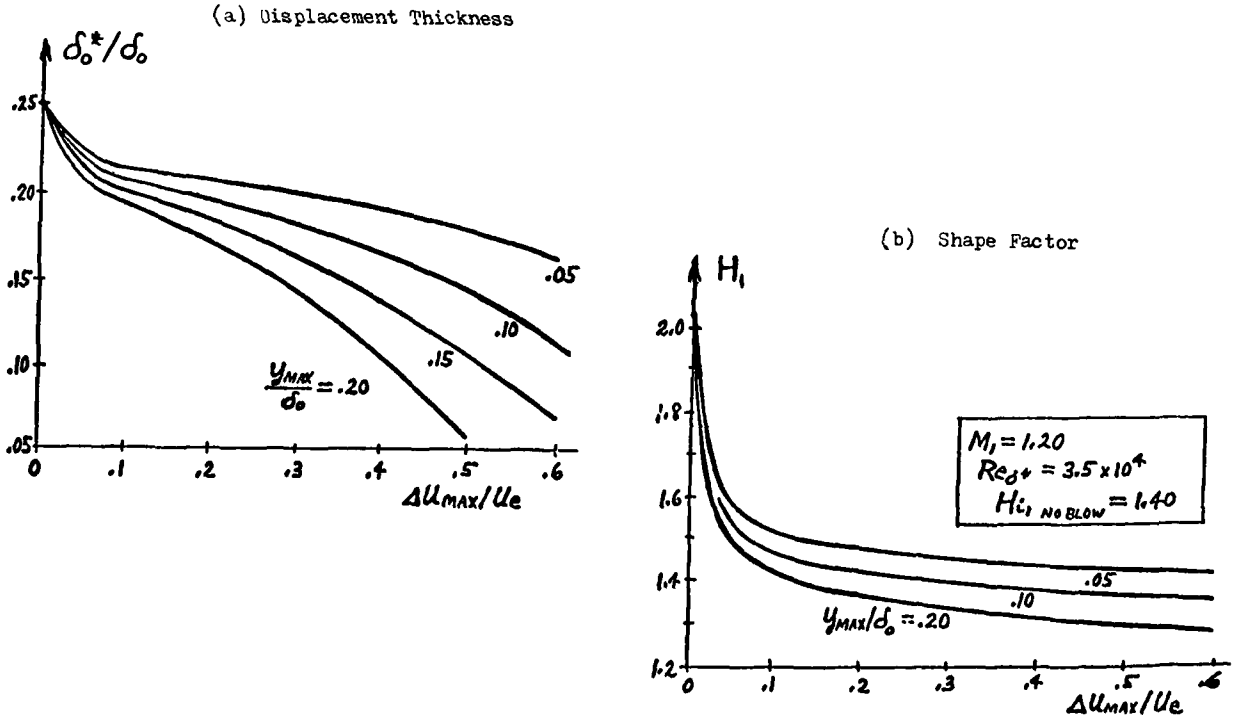


Fig. 10 Injection Effect on Integral Properties of the Boundary Layer

ROUND TABLE DISCUSSION

Dr. Orlik-Rückemann, Canada

I have been asked to chair this final session of our symposium. Those of you who have been to meetings of the Fluid Dynamics Panel before, know that it is one of the customs of our panel to appoint one or two specialists in the field to act as technical evaluators of a symposium. This normally takes the form of a report being issued several weeks after the meeting, and this is then distributed to all of the participants as well as to panel members. It is far less usual, however, to get the same technical evaluators to agree to share with the attendees their views about the symposium already at the closing session of the meeting, without having the benefit of sitting back and examining and sifting through the material and notes from the meeting just concluded. This time we have two technical evaluators, Dr. van den Berg on my far left and Dr. Oskam on my immediate left, both from NLR in Amsterdam. They have been kind enough to offer us the benefit of their comments and the immediate fresh assessment of the meeting right now. Dr. Oskam will lead off, followed by Dr. van den Berg, after which we will throw the floor open for the general discussion from the floor.

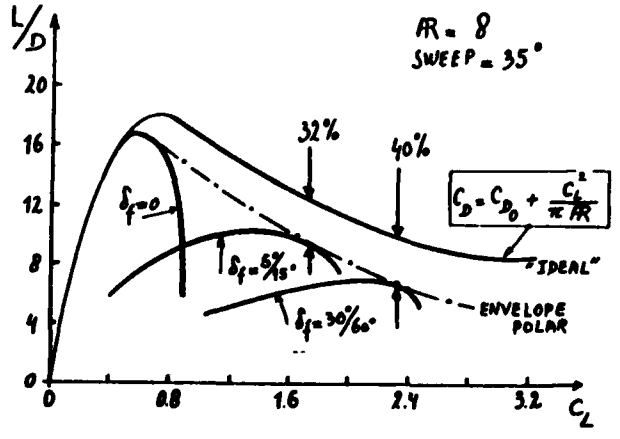
Dr. Oskam, NLR

First of all I would like to thank the chairman of the program committee, Professor Reshotko, for this opportunity to summarize the main points of the papers that have been presented during the past two and a half days. Since I am sharing this opportunity with my colleague, we have divided the task and decided that I should take care of the high-lift part.

The first day of our meeting the subject matter was aerodynamic improvement through high-lift systems. As I recall, the presentations we heard were primarily dealing with high-lift aerodynamics of transport-type aircraft during take-off and landing. The only exception at this point was the paper by Mr. Whittley who gave us a fine update on the augmenter wing. From this presentation I got the clear impression that this powered-lift STOL concept is now validated and ready for application. Getting back to the papers on transport-type aircraft, I must say that the invited speakers, Mr. Butter and Mr. Dillner, really covered quite a wide scope of issues. As you have also listened to the survey paper by Mr. Butter, you will recall the complicated flow processes he talked about. I fully agree with him that our present knowledge of all the relevant flow processes of the flow around even a 2-dimensional multi-element wing is not yet complete. However, I think that some progress is being made in this area. I just like to mention the paper by Mrs. Porcheron describing a very detailed study of a 2-D high-lift flow. Such a flow is an ideal test case for those researchers who are developing 2-D high-lift codes. I think that such an experiment is ideal for code validation. However, I am not sure that turbulence data of such a complicated situation is really sufficient for developing a good turbulence model of wakes subjected to large adverse pressure gradients. I feel that there is also a need for a more fundamental building block experiment in which the critical flow process, that is the adverse pressure gradient wake, is isolated from the complete high-lift configuration. This would enable one, in principle, to investigate and model the turbulence in the loaded wake without having the complication of all the other flow processes. I consider this to be a very important problem, because it directly relates to aerodynamic performance in 2-D high-lift. The full-potential calculation method reported by Mr. Suddhoo, dealing with 3-component airfoils, may be very useful as a independent numerical check for previously developed methods, such as the transonic panel method I talked about myself. I think it would be very instructive to see how well the various full-potential numerical solutions should converge to the genuine solution if the mesh is sufficiently refined. It shall be interesting to see whether they do.

I have observed all of the speakers in the high-lift session did recognize that the understanding and quantitative knowledge of Reynolds number effects is essential in high-lift aircraft design. However, I cannot make the same statement about free stream Mach number effects in high-lift aerodynamics. I think it is fair to say that these non-linear compressibility effects in high-lift are not that well-known. However, Mr. Fiddes, and others, have reminded us of the strong adverse effect an increasing free-stream Mach number can have on the maximum lift performance of high-lift systems. However, Mr. Dillner told us that in his experience supercritical leading edge flow should be avoided right from the beginning in any high-lift design for transport aircraft. I hope that we can have some comments on this point during the discussion.

The last thing I would like to tell you about during these summarizing remarks concerns the potential performance improvements one can expect for mechanical high-lift systems. In my opinion this is an imortant issue which has not been addressed as yet at this conference. As a matter of fact I found a figure in the paper of Mr. Butter. This figure can also be found in the paper of Mr. Dillner, but it has not been shown as yet. Let me just put it on the projector.



POTENTIAL
PERFORMANCE
IMPROVEMENT
FOR MECHANICAL
HIGH-LIFT SYSTEMS

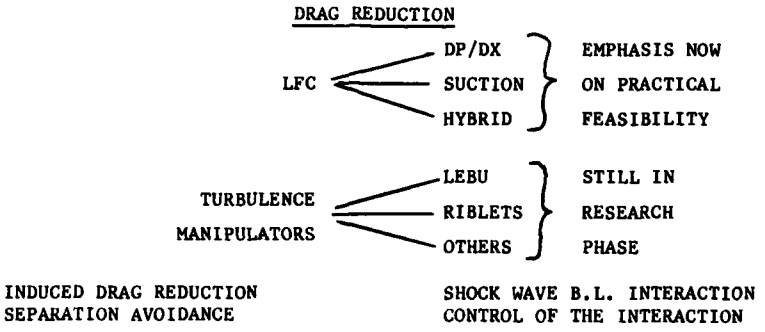
The point I really want to make should actually be formulated as a question. But let me first explain the slide. This slide shows three drag polars plotted in terms of lift-to-drag ratio versus lift coefficient. These three polars represent measured data for a fixed aspect ratio of 8 and a fixed wing sweep of 35 degrees; the first one is the cruise configuration, the second one is for take-off geometry and the third one for a landing configuration. The dash-dotted line reprsents the envelope of these three polars: the envelope polar. The "ideal" polar in this figure represents the well-known drag formula,

$$C_D = C_{D_o} + \frac{C_L^2}{\pi AR}$$

where C_{D_o} is the zero-lift drag of the cruise configuration. This "ideal" polar which applies only to the cruise configuration at low lift has been extended to high values of the lift. This "ideal" serves as a well-defined, hypothetical reference curve which can be used to express the performance level, and improvement, of mechanical high-lift systems. Mr. Dillner told us that the lift-to-drag ratio of the take-off configuration, which is moving along the envelope polar, was found to be the real sizer in terms of wing area for their energy efficient transport study. The question I have is: Has the position of this envelope polar relative to the "ideal" polar really changed during the past ten years, or are we just moving up and down the envelope polar and only optimize for wing sweep, aspect ratio and high-lift settings with fixed technology. I know from the paper by Mr. Van Egmond about his inverse slat design that you can do something in that direction, in two-dimensions; that is increase the lift-to-drag ratio at constant lift coefficient. This would represent an increase in the level of technology. However, I would like to encourage the aircraft specialists in the audience to fill us in at this point, and tell us whether the lift-to-drag performance level of mechanical high-lift systems has changed during the last ten years, or how large the potential for improvement really is.

Dr. van den Berg, NLR

The Symposium falls apart in three rather separate subjects. My colleague has covered already the high-lift part. I will now discuss first the papers on drag reduction. Actually, I do not intend to treat here the papers individually. Instead I will stick to a general discussion on what is apparently going on in the field. To guide me and you in this, I have produced this overhead sheet.



Two main routes are apparent in drag reduction research. The first one is the strive for laminar boundary layer flow. The gains to be achieved by keeping the boundary layer laminar are large. To achieve laminar flow most commonly one applies favourable pressure gradients or suction or both. As appeared from the presentations at this Symposium, the state of the art in this field is well advanced. The emphasis is now on the practical feasibility of the laminar flow concept for wings. Extensive flight tests simulating normal airline service are now being carried out. It is likely that soon the laminar flow control research work will have reached the stage that sufficient information is available to consider the application in an actual commercial airplane design. The other main route in drag reduction is manipulation of the turbulence in the boundary layer. The gains to be achieved here are much less, but may still be well worthwhile. One way is to alter the structure of the turbulence in the outer region of the boundary layer by so-called large eddy break-up devices ("LEBU's"). The turbulence properties in the wall region can be affected by changing the surface geometry, for instance by application of streamwise riblets in the surface.

To obtain an impression of the gains, which can be hoped for when manipulating turbulence, some calculations were carried out with a boundary layer calculation method at NLR. The boundary layer calculation method employs a simple mixing length turbulence model. The table here gives the effects of alterations of the empirical constants in the turbulence model. A reduction of the mixing length in the outer region of the boundary layer is what one would expect a LEBU to do. The effect of riblets on the surface can probably be represented as an increase of the viscous sublayer thickness in the turbulence model. The table shows that a mixing length reduction in the wall region would be most effective, but it is less likely that this is achieved either by LEBU's or riblets. The results emphasize the moderate drag reductions to be expected from turbulence manipulators, as the assumed changes of the mixing length and sublayer thickness seem to me already very large.

TURBULENT DRAG REDUCTION ACCORDING TO B.L. CALCS

ASSUMED CHANGE IN TURB. MODEL	FLOW CONDITION		
	ZERO PRESS. GRAD.	ADVERSE PRESS. GRAD.	FAVOURABLE PRESS. GRAD.
Mixing length in outer region reduced with factor two ("LEBU")	23%	Negligible Reduction	Little History Effects
Viscous sublayer Thickness increased with factor two ("Riblets")	24%		
Mixing length in wall region reduced with factor two	48%		

The table contains also remarks on the expected effect of a mixing length reduction in the outer region (LEBU's) in flows with a pressure gradient. The boundary layer calculations showed that the drag reduction obtained will be negligible in this case for adverse pressure gradient flows. When the pressure gradient is favourable there is another problem. Reducing the mixing length in the outer region by LEBU's relies very much on the large role of history effects in the tubulence development, so that one LEBU covers an extensive downstream region. In favourable pressure gradient flows the history effects are small, however. It is concluded that the effectiveness of LEBU's in non-zero pressure gradient flows may be disappointing, and that this should be investigated thoroughly.

When comparing turbulence drag reduction research with the laminar flow control work, it is evident that the first is still in a very early phse of development. The papers delivered at the Symposium showed that progress is made at various places, but that much still has to be done. A problem is the large variety of devices which might be effective in reducing the drag. Better insight in what the devices actually do to the turbulence could be of help in directing the research. The most important conclusion, which can be drawn at the moment, is that it has become very clear that turbulence can be manipulated to a certain extent and that this can be employed to our advantage. In a number of papers other means for drag reduction were discussed. It is not appropriate to mention them individually in this global review. Yet it may be useful to remind that the induced drag and separation regions if present, contribute considerably to the drag and consequently improvements here are soon worthwhile. This lead us to the last part of the Symposium, which concerned shock-wave boundary layer interaction work. Reductions in the detrimental effects of shock-wave boundary layer interactions may be as important as other means for drag reduction. The research performed in this field is very interesting. However, apart from the review paper yesterday, the papers on shock-wave boundary layer interaction were only delivered this morning. I do not feel able to give an opinion at such short term. This has to be postponed to the evaluation report, which Dr. Oskam and I will write later.

Dr. Orlik-Rückemann

Thank you very much. I would like to again thank both our technical evaluators; we all appreciate that it is very difficult to prepare this kind of comment immediately after the meeting, and I think they have done a really very good job. Now we will open the general session of comments from the audience. I would first like to remind you that this session is being recorded, so that you have to identify yourself when you take the mike. Secondly, this is not an ordinary round table discussion, so you are not necessarily addressing your questions to the two technical evaluators, but rather to the audience at large. So any questions, comments or suggestions for further work, or whatever else is on your mind should be expressed in this way. Finally, we should, to have some order in the comments, take the three parts of the symposium one at a time, at least initially. At this time therefore, I would like to open comments and discussions on the part dealing with the high lift systems. Are there any comments?

Mr. D. Butter (British Aerospace)

I would very briefly like to comment on the slide that Dr. Oskam put up. I think that I mentioned in my paper that the major changes that are going to come in high lift design are in fact going to be in L/D. It has been very much neglected in the past and unless anyone would object, I would say that the current technology hasn't improved that figure. This is borne out by the fact that Bert Dillner's curve is almost the same as mine which was taken from a paper 10 or 11 years ago. We have to be careful though, because

the gap between the envelope polar and the ideal is not just a simple case of changing the profile drag of various bits and pieces. It involves all the complex three-dimensional aspects of flap span, cutouts and even including the effect of trim drag. So, it is not straight forward as to how we close that gap. I think that is where the improvements are going to come. If you look at the top end of the C_L curve, you can see that there is a great deal of scope in improving L/D in that region. Returning to this question of compressibility, I would just like to add that I think that we must not get mistaken or tied up with the occurrence of shock waves on these slats. The problem is in fact compressibility and not the appearance of shock waves. We have to be able to calculate in these methods the effects of compressibility, so that we can design the optimum configuration.

Mr. Perrier, Dassault

Je fais un commentaire en francais, J'espère que le traducteur va arriver à réussir à traduire l'équivalent des termes techniques. Si on regarde la courbe de M. Oskam, on est peut être un petit peu exagérément surpris de l'écart de 30 à 40 % qu'il y a entre la valeur théorique et la valeur réelle mesurée en vol. Je crois que c'est une très mauvaise présentation parce que, quand on fait le bilan, on s'apercoit qu'il y a trois termes differents dans cet écart. Un premier terme qui est l'écart de trainée induite. Le terme presenté sous la forme d'un écart sur une aile elliptique ignore complètement qu'il y a un fuselage et que les volets ne vont pas jusqu'en bout d'aile et que souvent on les interrompt pour les moteurs ou pour mettre un aileron grande vitesse. Quand on fait le bilan de ce que coûtent en trainée induite ces coupures, on trouve en general une valeur de 10 %. C'est à dire, le tiers de l'écart qui est présenté. Ensuite, il y a une deuxième cause très importante, qui est le fait qu'on a representé la polaire en écart par rapport à la polaire lisse, c'est à dire que le CD_o, donné sur la surface de départ. Si on tient compte du fait qu'il y a des survitesses dans les fentes et qu'il y a une augmentation de surface, on trouve en général une augmentation de CD_o qui est très importante quant on fait usage de les hypersustentateurs. Nous avons fait chez Dassault sur au moins deux avions, le Falcon 50 et le Falcon 900, un bilan très complet de la finesse estimée par un calcul tri-dimensionnel. On trouve dans ce cas là que les effets qui devraient être pris en compte pour améliorer les performances ne portent plus qu'à peu près sur 5 %. En conclusion, on ne peut guére espérer mieux qu'une alelioration de 5% en finesse pour les dessins actuels, c'est à dire en tenant compte de la présence du fuselage, d'ailerons et d'interruptions obligatoires sur les volets.

Dr. B. Oskam

I would like to thank the speaker for his remarks on this curve. I don't think that I wanted to imply that you really could recover the 32%. I think that what I actually wanted to say is how hard a job it would be to recover a little bit of it, because I full well know that in a high lift situation you really don't have an elliptic load, you really don't get up to a cruise configuration which is very clean because you have highly loaded wakes or you have a lot of viscous processes, which you cannot do without. So I think that I agree with you that you can only recover a part of it. The question I posed is how do you go about it, how hard is it? Do you really need CFD or can boundary layer control help you? Is it worthwhile to employ boundary layer control in a high lift situation such that we can push the boundary a little bit.

Dr. Orlik-Rückemann

Thank you very much. I would like now to suggest that we turn our attention to Part II of this symposium, namely Drag Reduction. Are there any comments on that part of the symposium?

Mr. J. Slooff, NLR

I would like to say something on the possible interaction between high lift and laminar flow control. .If one looks at the shapes that apparently go with laminar flow control, or natural laminar flow for that matter, they look quite distinctive from conventional wing and airfoil sections. One might wonder what effect that these shapes have on the high lift, low speed performance. Nobody addressed that subject at this symposium. I wonder if somebody could comment.

Mr. R. Wagner (NASA)

The airfoil that I showed yesterday has a very pronounced undercut in the leading edge. That is done to simplify the achievement of laminar flow. However, the velocity level on the undercut is also low enough that it is believed that the local Reynolds numbers would be low enough that you could install a leading edge Krueger without tripping the flow. That airfoil is intended to have such a high lift device. In our studies with the industry, they have looked at more or less conventional supercritical airfoils. Their studies indicate that these airfoils are in fact compatible with laminar flow control. The Lockheed approach is to use a very large wing that would not require a leading edge device; Douglas has introduced a leading edge Krueger, but plans to laminarize only the upper surface. Each of these approaches work because the benefits of laminar flow are so large that you can compromise appreciably on the performance of the airplane and still get a large payoff.

Dr. Orlik-Rückemann

Thank you very much. Are there any further comments on that part or drag reduction itself? Dr. Roberts.

Dr. L. Roberts (AGARD)

I would like to make the observation that once we have introduced a blowing system which would be necessary for laminar control, then it opens up the possibility of using the same blowing system for something akin to propulsive lift, so that we can simplify possibly the mechanical high lift devices and replace them by some pneumatic devices that provide trailing edge blowing. I wonder whether Bert Dillner or the DeHavilland representative might wish to comment, if they are still here, on that possibility.

Mr. C. Bore (British Aerospace)

Len Roberts posed some questions to the Canadian, Don Whittley, but I know he left yesterday. Since I have been rather in sympathy for years with some of the notions that he was putting forward, I will comment on some of the implications of the augmentor wing concepts. There are two main points that have not received much discussion this week. They both arise from the fact that the main boundary layer enters between the twin augmentor flaps, leaving a very thin boundary layer on the outside towards the trailing edge. There is an element of wake propulsion implicit in the flow that is re-energized in the augmentor duct. *With wake propulsion one can get propulsive efficiency improved. Some studies we did 25 years ago* suggested that something like 10% improvement in fuel consumption could result from this increase in overall propulsive efficiency (which theoretically - believe it or not - could exceed 100%). In those days fuel was cheap, and the means for achieving wake propulsion seemed problematic, but with fuel now far more expensive, and the RB.419 engine better worked out, the prospect is far more enticing. It is likely that this form of wake propulsion could be applied to the fuselage as well as to the wing. Thus wake propulsion is a substantial means towards improving overall fuel economy that has not received much attention at this symposium.

The other point that arises from thin boundary layer at the wing trailing edge concerns lift dependent profile drag, which is sensitive to the boundary layer thickness at the trailing edge. We have discussed reducing profile drag, and considered reducing lift dependent drag by increasing aspect ratio. My point here amounts to noting that the lift dependent profile drag can be reduced greatly by producing thinner boundary layer at the trailing edge.

Dr. J. McCroskey (US Army)

Dr. van den Berg, if I understood your presentation, you point out the possibilities of being perhaps rather limited in what the turbulence manipulators can do for both adverse and favorable pressure gradients in the outer part of the flow, and you left blank those regions for the riblets and other devices. Admittedly, you might not wish to put numbers there, but what about the conclusions for what goes in those blanks. Is that case hopeless also?

Dr. B. van den Berg (NLR)

No, it is not. The gains in zero and non-zero pressure gradient are more similar in that case. No numbers have been inserted in the table for the non-zero pressure gradient flows, because the translation of the boundary layer calculation results to a corresponding drag value is not as evident as it is in zero-pressure gradient. It is perhaps good to add that the results in the table reflect the general experience, which is obtained from attempts to adapt the empirical constants in a turbulence model to measured boundary layer momentum thickness increments. You then find that model changes in the outer region do not help you very much in adverse pressure gradient flows (because of counteracting effects of the changed skin friction and boundary layer shape factor).

Dr. Orlik-Rückemann

Gentlemen, we will have to get out of this hall in 10 minutes, so let's take a couple more questions on drag reduction and then, if we can, one or two on shock wave boundary layer interactions. There is a question there from the Program Committee Chairman.

Prof. E. Reshotko (Case Western Reserve)

I wonder if I can have Dr. van den Berg's first summary slide to talk from. If Dennis Bushnell were here, he would have stood up long before this to make a comment that would be related to the one that I will make. I will give my own version of it. I can't give Dennis'. You see in this slide the number of means of drag reduction that have been discussed and that are potentially available, and you might wonder what an airplane incorporating these methods of drag reduction would look like. Another question is: how much drag reduction can one look forward to?

Well, let us assume for the moment that induced drag comprises about 40 percent of the drag of a present configuration and that we can work on the remaining 60 percent. It would seem that LFC of a wing would reduce the aircraft drag by perhaps 25 percent or so and that we have attainable perhaps another 5 to 10 percent in drag reduction from the turbulence manipulators. That would be a total reduction in aircraft drag approaching 35 percent. If 30 to 35 percent of the 60 percent can be eliminated, this brings up the question of what the airplane should look like at that point. Normally, we try to arrange some balance between induced drag and friction drag for either best endurance or best range or some other performance parameter. It means that if the parasite drag, if the friction drag is reduced by as much as indicated above, we should also look at means for reducing the induced drag. This might mean going to larger aspect ratios. It might also mean that, in order to implement drag reduction, we should seek aircraft that have a lower sweep angle and have perhaps a slightly reduced flight Mach number in the 0.7 to 0.75 range rather than the 0.8 to 0.85 range that we associate with present day aircraft. Block times would not be affected all that much with such a reduction in flight speed, but it would be a much happier airplane under those circumstances. I think that someone brought up the idea of forward sweep as a possibility. This is one of the possible answers to leading edge contamination, although it is really not necessary if the sweep angle is reduced for conventional sweep. It would seem that with the opportunities for drag reduction that are indicated, we should reconsider some of the configurational aspects in order to optimize the aircraft.

Dr. A.G. Panaras, Greece

I have a comment on the controversial issue of the effect of the Reynolds number on the length of the interaction of a turbulent boundary layer with a normal shock wave, that J. Delery has mentioned. Some results from a recent theoretical work of the present speaker clarify this issue (Z. Flugwiss Weltraumforsch 7 (1983), Heft 6). The figure shows both the wall pressure distribution and the displacement thickness for a boundary layer developing along a flat plate, for a constant Mach number M_e and two quite different values of Reynolds number. The value of the kinematic shape factor H_{1i} is different for each case and corresponds to the flat plate velocity profile for each Reynolds number. It may be observed in this figure, that the higher the Reynolds number, the nearer the pressure distribution is to the solid wall reflection (a shorter interaction length and a higher pressure level downstream of the shock). However, the corresponding distributions of the displacement thickness do not show a significant difference. These distributions almost coincide and give the impression that the interaction length is independent of the Reynolds number. Thus, experimental results based on the measurement of the development of the boundary layer will rather show independence of the transonic interaction length from the value of the Reynolds number, in contradiction to results based on the wall pressure distribution.

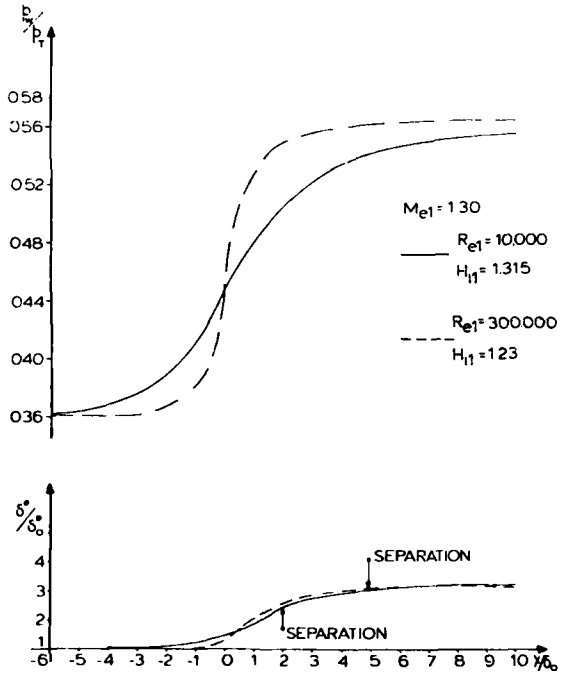


FIG 5 REYNOLDS NUMBER EFFECT

Dr. Orlik-Rückemann

At this time I am afraid that we have run out of time. I regret that there is no more time to discuss shock wave boundary layer interactions. I would like to thank once again our technical evaluators and the audience for the discussions, and I would like to turn the meeting over to the Program Committee Chairman, Prof. Reshotko.

Prof. Reshotko

Thank you Mr. Chairman. It is my pleasure, particularly at closing to make a few remarks, because I know that after these remarks I am through. The first interesting thing for me with this conference is that when it was conceived, it was conceived as a symposium where we could bring together people who are active in the applications of boundary layer control together with people who are investigating the fundamentals of boundary layer control. I think that we were a bit concerned in the beginning whether these two groups would be speaking the same language. To my very pleasant surprise, I find that everyone here was in fact speaking the same language, that the people in the aircraft industry who are concerned with techniques of boundary layer control are using the same sophistication in their work in terms of computation, experimentation, instrumentation, and in what they are looking for, as are the people who are doing the basic research. I believe that this enables us to look to a very promising future for the applications of boundary layer control to practical aerodynamics. I wish at this time to thank all the participants, the authors, those who are going to prepare the technical evaluation report, and not least of all, our hosts. We had a very shaky first day, but our hosts have responded admirably to the challenge of making everything work, and yesterday and today everything has worked. It has made for a most pleasant finish to our symposium. I do want to thank our hosts of the Belgian Air Force for their efforts and for their accomplishments. There are also people who have been in the anonymous region up there, behind the glass - the translators - who have also done a most admirable job in keeping all of us informed in our own language of what was going on within this room. I thank them as well. The technical program of this symposium is now over, and I turn the meeting over to the Chairman of the Fluid Dynamics Panel, Dr. Roberts.

Dr. L. Roberts

Thank you, Eli. Before closing the meeting, I would like to remind you of some of the future activities of the Fluid Dynamics Panel that you can anticipate over the next year. This is a certain amount of free advertising for us. Next week or rather the week after, we have the second part of our special course on V-STOL aerodynamics, the first time it was given at VKI a few weeks ago, and it will be repeated at the Ames Research Center in the US for those of you who are interested in that field. In October of this year we will have a symposium on Aerodynamics and Acoustics of Propellors, and this will take place in Toronto, Canada, October 1 to October 4. Next April we will have a special course at VKI on Cryogenic Technology in Windtunnel Testing, and in May we have our spring symposium, a year from now, on Unsteady Aerodynamics/Fundamentals and Applications to Aircraft Dynamics. That will be at Göttingen, Germany. Also in May of next year we will have a special course at VKI on Aircraft Drag Prediction and Reduction. That will be held in late May at VKI and also in June at NASA Langley. One year from October, to complete our 1985 program, a symposium on Store Airframe Aerodynamics will be held in Athens, Greece. I would ask you to inform your colleagues and friends with respect to the future activities of FDP and help us to spread his information. Let me add my thanks to all of those who have supported this, especially Prof. Reshotko and his program committee for formulating such a good program, and all of those who made it work, including our support staff. I would like to thank you, the audience, also for participating, and I think that the difference between the first day and the second day in terms of the ability to have all of our equipment working also reflected in the amount of time that was available for the discussions. I was very happy to have seen such a lot of participation from the audience on those last two days. Thank you for your forbearance during the times when we were getting our equipment working and thank you for your participation. With that I close this meeting and wish you a safe journey home.

REPORT DOCUMENTATION PAGE

1. Recipient's Reference	2. Originator's Reference	3. Further Reference	4. Security Classification of Document
	AGARD-CP-365	ISBN 92-835-0358-9	UNCLASSIFIED

5. Originator Advisory Group for Aerospace Research and Development
North Atlantic Treaty Organization
7 rue Ancelle, 92200 Neuilly sur Seine, France

6. Title IMPROVEMENT OF AERODYNAMIC PERFORMANCE THOUGH BOUNDARY LAYER CONTROL AND HIGH LIFT SYSTEMS

7. Presented at the Fluid Dynamics Panel Symposium in Brussels, Belgium, 21-23 May 1984.

8. Author(s)/Editor(s)	9. Date
Various	August 1984
10. Author's/Editor's Address	**11. Pages**
Various	436

12. Distribution Statement This document is distributed in accordance with AGARD policies and regulations, which are outlined on the Outside Back Covers of all AGARD publications.

13. Keywords/Descriptors

Boundary layer control
High lift devices
Aerodynamic characteristics
Control surfaces
Intake systems
Exhaust systems
Boundary layer flow

14. Abstract

There has been an increased experimental understanding of boundary layer structure and behaviour particularly in the turbulent regime as well as significant improvements in our knowledge of the factors affecting the boundary-layer transition in arbitrary flow fields.

It was intended that this Symposium bring together the practitioners of the various applications of boundary layer control with those interested in the underlying fluid mechanics for the purpose of mutual learning and understanding.

Contributions covered theoretical and experimental developments in the use of both traditional and non-traditional means of boundary layer control for external flow applications such as lift-augmentation, drag reduction and improved effectiveness of controls, and for internal flow applications such as air intakes and exit configurations. Techniques included shaping (geometry) suction and blowing; transverse blowing; vortex generators; heating and cooling; and turbulent boundary layer manipulation.

The special emphasis on high-lift systems included consideration of the techniques of boundary layer control on characteristics of wings and wing-body arrangements that involve flaps, slats and jets (blown flaps), and vortex flaps.

AGARD Conference Proceedings No.365
Advisory Group for Aerospace Research and Development, NATO
IMPROVEMENT OF AERODYNAMIC PERFORMANCE THROUGH BOUNDARY LAYER CONTROL AND HIGH LIFT SYSTEMS
Published August 1984
436 pages

There has been an increased experimental understanding of boundary layer structure and behaviour particularly in the turbulent regime as well as significant improvements in our knowledge of the factors affecting the boundary-layer transition in arbitrary flow fields.

It was intended that this Symposium bring together the

P.T.O

AGARD-CP-365

Boundary layer control
High lift devices
Aerodynamic characteristics
Control surfaces
Intake systems
Exhaust systems
Boundary layer flow

AGARD Conference Proceedings No.365
Advisory Group for Aerospace Research and Development, NATO
IMPROVEMENT OF AERODYNAMIC PERFORMANCE THROUGH BOUNDARY LAYER CONTROL AND HIGH LIFT SYSTEMS
Published August 1984
436 pages

There has been an increased experimental understanding of boundary layer structure and behaviour particularly in the turbulent regime as well as significant improvements in our knowledge of the factors affecting the boundary-layer transition in arbitrary flow fields.

It was intended that this Symposium bring together the

P.T.O

AGARD-CP-365

Boundary layer control
High lift devices
Aerodynamic characteristics
Control surfaces
Intake systems
Exhaust systems
Boundary layer flow

AGARD Conference Proceedings No.365
Advisory Group for Aerospace Research and Development, NATO
IMPROVEMENT OF AERODYNAMIC PERFORMANCE THROUGH BOUNDARY LAYER CONTROL AND HIGH LIFT SYSTEMS
Published August 1984
436 pages

There has been an increased experimental understanding of boundary layer structure and behaviour particularly in the turbulent regime as well as significant improvements in our knowledge of the factors affecting the boundary-layer transition in arbitrary flow fields.

It was intended that this Symposium bring together the

P.T.O

AGARD-CP-365

Boundary layer control
High lift devices
Aerodynamic characteristics
Control surfaces
Intake systems
Exhaust systems
Boundary layer flow

AGARD Conference Proceedings No.365
Advisory Group for Aerospace Research and Development, NATO
IMPROVEMENT OF AERODYNAMIC PERFORMANCE THROUGH BOUNDARY LAYER CONTROL AND HIGH LIFT SYSTEMS
Published August 1984
436 pages

There has been an increased experimental understanding of boundary layer structure and behaviour particularly in the turbulent regime as well as significant improvements in our knowledge of the factors affecting the boundary-layer transition in arbitrary flow fields.

It was intended that this Symposium bring together the

P.T.O

AGARD-CP-365

Boundary layer control
High lift devices
Aerodynamic characteristics
Control surfaces
Intake systems
Exhaust systems
Boundary layer flow

practitioners of the various applications of boundary layer control with those interested in the underlying fluid mechanics for the purpose of mutual learning and understanding.

Contributions covered theoretical and experimental developments in the use of both traditional and non-traditional means of boundary layer control for external flow applications such as lift-augmentation, drag reduction and improved effectiveness of controls, and for internal flow applications such as air intakes and exit configurations. Techniques included shaping (geometry) suction and blowing; transverse blowing; vortex generators; heating and cooling; and turbulent boundary layer manipulators.

The special emphasis on high-lift systems included consideration of the techniques of boundary layer control on characteristics of wings and wing-body arrangements that involve flaps, slats and jets (blowing flaps), and vortex flaps.

ISBN 92-835-0358-9

practitioners of the various applications of boundary layer control with those interested in the underlying fluid mechanics for the purpose of mutual learning and understanding.

Contributions covered theoretical and experimental developments in the use of both traditional and non-traditional means of boundary layer control for external flow applications such as lift-augmentation, drag reduction and improved effectiveness of controls, and for internal flow applications such as air intakes and exit configurations. Techniques included shaping (geometry) suction and blowing; transverse blowing; vortex generators; heating and cooling; and turbulent boundary layer manipulators.

The special emphasis on high-lift systems included consideration of the techniques of boundary layer control on characteristics of wings and wing-body arrangements that involve flaps, slats and jets (blowing flaps), and vortex flaps.

ISBN 92-835-0358-9

practitioners of the various applications of boundary layer control with those interested in the underlying fluid mechanics for the purpose of mutual learning and understanding.

Contributions covered theoretical and experimental developments in the use of both traditional and non-traditional means of boundary layer control for external flow applications such as lift-augmentation, drag reduction and improved effectiveness of controls, and for internal flow applications such as air intakes and exit configurations. Techniques included shaping (geometry) suction and blowing; transverse blowing; vortex generators; heating and cooling; and turbulent boundary layer manipulators.

The special emphasis on high-lift systems included consideration of the techniques of boundary layer control on characteristics of wings and wing-body arrangements that involve flaps, slats and jets (blowing flaps), and vortex flaps.

ISBN 92-835-0358-9

practitioners of the various applications of boundary layer control with those interested in the underlying fluid mechanics for the purpose of mutual learning and understanding.

Contributions covered theoretical and experimental developments in the use of both traditional and non-traditional means of boundary layer control for external flow applications such as lift-augmentation, drag reduction and improved effectiveness of controls, and for internal flow applications such as air intakes and exit configurations. Techniques included shaping (geometry) suction and blowing; transverse blowing; vortex generators; heating and cooling; and turbulent boundary layer manipulators.

The special emphasis on high-lift systems included consideration of the techniques of boundary layer control on characteristics of wings and wing-body arrangements that involve flaps, slats and jets (blowing flaps), and vortex flaps.

ISBN 92-835-0358-9

END

FILMED

12-84

DTIC